Standard Model and Related Topics

9. Quantum Chromodynamics

Revised August 2019 by J. Huston (Michigan State U.), K. Rabbertz (KIT) and G. Zanderighi (MPI Munich).

9.1 Basics

Quantum Chromodynamics (QCD), the gauge field theory that describes the strong interactions of colored quarks and gluons, is the SU(3) component of the SU(3)×SU(2)×U(1) Standard Model of Particle Physics. The Lagrangian of QCD is given by

$$\mathcal{L} = \sum_q \bar{\psi}_{q,a}(i\gamma^\mu \partial_\mu \delta_{ab} - g_s \gamma^\mu t^C_{ab} \mathcal{A}^C_\mu - m_q \delta_{ab})\psi_{q,b} - \frac{1}{4} F^A_{\mu\nu} F^{A\,\mu\nu}\,, \tag{9.1}$$

where repeated indices are summed over. The γ^μ are the Dirac γ-matrices. The $\psi_{q,a}$ are quark-field spinors for a quark of flavor q and mass m_q, with a color-index a that runs from $a = 1$ to $N_c = 3$, *i.e.* quarks come in three "colors." Quarks are said to be in the fundamental representation of the SU(3) color group.

The $\mathcal{A}^C_\mu$ correspond to the gluon fields, with C running from 1 to $N_c^2 - 1 = 8$, *i.e.* there are eight kinds of gluon. Gluons transform under the adjoint representation of the SU(3) color group. The t^C_{ab} correspond to eight 3×3 matrices and are the generators of the SU(3) group (*cf.* the section on "SU(3) isoscalar factors and representation matrices" in this *Review*, with $t^C_{ab} \equiv \lambda^C_{ab}/2$). They encode the fact that a gluon's interaction with a quark rotates the quark's color in SU(3) space. The quantity g_s (or $\alpha_s = \frac{g_s^2}{4\pi}$) is the QCD coupling constant. Besides quark masses, who have electroweak origin, it is the only fundamental parameter of QCD. Finally, the field tensor $F^A_{\mu\nu}$ is given by

$$\begin{aligned} F^A_{\mu\nu} &= \partial_\mu \mathcal{A}^A_\nu - \partial_\nu \mathcal{A}^A_\mu - g_s\, f_{ABC} \mathcal{A}^B_\mu \mathcal{A}^C_\nu\,, \\ [t^A, t^B] &= i f_{ABC} t^C\,, \end{aligned} \tag{9.2}$$

where the f_{ABC} are the structure constants of the SU(3) group.

Neither quarks nor gluons are observed as free particles. Hadrons are color-singlet (*i.e.* color-neutral) combinations of quarks, anti-quarks, and gluons.

Ab-initio predictive methods for QCD include lattice gauge theory and perturbative expansions in the coupling. The Feynman rules of QCD involve a quark-antiquark-gluon ($q\bar{q}g$) vertex, a 3-gluon vertex (both proportional to g_s), and a 4-gluon vertex (proportional to g_s^2). A full set of Feynman rules is to be found for example in Refs. [1, 2].

Useful color-algebra relations include: $t^A_{ab} t^A_{bc} = C_F \delta_{ac}$, where $C_F \equiv (N_c^2 - 1)/(2N_c) = 4/3$ is the color-factor ("Casimir") associated with gluon emission from a quark; $f_{ACD} f_{BCD} = C_A \delta_{AB}$, where $C_A \equiv N_c = 3$ is the color-factor associated with gluon emission from a gluon; $t^A_{ab} t^B_{ab} = T_R \delta_{AB}$, where $T_R = 1/2$ is the color-factor for a gluon to split to a $q\bar{q}$ pair.

There is freedom for an additional CP-violating term to be present in the QCD Lagrangian, $\theta \frac{\alpha_s}{8\pi} F^A_{\mu\nu} \tilde{F}^{A\,\mu\nu}$, where $\tilde{F}^{A\,\mu\nu}$ is the dual of the gluon field tensor, $\frac{1}{2}\epsilon_{\mu\nu\sigma\rho} F^{A\,\sigma\rho}$, where $\epsilon_{\mu\nu\sigma\rho}$ is the fully antisymmetric Levi-Civita symbol. Experimental limits on ultracold neutrons [3, 4] and atomic mercury [5] constrain the QCD vacuum angle to satisfy $|\theta| \lesssim 10^{-10}$. Further discussion is to be found in Ref. [6] and in the Axions section in the Listings of this *Review*.

This section will concentrate mainly on perturbative aspects of QCD as they relate to collider physics. Related textbooks and lecture notes include Refs. [1, 2, 7–9]. Aspects specific to Monte Carlo event generators are reviewed in the dedicated section 41. Lattice QCD is also reviewed in a section of its own, Sec. 17, with further discussion of perturbative and non-perturbative aspects to be found in the sections on "Quark Masses", "The CKM quark-mixing matrix", "Structure Functions", "Fragmentation Functions", "Passage of Particles Through Matter" and "Heavy-Quark and Soft-Collinear Effective Theory" in this *Review*.

9.1.1 *Running coupling*

In the framework of perturbative QCD (pQCD), predictions for observables are expressed in terms of the renormalized coupling $\alpha_s(\mu_R^2)$, a function of an (unphysical) renormalization scale μ_R. When one takes μ_R close to the scale of the momentum transfer Q in a given process, then $\alpha_s(\mu_R^2 \simeq Q^2)$ is indicative of the effective strength of the strong interaction in that process.

The coupling satisfies the following renormalization group equation (RGE):

$$\mu_R^2 \frac{d\alpha_s}{d\mu_R^2} = \beta(\alpha_s) = -(b_0 \alpha_s^2 + b_1 \alpha_s^3 + b_2 \alpha_s^4 + \cdots)\,, \tag{9.3}$$

where $b_0 = (11C_A - 4n_f T_R)/(12\pi) = (33 - 2n_f)/(12\pi)$ is referred to as the 1-loop β-function coefficient, the 2-loop coefficient is $b_1 = (17C_A^2 - n_f T_R(10C_A + 6C_F))/(24\pi^2) = (153 - 19n_f)/(24\pi^2)$, and the 3-loop coefficient is $b_2 = (2857 - \frac{5033}{9} n_f + \frac{325}{27} n_f^2)/(128\pi^3)$ for the SU(3) values of C_A and C_F. Here n_f is the number of quark flavours. The 4-loop coefficient, b_3, is to be found in Refs. [10, 11], while the 5-loop coefficient, b_4, is in Refs. [12–16]. The coefficients b_2 and b_3 (and beyond) are renormalization-scheme-dependent and given here in the modified minimal subtraction ($\overline{\rm MS}$) scheme [17], by far the most widely used scheme in QCD and the one adopted in the following.

The minus sign in Eq. (9.3) is the origin of Asymptotic Freedom [18, 19], *i.e.* the fact that the strong coupling becomes weak for processes involving large momentum transfers ("hard processes"). For momentum transfers in the 0.1–1 TeV range, $\alpha_s \sim 0.1$, while the theory is strongly interacting for scales around and below 1 GeV.

The β-function coefficients, the b_i, are given for the coupling of an *effective theory* in which n_f of the quark flavors are considered light ($m_q \ll \mu_R$), and in which the remaining heavier quark flavors decouple from the theory. One may relate the coupling for the theory with $n_f + 1$ light flavors to that with n_f flavors through an equation of the form

$$\begin{aligned} \alpha_s^{(n_f+1)}(\mu_R^2) =& \alpha_s^{(n_f)}(\mu_R^2) \times \\ & \times \left(1 + \sum_{n=1}^{\infty} \sum_{\ell=0}^{n} c_{n\ell}\, [\alpha_s^{(n_f)}(\mu_R^2)]^n \ln^\ell \frac{\mu_R^2}{m_h^2}\right), \end{aligned} \tag{9.4}$$

where m_h is the mass of the $(n_f+1)^{\rm th}$ flavor, and the first few $c_{n\ell}$ coefficients are $c_{11} = \frac{1}{6\pi}$, $c_{10} = 0$, $c_{22} = c_{11}^2$, $c_{21} = \frac{11}{24\pi^2}$, and $c_{20} = -\frac{11}{72\pi^2}$ when m_h is the $\overline{\rm MS}$ mass at scale m_h, while $c_{20} = \frac{7}{24\pi^2}$ when m_h is the pole mass (mass definitions are discussed below in Sec. (9.1.2) and in the review on "Quark Masses"). Terms up to $c_{4\ell}$ are to be found in Refs. [20, 21]. Numerically, when one chooses $\mu_R = m_h$, the matching is a modest effect, owing to the zero value for the c_{10} coefficient. Relations between n_f and (n_f+2) flavors where the two heavy flavors are close in mass are given to three loops in Ref. [22].

Working in an energy range where the number of flavors is taken constant, a simple exact analytic solution exists for Eq. (9.3) only if one neglects all but the b_0 term, giving $\alpha_s(\mu_R^2) = (b_0 \ln(\mu_R^2/\Lambda^2))^{-1}$. Here Λ is a constant of integration, which corresponds to the scale where the perturbatively-defined coupling would diverge. Its value is indicative of the energy range where non-perturbative dynamics dominates. A convenient approximate analytic solution to the RGE that includes terms up to b_4 is given by solving iteratively Eq. (9.3)

$$\begin{aligned} \alpha_s(\mu_R^2) \simeq \frac{1}{b_0 t}\Bigg(1 - \frac{b_1}{b_0^2}\frac{\ell}{t} + \frac{b_1^2(\ell^2 - \ell - 1) + b_0 b_2}{b_0^4 t^2} + \\ + \frac{b_1^3\left(-2\ell^3 + 5\ell^2 + 4\ell - 1\right) - 6 b_0 b_2 b_1 \ell + b_0^2 b_3}{2 b_0^6 t^3} + \\ + \frac{18 b_0 b_2 b_1^2\left(2\ell^2 - \ell - 1\right) + b_1^4\left(6\ell^4 - 26\ell^3 - 9\ell^2 + 24\ell + 7\right)}{6 b_0^8 t^4} \\ + \frac{-b_0^2 b_3 b_1(12\ell + 1) + 2 b_0^2\left(5 b_2^2 + b_0 b_4\right)}{6 b_0^8 t^4}\Bigg), \end{aligned} \tag{9.5}$$

with $t \equiv \ln \frac{\mu_R^2}{\Lambda^2}$ and $\ell = \ln t$, again parametrized in terms of a constant Λ. Note that Eq. (9.5) is one of several possible approximate 4-loop solutions for $\alpha_s(\mu_R^2)$, and that a value for Λ only defines $\alpha_s(\mu_R^2)$ once one knows which particular approximation is being used. An alternative to the use of formulas such as Eq. (9.5) is to solve the RGE exactly, numerically (including the discontinuities, Eq. (9.4), at flavor thresholds). In such cases the quantity Λ does not directly arise (though it can be defined, *cf.* Eqs. (1–3) of Ref. [23]). For these reasons, in determinations of the coupling, it has become standard practice to quote the value of α_s at a given scale (typically the mass of the Z boson, M_Z) rather than to quote a value for Λ.

A discussion of determinations of the coupling and a graph illustrating its scale dependence ("running") are to be found in Section 9.4. The RunDec package [24–26] is often used to calculate the evolution of the coupling. For a discussion of electroweak effects in the evolution of the QCD coupling, see Ref. [27] and references therein.

9.1.2 *Quark masses*

Free quarks have never been observed, which is understood as a result of a long-distance, confining property of the strong QCD force: up, down, strange, charm, and bottom quarks all *hadronize*, *i.e.* become part of a meson or baryon, on a timescale $\sim 1/\Lambda$; the top quark instead decays before it has time to hadronize. This means that the question of what one means by the quark mass is a complex one, which requires one to adopt a specific prescription. A perturbatively defined prescription is the pole mass, m_q, which corresponds to the position of the divergence of the propagator. This is close to one's physical picture of mass. However, when relating it to observable quantities, it suffers from substantial non-perturbative ambiguities (see *e.g.* Ref. [28–30]). An alternative is the $\overline{\rm MS}$ mass, $\overline{m}_q(\mu_R^2)$, which depends on the renormalization scale μ_R.

Results for the masses of heavier quarks are often quoted either as the pole mass or as the $\overline{\rm MS}$ mass evaluated at a scale equal to the mass, $\overline{m}_q(\overline{m}_q^2)$; light quark masses are often quoted in the $\overline{\rm MS}$ scheme at a scale $\mu_R \sim 2\,\text{GeV}$. The pole and $\overline{\rm MS}$ masses are related by a series that starts as $m_q = \overline{m}_q(\overline{m}_q^2)(1 + \frac{4\alpha_s(\overline{m}_q^2)}{3\pi} + \mathcal{O}(\alpha_s^2))$, while the scale-dependence of $\overline{\rm MS}$ masses is given at lowest order by

$$\mu_R^2 \frac{d\overline{m}_q(\mu_R^2)}{d\mu_R^2} = \left[-\frac{\alpha_s(\mu_R^2)}{\pi} + \mathcal{O}(\alpha_s^2)\right]\overline{m}_q(\mu_R^2)\,. \tag{9.6}$$

A more detailed discussion is to be found in a dedicated section of the *Review*, "Quark Masses", with detailed formulas also in Ref. [31] and references therein.

In perturbative QCD calculations of scattering processes, it is common to work in an approximation in which one neglects (*i.e.* sets to zero) the masses of all quarks, whose mass is significantly smaller than the momentum transfer in the process.

9.2 Structure of QCD predictions

9.2.1 *Fully inclusive cross sections*

The simplest observables in perturbative QCD are those that do not involve initial-state hadrons and that are fully inclusive with respect to details of the final state. One example is the total cross section for $e^+e^- \to$ hadrons at center-of-mass energy Q, for which one can write

$$\frac{\sigma(e^+e^- \to \text{hadrons}, Q)}{\sigma(e^+e^- \to \mu^+\mu^-, Q)} \equiv R(Q) = R_{\rm EW}(Q)(1 + \delta_{\rm QCD}(Q))\,, \tag{9.7}$$

where $R_{\rm EW}(Q)$ is the purely electroweak prediction for the ratio and $\delta_{\rm QCD}(Q)$ is the correction due to QCD effects. To keep the discussion simple, we can restrict our attention to energies $Q \ll M_Z$, where the process is dominated by photon exchange (neglecting electroweak and finite-quark-mass corrections $R_{\rm EW} = N_c \sum_q e_q^2$, where the e_q are the electric charges of the quarks) and

$$\delta_{\rm QCD}(Q) = \sum_{n=1}^{\infty} c_n \cdot \left(\frac{\alpha_s(Q^2)}{\pi}\right)^n + \mathcal{O}\left(\frac{\Lambda^4}{Q^4}\right)\,. \tag{9.8}$$

The first four terms in the α_s series expansion are then to be found in Ref. [32],

$$c_1 = 1\,, \qquad c_2 = 1.9857 - 0.1152 n_f\,, \tag{9.9a}$$

$$c_3 = -6.63694 - 1.20013 n_f - 0.00518 n_f^2 - 1.240\eta\,, \tag{9.9b}$$

$$c_4 = -156.61 + 18.775 n_f - 0.7974 n_f^2 + 0.0215 n_f^3 - (17.828 - 0.575 n_f)\eta\,, \tag{9.9c}$$

with $\eta = (\sum e_q)^2/(3\sum e_q^2)$. For corresponding expressions including also Z exchange and finite-quark-mass effects, see Refs. [33–35].

A related series holds also for the QCD corrections to the hadronic decay width of the τ lepton, which essentially involves an integral of $R(Q)$ over the allowed range of invariant masses of the hadronic part of the τ decay (see *e.g.* Ref. [36]). The series expansions for QCD corrections to Higgs-boson hadronic (partial) decay widths in the limit of heavy top quark and massless light flavours at N^{4}LO are given in Ref. [37].

One characteristic feature of Eqs. (9.8) and (9.9) is that the coefficients of α_s^n increase order by order: calculations in perturbative QCD tend to converge more slowly than would be expected based just on the size of α_s. The situation is significantly worse near thresholds or in the presence of tight kinematic cuts. Another feature is the existence of an extra "power-correction" term $\mathcal{O}(\Lambda^4/Q^4)$ in Eq. (9.8), which accounts for contributions that are fundamentally non-perturbative. All high-energy QCD predictions involve power corrections $(\Lambda/Q)^p$, although typically the suppression of these corrections with Q is smaller than given in Eq. (9.8) where $p = 4$. The exact power p depends on the observable and, for many processes and observables, it is possible to introduce an operator product expansion and associate power suppressed terms with specific higher-dimension (non-perturbative) operators [38].

Scale dependence. In Eq. (9.8) the renormalization scale for α_s has been chosen equal to Q. The result can also be expressed in terms of the coupling at an arbitrary renormalization scale μ_R,

$$\delta_{\rm QCD}(Q) = \sum_{n=1}^{\infty} \overline{c}_n\left(\frac{\mu_R^2}{Q^2}\right) \cdot \left(\frac{\alpha_s(\mu_R^2)}{\pi}\right)^n + \mathcal{O}\left(\frac{\Lambda^4}{Q^4}\right)\,, \tag{9.10}$$

where $\overline{c}_1(\mu_R^2/Q^2) \equiv c_1$, $\overline{c}_2(\mu_R^2/Q^2) = c_2 + \pi b_0 c_1 \ln(\mu_R^2/Q^2)$, $\overline{c}_3(\mu_R^2/Q^2) = c_3 + (2b_0c_2\pi + b_1c_1\pi^2) \times \ln(\mu_R^2/Q^2) + b_0^2c_1\pi^2 \ln^2(\mu_R^2/Q^2)$, *etc.* Given an infinite number of terms in the α_s expansion, the μ_R dependence of the $\overline{c}_n(\mu_R^2/Q^2)$ coefficients will exactly cancel that of $\alpha_s(\mu_R^2)$, and the final result will be independent of the choice of μ_R: physical observables do not depend on unphysical scales.[1]

With just terms up to some finite $n = N$, a residual μ_R dependence will remain, which implies an uncertainty on the prediction of $R(Q)$ due to the arbitrariness of the scale choice. This uncertainty will be $\mathcal{O}(\alpha_s^{N+1})$, *i.e.* of the same order as the neglected higher-order terms. For this reason it is customary to use QCD predictions' scale dependence as an estimate of the uncertainties due to neglected terms. One usually takes a central value for $\mu_R \sim Q$, in order to avoid the poor convergence of the perturbative series that results from the large $\ln^{n-1}(\mu_R^2/Q^2)$ terms in the $\overline{c}_n$ coefficients when $\mu_R \ll Q$ or $\mu_R \gg Q$. Uncertainties are then

[1] With respect to pQCD there is an important caveat to this statement: at sufficiently high orders, perturbative series generally suffer from "renormalon" divergences $\alpha_s^n n!$ (reviewed in Ref. [28]). This phenomenon is not usually visible with the limited number of perturbative terms available today. However it is closely connected with non-perturbative contributions and sets a limit on the possible precision of perturbative predictions. The cancellation of scale dependence will also ultimately be affected by this renormalon-induced breakdown of perturbation theory.

commonly determined by varying μ_R by a factor of two up and down around the central scale choice. A more detailed discussion on the accuracy of theoretical predictions and on ways to estimate the theoretical uncertainties can be found in Section 9.2.4.

9.2.2 *Processes with initial-state hadrons*

Deep-Inelastic Scattering. To illustrate the key features of QCD cross sections in processes with initial-state hadrons, let us consider deep-inelastic scattering (DIS), $ep \to e + X$, where an electron e with four-momentum k emits a highly off-shell photon (momentum q) that interacts with the proton (momentum p). For photon virtualities $Q^2 \equiv -q^2$ far above the squared proton mass (but far below the Z mass), the differential cross section in terms of the kinematic variables Q^2, $x = Q^2/(2p\cdot q)$ and $y = (q\cdot p)/(k\cdot p)$ is

$$\frac{d^2\sigma}{dxdQ^2} = \frac{4\pi\alpha^2}{2xQ^4}\left[(1+(1-y)^2)F_2(x,Q^2) - y^2F_L(x,Q^2)\right], \tag{9.11}$$

where α is the electromagnetic coupling and $F_2(x,Q^2)$ and $F_L(x,Q^2)$ are proton structure functions, which encode the interaction between the photon (in given polarization states) and the proton. In the presence of parity-violating interactions (*e.g.* νp scattering) an additional F_3 structure function is present. For an extended review, including equations for the full electroweak and polarized cases, see Sec. 18 of this *Review*.

Structure functions are not calculable in perturbative QCD, nor is any other cross section that involves QCD interactions and initial-state hadrons. To zeroth order in α_s, the structure functions are given directly in terms of non-perturbative parton (quark or gluon) distribution functions (PDFs),

$$F_2(x,Q^2) = x\sum_q e_q^2 f_{q/p}(x)\,, \qquad F_L(x,Q^2) = 0\,, \tag{9.12}$$

where $f_{q/p}(x)$ is the non-perturbative PDF for quarks of type q inside the proton, *i.e.* the number density of quarks of type q inside a fast-moving proton that carry a fraction x of its longitudinal momentum (the quark flavor index q, here, is not to be confused with the photon momentum q in the lines preceding Eq. (9.11)). Recently, some first determinations on lattice started to appear [39–43] but there is also some debate about the underlying methods [44]. Accordingly, for all practical uses, PDFs are currently determined from data (*cf.* Sec. 18 of this *Review* and also Refs. [45, 46]) [2].

The above result, with PDFs $f_{q/p}(x)$ that are independent of the scale Q, corresponds to the "quark-parton model" picture in which the photon interacts with point-like free quarks, or equivalently, one has incoherent elastic scattering between the electron and individual constituents of the proton. As a consequence, in this picture also F_2 and F_L are independent of Q [50]. When including higher orders in pQCD,

$$F_2(x,Q^2) = x\sum_{n=0}^{\infty}\frac{\alpha_s^n(\mu_R^2)}{(2\pi)^n}\times$$
$$\times\sum_{i=q,g}\int_x^1\frac{dz}{z}C_{2,i}^{(n)}(z,Q^2,\mu_R^2,\mu_F^2)f_{i/p}\left(\frac{x}{z},\mu_F^2\right) + \mathcal{O}\left(\frac{\Lambda^2}{Q^2}\right). \tag{9.13}$$

Just as in Eq. (9.10), we have a series in powers of $\alpha_s(\mu_R^2)$, each term involving a coefficient $C_{2,i}^{(n)}$ that can be calculated using Feynman graphs. At variance with the parton model, the PDFs in pQCD depend on an additional scale, the factorization scale μ_F, whose significance will be discussed in the following. Another important difference is the additional integral over z. The parton that comes from the proton can undergo a splitting before it interacts with the photon. As a result, the $C_{2,i}^{(n)}$ coefficients are functions that depend on the ratio, z, of the parton's momentum before and after radiation, and one must integrate over that ratio. For the electromagnetic component of DIS with light quarks and gluons, the zeroth order coefficient functions are $C_{2,q}^{(0)} = e_q^2\delta(1-z)$ and $C_{2,g}^{(0)} = 0$. Corrections are known up to $\mathcal{O}(\alpha_s^3)$ (next-to-next-to-next-to-leading order, N^{3}LO) for both electromagnetic [51] and weak currents [52, 53]. For heavy-quark production they are known to $\mathcal{O}(\alpha_s^2)$ [54, 55] (next-to-leading order, NLO, insofar as the series starts at $\mathcal{O}(\alpha_s)$). For precise comparisons of LHC cross sections with theoretical predictions, the photon PDF of the proton is also needed. It has been computed precisely in Ref. [56] and has now been implemented in most global PDF fits.

The majority of the emissions that modify a parton's momentum are collinear (parallel) to that parton, and do not depend on the fact that the parton is destined to interact with a photon. It is natural to view these emissions as modifying the proton's structure rather than being part of the coefficient function for the parton's interaction with the photon. Technically, one uses a procedure known as *collinear factorization* to give a well-defined meaning to this distinction, most commonly through the $\overline{\rm MS}$ factorization scheme, defined in the context of dimensional regularization. The $\overline{\rm MS}$ factorization scheme involves an arbitrary choice of *factorization scale*, μ_F, whose meaning can be understood roughly as follows: emissions with transverse momenta above μ_F are included in the $C_{2,q}^{(n)}(z,Q^2,\mu_R^2,\mu_F^2)$; emissions with transverse momenta below μ_F are accounted for within the PDFs, $f_{i/p}(x,\mu_F^2)$. While collinear factorization is generally believed to be valid for suitable (sufficiently inclusive) observables in processes with hard scales, Ref. [57], which reviews the factorization proofs in detail, is cautious in the statements it makes about their exhaustivity, notably for the hadron-collider processes which we shall discuss below. Further discussion is to be found in Refs. [58, 59].

The PDFs' resulting dependence on μ_F is described by the Dokshitzer-Gribov-Lipatov-Altarelli-Parisi (DGLAP) equations [60], which to leading order (LO) read[3]

$$\mu_F^2\frac{\partial f_{i/p}(x,\mu_F^2)}{\partial\mu_F^2} = \sum_j\frac{\alpha_s(\mu_F^2)}{2\pi}\int_x^1\frac{dz}{z}P_{i\leftarrow j}^{(1)}(z)f_{j/p}\left(\frac{x}{z},\mu_F^2\right), \tag{9.14}$$

with, for example, $P_{q\leftarrow g}^{(1)}(z) = T_R(z^2+(1-z)^2)$. The other LO splitting functions are listed in Sec. 18 of this *Review*, while results up to NLO, α_s^2, and NNLO, α_s^3, are given in Refs. [61] and [62] respectively. At N^{3}LO accuracy, only partial results are currently available Ref. [63–65].

Splitting functions for polarized PDFs are given in Ref. [66]. Beyond LO, the coefficient functions are also μ_F dependent, for example $C_{2,i}^{(1)}(x,Q^2,\mu_R^2,\mu_F^2) = C_{2,i}^{(1)}(x,Q^2,\mu_R^2,Q^2) - \ln\left(\frac{\mu_F^2}{Q^2}\right)\sum_j\int_x^1\frac{dz}{z}\times C_{2,j}^{(0)}(\frac{x}{z})P_{j\leftarrow i}^{(1)}(z)$. In certain contexts, higher-order QED and mixed QED-QCD corrections to the splitting functions are also needed [67].

As with the renormalization scale, the choice of factorization scale is arbitrary, but if one has an infinite number of terms in the perturbative series, the μ_F-dependencies of the coefficient functions and PDFs will compensate each other fully. Given only N terms of the series, a residual $\mathcal{O}(\alpha_s^{N+1})$ uncertainty is associated with the ambiguity in the choice of μ_F. As with μ_R, varying μ_F provides an input in estimating uncertainties on predictions. In inclusive DIS predictions, the default choice for the scales is

[2] PDFs can be determined from data in a global fit at LO, NLO and NNLO, depending on the order of the matrix elements used to describe the data. In modern global PDF fits, data are included from DIS, DY, jets and $t\bar{t}$ processes, and more LHC collider data, with the global PDF fits using 3000-4000 data points. There is a large change in the PDFs from LO to NLO, with a much smaller change from NLO to NNLO. LO PDFs can be unreliable for collider predictions, especially at low and high x. The uncertainties for the resulting PDFs are determined from the experimental uncertainties of the data that serves as input to the global PDF fits. The PDF uncertainties can either be determined through a Hessian approach or through the use of Monte Carlo replicas. It is now relatively straightforward to convert results from one approach to the other. The PDF4LHC15 PDF set is formed by combining replicas of the CT14, MMHT2014 and NNPDF3.0 PDF sets, at NLO and at NNLO [47]. Recently, theoretical uncertainties related to missing higher orders have been included in global PDF determinations but so far only at NLO [48, 49].

[3] LO is generally taken to mean the lowest order at which a quantity is non-zero.

usually $\mu_R = \mu_F = Q$.

As is the case for the running coupling, in DGLAP evolution one can introduce flavor thresholds near the heavy quark masses: below a given heavy quark's mass, that quark is not considered to be part of the proton's structure, while above it is considered to be part of the proton's structure and evolves with massless DGLAP splitting kernels. With appropriate parton distribution matching terms at threshold, such a variable flavor number scheme (VFNS), when used with massless coefficient functions, gives the full heavy-quark contributions at high Q^2 scales. For scales near the threshold, it is instead necessary to appropriately adapt the standard massive coefficient functions to account for the heavy-quark contribution already included in the PDFs [68–70].

At sufficiently small x and Q^2 in inclusive DIS, resummation of small x logarithms may be necessary [71,72]. This may in fact have been observed in Refs. [73] based on HERA data [74], in a kinematic region where useful information for PDFs for collider predictions is present. A better description of the data in this region can be gained by small x resummation matched to NNLO [73,75], or by the inclusion of power-suppressed contributions [76] or by using an x-dependent factorization scale in the NNLO DIS predictions [77].

Hadron-hadron collisions. The extension to processes with two initial-state hadrons can be illustrated with the example of the total (inclusive) cross section for W boson production in collisions of hadrons h_1 and h_2, which can be written as

$$\sigma(h_1 h_2 \to W + X) = \sum_{n=0}^{\infty} \alpha_s^n(\mu_R^2) \times \sum_{i,j} \int dx_1 dx_2 \, f_{i/h_1}\left(x_1, \mu_F^2\right) f_{j/h_2}\left(x_2, \mu_F^2\right) \times \hat{\sigma}^{(n)}_{ij\to W+X}\left(x_1 x_2 s, \mu_R^2, \mu_F^2\right) + \mathcal{O}\left(\frac{\Lambda^2}{M_W^4}\right), \tag{9.15}$$

where s is the squared center-of-mass energy of the collision. At LO, $n = 0$, the hard (partonic) cross section $\hat{\sigma}^{(0)}_{ij\to W+X}(x_1 x_2 s, \mu_R^2, \mu_F^2)$ is simply proportional to $\delta(x_1 x_2 s - M_W^2)$, in the narrow W-boson width approximation (see Sec. 50 of this *Review* for detailed expressions for this and other hard scattering cross sections). It is non-zero only for choices of i, j that can directly give a W, such as $i = u$, $j = \bar{d}$. At higher orders, $n \geq 1$, new partonic channels contribute, such as gq, and $x_1 x_2 s \geq M_W^2$ in the narrow W-boson width approximation.

Eq. (9.15) involves a collinear factorization between the hard cross section and the PDFs, just like Eq. (9.13). As long as the same factorization scheme is used in DIS and pp or $p\bar{p}$ (usually the $\overline{\text{MS}}$ scheme), then PDFs extracted in DIS can be directly used in pp and $p\bar{p}$ predictions [57,78] (with the anti-quark distributions in an anti-proton being the same as the quark distributions in a proton).

Fully inclusive hard cross sections are known to NNLO, *i.e.* corrections up to relative order α_s^2, for Drell-Yan (DY) lepton-pair and vector-boson production [79,80], Higgs-boson production in association with a vector boson [81], Higgs-boson production via vector-boson fusion [82] (in an approximation that factorizes the production of the two vector bosons), Higgs-pair production with full m_t dependence [83], top-antitop production [84] and vector-boson pair production [85–87].[4] Inclusive Higgs production through gluon fusion in the large m_t limit was calculated at N^{3}LO [88,89]. A calculation at this order, differential in the Higgs rapidity has also been presented recently [90]. Vector-boson fusion Higgs production is also known to N^{3}LO [91] in the factorized approximation. A discussion of many other calculations for Higgs production processes is to be found in Ref. [92].

Photoproduction. γp (and $\gamma\gamma$) collisions are similar to pp collisions, with the subtlety that the photon can behave in two ways: there is "direct" photoproduction, in which the photon behaves as a point-like particle and takes part directly in the hard collision, with hard subprocesses such as $\gamma g \to q\bar{q}$; there is also resolved photoproduction, in which the photon behaves like a hadron, with non-perturbative partonic substructure and a corresponding PDF for its quark and gluon content, $f_{i/\gamma}(x, Q^2)$. While useful to understand the general structure of γp collisions, the distinction between direct and resolved photoproduction is not well defined beyond leading order, as discussed for example in Ref. [93].

The high-energy (BFKL) limit. In situations in which the total center-of-mass energy $\sqrt{s}$ is much larger than all other momentum-transfer scales in the problem (*e.g.* Q in DIS, m_b for $b\bar{b}$ production in pp collisions, *etc.*), each power of α_s beyond LO can be accompanied by a power of $\ln(s/Q^2)$ (or $\ln(s/m_b^2)$, *etc.*). This is variously referred to as the high-energy, small-x or Balitsky-Fadin-Kuraev-Lipatov (BFKL) limit [72,94,95]. Currently it is possible to account for the dominant and first sub-dominant [96,97] power of $\ln s$ at each order of α_s, and also to estimate further sub-dominant contributions that are numerically large (see Refs. [98–101] and references therein). Progress towards NNLO is discussed in Ref. [102].

Physically, the summation of all orders in α_s can be understood as leading to a growth with s of the gluon density in the proton. At sufficiently high energies this implies non-linear effects (commonly referred to as parton saturation), whose treatment has been the subject of intense study (see for example Refs. [103,104] and references thereto).

9.2.3 *Cross sections with phase-space restrictions*

QCD final states always consist of hadrons, while perturbative QCD calculations deal with partons. Physically, an energetic parton fragments ("showers") into many further partons, which then, on later timescales, undergo a transition to hadrons ("hadronization"). Fixed-order perturbation theory captures only a small part of these dynamics. This does not matter for the fully inclusive cross sections discussed above: the showering and hadronization stages are approximately unitary, *i.e.* they do not substantially change the overall probability of hard scattering, because they occur long after it has taken place (they introduce at most a correction proportional to a power of the ratio of timescales involved, *i.e.* a power of Λ/Q, where Q is the hard scattering scale).

Less inclusive measurements, in contrast, may be affected by the extra dynamics. For those sensitive just to the main directions of energy flow (jet rates, event shapes, *cf.* Sec. 9.3.1) fixed-order perturbation theory is often still adequate, because showering and hadronization do not substantially change the overall energy flow. This means that one can make a prediction using just a small number of partons, which should correspond well to a measurement of the same observable carried out on hadrons. For observables that instead depend on distributions of individual hadrons (which, *e.g.*, are the inputs to detector simulations), it is mandatory to account for showering and hadronization. The range of predictive techniques available for QCD final states reflects this diversity of needs of different measurements.

While illustrating the different methods, we shall for simplicity mainly use expressions that hold for e^+e^- scattering. The extension to cases with initial-state partons will be mostly straightforward (space constraints unfortunately prevent us from addressing diffraction and exclusive hadron-production processes; extensive discussion is to be found in Refs. [105,106]).

9.2.3.1 *Soft and collinear limits*

Before examining specific predictive methods, it is useful to be aware of a general property of QCD matrix elements in the soft and collinear limits. Consider a squared tree-level matrix element $|M_n^2(p_1, \ldots, p_n)|$ for the process $e^+e^- \to n$ partons with momenta $p_1, \ldots, p_n$, and a corresponding phase-space integration measure $d\Phi_n$. If particle n is a gluon, which becomes collinear (parallel) to another particle i and additionally its momentum tends to zero

[4] Processes with jets or photons in the final state have divergent cross sections unless one places a cut on the jet or photon momentum. Accordingly, they are discussed below in Section 9.2.3.2.

(is "soft"), the matrix element simplifies as follows,

$$\lim_{\theta_{in}\to 0,\, E_n\to 0} d\Phi_n |M_n^2(p_1,\ldots,p_n)| \\ = d\Phi_{n-1}|M_{n-1}^2(p_1,\ldots,p_{n-1})| \frac{\alpha_s C_i}{\pi}\frac{d\theta_{in}^2}{\theta_{in}^2}\frac{dE_n}{E_n}\,, \qquad (9.16)$$

where $C_i = C_F$ (C_A) if i is a quark (gluon). This formula has non-integrable divergences both for the inter-parton angle $\theta_{in} \to 0$ and for the gluon energy $E_n \to 0$, which are mirrored also in the structure of divergences in loop diagrams. These divergences are important for at least two reasons: firstly, they govern the typical structure of events (inducing many emissions either with low energy or at small angle with respect to hard partons); secondly, they will determine which observables can be calculated within perturbative QCD.

9.2.3.2 *Fixed-order predictions*

Let us consider an observable $\mathcal{O}$ that is a function $\mathcal{O}_n(p_1,\ldots,p_n)$ of the four-momenta of the n final-state particles in an event (either partons or hadrons). In what follows, we shall consider the cross section for events weighted with the value of the observable, $\sigma_{\mathcal{O}}$. As examples, if $\mathcal{O}_n \equiv 1$ for all n, then $\sigma_{\mathcal{O}}$ is just the total cross section; if $\mathcal{O}_n \equiv \hat{\tau}(p_1,\ldots,p_n)$ where $\hat{\tau}$ is the value of the Thrust for that event (see Sec. 9.3.1.2), then the average value of the Thrust is $\langle\tau\rangle = \sigma_{\mathcal{O}}/\sigma_{\rm tot}$; if $\mathcal{O}_n \equiv \delta(\tau - \hat{\tau}(p_1,\ldots,p_n))$ then one gets the differential cross section as a function of the Thrust, $\sigma_{\mathcal{O}} \equiv d\sigma/d\tau$.

In the expressions below, we shall omit to write the non-perturbative power correction term, which for most common observables is proportional to a single power of Λ/Q.

Leading Order. If the observable $\mathcal{O}$ is non-zero only for events with at least n final-state particles, then the LO QCD prediction for the weighted cross section in e^+e^- annihilation is

$$\sigma_{\mathcal{O},LO} = \alpha_s^{n-2}(\mu_R^2)\int d\Phi_n |M_n^2(p_1,\ldots,p_n)|\,\mathcal{O}_n(p_1,\ldots,p_n)\,, \qquad (9.17)$$

where the squared tree-level matrix element, $|M_n^2(p_1,\ldots,p_n)|$, including relevant symmetry factors, has been summed over all subprocesses (*e.g.* $e^+e^- \to q\bar{q}q\bar{q}$, $e^+e^- \to q\bar{q}gg$) and has had all factors of α_s extracted in front. In processes other than e^+e^- collisions, the center-of-mass energy of the LO process is generally not fixed, and so the powers of the coupling are often brought inside the integrals, with the scale μ_R chosen event by event, as a function of the event kinematics.

Other than in the simplest cases (see the review on Cross Sections in this *Review*), the matrix elements in Eq. (9.17) are usually calculated automatically with programs such as CompHEP [107], MadGraph [108], Alpgen [109], Comix/Sherpa [110], and Helac/Phegas [111]. Some of these (CompHEP, MadGraph) use formulas obtained from direct evaluations of Feynman diagrams. Others (Alpgen, Helac/Phegas and Comix/Sherpa) use methods designed to be particularly efficient at high multiplicities, such as Berends-Giele recursion [112], which builds up amplitudes for complex processes from simpler ones (see also Refs. [113–116] for reviews on the topic and for other tree-level calculational methods).

The phase-space integration is usually carried out by Monte Carlo sampling, in order to deal with the possibly involved kinematic cuts that are used in the corresponding experimental measurements. Because of the divergences in the matrix element, Eq. (9.16), the integral converges only if the observable vanishes for kinematic configurations in which one of the n particles is arbitrarily soft or it is collinear to another particle. As an example, the cross section for producing any configuration of n partons will lead to an infinite integral, whereas a finite result will be obtained for the cross section for producing n deposits of energy (or jets, see Sec. 9.3.1.1), each above some energy threshold and well separated from each other in angle.

At a practical level, LO calculations can be carried out for $2 \to n$ processes with $n \lesssim 6-10$. The exact upper limit depends on the process, the method used to evaluate the matrix elements (recursive methods are more efficient), and the extent to which the phase-space integration can be optimized to work around the large variations in the values of the matrix elements.

NLO. Given an observable that is non-zero starting from n final-state particles, its prediction at NLO involves supplementing the LO result, Eq. (9.17), with the $2 \to (n+1)$-particle squared tree-level matrix element ($|M_{n+1}^2|$), and the interference of a $2 \to n$ tree-level and $2 \to n$ 1-loop amplitude ($2\mathrm{Re}(M_n M_{n,1-\rm loop}^*)$),

$$\sigma_{\mathcal{O}}^{NLO} = \sigma_{\mathcal{O}}^{LO} + \alpha_s^{n-1}(\mu_R^2)\int d\Phi_{n+1}|M_{n+1}^2(p_1,\ldots,p_{n+1})| \\ \times \mathcal{O}_{n+1}(p_1,\ldots,p_{n+1}) \;+\; \alpha_s^{n-1}(\mu_R^2) \\ \times \int d\Phi_n\, 2\mathrm{Re}\left[\, M_n(p_1,\ldots,p_n)\, M_{n,1-\rm loop}^*(p_1,\ldots,p_n)\,\right] \\ \times \mathcal{O}_n(p_1,\ldots,p_n)\,. \qquad (9.18)$$

Relative to LO calculations, two important issues appear in the NLO calculations. Firstly, the extra complexity of loop-calculations relative to tree-level calculations means that automated calculations started to appear only about fifteen years ago (see below). Secondly, loop amplitudes are infinite in 4 dimensions, while tree-level amplitudes are finite, but their *integrals* are infinite, due to the divergences of Eq. (9.16). These two sources of infinities have the same soft and collinear origins and cancel after the integration only if the observable $\mathcal{O}$ satisfies the property of infrared and collinear safety, which means that the observable is non-sensitive to soft emissions or to collinear splittings, *i.e.*

$$\begin{aligned} &\mathcal{O}_{n+1}(p_1,\ldots,p_s,\ldots,p_n) \quad \to \mathcal{O}_n(p_1,\ldots,p_{s-1},p_{s+1},\ldots,p_n) \\ &\qquad\qquad \text{if } p_s \to 0 \\ &\mathcal{O}_{n+1}(p_1,\ldots,p_a,p_b,\ldots,p_n) \;\to \mathcal{O}_n(p_1,\ldots,p_a+p_b,\ldots,p_n) \\ &\qquad\qquad \text{if } p_a \,||\, p_b\,. \end{aligned} \qquad (9.19)$$

Examples of infrared-safe quantities include event-shape distributions and jet cross sections (with appropriate jet algorithms, see below). Unsafe quantities include the distribution of the momentum of the hardest QCD particle (which is not conserved under collinear splitting), observables that require the complete absence of radiation in some region of phase space (*e.g.* rapidity gaps or 100% isolation cuts, which are affected by soft emissions), or the particle multiplicity (affected by both soft and collinear emissions). The non-cancellation of divergences at NLO due to infrared or collinear unsafety compromises the usefulness not only of the NLO calculation, but also that of a LO calculation, since LO is only an acceptable approximation if one can prove that higher-order terms are smaller. Infrared and collinear unsafety usually also imply large non-perturbative effects.

As with LO calculations, the phase-space integrals in Eq. (9.18) are usually carried out by Monte Carlo integration, so as to facilitate the study of arbitrary observables. Various methods exist to obtain numerically efficient cancellation among the different infinities. These include notably dipole [117], FKS [118] and antenna [119] subtraction.

Thanks to new ideas like the OPP method [120], generalised [121] and D-dimensional [122] unitarity, onshell methods [123], and on the fly reduction algorithms [124], recent years have seen a breakthrough in the calculation of one-loop matrix elements (for reviews on unitarity based method see Ref. [125,126]). Thanks to these innovative methods, automated NLO calculations tools have been developed and a number of programs are available publicly: Madgraph5_aMC@NLO [108] and Helac-NLO [127] provide full frameworks for NLO calculations; GoSam [128], Njet [129], OpenLoops [130] and Recola [131] calculate just the 1-loop part and are typically interfaced with an external tool such as Sherpa [132] for a combination with the appropriate tree-level amplitudes. Other tools such as NLOJet++ [133], MCFM [134], VBFNLO [135], the Phox family [136] or BlackHat [137] implement analytic calculations for a selected class of processes. Given that NLO computation for high-multiplicity final states is numerically demanding,

procedures [138–141] have been developed for *a posteriori* PDF and scale change. These methods represent NLO (or NNLO) results, for a given set of cuts and binning, as an effective coefficient function on a grid in parton momentum fractions and factorization scales.

Recently, a lot of attention has also been paid to the calculation of NLO electroweak corrections. Electroweak corrections are especially important for transverse momenta significantly above the W and Z masses, because they are enhanced by two powers of $\ln p_t/M_W$ for each power of the electroweak coupling, and close to Sudakov peaks, where most of the data lie and the best experimental precision can be achieved. In some cases the above programs (or development versions of them) can be used to calculate also NLO electroweak or beyond-standard-model corrections [142–148].

Given the progress in QCD and EW fixed-order computations, the largest unknown from fixed-order corrections is often given by the mixed QCD-electroweak corrections of $\mathcal{O}(\alpha_s\alpha)$. These mixed two-loop corrections are often available only in an approximate form [149–154] and first three-loop results $\mathcal{O}(\alpha_s^2\alpha)$ in the case of Higgs productions started to appear recently [155].

NNLO. Conceptually, NNLO and NLO calculations are similar, except that one must add a further order in α_s, consisting of: the squared $(n+2)$-parton tree-level amplitude, the interference of the $(n+1)$-parton tree-level and 1-loop amplitudes, the interference of the n-parton tree-level and 2-loop amplitudes, and the squared n-parton 1-loop amplitude.

Each of these elements involves large numbers of soft and collinear divergences, satisfying relations analogous to Eq. (9.16) which now involve multiple collinear or soft particles and higher loop orders (see *e.g.* Refs. [156–158]). Arranging for the cancellation of the divergences after numerical Monte Carlo integration has been one of the significant challenges of NNLO calculations, as has been the determination of the relevant 2-loop amplitudes. For the cancellations of divergences a wide range of methods has been developed. Some of them [159–163] retain the approach, inherent in NLO methods, of directly combining the separate loop and tree-level amplitudes. Others combine a suitably chosen, partially inclusive $2 \to n$ NNLO calculation with a fully differential $2 \to n+1$ NLO calculation [164–167].

Quite a number of processes have been calculated differentially at NNLO so far. The state of the art for e^+e^- collisions is $e^+e^- \to$ 3 jets [168–170]. For DIS, dijet production is known at NNLO [171] and the description jet production has been recently pushed even to N^{3}LO using the Projection-to-Born method [172,173]. For hadron colliders, all $2 \to 1$ processes are known, specifically vector boson [174, 175] and Higgs boson production [164, 176]. For most of the above calculations there exist public codes (EERAD3 for e^+e^-, DYNNLO, FEWZ and MATRIX for W and Z production, Fehipro and HNNLO for Higgs production), links to which are to be found among the above references. Substantial progress has been made in the past couple of years for hadron-collider $2 \to 2$ processes, with calculations having been performed for nearly all relevant processes: ZZ [86] WW [85] and WZ [177], $\gamma\gamma$ [178,179], $Z\gamma$ [180] and $W\gamma$ [181] (many of these colour singlet processes are available also in MCFM [182] or MATRIX [87]), inclusive photon [183,184], $\gamma+$ jet [184,185], $W+$ jet [165], $Z+$ jet [185–187] $H+$ jet [188–191], WH [192] and ZH [193], t-channel single-top [194,195], $t\bar{t}$ production [196], dijet production [197], and HH [198] (in large-top-mass approximation, see also the exact (two-loop) NLO result [83]). One $2 \to 3$ process is known at NNLO, Higgs production through vector-boson fusion, using an approximation in which the two underlying DIS-like $q \to qV$ scatterings are factorised, the so-called structure function approximation [167, 199]. Corrections beyond the structure function approximation are expected to be small, on the order of a percent or less [200].

The Les Houches precision wishlist compiles predictions needed to fully exploit the data that will be taken at the High Luminosity LHC [201]. Most of the needed calculations require accuracy of at least NNLO QCD and NLO EW, and many require the prediction of $2 \to 3$ processes, such as $W/Z+ \geq 2$ jets, $H+ \geq 2$ jets, and ttH to NNLO.

As discussed in this section, calculations at NLO can now be relatively easily generated by non-experts using the programs described. However, many NNLO calculations can be too complex and CPU-intensive to allow such an approach. In these cases, the relevant matrix element information can be stored in a grid format (or in ROOT ntuples) allowing predictions to be generated on-the-fly, similar to what has been available at NLO.

9.2.3.3 *Resummation*

Many experimental measurements place tight constraints on emissions in the final state. For example, in e^+e^- events, that (one minus) the Thrust should be less than some value $\tau \ll 1$, or, in $pp \to Z$, events that the Z-boson transverse momentum or the transverse momentum of the accompanying jet should be much smaller than the Z-boson mass. A further example is the production of heavy particles or jets near threshold (so that little energy is left over for real emissions) in DIS and pp collisions.

In such cases, the constraint vetoes a significant part of the integral over the soft and collinear divergence of Eq. (9.16). As a result, there is only a partial cancellation between real emission terms (subject to the constraint) and loop (virtual) contributions (not subject to the constraint), causing each order of α_s to be accompanied by a large coefficient $\sim L^2$, where *e.g.* $L = \ln\tau$ or $L = \ln(M_Z/p_t^Z)$. One ends up with a perturbative series, whose terms go as $\sim (\alpha_s L^2)^n$. It is not uncommon that $\alpha_s L^2 \gg 1$, so that the perturbative series converges very poorly if at all.[5] In such cases one may carry out a "resummation", which accounts for the dominant logarithmically enhanced terms to all orders in α_s, by making use of known properties of matrix elements for multiple soft and collinear emissions, and of the all-orders properties of the divergent parts of virtual corrections, following original works such as Refs. [202–211] and also through soft-collinear effective theory [212, 213] (*cf.* also the section on "Heavy-Quark and Soft-Collinear Effective Theory" in this *Review*, as well as Ref. [214]).

For cases with double logarithmic enhancements (two powers of logarithm per power of α_s), there are two classification schemes for resummation accuracy. Writing the cross section including the constraint as $\sigma(L)$ and the unconstrained (total) cross section as $\sigma_{\rm tot}$, the series expansion takes the form

$$\sigma(L) \simeq \sigma_{\rm tot} \sum_{n=0}^{\infty} \sum_{k=0}^{2n} R_{nk} \alpha_s^n(\mu_R^2) L^k, \qquad L \gg 1\,, \tag{9.20}$$

and leading log (LL) resummation means that one accounts for all terms with $k = 2n$, next-to-leading-log (NLL) includes additionally all terms with $k = 2n-1$, *etc.* Often $\sigma(L)$ (or its Fourier or Mellin transform) *exponentiates* [6],

$$\sigma(L) \simeq \sigma_{\rm tot} \exp\left[\sum_{n=1}^{\infty} \sum_{k=0}^{n+1} G_{nk} \alpha_s^n(\mu_R^2) L^k\right], \qquad L \gg 1\,, \tag{9.21}$$

where one notes the different upper limit on k ($\leq n+1$) compared to Eq. (9.20). This is a more powerful form of resummation: the G_{12} term alone reproduces the full LL series in Eq. (9.20). With the form Eq. (9.21) one still uses the nomenclature LL, but this now means that all terms with $k = n+1$ are included, and NLL implies all terms with $k = n$, *etc.*

For a large number of observables, NLL resummations are available in the sense of Eq. (9.21) (see Refs. [218–220] and references therein). NNLL has been achieved for the DY and Higgs-boson p_t distributions [221–224] (also available in the CuTe [225], HRes [226] and ResBos [227] families of programs and also differentially in vector-boson decay products [228]) and related variables [229], for the p_t of vector-boson pairs [230], for the back-to-back energy-energy correlation in e^+e^- [231], the jet broadening

[5] To be precise one should be aware of two causes of the divergence of perturbative series. That which interests us here is associated with the presence of a new large parameter (*e.g.* ratio of scales). It is distinct from the "renormalon" induced factorial divergences of perturbation theory which were discussed above.

[6] Whether or not this happens depends on the quantity being resummed. A classic example involves two-jet rate in e^+e^- collisions as a function of a jet-resolution parameter $y_{\rm cut}$. The logarithms of $1/y_{\rm cut}$ exponentiate for the k_t (Durham) jet algorithm [215], but not [216] for the JADE algorithm [217] (both are discussed below in Sec. 9.3.1.1).

in e^+e^- collisions [232], the jet-veto survival probability in Higgs and Z boson production in pp collisions [233, 234] [7], an event-shape type observable known as the beam Thrust [235], hadron-collider jet masses in specific limits [236] (see also Ref. [237]), the production of top anti-top pairs near threshold [238–240] (and references therein), and high-p_t W and Z production [241]. Automation of NNLL jet-veto resummations for different processes has been achieved in Ref. [242] (*cf.* also the NLL automation in Ref. [243]), while automation for a certain class of e^+e^- observables has been achieved in Ref. [244]. N^{3}LL resummations are available for the Thrust variable, C-parameter and heavy-jet mass in e^+e^- annihilations [245–247] (confirmed for Thrust at NNLL in Ref. [248]), for p_t distribution of the Higgs boson [249] and weak gauge bosons [250] and for Higgs- and vector-boson production near threshold [251]. An extensive discussion of jet masses for heavy-quark induced jets has been given in Ref. [252] (see also Ref. [253]). In order to make better contact with experimental measurements, recent years have seen an increasing interest in resummations in exclusive phase-space regions and joint resummations [254–260]. Finally, there has also been considerable progress in resummed calculations for jet substructure, whose observables involve more complicated definitions than is the case for standard resummations [261–267], see also Refs. [268, 269]. The inputs and methods involved in these various calculations are somewhat too diverse to discuss in detail here, so we recommend that the interested reader consult the original references for further details.

9.2.3.4 *Fragmentation functions*

Since the parton-hadron transition is non-perturbative, it is not possible to perturbatively calculate quantities such as the energy-spectra of specific hadrons in high-energy collisions. However, one can factorize perturbative and non-perturbative contributions via the concept of fragmentation functions. These are the final-state analogue of the parton distribution functions which are used for initial-state hadrons. Like parton distribution functions, they depend on a (fragmentation) factorization scale and satisfy a DGLAP evolution equation.

It should be added that if one ignores the non-perturbative difficulties and just calculates the energy and angular spectrum of partons in perturbative QCD with some low cutoff scale $\sim \Lambda$ (using resummation to sum large logarithms of $\sqrt{s}/\Lambda$), then this reproduces many features of the corresponding hadron spectra [270]. This is often taken to suggest that hadronization is "local", in this sense it mainly involves partons that are close both in position and in momentum.

Section 19 of this *Review* provides further information (and references) on these topics, including also the question of heavy-quark fragmentation.

9.2.3.5 *Parton-shower Monte Carlo generators*

Parton-shower Monte Carlo (MC) event generators like PYTHIA [271–273], HERWIG [274–276] and SHERPA [132] provide fully exclusive simulations of QCD events.[8] Because they provide access to "hadron-level" events, they are a crucial tool for all applications that involve simulating the response of detectors to QCD events. Here we give only a brief outline of how they work and refer the reader to Sec. 41 and Ref. [278] for a full overview.

The MC generation of an event involves several stages. It starts with the random generation of the kinematics and partonic channels of whatever *hard scattering process* the user has requested at some high scale Q_0 (for complex processes, this may be carried out by an external program). This is followed by a *parton shower*, usually based on the successive random generation of gluon emissions (or $g \to q\bar{q}$ splittings). Emissions are ordered according to some ordering variable. Common choices of scale for the ordering of emissions are virtuality, transverse momentum or angle. Each emission is generated at a scale lower than the previous emission, following a (soft and collinear resummed) perturbative QCD distribution, which depends on the momenta of all previous emissions. Parton showering stops at a scale of order 1 GeV, at which point a *hadronization model* is used to convert the resulting partons into hadrons. One widely-used model involves stretching a color "string" across quarks and gluons, and breaking it up into hadrons [279, 280]. Another breaks each gluon into a $q\bar{q}$ pair and then groups quarks and anti-quarks into colorless "clusters", which then give the hadrons [274]. As both models are tuned primarily to LEP data, the cluster and string models provide similar results for most observables [281]. For pp and γp processes, modeling is also needed to treat the collision between the two hadron remnants, which generates an *underlying event* (UE), usually implemented via additional $2 \to 2$ scatterings ("multiple parton interactions") at a scale of a few GeV, following Ref. [282]. The parameter values for the multiple parton interaction models must be determined from fits to the underlying event levels from LHC collision data. As the different Monte Carlo programs fit to essentially the same data, there should be similar results for each program. One complication, however, is the non-universality of the underlying event for different physics processes.

A deficiency of the soft and collinear approximations that underlie parton showers is that they may fail to reproduce the full pattern of hard wide-angle emissions, important, for example, in many new physics searches. It is therefore common to use LO multi-parton matrix elements to generate hard high-multiplicity partonic configurations as additional starting points for the showering, supplemented with some prescription (CKKW [283], MLM [284]) for consistently merging samples with different initial multiplicities. Monte Carlo generators, as described above, compute cross sections for the requested hard process that are correct at LO.

A wide variety of processes are available in MC implementations that are correct also to NLO, using the MC@NLO [285] or POWHEG [286] prescriptions, notably through the Madgraph5_aMC@NLO [108], POWHEGBox [287] and Sherpa [110] programs. Techniques have also been developed to combine NLO plus shower accuracy for different multiplicities of final-state jets [288]. Building in part on some of that work, several groups have also obtained NNLO plus shower accuracy for Drell-Yan and Higgs production [289], as well as for a handful of $2 \to 2$ processes [290–292].

In general, we expect parton-shower matched predictions to differ from the underlying fixed-order results in regions where (1) there is a large sensitivity to jet shapes (for instance small R jets), (2) there is a restriction in phase space such that soft gluon resummation effects become important, (3) the observable contains multiple disparate scales, (4) there are perturbative instabilities at fixed order, *e.g.* related to kinematical cuts, and (5) the observable is sensitive to higher multiplicity states than those described by the fixed-order calculation [281].

9.2.4 *Accuracy of predictions*

Estimating the accuracy of perturbative QCD predictions is not an exact science. It is often said that LO calculations are accurate to within a factor of two. This is based on experience with NLO corrections in the cases where these are available. In processes involving new partonic scattering channels at NLO and/or large ratios of scales (such as jet observables in processes with vector bosons, or the production of high-p_t jets containing B-hadrons), the ratio of the NLO to LO predictions, commonly called the "K-factor", can be substantially larger than two. NLO corrections tend to be large for processes for which there is a great deal of color annihilation in the interaction. In addition, NLO corrections tend to decrease as more final state legs are added.

For calculations beyond LO, a conservative approach to estimate the perturbative uncertainty is to take it to be the last known perturbative correction; a more widely used method is to estimate it from the change in the prediction when varying the renormalization and factorization scales around a central value Q that is taken close to the physical scale of the process. A conventional range of variation is $Q/2 < \mu_R, \mu_F < 2Q$, varying the two scales independently with the restriction $\frac{1}{2}\mu_R < \mu_F < 2\mu_R$ [293]. This constraint limits the risk of misleadingly small uncertainties due

[7] A veto on the jet phase space can be severe, for example by requiring exactly zero jets above a given transverse momentum cut accompanying a Higgs boson, or relatively mild, for example by placing a transverse momentum cut of 30 GeV on the measurement of the production of a Higgs boson with one or more jets. In general, inclusive cross sections are preferable, as uncertainties on both the theoretical and experimental sides are smaller.

[8] The program ARIADNE [277] has also been widely used for simulating e^+e^- and DIS collisions.

to fortuitous cancellations between the μ_F and μ_R dependence when both are varied together, while avoiding the appearance of large logarithms of μ_R^2/μ_F^2 when both are varied completely independently. Where possible, it can be instructive to examine the two-dimensional scale distributions (μ_R *vs.* μ_F) to obtain a better understanding of the interplay between μ_R and μ_F. This procedure should not be assumed to always estimate the full uncertainty from missing higher orders, but it does indicate the size of one important known source of higher-order ambiguity.[9]

For processes involving jets in the final state, estimates of the uncertainties at NNLO, along the lines described above, can be misleading for jets of smaller radii, due to accidental cancellations. Procedures are available to provide more reasonable estimates of the uncertainties in those cases [281, 302]. In addition, care must be taken as to the form of the central scale [303].

Calculations that involve resummations usually have an additional source of uncertainty associated with the choice of argument of the logarithms being resummed, *e.g.* $\ln(2\frac{p_t^Z}{M_Z})$ as opposed to $\ln(\frac{1}{2}\frac{p_t^Z}{M_Z})$. In addition to varying renormalization and factorization scales, it is therefore also advisable to vary the argument of the logarithm by a suitable factor in either direction with respect to the "natural" argument.

The accuracy of QCD predictions is limited also by non-perturbative corrections, which typically scale as a power of Λ/Q.[10] For measurements that are directly sensitive to the structure of the hadronic final state, the corrections are usually linear in Λ/Q. The non-perturbative corrections are further enhanced in processes with a significant underlying event (*i.e.* in pp and $p\bar{p}$ collisions) and in cases where the perturbative cross sections fall steeply as a function of p_t or some other kinematic variable, for example in inclusive jet spectra or dijet mass spectra. In general, the underlying event for a hard scattering process, such as dijet production, is of a similar order, but somewhat harder, than the average energy density in a minimum-bias event. Under high-luminosity running conditions, such as 13 TeV at the LHC, there can be on the order of 50 minimum-bias interactions occurring at each beam-beam crossing. This additional energy needs to be corrected for, and is typically removed by subtracting a rapidity-dependent transverse energy density determined on an event-by-event basis [304]. This subtraction, of necessity, also removes the underlying event, which must be added back in to restore the measured event to the hadron level.

Non-perturbative corrections are commonly estimated from the difference between Monte Carlo events at the parton level and after hadronization. An issue to be aware of with this procedure is that "parton level" is not a uniquely defined concept. For example, in an event generator it depends on a (somewhat arbitrary and tunable) internal cutoff scale that separates the parton showering from the hadronization. In contrast, no such cutoff scale exists in an NLO or NNLO partonic calculation. There exist alternative methods for estimating hadronization corrections, that attempt to analytically deduce non-perturbative effects in one observable based on measurements of other observables (see the reviews [28, 305]). While they directly address the problem of different possible definitions of parton level, it should also be said that they are far less flexible than Monte Carlo programs and not always able to provide equally good descriptions of the data.

One of the main issues is whether the fixed partonic final state of a NLO or NNLO prediction can match the parton shower in its ability to describe the experimental jet shape (minus any underlying event). NNLO calculations provide a better match to the parton shower predictions than do NLO ones, as might be expected from the additional gluon available to describe the jet shape. The hadronization predictions appear to work for both orders, but at an unknown accuracy. The impact of any error should fall as a power correction.

[9] A number of prescriptions also exist for setting the scale automatically, *e.g.* Refs. [294–298], eliminating uncertainties from scale variation, though not from the truncation of the perturbative series itself. Recently, there have also been studies of how to estimate uncertainties from missing higher orders that go beyond scale variations [299–301].

[10] In some circumstances, the scale in the denominator could be a smaller kinematic or physical scale that depends on the observable.

9.3 Experimental studies of QCD

Since we are not able to directly measure partons (quarks or gluons), but only hadrons and their decay products, a central issue for every experimental study of perturbative QCD is establishing a correspondence between observables obtained at the partonic and the hadronic level. The only theoretically sound correspondence is achieved by means of *infrared and collinear safe* quantities, which allow one to obtain finite predictions at any order of perturbative QCD.

As stated above, the simplest case of infrared- and collinear-safe observables are total cross sections. More generally, when measuring fully inclusive observables, the final state is not analyzed at all regarding its (topological, kinematical) structure or its composition. Basically the relevant information consists in the rate of a process ending up in a partonic or hadronic final state. In e^+e^- annihilation, widely used examples are the ratios of partial widths or branching ratios for the electroweak decay of particles into hadrons or leptons, such as Z or τ decays, (*cf.* Sec. 9.2.1). Such ratios are often favored over absolute cross sections or partial widths because of large cancellations of experimental and theoretical systematic uncertainties. The strong suppression of non-perturbative effects, $\mathcal{O}(\Lambda^4/Q^4)$, is one of the attractive features of such observables, however, at the same time, the sensitivity to radiative QCD corrections is small, which for example affects the statistical uncertainty when using them for the determination of the strong coupling constant. In the case of τ decays not only the hadronic branching ratio is of interest, but also moments of the spectral functions of hadronic tau decays, which sample different parts of the decay spectrum and thus provide additional information. Other examples of fully inclusive observables are structure functions (and related sum rules) in DIS. These are extensively discussed in Sec. 18 of this *Review*.

On the other hand, often the structure or composition of the final state are analyzed and cross sections differential in one or more variables characterizing this structure are of interest. Examples are jet rates, jet substructure, event shapes or transverse momentum distributions of jets or vector bosons in hadron collisions. The case of fragmentation functions, *i.e.* the measurement of hadron production as a function of the hadron momentum relative to some hard scattering scale, is discussed in Sec. 19 of this *Review*.

It is worth mentioning that, besides the correspondence between the parton and hadron level, also a correspondence between the hadron level and the actually measured quantities in the detector has to be established. The simplest examples are corrections for finite experimental acceptance and efficiencies. Whereas acceptance corrections essentially are of theoretical nature, since they involve extrapolations from the measurable (partial) to the full phase space, other corrections such as for efficiency, resolution and response are of experimental nature. For example, measurements of differential cross sections such as jet rates require corrections in order to relate, *e.g.*, the energy deposits in a calorimeter to the jets at the hadron level. Typically detector simulations and/or data-driven methods are used in order to obtain these corrections. Care should be taken here in order to have a clear separation between the parton-to-hadron level and hadron-to-detector level corrections. Finally, for the sake of an easy comparison to the results of other experiments and/or theoretical calculations, it is suggested to provide, whenever possible, measurements corrected for detector effects and/or all necessary information related to the detector response (*e.g.*, the detector response matrix).

9.3.1 *Hadronic final-state observables*

9.3.1.1 *Jets*

In hard interactions, final-state partons and hadrons appear predominantly in collimated bunches, which are generically called *jets*. To a first approximation, a jet can be thought of as a hard parton that has undergone soft and collinear showering and then hadronization. Jets are used both for testing our understanding and predictions of high-energy QCD processes, and also for identifying the hard partonic structure of decays of massive particles such as top quarks and W, Z and Higgs bosons.

In order to map observed hadrons onto a set of jets, one uses a *jet definition*. The mapping involves explicit choices: for example when a gluon is radiated from a quark, for what range of kinematics should the gluon be part of the quark jet, or instead form a separate jet? Good jet definitions are infrared and collinear safe, simple to use in theoretical and experimental contexts, applicable to any type of inputs (parton or hadron momenta, charged particle tracks, and/or energy deposits in the detectors) and lead to jets that are not too sensitive to non-perturbative effects.

An extensive treatment of the topic of jet definitions is given in Ref. [306] (for e^+e^- collisions) and Refs. [307–309]. Here we briefly review the two main classes: cone algorithms, extensively used at older hadron colliders, and sequential recombination algorithms, more widespread in e^+e^- and ep colliders and at the LHC.

Very generically, most (iterative) cone algorithms start with some seed particle i, sum the momenta of all particles j within a cone of opening-angle R, typically defined in terms of rapidity and azimuthal angle. They then take the direction of this sum as a new seed and repeat until the direction of the cone is stable, and call the contents of the resulting stable cone a jet if its transverse momentum is above some threshold $p_{t,\min}$. The parameters R and $p_{t,\min}$ should be chosen according to the needs of a given analysis.

There are many variants of the cone algorithm, and they differ in the set of seeds they use and the manner in which they ensure a one-to-one mapping of particles to jets, given that two stable cones may share particles ("overlap"). The use of seed particles is a problem w.r.t. infrared and collinear safety. Seeded algorithms are generally not compatible with higher-order (or sometimes even leading-order) QCD calculations, especially in multi-jet contexts, as well as potentially subject to large non-perturbative corrections and instabilities. Seeded algorithms (JetCLU, MidPoint, and various other experiment-specific iterative cone algorithms) are therefore to be deprecated. Such algorithms are not used at the LHC, but were at the Fermilab Tevatron, where data still provide useful information, for example for global PDF fits. A modern alternative is to use a seedless variant, SISCone [310].

Sequential recombination algorithms at hadron colliders (and in DIS) are characterized by a distance $d_{ij} = \min(k_{t,i}^{2p}, k_{t,j}^{2p})\Delta_{ij}^2/R^2$ between all pairs of particles i, j, where Δ_{ij} is their separation in the rapidity-azimuthal plane, $k_{t,i}$ is the transverse momentum w.r.t. the incoming beams, and R is a free parameter. At the LHC, R is typically in the range from 0.4 to 0.7. They also involve a "beam" distance $d_{iB} = k_{t,i}^{2p}$. One identifies the smallest of all the d_{ij} and d_{iB}, and if it is a d_{ij}, then i and j are merged into a new pseudo-particle (with some prescription, a recombination scheme, for the definition of the merged four-momentum). If the smallest distance is a d_{iB}, then i is removed from the list of particles and called a jet. As with cone algorithms, one usually considers only jets above some transverse-momentum threshold $p_{t,\min}$. The parameter p determines the kind of algorithm: $p = 1$ corresponds to the (*inclusive-*)k_t algorithm [215, 311, 312], $p = 0$ defines the *Cambridge-Aachen* algorithm [313, 314], while for the *anti-*k_t algorithm $p = -1$ [315]. All these variants are infrared and collinear safe. Whereas the former two lead to irregularly shaped jet boundaries, the latter results in cone-like boundaries. The *anti-*k_t algorithm has become the de-facto standard for the LHC experiments.

In e^+e^- annihilation the k_t algorithm [215] uses $y_{ij} = 2\min(E_i^2, E_j^2)(1-\cos\theta_{ij})/Q^2$ as distance measure between two particles/partons i and j and repeatedly merges the pair with smallest y_{ij}, until all y_{ij} distances are above some threshold $y_{\rm cut}$, the jet resolution parameter. Q is a measure of the overall hardness of the event. The (pseudo)-particles that remain at this point are called the jets. Here it is $y_{\rm cut}$ (rather than R and $p_{t,\min}$) that should be chosen according to the needs of the analysis. The two-jet rate in the k_t algorithm has the property that logarithms $\ln(1/y_{\rm cut})$ exponentiate. This is one reason why it is preferred over the earlier JADE algorithm [217], which uses the distance measure $y_{ij} = 2\,E_i\,E_j\,(1-\cos\theta_{ij})/Q^2$. Note that other variants of sequential recombination algorithms for e^+e^- annihilations, using different definitions of the resolution measure y_{ij}, exhibit much larger sensitivities to fragmentation and hadronization effects than the k_t and JADE algorithms [316]. Efficient implementations of the above algorithms are available through the *FastJet* package [317].

9.3.1.2 *Event Shapes*

Event-shape variables are functions of the four momenta of the particles in the final state and characterize the topology of an event's energy flow. They are sensitive to QCD radiation (and correspondingly to the strong coupling) insofar as gluon emission changes the shape of the energy flow.

The classic example of an event shape is the *Thrust* [318, 319] in e^+e^- annihilations, defined as

$$\hat{\tau} = \max_{\vec{n}_\tau} \frac{\sum_i |\vec{p}_i \cdot \vec{n}_\tau|}{\sum_i |\vec{p}_i|} \,, \tag{9.22}$$

where $\vec{p}_i$ are the momenta of the particles or the jets in the final-state and the maximum is obtained for the Thrust axis $\vec{n}_\tau$. In the Born limit of the production of a perfect back-to-back $q\bar{q}$ pair, the limit $\hat{\tau} \to 1$ is obtained, whereas a perfectly spherical many-particle configuration leads to $\hat{\tau} \to 1/2$. Further event shapes of similar nature have been extensively measured at LEP and at HERA, and for their definitions and reviews we refer to Refs. [1, 7, 305, 320, 321]. The energy-energy correlation function [322], namely the energy-weighted angular distribution of produced hadron pairs, and its associated asymmetry are further shape variables which have been studied in detail at e^+e^- colliders. For hadron colliders the appropriate modification consists in only taking the transverse momentum component [323]. More recently, the event shape *N-jettiness* has been proposed [324], that measures the degree to which the hadrons in the final state are aligned along N jet axes or the beam direction. It vanishes in the limit of exactly N infinitely narrow jets.

Phenomenological discussions of event shapes at hadron colliders can be found in Refs. [324–328]. Measurements of hadronic event-shape distributions have been published by CDF [329], ATLAS [330–335] and CMS [336–339].

Event shapes are used for many purposes. These include measuring the strong coupling, tuning the parameters of Monte Carlo programs, investigating analytical models of hadronization and distinguishing QCD events from events that might involve decays of new particles (giving event-shape values closer to the spherical limit).

9.3.1.3 *Jet substructure, quark vs. gluon jets*

Jet substructure, which can be resolved by finding subjets or by measuring jet shapes, is sensitive to the details of QCD radiation in the shower development inside a jet and has been extensively used to study differences in the properties of quark and gluon induced jets, strongly related to their different color charges. In general, there is clear experimental evidence that gluon jets have a softer particle spectrum and are "broader" than (light-) quark jets (as expected from perturbative QCD) when looking at observables such as the jet shape $\Psi(r/R)$. This is the fractional transverse momentum contained within a sub-cone of cone-size r for jets of cone-size R. It is sensitive to the relative fractions of quark and gluon jets in an inclusive jet sample and receives contributions from soft-gluon initial-state radiation and the underlying event. Therefore, it has been widely employed for validation and tuning of Monte Carlo parton-shower models. Furthermore, this quantity turns out to be sensitive to the modification of the gluon radiation pattern in heavy ion collisions (see *e.g.* Ref. [340]).

The most recent jet shape measurements using proton-proton collision data have been presented for inclusive jet samples [341–343] and for top-quark production [344]. Further discussions, references and summaries can be found in Refs. [321,345,346] and Sec. 4 of Ref. [347].

The use of jet substructure has also been investigated in order to distinguish QCD jets from jets that originate from hadronic decays of boosted massive particles (high-p_t electroweak bosons, top quarks and hypothesized new particles). A considerable number of experimental studies have been carried out with Tevatron and LHC data, in order to investigate on the performance of the

proposed algorithms for resolving jet substructure and to apply them to searches for new physics, as well as to the reconstruction of boosted top quarks, vector bosons and the Higgs boson. For reviews of this rapidly growing field, see sec. 5.3 of Ref. [307], Ref. [348] and Refs. [347,349–352]. Perhaps no other sub-field has benefited as much from machine learning techniques as the study of jet substructure. As a jet can have O(100) constituents each with kinematic and other information, jet substructure analysis is naturally a highly multivariate problem. Deep learning techniques can use all of the available information to study jets in their natural high dimensionality. Such techniques have not only improved discrimination between different final states/types of jets, but have also improved our understanding of perturbative QCD. See for example the review in Ref. [268].

9.3.2 *QCD measurements at colliders*

There exists a wealth of data on QCD-related measurements in e^+e^-, ep, pp, and $p\bar{p}$ collisions, to which a short overview like this would not be able to do any justice. Extensive reviews of the subject have been published in Refs. [320, 321] for e^+e^- colliders and in Ref. [353] for ep scattering, whereas for hadron colliders comprehensive overviews are given in, *e.g.*, Refs. [308, 346] and Refs. [2, 354–356].

Below we concentrate our discussion on measurements that are most sensitive to hard QCD processes with focus on jet production.

9.3.2.1 e^+e^- *colliders*

Analyses of jet production in e^+e^- collisions are mostly based on data from the JADE experiment at center-of-mass energies between 14 and 44 GeV, as well as on LEP collider data at the Z resonance and up to 209 GeV. The analyses cover the measurements of (differential or exclusive) jet rates (with multiplicities typically up to 4, 5 or 6 jets), the study of 3-jet events and particle production between the jets, as well as 4-jet production and angular correlations in 4-jet events.

Event-shape distributions from e^+e^- data have been an important input to the tuning of parton shower MC models, typically matched to matrix elements for 3-jet production. In general these models provide good descriptions of the available, highly precise data. Especially for the large LEP data sample at the Z peak, the statistical uncertainties are mostly negligible and the experimental systematic uncertainties are at the percent level or even below. These are usually dominated by the uncertainties related to the MC model dependence of the efficiency and acceptance corrections (often referred to as "detector corrections").

Observables measured in e^+e^- collisions have been used for determinations of the strong coupling constant (*cf.* Section 9.4 below) and for putting constraints on the QCD color factors (*cf.* Sec. 9.1 for their definitions), thus probing the non-Abelian nature of QCD. Typically, cross sections can be expressed as functions of these color factors, for example $\sigma = f(\alpha_s C_F, C_A/C_F, n_f T_R/C_F)$. Angular correlations in 4-jet events give sensitivity at leading order. Some sensitivity to these color factors, although only at NLO, is also obtained from event-shape distributions. Scaling violations of fragmentation functions and the different subjet structure in quark and gluon induced jets also give access to these color factors. In order to extract absolute values, *e.g.* for C_F and C_A, certain assumptions have to be made for other parameters, such as T_R, n_f or α_s, since typically only combinations (ratios, products) of all the relevant parameters appear in the perturbative predictions. A compilation of results [321] quotes world average values of $C_A = 2.89 \pm 0.03(\text{stat}) \pm 0.21(\text{syst})$ and $C_F = 1.30 \pm 0.01(\text{stat}) \pm 0.09(\text{syst})$, with a correlation coefficient of 82%. These results are in perfect agreement with the expectations from SU(3) of $C_A = 3$ and $C_F = 4/3$.

9.3.2.2 *DIS and photoproduction*

Jet measurements in ep collisions, both in the DIS and photoproduction regimes, allow for tests of QCD factorization (as they involve only one initial state proton and thus one PDF function), and provide sensitivity to both the gluon distribution and to the strong coupling constant. Calculations are available at NNLO in both regimes [357, 358]. Experimental uncertainties of the order of 5–10% have been achieved, mostly dominated by the jet energy scale, whereas statistical uncertainties are negligible to a large extent. For comparison to theoretical predictions, at large jet p_t the PDF uncertainty dominates the theoretical uncertainty (typically of order 5–10%, in some regions of phase space up to 20%), therefore jet observables become useful inputs for PDF fits.

In general, the data are well described by the NLO and NNLO matrix-element calculations, combined with DGLAP evolution equations, in particular at large Q^2 and central values of jet pseudo-rapidity. At low values of Q^2 and x, in particular for large jet pseudo-rapidities, certain features of the data have been interpreted as requiring BFKL-type evolution, though the predictions for such schemes are still limited. It is worth noting that there is lack of consensus throughout the community regarding this need of BFKL-evolution at currently probed x, Q^2 values, and an alternative approach [359], which implements the merging of LO matrix-element based event generation with a parton shower (using the SHERPA framework), successfully describes the data in all kinematical regions, including the low Q^2, low x domain. At moderately small x values, it should perhaps not be surprising that the BFKL approach and fixed-order matrix-element merging with parton showers may both provide adequate descriptions of the data, because some part of the multi-parton phase space that they model is common to both approaches.

In the case of photoproduction, a wealth of measurements with low p_t jets were performed in order to constrain the photon content of the proton. The uncertainties related to such photon PDFs play a minor role at high jet p_t, which has allowed for precise tests of pQCD calculations.

A few examples of recent measurements can be found in Refs. [360–364] for photoproduction and in Refs. [365–374] for DIS.

9.3.2.3 *Hadron-hadron colliders*

The spectrum of observables and the number of measurements performed at hadron colliders is enormous, probing many regions of phase space and covering a huge range of cross sections, as illustrated in Fig. 9.1 for the case of the ATLAS and CMS experiments at the LHC. In general, the theory agreement with data is excellent for a wide variety of processes, indicating the success of perturbative QCD with the PDF and strong coupling inputs. For the sake of brevity, in the following only certain classes of those measurements will be discussed, which allow addressing particular aspects of the various QCD studies performed. Most of our discussion will focus on LHC results, which are available for center-of-mass energies of 2.76, 5, 7, 8 and 13 TeV with integrated luminosities of up to 140 fb^{-1}. Generally speaking, besides representing a general test of the standard model and QCD in particular, these measurements serve several purposes, such as: (i) probing pQCD and its various approximations and implementations in MC models, in order to quantify the order of magnitude of not yet calculated contributions and to gauge their precision when used as background predictions, or (ii) extracting/constraining model parameters such as the strong coupling constant or PDFs. Indeed, data from the LHC is becoming increasingly important for the determination of both, PDFs and the strong coupling constant.

The final states measured at the LHC include single, double and triple gauge boson production, top production (single top, top pair and four top production), Higgs boson production, alone and in conjunction with a W or Z boson, and with a top quark pair. Many/most of these events are accompanied by additional jets. So far only relatively loose limits have been placed on double Higgs production. The volume of LHC results prohibits a comprehensive description in this *Review*; hence, only a few highlights will be presented.

Among the most important cross sections measured, and the one with the largest dynamic range, is the inclusive jet spectrum as a function of the jet transverse momentum (p_t), for several rapidity regions and for p_t up to 700 GeV at the Tevatron and ~ 3.5 TeV at the LHC. It is worth noting that this upper limit in p_t corresponds to a distance scale of $\sim 10^{-19}$ m: no other experiment so far is able to directly probe smaller distance scales of nature than this measurement. The Tevatron inclusive jet measurements in Run 2 (Refs. [377–380]) were carried out with the MidPoint jet clustering algorithm (or its equivalent) and with the k_t jet

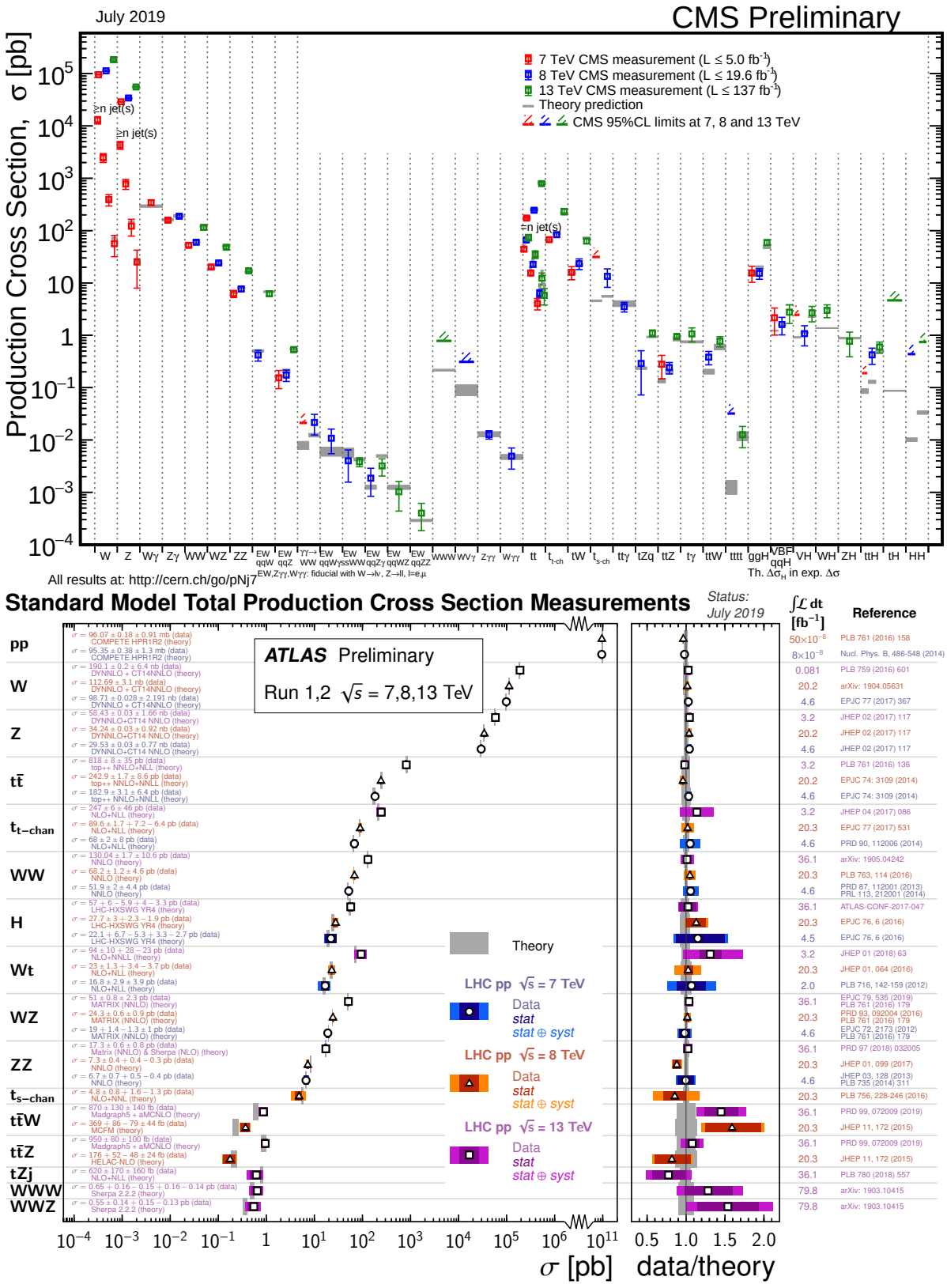

Figure 9.1: Overview of cross section measurements for a wide class of processes and observables, as obtained by the CMS [375] and ATLAS [376] experiments at the LHC, for centre-of-mass energies of 7, 8 and 13 TeV. Also shown are the theoretical predictions and their uncertainties.

clustering algorithm. Most of the LHC measurements use the *anti-k_t* algorithm, with a variety of jet radii. The use of multiple jet radii in the same analysis allows a better understanding of the underlying QCD dynamics. Measurements by ALICE, ATLAS and CMS have been published in Refs. [381–389].

In general, we observe a good description of the data by the NLO and NNLO QCD predictions over about 11 orders of magnitude in cross section. as long as care is taken for the form of

the central scale choice [303]. The experimental systematic uncertainties are dominated by the jet energy scale uncertainty, quoted to be in the range of a few percent (see for instance the review in Ref. [390]), leading to uncertainties of $\sim 5-30\%$ on the cross section, increasing with p_t and rapidity. The PDF uncertainties dominate the theoretical uncertainty at large p_t and rapidity. In fact, inclusive jet data are one of the most important inputs to global PDF fits, in particular for constraining the high-x gluon PDF [77, 391]. Constraints on the PDFs can also be obtained from ratios of inclusive cross sections at different center-of-mass energies [382, 387]. In general, ratios of jet cross sections are a means to (at least partially) cancel the jet energy scale uncertainties and thus provide jet observables with significantly improved precision.

Dijet events are analyzed in terms of their invariant mass or average dijet p_t and angular distributions, which allows for tests of NLO and NNLO QCD predictions (see *e.g.* Refs. [386,392,393] for recent LHC results), and for setting stringent limits on deviations from the Standard Model, such as quark compositeness or contact interactions (some examples can be found in Refs. [389,394–400]). Furthermore, dijet azimuthal correlations between the two leading jets, normalized to the total dijet cross section, are an extremely valuable tool for studying the spectrum of gluon radiation in the event. The azimuthal separation of the two leading jets is sensitive to multi-jet production, avoiding at the same time large systematic uncertainties from the jet energy calibration. For example, results from the Tevatron [401, 402] and the LHC [335, 403–407] show that the LO (non-trivial) prediction for this observable, with at most three partons in the final state, is not able to describe the data for an azimuthal separation below $2\pi/3$, where NLO contributions (with 4 partons) restore the agreement with data. In addition, this observable can be employed to tune Monte Carlo predictions of soft gluon radiation. Further examples of dijet observables that probe special corners of phase space are those that involve forward (large rapidity) jets and where a large rapidity separation, possibly also a rapidity gap, is required between the two jets. Reviews of such measurements can be found in Ref. [346], showing that no single prediction is capable of describing the data in all phase-space regions. In particular, no conclusive evidence for BFKL effects in these observables has been established so far.

Beyond dijet final states, measurements of the production of three or more jets, including cross section ratios, have been performed (see Refs. [346,408] for recent reviews), as a means of testing perturbative QCD predictions, determining the strong coupling constant (at NLO precision so far), and probing/tuning MC models, in particular those combining multi-parton matrix elements with parton showers.

W and Z production serve as benchmark cross sections at the LHC. The large boson mass provides a stability for the perturbative predictions which results in better theoretical precision. In terms of experimental precision, measurements of inclusive vector boson (W, Z) production provide the most precisely determined observables at hadron colliders so far. This is because the experimental signatures are based on leptons which are measured much more accurately than jets or photons. At the LHC [409–416], the dominant uncertainty stems from the luminosity determination ($\leq$2–4%), while other uncertainties (*e.g.* statistics, lepton efficiencies) are controlled at the $\sim$0.5–3% level. The uncertainty from the acceptance correction of about $\sim$1–2% can be reduced by measuring so-called fiducial cross sections, ie. by applying kinematic cuts also to the particle level of the theoretical predictions. A further reduction or even complete elimination of particular uncertainties (*e.g.* luminosity) is achieved by measuring cross section ratios (W/Z or W^+/W^-) or differential distributions that are normalised to the inclusive cross section. On the theory side, as discussed earlier in this *Review*, the production of these color-singlet states has been calculated up to NNLO accuracy, with some progress towards N^{3}LO. Since the dominant theoretical uncertainty is related to the choice of PDFs, these high-precision data provide useful handles for PDF determinations.

Further insights are obtained from measurements of differential vector boson production, as a function of the invariant dilepton mass, the boson's rapidity or its transverse momentum. For example, the dilepton invariant mass distribution has been measured [417–422] for masses between 15 and 3000 GeV, covering more than 8 orders of magnitude in cross section. NNLO QCD predictions, together with modern PDF sets and including higher-order electroweak and QED final-state radiation corrections, describe the data to within 5–10% over this large range, whereas NLO predictions show larger deviations, unless matched to a parton shower.

Similar conclusions can be drawn from the observed rapidity distribution of the dilepton system (see *e.g.* Refs. [409, 418, 423]) or, in the case of W production, from the observed charged lepton rapidity distribution and its charge asymmetry. The latter is particularly sensitive to differences among PDF sets [409, 424–426], also thanks to the high precision achieved by the ATLAS and CMS experiments for central rapidity ranges. These measurements are nicely extended to the very forward region, up to 4.5 in lepton rapidity, by the LHCb experiment.

An overview of this kind of measurements can be found in Ref. [346]. There one can also find a discussion of and references to LHC results from studies of the vector boson's transverse momentum distribution, p_t^V (see also Refs. [427–429]). This observable covers a wide kinematic range and probes different aspects of higher-order QCD effects. It is sensitive to jet production in association with the vector boson, without suffering from the large jet energy scale uncertainties. In the p_t^V region of several tens of GeV to over 1 TeV, the NNLO predictions for V+jet [11] can be used to predict the high p_t boson transverse cross section. The NNLO predictions agree with the data to within about 10%, and agree somewhat better at high transverse momentum than do the NLO predictions [430]. At transverse momenta below $\sim$20 GeV, the fixed-order predictions fail and soft-gluon resummation is needed to restore the agreement with data. The soft gluon resummation can either be performed analytically, or effectively using parton showering implemented in Monte Carlo programs.

The addition of jets to the final state extends the kinematic range as well as increasing the complexity of the calculation/measurements.[12] The number of results obtained both at the Tevatron and at the LHC is extensive. Recent summaries can be found in Refs. [346, 432]. Some more recent results can be found in Refs. [430, 433–436].

The measurements cover a very large phase space, *e.g.* with jet transverse momenta between 30 GeV and $\sim$ 1.5 TeV and jet rapidities up to $|y| < 4.4$ [430]. Jet multiplicities as high as seven jets accompanying the vector boson have already been probed at the LHC, together with a substantial number of other kinematical observables, such as angular correlations among the various jets or among the jets and the vector boson, or the sum of jet transverse momenta, H_T. Whereas the jet p_t and H_T distributions are dominated by jet energy scale uncertainties at levels similar to those discussed above for inclusive jet production, angular correlations and jet multiplicity ratios have been measured with a precision of $\sim$ 10%, see *e.g.* Refs. [337, 437].

NLO calculations for up to five jets [438] in addition to the vector boson are in good agreement with the data over that phase space, where the calculations are applicable; that is, one can not expect such predictions to work for *e.g.* the p_t distribution of the n + 1st jet with $V + n$ jets calculated at NLO. However, with the higher kinematic reach achieved by the LHC experiments, some more detailed observations can be made. NLO fixed-order predictions describe the W boson p_t distribution and the lead jet p_t distribution reasonably well at transverse momenta below around 500 GeV, but predict smaller cross sections than the data at higher transverse momenta. Predictions for V+jet at NNLO improve the description of the data. MC models that implement parton shower matching to matrix elements (either at LO or NLO) have mixed results.

The challenges get even more severe in the case of vector boson plus heavy quark (b, c) production, both because of theoretical

[11] For these calculations, there is a requirement of the presence of a jet, but the p_t cut is typically small (30 GeV) compared to the high p_t region being discussed here.

[12] For reliable predictions, the scale used in the higher order calculations should be proportional to the sum of the transverse momenta of all of the objects in the final state [431].

issues (an additional scale is introduced by the heavy quark mass and different schemes exist for the handling of heavy quarks and their mass effects in the initial and/or final state) and because of additional experimental uncertainties related to the heavy-flavour tagging. A review of heavy quark production at the LHC can be found in Ref. [439]. There it is stated that studies of b-jet production with or without associated W and Z bosons reveal the di-b-jet p_t and mass spectra to be well modelled, within experimental and theoretical uncertainties, by most generators on the market. However, sizable differences between data and predictions are seen in the modelling of events with single b jets, particularly at large b-jet p_t, where gluon splitting processes become dominant, as also confirmed by studies of b-hadron and b-jet angular correlations.

The precision reached in photon measurements is in between that for lepton and jet measurements. The photon 4-vectors can be measured at about the same precision as the lepton 4-vectors in Drell-Yan production, but there are greater challenges encountered in photon reconstruction (for example isolation) and in purity determination. Note, though, that the photon purity approaches unity as the photon p_t increases. At high p_t, it becomes increasingly difficult for a jet to fragment into an isolated neutral electromagnetic cluster which mimics the photon signature. The inclusive photon cross section can be measured [392, 440–443], as well as the production of a photon accompanied by one or more jets [443–445, 445–448]. The kinematic range for photon production is less than that for jet production because of the presence of the electromagnetic coupling, but still reaches about 2 TeV. Better agreement is obtained with NNLO predictions for photon production than for NLO predictions, except when the latter are matched to matrix element plus parton shower predictions. Photon production in association with a heavy-flavor jet is a useful input for the determination of the b and c quark PDFs [449].

Electroweak corrections are expected to become more and more relevant now that the TeV energy range starts to be explored. For example, such corrections were found [450] to be sizable (tens of percent) when studying the ratio $(d\sigma^{\gamma}/dp_t)/(d\sigma^{Z}/dp_t)$ in $\gamma\,(Z)$+jet production, p_t being the boson's transverse momentum, and might account for (some of) the differences observed in a CMS measurement [451] of this quantity.

A number of interesting developments, in terms of probing higher-order QCD effects, have occurred in the sector of diboson production, in particular for the WW and $\gamma\gamma$ cases. Regarding the former, an early disagreement of about 10% between the LHC measurements and the NLO predictions had led to a number of speculations of possible new physics effects in this channel. However, more recent ATLAS and CMS measurements [452–455] are in agreement with the NNLO prediction [85]. The statistical reach of the LHC has resulted in evidence for triple massive gauge boson production [456].

In the case of diphoton production, ATLAS [457, 458] and CMS [459] have provided accurate measurements, in particular for phase-space regions that are sensitive to radiative QCD corrections (multi-jet production), such as small azimuthal photon separation. While there are large deviations between data and NLO predictions in this region, a calculation [178] at NNLO accuracy manages to mostly fill this gap. This is an interesting example where scale variations can not provide a reliable estimate of missing contributions beyond NLO, since at NNLO new channels appear in the initial state (gluon fusion in this case). These missing channels can be included in a matrix element plus parton shower calculation in which two additional jets are included at NLO. The result is a similar level of agreement as that obtained at NNLO. Three photon production has also been measured [460].

In terms of heaviest particle involved, top-quark production at the LHC has become an important tool for probing higher-order QCD calculations, thanks to very impressive achievements both on the experimental and theoretical side, as extensively summarised in Ref. [461]. Regarding $t\bar{t}$ production, the most precise inclusive cross section measurements are achieved using the dilepton ($e\,\mu$) final state, with a total uncertainty of 4% [462–465]. This is of about the same size as the uncertainty on the most advanced theoretical predictions [84, 466–468], obtained at NNLO with additional soft-gluon resummation at NNLL accuracy [469]. There is excellent agreement between data and the QCD predictions.

The $t\bar{t}$ final state allows multiple observables to be measured. A large number of differential cross section measurements have been performed at 7, 8 and 13 TeV centre-of-mass energy, studying distributions such as the top-quark p_t and rapidity, the transverse momentum and invariant mass of the $t\bar{t}$ system (probing scales up to the TeV range), or the number of additional jets. These measurements have been compared to a wide range of predictions, at fixed order up to NNLO as well as using LO or NLO matrix elements matched to parton showers. Each of the observables provides information on the high x gluon and have been used in global PDF fits. While in general there is reasonable agreement observed with data, most MC simulations predict a somewhat harder top-quark p_t distribution than seen in data.

Thanks to both the precise measurements of, and predictions for, the inclusive top-pair cross section, which is sensitive to the strong coupling constant and the top-quark mass, this observable has been used to measure the strong coupling constant at NNLO accuracy from hadron collider data [470, 471] (*cf.* Section 9.4 below), as well as to obtain a measurement of the top-quark's pole mass without employing direct reconstruction methods [470, 472, 473].

The Higgs boson lends itself to being a tool for QCD studies, especially as the dominant production mechanism is gg fusion, which is subject to very large QCD corrections. Higgs boson production has been measured in the ZZ, $\gamma\gamma$, WW and $\tau\tau$ decay channels. The experimental cross section is now known with a precision approaching 10% [474, 475], similar to the size of the theoretical uncertainty [92], of which the PDF+α_s uncertainty is the largest component. The experimental precision has allowed detailed fiducial and differential cross section measurements. For example, with the diphoton final state, the transverse momentum of the Higgs boson can be measured out to 350-400 GeV [476, 477], where top quark mass effects become important. The production of a Higgs boson with up to 4 jets has been measured [476, 478]. The experimental cross sections have been compared to NNLO predictions (for $H+\geq 1$ jet), NLO for 2 and 3 jets, and NNLO+NNLL for the transverse momentum distribution. In addition, finite top quark mass effects have been taken into account at NLO. The use of the boosted $H \to b\bar{b}$ topology allows probes of Higgs boson transverse momenta on the order of 600 GeV [478]. So far the agreement with the perturbative QCD corrections is good.

9.4 Determinations of the strong coupling constant

Beside the quark masses, the only free parameter in the QCD Lagrangian is the strong coupling constant α_s. The coupling constant in itself is not a physical observable, but rather a quantity defined in the context of perturbation theory, which enters predictions for experimentally measurable observables, such as R in Eq. (9.7). The value of the strong coupling constant must be inferred from such measurements and is subject to experimental and theoretical uncertainties. The incomplete knowledge of α_s propagates into uncertainties in numerous precision tests of the Standard Model. Here we present an update of the 2016 PDG average value of $\alpha_s(M_Z^2)$ and its uncertainty [479], which were retained in the 2018 edition of this *Review* [480].[13]

Many experimental observables are used to determine α_s. A number of recent determinations are collected in Ref. [484]. Further discussions and considerations on determinations of α_s can also be found in Refs. [485, 486]. Such considerations include:

- The observable's sensitivity to α_s as compared to the experimental precision. For example, for the e^+e^- cross section to hadrons (*cf.* R in Sec. 9.2.1), QCD effects are only a small correction, since the perturbative series starts at order α_s^0; 3-jet production or event shapes in e^+e^- annihilations are directly sensitive to α_s since they start at order α_s; the hadronic decay width of heavy quarkonia, $\Gamma(\Upsilon \to \text{hadrons})$, is very sensitive to α_s since its leading order term is $\propto \alpha_s^3$.

[13] ♯ The time evolution of α_s combinations can be followed by consulting Refs. [481–483] as well as earlier editions of this *Review*.

- The accuracy of the perturbative prediction, or equivalently of the relation between α_s and the value of the observable. The minimal requirement is generally considered to be an NLO prediction. Some observables (many inclusive ones as well as 3-jet rates and event shapes in e^+e^- collisions) are known to NNLO since quite some time. Recent additions to the list of processes calculated up to NNLO comprise inclusive jet and dijet production in DIS and pp or $p\bar{p}$ collisions. Likewise, $t\bar{t}$ and W/Z+jet production cross sections have been computed up to NNLO for pp and $p\bar{p}$ scattering. The e^+e^- hadronic cross section and τ branching fraction to hadrons are even known to N^{3}LO, where one denotes the LO as the first non-trivial term. In certain cases, fixed-order predictions are supplemented with resummation. The precise magnitude of the associated theory uncertainties usually is estimated as discussed in Sec. 9.2.4.
- The size of non-perturbative effects. Sufficiently inclusive quantities, like the e^+e^- cross section to hadrons, have small non-perturbative contributions $\sim \Lambda^4/Q^4$. Others, such as event-shape distributions, have typically contributions $\sim \Lambda/Q$.
- The scale at which the measurement is performed. An uncertainty δ on a measurement of $\alpha_s(Q^2)$, at a scale Q, translates to an uncertainty $\delta' = (\alpha_s^2(M_Z^2)/\alpha_s^2(Q^2)) \cdot \delta$ on $\alpha_s(M_Z^2)$. For example, this enhances the already important impact of precise low-Q measurements, such as from τ decays, in combinations performed at the M_Z scale.

The selection of results from which to determine the world average value of $\alpha_s(M_Z^2)$ is restricted to those that are

- published in a peer-reviewed journal at the time of writing this report,
- based on the most complete perturbative QCD predictions of at least NNLO accuracy,
- accompanied by reliable estimates of all experimental and theoretical uncertainties.

We note that all determinations of $\alpha_s(M_Z^2)$ entering the average of the lattice gauge community as summarised comprehensively in the FLAG2019 report [487] are published in peer-reviewed journals, although the FLAG report itself that only describes the averaging procedure is not.

We also note that a prediction in perturbative QCD for the determination of $\alpha_s(M_Z^2)$ at NNLO accuracy requires the calculation of at least three consecutive terms in powers $p > 0$ of α_s^p. Although this condition is fulfilled, measurements from jet production in DIS and at hadron colliders (with one exception) are still excluded, because the determination of $\alpha_s(M_Z^2)$ has not yet been upgraded to NNLO. Nevertheless, the NLO analyses will be discussed in this *Review*, as they are important ingredients for the experimental evidence of the energy dependence of α_s, *i.e.* for Asymptotic Freedom, one of the key features of QCD.

In order to calculate the world average value of $\alpha_s(M_Z^2)$, as in earlier editions we apply an intermediate step of pre-averaging results within the sub-fields now labelled "Hadronic τ decays and low Q^2 continuum" (τ decays and low Q^2), "Heavy quarkonia decays" ($Q\bar{Q}$ bound states), "Deep-inelastic scattering and global PDF fits" (DIS & PDF fits), "Hadronic final states of e^+e^- annihilations" (e^+e^- jets & shapes), "Hadron collider results" (hadron collider), and "Electroweak precision fit" (electroweak) as explained in the following sections. For each sub-field, the *unweighted average* of all selected results is taken as the pre-average value of $\alpha_s(M_Z^2)$, and the unweighted average of the quoted uncertainties is assigned to be the respective overall error of this pre-average.[14] At variance with previous reviews, for the "Lattice QCD" (lattice) sub-field we do not perform a pre-averaging; instead, we adopt for this sub-field the FLAG2019 average value and uncertainty derived in Ref. [487].

Assuming that the six sub-fields (excluding lattice) are largely independent of each other, we determine a non-lattice world average value using a 'χ^2 *averaging*' method. In a last step we perform an unweighted average of the values and uncertainties of $\alpha_s(M_Z^2)$ from our non-lattice result and the lattice result presented in the FLAG 2019 report [487].

9.4.1 *Hadronic τ decays and low Q^2 continuum:*

Based on complete N^{3}LO predictions [36], analyses of the τ hadronic decay width and spectral functions have been performed, *e.g.* in Refs. [36,488–493], and lead to precise determinations of α_s at the energy scale of M_τ^2. They are based on different approaches to treat perturbative and non-perturbative contributions, the impacts of which have been a matter of intense discussions since a long time, see *e.g.* Refs. [492–495]. In particular, in τ decays there is a significant difference between results obtained using fixed-order (FOPT) or contour improved perturbation theory (CIPT), such that analyses based on CIPT generally arrive at larger values of $\alpha_s(M_\tau^2)$ than those based on FOPT. In addition, some results show differences in $\alpha_s(M_\tau^2)$ between different groups using the same data sets and perturbative calculations, most likely due to different treatments of the non-perturbative contributions, *cf.* Ref. [493] with Refs. [492, 496].

Here, we largely keep the same input calculations as in the previous review, with only the following changes. The result of Ref. [492] has been replaced by the one of Ref. [495]. From Ref. [493] we use the values resulting from a combination of ALEPH and OPAL data instead of ALEPH data alone. Moreover, we include the new α_s determination obtained from $R(s)$ below the charm threshold [497]. Here, the average from the FOPT and CIPT results gives $\alpha_s(M_\tau^2) = 0.301 \pm 0.019$, where the difference between the two amounts to 2% at m_τ. This corresponds to $\alpha_s(M_Z^2) = 0.1162 \pm 0.0025$.

In summary, we determine the pre-average value of $\alpha_s(M_Z^2)$ for this sub-field from studies that employ both FOPT and CIPT expansions, and that account for the difference among these in the quoted overall uncertainty: $\alpha_s(M_Z^2) = 0.1202 \pm 0.0019$ [36], $\alpha_s(M_Z^2) = 0.1199 \pm 0.0015$ [496], $\alpha_s(M_Z^2) = 0.1175 \pm 0.0017$ [493], $\alpha_s(M_Z^2) = 0.1197 \pm 0.0015$ [495], and $\alpha_s(M_Z^2) = 0.1162 \pm 0.0025$ [497]. Additionally, we include the result from τ decay and lifetime measurements, obtained in Sec. *Electroweak Model and constraints on New Physics* of the 2018 edition of this *Review*, $\alpha_s(M_Z^2) = 0.1184 \pm 0.0019$. The latter result, being a global fit of τ data, involve some correlations with the other extractions of this category. However, since we perform an unweighted average of the central value and uncertainty, we do not need to worry about double counting.

All these results are summarised in Fig. 9.2. Determining the unweighted average of the central values and their overall uncertainties, we arrive at $\alpha_s(M_Z^2) = 0.1187 \pm 0.0018$, which we will use as the first input for determining the world average value of $\alpha_s(M_Z^2)$. This corresponds to $\alpha_s(M_\tau^2) = 0.325 \pm 0.016$.

9.4.2 *Heavy quarkonia decays:*

For a long time, the best determination of the strong coupling constant from radiative Υ decays was the one of Ref. [498], which resulted in $\alpha_s(M_Z^2) = 0.119^{+0.006}_{-0.005}$. This determination is based on QCD at NLO only, so it will not be considered for the final extraction of the world average value of α_s; it is, however, an important ingredient for the demonstration of Asymptotic Freedom as given in Fig. 9.3. More recently, two determinations have been performed [499, 500] that are based on N^{3}LO accurate predictions. Reference [499] performs a simultaneous fit of the strong coupling and the bottom mass $\overline{m}_b$, including states with principal quantum number up to $n \leq 2$ in order to break the degeneracy between α_s and $\overline{m}_b$, finding $\alpha_s(M_Z^2) = 0.1178 \pm 0.0051$. Reference [500] instead uses as input of the fit the renormalon-free energy combination of B_c and bottomonium η_b and charmonium η_c, $M_{B_c} - M_{\eta_b}/2 - M_{\eta_c}/2$, which is weakly dependent on the heavy quark masses, but shows a good dependence on α_s. Using this observable, they obtain $\alpha_s(M_Z^2) = 0.1178 \pm 0.0051$. These two determinations satisfy our criteria to be included in the world

[14] In the previous review, if this error appeared to be smaller than the unweighted standard deviation - *i.e.* the *spread* - of the results, the standard deviation was taken as the overall uncertainty instead. This was done in order to arrive at an unbiased estimator of the average value of $\alpha_s(M_Z^2)$ from a given sub-field, and to avoid that singular, optimistic estimates of systematic uncertainties unduly bias the uncertainty of the sub-field average. Here we find that, for all six sub-fields, the quoted error is larger than the standard deviation.

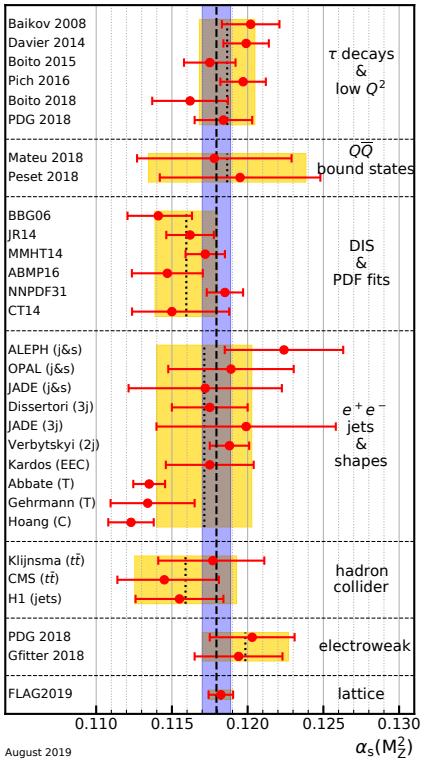

Figure 9.2: Summary of determinations of $\alpha_s(M_Z^2)$ from the seven sub-fields discussed in the text. The yellow (light shaded) bands and dotted lines indicate the pre-average values of each sub-field. The dashed line and blue (dark shaded) band represent the final world average value of $\alpha_s(M_Z^2)$.

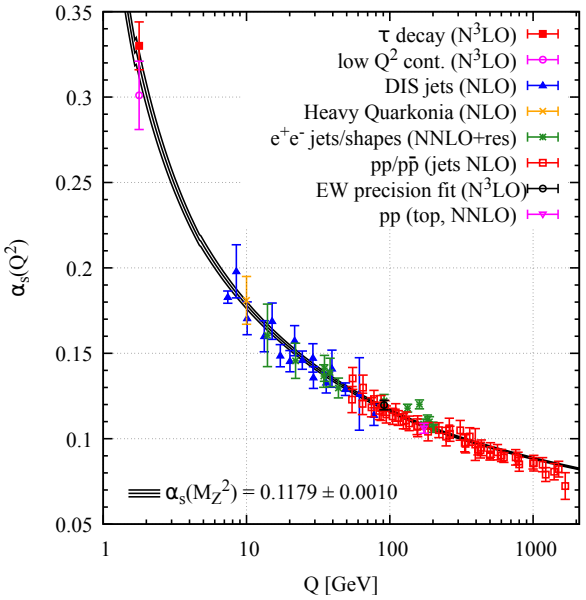

Figure 9.3: Summary of measurements of α_s as a function of the energy scale Q. The respective degree of QCD perturbation theory used in the extraction of α_s is indicated in brackets (NLO: next-to-leading order; NNLO: next-to-next-to-leading order; NNLO+res.: NNLO matched to a resummed calculation; N^{3}LO: next-to-NNLO).

average and are at the moment the only input values in the Heavy-quarkonia category. Their unweighted combination leads to the pre-average for this category of $\alpha_s(M_Z^2) = 0.1187 \pm 0.0052$. We note that, while we include this result in our final average, because of the large uncertainty of the two determinations in this category, removing this pre-average would not change the final result within the quoted uncertainty.

9.4.3 *Deep-inelastic scattering and global PDF fits:*

Studies of DIS final states have led to a number of precise determinations of α_s: a combination [501] of precision measurements at HERA, based on NLO fits to inclusive jet cross sections in neutral current DIS at high Q^2, provides combined values of α_s at different energy scales Q, as shown in Fig. 9.3, and quotes a combined result of $\alpha_s(M_Z^2) = 0.1198 \pm 0.0032$. A more recent study of multijet production [373], based on improved reconstruction and data calibration, confirms the general picture, albeit with a somewhat smaller value of $\alpha_s(M_Z^2) = 0.1165 \pm 0.0039$, still at NLO. An evaluation of inclusive jet production, including *approximate* NNLO contributions [502], reduces the theoretical prediction for jet production in DIS, improves the description of the final HERA data in particular at high photon virtuality Q^2 and increases the central fit value of the strong coupling constant.

Another class of studies, analyzing structure functions at NNLO QCD (and partly beyond), provide results that serve as relevant inputs for the world average of α_s. Most of these studies do *not*, however, explicitly include estimates of theoretical uncertainties when quoting fit results of α_s. In such cases we add, in quadrature, half of the difference between the results obtained in NNLO and NLO to the quoted errors: a combined analysis of non-singlet structure functions from DIS [503], based on QCD predictions up to N^{3}LO in some of its parts, results in $\alpha_s(M_Z^2) = 0.1141 \pm 0.0022$ (BBG). Studies of singlet and non-singlet structure functions, based on NNLO predictions, result in $\alpha_s(M_Z^2) = 0.1162 \pm 0.0017$ [504] (JR14). The AMBP group [505, 506] determined a set of parton distribution functions using data from HERA, NOMAD, CHORUS, from Tevatron and the LHC for the Drell-Yan process and the hadro-production of single-top and top-quark pairs and determined $\alpha_s(M_Z^2) = 0.1147 \pm 0.0024$ [505]. The MMHT group [507], also including hadron collider data, determined a new set of parton density functions (MMHT2014) together with $\alpha_s(M_Z^2) = 0.1172 \pm 0.0013$. Similarly, the CT group [508] determined the CT14 parton density set together with $\alpha_s(M_Z^2) = 0.1150^{+0.0036}_{-0.0024}$. The NNPDF group [509] presented NNPDF3.1 parton distribution functions together with $\alpha_s(M_Z^2) = 0.1185 \pm 0.0012$.

We note that criticism has been expressed on some of the above extractions. Among the issues raised, we mention the neglect of singlet contributions at $x \geq 0.3$ in pure non-singlet fits [510], the impact and detailed treatment of particular classes of data in the fits [510, 511], possible biases due to insufficiently flexible parametrizations of the PDFs [512] and the use of a fixed-flavor number scheme [513, 514].

Summarizing the results from world data on structure functions, taking the *unweighted average* of the central values and errors of all selected results, leads to a pre-average value of $\alpha_s(M_Z^2) = 0.1161 \pm 0.0018$, see Fig. 9.2.

9.4.4 *Hadronic final states of e^+e^- annihilations:*

Re-analyses of event shapes in e^+e^- annihilation (j&s), measured around the Z peak and at LEP2 center-of-mass energies up to 209 GeV, using NNLO predictions matched to NLL resummation and Monte Carlo models to correct for hadronization effects, resulted in $\alpha_s(M_Z^2) = 0.1224 \pm 0.0039$ (ALEPH) [515], with a dominant theoretical uncertainty of 0.0035, and in $\alpha_s(M_Z^2) = 0.1189 \pm 0.0043$ (OPAL) [516]. Similarly, an analysis of JADE data [517] at center-of-mass energies between 14 and 46 GeV gives $\alpha_s(M_Z^2) = 0.1172 \pm 0.0051$, with contributions from the hadronization model and from perturbative QCD uncertainties of 0.0035 and 0.0030, respectively. Precise determinations of α_s from 3-jet production alone (3j), at NNLO, resulted in $\alpha_s(M_Z^2) = 0.1175 \pm 0.0025$ [518] from ALEPH data and in $\alpha_s(M_Z^2) = 0.1199 \pm 0.0059$ [519] from JADE. A recent determination is based on an NNLO+NNLL accurate calculation that allows to fit the region of lower 3-jet rate (2j) using data collected at LEP and PETRA at different energies. This fit gives $\alpha_s(M_Z^2) = 0.1188 \pm 0.0013$ [520], where the dominant uncertainty is the hadronization uncertainty, which is estimated

from Monte Carlo simulations. A fit of energy-energy-correlation (EEC) also based on an NNLO+NNLL calculation together with a Monte Carlo based modelling of hadronization corrections gives $\alpha_s(M_Z^2) = 0.1175 \pm 0.0029$ [521]. These results are summarized in the upper seven rows of the e^+e^- sector of Fig. 9.2.

Another class of α_s determinations is based on analytic modelling of non-perturbative and hadronization effects, rather than on Monte Carlo models [522–525], using methods like power corrections, factorization of soft-collinear effective field theory, dispersive models and low scale QCD effective couplings. In these studies, the world data on Thrust distributions (T), or - most recently - C-parameter distributions (C), are analysed and fitted to perturbative QCD predictions at NNLO matched with resummation of leading logs up to N^3LL accuracy, see Sec. 9.2.3.3. The results are $\alpha_s(M_Z^2) = 0.1135 \pm 0.0011$ [523] and $\alpha_s(M_Z^2) = 0.1134^{+0.0031}_{-0.0025}$ [524] from Thrust, and $\alpha_s(M_Z^2) = 0.1123 \pm 0.0015$ [525] from C-parameter. They are displayed in the lower three rows of the e^+e^- sector of Fig. 9.2.

The determination of Ref. [522], $\alpha_s(M_Z^2) = 0.1164^{+0.0028}_{-0.0024}$, is no longer included in the average as it is superseded by other determinations that use the same Thrust data but rely on more accurate theoretical predictions. Not included in the computation of the world average but worth mentioning are a computation of the NLO corrections to 5-jet production and comparison to the measured 5-jet rates at LEP [526], giving $\alpha_s(M_Z^2) = 0.1156^{+0.0041}_{-0.0034}$, and a computation of non-perturbative and perturbative QCD contributions to the scale evolution of quark and gluon jet multiplicities, including resummation, resulting in $\alpha_s(M_Z^2) = 0.1199 \pm 0.0026$ [527].

We note that there is criticism on both classes of α_s extractions described above: those based on corrections of non-perturbative hadronization effects using QCD-inspired Monte Carlo generators (since the parton level of a Monte Carlo simulation is not defined in a manner equivalent to that of a fixed-order calculation), as well as studies based on non-perturbative analytic modelling, as their systematics have not yet been fully verified. For the latter case, Refs. [523, 525] quote surprisingly small overall experimental, hadronization, and theoretical uncertainties of only 2, 5, and 9 per-mille, respectively, which calls for an independent confirmation.

In view of these open questions, the determination of the *unweighted average* and uncertainties is intended to provide the most appropriate and unbiased estimate of the average value of $\alpha_s(M_Z^2)$ for this sub-field, which results in $\alpha_s(M_Z^2) = 0.1171 \pm 0.0031$.

9.4.5 *Hadron collider results:*

Until recently, determinations of α_s using hadron collider data, mostly from jet or $t\bar{t}$ production processes, could be performed at NLO only. In the meantime, NNLO calculations have become available for $t\bar{t}$ [84, 466, 468] and for inclusive jet and dijet production [197, 528, 529]. Both can be supplemented by electroweak corrections [530–532], which become important for high-p_T collisions at the LHC; for $t\bar{t}$ logarithms have been resummed [469]. Z+jet production, studied with respect to an α_s determination at NLO from multi-jet events in Ref. [533], is also known at NNLO for the 1-jet case [187, 534].

The first determination of α_s at NNLO accuracy in QCD has been reported by CMS [470] from the $t\bar{t}$ production cross section at $\sqrt{s} = 7$ TeV: $\alpha_s(M_Z^2) = 0.1151^{+0.0028}_{-0.0027}$, whereby the dominating contributions to the overall uncertainty are experimental ($^{+0.0017}_{-0.0018}$), from parton density functions ($^{+0.0013}_{-0.0011}$) and the value of the top quark pole mass (± 0.0013). In the last *Review* this opened up a new sub-field on its own. In the meantime, multiple datasets on $t\bar{t}$ production from Tevatron at $\sqrt{s} = 1.96$ TeV and from LHC at $\sqrt{s} = 7$, 8, and 13 TeV have been analyzed simultaneously to determine α_s [471] to

$$\alpha_s(M_Z^2) = 0.1177^{+0.0034}_{-0.0036},$$

where the largest uncertainties are associated with missing higher orders and with PDFs. Since this combined analysis contains among other things an updated measurement as compared to the dataset used by CMS, the latter is replaced in the averaging by the new combined result. A second entry into this sub-field is given by an analysis of new $t\bar{t}$ production data at $\sqrt{s} = 13$ TeV from the CMS collaboration [464]. From the four values presented for the chosen PDF sets, the unweighted average is taken:

$$\alpha_s(M_Z^2) = 0.1145^{+0.0036}_{-0.0031}.$$

From jet production only one α_s determination has been performed yet at NNLO using DIS data of the H1 Collaboration [374]. Two strategies are pursued for the extraction of α_s, one using predetermined PDFs as input and a second strategy fitting the proton PDFs together with the strong coupling constant. From the first approach we choose the result with the smallest total uncertainty, $\alpha_s(M_Z^2) = 0.1168 \pm 0.0030$, where the analysis is restricted to the phase space with the most precise theoretical prediction at the cost of excluding numerous data points at lower scale values. The second approach gives $\alpha_s(M_Z^2) = 0.1142 \pm 0.0028$, which we combine with the first result to our unweighted input average:

$$\alpha_s(M_Z^2) = 0.1155 \pm 0.0029.$$

As unweighted pre-average for this sub-field we obtain: $\alpha_s(M_Z^2) = 0.1159 \pm 0.0034$. Also worth mentioning is a recent still unpublished extraction of $\alpha_s(M_Z^2) = 0.1170 \pm 0.0030$ [535] using HERA jet data and relying on fast interpolation grid techniques.

Many further α_s determinations from jet measurements either could not yet be advanced to NNLO accuracy or the NNLO predictions are not yet available as is the case for observables requiring three or more jets in the final state. A selection of results from inclusive jet [373, 387, 536–541] and multi-jet measurements [332, 334, 335, 373, 542–546] is presented in Fig. 9.4, where the uncertainty in most cases is dominated by the impact of missing higher orders estimated through scale variations. The multi-jet α_s determinations are based on 3-jet cross sections (m3j), 3- to 2-jet cross-section ratios (R32), dijet angular decorrelations (RdR, RdPhi), and transverse energy-energy-correlations and their asymmetry (TEEC, ATEEC). The H1 result is extracted from a fit to inclusive 1-, 2-, and 3-jet cross sections (nj) simultaneously.

The CMS Collaboration has also derived an α_s value at NLO from dijet production at $\sqrt{s} = 8$ TeV [393], but only in combination with a PDF fit. The last point of the inclusive jet sub-field from Ref. [541] is derived from a simultaneous fit to six datasets from different experiments and partially includes data used already for the other data points, *e.g.* the CMS result at 7 TeV.

All NLO results are within their large uncertainties in agreement with the world average and the associated analyses provide valuable new values for the scale dependence of α_s at energy scales now extending up to almost 2.0 TeV as shown in Fig. 9.3.

9.4.6 *Electroweak precision fit:*

For this category, we update the global electroweak fit result of Ref. [547] to the one of Ref. [548], which now includes kinematic top quark and W boson mass measurements from the LHC, new determinations of the effective leptonic electroweak mixing angles from the Tevatron, a Higgs mass measurement from ATLAS and CMS, and a new evaluation of the hadronic contribution to the running of the electromagnetic coupling at the Z-boson mass. In addition, we use the newer results of the electroweak fit at the Z mass pole from LEP and SLC data presented in Sec. *Electroweak Model and constraints on New Physics* of the 2018 edition of this *Review*. Both very similar results, $\alpha_s(M_Z^2) = 0.1203 \pm 0.0028$ [480], $\alpha_s(M_Z^2) = 0.1194 \pm 0.0029$ [548], are also in perfect agreement with the original result obtained from LEP and SLD data [549]. Our pre-averaging gives $\alpha_s(M_Z^2) = 0.1199 \pm 0.0029$.

We note, however, that results from electroweak precision data strongly depend on the strict validity of Standard Model predictions and the existence of the minimal Higgs mechanism to implement electroweak symmetry breaking. Any - even small - deviation of nature from this model could strongly influence this extraction of α_s.

9.4.7 *Lattice QCD:*

Several methods exist to extract the strong coupling constant from lattice QCD, as reviewed also in Sec. *Lattice QCD* of this *Review*.

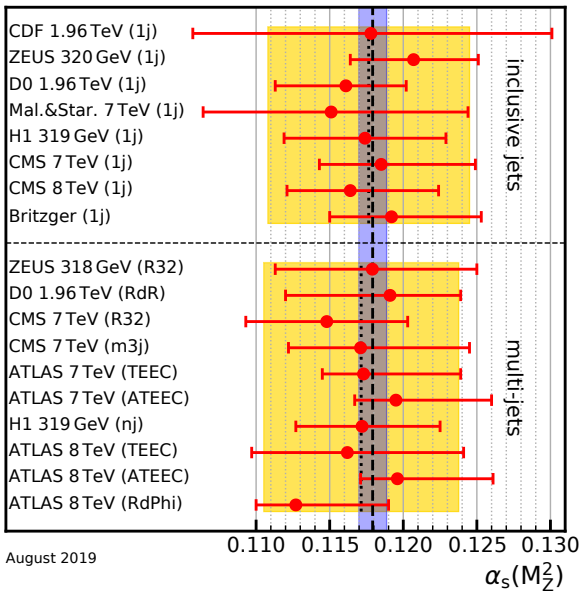

Figure 9.4: Summary of determinations of $\alpha_s(M_Z^2)$ at NLO from inclusive and multi-jet measurements at hadron colliders. The uncertainty is dominated by estimates of the impact of missing higher orders. The yellow (light shaded) bands and dotted lines indicate average values for the two sub-fields. The dashed line and blue (dark shaded) band represent the final world average value of $\alpha_s(M_Z^2)$.

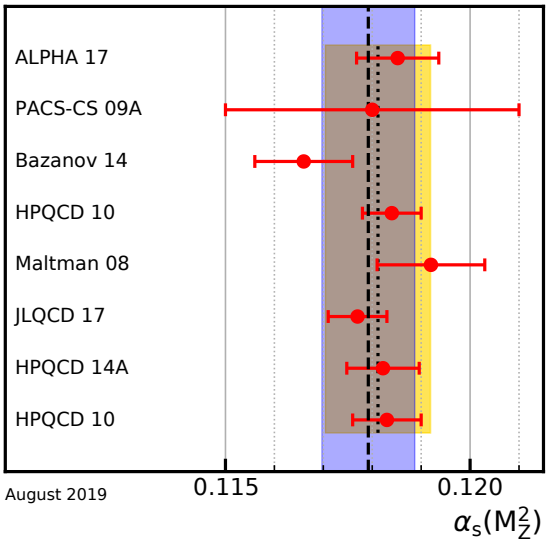

Figure 9.5: Lattice determinations that enter the FLAG2019 average. The yellow (light shaded) band and dotted line indicates the average value for this sub-field. The dashed line and blue (dark shaded) band represent the final world average value of $\alpha_s(M_Z^2)$.

The Flavour Lattice Averaging Group (FLAG) has recently considered the most up-to-date determinations and combined them to produce an update of their average α_s [487]. Their final result is obtained by considering seventeen possible input calculations [550–567] and by retaining in their final average only those eight [551–553, 556, 559–561, 563] that fulfill their predefined quality criteria. These determinations, together with their uncertainties, are displayed in Fig. 9.5. The yellow (light shaded) band and dotted line indicate the FLAG 2018 average, while the dashed line and blue (dark shaded) band represent the world average (see later). The level of agreement of individual results to the world average, or to the non-lattice world average is very similar. The criteria applied are detailed in the Sec. 9.2.1 of Ref. [487]. We note that, as in our case, the calculation must be published in a peer-reviewed journal for it to be eligible to be included in the FLAG average. We also note that the criteria applied now are considered relatively loose by the FLAG collaboration and they have already formulated more stringent criteria. It is likely that in future FLAG averages only results satisfying these stricter criteria will be included in their averaging.

Similarly to what is done here, the FLAG collaboration built pre-averages of results that belong to different classes. The categories that currently contribute to the average are: step-scaling methods ($\alpha_s(M_Z^2) = 0.11848^{+0.00081}_{-0.00081}$), the potential at short distances ($\alpha_s(M_Z^2) = 0.11660^{+0.00160}_{-0.00160}$), Wilson loops ($\alpha_s(M_Z^2) = 0.11858^{+0.00120}_{-0.00120}$), and heavy-quark current two-point functions ($\alpha_s(M_Z^2) = 0.11824^{+0.00150}_{-0.00150}$).

Other categories like the vacuum polarization at short distances, the calculation of QCD vertices, or of the eigenvalue spectrum of the Dirac operator have not yet published results that fulfill all requirements to be included in the average. Ref. [568] has been completed after the publication of Ref. [487], hence these results have not been considered in the last FLAG average.

The final value is obtained by performing an unweighted average of the pre-averages. In order to be conservative, the final uncertainty is not the combined uncertainty of the pre-averages, rather it is taken to be the smallest uncertainty of the pre-averages, which is the uncertainty of the step-scaling category and is dominated by the ALPHA 17 result [563]. The final FLAG average (rounded to four digits) is

$$\alpha_s(M_Z^2) = 0.1182 \pm 0.0008\,, \qquad \text{(lattice)}\,. \tag{9.23}$$

We believe that this result expresses to a large extent the consensus of the lattice community and that the imposed criteria and the rigorous assessment of systematic uncertainties qualify for a direct inclusion of this FLAG average here. In contrast to the previous review, we therefore decided to adopt the FLAG average with its uncertainty as our value of α_s for the lattice category. Moreover, this lattice result will not be directly combined with any other sub-field average, but with our non-lattice average to give our final world average value for α_s.

9.4.8 *Determination of the world average value of $\alpha_s(M_Z^2)$:*

Obtaining a world average value for $\alpha_s(M_Z^2)$ is a non-trivial exercise. A certain arbitrariness and subjective component is inevitable because of the choice of measurements to be included in the average, the treatment of (non-Gaussian) systematic uncertainties of mostly theoretical nature, as well as the treatment of correlations among the various inputs, of theoretical as well as experimental origin.

We have chosen to determine pre-averages for sub-fields of measurements that are considered to exhibit a maximum of independence among each other, considering experimental as well as theoretical issues. The seven pre-averages are summarized in Fig. 9.2. We recall that these are exclusively obtained from extractions that are based on (at least) full NNLO QCD predictions, and are published in peer-reviewed journals at the time of completing this *Review*. To obtain our final world average, we first combine six pre-averages, excluding the lattice result, using a χ^2 *averaging method*. This gives

$$\alpha_s(M_Z^2) = 0.1176 \pm 0.0011\,, \qquad \text{(without lattice)}\,. \tag{9.24}$$

This result is fully compatible with the lattice pre-average Eq. (9.23) and has a comparable error. In order to be conservative, we combine these two numbers using an unweighted average and take as an uncertainty the average between these two uncertainties. This gives our final world average value

$$\alpha_s(M_Z^2) = 0.1179 \pm 0.0010\,. \tag{9.25}$$

This world average value is in very good agreement with the last version of this *Review*, which was $\alpha_s(M_Z^2) = 0.1181 \pm 0.0011$, with only a slightly lower central value and decreased overall uncertainty. Performing a weighted average of all seven categories

gives $\alpha_s(M_Z^2) = 0.1180 \pm 0.0007$. Our uncertainty instead is about 50% larger.

Notwithstanding the many open issues still present within each of the sub-fields summarised in this *Review*, the wealth of available results provides a rather precise and reasonably stable world average value of $\alpha_s(M_Z^2)$, as well as a clear signature and proof of the energy dependence of α_s, in full agreement with the QCD prediction of Asymptotic Freedom. This is demonstrated in Fig. 9.3, where results of $\alpha_s(Q^2)$ obtained at discrete energy scales Q, now also including those based just on NLO QCD, are summarised. Thanks to the results from the Tevatron and from the LHC, the energy scales, at which α_s is determined, now extend up to almost 2 TeV.[15]

9.5 Acknowledgments

We are grateful to S. Bethke, G. Dissertori, D. d'Enterria, C. Glasman, A. Hoang, D. Lombardi, G.P. Salam, and B. Webber for discussions and for their comments on the manuscript, and to J. Andersen, A. Bazavov, H.-L. Win, and J. Smillie for useful discussions.

References

[1] R. K. Ellis, W. J. Stirling and B. R. Webber, Camb. Monogr. Part. Phys. Nucl. Phys. Cosmol. **8**, 1 (1996).

[2] J. Campbell, J. Huston, F. Krauss *"The Black Book of Quantum Chromodynamics, a Primer for the QCD Era,"*Oxford University Press, UK (2017).

[3] C. A. Baker *et al.*, Phys. Rev. Lett. **97**, 131801 (2006), [hep-ex/0602020].

[4] J. M. Pendlebury *et al.*, Phys. Rev. **D92**, 9, 092003 (2015), [arXiv:1509.04411].

[5] B. Graner *et al.*, Phys. Rev. Lett. **116**, 16, 161601 (2016), [Erratum: Phys. Rev. Lett.119,no.11,119901(2017)], [arXiv:1601.04339].

[6] J. E. Kim and G. Carosi, Rev. Mod. Phys. **82**, 557 (2010), [arXiv:0807.3125].

[7] G. Dissertori, I. G. Knowles and M. Schmelling, *High energy experiments and theory,* Oxford, UK: Clarendon (2003).

[8] R. Brock *et al.* (CTEQ), Rev. Mod. Phys. **67**, 157 (1995); see also http://www.phys.psu.edu/∼cteq/ handbook/v1.1/handbook.pdf/.

[9] K. Melnikov, CERN Yellow Rep. School Proc. **3**, 37 (2018).

[10] T. van Ritbergen, J. A. M. Vermaseren and S. A. Larin, Phys. Lett. **B400**, 379 (1997), [hep-ph/9701390].

[11] M. Czakon, Nucl. Phys. **B710**, 485 (2005), [hep-ph/0411261].

[12] P. A. Baikov, K. G. Chetyrkin and J. H. Kühn, Phys. Rev. Lett. **118**, 8, 082002 (2017), [arXiv:1606.08659].

[13] T. Luthe *et al.*, JHEP **07**, 127 (2016), [arXiv:1606.08662].

[14] F. Herzog *et al.*, JHEP **02**, 090 (2017), [arXiv:1701.01404].

[15] T. Luthe *et al.*, JHEP **10**, 166 (2017), [arXiv:1709.07718].

[16] K. G. Chetyrkin *et al.*, JHEP **10**, 179 (2017), [Addendum: JHEP12,006(2017)], [arXiv:1709.08541].

[17] W. A. Bardeen *et al.*, Phys. Rev. **D18**, 3998 (1978).

[18] D. J. Gross and F. Wilczek, Phys. Rev. Lett. **30**, 1343 (1973), [,271(1973)].

[19] H. D. Politzer, Phys. Rev. Lett. **30**, 1346 (1973), [,274(1973)].

[20] Y. Schroder and M. Steinhauser, JHEP **01**, 051 (2006), [hep-ph/0512058].

[21] K. G. Chetyrkin, J. H. Kuhn and C. Sturm, Nucl. Phys. **B744**, 121 (2006), [hep-ph/0512060].

[15] We note, however, that in many such studies, like those based on exclusive states of jet multiplicities, the relevant energy scale of the measurement is not uniquely defined. For instance, in studies of the ratio of 3- to 2-jet cross sections at the LHC, the relevant scale was taken to be the average of the transverse momenta of the two leading jets [543], but could alternatively have been chosen to be the transverse momentum of the 3^{rd} jet.

[22] A. G. Grozin *et al.*, JHEP **09**, 066 (2011), [arXiv:1107.5970].

[23] M. Dalla Brida *et al.* (ALPHA), Phys. Rev. Lett. **117**, 18, 182001 (2016), [arXiv:1604.06193].

[24] K. G. Chetyrkin, J. H. Kuhn and M. Steinhauser, Comput. Phys. Commun. **133**, 43 (2000), [hep-ph/0004189].

[25] B. Schmidt and M. Steinhauser, Comput. Phys. Commun. **183**, 1845 (2012), [arXiv:1201.6149].

[26] F. Herren and M. Steinhauser, Comput. Phys. Commun. **224**, 333 (2018), [arXiv:1703.03751].

[27] A. V. Bednyakov, Phys. Lett. **B741**, 262 (2015), [arXiv:1410.7603].

[28] M. Beneke, Phys. Rept. **317**, 1 (1999), [hep-ph/9807443].

[29] M. Beneke *et al.*, Phys. Lett. **B775**, 63 (2017), [arXiv:1605.03609].

[30] A. H. Hoang, C. Lepenik and M. Preisser, JHEP **09**, 099 (2017), [arXiv:1706.08526].

[31] P. Marquard *et al.*, Phys. Rev. Lett. **114**, 14, 142002 (2015), [arXiv:1502.01030].

[32] P. A. Baikov *et al.*, Phys. Lett. **B714**, 62 (2012), [arXiv:1206.1288].

[33] K. G. Chetyrkin, J. H. Kuhn and A. Kwiatkowski (1996), [Phys. Rept.277,189(1996)], [hep-ph/9503396].

[34] Y. Kiyo *et al.*, Nucl. Phys. **B823**, 269 (2009), [arXiv:0907.2120].

[35] P. A. Baikov *et al.*, Phys. Rev. Lett. **108**, 222003 (2012), [arXiv:1201.5804].

[36] P. A. Baikov, K. G. Chetyrkin and J. H. Kuhn, Phys. Rev. Lett. **101**, 012002 (2008), [arXiv:0801.1821].

[37] F. Herzog *et al.*, JHEP **08**, 113 (2017), [arXiv:1707.01044].

[38] V. A. Novikov *et al.*, Nucl. Phys. **B174**, 378 (1980).

[39] H.-W. Lin *et al.*, Phys. Rev. **D91**, 054510 (2015), [arXiv:1402.1462]; C. Alexandrou *et al.*, Phys. Rev. **D92**, 014502 (2015), [arXiv:1504.07455].

[40] H.-W. Lin *et al.*, Prog. Part. Nucl. Phys. **100**, 107 (2018), [arXiv:1711.07916].

[41] C. Alexandrou *et al.*, Phys. Rev. Lett. **121**, 11, 112001 (2018), [arXiv:1803.02685].

[42] J.-W. Chen *et al.* (2018), [arXiv:1803.04393].

[43] K. Cichy, L. Del Debbio and T. Giani (2019), [arXiv:1907.06037].

[44] G. C. Rossi and M. Testa, Phys. Rev. **D96**, 1, 014507 (2017), [arXiv:1706.04428].

[45] J. Gao, L. Harland-Lang and J. Rojo, Phys. Rept. **742**, 1 (2018), [arXiv:1709.04922].

[46] K. Kovařík, P. M. Nadolsky and D. E. Soper (2019), [arXiv:1905.06957].

[47] J. Butterworth *et al.*, J. Phys. **G43**, 023001 (2016), [arXiv:1510.03865].

[48] R. Abdul Khalek *et al.* (NNPDF) (2019), [arXiv:1905.04311].

[49] R. Abdul Khalek *et al.* (NNPDF) (2019), [arXiv:1906.10698].

[50] J. D. Bjorken and E. A. Paschos, Phys. Rev. **185**, 1975 (1969).

[51] J. A. M. Vermaseren, A. Vogt and S. Moch, Nucl. Phys. **B724**, 3 (2005), [hep-ph/0504242].

[52] S. Moch, J. A. M. Vermaseren and A. Vogt, Nucl. Phys. **B813**, 220 (2009), [arXiv:0812.4168].

[53] J. Davies *et al.*, PoS **DIS2016**, 059 (2016), [arXiv:1606.08907].

[54] E. Laenen *et al.*, Nucl. Phys. **B392**, 162 (1993); S. Riemersma, J. Smith and W. L. van Neerven, Phys. Lett. **B347**, 143 (1995), [hep-ph/9411431].

[55] J. Blümlein *et al.* (2019), [arXiv:1903.06155].

[56] A. Manohar *et al.*, Phys. Rev. Lett. **117**, 24, 242002 (2016), [arXiv:1607.04266].

[57] J. C. Collins, D. E. Soper and G. F. Sterman, Adv. Ser. Direct. High Energy Phys. **5**, 1 (1989), [hep-ph/0409313].

[58] J.C. Collins, *Foundations of Perturbative QCD*, Cambridge University Press, 2011.

[59] G. C. Nayak, J.-W. Qiu and G. F. Sterman, Phys. Rev. **D72**, 114012 (2005), [hep-ph/0509021].

[60] V. N. Gribov and L. N. Lipatov, Sov. J. Nucl. Phys. **15**, 438 (1972), [Yad. Fiz.15,781(1972)]; L. N. Lipatov, Sov. J. Nucl. Phys. **20**, 94 (1975), [Yad. Fiz.20,181(1974)]; G. Altarelli and G. Parisi, Nucl. Phys. **B126**, 298 (1977); Y. L. Dokshitzer, Sov. Phys. JETP **46**, 641 (1977), [Zh. Eksp. Teor. Fiz.73,1216(1977)].

[61] G. Curci, W. Furmanski and R. Petronzio, Nucl. Phys. **B175**, 27 (1980); W. Furmanski and R. Petronzio, Phys. Lett. **97B**, 437 (1980).

[62] A. Vogt, S. Moch and J. A. M. Vermaseren, Nucl. Phys. **B691**, 129 (2004), [hep-ph/0404111]; S. Moch, J. A. M. Vermaseren and A. Vogt, Nucl. Phys. **B688**, 101 (2004), [hep-ph/0403192].

[63] S. Moch *et al.*, JHEP **10**, 041 (2017), [arXiv:1707.08315].

[64] A. Vogt *et al.*, PoS **RADCOR2017**, 046 (2018), [arXiv:1801.06085].

[65] A. Vogt *et al.*, PoS **LL2018**, 050 (2018), [arXiv:1808.08981].

[66] S. Moch, J. A. M. Vermaseren and A. Vogt, Nucl. Phys. **B889**, 351 (2014), [arXiv:1409.5131].

[67] D. de Florian, G. F. R. Sborlini and G. Rodrigo, Eur. Phys. J. **C76**, 5, 282 (2016), [arXiv:1512.00612]; D. de Florian, G. F. R. Sborlini and G. Rodrigo, JHEP **10**, 056 (2016), [arXiv:1606.02887].

[68] R. S. Thorne, Phys. Rev. **D73**, 054019 (2006), [hep-ph/0601245].

[69] S. Forte *et al.*, Nucl. Phys. **B834**, 116 (2010), [arXiv:1001.2312].

[70] M. Guzzi *et al.*, Phys. Rev. **D86**, 053005 (2012), [arXiv:1108.5112].

[71] V. S. Fadin, E. A. Kuraev and L. N. Lipatov, Phys. Lett. **60B**, 50 (1975).

[72] I. I. Balitsky and L. N. Lipatov, Sov. J. Nucl. Phys. **28**, 822 (1978), [Yad. Fiz.28,1597(1978)].

[73] R. D. Ball *et al.*, Eur. Phys. J. **C78**, 4, 321 (2018), [arXiv:1710.05935].

[74] H. Abramowicz *et al.* (H1, ZEUS), Eur. Phys. J. **C75**, 12, 580 (2015), [arXiv:1506.06042].

[75] H. Abdolmaleki *et al.* (xFitter Developers' Team), Eur. Phys. J. **C78**, 8, 621 (2018), [arXiv:1802.00064].

[76] L. A. Harland-Lang *et al.*, Eur. Phys. J. **C76**, 4, 186 (2016), [arXiv:1601.03413].

[77] T.-J. Hou *et al.* (2019), [arXiv:1908.11238].

[78] J. C. Collins, D. E. Soper and G. F. Sterman, Nucl. Phys. **B261**, 104 (1985).

[79] R. Hamberg, W. L. van Neerven and T. Matsuura, Nucl. Phys. **B359**, 343 (1991), [Erratum: Nucl. Phys.B644,403(2002)].

[80] R. V. Harlander and W. B. Kilgore, Phys. Rev. Lett. **88**, 201801 (2002), [hep-ph/0201206].

[81] O. Brein, A. Djouadi and R. Harlander, Phys. Lett. **B579**, 149 (2004), [hep-ph/0307206].

[82] P. Bolzoni *et al.*, Phys. Rev. Lett. **105**, 011801 (2010), [arXiv:1003.4451].

[83] S. Borowka *et al.*, Phys. Rev. Lett. **117**, 1, 012001 (2016), [Erratum: Phys. Rev. Lett.117,no.7,079901(2016)], [arXiv:1604.06447].

[84] M. Czakon, P. Fiedler and A. Mitov, Phys. Rev. Lett. **110**, 252004 (2013), [arXiv:1303.6254].

[85] T. Gehrmann *et al.*, Phys. Rev. Lett. **113**, 21, 212001 (2014), [arXiv:1408.5243].

[86] F. Cascioli *et al.*, Phys. Lett. **B735**, 311 (2014), [arXiv:1405.2219].

[87] M. Grazzini, S. Kallweit and M. Wiesemann, Eur. Phys. J. **C78**, 7, 537 (2018), [arXiv:1711.06631].

[88] C. Anastasiou *et al.*, Phys. Rev. Lett. **114**, 212001 (2015), [arXiv:1503.06056]; C. Anastasiou *et al.*, JHEP **05**, 058 (2016), [arXiv:1602.00695].

[89] B. Mistlberger, JHEP **05**, 028 (2018), [arXiv:1802.00833].

[90] F. Dulat, B. Mistlberger and A. Pelloni, Phys. Rev. **D99**, 3, 034004 (2019), [arXiv:1810.09462].

[91] F. A. Dreyer and A. Karlberg, Phys. Rev. Lett. **117**, 7, 072001 (2016), [arXiv:1606.00840].

[92] D. de Florian *et al.* (LHC Higgs Cross Section Working Group) (2016), [arXiv:1610.07922].

[93] M. Greco and A. Vicini, Nucl. Phys. **B415**, 386 (1994).

[94] L. N. Lipatov, Sov. J. Nucl. Phys. **23**, 338 (1976), [Yad. Fiz.23,642(1976)].

[95] E. A. Kuraev, L. N. Lipatov and V. S. Fadin, Sov. Phys. JETP **45**, 199 (1977), [Zh. Eksp. Teor. Fiz.72,377(1977)].

[96] V. S. Fadin and L. N. Lipatov, Phys. Lett. **B429**, 127 (1998), [hep-ph/9802290].

[97] M. Ciafaloni and G. Camici, Phys. Lett. **B430**, 349 (1998), [hep-ph/9803389].

[98] G. Altarelli, R. D. Ball and S. Forte, Nucl. Phys. **B799**, 199 (2008), [arXiv:0802.0032].

[99] M. Ciafaloni *et al.*, JHEP **08**, 046 (2007), [arXiv:0707.1453].

[100] C. D. White and R. S. Thorne, Phys. Rev. **D75**, 034005 (2007), [hep-ph/0611204].

[101] E. Iancu *et al.*, Phys. Lett. **B744**, 293 (2015), [arXiv:1502.05642].

[102] N. Gromov, F. Levkovich-Maslyuk and G. Sizov, Phys. Rev. Lett. **115**, 25, 251601 (2015), [arXiv:1507.04010]; V. N. Velizhanin (2015), [arXiv:1508.02857]; S. Caron-Huot and M. Herranen, JHEP **02**, 058 (2018), [arXiv:1604.07417].

[103] I. Balitsky, Nucl. Phys. **B463**, 99 (1996), [hep-ph/9509348].

[104] Y. V. Kovchegov, Phys. Rev. **D60**, 034008 (1999), [hep-ph/9901281].

[105] A. Hebecker, Phys. Rept. **331**, 1 (2000), [hep-ph/9905226].

[106] A. V. Belitsky and A. V. Radyushkin, Phys. Rept. **418**, 1 (2005), [hep-ph/0504030].

[107] E. Boos *et al.* (CompHEP), Nucl. Instrum. Meth. **A534**, 250 (2004), [hep-ph/0403113]; `http://compep.sinp.su.ru/`.

[108] J. Alwall *et al.*, JHEP **07**, 079 (2014), [arXiv:1405.0301]; `https://launchpad.net/mg5amcnlo`.

[109] M. L. Mangano *et al.*, JHEP **07**, 001 (2003), [hep-ph/0206293]; `http://cern.ch/mlm/alpgen/`.

[110] T. Gleisberg and S. Hoeche, JHEP **12**, 039 (2008), [arXiv:0808.3674]; `https://sherpa.hepforge.prg/trac/wiki`.

[111] A. Cafarella, C. G. Papadopoulos and M. Worek, Comput. Phys. Commun. **180**, 1941 (2009), [arXiv:0710.2427]; `http://cern.ch/helac-phegas/`.

[112] F. A. Berends and W. T. Giele, Nucl. Phys. **B306**, 759 (1988).

[113] L. J. Dixon, in "QCD and beyond. Proceedings, Theoretical Advanced Study Institute in Elementary Particle Physics, TASI-95, Boulder, USA, June 4-30, 1995," 539–584 (1996), [hep-ph/9601359], URL `http://www-public.slac.stanford.edu/sciDoc/docMeta.aspx?slacPubNumber=SLAC-PUB-7106`.

[114] R. Britto, F. Cachazo and B. Feng, Nucl. Phys. **B715**, 499 (2005), [hep-th/0412308].

[115] F. Cachazo, P. Svrcek and E. Witten, JHEP **09**, 006 (2004), [hep-th/0403047].

[116] S. Badger *et al.*, Phys. Rev. **D87**, 3, 034011 (2013), [arXiv:1206.2381].

[117] S. Catani and M. H. Seymour, Nucl. Phys. **B485**, 291 (1997), [Erratum: Nucl. Phys.B510,503(1998)], [hep-ph/9605323].

[118] S. Frixione, Z. Kunszt and A. Signer, Nucl. Phys. **B467**, 399 (1996), [hep-ph/9512328].

[119] D. A. Kosower, Phys. Rev. **D57**, 5410 (1998), [hep-ph/9710213]; J. M. Campbell, M. A. Cullen and E. W. N. Glover, Eur. Phys. J. **C9**, 245 (1999), [hep-ph/9809429]; D. A. Kosower, Phys. Rev. **D71**, 045016 (2005), [hep-ph/0311272].

[120] G. Ossola, C. G. Papadopoulos and R. Pittau, Nucl. Phys. **B763**, 147 (2007), [hep-ph/0609007].

[121] R. Britto, F. Cachazo and B. Feng, Nucl. Phys. **B725**, 275 (2005), [hep-th/0412103].

[122] R. K. Ellis *et al.*, Nucl. Phys. **B822**, 270 (2009), [arXiv:0806.3467].

[123] C. F. Berger and D. Forde, Ann. Rev. Nucl. Part. Sci. **60**, 181 (2010), [arXiv:0912.3534].

[124] F. Cascioli, P. Maierhofer and S. Pozzorini, Phys. Rev. Lett. **108**, 111601 (2012), [arXiv:1111.5206].

[125] Z. Bern, L. J. Dixon and D. A. Kosower, Annals Phys. **322**, 1587 (2007), [arXiv:0704.2798].

[126] R. K. Ellis *et al.*, Phys. Rept. **518**, 141 (2012), [arXiv:1105.4319].

[127] G. Bevilacqua *et al.*, Comput. Phys. Commun. **184**, 986 (2013), [arXiv:1110.1499]; `http://cern.ch/helax-phegas/`.

[128] G. Cullen *et al.*, Eur. Phys. J. **C74**, 8, 3001 (2014), [arXiv:1404.7096]; `http://gosam.hepforge.org/`.

[129] S. Badger *et al.*, Comput. Phys. Commun. **184**, 1981 (2013), [arXiv:1209.0100]; `https://bitbucket.org/njet/wiki/Home/`.

[130] F. Buccioni, S. Pozzorini and M. Zoller, Eur. Phys. J. **C78**, 1, 70 (2018), [arXiv:1710.11452]; `https://openloops.hepforge.org/`.

[131] S. Actis *et al.*, Comput. Phys. Commun. **214**, 140 (2017), [arXiv:1605.01090].

[132] T. Gleisberg *et al.*, JHEP **02**, 007 (2009), [arXiv:0811.4622]; `http://projects.hepforge.org/sherpa`.

[133] Z. Nagy, Phys. Rev. **D68**, 094002 (2003), [hep-ph/0307268]; `http://www.desy.de.~znagy/Site/NLOJet++.html`.

[134] J. M. Campbell and R. K. Ellis, Phys. Rev. **D62**, 114012 (2000), [hep-ph/0006304].

[135] J. Baglio *et al.* (2011), [arXiv:1107.4038]; http://www-itp.particle.uni-karlsruhe.de/~vbfnloweb.

[136] T. Binoth *et al.*, Eur. Phys. J. **C16**, 311 (2000), [hep-ph/9911340]; `http://lapth.in2p3.fr/PHOX_FAMILY/`.

[137] Z. Bern *et al.*, PoS **LL2012**, 018 (2012), [arXiv:1210.6684].

[138] T. Kluge, K. Rabbertz and M. Wobisch, *FastNLO: Fast pQCD calculations for PDF fits* (2006), [hep-ph/0609285], URL `http://lss.fnal.gov/cgi-bin/find_paper.pl?conf-06-352`; `http://fastnlo.hepforge.org/`.

[139] T. Carli *et al.*, Eur. Phys. J. **C66**, 503 (2010), [arXiv:0911.2985]; `https://applgrid.hepforge.org/`.

[140] L. Del Debbio, N. P. Hartland and S. Schumann, Comput. Phys. Commun. **185**, 2115 (2014), [arXiv:1312.4460]; `http://mcgrid.hepforge.org/`.

[141] V. Bertone *et al.*, JHEP **08**, 166 (2014), [arXiv:1406.7693]; `https://amcfast.hepforge.org/`.

[142] G. Cullen, N. Greiner and G. Heinrich, Eur. Phys. J. **C73**, 4, 2388 (2013), [arXiv:1212.5154].

[143] S. Kallweit *et al.*, JHEP **04**, 012 (2015), [arXiv:1412.5157].

[144] A. Denner *et al.*, JHEP **04**, 018 (2015), [arXiv:1412.7421].

[145] M. Chiesa, N. Greiner and F. Tramontano, J. Phys. **G43**, 1, 013002 (2016), [arXiv:1507.08579].

[146] S. Frixione *et al.*, JHEP **06**, 184 (2015), [arXiv:1504.03446].

[147] B. Biedermann *et al.*, Eur. Phys. J. **C77**, 492 (2017), [arXiv:1704.05783].

[148] R. Frederix *et al.*, JHEP **07**, 185 (2018), [arXiv:1804.10017].

[149] C. Anastasiou, R. Boughezal and F. Petriello, JHEP **04**, 003 (2009), [arXiv:0811.3458].

[150] S. Dittmaier, A. Huss and C. Schwinn, Nucl. Phys. **B885**, 318 (2014), [arXiv:1403.3216].

[151] S. Dittmaier, A. Huss and C. Schwinn, Nucl. Phys. **B904**, 216 (2016), [arXiv:1511.08016].

[152] D. de Florian, M. Der and I. Fabre, Phys. Rev. **D98**, 9, 094008 (2018), [arXiv:1805.12214].

[153] M. Bonetti, K. Melnikov and L. Tancredi, Phys. Rev. **D97**, 5, 056017 (2018), [Erratum: Phys. Rev.D97,no.9,099906(2018)], [arXiv:1801.10403].

[154] C. Anastasiou *et al.*, JHEP **03**, 162 (2019), [arXiv:1811.11211].

[155] M. Bonetti, K. Melnikov and L. Tancredi, Phys. Rev. **D97**, 3, 034004 (2018), [arXiv:1711.11113].

[156] Z. Bern *et al.*, Nucl. Phys. **B425**, 217 (1994), [hep-ph/9403226].

[157] J. M. Campbell and E. W. N. Glover, Nucl. Phys. **B527**, 264 (1998), [hep-ph/9710255].

[158] S. Catani and M. Grazzini, Phys. Lett. **B446**, 143 (1999), [hep-ph/9810389].

[159] T. Binoth and G. Heinrich, Nucl. Phys. **B585**, 741 (2000), [hep-ph/0004013].

[160] C. Anastasiou, K. Melnikov and F. Petriello, Phys. Rev. **D69**, 076010 (2004), [hep-ph/0311311].

[161] A. Gehrmann-De Ridder, T. Gehrmann and E. W. N. Glover, JHEP **09**, 056 (2005), [hep-ph/0505111].

[162] G. Somogyi, Z. Trocsanyi and V. Del Duca, JHEP **01**, 070 (2007), [hep-ph/0609042].

[163] M. Czakon, Phys. Lett. **B693**, 259 (2010), [arXiv:1005.0274].

[164] S. Catani and M. Grazzini, Phys. Rev. Lett. **98**, 222002 (2007), [hep-ph/0703012]; `http://theory.fi.infn.it/grazzini/codes.html`.

[165] R. Boughezal *et al.*, Phys. Rev. Lett. **115**, 6, 062002 (2015), [arXiv:1504.02131].

[166] J. Gaunt *et al.*, JHEP **09**, 058 (2015), [arXiv:1505.04794].

[167] M. Cacciari *et al.*, Phys. Rev. Lett. **115**, 8, 082002 (2015), [Erratum: Phys. Rev. Lett.120,no.13,139901(2018)], [arXiv:1506.02660].

[168] A. Gehrmann-De Ridder *et al.*, Phys. Rev. Lett. **99**, 132002 (2007), [arXiv:0707.1285]; A. Gehrmann-De Ridder *et al.*, JHEP **12**, 094 (2007), [arXiv:0711.4711]; A. Gehrmann-De Ridder *et al.*, Phys. Rev. Lett. **100**, 172001 (2008), [arXiv:0802.0813].

[169] A. Gehrmann-De Ridder *et al.*, Comput. Phys. Commun. **185**, 3331 (2014), [arXiv:1402.4140]; `https://eerad3.epforge.org/`.

[170] S. Weinzierl, Phys. Rev. Lett. **101**, 162001 (2008), [arXiv:0807.3241]; S. Weinzierl, JHEP **06**, 041 (2009), [arXiv:0904.1077].

[171] J. Currie, T. Gehrmann and J. Niehues, Phys. Rev. Lett. **117**, 4, 042001 (2016), [arXiv:1606.03991].

[172] J. Currie *et al.*, JHEP **05**, 209 (2018), [arXiv:1803.09973].

[173] T. Gehrmann *et al.*, Phys. Lett. **B792**, 182 (2019), [arXiv:1812.06104].

[174] K. Melnikov and F. Petriello, Phys. Rev. **D74**, 114017 (2006), [hep-ph/0609070]; `http://gate.hep.anl.gov/fpetriello/FEWZ.html`.

[175] S. Catani *et al.*, Phys. Rev. Lett. **103**, 082001 (2009), [arXiv:0903.2120]; `http://theory.fi.infn.it/gazzani/dy.html`.

[176] C. Anastasiou, K. Melnikov and F. Petriello, Nucl. Phys. **B724**, 197 (2005), [hep-ph/0501130]; `http://www.phys.ethz.ch/~pheno/fehipro/`.

[177] M. Grazzini *et al.*, JHEP **05**, 139 (2017), [arXiv:1703.09065].

[178] S. Catani *et al.*, Phys. Rev. Lett. **108**, 072001 (2012), [Erratum: Phys. Rev. Lett.117,no.8,089901(2016)], [arXiv:1110.2375].

[179] J. M. Campbell *et al.*, JHEP **07**, 148 (2016), [arXiv:1603.02663].

[180] M. Grazzini *et al.*, Phys. Lett. **B731**, 204 (2014), [arXiv:1309.7000].

[181] M. Grazzini, S. Kallweit and D. Rathlev, JHEP **07**, 085 (2015), [arXiv:1504.01330].

[182] R. Boughezal *et al.*, Eur. Phys. J. **C77**, 1, 7 (2017), [arXiv:1605.08011].

[183] J. M. Campbell, R. K. Ellis and C. Williams, Phys. Rev. Lett. **118**, 22, 222001 (2017), [arXiv:1612.04333].

[184] X. Chen *et al.*, Submitted to: J. High Energy Phys. (2019), [arXiv:1904.01044].

[185] J. M. Campbell, R. K. Ellis and C. Williams, Phys. Rev. **D96**, 1, 014037 (2017), [arXiv:1703.10109].

[186] A. Gehrmann-De Ridder *et al.*, Phys. Rev. Lett. **117**, 2, 022001 (2016), [arXiv:1507.02850].

[187] R. Boughezal *et al.*, Phys. Rev. Lett. **116**, 15, 152001 (2016), [arXiv:1512.01291].

[188] R. Boughezal *et al.*, Phys. Rev. Lett. **115**, 8, 082003 (2015), [arXiv:1504.07922].

[189] R. Boughezal *et al.*, Phys. Lett. **B748**, 5 (2015), [arXiv:1505.03893].

[190] F. Caola, K. Melnikov and M. Schulze, Phys. Rev. **D92**, 7, 074032 (2015), [arXiv:1508.02684].

[191] X. Chen *et al.*, JHEP **10**, 066 (2016), [arXiv:1607.08817].

[192] G. Ferrera, M. Grazzini and F. Tramontano, Phys. Rev. Lett. **107**, 152003 (2011), [arXiv:1107.1164].

[193] G. Ferrera, M. Grazzini and F. Tramontano, Phys. Lett. **B740**, 51 (2015), [arXiv:1407.4747].

[194] M. Brucherseifer, F. Caola and K. Melnikov, Phys. Lett. **B736**, 58 (2014), [arXiv:1404.7116].

[195] E. L. Berger *et al.*, Phys. Rev. **D94**, 7, 071501 (2016), [arXiv:1606.08463].

[196] M. Czakon, P. Fiedler and A. Mitov, Phys. Rev. Lett. **115**, 5, 052001 (2015), [arXiv:1411.3007].

[197] J. Currie, E. W. N. Glover and J. Pires, Phys. Rev. Lett. **118**, 7, 072002 (2017), [arXiv:1611.01460].

[198] D. de Florian and J. Mazzitelli, Phys. Rev. Lett. **111**, 201801 (2013), [arXiv:1309.6594].

[199] J. Cruz-Martinez *et al.*, Phys. Lett. **B781**, 672 (2018), [arXiv:1802.02445].

[200] T. Liu, K. Melnikov and A. A. Penin (2019), [arXiv:1906.10899].

[201] *Les Houches 2017: Physics at TeV Colliders Standard Model Working Group Report* (2018), [arXiv:1803.07977], URL `http://lss.fnal.gov/archive/2018/conf/fermilab-conf-18-122-cd-t.pdf`.

[202] Y. L. Dokshitzer, D. Diakonov and S. I. Troian, Phys. Rept. **58**, 269 (1980).

[203] G. Parisi and R. Petronzio, Nucl. Phys. **B154**, 427 (1979).

[204] G. Curci, M. Greco and Y. Srivastava, Nucl. Phys. **B159**, 451 (1979).

[205] A. Bassetto, M. Ciafaloni and G. Marchesini, Nucl. Phys. **B163**, 477 (1980).

[206] J. C. Collins and D. E. Soper, Nucl. Phys. **B193**, 381 (1981), [Erratum: Nucl. Phys.B213,545(1983)].

[207] J. C. Collins and D. E. Soper, Nucl. Phys. **B197**, 446 (1982).

[208] J. Kodaira and L. Trentadue, Phys. Lett. **112B**, 66 (1982).

[209] J. Kodaira and L. Trentadue, Phys. Lett. **123B**, 335 (1983).

[210] J. C. Collins, D. E. Soper and G. F. Sterman, Nucl. Phys. **B250**, 199 (1985).

[211] S. Catani *et al.*, Nucl. Phys. **B407**, 3 (1993).

[212] C. W. Bauer *et al.*, Phys. Rev. **D63**, 114020 (2001), [hep-ph/0011336].

[213] C. W. Bauer, D. Pirjol and I. W. Stewart, Phys. Rev. **D65**, 054022 (2002), [hep-ph/0109045].

[214] T. Becher, A. Broggio and A. Ferroglia, Lect. Notes Phys. **896**, pp.1 (2015), [arXiv:1410.1892].

[215] S. Catani *et al.*, Phys. Lett. **B269**, 432 (1991).

[216] N. Brown and W. J. Stirling, Phys. Lett. **B252**, 657 (1990).

[217] W. Bartel *et al.* (JADE), Z. Phys. **C33**, 23 (1986), [,53(1986)].

[218] N. Kidonakis, G. Oderda and G. F. Sterman, Nucl. Phys. **B531**, 365 (1998), [hep-ph/9803241].

[219] R. Bonciani *et al.*, Phys. Lett. **B575**, 268 (2003), [hep-ph/0307035].

[220] A. Banfi, G. P. Salam and G. Zanderighi, JHEP **03**, 073 (2005), [hep-ph/0407286].

[221] D. de Florian and M. Grazzini, Phys. Rev. Lett. **85**, 4678 (2000), [hep-ph/0008152].

[222] G. Bozzi *et al.*, Nucl. Phys. **B737**, 73 (2006), [hep-ph/0508068]; `http://theory.fi.infn.it/grazzini/codes.html`.

[223] G. Bozzi *et al.*, Phys. Lett. **B696**, 207 (2011), [arXiv:1007.2351].

[224] T. Becher and M. Neubert, Eur. Phys. J. **C71**, 1665 (2011), [arXiv:1007.4005].

[225] T. Becher, M. Neubert, and D. Wilhelm, `http://cute.hepforge.org/`.

[226] D. de Florian *et al.*, JHEP **06**, 132 (2012), [arXiv:1203.6321]; `http://theory.fi.infn.it/grazzini/codes.html`.

[227] C. Balazs and C. P. Yuan, Phys. Rev. **D56**, 5558 (1997), [hep-ph/9704258].

[228] S. Catani *et al.*, JHEP **12**, 047 (2015), [arXiv:1507.06937].

[229] A. Banfi *et al.*, Phys. Lett. **B715**, 152 (2012), [arXiv:1205.4760].

[230] M. Grazzini *et al.*, JHEP **08**, 154 (2015), [arXiv:1507.02565].

[231] D. de Florian and M. Grazzini, Nucl. Phys. **B704**, 387 (2005), [hep-ph/0407241].

[232] T. Becher and G. Bell, JHEP **11**, 126 (2012), [arXiv:1210.0580].

[233] A. Banfi *et al.*, Phys. Rev. Lett. **109**, 202001 (2012), [arXiv:1206.4998]; T. Becher, M. Neubert and L. Rothen, JHEP **10**, 125 (2013), [arXiv:1307.0025].

[234] I. W. Stewart *et al.*, Phys. Rev. **D89**, 5, 054001 (2014), [arXiv:1307.1808].

[235] I. W. Stewart, F. J. Tackmann and W. J. Waalewijn, Phys. Rev. Lett. **106**, 032001 (2011), [arXiv:1005.4060].

[236] Y.-T. Chien *et al.*, Phys. Rev. **D87**, 1, 014010 (2013), [arXiv:1208.0010]; T. T. Jouttenus *et al.*, Phys. Rev. **D88**, 5, 054031 (2013), [arXiv:1302.0846].

[237] M. Dasgupta *et al.*, JHEP **10**, 126 (2012), [arXiv:1207.1640].

[238] V. Ahrens *et al.*, JHEP **09**, 097 (2010), [arXiv:1003.5827].

[239] M. Aliev *et al.*, Comput. Phys. Commun. **182**, 1034 (2011), [arXiv:1007.1327].

[240] N. Kidonakis, Phys. Rev. **D82**, 114030 (2010), [arXiv:1009.4935].

[241] T. Becher, C. Lorentzen and M. D. Schwartz, Phys. Rev. Lett. **108**, 012001 (2012), [arXiv:1106.4310].

[242] T. Becher *et al.*, Eur. Phys. J. **C75**, 4, 154 (2015), [arXiv:1412.8408].

[243] E. Gerwick *et al.*, JHEP **02**, 106 (2015), [arXiv:1411.7325].

[244] A. Banfi *et al.*, JHEP **05**, 102 (2015), [arXiv:1412.2126].

[245] T. Becher and M. D. Schwartz, JHEP **07**, 034 (2008), [arXiv:0803.0342].

[246] A. H. Hoang *et al.*, Phys. Rev. **D91**, 9, 094017 (2015), [arXiv:1411.6633].

[247] Y.-T. Chien and M. D. Schwartz, JHEP **08**, 058 (2010), [arXiv:1005.1644].

[248] P. F. Monni, T. Gehrmann and G. Luisoni, JHEP **08**, 010 (2011), [arXiv:1105.4560].

[249] W. Bizon *et al.*, JHEP **02**, 108 (2018), [arXiv:1705.09127].

[250] W. Bizon *et al.* (2019), [arXiv:1905.05171].

[251] S. Catani *et al.*, Nucl. Phys. **B888**, 75 (2014), [arXiv:1405.4827].

[252] S. Fleming *et al.*, Phys. Rev. **D77**, 074010 (2008), [hep-ph/0703207].

[253] A. H. Hoang, P. Pietrulewicz and D. Samitz, Phys. Rev. **D93**, 3, 034034 (2016), [arXiv:1508.04323].

[254] A. Banfi *et al.*, JHEP **04**, 049 (2016), [arXiv:1511.02886].

[255] A. J. Larkoski and I. Moult, Phys. Rev. **D93**, 014017 (2016), [arXiv:1510.08459].

[256] G. Lustermans, W. J. Waalewijn and L. Zeune, Phys. Lett. **B762**, 447 (2016), [arXiv:1605.02740].

[257] C. Muselli, S. Forte and G. Ridolfi, JHEP **03**, 106 (2017), [arXiv:1701.01464].

[258] M. Bonvini and S. Marzani, Phys. Rev. Lett. **120**, 20, 202003 (2018), [arXiv:1802.07758].

[259] M. Procura, W. J. Waalewijn and L. Zeune, JHEP **10**, 098 (2018), [arXiv:1806.10622].

[260] G. Lustermans *et al.*, JHEP **03**, 124 (2019), [arXiv:1901.03331].

[261] I. Feige *et al.*, Phys. Rev. Lett. **109**, 092001 (2012), [arXiv:1204.3898].

[262] M. Dasgupta *et al.*, JHEP **09**, 029 (2013), [arXiv:1307.0007].

[263] A. J. Larkoski *et al.*, JHEP **05**, 146 (2014), [arXiv:1402.2657].

[264] M. Dasgupta, A. Powling and A. Siodmok, JHEP **08**, 079 (2015), [arXiv:1503.01088].

[265] A. J. Larkoski, I. Moult and D. Neill, JHEP **05**, 117 (2016), [arXiv:1507.03018].

[266] C. Frye *et al.*, JHEP **07**, 064 (2016), [arXiv:1603.09338].

[267] A. J. Larkoski, I. Moult and D. Neill, JHEP **02**, 144 (2018), [arXiv:1710.00014].

[268] A. J. Larkoski, I. Moult and B. Nachman (2017), [arXiv:1709.04464].

[269] S. Marzani, G. Soyez and M. Spannowsky (2019), [Lect. Notes Phys.958,pp.(2019)], [arXiv:1901.10342].

[270] Yu.L. Dokshitzer *et al.*, *"Basics of perturbative QCD,"* Gif-sur-Yvette, France: Éditions frontières (1991), see also `http://www.lpthe.jussieu.fr/~yuri/BPQCD/cover.html`.

[271] T. Sj ostrand *et al.*, Comput. Phys. Commun. **135**, 238 (2001), [hep-ph/0010017].

[272] T. Sj ostrand, S. Mrenna and P. Z. Skands, JHEP **05**, 026 (2006), [hep-ph/0603175]; `http://projects.hepforge.org/pythia6/`.

[273] T. Sjostrand *et al.*, Comput. Phys. Commun. **191**, 159 (2015), [arXiv:1410.3012]; `http://home.thep.lu.se/~torbjorn/Pythia.html`.

[274] B. R. Webber, Nucl. Phys. **B238**, 492 (1984).

[275] G. Corcella *et al.*, JHEP **01**, 010 (2001), [hep-ph/0011363]; `http://www.hep.phy.cam.ac.uk/theory/webber/Herwig/`.

[276] M. Bahr *et al.*, Eur. Phys. J. **C58**, 639 (2008), [arXiv:0803.0883]; `http://projects.hepforge.org/herwig/`.

[277] L. Lonnblad, Comput. Phys. Commun. **71**, 15 (1992).

[278] A. Buckley *et al.*, Phys. Rept. **504**, 145 (2011), [arXiv:1101.2599].

[279] B. Andersson *et al.*, Phys. Rept. **97**, 31 (1983).

[280] T. Sjostrand, Nucl. Phys. **B248**, 469 (1984).

[281] J. Bellm *et al.* (2019), [arXiv:1903.12563].

[282] T. Sjostrand and M. van Zijl, Phys. Rev. **D36**, 2019 (1987).

[283] S. Catani *et al.*, JHEP **11**, 063 (2001), [hep-ph/0109231].

[284] J. Alwall *et al.*, Eur. Phys. J. **C53**, 473 (2008), [arXiv:0706.2569].

[285] S. Frixione and B. R. Webber, JHEP **06**, 029 (2002), [hep-ph/0204244].

[286] P. Nason, JHEP **11**, 040 (2004), [hep-ph/0409146].

[287] S. Alioli *et al.*, JHEP **06**, 043 (2010), [arXiv:1002.2581]; `http://powhegbox.mib.infn.it/`.

[288] S. Plätzer, JHEP **08**, 114 (2013), [arXiv:1211.5467]; R. Frederix and S. Frixione, JHEP **12**, 061 (2012), [arXiv:1209.6215]; K. Hamilton *et al.*, JHEP **05**, 082 (2013), [arXiv:1212.4504].

[289] K. Hamilton *et al.*, JHEP **10**, 222 (2013), [arXiv:1309.0017]; A. Karlberg, E. Re and G. Zanderighi, JHEP **09**, 134 (2014), [arXiv:1407.2940]; S. Höche, Y. Li and S. Prestel, Phys. Rev. **D91**, 7, 074015 (2015), [arXiv:1405.3607]; S. Höche, Y. Li and S. Prestel, Phys. Rev. **D90**, 5, 054011 (2014), [arXiv:1407.3773]; S. Alioli *et al.*, Phys. Rev. **D92**, 9, 094020 (2015), [arXiv:1508.01475]; P. F. Monni *et al.* (2019), [arXiv:1908.06987].

[290] W. Astill *et al.*, JHEP **06**, 154 (2016), [arXiv:1603.01620].

[291] W. Astill *et al.*, JHEP **11**, 157 (2018), [arXiv:1804.08141].

[292] E. Re, M. Wiesemann and G. Zanderighi, JHEP **12**, 121 (2018), [arXiv:1805.09857].

[293] M. Cacciari *et al.*, JHEP **04**, 068 (2004), [hep-ph/0303085].

[294] P. M. Stevenson, Phys. Lett. **100B**, 61 (1981).

[295] P. M. Stevenson, Phys. Rev. **D23**, 2916 (1981).

[296] G. Grunberg, Phys. Rev. **D29**, 2315 (1984).

[297] S. J. Brodsky, G. P. Lepage and P. B. Mackenzie, Phys. Rev. **D28**, 228 (1983).

[298] S.-Q. Wang *et al.* (2019), [arXiv:1908.00060].

[299] M. Cacciari and N. Houdeau, JHEP **09**, 039 (2011), [arXiv:1105.5152].

[300] A. David and G. Passarino, Phys. Lett. **B726**, 266 (2013), [arXiv:1307.1843].

[301] E. Bagnaschi *et al.*, JHEP **02**, 133 (2015), [arXiv:1409.5036].

[302] M. Dasgupta *et al.*, JHEP **06**, 057 (2016), [arXiv:1602.01110].

[303] J. Currie *et al.*, JHEP **10**, 155 (2018), [arXiv:1807.03692].

[304] G. Soyez *et al.*, Phys. Rev. Lett. **110**, 16, 162001 (2013), [arXiv:1211.2811].

[305] M. Dasgupta and G. P. Salam, J. Phys. **G30**, R143 (2004), [hep-ph/0312283].

[306] S. Moretti, L. Lonnblad and T. Sjostrand, JHEP **08**, 001 (1998), [hep-ph/9804296].

[307] G. P. Salam, Eur. Phys. J. **C67**, 637 (2010), [arXiv:0906.1833].

[308] S. D. Ellis *et al.*, Prog. Part. Nucl. Phys. **60**, 484 (2008), [arXiv:0712.2447].

[309] M. Cacciari, Int. J. Mod. Phys. **A30**, 31, 1546001 (2015), [arXiv:1509.02272].

[310] G. P. Salam and G. Soyez, JHEP **05**, 086 (2007), [arXiv:0704.0292].

[311] S. Catani *et al.*, Nucl. Phys. **B406**, 187 (1993).

[312] S. D. Ellis and D. E. Soper, Phys. Rev. **D48**, 3160 (1993), [hep-ph/9305266].

[313] Y. L. Dokshitzer *et al.*, JHEP **08**, 001 (1997), [hep-ph/9707323].

[314] M. Wobisch and T. Wengler, in "Monte Carlo generators for HERA physics. Proceedings, Workshop, Hamburg, Germany, 1998-1999," 270–279 (1998), [hep-ph/9907280].

[315] M. Cacciari, G. P. Salam and G. Soyez, JHEP **04**, 063 (2008), [arXiv:0802.1189].

[316] S. Bethke *et al.*, Nucl. Phys. **B370**, 310 (1992), [Erratum: Nucl. Phys.B523,681(1998)].

[317] M. Cacciari and G. P. Salam, Phys. Lett. **B641**, 57 (2006), [hep-ph/0512210]; M. Cacciari, G. P. Salam and G. Soyez, Eur. Phys. J. **C72**, 1896 (2012), [arXiv:1111.6097].

[318] S. Brandt *et al.*, Phys. Lett. **12**, 57 (1964).

[319] E. Farhi, Phys. Rev. Lett. **39**, 1587 (1977).

[320] O. Biebel, Phys. Rept. **340**, 165 (2001).

[321] S. Kluth, Rept. Prog. Phys. **69**, 1771 (2006), [hep-ex/0603011].

[322] C. L. Basham *et al.*, Phys. Rev. Lett. **41**, 1585 (1978).

[323] A. Ali, E. Pietarinen and W. J. Stirling, Phys. Lett. **141B**, 447 (1984).

[324] I. W. Stewart, F. J. Tackmann and W. J. Waalewijn, Phys. Rev. Lett. **105**, 092002 (2010), [arXiv:1004.2489].

[325] A. Banfi, G. P. Salam and G. Zanderighi, JHEP **08**, 062 (2004), [hep-ph/0407287].

[326] A. Banfi, G. P. Salam and G. Zanderighi, JHEP **06**, 038 (2010), [arXiv:1001.4082].

[327] T. Becher, X. Garcia i Tormo and J. Piclum, Phys. Rev. **D93**, 5, 054038 (2016), [Erratum: Phys. Rev.D93,no.7,079905(2016)], [arXiv:1512.00022].

[328] A. Gao *et al.*, Phys. Rev. Lett. **123**, 6, 062001 (2019), [arXiv:1901.04497].

[329] T. Aaltonen *et al.* (CDF), Phys. Rev. **D83**, 112007 (2011), [arXiv:1103.5143].

[330] G. Aad *et al.* (ATLAS), Eur. Phys. J. **C72**, 2211 (2012), [arXiv:1206.2135].

[331] G. Aad *et al.* (ATLAS), Phys. Rev. **D88**, 3, 032004 (2013), [arXiv:1207.6915].

[332] G. Aad *et al.* (ATLAS), Phys. Lett. **B750**, 427 (2015), [arXiv:1508.01579].

[333] G. Aad *et al.* (ATLAS), Eur. Phys. J. **C76**, 7, 375 (2016), [arXiv:1602.08980].

[334] M. Aaboud *et al.* (ATLAS), Eur. Phys. J. **C77**, 12, 872 (2017), [arXiv:1707.02562].

[335] M. Aaboud *et al.* (ATLAS), Phys. Rev. **D98**, 9, 092004 (2018), [arXiv:1805.04691].

[336] V. Khachatryan *et al.* (CMS), Phys. Lett. **B699**, 48 (2011), [arXiv:1102.0068].

[337] S. Chatrchyan *et al.* (CMS), Phys. Lett. **B722**, 238 (2013), [arXiv:1301.1646].

[338] V. Khachatryan *et al.* (CMS), JHEP **10**, 87 (2014), [arXiv:1407.2856].

[339] A. M. Sirunyan *et al.* (CMS), JHEP **12**, 117 (2018), [arXiv:1811.00588].

[340] S. Chatrchyan *et al.* (CMS), Phys. Lett. **B730**, 243 (2014), [arXiv:1310.0878].

[341] G. Aad *et al.* (ATLAS), Phys. Rev. **D83**, 052003 (2011), [arXiv:1101.0070].

[342] S. Chatrchyan *et al.* (CMS), JHEP **06**, 160 (2012), [arXiv:1204.3170].

[343] B. B. Abelev *et al.* (ALICE), Phys. Rev. **D91**, 11, 112012 (2015), [arXiv:1411.4969].

[344] G. Aad *et al.* (ATLAS), Eur. Phys. J. **C73**, 12, 2676 (2013), [arXiv:1307.5749].

[345] C. Glasman (H1, ZEUS), Nucl. Phys. Proc. Suppl. **191**, 121 (2009), [arXiv:0812.0757].

[346] T. Carli, K. Rabbertz and S. Schumann, in T. Schörner-Sadenius, editor, "The Large Hadron Collider: Harvest of Run 1," 139–194 (2015), [arXiv:1506.03239].

[347] A. Abdesselam *et al.*, Eur. Phys. J. **C71**, 1661 (2011), [arXiv:1012.5412].

[348] D. Krohn, J. Thaler and L.-T. Wang, JHEP **02**, 084 (2010), [arXiv:0912.1342].

[349] A. Altheimer *et al.*, J. Phys. **G39**, 063001 (2012), [arXiv:1201.0008].

[350] A. Altheimer *et al.*, Eur. Phys. J. **C74**, 3, 2792 (2014), [arXiv:1311.2708].

[351] P. C. Stichel and W. J. Zakrzewski, Eur. Phys. J. **C75**, 1, 9 (2015), [arXiv:1409.1363].

[352] D. Adams *et al.*, Eur. Phys. J. **C75**, 9, 409 (2015), [arXiv:1504.00679].

[353] T. Schorner-Sadenius, Eur. Phys. J. **C72**, 2060 (2012), [Erratum: Eur. Phys. J.C72,2133(2012)].

[354] J. M. Campbell, J. W. Huston and W. J. Stirling, Rept. Prog. Phys. **70**, 89 (2007), [hep-ph/0611148].

[355] M. L. Mangano, Phys. Usp. **53**, 109 (2010), [Usp. Fiz. Nauk180,113(2010)].

[356] J. M. Butterworth, G. Dissertori and G. P. Salam, Ann. Rev. Nucl. Part. Sci. **62**, 387 (2012), [arXiv:1202.0583].

[357] J. Currie *et al.*, JHEP **07**, 018 (2017), [arXiv:1703.05977].

[358] M. Klasen, G. Kramer and M. Michael, Phys. Rev. **D89**, 7, 074032 (2014), [arXiv:1310.1724].

[359] T. Carli, T. Gehrmann and S. Hoeche, Eur. Phys. J. **C67**, 73 (2010), [arXiv:0912.3715].

[360] S. Chekanov *et al.* (ZEUS), Nucl. Phys. **B792**, 1 (2008), [arXiv:0707.3749].

[361] S. Chekanov *et al.* (ZEUS), Phys. Rev. **D76**, 072011 (2007), [arXiv:0706.3809].

[362] A. Aktas *et al.* (H1), Phys. Lett. **B639**, 21 (2006), [hep-ex/0603014].

[363] H. Abramowicz *et al.* (ZEUS), Eur. Phys. J. **C71**, 1659 (2011), [arXiv:1104.5444].

[364] H. Abramowicz *et al.* (ZEUS), Nucl. Phys. **B864**, 1 (2012), [arXiv:1205.6153].

[365] F. D. Aaron *et al.* (H1), Eur. Phys. J. **C65**, 363 (2010), [arXiv:0904.3870].

[366] F. D. Aaron *et al.* (H1), Eur. Phys. J. **C54**, 389 (2008), [arXiv:0711.2606].

[367] S. Chekanov *et al.* (ZEUS), Eur. Phys. J. **C52**, 515 (2007), [arXiv:0707.3093].

[368] S. Chekanov *et al.* (ZEUS), Phys. Rev. **D78**, 032004 (2008), [arXiv:0802.3955].

[369] H. Abramowicz *et al.* (ZEUS), Eur. Phys. J. **C70**, 965 (2010), [arXiv:1010.6167].

[370] H. Abramowicz *et al.* (ZEUS), Phys. Lett. **B691**, 127 (2010), [arXiv:1003.2923].

[371] S. Chekanov *et al.* (ZEUS), Phys. Rev. **D85**, 052008 (2012), [arXiv:0808.3783].

[372] F. D. Aaron *et al.* (H1), Eur. Phys. J. **C67**, 1 (2010), [arXiv:0911.5678].

[373] V. Andreev *et al.* (H1), Eur. Phys. J. **C75**, 2, 65 (2015), [arXiv:1406.4709].

[374] V. Andreev *et al.* (H1), Eur. Phys. J. **C77**, 11, 791 (2017), [arXiv:1709.07251].

[375] `http://twiki.cern.ch/twiki/bin/view/CMSPublic/PhysicsResultsCombined`.

[376] `http://atlas.web.cern.ch/Atlas/GROUPS/PHYSICS/CombinedSummaryPlots/SM`.

[377] A. Abulencia *et al.* (CDF), Phys. Rev. **D75**, 092006 (2007), [Erratum: Phys. Rev.D75,119901(2007)], [hep-ex/0701051].

[378] T. Aaltonen *et al.* (CDF), Phys. Rev. **D78**, 052006 (2008), [Erratum: Phys. Rev.D79,119902(2009)], [arXiv:0807.2204].

[379] V. M. Abazov *et al.* (D0), Phys. Rev. Lett. **101**, 062001 (2008), [arXiv:0802.2400].

[380] V. M. Abazov *et al.* (D0), Phys. Rev. **D85**, 052006 (2012), [arXiv:1110.3771].

[381] B. Abelev *et al.* (ALICE), Phys. Lett. **B722**, 262 (2013), [arXiv:1301.3475].

[382] G. Aad *et al.* (ATLAS), Eur. Phys. J. **C73**, 8, 2509 (2013), [arXiv:1304.4739].

[383] G. Aad *et al.* (ATLAS), JHEP **02**, 153 (2015), [Erratum: JHEP09,141(2015)], [arXiv:1410.8857].

[384] M. Aaboud *et al.* (ATLAS), JHEP **09**, 020 (2017), [arXiv:1706.03192].

[385] V. Khachatryan *et al.* (CMS), Eur. Phys. J. **C76**, 5, 265 (2016), [arXiv:1512.06212].

[386] S. Chatrchyan *et al.* (CMS), Phys. Rev. **D87**, 11, 112002 (2013), [Erratum: Phys. Rev.D87,no.11,119902(2013)], [arXiv:1212.6660].

[387] V. Khachatryan *et al.* (CMS), JHEP **03**, 156 (2017), [arXiv:1609.05331].

[388] V. Khachatryan *et al.* (CMS), Eur. Phys. J. **C76**, 8, 451 (2016), [arXiv:1605.04436].

[389] M. Aaboud *et al.* (ATLAS), JHEP **05**, 195 (2018), [arXiv:1711.02692].

[390] A. Schwartzman, Int. J. Mod. Phys. **A30**, 31, 1546002 (2015), [arXiv:1509.05459].

[391] J. Rojo, Int. J. Mod. Phys. **A30**, 1546005 (2015), [arXiv:1410.7728].

[392] G. Aad *et al.* (ATLAS), JHEP **05**, 059 (2014), [arXiv:1312.3524].

[393] A. M. Sirunyan *et al.* (CMS), Eur. Phys. J. **C77**, 11, 746 (2017), [arXiv:1705.02628].

[394] T. Aaltonen *et al.* (CDF), Phys. Rev. **D79**, 112002 (2009), [arXiv:0812.4036].

[395] V. M. Abazov *et al.* (D0), Phys. Rev. Lett. **103**, 191803 (2009), [arXiv:0906.4819].

[396] S. Chatrchyan *et al.* (CMS), JHEP **05**, 055 (2012), [arXiv:1202.5535].

[397] V. Khachatryan *et al.* (CMS), Phys. Lett. **B746**, 79 (2015), [arXiv:1411.2646].

[398] A. M. Sirunyan *et al.* (CMS), JHEP **07**, 013 (2017), [arXiv:1703.09986].

[399] G. Aad *et al.* (ATLAS), JHEP **01**, 029 (2013), [arXiv:1210.1718].

[400] M. Aaboud *et al.* (ATLAS), Phys. Rev. **D96**, 5, 052004 (2017), [arXiv:1703.09127].

[401] V. M. Abazov *et al.* (D0), Phys. Rev. Lett. **94**, 221801 (2005), [hep-ex/0409040].

[402] V. M. Abazov *et al.* (D0), Phys. Lett. **B721**, 212 (2013), [arXiv:1212.1842].

[403] G. Aad *et al.* (ATLAS), Phys. Rev. Lett. **106**, 172002 (2011), [arXiv:1102.2696].

[404] V. Khachatryan *et al.* (CMS), Phys. Rev. Lett. **106**, 122003 (2011), [arXiv:1101.5029].

[405] V. Khachatryan *et al.* (CMS), Eur. Phys. J. **C76**, 10, 536 (2016), [arXiv:1602.04384].

[406] A. M. Sirunyan *et al.* (CMS), Eur. Phys. J. **C78**, 7, 566 (2018), [arXiv:1712.05471].

[407] A. M. Sirunyan *et al.* (CMS) (2019), [arXiv:1902.04374].

[408] P. Kokkas, Int. J. Mod. Phys. **A30**, 31, 1546004 (2015), [arXiv:1509.02144].

[409] M. Aaboud *et al.* (ATLAS), Eur. Phys. J. **C77**, 6, 367 (2017), [arXiv:1612.03016].

[410] G. Aad *et al.* (ATLAS), Phys. Lett. **B759**, 601 (2016), [arXiv:1603.09222].

[411] R. Aaij *et al.* (LHCb), JHEP **08**, 039 (2015), [arXiv:1505.07024].

[412] S. Chatrchyan *et al.* (CMS), JHEP **10**, 132 (2011), [arXiv:1107.4789].

[413] S. Chatrchyan *et al.* (CMS), Phys. Rev. Lett. **112**, 191802 (2014), [arXiv:1402.0923].

[414] R. Aaij *et al.* (LHCb), JHEP **06**, 058 (2012), [arXiv:1204.1620].

[415] R. Aaij *et al.* (LHCb), JHEP **01**, 155 (2016), [arXiv:1511.08039].

[416] R. Aaij *et al.* (LHCb), JHEP **09**, 136 (2016), [arXiv:1607.06495].

[417] S. Chatrchyan *et al.* (CMS), JHEP **10**, 007 (2011), [arXiv:1108.0566].

[418] V. Khachatryan *et al.* (CMS), Eur. Phys. J. **C75**, 4, 147 (2015), [arXiv:1412.1115].

[419] G. Aad *et al.* (ATLAS), Phys. Lett. **B725**, 223 (2013), [arXiv:1305.4192].

[420] G. Aad *et al.* (ATLAS), JHEP **06**, 112 (2014), [arXiv:1404.1212].

[421] G. Aad *et al.* (ATLAS), JHEP **08**, 009 (2016), [arXiv:1606.01736].

[422] A. M. Sirunyan *et al.* (CMS), Submitted to: JHEP (2018), [arXiv:1812.10529].

[423] M. Aaboud *et al.* (ATLAS), JHEP **12**, 059 (2017), [arXiv:1710.05167].

[424] S. Chatrchyan *et al.* (CMS), Phys. Rev. **D90**, 3, 032004 (2014), [arXiv:1312.6283].

[425] V. Khachatryan *et al.* (CMS), Eur. Phys. J. **C76**, 8, 469 (2016), [arXiv:1603.01803].

[426] G. Aad *et al.* (ATLAS), Submitted to: Eur. Phys. J. (2019), [arXiv:1904.05631].

[427] G. Aad *et al.* (ATLAS), Eur. Phys. J. **C76**, 5, 291 (2016), [arXiv:1512.02192].

[428] V. Khachatryan *et al.* (CMS), JHEP **02**, 096 (2017), [arXiv:1606.05864].

[429] A. M. Sirunyan *et al.* (CMS), JHEP **03**, 172 (2018), [arXiv:1710.07955].

[430] M. Aaboud *et al.* (ATLAS), JHEP **05**, 077 (2018), [arXiv:1711.03296].

[431] C. F. Berger *et al.*, Phys. Rev. **D80**, 074036 (2009), [arXiv:0907.1984].

[432] U. Blumenschein, Int. J. Mod. Phys. **A30**, 31, 1546007 (2015), [arXiv:1509.04885].

[433] G. Aad *et al.* (ATLAS) (2019), [arXiv:1907.06728].

[434] V. Khachatryan *et al.* (CMS), Phys. Rev. **D95**, 052002 (2017), [arXiv:1610.04222].

[435] A. M. Sirunyan *et al.* (CMS), Phys. Rev. **D96**, 7, 072005 (2017), [arXiv:1707.05979].

[436] A. M. Sirunyan *et al.* (CMS), Eur. Phys. J. **C78**, 11, 965 (2018), [arXiv:1804.05252].

[437] G. Aad *et al.* (ATLAS), JHEP **07**, 032 (2013), [arXiv:1304.7098].

[438] Z. Bern *et al.*, Phys. Rev. **D88**, 1, 014025 (2013), [arXiv:1304.1253].

[439] M. Voutilainen, Int. J. Mod. Phys. **A30**, 31, 1546008 (2015), [arXiv:1509.05026].

[440] G. Aad *et al.* (ATLAS), JHEP **08**, 005 (2016), [arXiv:1605.03495].

[441] G. Aad *et al.* (ATLAS) (2019), [arXiv:1908.02746].

[442] S. Chatrchyan *et al.* (CMS), Phys. Rev. **D84**, 052011 (2011), [arXiv:1108.2044].

[443] S. Chatrchyan *et al.* (CMS), JHEP **06**, 009 (2014), [arXiv:1311.6141].

[444] G. Aad *et al.* (ATLAS), Phys. Rev. **D89**, 5, 052004 (2014), [arXiv:1311.1440].

[445] M. Aaboud *et al.* (ATLAS), Phys. Lett. **B780**, 578 (2018), [arXiv:1801.00112].

[446] M. Aaboud *et al.* (ATLAS), Nucl. Phys. **B918**, 257 (2017), [arXiv:1611.06586].

[447] A. M. Sirunyan *et al.* (CMS), Eur. Phys. J. **C79**, 1, 20 (2019), [arXiv:1807.00782].

[448] A. M. Sirunyan *et al.* (CMS) (2019), [arXiv:1907.08155].

[449] M. Aaboud *et al.* (ATLAS), Phys. Lett. **B776**, 295 (2018), [arXiv:1710.09560].

[450] J. H. Kuhn *et al.*, JHEP **03**, 059 (2006), [hep-ph/0508253].

[451] V. Khachatryan *et al.* (CMS), JHEP **10**, 128 (2015), [Erratum: JHEP04,010(2016)], [arXiv:1505.06520].

[452] G. Aad *et al.* (ATLAS), JHEP **09**, 029 (2016), [arXiv:1603.01702].

[453] M. Aaboud *et al.* (ATLAS), Phys. Lett. **B773**, 354 (2017), [arXiv:1702.04519].

[454] M. Aaboud *et al.* (ATLAS) (2019), [arXiv:1905.04242].

[455] V. Khachatryan *et al.* (CMS), Eur. Phys. J. **C76**, 7, 401 (2016), [arXiv:1507.03268].

[456] G. Aad *et al.* (ATLAS) (2019), [arXiv:1903.10415].

[457] G. Aad *et al.* (ATLAS), JHEP **01**, 086 (2013), [arXiv:1211.1913].

[458] M. Aaboud *et al.* (ATLAS), Phys. Rev. **D95**, 11, 112005 (2017), [arXiv:1704.03839].

[459] S. Chatrchyan *et al.* (CMS), Eur. Phys. J. **C74**, 11, 3129 (2014), [arXiv:1405.7225].

[460] M. Aaboud *et al.* (ATLAS), Phys. Lett. **B781**, 55 (2018), [arXiv:1712.07291].

[461] K. Kröninger, A. B. Meyer and P. Uwer, in T. Schörner-Sadenius, editor, "The Large Hadron Collider: Harvest of Run 1," 259–300 (2015), [arXiv:1506.02800].

[462] M. Aaboud *et al.* (ATLAS), Phys. Rev. **D94**, 9, 092003 (2016), [arXiv:1607.07281].

[463] M. Aaboud *et al.* (ATLAS), Eur. Phys. J. **C77**, 5, 292 (2017), [arXiv:1612.05220].

[464] A. M. Sirunyan *et al.* (CMS), Eur. Phys. J. **C79**, 5, 368 (2019), [arXiv:1812.10505].

[465] A. M. Sirunyan *et al.* (CMS), Submitted to: Eur. Phys. J. (2019), [arXiv:1904.05237].

[466] M. Czakon, D. Heymes and A. Mitov, Phys. Rev. Lett. **116**, 8, 082003 (2016), [arXiv:1511.00549].

[467] S. Catani *et al.*, Phys. Rev. **D99**, 5, 051501 (2019), [arXiv:1901.04005].

[468] S. Catani *et al.*, JHEP **07**, 100 (2019), [arXiv:1906.06535].

[469] M. Czakon *et al.*, JHEP **05**, 149 (2018), [arXiv:1803.07623].

[470] S. Chatrchyan *et al.* (CMS), Phys. Lett. **B728**, 496 (2014), [Erratum: Phys. Lett.B738,526(2014)], [arXiv:1307.1907].

[471] T. Klijnsma *et al.*, Eur. Phys. J. **C77**, 11, 778 (2017), [arXiv:1708.07495].

[472] G. Aad *et al.* (ATLAS), Eur. Phys. J. **C74**, 10, 3109 (2014), [Addendum: Eur. Phys. J.C76,no.11,642(2016)], [arXiv:1406.5375].

[473] A. M. Sirunyan *et al.* (CMS), JHEP **09**, 051 (2017), [arXiv:1701.06228].

[474] M. Aaboud *et al.* (ATLAS), Phys. Lett. **B786**, 114 (2018), [arXiv:1805.10197].

[475] A. M. Sirunyan *et al.* (CMS), Phys. Lett. **B792**, 369 (2019), [arXiv:1812.06504].

[476] M. Aaboud *et al.* (ATLAS), Phys. Rev. **D98**, 052005 (2018), [arXiv:1802.04146].

[477] A. M. Sirunyan *et al.* (CMS), JHEP **01**, 183 (2019), [arXiv:1807.03825].

[478] A. M. Sirunyan *et al.* (CMS Collaboration), Phys. Lett. B **792**, arXiv:1812.06504. CMS-HIG-17-028-003, 369. 28 p (2018), submitted to Phys.Lett., URL `http://cds.cern.ch/record/2651932`.

[479] C. Patrignani *et al.* (Particle Data Group), Chin. Phys. **C40**, 10, 100001 (2016).

[480] M. Tanabashi *et al.* (Particle Data Group), Phys. Rev. **D98**, 3, 030001 (2018).

[481] S. Bethke, Prog. Part. Nucl. Phys. **58**, 351 (2007), [hep-ex/0606035].

[482] S. Bethke, Eur. Phys. J. **C64**, 689 (2009), [,111(2009)], [arXiv:0908.1135].

[483] S. Bethke, J. Phys. **G26**, R27 (2000), [hep-ex/0004021].

[484] D. d'Enterria *et al.*, in "Workshop on precision measurements of the QCD coupling constant (alphas-2019) Trento, Trentino, Italy, February 11-15, 2019," (2019), [arXiv:1907.01435].

[485] G. P. Salam, in A. Levy, S. Forte and G. Ridolfi, editors, "From My Vast Repertoire ...: Guido Altarelli's Legacy," 101–121 (2019), [arXiv:1712.05165].

[486] A. Pich *et al.*, in "13th Conference on Quark Confinement and the Hadron Spectrum (Confinement XIII) Maynooth, Ireland, July 31-August 6, 2018," (2018), [arXiv:1811.11801].

[487] S. Aoki *et al.* (Flavour Lattice Averaging Group) (2019), [arXiv:1902.08191].

[488] M. Beneke and M. Jamin, JHEP **09**, 044 (2008), [arXiv:0806.3156].

[489] K. Maltman and T. Yavin, Phys. Rev. **D78**, 094020 (2008), [arXiv:0807.0650].

[490] S. Narison, Phys. Lett. **B673**, 30 (2009), [arXiv:0901.3823].

[491] I. Caprini and J. Fischer, Eur. Phys. J. **C64**, 35 (2009), [arXiv:0906.5211].

[492] A. Pich, Prog. Part. Nucl. Phys. **75**, 41 (2014), [arXiv:1310.7922].

[493] D. Boito *et al.*, Phys. Rev. **D91**, 3, 034003 (2015), [arXiv:1410.3528].

[494] G. Altarelli, PoS **Corfu2012**, 002 (2013), [arXiv:1303.6065].

[495] A. Pich and A. Rodríguez-Sánchez, Phys. Rev. **D94**, 3, 034027 (2016), [arXiv:1605.06830].

[496] M. Davier *et al.*, Eur. Phys. J. **C74**, 3, 2803 (2014), [arXiv:1312.1501].

[497] D. Boito *et al.*, Phys. Rev. **D98**, 7, 074030 (2018), [arXiv:1805.08176].

[498] N. Brambilla *et al.*, Phys. Rev. **D75**, 074014 (2007), [hep-ph/0702079].

[499] V. Mateu and P. G. Ortega, JHEP **01**, 122 (2018), [arXiv:1711.05755].

[500] C. Peset, A. Pineda and J. Segovia, JHEP **09**, 167 (2018), [arXiv:1806.05197].

[501] C. Glasman (H1, ZEUS), J. Phys. Conf. Ser. **110**, 022013 (2008), [arXiv:0709.4426].

[502] T. Biekötter, M. Klasen and G. Kramer, Phys. Rev. **D92**, 7, 074037 (2015), [arXiv:1508.07153].

[503] J. Blumlein, H. Bottcher and A. Guffanti, Nucl. Phys. **B774**, 182 (2007), [hep-ph/0607200].

[504] P. Jimenez-Delgado and E. Reya, Phys. Rev. **D89**, 7, 074049 (2014), [arXiv:1403.1852].

[505] S. Alekhin *et al.*, Phys. Rev. **D96**, 1, 014011 (2017), [arXiv:1701.05838].

[506] S. Alekhin, J. Blümlein and S. Moch, Eur. Phys. J. **C78**, 6, 477 (2018), [arXiv:1803.07537].

[507] L. A. Harland-Lang *et al.*, Eur. Phys. J. **C75**, 9, 435 (2015), [arXiv:1506.05682].

[508] S. Dulat *et al.*, Phys. Rev. **D93**, 3, 033006 (2016), [arXiv:1506.07443].

[509] R. D. Ball *et al.* (NNPDF), Eur. Phys. J. **C78**, 5, 408 (2018), [arXiv:1802.03398].

[510] R. S. Thorne and G. Watt, JHEP **08**, 100 (2011), [arXiv:1106.5789].

[511] S. Alekhin, J. Blumlein and S. Moch, Eur. Phys. J. **C71**, 1723 (2011), [arXiv:1101.5261].

[512] R. D. Ball *et al.* (NNPDF), Phys. Lett. **B704**, 36 (2011), [arXiv:1102.3182].

[513] R. D. Ball *et al.* (NNPDF), Phys. Lett. **B723**, 330 (2013), [arXiv:1303.1189].

[514] R. S. Thorne, PoS **DIS2013**, 042 (2013), [arXiv:1306.3907].

[515] G. Dissertori *et al.*, JHEP **08**, 036 (2009), [arXiv:0906.3436].

[516] G. Abbiendi *et al.* (OPAL), Eur. Phys. J. **C71**, 1733 (2011), [arXiv:1101.1470].

[517] S. Bethke *et al.* (JADE), Eur. Phys. J. **C64**, 351 (2009), [arXiv:0810.1389].

[518] G. Dissertori *et al.*, Phys. Rev. Lett. **104**, 072002 (2010), [arXiv:0910.4283].

[519] J. Schieck *et al.* (JADE), Eur. Phys. J. **C73**, 3, 2332 (2013), [arXiv:1205.3714].

[520] A. Verbytskyi *et al.*, JHEP **08**, 129 (2019), [arXiv:1902.08158].

[521] A. Kardos *et al.*, Eur. Phys. J. **C78**, 6, 498 (2018), [arXiv:1804.09146].

[522] R. A. Davison and B. R. Webber, Eur. Phys. J. **C59**, 13 (2009), [arXiv:0809.3326].

[523] R. Abbate *et al.*, Phys. Rev. **D83**, 074021 (2011), [arXiv:1006.3080].

[524] T. Gehrmann, G. Luisoni and P. F. Monni, Eur. Phys. J. **C73**, 1, 2265 (2013), [arXiv:1210.6945].

[525] A. H. Hoang *et al.*, Phys. Rev. **D91**, 9, 094018 (2015), [arXiv:1501.04111].

[526] R. Frederix *et al.*, JHEP **11**, 050 (2010), [arXiv:1008.5313].

[527] P. Bolzoni, B. A. Kniehl and A. V. Kotikov, Nucl. Phys. **B875**, 18 (2013), [arXiv:1305.6017].

[528] J. Currie *et al.*, Phys. Rev. Lett. **119**, 15, 152001 (2017), [arXiv:1705.10271].

[529] M. Czakon *et al.* (2019), [arXiv:1907.12911].

[530] S. Dittmaier, A. Huss and C. Speckner, JHEP **11**, 095 (2012), [arXiv:1210.0438].

[531] R. Frederix *et al.*, JHEP **04**, 076 (2017), [arXiv:1612.06548].

[532] M. Czakon *et al.*, JHEP **10**, 186 (2017), [arXiv:1705.04105].

[533] M. Johnson and D. Maître, Phys. Rev. **D97**, 5, 054013 (2018), [arXiv:1711.01408].

[534] A. Gehrmann-De Ridder *et al.*, JHEP **07**, 133 (2016), [arXiv:1605.04295].

[535] D. Britzger *et al.* (2019), [arXiv:1906.05303].

[536] T. Affolder *et al.* (CDF), Phys. Rev. Lett. **88**, 042001 (2002), [hep-ex/0108034].

[537] S. Chekanov *et al.* (ZEUS), Phys. Lett. B **649**, 12 (2007), [hep-ex/0701039].

[538] V. M. Abazov *et al.* (D0), Phys. Rev. **D80**, 111107 (2009), [arXiv:0911.2710].

[539] B. Malaescu and P. Starovoitov, Eur. Phys. J. **C72**, 2041 (2012), [arXiv:1203.5416].

[540] V. Khachatryan *et al.* (CMS), Eur. Phys. J. **C75**, 6, 288 (2015), [arXiv:1410.6765].

[541] D. Britzger *et al.*, Eur. Phys. J. **C79**, 1, 68 (2019), [arXiv:1712.00480].

[542] S. Chekanov *et al.* (ZEUS), Eur. Phys. J. **C44**, 183 (2005), [hep-ex/0502007].

[543] S. Chatrchyan *et al.* (CMS), Eur. Phys. J. **C73**, 10, 2604 (2013), [arXiv:1304.7498].

[544] V. M. Abazov *et al.* (D0), Phys. Lett. **B718**, 56 (2012), [arXiv:1207.4957].

[545] V. Khachatryan *et al.* (CMS), Eur. Phys. J. **C75**, 5, 186 (2015), [arXiv:1412.1633].

[546] V. Andreev *et al.* (H1), Eur. Phys. J. C **77**, 4, 215 (2017), [arXiv:1611.03421].

[547] M. Baak *et al.* (Gfitter Group), Eur. Phys. J. **C74**, 3046 (2014), [arXiv:1407.3792].

[548] J. Haller *et al.*, Eur. Phys. J. **C78**, 8, 675 (2018), [arXiv:1803.01853].

[549] S. Schael *et al.* (ALEPH, DELPHI, L3, OPAL, SLD, LEP Electroweak Working Group, SLD Electroweak Group, SLD Heavy Flavour Group), Phys. Rept. **427**, 257 (2006), [hep-ex/0509008].

[550] I. Allison *et al.* (HPQCD), Phys. Rev. **D78**, 054513 (2008), [arXiv:0805.2999].

[551] K. Maltman *et al.*, Phys. Rev. **D78**, 114504 (2008), [arXiv:0807.2020].

[552] S. Aoki *et al.* (PACS-CS), JHEP **10**, 053 (2009), [arXiv:0906.3906].

[553] C. McNeile *et al.*, Phys. Rev. **D82**, 034512 (2010), [arXiv:1004.4285].

[554] E. Shintani *et al.*, Phys. Rev. **D82**, 7, 074505 (2010), [Erratum: Phys. Rev.D89,no.9,099903(2014)], [arXiv:1002.0371].

[555] B. Blossier *et al.*, Phys. Rev. **D85**, 034503 (2012), [arXiv:1110.5829].

[556] A. Bazavov *et al.*, Phys. Rev. **D86**, 114031 (2012), [arXiv:1205.6155].

[557] B. Blossier *et al.*, Phys. Rev. Lett. **108**, 262002 (2012), [arXiv:1201.5770].

[558] B. Blossier *et al.* (ETM), Phys. Rev. **D89**, 1, 014507 (2014), [arXiv:1310.3763].

[559] B. Chakraborty *et al.*, Phys. Rev. **D91**, 5, 054508 (2015), [arXiv:1408.4169].

[560] A. Bazavov *et al.*, Phys. Rev. **D90**, 7, 074038 (2014), [arXiv:1407.8437].

[561] K. Nakayama, B. Fahy and S. Hashimoto, Phys. Rev. **D94**, 5, 054507 (2016), [arXiv:1606.01002].

[562] Y. Maezawa and P. Petreczky, Phys. Rev. **D94**, 3, 034507 (2016), [arXiv:1606.08798].

[563] M. Bruno *et al.* (ALPHA), Phys. Rev. Lett. **119**, 10, 102001 (2017), [arXiv:1706.03821].

[564] R. J. Hudspith *et al.* (2018), [arXiv:1804.10286].

[565] H. Takaura *et al.*, Phys. Lett. **B789**, 598 (2019), [arXiv:1808.01632].

[566] H. Takaura *et al.*, JHEP **04**, 155 (2019), [arXiv:1808.01643].

[567] K. Nakayama, H. Fukaya and S. Hashimoto, Phys. Rev. **D98**, 1, 014501 (2018), [arXiv:1804.06695].

[568] A. Bazavov *et al.* (2019), [arXiv:1907.11747].

10. Electroweak Model and Constraints on New Physics

Revised March 2020 by J. Erler (IF-UNAM; U. of Mainz) and A. Freitas (Pittsburg U.).

10.1 Introduction

The standard model of the electroweak interactions (SM) [1–4] is based on the gauge group SU(2) × U(1), with gauge bosons W^i_μ, $i = 1, 2, 3$, and B_μ for the SU(2) and U(1) factors, respectively, and the corresponding gauge coupling constants g and g'. The left-handed fermion fields of the $i^{\rm th}$ fermion family transform as doublets $\Psi_i = \begin{pmatrix}\nu_i \\ \ell_i^-\end{pmatrix}$ and $\begin{pmatrix}u_i \\ d'_i\end{pmatrix}$ under SU(2), where $d'_i \equiv \sum_j V_{ij}\, d_j$, and V is the Cabibbo-Kobayashi-Maskawa mixing [5, 6] matrix[1]. The right-handed fields are SU(2) singlets. From Higgs and electroweak precision data it is known that there are precisely three sequential fermion families.

A complex scalar Higgs doublet, ϕ, is added to the model for mass generation through spontaneous symmetry breaking with potential[2] given by,

$$V(\phi) = \mu^2 \phi^\dagger \phi + \frac{\lambda^2}{2}(\phi^\dagger \phi)^2 \ , \qquad \phi \equiv \begin{pmatrix}\phi^+ \\ \phi^0\end{pmatrix} \ . \tag{10.1}$$

For μ^2 negative, ϕ develops a vacuum expectation value, $v/\sqrt{2} = |\mu|/\lambda$, where $v = 246.22$ GeV, breaking part of the electroweak (EW) gauge symmetry, after which only one neutral Higgs scalar, H, remains in the physical particle spectrum. In non-minimal models there are additional charged and neutral scalar Higgs particles. Higgs boson physics is reviewed in the Section on the "Status of Higgs Boson Physics" in this *Review*.

After symmetry breaking the Lagrangian for the fermion fields, ψ_i, is

$$\begin{aligned}\mathscr{L}_F = &\sum_i \bar\psi_i \left(i\,\partial\!\!\!/ - m_i - \frac{m_i H}{v}\right)\psi_i \\ &- \frac{g}{2\sqrt{2}} \sum_i \overline{\Psi}_i\, \gamma^\mu\, (1-\gamma^5)(T^+\, W^+_\mu + T^-\, W^-_\mu)\, \Psi_i \\ &- e \sum_i Q_i\, \bar\psi_i\, \gamma^\mu\, \psi_i\, A_\mu \\ &- \frac{g}{2\cos\theta_W} \sum_i \bar\psi_i\, \gamma^\mu (g^i_V - g^i_A \gamma^5)\, \psi_i\, Z_\mu \ .\end{aligned} \tag{10.2}$$

Here $\theta_W \equiv \tan^{-1}(g'/g)$ is the weak mixing angle and $e = g \sin\theta_W$ is the positron electric charge. Furthermore,

$$A_\mu \equiv B_\mu \cos\theta_W + W^3_\mu \sin\theta_W \ , \tag{10.3a}$$

$$W^\pm_\mu \equiv \frac{W^1_\mu \mp i W^2_\mu}{\sqrt{2}} \ , \tag{10.3b}$$

$$Z_\mu \equiv -B_\mu \sin\theta_W + W^3_\mu \cos\theta_W \ , \tag{10.3c}$$

are the photon field (γ) and the charged ($W^\pm$) and neutral (Z) weak boson fields, respectively.

The Yukawa coupling of H to ψ_i in the first term in $\mathscr{L}_F$, which is flavor diagonal in the minimal model, is $g m_i/2M_W$. The boson masses in the EW sector are given (at tree level, *i.e.*, to lowest order in perturbation theory) by,

$$M_H = \lambda\, v \ , \tag{10.4a}$$

$$M_W = \frac{gv}{2} = \frac{ev}{2\sin\theta_W} \ , \tag{10.4b}$$

$$M_Z = \sqrt{g^2 + g'^2}\ \frac{v}{2} = \frac{ev}{2\sin\theta_W \cos\theta_W} \ , \tag{10.4c}$$

$$M_\gamma = 0 \ . \tag{10.4d}$$

The second term in $\mathscr{L}_F$ represents the charged-current weak interaction [8–10], where T^+ and T^- are the weak isospin raising and lowering operators. For example, the coupling of a W to an electron and a neutrino is

$$-\frac{e}{2\sqrt{2}\sin\theta_W}\left[W^-_\mu\ \bar e\, \gamma^\mu (1-\gamma^5)\nu + W^+_\mu\ \bar\nu\, \gamma^\mu\, (1-\gamma^5) e\right] \ . \tag{10.5}$$

For momenta small compared to M_W, this term gives rise to the effective four-fermion interaction with the Fermi constant given by $G_F/\sqrt{2} = 1/2v^2 = g^2/8M^2_W$. CP violation is incorporated into the EW model by a single observable phase in V_{ij}.

The third term in $\mathscr{L}_F$ describes electromagnetic interactions (QED) [11, 12], and the last is the weak neutral-current interaction [9, 10, 13]. The vector and axial-vector couplings are

$$g^i_V \equiv t_{3L}(i) - 2Q_i \sin^2\theta_W \ , \tag{10.6a}$$

$$g^i_A \equiv t_{3L}(i) \ , \tag{10.6b}$$

where $t_{3L}(i)$ is the weak isospin of fermion i ($+1/2$ for u_i and ν_i; $-1/2$ for d_i and e_i) and Q_i is the charge of ψ_i in units of e.

The first term in Eq. (10.2) also gives rise to fermion masses, and in the presence of right-handed neutrinos to Dirac neutrino masses. The possibility of Majorana masses is discussed in the Section on "Neutrino Mass, Mixing, and Oscillations" in this *Review*.

10.2 Renormalization and radiative corrections

In addition to the Higgs boson mass, M_H, the fermion masses and mixings, and the strong coupling constant, α_s, the SM has three parameters. The set with the smallest experimental errors contains the Z mass[3], the Fermi constant, and the fine structure

[1] Constraints on V and tests of universality are discussed in Ref. [7] and in the Section on the "CKM Quark-Mixing Matrix" in this *Review*. The extension of the formalism to allow an analogous leptonic mixing matrix is discussed in the Section on "Neutrino Masses, Mixing, and Oscillations" in this *Review*.

[2] There is no generally accepted convention to write the quartic term. Our numerical coefficient simplifies Eq. (10.4a) below and the squared coupling preserves the relation between the number of external legs and the power counting of couplings at a given loop order. This structure also naturally emerges from physics beyond the SM, such as Supersymmetry.

[3] We emphasize that in the fits described in Sec. 10.6 and Sec. 10.7 the values of the SM parameters are affected by all observables that depend on

constant, to be discussed in turn (the numerical values quoted in Sections 10.2−10.4 correspond to the main fit result in Table 10.7).

The Z boson mass, $M_Z = 91.1876 \pm 0.0021$ GeV, has been determined from the Z lineshape scan at LEP 1 [14]. This value of M_Z corresponds to a definition based on a Breit-Wigner shape with an energy-dependent width[4] (see the Section on the "Z Boson" in this *Review*).

10.2.1 *The Fermi constant*

The Fermi constant, $G_F = 1.1663787(6) \times 10^{-5}$ GeV^{-2}, is derived from the μ lifetime formula[5],

$$\frac{\hbar}{\tau_\mu} = \frac{G_F^2 m_\mu^5}{192\pi^3} F(\rho) \left[1 + H_1(\rho)\frac{\widehat{\alpha}(m_\mu)}{\pi} + H_2(\rho)\frac{\widehat{\alpha}^2(m_\mu)}{\pi^2}\right] , \tag{10.7}$$

where $\rho = m_e^2/m_\mu^2$, and where

$$F(\rho) = 1 - 8\rho + 8\rho^3 - \rho^4 - 12\rho^2 \ln\rho = 0.99981295 , \tag{10.8a}$$

$$H_1(\rho) = \frac{25}{8} - \frac{\pi^2}{2} - \left(9 + 4\pi^2 + 12\ln\rho\right)\rho + 16\pi^2\rho^{3/2} + \mathcal{O}(\rho^2) = -1.80793 , \tag{10.8b}$$

$$H_2(\rho) = \frac{156815}{5184} - \frac{518}{81}\pi^2 - \frac{895}{36}\zeta(3) + \frac{67}{720}\pi^4 + \frac{53}{6}\pi^2\ln 2 - (0.042 \pm 0.002)_{\rm had} - \frac{5}{4}\pi^2\sqrt{\rho} + \mathcal{O}(\rho) = 6.64 , \tag{10.8c}$$

$$\widehat{\alpha}(m_\mu)^{-1} = \alpha^{-1} + \frac{1}{3\pi}\ln\rho + \mathcal{O}(\alpha) = 135.901 . \tag{10.8d}$$

H_1 and H_2 capture the QED corrections within the Fermi model. The results for $\rho = 0$ have been obtained in Refs. [16] and [17,18] for H_1 and H_2, respectively, where the term in parentheses is from the hadronic vacuum polarization [17]. The mass corrections to H_1 have been known for some time [19], while those to H_2 are more recent [20]. Notice the term linear in m_e whose appearance was unforeseen and can be traced to the use of the muon pole mass in the prefactor [20]. The remaining uncertainty in G_F is mostly experimental and has been reduced by an order of magnitude by the MuLan collaboration [15] at the PSI.

10.2.2 *The electromagnetic coupling*

The fine structure constant, α, can be extracted from the $e^\pm$ anomalous magnetic moment [21], $a_e = (1159652180.91 \pm 0.26) \times 10^{-12}$ [22], which gives the value $\alpha^{-1} = 137.035999150(33)$. Another approach combines measurements of the Rydberg constant and atomic masses with interferometry of atomic recoil kinematics. Applied to ^{87}Rb [23] and ^{133}Cs [24], this method implies the results $\alpha^{-1} = 137.035998997(85)$ and $\alpha^{-1} = 137.035999047(28)$, respectively, which can be combined to give $\alpha^{-1} = 137.035999042(26)$. Finally, combining the anomalous magnetic moment and atomic interferometry methods leads to the world average of $\alpha^{-1} = 137.035999084(21)$, but notice that they also show a 2.6 σ discrepancy. If this is interpreted as due to physics beyond the SM (BSM), the new physics would contribute to a_e with opposite sign compared to the $\mu^\pm$ anomalous magnetic moment, a_μ, to be discussed in Section 10.4.2.

In most EW renormalization schemes, it is convenient to define a running α dependent on the energy scale of the process, with $\alpha^{-1} \approx 137.036$ appropriate at very low energy, *i.e.* close to the Thomson limit. The OPAL [25] and L3 [26] collaborations at LEP could also observe the running directly in small and large angle Bhabha scattering, respectively. For scales above a few hundred MeV the low energy hadronic contribution to vacuum polarization introduces a theoretical uncertainty in α. In the modified minimal subtraction ($\overline{\rm MS}$) scheme[6] [27] (used for this *Review*), and with $\alpha_s(M_Z) = 0.1185 \pm 0.0016$ we have $\widehat{\alpha}^{(4)}(m_\tau)^{-1} = 133.472 \pm 0.007$ and $\widehat{\alpha}^{(5)}(M_Z)^{-1} = 127.952 \pm 0.009$. The latter corresponds to a quark sector contribution (without the top) to the conventional (on-shell) QED coupling,

$$\alpha(M_Z) = \frac{\alpha}{1 - \Delta\alpha(M_Z)} , \tag{10.9}$$

of $\Delta\alpha^{(5)}_{\rm had}(M_Z) = 0.02766 \pm 0.00007$. These values are updated from Ref. [28] with $\Delta\alpha^{(5)}_{\rm had}(M_Z)$ moved downwards and its uncertainty reduced (partly due to a more precise charm quark mass). Its correlation with a_μ, as well as the non-linear α_s dependence of $\widehat{\alpha}(M_Z)$ and the resulting correlation with the input variable α_s, are fully taken into account in the fits. This is done by using as actual input (fit constraint) instead of $\Delta\alpha^{(5)}_{\rm had}(M_Z)$ the low energy contribution by the three light quarks, $\Delta\alpha^{(3)}_{\rm had}(2.0\ {\rm GeV}) = (58.84 \pm 0.51) \times 10^{-4}$ [29], and by calculating the perturbative and heavy quark contributions to $\widehat{\alpha}(M_Z)$ in each call of the fits according to [28]. Part of the error ($\pm 0.37 \times 10^{-4}$) is from e^+e^- annihilation data below 2 GeV, as well as isospin rotated data from τ decays into two- and four-pion final states [30] (including uncertainties from isospin breaking effects [31]), but uncalculated higher order perturbative ($\pm 0.21 \times 10^{-4}$) and non-perturbative ($\pm 0.28 \times 10^{-4}$ [29]) QCD corrections and the $\overline{\rm MS}$ quark mass values (see below) also contribute. Various evaluations of $\Delta\alpha^{(5)}_{\rm had}(M_Z)$ are summarized in Table 10.1, where the relation[7] between the $\overline{\rm MS}$ and on-shell definitions (obtained using Ref [34]) is given by,

$$\begin{aligned}\Delta\widehat{\alpha}(M_Z) = \Delta\alpha(M_Z) + \frac{\alpha}{\pi}\Bigg[&\frac{100}{27} - \frac{1}{6} - \frac{7}{4}\ln\frac{M_Z^2}{M_W^2} \\ &+ \frac{\alpha_s(M_Z)}{\pi}\left(\frac{605}{108} - \frac{44}{9}\zeta(3)\right) \\ &+ \frac{\alpha_s^2}{\pi^2}\left(\frac{976481}{23328} - \frac{253}{36}\zeta(2) - \frac{781}{18}\zeta(3) + \frac{275}{27}\zeta(5)\right)\Bigg] \\ &= 0.007127(2) ,\end{aligned} \tag{10.10}$$

and where the first entry of the lowest order term is from fermions and the other two are from $W^\pm$ loops, which are usually excluded from the on-shell definition. Fermion mass effects and corrections of $\mathcal{O}(\alpha\alpha_s^3)$ and $\mathcal{O}(\alpha^2)$ contributing to Eq. (10.10) are small, partly cancel each other and are not included here. The most recent results on $\Delta\alpha^{(5)}_{\rm had}(M_Z)$ [29,35–37] typically assume the validity of perturbative QCD (PQCD) at scales of $\sim$ 2 GeV or above and are in good agreement with each other. In regions where PQCD is not trusted, one can use $e^+e^- \to$ hadrons cross-section data and τ decay spectral functions [38], where the latter derive from OPAL [39], CLEO [40], ALEPH [41], and Belle [42]. Recently, new data for various $e^+e^- \to$ hadrons channels was obtained from BaBar, BES III, CLEO, the SND and CMD-3 experiments at VEPP-2000, and the KEDR experiments at VEPP-4M (for a list of references see, *e.g.*, Ref. [29]). While VEPP-2000 and VEPP-4M scanned center-of-mass (CM) energies up to 2 GeV and between about 3 and 4 GeV, respectively, the BaBar collaboration studied multi-hadron events radiatively returned from the $\Upsilon(4S)$,

them. This is of no practical consequence for α and G_F, however, since they are very precisely known.

[4] The theoretically consistent and gauge-invariant definition of the Z-boson mass through the complex pole of the propagator would instead lead to a Breit-Wigner with a constant width. The two definitions differ numerically, and this difference has to be accounted for in theoretical calculations.

[5] In the spirit of the Fermi theory, we incorporated the small propagator correction, $3/5\ m_\mu^2/M_W^2$, into Δr (see below). This is also the convention adopted by the MuLan collaboration [15]. While this breaks with historical consistency, the numerical difference was negligible in the past.

[6] In this Section we denote quantities defined in the $\overline{\rm MS}$ scheme by a caret; the exception is the strong coupling constant, α_s, which will always correspond to the $\overline{\rm MS}$ definition and where the caret will be dropped.

[7] In practice, $\alpha(M_Z)$ is directly evaluated in the $\overline{\rm MS}$ scheme using the FORTRAN package GAPP [32], including the QED contributions of both leptons and quarks. The leptonic three-loop contribution in the on-shell scheme has been obtained in Ref. [33].

reconstructing the radiated photon and normalizing to $\mu^\pm\gamma$ final states. The precision of these results generally exceeds those from τ decays. There are significant discrepancies between the older (CMD-2) and newer (CMD-3) measurements of $e^+e^- \to K^+K^-$, which could be due to difficulties in determining the detection efficiency of low-momentum kaons. The radiative return data from BaBar is expected to be more reliable for this channel owing to an additional boost of the final-state hadrons.

10.2.3 *Quark masses*

Further free parameters entering into Eq. (10.2) are the quark and lepton masses, where m_i is the mass of the $i^{\rm th}$ fermion ψ_i. For the light quarks, as described in the Section on "Quark Masses" in this *Review*, $\widehat{m}_u = 2.16^{+0.49}_{-0.26}$ MeV, $\widehat{m}_d = 4.67^{+0.48}_{-0.17}$ MeV, and $\widehat{m}_s = 93^{+11}_{-\ 5}$ MeV. These are running $\overline{\rm MS}$ masses evaluated at the scale $\mu = 2$ GeV. For the charm mass we use the constraint [51],

$$\widehat{m}_c(\widehat{m}_c) = 1274 \pm 8 + 2616[\alpha_s(M_Z) - 0.1182] \text{ MeV} , \quad (10.11)$$

which is based on QCD sum rules [52, 53], and recalculate $\widehat{m}_c$ in each call of our fits to account for its α_s dependence. Similarly, for the bottom quark mass we use,

$$\widehat{m}_b(\widehat{m}_b) = 4180 \pm 8 + 108[\alpha_s(M_Z) - 0.1182] \text{ MeV} , \quad (10.12)$$

with a theoretical correlation of about 60% arising mostly from the PQCD truncation uncertainty which is similar for $\widehat{m}_c(\widehat{m}_c)$ and $\widehat{m}_b(\widehat{m}_b)$. To improve the precisions in $\widehat{m}_c(\widehat{m}_c)$ and $\widehat{m}_b(\widehat{m}_b)$ in the future it would help to remeasure the threshold regions of the heavy quarks, as well as the electronic decay widths of the narrow $c\bar{c}$ and $b\bar{b}$ resonances.

The top quark "pole" mass (the quotation marks are a reminder that the experiments do not strictly measure the pole mass and that quarks do not form asymptotic states), has been kinematically reconstructed by the Tevatron collaborations, CDF and DØ, in leptonic, hadronic, and mixed channels with the result $m_t = 174.30 \pm 0.35_{\rm\,stat.} \pm 0.54_{\rm\,syst.}$ GeV [54]. Likewise, using data from CM energies $\sqrt{s} = 7$ and 8 TeV (Run 1), ATLAS and CMS (including alternative technique measurements) at the LHC obtained $m_t = 172.69 \pm 0.25_{\rm\,stat.} \pm 0.41_{\rm\,syst.}$ GeV [55] and $m_t = 172.43 \pm 0.13_{\rm\,stat.} \pm 0.46_{\rm\,syst.}$ GeV [56], respectively. In addition, there are first results with $\sqrt{s} = 13$ TeV data (Run 2). CMS obtained $m_t = 172.26 \pm 0.07_{\rm\,mostly\,stat.} \pm 0.61_{\rm\,syst.}$ GeV [57] in the lepton + jets and all-jets channels, and $m_t = 172.33 \pm 0.14_{\rm\,stat.} \pm 0.69_{\rm\,syst.}$ GeV [58] in the di-lepton channel. Using a leptonic invariant mass and thus featuring reduced correlation with the more traditional analysis approaches, ATLAS quotes $m_t = 174.48 \pm 0.40_{\rm\,stat.} \pm 0.67_{\rm\,syst.}$ GeV [59] from the lepton + jets channel. While there seems to be generally good agreement between all these measurements, we observe a 2.8 σ discrepancy (or more in case of correlated systematics) between the two most precise determinations, 174.98 ± 0.76 GeV [60] (by the DØ collaboration) and 172.25 ± 0.63 GeV [61] (by the CMS collaboration), both from the lepton + jets channels. In addition, the latter is also 2.2 σ lower than the preliminary result of Ref. [59]. Assuming a systematic error component of 0.17 GeV (the QCD, PDF and Monte Carlo type errors at ATLAS at Run 1) is common to all six results, we arrive at the combination,

$$m_t = 172.89 \pm 0.28_{\rm\,exp.} \text{ GeV} + \Delta m_{\rm MC} , \quad (10.13)$$

where $\Delta m_{\rm MC}$ is defined to account for any difference between the top pole mass, m_t, and the mass parameter implemented in the Monte Carlo event generators employed by the experimental groups. $\Delta m_{\rm MC}$ is expected to be of order $\alpha_s(Q_0)Q_0$ with a low scale $Q_0 \sim \mathcal{O}(1\text{ GeV})$ [62], but its value is unknown in hadron collider environments so that we will treat it as an uncertainty instead, and choose for definiteness $Q_0 = \Gamma_t = 1.42$ GeV to arrive at $\Delta m_{\rm MC} = 0 \pm 0.52$ GeV. We further assume that an uncertainty [63] of ± 0.32 GeV in the relation [64] between m_t and the $\overline{\rm MS}$ definition, $\widehat{m}_t(\widehat{m}_t)$, entering electroweak radiative correction libraries, including the renormalon ambiguity [65], is already included in $\Delta m_{\rm MC}$, as m_t merely serves as an intermediate bookkeeping device in Ref. [62]. A promising future direction to arrive at a competitive independent constraint on m_t is to analyze differential top quark pair production cross-sections at next-to-next-to-leading order (NNLO) [66], as m_t extraction based on them are easier to interpret, and experimentally they have become much more precise recently [67,68]. The combination in Eq. (10.13) differs slightly from the average, $m_t = 172.9 \pm 0.4_{\rm\,exp.}$ GeV, which appears in the Top Quark Listings in this *Review*, as its uncertainty has been scaled up by a factor of 1.3. For more details and references, see the Section on the "Top Quark" and the Quarks Listings in this *Review*.

10.2.4 *The weak mixing angle*

The observables $\sin^2\theta_W$ and M_W can be calculated from M_Z, $\widehat{\alpha}(M_Z)$, and G_F, when values for m_t and M_H are given, or conversely, M_H can be constrained by $\sin^2\theta_W$ and M_W. The value of $\sin^2\theta_W$ is extracted from neutral-current processes (see Sec. 10.3) and Z pole observables (see Sec. 10.5.3) and depends on the renormalization prescription. There are a number of popular schemes [9] leading to values which differ by small factors depending on m_t and M_H. The notation for these schemes is shown in Table 10.2.

(i) The on-shell scheme [70] promotes the tree-level formula $\sin^2\theta_W = 1 - M_W^2/M_Z^2$ to a definition of the renormalized $\sin^2\theta_W$ to all orders in perturbation theory, *i.e.*,

$$\sin^2\theta_W \to s_W^2 \equiv 1 - \frac{M_W^2}{M_Z^2} , \quad (10.14a)$$

$$M_W = \frac{A_0}{s_W(1-\Delta r)^{1/2}} , \qquad M_Z = \frac{M_W}{c_W} , \quad (10.14b)$$

where $c_W \equiv \cos\theta_W$, $A_0 = (\pi\alpha/\sqrt{2}G_F)^{1/2} = 37.28038(1)$ GeV, and Δr includes the radiative corrections relating α, $\alpha(M_Z)$, G_F, M_W, and M_Z. One finds $\Delta r \sim \Delta r_0 - \rho_t \tan^{-2}\theta_W$, where $\Delta r_0 = 1 - \alpha/\widehat{\alpha}(M_Z) = 0.06629(7)$ is due to the running of α, and

$$\rho_t = \frac{3G_F m_t^2}{8\sqrt{2}\pi^2} = 0.00937 \times \frac{m_t^2}{(172.89\text{ GeV})^2} , \quad (10.15)$$

represents the dominant (quadratic) m_t dependence. There are additional contributions to Δr from bosonic loops, including those which depend logarithmically on M_H and higher-order corrections[8]. One has $\Delta r = 0.03652 \mp 0.00021 \pm 0.00007$, where the first uncertainty is from m_t and the second is from $\alpha(M_Z)$. Thus the value of s_W^2 extracted from M_Z includes an uncertainty (∓ 0.00007) from the currently allowed range of m_t. This scheme is simple conceptually. However, the relatively large ($\sim 3\%$) correction from ρ_t causes large spurious contributions in higher orders. s_W^2 depends not only on the gauge couplings but also on the spontaneous-symmetry breaking, and it is awkward in the presence of any extension of the SM which perturbs the value of M_Z (or M_W). Other definitions are motivated by the tree-level coupling constant definition $\theta_W = \tan^{-1}(g'/g)$:

(ii) In particular, the $\overline{\rm MS}$ scheme introduces the quantity,

$$\sin^2\widehat{\theta}_W(\mu) \equiv \frac{\widehat{g}'^2(\mu)}{\widehat{g}^{\,2}(\mu) + \widehat{g}'^2(\mu)} , \quad (10.16)$$

where the couplings $\widehat{g}$ and $\widehat{g}'$ are defined by modified minimal subtraction and the scale μ is conveniently chosen to be M_Z for many EW processes. The value of $\widehat{s}_Z^2 \equiv \sin^2\widehat{\theta}_W(M_Z)$ extracted from M_Z is less sensitive than s_W^2 to m_t (by a factor of $\tan^2\theta_W$), and is less sensitive to most types of new physics. It is also very useful for comparing with the predictions of grand unification. There are actually several variant definitions of $\sin^2\widehat{\theta}_W(M_Z)$, differing according

[8] All explicit numbers quoted here and below include the two- and three-loop corrections described near the end of Sec. 10.2.

Table 10.1: Evaluations of the on-shell $\Delta\alpha^{(5)}_{\rm had}(M_Z)$ by different groups (for a more complete list of evaluations see the 2012 edition of this *Review*). For better comparison we adjusted central values and errors to correspond to a common and fixed value of $\alpha_s(M_Z) = 0.120$. References quoting results without the top quark decoupled are converted to the five flavor definition. Ref. [43] uses $\Lambda_{\rm QCD} = 380 \pm 60$ MeV; for the conversion we assumed $\alpha_s(M_Z) = 0.118 \pm 0.003$.

Reference	Result	Comment
Geshkenbein, Morgunov [44]	0.02780 ± 0.00006	$\mathcal{O}(\alpha_s)$ resonance model
Swartz [45]	0.02754 ± 0.00046	use of fitting function
Krasnikov, Rodenberg [46]	0.02737 ± 0.00039	PQCD for $\sqrt{s} > 2.3$ GeV
Kühn & Steinhauser [47]	0.02778 ± 0.00016	full $\mathcal{O}(\alpha_s^2)$ for $\sqrt{s} > 1.8$ GeV
Groote *et al.* [43]	0.02787 ± 0.00032	use of QCD sum rules
Martin *et al.* [48]	0.02741 ± 0.00019	incl. new BES data
de Troconiz, Yndurain [49]	0.02754 ± 0.00010	PQCD for $s > 2$ GeV^2
Burkhardt, Pietrzyk [50]	0.02750 ± 0.00033	PQCD for $\sqrt{s} > 12$ GeV
Erler, Ferro-Hernández [35]	0.02761 ± 0.00010	conv. from $\overline{\rm MS}$ scheme
Jegerlehner [36]	0.02755 ± 0.00013	Euclidean split technique
Davier *et al.* [29]	0.02760 ± 0.00010	PQCD for $\sqrt{s} = 1.8$–3.7 & > 5 GeV
Keshavarzi *et al.* [37]	0.02761 ± 0.00011	PQCD for $\sqrt{s} > 11.2$ GeV

Table 10.2: Notations used to indicate the various schemes discussed in the text. Each definition of $\sin^2\theta_W$ leads to values that differ by small factors depending on m_t and M_H. Numerical values and the uncertainties induced by the imperfectly known SM parameters and unknown higher orders [69] are also given for illustration.

Scheme	Notation	Value	Uncertainty
On-shell	s^2_W	0.22337	± 0.00010
$\overline{\rm MS}$	$\widehat{s}^2_Z$	0.23121	± 0.00004
$\overline{\rm MS}$ND	$\widehat{s}^2_{\rm ND}$	0.23141	± 0.00004
$\overline{\rm MS}$	$\widehat{s}^2_0$	0.23857	± 0.00005
Effective angle	$\bar{s}^2_\ell$	0.23153	± 0.00004

to whether or how finite $\alpha \ln(m_t/M_Z)$ terms are decoupled (subtracted from the couplings). One cannot entirely decouple the $\alpha \ln(m_t/M_Z)$ terms from all EW quantities because $m_t \gg m_b$ breaks SU(2) symmetry. The scheme that will be adopted here decouples the $\alpha \ln(m_t/M_Z)$ terms from the γ–Z mixing [27, 71], essentially eliminating any $\ln(m_t/M_Z)$ dependence in the formulae for asymmetries at the Z pole when written in terms of $\widehat{s}^2_Z$. (A similar definition is used for $\widehat{\alpha}$.) The on-shell and $\overline{\rm MS}$ definitions are related by

$$\widehat{s}^2_Z = c\,(m_t, M_H) s^2_W = (1.0351 \pm 0.0003) s^2_W \ . \qquad (10.17)$$

The quadratic m_t dependence is given by $c \sim 1 + \rho_t/\tan^2\theta_W$. The expressions for M_W and M_Z in the $\overline{\rm MS}$ scheme are

$$M_W = \frac{A_0}{\widehat{s}_Z (1 - \Delta\widehat{r}_W)^{1/2}} \ , \qquad M_Z = \frac{M_W}{\widehat{\rho}^{\,1/2}\widehat{c}_Z} \ , \qquad (10.18)$$

and one predicts $\Delta\widehat{r}_W = 0.06918 \pm 0.00007$. $\Delta\widehat{r}_W$ has no quadratic m_t dependence, because shifts in M_W are absorbed into the observed G_F, so that the error in $\Delta\widehat{r}_W$ is almost entirely due to $\Delta r_0 = 1 - \alpha/\widehat{\alpha}(M_Z)$. The quadratic m_t dependence has been shifted into $\widehat{\rho} \sim 1 + \rho_t$, where including bosonic loops, $\widehat{\rho} = 1.01019 \pm 0.00009$.

(iii) A variant $\overline{\rm MS}$ quantity $\widehat{s}^2_{\rm ND}$ (used in the 1992 edition of this *Review*) does not decouple the $\alpha \ln(m_t/M_Z)$ terms [72]. It is related to $\widehat{s}^2_Z$ by

$$\widehat{s}^2_Z = \frac{\widehat{s}^2_{\rm ND}}{1 + \frac{\alpha}{\pi}\widehat{d}} \ , \qquad d = \frac{1}{3}\left(\frac{1}{\widehat{s}^2} - \frac{8}{3}\right)\left[\left(1 + \frac{\alpha_s}{\pi}\right)\ln\frac{m_t}{M_Z} - \frac{15\alpha_s}{8\pi}\right] \ . \qquad (10.19)$$

Thus, $\widehat{s}^2_Z - \widehat{s}^2_{\rm ND} = -0.0002$.

(iv) Some of the low-energy experiments discussed in the next section are sensitive to the weak mixing angle at almost vanishing momentum transfer [35,73–75]. Thus, Table 10.2 also includes $\widehat{s}^2_0 \equiv \sin^2\widehat{\theta}_W(0)$.

(v) Yet another definition, the effective angle [76, 77], $\bar{s}^2_f \equiv \sin\theta^f_{\rm eff}$, for the Z vector coupling to fermion f, is based on Z pole observables and described in Sec. 10.5.

10.2.5 *Radiative corrections*

Experiments are at such level of precision [69] that complete one-loop, dominant two-loop, and partial three and four-loop radiative corrections must be applied. For neutral-current and Z pole processes, these corrections are conveniently divided into two classes:

1. QED diagrams involving the emission of real photons or the exchange of virtual photons in loops, but not including vacuum polarization diagrams. These graphs often yield finite and gauge-invariant contributions to observable processes. However, they are dependent on energies, experimental cuts, *etc.*, and must be calculated individually for each experiment.
2. EW corrections, including $\gamma\gamma$, γZ, ZZ, and WW vacuum polarization diagrams, as well as vertex corrections, box graphs, *etc.*, involving virtual W and Z bosons. One-loop corrections [78] are included for all processes, and many two-loop corrections are also important. In particular, two-loop corrections involving the top quark modify ρ_t in $\widehat{\rho}$, Δr, and elsewhere by

$$\rho_t \to \rho_t \left[1 + R(M_H, m_t)\,\frac{\rho_t}{3}\right] \ . \qquad (10.20)$$

$R(M_H, m_t)$ can be described as an expansion in M^2_Z/m^2_t, for which the leading m^4_t/M^4_Z [79, 80] and next-to-leading m^2_t/M^2_Z [81, 82] terms are known. The complete two-loop calculation of Δr (without further approximation) has been performed in Refs. [83–87]. More recently, Ref. [88] obtained

the $\overline{\rm MS}$ quantities $\Delta\widehat{r}_W$ and $\widehat{\rho}$ to two-loop accuracy, confirming the prediction of M_W in the on-shell scheme from Refs. [85, 89] within about 4 MeV. Similarly, the EW two-loop corrections for the relation between $\bar{s}^2_{\ell,b}$ and s^2_W are known [90–95], as well as for the partial decay and total decay widths and the effective couplings of the Z boson [96–99]. For $\bar{s}_{s,c}$ only two-loop corrections from diagrams with closed fermion loops are available [100], but given the experimental precision this is more than adequate.

The mixed QCD-EW contributions to gauge boson self-energies of order $\alpha\alpha_s m_t^2$ [101, 102], $\alpha\alpha_s^2 m_t^2$ [103, 104], and $\alpha\alpha_s^3 m_t^2$ [105–107] increase the predicted value of m_t by 6%. This is, however, almost entirely an artifact of using the pole mass definition for m_t. The equivalent corrections when using the $\overline{\rm MS}$ definition $\widehat{m}_t(\widehat{m}_t)$ increase m_t by less than 0.5%. The sub-leading $\alpha\alpha_s$ corrections [108–111] are also included. Further three-loop corrections of order $\alpha\alpha_s^2$ [112,113], $\alpha^3 m_t^6$, and $\alpha^2\alpha_s m_t^4$ [114, 115], are rather small. The same is true for $\alpha^3 M_H^4$ [116] corrections unless M_H approaches 1 TeV. The theoretical uncertainty from unknown higher-order corrections [69] is estimated to amount to 4 MeV for the prediction of M_W [89] and 4.5×10^{-5} for $\bar{s}^2_\ell$ [100].

Throughout this *Review* we utilize EW radiative corrections from the program GAPP [32], which works entirely in the $\overline{\rm MS}$ scheme, and which is independent of the package ZFITTER [117].

10.3 Low energy electroweak observables

In the following we discuss EW precision observables obtained at low momentum transfers [118], *i.e.*, $Q^2 \ll M_Z^2$. It is convenient to write the four-fermion interactions relevant to ν-hadron, ν-e, as well as parity violating e-hadron and e-e neutral-current processes, in a form that is valid in an arbitrary gauge theory (assuming massless left-handed neutrinos). One has[9],

$$-\mathscr{L}^{\nu e} = \frac{G_F}{\sqrt{2}}\,\bar{\nu}\gamma_\mu(1-\gamma^5)\nu\;\bar{e}\,\gamma^\mu(g^{\nu e}_{LV} - g^{\nu e}_{LA}\,\gamma^5)e\;, \tag{10.21a}$$

$$-\mathscr{L}^{\nu h} = \frac{G_F}{\sqrt{2}}\,\bar{\nu}\,\gamma_\mu(1-\gamma^5)\nu\sum_q\Big[g^{\nu q}_{LL}\,\bar{q}\,\gamma^\mu(1-\gamma^5)q + g^{\nu q}_{LR}\,\bar{q}\,\gamma^\mu(1+\gamma^5)q\Big] \tag{10.21b}$$

$$-\mathscr{L}^{ee} = -\frac{G_F}{\sqrt{2}}\,g^{ee}_{AV}\,\bar{e}\,\gamma_\mu\gamma^5 e\,\bar{e}\,\gamma^\mu e\;, \tag{10.21c}$$

$$-\mathscr{L}^{eh} = -\frac{G_F}{\sqrt{2}}\sum_q\Big[g^{eq}_{AV}\,\bar{e}\,\gamma_\mu\gamma^5 e\,\bar{q}\,\gamma^\mu q + g^{eq}_{VA}\,\bar{e}\,\gamma_\mu e\,\bar{q}\,\gamma^\mu\gamma^5 q\Big]\;, \tag{10.21d}$$

where one must include the charged-current contribution for ν_e-e and $\bar{\nu}_e$-e and the parity conserving QED contribution for electron scattering. The SM tree level expressions for the four-Fermi couplings are given in Table 10.3. Note that they differ from the respective products of the gauge couplings in (10.6) in the radiative corrections and in the presence of possible physics beyond the SM.

10.3.1 *Neutrino scattering*

The cross-section in the laboratory system for $\nu_\mu e \to \nu_\mu e$ or $\bar{\nu}_\mu e \to \bar{\nu}_\mu e$ elastic scattering [9,119] is (in this subsection we drop the redundant index L in the effective neutrino couplings),

$$\frac{d\sigma_{\nu,\bar{\nu}}}{dy} = \frac{G_F^2 m_e E_\nu}{2\pi}\Big[\,(g_V^{\nu e}\pm g_A^{\nu e})^2 + (g_V^{\nu e}\mp g_A^{\nu e})^2(1-y)^2 - (g_V^{\nu e 2} - g_A^{\nu e 2})\frac{y\,m_e}{E_\nu}\Big]\;, \tag{10.22}$$

where the upper (lower) sign refers to $\nu_\mu(\bar{\nu}_\mu)$, and $y \equiv T_e/E_\nu$ (which runs from 0 to $(1+m_e/2E_\nu)^{-1}$) is the ratio of the kinetic energy of the recoil electron to the incident ν or $\bar{\nu}$ energy. For $E_\nu \gg m_e$ this yields a total cross-section

$$\sigma = \frac{G_F^2 m_e E_\nu}{2\pi}\left[(g_V^{\nu e}\pm g_A^{\nu e})^2 + \frac{1}{3}(g_V^{\nu e}\mp g_A^{\nu e})^2\right]\;. \tag{10.23}$$

The most accurate measurements of $\sin^2\theta_W$ from ν-lepton scattering (see Sec. 10.6) are from the ratio $R \equiv \sigma_{\nu_\mu e}/\sigma_{\bar{\nu}_\mu e}$, in which many of the systematic uncertainties cancel. The results are $\sin^2\theta_W = 0.211 \pm 0.037$ [120], $\sin^2\theta_W = 0.195 \pm 0.022$ [121], and $\sin^2\theta_W = 0.2324 \pm 0.0083$ [122], where radiative corrections (other than m_t effects) are small compared to the precision of present experiments and have negligible effect. As shown in Fig. 10.1, one can determine $g^{\nu e}_{V,A}$ from the experimental data as well. The cross-sections for ν_e-e and $\bar{\nu}_e$-e may be obtained from Eq. (10.22) by replacing $g^{\nu e}_{V,A}$ by $g^{\nu e}_{V,A}+1$, where the 1 is due to the charged-current contribution.

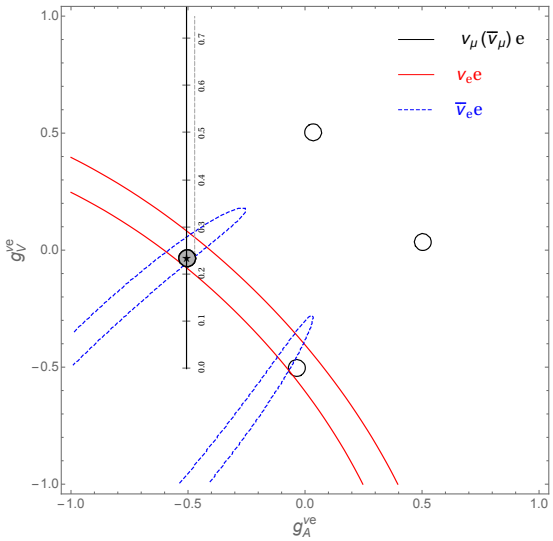

Figure 10.1: Allowed contours in $g_A^{\nu e}$ *vs.* $g_V^{\nu e}$ from neutrino-electron scattering and the SM prediction as a function of $\widehat{s}^2_Z$. (The SM best fit value, $\widehat{s}^2_Z = 0.23121$, is also indicated.) The ν_e-e [123, 124] and $\bar{\nu}_e$-e [125] constraints are at 1 σ, while each of the four equivalent $\nu_\mu(\bar{\nu}_\mu)$-e [120–122] solutions ($g_{V,A} \to -g_{V,A}$ and $g_{V,A} \to g_{A,V}$) are at the 90% CL. The global best fit region (shaded) almost exactly coincides with the corresponding $\nu_\mu(\bar{\nu}_\mu)$-e region. The solution near $g_A = 0$ and $g_V = -0.5$ is eliminated by $e^+e^- \to \ell^+\ell^-$ data under the weak additional assumption that the neutral current is dominated by the exchange of a single Z boson.

A precise determination of the on-shell s^2_W, which depends only very weakly on m_t and M_H, is obtained from deep inelastic scattering (DIS) of neutrinos [119,126] from (approximately) isoscalar targets. The ratio $R_\nu \equiv \sigma^{NC}_{\nu N}/\sigma^{CC}_{\nu N}$ of neutral-to-charged-current cross-sections has been measured to 1% accuracy by CDHS [127] and CHARM [128] at CERN. CCFR [129] at Fermilab has obtained an even more precise result, so it is important to obtain theoretical expressions for R_ν and $R_{\bar{\nu}} \equiv \sigma^{NC}_{\bar{\nu}N}/\sigma^{CC}_{\bar{\nu}N}$ to comparable accuracy. Fortunately, many of the uncertainties from the strong interactions and neutrino spectra cancel in the ratio. A large theoretical uncertainty is associated with the c-threshold,

[9] We use here slightly different definitions (and to avoid confusion also a different notation) for the coefficients of these four-Fermi operators than we did in previous editions of this *Review*. The new couplings [13] are defined in the static limit, $Q^2 \to 0$, with specific radiative corrections included, while others (more experiment specific ones) are assumed to be removed by the experimentalist. They are convenient in that their determinations from very different types of processes can be straightforwardly combined.

Table 10.3: SM tree level expressions for the neutral-current parameters for ν-hadron, ν-e, and e^- scattering processes. To obtain the SM values in the last column, the tree level expressions have to be multiplied by the low-energy neutral-current ρ parameter, $\rho_{\rm NC} = 1.00063$, and further vertex and box corrections need to be added as detailed in Ref. [13]. The dominant m_t dependence is again given by $\rho_{\rm NC} \sim 1 + \rho_t$.

Quantity	SM tree level	SM value
$g_{LV}^{\nu_\mu e}$	$-\frac{1}{2} + 2\,\widehat{s}_0^2$	-0.0398
$g_{LA}^{\nu_\mu e}$	$-\frac{1}{2}$	-0.5064
$g_{LL}^{\nu_\mu u}$	$\frac{1}{2} - \frac{2}{3}\,\widehat{s}_0^2$	0.3458
$g_{LL}^{\nu_\mu d}$	$-\frac{1}{2} + \frac{1}{3}\,\widehat{s}_0^2$	-0.4288
$g_{LR}^{\nu_\mu u}$	$-\frac{2}{3}\,\widehat{s}_0^2$	-0.1552
$g_{LR}^{\nu_\mu d}$	$\frac{1}{3}\,\widehat{s}_0^2$	0.0777
g_{AV}^{ee}	$\frac{1}{2} - 2\,\widehat{s}_0^2$	0.0227
g_{AV}^{eu}	$-\frac{1}{2} + \frac{4}{3}\,\widehat{s}_0^2$	-0.1888
g_{AV}^{ed}	$\frac{1}{2} - \frac{2}{3}\,\widehat{s}_0^2$	0.3419
g_{VA}^{eu}	$-\frac{1}{2} + 2\,\widehat{s}_0^2$	-0.0352
g_{VA}^{ed}	$\frac{1}{2} - 2\,\widehat{s}_0^2$	0.0249

which mainly affects σ^{CC}. Using the slow rescaling prescription [130, 131] the central value of $\sin^2\theta_W$ from CCFR varies as $0.0111(m_c/\text{GeV}-1.31)$, where m_c is the effective mass which is numerically close to the $\overline{\rm MS}$ mass $\widehat{m}_c(\widehat{m}_c)$, but their exact relation is unknown at higher orders. For $m_c = 1.31 \pm 0.24$ GeV, which was determined from ν-induced di-muon production [132], this contributes ± 0.003 to the total uncertainty of $\Delta \sin^2\theta_W = \pm 0.004$, where the experimental uncertainty was also ± 0.003. This uncertainty largely cancels, however, in the Paschos-Wolfenstein ratio [133],

$$R^- = \frac{\sigma_{\nu N}^{NC} - \sigma_{\bar\nu N}^{NC}}{\sigma_{\nu N}^{CC} - \sigma_{\bar\nu N}^{CC}} \ . \tag{10.24}$$

It was measured by Fermilab's NuTeV collaboration [134] for the first time, and required a high-intensity and high-energy anti-neutrino beam.

A simple zero$^{\rm th}$-order approximation is,

$$R_\nu = g_L^2 + g_R^2 r \ , \qquad R_{\bar\nu} = g_L^2 + \frac{g_R^2}{r} \ , \tag{10.25a}$$

$$R^- = g_L^2 - g_R^2 \ , \qquad r \equiv \frac{\sigma_{\bar\nu N}^{CC}}{\sigma_{\nu N}^{CC}} \ , \tag{10.25b}$$

where r is the ratio of $\bar\nu$ to ν charged-current cross-sections which can be measured directly[10], and

$$g_L^2 \equiv (g_{LL}^{\nu_\mu u})^2 + (g_{LL}^{\nu_\mu d})^2 \approx \frac{1}{2} - \sin^2\theta_W + \frac{5}{9}\sin^4\theta_W \ , \tag{10.26a}$$

$$g_R^2 \equiv (g_{LR}^{\nu_\mu u})^2 + (g_{LR}^{\nu_\mu d})^2 \approx \frac{5}{9}\sin^4\theta_W \ . \tag{10.26b}$$

In practice, Eq. (10.25b) must be corrected for quark mixing, quark sea effects, c quark threshold effects, non-isoscalarity, W–Z propagator differences, the finite muon mass, QED and EW radiative corrections. Details of the neutrino spectra, experimental cuts, x and Q^2 dependence of structure functions, and longitudinal structure functions, enter only at the level of these corrections and therefore lead to very small uncertainties. CCFR quotes $s_W^2 = 0.2236 \pm 0.0041$ for the reference values $(m_t, M_H) = (175, 150)$ GeV with very little sensitivity to (m_t, M_H).

The NuTeV collaboration found $s_W^2 = 0.2277 \pm 0.0016$ (for the same reference values), which was 3.0 σ higher than the SM prediction [134]. However, since then several groups have raised concerns about the interpretation of the NuTeV result, which could affect the extracted $g_{L,R}^2$ (and thus s_W^2) including their uncertainties and correlation. These include the assumption of symmetric strange and anti-strange sea quark distributions, the electron neutrino contamination from K_{e3} decays, isospin symmetry violation in the parton distribution functions and from QED splitting effects, nuclear shadowing effects, and a more complete treatment of EW and QCD radiative corrections. A more detailed discussion and a list of references can be found in the 2016 edition of this *Review*. The precise impact of these effects would need to be evaluated carefully by the collaboration, but in the absence of such an effort we do not include the νDIS constraints in our default set of fits.

Very recently, the COHERENT collaboration was the first to observe the coherent elastic neutrino nucleus scattering (CEνNS) process [135] on a target consisting mostly of ^{133}Cs and ^{127}I, and at the opposite end of the kinematic scale where the momentum transfer is significantly smaller than the inverse of the nuclear radius. The coherence enhances the process roughly proportional to the square of the number of neutrons in the nuclei, but the process is difficult to observe as the experimental signature is a mere keV scale nuclear recoil.

10.3.2 *Parity violating lepton scattering*

Reviews on weak polarized electron scattering may be found in Refs. [9, 136]. The SLAC polarized electron-deuteron DIS (eDIS) experiment [137] measured the parity violating right-left asymmetry,

$$A_{RL} \equiv \frac{\sigma_R - \sigma_L}{\sigma_R + \sigma_L} \ , \tag{10.27}$$

where $\sigma_{R,L}$ is the cross-section for the deep-inelastic scattering of a right- or left-handed electron, $e_{R,L}N \to e\text{X}$. In the quark parton model,

$$\frac{A_{RL}}{Q^2} = a_1 + a_2\,\frac{1-(1-y)^2}{1+(1-y)^2} \ , \tag{10.28}$$

where $Q^2 > 0$ is the momentum transfer and y is the fractional energy transfer from the electron to the hadrons. For the deuteron or other isoscalar targets, one has, neglecting the s quark and anti-quarks,

$$a_1 = \frac{3G_F}{5\sqrt{2}\pi\alpha}\left(g_{AV}^{eu} - \frac{1}{2}g_{AV}^{ed}\right) \approx \frac{3G_F}{5\sqrt{2}\pi\alpha}\left(-\frac{3}{4} + \frac{5}{3}\widehat{s}_0^2\right) \ , \tag{10.29a}$$

$$a_2 = \frac{3G_F}{5\sqrt{2}\pi\alpha}\left(g_{VA}^{eu} - \frac{1}{2}g_{VA}^{ed}\right) \approx \frac{9G_F}{5\sqrt{2}\pi\alpha}\left(\widehat{s}_0^2 - \frac{1}{4}\right) \ . \tag{10.29b}$$

The Jefferson Lab Hall A collaboration [138, 139] improved on the SLAC result by measuring A_{RL} at $Q^2 = 1.085$ GeV^2 and

[10] In the simple parton model, ignoring hadron energy cuts, $r \approx (1 + 3\epsilon)/(3 + \epsilon)$, where $\epsilon \sim 0.125$ is the ratio of the fraction of the nucleon's momentum carried by anti-quarks to that carried by quarks.

1.901 GeV^2, and determined the weak mixing angle to 2% precision, $\widehat{s}^2(161\text{ MeV}) = 0.2403 \pm 0.0043$. In another polarized electron scattering experiment on deuterons, but in the quasi-elastic kinematic regime, the SAMPLE experiment [140, 141] at MIT-Bates extracted the combination $g_{VA}^{eu} - g_{VA}^{ed}$ at Q^2 values of 0.038 GeV^2 and 0.091 GeV^2. What was actually determined were nucleon form factors from which the quoted results were obtained by the removal of a multi-quark radiative correction [142]. Other linear combinations of the effective couplings have been determined in polarized lepton scattering at CERN in μ-^{12}C DIS [143] (the observable was the double charge-helicity cross-section asymmetry), at Mainz in e-^{9}Be (quasi-elastic) [144], and at Bates in e-^{12}C (elastic) [145]. More recent polarized electron scattering experiments, *i.e.*, SAMPLE, the PVA4 experiment at Mainz, and the HAPPEX and GØ experiments at Jefferson Lab, have focussed on the strange quark content of the nucleon [146].

A_{RL} can also be measured in fixed target polarized Møller scattering, $e^-e^- \to e^-e^-$, and reads [147],

$$\frac{A_{RL}}{Q^2} = -2\, g_{AV}^{ee} \frac{G_F}{\sqrt{2}\pi\alpha} \frac{1-y}{1+y^4+(1-y)^4} \ . \tag{10.30}$$

It has been determined at low $Q^2 = 0.026$ GeV^2 in the SLAC E158 experiment [148], with the result, $A_{RL} = (-1.31 \pm 0.14_{\text{stat.}} \pm 0.10_{\text{syst.}}) \times 10^{-7}$. Expressed in terms of the weak mixing angle in the $\overline{\text{MS}}$ scheme this yields $\widehat{s}^2(161\text{ MeV}) = 0.2403 \pm 0.0013$, and as shown in Fig. 10.2 established the scale dependence of the weak mixing angle at the level of 6.4 σ. One also extracts the model-independent effective coupling, $g_{AV}^{ee} = 0.0190 \pm 0.0027$ [13]. One-loop radiative corrections and implications are discussed in Ref. [73].

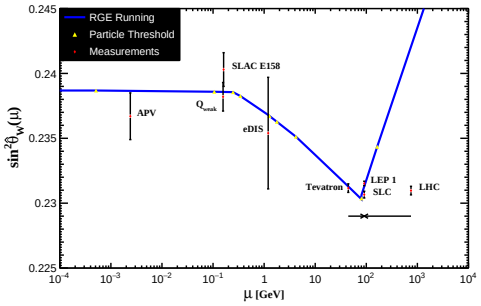

Figure 10.2: Scale dependence of the weak mixing angle defined in the $\overline{\text{MS}}$ scheme [35, 74] (for the scale dependence in a mass-dependent renormalization scheme, see Ref. [73]). The minimum of the curve corresponds to $\mu = M_W$, below which we switch to an effective theory with the $W^\pm$ bosons integrated out, and where the β-function for $\widehat{s}^2(\mu)$ changes sign. At M_W and each fermion mass there are also discontinuities arising from scheme dependent matching terms, which are necessary to ensure that the various effective field theories within a given loop order describe the same physics. However, in the $\overline{\text{MS}}$ scheme these are very small numerically and barely visible in the figure provided one decouples quarks at $\mu = \widehat{m}_q(\widehat{m}_q)$. The width of the curve exceeds the theory uncertainty from strong interaction effects which at low energies is at the level of $\pm 2 \times 10^{-5}$ [35]. The Tevatron and LHC measurements are strongly dominated by invariant masses of the final-state di-lepton pair of $\mathcal{O}(M_Z)$ and can thus be considered as additional Z pole data points. For clarity we displayed the Tevatron and LHC points horizontally to the left and right, respectively.

In a similar experiment and at about the same $Q^2 = 0.0248$ GeV^2, the Q_{weak} collaboration at Jefferson Lab obtained $A_{RL} = (-2.265 \pm 0.073_{\text{stat.}} \pm 0.058_{\text{syst.}}) \times 10^{-7}$ [149, 150] in elastic $e^-p \to e^-p$ scattering. To extract the physical quantity of interest, the weak charge of the proton [151], a large ($\approx 30\%$) correction had to be applied to A_{RL} arising from electromagnetic, strange, and axial form factors. This was achieved by performing a global fit [152] including a large number of A_{RL} data points at larger Q^2, dominated by the HAPPEX result at $Q^2 = 0.109$ GeV^2 [153]. Finally, the constraint, $2g_{AV}^{eu} + g_{AV}^{ed} = 0.0356 \pm 0.0023$, which translates into a weak mixing angle measurement of $\widehat{s}^2(157\text{ MeV}) = 0.2382 \pm 0.0011$, could be deduced, after correcting for a relatively large and uncertain contribution from the γZ box diagram [154–157].

10.3.3 *Atomic parity violation*

There are precise measurements of atomic parity violation (APV) [9, 158, 159] in ^{133}Cs [160, 161] (at the 0.4% level [160]), ^{205}Tl [162, 163], ^{208}Pb [164], and ^{209}Bi [165]. The EW physics is contained in the nuclear weak charges $Q_W(Z,N)$, where Z and N are the numbers of protons and neutrons in the nucleus. In terms of the nucleon vector couplings,

$$g_{AV}^{ep} \equiv 2g_{AV}^{eu} + g_{AV}^{ed} \approx -\frac{1}{2} + 2\widehat{s}_0^2 \ , \tag{10.31a}$$

$$g_{AV}^{en} \equiv g_{AV}^{eu} + 2g_{AV}^{ed} \approx +\frac{1}{2} \ , \tag{10.31b}$$

one has,

$$Q_W(Z,N) \equiv -2\left[Z(g_{AV}^{ep} + 0.00005) + N(g_{AV}^{en} + 0.00006)\right] \times \left(1 - \frac{\alpha}{2\pi}\right) \ , \tag{10.32}$$

where the numerically small adjustments are discussed in Ref. [13] and include the result of the γZ-box correction from Ref. [166].

E.g., $Q_W(^{133}_{78}\text{Cs})$ is extracted by measuring experimentally the ratio of the parity violating amplitude, E_{PNC}, to the Stark vector transition polarizability, β, and by calculating theoretically E_{PNC} in terms of Q_W. One can then write,

$$Q_W(^{133}_{78}\text{Cs}) = N \left(\frac{\text{Im}\, E_{\text{PNC}}}{\beta}\right)_{\text{exp.}} \left(\frac{|e|\, a_B}{\text{Im}\, E_{\text{PNC}}} \frac{Q_W}{N}\right)_{\text{th.}} \times \left(\frac{\beta}{a_B^3}\right)_{\text{exp.+th.}} \left(\frac{a_B^2}{|e|}\right) \ , \tag{10.33}$$

where a_B is the Bohr radius. There are currently two semi-empirical approaches to β of similar precision. The ratio of the off-diagonal hyperfine amplitude to the vector polarizability was measured directly by the Boulder group [167]. Combined with the hyperfine amplitude, computed precisely in Ref. [168], one finds $\beta = (26.957 \pm 0.044_{\text{exp.}} \pm 0.027_{\text{th.}})\, a_B^3$. Alternatively, one can combine [169] the measurement of the ratio of scalar to vector transition polarizabilities [170] with the recent calculation of the scalar polarizability [171] to obtain $\beta = (27.139 \pm 0.030_{\text{exp.}} \pm 0.030_{\text{th.}})\, a_B^3$, in agreement with earlier results [172, 173] based on this approach. The two determinations average to $\beta = (27.064 \pm 0.025_{\text{exp.}} \pm 0.021_{\text{th.}})\, a_B^3$, while they differ by 2.7 σ.

The uncertainties associated with the atomic wave function calculations are relatively small for cesium [9, 174–176]. State-of-the-art many-body atomic structure computations of the parity non-conserving amplitude, $\text{Im}\, E_{\text{PNC}} = (0.8977 \pm 0.0040) \times 10^{-11} |e|\, a_B\, Q_W/N$ [177–182], together with the measurements [160, 161] which can be combined to give $\text{Im}\, E_{\text{PNC}}/\beta = -1.5924 \pm 0.0055$ mV/cm, imply,

$$Q_W(^{133}_{78}\text{Cs}) = -72.82 \pm 0.26_{\text{exp.}} \pm 0.33_{\text{th.}} \ , \tag{10.34}$$

or equivalently the constraint, $55g_{AV}^{ep} + 78g_{AV}^{en} = 36.46 \pm 0.21$. Within the SM this can also be translated into a determination of the weak mixing angle, $\widehat{s}^2(2.4\text{ MeV}) = 0.2367 \pm 0.0018$, where the scale setting follows the estimate in Ref. [183] for the typical momentum transfer for parity violation experiments in Cs (the corresponding estimate for Tl amounts to 8 MeV). By comparing different hyperfine transitions, the Boulder experiment in cesium also observed the parity violating weak corrections to the nuclear electromagnetic vertex, called the nuclear anapole moment [184–186].

The theoretical atomic structure uncertainties are 3% for thallium [187] and even larger for the other atoms. However, they mostly cancel if one takes ratios of parity violation in different isotopes [188]. The first result of this type of experiment was announced very recently by the Mainz group [189], who studied APV in ^{100}Yb, ^{102}Yb, ^{104}Yb, and ^{106}Yb, at the 0.5% level. The resulting three ratios can be interpreted as a measurement of $\widehat{s}_0^2 = 0.258 \pm 0.052$, and represent a very complementary approach to search for BSM physics [190]. If the precision increases in the future, one would ultimately face uncertainties from differences in the neutron charge radii [191, 192]. These can be constrained experimentally [193], *e.g.*, by measuring A_{RL} in heavier nuclei as done by the PREX collaboration at Jefferson Lab on ^{208}Pb [194].

10.4 Precision flavor physics

In addition to cross-sections, asymmetries, parity violation, W, Z, Higgs and other collider physics, there is a large number of experiments and observables testing the flavor structure of the SM. These are addressed elsewhere in this *Review*, and are generally not included in this Section. However, we identify three precision observables with sensitivity to similar types of new physics as the other processes discussed here. The branching fraction of the flavor changing transition $b \to s\gamma$ is of comparatively low precision, but since it is a loop-level process (in the SM) its sensitivity to new physics (and SM parameters, such as heavy quark masses) is enhanced. A discussion can be found in the 2010 edition of this *Review*.

The τ lepton lifetime and leptonic branching ratios are primarily sensitive to α_s and not affected significantly by many types of new physics. However, having an independent and reliable low energy measurement of α_s in a global analysis allows the comparison with the Z lineshape determination of α_s which shifts easily in the presence of new physics contributions. By far the most precise observable discussed here is the anomalous magnetic moment of the muon. Its combined experimental and theoretical uncertainty is smaller than typical electroweak scale contributions. The electron magnetic moment is measured to even greater precision, and as discussed in Sec. 10.2.2 can be used to determine α. Its new physics sensitivity, however, is suppressed by an additional factor of m_e^2/m_μ^2, unless there is a new light degree of freedom such as a dark Z [195] boson.

10.4.1 *The τ lifetime*

The extraction of α_s from the τ lifetime τ_τ [196,197] is standing out from other determinations because of a variety of independent reasons:

(i) The τ-scale is low, so that upon extrapolation to the Z scale (where it can be compared to the theoretically clean Z lineshape determinations) the α_s error shrinks by about an order of magnitude.

(ii) Yet, this scale is high enough that perturbation theory and the operator product expansion (OPE) can be applied.

(iii) These observables are fully inclusive and thus free of fragmentation and hadronization effects that would have to be modeled or measured.

(iv) Duality violation (DV) effects are most problematic near the branch cut but there they are suppressed by a double zero at $s = m_\tau^2$.

(v) There are data [39, 41, 198] to constrain non-perturbative effects both within and breaking the OPE.

(vi) A complete four-loop order QCD calculation is available [199–203] in the massless limit.

(vii) Large effects associated with the QCD β-function can be re-summed [204] in what has become known as contour improved perturbation theory (CIPT).

However, while CIPT certainly shows faster convergence in the lower (calculable) orders, doubts have been cast on the method by the observation that at least in a specific model [205], which includes the exactly known coefficients and theoretical constraints on the large-order behavior, ordinary fixed order perturbation theory (FOPT) may nevertheless give a better approximation to the full result. We therefore use the expressions [53, 203, 206],

$$\tau_\tau = \hbar \frac{1 - \mathcal{B}_\tau^s}{\Gamma_\tau^e + \Gamma_\tau^\mu + \Gamma_\tau^{ud}} = 290.75 \pm 0.36 \text{ fs} \,, \tag{10.35}$$

and

$$\Gamma_\tau^{ud} = \frac{G_F^2 m_\tau^5 |V_{ud}|^2}{64\pi^3} S(m_\tau, M_Z) \left(1 + \frac{3}{5}\,\frac{m_\tau^2 - m_\mu^2}{M_W^2}\right) \times \left[1 + \frac{\alpha_s(m_\tau)}{\pi} + 5.202\,\frac{\alpha_s^2}{\pi^2} + 26.37\,\frac{\alpha_s^3}{\pi^3} + 127.1\,\frac{\alpha_s^4}{\pi^4} + \frac{\widehat{\alpha}}{\pi}\left(\frac{85}{24} - \frac{\pi^2}{2}\right) + \delta_{\rm NP}\right] \,, \tag{10.36}$$

where Γ_τ^e and Γ_τ^μ can be taken from Eq. (10.7) with obvious replacements. The relative fraction of strangeness changing ($\Delta S = -1$) decays, $\mathcal{B}_\tau^s = 0.0292 \pm 0.0004$, is based on experimental data since the value for the strange quark mass, $\widehat{m}_s(m_\tau)$, is not well known and the QCD expansion proportional to $\widehat{m}_s^2$ converges poorly and cannot be trusted. $S(m_\tau, M_Z) = 1.01907 \pm 0.0003$ is a logarithmically enhanced EW correction factor [207] with higher orders re-summed [208].

$\delta_{\rm NP}$ collects non-perturbative and quark-mass suppressed contributions, including the dimension four, six and eight terms in the OPE, as well as DV effects. We use the average $\delta_{\rm NP} = 0.0141 \pm 0.0072$ derived from the τ decay spectral functions provided by OPAL [39] and ALEPH [41,198], which give $\delta_{\rm NP} = 0.000 \pm 0.012$ and $\delta_{\rm NP} = 0.022 \pm 0.009$, respectively. These numbers are based on the original analyses in Refs. [209, 210], but are modified to correspond to a strict FOPT analysis as is appropriate for our purpose[11] (for alternative analyses, see Refs. [197, 198, 211]).

The dominant uncertainty arises from the truncation of the FOPT series and is conservatively taken as the α_s^4 term (this is re-calculated in each call of the fits, leading to an α_s-dependent and thus asymmetric error) until a better understanding of the numerical differences between FOPT and CIPT has been gained. Our perturbative error covers almost the entire range from using CIPT to assuming that the nearly geometric series in Eq. (10.36) continues to higher orders. The experimental uncertainty in Eq. (10.35) is from the combination of the two leptonic branching ratios with the direct τ_τ. Included are also various smaller uncertainties (± 0.15 fs) from other sources. Based on the method of Refs. [53, 212], we obtain in total

$$\alpha_s^{(4)}(m_\tau) = 0.312^{+0.016}_{-0.013} \,, \qquad \alpha_s^{(5)}(M_Z) = 0.1170^{+0.0019}_{-0.0017} \,, \tag{10.37}$$

which represents a 1.5% determination of $\alpha_s(M_Z)$. For more details, see Refs. [209,210] where the τ spectral functions themselves and an estimate of the unknown α_s^5 term were used as additional inputs.

10.4.2 *The muon anomalous magnetic moment*

The world average of the muon anomalous magnetic moment[12],

$$a_\mu^{\rm exp} = \frac{g_\mu - 2}{2} = (1165920.91 \pm 0.63) \times 10^{-9} \,, \tag{10.38}$$

is dominated by the final result of the BNL E821 collaboration [213]. The QED contribution has been calculated to five loops [214–216] (fully analytic to three loops [217–221] and semi-analytic to four loops [222]). The estimated SM EW contribution [223–228], $a_\mu^{\rm EW} = (1.54 \pm 0.01) \times 10^{-9}$, includes two-

[11] We are indebted to Diogo Boito, Maarten Golterman, Kim Maltman and Santiago Peris for privately communicating these results to us.

[12] In what follows, we summarize the most important aspects of a_μ and give some details on the evaluation in our fits. For more details and references, see the Section on the "Muon Anomalous Magnetic Moment" in this *Review*. There are some numerical differences, which are well understood and arise because internal consistency of the fits requires the calculation of all observables from analytical expressions and common inputs and fit parameters, so that an independent evaluation is necessary for this Section. Note, that in the spirit of a global analysis based on all available information we have chosen here to also include τ decay data [30], corrected for isospin breaking effects [31].

loop [229–233] and leading three-loop [234, 235] corrections and is at the level of twice the current uncertainty.

The limiting factor in the interpretation of the result are the uncertainties from hadronic effects. The most recent evaluations of the leading-order (two-loop) hadronic vacuum polarization contribution obtained $a_\mu^{\rm had,VP}(\alpha^2) = (68.81 \pm 0.41) \times 10^{-9}$ [236], $a_\mu^{\rm had,VP}(\alpha^2) = (69.39 \pm 0.40) \times 10^{-9}$ [29], and $a_\mu^{\rm had,VP}(\alpha^2) = (69.28 \pm 0.24) \times 10^{-9}$ [37]. These are mainly based on data from $e^+e^- \to$ hadrons (see, *e.g.*, Ref. [29] for references). Our analysis combines the e^+e^- [29] and τ-decay data [30,31] for contributions up to $\sqrt{s} = 2$ GeV, $a_\mu^{\rm had,VP}(\alpha^2, 2\ {\rm GeV}) = (64.49 \pm 0.33) \times 10^{-9}$, with analytical PQCD expressions for energies beyond 2 GeV and for the c and b quark contributions [221]. By now there are also precise results for the determination of $a_\mu^{\rm had,VP}(\alpha^2)$ from lattice QCD calculations [237] at the 2–3% level [238–242], while the most recent one has a 0.6% quoted uncertainty [243] (for a comparative appraisal and further references, see Ref. [244]). The result of Ref. [243], $(71.24 \pm 0.45) \times 10^{-9}$, has a more than 3 σ conflict with the data-driven evaluations, while there is very good statistical agreement among the different lattice results, assuming them to be uncorrelated (χ^2/d.o.f. = 5.1/5). If confirmed, the recent lattice determinations for $a_\mu^{\rm had,VP}(\alpha^2)$ may point to a problem with the data-driven approach to this quantity.

The other hadronic uncertainty is induced by the three-loop light-by-light scattering amplitude, where a number of independent model calculations yield results which are in reasonable agreement with each other, $a_\mu^{\rm had,\gamma\times\gamma}(\alpha^3) = (1.36 \pm 0.25) \times 10^{-9}$ [245], $a_\mu^{\rm had,\gamma\times\gamma}(\alpha^3) = 1.37^{+0.15}_{-0.27} \times 10^{-9}$ [246], $a_\mu^{\rm had,\gamma\times\gamma}(\alpha^3) = (1.05 \pm 0.26) \times 10^{-9}$ [247], and $a_\mu^{\rm had,\gamma\times\gamma}(\alpha^3) = (1.03 \pm 0.29) \times 10^{-9}$ [236], but the sign of this effect is opposite [248] to the one quoted in the 2002 edition of this *Review*. There is also an upper bound given by $a_\mu^{\rm had,\gamma\times\gamma}(\alpha^3) < 1.59 \times 10^{-9}$ [246] but this requires an *ad hoc* assumption, too. An effort to improve the evaluation of the light-by-light contribution by using experimental input where available yields a slightly lower value, $a_\mu^{\rm had,\gamma\times\gamma}(\alpha^3) = (0.87 \pm 0.13) \times 10^{-9}$ [249]. A first complete result from lattice simulations, $a_\mu^{\rm had,\gamma\times\gamma}(\alpha^3) = (0.79 \pm 0.35) \times 10^{-9}$ [250], accounting for all systematic errors, is consistent with the model and data-driven calculations. For the fits, we take the result from Ref. [236], shifted by 2×10^{-11} to account for the more accurate charm quark treatment of Ref. [246], and with increased error to cover all recent evaluations, resulting in $a_\mu^{\rm had,\gamma\times\gamma}(\alpha^3) = (1.05 \pm 0.33) \times 10^{-9}$.

Sub-leading hadronic vacuum polarization effects at three-loop [251] and four-loop order [252] contribute $a_\mu^{\rm had,VP}(\alpha^3) = (-0.983 \pm 0.004) \times 10^{-9}$ [37] and $a_\mu^{\rm had,VP}(\alpha^4) = (0.124 \pm 0.001) \times 10^{-9}$ [252], respectively. The correlations with the two-loop hadronic contribution and with $\Delta\alpha(M_Z)$ (see Sec. 10.2) were considered in Ref. [221]. The contributions with a hadronic light-by-light scattering subgraph have been estimated in Ref. [253], with the result, $a_\mu^{\rm had,\gamma\times\gamma}(\alpha^4) = (0.03 \pm 0.02) \times 10^{-9}$.

Altogether, the SM prediction is

$$a_\mu^{\rm theory} = (1165918.46 \pm 0.47) \times 10^{-9} \ , \qquad (10.39)$$

where the error is from the hadronic uncertainties excluding parametric ones such as from α_s and the heavy quark masses. We evaluate the correlation of the total (experimental plus theoretical) uncertainty in a_μ with $\Delta\alpha(M_Z)$ to amount to roughly 30%. The overall 3.1 σ discrepancy between $a_\mu^{\rm theory}$ and $a_\mu^{\rm exp}$ could be due to fluctuations (the E821 result is statistics dominated) or underestimates of the theoretical uncertainties. On the other hand, the deviation could also arise from physics beyond the SM, such as supersymmetric models with large $\tan\beta$ and moderately light superparticle masses [254], or a dark Z boson [195].

10.5 Physics of the massive electroweak bosons

If the CM energy $\sqrt{s}$ is large compared to the fermion mass m_f, the unpolarized Born cross-section for $e^+e^- \to f\bar{f}$ [255] can be written as,

$$\frac{d\sigma}{d\cos\theta} = \frac{\pi\alpha^2(s)}{2s}\left[F_1(1+\cos^2\theta) + 2F_2\cos\theta\right] + B \ , \qquad (10.40a)$$

$$F_1 = Q_e^2 Q_f^2 - 2\chi Q_e Q_f \bar{g}_V^e \bar{g}_V^f \cos\delta_R + \chi^2(\bar{g}_V^{e2} + \bar{g}_A^{e2})(\bar{g}_V^{f2} + \bar{g}_A^{f2}) \ , \qquad (10.40b)$$

$$F_2 = -2\chi Q_e Q_f \bar{g}_A^e \bar{g}_A^f \cos\delta_R + 4\chi^2 \bar{g}_V^e \bar{g}_A^e \bar{g}_V^f \bar{g}_A^f \ , \qquad (10.40c)$$

where,

$$\tan\delta_R = \frac{\overline{M}_Z\overline{\Gamma}_Z}{\overline{M}_Z^2 - s} \ , \quad \chi = \frac{G_F}{2\sqrt{2}\pi\alpha(s)} \frac{s\overline{M}_Z^2}{\left[(\overline{M}_Z^2 - s)^2 + \overline{M}_Z^2\overline{\Gamma}_Z^2\right]^{1/2}} \ . \qquad (10.41)$$

B accounts for box graphs involving virtual Z and W bosons, and the $\bar{g}_{V,A}^f$ are defined in Eq. (10.42) below. $\overline{M}_Z$ and $\overline{\Gamma}_Z$ correspond to mass and width definitions based on a Breit-Wigner shape with an energy-independent width (see the Section on the "Z Boson" in this *Review*). The differential cross-section receives important corrections from QED effects in the initial and final state, and interference between the two [256]. For $q\bar{q}$ production, there are additional final-state QCD corrections, which are relatively large. Note also that the equations above are written in the CM frame of the incident e^+e^- system, which may be boosted due to the initial-state QED radiation.

Some of the leading virtual EW corrections are captured by the running QED coupling $\alpha(s)$ and the Fermi constant G_F. The remaining corrections to the $Zf\bar{f}$ interactions are absorbed by replacing the tree-level couplings in Eq. (10.6) with the s-dependent *effective couplings* [14],

$$\bar{g}_V^f = \sqrt{\rho_f}\left(t_{3L}^f - 2Q_f\kappa_f\sin^2\theta_W\right) \ , \qquad (10.42a)$$

$$\bar{g}_A^f = \sqrt{\rho_f}\, t_{3L}^f \ . \qquad (10.42b)$$

In these equations, the effective couplings are to be taken at the scale $\sqrt{s}$, but for notational simplicity we do not show this explicitly. At tree-level, $\rho_f = \kappa_f = 1$, but inclusion of EW radiative corrections leads to $\rho_f \neq 1$ and $\kappa_f \neq 1$, which depend on the fermion f and on the renormalization scheme. In the on-shell scheme, the quadratic m_t dependence is given by,

$$\rho_f \sim 1 + \rho_t \ , \qquad \kappa_f \sim 1 + \frac{\rho_t}{\tan^2\theta_W} \ , \qquad (10.43)$$

while in $\overline{\rm MS}$, $\widehat{\rho}_f \sim \widehat{\kappa}_f \sim 1$, for $f \neq b$, and

$$\widehat{\rho}_b \sim 1 - \frac{4}{3}\rho_t \ , \qquad \widehat{\kappa}_b \sim 1 + \frac{2}{3}\rho_t \ . \qquad (10.44)$$

In the $\overline{\rm MS}$ scheme the normalization is changed according to $G_F M_Z^2/2\sqrt{2}\pi \to \widehat{\alpha}/4\widehat{s}_Z^2\widehat{c}_Z^2$ in the second Eq. (10.41).

As reviewed in Sec. 10.2.5, for the high precision Z pole observables discussed below, many additional bosonic and fermionic loop effects, vertex corrections, and higher order contributions, *etc.*, must be included. For example, in the $\overline{\rm MS}$ scheme one then has $\widehat{\rho}_\ell = 0.9977$, $\widehat{\kappa}_\ell = 1.0014$, $\widehat{\rho}_b = 0.9866$, and $\widehat{\kappa}_b = 1.0068$.

To connect to measured quantities, it is convenient to define an effective angle

$$\bar{s}_f^2 \equiv \sin^2\bar{\theta}_{Wf} \equiv \widehat{\kappa}_f\widehat{s}_Z^2 = \kappa_f s_W^2 \ , \qquad (10.45)$$

in terms of which $\bar{g}_V^f$ and $\bar{g}_A^f$ are given by $\sqrt{\rho_f}$ times their tree-level formulae. One finds that the $\widehat{\kappa}_f$ ($f \neq b$) are almost independent of m_t and M_H, and thus one can write,

$$\bar{s}_\ell^2 = \widehat{s}_Z^2 + 0.00032 \ , \qquad (10.46)$$

while the κ_f for the on-shell scheme are m_t dependent.

10.5.1 *Electroweak physics off the Z pole*

Experiments at PEP, PETRA and TRISTAN have measured the unpolarized forward-backward asymmetry, A_{FB}, and the total cross-section relative to pure QED, R, for $e^+e^- \to \ell^+\ell^-$, $\ell = \mu$ or τ at CM energies $\sqrt{s} < M_Z$. They are defined as

$$A_{FB} \equiv \frac{\sigma_F - \sigma_B}{\sigma_F + \sigma_B} \ , \qquad R = \frac{\sigma}{\mathcal{R}_{\rm ini} \otimes 4\pi\alpha^2/3s} \ , \tag{10.47}$$

where σ_F (σ_B) is the cross-section for ℓ^- to travel forward (backward) with respect to the e^- direction, and $\mathcal{R}_{\rm ini}\otimes$ denotes convolution with initial-state QED corrections. Neglecting box graph contributions, they are given by,

$$A_{FB} = \frac{3}{4}\frac{F_2}{F_1} \ , \qquad R = F_1 \ . \tag{10.48}$$

For the available data, it is sufficient to approximate the EW corrections through the leading running $\alpha(s)$ and quadratic m_t contributions [257], as described above. Reviews and formulae for $e^+e^- \to$ hadrons may be found in [9, 258, 259].

LEP 2 [260] ran at several energies above the Z pole up to ~ 209 GeV. Measurements were made of a number of observables, including the total production cross-sections of $f\bar{f}$ pairs for $f = \mu, \tau$, and q (hadrons), of four-fermion final states, of $\gamma\gamma$, ZZ, WW, $WW\gamma$, and WWZ, as well as of single resonant W and Z bosons. The differential cross-sections for all three lepton flavors, and the leptonic and hadronic W branching ratios were also extracted.

Among the most important LEP 2 results were the measurements [260] of the W boson mass,

$$M_W = 80.376 \pm 0.025_{\rm\,stat.} \pm 0.022_{\rm\,syst.}\ {\rm GeV\ (LEP\ 2)} \ , \tag{10.49}$$

which were dominated by kinematic reconstruction, but included the complementary albeit statistics limited and thus much less precise determination from a WW threshold cross section scan. The kinematic method was also employed at the Tevatron [261] and by ATLAS [263]. They quote,

$$M_W = 80.387 \pm 0.016\ {\rm GeV\ (Tevatron)} \ , \tag{10.50a}$$

$$M_W = 80.3695 \pm 0.0068_{\rm\,stat.} \pm 0.0106_{\rm\,syst.} \pm 0.0136_{\rm\,th.}\ {\rm GeV\ (ATLAS)} \ . \tag{10.50b}$$

We assume an error component of 7 MeV to be common between the two hadron collider determinations. This is smaller than the 10 MeV PDF uncertainty quoted by CDF, because the larger CM energy at the LHC enhances the sensitivity to second generation quark PDFs, in addition to the greater sea quark PDF dependence of the Drell-Yan process in the pp environment. There may also be some correlation due to other production modeling uncertainties. This implies for the average,

$$M_W = 80.379 \pm 0.012\ {\rm GeV\ (world\ average)} \ . \tag{10.51}$$

For details and references, see the Section on the "Mass and Width of the W Boson" in this *Review*.

Strong constraints on anomalous triple and quartic gauge couplings have been obtained at LEP 2, the Tevatron, and the LHC. These are described in detail in the three Sections on the "Extraction of Triple Gauge Couplings (TGCs)", "Anomalous W/Z Quartic Couplings (QGCs)", and "Anomalous $ZZ\gamma$, $Z\gamma\gamma$, and ZZV Couplings" in this *Review*.

After their discovery of the Higgs boson [264, 265], the LHC experiments are now performing high precision measurements of its mass. We average the results, $M_H = 124.97 \pm 0.16_{\rm\,stat.} \pm 0.18_{\rm\,syst.}$ GeV from ATLAS [266], and $M_H = 125.38 \pm 0.11_{\rm\,stat.} \pm 0.09_{\rm\,syst.}$ GeV from CMS [267], by conservatively treating the smaller systematic error as common among the two determinations, and arrive at,

$$M_H = 125.30 \pm 0.09_{\rm\,stat.} \pm 0.09_{\rm\,syst.}\ {\rm GeV\ (LHC)} \ . \tag{10.52}$$

For further references and many more details on Higgs boson properties, see the Section on the "Status of Higgs Boson Physics" in this *Review*. The principal non-Z pole observables discussed here and in Sections 10.2−10.4 are summarized in Table 10.4.

10.5.2 *Z pole physics*

High precision measurements of various Z pole ($\sqrt{s} \approx M_Z$) observables [9, 276, 277] have been performed at LEP 1 and SLC [14, 273, 274, 278, 279], as summarized in Table 10.5. These include the Z mass and total width, Γ_Z, and partial widths $\Gamma_{f\bar{f}}$ for $Z \to f\bar{f}$, where $f = e$, μ, τ, light hadrons, b, and c. It is convenient to use the variables M_Z, Γ_Z,

$$\sigma_{\rm had} \equiv \frac{12\pi\Gamma_{e^+e^-}\Gamma_{\rm had}}{M_Z^2\,\Gamma_Z^2} \ , \qquad R_\ell \equiv \frac{\Gamma_{\rm had}}{\Gamma_{\ell^+\ell^-}} \ , \qquad R_q \equiv \frac{\Gamma_{q\bar{q}}}{\Gamma_{\rm had}} \ , \tag{10.53}$$

for $\ell = e, \mu$ or τ, and $q = b$ or c, where $\Gamma_{\rm had}$ is the partial width into hadrons. Most of these are weakly correlated experimentally. The three values for R_ℓ are consistent with lepton universality (although R_τ is somewhat low compared to R_e and R_μ), but we use the general analysis in which the three observables are treated as independent. Similar remarks apply to $A_{FB}^{0,\ell}$ defined through Eq. (10.54) with $P_e = 0$, where $A_{FB}^{0,\tau}$ is somewhat high. Initial-state radiation reduces the peak cross section by more than 25%, where $\mathcal{O}(\alpha^3)$ QED effects induce a large anti-correlation (−30%) between Γ_Z and $\sigma_{\rm had}$. The anti-correlation between R_b and R_c amounts to −18% [14]. The R_ℓ are insensitive to m_t except for the $Z \to b\bar{b}$ vertex, final-state corrections, and the implicit dependence through $\sin^2\theta_W$. Thus, they are especially useful for constraining α_s.

Very important constraints follow from measurements of various Z pole asymmetries. These include the forward-backward asymmetry, A_{FB}, and the polarization or left-right asymmetry, A_{LR}, defined analogously to Eq. (10.27). The latter was measured precisely by the SLD collaboration at the SLC [273], and has the advantages of being very sensitive to $\bar{s}_\ell^2$ and that systematic uncertainties largely cancel. After removing initial-state QED corrections and contributions from photon exchange, γ–Z interference, as well as the EW boxes in Eq. (10.40a), one can use the effective tree-level expressions,

$$A_{LR} = A_e P_e \ , \qquad A_{FB} = \frac{3}{4} A_f \, \frac{A_e + P_e}{1 + P_e A_e} \ , \tag{10.54}$$

where,

$$A_f \equiv \frac{2\bar{g}_V^f \bar{g}_A^f}{\bar{g}_V^{f2} + \bar{g}_A^{f2}} = \frac{1 - 4|Q_f|\bar{s}_f^2}{1 - 4|Q_f|\bar{s}_f^2 + 8(|Q_f|\bar{s}_f^2)^2} \ . \tag{10.55}$$

P_e is the initial e^- polarization, so that the second equality in Eq. (10.56) is reproduced for $P_e = 1$, and the Z pole forward-backward asymmetries at LEP 1 ($P_e = 0$) are given by $A_{FB}^{(0,f)} = \frac{3}{4} A_e A_f$ for $f = e$, μ, τ, b, c, s [14], and q, and where $A_{FB}^{(0,q)}$ refers to the hadronic charge asymmetry. Corrections for t-channel exchange and s/t-channel interference cause $A_{FB}^{(0,e)}$ to be strongly anti-correlated with R_e (−37%). Very recently, the m_b-dependence [280] of the $\mathcal{O}(\alpha_s^2)$ QCD correction [281], affecting the reference axis of the b quark asymmetry [282], increased the extracted[13] $A_{FB}^{(0,b)}$ by about $0.2\,\sigma$. The correlation between $A_{FB}^{(0,b)}$ and $A_{FB}^{(0,c)}$ amounts to 15%.

In addition, SLD extracted the final-state couplings A_b, A_c [14], A_s [278], A_τ, and A_μ [274], from left-right forward-backward asymmetries, using

$$A_{LR}^{FB}(f) = \frac{\sigma_{LF}^f - \sigma_{LB}^f - \sigma_{RF}^f + \sigma_{RB}^f}{\sigma_{LF}^f + \sigma_{LB}^f + \sigma_{RF}^f + \sigma_{RB}^f} = \frac{3}{4} A_f \ , \tag{10.56}$$

where, for example, σ_{LF}^f is the cross-section for a left-handed incident electron to produce a fermion f traveling in the forward hemisphere. Similarly, A_τ and A_e were measured at LEP 1 [14] through the τ polarization, $\mathcal{P}_\tau$, as a function of the scattering

[13] We are grateful to Werner Bernreuther and Long Chen for the recalculation of their result employing the more appropriate $\overline{\rm MS}$ mixing angle, $\widehat{s^2_Z}$, instead of the on-shell quantity, s^2_W.

Table 10.4: Non-Z pole observables, compared with the SM best fit predictions. The first M_W and Γ_W values are from the Tevatron [261,262], the second ones from LEP 2 [260], while the third M_W is from ATLAS [263]. The entry of m_t differs from the one in the Particle Listings as it includes an additional theory error. The world averages for $g^{\nu e}_{V,A}$ are dominated by the CHARM II [122] results, $g^{\nu e}_V = -0.035 \pm 0.017$ and $g^{\nu e}_A = -0.503 \pm 0.017$. The τ_τ value is the τ lifetime world average computed by combining the direct measurements with values derived from the leptonic branching ratios [53]; in this case, the theory error is included in the SM prediction. In all other SM predictions, the uncertainty is parametric from M_Z, M_H, m_t, m_b, m_c, $\widehat{\alpha}(M_Z)$, and α_s, and theoretical from unknown higher orders [69], where correlations due to both types have been accounted for. The column denoted by Pull gives the standard deviations.

Quantity	Value	Standard Model	Pull
m_t [GeV]	172.89 ± 0.59	173.19 ± 0.55	-0.5
M_H [GeV]	125.30 ± 0.13	125.30 ± 0.13	0.0
M_W [GeV]	80.387 ± 0.016	80.361 ± 0.006	1.6
	80.376 ± 0.033		0.5
	80.370 ± 0.019		0.5
Γ_W [GeV]	2.046 ± 0.049	2.090 ± 0.001	-0.9
	2.195 ± 0.083		1.3
$g^{\nu e}_V$	-0.040 ± 0.015	-0.0398 ± 0.0001	0.0
$g^{\nu e}_A$	-0.507 ± 0.014	-0.5064	0.0
$Q_W(e)$	-0.0403 ± 0.0053	-0.0476 ± 0.0002	1.4
$Q_W(p)$	0.0719 ± 0.0045	0.0711 ± 0.0002	0.2
Q_W(Cs)	-72.82 ± 0.42	-73.23 ± 0.01	1.0
Q_W(Tl)	-116.4 ± 3.6	-116.88 ± 0.02	0.1
$\widehat{s}^2_Z$(eDIS)	0.2299 ± 0.0043	0.23121 ± 0.00004	-0.3
τ_τ [fs]	290.75 ± 0.36	288.90 ± 2.24	0.8
$\frac{1}{2}(g_\mu - 2 - \frac{\alpha}{\pi})$	$(4511.18 \pm 0.78) \times 10^{-9}$	$(4508.74 \pm 0.03) \times 10^{-9}$	3.1

angle θ, which can be written as,

$$\mathcal{P}_\tau = -\frac{A_\tau(1+\cos^2\theta) + 2A_e\cos\theta}{(1+\cos^2\theta) + 2A_\tau A_e\cos\theta} \ . \qquad (10.57)$$

The average polarization, $\langle\mathcal{P}_\tau\rangle$, obtained by integrating over $\cos\theta$ in the numerator and denominator of Eq. (10.57), yields $\langle\mathcal{P}_\tau\rangle = -A_\tau$, and A_e can be extracted from the $\mathcal{P}_\tau$ angular distribution. The initial-state coupling, A_e, was also determined through the left-right charge asymmetry [279] and in polarized Bhabba scattering [274] at the SLC. Because $\bar{g}^\ell_V$ is very small, not only $A^0_{LR} = A_e$, $A^{(0,\ell)}_{FB}$, and $\mathcal{P}_\tau$, but also $A^{(0,q)}_{FB}$ for $q = b$, c, and s, as well as the hadronic asymmetries are mainly sensitive to $\bar{s}^2_\ell$.

As an example of the precision of the Z pole observables, the values of $\bar{g}^f_A$ and $\bar{g}^f_V$ for $f = e, \mu, \tau$, and ℓ, extracted from the LEP and SLC lineshape and asymmetry data, are shown in Fig. 10.3. It may be compared with Fig. 10.1 as the two sets of parameters coincide at the SM at tree-level.

As for hadron colliders, the forward-backward asymmetry, A_{FB}, for e^+e^- and $\mu^+\mu^-$ final states (with invariant masses restricted to or dominated by values around M_Z) in $p\bar{p}$ collisions has been measured by the CDF [283] and DØ [284] collaborations, and the values $\bar{s}^2_\ell = 0.23221 \pm 0.00046$ and $\bar{s}^2_\ell = 0.23095 \pm 0.00040$ were extracted, respectively. The combination of these measurements (which differ by more than 2 σ) yields [268],

$$\bar{s}^2_\ell = 0.23148 \pm 0.00033 \text{ (Tevatron)} \ . \qquad (10.58)$$

By varying the invariant mass and the scattering angle (and assuming the electron couplings), information on the effective Z couplings to light quarks, $\bar{g}^{u,d}_{V,A}$, could also be obtained [285,286], but with large uncertainties, mutual correlations, and not independently of $\bar{s}^2_\ell$ above. Similar analyses have also been reported by the H1 [287] and ZEUS [288] collaborations at HERA and by the LEP collaborations [14]. This kind of measurement is harder in the pp environment due to the difficulty to assign the initial quark and antiquark in the underlying Drell-Yan process to the protons, thus requiring excellent control of uncertainties from parton distribution functions. ATLAS obtained $\bar{s}^2_\ell = 0.2308 \pm 0.0012$ using 7 TeV data [269] and $\bar{s}^2_\ell = 0.23140 \pm 0.00036$ at 8 TeV [270],

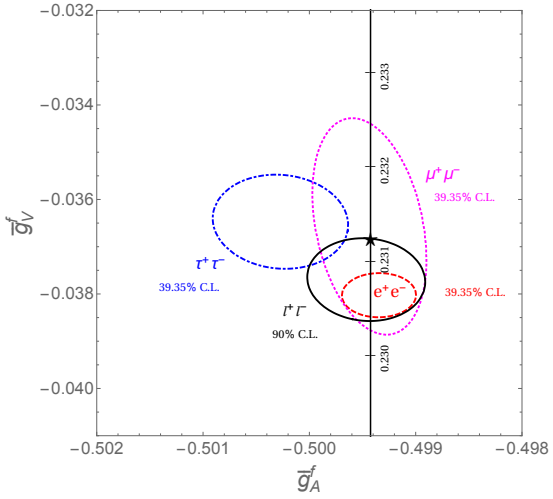

Figure 10.3: 1 σ (39.35% CL) contours of the effective couplings $\bar{g}^f_A$ and $\bar{g}^f_V$ for $f = e, \mu$ and τ from LEP and SLC, compared to the SM expectation as a function of $\widehat{s}^2_Z$. (The SM best fit value $\widehat{s}^2_Z = 0.23121$ is also indicated.) Also shown is the 90% CL allowed region in $\bar{g}^\ell_{A,V}$ obtained assuming lepton universality.

while CMS measured $\bar{s}^2_\ell = 0.23101 \pm 0.00053$ (8 TeV) [271] and LHCb reported $\bar{s}^2_\ell = 0.23142 \pm 0.00106$ (from both 7 and 8 TeV data, but only analyzing $\mu^+\mu^-$ final state) [272]. Assuming that the smallest theoretical and PDF uncertainty (± 0.00024 from ATLAS [270]) is fully correlated among the four determinations, they combine to

$$\bar{s}^2_\ell = 0.23129 \pm 0.00033 \text{ (LHC)} \ . \qquad (10.59)$$

10.5.3 *W and Z decays*

The partial decay widths for gauge bosons to decay into massless fermions $f_1\bar{f}_2$ (the numerical values include the small EW

Table 10.5: Principal Z pole observables and their SM predictions (*cf.* Table 10.4). The first $\bar{s}^2_\ell$ is the effective weak mixing angle extracted from the hadronic charge asymmetry at LEP 1 [14], the second is the combined value from the Tevatron [268], and the third is from the LHC [269–272]. The values of A_e are (i) from A_{LR} for hadronic final states [273]; (ii) from A_{LR} for leptonic final states and from polarized Bhabba scattering [274]; and (iii) from the angular distribution of the τ polarization at LEP 1 [14]. The A_τ values are from SLD [274] and the total τ polarization, respectively. Note that the SM errors in Γ_Z, the R_ℓ, and $\sigma_{\rm had}$ are largely dominated by the uncertainty in α_s.

Quantity	Value	Standard Model	Pull
M_Z [GeV]	91.1876 ± 0.0021	91.1882 ± 0.0020	-0.3
Γ_Z [GeV]	2.4955 ± 0.0023	2.4942 ± 0.0009	0.6
$\sigma_{\rm had}$ [nb]	41.481 ± 0.033	41.482 ± 0.008	0.0
R_e	20.804 ± 0.050	20.736 ± 0.010	1.4
R_μ	20.784 ± 0.034	20.735 ± 0.010	1.4
R_τ	20.764 ± 0.045	20.781 ± 0.010	-0.4
R_b	0.21629 ± 0.00066	0.21581 ± 0.00002	0.7
R_c	0.1721 ± 0.0030	0.17221 ± 0.00003	0.0
$A_{FB}^{(0,e)}$	0.0145 ± 0.0025	0.01619 ± 0.00007	-0.7
$A_{FB}^{(0,\mu)}$	0.0169 ± 0.0013		0.5
$A_{FB}^{(0,\tau)}$	0.0188 ± 0.0017		1.5
$A_{FB}^{(0,b)}$	0.0996 ± 0.0016	0.1030 ± 0.0002	-2.1
$A_{FB}^{(0,c)}$	0.0707 ± 0.0035	0.0736 ± 0.0002	-0.8
$A_{FB}^{(0,s)}$	0.0976 ± 0.0114	0.1031 ± 0.0002	-0.5
$\bar{s}^2_\ell$	0.2324 ± 0.0012	0.23153 ± 0.00004	0.7
	0.23148 ± 0.00033		-0.2
	0.23129 ± 0.00033		-0.7
A_e	0.15138 ± 0.00216	0.1469 ± 0.0003	2.1
	0.1544 ± 0.0060		1.2
	0.1498 ± 0.0049		0.6
A_μ	0.142 ± 0.015		-0.3
A_τ	0.136 ± 0.015		-0.7
	0.1439 ± 0.0043		-0.7
A_b	0.923 ± 0.020	0.9347	-0.6
A_c	0.670 ± 0.027	0.6677 ± 0.0001	0.1
A_s	0.895 ± 0.091	0.9356	-0.4

Table 10.6: Results derived from Table 10.5 and the corresponding covariance matrices [14, 275], and the SM predictions for the partial and total Z decay widths [in MeV]. In the (second) third column lepton universality is (not) assumed.

Quantity	Value	Value (universal)	Standard Model
$\Gamma_{e^+e^-}$	83.87 ± 0.12	83.942 ± 0.085	83.964 ± 0.009
$\Gamma_{\mu^+\mu^-}$	83.95 ± 0.18	83.941 ± 0.085	83.963 ± 0.009
$\Gamma_{\tau^+\tau^-}$	84.03 ± 0.21	83.759 ± 0.085	83.780 ± 0.009
$\Gamma_{\rm inv}$	498.9 ± 2.5	500.5 ± 1.5	501.464 ± 0.047
$\Gamma_{u\bar{u}}$	—	—	299.91 ± 0.20
$\Gamma_{c\bar{c}}$	300.3 ± 5.3	300.0 ± 5.2	299.83 ± 0.20
$\Gamma_{d\bar{d}}, \Gamma_{s\bar{s}}$	—	—	382.79 ± 0.14
$\Gamma_{b\bar{b}}$	377.4 ± 1.3	377.0 ± 1.2	375.75 ∓ 0.18
$\Gamma_{\rm had}$	1744.8 ± 2.6	1743.2 ± 1.9	1741.06 ± 0.85
Γ_Z	2495.5 ± 2.3	2495.5 ± 2.3	2494.23 ± 0.86

radiative corrections and final-state mass effects) are given by,

$$\Gamma(W^+ \to e^+\nu_e) = \frac{M_W^3}{12\pi v^2} = 226.35 \pm 0.05\,\text{MeV}\ , \tag{10.60a}$$

$$\Gamma(W^+ \to u_i\bar{d}_j) = \frac{M_W^3}{12\pi v^2}\,|V_{ij}|^2\mathcal{R}_V^q = (705.4 \pm 0.4\,\text{MeV})|V_{ij}|^2\ , \tag{10.60b}$$

$$\Gamma(Z \to f\bar{f}) = \frac{M_Z^3}{12\pi v^2}\left[\mathcal{R}_V^f\,\bar{g}_V^{f2} + \mathcal{R}_A^f\,\bar{g}_A^{f2}\right]\ , \tag{10.60c}$$

where the result for the latter are shown in Table 10.6. Final-state QED and QCD corrections [289] to the vector and axial-vector form factors are given by,

$$\mathcal{R}_{V,A}^f = N_C\left[1 + \frac{3}{4}\left(Q_f^2\frac{\alpha(s)}{\pi} + \frac{N_C^2-1}{2N_C}\frac{\alpha_s(s)}{\pi}\right) + \cdots\right]\ , \tag{10.61}$$

where $N_C = 3$ (1) is the color factor for quarks (leptons) and the dots indicate finite fermion mass effects proportional to m_f^2/s which are different for $\mathcal{R}_V^f$ and $\mathcal{R}_A^f$, as well as higher-order QCD corrections [290], which are known to $\mathcal{O}(\alpha_s^4)$ [203]. These include

singlet contributions starting from two-loop order which are large, strongly top quark mass dependent, family universal, and flavor non-universal [291–295]. The $\mathcal{O}(\alpha^2)$ self-energy corrections from Ref. [296] are also taken into account.

For the W decay into quarks, Eq. (10.60b), only the universal massless part (non-singlet and $m_q = 0$) of the final-state QCD radiator function in $\mathcal{R}_V$ from Eq. (10.61) is used, and the QED corrections are modified. Expressing the widths in terms of $G_F M_{W,Z}^3$ incorporates the largest radiative corrections from the running QED coupling. EW corrections to the Z widths are then taken into account through the effective couplings $\bar{g}^{\,i\,2}_{V,A}$. Hence, in the on-shell scheme the Z widths are proportional to $\rho_i \sim 1 + \rho_t$. There is additional (negative) quadratic m_t dependence in the $Z \to b\bar{b}$ vertex corrections [297, 298] which causes $\Gamma_{b\bar{b}}$ to decrease with m_t. The dominant effect is to multiply $\Gamma_{b\bar{b}}$ by the vertex correction $1 + \delta\rho_{b\bar{b}}$, where $\delta\rho_{b\bar{b}} \sim 10^{-2}(-\frac{1}{2}m_t^2/M_Z^2 + \frac{1}{5})$. In practice, the corrections are included in $\widehat{\rho}_b$ and $\widehat{\kappa}_b$, as discussed in Sec. 10.5.

Starting at $\mathcal{O}(\alpha\alpha_s)$, the factorized form indicated in Eq. (10.60) is violated and corrections need to be included [299–301]. They add coherently, resulting in a sizable effect, and shift $\alpha_s(M_Z)$ when extracted from Z lineshape observables by about +0.0007. Similar non-factorizable corrections are also known for mixed QED-EW corrections [97, 98, 100, 302].

For three fermion families the total widths of the Z [303–307] and W [308, 309] bosons are predicted to be,

$$\Gamma_Z = 2.4942 \pm 0.0009\,\text{GeV}\,, \qquad \Gamma_W = 2.0896 \pm 0.0008\,\text{GeV}\,. \tag{10.62}$$

The uncertainties in these predictions are almost entirely induced by the parametric error in $\alpha_s(M_Z) = 0.1185 \pm 0.0016$ from the global fit. These predictions can be compared with the experimental results, $\Gamma_Z = 2.4955 \pm 0.0023$ GeV [14, 275] and $\Gamma_W = 2.085 \pm 0.042$ GeV [260, 262] (see the Gauge & Higgs Bosons Particle Listings). The measurements of the total and partical widths are generally in good agreement with the SM. The exception is the branching ratio $W \to \tau + \nu_\tau$ from LEP 2, which is 2.6 σ larger than the electron-muon average [260].

The invisible decay width, $\Gamma_{\text{inv}} = \Gamma_Z - \Gamma_{e^+e^-} - \Gamma_{\mu^+\mu^-} - \Gamma_{\tau^+\tau^-} - \Gamma_{\text{had}}$, can be used to determine the number of neutrino flavors, N_ν, much lighter than $M_Z/2$. The hadronic peak cross section, and therefore the extracted Γ_{had}, depends strongly on the knowledge of the LEP 1 luminosity derived from small-angle Bhabha scattering. However, the prediction for the Bhabha cross-section was very recently found to be overestimated, and consequently the luminosity underestimated [275]. The updated analysis involved an improved Z lineshape fit, significantly reducing σ_{had}, while slightly increasing Γ_Z, with the result, $N_\nu = 2.9963 \pm 0.0074$ [275]. In practice, we determine N_ν by allowing it as an additional fit parameter and obtain,

$$N_\nu = 3.0026 \pm 0.0061\,, \tag{10.63}$$

which is now in perfect agreement with the observed number of fermion generations and $N_\nu = 3$ (a 1.3 σ deviation was observed in the 2018 edition of this *Review* before including the correction in the luminosity determination).

10.6 Global fit results

In this section, we present the results of global fits, subject to the experimental data and theoretical constraints discussed in Section 10.2−10.4. For earlier analyses, see Refs. [14, 69, 310–313] and previous editions of this *Review*. The values for m_t, M_W [260, 261, 263], Γ_W [260, 262], the weak charges of the electron [148], the proton [149], cesium [160, 161] and thallium [162, 163], the weak mixing angle extracted from eDIS [138], $\nu_\mu(\bar{\nu}_\mu)$-e scattering [120–122], the τ lifetime, and the μ anomalous magnetic moment [213] are listed in Table 10.4. Likewise, Table 10.5 summarizes the principal Z pole observables, where the LEP 1 averages of the ALEPH, DELPHI, L3, and OPAL results include common systematic uncertainties and correlations [14, 275]. The heavy flavor results [14, 280] of LEP 1 and SLD are based on common inputs, and are thus correlated, as well.

Also shown in both tables are the SM predictions for the values of M_Z, M_H, $\alpha_s(M_Z)$, $\Delta\alpha^{(3)}_{\text{had}}$ and the heavy quark masses shown in Table 10.7. The predictions result from a global least-square (χ^2) fit to all data using the minimization package MINUIT [314] and the EW library GAPP [32]. In most cases, we treat all input errors (the uncertainties of the values) as Gaussian. The reason is not that we assume that theoretical and systematic errors are intrinsically bell-shaped (which they are not) but because in most cases the input errors are either dominated by the statistical components or they are combinations of many different (including statistical) error sources, which should yield approximately Gaussian *combined* errors by the large number theorem. An exception is the theory dominated error on the τ lifetime, which we recalculate in each χ^2-function call since it depends itself on α_s. Sizes and shapes of the output errors (the uncertainties of the predictions and the SM fit parameters) are fully determined by the fit, and 1 σ errors are defined to correspond to $\Delta\chi^2 = \chi^2 - \chi^2_{\text{min}} = 1$, and do not necessarily correspond to the 68.3% probability range or the 39.3% probability contour (for 2 parameters).

The agreement is generally very good. Despite the few discrepancies addressed in the following, the global electroweak fit describes the data very well, with an excellent $\chi^2/\text{d.o.f.} = 40.8/41$. The probability of a larger χ^2 is 48%, and only $g_\mu - 2$ is currently showing a larger (3.1 σ) conflict. In addition, A^0_{LR} (SLD) from hadronic final states and $A^{(0,b)}_{FB}$ (LEP 1) deviate at the 2 σ level. g^2_L from NuTeV is nominally in conflict with the SM, as well, but the precise status is unresolved (see Sec. 10.3.1). We also emphasize that there are a number of discrepancies among individual measurements of certain quantities, as discussed in previous sections, but that they are not reflected in the overall χ^2 of the fit as only the corresponding combinations are used as constraints.

A_b can be extracted from $A^{(0,b)}_{FB}$ when $A_e = 0.1501 \pm 0.0016$ is taken from a fit to leptonic asymmetries (using lepton universality). The result, $A_b = 0.885 \pm 0.017$, is 2.9 σ below the SM prediction[14] and also 1.4 σ below $A_b = 0.923 \pm 0.020$ obtained from $A^{FB}_{LR}(b)$ at SLD. Thus, it appears that at least some of the problem in A_b is due to a statistical fluctuation or other experimental effect in one of the asymmetries. Note, however, that the uncertainty in $A^{(0,b)}_{FB}$ is strongly statistics dominated. The combined value, $A_b = 0.901 \pm 0.013$ deviates by 2.6 σ.

The left-right asymmetry, $A^0_{LR} = 0.15138 \pm 0.00216$ [273], from hadronic decays at SLD, differs by 2.1 σ from the SM expectation of 0.1469 ± 0.0003. The combined value of $A_\ell = 0.1513 \pm 0.0021$ from SLD (using lepton-family universality and including correlations) is also 2.1 σ above the SM prediction; but there is experimental agreement between this SLD value and the LEP 1 value, $A_\ell = 0.1481 \pm 0.0027$, obtained from a fit to $A^{(0,\ell)}_{FB}$, $A_e(\mathcal{P}_\tau)$, and $A_\tau(\mathcal{P}_\tau)$, again assuming universality.

The observables in Table 10.4 and Table 10.5, as well as some other less precise observables, are used in the global fits described below. In all fits, the errors include full statistical, systematic, and theoretical uncertainties. The correlations from the LEP 1 lineshape and τ polarization measurements, the LEP/SLD heavy flavor observables, the SLD lepton asymmetries, and the ν-e scattering observables, are included. The theoretical correlations between $\Delta\alpha^{(5)}_{\text{had}}$, $\widehat{s}^2_0$, and $g_\mu - 2$, and between the M_W extractions from ATLAS and the Tevatron, are also accounted for.

The electroweak data allow a simultaneous determination of M_Z, m_t, and $\alpha_s(M_Z)$. The direct measurements of M_H at the LHC [266, 267] have reached a precision that the global fit result for M_H coincides with the constraint in Eq. (10.52) with negligible correlations with the other fit parameters. $\widehat{m}_c$, $\widehat{m}_b$, and $\Delta\alpha^{(3)}_{\text{had}}$ are also allowed to float in the fits, subject to the theoretical constraints [28, 51] described in Sec. 10.2, and are correlated with α_s, which in turn is determined mainly through R_ℓ, Γ_Z, σ_{had}, and τ_τ. The global fit to all data, including the hadron collider m_t average in Eq. (10.13), yields the results in Table 10.7, while those

[14] Alternatively, one can use $A_\ell = 0.1481 \pm 0.0027$, which is from LEP 1 alone and in excellent agreement with the SM, and obtain $A_b = 0.897 \pm 0.022$ which is 1.7 σ low. This illustrates that some of the discrepancy is related to the one in A_{LR}.

Table 10.7: Principal SM fit result including mutual correlations.

M_Z [GeV]	91.1882 ± 0.0020	1.00	−0.07	0.00	0.00	0.02	0.02
$\widehat{m}_t(\widehat{m}_t)$ [GeV]	163.51 ± 0.55	−0.07	1.00	0.00	−0.11	−0.22	0.04
$\widehat{m}_b(\widehat{m}_b)$ [GeV]	4.180 ± 0.008	0.00	0.00	1.00	0.20	−0.02	0.00
$\widehat{m}_c(\widehat{m}_c)$ [GeV]	1.275 ± 0.009	0.00	−0.11	0.20	1.00	0.47	0.00
$\alpha_s(M_Z)$	0.1185 ± 0.0016	0.02	−0.22	−0.02	0.47	1.00	−0.03
$\Delta\alpha^{(3)}_{\rm had}(2\ {\rm GeV})$	0.00592 ± 0.00005	0.02	0.04	0.00	0.00	−0.03	1.00

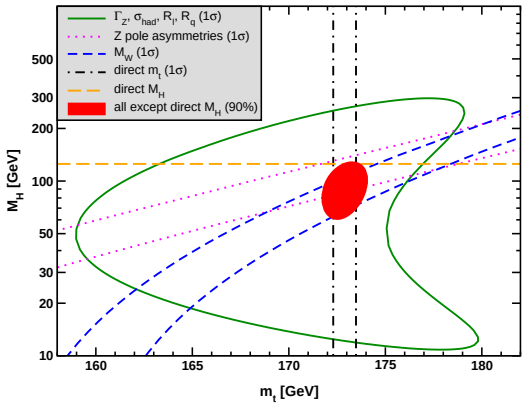

Figure 10.4: Fit result and one-standard-deviation (39.35% for the closed contours and 68% for the others) uncertainties in M_H as a function of m_t for various inputs, and the 90% CL region ($\Delta\chi^2 = 4.605$) allowed by all data. $\alpha_s(M_Z) = 0.1185$ is assumed except for the fits including the Z lineshape. The width of the horizontal dashed band is not visible on the scale of the plot.

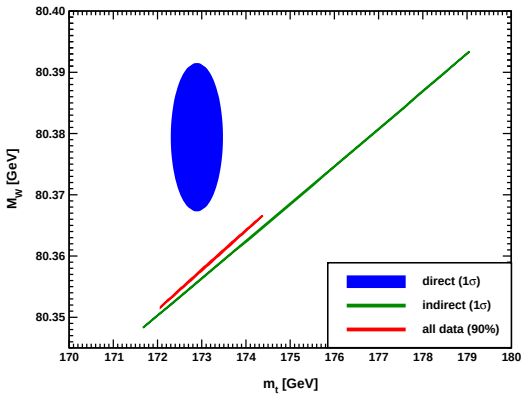

Figure 10.5: One-standard-deviation (39.35%) regions in M_W as a function of m_t for the direct and indirect data, and the 90% CL region ($\Delta\chi^2 = 4.605$) allowed by all data.

for the weak mixing angle in various schemes are summarized in Table 10.2.

Removing the kinematic constraint on M_H from LHC gives the loop-level determination from the precision data,

$$M_H = 90^{+18}_{-16}\ {\rm GeV}\ , \tag{10.64}$$

which is 1.8 σ below the value in Eq. (10.52). The latter is also slightly outside the 90% central confidence range,

$$64\ {\rm GeV} < M_H < 122\ {\rm GeV}\ . \tag{10.65}$$

This is mostly a reflection of the Tevatron determination of M_W, which is 1.6 σ higher than the SM best fit value in Table 10.4. This is shown in Fig. 10.4 where one sees that the precision data together with M_H from the LHC prefer m_t to be closer to the upper end of its 1 σ allowed range.

Conversely, one can remove the explicit M_W and Γ_W constraints from the global fit and use $M_H = 125.30 \pm 0.13$ GeV to obtain $M_W = 80.357 \pm 0.006$ GeV, which is 1.7 σ below the world average in Eq. (10.51). Finally, one can carry out a fit without including the direct constraint, $m_t = 172.89 \pm 0.59$ GeV, from the hadron colliders. One obtains $m_t = 176.3 \pm 1.9$ GeV, which is 1.7 σ higher than the collider average. (The indirect prediction is for the $\overline{\rm MS}$ mass definition, $\widehat{m}_t(\widehat{m}_t) = 166.4 \pm 1.8$ GeV, which is in the end converted to the pole mass.) The situation is summarized in Fig. 10.5 showing the 1 σ contours in the $M_W - m_t$ plane from the direct and indirect determinations, as well as the combined 90% CL region.

In view of these tensions it is instructive to study the effect of doubling the uncertainty in $\Delta\alpha^{(3)}_{\rm had}(2\ {\rm GeV}) = (58.84 \pm 0.51) \times 10^{-4}$ (see Sec. 10.2) on the loop-level determination of the Higgs boson mass. The result, $M_H = 88^{+18}_{-17}$ GeV, deviates even slightly *more* (1.9 σ) than Eq. (10.64), and demonstrates that the uncertainty in $\Delta\alpha_{\rm had}$ is currently of only secondary importance. Note also that a shift of $\pm 10^{-4}$ in $\Delta\alpha^{(3)}_{\rm had}(2\ {\rm GeV})$ corresponds to a shift of ∓ 4.4 GeV in M_H. The hadronic contribution to $\alpha(M_Z)$ is correlated with $g_\mu - 2$ (see Sec. 10.4). The measurement of the latter is higher than the SM prediction, and its inclusion in the fit favors a larger $\alpha(M_Z)$ and a lower M_H from the precision data (currently by 2.3 GeV).

The weak mixing angle can be determined from Z pole observables, M_W, and a variety of neutral-current processes spanning a very wide Q^2 range. The results (for older low energy neutral-current data see Refs. [310–313], as well as earlier editions of this *Review*) shown in Table 10.8 are in reasonable agreement with each other, indicating the quantitative success of the SM. One of the largest discrepancies is the value $\widehat{s}^2_Z = 0.23176 \pm 0.00027$ from $A^{(0,b)}_{FB}$ and $A^{(0,c)}_{FB}$, which is 2.0 σ above the value 0.23121 ± 0.00004 from the global fit to all data. Similarly, $\widehat{s}^2_Z = 0.23064 \pm 0.00028$ from the SLD asymmetries (in both cases when combined with M_Z, Γ_Z, and m_t) is 2.0 σ low.

The extracted Z pole value of $\alpha_s(M_Z)$ is based on a formula with negligible theoretical uncertainty if one assumes the exact validity of the SM. One should keep in mind, however, that this value, $\alpha_s(M_Z) = 0.1221 \pm 0.0027$, which increased after the updated analysis in Ref. [275], is very sensitive to certain types of new physics such as non-universal vertex corrections. In contrast, the value derived from τ decays, $\alpha_s(M_Z) = 0.1170^{+0.0019}_{-0.0017}$, is theory dominated but less sensitive to new physics. The agreement between the two values is only marginal, but the latter does agree well with the averages deduced from DIS and global PDF fits (0.1161 ± 0.0018), hadronic final states of e^+e^- annihilations (0.1171 ± 0.0031), hadron colliders (0.1159 ± 0.0034), as well as lattice QCD simulations (0.1182 ± 0.0008). For more details, other determinations, and references, see the Section on "Quantum Chromodynamics" in this *Review*.

Using $\alpha(M_Z)$ and $\widehat{s}^2_Z$ as inputs, one can predict $\alpha_s(M_Z)$ assuming grand unification. One finds $\alpha_s(M_Z) = 0.13 \pm 0.01$ [317,318] for the simplest theories based on the minimal supersymmetric extension of the SM, where the uncertainty is from the unknown particle thresholds. This is slightly larger, but consistent with $\alpha_s(M_Z) = 0.1185 \pm 0.0016$ from our fit and most other determinations, while minimal non-supersymmetric theories predict much lower and excluded values (see the Section on "Grand Unified The-

Table 10.8: Values of $\widehat{s}^2_Z$, s^2_W, α_s, m_t and M_H for various data sets. In the fit to the LHC data, the α_s constraint is from a combined NNLO analysis of inclusive electroweak boson production cross-sections at the LHC [315]. Likewise, for the Tevatron fit we use the α_s result from the inclusive jet cross-section at DØ [316].

data set	$\widehat{s}^2_Z$	s^2_W	$\alpha_s(M_Z)$	m_t [GeV]	M_H [GeV]
all data	0.23121(4)	0.22337(10)	0.1185(16)	173.2 ± 0.6	125
all data except M_H	0.23107(9)	0.22309(19)	0.1189(17)	172.9 ± 0.6	$90^{+\ 18}_{-\ 16}$
all data except M_Z	0.23111(6)	0.22334(10)	0.1185(16)	172.9 ± 0.6	125
all data except M_W	0.23123(4)	0.22345(11)	0.1189(17)	172.9 ± 0.6	125
all data except m_t	0.23113(6)	0.22305(21)	0.1190(17)	176.3 ± 1.9	125
$M_{H,Z} + \Gamma_Z + m_t$	0.23126(8)	0.22351(17)	0.1215(47)	172.9 ± 0.6	125
LHC	0.23113(10)	0.22337(13)	0.1188(16)	172.7 ± 0.6	125
Tevatron + M_Z	0.23102(13)	0.22295(30)	0.1160(44)	174.3 ± 0.8	$99^{+\ 32}_{-\ 26}$
LEP 1 + LEP 2	0.23137(18)	0.22353(46)	0.1235(29)	178 ± 11	201^{+279}_{-113}
LEP 1 + SLD	0.23116(17)	0.22348(58)	0.1221(27)	169 ± 10	$80^{+101}_{-\ 39}$
SLD + $M_Z + \Gamma_Z + m_t$	0.23064(28)	0.22227(54)	0.1188(48)	172.9 ± 0.6	$37^{+\ 30}_{-\ 21}$
$A^{(b,c)}_{FB} + M_Z + \Gamma_Z + m_t$	0.23176(27)	0.22467(66)	0.1266(46)	172.9 ± 0.6	280^{+145}_{-100}
$M_{W,Z} + \Gamma_{W,Z} + m_t$	0.23103(12)	0.22302(25)	0.1198(44)	172.9 ± 0.6	$84^{+\ 24}_{-\ 20}$
low energy + $M_{H,Z}$	0.23176(94)	0.2254(35)	0.1171(18)	156 ± 29	125

Table 10.9: Values of model-independent neutral-current parameters, compared with the SM predictions, where the uncertainties in the latter are $\lesssim 0.0001$, throughout.

Quantity	Experimental Value	Standard Model	Correlation	
$g^{\nu e}_{LV}$	-0.040 ± 0.015	-0.0398		-0.05
$g^{\nu e}_{LA}$	-0.507 ± 0.014	-0.5064		
$g^{eu}_{AV} + 2\,g^{ed}_{AV}$	0.4927 ± 0.0031	0.4950	-0.88	0.20
$2\,g^{eu}_{AV} - g^{ed}_{AV}$	-0.7165 ± 0.0068	-0.7195		-0.22
$2\,g^{eu}_{VA} - g^{ed}_{VA}$	-0.13 ± 0.06	-0.0954		
g^{ee}_{VA}	0.0190 ± 0.0027	0.0227		

ories" in this *Review*).

Most of the parameters relevant to ν-hadron, ν-e, e-hadron, and e-e processes are determined uniquely and precisely from the data in "model-independent" fits, *i.e.*, fits allowing for an arbitrary EW gauge theory. The values for the parameters defined in Eq. (10.21) are given in Table 10.9 along with the predictions of the SM. The agreement is very good. (The ν-hadron results including NuTeV [134] and other ν-DIS data can be found in the 2006 edition of this *Review*, and fits with modified NuTeV constraints in the 2008 and 2010 editions.)

10.7 Constraints on new physics

The masses and decay properties of the electroweak bosons and low energy data can be used to search for and set limits on deviations from the SM. We will mainly discuss the effects of exotic particles (with heavy masses $M_{\rm new} \gg M_Z$ in an expansion in $M_Z/M_{\rm new}$) on the gauge boson self-energies. (Brief remarks are made on new physics which is not of this type.) Most of the effects on precision measurements can be described by three gauge self-energy parameters S, T, and U. We will define these, as well as the related parameters ρ_0, ϵ_i, and $\widehat{\epsilon}_i$, to arise from new physics only. In other words, they are equal to zero ($\rho_0 = 1$) exactly in the SM, and do not include any (loop induced) contributions that depend on m_t or M_H, which are treated separately. Our treatment differs from most of the original papers.

The dominant effect of many extensions of the SM can be described by the ρ_0 parameter,

$$\rho_0 \equiv \frac{M_W^2}{M_Z^2\,\widehat{c}^2_Z\,\widehat{\rho}}\,, \tag{10.66}$$

which describes new sources of SU(2) breaking that cannot be accounted for by the SM Higgs doublet or by m_t effects. $\widehat{\rho}$ is calculated as in Eq. (10.18) assuming the validity of the SM. In the presence of $\rho_0 \neq 1$, Eq. (10.66) generalizes the second Eq. (10.18) while the first remains unchanged. Provided that the new physics which yields $\rho_0 \neq 1$ is a small perturbation which does not significantly affect other radiative corrections, ρ_0 can be regarded as a phenomenological parameter which multiplies G_F in Eqs. (10.21) and (10.41), as well as Γ_Z in Eq. (10.60c). There are enough data to determine ρ_0, M_H, m_t, and α_s, simultaneously. From the global fit,

$$\rho_0 = 1.00038 \pm 0.00020\,, \tag{10.67a}$$

$$\alpha_s(M_Z) = 0.1188 \pm 0.0017\,, \tag{10.67b}$$

where as before the uncertainty is from the experimental inputs and includes an estimate of the error from unknown higher-order electroweak corrections. The result in Eq. (10.67a) is 1.9 σ above the SM expectation, $\rho_0 = 1$. It can be used to constrain higher-dimensional Higgs representations to have vacuum expectation values of less than a few percent of those of the doublets. Indeed, the relation between M_W and M_Z is modified if there are Higgs multiplets with weak isospin $> 1/2$ and significant vacuum expectation values. For a general (charge-conserving) Higgs structure,

$$\rho_0 = \frac{\sum_i [t_i(t_i+1) - t^2_{3i}]|v_i|^2}{2\sum_i t^2_{3i}|v_i|^2}\,, \tag{10.68}$$

where v_i is the expectation value of the neutral component of a Higgs multiplet with weak isospin t_i and third component t_{3i}. In order to calculate to higher orders in such theories one must define a set of four fundamental renormalized parameters which one may conveniently choose to be α, G_F, M_Z, and M_W, since M_W and M_Z are directly measurable. Then $\widehat{s}^2_Z$ and ρ_0 can be considered dependent parameters.

Eq. (10.67a) can also be used to constrain other types of new physics. For example, non-degenerate multiplets of heavy

fermions or scalars break the vector part of weak SU(2) and lead to a decrease in the value of M_Z/M_W. Each non-degenerate SU(2) doublet $\binom{f_1}{f_2}$ yields a positive contribution to ρ_0 [319–321] of

$$\frac{N_C\, G_F}{8\sqrt{2}\pi^2}\Delta m^2 \ , \tag{10.69}$$

where

$$\Delta m^2 \equiv m_1^2 + m_2^2 - \frac{4m_1^2 m_2^2}{m_1^2 - m_2^2}\ln\frac{m_1}{m_2} \geq (m_1 - m_2)^2 \ , \tag{10.70}$$

and $N_C = 1$ (3) for color singlets (triplets). Eq. (10.67a) taken together with Eq. (10.69) implies the following constraint on the mass splitting at the 90% CL,

$$(14\ \text{GeV})^2 < \sum_i \frac{N_C^i}{3}\,\Delta m_i^2 < (48\ \text{GeV})^2 \ , \tag{10.71}$$

where the sum runs over all new-physics doublets, for example fourth-family quarks or leptons, $\binom{t'}{b'}$ or $\binom{\nu'}{\ell'-}$, vector-like fermion doublets (which contribute to the sum in Eq. (10.71) with an extra factor of 2), and scalar doublets such as $\binom{\tilde{t}}{\tilde{b}}$ in Supersymmetry (in the absence of L–R mixing).

Non-degenerate multiplets usually imply $\rho_0 > 1$. Similarly, heavy Z' bosons decrease the prediction for M_Z due to mixing and generally lead to $\rho_0 > 1$ [322]. On the other hand, extra Higgs doublets participating in spontaneous symmetry breaking [323–325] or heavy lepton doublets involving Majorana neutrinos [326], both of which have more complicated expressions, and the v_i of higher-dimensional Higgs representations can contribute to ρ_0 with either sign.

A number of authors [327–329] have considered the general effects on neutral-current, Z and W boson observables of various types of heavy (*i.e.*, $M_{\rm new} \gg M_Z$) physics which contribute to the W and Z self-energies but which do not have any direct coupling to the ordinary fermions (an alternative formulation is given by Ref. [330]). In addition to non-degenerate multiplets, which break the vector part of weak SU(2), these include heavy degenerate multiplets of chiral fermions which break the axial generators.

Such effects can be described by just three parameters, S, T, and U [331], at the (EW) one-loop level[15]. T is proportional to the difference between the W and Z self-energies at $Q^2 = 0$ (*i.e.*, vector SU(2)-breaking), while S ($S + U$) is associated with the difference between the Z (W) self-energy at $Q^2 = M_{Z,W}^2$ and $Q^2 = 0$ (axial SU(2)-breaking). Denoting the contributions of new physics to the various self-energies by $\Pi_{ij}^{\rm new}$, we have

$$\widehat{\alpha}(M_Z)T \equiv \frac{\Pi_{WW}^{\rm new}(0)}{M_W^2} - \frac{\Pi_{ZZ}^{\rm new}(0)}{M_Z^2} \ , \tag{10.72a}$$

$$\frac{\widehat{\alpha}(M_Z)}{4\widehat{s}_Z^2\widehat{c}_Z^2}S \equiv \frac{\Pi_{ZZ}^{\rm new}(M_Z^2) - \Pi_{ZZ}^{\rm new}(0)}{M_Z^2} - \frac{\widehat{c}_Z^2 - \widehat{s}_Z^2}{\widehat{c}_Z\widehat{s}_Z}\frac{\Pi_{Z\gamma}^{\rm new}(M_Z^2)}{M_Z^2} - \frac{\Pi_{\gamma\gamma}^{\rm new}(M_Z^2)}{M_Z^2} \ , \tag{10.72b}$$

$$\frac{\widehat{\alpha}(M_Z)}{4\widehat{s}_Z^2}(S+U) \equiv \frac{\Pi_{WW}^{\rm new}(M_W^2) - \Pi_{WW}^{\rm new}(0)}{M_W^2} - \frac{\widehat{c}_Z}{\widehat{s}_Z}\frac{\Pi_{Z\gamma}^{\rm new}(M_Z^2)}{M_Z^2} - \frac{\Pi_{\gamma\gamma}^{\rm new}(M_Z^2)}{M_Z^2} \ . \tag{10.72c}$$

S, T, and U are defined with a factor proportional to $\widehat{\alpha}$ removed, so that they are expected to be of order unity in the presence of new physics. In the $\overline{\rm MS}$ scheme as defined in Ref. [71], the last two terms in Eqs. (10.72b) and (10.72c) can be omitted, as was done in some earlier editions of this *Review*. These parameters are related to other parameter sets, S_i [71], $\widehat{\epsilon}_i$ [335], and h_i [336], by

$$T = h_V = \frac{\widehat{\epsilon}_1}{\widehat{\alpha}(M_Z)} \ , \tag{10.73a}$$

$$S = h_{AZ} = S_Z = 4\,\widehat{s}_Z^2\frac{\widehat{\epsilon}_3}{\widehat{\alpha}(M_Z)} \ , \tag{10.73b}$$

$$U = h_{AW} - h_{AZ} = S_W - S_Z = -4\,\widehat{s}_Z^2\,\frac{\widehat{\epsilon}_2}{\widehat{\alpha}(M_Z)} \ . \tag{10.73c}$$

A heavy non-degenerate multiplet of fermions or scalars contributes positively to T as

$$\rho_0 - 1 = \frac{1}{1 - \widehat{\alpha}(M_Z)T} - 1 \approx \widehat{\alpha}(M_Z)T \ , \tag{10.74}$$

where $\rho_0 - 1$ is given in Eq. (10.69). The effects of non-standard Higgs representations cannot be separated from heavy non-degenerate multiplets unless the new physics has other consequences, such as vertex corrections. Most of the original papers defined T to include the effects of loops only. However, we will redefine T to include all new sources of SU(2) breaking, including non-standard Higgs, so that T and ρ_0 are equivalent by Eq. (10.74).

A multiplet of heavy degenerate chiral fermions yields

$$S = \frac{N_C}{3\pi}\sum_i \left(t_{3i}^L - t_{3i}^R\right)^2 \ , \tag{10.75}$$

where $t_{3i}^{L,R}$ is the 3$^{\rm rd}$ component of weak isospin of the left-(right-) handed component of fermion i. For example, a heavy degenerate ordinary or mirror family would contribute $2/3\pi$ to S. In models with warped extra dimensions [337], sizeable corrections to the S parameter are generated through mixing between the SM gauge bosons and their Kaluza-Klein (KK) excitations, and one finds $S \approx 30\, v^2 M_{KK}^{-2}$ [338], where M_{KK} is the mass scale of the KK gauge bosons. Large positive values of S can also be generated in models with dynamical electroweak symmetry breaking, where the Higgs boson is composite. In simple composite Higgs models, the dominant contribution stems from heavy spin-1 resonances of the strong dynamics leading to $S \approx 4\pi v^2(M_V^{-2} + M_A^{-2})$, where $M_{V,A}$ are the masses of the lightest vector and axial-vector resonances, respectively [339].

Negative values of S are possible, for example, in models of walking Technicolor [340–347], or from loops involving scalars or Majorana particles [348,349]. The simplest origin of $S < 0$ would probably be an additional heavy Z' boson [322]. Supersymmetric extensions of the SM [350, 351] generally give very small effects. For more details and references, see Refs. [352–361] and the Sections on "Supersymmetry" in this *Review*. Most simple types of new physics yield $U = 0$, although there are counter-examples, such as the effects of anomalous triple gauge vertices [335].

The SM expressions for observables are replaced by,

$$M_Z^2 = M_{Z0}^2\,\frac{1 - \widehat{\alpha}(M_Z)T}{1 - G_F M_{Z0}^2 S/2\sqrt{2}\pi} \ , \tag{10.76a}$$

$$M_W^2 = M_{W0}^2\,\frac{1}{1 - G_F M_{W0}^2 (S+U)/2\sqrt{2}\pi} \ , \tag{10.76b}$$

where M_{Z0} and M_{W0} are the SM expressions (as functions of m_t and M_H) in the $\overline{\rm MS}$ scheme. Furthermore,

$$\Gamma_Z = \frac{M_Z^3\beta_Z}{1 - \widehat{\alpha}(M_Z)T} \ , \tag{10.77a}$$

$$\Gamma_W = M_W^3\beta_W \ , \tag{10.77b}$$

$$A_i = \frac{A_{i0}}{1 - \widehat{\alpha}(M_Z)T} \ , \tag{10.77c}$$

[15] Three additional parameters are needed if the new physics scale is comparable to M_Z [332]. Further generalizations, including effects relevant to LEP 2 and Drell-Yan production at the LHC, are described in Refs. [333] and [334], respectively.

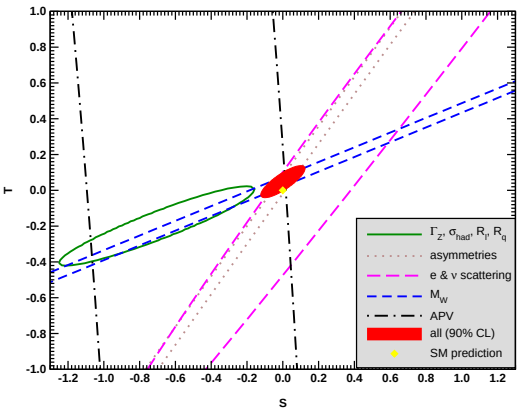

Figure 10.6: 1 σ constraints (39.35% for the closed contours and 68% for the others) on S and T (for $U = 0$) from various inputs combined with M_Z. S and T represent the contributions of new physics only. Data sets not involving M_W or Γ_W are insensitive to U. With the exception of the fit to all data, we fix $\alpha_s = 0.1185$. The black dot indicates the Standard Model values $S = T = 0$.

where $\beta_{Z,W}$ are the SM expressions for the reduced widths Γ_{Z0}/M_{Z0}^3 and Γ_{W0}/M_{W0}^3, M_Z and M_W are the physical masses, and A_i (A_{i0}) is a neutral-current amplitude (in the SM).

The data allows for a simultaneous determination of M_H and m_t (from the hadron colliders), S (from M_Z), T (mainly from Γ_Z), U (from M_W), $\widehat{s}_Z^2 = 0.23112 \pm 0.00013$ (from the Z pole asymmetries), and $\alpha_s(M_Z) = 0.1189 \pm 0.0018$ (from R_ℓ, $\sigma_{\rm had}$, and τ_τ), giving,

$$S = -0.01 \pm 0.10 \ , \tag{10.78a}$$

$$T = \ \ 0.03 \pm 0.12 \ , \tag{10.78b}$$

$$U = \ \ 0.02 \pm 0.11 \ , \tag{10.78c}$$

with little correlation among the SM parameters, where the uncertainties are from unknown higher orders in the SM predictions and the inputs. The parameters in Eq. (10.78), which by definition are due to new physics only, are in excellent agreement with the SM values of zero. Fixing $U = 0$, which is motivated by the fact that U is suppressed by an additional factor $M_{\rm new}^2/M_Z^2$ compared to S and T [362], greatly improves the precision on S and particularly T,

$$S = 0.00 \pm 0.07 \ , \tag{10.79a}$$

$$T = 0.05 \pm 0.06 \ . \tag{10.79b}$$

If only any one of the three parameters is allowed, then this parameter would deviate at the 1.6 to 1.9 σ level, reflecting the deviation in M_W. Using Eq. (10.74), the value of ρ_0 corresponding to T in Eqs. (10.78) is 1.0002 ± 0.0009, while the one corresponding to Eqs. (10.79) is 1.0004 ± 0.0005. Thus, the multi-parameter fits are consistent with $\rho_0 = 1$, in contrast to the fit with $S = U = 0$ in Eq. (10.67a). There is a strong correlation (92%) between the S and T parameters. The U parameter is -80% (-93%) anti-correlated with S (T). The allowed regions in S–T (for $U = 0$) are shown in Fig. 10.6. From Eq. (10.78) one obtains $S < 0.14$ and $T < 0.22$ at 95% CL, where the former puts the constraint $M_{KK} \gtrsim 3.6$ TeV on the masses of KK gauge bosons in warped extra dimensions. In minimal composite Higgs models, the bound on S requires $M_V \gtrsim 4$ TeV [363], but this constraint can be relaxed, *e.g.*, if the fermionic sector is also allowed to be partially composite [364, 365].

The S parameter can also be used to constrain the number of fermion families, *under the assumption* that there are no new contributions to T or U and therefore that any new families are degenerate; then an extra generation of SM fermions is excluded at the 8 σ level corresponding to $N_F = 2.75 \pm 0.15$. This can be compared to the fit to the number of light neutrinos given in Eq. (10.63), $N_\nu = 3.0026 \pm 0.0061$, but the S parameter fits are valid even for a very heavy fourth family neutrino. Allowing T to vary as well, the constraint on a fourth family is weaker [366]. However, a heavy fourth family would increase the Higgs production cross-section through gluon fusion by a factor of about 9 [367], which is in considerable tension with the observed Higgs signal at the LHC [368]. Combining the limits from electroweak precision data with the measured Higgs production rate and limits from direct searches for heavy quarks [369], a fourth family of chiral fermions is now excluded by more than five standard deviations [370, 371]. Similar remarks apply to a heavy mirror family [372] involving right-handed SU(2) doublets and left-handed singlets. In contrast, new doublets that receive most of their mass from a different source than the Higgs vacuum expectation value, such as vector-like fermion doublets or scalar doublets in Supersymmetry, give small or no contribution to S, T, U, and the Higgs production cross-section and are therefore still allowed. Partial or complete vector-like fermion families are predicted in many Grand Unified Theories [373] (see the Section on "Grand Unified Theories" in this *Review*), and many other models including supersymmetric and superstring inspired ones [374–377].

As discussed in Sec. 10.6, there is a 3.6% deviation in the asymmetry parameter A_b. Assuming that this is due to new physics affecting preferentially the third generation, we can perform a fit allowing additional $Z \to b\bar{b}$ vertex corrections ρ_b and κ_b as in Eq. (10.42) (here defined to be due to new physics only with the SM contributions removed), as well as S, T, U, and the SM parameters, with the result,

$$\rho_b = 0.058 \pm 0.020 \ , \tag{10.80a}$$

$$\kappa_b = 0.185 \pm 0.067 \ , \tag{10.80b}$$

with an almost perfect correlation of 99% (because R_b is much better determined than A_b). The central values of the oblique parameters are consistent with their SM values of zero, and there is little change in the SM parameters, except that the value of $\alpha_s(M_Z)$ is lower by 0.0008 compared to the SM fit. Given that an $\mathcal{O}(20\%)$ correction to κ_b would be necessary, it would be difficult to account for the deviation in A_b by new physics that enters only at the level of radiative corrections. Thus, if it is due to new physics, it is most likely of tree-level type affecting preferentially the third generation. Examples include the decay of a scalar neutrino resonance [378], mixing of the b quark with heavy exotics [379], and a heavy Z' with family non-universal couplings [380, 381]. It is difficult, however, to simultaneously account for R_b without tuning, which has been measured on the Z peak and off-peak [382] at LEP 1.

There is no simple parametrization to describe the effects of every type of new physics on every possible observable. The S, T, and U formalism describes many types of heavy physics which affect only the gauge self-energies, and it can be applied to all precision observables. However, new physics which couples directly to ordinary fermions cannot be fully parametrized in the S, T, and U framework. Examples include heavy Z' bosons [322], mixing with exotic fermions [9, 383, 384], leptoquark exchange [260, 385, 386], supersymmetric models, strong EW dynamics [364], Little Higgs models [387, 388], and TeV-scale extra spatial dimensions [389–392] (for more details and references, see the Section on "Extra Dimensions" in this *Review*). These types of new physics can be parametrized in a model-independent way by using an effective field theory description [393–396]. Here the SM is extended by a set of higher-dimensional operators, denoted $\mathcal{O}_i$,

$$\mathcal{L} = \mathcal{L}_{\rm SM} + \sum_{d>4} \sum_i \frac{C_i}{\Lambda^{d-4}} \mathcal{O}_i \ , \tag{10.81}$$

where Λ is the characteristic scale of the new physics sector, which is assumed to satisfy $\Lambda \gg v$. For EW precision observables, the leading new operators enter at dimension $d = 6$. Note that S and T can be identified with two of these operators (or linear combinations thereof, depending on the chosen operator basis), while U corresponds to a dimension-8 operator [362, 397]. With current data on M_W and Z pole observables, Λ is constrained to

be larger than $\mathcal{O}$(TeV) if the Wilson coefficients C_i are of order unity [398–402].

An alternate formalism [403] defines parameters, ϵ_1, ϵ_2, ϵ_3, and ϵ_b in terms of the specific observables M_W/M_Z, $\Gamma_{\ell\ell}$, $A_{FB}^{(0,\ell)}$, and R_b. The definitions coincide with those for $\widehat{\epsilon}_i$ in Eqs. (10.72) and (10.73c) for physics which affects gauge self-energies only, but the ϵ's now parametrize arbitrary types of new physics. However, the ϵ_i are not related to other observables unless additional model-dependent assumptions are made.

Limits on new four-Fermi operators and on leptoquarks using LEP 2 and lower energy data are given in Refs. [260, 404–406], while constraints on various types of new physics are addressed in Refs. [9, 151, 277, 407, 408]. For a particularly well motivated and explored type of physics beyond the SM, see the Section on "Z'-Boson Searches" in this *Review*.

Acknowledgments

It is a pleasure to thank Rodolfo Ferro-Hernández for discussions, for performing some of the calculations and checks, and for producing the plot in Fig. 10.2. J.E. is supported by the German–Mexican research collaboration grant SP 778/4–1 (DFG) and 278017 (CONACyT). A.F. is supported in part by the National Science Foundation under grant no. PHY–1820760.

References

[1] S. Glashow, Nucl. Phys. **22**, 579 (1961).

[2] S. Weinberg, Phys. Rev. Lett. **19**, 1264 (1967).

[3] A. Salam, Conf. Proc. C **680519**, 367 (1968).

[4] S. Glashow, J. Iliopoulos and L. Maiani, Phys. Rev. D **2**, 1285 (1970).

[5] N. Cabibbo, Phys. Rev. Lett. **10**, 531 (1963).

[6] M. Kobayashi and T. Maskawa, Prog. Theor. Phys. **49**, 652 (1973).

[7] S. Descotes-Genon and P. Koppenburg, Ann. Rev. Nucl. Part. Sci. **67**, 97 (2017), [arXiv:1702.08834].

[8] E. Commins and P. Bucksbaum, *Weak Interactions of Leptons and Quarks*, Cambridge Univ. Pr., Cambridge, USA (1983), ISBN 978-0-521-27370-1.

[9] P. Langacker, editor, *Precision tests of the standard electroweak model*, volume 14, WSP, Singapore (1996).

[10] P. Langacker, *The standard model and beyond*, CRC Pr., Boca Raton, USA (2010), ISBN 978-1-4200-7906-7.

[11] T. Kinoshita, editor, *Quantum electrodynamics*, volume 7, WSP, Singapore (1990).

[12] S. G. Karshenboim, Phys. Rept. **422**, 1 (2005), [hep-ph/0509010].

[13] J. Erler and S. Su, Prog. Part. Nucl. Phys. **71**, 119 (2013), [arXiv:1303.5522].

[14] S. Schael *et al.* (ALEPH, DELPHI, L3, OPAL, SLD, LEP Electroweak Working Group, SLD Electroweak Group, SLD Heavy Flavour Group), Phys. Rept. **427**, 257 (2006), [hep-ex/0509008].

[15] D. Webber *et al.* (MuLan), Phys. Rev. Lett. **106**, 041803 (2011), [arXiv:1010.0991].

[16] T. Kinoshita and A. Sirlin, Phys. Rev. **113**, 1652 (1959).

[17] T. van Ritbergen and R. G. Stuart, Nucl. Phys. B **564**, 343 (2000), [hep-ph/9904240].

[18] M. Steinhauser and T. Seidensticker, Phys. Lett. B **467**, 271 (1999), [hep-ph/9909436].

[19] Y. Nir, Phys. Lett. B **221**, 184 (1989).

[20] A. Pak and A. Czarnecki, Phys. Rev. Lett. **100**, 241807 (2008), [arXiv:0803.0960].

[21] T. Aoyama, T. Kinoshita and M. Nio, Atoms **7**, 1, 28 (2019).

[22] P. J. Mohr, D. B. Newell and B. N. Taylor, Rev. Mod. Phys. **88**, 3, 035009 (2016), [arXiv:1507.07956].

[23] R. Bouchendira *et al.*, Phys. Rev. Lett. **106**, 080801 (2011), [arXiv:1012.3627].

[24] R. H. Parker *et al.*, Science **360**, 191 (2018), [arXiv:1812.04130].

[25] G. Abbiendi *et al.* (OPAL), Eur. Phys. J. C **45**, 1 (2006), [hep-ex/0505072].

[26] P. Achard *et al.* (L3), Phys. Lett. B **623**, 26 (2005), [hep-ex/0507078].

[27] S. Fanchiotti, B. A. Kniehl and A. Sirlin, Phys. Rev. D **48**, 307 (1993), [hep-ph/9212285].

[28] J. Erler, Phys. Rev. D **59**, 054008 (1999), [hep-ph/9803453].

[29] M. Davier *et al.*, Eur. Phys. J. C **80**, 3, 241 (2020), [arXiv:1908.00921].

[30] F. Jegerlehner, EPJ Web Conf. **118**, 01016 (2016), [arXiv:1511.04473].

[31] F. Jegerlehner and R. Szafron, Eur. Phys. J. C **71**, 1632 (2011), [arXiv:1101.2872].

[32] J. Erler (1999), [hep-ph/0005084].

[33] M. Steinhauser, Phys. Lett. B **429**, 158 (1998), [hep-ph/9803313].

[34] K. Chetyrkin, J. H. Kuhn and M. Steinhauser, Nucl. Phys. B **482**, 213 (1996), [hep-ph/9606230].

[35] J. Erler and R. Ferro-Hernández, JHEP **03**, 196 (2018), [arXiv:1712.09146].

[36] *Theory report on the 11th FCC-ee workshop* (2019), [arXiv:1905.05078].

[37] A. Keshavarzi, D. Nomura and T. Teubner, Phys. Rev. D **101**, 1, 014029 (2020), [arXiv:1911.00367].

[38] M. Davier *et al.*, Eur. Phys. J. C **71**, 1515 (2011), [Erratum: Eur.Phys.J.C 72, 1874 (2012)], [arXiv:1010.4180].

[39] K. Ackerstaff *et al.* (OPAL), Eur. Phys. J. C **7**, 571 (1999), [hep-ex/9808019].

[40] S. Anderson *et al.* (CLEO), Phys. Rev. D **61**, 112002 (2000), [hep-ex/9910046].

[41] S. Schael *et al.* (ALEPH), Phys. Rept. **421**, 191 (2005), [hep-ex/0506072].

[42] M. Fujikawa *et al.* (Belle), Phys. Rev. D **78**, 072006 (2008), [arXiv:0805.3773].

[43] S. Groote *et al.*, Phys. Lett. B **440**, 375 (1998), [hep-ph/9802374].

[44] B. Geshkenbein and V. Morgunov, Phys. Lett. B **352**, 456 (1995).

[45] M. L. Swartz, Phys. Rev. D **53**, 5268 (1996), [hep-ph/9509248].

[46] N. Krasnikov and R. Rodenberg, Nuovo Cim. A **111**, 217 (1998), [hep-ph/9711367].

[47] J. H. Kuhn and M. Steinhauser, Phys. Lett. B **437**, 425 (1998), [hep-ph/9802241].

[48] A. D. Martin, J. Outhwaite and M. Ryskin, Phys. Lett. B **492**, 69 (2000), [hep-ph/0008078].

[49] J. de Troconiz and F. Yndurain, Phys. Rev. D **65**, 093002 (2002), [hep-ph/0107318].

[50] H. Burkhardt and B. Pietrzyk, Phys. Rev. D **84**, 037502 (2011), [arXiv:1106.2991].

[51] J. Erler, P. Masjuan and H. Spiesberger, Eur. Phys. J. C **77**, 2, 99 (2017), [arXiv:1610.08531].

[52] V. Novikov *et al.*, Phys. Rept. **41**, 1 (1978).

[53] J. Erler and M. Luo, Phys. Lett. B **558**, 125 (2003), [hep-ph/0207114].

[54] T. Aaltonen *et al.* (CDF, DØ, Tevatron Electroweak Working Group) (2016), [arXiv:1608.01881].

[55] M. Aaboud *et al.* (ATLAS), Eur. Phys. J. C **79**, 4, 290 (2019), [arXiv:1810.01772].

[56] Technical Report CMS-PAS-TOP-15-012, CERN, Geneva (2016), URL `https://cds.cern.ch/record/2235162`.

[57] A. M. Sirunyan *et al.* (CMS), Eur. Phys. J. C **79**, 4, 313 (2019), [arXiv:1812.10534].

[58] A. M. Sirunyan *et al.* (CMS), Eur. Phys. J. C **79**, 5, 368 (2019), [arXiv:1812.10505].

[59] Technical Report ATLAS-CONF-2019-046, CERN, Geneva (2019), URL `https://cds.cern.ch/record/2693954`.

[60] V. M. Abazov *et al.* (DØ), Phys. Rev. Lett. **113**, 032002 (2014), [arXiv:1405.1756].

[61] A. M. Sirunyan *et al.* (CMS), Eur. Phys. J. C **78**, 11, 891 (2018), [arXiv:1805.01428].

[62] A. H. Hoang, S. Plätzer and D. Samitz, JHEP **10**, 200 (2018), [arXiv:1807.06617].

[63] M. Beneke *et al.*, Phys. Lett. B **775**, 63 (2017), [arXiv:1605.03609].

[64] P. Marquard *et al.*, Phys. Rev. Lett. **114**, 14, 142002 (2015), [arXiv:1502.01030].

[65] M. Beneke, Phys. Rept. **317**, 1 (1999), [hep-ph/9807443].

[66] S. Catani *et al.*, JHEP **07**, 100 (2019), [arXiv:1906.06535].

[67] Technical Report CMS-PAS-TOP-18-004, CERN, Geneva (2018), URL `https://cds.cern.ch/record/2647989`.

[68] G. Aad *et al.* (ATLAS), JHEP **11**, 150 (2019), [arXiv:1905.02302].

[69] J. Erler and M. Schott, Prog. Part. Nucl. Phys. **106**, 68 (2019), [arXiv:1902.05142].

[70] A. Sirlin, Phys. Rev. D **22**, 971 (1980).

[71] W. J. Marciano and J. L. Rosner, Phys. Rev. Lett. **65**, 2963 (1990), [Erratum: Phys.Rev.Lett. 68, 898 (1992)].

[72] G. Degrassi, S. Fanchiotti and A. Sirlin, Nucl. Phys. B **351**, 49 (1991).

[73] A. Czarnecki and W. J. Marciano, Int. J. Mod. Phys. A **15**, 2365 (2000), [hep-ph/0003049].

[74] J. Erler and M. J. Ramsey-Musolf, Phys. Rev. D **72**, 073003 (2005), [hep-ph/0409169].

[75] K. Kumar *et al.*, Ann. Rev. Nucl. Part. Sci. **63**, 237 (2013), [arXiv:1302.6263].

[76] G. Degrassi and A. Sirlin, Nucl. Phys. B **352**, 342 (1991).

[77] P. Gambino and A. Sirlin, Phys. Rev. D **49**, 1160 (1994), [hep-ph/9309326].

[78] W. Hollik, Fortsch. Phys. **38**, 165 (1990).

[79] R. Barbieri *et al.*, Nucl. Phys. B **409**, 105 (1993).

[80] J. Fleischer, O. Tarasov and F. Jegerlehner, Phys. Lett. B **319**, 249 (1993).

[81] G. Degrassi, P. Gambino and A. Vicini, Phys. Lett. B **383**, 219 (1996), [hep-ph/9603374].

[82] G. Degrassi, P. Gambino and A. Sirlin, Phys. Lett. B **394**, 188 (1997), [hep-ph/9611363].

[83] A. Freitas *et al.*, Phys. Lett. B **495**, 338 (2000), [Erratum: Phys.Lett.B 570, 265 (2003)], [hep-ph/0007091].

[84] M. Awramik and M. Czakon, Phys. Lett. B **568**, 48 (2003), [hep-ph/0305248].

[85] A. Freitas *et al.*, Nucl. Phys. B **632**, 189 (2002), [Erratum: Nucl.Phys.B 666, 305–307 (2003)], [hep-ph/0202131].

[86] M. Awramik and M. Czakon, Phys. Rev. Lett. **89**, 241801 (2002), [hep-ph/0208113].

[87] A. Onishchenko and O. Veretin, Phys. Lett. B **551**, 111 (2003), [hep-ph/0209010].

[88] G. Degrassi, P. Gambino and P. P. Giardino, JHEP **05**, 154 (2015), [arXiv:1411.7040].

[89] M. Awramik *et al.*, Phys. Rev. D **69**, 053006 (2004), [hep-ph/0311148].

[90] M. Awramik *et al.*, Phys. Rev. Lett. **93**, 201805 (2004), [hep-ph/0407317].

[91] W. Hollik, U. Meier and S. Uccirati, Nucl. Phys. B **731**, 213 (2005), [hep-ph/0507158].

[92] M. Awramik, M. Czakon and A. Freitas, Phys. Lett. B **642**, 563 (2006), [hep-ph/0605339].

[93] W. Hollik, U. Meier and S. Uccirati, Nucl. Phys. B **765**, 154 (2007), [hep-ph/0610312].

[94] M. Awramik *et al.*, Nucl. Phys. B **813**, 174 (2009), [arXiv:0811.1364].

[95] I. Dubovyk *et al.*, Phys. Lett. B **762**, 184 (2016), [arXiv:1607.08375].

[96] A. Freitas, Phys. Lett. B **730**, 50 (2014), [arXiv:1310.2256].

[97] A. Freitas, JHEP **04**, 070 (2014), [arXiv:1401.2447].

[98] I. Dubovyk *et al.*, Phys. Lett. B **783**, 86 (2018), [arXiv:1804.10236].

[99] I. Dubovyk *et al.*, JHEP **08**, 113 (2019), [arXiv:1906.08815].

[100] M. Awramik, M. Czakon and A. Freitas, JHEP **11**, 048 (2006), [hep-ph/0608099].

[101] A. Djouadi and C. Verzegnassi, Phys. Lett. B **195**, 265 (1987).

[102] A. Djouadi, Nuovo Cim. A **100**, 357 (1988).

[103] K. Chetyrkin, J. H. Kuhn and M. Steinhauser, Phys. Lett. B **351**, 331 (1995), [hep-ph/9502291].

[104] L. Avdeev *et al.*, Phys. Lett. B **336**, 560 (1994), [Erratum: Phys.Lett.B 349, 597–598 (1995)], [hep-ph/9406363].

[105] Y. Schroder and M. Steinhauser, Phys. Lett. B **622**, 124 (2005), [hep-ph/0504055].

[106] K. Chetyrkin *et al.*, Phys. Rev. Lett. **97**, 102003 (2006), [hep-ph/0605201].

[107] R. Boughezal and M. Czakon, Nucl. Phys. B **755**, 221 (2006), [hep-ph/0606232].

[108] B. A. Kniehl, J. H. Kuhn and R. Stuart, Phys. Lett. B **214**, 621 (1988).

[109] B. A. Kniehl, Nucl. Phys. B **347**, 86 (1990).

[110] F. Halzen and B. A. Kniehl, Nucl. Phys. B **353**, 567 (1991).

[111] A. Djouadi and P. Gambino, Phys. Rev. D **49**, 3499 (1994), [Erratum: Phys.Rev.D 53, 4111 (1996)], [hep-ph/9309298].

[112] A. Anselm, N. Dombey and E. Leader, Phys. Lett. B **312**, 232 (1993).

[113] K. Chetyrkin, J. H. Kuhn and M. Steinhauser, Phys. Rev. Lett. **75**, 3394 (1995), [hep-ph/9504413].

[114] J. van der Bij *et al.*, Phys. Lett. B **498**, 156 (2001), [hep-ph/0011373].

[115] M. Faisst *et al.*, Nucl. Phys. B **665**, 649 (2003), [hep-ph/0302275].

[116] R. Boughezal, J. Tausk and J. van der Bij, Nucl. Phys. B **725**, 3 (2005), [hep-ph/0504092].

[117] A. Arbuzov *et al.*, Comput. Phys. Commun. **174**, 728 (2006), [hep-ph/0507146].

[118] J. Erler and M. J. Ramsey-Musolf, Prog. Part. Nucl. Phys. **54**, 351 (2005), [hep-ph/0404291].

[119] J. Formaggio and G. Zeller, Rev. Mod. Phys. **84**, 1307 (2012), [arXiv:1305.7513].

[120] J. Dorenbosch *et al.* (CHARM), Z. Phys. C **41**, 567 (1989), [Erratum: Z.Phys.C 51, 142 (1991)].

[121] L. Ahrens *et al.*, Phys. Rev. D **41**, 3297 (1990).

[122] P. Vilain *et al.* (CHARM-II), Phys. Lett. B **335**, 246 (1994).

[123] R. Allen *et al.*, Phys. Rev. D **47**, 11 (1993).

[124] L. Auerbach *et al.* (LSND), Phys. Rev. D **63**, 112001 (2001), [hep-ex/0101039].

[125] M. Deniz *et al.* (TEXONO), Phys. Rev. D **81**, 072001 (2010), [arXiv:0911.1597].

[126] J. M. Conrad, M. H. Shaevitz and T. Bolton, Rev. Mod. Phys. **70**, 1341 (1998), [hep-ex/9707015].

[127] A. Blondel *et al.*, Z. Phys. C **45**, 361 (1990).

[128] J. Allaby *et al.* (CHARM), Z. Phys. C **36**, 611 (1987).

[129] K. S. McFarland *et al.* (CCFR, E744, E770), Eur. Phys. J. C **1**, 509 (1998), [hep-ex/9701010].

[130] R. Barnett, Phys. Rev. D **14**, 70 (1976).

[131] H. Georgi and H. Politzer, Phys. Rev. D **14**, 1829 (1976).

[132] S. Rabinowitz *et al.*, Phys. Rev. Lett. **70**, 134 (1993).

[133] E. Paschos and L. Wolfenstein, Phys. Rev. D **7**, 91 (1973).

[134] G. Zeller *et al.* (NuTeV), Phys. Rev. Lett. **88**, 091802 (2002), [Erratum: Phys.Rev.Lett. 90, 239902 (2003)], [hep-ex/0110059].

[135] D. Akimov *et al.* (COHERENT), Science **357**, 6356, 1123 (2017), [arXiv:1708.01294].

[136] J. Erler *et al.*, Ann. Rev. Nucl. Part. Sci. **64**, 269 (2014), [arXiv:1401.6199].

[137] C. Prescott *et al.*, Phys. Lett. B **84**, 524 (1979).

[138] D. Wang *et al.* (PVDIS), Nature **506**, 7486, 67 (2014).

[139] D. Wang *et al.*, Phys. Rev. C **91**, 4, 045506 (2015), [arXiv:1411.3200].

[140] R. Hasty *et al.* (SAMPLE), Science **290**, 2117 (2000), [arXiv:nucl-ex/0102001].

[141] E. Beise, M. Pitt and D. Spayde, Prog. Part. Nucl. Phys. **54**, 289 (2005), [arXiv:nucl-ex/0412054].

[142] S.-L. Zhu *et al.*, Phys. Rev. D **62**, 033008 (2000), [hep-ph/0002252].

[143] A. Argento *et al.*, Phys. Lett. B **120**, 245 (1983).

[144] W. Heil *et al.*, Nucl. Phys. B **327**, 1 (1989).

[145] P. Souder *et al.*, Phys. Rev. Lett. **65**, 694 (1990).

[146] D. Armstrong and R. McKeown, Ann. Rev. Nucl. Part. Sci. **62**, 337 (2012), [arXiv:1207.5238].

[147] E. Derman and W. J. Marciano, Annals Phys. **121**, 147 (1979).

[148] P. Anthony *et al.* (SLAC E158), Phys. Rev. Lett. **95**, 081601 (2005), [hep-ex/0504049].

[149] D. Androić *et al.* (Qweak), Nature **557**, 7704, 207 (2018), [arXiv:1905.08283].

[150] R. D. Carlini *et al.*, Ann. Rev. Nucl. Part. Sci. **69**, 191 (2019).

[151] J. Erler, A. Kurylov and M. J. Ramsey-Musolf, Phys. Rev. D **68**, 016006 (2003), [hep-ph/0302149].

[152] R. D. Young *et al.*, Phys. Rev. Lett. **99**, 122003 (2007), [arXiv:0704.2618].

[153] A. Acha *et al.* (HAPPEX), Phys. Rev. Lett. **98**, 032301 (2007), [arXiv:nucl-ex/0609002].

[154] M. Gorchtein and C. Horowitz, Phys. Rev. Lett. **102**, 091806 (2009), [arXiv:0811.0614].

[155] M. Gorchtein, C. Horowitz and M. J. Ramsey-Musolf, Phys. Rev. C **84**, 015502 (2011), [arXiv:1102.3910].

[156] N. Hall *et al.*, Phys. Lett. B **753**, 221 (2016), [arXiv:1504.03973].

[157] J. Erler *et al.*, Phys. Rev. D **100**, 5, 053007 (2019), [arXiv:1907.07928].

[158] M. Bouchiat and C. Bouchiat, Phys. Lett. B **48**, 111 (1974).

[159] M. Safronova *et al.*, Rev. Mod. Phys. **90**, 2, 025008 (2018), [arXiv:1710.01833].

[160] C. Wood *et al.*, Science **275**, 1759 (1997).

[161] J. Guena, M. Lintz and M. Bouchiat, Phys. Rev. A **71**, 042108 (2005), [arXiv:physics/0412017].

[162] N. Edwards *et al.*, Phys. Rev. Lett. **74**, 2654 (1995).

[163] P. Vetter *et al.*, Phys. Rev. Lett. **74**, 2658 (1995).

[164] D. Meekhof *et al.*, Phys. Rev. Lett. **71**, 3442 (1993).

[165] M. Macpherson *et al.*, Phys. Rev. Lett. **67**, 20, 2784 (1991).

[166] P. Blunden, W. Melnitchouk and A. Thomas, Phys. Rev. Lett. **109**, 262301 (2012), [arXiv:1208.4310].

[167] S. Bennett and C. E. Wieman, Phys. Rev. Lett. **82**, 2484 (1999), [Erratum: Phys.Rev.Lett. 82, 4153 (1999), Erratum: Phys.Rev.Lett. 83, 889 (1999)], [hep-ex/9903022].

[168] V. Dzuba and V. Flambaum., Phys. Rev. A **62**, 052101 (2000), [arXiv:physics/0005038].

[169] V. Dzuba, V. Flambaum and O. Sushkov, Phys. Rev. A **56**, 4357 (1997), [hep-ph/9709251].

[170] D. Cho *et al.*, Phys. Rev. A **55**, 1007 (1997).

[171] G. Toh *et al.*, Phys. Rev. Lett. **123**, 7, 073002 (2019), [arXiv:1905.02768].

[172] A. A. Vasilyev *et al.*, Phys. Rev. A **66**, 020101 (2002).

[173] V. Dzuba, V. Flambaum and J. Ginges, Phys. Rev. D **66**, 076013 (2002), [hep-ph/0204134].

[174] J. Ginges and V. Flambaum, Phys. Rept. **397**, 63 (2004), [arXiv:physics/0309054].

[175] A. Derevianko and S. G. Porsev, Eur. Phys. J. A **32**, 4, 517 (2007), [hep-ph/0608178].

[176] B. Roberts, V. Dzuba and V. Flambaum, Ann. Rev. Nucl. Part. Sci. **65**, 63 (2015), [arXiv:1412.6644].

[177] A. Derevianko, Phys. Rev. Lett. **85**, 1618 (2000), [hep-ph/0005274].

[178] W. Johnson, I. Bednyakov and G. Soff, Phys. Rev. Lett. **87**, 233001 (2001), [Erratum: Phys.Rev.Lett. 88, 079903 (2002)], [hep-ph/0110262].

[179] M. Kuchiev and V. Flambaum, Phys. Rev. Lett. **89**, 283002 (2002), [hep-ph/0206124].

[180] A. Milstein, O. Sushkov and I. Terekhov, Phys. Rev. Lett. **89**, 283003 (2002), [hep-ph/0208227].

[181] S. Porsev, K. Beloy and A. Derevianko, Phys. Rev. Lett. **102**, 181601 (2009), [arXiv:0902.0335].

[182] V. Dzuba *et al.*, Phys. Rev. Lett. **109**, 203003 (2012), [arXiv:1207.5864].

[183] C. Bouchiat and C. Piketty, Phys. Lett. B **128**, 73 (1983).

[184] I. Zel'dovich, J. Exp. Theor. Phys. **6**, 1184 (1958).

[185] V. Flambaum and D. Murray, Phys. Rev. C **56**, 1641 (1997), [arXiv:nucl-th/9703050].

[186] W. Haxton and C. E. Wieman, Ann. Rev. Nucl. Part. Sci. **51**, 261 (2001), [arXiv:nucl-th/0104026].

[187] V. Dzuba *et al.*, J. Phys. B **20**, 3297 (1987).

[188] J. L. Rosner, Phys. Rev. D **53**, 2724 (1996), [hep-ph/9507375].

[189] D. Antypas *et al.*, Nature Phys. **15**, 2, 120 (2019), [arXiv:1804.05747].

[190] M. Ramsey-Musolf, Phys. Rev. C **60**, 015501 (1999), [hep-ph/9903264].

[191] S. Pollock, E. Fortson and L. Wilets, Phys. Rev. C **46**, 2587 (1992), [arXiv:nucl-th/9211004].

[192] B. Chen and P. Vogel, Phys. Rev. C **48**, 1392 (1993), [arXiv:nucl-th/9303003].

[193] C. Horowitz *et al.*, Phys. Rev. C **63**, 025501 (2001), [arXiv:nucl-th/9912038].

[194] S. Abrahamyan *et al.*, Phys. Rev. Lett. **108**, 112502 (2012), [arXiv:1201.2568].

[195] H. Davoudiasl, H.-S. Lee and W. J. Marciano, Phys. Rev. D **86**, 095009 (2012), [arXiv:1208.2973].

[196] E. Braaten, S. Narison and A. Pich, Nucl. Phys. B **373**, 581 (1992).

[197] A. Pich, Prog. Part. Nucl. Phys. **75**, 41 (2014), [arXiv:1310.7922].

[198] M. Davier *et al.*, Eur. Phys. J. C **74**, 3, 2803 (2014), [arXiv:1312.1501].

[199] K. Chetyrkin, A. Kataev and F. Tkachov, Phys. Lett. B **85**, 277 (1979).

[200] M. Dine and J. Sapirstein, Phys. Rev. Lett. **43**, 668 (1979).

[201] S. Gorishnii, A. Kataev and S. Larin, Phys. Lett. B **259**, 144 (1991).

[202] L. R. Surguladze and M. A. Samuel, Phys. Rev. Lett. **66**, 560 (1991), [Erratum: Phys.Rev.Lett. 66, 2416 (1991)].

[203] P. Baikov, K. Chetyrkin and J. H. Kuhn, Phys. Rev. Lett. **101**, 012002 (2008), [arXiv:0801.1821].

[204] F. Le Diberder and A. Pich, Phys. Lett. B **286**, 147 (1992).

[205] M. Beneke and M. Jamin, JHEP **09**, 044 (2008), [arXiv:0806.3156].

[206] E. Braaten and C.-S. Li, Phys. Rev. D **42**, 3888 (1990).

[207] W. Marciano and A. Sirlin, Phys. Rev. Lett. **61**, 1815 (1988).

[208] J. Erler, Rev. Mex. Fis. **50**, 200 (2004), [hep-ph/0211345].

[209] D. Boito *et al.*, Phys. Rev. D **85**, 093015 (2012), [arXiv:1203.3146].

[210] D. Boito *et al.*, Phys. Rev. D **91**, 3, 034003 (2015), [arXiv:1410.3528].

[211] A. Pich and A. Rodríguez-Sánchez, Phys. Rev. D **94**, 3, 034027 (2016), [arXiv:1605.06830].

[212] J. Erler (2011), [arXiv:1102.5520].

[213] G. Bennett *et al.* (Muon g-2), Phys. Rev. Lett. **92**, 161802 (2004), [hep-ex/0401008].

[214] T. Aoyama *et al.*, Phys. Rev. Lett. **109**, 111808 (2012), [arXiv:1205.5370].

[215] T. Aoyama *et al.*, PTEP **2012**, 01A107 (2012).

[216] P. Baikov, A. Maier and P. Marquard, Nucl. Phys. B **877**, 647 (2013), [arXiv:1307.6105].

[217] G. Li, R. Mendel and M. A. Samuel, Phys. Rev. D **47**, 1723 (1993).

[218] S. Laporta and E. Remiddi, Phys. Lett. B **301**, 440 (1993).

[219] S. Laporta and E. Remiddi, Phys. Lett. B **379**, 283 (1996), [hep-ph/9602417].

[220] A. Czarnecki and M. Skrzypek, Phys. Lett. B **449**, 354 (1999), [hep-ph/9812394].

[221] J. Erler and M. Luo, Phys. Rev. Lett. **87**, 071804 (2001), [hep-ph/0101010].

[222] S. Laporta, Phys. Lett. B **772**, 232 (2017), [arXiv:1704.06996].

[223] S. J. Brodsky and J. D. Sullivan, Phys. Rev. **156**, 1644 (1967).

[224] T. Burnett and M. Levine, Phys. Lett. B **24**, 467 (1967).

[225] R. Jackiw and S. Weinberg, Phys. Rev. D **5**, 2396 (1972).

[226] I. Bars and M. Yoshimura, Phys. Rev. D **6**, 374 (1972).

[227] K. Fujikawa, B. Lee and A. Sanda, Phys. Rev. D **6**, 2923 (1972).

[228] W. A. Bardeen, R. Gastmans and B. Lautrup, Nucl. Phys. B **46**, 319 (1972).

[229] T. Kukhto *et al.*, Nucl. Phys. B **371**, 567 (1992).

[230] S. Peris, M. Perrottet and E. de Rafael, Phys. Lett. B **355**, 523 (1995), [hep-ph/9505405].

[231] A. Czarnecki, B. Krause and W. J. Marciano, Phys. Rev. D **52**, 2619 (1995), [hep-ph/9506256].

[232] A. Czarnecki, B. Krause and W. J. Marciano, Phys. Rev. Lett. **76**, 3267 (1996), [hep-ph/9512369].

[233] C. Gnendiger, D. Stöckinger and H. Stöckinger-Kim, Phys. Rev. D **88**, 053005 (2013), [arXiv:1306.5546].

[234] G. Degrassi and G. Giudice, Phys. Rev. D **58**, 053007 (1998), [hep-ph/9803384].

[235] A. Czarnecki, W. J. Marciano and A. Vainshtein, Phys. Rev. D **67**, 073006 (2003), [Erratum: Phys.Rev.D 73, 119901 (2006)], [hep-ph/0212229].

[236] F. Jegerlehner, EPJ Web Conf. **166**, 00022 (2018), [arXiv:1705.00263].

[237] H. B. Meyer and H. Wittig, Prog. Part. Nucl. Phys. **104**, 46 (2019), [arXiv:1807.09370].

[238] T. Blum *et al.* (RBC, UKQCD), Phys. Rev. Lett. **121**, 2, 022003 (2018), [arXiv:1801.07224].

[239] D. Giusti *et al.*, Phys. Rev. D **99**, 11, 114502 (2019), [arXiv:1901.10462].

[240] E. Shintani and Y. Kuramashi (PACS), Phys. Rev. D **100**, 3, 034517 (2019), [arXiv:1902.00885].

[241] C. Davies *et al.* (Fermilab Lattice, LATTICE-HPQCD, MILC), Phys. Rev. D **101**, 3, 034512 (2020), [arXiv:1902.04223].

[242] A. Gérardin *et al.*, Phys. Rev. D **100**, 1, 014510 (2019), [arXiv:1904.03120].

[243] S. Borsanyi *et al.* (2020), [arXiv:2002.12347].

[244] C. Lehner and A. S. Meyer (2020), [arXiv:2003.04177].

[245] K. Melnikov and A. Vainshtein, Phys. Rev. D **70**, 113006 (2004), [hep-ph/0312226].

[246] J. Erler and G. Toledo Sanchez, Phys. Rev. Lett. **97**, 161801 (2006), [hep-ph/0605052].

[247] J. Prades, E. de Rafael and A. Vainshtein **20**, 303 (2009), [arXiv:0901.0306].

[248] M. Knecht and A. Nyffeler, Phys. Rev. D **65**, 073034 (2002), [hep-ph/0111058].

[249] I. Danilkin, C. F. Redmer and M. Vanderhaeghen, Prog. Part. Nucl. Phys. **107**, 20 (2019), [arXiv:1901.10346].

[250] T. Blum *et al.* (2019), [arXiv:1911.08123].

[251] B. Krause, Phys. Lett. B **390**, 392 (1997), [hep-ph/9607259].

[252] A. Kurz *et al.*, Phys. Lett. B **734**, 144 (2014), [arXiv:1403.6400].

[253] G. Colangelo *et al.*, Phys. Lett. B **735**, 90 (2014), [arXiv:1403.7512].

[254] J. L. Lopez, D. V. Nanopoulos and X. Wang, Phys. Rev. D **49**, 366 (1994), [hep-ph/9308336].

[255] G. Passarino and M. Veltman, Nucl. Phys. B **160**, 151 (1979).

[256] W. Hollik and G. Duckeck, Springer Tracts Mod. Phys. **162**, 1 (2000).

[257] B. Lynn and R. Stuart, Nucl. Phys. B **253**, 216 (1985).

[258] S. L. Wu, Phys. Rept. **107**, 59 (1984).

[259] R. Marshall, Z. Phys. C **43**, 607 (1989).

[260] S. Schael *et al.* (ALEPH, DELPHI, L3, OPAL, LEP Electroweak), Phys. Rept. **532**, 119 (2013), [arXiv:1302.3415].

[261] T. A. Aaltonen *et al.* (CDF, DØ), Phys. Rev. D **88**, 5, 052018 (2013), [arXiv:1307.7627].

[262] Technical Report TEVEWWG/WZ 2010/01, FERMILAB, Batavia (2010), [arXiv:1003.2826], URL `https://www-d0.fnal.gov/Run2Physics/WWW/results/prelim/EW/E34`.

[263] M. Aaboud *et al.* (ATLAS), Eur. Phys. J. C **78**, 2, 110 (2018), [Erratum: Eur.Phys.J.C 78, 898 (2018)], [arXiv:1701.07240].

[264] G. Aad *et al.* (ATLAS), Phys. Lett. B **716**, 1 (2012), [arXiv:1207.7214].

[265] S. Chatrchyan *et al.* (CMS), Phys. Lett. B **716**, 30 (2012), [arXiv:1207.7235].

[266] M. Aaboud *et al.* (ATLAS), Phys. Lett. B **784**, 345 (2018), [arXiv:1806.00242].

[267] A. M. Sirunyan *et al.* (CMS) (2020), [arXiv:2002.06398].

[268] T. A. Aaltonen *et al.* (CDF, DØ), Phys. Rev. D **97**, 11, 112007 (2018), [arXiv:1801.06283].

[269] G. Aad *et al.* (ATLAS), JHEP **09**, 049 (2015), [arXiv:1503.03709].

[270] Technical Report ATLAS-CONF-2018-037, CERN, Geneva (2018), URL `https://cds.cern.ch/record/2630340`.

[271] A. M. Sirunyan *et al.* (CMS), Eur. Phys. J. C **78**, 9, 701 (2018), [arXiv:1806.00863].

[272] R. Aaij *et al.* (LHCb), JHEP **11**, 190 (2015), [arXiv:1509.07645].

[273] K. Abe *et al.* (SLD), Phys. Rev. Lett. **84**, 5945 (2000), [hep-ex/0004026].

[274] K. Abe *et al.* (SLD), Phys. Rev. Lett. **86**, 1162 (2001), [hep-ex/0010015].

[275] P. Janot and S. Jadach, Phys. Lett. B **803**, 135319 (2020), [arXiv:1912.02067].

[276] D. Kennedy *et al.*, Nucl. Phys. B **321**, 83 (1989).

[277] S. Riemann, Rept. Prog. Phys. **73**, 126201 (2010).

[278] K. Abe *et al.* (SLD), Phys. Rev. Lett. **85**, 5059 (2000), [hep-ex/0006019].

[279] K. Abe *et al.* (SLD), Phys. Rev. Lett. **78**, 17 (1997), [hep-ex/9609019].

[280] W. Bernreuther *et al.*, JHEP **01**, 053 (2017), [arXiv:1611.07942].

[281] S. Catani and M. H. Seymour, JHEP **07**, 023 (1999), [hep-ph/9905424].

[282] A. Djouadi, J. H. Kuhn and P. Zerwas, Z. Phys. C **46**, 411 (1990).

[283] T. A. Aaltonen *et al.* (CDF), Phys. Rev. D **93**, 11, 112016 (2016), [Addendum: Phys.Rev.D 95, 119901 (2017)], [arXiv:1605.02719].

[284] V. M. Abazov *et al.* (DØ), Phys. Rev. Lett. **120**, 24, 241802 (2018), [arXiv:1710.03951].

[285] V. Abazov *et al.* (DØ), Phys. Rev. D **84**, 012007 (2011), [arXiv:1104.4590].

[286] D. Acosta *et al.* (CDF), Phys. Rev. D **71**, 052002 (2005), [hep-ex/0411059].

[287] A. Aktas *et al.* (H1), Phys. Lett. B **632**, 35 (2006), [hep-ex/0507080].

[288] H. Abramowicz *et al.* (ZEUS), Phys. Rev. D **93**, 9, 092002 (2016), [arXiv:1603.09628].

[289] D. Albert *et al.*, Nucl. Phys. B **166**, 460 (1980).

[290] K. Chetyrkin, J. H. Kuhn and A. Kwiatkowski, Phys. Rept. **277**, 189 (1996), [hep-ph/9503396].

[291] B. A. Kniehl and J. H. Kuhn, Nucl. Phys. B **329**, 547 (1990).

[292] K. Chetyrkin and A. Kwiatkowski, Phys. Lett. B **319**, 307 (1993), [hep-ph/9310229].

[293] S. Larin, T. van Ritbergen and J. Vermaseren, Phys. Lett. B **320**, 159 (1994), [hep-ph/9310378].

[294] K. Chetyrkin and O. Tarasov, Phys. Lett. B **327**, 114 (1994), [hep-ph/9312323].

[295] P. Baikov *et al.*, Phys. Rev. Lett. **108**, 222003 (2012), [arXiv:1201.5804].

[296] A. Kataev, Phys. Lett. B **287**, 209 (1992).

[297] B. W. Lynn and R. G. Stuart, Phys. Lett. B **252**, 676 (1990).

[298] J. Bernabeu, A. Pich and A. Santamaria, Nucl. Phys. B **363**, 326 (1991).

[299] A. Czarnecki and J. H. Kuhn, Phys. Rev. Lett. **77**, 3955 (1996), [hep-ph/9608366].

[300] R. Harlander, T. Seidensticker and M. Steinhauser, Phys. Lett. B **426**, 125 (1998), [hep-ph/9712228].

[301] J. Fleischer *et al.*, Phys. Lett. B **459**, 625 (1999), [hep-ph/9904256].

[302] P. A. Grassi, B. A. Kniehl and A. Sirlin, Phys. Rev. Lett. **86**, 389 (2001), [hep-th/0005149].

[303] A. Akhundov, D. Bardin and T. Riemann, Nucl. Phys. B **276**, 1 (1986).

[304] F. Jegerlehner, Z. Phys. C **32**, 425 (1986), [Erratum: Z.Phys.C 38, 519 (1988)].

[305] W. Beenakker and W. Hollik, Z. Phys. C **40**, 141 (1988).

[306] D. Bardin *et al.*, Z. Phys. C **44**, 493 (1989).

[307] A. Borrelli *et al.*, Nucl. Phys. B **333**, 357 (1990).

[308] A. Denner and T. Sack, Z. Phys. C **46**, 653 (1990).

[309] A. Denner, Fortsch. Phys. **41**, 307 (1993), [arXiv:0709.1075].

[310] U. Amaldi *et al.*, Phys. Rev. D **36**, 1385 (1987).

[311] G. Costa *et al.*, Nucl. Phys. B **297**, 244 (1988).

[312] P. Langacker and M. Luo, Phys. Rev. D **44**, 817 (1991).

[313] J. Erler and P. Langacker, Phys. Rev. D **52**, 441 (1995), [hep-ph/9411203].

[314] F. James and M. Roos, Comput. Phys. Commun. **10**, 343 (1975).

[315] D. d'Enterria and A. Poldaru (2019), [arXiv:1912.11733].

[316] V. Abazov *et al.* (DØ), Phys. Rev. D **80**, 111107 (2009), [arXiv:0911.2710].

[317] J. Bagger, K. T. Matchev and D. Pierce, Phys. Lett. B **348**, 443 (1995), [hep-ph/9501277].

[318] P. Langacker and N. Polonsky, Phys. Rev. D **52**, 3081 (1995), [hep-ph/9503214].

[319] M. Veltman, Nucl. Phys. B **123**, 89 (1977).

[320] M. S. Chanowitz, M. Furman and I. Hinchliffe, Phys. Lett. B **78**, 285 (1978).

[321] J. van der Bij and F. Hoogeveen, Nucl. Phys. B **283**, 477 (1987).

[322] P. Langacker and M. Luo, Phys. Rev. D **45**, 278 (1992).

[323] A. Denner, R. Guth and J. H. Kuhn, Phys. Lett. B **240**, 438 (1990).

[324] W. Grimus *et al.*, J. Phys. G **35**, 075001 (2008), [arXiv:0711.4022].

[325] H. E. Haber and D. O'Neil, Phys. Rev. D **83**, 055017 (2011), [arXiv:1011.6188].

[326] S. Bertolini and A. Sirlin, Phys. Lett. B **257**, 179 (1991).

[327] M. Golden and L. Randall, Nucl. Phys. B **361**, 3 (1991).

[328] B. Holdom and J. Terning, Phys. Lett. B **247**, 88 (1990).

[329] M. E. Peskin and T. Takeuchi, Phys. Rev. Lett. **65**, 964 (1990).

[330] K. Hagiwara *et al.*, Z. Phys. C **64**, 559 (1994), [Erratum: Z.Phys.C 68, 352 (1995)], [hep-ph/9409380].

[331] M. E. Peskin and T. Takeuchi, Phys. Rev. D **46**, 381 (1992).

[332] I. Maksymyk, C. Burgess and D. London, Phys. Rev. D **50**, 529 (1994), [hep-ph/9306267].

[333] R. Barbieri *et al.*, Nucl. Phys. B **703**, 127 (2004), [hep-ph/0405040].

[334] M. Farina *et al.*, Phys. Lett. B **772**, 210 (2017), [arXiv:1609.08157].

[335] G. Altarelli and R. Barbieri, Phys. Lett. B **253**, 161 (1991).

[336] D. Kennedy and P. Langacker, Phys. Rev. D **44**, 1591 (1991).

[337] L. Randall and R. Sundrum, Phys. Rev. Lett. **83**, 3370 (1999), [hep-ph/9905221].

[338] M. Carena *et al.*, Nucl. Phys. B **759**, 202 (2006), [hep-ph/0607106].

[339] R. Contino (2011), [arXiv:1005.4269].

[340] E. Gates and J. Terning, Phys. Rev. Lett. **67**, 1840 (1991).

[341] R. Sundrum, Nucl. Phys. B **395**, 60 (1993), [hep-ph/9205203].

[342] R. Sundrum and S. D. Hsu, Nucl. Phys. B **391**, 127 (1993), [hep-ph/9206225].

[343] M. A. Luty and R. Sundrum, Phys. Rev. Lett. **70**, 529 (1993), [hep-ph/9209255].

[344] T. Appelquist and J. Terning, Phys. Lett. B **315**, 139 (1993), [hep-ph/9305258].

[345] D. D. Dietrich, F. Sannino and K. Tuominen, Phys. Rev. D **72**, 055001 (2005), [hep-ph/0505059].

[346] N. D. Christensen and R. Shrock, Phys. Lett. B **632**, 92 (2006), [hep-ph/0509109].

[347] M. Harada, M. Kurachi and K. Yamawaki, Prog. Theor. Phys. **115**, 765 (2006), [hep-ph/0509193].

[348] H. Georgi, Nucl. Phys. B **363**, 301 (1991).

[349] M. J. Dugan and L. Randall, Phys. Lett. B **264**, 154 (1991).

[350] H. E. Haber and G. L. Kane, Phys. Rept. **117**, 75 (1985).

[351] A. Djouadi, Phys. Rept. **459**, 1 (2008), [hep-ph/0503173].

[352] R. Barbieri *et al.*, Nucl. Phys. B **341**, 309 (1990).

[353] R. Barbieri, M. Frigeni and F. Caravaglios, Phys. Lett. B **279**, 169 (1992).

[354] J. Erler and D. M. Pierce, Nucl. Phys. B **526**, 53 (1998), [hep-ph/9801238].

[355] G.-C. Cho and K. Hagiwara, Nucl. Phys. B **574**, 623 (2000), [hep-ph/9912260].

[356] G. Altarelli *et al.*, JHEP **06**, 018 (2001), [hep-ph/0106029].

[357] S. Heinemeyer, W. Hollik and G. Weiglein, Phys. Rept. **425**, 265 (2006), [hep-ph/0412214].

[358] S. P. Martin, K. Tobe and J. D. Wells, Phys. Rev. D **71**, 073014 (2005), [hep-ph/0412424].

[359] M. Ramsey-Musolf and S. Su, Phys. Rept. **456**, 1 (2008), [hep-ph/0612057].

[360] S. Heinemeyer *et al.*, JHEP **04**, 039 (2008), [arXiv:0710.2972].

[361] O. Buchmueller *et al.*, Eur. Phys. J. C **72**, 2020 (2012), [arXiv:1112.3564].

[362] B. Grinstein and M. B. Wise, Phys. Lett. B **265**, 326 (1991).

[363] A. Pich, I. Rosell and J. Sanz-Cillero, JHEP **01**, 157 (2014), [arXiv:1310.3121].

[364] C. T. Hill and E. H. Simmons, Phys. Rept. **381**, 235 (2003), [Erratum: Phys.Rept. 390, 553–554 (2004)], [hep-ph/0203079].

[365] G. Panico and A. Wulzer **913** (2016), [arXiv:1506.01961].

[366] J. Erler and P. Langacker, Phys. Rev. Lett. **105**, 031801 (2010), [arXiv:1003.3211].

[367] J. Gunion, D. W. McKay and H. Pois, Phys. Rev. D **53**, 1616 (1996), [hep-ph/9507323].

[368] A. Lenz, Adv. High Energy Phys. **2013**, 910275 (2013).

[369] S. Chatrchyan *et al.* (CMS), Phys. Rev. D **86**, 112003 (2012), [arXiv:1209.1062].

[370] A. Djouadi and A. Lenz, Phys. Lett. B **715**, 310 (2012), [arXiv:1204.1252].

[371] O. Eberhardt *et al.*, Phys. Rev. Lett. **109**, 241802 (2012), [arXiv:1209.1101].

[372] J. Maalampi and M. Roos, Phys. Rept. **186**, 53 (1990).

[373] P. Langacker, Phys. Rept. **72**, 185 (1981).

[374] J. L. Hewett and T. G. Rizzo, Phys. Rept. **183**, 193 (1989).

[375] J. Kang, P. Langacker and B. D. Nelson, Phys. Rev. D **77**, 035003 (2008), [arXiv:0708.2701].

[376] S. P. Martin, Phys. Rev. D **81**, 035004 (2010), [arXiv:0910.2732].

[377] P. W. Graham *et al.*, Phys. Rev. D **81**, 055016 (2010), [arXiv:0910.3020].

[378] J. Erler, J. L. Feng and N. Polonsky, Phys. Rev. Lett. **78**, 3063 (1997), [hep-ph/9612397].

[379] D. Choudhury, T. M. Tait and C. Wagner, Phys. Rev. D **65**, 053002 (2002), [hep-ph/0109097].

[380] J. Erler and P. Langacker, Phys. Rev. Lett. **84**, 212 (2000), [hep-ph/9910315].

[381] P. Langacker and M. Plumacher, Phys. Rev. D **62**, 013006 (2000), [hep-ph/0001204].

[382] P. Abreu *et al.* (DELPHI), Eur. Phys. J. C **10**, 415 (1999).

[383] P. Langacker and D. London, Phys. Rev. D **38**, 886 (1988).

[384] F. del Aguila, J. de Blas and M. Perez-Victoria, Phys. Rev. D **78**, 013010 (2008), [arXiv:0803.4008].

[385] M. Chemtob, Prog. Part. Nucl. Phys. **54**, 71 (2005), [hep-ph/0406029].

[386] R. Barbier *et al.*, Phys. Rept. **420**, 1 (2005), [hep-ph/0406039].

[387] T. Han, H. E. Logan and L.-T. Wang, JHEP **01**, 099 (2006), [hep-ph/0506313].

[388] M. Perelstein, Prog. Part. Nucl. Phys. **58**, 247 (2007), [hep-ph/0512128].

[389] I. Antoniadis (2001), [hep-th/0102202].

[390] M. Carena *et al.*, Phys. Rev. D **68**, 035010 (2003), [hep-ph/0305188].

[391] K. Agashe *et al.*, JHEP **08**, 050 (2003), [hep-ph/0308036].

[392] I. Gogoladze and C. Macesanu, Phys. Rev. D **74**, 093012 (2006), [hep-ph/0605207].

[393] S. Weinberg, Phys. Rev. Lett. **43**, 1566 (1979).

[394] W. Buchmuller and D. Wyler, Nucl. Phys. B **268**, 621 (1986).

[395] B. Grzadkowski *et al.*, JHEP **10**, 085 (2010), [arXiv:1008.4884].

[396] R. Contino *et al.*, JHEP **07**, 035 (2013), [arXiv:1303.3876].

[397] K. Hagiwara *et al.*, Phys. Rev. D **48**, 2182 (1993).

[398] A. Falkowski, F. Riva and A. Urbano, JHEP **11**, 111 (2013), [arXiv:1303.1812].

[399] A. Pomarol and F. Riva, JHEP **01**, 151 (2014), [arXiv:1308.2803].

[400] J. Ellis, V. Sanz and T. You, JHEP **03**, 157 (2015), [arXiv:1410.7703].

[401] A. Efrati, A. Falkowski and Y. Soreq, JHEP **07**, 018 (2015), [arXiv:1503.07872].

[402] J. de Blas *et al.*, PoS **EPS-HEP2017**, 467 (2017), [arXiv:1710.05402].

[403] G. Altarelli, R. Barbieri and S. Jadach, Nucl. Phys. B **369**, 3 (1992), [Erratum: Nucl.Phys.B 376, 444 (1992)].

[404] G.-C. Cho, K. Hagiwara and S. Matsumoto, Eur. Phys. J. C **5**, 155 (1998), [hep-ph/9707334].

[405] K. Cheung, Phys. Lett. B **517**, 167 (2001), [hep-ph/0106251].

[406] Z. Han and W. Skiba, Phys. Rev. D **71**, 075009 (2005), [hep-ph/0412166].

[407] P. Langacker, M. Luo and A. K. Mann, Rev. Mod. Phys. **64**, 87 (1992).

[408] P. Langacker, Rev. Mod. Phys. **81**, 1199 (2009), [arXiv:0801.1345].

11. Status of Higgs Boson Physics

Revised August 2019 by M. Carena (FNAL; Chicago U.; Chicago U., Kavli Inst.), C. Grojean (Theoriegruppe, DESY, Hamburg; Physik, Humboldt U.), M. Kado (Rome U. Sapienza; INFN, Rome; U. Paris-Saclay, IJCLab) and V. Sharma (UC San Diego).

11.1 Introduction

Understanding the mechanism that breaks the electroweak symmetry and generates the masses of the known elementary particles has been one of the fundamental endeavours in particle physics for several decades. The discovery in 2012 by the ATLAS [1] and the CMS [2] collaborations of a new resonance with a mass of approximately 125 GeV and the subsequent studies of its properties with the full data set from Run 1, from 2009 to 2012, with a centre-of-mass energy of 7 TeV and 8 TeV, conclusively provided a first portrait of the Electroweak Symmetry Breaking (EWSB) mechanism. The data collected during the LHC Run 2, from 2015 to 2018, with a higher centre-of-mass energy of 13 TeV and more conspicuous dataset, put in solid grounds the compatibility of the measured resonance with the Higgs boson of the Standard Model (SM) [3].

In the SM, the electroweak interactions are described by a gauge field theory invariant under the $\mathrm{SU}(2)_L \times \mathrm{U}(1)_Y$ symmetry group. The mechanism of EWSB [4] provides a general framework to keep untouched the structure of these gauge interactions at high energies and still generate the observed masses of the W and Z gauge bosons. The EWSB mechanism posits a self-interacting complex EW doublet scalar field, whose CP-even neutral component acquires a vacuum expectation value (VEV) $v \approx 246\,\mathrm{GeV}$, which sets the scale of the symmetry breaking. Three massless Goldstone bosons are generated and are absorbed to give masses to the W and Z gauge bosons. The remaining component of the complex doublet becomes the Higgs boson – a new, and so far unique, fundamental scalar particle. The masses of all fermions are also a consequence of EWSB since the Higgs doublet is postulated to couple to the fermions through Yukawa interactions

The initial measurements during the LHC Run 1 were accessible mainly through production and decay channels related to the couplings of the Higgs boson to the vector gauge bosons (the mediators of the electroweak interactions, $W^{\pm}$, Z and γ, as well as the gluons, g, mediators of the strong interactions).

The outstanding performance of the LHC Run 2, made it possible for the ATLAS and CMS experiments to independently and unambiguously establish the couplings of the Higgs boson to the charged fermions of the third generation (the top quark, the bottom quark, and the tau). These observations of fundamental importance were made with partial Run 2 datasets.

In all observed production and decay modes measured so far, the rates and differential measurements are found to be consistent, within experimental and theoretical uncertainties, with the SM predictions. In high resolution decay channels, such as the ones with four leptons (electrons or muons) or diphoton final states, the mass of the Higgs boson has been measured at the permill precision level.

Nevertheless, several channels are still out of reach experimentally and the couplings of the Higgs boson to light fermions are yet to be proven. Moreover, within the current precision, a more complex sector with additional states is not ruled out, nor has it been established whether the Higgs boson is an elementary particle or whether it has an internal structure like any other scalar particles observed before it.

Without the Higgs boson, the calculability of the SM would have been spoiled. In particular, perturbative unitarity [5] would be lost at high energies since the longitudinal W/Z boson scattering amplitude would grow with the centre-of-mass energy. In addition, the radiative corrections to the gauge boson self-energies would exhibit dangerous logarithmic divergences that would be difficult to reconcile with EW precision data. With the discovery of the Higgs boson, the SM is a spontaneously broken gauge theory and, as such, it could a priori be consistently extrapolated well above the masses of the W and Z bosons. Hence, formally there is no need for new physics at the EW scale. However, as the SM Higgs boson is a scalar particle, at the quantum level it has sensitivity to possible new physics scales. Quite generally, the Higgs boson mass is affected by the presence of heavy particles and receives quantum corrections which destabilise the weak scale barring a large fine tuning of unrelated parameters. This is known as the Higgs naturalness or hierarchy problem [6]. It has been the prime argument for expecting new physics right at the TeV scale. New theoretical paradigms have been imagined, such as a new fermion-boson symmetry called supersymmetry (SUSY) [7] (for recent reviews, see Refs. [8, 9]), or the existence of strong interactions at a scale of the order of a TeV from which the Higgs boson would emerge as a composite state [10] (see Refs. [11, 12] for recent reviews). Alternatively, new agents stabilising the weak scale could also be light but elusive, like in models of neutral naturalness [13,14]. Other more recent scenarios [15], instead, rely on the cosmological evolution of the Universe to drive the Higgs boson mass to a value much smaller than the cutoff of the theory and aim at alleviating the hierarchy problem without the need for TeV scale new physics, even thought there might still be interesting and spectacular signatures [15, 16]. Beyond the naturalness problem, extensions of the SM Higgs sector without other low-energy particles have been proposed, for example, to provide explanations for the fermion mass hierarchies, see e.g. Ref. [17], to account for the Dark Matter abundance, see e.g. Ref. [18], or to modify the properties of the electroweak phase transition [19]. Such models with additional scalars provide grounds to explore new Higgs boson signals in concrete and complete scenarios, with different types of coupling structure to fermions and gauge bosons.

The Higgs boson is anyway special and, in the eight years since its discovery, it became a powerful tool to explore the manifestations of the SM and to probe the physics landscape beyond it. It might offer direct insights on what comes beyond the weak scale through possible sizeable effects on the Higgs boson properties. The Higgs boson couplings, however, are observed to be in good agreement with their SM predictions. This, together with the strong bounds from precision electroweak and flavour data, leaves open the possibility that the Higgs boson may well be elementary, weakly coupled and solitary up to the Planck scale, rendering the EW vacuum potentially metastable [20].

After completion of the first two runs, the LHC has only gathered approximately 5% of its projected full dataset. During the second long shut down currently underway, the LHC is undergoing important upgrades in order to prepare for its high luminosity phase. The foreseen larger datasets to be collected during Run 3 and ultimately during the High Luminosity LHC (HL-LHC), will enable yet more fundamental and challenging measurements to explore new physics.

This review is organised as follow. Section 11.2 is a theoretical review of the SM Higgs boson, its properties, production mechanisms and decay rates. In Section 11.3, the experimental measurements are described. In Section 11.4, the combination of the main Higgs boson production and decay channels is presented. In Section 11.5, measurements of the main quantum numbers and CP properties of the Higgs boson are reported and the bounds on its total width are discussed. In Section 11.6, a general theoretical framework to describe the deviations of the Higgs boson couplings from the SM predictions is introduced and the experimental measurements of these Higgs couplings is reviewed. Measurements of differential cross sections are outlined. Section 11.7 presents, in detail, some interesting models proposed for extensions of the SM Higgs sector, addressing the hierarchy problem or not, and considers their experimental signatures. Section 11.8 provides a short summary and a brief outlook.

11.2 The Standard Model and the mechanism of electroweak symmetry breaking

In the SM [3], electroweak symmetry breaking [4] is responsible for generating mass for the W and Z gauge bosons rendering the weak interactions short ranged. The SM scalar potential reads:

$$V(\Phi) = m^2\Phi^\dagger\Phi + \lambda(\Phi^\dagger\Phi)^2 \tag{11.1}$$

with the Higgs field Φ being a self-interacting $\mathrm{SU}(2)_L$ complex doublet (four real degrees of freedom) with weak hypercharge $Y{=}1$ (the hypercharge is normalised such that $Q = T_{3L} + Y/2$, Q being the electric charge and T_{3L} the eigenvalue of the diagonal generator of $\mathrm{SU}(2)_L$):

$$\Phi = \frac{1}{\sqrt{2}}\begin{pmatrix}\sqrt{2}\phi^+\\ \phi^0 + ia^0\end{pmatrix}, \tag{11.2}$$

where ϕ^0 and a^0 are the CP-even and CP-odd neutral components, and ϕ^+ is the complex charged component of the Higgs doublet, respectively. $V(\Phi)$ is the most general renormalisable scalar potential. If the quadratic term is negative, the neutral component of the scalar doublet acquires a non-zero vacuum expectation value (VEV)

$$\langle\Phi\rangle = \frac{1}{\sqrt{2}}\begin{pmatrix}0\\ v\end{pmatrix}, \tag{11.3}$$

with $\phi^0 = H + \langle\phi^0\rangle$ and $\langle\phi^0\rangle \equiv v$, inducing the spontaneous breaking of the SM gauge symmetry $\mathrm{SU}(3)_C \times \mathrm{SU}(2)_L \times \mathrm{U}(1)_Y$ into $\mathrm{SU}(3)_C \times \mathrm{U}(1)_{\mathrm{em}}$. The global minimum of the theory defines the ground state, and spontaneous symmetry breaking implies that there is a (global and/or local) symmetry of the system that is not respected by the ground state. From the four generators of the $\mathrm{SU}(2)_L \times \mathrm{U}(1)_Y$ SM gauge group, three are spontaneously broken, implying that they lead to non-trivial transformations of the ground state and indicate the existence of three massless Goldstone bosons identified with three of the four Higgs field degrees of freedom. The Higgs field couples to the W_μ and B_μ gauge fields associated with the $\mathrm{SU}(2)_L \times \mathrm{U}(1)_Y$ local symmetry through the covariant derivative appearing in the kinetic term of the Higgs Lagrangian,

$$\mathcal{L}_{\mathrm{Higgs}} = (D_\mu\Phi)^\dagger(D^\mu\Phi) - V(\Phi), \tag{11.4}$$

where $D_\mu\Phi = (\partial_\mu + ig\sigma^a W^a_\mu/2 + ig'YB_\mu/2)\Phi$, g and g' are the $\mathrm{SU}(2)_L$ and $\mathrm{U}(1)_Y$ gauge couplings, respectively, and $\sigma^a, a = 1,2,3$ are the usual Pauli matrices. As a result, the neutral and the two charged massless Goldstone degrees of freedom mix with the gauge fields corresponding to the broken generators of $\mathrm{SU}(2)_L \times \mathrm{U}(1)_Y$ and become, in the unitarity gauge, the longitudinal components of the Z and W physical gauge bosons, respectively. The Z and W gauge bosons acquire masses,

$$m_W^2 = \frac{g^2v^2}{4}, \quad m_Z^2 = \frac{(g'^2+g^2)v^2}{4}. \tag{11.5}$$

The fourth generator remains unbroken since it is the one associated to the conserved $\mathrm{U}(1)_{\mathrm{em}}$ gauge symmetry, and its corresponding gauge field, the photon, remains massless. Similarly the eight color gauge bosons, the gluons, corresponding to the conserved $\mathrm{SU}(3)_C$ gauge symmetry with 8 unbroken generators, also remain massless (though confined inside hadrons and mesons as the result of the asymptotic freedom behaviour of QCD). Hence, from the initial four degrees of freedom of the Higgs field, two are absorbed by the $W^\pm$ gauge bosons, one by the Z gauge boson, and there is one remaining degree of freedom, H, that is the physical Higgs boson — a new scalar particle first imagined by P. Higgs [4]. The Higgs boson is neutral under the electromagnetic interactions and transforms as a singlet under $\mathrm{SU}(3)_C$ and hence does not couple at tree level to the massless photons and gluons.

The fermions of the SM acquire mass through renormalisable interactions between the Higgs field and the fermions: the Yukawa interactions,

$$\mathcal{L}_{\mathrm{Yukawa}} = -\hat{h}_{d_{ij}}\,\bar{q}_{L_i}\Phi\,d_{R_j} - \hat{h}_{u_{ij}}\,\bar{q}_{L_i}\tilde{\Phi}u_{R_j} - \hat{h}_{l_{ij}}\,\bar{l}_{L_i}\Phi\,e_{R_j} + h.c., \tag{11.6}$$

which respect the symmetries of the SM but generate fermion masses once EWSB occurs. In the Lagrangian above, $\tilde{\Phi} = i\sigma_2\Phi^*$ and q_L (l_L) and u_R, d_R (e_R) are the quark (lepton) $\mathrm{SU}(2)_L$ doublets and singlets, respectively, while in each term, $\hat{h}_{X_{ij}}$ is parametrised by a 3×3 matrix in family space. The mass term for neutrinos is omitted, but could be added in an analogous manner to the up-type quarks when right-handed neutrinos are supplementing the SM particle content (neutrinos can also acquire Majorana masses via non-renormalisable dimension-5 interactions with the Higgs field [21]). Once the Higgs field acquires a VEV, and after rotation to the fermion mass eigenstate basis that also diagonalises the Higgs-fermion interactions, $\hat{h}_{f_{ij}} \to h_{f_i}\delta_{ij}$, all fermions acquire a mass given by $m_{f_i} = h_{f_i}v/\sqrt{2}$. The indices $i,j = 1,2,3$ refer to the three families in the up-quark, down-quark or charged lepton sectors. It should be noted that the EWSB mechanism provides no additional insight on possible underlying reasons for the large variety of masses of the fermions, often referred to as the flavour hierarchy. The fermion masses, accounting for a large number of the free parameters of the SM, are simply translated into Yukawa couplings.

11.2.1 *The SM Higgs boson mass, couplings and quantum numbers*

The SM Higgs boson is a CP-even scalar of spin 0. Its mass is given by $m_H = \sqrt{2\lambda}\,v$, where λ is the self coupling parameter in $V(\Phi)$. The expectation value of the Higgs field, $v = (\sqrt{2}G_F)^{-1/2} \approx 246\,\mathrm{GeV}$, is fixed by the Fermi coupling G_F, which is determined with a precision of 0.6 ppm from muon decay measurements [22]. The quartic coupling λ is a free parameter in the SM, and hence, there is no a priori prediction for the Higgs mass. Moreover the sign of the mass parameter $m^2 = -\lambda v^2$ has to be negative for the EW symmetry breaking to take place, but there is no a priori understanding of what decides of this sign. The experimentally measured Higgs boson mass, $m_H = 125.10 \pm 0.14\,\mathrm{GeV}$ [22], implies that $\lambda \simeq 0.13$ and $|m| \simeq 88.4\,\mathrm{GeV}$.

The Higgs boson couplings to the fundamental particles are set by their masses. This is a new type of interaction; very weak for light particles, such as up and down quarks, and electrons, but strong for heavy particles such as the W and Z bosons and the top quark. More precisely, the SM Higgs couplings to fundamental fermions are linearly proportional to the fermion masses, whereas the couplings to bosons are proportional to the square of the boson masses. The SM Higgs boson couplings to gauge bosons and fermions, as well as the Higgs boson self coupling, are summarised in the following Lagrangian:

$$\mathcal{L} = -g_{Hf\bar{f}}\bar{f}fH + \frac{g_{HHH}}{6}H^3 + \frac{g_{HHHH}}{24}H^4 + \delta_V V_\mu V^\mu \left(g_{HVV}H + \frac{g_{HHVV}}{2}H^2\right) \quad (11.7)$$

with

$$g_{Hf\bar{f}} = \frac{m_f}{v},\ g_{HVV} = \frac{2m_V^2}{v},\ g_{HHVV} = \frac{2m_V^2}{v^2},\ g_{HHH} = \frac{3m_H^2}{v},\ g_{HHHH} = \frac{3m_H^2}{v^2}, \quad (11.8)$$

where $V = W^\pm$ or Z and $\delta_W = 1, \delta_Z = 1/2$. As a result, the dominant mechanisms for Higgs boson production and decay involve the coupling of H to W, Z and/or the third generation quarks and leptons. The Higgs boson coupling to gluons [23,24] is induced at leading order by a one-loop process in which H couples to a virtual $t\bar{t}$ pair (with minor contributions from the other lighter quarks). Likewise, the Higgs boson coupling to photons is also generated via loops, although in this case the one-loop graph with a virtual W^+W^- pair provides the dominant contribution [25] and it is interfering with the smaller contribution involving a virtual $t\bar{t}$ pair (as such, the Higgs coupling to photons is sensitive to the relative phase of the interactions between bosons and fermions).

11.2.2 *The SM custodial symmetry*

The SM Higgs Lagrangian, $\mathcal{L}_{\text{Higgs}} + \mathcal{L}_{\text{Yukawa}}$ of Eq. (11.4) and Eq. (11.6), is, by construction, $\text{SU}(2)_L \times \text{U}(1)_Y$ gauge invariant, but it also has an approximate global symmetry. In the limit $g' \to 0$ and $h_f \to 0$, the Higgs sector has a global $\text{SU}(2)_R$ symmetry, and hence it is invariant under a global $\text{SU}(2)_L \times \text{SU}(2)_R$ symmetry, with $\text{SU}(2)_L$ just being the global variant of the SM chiral gauge symmetry. This symmetry is preserved for non-vanishing Yukawa couplings, provided $h_u = h_d$. Once the Higgs acquires a VEV, both the $\text{SU}(2)_L$ and $\text{SU}(2)_R$ symmetry groups are broken but the diagonal subgroup $\text{SU}(2)_{L+R}$ remains unbroken and it is the subgroup that defines the custodial symmetry of the SM [26].

In the limit $g' \to 0$, the W and Z gauge bosons have equal mass and form a triplet of the $\text{SU}(2)_{L+R}$ unbroken global symmetry. Using the expressions for the W and Z gauge boson masses in term of the gauge couplings, one obtains at tree level

$$\frac{m_W^2}{m_Z^2} = \frac{g^2}{g'^2 + g^2} = \cos^2\theta_W \quad \text{or} \quad \rho \equiv \frac{m_W^2}{m_Z^2 \cos^2\theta_W} = 1. \quad (11.9)$$

The custodial symmetry protects the above relation from large radiative corrections. All corrections to the ρ parameter are therefore proportional to terms that break the custodial symmetry. For instance, radiative corrections involving the Higgs boson are proportional to $\sin^2\theta_W$, $\delta\rho = -11G_F m_Z^2 \sin^2\theta_W \log(m_H^2/m_Z^2)/(24\sqrt{2}\pi^2)$, and vanish in the limit $g' \to 0$. Since $m_t \neq m_b$, there are also relevant radiative corrections generated by massive fermions. They are proportional to $m_t^2 + m_b^2 - 2(m_t^2 m_b^2)\log(m_t^2/m_b^2)/(m_t^2 - m_b^2)$ and would indeed vanish for $m_t = m_b$ [27].

11.2.3 *Stability of the Higgs potential*

The discovery of the Higgs boson with $m_H \approx 125\,\text{GeV}$ has far reaching consequences within the SM framework. In particular, the precise value of m_H determines the value of the quartic coupling λ at the electroweak scale and makes it possible to study its behavior up to high energy scales. A larger value of m_H would have implied that the self coupling λ would become non-perturbative at some scale Λ that could be well below the Planck scale [28].

However, for the value of Higgs boson mass experimentally measured, the EW vacuum of the Higgs potential is most likely metastable [20]. The high energy evolution of λ shows that it becomes negative at energies $\Lambda = \mathcal{O}(10^{11})\,\text{GeV}$ (even though λ could remain positive till higher energy, maybe all the way to the Planck scale, if the top quark mass exceeds its current measured value by 3σ). When this occurs, the SM Higgs potential develops an instability and the long term existence of the EW vacuum is challenged. This behaviour may call for new physics at an intermediate scale before the instability develops, i.e., below M_{Planck}, even though new physics at M_{Planck} could influence the stability of the EW vacuum and possibly modify this conclusion [29]. The consequences of the instability of the EW vacuum on high-scale inflation have been discussed in Ref. [30]. It was also noticed that Higgs field fluctuations during inflation could seed the formation of primordial black holes, possibly making up the Dark Matter relic abundance [31] or they could produce a stochastic background of gravitational waves with characteristic structures [32], offering a probe of the EW vacuum near criticality.

The lifetime of the EW metastable vacuum is determined by the rate of quantum tunnelling from this vacuum into the true vacuum of the theory (for the most recent computation of the EW vacuum lifetime within the SM, see Ref. [33]). Within the SM, the running of the Higgs self coupling slows down at high energies with a cancellation of its β-function at energies just one to two orders of magnitude below the Planck scale [34]. This slow evolution of the quartic coupling is responsible for saving the EW vacuum from premature collapse. It might also help the Higgs boson to play the role of an inflaton [35] (see, however, Ref. [36] for potential issues with this Higgs-boson-as-an-inflaton idea).

11.2.4 *Higgs boson production and decay mechanisms*

Reviews of the SM Higgs boson's properties and phenomenology, with an emphasis on the impact of loop corrections to the Higgs boson decay rates and cross sections, can be found in Refs. [37–44].

11.2.4.1 *Production mechanisms at hadron colliders*

The main production mechanisms at the Tevatron collider and the LHC are gluon fusion (ggF), weak-boson fusion (VBF), associated production with a gauge boson (VH), and associated production with a pair of $t\bar{t}$ quarks ($t\bar{t}H$) or with a single top quark (tHq). Figure 11.1 depicts representative diagrams for these dominant Higgs boson production processes.

The state-of-the-art of the theoretical calculations in the main different production channels is summarized in Table 11.1.

The cross sections for the production of a SM Higgs boson as a function of $\sqrt{s}$, the center of mass energy, for pp collisions, including bands indicating the theoretical uncertainties, are summarised in Fig. 11.2 (left) [45]. A detailed discussion, including uncertainties in the theoretical calculations due to missing higher-order effects and experimental uncertainties on the determination of SM parameters involved in the calculations, can be found in Refs. [41–44]. These references also contain state-of-the-art discussions on the impact of PDF uncertainties, QCD scale uncertainties and uncertainties due to different procedures for including higher-order corrections matched to parton shower simulations, as well as uncertainties due to hadronisation and parton-shower events.

Table 11.2 summarises the Higgs boson production cross sections and relative uncertainties for a Higgs boson mass of 125 GeV, for $\sqrt{s} = 7$, 8, 13 and 14 TeV. The Higgs boson production cross sections in $p\bar{p}$ collisions at $\sqrt{s} = 1.96\,\text{TeV}$ for the Tevatron are obtained from Ref. [46].

i. *Gluon fusion production mechanism*

At high-energy hadron colliders, the Higgs boson production mechanism with the largest cross section is the gluon-fusion process, $gg \to H + X$, mediated by the exchange of a virtual, heavy top quark [47]. Contributions from lighter quarks propagating in the loop are suppressed proportionally to m_q^2. QCD radiative corrections to the gluon-fusion process are very important and have been studied in detail. Including the full dependence on the

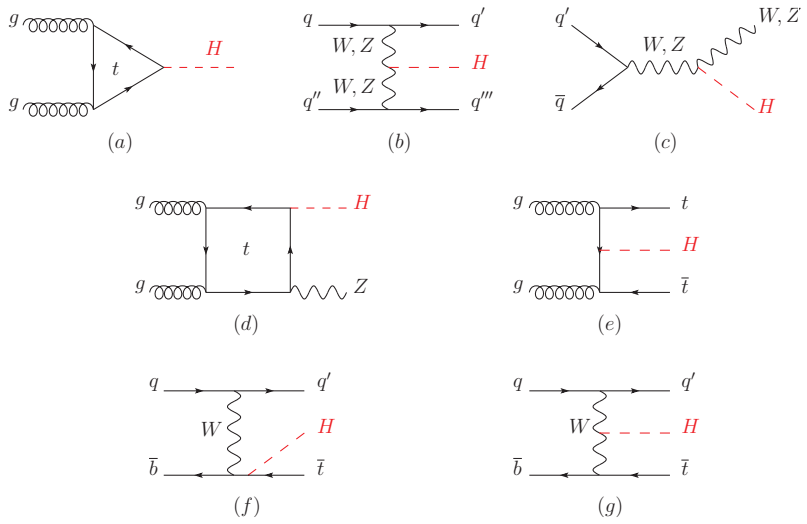

Figure 11.1: Main leading order Feynman diagrams contributing to the Higgs boson production in (a) gluon fusion, (b) Vector-boson fusion, (c) Higgs-strahlung (or associated production with a gauge boson at tree level from a quark-quark interaction), (d) associated production with a gauge boson (at loop level from a gluon-gluon interaction), (e) associated production with a pair of top quarks (there is a similar diagram for the associated production with a pair of bottom quarks), (f-g) production in association with a single top quark

Table 11.1: State-of-the-art of the theoretical calculations in the main Higgs boson production channels in the SM, and the major MC tools used in the simulations

ggF	VBF	VH	$t\bar{t}H$
Fixed order:	Fixed order:	Fixed order:	Fixed order:
N3LO QCD + NLO EW	NNLO QCD	NLO QCD+EW	NLO QCD+EW
`(HIGLU, iHixs, FeHiPro, HNNLO)`	`(VBF@NNLO)`	`(V2HV and HAWK)`	`(Powheg)`
Resummed:	Fixed order:	Fixed order:	`(MG5_aMC@NLO)`
NNLO + NNLL QCD	NLO QCD + NLO EW	NNLO QCD	
`(HRes)`	`(HAWK)`	`(VH@NNLO)`	
Higgs p_T:			
NNLO+NNLL			
`(HqT, HRes)`			
Jet Veto:			
N3LO+NNLL			

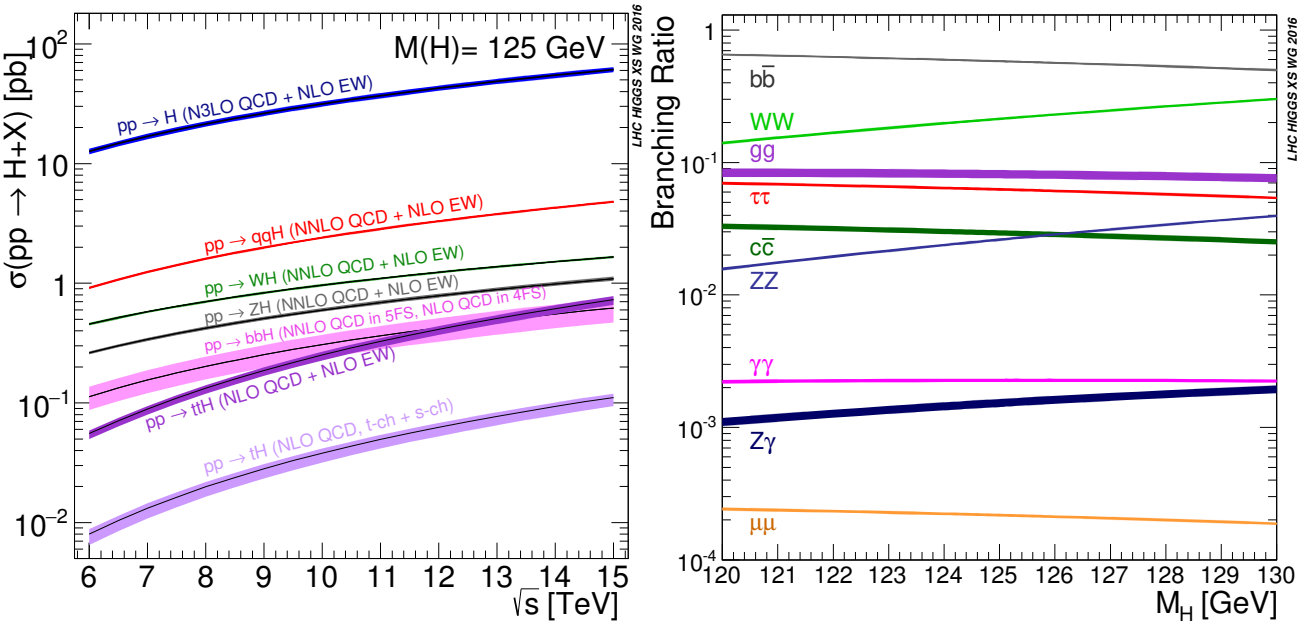

Figure 11.2: (Left) The SM Higgs boson production cross sections as a function of the center of mass energy, $\sqrt{s}$, for pp collisions [45]. The VBF process is indicated here as qqH. The theoretical uncertainties are indicated as bands. (Right) The branching ratios for the main decays of the SM Higgs boson near $m_H = 125\,\text{GeV}$ [43, 44]. The theoretical uncertainties are indicated as bands.

(top, bottom, charm) quark and Higgs boson masses, the cross section has been calculated at the next-to-leading order (NLO)

Table 11.2: The SM Higgs boson production cross sections for $m_H = 125\,\text{GeV}$ in pp collisions ($p\bar{p}$ collisions at $\sqrt{s} = 1.96\,\text{TeV}$ for the Tevatron), as a function of the center of mass energy, $\sqrt{s}$. The predictions for the LHC energies are taken from Refs. [41–44], the ones for the Tevatron energy are from Ref. [46]. The predictions for the ggF channel at the LHC include the latest N3LO results leading to reduced theoretical uncertainties by a factor around 2 compared to the NNLO+NLL results. The total uncertainties are estimated assuming no correlations between α_S and PDF uncertainties.

$\sqrt{s}$ (TeV)	Production cross section (in pb) for $m_H = 125\,\text{GeV}$					
	ggF	VBF	WH	ZH	$t\bar{t}H$	total
1.96	$0.95^{+17\%}_{-17\%}$	$0.065^{+8\%}_{-7\%}$	$0.13^{+8\%}_{-8\%}$	$0.079^{+8\%}_{-8\%}$	$0.004^{+10\%}_{-10\%}$	1.23
7	$16.9^{+4.4\%}_{-7.0\%}$	$1.24^{+2.1\%}_{-2.1\%}$	$0.58^{+2.2\%}_{-2.3\%}$	$0.34^{+3.1\%}_{-3.0\%}$	$0.09^{+5.6\%}_{-10.2\%}$	19.1
8	$21.4^{+4.4\%}_{-6.9\%}$	$1.60^{+2.3\%}_{-2.1\%}$	$0.70^{+2.1\%}_{-2.2\%}$	$0.42^{+3.4\%}_{-2.9\%}$	$0.13^{+5.9\%}_{-10.1\%}$	24.2
13	$48.6^{+4.6\%}_{-6.7\%}$	$3.78^{+2.2\%}_{-2.2\%}$	$1.37^{+2.6\%}_{-2.6\%}$	$0.88^{+4.1\%}_{-3.5\%}$	$0.50^{+6.8\%}_{-9.9\%}$	55.1
14	$54.7^{+4.6\%}_{-6.7\%}$	$4.28^{+2.2\%}_{-2.2\%}$	$1.51^{+1.9\%}_{-2.0\%}$	$0.99^{+4.1\%}_{-3.7\%}$	$0.60^{+6.9\%}_{-9.8\%}$	62.1

in α_s [48, 49]. To a very good approximation, the leading top-quark contribution can be evaluated in the limit $m_t \to \infty$ by matching the SM to an effective theory. The gluon-fusion amplitude is then evaluated from an effective Lagrangian containing a local $HG^a_{\mu\nu}G^{a\,\mu\nu}$ operator [23, 24]. In this approximation, the cross section is known at next-to-next-to-next-to-leading order (N3LO) [50]. The validity of the effective theory with infinite m_t is greatly enhanced by rescaling the result by the exact LO result: $\sigma = (\sigma^{\text{LO}}_{m_t}/\sigma^{\text{LO}}_{m_t=\infty}) \times \sigma_{m_t=\infty}$ [44]. The large top-quark mass approximation, after this rescaling of the cross section, yields a NNLO result that has been established to be at the percent level accuracy [51]. Further progress is made to include full top mass dependence at NNLO [52].

The LO and NLO QCD corrections [53] amount to about 80% of the total N3LO cross section. The NNLO corrections [54] further enhance the cross section by approximately 30% of the LO plus NLO result (at $\mu_f = \mu_r = m_H/2$). Electroweak radiative corrections have been computed at NLO and increase the LO cross section by about 5% for $m_H \simeq 125\,\text{GeV}$ [55]. Mixed QCD-EW corrections are now being investigated with encouraging results on the computation of the exact 3-loop amplitude [56] complementing the results obtained in either limit of heavy [57] or massless [58] gauge bosons.

At N3LO, the perturbation series is rather stable with a mere enhancement of 3% of the total cross section, with a central value quite insensitive to threshold resummation effects with the scale choice mentioned above [44, 50, 59]. At the LHC with a center-of-mass energy of 13 TeV, the most up-to-date value for the production cross section of a 125 GeV Higgs boson amounts to [44]

$$\sigma^{\text{N3LO}}_{\text{ggF}} = 48.6\,\text{pb}^{+2.2\,\text{pb}\,(+4.6\%)}_{-3.3\,\text{pb}\,(-6.7\%)}\,(\text{theory}) \pm 1.6\,\text{pb}\,(3.2\%)\,(\text{PDF}+\alpha_s). \tag{11.10}$$

Besides considering the inclusive Higgs boson production cross section at the LHC, it is important to study differential distributions in order to probe the properties of the Higgs boson in a detailed way. A more exclusive account of Higgs boson production is also required because experimental analyses often impose cuts on the final states in order to improve the signal-to-background ratio. To this end, it is useful to define benchmark cuts and compare the differential distributions obtained at various levels of theoretical accuracy (i.e., at NLO or NNLO) with Monte-Carlo generators. In the infinite top mass limit, the Higgs boson p_T distribution is known at NNLO [60, 61] (see Ref. [62] for a recent reappraisal) and heavy quark mass effects, including top-bottom interferences, have been computed at NLO [63], revealing a non-trivial logarithmic structure that will make resummation difficult [64]. A programatic approach for a fixed-order/resummation matching of the top-bottom interferences has been proposed [65]. Many search modes for the Higgs boson are carried out by separating the events according to the number of jets or the transverse momentum and rapidity of the Higgs boson. For $p_T < 35\,\text{GeV}$, predictions for the transverse-momentum distribution can only be trusted after large logarithms of the form $\alpha_s^n \ln^k(m_H/p_T^{\text{veto}})$, $k \leq 2n-1$, and (non-Sudakov) double logarithms of the form $g_{Hq\bar{q}}\, m_q/m_H[\ln^2(m_H/m_q), \ln^2(p_T/m_q)]$ have been resummed. This has been accomplished with N3LL accuracy [66] and the results have been matched onto the fixed-order prediction at NNLO [67]. In addition, impressive progress is made to improve the calculation of the Higgs boson production cross section with a jet veto (the "0-jet bin" or in the presence of a veto bounding the transverse momentum of the hardest accompanying jet) [68], reaching N2LL accuracy matched to N3LO. These accurate predictions for the jet-veto cross section are required, e.g., to suppress the $t\bar{t}$ background in the $H \to WW$ channel [69]. Electroweak corrections have been studied in Ref. [70]. Note that in the boosted regime, at $p_T \sim 1\,\text{TeV}$, VH takes over ggF as the dominant channel [71].

ii. *Vector boson fusion production mechanism*

The SM Higgs boson production mode with the second-largest cross section at the LHC is vector boson fusion. At the Tevatron collider, VBF also occurred, but for $m_H = 125\,\text{GeV}$ had a smaller cross section than Higgs boson production in association with a W or Z boson. Higgs boson production via VBF, $qq \to qqH$, proceeds by the scattering of two (anti-)quarks, mediated by t- or u-channel exchange of a W or Z boson, with the Higgs boson radiated off the weak-boson propagator. The scattered quarks give rise to two back-to-back hard jets in the forward and backward regions of the detector [72]. Because of the color-singlet nature of the weak-gauge boson exchange, gluon radiation from the central-rapidity regions is strongly suppressed. These characteristic features of VBF processes can be exploited to distinguish them from overwhelming QCD backgrounds, including gluon-fusion induced Higgs boson + 2 jet production, and from s-channel WH or ZH production with a hadronically decaying weak gauge boson. After the application of specific selection cuts, the VBF channel provides a clean environment, not only for the Higgs boson searches originally performed, but also for the subsequent determination of Higgs boson couplings at the LHC.

At the inclusive level, the cross-section is known at N3LO [73], with a residual uncertainty of the order of few permill. However, this result is obtained in the DIS/factorised approximation [74] where the fusing gauge bosons are emitted from the two quark legs independently. While, the exact NNLO VBF calculation will remain out-of-reach in the near future, the leading non-factorisable contributions with two forward jets have been estimated [75]. They give some corrections, also of the order of few permill, to inclusive quantities, but they are an order of magnitude larger for differential observables. Full NNLO QCD and NLO EW results in the DIS approximation are known [76] and the residual uncertainty is of the order of a few percent but is quite sensitive to the tagging jet cuts and jet radius modelling [77].

iii. *WH and ZH associated production mechanism*

The next most relevant Higgs boson production mechanisms after ggF and VBF at the LHC, and the most relevant ones after ggF at the Tevatron collider, are associated production with W and Z gauge bosons. The cross sections for the associated production processes, $pp \to VH + X$, with $V = W^{\pm}, Z$ receive contributions at NLO given by NLO QCD corrections to the Drell–Yan cross section [78, 79] and from NLO EW corrections. The latter, unlike the QCD corrections, do not respect the factorisation into Drell–Yan production since there are irreducible box contributions already at one loop [80]. At NNLO, the Drell–Yan-like corrections

to WH production also give the bulk of the corrections to ZH production [81]. For ZH production there are, however, gluon-gluon induced contributions that do not involve a virtual Z gauge boson but are such that the Z gauge boson and H boson couple to gluons via top-quark loops [82], see diagram (d) in Fig. 11.1. In addition, WH and ZH production receive non Drell–Yan-like corrections in the $q\bar{q}'$ and $q\bar{q}$ initiated channels, respectively, at the NNLO level, where the Higgs boson is radiated off top-quark loops [83]. The full QCD corrections up to NNLO order, the NLO EW corrections and the NLO corrections to the gluon-gluon channel are available in `VH@NNLO` [84].

As neither the Higgs boson nor the weak gauge bosons are stable particles, their decays also have to be taken into account. Providing full kinematical information for the decay products can furthermore help in the suppression of large QCD backgrounds. Differential distributions for the processes $pp \to WH \to \bar{\nu}_\ell \ell H$ and $pp \to ZH \to \ell^+\ell^- H/\nu_\ell \bar{\nu}_\ell H$, including NLO QCD and EW corrections, have been presented in Ref. [85]. The NNLO QCD corrections to differential observables for WH production at the LHC, including the leptonic decays of the W boson and the decay of the Higgs boson into a $b\bar{b}$ pair, are presented in Ref. [86]. Calculations at the same level, including also the ZH process have been performed [87]. The WH production mode has also been matched to a parton shower at NNLO accuracy [88]. Full NNLO results for both the production and decay are available [89] and show a large impact of radiation from the final-state bottoms. The WH and ZH production modes, especially in the boosted regime, provide a relatively clean environment for studying the decay of the Higgs boson into bottom quarks [90].

iv. *Higgs boson production in association with $t\bar{t}$*

Higgs boson radiation off top quarks, $pp \to t\bar{t}H$, provides a direct probe of the top-Higgs Yukawa coupling. The LO cross section for this production process was computed in Ref. [91]. Later, the NLO(+NNLL) QCD [92] and NLO EW corrections [93] were evaluated yielding a moderate increase in the total cross section of at most 20%, but significantly reducing the scale dependence of the inclusive cross section. The EW corrections can be enhanced by large electroweak Sudakov logarithms in particular in the boosted regime often used in the phenomenological analyses [94]. The total theoretical errors, estimated by combining the uncertainties from factorisation and renormalisation scales, strong gauge coupling, and parton distributions, amount to 10–15% of the corresponding inclusive cross section. Interfaces between NLO QCD calculations for $t\bar{t}H$ production with parton-shower Monte-Carlo programs have been provided in Ref. [95]. These programs provide the most flexible tools to date for the computation of differential distributions, including experimental selection cuts and vetoes on the final-state particles and their decay products. The fixed-order NLO QCD calculation have been interfaced with the standard Parton Shower Monte-Carlo generators, allowing an accurate description of the $t\bar{t}H$ signal, from the energy scale of the hard scattering to the hadronisation energy scale. The exploitation of this channel requires, however, a proper description of the background, in particular $t\bar{t}b\bar{b}$, which exhibits a huge k-factor[1] enhancement from shower effects, see Ref. [44] for a detailed discussion.

v. *Other single Higgs boson production mechanisms at the LHC*

The Higgs boson production in association with a single top quark, though subdominant, can bring valuable information, in particular regarding the sign of the top Yukawa coupling. This is due to an almost totally destructive interference between two large contributions, one where the Higgs boson couples to a space-like W boson and the other where it couples to the top quark. This process has been computed at NLO in a five-flavour scheme [96] and amounts to about 90 fb at $\sqrt{s} = 14\,\text{TeV}$ (with the opposite sign of the top Yukawa coupling, the cross section increases by one order of magnitude while the cross section for associated production with a pair of top quarks is unaffected).

The Higgs boson production in association with a pair of bottom quarks ($b\bar{b}H$) is known at NNLO in the case of five quark flavours [97–99]. The coupling of the Higgs boson to a b-quark is suppressed in the SM by the bottom-quark mass over the Higgs VEV, m_b/v, implying that associated production of a SM Higgs boson with b-quarks is small at the LHC. Yet, at high energy, large logarithms are present and need to be resummed, leading to an enhancement of the inclusive cross section. At $\sqrt{s} = 14\,\text{TeV}$, the $b\bar{b}H$ cross section can be as large as 550 fb, still two orders of magnitude below the ggF production cross section. In a two Higgs doublet model or a SUSY model, which will be discussed in Section 11.7, this coupling is proportional to the ratio of neutral Higgs boson vacuum expectation values, $\tan\beta$, and can be significantly enhanced for large values of this ratio. Consequently, the $b\bar{b}H$ mode can even become the dominant production process for the Higgs boson, unlike in the SM.

The Higgs boson production in association with charm quarks is also known at NNLO and its cross section is approximately 85 fb at $\sqrt{s} = 13\,\text{TeV}$ [44].

vi. *Double Higgs boson production at the LHC*

The main interest in the double Higgs boson production is that it can provide invaluable information on the Higgs potential. In particular, it gives access to the Higgs trilinear self coupling. The dominant production is via gluon fusion $gg \to HH$. It accounts for more than 90% of the total inclusive cross-section, the subleading production mechanisms are VBF $HHjj$ (around 1.7 fb at 13 TeV), HHW (0.50 fb), HHZ (0.36 fb) and $t\bar{t}HH$ (0.8 fb). The fixed order QCD corrections, computed in the infinite top mass limit, are large, typically doubling the cross section from LO to NLO [100] and further enhancing it by 20% from NLO to NNLO [101] to reach at 13 TeV [45]

$$\sigma(gg \to HH)^{\text{NNLO, FTa}}_{\text{ggF}} = 31.05\,\text{fb}^{+2.2\%}_{-5.0\%}\,(\text{theory}) \pm 3\%\,(\text{PDF} + \alpha_s) \pm 2.6\%\,(m_t). \tag{11.11}$$

Recently, the complete NLO corrections with all top quark mass effects also became available numerically [102, 103], intriguingly revealing a k-factor much less flat than predicted in the large top mass approximations. The non-trivial dependence of the results on the renormalisation scheme and scale for the top quark mass [103] questions the assessment of the scale uncertainty and would warrant a proper NNLO computation that will however remain out of reach for quite some time. At the differential level, the destructive interference between the box and the triangle contributions complicates the predictions made in the infinite top mass limit for both the HH invariant mass and the leading Higgs boson p_T distributions. With an inclusive cross section of about 35 fb at $\sqrt{s} = 13\,\text{TeV}$ and a difficult signal vs background discrimination, the double Higgs boson production remains a challenging channel to probe and will greatly benefit from the high-luminosity run of the LHC [104].

11.2.4.2 *Production mechanisms at e^+e^- colliders*

The dominant Higgs boson production cross sections at an e^+e^- collider are from the Higgs-strahlung process [23, 105], $e^+e^- \to ZH$, and the WW fusion process [106], $e^+e^- \to \bar{\nu}_e\nu_e W^*W^* \to \bar{\nu}_e\nu_e H$. The cross-section for the Higgs-strahlung process scales as s^{-1} and is predominant at low energies, while the cross-section for the WW fusion process scales as $\ln(s/m_H^2)$ and dominates at high energies [107]. The ZZ fusion mechanism, $e^+e^- \to e^+e^- Z^*Z^* \to e^+e^- H$, also contributes to the Higgs boson production, with a cross-section suppressed by an order of magnitude with respect to that of WW fusion. The process $e^+e^- \to t\bar{t}H$ [108] becomes important for $\sqrt{s} \geq 500\,\text{GeV}$. For a more detailed discussion of Higgs boson production properties at lepton colliders, see for example Ref. [109].

[1] the k-factor is defined as the ratio of a physical quantity with and without radiative corrections included.

11.2.4.3 *SM Higgs boson branching ratios and total width*

For the understanding and interpretation of the experimental results, the computation of all relevant Higgs boson decay widths is essential, including an estimate of their uncertainties and, when appropriate, the effects of Higgs boson decays into off-shell particles with successive decays into lighter SM ones. A Higgs boson mass of about 125 GeV allows to explore the Higgs boson couplings to many SM particles. In particular the dominant decay modes are $H \to b\bar{b}$ and $H \to WW^*$, followed by $H \to gg$, $H \to \tau^+\tau^-$, $H \to c\bar{c}$ and $H \to ZZ^*$. With much smaller rates follow the Higgs boson decays into $H \to \gamma\gamma$, $H \to \gamma Z$ and $H \to \mu^+\mu^-$. Since the decays into gluons, diphotons and $Z\gamma$ are loop induced, they provide indirect information on the Higgs boson couplings to WW, ZZ and $t\bar{t}$ in different combinations. The uncertainties in the branching ratios include the missing higher-order corrections in the theoretical calculations as well as the errors in the SM input parameters, in particular fermion masses and the QCD gauge coupling, involved in the decay. In the following the state-of-the-art of the theoretical calculations will be discussed and the reader is referred to Refs. [41–44, 110] for detail.

The evaluation of the radiative corrections to the fermionic decays of the SM Higgs boson are implemented in HDECAY [111] at different levels of accuracy. The computations of the $H \to b\bar{b}$ and $H \to c\bar{c}$ decays include the complete massless QCD corrections up to N4LO, with a corresponding scale dependence of about 0.1% [112]. Both the electroweak corrections to $H \to b\bar{b}$, $c\bar{c}$ as well as $H \to \tau^+\tau^-$ are known at NLO [113] providing predictions with an overall accuracy of about 1–2% for $m_H \simeq 125\,\text{GeV}$.

The loop induced decays of the SM Higgs boson are known fully at NLO and partially beyond that approximation. For $H \to gg$, the QCD corrections are known up to N3LO in the limit of heavy top quarks [49,114] and the uncertainty from the scale dependence is about 3%. For the $H \to \gamma\gamma$, the full NLO QCD corrections are available [49, 115] and the three-loop QCD corrections have also been evaluated [116]. The NLO electroweak corrections to $H \to gg$ and $H \to \gamma\gamma$ have been computed in Ref. [117]. All these corrections are implemented in HDECAY [111]. For $m_H \simeq 125\,\text{GeV}$, the overall impact of known QCD and EW radiative effects turns out to be well below 1%. In addition, the contribution of the $H \to \gamma e^+ e^-$ decay via virtual photon conversion has been computed in Ref. [118]. The partial decay width $H \to Z\gamma$ is only implemented at LO in HDECAY, including the virtual W, top-, bottom-, and τ-loop contributions. The QCD corrections have been calculated and are at the percent level [119]. The theoretical uncertainty due to unknown electroweak corrections is estimated to be less than 5%, an accuracy that will be hard to achieve in the measurement of this process at the LHC.

Table 11.3: The branching ratios and the relative uncertainty [43, 44] for a SM Higgs boson with $m_H = 125\,\text{GeV}$.

Decay channel	Branching ratio	Rel. uncertainty
$H \to \gamma\gamma$	2.27×10^{-3}	2.1%
$H \to ZZ$	2.62×10^{-2}	±1.5%
$H \to W^+W^-$	2.14×10^{-1}	±1.5%
$H \to \tau^+\tau^-$	6.27×10^{-2}	±1.6%
$H \to b\bar{b}$	5.82×10^{-1}	$^{+1.2\%}_{-1.3\%}$
$H \to c\bar{c}$	2.89×10^{-2}	$^{+5.5\%}_{-2.0\%}$
$H \to Z\gamma$	1.53×10^{-3}	±5.8%
$H \to \mu^+\mu^-$	2.18×10^{-4}	±1.7%

The decays $H \to WW/ZZ \to 4f$ can be simulated with the `Prophecy4f` Monte-Carlo generator [120] that includes complete NLO QCD and EW corrections for Higgs decays into any possible four-fermion final state. All calculations are consistently performed with off-shell gauge bosons, without any on-shell approximation. For the SM Higgs boson, the missing higher-order corrections are estimated to be roughly 0.5%. Such uncertainties will have to be combined with the parametric uncertainties, in particular those associated to the bottom-quark mass and the strong gauge coupling, to arrive at the full theory uncertainty. A detailed treatment of the differential distributions for a Higgs boson decay into four charged leptons in the final state is discussed in Refs. [43, 121].

The total width of a 125 GeV SM Higgs boson is $\Gamma_H = 4.07 \times 10^{-3}\,\text{GeV}$, with a relative uncertainty of $^{+4.0\%}_{-3.9\%}$. The branching ratios for the most relevant decay modes of the SM Higgs boson as a function of m_H, including the most recent theoretical uncertainties, are shown in Fig. 11.2 (right) and listed for $m_H = 125\,\text{GeV}$ in Table 11.3. Further details of these calculations can be found in the reviews [41–44] and references therein.

11.3 The experimental profile of the Higgs boson

The observation [1, 2] at the LHC of a narrow resonance with a mass of about 125 GeV was an important landmark in the decades-long direct search [46, 122] for the SM Higgs boson. This was followed by a detailed exploration of properties of the Higgs boson at the different runs of the LHC at $\sqrt{s} = 7$, 8 and 13 TeV.

The dataset at $\sqrt{s}$ =13 TeV in the Run 2 phase of the LHC operation corresponds to an integrated luminosity of about $156\,\text{fb}^{-1}$ see Table 11.4. The datasets effectively useful for analysis need to take into account the data-taking efficiency with fully operational detectors and the data quality efficiency. The typical total inefficiency for both ATLAS and CMS is approximately 10%, where approximately half is due to the data taking inefficiency and half from data quality.

In this section, most of the references for the Run 1 measurements that have been updated at the Run 2 are given in the previous version of this review [123] and are not repeated herein.

Table 11.4: The LHC *pp* collision centre-of-mass energies and delivered data samples.

Year	$\sqrt{s}$ (TeV)	$\int$ L.dt (fb^{-1})	Period
2010	7	0.04	Run 1
2011	7	6.1	Run 1
2012	8	23.3	Run 1
2015	13	4.2	Run 2
2016	13	40.8	Run 2
2017	13	50.2	Run 2
2018	13	60.6	Run 2

11.3.1 *The principal decay channels to vector bosons*

For a given m_H, the sensitivity of a channel depends on the production cross section of the Higgs boson, its decay branching fraction, the reconstructed mass resolution, the selection efficiency and the level of background in the final state. For a low-mass Higgs boson ($110\,\text{GeV} < m_H < 150\,\text{GeV}$) for which the SM width would be only a few MeV, five decay channels play an important role at the LHC. In the $H \to \gamma\gamma$ and $H \to ZZ^* \to 4\ell$ channels, all final state particles can be very precisely measured and the reconstructed m_H resolution is excellent (typically 1-2%). While the $H \to W^+W^- \to \ell^+\nu_\ell\ell'^-\bar{\nu}_{\ell'}$ channel has relatively large branching fraction, however, due to the presence of neutrinos which are not reconstructed in the final state, the m_H resolution, obtained through observables sensitive to the Higgs boson mass such as the transverse mass, is poor (approximately 20%). The $H \to b\bar{b}$ and the $H \to \tau^+\tau^-$ channels suffer from large backgrounds and lead to an intermediate mass resolution of about 10% and 15% respectively.

With the increase in the size of datasets, measurements in the most sensitive channels are now carried out differentially or in exclusive modes depending on specific production characteristics. These measurements are discussed in Section 11.6.2.4.

The candidate events in each Higgs boson decay channel are split into several mutually exclusive categories (or event tags) based on the specific topological, kinematic or other features present in the event. The categorization of events increases the sensitivity of the overall analysis and allows a separation of different Higgs boson production processes. Most categories are dominated by signal from one Higgs boson decay mode but contain an admixture of various Higgs boson production processes. For example, a typical VBF selection requires Higgs boson candidates to be accompanied by two energetic jets (≥ 30 GeV) with a large dijet mass (≥ 400 GeV) and separated by a large pseudo-rapidity ($\Delta\eta_{jj} \geq 3.5$) [124]. While such a category is enriched in Higgs bosons produced via VBF, the contamination from the ggF production mechanism can be significant. Hence, a measurement of the signal rate in the VBF category does not imply a measurement of VBF production cross section since one cannot resolve the contamination from ggF. Simulations are used to determine the relative contributions of the various Higgs boson production modes in each specific categories.

An important difference between the Run 1 and Run 2 results, in particular when comparing signal strengths, and therefore in the measurement of the couplings of the Higgs boson as discussed in Section 11.4, is that values and errors of the predicted cross sections have been improved (mostly the scale and PDF uncertainties). The theoretical predictions are however compatible and therefore, the signal strengths can be compared on a sound basis.

11.3.1.1 $H \to \gamma\gamma$

In the $H \to \gamma\gamma$ channel, a search is performed for a narrow peak over a smoothly falling background in the invariant mass distribution of two high p_T photons. The background in this channel is conspicuous and stems from prompt $\gamma\gamma$ processes for the irreducible backgrounds, and the γ+jet and dijet processes for the reducible backgrounds where one jet fragments typically into a leading π^0. In order to optimise search sensitivity and also to separate the various Higgs boson production modes, ATLAS and CMS split events into several mutually exclusive categories. Diphoton events containing a high p_T muon or electron, or missing energy ($E_T^{\rm miss}$) consistent with the decay of a W or Z boson, are tagged in the VH production category. Diphoton events containing energetic dijets with a large mass and pseudo-rapidity difference are assigned to the VBF production category, and the remaining events are considered either in the VH category when the two jets are compatible with the hadronic decay of a W or a Z, or in the ggF production category. While the leptonic VH category is relatively pure, the VBF category has significant contamination from the gluon fusion process. Events which are not picked by any of the above selections are further categorised according to their expected $m_{\gamma\gamma}$ resolution and signal-to-background ratio. Categories with good m_H resolution and larger signal-to-background ratio contribute most to the sensitivity of the search.

Both ATLAS and CMS have studied in detail the calibration of the energy response of photons, in particular using $Z \to e^+e^-$, $Z \to \mu^+\mu^-\gamma$ and the response of muons in the calorimeter (for ATLAS) from $Z \to \mu^+\mu^-$ events. This information is used to correct the simulated signal mass line-shapes. In each category, parametric signal models are adjusted to these line-shapes to provide a functional form for the signal. Simple monotonic functional forms of the backgrounds are determined by a fit to the $m_{\gamma\gamma}$ distribution in each category (typically exponential, Bernstein polynomials, Laurent series or power laws). All categories are fitted simultaneously to determine the signal yield at the measured combined Run 1 mass of 125.09± GeV [127] discussed in Section 11.3.2. The $m_{\gamma\gamma}$ distribution after combining all categories is shown in Fig. 11.3, using the full ATLAS Run 2 dataset.

The signal strength, $\mu = (\sigma \cdot {\rm BR})_{\rm obs}/(\sigma \cdot {\rm BR})_{\rm SM}$, which is the observed product of the Higgs boson production cross section (σ) and its branching ratio (BR) normalised to the corresponding SM values, is 1.17 ± 0.27 for ATLAS in Run 1 and 1.02 ± 0.14 in Run 2 [128] (where this signal strength measurement is estimated from the measured fiducial cross sections and thus neglects acceptance systematic uncertainties, which are not expected to be dominant in particular given that the measurement is inclusive). The signal strengths [2] measured in Run 1 and Run 2 by the CMS collaboration are $1.18^{+0.26}_{-0.23}$ and $1.18^{+0.17}_{-0.14}$ [129] respectively.

11.3.1.2 $H \to ZZ^* \to \ell^+\ell^-\ell'^+\ell'^-$

In the $H \to ZZ^* \to \ell^+\ell^-\ell'^+\ell'^-$ channel, a search is performed for a narrow mass peak over a small continuous background dominated by non-resonant ZZ^* production from $q\bar{q}$ annihilation and gg fusion processes. The contribution and the shape of this irreducible background is taken from simulation. The subdominant and reducible backgrounds stem from Z+$b\bar{b}$, $t\bar{t}$ and Z+jets events. Their contribution is suppressed by requirements on lepton isolation and lepton impact parameter and their yield is estimated from control samples in data.

To help to distinguish the Higgs boson signal from the dominant non-resonant ZZ^* background, both ATLAS and CMS [130] use a matrix element likelihood approach to construct a kinematic discriminant built for each 4ℓ event based on the ratio of complete leading-order matrix elements $|\mathcal{M}_{\rm sig}{}^2/\mathcal{M}_{\rm bkg}{}^2|$ for the signal ($gg \to H \to 4\ell$) and background ($q\bar{q} \to ZZ \to 4\ell$) hypotheses. To further enhance the sensitivity, experiments also use multivariate techniques.

To improve the sensitivity to more exclusive production processes such as VBF, VH and $t\bar{t}H$, the experiments divide 4ℓ events into mutually exclusive categories. Events are categorised in terms of the number of reconstructed jets, the number of additional leptons (from the decay of a vector boson in the associated production mode), number of jet tagged as containing a b-hadron, the transverse momentum of the Higgs boson (or e.g. its associated vector boson) and missing transverse momentum. The exclusive processes are also further separated in different kinematic regions in a framework referred to as Simplified Template Cross Sections (see Section 11.6.2.4). Dijets with a large mass and pseudo-rapidity difference populate the VBF category. ATLAS requires the presence of an additional lepton in the VH category. In events with less than two jets, CMS uses the $p_T^{4\ell}$ to distinguish between production via the gluon fusion and the VH/VBF processes.

Since the $m_{4\ell}$ resolutions and the reducible background levels are different in the 4μ, $4e$ and $2e2\mu$ sub-channels, they are analysed separately and the results are then combined. The distribution of the reconstructed invariant mass of the four leptons for CMS [126] is given in Fig. 11.3 (right), showing a clear excess at a mass of approximately $m_H = 125$ GeV. Both experiments also observe a clear peak at $m_{4\ell} = 91$ GeV from the production of a Z boson on-mass-shell and decaying to four leptons due typically to the emission of an off-shell photon from one of the primary leptons from the Z boson decay.

The signal strengths μ for the inclusive $H \to 4\ell$ production measured by ATLAS and CMS are $1.44^{+0.40}_{-0.33}$ at $m_H = 125.36$ GeV and $0.93^{+0.29}_{-0.25}$ at $m_H = 125.6$ GeV respectively, in Run 1. The signal strengths measured by ATLAS and CMS in Run 2 are 1.04 ± 0.10 [131] and 0.94 ± 0.10 [126] respectively (the ATLAS measurement is made at the combined Run 1 Higgs boson mass of $m_H = 125.09$ GeV while the m_H is profiled in the CMS analysis). The dominant uncertainty in these measurements remains the statistical uncertainty.

11.3.1.3 *Measurement of the Higgs boson mass*

To measure the mass of the Higgs boson, ATLAS and CMS collaborations rely on the two high mass-resolution and sensitive channels, $\gamma\gamma$ and $ZZ^*/4\ell$. The ATLAS and CMS approaches are very similar in these two analyses with small differences on the usage of categories, additional discriminating variables and per-event errors. In these two channels, the mass resolutions range from 1.4 GeV to 2 GeV for ATLAS and from 1.0 GeV to 2.8 GeV for CMS (see Ref. [127] and the reconstruction-performance references therein). The best mass resolution is obtained for both experiments in the diphoton channel for central diphoton pairs (typically for events where both photons are not converted). The signal strengths in the $\gamma\gamma$ and ZZ channels are assumed to be

[2] The Run 1 results for ATLAS and CMS are at fixed values of $m_H = 125.4$ GeV and 124.7 GeV, respectively.

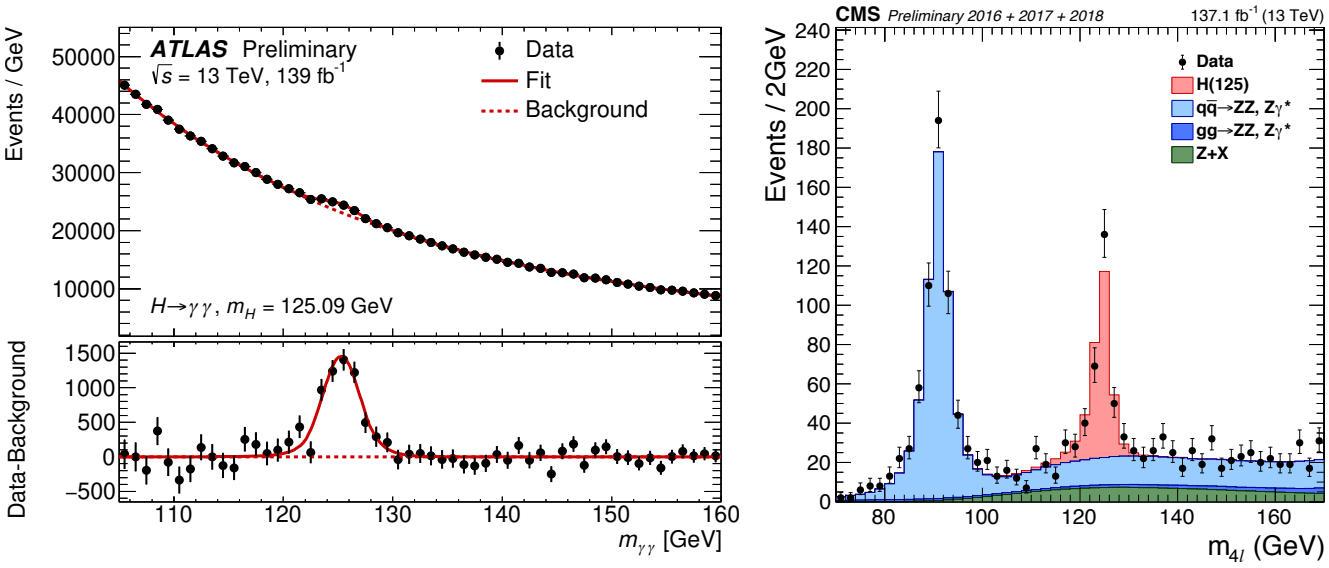

Figure 11.3: (Left) The invariant mass distribution of diphoton candidates, with each event weighted by the ratio of signal-to-background in each event category, observed by ATLAS [125] at Run 2. The residuals of the data with respect to the fitted background are displayed in the lower panel. (Right) The $m_{4\ell}$ distribution from CMS [126] Run 2 data.

independent and not constrained to the expected rate ($\mu = 1$) for the SM Higgs boson.

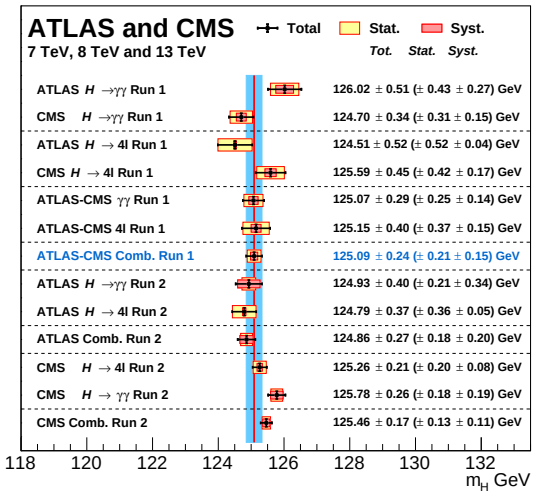

Figure 11.4: Summary of the CMS and ATLAS mass measurements in the $\gamma\gamma$ and ZZ channels in Run 1 and Run 2.

Figure 11.4 summarizes all measurements of the Higgs boson mass, including the individual and combined Run 1 measurements [127] and the Run 2 measurement by ATLAS [132] and CMS [130, 133] for both the diphoton and the 4ℓ channels.

In the diphoton channel, as discussed in Section 11.5.3.2, a mass shift is expected to be induced by the deformation of the mass line-shape of the signal in presence of background, from the interference between the Higgs boson production and the continuum irreducible background. It is a small but non negligible effect of approximately 35 MeV [134] for a Higgs boson width close to that of the SM. This effect could be larger if the width of the Higgs boson were to be substantially larger. This effect estimated by ATLAS with a full simulation is still relatively small with respect to the total uncertainty on the mass and is therefore neglected.

11.3.1.4 $H \to W^+W^- \to \ell^+\nu\ell^-\overline{\nu}$

In this intricate channel, experiments search for an excess of events with two leptons of opposite charge accompanied by missing energy and/or jets. A typical event selection is described below in order to give an idea of the main challenges. Specific selections vary between experiments and between Run 1 and Run 2 analyses. Events are divided into several categories depending on the lepton flavour combination (e^+e^-, $\mu^+\mu^-$and $e^\pm\mu^\mp$) and the number of accompanying jets ($N_{\text{jet}} = 0, 1, \geq 2$). In the ATLAS analysis, the $N_{\text{jet}} \geq 2$ category is optimised for the VBF production process by selecting two leading jets with a large pseudo-rapidity difference and with a large mass ($m_{jj} > 500$ GeV).

Backgrounds contributing to this channel are numerous and depend on the category of selected events. Reducing them and accurately estimating the remainder is a major challenge in this analysis. For events with opposite-flavour leptons and no accompanying high p_T jets, the dominant background stems from non-resonant WW production. Events with same-flavour leptons suffer from large Drell–Yan contamination (note that also the opposite-flavour leptons analysis has Drell–Yan $\tau\bar{\tau}$ background in 0-jet category). The $t\bar{t}$, tW and W + jets (with the jet misidentified as a lepton) events contaminate all categories. Non-resonant WZ, ZZ and $W\gamma$ processes also contribute to the background at a sub-leading level.

A requirement of large missing transverse energy (E_T^{miss}) is used to reduce the Drell–Yan and multijet backgrounds. In the e^+e^- and $\mu^+\mu^-$ categories, events with $m_{\ell\ell}$ consistent with the Z mass are vetoed. The $t\bar{t}$ background is suppressed by a veto against identified b-jets or low p_T muons assumed to be coming from semi-leptonic b-hadron decays within jets (this soft muon veto was not applied anymore in Run 2 analysis) and tight isolation requirements diminish the W+jets background. The scalar nature of the Higgs boson and the $V - A$ nature of the W boson decay implies that the two charged leptons in the final state are preferentially emitted at small angles with respect to each other. Therefore the dilepton invariant mass ($m_{\ell\ell}$) and the azimuthal angle difference between the leptons ($\Delta\phi_{\ell\ell}$) are used to discriminate between the signal and non-resonant WW events [135]. The transverse mass, constructed from the dilepton p_T ($p_T^{\ell\ell}$), E_T^{miss} and the azimuthal angle between E_T^{miss} and $p_T^{\ell\ell}$, is defined as $m_T = \sqrt{2p_T^{\ell\ell}E_T^{\text{miss}}(1 - \cos\Delta\phi_{E_T^{\text{miss}}\ell\ell})}$ and serves as an effective discriminant against backgrounds. The transverse mass variable also tracks the Higgs boson mass but with a poor mass resolution. Background rates except for the small contributions typically from non-resonant WZ, ZZ and $W\gamma$ are evaluated from data control samples with floating normalisation.

ATLAS fitted the m_T distributions and observed an excess at $m_H = 125.36$ GeV with a local significance of 6.1σ similar to that expected from a 125 GeV SM Higgs boson. The measured inclusive

signal strength is $\mu = 1.09^{+0.23}_{-0.21}$. In the VBF category, an excess with a significance of 3.2σ corresponding to a signal strength of $\mu = 1.27^{+0.53}_{-0.45}$ is observed. The CMS analysis of 0- and 1-jet categories, using all lepton flavour combinations, shows an excess with an observed significance of 4.3σ, lower than the expected sensitivity of 5.8σ for a 125.6 GeV SM Higgs boson. CMS observes no significant excess in the VBF production mode and sets a 95% CL limit on the signal strength of $\mu_{\rm VBF} < 1.7$ for $m_H = 125.6$ GeV.

ATLAS and CMS have also searched for the associated Higgs boson production in this channel. The signal consists of up to three (WH) or four (ZH) high p_T isolated leptons with missing transverse energy and low hadronic activity. The major backgrounds stem from triboson and diboson production where each boson decays leptonically. ATLAS observes [136] an excess at $m_H = 125.36$ GeV with a local significance of 2.5σ corresponding to a $\mu_{VH} = 3.0^{+1.6}_{-1.0}$. CMS instead sets a 95% CL limit of $\mu_{VH} < 4.7$.

In this difficult channel, the full Run 2 dataset has not yet been analysed by ATLAS nor CMS. There have been partial analyses made with Run 2 data at 13 TeV by both ATLAS and CMS. ATLAS has analysed the $WW \to e\nu\mu\nu$ decay mode in the gluon fusion, the VBF and VH production modes with 2015 and 2016 datasets [137,138]. With this limited dataset the measured gluon fusion signal strength yielded [138] $\mu_{\rm ggF} = 1.10 \pm 0.20$, with the largest uncertainties being the experimental systematic uncertainties.

CMS has performed a more complete analysis with the full 2016 dataset, with most production channels covering both the opposite- and same-flavour final states of opposite charge leptons (electrons or muons), obtaining a combined signal strength of $\mu_{\rm WW} = 1.28 \pm 0.18$ [139]. This analysis aims at several production modes (ggF, VBF and VH – with the vector boson reconstructed both in jet and leptonic decay modes).

11.3.2 *Decays to third generation fermions ($b\bar{b}$ and $\tau^+\tau^-$)*

In the SM, fermions acquire a mass through gauge invariant interactions with the Higgs field which is also responsible for the electroweak symmetry breaking and thus for generating the masses of gauge bosons (see Section 11.2 for more details). While this minimal solution is very elegant, there is no fundamental reason for it to be the case, and probing the couplings of the Higgs boson to fermions is therefore of fundamental importance, in particular since BSM physics can largely change the SM predictions.

The discovery of the Higgs boson was made essentially through bosonic final states. These decays probed mostly the couplings of the Higgs boson to vector bosons (the decay of the Higgs boson to photons occurring only through loops is also dominated in the SM by the coupling of the Higgs boson to W bosons). However, the predominant Higgs boson production mode is the gluon fusion, occurring only through loops dominated by the coupling of the Higgs boson to fermions. The observation of the Higgs boson in the two photons or two gluons decay modes is also an indirect evidence for the coupling of the Higgs boson to fermions (and in particular to the top quark). Nevertheless, the observation of either decays to fermions or production modes which unambiguously proceed through fermion couplings provide direct probes of the coupling of the Higgs boson to fermions and is thus of fundamental importance.

At hadron colliders, the most promising channel for probing the coupling of the Higgs field to the quarks and leptons are $H \to b\bar{b}$ and $H \to \tau^+\tau^-$, respectively. For a Higgs boson with $m_H \approx 125$ GeV, the branching fraction to $b\bar{b}$ is about 58% and to $\tau^+\tau^-$ is about 6%. Nevertheless, the presence of very large backgrounds makes the isolation of a Higgs boson signal in these channels quite challenging.

One of the most prominent goals of the LHC Run 2 for ATLAS and CMS was the direct observation of the Yukawa coupling of the Higgs boson to fermions of the third generation (bottom quarks, tau leptons and top quarks). This goal has been reached independently by both ATLAS and CMS and with only partial Run 2 datasets.

11.3.2.1 $H \to \tau^+\tau^-$

In the $H \to \tau^+\tau^-$ search, τ leptons decaying to electrons (τ_e), muons (τ_μ) and hadrons (τ_{had}) are considered. The $\tau^+\tau^-$ invariant mass ($m_{\tau\tau}$) is reconstructed from a kinematic fit of the visible products from the two τ leptons and the missing energy observed in the event. Due to the presence of missing neutrinos, the $m_{\tau\tau}$ resolution is poor ($\approx 15\%$). As a result, a broad excess over the expected background in the $m_{\tau\tau}$ distribution is searched for. The major sources of background stem from Drell–Yan $Z \to \tau^+\tau^-$ and $Z \to e^+e^-$, W+jets, $t\bar{t}$ and multijet production. Events in all sub-channels are divided into categories based on the number and kinematic properties of additional energetic jets in the event and the transverse momentum of the reconstructed Higgs boson and the distance ΔR distance between the two τ's. The sensitivity of the search is generally higher for categories with one or more additional jets. The VBF category, consisting of a τ pair with two energetic jets separated by a large pseudo-rapidity, has the best signal-to-background ratio and search sensitivity, followed by the $\tau^+\tau^-$+1 jet category. The signal to background discrimination relies in part on the $m_{\tau\tau}$ resolution, which improves with the boost of the Higgs boson. The non-VBF categories are further subdivided according to the observed boost of the $\tau^+\tau^-$ system. CMS primarily uses the reconstructed $m_{\tau\tau}$ as the final discriminating variable while ATLAS combines various kinematic properties of each event categories with multivariate techniques to build the final discriminant [140].

Searches for $H \to \tau^+\tau^-$ decays in the VH production mode are also performed in final states where the W or Z boson decays into leptons or jets. The irreducible background in this search arises from non-resonant WZ and ZZ diboson production. The reducible backgrounds originate from W, Z, and $t\bar{t}$ events that contain at least one fake lepton in the final state due to a misidentified jet. The shape and yield of the major backgrounds in each category are estimated from control samples in data. Contributions from non-resonant WZ and ZZ diboson production are estimated from simulations but corrected for reconstruction efficiency using control samples formed from observed data.

For CMS, the significance of the observed excess at $m_H = 125$ GeV in Run 1 is 3.2σ, close to the expected 3.7σ sensitivity, and corresponds to a signal strength of $\mu = 0.86 \pm 0.29$. The observed (expected) deviation from the background-only hypothesis in ATLAS corresponds to a local significance of 4.5σ (3.4σ) and the best fit value of the signal strength is $\mu = 1.43^{+0.43}_{-0.37}$ [140].

When the ATLAS and CMS $H \to \tau\tau$ Run 1 measurements are combined [141], the significance of the observed excess corresponding to $m_H = 125.09$ GeV is 5.5σ and the combined signal strength is $\mu = 1.11^{+0.24}_{-0.22}$, consistent with the SM expectation.

The Run 1 evidence was strong only through the combination of the two experiments. The Run 2 larger dataset at a greater centre-of-mass energy is essential to further confirm this observation and perform first precision measurements in this important channel.

ATLAS has analysed its 2015 and 2016 dataset so far, providing further evidence at the 4.4σ level with an expected significance of 4.1σ. When combined with the Run 1 data the single experiment observation significance is 6.4σ (5.4σ expected) [142].

In the CMS analysis of the 2016 data [143], the strategy was improved using additional categories aiming at the inclusive production of the Higgs boson and binned in transverse momentum of the $\tau^+\tau^-$ system, and for the VBF production, the analysis is binned as a function of the dijet mass. This analysis reached a sensitivity of 4.7σ with a dataset corresponding to an integrated luminosity of 35.9 fb^{-1}. CMS observes an excess with a significance of 4.9σ. In combination with the Run 1 results, this provides an unambiguous observation of the direct coupling of the Higgs boson to taus, in the VBF production mode.

CMS has then also extended to additional production modes via the associated production with a vector boson [144] and analysed a larger dataset corresponding to an integrated luminosity of almost 80 fb^{-1} of data collected in 2016 and 2017, providing results which complete the Run 1 search for an unambiguous observation of the direct decay of the Higgs bosons to a pair of taus (and measurements of cross sections times branching-fractions) [145].

11.3.2.2 $H \to b\bar{b}$

In the search for the decay of the Higgs boson to a pair of b-quarks, the most sensitive production modes are the associated WH and ZH processes allowing use of the leptonic W and Z decays for triggering, and to purify the signal and reject QCD backgrounds. The W bosons are reconstructed via their leptonic decay $W \to \ell\bar{\nu}_\ell$ where $\ell = e, \mu$ or τ. The Z bosons are reconstructed via their decay into $e^+e^-, \mu^+\mu^-$or $\nu\bar{\nu}$. The Higgs boson candidate mass is reconstructed from two b-tagged jets in the event. Backgrounds arise from production of W and Z bosons in association with gluon, light and heavy-flavoured jets (V+jets), $t\bar{t}$, diboson (ZZ and WZ with $Z \to b\bar{b}$) and QCD multi-jet processes. Due to the limited $m_{b\bar{b}}$ mass resolution, a SM Higgs boson signal is expected to appear as a broad enhancement in the reconstructed dijet mass distribution. The crucial elements in this search are b-jet tagging with high efficiency and low fake rate, accurate estimate of b-jet momentum and estimate of backgrounds from various signal depleted control samples constructed from data.

At the Tevatron, the $H \to b\bar{b}$ channel contributes the majority of the Higgs boson search sensitivity below $m_H = 130\,\text{GeV}$. To separate signal from background, CDF and D0 use multivariate analysis (MVA) techniques that combine several discriminating variables into a single final discriminant. Each channel is divided into exclusive sub-channels according to various lepton, jet multiplicity, and b-tagging characteristics in order to group events with similar signal-to-background ratio and thus optimise the overall search sensitivity. The combined CDF and D0 data show [46,146] an excess of events with respect to the predicted background in the 115–140 GeV mass range in the most sensitive bins of the discriminant distributions suggesting the potential presence of a signal. At $m_H = 125\,\text{GeV}$, the observed signal strength is $\mu = 1.59^{+0.69}_{-0.72}$.

At the LHC, in order to reduce the dominant V+jets background, following Ref. [90], experiments select a region in the VH production phase space where the vector boson is significantly boosted and recoils from the $H \to b\bar{b}$ candidate with a large azimuthal angle $\Delta\phi_{VH}$. For each channel, events are categorised into different $p_T(V)$ regions with varying signal/background ratios. Events with higher $p_T(V)$ have smaller backgrounds and better $m_{b\bar{b}}$ resolution. CMS uses MVA classifiers based on kinematic, topological and quality of b-jet tagging and trained on different values of m_H to separate Higgs boson signal in each category from backgrounds. The MVA outputs for all categories are then fit simultaneously.

The nominal results from ATLAS are also based on a combination of (i) a multivariate analysis of their 8 TeV data, incorporating various kinematic variables in addition to $m_{b\bar{b}}$ and b-tagging information and (ii) a statistical analysis of their 7 TeV data centred on $m_{b\bar{b}}$ as the main discriminant. In both cases, customised control samples devised from data are used to constrain the contributions of the dominant background processes.

The direct observation of the Higgs boson decaying to a pair of b-quarks, a major result of Run 2, was obtained by both ATLAS and CMS independently after the update of their search with similar analyses as those performed at Run 1 but with a larger dataset of approximately $80\,\text{fb}^{-1}$ of data collected in 2015, 2016 and 2017. The increase in signal cross sections of nearly a factor of 3 at the centre-of-mass energy of 13 TeV with respect to 7 TeV, has also been instrumental in bringing the two experiments to the required sensitivity to claim an evidence for this decay mode in the VH production mode (in the high transverse momentum of the vector boson fiducial region of interest for this channel). The expected significance for a SM Higgs boson is 4.3σ for ATLAS [147] and 4.9σ for CMS [148]. Both ATLAS and CMS observe significant excesses corresponding to 4.9σ and 4.8σ respectively with Run 2 data only. When combined with results obtained in Run 1, the observed (expected) significance of the excesses are 5.4σ (5.5σ) and 5.6σ (5.5σ) respectively. These results provide direct evidence for the Higgs boson decay to a $b\bar{b}$ through the VH production mode. All these results are summarised in Table 11.5. It should be noted that the sensitivity of these analyses are already limited by systematic uncertainties.

This channel has also been exploited by ATLAS to produce a measurement at higher transverse momentum of the vector boson in the framework of Simplified Template Cross Sections (STXS) discussed in Section 11.6.2.4 [149]. In this case, at higher transverse momentum, the statistical uncertainty still dominates.

Also, the LHCb collaboration has performed a search for the VH production with subsequent decay of the Higgs boson to a pair of b-quarks [150] with $1.98\,\text{fb}^{-1}$ of data taken at a centre-of-mass energy of 8 TeV. The final state is required to have two reconstructed b quarks and one lepton in the LHCb acceptance of $2 < \eta < 5$. The sensitivity of this search is an expected 95% CL exclusion of 84 times the SM production rate. This analysis is also used to set a limit on the VH production with the subsequent decay of the Higgs boson in a pair of c quarks with a 95% CL limit at 6.4×10^3 times the SM production rate, while the expected sensitivity corresponds to an exclusion of 7.9×10^3 times the SM production rate.

ATLAS and CMS have also searched for $H \to b\bar{b}$ in the VBF production mode. The event topology consists of two VBF-tagging energetic light-quark jets in the forward and backward direction relative to the beam direction and two b-tagged jets in the central region of the detector. Due to the electroweak nature of the process, for the signal events, no additional energetic jet activity (excluding that from the Higgs boson) is expected in the rapidity gap between the two VBF-tagging jets. The dominant background in this search stems from QCD production of multi-jet events and the hadronic decays of vector bosons accompanied by additional jets. A contribution of Higgs boson events produced in the ggF process but with two or more associated jets is expected in the signal sample. The signal is expected as a broad enhancement in the $m_{b\bar{b}}$ distribution over the smoothly falling contribution from the SM background processes. Both ATLAS [151] and CMS [152] have produced results in this channel with Run 1 data, but with limited sensitivity. Both experiments performed a similar analysis with Run 2 data [153]. The results are summarised in Table 11.5.

Two of the main difficulties for the VBF production mode are the large QCD background and the difficulty in triggering events fully hadronic events. Both difficulties are addressed, by the proposal made in Ref. [154], where the requirement of an additional photon in the final state reduces the background through an interference effect and enhances the possibilities for triggering. This analysis has been carried out by ATLAS at Run 2 [153] (see Table 11.5).

The sensitivity in the inclusive search for the Higgs boson in the ggF production mode with $H \to b\bar{b}$ is limited by the overwhelming background from the inclusive production of $pp \to b\bar{b} + X$ via the strong interaction. For this reason, no meaningful results exist with the Run 1 dataset for this production mode. With the increase in centre-of-mass energy to 13 TeV, and by taking advantage of the harder transverse momentum spectrum of the $gg \to H$ production mode with respect to the QCD background, a search for high p_T Higgs boson decaying to a pair of b quarks in association with an energetic Initial State Radiation (ISR) jet, has been performed by ATLAS [155] and CMS [156]. For this analysis with the Run 2 data, ATLAS and CMS require jets clustered with the anti-k_T algorithm [157] with a distance parameter of 1.0 and 0.8 respectively, with a transverse momentum in excess of 480 GeV and 450 GeV respectively. As in the case of VH production mode, this analysis is sensitive also to the $VZ, Z \to b\bar{b}$ production, which is an important step in the validation of the analysis chain. The $Z \to b\bar{b}$ decay is observed with a significance of 5.8σ, in good agreement with the expected sensitivity of 5.1σ. CMS provides an expected sensitivity to the observation of a Higgs boson of 0.7σ. This estimate has a non negligible uncertainty from the precise estimate of the fiducial signal cross section in the specific acceptance of this analysis. Both ATLAS and CMS observe small and non significant excesses at $m_H = 125\,\text{GeV}$ of 1.6σ and 1.5σ respectively. These results are reported in Table 11.5.

Another important production mode sensitive to the decay of the Higgs boson to bottom quarks, is the associated production with a pair of top quarks. The results of the searches for this process have been combined with the channels described above, to provide an additional constraint on the Yukawa coupling of

Table 11.5: Summary of the results of measurements for a Higgs boson decaying to a pair of b-quarks by ATLAS and CMS. The results are given in terms of measured signal strength. When available, the statistical and systematic contributions to the total uncertainty are reported separately and in this order.

$H \to b\bar{b}$	Tevatron	ATLAS Run 1	CMS Run 1	ATLAS Run 2	CMS Run 2
VH	1.6 ± 0.7	$0.52 \pm 0.32 \pm 0.24$	1.0 ± 0.5	$1.16 \pm 0.16\,^{+0.21}_{-0.19}$	1.01 ± 0.22
VBF (γ)	—	-0.8 ± 2.3	$2.8 \pm 1.4 \pm 0.8$	2.5 ± 1.3	1.3 ± 1.2
$t\bar{t}H$	—	$1.4 \pm 0.6 \pm 0.8$	0.7 ± 1.9	$0.79 \pm 0.29 \pm 0.53$	$1.49 \pm 0.21 \pm 0.39$
Inclusive	—	—	—	$5.8 \pm 3.1 \pm 2.5$	2.3 ± 1.7

the Higgs boson to bottom quarks. The channels corresponding to this production mode are described in Section 11.3.3. The results are, however, also reported in Table 11.5.

11.3.3 *Higgs boson production in association with top quarks or in top decays*

11.3.3.1 *The associated production with top quark pairs*

As discussed in Section 11.2, the coupling of the Higgs boson to top quarks plays a special role in the electroweak symmetry breaking mechanism in the SM, as well as in its possible extensions. Substantial indirect evidence of this coupling is provided by the compatibility of observed rates of the Higgs boson in the principal discovery channels, given that the main production process – the gluon fusion – is dominated by a top quark loop. Direct evidence of this coupling at the LHC and the future e^+e^- colliders will be mainly available through the $t\bar{t}H$ final state and will permit a clean measurement of the top quark-Higgs boson Yukawa coupling. The $t\bar{t}H$ production cross section at the LHC is small in comparison with the ggF or even VH production modes. The production cross section for a 125 GeV Higgs boson in pp collisions at $\sqrt{s} = 8$ TeV of about 130 fb made it challenging to measure the $t\bar{t}H$ process with the LHC Run 1 dataset. However, in Run 2, the increase in cross section at $\sqrt{s} = 13$ TeV is substantial, reaching approximately 500 fb. For a sensitive search, at Run 1, it was important to target as many accessible experimental signatures as possible. The analysis channels for such complex final states can be separated in four classes according to the decays of the Higgs boson. In each of these classes, most of the decay final states of the top quarks are considered (fully hadronic, semi-leptonic and dilepton decay final states).

The first analysis in this ensemble is the search for $t\bar{t}H$ production in the $H \to \gamma\gamma$ channel. This analysis relies on the search for a narrow mass peak in the $m_{\gamma\gamma}$ distribution. The background is estimated from the $m_{\gamma\gamma}$ sidebands. The sensitivity in this channel is mostly limited by the available statistics. The second analysis is the search for the Higgs boson decaying to ZZ^* and subsequently to four leptons (electrons and/or muons). This channel is currently limited by the low statistics due to the small branching fraction of the Z decays to leptons. The third analysis is the search in the $H \to b\bar{b}$ channel. This search is intricate due to the large backgrounds, both physical and combinatorial in resolving the $b\bar{b}$ system from the Higgs boson decay, in events with six jets and four b-tagged jets. Already with the Run 1 dataset, the sensitivity of this analysis was strongly impacted by the systematic uncertainties on the background predictions. The fourth analysis channel is a specific search for $\tau^+\tau^-$ where the two tau leptons decay to hadrons. Finally, the W^+W^- , $\tau^+\tau^-$ and ZZ^* final states can be searched for inclusively in multilepton event topologies (not including the resonant $H \to 4\ell$ channel that is covered in a more specific analysis). The corresponding $t\bar{t}H$ modes can be decomposed in terms of the decays of the Higgs boson and those of the top quarks as having two b-quarks and four W bosons (or two W and two taus, or two W and two Z) in the final state.

ATLAS and CMS have provided a complete set of results in these channels and their combination with the Run 1 data [158, 159]. Results for most of these channels have been updated with Run 2 data.

With the large increase in production cross section for the $t\bar{t}H$ associated production process of a factor of 3.9 from 7 TeV to 13 TeV, an outstanding goal of the Run 2 physics program was the direct observation of the top Yukawa coupling through this production mode. As could be seen in the Run 1 results, the $H \to b\bar{b}$ channel sensitivity was already dominated by systematic uncertainties and the multilepton channel had already large systematic uncertainties, while channels such as the $H \to \gamma\gamma$ had very limited sensitivity due to the low statistics. With a conspicuous amount of data, the hierarchy of channels was therefore bound to change.

ATLAS and CMS have analysed Run 2 data in all the sensitive decay channels for this production mode, with datasets of variable size of up to the full Run 2 dataset in the case where it matters the most, i.e., the $t\bar{t}(H \to \gamma\gamma)$ channel. With this partial analysis of the Run 2 data, ATLAS and CMS were able to independently observe the production of the Higgs boson in association with a pair of top quarks, and therefore the Yukawa coupling of the Higgs boson to the top quark [160]. This observation is particularly important in comparison to the indirect evidence through the gluon fusion production process dominated by the top quark loop.

The observation made independently by the two experiments was based on all the channels that were studied at the Run 1. ATLAS used up to 79.8 fb^{-1} of Run 2 data and CMS has used its 2016 dataset of 35.9 fb^{-1}. ATLAS reached an expected sensitivity of 4.9σ and an observed significance of 5.8σ with the Run 2 partial dataset alone, and 6.3σ (with 5.1σ expected) in combination with the Run 1 results. CMS reached a sensitivity of 4.2σ and observed an excess with respect to the background-only hypothesis of 5.2σ, combining the Run 1 and Run 2 results.

With the larger Run 2 dataset, the dominant mode is the $t\bar{t}(H \to \gamma\gamma)$ channel, where a narrow peak over a continuous background is searched for. At Run 2, this channel has reached a signal-to-background ratio in excess of 1 in the most signal-like categories. This is in contrast with the inclusive diphoton channel Higgs channels where the signal-to-background ratios are of the order of a few percent. ATLAS has analysed the entire Run 2 dataset reaching an observed (expected) sensitivity of 4.9σ (4.2σ) [161] and CMS has utilised 77.4 fb^{-1} of Run 2 data for this channel with an observed (expected) sensitivity of 4.1σ (2.7σ) [162], providing nearly unambiguous observations in this channel alone. These results are largely dominated by statistical uncertainty and are therefore expected to improve significantly with more data. These results with the full dataset from ATLAS [161] and with a larger Run 2 dataset for CMS [162] are not part of the ATLAS and CMS combinations and therefore provide substantially more evidence for the direct coupling of the Higgs boson to the top quark.

The resonant search for the resonant Higgs boson decay to four leptons in the associated production with a pair of top quarks has also been updated in ATLAS [131] with the full Run 2 dataset and reported in Table 11.6, but it is also not included in the combination.

An update of the $H \to b\bar{b}$ channel made by CMS with a partial Run 2 dataset of 41.5 fb^{-1} [163], using in particular the fully hadronic channel, is not in combination either. It is nevertheless reported in Table 11.5.

For the so-called "multi-lepton" channels which cover mostly

the WW, ZZ and $\tau\tau$ decay modes, ATLAS and CMS have analysed only part of the Run 2 datasets [164].

All results are summarized in Table 11.6.

11.3.3.2 *The associated production with a single top quark*

An additional production mode of the Higgs boson in association with a top quark is the single top associated production mode. There is an interesting similarity between this production mode and the $H \to \gamma\gamma$ decay mode. Both processes proceed through either the top Yukawa coupling or the interaction of the Higgs boson with the W boson, with a negative interference between the two. Representative Feynman diagrams for this production process are shown in Fig. 11.1. Contrary to the diphoton decay channel, in this production mode the interference occurs at the tree level and is dominant. This process can therefore be used to further discriminate a negative relative sign between the couplings of the Higgs boson to fermions and its couplings to gauge bosons [165].

ATLAS and CMS have produced specific searches for the tH production mode with the Run 1 and Run 2 data exploiting a variety of Higgs boson decay modes resulting in final states with photons, bottom quarks, and multiple charged leptons, including tau leptons. In particular, with the Run 2 data, CMS has searched for multi-leptonic decay signatures from the $H \to WW^*$, $H \to \tau^+\tau^-$ and $H \to ZZ^*$ modes [166]. This analysis restricts values of κ_t, the top-Higgs coupling normalized to its SM value, to $[-1.25, 1.60]$ at 95% CL. CMS has also performed an analysis of the 2015 dataset to search for the $H \to b\bar{b}$ mode [167], yielding much less stringent constraints.

The diphoton channel has also been used to search specifically for this production mode by ATLAS using Run 1 data, yielding the restricted range of allowed values of κ_t at the 95% CL to $[-1.3, 8]$.

The strongest constraint on the negative (relative) sign of κ_t was obtained by CMS with a recent analysis of the 2016 dataset [168] in the multilepton ($H \to WW$, $H \to ZZ$, $H \to \tau\tau$) and $H \to bb$ channels, all combined with a reinterpretation of the $H \to \gamma\gamma$ analysis channel aiming at measuring the $pp \to t\bar{t}H$ production mode. Negative values of κ_t are disfavoured at approximately 1.5σ and values of κ_t below -0.9 are excluded at 95% CL.

11.3.3.3 *Flavour changing neutral current decays of the top quark*

The discovery of the Higgs boson at a mass smaller than the top quark mass opened a new decay channel for the top quark. The decays of the top quark to a Higgs boson and a charm or an up quark proceed through a Flavour Changing Neutral Current (FCNC) which are forbidden at tree level and suppressed at higher orders through the Glashow–Iliopoulos–Maiani (GIM) mechanism [3]. The SM prediction for these branching fractions is $\mathrm{BR}(t \to Hc) = 10^{-15}$ and two orders of magnitude less for the Hu final state. These decay channels of the top quark are, therefore, very interesting to probe possible FCNC interactions in the Yukawa couplings to the quark sector, see Section 11.7.

ATLAS has searched for FCNC top decays specifically in channels involving a Higgs boson with subsequent decays to two photons and a pair of b-quarks [169]. It has also reinterpreted a search for the $t\bar{t}H$ production in the multilepton final state (discussed in Section 11.3.6.1) [159]. The latter channel covers Higgs boson decays to a pair of W bosons and a pair of taus. No significant excess was observed in any of the specific channels (as discussed in Section 11.3.6.1, a slight excess is observed in the $t\bar{t}H$ multilepton channel) and 95% CL upper limits are set on $\mathrm{BR}(t \to Hc) < 0.46\%$ with an expected sensitivity of 0.25% and $\mathrm{BR}(t \to Hu) < 0.45\%$ with an expected sensitivity of 0.29%. CMS has performed a search for these FCNC top decays in the diphoton and multi-lepton channels [170], placing a 95% CL upper limit on $\mathrm{BR}(t \to Hc) < 0.40\%$ with an expected sensitivity of 0.43%.

From these limits on branching fractions, constraints on non-flavour-diagonal Yukawa couplings of a FCNC Lagrangian of the form:

$$\mathcal{L}_{\mathrm{FCNC}} = \lambda_{tcH}\bar{t}Hc + \lambda_{tuH}\bar{t}Hu + h.c. \qquad (11.12)$$

can be derived. The 95% CL observed (expected) upper limits from ATLAS on the $|\lambda_{tcH}|$ and $|\lambda_{tuH}|$ couplings are 0.13 (0.10) and 0.13 (0.10), respectively.

The results above are derived from the combination of several channels for searches performed with Run 1 data. Both ATLAS and CMS have produced updates of individual channels with Run 2 data. ATLAS has searched for FCNC top decays with subsequent decays of the Higgs boson to a pair of photons [171], yielding a 95% CL upper limit on $\mathrm{BR}(t \to Hc) < 0.22\%$ with an expected sensitivity of 0.16%. CMS has searched for FCNC top decays with subsequent decays of the Higgs boson to a pair of b-quarks [172], yiedling a 95% CL upper limit on $\mathrm{BR}(t \to Hc) < 0.47\%$ with an expected sensitivity of 0.44%.

11.3.4 *Higgs boson pair production*

Higgs boson pair production in the SM is a rare but very important mode to measure and search for. The measurement of Higgs boson pair production is essential to directly constrain the trilinear Higgs boson self coupling and the search for Higgs boson pair resonances is key in a variety of BSM models. The latter searches are discussed in Section 11.7.7.

In the SM, the main non-resonant production mode of two Higgs bosons proceeds through a loop, mainly of top quarks, see Fig. 11.5 (a). Another production mode is via the trilinear coupling of the Higgs boson, see Fig. 11.5 (b), whose amplitude is not negligible compared to the former. These diagrams interfere negatively, making the overall production rate smaller than what would be expected in the absence of a trilinear coupling.

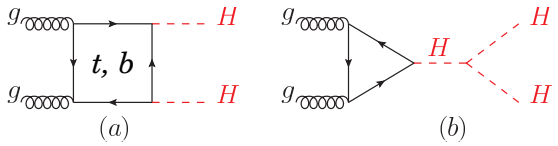

Figure 11.5: Feynman diagrams contributing at leading order to Higgs boson pair production through (a) a top- and bottom-quark loop and (b) through the self coupling of the Higgs boson.

11.3.4.1 *Searches for Higgs boson pair production*

The searches for Higgs boson pair production both resonant and non-resonant are very interesting probes for a variety of BSM theories, and they can be done in a large number of Higgs boson decay channels. At Run 1, ATLAS and CMS have searched for both resonant and non resonant Higgs boson pair production in the following channels: (i) $HH \to b\bar{b}\gamma\gamma$; (ii) $HH \to b\bar{b}\tau^+\tau^-$; (iii) $HH \to b\bar{b}b\bar{b}$; (iv) $HH \to WW^*\gamma\gamma$; (v) in final states containing multiple leptons (electrons or muons) covering the WW^*WW^*, WW^*ZZ^*, ZZ^*ZZ^*, $ZZ^*\tau^+\tau^-$, $WW^*\tau^+\tau^-$, $ZZ^*b\bar{b}$, $\tau^+\tau^-\tau^+\tau^-$ channels; and (vi) $\gamma\gamma\tau^+\tau^-$ channels.

At Run 2, similarly to the $t\bar{t}H$ production process, the di-Higgs production gains a substantial increase in production cross section of a factor in excess of 3 from 8 TeV to 13 TeV, and most of these channels have been updated both by ATLAS [173] and CMS [174] using the 2016 datasets with the addition of the (vii) $HH \to b\bar{b}b\bar{b}$ channels. The detailed description of the analyses can be found in references within the combination results published by the collaborations [173, 174]. All the results and their combinations are summarised in Table 11.7.

11.3.4.2 *The Higgs boson self coupling*

The Higgs boson self coupling is an extremely important direct probe of the Higgs potential with implications on our understanding of the electroweak phase transition. Constraints on the trilinear self coupling from HH processes is an outstanding long term goal of the LHC and the reach in sensitivity has been reappraised in the light of the recent HH analyses from ATLAS and CMS, shedding a different light on the achievable sensitivity [104]. Constraints from the HHH final state on the quartic Higgs boson self coupling are out of reach at the LHC due mostly to the very small production rates and intricate final states.

In the SM, the Higgs boson pair production through the trilinear Higgs boson self coupling has an on-shell component and a large off-shell component. The on-shell $H \to H^*H^*$ is strongly disfavoured, requiring two off-shell Higgs bosons in the final state.

Table 11.6: Summary of the results of searches for a Higgs boson in association with a top quark pair by ATLAS and CMS. The results are given in terms of a measured signal strength. When available, the statistical and systematic contributions to the total uncertainty are reported separately and in this order. The ATLAS [161] and CMS [162] diphoton results indicated by (∗) are not included in the overall combinations which include versions of the diphoton analyses with smaller Run 2 datasets. The combination includes the $t\bar{t}(H \to b\bar{b})$ channels reported in Table 11.5.

$t\bar{t}H$	ATLAS Run 1	CMS Run 1	ATLAS Run 2	CMS Run 2
$H \to \gamma\gamma$	$1.3\,^{+2.6}_{-1.7}\,^{+2.5}_{-1.7}$	$1.2\,^{+2.5}_{-1.7}\,^{+2.6}_{-1.8}$	$1.38\,^{+0.33}_{-0.31}\,^{+0.26}_{-0.18}$ (∗)	$2.27^{+0.86}_{-0.74}$ (∗)
$H \to 4\ell$	—	—	$1.2\,^{+1.4}_{-0.8}$ (∗)	0.0 ± 1.2 (∗)
$WW/\tau\tau/ZZ$	$1.4 \pm 0.6 \pm 1.0$	3.3 ± 1.4	$1.56\,^{+0.30}_{-0.29}\,^{+0.30}_{-0.27}$	$0.96\,^{+0.34}_{-0.31}$
Comb.	$1.7 \pm 0.5 \pm 0.8$	$2.6\,^{+1.0}_{-0.9}$	$1.32 \pm 0.18\,^{+0.21}_{-0.19}$	$1.49 \pm 0.16\,^{+0.27}_{-0.21}$

Table 11.7: Summary of the final states investigated in the search for Higgs boson pair production by ATLAS and CMS, most analyses make use of the 2016 Run 2 dataset corresponding to integrated luminosities of up to 36 fb^{-1}. For ATLAS, the result indicated by (*) uses mostly the $b\bar{b}W^+W^-$ channel. Results are 95% CL upper limits on the observed (expected) SM signal strengths.

Channel	ATLAS	CMS
$b\bar{b}\gamma\gamma$	20.3 (26)	23.6 (18.8)
$b\bar{b}b\bar{b}$	12.9 (21)	74.6 (36.9)
$b\bar{b}\tau^+\tau^-$	12.5 (15)	31.4 (25.1)
$W^+W^-W^+W^-$	160 (120)	–
$W^+W^-\gamma\gamma$	230 (170)	–
$b\bar{b}VV$	305 (305)*	79 (89)
Combination	6.9 (10)	22.2 (12.8)

The sensitivity region to the trilinear coupling production as in Fig. 11.5 (b), is mainly in the kinematic region where the two Higgs boson in the final state are on-shell and the Higgs boson acts as a propagator (off-shell). As discussed in the introduction to this section, this process interferes negatively with the background Higgs boson pair production (Fig. 11.5 (a)).

The measurement of the trilinear coupling requires separating the contributions of the diagram of Fig. 11.5 (b) from the box diagram of Fig. 11.5 (b), and therefore a precise knowledge of the top-Yukawa coupling is needed. Each diagram alone would produce rather distinct m_{HH} distribution. And, for values of the trilinear coupling close to the SM value, an additional discriminating feature of the signal with respect to one obtained with the box contribution alone is a deficit in the number of events. With large variations of the trilinear coupling, an excess of events over the SM prediction would be observed (for a value of the trilinear coupling about 6 times larger than its SM value, the number of events is equal to the SM expectation). Additional sensitivity to the trilinear coupling is also obtained from the kinematical distributions of the signal taking in particular into account the effect of the HH mass distribution which discriminates the main contributions of Fig. 11.5. This further discrimination is instrumental in resolving the degeneracy in the total cross section mentioned above. The bounds obtained by ATLAS [173] and CMS [174] are the following:

$$\begin{aligned} &\text{(ATLAS)} \; -5.0 < \kappa_\lambda < 12.0 \,\text{(observed)}, \\ &\qquad\quad -5.8 < \kappa_\lambda < 12.0 \,\text{(expected)}, \\ &\text{(CMS)} \; -11.8 < \kappa_\lambda < 18.8 \,\text{(observed)}, \\ &\qquad\quad -7.1 < \kappa_\lambda < 13.6 \,\text{(expected)}, \end{aligned} \tag{11.13}$$

where κ_λ is the ratio between the trilinear coupling value left free in the fit and its expected value in the SM ($\kappa_\lambda = 1$ corresponds to the SM). These results are also illustrated in Fig. 11.6.

The analyses performed at Run 2 bring substantial improvements from those of Run 1, and they were used to reappraise the sensitivity of the LHC in the High Luminosity regime in the framework of the update of the European Strategy for Particle Physics [104]. The result in terms of bounds on the trilinear coupling are shown in Fig. 11.6, indicating that the significance of the observation of the HH process reaches 4σ. It is also apparent that the degeneracy of secondary minimum at intermediate values of κ_λ is resolved by the use of the kinematic discriminants. Indeed, this secondary minimum is expected to be excluded at 99.4% CL. This is very important to allow the measurement in the vicinity of the SM value at one standard deviation and to provide a meaningful confidence interval. At HL-LHC, the foreseen precision on κ_λ is approximately 50%.

Significantly higher precisions can be reached at pp colliders (and e^+e^- colliders) at higher centre-of-mass energies. The foreseen precision for a High-Energy (HE) LHC at a centre-of-mass energy of 27 TeV is expected to be within 10% to 20% [104]. At a very large hadron collider at a centre-of-mass energy of 100 TeV, a 5% sensitivity is expected to be reached, provided that the theoretical and parametric uncertainties are kept at the 1% level.

Indirect constraints on the Higgs boson trilinear coupling from single Higgs boson production processes will be discussed in Section 11.6.2.5.

11.3.5 *Searches for rare decays of the Higgs boson*

11.3.5.1 *$H \to Z\gamma$ and the Dalitz $H \to \ell^+\ell^-\gamma$ decay*

The search for $H \to Z\gamma$ is performed in the final states where the Z boson decays into opposite sign and same flavour leptons ($\ell^+\ell^-$), ℓ here refers to e or μ. While the branching fraction for $H \to Z\gamma$ is comparable to $H \to \gamma\gamma$ (about 10^{-3}) at $m_H = 125$ GeV, the observable signal yield is brought down by the small branching ratio of $Z \to (e^+e^- + \mu^+\mu^-) = 6.7 \times 10^{-2}$. In these channels, the $m_{\ell\ell\gamma}$ mass resolution is excellent (1–3%), therefore the analyses search for a narrow mass peak over a continuous background. The major backgrounds arise from the $Z + \gamma$ final state radiation in Drell–Yan decays and from the Z + jets processes where a jet is misidentified as a photon. The ratio of signal over background in this channel is typically of the order of 0.5%. In a narrow window of a few GeV around 125 GeV, several hundreds of events are expected in a Run 2 dataset corresponding to approximately 36 fb^{-1}.

Events are divided into mutually exclusive categories on the basis of the expected $m_{Z\gamma}$ resolution and the signal-to-background ratio. A VBF category is formed for $H \to Z\gamma$ candidates which

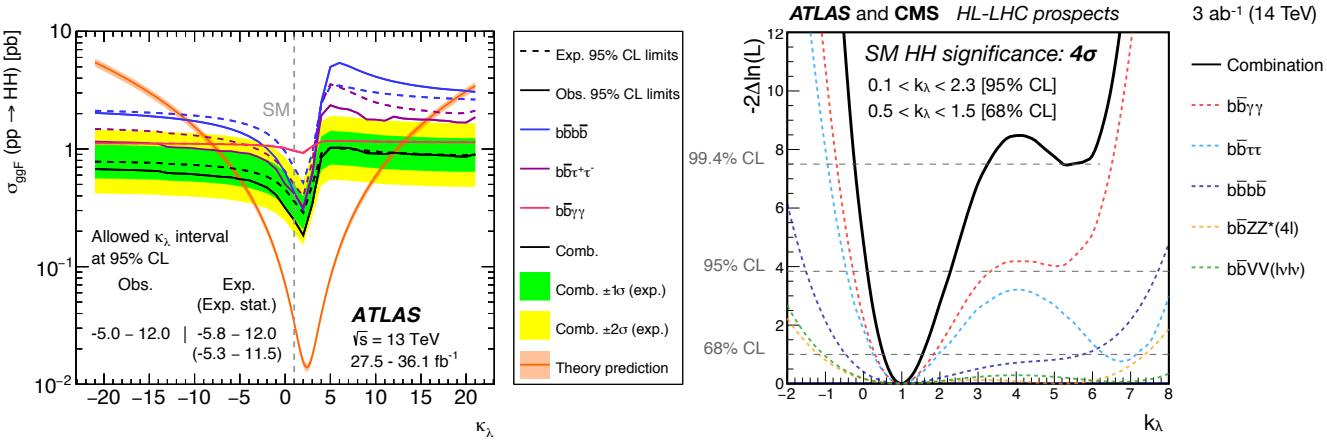

Figure 11.6: (Left) Upper limit obtained by ATLAS on the total $pp \to HH$ production cross section as a function of the trilinear coupling modifier κ_λ. The variation of the limit corresponds to variations in the signal acceptance. The expected total production cross section is also illustrated (red). (Right) Expected combined ATLAS and CMS likelihood for the searches for the $pp \to HH$ production at the High Luminosity LHC. The channels used in the combination are indicated in the figure.

are accompanied by two energetic jets separated by a large pseudo-rapidity. While this category contains only about 2% of the total event count, the signal-to-noise ratio is about an order of magnitude higher. The search for a Higgs boson is conducted independently in each category and the results from all categories are then combined.

No excess of events is observed in either ATLAS or CMS in the Run 1 data. The CMS expected and observed 95% CL upper limits for $m_H = 125\,\text{GeV}$ on the signal strength μ are 10.0 and 9.5 respectively. The ATLAS expected and observed upper limits on the signal strength μ are 9.0 and 11.0 respectively, for $m_H = 125.5\,\text{GeV}$.

The CMS analysis also extended the search for the so-called Dalitz Higgs boson decays $H \to \gamma^*\gamma \to \ell^+\ell^-\gamma$ in the low mass γ^* range of $m_{\ell\ell} < 20\,\text{GeV}$. This decay mode has a substantially larger branching fraction compared to the $Z\gamma$ decay, as $\Gamma(H \to \gamma^*\gamma \to e^+e^-\gamma) \sim 3.5\% \times \Gamma(H \to \gamma\gamma)$ and $\Gamma(H \to \gamma^*\gamma \to \mu^+\mu^-\gamma) \sim 1.7\% \times \Gamma(H \to \gamma\gamma)$, while $\Gamma(H \to Z\gamma) = 2.3\% \times \Gamma(H \to \gamma\gamma)$ (which does not account for the subsequent decay of the Z boson to electrons or muons). The limits in this channel are therefore stronger and CMS has observed an upper limit of 6.7 times the SM branching ratio [175].

ATLAS has performed an analysis of the full 2015 and 2016 Run 2 data to search for the $Z\gamma$ decay mode [176]. No significant excess was observed and 95% CL observed (expected) upper limits on the signal strength are 6.6 (5.2).

CMS has repeated its $Z\gamma$ and $\gamma^*\gamma$ analyses with the 2016 dataset and obtained much more stringent observed limits on cross section times the corresponding branching fractions of 1.4 and 4.0 (6.1 and 11.4) times the SM cross section for $H \to \gamma^*\gamma$ ($H \to Z\gamma$) [177]. CMS also performed a combination of the two modes, obtaining a combined observed (expected) limit of 3.9 (2.0) times the SM branching fractions.

11.3.5.2 $H \to \mu^+\mu^-$

The branching fraction in the $H \to \mu^+\mu^-$ channel for a 125 GeV SM Higgs boson is 2.2×10^{-4}, about ten times smaller than that for $H \to \gamma\gamma$. The dominant and irreducible background arises from the $Z/\gamma^* \to \mu^+\mu^-$ process which has a rate several orders of magnitude larger than that from the SM Higgs boson signal. Due to the precise muon momentum measurement achieved by ATLAS and CMS, the $m_{\mu^+\mu^-}$ mass resolution is very good ($\approx$ 2–3% for ATLAS and $\approx$ 1–3% for CMS depending on the selected categories; a better resolution is expected for CMS due its higher field in the inner detector). A search is performed for a narrow peak over a large but smoothly falling background. For optimal search sensitivity, events are divided into several categories. Either taking advantage of the superior muon momentum measurement in the central region, events can be subdivided by the pseudo-rapidity of the muons, or designing selections aiming at specific production processes such in particular as the vector boson fusion.

No excess in the $m_{\mu^+\mu^-}$ spectrum is observed near 125 GeV. From an analysis of the Run 1 data, ATLAS sets an observed (expected) 95% CL upper limit on the signal strength $\mu < 7.0$ (7.2). The CMS analysis of its 7 and 8 TeV data sets an observed (expected) limit of $\mu < 7.4$ (6.5).

ATLAS performed a reoptimised analysis using the full Run 2 dataset and categorising events in number of jets including VBF-topology specific categories [178]. The data showed a non-significance excess with a best-fit value of the signal strength for Higgs boson with a mass of 125 GeV, $\mu = 0.5 \pm 0.7$. The data subsequently yielded an observed (expected) 95% CL upper limit on the signal strength of 1.7 (1.3) , assuming $\text{BR}(H \to \mu\mu) = 0$, (while the expected limit assuming the SM value for $\text{BR}(H \to \mu\mu)$ is 2.2).

CMS, having analysed its 2016 dataset of Run 2, has obtained an observed (expected) limit on the production cross section times the branching fraction to a pair of muons of 3.0 (2.5) times the SM expectation [179]. In combination with the Run 1 data, the limit improves to 2.2 times the SM expectation. A non significant excess is also observed (with a significance of approximately 1σ) and the best fit signal strength is $1.0 \pm 1.0\,(\text{stat}) \pm 0.1\,(\text{syst})$.

11.3.5.3 $H \to e^+e^-$

A search similar to the $H \to \mu^+\mu^-$ is performed by CMS in the di-electron channel. In this search channel, the contribution from the peaking background from Higgs boson decays to diphotons mis-identified as di-electrons (when mostly converted photons are faking electrons) needs to be assessed. The sensitivity to the SM Higgs decays is negligible given the extremely small branching fraction to e^+e^-, approximately 40'000 times smaller than the branching fraction to dimuons. It is nevertheless interesting to probe this decay channel to search for potential large anomalous couplings. Assuming a SM Higgs boson production cross section, the observed limit on the branching fraction at the 95% CL is 0.0019, five orders of magnitude larger than the expected SM prediction. It is also important to note that processes not depending on the electron Yukawa coupling such as the $H \to e^+e^-\gamma$ (where the photon is soft), are sizeably larger than the direct Yukawa coupling process, but also much smaller than the current constraints, making any interpretation in terms of constraint on the electron Yukawa couplings far from straightforward.

At Run 2, ATLAS has also performed a search for the $H \to e^+e^-$ decay mode with the full dataset, improving the current limit by a factor of approximately 5, with a limit of 3.6×10^{-4} on the branching fraction [180].

11.3.5.4 *Lepton flavour violating (LFV) Higgs boson decays*

Given the Yukawa suppression of the couplings of the Higgs boson to quarks and leptons of the first two generations and the small total width of the Higgs boson, new physics contributions could easily have sizable branching fractions. One very interesting possibility is the Lepton Flavour Violating (LFV) decays of the Higgs boson, in particular in the $\tau\mu$ and τe modes. These decays are suppressed in the SM but they could easily be enhanced in theories such as two-Higgs-doublet models (discussed in Section 11.7).

There are already constraints on LFV Yukawa couplings $|Y_{\tau\mu}|$ from channels such as the $\tau \to 3\mu$ or $\tau \to \mu\gamma$, or a reinterpretation of the search for Higgs boson decays to $\tau^+\tau^-$. A direct search at the LHC, however, complements these indirect limits. The search for LFV decays in the $\tau\mu$ channel have been done with the Run 1 dataset in several channels according to the subsequent decay of the τ. The results from CMS [181] and from ATLAS for the hadronic [182], the leptonic [183] decays of the tau, and their combination [183] are reported in Table 11.8. It is interesting to note that the analysis strategies at Run 1 for the di-lepton $\tau_{\rm lep}\mu$ channel are very different between ATLAS [183] and CMS [181].

As shown in Table 11.8, an excess was observed in this channel by CMS with a significance of 2.5σ, while in ATLAS analysis, the excess is smaller, about 1σ at Run 1. CMS has performed the search again with the full 2016 Run 2 dataset [184], relying on a multivariate analysis. The observed best fit branching fraction is $(0.00 \pm 0.12)\%$. These limits are reported in Table 11.8.

ATLAS and CMS have also performed a search for the LFV Higgs boson decays in the τe and μe channels [183–185]. No significant excess was observed and 95% CL limits are reported in Table 11.8, for the τe channel only. For the μe channel, the constraints from the $\mu \to e\gamma$ experiments [186] are much stronger than those from the direct LFV Higgs boson decay search. However these indirect constraints can be relaxed by the cancellation of LFV effects from new physics.

At Run 2, ATLAS has performed searches for LFV decays of the Higgs boson in the $e\tau$ and $\mu\tau$ channels [187] as well as in the $e\mu$ channel [180]. The searches for the $H \to e\tau$ and $H \to \mu\tau$ decays where done with the 2016 data only and yielded upper limits on the LFV decay branching fraction of 0.47% (0.34%) and 0.28% (0.37%), respectively.

CMS has also searched for LFV decays with the 2016 dataset at Run 2 and obtained observed (expected) limits on the LFV branching fraction of $\mathrm{BR}(H \to \mu\tau) < 0.25\%$ (0.25%) and $\mathrm{BR}(H \to e\tau) < 0.61\%$ (0.37%), at the 95% CL [188]. These limits were also interpreted in terms of constraints on the corresponding off-diagonal Yukawa couplings.

The results obtained by ATLAS and CMS at Run 2 do not confirm the excesses observed at Run 1.

11.3.5.5 *Probing charm- and light-quark-Yukawa couplings*

Probing the Yukawa couplings to quarks of the second or even the first generation is extremely challenging given the overwhelming backgrounds and very small rates.

The possibility of probing the Yukawa coupling to the charm has been discussed in Ref. [189] where indirect bounds are estimated from a combined fit to the Higgs data and the importance of using charm tagging is emphasised. Searches in the VH production mode have then been carried out, in the channels very similarly to those aiming at the b-quark Yukawa coupling, by both ATLAS [190] and CMS [191] with Run 2 data. The upper limits obtained (expected) on the VH production cross section times the charm quark decay branching fraction of the Higgs boson are:

$$\text{(ATLAS)}\ \ \sigma(ZH) \times \mathrm{BR}(H \to c\bar{c}) < 2.7\ \ (3.9^{+2.1}_{-1.1})\,\text{pb}, \quad (11.14)$$

$$\text{(CMS)}\ \ \frac{\sigma(VH) \times \mathrm{BR}(H \to c\bar{c})}{\sigma(VH)_{SM} \times \mathrm{BR}(H \to c\bar{c})_{SM}} < 70\ \ (37^{+16}_{-10}). \quad (11.15)$$

The ATLAS search [190] was done in the ZH channel where the Z boson decays to a pair of leptons (electrons or muons) only. The expected cross section times branching fraction $\sigma(ZH) \times \mathrm{BR}(H \to c\bar{c})$ is $26\,\mathrm{fb}^{-1}$.

Another possibility to access the charm Yukawa coupling has been discussed in Ref. [192]. It relies on the decays of the Higgs boson to a final state with charmonium: $H \to J/\Psi\gamma$. Higgs boson decays in this final state have been searched for by ATLAS [193]. The sensitivity of this analysis is, however, several orders of magnitude above the branching fraction estimated in the SM: $\mathrm{BR}(H \to J/\Psi\gamma) = (2.8 \pm 0.2) \times 10^{-6}$. ATLAS [193] has also searched for Higgs boson decays to $\Upsilon(nS)\gamma$ where $(n = 1, 2, 3)$, a channel with much lower sensitivity than the $H \to b\bar{b}$ to the Yukawa coupling to b-quarks.

More recently, ATLAS has searched, , with a specific trigger, for another quarkonia final state where the Higgs boson decays to $\phi\gamma$ [194] at the LHC Run 2 and a center-of-mass energy of 13 TeV. This channel could probe deviations from the strange-quark Yukawa coupling. Its sensitivity is several orders of magnitude above the SM expectation. Other quarkonia final states, such as the $\rho\gamma$, which could potentially probe the Yukawa coupling to light quarks, can also be searched for.

CMS has also performed a search of the decays of the Higgs boson in the $J/\Psi J/\Psi$ and $\Upsilon\Upsilon$ decay to cover the cases where the photon in the $J/\Psi\gamma$ decay is virtual and transforms into a J/Ψ meson, These decays provide an additional channel potentially sensitive to BSM phenomena [195].

11.3.5.6 *Rare decays outlook*

Rare decays such as those described in the above sections have clearly a limited sensitivity. However, they already deliver interesting messages. For example, if the coupling of the Higgs boson to muons was as strong as it is to top quarks, this mode should have been observed. Therefore, it can be concluded that the observed couplings of the Higgs boson are manifestly non-universal. Further developing these rare decay modes is an important component of the High Luminosity program of the LHC in order to directly probe the couplings of the Higgs boson, and to potentially measure the Yukawa coupling to the fermions of the second generation, in particular to muons. It is also an integral part of the physics program of the discussed potential future Higgs boson factories.

11.3.6 *Searches for non-SM decay channels*

The main decay and production properties of the observed Higgs boson are consistent with the SM predictions. The Higgs boson may, however, have other decay channels beyond those anticipated in the SM. Among these, and of great interest, are the invisible decays into stable particles, such as DM particle candidates, that interact very weakly with the detector, and that remain undetected. Other non standard decay channels that have been investigated are the decays of the Higgs particle to hidden valley or dark particles.

11.3.6.1 *Invisible decays of the Higgs boson*

The discovery of the Higgs boson immediately raised the question of its couplings to DM and how it could be used to reveal at colliders the existence of a dark sector coupled to the SM via the Higgs boson portal, see Ref. [196] and references therein. If kinematically accessible and with a sufficiently large coupling to the Higgs boson, DM particles, such as, e.g., neutralinos in SUSY models, graviscalars in models with extra dimensions or heavy neutrinos in the context of four-generation fermion models, would manifest themselves as invisible decays of the Higgs boson, thus strongly motivating searches for the invisible decays of the Higgs boson.

To identify an invisibly decaying Higgs boson at the LHC, it must be produced in association with other particles. Searches for invisible decays of the Higgs particle at the LHC have been carried out in the three associated production modes of the Higgs boson with the highest SM cross sections and target events with large missing energy.

The ggF production mode has the largest SM cross section but it usually results in the Higgs boson being created alone and hence leaving no characteristic signature in the detector of its invisible decay. One way to search for invisible decays in ggF production mode is to look for events with the monojet topology arising from initial state gluon radiation and containing missing energy. The major irreducible background in such searches stems from Z + jets

Table 11.8: Summary of the results of searches for lepton flavour violating decays of the Higgs boson in the $\tau\mu$ and τe channels from ATLAS and CMS. For the result with *, the expected sensitivity was not reported but appears consistent with the observed one.

	ATLAS (Run 1)	CMS (Run 1)	CMS (Run 2)
BR($H \to \tau\mu$)	$(0.53 \pm 0.51)\%$	$(0.84^{+0.39}_{-0.37})\%$	$(0.00 \pm 0.12)\%$
95% CL Obs. (Exp.)	1.43% (1.01%)	1.51% (0.75%)	0.25% (0.25%)
$H \to \tau e$ 95% CL Obs. (Exp.)	1.02% (1.21%)	0.69%*	0.61% (0.37%)

events where the Z boson decays into a pair of neutrinos [197]. The analysis with the best sensitivity targets the VBF production topology but it suffers from large backgrounds arising from events with two jets and large missing energy. The VH mode has much smaller cross section but the presence of a W or Z boson allows a variety of final states that can be tagged with relatively low background.

ATLAS and CMS have searched for such final states at Run 1 and have observed no significant excess over the predicted backgrounds (for references, see the previous edition of this review [123]). Table 11.9 summarizes the 95% CL limits on the invisible decays of the Higgs boson assuming a SM Higgs boson production cross section and the corresponding detector acceptances.

ATLAS has performed the search for invisible decays of the Higgs boson at Run 2 with the 2015 and 2016 datasets, corresponding to an integrated luminosity of approximately 36 fb^{-1}, in the VBF production [198], the ZH associated production where the Z boson subsequently decays to a pair of leptons [199], and the VH associated production where the vector boson (a W or a Z) subsequently decays hadonically [200]. The most stringent constraint is obtained through the VBF channel. All results and their combination [201] are reported in Table 11.9. Combined with the Run 1 results, the ATLAS limit on the invisible branching fraction reaches 26%, with an expected sensitivity of 17% [201].

CMS has updated the search for invisible decays of the Higgs boson in the vector boson fusion and the associated production with a vector boson channels (both with subsequent leptonic [202] and hadronic decays [203]) using Run 2 data collected in 2016 [204]. It has produced a combination with Run 1 channels, yielding a limit on the invisible branching fraction of 19%, with an expected sensitivity of 15% [204].

CMS has also reinterpreted a search for scalar top quarks in the all-hadronic, semi-leptonic and fully leptonic final state with the 2016 data of Run 2 to set limits on the invisible Higgs decays through the $pp \to t\bar{t}H$ production mode [205]. The results of the search are reported in Table 11.9.

This constraint can then be further used to probe Higgs portal models to DM [196], where an additional weakly interacting particle χ with mass lower than $m_H/2$ is introduced as DM candidate and where the Higgs boson is considered as the only mediator between the SM particles and DM. In this model, it is interesting to express the limit on the invisible branching fraction in terms of strength of interaction of DM with standard matter, i.e., in terms of it interaction cross section with nucleons $\sigma_{\chi-N}$. In this model, the couplings of the Higgs boson to SM particles are assumed to be those of the SM and the interaction of the Higgs boson with the nucleon is parametrised in a Higgs-Nucleon form factor estimated using lattice QCD calculations [196]. The exclusion limits from the constraints on invisible Higgs boson decays, both direct and indirect from the measurement of the coupling properties of the Higgs boson can be compared to direct detection experiments. For comparison, the limit at 90% CL on the invisible branching fraction of $\text{BR}_{\text{inv}} < 19\%$ [204] is used and converted into limits on $\sigma_{\chi-N}$ under several hypotheses on the nature of DM particles depending mainly on their spin (scalar- or fermion-like). The vector DM hypothesis is not included since (renormalisable) models of vectorial DM require an extended dark sector that could imply modifications of the signal. The results are shown in Fig. 11.7.

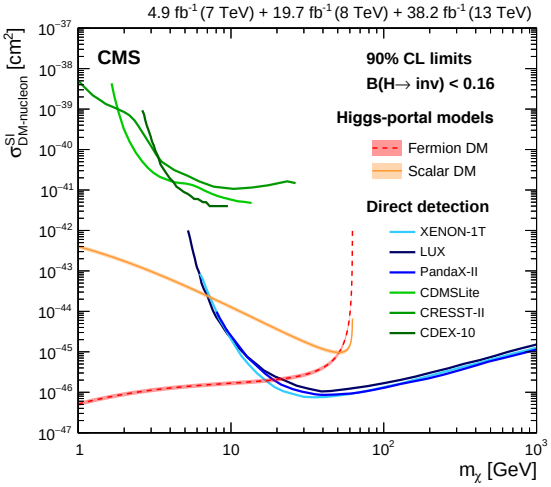

Figure 11.7: 90% CL upper limits on the WIMP-nucleon scattering cross section as a function of the DM particle mass. Spin-independent results excluded and favored regions from direct detection experiments are also shown.

11.3.6.2 *Exotic Higgs boson decays*

The 125 GeV Higgs boson serves not only as a probe for potential DM candidates, but also to search for other exotic particles arising from fields associated with a low-mass hidden sector. Such hidden sectors are composed of fields that are singlet under the SM gauge group $\text{SU}(3) \times \text{SU}(2) \times U(1)$. These models are referred to as hidden valley models [206]. Since a light Higgs boson is a particle with a narrow width, even modest couplings to new states can give rise to a significant modification of the Higgs boson phenomenology through exotic decays. Simple hidden valley models exist in which the Higgs boson decays to an invisible fundamental particle, which has a long lifetime to decay back to SM particles through a small mixing with the SM Higgs boson, see Ref. [206] for a concrete example. The Higgs boson may also decay to a pair of hidden valley "v-quarks," which subsequently hadronise in the hidden sector, forming "v-mesons." These mesons often prefer to decay to the heaviest state kinematically available, so that a possible signature is $H \to 4b$. Some of the v-mesons may be stable, implying a mixed missing energy plus heavy flavour final state. In other cases, the v-mesons may decay to leptons, implying the presence of low mass lepton resonances in high-H_T events [207]. Other scenarios have been studied [208] in which the Higgs boson decays predominantly into light hidden sector particles, either directly, or through light SUSY states, and with subsequent cascades that increase the multiplicity of hidden sector particles. In such scenarios, the high-multiplicity hidden-sector particles, after decaying back into the SM, appear in the detector as clusters of collimated leptons known as "lepton jets".

A variety of models have been investigated searching for final states involving dark photons and hidden valley scalars. The resulting topologies typically have leptons or light hadrons which in some cases can be prompt (i.e., originating from the hard process interaction point) or not and are in some cases collimated and reconstructed as jets [209, 210], and long lived weakly interacting particles. The latter occur not only in hidden valley scenarios, but also in gauge-mediated extensions of the minimal SUSY standard model (MSSM), the MSSM with R-parity violation, and inelastic DM scenarios [211]. Finally, CMS has performed a search for pair production of light bosons [212]. Such a scenario can occur in SUSY models with additional hidden (or dark) valleys.

Table 11.9: Summary of the channels searched for and the corresponding 95% CL limits from ATLAS and CMS on the branching fraction for the Higgs boson decay to invisible particles assuming a SM Higgs boson production cross section. The results in parentheses are the expected exclusions.

	ATLAS (Run 1)	ATLAS (Run 2)	CMS (Run 1)	CMS (Run 2)
ggF (monojet); $H \to$ inv.	–	–	67 (71) %	66 (59)%
VBF; $H \to$ inv.	28 (31) %	37 (28) %	57 (40) %	33 (25) %
ZH; $Z \to \ell^+\ell^-$; $H \to$ inv.	75 (62)%	67 (39) %	75 (91) %	40 (42)%
VH; $Z, W \to jj$; $H \to$ inv.	78 (86)%	83 (58) %	–	50 (48)%
ZH; $Z \to b\bar{b}$; $H \to$ inv.	–	–	182 (189)%	–
Combination	25 (27)%	38 (21)%	–	26 (20) %
Run 1 & 2 Combination	26 (17)%		19 (15)%	
$t\bar{t}H$; $H \to$ inv.	–	–	–	46 (48)%

11.4 Combining the main channels

The analysis strategy used by the LHC experiments to perform the searches for the Higgs boson has been based on the Higgs boson decay modes. It is a natural choice given that it focusses on the decay products of the object searched for. However, for each channel, exclusive sub-channels have been defined according to the Higgs boson production processes and, in the results presented, these sub-channels have been combined. The natural extension of this approach in order to probe further the production and decay modes of the Higgs boson is to combine the analysis channels together. Such a combination is also used in Section 11.6 to further measure the coupling properties of the Higgs boson.

At the LHC, the total cross section cannot be measured in any of the production modes. As a consequence, neither the absolute branching fractions nor the total width of the Higgs boson can be directly measured, at least if the width is of the SM size. However, a combined measurement of the large variety of categories described in Section 11.3, with different sensitivities to various production and decay modes, permits a wide variety of measurements of the production, decay and coupling properties. These measurements require, in general, a limited but nevertheless restrictive number of assumptions.

In this section, three sets of results will be given. The first one is the ATLAS and CMS Run 1 combination [141]. The other two are the individual combinations of ATLAS and CMS independently with partial Run 2 dataset. It is important to note that, between the Run 1 and the Run 2 results, the signal theoretical systematic uncertainties have improved significantly.

The Run 1 full combination results were derived by the two collaborations, taking rigorously into account all correlations in the systematic uncertainties and in the large number of channels and their categories.

At Run 2, ATLAS [213] and CMS [214] have already produced combined measurements of the coupling properties of the Higgs boson with partial datasets, of up to $80\,\text{fb}^{-1}$ and up to $36\,\text{fb}^{-1}$ respectively.

In this section, only the results on the main Higgs boson production and decay modes will be discussed. Only a brief presentation of the combination framework is given here (a more detailed description is given in Ref. [215]). This framework will also be used in Section 11.6 to discuss the measurements of the coupling properties of the Higgs boson.

11.4.1 *Principles of the combination*

The combination of the Higgs boson analysis channels in each experiment and for the two experiments together was done using a fit of a signal and background model to the data. As described above, the data was made of a large number of categories, aiming at reconstructing exclusive production and decay modes. In the combination of ATLAS and CMS [141], there were approximately 600 categories. The combination was a simultaneous fit to all these categories, using a reduced number of parameters of interest and a Higgs boson mass fixed at its measured value (see Section 11.3.2). The much larger number of categories present in the ATLAS and CMS combination [141] is due to additional separation in terms of finer exclusive production regions, decay channels of the Z and the W bosons, and taus, control regions where little-to-no signal is present, and different center-of-mass energies. It should be noted that the individual combination performed by ATLAS [216] included two additional decay channels: the $\mu^+\mu^-$ and $Z\gamma$. For the sake of simplicity these channels were omitted in the ATLAS–CMS combination. In addition, a $H \to b\bar{b}$ analysis performed by CMS, see the reference in Ref [123], and included in its own combination, has been omitted from the ATLAS–CMS combination.

In their Run 2 individual combinations, ATLAS and CMS have not considered the $Z\gamma$ channel. The CMS experiment has included the $\mu\mu$ channel.

The key to understand how the combination of channels works relies on the combination master formula, which expresses for each category, indexed by c, of a given channel (typically a category covers mostly one decay mode, but possibly various production modes), the measured number of signal events n_s^c as a function of a limited number of parameters as follows:

$$n_s^c = \left(\sum_{i,f} \mu_i \, \sigma_i^{\text{SM}} \times A_{if}^c \times \varepsilon_{if}^c \times \mu_f \, \text{BR}_f^{\text{SM}} \right) \times \mathcal{L}^c. \quad (11.16)$$

The production index is defined as $i \in \{\text{ggF}, \text{VBF}, VH, t\bar{t}H\}$ and the decay index is defined as $f \in \{\gamma\gamma, WW, ZZ, bb, \tau\tau\}$, while σ_i^{SM} and BR_f^{SM} are the corresponding production cross sections and decay branching fractions, estimated as described in Section 11.2, assuming that the Higgs boson is that of the SM. A_{if}^c and ε_{if}^c are the signal acceptance and the reconstruction efficiency for the given production and decay modes in the category c. $\mathcal{L}^c$ is the integrated luminosity used for that specific category. For the purpose of this review, these parameters can be considered as fixed[3].

The parameters of interest in the master formula are the signal strength parameters μ_i and μ_f. It is important to note that the formula relies on the factorisation of the production cross section and decay branching fraction, which assumes the narrow width approximation. The width of the Higgs boson will be discussed in Section 11.5, however, for the precision needed here, the fact that the Higgs boson has been observed in decay channels with high mass resolution as a resonance is sufficient to validate this hypothesis. It is also manifest in the above equation that the ten parameters for the production modes (μ_i) and decay modes (μ_f) cannot be determined simultaneously. This illustrates that total cross sections or branching fractions cannot be measured without further assumptions in this fit.

The master formula also illustrates an important caveat to the measurement of signal strength parameters. In case these are interpreted as scale factors of the production cross sections or branching fractions, then all the other quantities such as the acceptances and efficiencies, A_{if}^c and ε_{if}^c, need to be assumed as independent and fixed to their estimated values for the SM Higgs boson. An additional important caveat to note concerning these combined results is that only the normalisation is varied, while the discriminating variables for the signal are not modified and

[3] In the combination performed by ATLAS and CMS, the systematic uncertainties on these parameters are taken into account by allowing these parameters to vary in the fit.

Table 11.10: Summary of the observation significances (with respect to the background only hypothesis) for the main production and decay processes at the LHC. Measured signal strengths are reported when the observation has been established unambiguously. Measured signal strengths are reported with the uncertainty of statistical nature first and systematic last, ATLAS has not reported these results in its Run 2 combination (NR). *The Run 2 VH significances reported in this table are obtained from the observation of the Higgs boson decays to b quarks, while the Run 1 combination corresponds to combination of all channels.

	Decay modes			
	ATLAS (Run 1)	CMS (Run 1)	ATLAS (Run 2)	CMS (Run 2)
$\gamma\gamma$	4.6σ (5.3σ)	5.2σ (4.6σ)	NR	$1.20\,^{+0.13\ +0.12}_{-0.11\ -0.09}$
ZZ	6.2σ (6.3σ)	8.1σ (6.5σ)	NR	$1.06\,^{+0.16\ +0.11}_{-0.15\ -0.08}$
WW	5.9σ (5.4σ)	6.5σ (4.7σ)	NR	$1.28\,^{+0.09\ +0.14}_{-0.09\ -0.13}$
$\tau^+\tau^-$	3.4σ (3.9σ)	4.5σ (3.8σ)	6.4σ (5.4σ)	5.9σ (5.9σ)
	Comb. 5.0σ (5.5σ)			
$b\bar{b}$	2.6σ (2.5σ)	1.4σ (2.1σ)	5.4σ (5.5σ)	5.5σ (5.6σ)
	Comb. 3.7σ (2.6σ)			
	Production modes			
	ATLAS and CMS (Run 1)		ATLAS (Run 2)	CMS (Run 2)
$qq \to qqH$ (VBF)	Comb. 5.4σ (4.6σ)		$1.21\,^{+0.18\ +0.16}_{-0.17\ -0.13}$	$0.73\,^{+0.24\ +0.17}_{-0.23\ -0.15}$
$pp \to VH$	Comb. 3.5σ (4.2σ)		5.3σ (4.8σ)*	4.8σ (4.9σ)*
$pp \to t\bar{t}H$	Comb. 4.4σ (2.2σ)		5.8σ (4.9σ)	5.2σ (4.2σ)

are still used in the fit. These caveats are of particular importance in the use of the combination to measure the coupling properties of the Higgs boson, as discussed in Section 11.6. For relatively small perturbations of the couplings of the Higgs boson from the SM values, this hypothesis is valid.

However, the products $\mu_i \times \mu_f$ can be considered as free parameters and in principle measurable (if there is sufficient sensitivity from specific categories). Measuring the products of signal strengths can be viewed as measuring the cross sections times the branching fraction, $\sigma \cdot \mathrm{BR}$. An illustration of the results for the Run 2 combinations of ATLAS and CMS is presented in Fig. 11.8 for the combination of ATLAS and CMS.

A coherent picture emerges (including the Run 1 results, see Ref. [123]) where an excellent consistency between the observation in each channel and the SM expectation. This multi-parameter fit quantifies the current experimental knowledge of the main production and decays modes. Run 2 results are also available [213, 214]. These are not included in the figure for the sake of simplicity. The Run 2 results are already competitive with the Run 1 results. In Fig. 11.8, the Run 1 results are kept for illustration purposes. The theoretical uncertainty in the aforementioned fit is not included in the measured values of the signal strengths but is illustrated on the unit value corresponding to the SM expectation.

Other fits involving ratios of cross sections, which are less sensitive to theory uncertainties, are performed and reported in Ref. [215].

The most constrained fit in the combination allows for only one single parameter to vary, i.e., $\forall(i,f), \mu_i = \mu_f = \mu$. This global-signal-strength model provides the simplest probe of the compatibility of the signal with the SM Higgs boson. Indeed, it is sensitive to any deviation from the SM Higgs boson couplings provided that these deviations do not cancel overall. The full Run 1 combination determines the global signal strength to be

$$\begin{aligned}\mu = 1.09 \pm 0.11 =& 1.09 \pm 0.07\ (\text{stat.})\ \pm 0.04\ (\text{expt.}) \\ & \pm 0.03\ (\text{th. bkg.})\ \pm 0.07\ (\text{th. sig.}),\end{aligned} \tag{11.17}$$

where the statistical, experimental uncertainties as well as the theoretical uncertainties on the background and on the signal are reported separately. The ATLAS Run 2 combination of the global signal strength yields [213]:

$$\begin{aligned}\mu = 1.11^{+0.09}_{-0.08} = 1.11\ & \pm 0.05\ (\text{stat.})\ ^{+0.05}_{-0.04}\ (\text{expt.}) \\ & \pm 0.03\ (\text{th. bkg.})\ ^{+0.05}_{-0.04}\ (\text{th. sig.}),\end{aligned} \tag{11.18}$$

while the CMS Run 2 combination yields [214]:

$$\begin{aligned}\mu = 1.17 \pm 0.10 = 1.17\ & \pm 0.06\ (\text{stat.})\ ^{+0.06}_{-0.05}\ (\text{th. sig.}) \\ & \pm 0.06\ (\text{other. syst.}).\end{aligned} \tag{11.19}$$

These overall signal strengths are fully compatible with the SM expectation, $\mu = 1$, with a precision of 10%. It is interesting to note that the main uncertainty in these measurements arises from the limited precision in the theoretical predictions for the signal production processes. The precision reached with the individual experiments combinations using partial Run 2 data sets have already exceeded the full Run 1 ATLAS and CMS combination precision.

11.4.2 *Main decay modes*

Despite the large number of decay channels, since the cross sections cannot be independently measured, from the measurements described in this section it is impossible to measure the decay branching fractions without a loss of generality. The simplest assumption that can be made is that the production cross sections are those of the SM, which is equivalent to assume that, for all i indices, $\mu_i = 1$. All branching fractions μ_f can then be measured in a simple 5 parameter fit. The results of these fits are reported in Table 11.10 in terms of significances to highlight their unambiguous observations: all the measured branching fractions are compatible with the SM values.

For the $\tau^+\tau^-$ channel, ATLAS and CMS were both only mildly sensitive at the Run 1 and have observed excesses in their data. The individual results were not sufficiently significant to claim an observation, however, in combination the evidence was very strong. It is really with the addition of the Run 2 data that the decay of the Higgs boson to tau pairs has been established by the two experiments independently and unambiguously (see Table 11.10 and Section 11.3.2).

As illustrated in Table 11.10, ATLAS and CMS were both less sensitive in the $H \to b\bar{b}$ decay mode. The available sensitivity

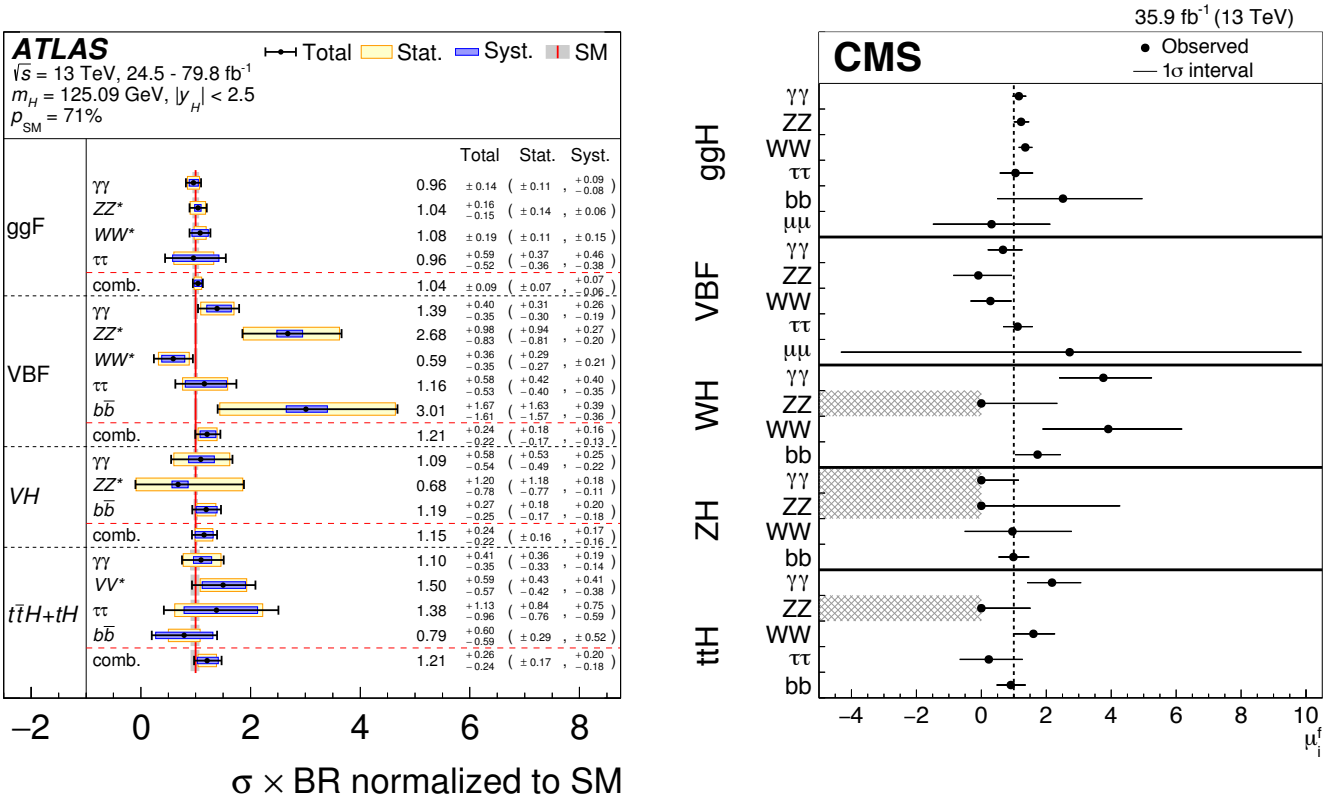

Figure 11.8: Combined measurements of the products $\sigma \cdot \mathrm{BR}$, normalised to the SM predictions, for the five main production and five main decay modes. The hatched combinations require more data for a meaningful confidence interval to be provided.

came mostly from the VH process. The combined significance of 3.7σ at Run 1 was sufficient to suggest evidence, however ATLAS and CMS observations were both low with respect to the rate expected in the SM. At Run 2, this channel benefited largely from the increased production cross sections at 13 TeV and the much larger dataset. In this case as well, it is with the addition of the Run 2 data that both experiments were able to establish a measurement in this channel (as discussed in Section 11.3.2).

These are major milestones of the LHC physics program.

11.4.3 *Main production modes*

Most analysis channels are divided into exclusive categories allowing for an increased overall sensitivity and permitting to access the various Higgs boson production modes. The cross sections of the main production modes can be measured assuming that the branching fractions are those of the SM, i.e., for all f indices $\mu_f = 1$. These assumptions lead to a 5 parameter combination. The results are reported in terms of significances of observation of the production modes in Table 11.10.

The gluon fusion production process is the dominant production mode. Although no numerical estimate of combined significance of observation for this process has been given by the experiments, it is considered as established due to the overwhelming evidence from the three main discovery channels. None of the other production modes have been firmly established by the experiments individually. However, the table shows that, for the VBF production mode, the combination had a large sensitivity and produced a combined observation of 5.4σ, therefore establishing this process with a rate compatible with that expected in the SM.

The VH production mode has only very recently been unambiguously observed by ATLAS and CMS independently (as discussed in Section 11.3.2) through the $V(H \to b\bar{b})$ channel. This is illustrated in the relative contributions of all channels to the VH process shown in Figure 11.8.

With the Run 2 data, all production processes have been established, and in particular the $pp \to t\bar{t}H$ process, which provides direct evidence of the coupling of the Higgs boson to top quarks. This is another milestone in the LHC physics program.

11.5 Main quantum numbers and width of the Higgs boson

11.5.1 *Main quantum numbers* J^{PC}

Probing the Higgs boson quantum numbers is essential to further unveiling its coupling properties. The measurements of the signal event yields in all the channels discussed in Sections 11.3 and 11.4, and their compatibility with the SM Higgs boson predictions, give a qualitative but, nonetheless, compelling indication of its nature. This qualitative picture is further complemented by the implications of the observation of the particle in the diphoton channel. According to the Landau–Yang theorem [217], the observation made in the diphoton channel excludes the spin-1 hypothesis and restricts possibilities for the spin to 0 or 2.

The Landau–Yang theorem does not apply if the observed state is not decaying to a pair of photons but to a pair of scalars subsequently decaying to two very collimated pairs of photons (as for example in the case of $H \to a_1 a_1 \to 4\gamma$). This possibility has not been rigorously excluded but is not experimentally favoured since tight selection criteria are applied on the electromagnetic shower shapes of the reconstructed photons. A more systematic analysis of shower shapes and the fraction of conversions could be performed to further discriminate between the single prompt photon and the two overlapping photons hypotheses. There are also potential theoretical loopholes concerning the applicability of the Landau–Yang theorem, such as off-shell vector boson decays. However, for the observed particle not to be of spin 0 and +1 parity would require an improbable conspiracy of effects. It is nevertheless important to test this hypothesis independently, in particular since the measurements of coupling properties of the Higgs boson assume that it is a CP-even state.

11.5.1.1 *Charge conjugation*

The charge conjugation quantum number is multiplicative, therefore given that the Higgs-like particle is observed in the $H \to \gamma\gamma$ channel, and given that photons are C-odd eigenstates, assuming C conservation, the observed neutral particle should be C-even.

11.5.1.2 *Spin and parity*

To probe the spin and parity quantum numbers of the discovered particle, a systematic analysis of its production and decay processes is performed in several analyses. These analyses are designed to be independent of the measured event yields and they rely instead on the production and the decay angles, and on the threshold distributions as long as a significant signal is observed, i.e., in situations when an excess over the expected background can be used to further discriminate between signal hypotheses. These analyses are based on probing various alternative models of spin and parity [218]. These models can be expressed in terms of an effective Lagrangian [219] or in terms of helicity amplitudes [220]. The two approaches are equivalent. In the following, the effective Lagrangian formalism is chosen to describe the models considered and a restricted number of models are discussed [219]. In the analysis performed by CMS [220], a larger number of models have been investigated, however, the main channels studied by both experiments are essentially the same and the main conclusions are similar and fully consistent.

i. *Spin-0 model*

The interaction Lagrangian relevant for the analysis of spin-0 particle interaction with a pair of W or Z bosons with either fixed or mixed SM and BSM CP-even couplings or CP-odd couplings, is the following [221]:

$$\begin{aligned}\mathcal{L}_0^{W,Z} \supset \Bigg\{ &\cos(\alpha)\kappa_{\rm SM}\left[\frac{1}{2}g_{HZZ}Z_\mu Z^\mu + g_{HWW}W_\mu^+ W^{-\mu}\right] \\ &- \frac{1}{4\Lambda}\left[\cos(\alpha)\kappa_{HZZ}Z_{\mu\nu}Z^{\mu\nu} + \sin(\alpha)\kappa_{AZZ}Z_{\mu\nu}\tilde{Z}^{\mu\nu}\right] \\ &- \frac{1}{2\Lambda}\left[\cos(\alpha)\kappa_{HWW}W^+_{\mu\nu}W^{-\mu\nu} + \sin(\alpha)\kappa_{AWW}W^+_{\mu\nu}\tilde{W}^{-\mu\nu}\right]\Bigg\} H,\end{aligned} \tag{11.20}$$

where $V^\mu = Z^\mu, W^{+\mu}$ are the vector boson fields, $V^{\pm\mu\nu}$ are the reduced field tensors and $\tilde{V}^{\pm\mu\nu} = 1/2\,\varepsilon^{\mu\nu\rho\sigma}V_{\rho\sigma}$ are the dual tensor fields. And Λ defines an effective theory energy scale. The factors $\kappa_{\rm SM}, \kappa_{HZZ}, \kappa_{HWW}, \kappa_{AZZ}, \kappa_{AWW}$ denote the coupling constants corresponding of the coupling of the SM and BSM CP-even and CP-odd components of the Higgs boson to the W and Z fields. The mixing angle α allows for the production of a CP-mixed state and the CP-symmetry is broken when $\alpha \neq 0, \pi$.

This formalism can be used to probe both CP-mixing for a spin-0 state, as discussed in Section 11.5.1.4 or specific alternative hypotheses, as discussed below in Section 11.5.1.3, such as a pure CP-odd state ($J^P = 0^-$) corresponding to $\alpha = \pi/2$, $\kappa_{\rm SM} = \kappa_{HVV} = 0$ and $\kappa_{AVV} = 1$. A BSM CP-even state $J^P = 0^+$ corresponds to $\alpha = 0$, $\kappa_{AVV} = 0$, $\kappa_{HVV} = 1$ and $\kappa_{\rm SM}$ arbitrary. These hypotheses are compared to the SM Higgs boson hypothesis corresponding to $\alpha = 0$ and $\kappa_{HVV} = \kappa_{AVV} = 0$ and $\kappa_{\rm SM} = 1$. This formalism has been adopted by the ATLAS experiment. The analysis of these benchmarks are illustrated in Fig. 11.9.

A different parametrisation of anomalous couplings of a spin-zero boson with two gauge bosons VV can also expressed in the general form of the scattering amplitude A:

$$\begin{aligned}A \sim &\left[a_1^{VV} - \frac{\kappa_1^{VV}q_1^2 + \kappa_2^{VV}q_2^2}{(\Lambda_1^{VV})^2} - \frac{\kappa_3^{VV}(q_1+q_2)^2}{(\Lambda_Q^{VV})^2}\right] m_{V_1}^2 \varepsilon_{V_1}^* \varepsilon_{V_2}^* \\ &+ a_2^{VV} f_{\mu\nu}^{*(1)} f^{*(2)\mu\nu} + a_3^{VV} f_{\mu\nu}^{*(1)} \tilde{f}^{*(2)\mu\nu}\end{aligned} \tag{11.21}$$

where ε_i is the polarization vector of the boson V_i, $f_{\mu\nu}^{*(i)} = \varepsilon_i^\mu q^\nu - \varepsilon_i^\nu q^\mu$ is a scalar tensor constructed from the vector boson V_i polarization and four momentum, $\tilde{f}_{\mu\nu}^{*(i)} = \frac{1}{2}\varepsilon_{\mu\nu\rho\sigma}f^{*(i)\rho\sigma}$ is the corresponding pseudo-scalar tensor. Λ_1 and Λ_Q are new physics scales, $a_{1,2,3}$ are coupling strength modifiers and $|\kappa_{(1,2,3)}^{VV}| = 0$ or 1. The custodial symmetry would require that $a^{WW} = a^{ZZ}$ and, at tree-level, the only non-zero contributions would come from the a_1 term. This parametrisation is used by CMS. It is fully equivalent to the interaction Lagrangian approach described above.

ii. *Spin-2 model*

The graviton-inspired interaction Lagrangian for a spin-2 boson $X^{\mu\nu}$ that does not carry any color, weak and electromagnetic charge and that uniquely interacts with the energy momentum tensor $\mathcal{T}^{V,f}$ of vector bosons V or fermions f, can be written as follows [221]:

$$\mathcal{L}_2 \supset \frac{1}{\Lambda}\left[\sum_V \xi_V \mathcal{T}_{\mu\nu}^V X^{\mu\nu} + \sum_f \xi_f \mathcal{T}_{\mu\nu}^f X^{\mu\nu}\right], \tag{11.22}$$

where the strength of the interaction is determined by the couplings ξ_V and ξ_f. The simplest scenarios, referred to as universal couplings (UC), correspond to $\xi_V = \xi_f$. They predict a large branching ratio to photons (of approximately 5%) and negligible couplings to massive gauge bosons (W and Z). They are therefore disfavoured, and other models are investigated where the couplings of the W, Z and γ are assumed to be independent. Universality of the couplings refers to $\xi_g = \xi_q$. Two other scenarios are considered: $\xi_q = 0$ and $\xi_q = 2\xi_g$. In these scenarios, a large enhancement of the tail of the transverse momentum of the spin-2 state is expected and requires a further selection requirement in order to probe the models within the range of validity of the effective field theory. Two requirements are considered, $p_T^X < 300\,\text{GeV}$ and $p_T^X < 125\,\text{GeV}$ [219]. The analysss of these benchmarks are discussed below and results are illustrated in Fig. 11.9.

11.5.1.3 *Probing fixed J^P scenarios*

At the LHC, the determination of the spin and CP properties of the Higgs boson is done independently from the total rates measurement, it uses a global angular helicity analysis and, when applicable, the study of threshold effects. The channels used for this analysis, $H \to \gamma\gamma$, $H \to WW^{(*)} \to \ell\nu\ell\nu$ and $H \to ZZ^{(*)} \to 4\ell$, are those where the observation of a signal is unambiguous.

At the Tevatron, an analysis using the threshold distribution in the associated production mode VH with subsequent decay to a pair of b quarks was performed by the D0 collaboration.

i. *The VH production at D0*

The mass of the VH system is a powerful discriminant to distinguish a $J^P = 0^+$, with a threshold behaviour in $d\sigma/dM^2 \sim \beta, \beta^3, \beta^5$ from a 0^+, 0^- and 2^+ state, respectively [222]. The VH mass observable not only discriminates signal hypotheses, but also has an increased separation between the 0^- and 2^+ hypotheses with respect to the backgrounds, thus allowing, with a small and not yet significant signal yield, to exclude that the observed state is 0^- at 98% CL [223] and 2^+ at the 99.9% CL [224], assuming a signal produced with their best fit signal strength (which was $\mu = 1.23$).

ii. *The $\gamma\gamma$ channel at the LHC*

In the $H \to \gamma\gamma$ channel, the analysis is performed inclusively using the production angle $\cos\theta_{CS}^*$ and the transverse momentum of the diphoton pair [219]. The polar angle in the rest frame is defined with respect to the bisector axis of the momenta of the incoming protons and is referred to as the polar angle in the Collins–Soper frame [225]. The SM Higgs boson signal distribution is expected to be uniform with a cutoff due to the selection requirements on the photons transverse momentum. The $H \to \gamma\gamma$ channel is mostly sensitive to the gluon-initiated spin-2 production scenarios, which yield a $\cos\theta_{CS}^*$ distribution peaking at values close to 1. The ATLAS limits are derived from a fit of the signal in bins of $\cos\theta_{CS}^*$ and diphoton transverse momentum and are summarised in Fig. 11.9 (right) (only combined results are shown). The data shows a good compatibility with the SM 0^+ hypothesis and contributes strongly to the exclusion of several spin-2 scenarios. The conclusions are the same from CMS results [220].

iii. *The $H \to WW^{(*)} \to \ell\nu\ell\nu$ channel at the LHC*

In the $H \to WW^{(*)} \to \ell\nu\ell\nu$ channel, the production and decay angles cannot be easily reconstructed due to the presence of neu-

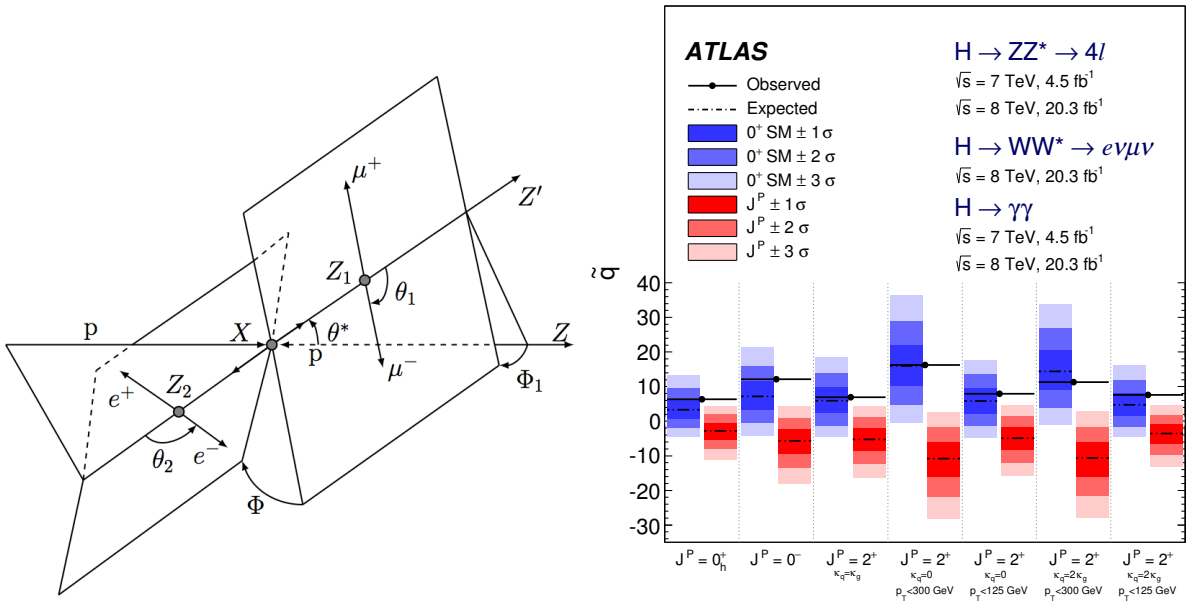

Figure 11.9: (Left) Definition of the production and decay angles defined for the $H \to ZZ^{(*)} \to 4\ell$ final state [220]. (Right) Expected distributions of the test statistic for the SM hypothesis (in blue) and several alternative spin and parity hypotheses (in red).

trinos in the final state, however, sensitivity arises from the $V-A$ structure of the decay of the W bosons. A scalar state thus yields a clear spin correlation pattern that implies that the charged leptons e or μ from the decays of the W bosons are produced close to one another in the transverse plane. This feature impacts observables such as the azimuthal angle between the two leptons $\Delta\Phi_{\ell\ell}$ or their invariant mass $m_{\ell\ell}$ in addition to the threshold behaviour of the decay. It can be used to discriminate between various spin and parity hypotheses. The approach adopted by ATLAS uses a multivariate discriminant, whereas CMS uses a 2D-fit of the dilepton mass and the transverse mass. Figure 11.9 (right) summarises the ATLAS results of the $H \to WW^{(*)} \to \ell\nu\ell\nu$ analyses alone and in combination with other channels. Spin-1 hypotheses (1^+ and 1^-) have also been tested in this channel by ATLAS and CMS. ATLAS and CMS exclude the 1^+ and 1^- hypotheses at more than 95% CL.

iv. *The $H \to ZZ^{(*)} \to 4\ell$ channel at the LHC*

The $H \to ZZ^{(*)} \to 4\ell$ coupling analysis, as described in Section 11.3, also uses a discriminant based on the 0^+ nature of the Higgs boson to further separate signal and background. In this analysis, this feature is used to discriminate between signal hypotheses. The observables sensitive to the spin and parity are [226] the masses of the two Z bosons (due to the threshold dependence of the mass of the off-shell Z boson), two production angle θ^* and Φ_1, and three decay angles, Φ, θ_1 and θ_2. The production and decay angles are defined as:

– θ_1 and θ_2, the angles between the negative final state lepton and the direction of flight of Z_1 and Z_2 in the rest frame.

– Φ, the angle between the decay planes of the four final state leptons expressed in the four lepton rest frame.

– Φ_1, the angle defined between the decay plane of the leading lepton pair and a plane defined by the vector of the Z_1 in the four lepton rest frame and the positive direction of the proton axis.

– θ^*, the production angle of the Z_1 defined in the four lepton rest frame with respect to the proton axis.

These angles are illustrated in Fig. 11.9 (left). There are two approaches to this analysis. The first, used by CMS, is a matrix element likelihood approach where a kinematic discriminant is defined based on the ratio of the signal and background probabilities. These probabilities are defined using the leading-order matrix elements. A similar approach is also performed by ATLAS as a cross check of their main result. The main approach adopted by ATLAS is the combination of sensitive observables with a Boosted Decision Tree. These analyses are sensitive to various J^P hypotheses and in particular discriminate the 0^+ hypothesis from the 0^-. In all scenarios investigated, and for both ATLAS and CMS, the data is compatible with the 0^+ hypothesis. ATLAS and CMS exclude a pure pseudo-scalar nature of the observed boson at CL_S levels of 98% and 99.8% [220].

11.5.1.4 *Probing CP-mixing and anomalous HVV couplings*

The careful study of the kinematic properties of the events observed in the $H \to ZZ^{(*)} \to 4\ell$ and $H \to WW^{(*)} \to \ell\nu\ell\nu$ channel, and in particular the angular distributions described above, allows one to further probe the HVV coupling beyond testing fixed hypotheses. Assuming that the observed particle is a spin-0 state, and using several discriminating observables in the $H \to ZZ^{(*)} \to 4\ell$ and $H \to WW^{(*)} \to \ell\nu\ell\nu$ channels, the anomalous terms in the formalism of Eq. (11.20) can be probed. In the approach of helicity amplitudes used by CMS [220], all terms are essentially equivalent, except for one additional phase which is neglected in Eq. (11.20).

Results are derived in terms of the parameters $\tilde{\kappa}_{HVV} = v\,\kappa_{HVV}/\Lambda$ and $\tilde{\kappa}_{AVV} = v\,\kappa_{AVV}/\Lambda$, and, more precisely, as measurements of $\tilde{\kappa}_{HVV}/\kappa_{\rm SM}$ and $\tan\alpha \cdot \tilde{\kappa}_{AVV}/\kappa_{\rm SM}$, as shown in Fig. 11.10. These parameters can be interpreted as mixing parameters of a tensor anomalous CP-even coupling and a CP-odd component. The measurements are made in the $H \to ZZ^{(*)} \to 4\ell$ and $H \to WW^{(*)} \to \ell\nu\ell\nu$ channels independently and then combined assuming that the $\tilde{\kappa}_{HVV}/\kappa_{\rm SM}$ and $\tan\alpha \cdot \tilde{\kappa}_{AVV}/\kappa_{\rm SM}$ are the same for the W and Z vector bosons. Only the combination of the WW and ZZ channels is shown in Fig. 11.10. The asymmetric shape of the likelihood as a function of $\tilde{\kappa}_{HWW,\,HZZ}/\kappa_{\rm SM}$ is mainly due to the interference between the BSM and the SM contributions that gives a maximal deviation from the SM predictions for negative relative values of the BSM couplings. In Fig. 11.10, the expected likelihood profiles for a SM Higgs boson are also displayed. While no significant deviation from the SM expectation is observed, the precision of the measurements of the mixing parameters is fairly low. The results and conclusions from the CMS measurements [220] are very similar.

An individual ZZ^* channel measurement has also been carried out with a partial Run 2 dataset by ATLAS [227]. CMS has performed a CP-mixing analysis of a partial Run 2 dataset of 36 pb^{-1} combined with the full Run 1 data using the ZZ^* channel [228]. In this analysis the CMS experiment sets constraints on the following parameters defined in the scattering amplitude

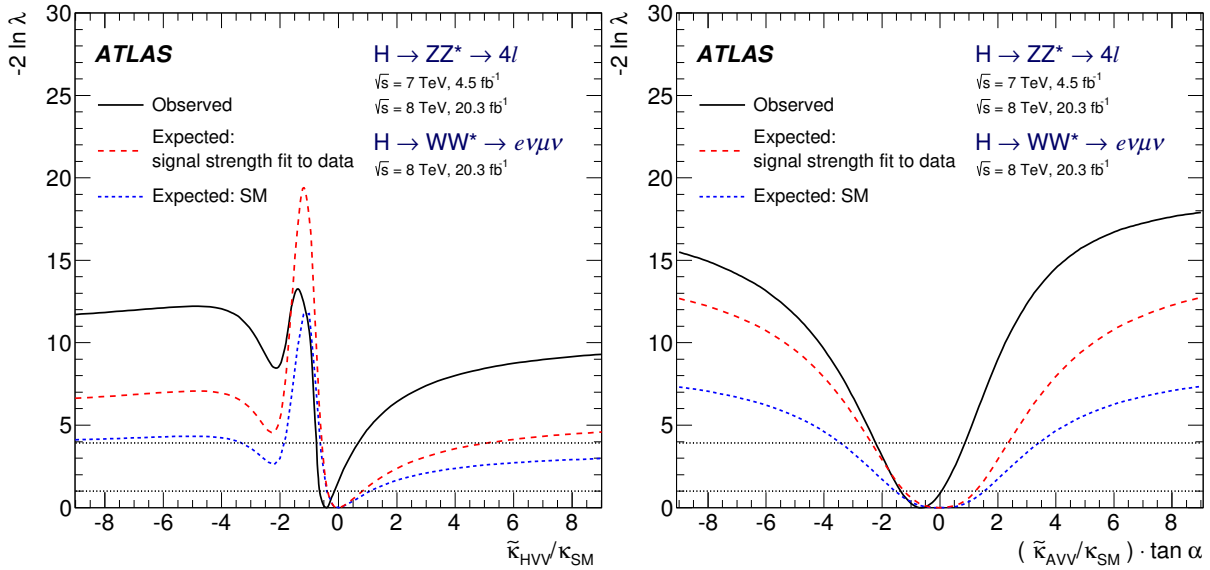

Figure 11.10: Likelihood profiles for the $\tilde{\kappa}_{HVV}$ and $\tilde{\kappa}_{AVV} \cdot \tan\alpha$ parameters, representing respectively CP-even and CP-odd anomalous couplings of the Higgs boson.

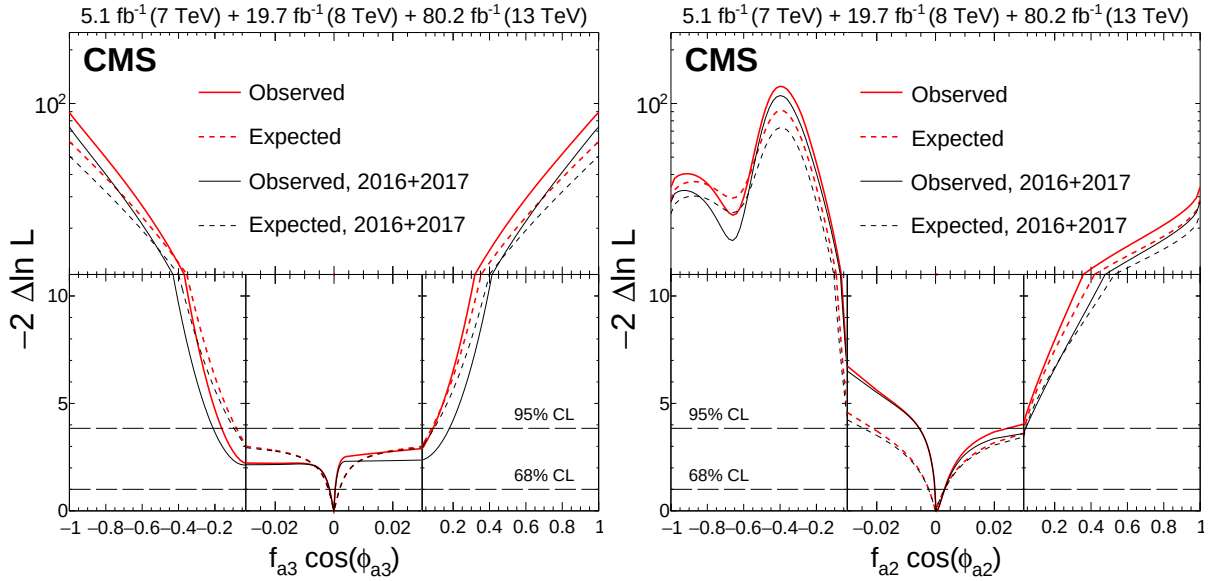

Figure 11.11: Observed (solid) and expected (dashed) likelihoods as a function of $f_{a_3}\cos(\phi_{a_3})$ (left), $f_{a_2}\cos(\phi_{a_2})$ (right) for the Run 1 and Run 2 datasets separately and combined.

parametrisation (11.21):

$$f_{a_i} = \frac{|a_i|^2\sigma_i}{\sum_{j=1,2,3}|a_j|^2\sigma_j}, \quad \phi_{a_i} = \arg\left(\frac{a_i}{a_1}\right), \tag{11.23}$$

where σ_i is the cross section for process with $a_i = 1$ and $a_{j\neq i} = 0$. The constraints on these parameters are shown in Fig. 11.11.

CP invariance in the HVV coupling can also be probed with the VBF production process in the $H \to \tau^+\tau^-$ channel. CMS has performed an analysis in this channel and has combined its results with the aforementioned ZZ^* channel using the same dataset [229].

ATLAS has also performed an analysis using optimal observables [230], defined as the ratio of the interference between the CP-odd and the SM contributions normalised to the SM matrix element squared, using the Run 1 data. In this study, the CP-mixing contributions are described in the framework of an effective field theory governed by a single parameter $\tilde{d}$, found to be consistent with its SM value of $\tilde{d} = 0$ and constrained to the interval [-0.11,0.05] at the 68% CL.

11.5.2 *Off-shell couplings of the Higgs boson*

In the dominant ggF production mode with a subsequent decay of the Higgs boson into a pair of Z bosons, the production cross section of an off-shell Higgs boson is known to be sizeable. This follows as a consequence of the enhanced couplings of the Higgs boson to the longitudinal polarisation of the massive vector bosons at high energy.

The off-shell to on-shell cross section ratio is approximately 8% in the SM [231]. Still the Higgs contribution to VV production at large invariant mass remains small compared to the background. It is nevertheless interesting to probe Higgs production in this regime as it is sensitive to new physics beyond the SM.

The difficulty in the off-shell VV analysis, beyond the small signal-to-background ratio, is due to a large negative interference between the signal and the $gg \to VV$ background.

The resulting presence of a SM Higgs boson signal in the far off-shell domain results in a deficit of events with respect to the expectation from background only events. It is only when the off-shell couplings of the Higgs boson are larger than expected in

the SM that the presence of a signal appears as an excess over the background expectation. One additional intricacy arises from the precision in the prediction of the rate for $gg \to VV$, a loop process at lowest order, and its interference with the signal. At the time of the publication of the original ATLAS and CMS results, a full NLO prediction had not been computed.

It is interesting to note that, in this regime, the Higgs boson is studied as a propagator and not as a particle. The measurement of its off-shell couplings is therefore absolute and does not rely on the knowledge of the total Higgs boson width. The off-shell coupling constraints can then be used to indirectly constrain the width of the Higgs boson, under specific assumptions detailed in Section 11.5.3.3.

This measurement has been carried out in the $H \to ZZ \to 4\ell$, $H \to ZZ \to \ell\ell\nu\nu$ and $H \to WW \to \ell\nu\ell\nu$ channels. To enhance the sensitivity of the analysis, the knowledge of the full kinematics of the events is important. In particular the signal and the background can be further distinguished by the invariant mass of the VV system, which is more accurately accessible in the $H \to ZZ \to 4\ell$ channel. Angular distributions also play an important role in this analysis. For these reasons, the $H \to ZZ^{(*)} \to 4\ell$ channel is significantly more sensitive than $H \to WW^{(*)} \to \ell\nu\ell\nu$. The CMS results in Refs. [232] include the VBF and VH processes through the selection of two additional jets in the final state. The ATLAS results do not have a specific selection for the VBF or VH production processes, but their contributions are taken into account.

Limits on the off-shell rates have been reported for the two channels by ATLAS [233] and CMS [232]. The combined results, assuming that the off-shell rates in the ZZ and WW channels scale equally, are given for two different hypotheses on the VBF production rate: fixing it to its SM value or scaling it as the gluon fusion rate. The observed (expected) limits on the off-shell rate fraction with respect to its SM expectation is 6.7 (9.1) for ATLAS [233] with the VBF rate fixed to its SM value and 2.4 (6.2) for CMS [232] where no assumption is made on the relative production rates of gluon-fusion and VBF. In both cases, the custodial symmetry is assumed and the ratio of the rates in the ZZ and WW decays are fixed to those of the SM. Results without this assumption have also been reported in Ref. [232].

Both ATLAS [234] and CMS [228] have performed off-shell Higgs boson analyses to constrain the off-shell Higgs boson production rates with partial Run 2 datasets, corresponding respectively to luminosities of $36.1\,\text{fb}^{-1}$ and $80.2\,\text{fb}^{-1}$. With the increase in centre-of-mass energy and luminosities, significantly better sensitivities are achieved. The ATLAS analysis is based on two decay channels, $H \to 4\ell$ and $H \to 2\ell 2\nu$, and the two main ggF and VBF production modes, while the CMS analysis is based on the $H \to 4\ell$ channel exclusively, but uses the exclusive VH categories. The results obtained have already reached an impressive sensitivity, with 95% CL upper limits on the off shell signal strength $\mu_{\text{off-shell}}$:

$$\begin{aligned} &\text{(ATLAS)}\ \ \mu_{\text{off-shell}} < 3.8\ \text{(obs)}\ \ [3.4\ \text{(exp)}], \\ &\text{(CMS)}\ \ \mu_{\text{off-shell}} < 2.28\ \text{(obs)}\ \ [3.2\ \text{(exp)}]. \end{aligned} \tag{11.24}$$

11.5.3 *The Higgs boson width*

In the SM, the Higgs boson width is very precisely predicted once the Higgs boson mass is known. For a mass of 125 GeV, the Higgs boson has a very narrow width of 4.1 MeV [44]. It is dominated by the fermionic decays partial width at approximately 75%, while the vector boson modes are suppressed and contribute 25% only.

At the LHC or the Tevatron, in all production modes, only the cross sections times branching fractions can be measured. As a consequence, the total width of the Higgs boson cannot be inferred from measurements of Higgs boson rates. Direct constraints on the Higgs boson width are much larger than the expected width of the SM Higgs boson.

11.5.3.1 *Direct constraints*

Analyses of the reconstructed mass line-shape in the two channels with a good mass resolution, the $H \to \gamma\gamma$ and $H \to ZZ^{(*)} \to 4\ell$ channels, allow for a direct measurement of the width of the SM Higgs boson. The intrinsic mass resolution in these channels is about 1–2 GeV, much larger than the expected width of the SM Higgs boson. As a result, only upper limits on the Higgs boson width have been set by ATLAS [235] and CMS [236]. The two main challenges of direct constraints on the width through the measurement of the line-shape are: (i) the modelling of resolution uncertainties and (ii) the modelling of the interference between the signal and the continuum background which can be sizeable for large widths, in particular in the range where direct constraints are set. Given that these interference effects are small with respect to the individual channels sensitivity, they are neglected in deriving constraints on the total width. The combined constraints, however, being more precise, could be affected by the interference. ATLAS [235] has therefore not combined the constraints on the width from the two channels. The results are reported in Table 11.11. These constraints are still three orders of magnitude larger than the expected SM width and are fully compatible with the SM hypothesis.

Another direct constraint on the Higgs boson width can be obtained, in the $H \to ZZ^{(*)} \to 4\ell$ channel, from the measurement of the average lifetime of the Higgs boson calculated from the displacement of the four-lepton vertex from the beam spot. This analysis has been carried out by CMS (see references in Ref. [123]), using the measured decay length. The measured $c\tau_H$ is $2^{+25}_{-2}\,\mu$m, yielding an observed (and expected) limit at the 95% CL of $c\tau_H < 57(56)\,\mu$m. From this upper limit on the lifetime of the Higgs boson, the 95% CL lower limit on its width is $\Gamma_H > 3.5 \times 10^{-12}$ GeV.

11.5.3.2 *Indirect constraints from mass shift in the diphoton channel*

In the diphoton channel, it was noticed in Ref. [237], that the effect of the interference between the main signal $gg \to H \to \gamma\gamma$ and the continuum irreducible background $gg \to \gamma\gamma$, taking into account detector resolution effects, is responsible for a non negligible mass shift. The size of the mass shift depends on the total width of the Higgs boson and it was suggested that measuring this mass shift could provide a constraint on the width [237]. It was further noticed that the mass shift has a dependence also on the diphoton transverse momentum. The total width of the Higgs boson could therefore be constrained using the diphoton channel alone.

Further studies were performed by ATLAS to estimate the size of the expected mass shift [134]. The expected shift in mass in the diphoton channel is 35 ± 9 MeV for the SM Higgs boson. Very preliminary studies of the sensitivity of this method to estimate the width of the Higgs boson in the High-Luminosity regime have been made by ATLAS [238] and yield an expected 95% CL upper limit on the total width of approximately 200 MeV from $3\,\text{ab}^{-1}$ of 14 TeV data.

11.5.3.3 *Indirect constraints from on-shell rate in the diphoton channel*

In the diphoton channel, it was noticed in Ref. [239], that the interference between the main signal $gg \to H \to \gamma\gamma$ amplitude and the continuum irreducible background $gg \to \gamma\gamma$ amplitude generates non-negligible change in the on-shell cross sections, as a result of the existence of a relative phase between these amplitudes. The size of this on-shell interference effect depends on the total width of the Higgs boson and it was suggested that measuring this on-shell cross section precisely could provide a constraint on the Higgs total width. This interference effect yields around 2% reduction for the $gg \to H \to \gamma\gamma$ cross section measurement. The current evaluation of this interference effect is performed at NLO and has a $^{+50\%}_{-30\%}$ uncertainty, due to the fact that the large relative phase is driven by the two-loop $gg \to \gamma\gamma$ background amplitude [237, 239]. This on-shell interference effect has a dependence on the p_T of the diphoton system and the photon polar angle in the diphoton rest frame, which can be further exploited to improve the measurement to constrain the Higgs total width.

Taking the ratios of the on-shell cross section of Higgs boson to diphoton channel and the cross section of Higgs boson to four-leptons channel where the interference effect is negligible could put bound on the Higgs boson total width. This ratio is free

Table 11.11: Run 1 observed (expected) direct 95% CL constraints on the width of the 125 GeV resonance from fits to the $\gamma\gamma$ and ZZ mass spectra and to the 4ℓ vertex lifetime. *The CMS measurement from the 4ℓ mass line-shape was performed using Run 2 data.

Exp.	$M_{\gamma\gamma}$ mass spectrum	$M_{4\ell}$ spectrum	4ℓ vertex lifetime
ATLAS	$< 5.0\,(6.2)$ GeV	$< 2.6\,(6.2)$ GeV	—
CMS	$< 2.4\,(3.1)$ GeV	$< 1.1\,(1.6)$ GeV*	$> 3.5 \times 10^{-12}$ GeV

from many dominant sources of systematic uncertainties for cross section measurements, i.e., PDF uncertainty and luminosity uncertainty, and can be further improved by the accumulation of the LHC data. From this cross section ratio measurement alone, a preliminary estimation of the current limit from this interference effect with current 30% precision puts an upper bound of 800 MeV on the Higgs boson total width and the limit improves to 60 MeV with $3\,\text{ab}^{-1}$ of 14 TeV data [239, 240].

11.5.3.4 *Indirect constraints from off-shell couplings*

Using simultaneously on-shell and off-shell measurements in the VV channels, it was noticed [231, 241] that the total width of the Higgs boson could be constrained. This can be illustrated from the parametrisation of the signal strength measurements both on-shell ($\mu_{\text{on-shell}}$) and off-shell ($\mu_{\text{off-shell}}$) as a function of the couplings modifiers κ_g and κ_V parameterising the main process $gg \to H \to VV$ (see Section 11.6.2 for the definition of these coupling modifiers). The on-shell and off-shell signal strengths can be written as:

$$\begin{aligned} \mu_{\text{on-shell}} &= \frac{\kappa^2_{g,\,\text{on-shell}}\,\kappa^2_{V,\,\text{on-shell}}}{\Gamma_H/\Gamma_{\text{SM}}}, \\ \mu_{\text{off-shell}} &= \kappa^2_{g,\,\text{off-shell}}\,\kappa^2_{V,\,\text{off-shell}}. \end{aligned} \tag{11.25}$$

A bound on the Higgs boson width can then be obtained from the measurements of the on-shell and off-shell signal strengths. This assumes that no new physics alters the Higgs boson couplings in the off-shell regime, i.e., that the running of its couplings is negligible in the off-shell regime [242,243]. Both ATLAS [233] and CMS [232] have used their off-shell production limits to constrain the width of the Higgs boson.

Both ATLAS and CMS analyses use the kinematic event characteristics to further gain in sensitivity to discriminate between the signal and background. The ATLAS analysis assumed that there are no anomalous couplings of the Higgs boson to vector bosons, and obtains 95% CL observed (expected) upper limit on the total width of $5.7\times\Gamma_{\text{SM}}$ ($9.0\times\Gamma_{\text{SM}}$) with the Run 1 dataset. In the CMS analysis, the observed (expected) limit on the total width is $6.2\times\Gamma_{\text{SM}}$ ($9.8\times\Gamma_{\text{SM}}$) for the ZZ channel only at Run 1.

In addition, in the CMS analysis, results are also derived allowing for anomalous couplings of the Higgs boson, therefore reducing the discriminating power of the kinematic variables used in the analysis but reducing the model dependence. The observed (expected) limit on the total width is $10.9\times\Gamma_{\text{SM}}$ ($17.4\times\Gamma_{\text{SM}}$).

CMS has also combined the ZZ and W^+W^- channels while keeping the gluon-fusion and VBF production processes separate. For the gluon fusion mode, the observed (expected) combined upper limit at the 95% CL on the total width of the Higgs boson is $2.4\times\Gamma_{\text{SM}}$ ($6.2\times\Gamma_{\text{SM}}$) [232], while for the VBF production mode the exclusion limits are $19.3\times\Gamma_{\text{SM}}$ ($34.4\times\Gamma_{\text{SM}}$) [232].

At Run 2, using the ATLAS [234] and CMS [228] analyses described in Section 11.5.2, the following bounds were obtained:

$$\begin{aligned} &\text{(ATLAS)}\ \ \Gamma_H/\Gamma_H^{SM} < 3.5\ \ [3.7\ (\text{exp})], \\ &\text{(CMS)}\ \ \Gamma_H < 9.16\ \ [13.7\ (\text{exp})]\ \text{MeV} \\ &\text{or}\ \ \Gamma_H\Gamma_H^{SM} = 3.2^{+2.8}_{-2.2}\ \ [4.1^{+5.0}_{-4.0}\ (\text{exp})]. \end{aligned} \tag{11.26, 11.27}$$

CMS has also performed this analysis considering possible anomalous HZZ couplings as discussed in Section 11.5.1.4. Neither the results nor the sensitivities are significantly affected by allowing specific anomalous coupling parameters to float in the fits.

ATLAS and CMS have also performed a study of the prospects for measuring the Higgs boson width mainly in the four lepton channel. Projecting to a luminosity of $3\,\text{ab}^{-1}$, it was concluded that, within assumptions similar to the ones mentioned above and assuming the SM central value, the observed (expected) combined upper limit at the 95% CL on the total width of the Higgs boson would be $3.8\times\Gamma_{\text{SM}}$ ($3.4\times\Gamma_{\text{SM}}$), i.e., the width of the Higgs boson could be constrained with the following precision [104]:

$$\Gamma_H = 4.1^{+0.7}_{-0.8}\,\text{MeV}. \tag{11.28}$$

11.6 Probing the coupling properties of the Higgs boson

As discussed in Section 11.2, within the SM, all the Higgs boson couplings are fixed unambiguously once all the particle masses are known. Any deviation in the measurement of the couplings of the Higgs boson could therefore signal BSM physics.

Measuring the Higgs boson couplings without relying on the SM assumption requires a general framework treating deviations from the SM coherently at the quantum level in order to provide theoretical predictions for relevant observables to be confronted with experimental data. An attempt in that direction has been formalised in the so-called κ-formalism [244], following earlier attempts [245] and initial phenomenological studies of the first hints of the existence of the Higgs boson [246]. In this LO-inspired approach, the SM Higgs boson couplings are rescaled by arbitrary factors, κ's, keeping the same Lorentz structure of the interactions. This formalism allows for simple interpretation of the signal strengths measured in the various Higgs channels. It it has been utilised to test various physics scenarios, like the existence of additional new particles contributing to the radiative Higgs boson production and decays, or to probe various symmetries of the SM itself, as for example the custodial symmetry. It only compares the experimental measurements to their best SM predictions and does not require any new BSM computations per se. And, from a more theoretical perspective, its relevance arises from the fact that it actually fully captures the leading effects in single Higgs processes of well motivated scenarios. Still, the κ-formalism has obvious limitations and certainly does not capture the most general deformations of the SM, even under the assumptions of heavy and decoupling new physics. A particularly acute shortcoming at the time Higgs physics is entering a precision era is the lack of proficiency to assert the richness of kinematical distributions beyond simple signal strength measurements. Several extensions and alternative approaches are being developed as part of the activities of the LHC Higgs Cross Section Working Group [45].

The Higgs Pseudo-Observable (HPO) approach [247] allows one to report the data in terms of a finite set of on-shell form factors parametrising amplitudes of physical processes subject to constraints from Lorentz invariance and other general requirements like analyticity, unitarity, and crossing symmetry. These form factors are expanded in powers of kinematical invariants of the process around the known poles of SM particles, assuming that poles from BSM particles are absent in the relevant energy regime. A set of HPOs have been proposed to characterise both the Higgs boson decays and the EW Higgs boson production channels, thus exploring different kinematical regimes. Prospective studies concluded that these HPOs can be measured/bounded at the percent level at the HL-LHC and could therefore be used to constrain some explicit models of new physics.

Another systematic approach to characterise the possible Higgs boson coupling deviations induced by BSM physics is the use of Effective Field Theories (EFT) [248,249]. This approach assumes again that the new physics degrees of freedom are sufficiently heavy to be integrated out and they give rise to effective interactions among the light SM particles. By construction, the effective Lagrangians cannot account for deviations in Higgs physics induced by light degrees of freedom, unless they are added themselves as extra fields in the effective Lagrangians. In Section 11.7, several examples of models with light degrees of freedom affect-

ing Higgs boson production and decay rates will be presented. The main advantage of EFTs is their prowess to relate different observables in different sectors and at different energies to constrain a finite set of effective interactions among the SM degrees of freedom. In an EFT, the SM Lagrangian is extended by a set of higher-dimensional operators, and it reproduces the low-energy limit of a more fundamental UV description. It will be assumed that the Higgs boson is part of a CP-even EW doublet, Φ, and that the Lagrangian is an analytic function of the gauge invariant $\Phi^\dagger\Phi$. This scenario is commonly refereed as SMEFT. Even though it is not fully established experimentally, this set-up is motivated by the measurements of the Higgs couplings to the different SM particles that show an alignement with their masses, such an alignement naturally follows under this assumption of a linear realisation of the $\mathrm{SU}(2)_L \times \mathrm{U}(1)_Y$ symmetry of the SM but would require an ad-hoc tuning otherwise. General Lagrangians bypassing this linear assumption have been explicitly written down, see for instance Ref. [250]. They rely on a chiral expansion with a specific power-counting, effectively resumming the expansion in powers of the Higgs field, usually referred as HEFT as opposed to SMEFT.

11.6.1 *Effective Lagrangian framework*

The SMEFT has the same field content and it respects the same linearly-realised $\mathrm{SU}(3)_C \times \mathrm{SU}(2)_L \times \mathrm{U}(1)_Y$ local symmetry as the SM. The difference is the presence of operators with canonical mass-dimension d larger than 4. These are organised in a systematic expansion in d, where each consecutive term is suppressed by a larger power of a high mass scale. Assuming baryon and lepton number conservation, the most general Lagrangian takes the form

$$\mathcal{L}_{\text{eff}} = \mathcal{L}_{\text{SM}} + \sum_i c_i^{(6)} \mathcal{O}_i^{(6)} + \sum_j c_j^{(8)} \mathcal{O}_j^{(8)} + \cdots . \qquad (11.29)$$

The contribution of the higher order operators of dimension d to physical amplitudes is suppressed by $(E/\Lambda)^{d-4}$, where E is the relevant energy scale of the process and Λ is the energy scale suppressing the higher-dimensional operators. The Wilson coefficients $c_i^{(d)}$ encode the virtual effects of the heavy new physics in low-energy observables. Their precise forms in terms of masses and couplings of the new particles can be obtained via matching with the ultraviolet (UV) completion of the SM, see, e.g., Ref. [251], or inferred using specific power-counting rules [248, 252].

The list of dimension-6 operators was first classified in a systematic way in Ref. [253] after the works of Ref. [254]. Subsequent analyses pointed out the presence of redundant operators, and a minimal and complete list of operators was finally provided in Ref. [255][4]. For a single family of fermions, there are 76 real ways to deform the SM generated by 59 independent operators. With the 3 families of fermions of the SM, flavour indices can be added to these 59 operators, and furthermore, new operator structures, that have been dismissed by means of Fierz transformations in the single family case, have to be considered, for a total of 2499 real deformations [258]. When considering Higgs data, one can reasonably focus on a relatively small subset of the 2499 operators of dimension 6. In particular the vast subset of 4-fermion operators, whether flavour and CP preserving or not, can be more strongly constrained by other processes. Thus, it makes sense to neglect this whole class, with the exception of one particular four-fermion interaction that contributes to the muon decay and thus directly affects the Fermi constant. The dipole operators, instead do directly affect Higgs boson production, however, under very general and plausible assumptions on the flavour structure of new physics, the coefficients of these operators display the same structure and the same chiral suppression of the Yukawa couplings. The consequence is that, with the possible exception of processes involving the top quark, their effect in Higgs boson production is expected to be negligible. Furthermore, as far as Higgs boson decays are concerned, the dipole operators only contribute to three (or more)-body final states (for instance $H \to \bar{b}b\gamma$) and as such they can easily be neglected too. Eliminating these two classes, there remain three other classes: 1) purely bosonic operators, 2) generalised Yukawas, 3) Higgs-fermion current operators. Operators in class 2 and 3, per se, can still contain CP- or flavour-violating terms, on which experimental constraints are rather strong. Under the assumption of flavour universality (respectively diagonality), one is left with 12 (14) parameters affecting EW precision measurements, diboson processes and single- and double-Higgs data and 7 (17) other parameters modifying the EW gauge boson couplings to fermions, see Ref. [44] for further technical details. Working in the unitary gauge and performing suitable redefinition of fields and input parameters the effective Lagrangian can be conveniently expressed in the parameterisation of Ref. [259], the so-called *Higgs basis* that conveniently single out these special less constrained parameters. Such a classification reflects the current experimental situation and the hierarchy in the sensitivity of the experimental measurements in the various sectors of the SM. As the sensitivity of the measurements in the Higgs sector improves, another and more general parametrisation of the SM deformation will have to be retained, in particular a parametrisation more suited for a treatment at the quantum level. In other bases of operators, in particular the so-called Warsaw basis [255] used in some experimental EFT analyses [128, 260, 261], one finds strong correlations among the operators affecting the EW gauge couplings to fermions, leaving 12 (14) linear combinations of operators with weaker constraints.

Section 11.6.2 illustrates how the Higgs data accumulated at the LHC can (partially) constrain the SM deformations, i.e., the dimension-6 operators of the SEMFT Lagrangian. Automatic tools are being developed to analyse the experimental data within an EFT framework, see the report [262] and references therein.

11.6.2 *Probing coupling properties*

As described in Section 11.3, a framework was developed by ATLAS and CMS [141], individually and together, to combine the very large number of exclusive categories aimed at reconstructing the five main decay modes and the five main production modes of the Higgs boson. The general conclusion of this combination, illustrating the compatibility of the observation with the SM expectations, is given in Section 11.3. The same framework with its master formula, Eq. (11.16), can be used to further measure coupling properties of the Higgs boson under specific additional assumptions.

11.6.2.1 *Combined measurements of the Higgs boson coupling properties*

i. *From effective Lagrangians to Higgs observables*

The κ framework, described in detail in Ref. [43, 244], facilitates the characterisation of Higgs coupling properties in terms of a series of Higgs coupling strength modifier parameters κ_i, which are defined as the ratios of the couplings of the Higgs bosons to particles i to their corresponding SM values. The κ framework assumes a single narrow resonance so that the zero-width approximation can be used to decompose the cross section as a product of two factors characterising the production and the decay of the Higgs boson. The κ parameters are introduced by expressing each of the these factors as their SM expectation multiplied by the square of a coupling strength modifier for the corresponding process at leading order:

$$\begin{aligned}(\sigma \cdot \mathrm{BR})(i \to \mathrm{H} \to f) &= \frac{\sigma_i^{SM}\kappa_i^2 \cdot \Gamma_f^{SM}\kappa_f^2}{\Gamma_H^{SM}\kappa_H^2} \quad \to \\ \to \quad \mu_i^f &\equiv \frac{\sigma \cdot \mathrm{BR}}{\sigma_{\mathrm{SM}} \cdot \mathrm{BR}_{\mathrm{SM}}} = \frac{\kappa_i^2 \cdot \kappa_f^2}{\kappa_H^2},\end{aligned} \qquad (11.30)$$

where μ_i^f is the rate relative to the SM expectation and κ_H^2 is an expression that adjusts the SM Higgs width to take into account the modifications induced by the deformed Higgs boson couplings. When all κ_i are set to 1, the SM is reproduced. For loop-induced processes, e.g. $H \to \gamma\gamma$, there is a choice of either resolving the coupling strength modification in its SM expectation,

[4] Complete enumerations of d=8 operators have been obtained [256] and some preliminary constraints on peculiar subsets of these operators have been derived from experimental measurements [257]. Still, in this review, the EFT Lagrangians will be truncated at the level of dimension-6 operators.

i.e., $\kappa_\gamma(\kappa_t, \kappa_W)$ or keeping κ_γ as an effective coupling strength parameter.

The κ-framework is the simplest parametrisation directly related to experimental measurements of the Higgs boson production and decay modes. For this reason, it has been widely used by the community. It can also be connected to the SMEFT formalism as follows. Restricting to the EFT directions not probed outside Higgs physics [263], the Higgs boson couplings are written in the unitary gauge as:

$$\begin{aligned}\mathcal{L} = {} & \kappa_Z \frac{m_Z^2}{v} Z_\mu Z^\mu H + \kappa_W \frac{2m_W^2}{v} W_\mu^+ W^{-\mu} H \\ & + \kappa_{VV} \frac{\alpha}{2\pi v} \left(\cos^2\theta_W Z_{\mu\nu} Z^{\mu\nu} + 2\, W_{\mu\nu}^+ W^{-\mu\nu}\right) H \\ & + \kappa_g \frac{\alpha_s}{12\pi v} G^a_{\mu\nu} G^{a\mu\nu} H + \kappa_\gamma \frac{\alpha}{2\pi v} A_{\mu\nu} A^{\mu\nu} H + \kappa_{Z\gamma} \frac{\alpha}{\pi v} A_{\mu\nu} Z^{\mu\nu} H \\ & + \kappa_3 \frac{m_H^2}{2v} H^3 \\ & - \left(\kappa_t \sum_{f=u,c,t} \frac{m_f}{v} + \kappa_b \sum_{f=d,s,b} \frac{m_f}{v} + \kappa_\tau \sum_{f=e,\mu,\tau} \frac{m_f}{v}\right) f\bar{f} H. \end{aligned} \tag{11.31}$$

The exact correspondence between the effective coefficients of the dimension-6 operators and the κ's can be found for instance in Ref. [44]. In the SM, the Higgs boson does not couple to massless gauge bosons at tree level, hence $\kappa_g = \kappa_\gamma = \kappa_{Z\gamma} = 0$. Nonetheless, the contact operators are generated radiatively by SM particles loops. In particular, the top quark gives a contribution to the 3 coefficients $\kappa_g, \kappa_\gamma, \kappa_{Z\gamma}$ that does not decouple in the infinite top mass limit. For instance, in that limit $\kappa_\gamma = \kappa_g = 1$ [23, 24, 264].

The coefficient for the contact interactions of the Higgs boson to the W and Z field strengths is not independent but obeys the relation

$$(1 - \cos^4\theta_W)\kappa_{VV} = \sin 2\theta_W \kappa_{Z\gamma} + \sin^2\theta_W \kappa_{\gamma\gamma}. \tag{11.32}$$

This relation is a general consequence of the custodial symmetry [265], which also imposes $\kappa_Z = \kappa_W$ at leading order ($\kappa_Z/\kappa_W - 1$ is a measure of custodial symmetry breaking and, as such, is already constrained by electroweak precision data and the bounds on anomalous gauge couplings). When the Higgs boson is part of a $\mathrm{SU}(2)_L$ doublet, the custodial symmetry in the bosonic sector could only be broken by the $\mathcal{O}_T = \frac{1}{2}\left(\Phi^\dagger \overleftrightarrow{D}^\mu \Phi\right)^2$ operator at the level of dimension-6 operators and it is accidentally realised among the interactions with four derivatives, like the contact interactions considered.

The coefficient κ_3 can be accessed directly only through double Higgs boson production processes, hence it will remain largely unconstrained at the LHC. Before the associated production of a Higgs boson with a pair of top quarks was observed, the Higgs boson coupling to the top quark was only probed indirectly via the one-loop gluon fusion production or the radiative decay into two photons. However, these two processes are only sensitive to the combinations of couplings $(\kappa_t + \kappa_g)$ and $(\kappa_t + \kappa_\gamma)$ and not to the individual couplings. Therefore a deviation in the Higgs boson coupling to the top quark can in principle always be masked by new contact interactions to photons and gluons (and this is precisely what is happening in minimal incarnations of composite Higgs models [266]). The current and still limited sensitivity, of the order of 20%, in the $t\bar{t}H$ channel leaves elongated ellipses in the direction $\kappa_g = \kappa_\gamma = 1 - \kappa_t$.

The operators already bounded by EW precision data and the limits on anomalous gauge couplings modify in general the Lorentz structure of the Higgs couplings and hence induce some modifications of the kinematical differential distributions [267]. A promising way to have a direct access to the effective coefficients of these operators in Higgs physics is to study the VH associated production with a W or a Z at large invariant mass of the VH system [268]. These differential distributions could also be a way to test the hypothesis that the Higgs boson belongs to a $\mathrm{SU}(2)_L$ doublet together with the longitudinal components of the massive electroweak gauge bosons.

ii. *Interpretations of the experimental data*

The measurements of the coupling properties of the Higgs boson are entirely based on the formalism of the effective Lagrangian described above. Measurements of coupling properties in this framework implies assessing the parameters of the model Eq. (11.31) or combinations of these parameters with different sets of assumptions.

These measurements are carried out with the combination framework described in Section 11.4, where the μ_i and μ_f signal strength parameters are further interpreted in terms of modifiers of the SM couplings κ_k where $k \in \{Z, W, f, g, \gamma, Z\gamma\}$ as in Eq. (11.31). The number of signal events per category for the various production modes are typically estimated at higher orders in the analyses but are scaled by these single LO-inspired factors, thus not taking into account possible intricacies and correlations of these parameters through the higher-order corrections. This approximation is valid within the level of precision of current results and their compatibility with the SM expectation.

In this formalism, further assumptions are explicitly made: (i) the signals observed in the different search channels originate from a single narrow resonance with a mass of 125 GeV; (ii) similarly to the combination described in Section 11.4, the narrow width approximation is assumed (to allow the decomposition of signal yields into products of production and decay signal strengths); (iii) the tensor structure of the couplings is assumed to be the same as that of a SM Higgs boson. This means in particular that the observed state is assumed to be a CP-even scalar as in the SM.

Loop-level couplings such as the $gg \to H$, $H \to \gamma\gamma$ and $H \to Z\gamma$ can either be treated effectively, with κ_g, κ_γ and $\kappa_{Z\gamma}$ as free parameters in the fit or these parameters can be expressed in terms of the know SM field content and as a function of the SM coupling modifiers, in the following way [269]:

$$\begin{aligned} \kappa_g^2(\kappa_t, \kappa_b, \kappa_c) = {} & 1.042\,\kappa_t^2 - 0.040\,\kappa_t\kappa_b + 0.002\,\kappa_b^2 \\ & - 0.005\kappa_t\kappa_c + 0.0005\kappa_b\kappa_c + 0.00002\kappa_c^2, \\ \kappa_\gamma^2(\kappa_F, \kappa_V) = {} & 1.59\,\kappa_V^2 - 0.66\,\kappa_V\kappa_F + 0.07\,\kappa_F^2, \\ \kappa_{Z\gamma}^2(\kappa_F, \kappa_V) = {} & 1.12\,\kappa_V^2 - 0.15\,\kappa_V\kappa_F + 0.03\,\kappa_F^2. \end{aligned} \tag{11.33}$$

The $\kappa_{Z\gamma}$ parametrisation has been used only in the ATLAS Run 1 combined measurements of the coupling properties of the Higgs boson. The $\mu^+\mu^-$ channels is included neither in the CMS and ATLAS-CMS Run 1 combinations, nor in the ATLAS [213] Run 2 individual combination, while it is included in the CMS [214] Run 2 combination.

The parametrisations are given for a Higgs boson mass hypothesis of 125.09 GeV (and in the last two expressions, all the Higgs-fermion couplings are assumed to be rescaled by an universal multiplicative factor κ_F). It can be noted from the expression of κ_γ that the coupling of the Higgs boson to photons is dominated by the loop of W bosons, and it is affected by the top quark loop mostly through its interference with the W loop. The sensitivity of the current measurements to the relative sign of the fermion and vector boson couplings to the Higgs boson is due to this large negative interference term. The κ_g parameter is expressed in terms of the scaling of production cross sections and therefore also depends on the pp collisions centre-of-mass energy. The parametrisations of κ_γ and $\kappa_{Z\gamma}$ are obtained from the scaling of partial widths and are only dependent on the Higgs boson mass hypothesis. Experiments use a more complete parametrisation with the contributions from the b-quarks, τ-leptons in the loops [43, 244].

The global fit is then performed expressing the μ_i and μ_f parameters in terms of a limited number of κ_k parameters or their ratios, under various assumptions. The parametrisation for the main production modes are: (i) $\mu_{\mathrm{ggF}} = \kappa_g^2$ for the gluon fusion and an effective coupling of the Higgs boson to the gluons; (ii) $\mu_{\mathrm{VBF},VH} = \kappa_V^2$ for the VBF and VH processes when the W and Z couplings are assumed to scale equally, and $\mu_{\mathrm{VBF}}^2(\kappa_W, \kappa_Z) = (\kappa_W^2\sigma_{WWH} + \kappa_Z^2\sigma_{ZZH})/(\sigma_{WWH} + \sigma_{ZZH})$, when the couplings to the W and Z bosons are varied independently (σ_{WWH} and

σ_{ZZH} denote the VBF cross sections via the fusion of a W and a Z boson respectively, the small interference term is neglected); (iii) $\mu_{t\bar{t}H} = \kappa_t^2$ for the $t\bar{t}H$ production mode. Numerically the production modes signal strengths as a function of the coupling modifiers to the SM fields are:

$$\begin{aligned}&\mu_{\rm ggF} = 1.06\kappa_t^2 + 0.01\kappa_b^2 - 0.07\kappa_t\kappa_b, \quad \text{and}\\ &\mu_{\rm VBF} = 0.74\kappa_W^2 + 0.26\kappa_Z^2.\end{aligned} \tag{11.34}$$

The decay mode signal strengths are parametrised as $\mu_k = \kappa_k^2/\kappa_H^2$ where $k \in \{Z, W, f, g, \gamma, Z\gamma\}$ denotes the decay mode and κ_H, the overall modifier of the total width that affects all the signal yields. κ_H is a priori an independent parameter. However, when it is assumed that the Higgs boson cannot decay to new particles beyond those of the SM, κ_H can also be treated as an effective parameter and expressed in terms of the coupling modifiers to the SM field content. Its general expression is:

$$\begin{aligned}\kappa_H^2 =& 0.57\kappa_b^2 + 0.06\kappa_\tau^2 + 0.03\kappa_c^2 + 0.22\kappa_W^2 + 0.03\kappa_Z^2 + 0.09\kappa_g^2\\ &+ 0.0023\kappa_\gamma^2.\end{aligned} \tag{11.35}$$

The general expression of the total width of the Higgs boson can be written as follows:

$$\Gamma_H = \frac{\kappa_H^2 \Gamma_H^{\rm SM}}{1 - {\rm BR}_{\rm BSM}} \tag{11.36}$$

where $\Gamma_H^{\rm SM}$ is the total width of the SM Higgs boson and ${\rm BR}_{\rm BSM}$ is the branching fraction of the Higgs boson to new particles beyond the SM.

Specific parametrisations will be made in order to address the following aspects of the coupling properties of the Higgs boson under different assumptions: (i) the relative couplings of the Higgs boson to fermions and bosons; (ii) the potential impact of the presence of new particles beyond the SM either in the loops or both in the loops and the decay of the H; and (iii) also, more general models either of coupling modifiers or their ratios, under different assumptions.

iii. *Couplings to bosons and fermions*

As it will be discussed in Section 11.7.6.3, it is interesting to probe a model where no additional field content is considered in the decay width of the Higgs boson and where the relative couplings of the Higgs boson to W- and Z-bosons is fixed to its SM value, i.e., $\kappa_W = \kappa_Z$, and where all Yukawa couplings scale with one coupling modifier. In this model, only the SM particles are assumed to contribute to the gluon fusion and the diphoton loops, and all fermion couplings modifiers are required to scale simultaneously with a unique factor κ_F while all vector boson couplings modifiers also scale with a common factor κ_V. It is a two-parameter fit with κ_V and κ_F as free variables of interest. The ATLAS-CMS combined results for each channel independently, the combinations of all channels for the two experiments separately and the results of the overall combination are all shown in Fig. 11.12.

The global fit is only sensitive to the relative sign of κ_V and κ_F. By convention, either κ_F or κ_V can be considered positive and negative values of κ_V or κ_F respectively can be considered. Such values are not excluded a priori, but would imply the existence of new physics at a light scale and would also raise questions about the validity of the perturbative treatment of the SM deformations and also about the stability of the vacuum [271]. Among the five main Higgs boson decay channels, only the $\gamma\gamma$ is sensitive to the sign of κ_F (or κ_V) through the interference of the W and t loops as shown in Eq. (11.33). The current global fit disfavours a negative value of κ_F at more than five standard deviations. A specific analysis for the Higgs boson production in association with a single top quark has been proposed in order to more directly probe the sign of κ_F (see references in Ref. [123]). All available experimental data show a fair agreement of the SM prediction of the couplings of the Higgs boson to fermions and gauge bosons. The results shown in Fig. 11.12 assume that $\kappa_F \geq 0$, however, in Ref. [141], a similar combination is done without this assumption. The observed exclusion is fully compatible with the SM expectation The ATLAS and CMS combined measurements with the Run 1 dataset lead to

$$\kappa_V = 1.04 \pm 0.05 \quad \text{and} \quad \kappa_F = 0.98^{+0.11}_{-0.10}, \tag{11.37}$$

and were already at an impressive 5% level of accuracy for the κ_V parameter. The ATLAS Run 2 combination yielded:

$$\kappa_V = 1.05 \pm 0.04 \quad \text{and} \quad \kappa_F = 1.05 \pm 0.09. \tag{11.38}$$

And the results for the CMS Run 2 are reported as likelihood contours shown in Fig. 11.12.

iv. *Probing new physics in the loops (and the decay)*

A more constrained model fully focussing on BSM scenarios with new heavy particles contributing to the loops and where all couplings to the SM particles are assumed to be the same as in the SM ($\kappa_W = \kappa_Z = \kappa_t = \kappa_b = \kappa_\tau = 1$) is also used to constrain the κ_g and κ_γ parameters only. In this model, it can be assumed that the new physics affecting the loops are either introducing new decay channels (i.e., ${\rm BR}_{\rm BSM}$ allowed to vary in the fit) or not (i.e., ${\rm BR}_{\rm BSM} = 0$). In the two cases, the results on the couplings through loops (to gluons and photons) do not change significantly. The constraints on ${\rm BR}_{\rm BSM}$ will be discussed in the next section, while here the focus will be on the effective couplings of the Higgs boson to gluons and photons. The contours of the combined likelihood in the $(\kappa_\gamma, \kappa_g)$ plane for the ATLAS and CMS experiments and their combination are shown in Fig. 11.13. The measured values of these parameters for the ATLAS and CMS Run 1 combination are:

$$\kappa_g = 0.78^{+0.13}_{-0.10} \quad \text{and} \quad \kappa_\gamma = 0.87^{+0.14}_{-0.09}. \tag{11.39}$$

At Run 2, the ATLAS combination yielded:

$$\kappa_g = 1.03^{+0.07}_{-0.06} \quad \text{and} \quad \kappa_\gamma = 1.00 \pm 0.06. \tag{11.40}$$

The CMS results are reported as likelihood contours in the $(\kappa_g, \kappa_\gamma)$ plane only, as shown in Fig. 11.13.

In this model as well, all results are fully compatible with the SM expectations.

v. *Coupling measurements and probing BSM physics in loops and in the decay*

In the models described above, it was either assumed that no new latent BSM degree of freedom distorts neither the loop-induced Higgs boson couplings to gluons and photons nor the total Higgs boson width, or that all tree level couplings to SM particles are SM-like. These assumptions can be relaxed.

In order to probe simultaneously the Higgs boson couplings to massive and massless particles, only the assumption ${\rm BR}_{\rm BSM} = 0$ is kept. The couplings to photons and gluons are then parametrised by independent effective couplings, κ_g and κ_γ, and κ_Z, κ_W, κ_t, $|\kappa_\tau|$, and $|\kappa_b|$ are measured simultaneously. The absolute values of certain coupling modifiers only indicate the degeneracy of combined likelihood for the two signs. It can be noted that when the coupling to gluons is not considered effective, there is some sensitivity to the sign of κ_b through the interference between the top- and bottom-quark loops in the gluon fusion process. In this analysis, the constraint on the top quark Yukawa coupling comes from the $t\bar{t}H$ direct search channels only. The complete set of results from this model is given in Table 11.12 for the ATLAS-CMS combination using the full Run 1 dataset [270] and for the ATLAS [213] and CMS [214] individual combinations using partial Run 2 datasets. Figure 11.14 also displays the results of the individual ATLAS and CMS combinations. A negative relative sign is allowed for the κ_W and κ_Z parameters without loss of generality. This convention is used in the ATLAS and CMS Run 1 combination and in the CMS Run 2 combination. Neglecting the very small interference between the W and Z exchanges in the VBF production and when treating the photon and gluon couplings as effective, the sensitivity to the negative signs of the

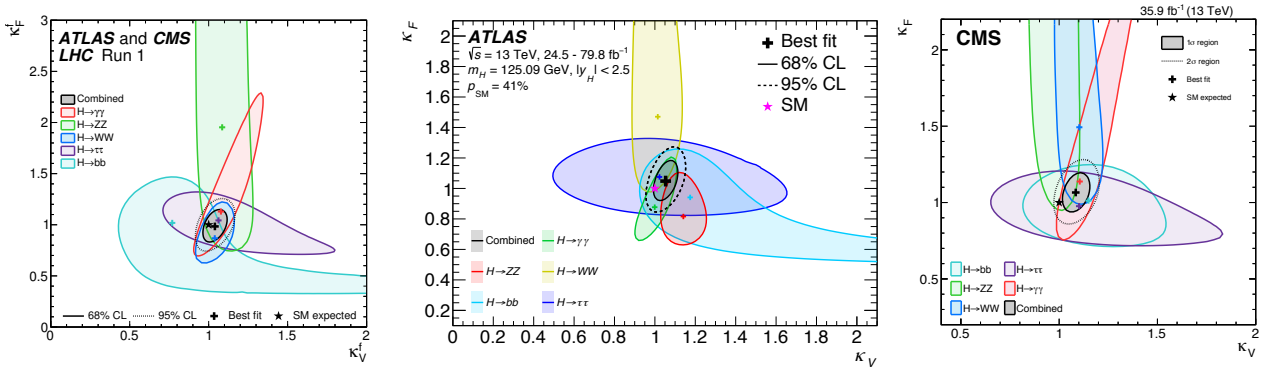

Figure 11.12: Likelihood contours in the (κ_F, κ_V) plane for the ATLAS-CMS Run 1 combination [270] (left) and the ATLAS [213] (center) and CMS [214] (right) individual Run 2 combinations.

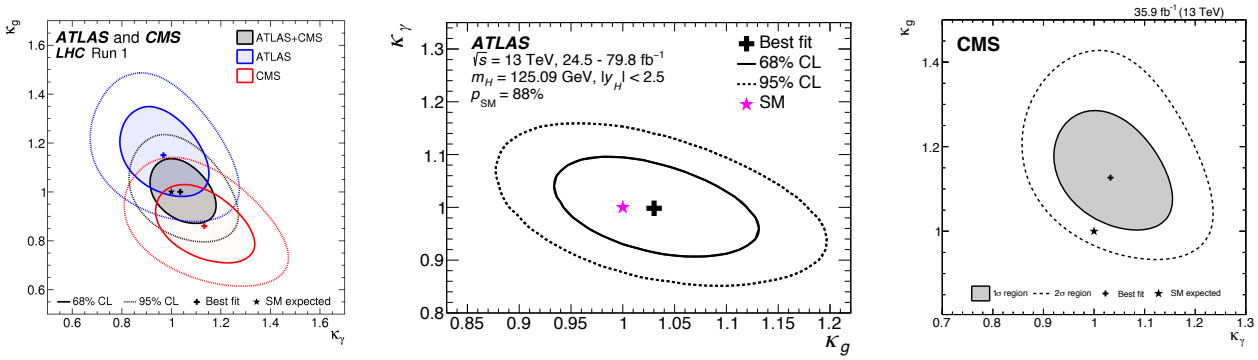

Figure 11.13: Likelihood contours in the $(\kappa_g, \kappa_\gamma)$ plane for the ATLAS-CMS [270] combination (left) and for the ATLAS [213] (center) and CMS [214] (right) individual Run 2 combinations.

couplings of the Higgs boson to the W and the top quark and that of the Z to the gluon come respectively from the tH and the $ggHZ$ production processes. In the case of the ATLAS Run 2 combination, only a relative negative sign of the coupling of the Higgs boson to the top quark is allowed. The cases reported in Table 11.12 of negative values of the couplings correspond to *quasi*-degenerate cases and the choice of sign is therefore not significant. For instance, the negative value of κ_W obtained by CMS in its Run 2 combination is due to tH contribution to the $t\bar{t}H$ channels as the specific tH analyses described in Section 11.3.3 are not included in the combination.

It is interesting to note that, with a partial Run 2 dataset, the sensitivity of individual experiments is already better than the one obtained at Run 1. This is in large part due to the improved systematic uncertainties related to the predictions of the Higgs boson production and decay that have been discussed in Section 11.2.

The results above are obtained under the assumption that the Higgs boson decays only to SM particles. This assumption is necessary since the signal rates cannot resolve separately κ_H and the absolute couplings of the Higgs boson to the SM particles. This degeneracy can, however, be resolved using an independent constraint on the Higgs boson width as the one derived from off-shell couplings measurements. This approach was used by the ATLAS experiment (see references in Ref. [123]), thus yielding a priori an absolute measurement of the couplings of the Higgs boson. The validity of the results obtained still relies on assumptions that have been discussed in Section 11.5.2. Another well-motivated assumption to resolve the aforementioned degeneracy preventing the determination of κ_H is inspired by unitarity conditions. Requiring that $\kappa_V \leq 1$ allows to free the $\mathrm{BR_{BSM}}$ parameter and further probe new physics in the decay of the Higgs boson. An intuitive understanding of how this constraint works can be given by a simple example. In the VBF $H \to W^+W^-$ channel, the number of signal events compared to the SM prediction is rescaled by $(1 - \mathrm{BR_{BSM}})\kappa_W^4/\kappa_H^2$, and, an observed signal close to the SM expectation cannot accommodate a large value of $\mathrm{BR_{BSM}}$ since the depletion factor $(1 - \mathrm{BR_{BSM}})$ cannot be compensated by an enhanced value $\kappa_W > 1$. Or, in other terms, if $\kappa_W \sim 1$ is preferred from other channels, a low signal in the VBF $H \to W^+W^-$ channel would be a sign of the presence of BSM physics in the Higgs boson decays. Within this framework, all the Higgs boson couplings to massive and massless SM particles can be measured in addition to $\mathrm{BR_{BSM}}$. The results of this combination are shown in Fig. 11.14 (left). The results for all parameters do not change significantly with respect to the previous fit that assumed $\mathrm{BR_{BSM}} = 0$. But a 95% CL bound on this parameter can now be obtained:

$$\mathrm{BR_{BSM}} < 34\% \ \text{(ATLAS)}, \quad \mathrm{BR_{BSM}} < 38\% \ \text{(CMS)}. \tag{11.41}$$

Both ATLAS and CMS in their Run 2 combinations have included the search for invisible decays of the Higgs boson [213,214], described in Section 11.3. This allows for a coherent interpretation of the constraints on invisible decays and the measurements in the visible channels as well as simultaneously constraining $\mathrm{BR_{inv}}$ and the overall branching fraction to potentially "visible" particles but to which none of the considered measurements are sensitive, as for example Higgs boson decays to light quarks or BSM particles decaying subsequently mainly to light quarks ($\mathrm{BR_{und}}$ referred to as branching fraction to undetected particles). The limits obtained on the invisible branching fractions are:

$$\mathrm{BR_{inv}} < 30\% \ \text{(ATLAS)}, \quad \mathrm{BR_{inv}} < 22\% \ \text{(CMS)}. \tag{11.42}$$

Models which are less sensitive to modelling systematic uncertainties and requiring no constraints on the natural width of the Higgs bosons have been considered, either through the ratio of cross section and branching ratios (see results in Ref. [123]) or through a more generic approach to avoid the degeneracy in the measurement of the coupling modifiers, probing the coupling properties of the Higgs boson through ratio of couplings. In the latter model, the cross section times branching fraction of the $gg \to H \to ZZ$ process is parametrised as a function of a single

Table 11.12: Coupling modifier combined measurements assuming the absence of perceptible new physics in the decay of the Higgs boson. No assumption is made for the loop level couplings of the Higgs boson to gluons and photons which are considered as effective.

	LHC Run 1	ATLAS Run 2	CMS Run 2	HL-LHC (expected)
κ_γ	$0.87^{+0.14}_{-0.09}$	1.05 ± 0.09	$1.07^{+0.10\,+0.09}_{-0.14\,-0.05}$	1.8%
κ_W	$0.87^{+0.13}_{-0.09}$	1.05 ± 0.09	$-1.13^{+0.15\,+0.06}_{-0.10\,-0.08}$	1.7%
κ_Z	-0.98 ± 0.10	1.11 ± 0.08	$1.00^{+0.09\,+0.06}_{-0.09\,-0.07}$	1.5%
κ_g	$0.78^{+0.13}_{-0.10}$	$0.99^{+0.11}_{-0.10}$	$1.18^{+0.10\,+0.12}_{-0.09\,-0.10}$	2.5%
κ_t	$1.40^{+0.24}_{-0.21}$	$1.09^{+0.15}_{-0.14}$	$0.98^{+0.08\,+0.12}_{-0.08\,-0.11}$	3.4%
κ_b	$0.49^{+0.27}_{-0.15}$	$1.03^{+0.19}_{-0.18}$	$1.17^{+0.18\,+0.20}_{-0.29\,-0.10}$	3.7%
κ_τ	$0.84^{+0.15}_{-0.11}$	$1.05^{+0.16}_{-0.15}$	$0.80^{+0.56\,+0.17}_{-0.81\,-0.00}$	1.9%

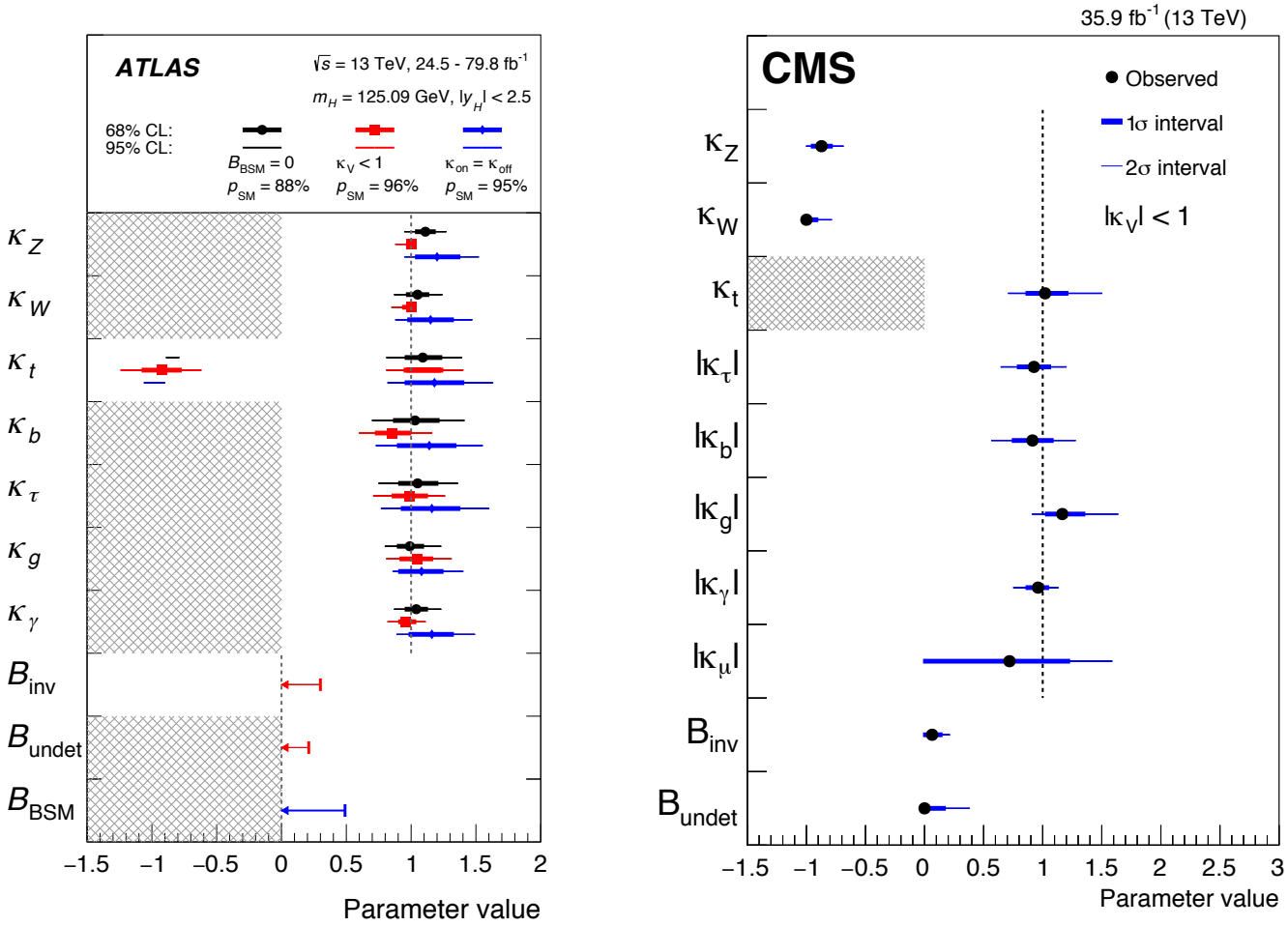

Figure 11.14: ATLAS [213] (left) and CMS [214] (right) combined measurements of coupling modifiers in the $\kappa_V < 1$ scenario, and in the case of the ATLAS measurements with the assumption $\mathrm{BR}_{\mathrm{BSM}} = 0$ and using the off-shell Higgs measurements.

coupling modifier:

$$\kappa_{gZ} = \kappa_g \times \frac{\kappa_Z}{\kappa_H} \tag{11.43}$$

Then all combination signals can be parametrised with the following ratios of coupling modifiers: (i) the $\lambda_{Zg} = \kappa_Z/\kappa_g$ ratio which is mainly probed by the measurements of the VBF and ZH production; (ii) the $\lambda_{tg} = \kappa_t/\kappa_g$ ratio constrained by the $t\bar{t}H$ production process; (iii) the $\lambda_{WZ} = \kappa_W/\kappa_Z$ ratio mainly probed by the WW and ZZ decay modes; (iv) the $\lambda_{\tau Z} = \kappa_\tau/\kappa_Z$ ratio constrained by the $\tau^+\tau^-$ channel; (v) the $\lambda_{bZ} = \kappa_b/\kappa_Z$ ratio probed mainly by the $VH(b\bar{b})$ channels; and (vi) the $\lambda_{\gamma Z} = \kappa_\gamma/\kappa_Z$ ratio constrained by the diphoton channel. In this parametrisation, the ZZ channel plays an important normalisation role (the results are discussed in detail in the previous edition of this review [123]).

11.6.2.2 *Differential cross sections*

To further characterise the production and decay properties of the Higgs boson, with the increase in size of the LHC datasets, measurements of fiducial and differential cross sections are being carried out by ATLAS and CMS both at Run 1 (the references can be found in the previous edition of this review [123]) and Run 2 [260, 272] and in several channels: (i) the diphoton, (ii) the four leptons, and (iii) the WW channels.

The definition of a fiducial volume as close as possible to the reconstruction level selection criteria is very important as it will

minimise the model dependence from possible variations in the signal reconstruction efficiencies. Minimising model dependence of unfolded fiducial differential cross section measurements is also key to ensure their usefulness to further probe and tune more accurate models in the future.

As an example in the diphoton channel for the ATLAS Run 1 analysis (similar criteria are used at Run 2 and by CMS), the selection criteria defining the fiducial volume are the following: the two highest transverse momentum (E_T), isolated final state photons, within $|\eta| < 2.37$ and with $105\,\text{GeV} < M_{\gamma\gamma} < 160\,\text{GeV}$ are selected (the transition region between the barrel and end-cap calorimeters is not removed); after the pair is selected, the same cut on $E_T/M_{\gamma\gamma}$ as in the event selection, i.e., in excess of 0.35 (0.25) for the two photons is applied. The requirement of the isolation of the photon to define the fiducial volume is particularly important to avoid potentially large variations of the reconstruction efficiency within this volume for production processes as different as the gluon fusion and $t\bar{t}H$.

While strict fiducial requirements are key to minimise model dependence, these make combinations of decay channels impossible. To gain precision in the measurement of the production properties of the Higgs boson, the fiducial volume defined on the decay products of the Higgs boson can be removed and channels can be combined relying on the extrapolation from the reconstruction acceptance using Monte Carlo simulations. This has been used to combine differential cross section for instance in the transverse momentum of the Higgs boson. Such hybrid approaches are also discussed in Section 11.6.2.4.

A large number of observables have been studied aiming at probing the accuracy of the modelling of the Higgs boson production simulations. Some examples include (i) the transverse momentum and pseudo rapidity of the objects, such as jets or leptons, produced in association with the Higgs boson in several modes, the principal distributions of the Higgs boson decay products such for instance in the diphoton channel; (ii) the production angle in the Collins–Soper frame [225] in the diphoton channel; (iii) the overall distribution of the Higgs boson transverse momentum.

The measured differential cross section in the Higgs boson transverse momentum by ATLAS and CMS using the full Run 2 datasets are illustrated in Fig. 11.15.

11.6.2.3 *Constraints on non-SM Higgs boson interactions in an effective Lagrangian*

An example of the possible use of differential cross sections in constraining non-SM Higgs boson couplings in an EFT is given by ATLAS [273]. In this analysis, differential cross section measured in the diphoton channel are used to constrain an effective Lagrangian where the SM is supplemented by dimension six CP-even operators of the Strongly Interacting Light Higgs (SILH) formulation [248] and corresponding CP-odd operators. The diphoton differential cross sections are mainly sensitive to the operators that affect the Higgs boson interactions with gauge bosons. CMS has also recently analysed [260] the Higgs boson transverse momentum distribution to constrain the Higgs boson couplings to top, bottom, and charm quarks as well as the effective coupling to gluons. This analysis is, however, not performed in an EFT framework.

The differential distributions used in this combination are: (i) the transverse momentum of the Higgs boson, (ii) the number of reconstructed jets produced in association with the diphoton pair, (iii) the invariant mass of the diphoton system and (iv) the difference in azimuthal angle of the leading and sub-leading jets in events with two or more jets. This analysis shows how differential information significantly improves the sensitivity to dimension-6 operators.

11.6.2.4 *Simplified Template Cross Sections (STXS)*

An overarching subject of discussion between the theory and experimental communities in the field of Higgs physics has been how experimentalists could best communicate their results for them to be most efficiently used by others for further interpretation.

In the field of precision SM measurements, the commonly used practise is that results are given at particle level within a well defined fiducial volume of phase space. The fiducial volume is usually defined close enough to the experimental reconstruction to minimise the possible variations of the reconstruction efficiency within the particle level fiducial volume. In this way, results minimise their dependence on theoretical uncertainties.

ATLAS and CMS have produced fiducial and unfolded cross sections based on all objects reconstructed in the events. These measurements could be used for further interpretation. However, performing a proper combination of channels taking into account all experimental systematic uncertainties is non trivial. A proposal [44, 274] was made by the LHC Higgs Cross Section Working Group to produce results in each decay channel with a well defined fiducial phase space of the Higgs boson (and not its decay products) and for other associated objects pertaining to all channels, such as jets and missing transverse momentum (MET). The definition of the fiducial regions is motivated by maximising the experimental sensitivity, isolating possible BSM effects, and minimising the dependence on theoretical uncertainties. The number of regions is also minimised to avoid the loss of experimental sensitivity. The observables that are measured in this approach are still the standard production cross sections (the gluon fusion, the vector boson fusion, the VH and $t\bar{t}H$ associated production modes) within the defined fiducial volumes.

In summary, this approach is hybrid. It is fiducial on specific objects to reduce the theory dependence and inclusive in the Higgs kinematics in order to allow for a more straightforward combination. This approach also allows the use of multivariate techniques to enhance the sensitivity within given fiducial regions, at the expense of a greater extrapolation and therefore increased model dependence.

The currently used Simplified Template Cross Sections (STXS) scheme covers, with a limited number of bins, the ggF process in four categories in number of jets (0, 1, 2 and 2 VBF-like jets, where VBF-like means a selection of two high invariant mass jets with large pseudo rapidity difference) further subdivided in four transverse momentum categories covering the full spectrum with the last bin being inclusive for $p_T > 200$GeV. The VH process is subdivided two categories depending on the number of reconstructed charged leptons corresponding to the decays of either a W boson or a Z boson, and two bins in transverse momentum. VBF and hadronic VH categories are defined using jet cuts and two bins in transverse momentum.

Measurements in this framework have been made in various decay channels. The first measurements have been performed in the main Higgs boson discovery channels. ATLAS has produced measurements of the diphoton and the 4ℓ channels with Run 2 data [125, 227, 236, 275, 276]. And full Run 2 results are available for the $H \to 4\ell$ channel from ATLAS [131] and CMS [277].

CMS has carried out a measurement of the STXS in the $H \to \tau^+\tau^-$ decay channel targeting the high transverse momentum of the Higgs boson [145], in particular in the channel where the Higgs boson is produced with one jet of transverse energy in excess of 200 GeV.

ATLAS [149] has made a measurement of the STXS aiming at the VH production mode in the $H \to b\bar{b}$ decay mode at high transverse momentum of the vector boson above 250 GeV, where the discrimination of the background further increases.

A combination of STXS across decay channels has also been carried out by ATLAS with a dataset corresponding to an integrated luminosity of up to $80\,\text{fb}^{-1}$ [213].

11.6.2.5 *Indirect constraints on the Higgs boson couplings*

The direct measurements at the LHC provide direct probes of the Higgs boson couplings to the vector bosons (photons, W, Z and gluons) and to a limited number of Yukawa couplings to fermions. Currently these include essentially the third generation fermions – tau leptons, bottom and top quarks. For the High-Luminosity run, prospective studies [104] have shown that a good precision will be reached in the measurement of the coupling of the Higgs boson to muons and an evidence of the Higgs boson trilinear self-coupling with a precision of the order of 50% can be achieved. For the couplings of the Higgs boson to the other light SM fermions, direct evidences will be hard to reach at the LHC. However, from the measurements of the main observed Higgs final

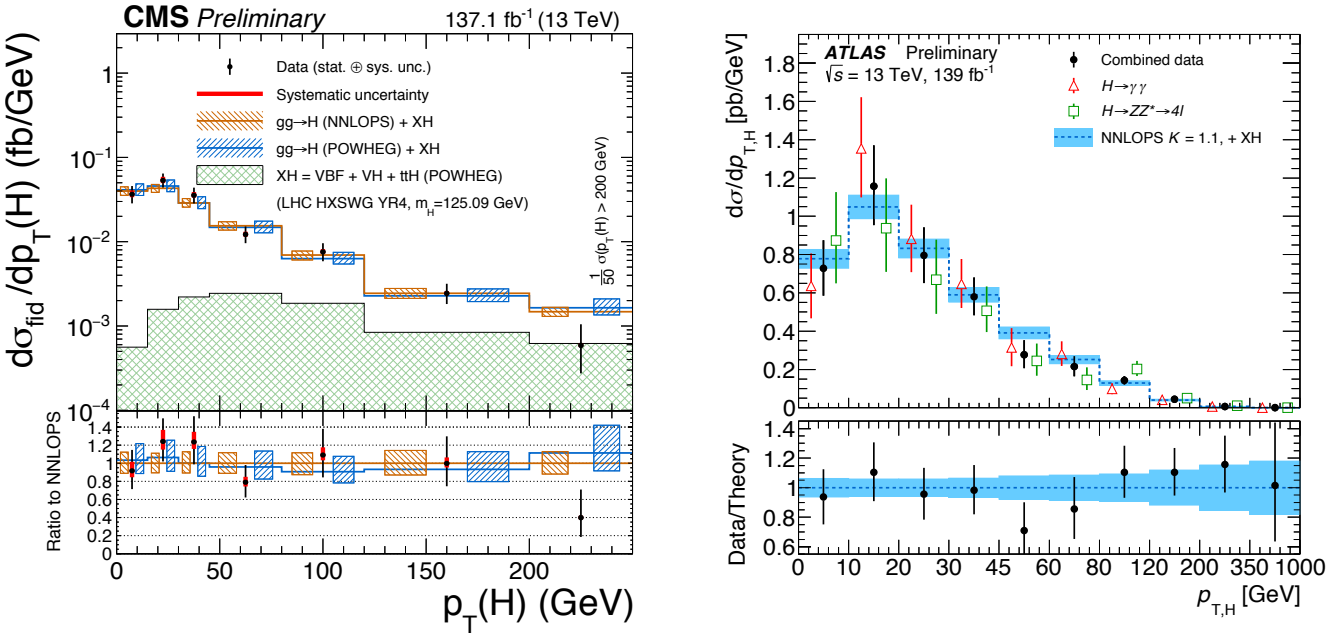

Figure 11.15: (Left) Fiducial differential, closely matching the reconstruction level selections, cross sections in Higgs boson transverse momentum in the $H \to 4\ell$ channel from the CMS experiment [126]. (Right) Partially fiducial combined cross sections using the $H \to \gamma\gamma$ and $H \to 4\ell$ channels from the ATLAS experiment [272].

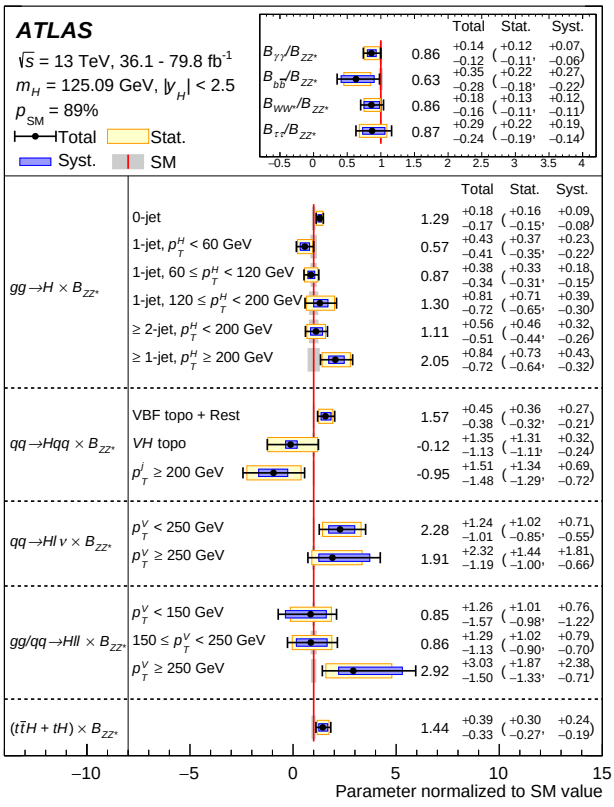

Figure 11.16: Simultaneous measurement of the simplified template cross sections times the branching fraction BR($H \to ZZ$) (normalised to their Standard Model expectations) and the ratios of branching fractions BR(f)/BR(ZZ) [213].

states, it is possible to constrain specific couplings through their radiative corrections to dominant processes. Two prime examples are: (i) the trilinear self-coupling can be constrained through loop corrections to the single Higgs boson production [278–280], see the interpretation carried out by ATLAS of the combination of the main decay channels [281]; (ii) the charm Yukawa coupling can be constrained from the differential cross section in Higgs boson transverse momentum [282], see the ATLAS [283] and CMS [260] analyses in the diphoton channel. These indirect constraints, however, require assumptions on the possible variations of all the other couplings.

ATLAS has also performed a preliminary combination of the single Higgs boson production measurements [284], using the approach and parametrisations of Ref. [279], which yield the following constraint:

$$-3.2 < \kappa_\lambda < 11.9. \qquad (11.44)$$

When combined with results of the double Higgs boson production searches, the following combined constraint on the Higgs boson trilinear coupling yields:

$$-2.3 < \kappa_\lambda < 10.3\,(\text{obs}) \quad [-5.1 < \kappa_\lambda < 11.2.\,(\text{exp})]. \qquad (11.45)$$

The *direct* and *indirect* constraints on the Higgs boson trilinear self-coupling are currently of similar strength. The double Higgs boson measurements are dominated by statistical uncertainties and are expected to improve much more rapidly than the precision on single Higgs boson measurements. Furthermore, it should be stressed that the constraints on the trilinear self-coupling obtained via the NLO fit of single Higgs boson data are less robust and more model-dependent since the NLO effects induced by a shift of the trilinear self-coupling compete with possible LO effects sourced by the deviations of the Higgs boson couplings to the other SM particles. The different effects can be disentangled by the measurements of various kinematical differential distributions in addition to the study of the inclusive rates [285], but the expected sensitivity in such global fits is not as promising as the one obtained when only the Higgs boson self-coupling is allowed to deviate from its SM value [286].

11.7 New physics models of EWSB in the light of the Higgs boson discovery

The discovery of a light scalar with couplings to gauge bosons and fermions that are consistent with SM predictions, together with the slow running of the Higgs boson self-coupling at high energies allow one to consider the SM as a valid perturbative description of nature all the way to the Planck scale. This picture is admittedly very attractive, but it posits that the Higgs boson

is an elementary scalar field, whose mass has quantum sensitivity to possible new physics scales. This EW/Higgs naturalness problem [6] has become much more definite after the Higgs boson discovery.

There are two broad classes of models addressing the naturalness problem[5]. One is based on SUSY [7] (for recent reviews, see Refs. [8, 9]). This is a weakly coupled approach to EWSB, maintaining the perturbativity of the SM, and, the Higgs boson remains elementary and the corrections to its mass are screened at the scale at which SUSY is broken so the value of the weak scale remains insensitive to the details of the physics at higher scales. These theories predict at least three neutral Higgs particles and a pair of charged Higgs particles [25]. One of the neutral Higgs bosons, most often the lightest CP-even one, has properties that could resemble those of the SM Higgs boson (at least in some regions of the parameter space). It is referred to as a SM-like Higgs boson, meaning that its couplings are close to the ones predicted in the SM. The other approach invokes the existence of strong interactions at a scale of the order of one TeV or above and these new interactions induce the breaking of the electroweak symmetry [288]. In the original incarnation, dubbed technicolor, the strong interactions themselves trigger EWSB without the need of a Higgs boson. Another possibility, more compatible with the ATLAS and CMS discovery, is that the strong interactions produce four light resonances identified with the Higgs doublet and EWSB proceeds through vacuum misalignment [10] (see Refs. [11, 12] for recent reviews). In that case, the Higgs boson itself has a finite size and thus never feels the UV degrees of freedom that would otherwise have dragged its mass to much higher scales. The Higgs boson could also correspond to the Goldstone boson associated with the spontaneous breaking of scale invariance, see Ref. [289] and references therein. However, this dilaton/radion scenario now requires a jumbled model-building to be consistent with the constraints from the coupling measurements. All these BSM scenarios can have important effects on the phenomenology of the Higgs boson. Also, in each case, the role of the Higgs boson in the unitarisation of scattering amplitudes is shared by other particles which remain targets of experimental searches.

The realisation of SUSY at low energies has many good qualities that render it attractive as a model of new physics. First of all since, for every SM degree of freedom, there is a superpartner of different spin but of equal mass and effective coupling to the SM-like Higgs boson, in the case of exact SUSY, an automatic cancellation of quantum corrections to the Higgs mass parameter holds. In practice, it is known that SUSY must be broken since no superpartners of the SM particles have been observed so far. The mass difference between the precise value of the mass of any particle and that of its corresponding superpartner is proportional to the correlated soft SUSY breaking parameter, generically called $M_{\rm SUSY}$. The quantum corrections to the Higgs boson mass parameter are proportional to $M^2_{\rm SUSY}$, and provided $M_{\rm SUSY}$ is of order of a few TeV, the low energy mass parameters of the Higgs sector become insensitive to physics at the GUT or Planck scale. Another interesting feature of SUSY theories is related to the dynamical generation of EWSB [290]. In the SM, a negative Higgs mass parameter, m^2, needs to be inserted by hand to induce EWSB, see Eq. (11.1). In SUSY, instead, even if the relevant Higgs mass parameter is positive in the ultraviolet, it may become negative and induce EWSB radiatively through the strong effect of the top quark-Higgs boson coupling in its renormalisation group evolution [290].

In the following, the Higgs sector will be explored in specific SUSY models. In all of them, it is often possible to find regions of the parameter space that accommodate one neutral Higgs boson with properties that resemble those of the SM Higgs boson, whereas additional neutral and charged Higgs bosons are also predicted and are intensively being sought for at the LHC (see Section 11.7.7). In the simplest SUSY model, accommodating a SM-like Higgs boson mass of about 125 GeV results in constraints on the stop sector, with at least one stop mass in the few TeV mass range. In non-minimal SUSY extensions of the SM (details and related references can be found in the previous edition of this review [123]), a SM-like Higgs boson with mass of 125 GeV can be accomodated with less restrictions on the stop sector. While naturalness dictates relatively light stops and - at the two loop level - also gluinos, the first and second generation of squarks and sleptons couple weakly to the Higgs sector and may be heavy. Moreover, small values of the μ parameter and therefore light Higgsinos, the fermionic superpartners of the Higgs bosons, would be a signature of a natural realization of electroweak symmetry breaking [291]. Such SUSY spectra, consisting of TeV range stop masses and light Higgsinos, continue to be under intense scrutiny by the experimental collaborations [292] in order to understand if such natural SUSY scenarios endure and can explain why the Higgs boson remains light.

In the context of weakly coupled models of EWSB, one can also consider multiple Higgs $\mathrm{SU}(2)_L$ doublets as well as additional Higgs singlets, triplets or even more complicated multiplet structures, with or without low energy SUSY. In general, for such models, one needs to take into account experimental constraints from precision measurements and flavour changing neutral currents. The LHC signatures of such extended Higgs sectors are largely shaped by the role of the exotic scalar fields in EWSB.

The idea that the Higgs boson itself could be a composite bound state emerging from a new strongly-coupled sector has been reconsidered thanks to the insights gained from the AdS/CFT duality. The composite Higgs boson idea is an incarnation of EWSB via strong dynamics that smoothly interpolates between the standard technicolor approach and the true SM limit. To avoid the usual conflict with EW data, it is sufficient, if not necessary, that a mass gap separates the Higgs resonance from the other resonances of the strong sector. Such a mass gap can naturally follow from dynamics if the strongly-interacting sector exhibits a global symmetry, G, broken dynamically to a subgroup H at the scale f, such that, in addition to the three Nambu–Goldstone bosons of SO(4)/SO(3) that describe the longitudinal components of the massive W and Z, the coset G/H contains a fourth Nambu–Goldstone boson that can be identified with the physical Higgs boson. Simple examples of such a coset are SU(3)/SU(2) or SO(5)/SO(4), the latter being favoured since it is invariant under the custodial symmetry. It is also possible to have non-minimal custodial cosets with extra Goldstone bosons leading to additional Higgs bosons in the spectrum, see for instance Ref. [293]. Modern incarnations of composite Higgs models have been recently investigated in the framework of 5D warped models where, according to the principles of the AdS/CFT correspondence, the holographic composite Higgs boson then originates from a component of a gauge field along the 5th dimension with appropriate boundary conditions.

A last crucial ingredient in the construction of viable composite Higgs boson models is the concept of partial compositeness [294], i.e., the idea that there are only linear mass mixings between elementary fields and composite states. After diagonalisation of the mass matrices, the SM particles, fermions and gauge bosons, are admixtures of elementary and composite states and thus they interact with the strong sector, and in particular with the Higgs boson, through their composite component. This setup has important consequences on the flavour properties, chiefly the suppression of large flavour changing neutral currents involving light fermions. It also plays an important role in dynamically generating a potential for the would-be Goldstone bosons. Partial compositeness also links the properties of the Higgs boson to the spectrum of the fermionic resonances, i.e., the partners of the top quark. As in the MSSM, these top partners are really the agents that trigger the EWSB and also generate the mass of the Higgs boson that otherwise would remain an exact Goldstone boson and hence massless. The bounds from the direct searches for the top partners, in addition to the usual constraints from EW precision data, force the minimal composite Higgs models into some unnatural corners of their parameter spaces [295].

11.7.1 *Higgs bosons in the minimal supersymmetric standard model (MSSM)*

The particle masses and interactions in a SUSY theory are uniquely defined as a function of the superpotential and the Käh-

[5] Another solution to the naturalness problem is to lower the fundamental scale of quantum gravity, like for instance in models with large extra-dimensions, see Ref. [287].

ler potential [9]. A fundamental theory of SUSY breaking, however, is unknown at this time. Nevertheless, one can parametrise the low-energy theory in terms of the most general set of soft SUSY-breaking operators [9]. The simplest realistic model of low-energy SUSY is the minimal SUSY extension of the SM (MSSM) [9, 296], that associates a SUSY partner to each gauge boson and chiral fermion of the SM, and provides a realistic model of physics at the weak scale. However, even in this minimal model with the most general set of soft SUSY-breaking terms, more than 100 new parameters are introduced. Fortunately, only a subset of these parameters impact the Higgs boson phenomenology either directly at tree-level or through quantum effects.

The MSSM contains the particle spectrum of a two-Higgs-doublet model (2HDM) extension of the SM and the corresponding SUSY partners. Two Higgs doublets, Φ_1 and Φ_2, with hypercharge $Y = -1$ and $Y = 1$, respectively, are required to ensure an anomaly-free SUSY extension of the SM and to generate mass for down-type quarks/charged leptons (Φ_1) and up-type quarks (Φ_2) [25]. The Higgs potential reads

$$\begin{aligned} V =& m_1^2 \Phi_1^\dagger \Phi_1 + m_2^2 \Phi_2^\dagger \Phi_2 - m_3^2 (\Phi_1^T i\sigma_2 \Phi_2 + \text{h.c.}) \\ &+ \frac{1}{2}\lambda_1 (\Phi_1^\dagger \Phi_1)^2 + \frac{1}{2}\lambda_2 (\Phi_2^\dagger \Phi_2)^2 + \lambda_3 (\Phi_1^\dagger \Phi_1)(\Phi_2^\dagger \Phi_2) \\ &+ \lambda_4 |\Phi_1^T i\sigma_2 \Phi_2|^2 + \frac{1}{2}\lambda_5 \left[(\Phi_1^T i\sigma_2 \Phi_2)^2 + \text{h.c.} \right] \\ &+ \left[[\lambda_6 (\Phi_1^\dagger \Phi_1) + \lambda_7 (\Phi_2^\dagger \Phi_2)] \Phi_1^T i\sigma_2 \Phi_2 + \text{h.c.} \right], \end{aligned} \tag{11.46}$$

where $m_i^2 = \mu^2 + m_{H_i}^2$ $(i = 1, 2)$, with μ being the supersymmetric Higgsino mass parameter and m_i the soft supersymmetric breaking mass parameters of the two Higgs doublets; $m_3^2 \equiv B\mu$ is associated to the B-term soft SUSY breaking parameter; and λ_i, for $i = 1$ to 7, are all the Higgs quartic couplings.

After the spontaneous breaking of the electroweak symmetry, five physical Higgs particles are left in the MSSM spectrum: one charged Higgs pair, $H^\pm$, one CP-odd neutral scalar, A, and two CP-even neutral states, H and h, with h being the lightest.[6] The Higgs sector at tree level depends on the electroweak gauge coupling constants and the vacuum expectation value v – or equivalently the Z gauge boson mass – and is determined by only two free parameters: $\tan\beta$ - the ratio of the two Higgs doublets' vacuum expectation values v_2/v_1 - and one Higgs boson mass, conventionally chosen to be the CP-odd Higgs boson mass, m_A. The other tree-level Higgs boson masses are then given in terms of these parameters. The tree level value of m_h is maximised not only for $m_A \gg m_Z$ but also for $\tan\beta \gg 1$. For $m_A \gg m_Z$ it acquires a maximum value $m_h = m_Z \cos 2\beta$.

Radiative corrections have a significant impact on the values of Higgs boson masses and couplings in the MSSM. The dominant radiative effects to the SM-like Higgs boson mass arise from the incomplete cancellation between top and scalar-top (stop) loops and at large $\tan\beta$ also from sbottom and stau loops. The stop, sbottom and stau masses and mixing angles depend on the SUSY Higgsino mass parameter μ and on the soft-SUSY-breaking parameters [9, 296]: M_Q, M_U, M_D, M_L, M_E, and A_t, A_b A_τ. The first three of these are the left-chiral and the right-chiral top and bottom scalar quark mass parameters. The next two are the left-chiral stau/sneutrino and the right-chiral stau mass parameters, and the last three are the trilinear parameters that enter in the off-diagonal squark/slepton mixing elements: $X_t \equiv A_t - \mu \cot\beta$ and $X_{b,\tau} \equiv A_{b,\tau} - \mu \tan\beta$. At one-loop, the electroweak gauginos yield a small contribution to the Higgs boson mass, and at the two-loop level, the masses of the gluinos also enter in the calculations. Radiative corrections to the Higgs boson masses have been computed using a number of techniques, with a variety of approximations; for a discussion see for example Refs. [39, 297, 298] and the corresponding section of the previous edition of this review [123].

The discovered SM-like Higgs boson, if interpreted as the lightest MSSM Higgs boson with a mass of about 125 GeV, provides information on the possible MSSM parameter space, see Fig. 11.17.

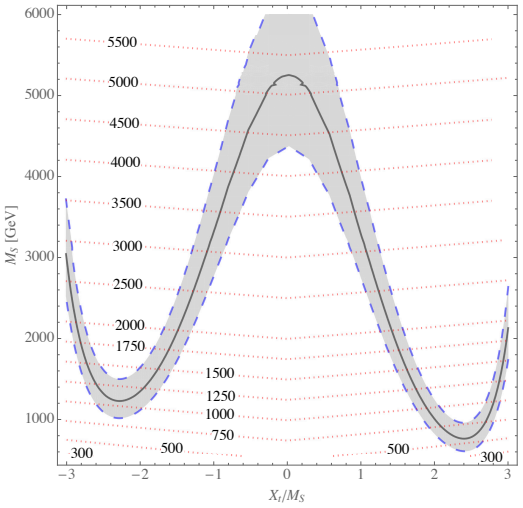

Figure 11.17: Values of the SUSY mass scale $M_{\rm SUSY} = M_S$ versus the stop mixing parameter normalised by the SUSY mass scale $X_t/M_{\rm SUSY}$, for fixed $\tan\beta = 20$, $\mu = 200$ GeV and $M_A = A_t = A_b = A_\tau = M_{\rm SUSY}$. The solid black line corresponds to $m_h = 125$ GeV while in the grey band m_h varies by ± 1 GeV. The red dotted lines are iso-values of the stop mass. This figure is based on Ref. [299].

The phenomenology of the Higgs sector depends on the couplings of the Higgs bosons to gauge bosons and fermions. At tree-level, the couplings of the two CP-even Higgs bosons to W and Z bosons are given in terms of the angles α, that diagonalises the CP-even Higgs boson squared-mass matrix, and β

$$g_{hVV} = g_V m_V \sin(\beta - \alpha), \quad g_{HVV} = g_V m_V \cos(\beta - \alpha), \tag{11.47}$$

where $g_V \equiv 2m_V/v$, for $V = W$ or Z ($g_V m_V$ is the SM hVV coupling). Observe that in the limit $\cos(\beta - \alpha) \to 0$, the lightest CP-even Higgs boson h behaves as the SM Higgs boson. This situation is called alignment and is achieved in specific regions of parameter space for $m_A \geq m_Z$ [300] or in the large $m_A \gg m_Z$ limit, in which alignment is achieved through decoupling [300, 301]. There are no tree-level couplings of A or $H^\pm$ to VV. The couplings of the Z boson to two neutral Higgs bosons are given by $g_{\phi AZ}(p_\phi - p_A)$, where $\phi = H$ or h, the momenta p_ϕ and p_A point into the vertex, and

$$g_{hAZ} = g_Z \cos(\beta - \alpha)/2, \quad g_{HAZ} = -g_Z \sin(\beta - \alpha)/2\,. \tag{11.48}$$

The expressions of the couplings between a charged Higgs boson, a neutral Higgs boson and the W boson as well as the expressions of the four-point couplings of vector bosons and Higgs bosons can be found in Ref. [25].

The tree-level Higgs boson couplings to fermions obey the following property: the neutral components of one Higgs doublet, Φ_1, couple exclusively to down-type fermion pairs while the neutral components of the other doublet, Φ_2, couple exclusively to up-type fermion pairs [25]. This Higgs-fermion coupling structure defines the Type-II 2HDM. In the MSSM, fermion masses are generated when both neutral Higgs components acquire a vacuum expectation value, and the relations between Yukawa couplings and fermion masses are (in third-generation notation)

$$h_{b,\tau} = \sqrt{2}\, m_{b,\tau}/(v \cos\beta), \quad h_t = \sqrt{2}\, m_t/(v \sin\beta)\,. \tag{11.49}$$

The couplings of the neutral Higgs bosons to $f\bar{f}$, relative to their

[6] Observe that in the SM sections of this review, H denotes the SM Higgs boson, whereas in the sections about SUSY, or extensions of the SM with two Higgs doublets, H is used for the heaviest CP-even Higgs boson, since this is the standard notation in the literature, and the 125 GeV SM-like light Higgs boson will be denoted by h. Generically, in the MSSM, the lightest CP-even Higgs boson is indeed SM-like and thus it is naturally identified with the 125 GeV Higgs boson discovered by ATLAS and CMS, while in 2HDM extensions, with or without SUSY, there could still be lighter scalar states below 125 GeV.

SM values, $g\,m_f/(2m_W)$, are given by

$$\begin{array}{ll} hb\bar{b}: & -\sin\alpha/\cos\beta, \qquad ht\bar{t}: \cos\alpha/\sin\beta\,, \\ Hb\bar{b}: & \cos\alpha/\cos\beta, \qquad Ht\bar{t}: \sin\alpha/\sin\beta\,, \\ Ab\bar{b}: & \gamma_5\tan\beta, \qquad At\bar{t}: \gamma_5\cot\beta\,. \end{array} \tag{11.50}$$

In each relation above, the factor listed for $b\bar{b}$ also pertains to $\tau^+\tau^-$. The charged Higgs boson couplings to fermion pairs, normalised to $g/(\sqrt{2}m_W)$, are given by

$$\begin{aligned} g_{H^-t\bar{b}} &: m_t\cot\beta\frac{1+\gamma_5}{2} + m_b\tan\beta\frac{1-\gamma_5}{2}, \\ g_{H^-\tau^+\nu} &: m_\tau\tan\beta\frac{1-\gamma_5}{2}\,. \end{aligned} \tag{11.51}$$

The non-standard neutral Higgs bosons have significantly enhanced couplings to down-type fermions at sizeable $\tan\beta$. Radiative corrections can modify significantly the values of the Higgs boson couplings to fermion pairs and to vector boson pairs, through a radiatively-corrected value for $\cos(\beta-\alpha)$ as well as from the one-loop vertex corrections to tree-level Higgs-fermion Yukawa couplings, see Ref. [9] and references therein, for a detailed discussion.

11.7.1.1 *MSSM Higgs boson phenomenology*

The MSSM parameters have to be arranged such that the mass, the CP properties, the decay and production properties of one of the neutral Higgs bosons agree with the LHC Higgs data. Given that present data allows only for moderate departures from the SM predictions, it implies that some degree of alignment is necessary.

The SM-like branching ratios of h can be modified if decays into SUSY particles are kinematically allowed, and, in particular, decays into a pair of the lightest SUSY particles – i.e., the lightest neutralinos, $\tilde{\chi}_1^0$ – can become dominant and would be invisible if R-parity is conserved [302]. Moreover, if light superpartners exist and couple to photons and/or gluons, the h loop-induced coupling to gg and $\gamma\gamma$ could deviate sizeably from the corresponding SM predictions (see for instance the review [297]), and would be in conflict with present data (see Section 11.3). For the heavier Higgs states, there are two possibilities to be considered[7]:

i) Alignment triggered by decoupling, hence $m_A \geq$ several hundred GeV: The HWW and HZZ couplings are very small. The dominant H, A decay branching ratios strongly depend on $\tan\beta$. The decay modes $H, A \to b\bar{b}, \tau^+\tau^-$ dominate when $\tan\beta$ is large (this holds even away from decoupling). For small $\tan\beta$, the $t\bar{t}$ decay mode dominates above its kinematic threshold. For the charged Higgs boson, $H^+ \to t\bar{b}$ dominates.

ii) Some degree of alignment without decoupling, hence $m_A \leq$ a few hundred GeV: The main difference with the previous case is that, in the low $\tan\beta$ regime ($\tan\beta \leq 5$), additional decay channels may be allowed which involve decays into the lightest SM-like Higgs boson; $A \to Zh$, $H \to hh$ as well as $H \to WW/ZZ$ decay modes are available (they are suppressed in the strict alignment limit). When kinematically open, the decays $A/H \to t\bar{t}$ become relevant or even dominant for sufficiently small $\tan\beta$. For the charged Higgs boson, $H^+ \to \tau^+\nu_\tau$ dominates below the $t\bar{b}$ threshold, and also $H^\pm \to W^\pm h$ may be searched for.

In both cases i) and ii), the heavier Higgs states, H, A and $H^\pm$, are roughly mass degenerate (with masses $\pm$ 20 GeV or less apart). If kinematically allowed, the heavy Higgs boson decays into charginos, neutralinos and third-generation squarks and sleptons can be important [305].

At hadron colliders, the dominant neutral Higgs boson production mechanism at moderate values of $\tan\beta$ is gluon fusion, mediated by loops containing heavy top and bottom quarks and the corresponding SUSY partners. The effect of light stops that may contribute to the gluon fusion production can be partially cancelled by mixing effects. Higgs boson radiation off bottom quarks becomes important for large $\tan\beta$, where at least two of the three neutral Higgs bosons have enhanced couplings to bottom-type fermions [306, 307]. Detailed discussions of the impact of radiative corrections in these search modes are presented for instance in Ref. [308]. The vector boson fusion and Higgs-strahlung production of the CP-even Higgs bosons as well as the associated production of neutral Higgs bosons with top quark pairs have lower production cross sections by at least an order of magnitude with respect to the dominant ones, depending on the precise region of MSSM parameter space [41–44]. Higgs boson pair production of non-standard MSSM Higgs bosons has been studied in Ref. [309]. For a discussion of charged Higgs boson production at LHC, see Refs. [42, 43, 310].

Strong production of a heavy neutral Higgs boson followed by its decay into top-quark pairs is a challenging channel, only most recently being searched for by ATLAS and CMS. Interference effects between the signal and the SM $t\bar{t}$ background need to be carefully taken into account [311].

Summarising, the additional Higgs bosons are sought for mainly via the channels:

$$\begin{aligned} & pp \to A/H \to \tau^+\tau^- \text{ (inclusive)}, \\ & b\bar{b}A/H, A/H \to \tau^+\tau^- \text{ (with } b\text{-tag)}, \\ & b\bar{b}A/H, A/H \to b\bar{b} \text{ (with } b\text{-tag)}, \\ & pp \to t\bar{t} \to H^\pm W^\mp b\bar{b},\ H^\pm \to \tau\nu_\tau\ , \\ & gb \to H^- t \ \text{ or } \ g\bar{b} \to H^+\bar{t},\ H^\pm \to \tau\nu_\tau\ . \end{aligned} \tag{11.52}$$

After the Higgs boson discovery, updated MSSM benchmarks scenarios have been defined to highlight interesting conditions for the MSSM Higgs boson searches [43, 304, 312]. The latest benchmark scenarios update [304], partly based in MSSM parameter space discussions in Ref. [312], considers six benchmarks to illustrate different aspects of Higgs phenomenology in the MSSM. They include one case with complex parameters, but they all assume R-parity conservation and no flavour mixing. Each scenario contains one CP-even scalar with mass around 125 GeV and SM-like couplings. These scenarios include a M_h^{125} scenario with relatively heavy superparticles, so the Higgs phenomenology at the LHC resembles that of a 2HDM with MSSM-inspired Higgs boson couplings. Other two scenarios are characterised by some of the superparticles – staus or electroweakinos – being relatively light, that in turn is of relevance for heavy neutral Higgs boson searches. In particular, the traditional $A/H \to \tau^+\tau^-$ search channel varies depending on the values of μ and M_2, that may enable the A/H decays into electroweakinos. Another two scenarios are characterised by the phenomenon of alignment without decoupling, in which one of the two neutral CP-even scalars has SM-like couplings independently of the mass spectrum of the remaining Higgs bosons, hence allowing for all the Higgs bosons to have relatively low mass values (about few hundred GeV). Finally there is one scenario which incorporates CP violation in the Higgs sector and gives rise to a strong admixture of the two heavier neutral states. All the above scenarios assume all parameters in the mass range from 1 to a few TeV, hence they are not applicable for values of $\tan\beta$ of order a few, for which a Higgs boson mass value of 125 GeV is out of reach. An additional study, EFTMSSM [313], proposes two scenarios specifically designed for the low $\tan\beta$ region and ensures a 125 GeV Higgs boson mass in almost the entire parameter space by employing a flexible supersymmetric mass scale, reaching values of up to 10^{16} GeV.

An alternative approach to reduce the large number of parameters relevant to the Higgs sector is to consider that, in the Higgs basis, the only important radiative corrections are those affecting the Higgs boson mass [314]. This approximation is called hMSSM and works well in large regions of parameter space but it breaks down for sizeable values of μ and A_t, and moderate values of $\tan\beta$, for which the radiative corrections to the mixing between the two CP even eigenstates become relevant. The effect of such radiative corrections is to allow for alignment for small to intermediate values of $\tan\beta$, independent of the specific value of m_A [315]. In

[7] In very special regions of the parameter space, there is still the possibility that the heavier CP-even Higgs state is identified with the 125 GeV Higgs boson discovered by ATLAS and CMS, see for instance the discussion in Ref. [303] and the benchmark M_H^{125} defined in Ref. [304].

addition, the hMSSM assumption that the right value of the Higgs boson mass may be obtained for all values of m_A and $\tan\beta$ is in conflict with the MSSM predictions for the Higgs boson mass for small values of m_A and $\tan\beta \simeq \mathcal{O}(1)$. The recent M_h^{125} [304] and EFTMSSM benchmarks [313], are designed to address the limitations of the hMSSM, in particular the low $\tan\beta$ region for the EFTMSSM.

The M_h^{125} scenarios are aiming at treating more rigorously all radiative correction to the observed Higgs boson mass as well as specifically taking into possibly intermediate to light MSSM colorless states as electroweakinos or staus [304]. The main M_h^{125} benchmark, however, assumes that super partners are heavy, so that the phenomenology of the observed Higgs boson is not altered except in its couplings due to the existence of another doublet. Another important example scenario, referred to as $M_h^{125}(\tilde{\chi})$, considers light electroweakinos and therefore the heavy Higgs bosons H and A can have sizeable decay rates to charginos and neutralinos, consequently suppressing the $\tau^+\tau^-$ decay rate. It is interesting to note that in this scenario the branching fraction of the Higgs boson to photons is enhanced for small values of $\tan\beta$ due to the presence of electroweakinos in the loop. These two scenarios are illustrated in Fig. 11.18.

The compatibility between the predicted and measured Higgs boson mass is an important constraint in these scenarios. The predictions are illustrated in Fig. 11.18. To use the predicted Higgs boson mass as a constraint (exclusion at nearly constant $\tan\beta$ at high M_A in the (M_A,$\tan\beta$) plane), it is important to account for the theoretical uncertainty on the prediction which is in excess of an order of magnitude larger than the experimental uncertainty on the measured mass of the Higgs boson. The theoretical uncertainty depends itself on the specific SUSY spectrum for a given MSSM parameter set and should be estimated accordingly, however, a more generic estimate of ± 3 GeV is made and found to be a conservative choice.

Reviews of the properties and phenomenology of the Higgs bosons of the MSSM can be found for example in Refs. [9,39,297]. Future precision measurements of the Higgs boson couplings to fermions and gauge bosons together with information on heavy Higgs boson searches will provide powerful information on the SUSY parameter space [315,316].

Improvements in our understanding of B-physics observables put indirect constraints on additional Higgs bosons in mass ranges that would be accessible in direct LHC searches. In particular, $\mathrm{BR}(B_s \to \mu^+\mu^-)$, $\mathrm{BR}(b \to s\gamma)$, and $\mathrm{BR}(B_u \to \tau\nu)$ play an important role within minimal flavour-violating (MFV) models [317], in which flavor effects proportional to the CKM matrix elements are induced as in the SM.

11.7.2 *Supersymmetry with singlet extensions*

The Higgs mass parameter μ is a SUSY parameter, and as such, it should naturally be of order M_{GUT} or M_{Planck}. The fact that phenomenologically it is required that μ be at the electroweak/TeV scale is known as the μ problem [318]. SUSY models with additional singlets can provide a solution to the μ problem, by promoting the μ parameter to a dynamical singlet superfield S that only interacts with the MSSM Higgs doublets through a coupling λ_S at the level of the superpotential. An effective μ is generated when the real scalar component of S acquires a vacuum expectation value v_S, yielding $\mu_{\mathit{eff}} = \lambda_S\, v_S$. After the minimization of the Higgs potential, the vacuum state relates the vacuum expectation values of the three CP-even neutral scalars, v_1, v_2 and v_S, to the scalar doublet and singlet soft SUSY breaking masses, hence, one expects that these VEVs should all be of order M_{SUSY} and therefore the μ problem is solved.

The addition of a singlet superfield to the MSSM may come along with additional symmetries imposed to the theory. Depending on such symmetries, different models with singlet extensions of the MSSM (xMSSM) have been proposed, see Ref. [319] for a general review. Among the most studied examples are the NMSSM with an additional discrete Z_3 symmetry (first introduced in Ref. [320]), the Nearly-Minimal SUSY SM (nMSSM), with additional discrete Z_5^R, and Z_7^R symmetries [321], and the U(1)$'$-extended MSSM (UMSSM) [322]. A Secluded U(1)$'$-extended MSSM (sMSSM) [323] contains three singlets in addition to the standard UMSSM Higgs boson singlet; this model is equivalent to the nMSSM in the limit that the additional singlet VEV's are large, and the trilinear singlet coupling, λ_S, is small [324].

A singlet extended SUSY Higgs sector opens new avenues for discovery. Since the singlet pseudoscalar particle may be identified as the pseudo-Goldstone boson of a spontaneously broken Peccei–Quinn symmetry, it may become naturally light [325]. Generally, there is mixing of the singlet sector with the MSSM Higgs sector, and for a sufficiently light, singlet-dominated scalar or pseudoscalar, h_S or A_S, respectively, the SM-like Higgs boson h may decay to pairs of h_S or A_S. The light scalar and/or pseudoscalar may subsequently decay to $\tau\tau$ or $b\bar{b}$ pairs. Such cascade decays are more difficult to detect than in standard searches due to the potentially soft decay products. There is also a rich phenomenology for the decays of the heavy CP-even and CP-odd doublets, H and A into two lighter Higgs bosons such as $H \to hh_S$, hh, h_Sh_S or $A \to A_Sh_S$, A_Sh as well as into a light Higgs boson and a gauge boson: $H \to A_SZ$; $A \to h_SZ$, hZ. If kinematically allowed, the heavy Higgs bosons decay into $t\bar{t}$. If the singlet-dominated scalar or pseudoscalar are somewhat heavier, the decays $h_S \to WW$ or $A_S \to h_SZ$ will be allowed.

In addition, the light singlet scenario in the NMSSM or nMSSM is typically associated with a light singlino-dominated neutralino. The recently discovered SM-like Higgs boson can then decay to pairs of this neutralino [326], opening an invisible decay mode that is not excluded by present data. All of the Higgs bosons can decay into electroweakinos depending on kinematics and on the singlino or Higgsino composition of the electroweakinos.

In models with extended singlets, at low $\tan\beta$, it is possible to trade the requirement of a large stop mixing by a sizeable trilinear Higgs-singlet Higgs coupling λ_S, rendering more freedom on the requirements for gluon fusion production. As in the MSSM, mixing in the Higgs sector – additionally triggered by the extra new parameter λ_S – can produce variations in the Higgs–$b\bar{b}$ and Higgs–$\tau^-\tau^+$ couplings that can alter the Higgs to ZZ/WW and to diphoton rates. Light charginos at low $\tan\beta$ can independently contribute to enhance the di-photon rate, without altering any other of the Higgs boson decay rates, see for instance Ref. [327].

There is much activity in exploring the NMSSM phenomenology in the light of the 125 GeV Higgs boson as well as in defining benchmark scenarios with new topologies including Higgs decay chains, see Refs. [44, 328] and references therein. An analytic understanding of the alignment condition in the NMSSM is presented in Ref. [329]. The NMSSM with a Higgs boson of mass 125 GeV can be compatible with stop masses of order of the electroweak/TeV scale, thereby reducing the degree of fine tuning necessary to achieve electroweak symmetry breaking. Interestingly, the alignment conditions point toward a more natural region of parameter space for electroweak symmetry breaking, while allowing for perturbativity of the theory up to the Planck scale and yielding a rich and interesting Higgs boson phenomenology at the LHC.

11.7.3 *Supersymmetry with extended gauge sectors*

In the MSSM, the tree-level value of the lightest CP-even Higgs boson mass originates from the D-term dependence of the scalar potential that comes from the SUSY kinetic terms in the Kähler potential. The D-terms lead to tree-level quartic couplings which are governed by the squares of the gauge couplings of the weak interactions, under which the Higgs boson has non-trivial charges. Hence, the lightest Higgs mass is bounded to be smaller than M_Z. In the presence of new gauge interactions at the TeV scale, and if the Higgs fields had non-trivial charges under them, new D-term contributions would lead to an enhancement of the tree-level Higgs boson mass value. Since the low energy gauge interactions reduce to the known $\mathrm{SU}(3)_c \times \mathrm{SU}(2)_L \times \mathrm{U}(1)_Y$ ones, in order for this mechanism to work, the extended gauge and Higgs sectors should be integrated out in a non-SUSY way. This means that there must be SUSY breaking terms that are of the order of, or larger than, the new gauge boson masses. The tree-level quartic couplings would then be enhanced through their dependence on the square of the gauge couplings of the extended Higgs sector. This effect will be suppressed when the heavy gauge boson masses are larger than the SUSY breaking scale and will acquire its full

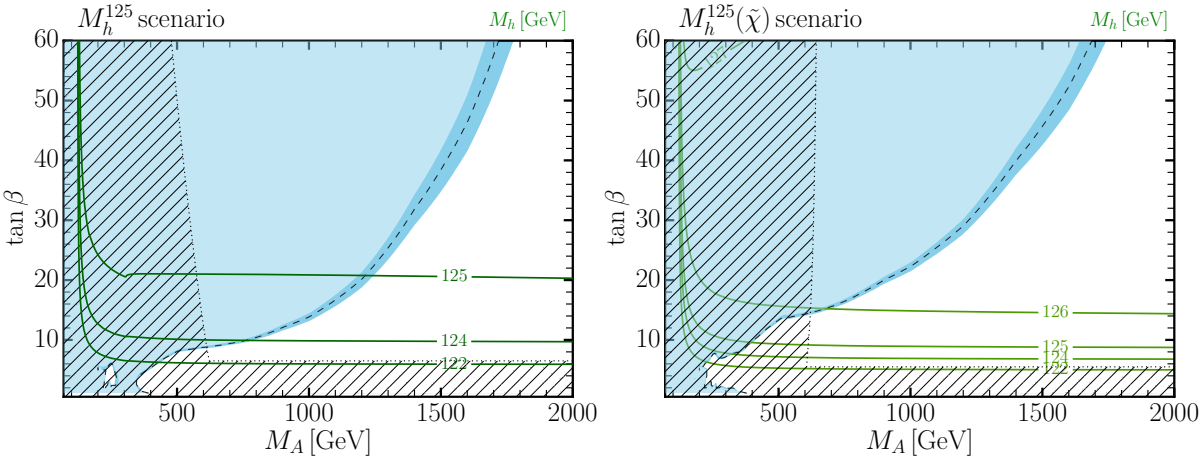

Figure 11.18: The 95% CL exclusion contours in the $(M_A, \tan\beta)$ parameter space for the M_h^{125} (right) and $M_h^{125}(\tilde{\chi})$(left) benchmark scenarios. The nearly vertical dotted line illustrated the lower limit on the mass of the A boson and the close-to horizontal dotted line represents the limit on $\tan\beta$ from the compatibility of the measured mass of the observed Higgs boson and the prediction using radiative corrections (mostly from the stop sector).

potential only for large values of this scale.

One of the simplest possibilities is to extend the weak interactions to a $\mathrm{SU}(2)_1 \times \mathrm{SU}(2)_2$ sector, such that the known weak interactions are obtained after the spontaneous breaking of these groups to $\mathrm{SU}(2)_L$ [330]. This example is briefly summarized in the previous editions of this review [123]. Assuming SUSY breaking terms of the order of the new gauge boson masses, enhancements of order 50% of the MSSM D-term contribution to the Higgs boson mass may be obtained. Such enhancements are sufficient to obtain the measured Higgs mass value without the need for very heavy stops or large stop mixing parameters. This gauge extension leads to new, heavy gauge and Higgs bosons, as well as new neutralinos and charginos, that depending on the region of parameter space can induce novel phenomenology at the LHC. Gauge extensions including new abelian gauge groups have also been considered.

Gauge extensions of the MSSM can also lead to an enhancement of the Higgs boson mass value by modifying the renormalisation group evolution of the Higgs quartic coupling to low energies. In the MSSM, the evolution of the quartic coupling is governed by the top-quark Yukawa interactions and depends on the fourth power of the top-quark Yukawa coupling. The neutralino and chargino contributions, which depend on the fourth power of the weak gauge couplings, are small due to the smallness of these couplings. Depending on the values of the soft SUSY breaking parameters in the gaugino and Higgsino sectors, the $\mathrm{SU}(2)_1$ gauginos may become light, with masses of the order of the weak scale. Since the $\mathrm{SU}(2)_1$ coupling may be significantly larger than the $\mathrm{SU}(2)_L$ one, for small values of the Higgsino mass parameter μ, the associated charginos and neutralinos may modify the evolution of the quartic coupling in a significant way [331]. This may lead to a significant increase of the lightest CP-even Higgs boson mass, even for small values of $\tan\beta \simeq 1$ for which the D-term contributions become small. Radiative corrections should be properly taken into account in this scenario as they might modify the tree-level result.

11.7.4 *Effects of CP violation*

SUSY scenarios with CP-violation (CPV) phases are theoretically appealing, since additional CPV beyond that observed in the K, D, and B meson systems is required to explain the observed cosmic matter-antimatter asymmetry. In the MSSM, CP-violation effects in the Higgs sector appear at the quantum level, while in singlet extensions of the MSSM CP-violation effects can already be effective at tree level. In general, CP-violation effects in the Higgs sector have significant constraints from electric dipole moments data [332].

In the MSSM, the gaugino mass parameters ($M_{1,2,3}$), the Higgsino mass parameter, μ, the bilinear Higgs squared-mass parameter, m_{12}^2, and the trilinear couplings of the squark and slepton fields to the Higgs fields, A_f, may carry non-trivial phases. The two parameter combinations $\arg[\mu A_f (m_{12}^2)^*]$ and $\arg[\mu M_i (m_{12}^2)^*]$ are invariant under phase redefinitions of the MSSM fields [333, 334]. Therefore, if one of these quantities is non-zero, there would be new sources of CP-violation affecting the Higgs sector through radiative corrections, see Ref. [335] and references therein. The mixing of the neutral CP-odd and CP-even Higgs boson states is no longer forbidden. Hence, m_A is no longer a physical parameter. However, the charged Higgs boson mass $m_{H^\pm}$ is still physical and can be used as an input for the computation of the neutral Higgs boson spectrum of the theory. For large values of $m_{H^\pm}$, corresponding to the decoupling limit, the properties of the lightest neutral Higgs boson state approach those of the SM Higgs boson. In particular, the upper bound on the lightest neutral Higgs boson mass takes the same value as in the CP-conserving case [334]. Nevertheless, there still can be significant mixing between the two heavier neutral mass eigenstates. For a detailed study of the Higgs boson mass spectrum and parametric dependence of the associated radiative corrections, see Ref. [335] and references therein.

Major variations to the Higgs boson phenomenology occur in the presence of explicit CPV phases. In the CPV case, vector boson pairs couple to all three neutral Higgs boson mass eigenstates, H_i $(i = 1, 2, 3)$, with couplings

$$\begin{aligned} g_{H_i VV} &= \cos\beta\, \mathcal{O}_{1i} + \sin\beta\, \mathcal{O}_{2i}\,, \\ g_{H_i H_j Z} &= \mathcal{O}_{3i}\, (\cos\beta\, \mathcal{O}_{2j} - \sin\beta\, \mathcal{O}_{1j}) \\ &\quad - \mathcal{O}_{3j}\, (\cos\beta\, \mathcal{O}_{2i} - \sin\beta\, \mathcal{O}_{1i})\,, \end{aligned} \tag{11.53}$$

where the $g_{H_i VV}$ couplings are normalised to the analogous SM coupling and the $g_{H_i H_j Z}$ have been normalised to $g_Z^{\mathrm{SM}}/2$. The orthogonal matrix $\mathcal{O}_{ij}$, only defined in the $p^2 \to 0$ limit, is relating the weak eigenstates to the mass eigenstates. It has non-zero off-diagonal entries mixing the CP-even and CP-odd components of the weak eigenstates. Moreover, CPV phases imply that all neutral Higgs bosons can couple to both scalar and pseudoscalar fermion bilinear densities. The couplings of the mass eigenstates H_i to fermions depend on the loop-corrected fermion Yukawa couplings (similarly to the CP conserving (CPC) case), on $\tan\beta$ and on $\mathcal{O}_{ji}$ [336].

The production processes of neutral MSSM Higgs bosons in the CPV scenario are similar to those in the CPC scenario. Regarding the decay properties, the lightest mass eigenstate, H_1, predominantly decays to $b\bar{b}$ if kinematically allowed, with a smaller fraction decaying to $\tau^+\tau^-$. If kinematically allowed, a SM-like neutral Higgs boson, H_2 or H_3 can decay predominantly to $H_1 H_1$ leading to many new interesting signals both at lepton and hadron colliders; otherwise it will decay preferentially to $b\bar{b}$.

The discovery of a 125 GeV Higgs boson has put strong constraints on the realisation of the CPV scenario within the MSSM. This is partly due to the fact that the observed Higgs boson rates are close to the SM values, and a large CP-violating component would necessarily induce a large variation in the rate of the SM-like Higgs boson decays into the weak gauge bosons $W^{\pm}$ and Z. The measured Higgs mass imposes additional constraints on the realisation of this scenario. Once all effects are considered, the CP-odd Higgs boson A component of the lightest Higgs boson tends to be smaller than about 10% [337]. This restriction can be alleviated in the NMSSM or more general two Higgs doublet models. CP-violating effects can still be significant in the heavy Higgs sector. For instance, the Higgs bosons H_2 and H_3 may be admixtures of CP-even and CP-odd scalars, and therefore both may be able to decay into pairs of weak gauge bosons. The observation of such decays would be a clear signal of CP-violation. In the MSSM, the proximity of the masses of H_2 and H_3 makes the measurement of such effect quite challenging, but in generic two Higgs doublet models, the mass splitting between the two heavy mass eigenstates may become larger, facilitating the detection of CP-violating effects at collider experiments [338].

11.7.5 *Non-supersymmetric extensions of the Higgs sector*

There are many ways to extend the minimal Higgs sector of the SM. In the preceding sections the phenomenology of SUSY Higgs sectors is considered, which at tree level implies a constrained type-II 2HDM (with restrictions on the Higgs boson masses and couplings). In the following discussion, more generic 2HDM's are presented (for some comprehensive reviews, see Ref. [339]). These models are theoretically less compelling since they do not provide an explanation for the SM Higgs naturalness problem, but can lead to different patterns of Higgs-fermion couplings, hence, to different phenomenology. It is also possible to consider models with a SM Higgs boson and one or more additional scalar SU(2) doublets that acquire no VEV and hence play no role in the EWSB mechanism. Such models are dubbed Inert Higgs Doublet Models (IHD) [340]. Without a VEV associated to it, a Higgs boson from an inert doublet has no tree-level coupling to gauge bosons and hence cannot decay into a pair of them. Moreover, imposing a Z_2 symmetry that prevents them from coupling to the fermions, it follows that, if the lightest inert Higgs boson is neutral, it becomes a good DM candidate with interesting associated collider signals. Various studies of IHD models in the light of a 125 GeV Higgs boson have been performed, see for instance Ref. [341], showing an interesting interplay between collider and direct DM detection signals.

An interesting type of 2HDMs are those in which an abelian flavour symmetry broken at the electroweak scales creates the fermion mass hierarchies and mixing angles [17]. This idea is based on the Froggatt–Nielsen model [342], where a flavon field couples differently to the SM fermions of different flavour charges. Such flavon acquires a vacuum expectation value, breaking the flavour symmetry but leaving both the flavour breaking and the new physics scales undetermined. In Refs. [343], it was proposed to relate the flavour breaking scale to the electroweak scale by identifying the flavon with the modulus square of the Higgs field. A 2HDM, however, provides a more compelling realisation of the electroweak scale flavour breaking idea. In the most ambitious constructions of two Higgs doublet flavour models (2HDFM), the textures of the Yukawa couplings are a result of an abelian flavour symmetry that only allows renormalisable Yukawa couplings of the top quark to the Higgs bosons. All other Yukawa couplings are generated by higher dimensional operators that produce hierarchical entries of the Yukawa matrices, explaining the observed quark masses and mixing angles. Flavour observables, LHC Higgs signal strength measurements, electroweak precision measurements, unitarity and perturbativity bounds, as well as collider searches for new scalar resonances result in precise predictions for the parameters of these 2HDFMs. In particular, correlated departures from SM Higgs boson couplings, as well as additional Higgs bosons with masses < 700 GeV must be observed at the LHC. Other incarnations of 2HDFMs can aim at only partially explaining the fermion mass hierarchies but are therefore less restrictive.

Other extensions of the Higgs sector can include multiple copies of $\mathrm{SU}(2)_L$ doublets [344], additional Higgs singlets [345], triplets or more complicated combinations of Higgs multiplets. It is also possible to enlarge the gauge symmetry beyond $\mathrm{SU}(2)_L \times \mathrm{U}(1)_Y$ along with the necessary Higgs field structure to generate gauge boson and fermion masses. There are two main experimental constraints on these extensions: (i) precision measurements which constrain $\rho = m_W^2/(m_Z^2 \cos^2\theta_W)$ to be very close to 1 and (ii) flavour changing neutral current (FCNC) effects. In electroweak models based on the SM gauge group, the tree-level value of ρ is determined by the Higgs multiplet structure. By suitable choices for the hypercharges, and in some cases the mass splitting between the charged and neutral Higgs sector or the vacuum expectation values of the Higgs fields, it is possible to obtain a richer combination of singlets, doublets, triplets and higher multiplets compatible with precision measurements. Concerning the constraints coming from FCNC effects, the Glashow–Weinberg (GW) criterion [346] states that, in the presence of multiple Higgs doublets, the tree-level FCNC's mediated by neutral Higgs bosons will be absent if all fermions of a given electric charge couple to no more than one Higgs doublet. An alternative way of suppressing FCNC in a two Higgs doublet model has been considered in Ref. [347], where it is shown that it is possible to have tree level FCNC completely fixed by the CKM matrix, as a result of an abelian symmetry.

11.7.5.1 *Two-Higgs-doublet models*

General two Higgs doublet models [339] can have a more diverse Higgs-fermion coupling structure than in SUSY, and can be viewed as a simple extension of the SM to realise the spontaneous breakdown of $\mathrm{SU}(2)_L \times \mathrm{U}(1)_Y$ to $\mathrm{U}(1)_{\mathrm{em}}$. Quite generally, if the two Higgs doublets contain opposite hypercharges, the scalar potential will contain mixing mass parameters of the kind $m_{12}^2 \Phi_1^T i\sigma_2 \Phi_2 + h.c.$. In the presence of such terms, both Higgs doublets will acquire vacuum expectation values, $v_1/\sqrt{2}$ and $v_2/\sqrt{2}$, respectively, and the gauge boson masses will keep their SM expressions with the Higgs VEV v replaced by $\sqrt{v_1^2 + v_2^2}$. Apart from the mass terms, the most generic renormalisable and gauge invariant scalar potential for two Higgs doublets with opposite hypercharges contains seven quartic couplings, as presented in Eq. (11.46).

Just as in the MSSM case, after electroweak symmetry breaking and in the absence of CP-violation, the physical spectrum contains a pair of charged Higgs bosons $H^{\pm}$, a CP-odd Higgs boson A and two neutral CP-even Higgs bosons, h and H. The angles α and β diagonalise the CP-even, and the CP-odd and charged Higgs sectors, respectively. The complete 2HDM is defined only after considering the interactions of the Higgs fields to fermions. Yukawa couplings of the generic form

$$- h_{ij}^a \bar{\Psi}_L^i H_a \Psi_R^j + h.c. \tag{11.54}$$

may be added to the renormalisable Lagrangian of the theory. Contrary to the SM, the two Higgs doublet structure does not ensure the alignment of the fermion mass terms $m_{ij} = h_{ij}^a v_a/\sqrt{2}$ with the Yukawa couplings h_{ij}^a. This implies that quite generally the neutral Higgs boson will mediate flavour changing interactions between the different mass eigenstates of the fermion fields. Such flavour changing interactions should be suppressed in order to describe properly the Kaon, D and B meson phenomenology. Based on the Glashow–Weinberg criterion, it is clear that the simplest way of avoiding such transitions is to assume the existence of a symmetry that ensures the couplings of the fermions of each given quantum number (up-type and down-type quarks, charged and neutral leptons) to only one of the two Higgs doublets. Different models may be defined depending on which of these fermion fields couple to a given Higgs boson, see Table 11.13. Models of type-I are those in which all SM fermions couple to a single Higgs field. In type-II models, down-type quarks and charged leptons couple to a common Higgs field, while the up-type quarks and neutral leptons couple to the other. In models of type-III (lepton-specific), quarks couple to one of the Higgs bosons, while leptons couple to the other. Finally, in models of type-IV (flipped), up-type quarks and charged leptons couple to one of the Higgs fields while down-quarks and neutral leptons couple to the other.

Table 11.13: Higgs boson couplings to up, down and charged lepton-type $SU(2)_L$ singlet fermions in the four discrete types of 2HDM models that satisfy the Glashow–Weinberg criterion.

Model	2HDM I	2HDM II	2HDM III	2HDM IV
u	Φ_2	Φ_2	Φ_2	Φ_2
d	Φ_2	Φ_1	Φ_2	Φ_1
e	Φ_2	Φ_1	Φ_1	Φ_2

The two Higgs doublet model phenomenology depends strongly on the size of the mixing angle α and therefore on the quartic couplings. For large values of m_A, $\sin\alpha \to -\cos\beta$, $\cos\alpha \to \sin\beta$, $\cos(\beta-\alpha) \to 0$, and the lightest CP-even Higgs boson h behaves as the SM Higgs boson. The same behaviour is obtained if the quartic couplings are such that $\mathcal{M}^2_{12}\sin\beta = -(\mathcal{M}^2_{11} - m^2_h)\cos\beta$. The latter condition represents a situation in which the couplings of h to fermions and weak gauge bosons become the same as in the SM, without decoupling the rest of the non-standard scalars and it is of particular interest due to the fact that the discovered Higgs boson has SM-like properties. This situation will be referred to as alignment, as in the MSSM case.

In analogy to the effects of CP violation in the SUSY 2HDM, some parameters of the Higgs potential can be complex and one has a model that is explicitly CP violating. The three neutral mass eigenstates mixed with each other and the Higgs phenomenology is analogous to the one described for the SUSY case above, with the caveat that when considering the neutral Higgs boson couplings to the scalar and pseudoscalar fermion bilinear densities, the proper weight should be considered for the respective 2HDM's.

In type-II Higgs doublet models, at large values of $\tan\beta$ and moderate values of m_A, the non-standard Higgs bosons H, A and $H^\pm$ couple strongly to bottom quarks and τ leptons. Hence the decay modes of the non-standard Higgs bosons tend to be dominated by the b-quark and τ-lepton modes, including top quarks or neutrinos in the case of the charged Higgs boson. However, for large and negative values of λ_4, the charged Higgs boson mass may be sufficiently heavy to allow on-shell decays $H^\pm \to W^\pm + (H, A)$, via a trilinear coupling

$$g_{H^\pm W^\mp H,A} \simeq \frac{M_W}{v}\sin(\beta-\alpha)(p_{H^+} - p_{H,A})\,, \quad (11.55)$$

where p_{H^+} and $p_{H,A}$ are the charged and neutral scalar Higgs boson momenta pointing into the vertex. On the other hand, for large and positive values of λ_5, the above charged Higgs boson decay into a $W^\pm$ and the CP-odd Higgs boson may be allowed, but the heavy Higgs boson H may be sufficiently heavy to decay into a CP-odd Higgs boson and an on-shell Z, $H \to Z + A$, via

$$g_{HZA} \simeq \frac{M_Z}{v}\sin(\beta-\alpha)(p_H - p_A). \quad (11.56)$$

The decay $H^\pm \to W^\pm + H$, on the other hand may be allowed only if $\lambda_4 < -\lambda_5$. The couplings controlling all the above decay modes are proportional to $\sin(\beta-\alpha)$ and therefore they are unsuppressed in the alignment limit. Moreover, these could still be the dominant decay modes at moderate values of $\tan\beta$, offering a way to evade the current bounds obtained assuming a dominant decay into b-quarks or τ-leptons.

The quartic couplings are restricted by the condition of stability of the effective potential as well as by the restriction of obtaining the proper value of the lightest CP-even Higgs boson mass. Close to the alignment limit, the lightest CP-even Higgs boson mass becomes approximately independent of m_A and is given by

$$\begin{aligned} m^2_h \simeq\; & v^2(\lambda_1\cos^4\beta + \lambda_2\sin^4\beta + 2\tilde{\lambda}_3 v^2\cos^2\beta\sin^2\beta \\ & + 4\lambda_6\cos^3\beta\sin\beta + 4\lambda_7\sin^3\beta\cos\beta)\,, \end{aligned} \quad (11.57)$$

where $\tilde{\lambda}_3 = \lambda_3 + \lambda_4 + \lambda_5$.

The stability conditions imply the positiveness of all masses, as well as the avoidance of run-away solutions to large negative values of the fields in the scalar potential. These conditions imply

$$\begin{aligned} & \lambda_1 \geq 0,\;\; \lambda_2 \geq 0,\;\; \lambda_3 + \lambda_4 - |\lambda_5| \geq -\sqrt{\lambda_1\lambda_2},\;\; \lambda_3 \geq -\sqrt{\lambda_1\lambda_2}, \\ & 2|\lambda_6 + \lambda_7| < \frac{\lambda_1+\lambda_2}{2} + \tilde{\lambda}_3, \end{aligned} \quad (11.58)$$

where the first four conditions are necessary and sufficient conditions in the case of $\lambda_6 = \lambda_7 = 0$, while the last one is a necessary condition in the case all couplings are non-zero. Therefore, to obtain the conditions that allow the decays $H^\pm \to W^\pm H, A$ and $H \to ZA$, λ_3 should take large positive values in order to compensate for the effects of λ_4 and λ_5. For more detailed discussions about 2HDM phenomenology, see for example Refs. [44, 339].

11.7.5.2 *Higgs triplets*

Electroweak triplet scalars are the simplest non-doublet extension of the SM that can participate in the spontaneous breakdown of $\mathrm{SU(2)}_L \times \mathrm{U(1)}_Y$ to $\mathrm{U(1)}_{\mathrm{em}}$. Two types of model have been developed in enough detail to make a meaningful comparison to LHC data: the Higgs triplet model (HTM) [348] and the Georgi–Machacek model (GM) [349].

The Higgs triplet model extends the SM by the addition of a complex $\mathrm{SU(2)}_L$ triplet scalar field Δ with hypercharge $Y = 2$, and a general gauge-invariant renormalisable potential $V(\Phi, \Delta)$ for Δ and the SM Higgs doublet Φ. The components of the triplet field can be parameterised as

$$\Delta = \frac{1}{\sqrt{2}}\begin{pmatrix} \Delta^+ & \sqrt{2}\Delta^{++} \\ v_\Delta + \delta + i\xi & -\Delta^+ \end{pmatrix}. \quad (11.59)$$

where Δ^+ is a singly-charged field, Δ^{++} is a doubly-charged field, δ is a neutral CP-even scalar, ξ is a neutral CP-odd scalar, and v_Δ is the triplet VEV. The general scalar potential mixes the doublet and triplet components. After electroweak symmetry breaking there are seven physical mass eigenstates, denoted $H^{\pm\pm}$, $H^\pm$, A, H, and h.

A distinguishing feature of the HTM is that it violates the custodial symmetry of the SM; thus the ρ parameter deviates from 1 even at tree level. Letting x denote the ratio of triplet and doublet VEVs, the tree level expression is

$$\rho = \frac{1+2x^2}{1+4x^2}\,. \quad (11.60)$$

The measured value of the ρ parameter then limits the triplet VEV to be quite small, $x \lesssim 0.03$, or $v_\Delta < 8\,\mathrm{GeV}$. This constraint severely limits the role of the triplet scalar in the EWSB mechanism.

The small VEV of the Higgs triplet in the HTM is a virtue from the point of view of generating neutrino masses without the necessity for introducing right-handed neutrino fields. The gauge invariant dimension four interaction

$$h_{\nu_{ij}}\,\ell_i^T C^{-1} i\sigma_2\,\Delta\,\ell_j\,, \quad (11.61)$$

where ℓ_i are the lepton doublets, C is the charge conjugation matrix, and $h_{\nu_{ij}}$ is a complex symmetric coupling matrix, generates a Majorana mass matrix for the neutrinos:

$$m_{\nu_{ij}} = \sqrt{2}h_{\nu_{ij}}\,v_\Delta\,. \quad (11.62)$$

This can be combined with the usual neutrino seesaw to produce what is known as the type-II seesaw [350].

The HTM suggests the exciting possibility of measuring parameters of the neutrino mass matrix at the LHC. If the doubly-charged Higgs boson is light enough and/or its couplings to W^+W^+ are sufficiently suppressed, then its primary decay is into same-sign lepton pairs: $H^{++} \to \ell_i^+\ell_j^+$; from Eq. (11.61) and Eq. (11.62), it is apparent that these decays are in general lepton-flavor violating with branchings proportional to elements of the neutrino mass matrix [351].

Precision electroweak data constrain the mass spectrum as well as the triplet VEV of the HTM [352]. These constraints favour a spectrum where H^{++} is the lightest of the exotic bosons, and

where the mass difference between H^+ and H^{++} is a few hundred GeV. The favoured triplet VEV is a few GeV, which also favours H^{++} decays into W^+W^+ over same-sign dileptons.

The GM model addresses the ρ parameter constraint directly by building in custodial symmetry. Writing the complex scalar doublet of the SM as a $(2,2)$ under $\mathrm{SU}(2)_L \times \mathrm{SU}(2)_R$, it is obvious that the next simplest construction respecting custodial symmetry is a scalar transforming like a $(3,3)$ [353]. These nine real degrees of freedom correspond to a complex electroweak triplet combined with a real triplet, with the scalar potential required to be invariant under $\mathrm{SU}(2)_R$. Under the custodial $\mathrm{SU}(2)_{L+R}$, they transform as $1 \oplus 3 \oplus 5$, with a CP-even neutral scalar as the custodial singlet (thus matching the SM Higgs boson), a CP-odd neutral scalar in the custodial triplet, and another CP-even neutral scalar in the custodial 5-plet.

The scalar components can be decomposed as

$$\Xi = \begin{pmatrix} \chi_3^* & \xi_1 & \chi_1 \\ -\chi_2^* & \xi_2 & \chi_2 \\ \chi_1^* & -\xi_1^* & \chi_3 \end{pmatrix}, \tag{11.63}$$

where ξ_2 is a real scalar and the others are complex scalars. Linear combinations of these scalars account for the neutral custodial singlet, a neutral and singly-charged field making up the custodial triplet, and neutral, singly-charged, and doubly-charged fields making up the custodial 5-plet.

When combined with the usual SM doublet field Φ, the electroweak scale v is now related to the doublet and triplet VEVs by

$$v^2 = v_\Phi^2 + 8v_\Xi^2 \, . \tag{11.64}$$

Note that the GM triplets by themselves are sufficient to explain electroweak symmetry breaking and the existence of a 125 GeV neutral boson along with a custodial triplet of Goldstone bosons; the complex doublet field in the GM model is required to generate fermion masses via the usual dimension four Yukawa couplings. This raises the question of whether one can rule out the possibility that the 125 GeV boson is the neutral member of a custodial 5-plet rather than a custodial singlet, without invoking decays to fermions. A conclusive answer is given by observing that the ratio of the branching fractions to W versus Z bosons is completely determined by the custodial symmetry properties of the boson. For a custodial 5-plet, the ratio of the signal strength to WW over that to ZZ is predicted to be 1/4 that of a SM Higgs boson [353], and thus already ruled out by the experimental results presented in Section 11.6.

Another interesting general feature of Higgs triplet models is that, after mixing, the SM-like neutral boson can have stronger couplings to WW and ZZ than predicted by the SM [354]; this is in contrast to mixing with additional doublets and singlet, which can only reduce the WW and ZZ couplings versus the SM. This emphasises that LHC Higgs data cannot extract model independent coupling strengths for the Higgs boson [244].

Because of the built-in custodial symmetry, the triplet VEV in the GM model can be large compared to the doublet VEV. The custodial singlet neutral boson from the triplets mixes with the neutral boson from the doublet. Two interesting special cases are (i) the triplet VEV is small and the 125 GeV boson is SM-like except for small deviations, and (ii) the 125 GeV boson is mostly the custodial singlet neutral boson from the electroweak triplets. The phenomenology of the doubly-charged and singly-charged bosons is similar to that of the HTM. The constraints on the GM model from precision electroweak data, LEP data, and current LHC data are summarised in Ref. [44].

11.7.6 *Composite Higgs models*

Within the SM, EWSB is posited but has no dynamical origin. Furthermore, the Higgs boson appears to be unnaturally light. A scenario that remedies these two catches is to consider the Higgs boson as a bound state of new dynamics becoming strong around the weak scale. The Higgs boson can be made significantly lighter than the other resonances of the strong sector if it appears as a pseudo-Nambu–Goldstone boson, see Refs. [11] for reviews.

11.7.6.1 *Little Higgs models*

The idea behind the Little Higgs boson models [355] is to identify the Higgs doublet as a (pseudo) Nambu–Goldstone boson while keeping some sizeable non-derivative interactions, in particular a largish Higgs quartic interaction. By analogy with QCD where the pions $\pi^{\pm,0}$ appear as Nambu–Goldstone bosons associated to the breaking of the chiral symmetry $\mathrm{SU(2)_L} \times \mathrm{SU(2)_R/SU(2)}$, switching on some interactions that break explicitly the global symmetry will generate masses for the would-be massless Nambu–Goldstone bosons of the order of $g\Lambda_{G/H}/(4\pi)$, where g is the coupling of the symmetry breaking interaction and $\Lambda_{G/H} = 4\pi f_{G/H}$ is the dynamical scale of the global symmetry breaking G/H. In the case of the Higgs boson, the top Yukawa interaction or the gauge interactions themselves will certainly break explicitly (part of) the global symmetry since they act non-linearly on the Higgs boson. Therefore, obtaining a Higgs boson mass around 125 GeV would demand a dynamical scale $\Lambda_{G/H}$ of the order of 1 TeV, which is known to lead to too large oblique corrections. Raising the strong dynamical scale by at least one order of magnitude requires an additional selection rule to ensure that a Higgs boson mass is generated at the 2-loop level only

$$m_H^2 = \frac{g^2}{16\pi^2}\Lambda_{G/H}^2 \to m_H^2 = \frac{g_1^2 g_2^2}{(16\pi^2)^2}\Lambda_{G/H}^2. \tag{11.65}$$

The way to enforce this selection rule is through a "collective breaking" of the global symmetry:

$$\mathcal{L} = \mathcal{L}_{G/H} + g_1\mathcal{L}_1 + g_2\mathcal{L}_2. \tag{11.66}$$

Each interaction $\mathcal{L}_1$ or $\mathcal{L}_2$ individually preserves a subset of the global symmetry such that the Higgs boson remains an exact Nambu–Goldstone boson whenever either g_1 or g_2 is vanishing. A mass term for the Higgs boson can be generated only by diagrams involving simultaneously both interactions. At one-loop, such diagrams are not quadratically divergent, so the Higgs boson mass is not UV sensitive. Explicitly, the cancellation of the SM quadratic divergences is achieved by a set of new particles around the Fermi scale: gauge bosons, vector-like quarks, and extra massive scalars, which are related, by the original global symmetry, to the SM particles with the same spin. Contrary to SUSY, the cancellation of the quadratic divergences is achieved by same-spin particles. These new particles, with definite couplings to SM particles as dictated by the global symmetries of the theory, are perfect goals for the LHC.

The simplest incarnation of the collective breaking idea, the so-called littlest Higgs boson model, is based on a non-linear σ-model describing the spontaneous breaking SU(5) down to SO(5). A subgroup $\mathrm{SU(2)_1 \times U(1)_1 \times SU(2)_2 \times U(1)_2}$ is weakly gauged. This model contains a weak doublet, that is identified with the Higgs doublet, and a complex weak triplet whose mass is not protected by collective breaking. Other popular little Higgs models are based on different coset spaces: minimal moose $(\mathrm{SU(3)^2/SU(3)})$, the simplest little Higgs $(\mathrm{SU(3)^2/SU(2)^2})$, the bestest little Higgs $(\mathrm{SO(6)^2/SO(6)})$. For comprehensive reviews, see Ref. [356].

Generically, oblique corrections in Little Higgs models are reduced either by increasing the coupling of one of the gauge groups (in the case of product group models) or by increasing the masses of the W and Z partners, leading ultimately to a fine-tuning of the order of a few percents (see for instance Ref. [357] and references therein). The compatibility of Little Higgs models with experimental data is significantly improved when the global symmetry involves a custodial symmetry as well as a T-parity [358] under which, in analogy with R-parity in SUSY models, the SM particles are even and their partners are odd. Such Little Higgs models would therefore appear in colliders as jet(s) with missing transverse energy [359] and the ATLAS and CMS searches for squarks and gluinos (see "Supersymmetry, Part II" in this review) can be recast to obtain limits on the masses of the heavy vector-like quarks. The T-even top partner, with an expected mass below 1 TeV to cancel the top loop quadratic divergence without too much fine-tuning, would decay dominantly into a $t + Z$ pair or into a $b + W$ pair or even into $t + H$. The latest CMS and ATLAS direct searches [360] for vector-like top partners put a lower bound

around 1.1–1.3 TeV (for various branching fraction combinations), excluding the most natural region of the parameter space of these models, i.e., imposing a fine-tuning below the percent level.

The motivation for Little Higgs models is to solve the little hierarchy problem, i.e., to push the need for new physics (responsible for the stability of the weak scale) up to around 10 TeV. Per se, Little Higgs models are effective theories valid up to their cut-off scale $\Lambda_{G/H}$. Their UV completions could either be weakly or strongly coupled.

11.7.6.2 *Models of partial compositeness*

Even in composite models, the Higgs boson cannot appear as a regular resonance of the strong sector without endangering the viability of the setup when confronted to data. The way out is that the Higgs boson appears as a pseudo Nambu–Goldstone boson: the new strongly coupled sector is supposed to be invariant under a global symmetry G spontaneously broken to a subgroup H at the scale f (the typical mass scale of the resonances of the strong sector is $m_\rho \sim g_\rho f$ with g_ρ the characteristic coupling of the strong sector). To avoid conflict with EW precision measurements, the strong interactions themselves should better not break the EW symmetry. Hence the SM gauge symmetry itself should be contained in H. See Table 11.14 for a few examples of coset spaces.

Table 11.14: Global symmetry breaking patterns and the corresponding Goldstone boson contents of the SM, the minimal composite Higgs model, the next to minimal composite Higgs model, and the minimal composite two Higgs doublet model. Note that the SU(3) model does not have a custodial invariance. a denotes a CP-odd scalar while h and H are CP-even scalars.

Model	Symmetry Pattern	Goldstones
SM	SO(4)/SO(3)	W_L, Z_L
–	SU(3)/SU(2)×U(1)	W_L, Z_L, H
MCHM	SO(5)/SO(4)	W_L, Z_L, H
NMCHM	SO(6)/SO(5)	W_L, Z_L, H, a
MC2HM	SO(6)/SO(4)×SO(2)	$W_L, Z_L, h, H, H^\pm, a$

The SM (light) fermions and gauge bosons cannot be part of the strong sector itself since LEP data have already put stringent bounds on the compositeness scale of these particles far above the TeV scale. The gauge bosons couple to the strong sector by a weak gauging of a SU(2)×U(1) subgroup of the global symmetry G. Inspiration for the construction of such models comes from the AdS/CFT correspondence: the components of a gauge field along an extra warped space dimension can be interpreted as the Goldstone bosons resulting from the breaking of global symmetry of the strong sector. The couplings of the SM fermions to the strong sector could a priori take two different forms:

(i) a bilinear coupling of two SM fermions to a composite scalar operator, $\mathcal{O}$, of the form $\mathcal{L} = y\,\bar{q}_L u_R \mathcal{O} + h.c.$, in simple analogy with the SM Yukawa interactions. This is the way fermion masses were introduced in technicolor theories and it generically comes with severe flavour problems and calls for extended model-building gymnastics [12] to circumvent them;

(ii) a linear mass mixing with fermionic vector-like operators: $\mathcal{L} = \lambda_L\,\bar{q}_L \mathcal{Q}_R + \lambda_R \bar{\mathcal{U}}_L u_R$. $\mathcal{Q}$ and $\mathcal{U}$ are two fermionic composite operators of mass M_Q and M_U.

Being part of the composite sector, the composite fermionic operators can have a direct coupling of generic order Y_* to the Higgs boson. In analogy with the photon-ρ mixing in QCD, once the linear mixings are diagonalised, the physical states are a linear combination of elementary and composite fields. Effective Yukawa couplings are generated and read for instance for the up-type quark

$$y = Y_* \sin\theta_L \sin\theta_R \tag{11.67}$$

where $\sin\theta_i = \lambda_i/\sqrt{M_{Q,U}^2 + \lambda_i^2}$, $i = L, R$, measure the amount of compositeness of the SM left- and right-handed up-type quark. If the strong sector is flavour-anarchic, i.e., if the couplings of the Higgs boson to the composite fermions does not exhibit any particular flavour structure, the relation Eq. (11.67) implies that the light fermions are mostly elementary states ($\sin\theta_i \ll 1$), while the third generation quarks need to have a sizable degree of compositeness. The partial compositeness paradigm offers an appealing dynamical explanation of the hierarchies in the fermion masses. In fact, assuming the strong sector to be almost conformal above the confinement scale, the low-energy values of the mass-mixing parameters $\lambda_{L,R}$ are determined by the (constant) anomalous dimension of the composite operator they mix with. If the UV scale at which the linear mixings are generated is large, then $\mathcal{O}(1)$ differences in the anomalous dimensions can generate naturally large hierarchies in the fermion masses via renormalisation group running [361]. While the introduction of partial compositeness greatly ameliorated the flavor problem of the original composite Higgs models, nevertheless, it did not solve the issue completely, at least in the case where the strong sector is assumed to be flavour-anarchic [362]. While the partial compositeness set-up naturally emerges in models built in space-times with extra dimensions, no fully realistic microscopic realisation of partial compositeness has been proposed in the literature.

Another nice aspect of the partial compositeness structure is the dynamical generation of the Higgs potential that is not arbitrary like in the SM. The Higgs boson being a pseudo-Nambu–Goldstone boson, its mass does not receive any contribution from the strong sector itself but it is generated at the one-loop level via the couplings of the SM particles to the strong sector since these interactions are breaking the global symmetries under which the Higgs doublet transforms non-linearly. Obtaining $v \ll f$, as required phenomenologically, requires some degree of tuning, which scales like $\xi \equiv v^2/f^2$. A mild tuning of the order of 10% ($\xi \approx 0.1$) is typically enough to comply with electroweak precision constraints. This is an important point: in partial compositeness models, the entire Higgs potential is generated at one loop, therefore the separation between v and f can only be obtained at a price of a tuning. This marks a difference with respect to the Little Higgs models which realise a parametric hierarchy between the quartic and mass terms through the collective symmetry breaking mechanism. In fact in Little Higgs models, the quartic coupling is a tree-level effect, leading to a potential

$$V(H) \approx \frac{g_{\rm SM}^2}{16\pi^2} m_\rho^2 H^2 + g_{\rm SM}^2 H^4, \tag{11.68}$$

where $g_{\rm SM}$ generically denotes the SM couplings. The minimisation condition reads $v^2/f^2 \sim g_\rho^2/(16\pi^2)$, therefore v is formally loop suppressed with respect to f. This is the major achievement of the Little Higgs constructions, which however comes at the price of the presence of sub-TeV vectors carrying EW quantum numbers and therefore giving rise generically to large oblique corrections to the propagators of the W and the Z gauge bosons.

After minimisation, the dynamically generated potential leads to an estimate of the Higgs boson mass as

$$m_H^2 \approx g_\rho^3\, y_t 2\pi^2 v^2. \tag{11.69}$$

It follows that the limit $f \to \infty$, i.e., $\xi \to 0$, is a true decoupling limit: all the resonances of the strong sector become heavy but the Higgs boson whose mass is protected by the symmetries of the coset G/H. When compared to the experimentally measured Higgs boson mass, this estimate puts an upper bound on the strength of the strong interactions: $g_\rho \lesssim 2$. In this limit of not so large coupling, the Higgs potential receives additional contributions. In particular, the fermionic resonances in the top sector which follow from the global symmetry structure of the new physics sector can help raising the Higgs boson mass. Using some dispersion relation techniques, the mass of the Higgs is connected to the resonance masses. In the minimal SO(5)/SO(4) model, it was shown [363] that a 125 GeV mass can be obtained if at least one of the fermionic resonances is lighter than $\sim 1.4\,f$. As in SUSY scenarios, the top sector is playing a crucial role in the dynamics of EWSB and can provide the first direct signs of new physics. The direct searches for these top partners, in particular

the ones with exotic electric charges 5/3, are already exploring the natural parameter spaces of these models [364].

The main physics properties of a pseudo Nambu–Goldstone Higgs boson can be captured in a model-independent way by a small number of higher-dimensional operators. Indeed, the strong dynamics at the origin of the composite Higgs boson singles out a few operators among the complete list discussed earlier in Section 11.6: these are the operators that involve extra powers of the Higgs doublets and they are therefore generically suppressed by a factor $1/f^2$ as opposed to the operators that involve extra derivatives or gauge bosons that are suppressed by a factor $1/(g_\rho^2 f^2)$. The relevant effective Lagrangian describing a strongly interacting light Higgs boson is:

$$\mathcal{L}_{\rm SILH} = \frac{c_H}{2f^2}\left(\partial_\mu\left(\Phi^\dagger\Phi\right)\right)^2 + \frac{c_T}{2f^2}\left(\Phi^\dagger \overleftrightarrow{D}^\mu \Phi\right)^2 - \frac{c_6\lambda}{f^2}\left(\Phi^\dagger\Phi\right)^3 + \left(\sum_f \frac{c_f\, y_f}{f^2}\Phi^\dagger\Phi\bar{f}_L\Phi f_R + \text{h.c.}\right). \tag{11.70}$$

Typically, these new interactions induce deviations in the Higgs boson couplings that scale like $\mathcal{O}(v^2/f^2)$. Hence the measurements of the Higgs boson couplings can be translated into some constraints on the compositeness scale, $4\pi f$, of the Higgs boson. The peculiarity of these composite models is that, due to the Goldstone nature of the Higgs boson, the direct couplings to photons and gluons are further suppressed and generically the coupling modifiers scale like

$$\kappa_{W,Z,f} \sim 1 + \mathcal{O}\left(\frac{v^2}{f^2}\right), \quad \kappa_{Z\gamma} \sim \mathcal{O}\left(\frac{v^2}{f^2}\right), \quad \kappa_{\gamma,g} \sim \mathcal{O}\left(\frac{v^2}{f^2}\times\frac{y_t^2}{g_\rho^2}\right), \tag{11.71}$$

where g_ρ denotes the typical coupling strength among the states of the strongly coupled sector and y_t is the top Yukawa coupling, the largest interaction that breaks the Goldstone symmetry. The $\kappa_{Z\gamma,\gamma,g}$ coupling modifiers are not generated by the strong coupling operators of Eq. (11.70) but by some subleading form-factor operator generated by loops of heavy resonances of the strong sector. The coupling modifiers also receive additional contributions from the other resonances of the strong sector, in particular the fermionic resonances of the top sector that are required to be light to generate a 125 GeV Higgs boson mass. Some indirect information on the resonance spectrum could thus be inferred by a precise measurement of the Higgs boson coupling deviations. However, it was realised, see in particular Ref. [266], that the task is actually complicated by the fact that, in the minimal models, these top partners give a contribution to both κ_t (resulting from a modification of the top Yukawa coupling) and κ_γ and κ_g (resulting from new heavy particles running into the loops) and the structure of interactions is such that the net effect vanishes for inclusive quantities like $\sigma(gg \to H)$ or $\Gamma(H \to \gamma\gamma)$ as a consequence of the Higgs low energy theorem [23, 24, 264]. So, one would need to rely on differential distribution, like the Higgs boson p_T distribution discussed in Section 11.2.4.1, to *see* the top partner effects in Higgs data [365]. The off-shell channel $gg \to H^* \to 4\ell$ [243] and the double Higgs boson production $gg \to HH$ [366] can also help to resolve the gluon loop and separate the top and top-partner contributions.

11.7.6.3 *Minimal composite Higgs models*

The minimal composite Higgs models (MCHM) are concrete examples of the partial compositeness paradigm. The Higgs doublet is described by the coset space SO(5)/SO(4) where a subgroup $\mathrm{SU}(2)_L\times\mathrm{U}(1)_Y$ is weakly gauged and under which the four Goldstone bosons transform as a doublet of hypercharge 1. There is some freedom on how the global symmetry is acting on the SM fermions: in MCHM4 the quarks and leptons are embedded into spinorial representations of SO(5), while in MHCM5 they are part of fundamental representations (it might also be interesting phenomenologically to consider larger representations like MCHM14 [367] with the SM fermions inside a representation of dimension 14). It is also possible to consider that fermions of different chirality and flavour are in different representations of SO(5), leading to a more varied phenomenology [368]. The non-linearly realised symmetry acting on the Goldstone bosons leads to general predictions of the coupling of the Higgs boson to the EW gauge bosons. For instance, it can be shown that the quadratic terms in the W and Z bosons read

$$m_W^2(H)\left(W_\mu W^\mu + \frac{1}{2\cos^2\theta_W}Z_\mu Z^\mu\right), \tag{11.72}$$

with $m_W(H) = \frac{gf}{2}\sin\frac{H}{f}$. Expanding around the EW vacuum, the expression of the weak scale is $v = f\sin(\langle H\rangle/f)$. And the values of the modified Higgs boson couplings to the W and Z become:

$$g_{HVV} = \frac{2m_V^2}{v}\sqrt{1-v^2/f^2}\,, \quad g_{HHVV} = \frac{2m_V^2}{v^2}(1-2v^2/f^2)\,. \tag{11.73}$$

Note that the Higgs boson couplings to gauge bosons is always suppressed compared to the SM prediction. This is a general result [369] that holds as long as the coset space is compact.

The Higgs boson couplings to the fermions depend on the representation which the SM fermions are embedded into. The most commonly used embeddings consider all fermion doublets and singlets in the same representations. While, in MCHM4 and MCHM5, the modifications of the couplings depend only on the Higgs boson compositeness scale, in MCHM14 the leading corrections depend also on the mass spectrum of the resonances [367]. This is due to the fact that more than one SO(5) invariant gives rise to SM fermion masses. The (κ_V, κ_f) experimental fit of the Higgs boson couplings can be used to derive a lower bound on the Higgs boson compositeness scale $4\pi f \gtrsim 9$ TeV, which is less stringent than the indirect bound obtained from EW precision data, $4\pi f \gtrsim 15$ TeV [370] but more robust and less subject on assumptions [371].

11.7.6.4 *Twin Higgs models*

In all composite models presented above, the particles responsible for canceling the quadratic divergences in the Higgs boson mass are charged under the SM gauge symmetries. In particular, the top partner carries color charge, implying a reasonably large minimal production cross section at the LHC. An alternative scenario, which is experimentally quite challenging and might explain the null result in various new physics searches, is the case nowadays referred to as "neutral naturalness" [13, 14], where the particles canceling the 1-loop quadratic divergences are neutral under the SM. The canonical example for such theories is the Twin Higgs model of Ref. [13]. This is an example of a pseudo-Goldstone boson model with an approximate global SU(4) symmetry broken to SU(3). The Twin Higgs model is obtained by gauging the $\mathrm{SU}(2)_A\times\mathrm{SU}(2)_B$ subgroup of SU(4), where $\mathrm{SU}(2)_A$ is identified with the SM $\mathrm{SU}(2)_L$, while $\mathrm{SU}(2)_B$ is the twin SU(2) group. Gauging this subgroup breaks the SU(4) symmetry explicitly, but quadratically divergent corrections do not involve the Higgs boson when the gauge couplings of the two SU(2) subgroups are equal, $g_A = g_B$. The SU(4)$\to$ SU(3) breaking will also result in the breaking of the twin $\mathrm{SU}(2)_B$ group and, as a result, three of the seven Goldstone bosons will be eaten, leaving 4 Goldstone bosons corresponding to the SM Higgs doublet. In fact, imposing the Z_2 symmetry on the full model will ensure the cancellation of all 1-loop quadratic divergences to the Higgs boson mass. Logarithmically divergent terms can, however, arise for example from gauge loops, leading to a Higgs boson mass of order $g^2 f/4\pi$, which is of the order of the physical Higgs boson mass for $f \sim 1$ TeV. The quadratic divergences from the top sector can be eliminated if the Z_2 protecting the Higgs boson mass remains unbroken by the couplings that result in the top Yukawa coupling. This can be achieved by introducing top partners charged under a twin $\mathrm{SU}(3)_C$. In this case, the quadratic divergences are cancelled by top partners that are neutral under the SM gauge symmetries.

Twin Higgs models are low-energy effective theories valid up to a cutoff scale of order $\Lambda \sim 4\pi f \sim 5$–10 TeV, beyond which a UV

completion has to be specified. The simplest such possibility is to also make the Higgs boson composite, and to UV complete the twin Higgs model via gauge and top partners at masses of the order of a few TeV. A concrete implementation is the holographic twin Higgs model [372], which also incorporates a custodial symmetry to protect the T-parameter from large corrections. It is based on a warped extra dimensional theory with a bulk SO(8) gauge group, which incorporates the SU(4) global symmetry discussed above enlarged to contain the $SU(2)_L \times SU(2)_R$ custodial symmetry. In addition the bulk contains either a full SU(7) group or an $SU(3) \times SU(3) \times U(1) \times U(1) \times Z_2$ subgroup of it to incorporate the QCD, its twin, and the hypercharge local symmetries. The breaking on the UV brane is to the SM symmetries and their twin symmetries, while on the IR brane SO(8) $\rightarrow$ SO(7), giving rise to the 7 Goldstone bosons, three of which will be again eaten by the twin W, Z. The main difference compared to ordinary composite Higgs models is that, in composite twin Higgs models, the cancellation of the one-loop quadratic divergences is achieved by the twin partners. They have a mass of order 700 GeV–1 TeV and they are uncharged under the SM gauge group. This allows the IR scale of the warped extra dimension to be raised to the multi-TeV range without reintroducing the hierarchy problem. The role of the composite partners is to UV complete the theory, rather than to cancel the one-loop quadratic divergences. For more details about the composite twin Higgs models, see Refs. [373].

11.7.7 *Searches for signatures of extended Higgs sectors*

The measurements described in Sections 11.3 to 11.6 have established the existence of one state of the electroweak symmetry breaking sector, compatible with a SM Higgs boson, but not that it is the only one. As was discussed above, several classes of models beyond the SM require extended Higgs sectors. The searches are typically designed to be as model-independent as possible[8] and can be categorised in the classes summarised as follows:

- **(i)** the search for an additional CP-even state mostly in the high mass domain decaying to vector bosons, which would correspond either to the heavy CP-even state in a generic 2HDM where the light state would be the discovered Higgs boson at 125 GeV or to a generic additional singlet;
- **(ii)** the search for a state in the high mass domain decaying to pairs of fermions, which would correspond to the CP-odd A or the heavy CP-even state H in a generic 2HDM;
- **(iii)** the search for charged Higgs bosons, which also appear in generic 2HDMs;
- **(iv)** the search for a CP-odd state a in the low mass region which appears in the NMSSM in a variety of final states, e.g., with one or two a bosons decaying to pairs of photons, muons, taus, and b-quarks;
- **(v)** the search for doubly charged Higgs bosons which are expected in extensions of the Higgs sector with triplets.

Below is a concise description of the most recent searches performed at the LHC and elsewhere. A summary of these searches in terms of final states is given in Table 11.15 where the corresponding references are given for more details.

11.7.7.1 *Searches for an additional CP-even state*

(a) Exclusion limits from LEP

The searches for the SM Higgs boson at LEP provided an absolute lower limit of 114 GeV on its mass. These searches are also relevant for non-SM Higgs bosons. These searches were interpreted as 95% CL upper bounds on the ratio of the coupling g_{HZZ} to its SM prediction as a function of the Higgs boson mass [122, 436]. These results have an impact on MSSM benchmarks such as the low-m_H scenario, which is also nearly ruled out by current direct constraints and charged Higgs boson limits from LHC. These results also impact scenarios of light CP-even Higgs boson of the NMSSM which are constrained to project predominantly onto the EW singlet component. Additional interest for these scenarios is due to the slight excess observed at LEP [122] at a Higgs boson mass hypothesis of approximately 98 GeV.

(b) Searches at the LHC

At the LHC, the searches for the SM Higgs boson before the 2012 discovery covered a wide range of mass hypotheses up to approximately 1 TeV. After the discovery, the SM Higgs boson searches have been reappraised to search for a heavy CP-even state, extending progressively the search mass range beyond 1 TeV. This state could be the heavy CP-even Higgs boson of a 2HDM, or a generic additional singlet. In both cases, the natural width of the additional H state can be very different from that of the SM Higgs boson. To preserve unitarity of the longitudinal vector boson scattering and the longitudinal vector boson scattering into fermion pairs, the couplings of the additional CP-even Higgs boson to gauge bosons and fermions should not be too large and should constrain the natural width to be smaller than that of a unique Higgs boson at high mass with couplings to fermions and gauge bosons as predicted by the SM (and provided that trilinear and quartic couplings are not too large and that no new state affects the heavy state total width). It is therefore reasonable to consider total widths for the high mass CP-even state smaller than the equivalent SM width. Two specific cases have been considered: (i) the SM width using the complex pole scheme (CPS), and (ii) the narrow width approximation. For the sake of generality, these searches are now done as a function of the Higgs boson mass and total width.

Searches for the Higgs boson in the channels $H \rightarrow \gamma\gamma$, $H \rightarrow Z\gamma$, $H \rightarrow WW^{(*)}$ leptonic and semi-leptonic, and in the $H \rightarrow ZZ^{(*)}$ searches in the 4ℓ, $\ell\ell q\bar{q}$ and $\ell\ell\nu\nu$ channels have also been done, but some of them are simple reinterpretations of the SM Higgs boson search in the CPS scheme. References for these searches are summarised in Table 11.15.

(c) Searches for an additional resonance decaying to a pair of Higgs bosons

In addition to the rare and expected Higgs boson pair production mode, high mass CP-even Higgs bosons can be searched for in the resonant double Higgs boson mode. Searches for such processes, where the Higgs boson is used as a tool for searches for BSM phenomena, have been carried out in a variety of distinct modes depending on the subsequent decays of each Higgs bosons. ATLAS and CMS have searched for the $H \rightarrow hh \rightarrow b\bar{b}\tau\tau$, $b\bar{b}\gamma\gamma$, $H \rightarrow hh \rightarrow 4b$, $H \rightarrow hh \rightarrow \gamma\gamma WW^*$, $H \rightarrow hh \rightarrow bbWW^*$, $H \rightarrow hh \rightarrow WW^*WW^*$ and $H \rightarrow hh \rightarrow bbZZ^*$ final states. For mass hypotheses of an additional Higgs boson below 500 GeV, the two dominant search channels are the $b\bar{b}\gamma\gamma$ and the $b\bar{b}\tau\tau$ channels. For masses above 500 GeV, the most powerful search is with the $4b$ final state. As illustrated in Figure 11.19, these searches provide useful limits in the low $\tan\beta$ and high mass domain. The list of references for these searches is given in Table 11.15.

(d) Searches for an additional state with the presence of the Higgs boson

In the post-discovery era, analyses searching for additional Higgs bosons need to take into account the presence of the 125 GeV Higgs boson. For searches with sufficiently high mass resolution to disentangle the additional states which are not degenerate in mass, the strength of the observed state and limits on the signal strength of a potential additional state can be set independently, as discussed in the next section. However, in some cases where channels do not have a sufficiently fine mass resolution to resolve states nearly degenerate in mass, specific analyses need to be designed. There are two examples of such analyses: (i) the search for an additional state in the $H \rightarrow WW^{(*)} \rightarrow \ell\nu\ell\nu$ channel in ATLAS, and (ii) the search for nearly degenerate states in the $H \rightarrow \gamma\gamma$ channel with the CMS detector.

In the $H \rightarrow WW^{(*)} \rightarrow \ell\nu\ell\nu$ channel, the search for an additional state is done using a boosted decision tree combining several discriminating kinematic characteristics to separate both the signal from the background and a high mass signal H from the lower mass state h [437]. A simultaneous fit of the two states h

[8] Still, most non-SUSY models are likely to include further states and dynamics above the weak scale to stabilise the scalar sector and this new and unknown physics may influence the searches described in this section in a way difficult to estimate.

Table 11.15: Summary of references to the searches for additional states from extended Higgs sectors. (BBr) denotes the BaBar experiment and (TeV), the Tevatron experiments. Results using the full Run 2 dataset are indicated by (*). V denotes either the W or the Z boson. Only Run 2 searches references are indicated except when searches have been carried out using Run 1 data only. References for Run 1 searches are available in Ref. [123].

	ATLAS	CMS	Other experiments
CP-even H			
$H \to \gamma\gamma$	[374]	[375]	—
$H \to \gamma\gamma$ (low mass)	[374]	[376]	—
$H \to Z\gamma$	[176]	[377]	—
$H \to ZZ \to 4\ell$	[378]	[379]	—
$H \to ZZ \to \ell\ell\nu\nu$	[378]	[380]	—
$H \to ZZ \to \ell\ell q\bar{q}$	[381]	[382]	—
$H \to ZZ \to \nu\nu q\bar{q}$	[381]	—	—
$H \to WW \to \ell\nu\ell\nu$	[383]	* [384]	—
$H \to WW \to \ell\nu q\bar{q'}$	[385]	[384]	—
$H \to VV \to q\bar{q'}q\bar{q'}(JJ)$	[386, 387]	—	—
$H \to VV$ combination	[388]	—	—
$H \to hh \to b\bar{b}\tau\tau, b\bar{b}\gamma\gamma, 4b,$ $\gamma\gamma WW^*, bbWW^*, WW^*WW^*, bbZZ^*$	* [389, 390]	[391–393]	—
CP-odd A (and/or CP-even H)			
$H, A \to \tau^+\tau^-$	* [394]	* [395]	[396, 397] (TeV) [398] (LHCb)
$A \to \tau^+\tau^-$ (low mass)	—	[399]	—
$H, A \to \mu^+\mu^-$	[400]	[401]	—
$H \to \mu\tau, e\tau$ LFV		[402]	—
$bj\mu^+\mu^-$ (low $\mu^+\mu^-$ mass)	* [403]	[404]	—
$H, A \to t\bar{t}$	* [387, 405]	[406]	
$H, A \to b\bar{b}$	[407]	[408]	[409, 410] (TeV)
$A \to hV \to b\bar{b}q\bar{q'}, b\bar{b}\ell\nu, b\bar{b}\ell\ell, \ell\ell\tau\tau, \nu\bar{\nu}b\bar{b}$	* [411]	[392, 412]	
$H \to ZA \to b\bar{b}\ell^+\ell^-$	—	[413]	—
Charged $H^\pm$			
$H^\pm \to \tau^\pm\nu$	* [414, 415]	* [416]	—
$H^\pm \to cs$	[417]	[418]	—
$H^\pm \to tb$	* [419]	[420]	—
$H^\pm \to W^\pm Z$	[421]	* [422]	—
$H^\pm \to W^\pm A$	—	* [423]	—
$H^\pm \to cb$	—	* [424]	—
CP-odd NMSSM a			
$a \to \mu^+\mu^-$	[425]	* [426]	—
$h \to aa \to 4\mu, 4\tau, 2\mu2\tau, 4\gamma,$	[427]	[428]	[429] (TeV)
$aa \to \mu^+\mu^-\mu^+\mu^-$	—	* [430]	—
$bb\mu\mu, bb\tau\tau$			[431] (LEP)
$\Upsilon_{1s,3s} \to a\gamma$	—	—	[432, 433] (BBr)
Doubly charged $H^{\pm\pm}$	* [434]	* [435]	—

and H is then made to test the presence of an additional state. In this case, the usual null hypothesis of background includes the SM signal.

The CMS search for nearly degenerate mass states decaying to a pair of photons [438] is more generic and could for instance apply to CP-odd Higgs bosons as well. It consists of a fit to the diphoton mass spectrum using two nearly degenerate mass templates.

(e) Type I 2HDM and fermiophobia

The measurements of coupling properties of the 125 GeV Higgs boson directly establish its couplings to fermions. However, the presence of an additional fermiophobic state, as predicted by Type I 2HDMs, is not excluded. Prior to the discovery, ATLAS and CMS have performed searches for a fermiophobic Higgs boson, i.e., produced through couplings with vector bosons only (VBF and VH) and decaying in two photons. CMS has further combined these results with searches in the W^+W^- and ZZ channels, assuming fermiophobic production and decay. This way, CMS excluded a fermiophobic Higgs boson in the range 110 GeV $< m_H <$ 188 GeV at the 95% CL. References for these Run 1 measurements can be found in Ref. [123]

11.7.7.2 *Searches for additional neutral states ($\phi \equiv h$, H, A) decaying to fermions*

(a) Exclusion limits from LEP

In e^+e^- collisions, around the centre-of-mass energies reached by LEP, the main production mechanisms of the neutral MSSM Higgs bosons were the Higgs-strahlung processes $e^+e^- \to hZ$, HZ and the pair production processes $e^+e^- \to hA$, HA, while the vector boson fusion processes played a marginal role. Higgs boson decays to $b\bar{b}$ and $\tau^+\tau^-$ were used in these searches.

The searches and limits from the four LEP experiments are described in Refs. [439]. The combined LEP data did not contain any excess of events which would imply the production of a Higgs boson. Combined limits were derived [436]. For $m_A \gg M_Z$, the limit on m_h is nearly that of the SM searches, as $\sin^2(\beta-\alpha) \approx 1$. For high values of $\tan\beta$ and low m_A ($m_A \leq m_h^{max}$), the $e^+e^- \to hA$ searches become the most important, and the lightest Higgs boson h is non SM-like. In this region, the 95% CL mass bounds are $m_h > 92.8$ GeV and $m_A > 93.4$ GeV. In the m_h^{max} scenario [440], values of $\tan\beta$ from 0.7 to 2.0 are excluded taking $m_t = 174.3$ GeV, while a much larger $\tan\beta$ region is excluded for other benchmark scenarios such as the no-mixing one.

A flavour-independent limit for Higgs bosons in the Higgs-strahlung process at LEP has also been set at 112 GeV [441].

Neutral Higgs bosons may also be produced by Yukawa processes $e^+e^- \to f\bar{f}\phi$, where the Higgs particle $\phi \equiv h$, H, A, is radiated off a massive fermion ($f \equiv b$ or $\tau^\pm$). These processes can be dominant at low masses, and whenever the $e^+e^- \to hZ$ and hA processes are suppressed. The corresponding ratios of

the $f\bar{f}h$ and $f\bar{f}A$ couplings to the SM coupling are $-\sin\alpha/\cos\beta$ and $\tan\beta$, respectively. The LEP data have been used to search for $b\bar{b}\,b\bar{b}$, $b\bar{b}\tau^+\tau^-$, and $\tau^+\tau^-\,\tau^+\tau^-$ final states [442]. Regions of low mass and high enhancement factors are excluded by these searches.

The searches for the Higgs boson at LEP also included the case where it does not predominantly decay to a pair of b quarks. All four collaborations conducted dedicated searches for the Higgs boson with reduced model dependence, assuming it is produced via the Higgs-strahlung process, and not addressing its flavour of decay, a lower limit on the Higgs boson mass of 112.9 GeV is set by combining the data of all four experiments [441].

Using an effective Lagrangian approach and combining results sensitive to the $h\gamma\gamma$, $hZ\gamma$ and hZZ couplings, an interpretation of several searches for the Higgs boson was made and set a lower limit of 106.7 GeV on the mass of a Higgs boson that can couple anomalously to photons [441].

(b) Searches at the Tevatron and the LHC

The best sensitivity is in the regime with low to moderate m_A and with large $\tan\beta$ which enhances the couplings of the Higgs bosons to down-type fermions. The corresponding limits on the Higgs boson production cross section times the branching ratio of the Higgs boson into down-type fermions can be interpreted in MSSM benchmark scenarios [443]. If $\phi = A, H$ for $m_A > m_h^{\max}$, and $\phi = A, h$ for $m_A < m_h^{\max}$, the most promising channels at the Tevatron are the inclusive $p\bar{p} \to \phi \to \tau^+\tau^-$ process, with contributions from both $gg \to \phi$ and $b\bar{b}\phi$ production, and $b\bar{b}\phi, \phi \to \tau^+\tau^-$ or $\phi \to b\bar{b}$, with $b\tau\tau$ or three tagged b-jets in the final state, respectively. Although the Higgs boson production via gluon fusion has a higher cross section in general than via associated production, it cannot be used to study the $\phi \to b\bar{b}$ decay mode since the signal is overwhelmed by the QCD background.

CDF and D0 have searched for neutral Higgs bosons produced in association with bottom quarks and which decay into $b\bar{b}$ [409, 410], or into $\tau^+\tau^-$ [396, 397]. The most recent searches in the $b\bar{b}\phi$ channel with $\phi \to b\bar{b}$ analyse approximately 2.6 fb^{-1} (CDF) and 5.2 fb^{-1} (D0) of data, seeking events with at least three b-tagged jets. The cross section is defined such that at least one b quark not from ϕ decay is required to have $p_T > 20$ GeV and $|\eta| < 5$. The invariant mass of the two leading jets as well as b-tagging variables are used to discriminate the signal from the backgrounds. The QCD background rates and shapes are inferred from data control samples, in particular, the sample with two b-tagged jets and a third, untagged jet. Separate-signal hypotheses are tested and limits are placed on $\sigma(p\bar{p} \to b\bar{b}\phi) \times \mathrm{BR}(\phi \to b\bar{b})$. A local excess of approximately 2.5σ significance has been observed in the mass range of 130–160 GeV, but D0's search is more sensitive and sets stronger limits. The D0 result had a $\mathcal{O}(2\sigma)$ local upward fluctuation in the 110 to 125 GeV mass range. These results have been superseded by the LHC searches and the excess seen by D0 has not been confirmed elsewhere.

A substantially larger sensitivity in the search for the $\phi \to \tau^+\tau^-$ is obtained with the ATLAS and CMS analyses. The higher centre-of-mass energy reached at the Run 2 brings a substantial, though not excessively large, increase in sensitivity due to the intermediate masses probed. Both ATLAS and CMS have reported the result of their searches in this important channel with the full 2016 dataset. The searches are performed in categories of the decays of the two tau leptons: $e\tau_{\mathrm{had}}$, $\mu\tau_{\mathrm{had}}$, $e\mu$, and $\mu\mu$, where τ_{had} denotes a tau lepton which decays to one or more hadrons plus a tau neutrino, e denotes $\tau \to e\nu\nu$, and μ denotes $\tau \to \mu\nu\nu$. The dominant background comes from $Z \to \tau^+\tau^-$ decays, although $t\bar{t}$, W+jets and Z+jets events contribute as well. Separating events into categories based on the number of b-tagged jets improves the sensitivity in the MSSM. The $b\bar{b}$ annihilation process and radiation of a Higgs boson from a b quark gives rise to events in which the Higgs boson is accompanied by a $b\bar{b}$ pair in the final state. Requiring the presence of one or more b-jets reduces the background from Z+jets. Data control samples are used to constrain background rates. The rates for jets to be identified as a hadronically decaying tau lepton are measured in dijet samples, and W+jets samples provide a measurement of the rate of events that, with a fake hadronic tau, can pass the signal selection requirements. Lepton fake rates are measured using samples of isolated lepton candidates and same-sign lepton candidates. Constraints from the ATLAS searches are shown in Fig. 11.19 (left) in the hMSSM approximation defined in Ref. [314]. The neutral Higgs boson searches consider the contributions of both the CP-odd and CP-even neutral Higgs bosons with enhanced couplings to bottom quarks, similarly to was done for the Tevatron results. In Fig. 11.19, decays of the charged Higgs boson into $\tau\nu$ and decays of the heavy Higgs boson into a pair of SM-like Higgs bosons or gauge bosons, or decays of A into hZ are also being constrained. In addition, decays of the neutral Higgs bosons into muon pairs are also being explored. In the m_h-mod+ scenario the region of $\tan\beta$ lower than 5 does not allow for a Higgs boson mass m_h close to 125 GeV. For the hMSSM scenario, instead, the SM-like Higgs boson mass is fixed as an input and hence the requirement that it is close to 125 GeV is always fulfilled, although this may imply other limitations as discussed in Section 11.7.1.1.

A search for $\phi \to \mu^+\mu^-$ has also been performed by ATLAS [400] and CMS [401].

Finally searches for a resonance decaying to a top quark pair were done by ATLAS [405, 444] and CMS [406, 445]. These searches were interpreted as searches for scalar resonances by ATLAS [405], however, an important component of these searches is an accurate treatment of the interference effects between the signal and the continuum background. These effects can yield a dip and peak structure instead of a simple peak [311]. ATLAS has performed a search for a high mass state decaying to a pair of top quarks taking into account the deformation in mass shape of the signal in the presence of the continuum background [446].

The LHC has the potential to explore a broad range of SUSY parameter space through the search for non-SM-like Higgs bosons. As illustrated in Fig. 11.19, the parameter space corresponding to large $\tan\beta$ values and large masses of the A boson are covered mostly by the searches in the $A, H \to \tau^+\tau^-$ channel. A projection of the combined sensitivity of ATLAS and CMS at the HL-LHC has been performed in Ref. [104], showing that, compared to the current sensitivity, the full HL-LHC luminosity can expand the exclusion domain by nearly 1 TeV. In the low $\tan\beta$ limit, the parameter space spanning large A boson masses is best excluded indirectly from the observed Higgs boson measurements. This is illustrated in the Mh125 scenario by the nearly horizontal exclusion which is due to the compatibility of the Higgs boson mass measurement with its prediction from radiative corrections (mostly from the stop sector). Nevertheless, Fig. 11.19 (right) shows a broad region with intermediate $\tan\beta$ and large values of m_A that is not accessed by current searches, and in which the most promising channel is the very difficult search for $t\bar{t}$ decays with its aforementioned intricacies. In this region of parameter space, it is possible that only the SM-like Higgs boson can be within the LHC's reach. If no other state of the EWSB sector than the 125 GeV state is discovered, it may be challenging to determine only from the Higgs sector whether there is a SUSY extension of the SM in nature.

11.7.7.3 *Searches for a CP-odd state decaying to hZ*

Similarly to the search for a CP-even high mass Higgs boson decaying to a pair of Higgs bosons, the search for a CP-odd states decaying to hZ was carried out at the LHC by ATLAS and CMS in various channels:

(i) $(Z \to \ell\ell)(h \to b\bar{b})$,
(ii) $(Z \to \nu\nu)(h \to b\bar{b})$,
(iii) $(Z \to \ell\ell)(h \to \tau\tau)$,
(iv) and $(Z \to \ell\ell)(h \to \tau\tau)$.

The searches where the A boson decays to a pair of b quarks have been performed both in the regime where both b-jets are resolved and in the boosted regime where the two b-jets are merged in a single larger radius jet. These searches have been used to constrain the parameter space of 2HDMs. In the MSSM, these searches place limits on small values of $\tan\beta$ for masses of A between 220 GeV and 360 GeV.

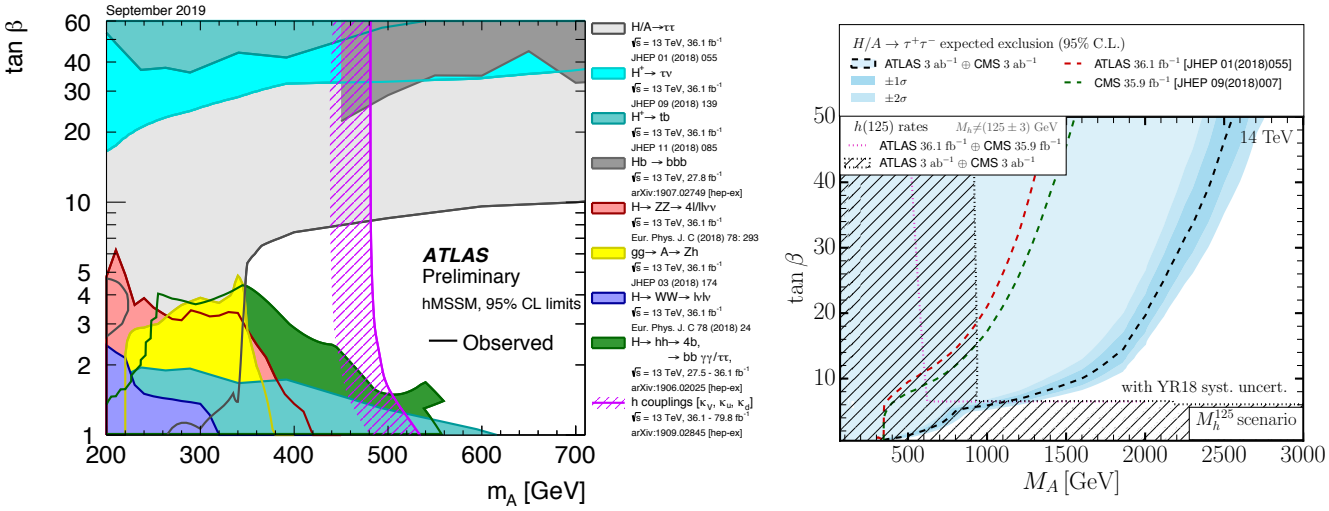

Figure 11.19: The 95% CL exclusion contours in the $(M_A, \tan\beta)$ parameter space for: (left) a summary of ATLAS Run 2 searches in the hMSSM and (right) the projected sensitivity for the combination of ATLAS and CMS searches in the $A, H \to \tau^+\tau^-$ channel at HL-LHC and the interpretation of the constraints from the measurements of the Higgs boson couplings in the Mh125 benchmark (the projected ATLAS sensitivity in the $A, H \to \tau^+\tau^-$ channel used for this projection was not optimised for high masses, when re-optimised similar sensitivities are obtained between ATLAS and CMS).

11.7.7.4 *Searches for low mass states*

Searches for pseudo-scalar Higgs boson at intermediate to low masses, below the Z mass (in the 25 GeV to 80 GeV mass range) have been performed by CMS both in the $\tau^+\tau^-$ [447] and the $\mu^+\mu^-$ [448] decay channels. A light pseudo-scalar in this mass range is excluded by current direct constraints in the MSSM but not in general 2HDMs [449]. These searches are done in the decay channels where the pseudo-scalar Higgs boson is produced in association with a pair of b-quarks and decays into a pair of taus or muons.

CMS has also reported an anomaly observed in the search for $\mu^+\mu^-$ resonances produced with one jet tagged as containing a b-hadron and a forward jet in the Run 1 data. A mild excess appeared in the di-muon mass distribution at approximately 28 GeV. Another very mild excess was then also found in the 2016 Run 2 data [404]. ATLAS then performed a similar analysis with the full Run 2 dataset corresponding to an integrated luminosity of approximately 139 fb^{-1}, and no significant excess was found [403].

Searches for low mass Higgs bosons were also performed in the diphoton channel by both ATLAS and CMS [450, 451] at Run 1. CMS has updated the results of this search with the full 2016 dataset [452]. A modest excess has been observed by CMS at a mass of 95.3 GeV with a local significance of 2.8σ (the corresponding global significance is 1.3σ). A slight excess was also seen by CMS in the 8 TeV data at a slightly higher mass of 97.6 GeV with a local significance of 2.0σ (1.47σ global). No significant excess has been observed in this region by ATLAS neither in the Run 1 nor Run 2 [374] data. It should, however, be noted that the ATLAS search does not reach the level of sensitivity to exclude at the 95% CL the excess seen in CMS. This mildly significant excess also coincides in mass with the excess observed at LEP and discussed in Section 11.7.7.1. It has therefore raised interest and speculations on its possible nature, see for instance Ref. [453] and references therein.

11.7.7.5 *Searches for charged Higgs bosons $H^\pm$*

At e^+e^- colliders, charged Higgs bosons can be pair produced in the s-channel via γ or Z boson exchange. This process is dominant in the LEP centre-of-mass energies range, i.e., up to 209 GeV. At higher centre-of-mass energies, other processes can play an important role such as the production in top quark decays via $t \to b + H^+$ if $m_{H^\pm} < m_t - m_b$ or via the one-loop process $e^+e^- \to W^\pm H^\mp$ [454, 455], which allows the production of a charged Higgs boson with $m_{H^\pm} > \sqrt{s}/2$, even when H^+H^- production is kinematically forbidden. Other single charged Higgs boson production mechanisms include $t\bar{b}H^-/\bar{t}bH^+$ production [108], $\tau^+\nu H^-/\tau^-\bar{\nu}H^+$ production [456], and a variety of processes in which $H^\pm$ is produced in association with a one or two other gauge and/or Higgs bosons [457].

At hadron colliders, charged Higgs bosons can be produced in several different modes depending on the value of its mass with respect to the top-quark mass. For light values of the charged Higgs boson mass, defined by Higgs boson masses smaller than the mass of the top quark (with experimental analyses typically considering masses up to $m_{H^\pm} \leq 160$ GeV), the top-quark decay $t \to Hb$ is allowed and the charged Higgs boson is light enough so that top-quark off-shell effects can be neglected. The cross section for the production of a light charged Higgs boson is simply given by the product of the top-pair production cross section and the branching ratio of a top quark into a charged Higgs boson. The top-pair production cross section is known up to NNLO in perturbative QCD [458], and relevant QCD and SUSY-QCD including NLO corrections to the branching ratio for $t \to H^+b$ have been computed in the literature, see Refs. [459–461] and references therein. At present, the theoretical accuracy for the production of a light charged Higgs boson is at the few percent level. For the intermediate mass range, values of $m_{H^\pm}$ near m_t, the finite top-width effects as well as the interplay between top-quark resonant and non-resonant diagrams cannot be neglected. Hence, the full process $pp \to H^\pm W^\mp b\bar{b}$ (with massive b-quarks) must be considered to perform a reliable perturbative calculation of the charged Higgs boson production cross section [461]. For heavy charged Higgs boson scenarios, with charged Higgs boson masses larger than the top-quark mass (typically above 180 GeV), the dominant charged Higgs boson production channel is the associated production with a top quark/antiquark and a (possibly low transverse momentum) bottom antiquark/quark. Theoretical calculation at NLO have been computed both at the inclusive and fully-differential level in the five-flavour scheme and in the four-flavour scheme, see Ref. [44] and references therein. Charged Higgs bosons can also be produced via associated production with $W^\pm$ bosons through $b\bar{b}$ annihilation and gg-fusion annihilation [462].

For charged Higgs boson production cross section predictions for the Tevatron and the LHC, see Refs. [42, 43, 310].

(a) Exclusion limits from LEP

Charged Higgs bosons have been searched for at LEP, where the combined data of the four experiments, ALEPH, DELPHI, L3, and OPAL, were sensitive to masses of up to about 90 GeV [436] in two decay channels, $\tau\nu$ and $c\bar{s}$. The combined LEP data exclude, at 95% CL, charged Higgs bosons with mass below 80 GeV (Type II scenario) or 72.5 GeV (Type I scenario) [463].

(b) Exclusion limits from Tevatron

Compared to the mass domain covered by LEP searches, the Tevatron covered a complementary range of charged Higgs boson masses. CDF and D0 have also searched for charged Higgs bosons in top quark decays with subsequent decays to $\tau\nu$ or to $c\bar{s}$ [464]. For the $H^+ \to c\bar{s}$ channel, the limits on $\mathrm{BR}(t \to H^+ b)$ from CDF and D0 are $\approx 20\%$ in the mass range $90\,\mathrm{GeV} < m_{H^+} < 160\,\mathrm{GeV}$ and assuming a branching fraction of 100% in this specific final state. $H^+ \to \tau^+\nu_\tau$ channel, D0's limits on $\mathrm{BR}(t \to H^+ b)$ are also $\approx 20\%$ in the same mass range and assuming a branching fraction of 100% in this final state. These limits are valid in general 2HDMs, and they have also been interpreted in terms of the MSSM [464].

(c) Exclusion limits from LHC

Similarly to the Tevatron, at the LHC, light charged Higgs bosons can be searched for in the decays of top quarks. The main initial production mode for light charged Higgs bosons ($m_{H^\pm} < m_t - m_b$) is top pair production. The subsequent decay modes of the charged Higgs boson for these searches are $\tau\nu$ and $c\bar{s}$. More recently, ATLAS and CMS have also searched for higher mass charged Higgs bosons ($m_{H^\pm} > m_t + m_b$) in $H^+ \to t\bar{b}$. The main production modes are the associated production of a charged Higgs boson in association with a top and a bottom quark or in association with a top quark only.

The decay $H^+ \to \tau^+\nu_\tau$ is searched typically in three final state topologies:

(i) lepton+jets: with $t\bar{t} \to \bar{b}WH^+ \to b\bar{b}(q\bar{q}')(\tau_{\mathrm{lep}}\nu)$, i.e., the W boson decays hadronically and the tau decays into an electron or a muon, with two neutrinos;

(ii) τ +lepton: with $t\bar{t} \to \bar{b}WH^+ \to b\bar{b}(l\nu)(\tau_{\mathrm{had}}\nu)$, i.e., the W boson decays leptonically (with $\ell = e$, μ) and the tau decays hadronically;

(iii) τ+jets: $t\bar{t} \to \bar{b}WH^+ \to b\bar{b}(q\bar{q}')(\tau_{\mathrm{had}}\nu)$, i.e., both the W boson and the τ decay hadronically.

CMS has also searched for the charged Higgs boson in the decay products of top quark pairs: $t\bar{t} \to H^\pm W^\mp b\bar{b}$ and $t\bar{t} \to H^+H^- b\bar{b}$ as well. Three types of final states with large missing transverse energy and jets originating from b-quark hadronisation have been analysed: the fully-hadronic channel with a hadronically decaying tau in association with jets, the dilepton channel with a hadronically decaying tau in association with an electron or muon and the dilepton channel with an electron-muon pair. The results of the searches at the LHC are illustrated in Figure 11.19.

Both ATLAS and CMS have also searched for high mass charged Higgs bosons decaying to a top and bottom quarks. The main production mode for this search is the associated production with one top quark (5-flavour scheme) or a top quark and and bottom quark (4-flavour scheme) in the final state. The s-channel production mode where the charged Higgs boson is produced alone in the final state at tree level is also considered. This search is particularly intricate and it is sensitive to the modelling of the top pair production background produced in association with additional partons and in particular b-quarks. No excess was found and the results are expressed in terms of exclusion limits of cross section times branching fractions.

ATLAS and CMS have also searched for charged Higgs bosons in top quark decays assuming $\mathrm{BR}(H^+ \to c\bar{s}) = 100\%$ [417, 418], and sets limits of $\approx$ 20% on $\mathrm{BR}(t \to H^+ b)$ in the $90\,\mathrm{GeV} < m_{H^+} < 160\,\mathrm{GeV}$ mass range.

In 2HDMs, the decay of the charged Higgs boson to a W and a Z boson is allowed only at loop level and is therefore suppressed. However the $H^\pm \to W^\pm Z$ decay channel is allowed in Higgs triplet models. ATLAS [421] has searched for such decays, requiring that the charged Higgs boson is produced through the fusion of vector bosons. No excess with respect to the SM backgrounds has been observed in this channel, and the results are interpreted in the Georgi–Machacek model [349] discussed in Section 11.7.5.2.

At the LHC, various other channels still remain to be explored, in particular searches involving additional neutral scalars in particular in the WH, WA channels (A is the pseudo-scalar MSSM Higgs boson), and in the Wa channel (a is the light CP-odd scalars of the NMSSM).

11.7.7.6 *Interpretation of the measurements of the coupling properties of the Higgs boson*

The 125 GeV Higgs boson being part of any hypothetically extended EWSB sector, it can be used through the compatibility of its measured couplings and mass with those predicted in specific models to provide constraints on these specific models parameters.

As discussed in Section 11.7.1.1, the mass of the Higgs boson limits drastically the MSSM parameter space and can be used to set limits on specific MSSM benchmarks. This is the case for the Mh125 scenario as illustrated in Figure 11.18 and in Figure 11.19, corresponding approximately to a lower limit on $\tan\beta$ in this model [104].

The measurements of the Higgs boson couplings, discussed in Section 11.6, can be interpreted in the framework of a constrained model where the couplings of the Higgs boson to vector bosons, up-type quarks, down-type quarks and leptons, are varied. In 2HDMs, these couplings are functions of the mixing angle α between the observed Higgs boson and the heavy CP-even neutral scalar, and of the ratio of the vacuum expectation values of the two doublets, $\tan\beta$. In the case of the MSSM, the two parameters are the A boson mass and $\tan\beta$ (the sole two parameters needed to describe the MSSM Higgs sector at tree level). The coupling measurements have been interpreted both by ATLAS [213] and CMS [214] in specific MSSM benchmarks and in 2HDMs. The exclusion contour in the hMSSM for the ATLAS combination [213] is illustrated in Figure 11.19.

11.7.7.7 *Searches for a light CP-odd Higgs boson*

A light pseudo-scalar boson a is present in any two Higgs doublet model enhanced with an additional singlet field. A prominent example is the NMSSM. The theoretical motivations for singlet extensions of the MSSM are discussed in Section 11.7.2. There is also a variety of other models with light additional spin-0 bosons such as two Higgs doublet models with a scalar, Little Higgs models or light scalar mediator to a dark sector.

In the framework of the NMSSM, the searches now focus on the low a mass region for several reasons:

(i) in the NMSSM, the light pseudo-scalar a boson can, as a pseudo-Goldstone boson, be a natural candidate for an axion;

(ii) scenarios where $m_a > 2m_b$ and a CP-even state h decaying to a pair of a ($m_h > 2m_a$) are excluded by direct searches at LEP in the four b's channel [429, 436, 465];

(iii) in the pre-discovery era, LEP limits on a CP-even Higgs boson resulted in fine tuning MSSM constraints [466] which could be evaded through non standard decays of the Higgs boson to aa;

(iv) in the NMSSM, a CP-odd a boson with a mass in the range 9.2–12 GeV can also account for the difference observed between the measured anomalous muon magnetic moment and its prediction [467].

The benchmark scenarios have also changed in the light of the Higgs boson discovery. The 125 GeV state could be the lightest or the next-to-lightest of the three CP-even states of the NMSSM. Light pseudo-scalar scenarios are still very interesting in particular for the potential axion candidate. There are three main types of direct searches for the light a boson:

(i) for masses below the Υ resonance, the search is for radiative decays $\Upsilon \to a\gamma$ at B-factories;

(ii) the inclusive search in high energy pp collisions at the LHC;

(iii) the search for decays of the observed CP-even Higgs h boson into a pair of a bosons.

Radiative decays $\Upsilon \to a\gamma$ have been searched for in various colliders, the most recent results are searches for radiative decays of the $\Upsilon(1s)$ to $a\gamma$ with a subsequent decay of the a boson to a pair of taus at CLEO [468], and the radiative decays of the $\Upsilon(1s, 2s, 3s)$ to $a\gamma$ with subsequent decays to a pair of muons or taus by BaBar [432, 433].

Direct inclusive searches for the light pseudo scalar a boson were performed in the $a \to \mu\mu$ channel at the Tevatron by D0 [429] and by ATLAS [425], CMS [426], and LHCb [151] at the LHC.

Finally, searches for the decays of the Higgs boson to a pair of a bosons where performed with subsequent decays to four photons, in the four muons final state, in the two muons and two taus final state, and in the four taus final state.

No significant excess in the searches for a light CP-odd a boson was found and limits on the production times branching fractions of the a boson have been set.

References for all these searches are summarised in Table 11.15.

11.7.7.8 *Searches for doubly charged Higgs bosons $H^{\pm\pm}$*

As discussed in Section 11.7.5, the generation of small neutrino masses via the standard EWSB mechanism described in Section 11.2 requires unnaturally small Yukawa couplings, provided that neutrinos are Dirac-type fermions. A Majorana mass term with a see-saw mechanism for neutrinos, would allow for naturally small masses and would also yield a framework for the appealing scenario of leptogenesis. However, within the SM, Majorana mass terms correspond to (non-renomalizable) dimension-5 operators. Such effective interactions can be generated via renormalisable interactions with an electroweak triplet of complex scalar fields (corresponding to a type-II see-saw mechanism). Other models such as the Zee–Babu model, with the introduction of two $\mathrm{SU}(2)_L$ singlets, also generate Majorana mass terms. The signature of such models would be the presence of doubly charged Higgs bosons $H^{\pm\pm}$.

The main production mechanisms of $H^{\pm\pm}$ bosons at hadron colliders are the pair production in the s-channel through the exchange of a Z boson or a photon and the associated production with a charged Higgs boson through the exchange of a W boson. Various searches for doubly charged Higgs bosons have been performed by ATLAS and CMS at Run 1 [469] and Run 2 [434, 435]. Typically, these searches aim at low values of the Higgs triplet vacuum expectation for which the doubly charged Higgs boson will decay mostly to leptons (for high values, the decay to W bosons will become predominant). These searches assume that the coupling to W bosons is negligible and that the main production mode is through the Drell–Yan process.

11.7.7.9 *Searches for non-standard production processes of the Higgs boson*

The discovery of the Higgs boson has also allowed for searches of BSM processes involving standard decays of the Higgs boson. One example directly pertaining to the search for additional states of the EWSB sector is the search for Higgs bosons in the cascade decay of a heavy CP-even Higgs boson decaying to charged Higgs boson and a W boson, and the charged Higgs boson subsequently decaying to H and another W boson. This search has been performed by ATLAS in $b\bar{b}$ decays of the 125 GeV Higgs boson [470].

11.7.7.10 *Outlook on searches for additional states*

The LHC program of searches for additional states covers a large variety of decay and production channels. Since the Higgs boson discovery, many new channels have been explored at the LHC, e.g., the searches for additional states decaying into hh or Vh or ZA. The search for charged Higgs bosons has been extended to include the WZ, WA and the very difficult $t\bar{b}$ decay channel.

11.8 Summary and outlook

Summary– The discovery of the Higgs boson is a major milestone in the history of particle physics as well as an extraordinary achievement of the LHC machine and the ATLAS and CMS experiments. Seven years after the discovery, substantial progress in the field of Higgs boson physics has been accomplished and a significant number of measurements probing the nature of this unique particle have been made. They are revealing an increasingly precise profile of the Higgs boson.

The LHC has now concluded its Run 2, delivering a dataset of 13 TeV pp collisions corresponding to an integrated luminosity of approximately 140 fb^{-1} of data collected by ATLAS and CMS. With the substantial increase in production rates at the higher center-of-mass energy and the larger datasets, new landmark results in Higgs physics have been achieved.

Three new results of fundamental importance have been achieved with partial Run 2 datasets by ATLAS and CMS independently: (i) the clear and unambiguous observation of the Higgs boson decay to taus; (ii) the clear and unambiguous observation of the Higgs boson decay to a pair of b quarks; (iii) the clear and unambiguous observation of the production of the Higgs boson through the $t\bar{t}H$ process. These results provide direct evidence for the Yukawa coupling of the Higgs boson to fermions of the third generation: taus, bottom quarks and top quarks, at rates compatible with those expected in the SM. These, and all other experimental measurements, are consistent with the EWSB mechanism of the SM.

New theoretical calculations and developments in Monte-Carlo simulation pertaining to Higgs physics are still occurring at a rapid pace. For example, the theoretical prediction for the dominant gluon fusion production mode now includes the latest N3LO result, which is twice as precise as previous N2LO calculations. With these improvements in the state-of-the-art theory predictions and the increase in luminosity and center-of-mass energy, Higgs physics has definitively entered a precision era. Its impact can already be seen on the latest Run 2 combined measurements of the Higgs boson couplings (see Section 11.6).

Since the discovery of the Higgs boson, new ideas have emerged to probe its rare decays and production modes, as well as to indirectly measure the Higgs boson width through the study of its off-shell couplings, or via on-shell interference effects. The Higgs boson has now become part of the standard toolkit in searches for new physics.

Many extensions of the SM at higher energies call for an enlargement of the EWSB sector. Hence, direct searches for additional scalar states can provide valuable insights on the dynamics of the EWSB mechanism. The ATLAS and CMS experiments have searched for additional Higgs bosons in the Run 2 data, and have imposed constraints in broad ranges of mass and couplings for various scenarios with an extended Higgs sector.

The landscape of Higgs physics has been extended extraordinarily since its discovery. The current dataset is approximately only five percent of the total dataset foreseen for the High Luminosity phase of the LHC project. The current precisions on the measurements of the couplings of the Higgs boson to gauge bosons and third generation fermions are typically of the order of 10–20%. The uncertainty on the Higgs boson coupling to the muon is approximately 100%, and the upper limits on the branching fraction to new invisible or undetected particles are approximately 20%. The sensitivity to the Higgs boson self-coupling has not reached the SM value yet and there is no information on how the Higgs field acquired its VEV in the early times of the Universe. This situation allows for new challenges to ultimately increase further the reach in precision and it also widens the possibilities of unveiling the true nature and the dynamics of the electroweak symmetry breaking.

Outlook– The unitarisation of the vector boson scattering (VBS) amplitudes, dominated at high energies by their longitudinal polarisation, has been the basis of the *no lose* theorem at the LHC, and was a determining consideration in the building of the accelerator and detectors. It motivated the existence of a Higgs boson or the observability of manifestations of strong dynamics at the TeV scale. Now that a Higgs boson has been found and its couplings to gauge bosons are consistent with the SM predictions, perturbative unitarity is preserved to a large extent with the sole exchange of the Higgs boson, and without the need for any additional states. VBS is, however, still an important channel to further investigate in order to better understand the nature of the Higgs sector and the possible completion of the SM at the TeV scale. In association with the double Higgs boson production channel by vector boson fusion, VBS could, for instance, confirm that the Higgs boson is part of a weak doublet and also establish whether it is an elementary object or a composite state that could emerge as a pseudo-Nambu–Goldstone boson from a new underlying broken symmetry.

The fermion-Higgs boson couplings are not governed by local

gauge symmetry. Thus, in addition to a new particle, the LHC has also discovered a new force, different in nature from the other fundamental interactions since it is non-universal and distinguishes between the three families of quarks and leptons. The existence of the Higgs boson embodies the problem of an unnatural cancellation among the quantum corrections to its mass if new physics is present at scales significantly higher than the EW scale. The non-observation of additional states which could stabilise the Higgs boson mass is a challenge for natural scenarios like SUSY or models with a new strong interaction in which the Higgs boson is not a fundamental particle. This increasingly pressing paradox starts questioning the principle of naturalness.

The search for the Higgs boson has occupied the particle physics community for the last 50 years. Its discovery has shaped and sharpened the physics programs of the LHC and of prospective future accelerators [471]. With the HL-LHC, the precision will improve by a factor 5–10 on all observables with respect to current data. Table 11.12 displays the expected sensitivities in the characterization of the Higgs boson at HL-LHC: in this table, the parameters κ_i specify by how much the coupling of the Higgs boson to a given particle i deviates from the SM expectation. The only channels which are expected to be limited by data statistics are the rare decays to muons and $Z\gamma$. In all other cases, the experimental systematic uncertainties are similar to the statistical uncertainties, but the dominant source of uncertainty arises from theory, and this remains the case even after assuming that, by the end of the HL-LHC run, the theory uncertainties can be reduced by a factor two compared to the current uncertainties, a hypothesis that appears realistic but still requires dedicated and concerted work [104]. For both hadron and lepton colliders, some theoretical progress is crucial to fully exploit and capitalise on the experimental data. In particular, the expected HL-LHC data together with rapid ongoing progress in theoretical calculations are defining a new era of precision Higgs boson measurements.

Acknowledgements

We would like to thank many of our colleagues for proofreading this review, for useful criticism and for their input in general: W. Altmannshofer, J. de Blas, G. Branco, J. Campbell, F. Caola, F. Cerutti, C. Csáki, R. Contino, J. Conway, N. Craig, A. David, S. Dawson, J.B. De Vivie, J. D'Hondt, G. Durieux, C. Englert, J.R. Espinosa, A. Falkowski, L. Fayard, W. Fischer, S. Forte, M. Grazzini, J. Gu, H. Haber, B. Heinemann, S. Heinemeyer, J. Hubisz, A. Korytov, B. Jäger, H. Ji, T. Junk, P. Langacker, J. Lykken, F. Maltoni, M.L. Mangano, B. Mansoulié, M. McCullough, R. Mishra, M. Mühlleitner, B. Murray, M. Neubert, A. Nisati, Y. Paul, G. Perez, G. Petrucciani, A. Pomarol, E. Pontón, R. Rattazzi, D. Rebuzzi, F. Riva, R. Salerno, E. Salvioni, N. Shah, G. Shaughnessy, M. Spira, O. Stål, A. Strumia, K. Tackmann, R. Tanaka, J. Terning, A. Vartak, C. Wagner, A. Weiler, A. Wulzer, and G. Zanderighi. We are also most grateful to the ATLAS, CDF, CMS and D0 collaborations for their help with this review.

M.C. is supported by Fermilab, that is operated by Fermi Research Alliance, LLC under Contract No. DE–AC02–07CH11359 with the United States Department of Energy. C.G. is supported by the Helmholtz Association and by the Deutsche Forschungsgemeinschaft under Germany's Excellence Strategy – EXC 2121 "Quantum Universe" – 390833306. V.S. is supported by the grant DE–SC0009919 of the United States Department of Energy.

References

[1] G. Aad *et al.* (ATLAS), Phys. Lett. **B716**, 1 (2012), [arXiv:1207.7214].

[2] S. Chatrchyan *et al.* (CMS), Phys. Lett. **B716**, 30 (2012), [arXiv:1207.7235].

[3] S.L. Glashow, Nucl. Phys. **20**, 579 (1961); S. Weinberg, Phys. Rev. Lett. **19**, 1264 (1967); A. Salam, *Elementary Particle Theory*, eds.: Svartholm, Almquist and Wiksells, Stockholm, 1968; S. L. Glashow, J. Iliopoulos and L. Maiani, Phys. Rev. **D2**, 1285 (1970).

[4] F. Englert and R. Brout, Phys. Rev. Lett. **13**, 321 (1964), [,157(1964)]; P. W. Higgs, Phys. Rev. **145**, 1156 (1966); G. S. Guralnik, C. R. Hagen and T. W. B. Kibble, Phys. Rev. Lett. **13**, 585 (1964), [,162(1964)].

[5] J. M. Cornwall, D. N. Levin and G. Tiktopoulos, Phys. Rev. Lett. **30**, 1268 (1973), [Erratum: Phys. Rev. Lett. **31**, 572 (1973)]; J. M. Cornwall, D. N. Levin and G. Tiktopoulos, Phys. Rev. **D10**, 1145 (1974), [Erratum: Phys. Rev. **D11**, 972 (1975)]; C. H. Llewellyn Smith, Phys. Lett. **46B**, 233 (1973); B. W. Lee, C. Quigg and H. B. Thacker, Phys. Rev. **D16**, 1519 (1977).

[6] K. G. Wilson, Phys. Rev. **D3**, 1818 (1971); G. 't Hooft, in *Proc. of 1979 Cargèse Institute on Recent Developments in Gauge Theories,* p. 135 Press, New York 1980; For a recent review, see G.F. Giudice, PoS EPS-HEP2013, 163 (2013).

[7] J. Wess and B. Zumino, Phys. Lett. **49B**, 52 (1974).

[8] S. P. Martin, Adv. Ser. Direct. High Energy Phys. 1–98 (1998), [hep-ph/9709356].

[9] B.C, Allanach and H.E. Haber, *Supersymmetry, Part I (Theory)*, in this volume.

[10] D. B. Kaplan and H. Georgi, Phys. Lett. **136B**, 183 (1984).

[11] B. Bellazzini, C. Csaki and J. Serra, Eur. Phys. J. **C74**, 5, 2766 (2014), [arXiv:1401.2457]; G. Panico and A. Wulzer, Lect. Notes Phys. **913**, pp.1 (2016), [arXiv:1506.01961]; C. Csaki, C. Grojean and J. Terning, Rev. Mod. Phys. **88**, 4, 045001 (2016), [arXiv:1512.00468].

[12] K.M. Black, R.S. Chivukula and M. Narain, *Dynamical Electroweak Symmetry Breaking: Implications of the H0*, in this volume.

[13] Z. Chacko, H.-S. Goh and R. Harnik, Phys. Rev. Lett. **96**, 231802 (2006), [hep-ph/0506256]; Z. Chacko, H.-S. Goh and R. Harnik, JHEP **01**, 108 (2006), [hep-ph/0512088].

[14] N. Craig *et al.*, JHEP **07**, 105 (2015), [arXiv:1501.05310]; N. Craig, S. Knapen and P. Longhi, Phys. Rev. Lett. **114**, 6, 061803 (2015), [arXiv:1410.6808].

[15] P. W. Graham, D. E. Kaplan and S. Rajendran, Phys. Rev. Lett. **115**, 22, 221801 (2015), [arXiv:1504.07551]; J. R. Espinosa *et al.*, Phys. Rev. Lett. **115**, 25, 251803 (2015), [arXiv:1506.09217]; G. Dvali (2019), [arXiv:1908.05984].

[16] T. Flacke *et al.*, JHEP **06**, 050 (2017), [arXiv:1610.02025].

[17] M. Bauer, M. Carena and K. Gemmler, JHEP **11**, 016 (2015), [arXiv:1506.01719]; M. Bauer, M. Carena and K. Gemmler, Phys. Rev. **D94**, 11, 115030 (2016), [arXiv:1512.03458].

[18] R. Barbieri, L. J. Hall and V. S. Rychkov, Phys. Rev. **D74**, 015007 (2006), [hep-ph/0603188].

[19] D. E. Morrissey and M. J. Ramsey-Musolf, New J. Phys. **14**, 125003 (2012), [arXiv:1206.2942].

[20] G. Degrassi *et al.*, JHEP **08**, 098 (2012), [arXiv:1205.6497]; S. Alekhin, A. Djouadi and S. Moch, Phys. Lett. **B716**, 214 (2012), [arXiv:1207.0980]; D. Buttazzo *et al.*, JHEP **12**, 089 (2013), [arXiv:1307.3536].

[21] S. Weinberg, Phys. Rev. Lett. **43**, 1566 (1979).

[22] See the particle listing section at `http://pdg.lbl.gov`.

[23] J. R. Ellis, M. K. Gaillard and D. V. Nanopoulos, Nucl. Phys. **B106**, 292 (1976).

[24] M. A. Shifman *et al.*, Sov. J. Nucl. Phys. **30**, 711 (1979), [Yad. Fiz.30,1368(1979)].

[25] J. F. Gunion *et al.*, *The Higgs Hunter's Guide*, Addison-Wesley (1990).

[26] P. Sikivie *et al.*, Nucl. Phys. **B173**, 189 (1980); H. Georgi, Ann. Rev. Nucl. Part. Sci. **43**, 209 (1993).

[27] M. J. G. Veltman, Nucl. Phys. **B123**, 89 (1977).

[28] M. Luscher and P. Weisz, Nucl. Phys. **B290**, 25 (1987); M. Luscher and P. Weisz, Nucl. Phys. **B295**, 65 (1988).

[29] V. Branchina, E. Messina and M. Sher, Phys. Rev. **D91**, 013003 (2015), [arXiv:1408.5302].

[30] A. Hook *et al.*, JHEP **01**, 061 (2015), [arXiv:1404.5953]; J. Kearney, H. Yoo and K. M. Zurek, Phys. Rev. **D91**, 12, 123537 (2015), [arXiv:1503.05193].

[31] J. R. Espinosa, D. Racco and A. Riotto, Phys. Rev. Lett. **120**, 12, 121301 (2018), [arXiv:1710.11196].

[32] J. R. Espinosa, D. Racco and A. Riotto, JCAP **1809**, 09, 012 (2018), [arXiv:1804.07732].

[33] A. Andreassen, W. Frost and M. D. Schwartz, Phys. Rev. **D97**, 5, 056006 (2018), [arXiv:1707.08124]; S. Chigusa, T. Moroi and Y. Shoji, Phys. Rev. Lett. **119**, 21, 211801 (2017), [arXiv:1707.09301].

[34] M. Shaposhnikov and C. Wetterich, Phys. Lett. **B683**, 196 (2010), [arXiv:0912.0208]; M. Holthausen, K. S. Lim and M. Lindner, JHEP **02**, 037 (2012), [arXiv:1112.2415].

[35] F. L. Bezrukov and M. Shaposhnikov, Phys. Lett. **B659**, 703 (2008), [arXiv:0710.3755]; F. L. Bezrukov, A. Magnin and M. Shaposhnikov, Phys. Lett. **B675**, 88 (2009), [arXiv:0812.4950].

[36] C. P. Burgess, H. M. Lee and M. Trott, JHEP **09**, 103 (2009), [arXiv:0902.4465]; J. L. F. Barbon and J. R. Espinosa, Phys. Rev. **D79**, 081302 (2009), [arXiv:0903.0355]; M. P. Hertzberg, JHEP **11**, 023 (2010), [arXiv:1002.2995].

[37] B. A. Kniehl, Phys. Rept. **240**, 211 (1994).

[38] M. Spira, Fortsch. Phys. **46**, 203 (1998), [hep-ph/9705337].

[39] M. Carena and H. E. Haber, Prog. Part. Nucl. Phys. **50**, 63 (2003), [hep-ph/0208209].

[40] A. Djouadi, Phys. Rept. **457**, 1 (2008), [hep-ph/0503172].

[41] S. Dittmaier *et al.* (LHC Higgs Cross Section Working Group), CERN Report **2011-002** (2011), [arXiv:1101.0593].

[42] S. Dittmaier *et al.* (LHC Higgs Cross Section Working Group), CERN Report **2012-002** (2012), [arXiv:1201.3084].

[43] S. Heinemeyer *et al.* (LHC Higgs Cross Section Working Group), CERN Report **2013-004** (2013), [arXiv:1307.1347].

[44] D. de Florian *et al.* (LHC Higgs Cross Section Working Group), CERN Report **2017-002** (2016), [arXiv:1610.07922].

[45] LHC Higgs Cross Section Working Group, `https://twiki.cern.ch/twiki/bin/view/LHCPhysics/LHCHXSWG`.

[46] T. Aaltonen *et al.* (CDF, D0), Phys. Rev. **D88**, 5, 052014 (2013), [arXiv:1303.6346].

[47] H. M. Georgi *et al.*, Phys. Rev. Lett. **40**, 692 (1978).

[48] D. Graudenz, M. Spira and P. M. Zerwas, Phys. Rev. Lett. **70**, 1372 (1993).

[49] M. Spira *et al.*, Nucl. Phys. **B453**, 17 (1995), [hep-ph/9504378].

[50] C. Anastasiou *et al.*, Phys. Rev. Lett. **114**, 212001 (2015), [arXiv:1503.06056]; C. Anastasiou *et al.*, JHEP **05**, 058 (2016), [arXiv:1602.00695].

[51] R. V. Harlander and K. J. Ozeren, JHEP **11**, 088 (2009), [arXiv:0909.3420]; A. Pak, M. Rogal and M. Steinhauser, JHEP **02**, 025 (2010), [arXiv:0911.4662].

[52] J. Davies *et al.*, Phys. Rev. **D100**, 3, 034017 (2019), [arXiv:1906.00982].

[53] S. Dawson, Nucl. Phys. **B359**, 283 (1991); A. Djouadi, M. Spira and P. M. Zerwas, Phys. Lett. **B264**, 440 (1991).

[54] R. V. Harlander and W. B. Kilgore, Phys. Rev. Lett. **88**, 201801 (2002), [hep-ph/0201206]; C. Anastasiou and K. Melnikov, Nucl. Phys. **B646**, 220 (2002), [hep-ph/0207004]; V. Ravindran, J. Smith and W. L. van Neerven, Nucl. Phys. **B665**, 325 (2003), [hep-ph/0302135].

[55] A. Djouadi and P. Gambino, Phys. Rev. Lett. **73**, 2528 (1994), [hep-ph/9406432]; S. Actis *et al.*, Phys. Lett. **B670**, 12 (2008), [arXiv:0809.1301]; U. Aglietti *et al.*, Phys. Lett. **B595**, 432 (2004), [hep-ph/0404071]; G. Degrassi and F. Maltoni, Phys. Lett. **B600**, 255 (2004), [hep-ph/0407249].

[56] M. Bonetti, K. Melnikov and L. Tancredi, Phys. Rev. **D97**, 5, 056017 (2018), [Erratum: Phys. Rev. **D97**, 9, 099906 (2018)], [arXiv:1801.10403].

[57] C. Anastasiou, R. Boughezal and F. Petriello, JHEP **04**, 003 (2009), [arXiv:0811.3458].

[58] C. Anastasiou *et al.*, JHEP **03**, 162 (2019), [arXiv:1811.11211].

[59] M. Bonvini *et al.*, JHEP **08**, 105 (2016), [arXiv:1603.08000]; B. Mistlberger, JHEP **05**, 028 (2018), [arXiv:1802.00833].

[60] R. Boughezal *et al.*, Phys. Rev. Lett. **115**, 8, 082003 (2015), [arXiv:1504.07922].

[61] X. Chen *et al.*, Phys. Lett. **B740**, 147 (2015), [arXiv:1408.5325].

[62] J. M. Campbell, R. K. Ellis and S. Seth (2019), [arXiv:1906.01020].

[63] J. M. Lindert *et al.*, Phys. Rev. Lett. **118**, 25, 252002 (2017), [arXiv:1703.03886]; J. M. Lindert *et al.*, Phys. Lett. **B782**, 210 (2018), [arXiv:1801.08226]; S. P. Jones, M. Kerner and G. Luisoni, Phys. Rev. Lett. **120**, 16, 162001 (2018), [arXiv:1802.00349]; T. Neumann, J. Phys. Comm. **2**, 9, 095017 (2018), [arXiv:1802.02981].

[64] S. Forte and C. Muselli, JHEP **03**, 122 (2016), [arXiv:1511.05561]; K. Melnikov and A. Penin, JHEP **05**, 172 (2016), [arXiv:1602.09020]; T. Liu and A. Penin, JHEP **11**, 158 (2018), [arXiv:1809.04950].

[65] F. Caola *et al.*, JHEP **09**, 035 (2018), [arXiv:1804.07632].

[66] W. Bizon *et al.*, JHEP **02**, 108 (2018), [arXiv:1705.09127]; X. Chen *et al.*, Phys. Lett. **B788**, 425 (2019), [arXiv:1805.00736].

[67] S. Catani and M. Grazzini, Eur. Phys. J. **C72**, 2013 (2012), [Erratum: Eur. Phys. J. **C72**, 2132 (2012)], [arXiv:1106.4652].

[68] A. Banfi, G. P. Salam and G. Zanderighi, JHEP **06**, 159 (2012), [arXiv:1203.5773]; T. Becher, M. Neubert and D. Wilhelm, JHEP **05**, 110 (2013), [arXiv:1212.2621]; A. Banfi *et al.*, JHEP **04**, 049 (2016), [arXiv:1511.02886]; J. K. L. Michel, P. Pietrulewicz and F. J. Tackmann, JHEP **04**, 142 (2019), [arXiv:1810.12911]; P. F. Monni, L. Rottoli and P. Torrielli (2019), [arXiv:1909.04704].

[69] I. Moult and I. W. Stewart, JHEP **09**, 129 (2014), [arXiv:1405.5534].

[70] W.-Y. Keung and F. J. Petriello, Phys. Rev. **D80**, 013007 (2009), [arXiv:0905.2775]; S. Bühler *et al.*, JHEP **07**, 115 (2012), [arXiv:1204.4415].

[71] LHC Higgs Cross Section Working Group, "Recommended predictions for the boosted-Higgs cross section", Note LHCHXSWG-2019-002, `https://cds.cern.ch/record/2669113`.

[72] V. D. Barger *et al.*, Phys. Rev. **D44**, 1426 (1991).

[73] F. A. Dreyer and A. Karlberg, Phys. Rev. Lett. **117**, 7, 072001 (2016), [arXiv:1606.00840].

[74] T. Han, G. Valencia and S. Willenbrock, Phys. Rev. Lett. **69**, 3274 (1992), [hep-ph/9206246].

[75] T. Liu, K. Melnikov and A. A. Penin (2019), [arXiv:1906.10899].

[76] M. Cacciari *et al.*, Phys. Rev. Lett. **115**, 8, 082002 (2015), [Erratum: Phys. Rev. Lett. **120**, 13,139901 (2018)], [arXiv:1506.02660]; J. Cruz-Martinez *et al.*, Phys. Lett. **B781**, 672 (2018), [arXiv:1802.02445].

[77] M. Rauch and D. Zeppenfeld, Phys. Rev. **D95**, 11, 114015 (2017), [arXiv:1703.05676].

[78] S. L. Glashow, D. V. Nanopoulos and A. Yildiz, Phys. Rev. **D18**, 1724 (1978); T. Han and S. Willenbrock, Phys. Lett. **B273**, 167 (1991); T. Han, G. Valencia, and S. Willenbrock, Phys. Rev. Lett. **69**, 3274 (1992); H. Baer, B. Bailey and J. F. Owens, Phys. Rev. **D47**, 2730 (1993); J. Ohnemus and W. J. Stirling, Phys. Rev. **D47**, 2722 (1993).

[79] A. Stange, W. J. Marciano and S. Willenbrock, Phys. Rev. **D49**, 1354 (1994), [hep-ph/9309294]; A. Stange, W. J. Marciano and S. Willenbrock, Phys. Rev. **D50**, 4491 (1994), [hep-ph/9404247].

[80] M. L. Ciccolini, S. Dittmaier and M. Kramer, Phys. Rev. **D68**, 073003 (2003), [hep-ph/0306234]; A. Denner *et al.*, JHEP **03**, 075 (2012), [arXiv:1112.5142].

[81] R. Hamberg, W. L. van Neerven and T. Matsuura, Nucl. Phys. **B359**, 343 (1991), [Erratum: Nucl. Phys. **B644**, 403 (2002)].

[82] O. Brein, A. Djouadi and R. Harlander, Phys. Lett. **B579**, 149 (2004), [hep-ph/0307206]; L. Altenkamp *et al.*, JHEP **02**, 078 (2013), [arXiv:1211.5015].

[83] O. Brein *et al.*, Eur. Phys. J. **C72**, 1868 (2012), [arXiv:1111.0761].

[84] O. Brein, R.V. Harlander, and T.J. Zirke, Comp. Phys. Comm. **184**, 998 (2013).

[85] A. Denner *et al.*, JHEP **03**, 075 (2012), [arXiv:1112.5142].

[86] G. Ferrera, M. Grazzini, and F. Tramontano, Phys. Rev. Lett. **107**, 152003 (2011).

[87] G. Ferrera, M. Grazzini and F. Tramontano, Phys. Lett. **B740**, 51 (2015), [arXiv:1407.4747]; J. M. Campbell, R. K. Ellis and C. Williams, JHEP **06**, 179 (2016), [arXiv:1601.00658].

[88] W. Astill *et al.*, JHEP **06**, 154 (2016), [arXiv:1603.01620].

[89] F. Caola *et al.*, Phys. Rev. **D97**, 7, 074022 (2018), [arXiv:1712.06954]; R. Gauld *et al.* (2019), [arXiv:1907.05836].

[90] J. M. Butterworth *et al.*, Phys. Rev. Lett. **100**, 242001 (2008), [arXiv:0802.2470].

[91] R. Raitio and W. W. Wada, Phys. Rev. **D19**, 941 (1979); Z. Kunszt, Nucl. Phys. **B247**, 339 (1984); J. F. Gunion, Phys. Lett. **B261**, 510 (1991); W. J. Marciano and F. E. Paige, Phys. Rev. Lett. **66**, 2433 (1991).

[92] W. Beenakker *et al.*, Phys. Rev. Lett. **87**, 201805 (2001), [hep-ph/0107081]; L. Reina and S. Dawson, Phys. Rev. Lett. **87**, 201804 (2001), [hep-ph/0107101]; S. Dawson *et al.*, Phys. Rev. **D67**, 071503 (2003), [hep-ph/0211438]; W. Beenakker *et al.*, Nucl. Phys. **B653**, 151 (2003), [hep-ph/0211352]; S. Dawson *et al.*, Phys. Rev. **D68**, 034022 (2003), [hep-ph/0305087].

[93] Y. Zhang *et al.*, Phys. Lett. **B738**, 1 (2014), [arXiv:1407.1110]; S. Frixione *et al.*, JHEP **09**, 065 (2014), [arXiv:1407.0823].

[94] T. Plehn, G. P. Salam and M. Spannowsky, Phys. Rev. Lett. **104**, 111801 (2010), [arXiv:0910.5472].

[95] R. Frederix *et al.*, Phys. Lett. **B701**, 427 (2011), [arXiv:1104.5613]; M. V. Garzelli *et al.*, EPL **96**, 1, 11001 (2011), [arXiv:1108.0387].

[96] F. Demartin *et al.*, Eur. Phys. J. **C75**, 6, 267 (2015), [arXiv:1504.00611].

[97] K.A. Assamagan *et al.*, [Higgs Working Group, "Physics at TeV Colliders" workshop, Les Houches, 2003], `arXiv:hep-ph/0406152` (2004).

[98] R. V. Harlander and W. B. Kilgore, Phys. Rev. **D68**, 013001 (2003), [hep-ph/0304035]; J. M. Campbell *et al.*, Phys. Rev. **D67**, 095002 (2003), [hep-ph/0204093]; S. Dawson *et al.*, Phys. Rev. Lett. **94**, 031802 (2005), [hep-ph/0408077]; S. Dittmaier, M. Krämer and M. Spira, Phys. Rev. **D70**, 074010 (2004), [hep-ph/0309204]; S. Dawson *et al.*, Phys. Rev. **D69**, 074027 (2004), [hep-ph/0311067].

[99] W. J. Stirling and D. J. Summers, Phys. Lett. **B283**, 411 (1992); F. Maltoni *et al.*, Phys. Rev. **D64**, 094023 (2001), [hep-ph/0106293].

[100] S. Dawson, S. Dittmaier and M. Spira, Phys. Rev. **D58**, 115012 (1998), [hep-ph/9805244].

[101] D. de Florian and J. Mazzitelli, Phys. Rev. Lett. **111**, 201801 (2013), [arXiv:1309.6594].

[102] S. Borowka *et al.*, Phys. Rev. Lett. **117**, 1, 012001 (2016), [Erratum: Phys. Rev. Lett. **117**, 7, 079901 (2016)], [arXiv:1604.06447].

[103] J. Baglio *et al.*, Eur. Phys. J. **C79**, 6, 459 (2019), [arXiv:1811.05692].

[104] M. Cepeda *et al.* (HL/HE WG2 group) (2019), [arXiv:1902.00134].

[105] B.L. Ioffe and V.A. Khoze, Sov. J. Nucl. Phys. **9**, 50 (1978).

[106] D. R. T. Jones and S. T. Petcov, Phys. Lett. **84B**, 440 (1979); R. N. Cahn and S. Dawson, Phys. Lett. **136B**, 196 (1984), [Erratum: Phys. Lett. **138B**, 464 (1984)]; G. L. Kane, W. W. Repko and W. B. Rolnick, Phys. Lett. **148B**, 367 (1984); G. Altarelli, B. Mele and F. Pitolli, Nucl. Phys. **B287**, 205 (1987); W. Kilian, M. Kramer and P. M. Zerwas, Phys. Lett. **B373**, 135 (1996), [hep-ph/9512355].

[107] B. A. Kniehl, Z. Phys. **C55**, 605 (1992); J. Fleischer and F. Jegerlehner, Nucl. Phys. **B216**, 469 (1983); A. Denner *et al.*, Z. Phys. **C56**, 261 (1992); B. A. Kniehl, Int. J. Mod. Phys. **A17**, 1457 (2002), [hep-ph/0112023].

[108] K. J. F. Gaemers and G. J. Gounaris, Phys. Lett. **77B**, 379 (1978); A. Djouadi, J. Kalinowski and P. M. Zerwas, Z. Phys. **C54**, 255 (1992); B. A. Kniehl, F. Madricardo and M. Steinhauser, Phys. Rev. **D66**, 054016 (2002), [hep-ph/0205312]; S. Dittmaier *et al.*, Phys. Lett. **B441**, 383 (1998), [hep-ph/9808433]; S. Dittmaier *et al.*, Phys. Lett. **B478**, 247 (2000), [hep-ph/0002035]; S. Dawson and L. Reina, Phys. Rev. **D59**, 054012 (1999), [hep-ph/9808443].

[109] A. Arbey *et al.*, Eur. Phys. J. **C75**, 8, 371 (2015), [arXiv:1504.01726].

[110] A. Denner *et al.*, Eur. Phys. J. **C71**, 1753 (2011), [arXiv:1107.5909].

[111] A. Djouadi, J. Kalinowski, and M. Spira, Comp. Phys. Comm. **108**, 56 (1998); A. Djouadi *et al.*, `arXiv:1003.1643 [hep-ph]` (2010).

[112] S. G. Gorishnii *et al.*, Mod. Phys. Lett. **A5**, 2703 (1990); S. G. Gorishnii *et al.*, Phys. Rev. **D43**, 1633 (1991); A. L. Kataev and V. T. Kim, Mod. Phys. Lett. **A9**, 1309 (1994); L. R. Surguladze, Phys. Lett. **B341**, 60 (1994), [hep-ph/9405325]; S. A. Larin, T. van Ritbergen and J. A. M. Vermaseren, Phys. Lett. **B362**, 134 (1995), [hep-ph/9506465]; K. G. Chetyrkin and A. Kwiatkowski, Nucl. Phys. **B461**, 3 (1996), [hep-ph/9505358]; K. G. Chetyrkin, Phys. Lett. **B390**, 309 (1997), [hep-ph/9608318]; P. A. Baikov, K. G. Chetyrkin and J. H. Kuhn, Phys. Rev. Lett. **96**, 012003 (2006), [hep-ph/0511063].

[113] J. Fleischer and F. Jegerlehner, Phys. Rev. **D23**, 2001 (1981); D. Yu. Bardin, B. M. Vilensky and P. K. Khristova, Sov. J. Nucl. Phys. **53**, 152 (1991), [Yad. Fiz.53,240(1991)]; A. Dabelstein and W. Hollik, Z. Phys. **C53**, 507 (1992); B. A. Kniehl, Nucl. Phys. **B376**, 3 (1992); A. Djouadi *et al.*, in "In *Munich/Annecy/Hamburg 1991, Proceedings, e+ e- collisions at 500-GeV, pt. A* 11-30," (1991).

[114] T. Inami, T. Kubota and Y. Okada, Z. Phys. **C18**, 69 (1983); K. G. Chetyrkin, B. A. Kniehl and M. Steinhauser, Phys. Rev. Lett. **79**, 353 (1997), [hep-ph/9705240]; P. A. Baikov and K. G. Chetyrkin, Phys. Rev. Lett. **97**, 061803 (2006), [hep-ph/0604194].

[115] H.-Q. Zheng and D.-D. Wu, Phys. Rev. **D42**, 3760 (1990); A. Djouadi *et al.*, Phys. Lett. **B257**, 187 (1991); S. Dawson and R. P. Kauffman, Phys. Rev. **D47**, 1264 (1993); A. Djouadi, M. Spira and P. M. Zerwas, Phys. Lett.

B311, 255 (1993), [hep-ph/9305335]; K. Melnikov and O. I. Yakovlev, Phys. Lett. **B312**, 179 (1993), [hep-ph/9302281]; M. Inoue *et al.*, Mod. Phys. Lett. **A9**, 1189 (1994).

[116] P. Maierhöfer and P. Marquard, Phys. Lett. **B721**, 131 (2013), [arXiv:1212.6233].

[117] U. Aglietti *et al.*, Phys. Lett. **B595**, 432 (2004), [hep-ph/0404071]; G. Degrassi and F. Maltoni, Phys. Lett. **B600**, 255 (2004), [hep-ph/0407249]; S. Actis *et al.*, Phys. Lett. **B670**, 12 (2008), [arXiv:0809.1301]; U. Aglietti *et al.*, Phys. Lett. **B600**, 57 (2004), [hep-ph/0407162]; G. Degrassi and F. Maltoni, Nucl. Phys. **B724**, 183 (2005), [hep-ph/0504137]; U. Aglietti *et al.*, FERMILAB-CONF (2006), [hep-ph/0612172].

[118] A. Abbasabadi *et al.*, Phys. Rev. **D55**, 5647 (1997), [hep-ph/9611209]; A. Abbasabadi and W. W. Repko, Phys. Rev. **D71**, 017304 (2005), [hep-ph/0411152]; A. Abbasabadi and W. W. Repko, JHEP **08**, 048 (2006), [hep-ph/0602087]; D. A. Dicus and W. W. Repko, Phys. Rev. **D87**, 7, 077301 (2013), [arXiv:1302.2159]; L.-B. Chen, C.-F. Qiao and R.-L. Zhu, Phys. Lett. **B726**, 306 (2013), [arXiv:1211.6058]; Y. Sun, H.-R. Chang and D.-N. Gao, JHEP **05**, 061 (2013), [arXiv:1303.2230]; G. Passarino, Phys. Lett. **B727**, 424 (2013), [arXiv:1308.0422].

[119] M. Spira, A. Djouadi and P. M. Zerwas, Phys. Lett. **B276**, 350 (1992).

[120] A. Bredenstein *et al.*, Phys. Rev. **D74**, 013004 (2006), [hep-ph/0604011]; A. Bredenstein *et al.*, JHEP **02**, 080 (2007), [hep-ph/0611234]; A. Bredenstein *et al.*, `Prophecy4f`: A Monte Carlo generator for a proper description of the Higgs decay into 4 fermions, `http://omnibus.uni-freiburg.de/~sd565/programs/prophecy4f/prophecy4f.html`.

[121] A. Ghinculov, Phys. Lett. **B337**, 137 (1994), [Erratum: Phys. Lett. **B346**, 426 (1995)], [hep-ph/9405394]; L. Durand, B. A. Kniehl and K. Riesselmann, Phys. Rev. **D51**, 5007 (1995), [hep-ph/9412311]; L. Durand, K. Riesselmann and B. A. Kniehl, Phys. Rev. Lett. **72**, 2534 (1994), [Erratum: Phys. Rev. Lett. **74**, 1699 (1995)].

[122] R. Barate *et al.* (LEP Working Group for Higgs boson searches, ALEPH, DELPHI, L3, OPAL), Phys. Lett. **B565**, 61 (2003), [hep-ex/0306033].

[123] M. Tanabashi *et al.* (Particle Data Group), Phys. Rev. **D98**, 3, 030001 (2018).

[124] Y. L. Dokshitzer, S. I. Troian and V. A. Khoze, Sov. J. Nucl. Phys. **46**, 712 (1987), [Yad. Fiz.46,1220(1987)].

[125] ATLAS Collaboration, ATLAS-CONF-2017-045 (2017).

[126] CMS Collaboration, CMS-PAS-HIG-19-001 (2019).

[127] G. Aad *et al.* (ATLAS, CMS), Phys. Rev. Lett. **114**, 191803 (2015), [arXiv:1503.07589].

[128] ATLAS Collaboration, ATLAS-CONF-2019-029 (2019).

[129] A. M. Sirunyan *et al.* (CMS), JHEP **11**, 185 (2018), [arXiv:1804.02716].

[130] A. M. Sirunyan *et al.* (CMS), JHEP **11**, 047 (2017), [arXiv:1706.09936].

[131] ATLAS Collaboration, ATLAS-CONF-2019-025 (2019).

[132] M. Aaboud *et al.* (ATLAS), Phys. Lett. **B784**, 345 (2018), [arXiv:1806.00242].

[133] CMS Collaboration, CMS-PAS-HIG-18-029 (2019).

[134] ATLAS Collaboration, ATL-PHYS-PUB-2016-009 (2016).

[135] M. Dittmar and H. K. Dreiner, Phys. Rev. **D55**, 167 (1997), [hep-ph/9608317].

[136] G. Aad *et al.* (ATLAS), JHEP **08**, 137 (2015), [arXiv:1506.06641].

[137] ATLAS Collaboration, ATLAS-CONF-2016-112 (2016).

[138] M. Aaboud *et al.* (ATLAS), Phys. Lett. **B789**, 508 (2019), [arXiv:1808.09054].

[139] A. M. Sirunyan *et al.* (CMS), Phys. Lett. **B791**, 96 (2019), [arXiv:1806.05246].

[140] G. Aad *et al.* (ATLAS), JHEP **04**, 117 (2015), [arXiv:1501.04943].

[141] ATLAS and CMS Collaboration, ATLAS-CONF-2015-044 and CMS-PAS-HIG-15-002 (2015).

[142] M. Aaboud *et al.* (ATLAS), Phys. Rev. **D99**, 072001 (2019), [arXiv:1811.08856].

[143] A. M. Sirunyan *et al.* (CMS), Phys. Lett. **B779**, 283 (2018), [arXiv:1708.00373].

[144] A. M. Sirunyan *et al.* (CMS), JHEP **06**, 093 (2019), [arXiv:1809.03590].

[145] CMS Collaboration, CMS-PAS-HIG-18-032 (2019).

[146] T. Aaltonen *et al.* (CDF, D0), Phys. Rev. Lett. **109**, 071804 (2012), [arXiv:1207.6436].

[147] M. Aaboud *et al.* (ATLAS), Phys. Lett. **B786**, 59 (2018), [arXiv:1808.08238].

[148] A. M. Sirunyan *et al.* (CMS), Phys. Rev. Lett. **121**, 12, 121801 (2018), [arXiv:1808.08242].

[149] M. Aaboud *et al.* (ATLAS), JHEP **05**, 141 (2019), [arXiv:1903.04618].

[150] LHCb Collaboration, LHCb-CONF-2016-006, CERN-LHCb-CONF-2016-006 (2016).

[151] M. Aaboud *et al.* (ATLAS), JHEP **11**, 112 (2016), [arXiv:1606.02181].

[152] V. Khachatryan *et al.* (CMS), Phys. Rev. **D92**, 3, 032008 (2015), [arXiv:1506.01010].

[153] M. Aaboud *et al.* (ATLAS), Phys. Rev. **D98**, 5, 052003 (2018), [arXiv:1807.08639]; CMS Collaboration, CMS-PAS-HIG-16-003 (2019).

[154] E. Gabrielli *et al.*, Nucl. Phys. **B781**, 64 (2007), [hep-ph/0702119].

[155] ATLAS Collaboration, ATLAS-CONF-2018-052 (2018).

[156] A. M. Sirunyan *et al.* (CMS), Phys. Rev. Lett. **120**, 7, 071802 (2018), [arXiv:1709.05543].

[157] M. Cacciari, G. P. Salam and G. Soyez, JHEP **04**, 063 (2008), [arXiv:0802.1189].

[158] V. Khachatryan *et al.* (CMS), Eur. Phys. J. **C75**, 6, 251 (2015), [arXiv:1502.02485].

[159] G. Aad *et al.* (ATLAS), Phys. Lett. **B749**, 519 (2015), [arXiv:1506.05988].

[160] M. Aaboud *et al.* (ATLAS), Phys. Lett. **B784**, 173 (2018), [arXiv:1806.00425]; A. M. Sirunyan *et al.* (CMS), Phys. Rev. Lett. **120**, 23, 231801 (2018), [arXiv:1804.02610].

[161] ATLAS Collaboration, ATLAS-CONF-2019-004 (2019).

[162] CMS Collaboration, CMS-PAS-HIG-18-018 (2019).

[163] CMS Collaboration, CMS-PAS-HIG-18-030 (2019).

[164] ATLAS Collaboration, ATLAS-CONF-2017-077 (2017); A. M. Sirunyan *et al.* (CMS), JHEP **08**, 066 (2018), [arXiv:1803.05485]; CMS Collaboration, CMS-PAS-HIG-18-019 (2018); ATLAS Collaboration, ATLAS-CONF-2019-045 (2019).

[165] M. Farina *et al.*, JHEP **05**, 022 (2013), [arXiv:1211.3736].

[166] CMS Collaboration, CMS-PAS-HIG-17-005 (2017).

[167] CMS Collaboration, CMS-PAS-HIG-16-019 (2016).

[168] A. M. Sirunyan *et al.* (CMS), Phys. Rev. **D99**, 9, 092005 (2019), [arXiv:1811.09696].

[169] G. Aad *et al.* (ATLAS), JHEP **12**, 061 (2015), [arXiv:1509.06047].

[170] V. Khachatryan *et al.* (CMS), JHEP **02**, 079 (2017), [arXiv:1610.04857].

[171] ATLAS Collaboration, JHEP **129**, 010 (2017).

[172] CMS Collaboration, CMS-PAS-TOP-2017-003 (2017).

[173] G. Aad *et al.* (ATLAS) (2019), [arXiv:1906.02025].

[174] A. M. Sirunyan *et al.* (CMS), Phys. Rev. Lett. **122**, 12, 121803 (2019), [arXiv:1811.09689].

[175] V. Khachatryan *et al.* (CMS), Phys. Lett. **B753**, 341 (2016), [arXiv:1507.03031].

[176] M. Aaboud *et al.* (ATLAS), JHEP **10**, 112 (2017), [arXiv:1708.00212].

[177] A. M. Sirunyan *et al.* (CMS), JHEP **11**, 152 (2018), [arXiv:1806.05996].

[178] ATLAS Collaboration, ATLAS-CONF-2019-028 (2019).

[179] A. M. Sirunyan *et al.* (CMS), Phys. Rev. Lett. **122**, 2, 021801 (2019), [arXiv:1807.06325].

[180] ATLAS Collaboration, ATLAS-CONF-2019-037 (2019).

[181] V. Khachatryan *et al.* (CMS), Phys. Lett. **B749**, 337 (2015), [arXiv:1502.07400].

[182] G. Aad *et al.* (ATLAS), JHEP **11**, 211 (2015), [arXiv:1508.03372].

[183] G. Aad *et al.* (ATLAS), Eur. Phys. J. **C77**, 2, 70 (2017), [arXiv:1604.07730].

[184] CMS Collaboration, CMS-PAS-HIG-17-001 (2017).

[185] V. Khachatryan *et al.* (CMS), Phys. Lett. **B763**, 472 (2016), [arXiv:1607.03561].

[186] R. Harnik, J. Kopp and J. Zupan, JHEP **03**, 026 (2013), [arXiv:1209.1397].

[187] G. Aad *et al.* (ATLAS) (2019), [arXiv:1907.06131].

[188] A. M. Sirunyan *et al.* (CMS), JHEP **06**, 001 (2018), [arXiv:1712.07173].

[189] C. Delaunay *et al.*, Phys. Rev. **D89**, 3, 033014 (2014), [arXiv:1310.7029].

[190] M. Aaboud *et al.* (ATLAS), Phys. Rev. Lett. **120**, 21, 211802 (2018), [arXiv:1802.04329].

[191] CMS Collaboration, CMS-PAS-HIG-18-031 (2019).

[192] G. Isidori, A. V. Manohar and M. Trott, Phys. Lett. **B728**, 131 (2014), [arXiv:1305.0663]; G. T. Bodwin *et al.*, Phys. Rev. **D88**, 5, 053003 (2013), [arXiv:1306.5770]; M. König and M. Neubert, JHEP **08**, 012 (2015), [arXiv:1505.03870].

[193] G. Aad *et al.* (ATLAS), Phys. Rev. Lett. **114**, 12, 121801 (2015), [arXiv:1501.03276].

[194] M. Aaboud *et al.* (ATLAS), Phys. Rev. Lett. **117**, 11, 111802 (2016), [arXiv:1607.03400].

[195] A. M. Sirunyan *et al.* (CMS), Phys. Lett. **B797**, 134811 (2019), [arXiv:1905.10408].

[196] A. Djouadi *et al.*, Eur. Phys. J. **C73**, 6, 2455 (2013), [arXiv:1205.3169].

[197] O. J. P. Eboli and D. Zeppenfeld, Phys. Lett. **B495**, 147 (2000), [hep-ph/0009158].

[198] M. Aaboud *et al.* (ATLAS), Phys. Lett. **B793**, 499 (2019), [arXiv:1809.06682].

[199] M. Aaboud *et al.* (ATLAS), Phys. Lett. **B776**, 318 (2018), [arXiv:1708.09624].

[200] M. Aaboud *et al.* (ATLAS), JHEP **10**, 180 (2018), [arXiv:1807.11471].

[201] M. Aaboud *et al.* (ATLAS), Phys. Rev. Lett. **122**, 23, 231801 (2019), [arXiv:1904.05105].

[202] A. M. Sirunyan *et al.* (CMS), Eur. Phys. J. **C78**, 4, 291 (2018), [arXiv:1711.00431].

[203] A. M. Sirunyan *et al.* (CMS), Phys. Rev. **D97**, 9, 092005 (2018), [arXiv:1712.02345].

[204] A. M. Sirunyan *et al.* (CMS), Phys. Lett. **B793**, 520 (2019), [arXiv:1809.05937].

[205] CMS Collaboration, CMS-PAS-HIG-18-008 (2019).

[206] M. J. Strassler and K. M. Zurek, Phys. Lett. **B651**, 374 (2007), [hep-ph/0604261]; M. J. Strassler and K. M. Zurek, Phys. Lett. **B661**, 263 (2008), [hep-ph/0605193].

[207] T. Han *et al.*, JHEP **07**, 008 (2008), [arXiv:0712.2041].

[208] A. Falkowski *et al.*, Phys. Rev. Lett. **105**, 241801 (2010), [arXiv:1007.3496].

[209] G. Aad *et al.* (ATLAS) (2019), [arXiv:1909.01246].

[210] CMS Collaboration, CMS-PAS-EXO-19-007 (2019).

[211] D. Tucker-Smith and N. Weiner, Phys. Rev. **D64**, 043502 (2001), [hep-ph/0101138].

[212] S. Chatrchyan *et al.* (CMS), Phys. Lett. **B726**, 564 (2013), [arXiv:1210.7619].

[213] G. Aad *et al.* (ATLAS) (2019), [arXiv:1909.02845].

[214] A. M. Sirunyan *et al.* (CMS), Eur. Phys. J. **C79**, 5, 421 (2019), [arXiv:1809.10733].

[215] C. Patrignani *et al.* (Particle Data Group), Chin. Phys. **C40**, 10, 100001 (2016).

[216] G. Aad *et al.* (ATLAS), Eur. Phys. J. **C76**, 1, 6 (2016), [arXiv:1507.04548].

[217] L. D. Landau, Dokl. Akad. Nauk Ser. Fiz. **60**, 2, 207 (1948); C.-N. Yang, Phys. Rev. **77**, 242 (1950).

[218] S. Bolognesi *et al.*, Phys. Rev. **D86**, 095031 (2012), [arXiv:1208.4018].

[219] G. Aad *et al.* (ATLAS), Eur. Phys. J. **C75**, 10, 476 (2015), [Erratum: Eur. Phys. J. **C76**, 3, 152 (2016)], [arXiv:1506.05669].

[220] V. Khachatryan *et al.* (CMS), Phys. Rev. **D92**, 1, 012004 (2015), [arXiv:1411.3441]; G. Aad *et al.* (ATLAS), Phys. Lett. **B726**, 120 (2013), [arXiv:1307.1432].

[221] P. Artoisenet *et al.*, JHEP **11**, 043 (2013), [arXiv:1306.6464].

[222] J. Ellis *et al.*, JHEP **11**, 134 (2012), [arXiv:1208.6002].

[223] D0 Collaboration, Note 6387-CONF (2013).

[224] D0 Collaboration, Note 6406-CONF (2013).

[225] J. C. Collins and D. E. Soper, Phys. Rev. **D16**, 2219 (1977).

[226] A. De Rujula *et al.*, Phys. Rev. **D82**, 013003 (2010), [arXiv:1001.5300].

[227] ATLAS Collaboration, ATLAS-CONF-2017-043 (2017).

[228] A. M. Sirunyan *et al.* (CMS), Phys. Rev. **D99**, 11, 112003 (2019), [arXiv:1901.00174].

[229] A. M. Sirunyan *et al.* (CMS), Submitted to: Phys. Rev. (2019), [arXiv:1903.06973].

[230] G. Aad *et al.* (ATLAS), Eur. Phys. J. **C76**, 12, 658 (2016), [arXiv:1602.04516].

[231] N. Kauer and G. Passarino, JHEP **08**, 116 (2012), [arXiv:1206.4803].

[232] V. Khachatryan *et al.* (CMS), JHEP **09**, 051 (2016), [arXiv:1605.02329].

[233] G. Aad *et al.* (ATLAS), Eur. Phys. J. **C75**, 7, 335 (2015), [arXiv:1503.01060].

[234] M. Aaboud *et al.* (ATLAS), Phys. Lett. **B786**, 223 (2018), [arXiv:1808.01191].

[235] G. Aad *et al.* (ATLAS), Phys. Rev. **D90**, 5, 052004 (2014), [arXiv:1406.3827].

[236] CMS Collaboration, CMS-PAS-HIG-16-041 (2017).

[237] L. J. Dixon and M. S. Siu, Phys. Rev. Lett. **90**, 252001 (2003), [hep-ph/0302233]; S. P. Martin, Phys. Rev. **D86**, 073016 (2012), [arXiv:1208.1533]; L. J. Dixon and Y. Li, Phys. Rev. Lett. **111**, 111802 (2013), [arXiv:1305.3854].

[238] ATLAS Collaboration, ATL-PHYS-PUB-2013-014 (2013).

[239] J. Campbell *et al.*, Phys. Rev. Lett. **119**, 18, 181801 (2017), [Addendum: Phys. Rev. Lett.119,19,199901(2017)], [arXiv:1704.08259].

[240] ATLAS Collaboration, ATL-PHYS-PUB-2014-016 (2014).

[241] F. Caola and K. Melnikov, Phys. Rev. **D88**, 054024 (2013), [arXiv:1307.4935]; J. M. Campbell, R. K. Ellis and C. Williams, JHEP **04**, 060 (2014), [arXiv:1311.3589]; J. M. Campbell, R. K. Ellis and C. Williams, Phys. Rev. **D89**, 5, 053011 (2014), [arXiv:1312.1628].

[242] C. Englert and M. Spannowsky, Phys. Rev. **D90**, 053003 (2014), [arXiv:1405.0285].

[243] A. Azatov *et al.*, Zh. Eksp. Teor. Fiz. **147**, 410 (2015), [J. Exp. Theor. Phys.120,354(2015)], [arXiv:1406.6338]; A. Azatov *et al.*, JHEP **09**, 123 (2016), [arXiv:1608.00977].

[244] A. David *et al.* (LHC Higgs Cross Section Working Group), "LHC HXSWG interim recommendations to explore the coupling structure of a Higgs-like particle," (2012), [arXiv:1209.0040].

[245] M. Dührssen, "Prospects for the measurement of Higgs boson coupling parameters in the mass range from 110–190 GeV," (2003); M. Duhrssen *et al.*, Phys. Rev. **D70**, 113009 (2004), [hep-ph/0406323]; R. Lafaye *et al.*, JHEP **08**, 009 (2009), [arXiv:0904.3866].

[246] J. R. Espinosa *et al.*, JHEP **05**, 097 (2012), [arXiv:1202.3697]; A. Azatov, R. Contino and J. Galloway, JHEP **04**, 127 (2012), [Erratum: JHEP **04**, 140 (2013)], [arXiv:1202.3415]; D. Carmi *et al.*, JHEP **07**, 136 (2012), [arXiv:1202.3144]; J. R. Espinosa *et al.*, JHEP **12**, 045 (2012), [arXiv:1207.1717].

[247] M. Gonzalez-Alonso *et al.*, Eur. Phys. J. **C75**, 128 (2015), [arXiv:1412.6038]; A. Greljo *et al.*, Eur. Phys. J. **C76**, 3, 158 (2016), [arXiv:1512.06135].

[248] G. F. Giudice *et al.*, JHEP **06**, 045 (2007), [hep-ph/0703164].

[249] S. Willenbrock and C. Zhang, Ann. Rev. Nucl. Part. Sci. **64**, 83 (2014), [arXiv:1401.0470]; I. Brivio and M. Trott, Phys. Rept. **793**, 1 (2019), [arXiv:1706.08945]; S. Dawson, C. Englert and T. Plehn, Phys. Rept. **816**, 1 (2019), [arXiv:1808.01324]; T. Cohen, PoS **TASI2018**, 011 (2019), [arXiv:1903.03622].

[250] F. Feruglio, Int. J. Mod. Phys. **A8**, 4937 (1993), [hep-ph/9301281]; G. Buchalla, O. Catà and C. Krause, Nucl. Phys. **B880**, 552 (2014), [Erratum: Nucl. Phys. **B913**, 475 (2016)], [arXiv:1307.5017]; R. Alonso *et al.*, Phys. Lett. **B722**, 330 (2013), [Erratum: Phys. Lett. **B726**, 926 (2013)], [arXiv:1212.3305]; A. V. Manohar, in "Les Houches summer school: EFT in Particle Physics and Cosmology Les Houches, Chamonix Valley, France, July 3-28, 2017," (2018), [arXiv:1804.05863]; I. Brivio *et al.*, JHEP **03**, 024 (2014), [arXiv:1311.1823].

[251] J. de Blas *et al.*, JHEP **03**, 109 (2018), [arXiv:1711.10391].

[252] A. Manohar and H. Georgi, Nucl. Phys. **B234**, 189 (1984); M. A. Luty, Phys. Rev. **D57**, 1531 (1998), [hep-ph/9706235]; D. Liu *et al.*, JHEP **11**, 141 (2016), [arXiv:1603.03064].

[253] W. Buchmuller and D. Wyler, Nucl. Phys. **B268**, 621 (1986).

[254] C. J. C. Burges and H. J. Schnitzer, Nucl. Phys. **B228**, 464 (1983); C. N. Leung, S. T. Love and S. Rao, Z. Phys. **C31**, 433 (1986).

[255] B. Grzadkowski *et al.*, JHEP **10**, 085 (2010), [arXiv:1008.4884].

[256] L. Lehman and A. Martin, JHEP **02**, 081 (2016), [arXiv:1510.00372]; B. Henning *et al.*, JHEP **08**, 016 (2017), [arXiv:1512.03433].

[257] C. Hays *et al.*, JHEP **02**, 123 (2019), [arXiv:1808.00442].

[258] R. Alonso *et al.*, JHEP **04**, 159 (2014), [arXiv:1312.2014].

[259] A. Falkowski, LHCHXSWG-INT-2015-001 (2015); A. Falkowski, Pramana **87**, 3, 39 (2016), [arXiv:1505.00046].

[260] A. M. Sirunyan *et al.* (CMS), Phys. Lett. **B792**, 369 (2019), [arXiv:1812.06504].

[261] M. Aaboud *et al.* (ATLAS), Phys. Rev. **D98**, 052005 (2018), [arXiv:1802.04146].

[262] F. Maltoni *et al.* (2019), [arXiv:1906.12310].

[263] R. S. Gupta, A. Pomarol and F. Riva, Phys. Rev. **D91**, 3, 035001 (2015), [arXiv:1405.0181].

[264] B. A. Kniehl and M. Spira, Z. Phys. **C69**, 77 (1995), [hep-ph/9505225].

[265] R. Contino *et al.*, JHEP **07**, 035 (2013), [arXiv:1303.3876].

[266] A. Azatov and J. Galloway, Phys. Rev. **D85**, 055013 (2012), [arXiv:1110.5646].

[267] G. Isidori and M. Trott, JHEP **02**, 082 (2014), [arXiv:1307.4051]; A. Pomarol and F. Riva, JHEP **01**, 151 (2014), [arXiv:1308.2803].

[268] J. Ellis, V. Sanz and T. You, JHEP **07**, 036 (2014), [arXiv:1404.3667]; A. Biekötter *et al.*, Phys. Rev. **D91**, 055029 (2015), [arXiv:1406.7320].

[269] LHC Higgs Cross Section Working Group, `https://twiki.cern.ch/twiki/bin/view/LHCPhysics/LHCHXSWG2KAPPA`.

[270] ATLAS and C. Collaboration (CMS) (2015).

[271] M. Reece, New J. Phys. **15**, 043003 (2013), [arXiv:1208.1765].

[272] ATLAS Collaboration, ATLAS-CONF-2019-032 (2019).

[273] G. Aad *et al.* (ATLAS), Phys. Lett. **B753**, 69 (2016), [arXiv:1508.02507].

[274] N. Berger *et al.* (2019), [arXiv:1906.02754].

[275] CMS Collaboration, CMS-PAS-HIG-16-040 (2017).

[276] ATLAS Collaboration, ATLAS-CONF-2018-028 (2018).

[277] ATLAS Collaboration, CMS-PAS-HIG-19-001 (2019).

[278] M. McCullough, Phys. Rev. **D90**, 1, 015001 (2014), [Erratum: Phys. Rev. **D92**, 3, 039903 (2015)], [arXiv:1312.3322].

[279] G. Degrassi *et al.*, JHEP **12**, 080 (2016), [arXiv:1607.04251].

[280] M. Gorbahn and U. Haisch, JHEP **10**, 094 (2016), [arXiv:1607.03773].

[281] ATLAS Collaboration, ATL-PHYS-PUB-2019-009 (2019).

[282] F. Bishara *et al.*, Phys. Rev. Lett. **118**, 12, 121801 (2017), [arXiv:1606.09253].

[283] T. A. collaboration (ATLAS) (2019).

[284] ATLAS Collaboration, ATLAS-CONF-2019-049 (2019).

[285] S. Di Vita *et al.*, JHEP **09**, 069 (2017), [arXiv:1704.01953]; F. Maltoni *et al.*, Eur. Phys. J. **C77**, 12, 887 (2017), [arXiv:1709.08649].

[286] B. Di Micco *et al.* (2019), [arXiv:1910.00012].

[287] J. Parsons, and A. Pomarol, *Extra Dimenions*, in this volume.

[288] S. Weinberg, Phys. Rev. **D13**, 974 (1976), [Addendum: Phys. Rev.D19,1277(1979)]; L. Susskind, Phys. Rev. **D20**, 2619 (1979); For a review, see C. T. Hill and E. H. Simmons, Phys. Reports **381**, 235 (2003) [Erratum: 390, 553 (2004)], [arXiv:hep-ph/0203079].

[289] Z. Chacko, R. Franceschini and R. K. Mishra, JHEP **04**, 015 (2013), [arXiv:1209.3259].

[290] L. E. Ibanez and G. G. Ross, Phys. Lett. **110B**, 215 (1982); L. E. Ibanez, Phys. Lett. **118B**, 73 (1982); J. R. Ellis, D. V. Nanopoulos and K. Tamvakis, Phys. Lett. **121B**, 123 (1983); L. Alvarez-Gaume, J. Polchinski and M. B. Wise, Nucl. Phys. **B221**, 495 (1983).

[291] S. Dimopoulos and G. F. Giudice, Phys. Lett. **B357**, 573 (1995), [hep-ph/9507282]; M. Papucci, J. T. Ruderman and A. Weiler, JHEP **09**, 035 (2012), [arXiv:1110.6926].

[292] ATLAS Collaboration, `https://twiki.cern.ch/twiki/bin/view/AtlasPublic/Publications`; CMS Collaboration, `http://cms-results.web.cern.ch/cms-results/public-results/publications/SUS/STOP.html`.

[293] J. Mrazek *et al.*, Nucl. Phys. **B853**, 1 (2011), [arXiv:1105.5403].

[294] D. B. Kaplan, Nucl. Phys. **B365**, 259 (1991).

[295] G. Panico *et al.*, JHEP **03**, 051 (2013), [arXiv:1210.7114].

[296] H. E. Haber and G. L. Kane, Phys. Rept. **117**, 75 (1985).

[297] A. Djouadi, Phys. Rept. **459**, 1 (2008), [hep-ph/0503173].

[298] S. Heinemeyer, W. Hollik and G. Weiglein, Phys. Rept. **425**, 265 (2006), [hep-ph/0412214].

[299] P. Draper, G. Lee and C. E. M. Wagner, Phys. Rev. **D89**, 5, 055023 (2014), [arXiv:1312.5743].

[300] J. F. Gunion and H. E. Haber, Phys. Rev. **D67**, 075019 (2003), [hep-ph/0207010].

[301] H. E. Haber and Y. Nir, Nucl. Phys. **B335**, 363 (1990).

[302] E. L. Berger *et al.*, Phys. Rev. **D66**, 095001 (2002), [hep-ph/0205342].

[303] P. Bechtle *et al.*, Eur. Phys. J. **C77**, 2, 67 (2017), [arXiv:1608.00638].

[304] E. Bagnaschi *et al.*, Eur. Phys. J. **C79**, 7, 617 (2019), [arXiv:1808.07542].

[305] A. Djouadi, J. Kalinowski and P. M. Zerwas, Z. Phys. **C57**, 569 (1993).

[306] G. Lee and C. E. M. Wagner, Phys. Rev. **D92**, 7, 075032 (2015), [arXiv:1508.00576].

[307] D. Dicus *et al.*, Phys. Rev. **D59**, 094016 (1999), [hep-ph/9811492].

[308] M. Carena *et al.*, JHEP **07**, 091 (2012), [arXiv:1203.1041].

[309] A. A. Barrientos Bendezu and B. A. Kniehl, Phys. Rev. **D64**, 035006 (2001), [hep-ph/0103018].

[310] LHC Higgs Cross Section Working Group, `https://twiki.cern.ch/twiki/bin/view/LHCPhysics/LHCHXSWGMSSMCharged`.

[311] A. Djouadi, J. Ellis and J. Quevillon, JHEP **07**, 105 (2016), [arXiv:1605.00542]; M. Carena and Z. Liu, JHEP **11**, 159 (2016), [arXiv:1608.07282].

[312] M. Carena *et al.*, Eur. Phys. J. **C26**, 601 (2003), [hep-ph/0202167]; M. Carena *et al.*, Eur. Phys. J. **C73**, 9, 2552 (2013), [arXiv:1302.7033].

[313] H. Bahl, S. Liebler and T. Stefaniak, Eur. Phys. J. **C79**, 3, 279 (2019), [arXiv:1901.05933].

[314] L. Maiani, A. D. Polosa and V. Riquer, Phys. Lett. **B718**, 465 (2012), [arXiv:1209.4816]; A. Djouadi and J. Quevillon, JHEP **10**, 028 (2013), [arXiv:1304.1787]; A. Djouadi *et al.*, Eur. Phys. J. **C73**, 2650 (2013), [arXiv:1307.5205].

[315] M. Carena *et al.*, Phys. Rev. **D91**, 3, 035003 (2015), [arXiv:1410.4969].

[316] M. Carena *et al.*, JHEP **04**, 015 (2014), [arXiv:1310.2248]; K. Blum, R. T. D'Agnolo and J. Fan, JHEP **01**, 057 (2013), [arXiv:1206.5303]; A. Djouadi *et al.*, JHEP **06**, 168 (2015), [arXiv:1502.05653].

[317] R. S. Chivukula and H. Georgi, Phys. Lett. **B188**, 99 (1987); L. J. Hall and L. Randall, Phys. Rev. Lett. **65**, 2939 (1990); A. J. Buras *et al.*, Phys. Lett. **B500**, 161 (2001), [hep-ph/0007085]; G. D'Ambrosio *et al.*, Nucl. Phys. **B645**, 155 (2002), [hep-ph/0207036].

[318] L. J. Hall, J. D. Lykken and S. Weinberg, Phys. Rev. **D27**, 2359 (1983); J. E. Kim and H. P. Nilles, Phys. Lett. **138B**, 150 (1984); G. F. Giudice and A. Masiero, Phys. Lett. **B206**, 480 (1988).

[319] U. Ellwanger, C. Hugonie and A. M. Teixeira, Phys. Rept. **496**, 1 (2010), [arXiv:0910.1785].

[320] P. Fayet, Nucl. Phys. **B90**, 104 (1975).

[321] C. Panagiotakopoulos and K. Tamvakis, Phys. Lett. **B469**, 145 (1999), [hep-ph/9908351]; A. Dedes *et al.*, Phys. Rev. **D63**, 055009 (2001), [hep-ph/0009125]; A. Menon, D. E. Morrissey and C. E. M. Wagner, Phys. Rev. **D70**, 035005 (2004), [hep-ph/0404184].

[322] M. Cvetic *et al.*, Phys. Rev. **D56**, 2861 (1997), [Erratum: Phys. Rev. **D58**, 119905 (1998)], [hep-ph/9703317]; P. Langacker and J. Wang, Phys. Rev. **D58**, 115010 (1998), [hep-ph/9804428].

[323] J. Erler, P. Langacker and T.-j. Li, Phys. Rev. **D66**, 015002 (2002), [hep-ph/0205001]; T. Han, P. Langacker and B. McElrath, Phys. Rev. **D70**, 115006 (2004), [hep-ph/0405244]; V. Barger *et al.*, Phys. Rev. **D73**, 115010 (2006), [hep-ph/0603247].

[324] V. Barger, P. Langacker and G. Shaughnessy, Phys. Rev. **D75**, 055013 (2007), [hep-ph/0611239].

[325] B. A. Dobrescu, G. L. Landsberg and K. T. Matchev, Phys. Rev. **D63**, 075003 (2001), [hep-ph/0005308]; R. Dermisek and J. F. Gunion, Phys. Rev. Lett. **95**, 041801 (2005), [hep-ph/0502105].

[326] O. J. P. Eboli and D. Zeppenfeld, Phys. Lett. **B495**, 147 (2000), [hep-ph/0009158]; H. Davoudiasl, T. Han and H. E. Logan, Phys. Rev. **D71**, 115007 (2005), [hep-ph/0412269].

[327] J.-J. Cao *et al.*, JHEP **03**, 086 (2012), [arXiv:1202.5821].

[328] LHC Higgs Cross Section Working Group, Beyond the Standard Model Higgs – NMSSM, `https://twiki.cern.ch/twiki/bin/view/LHCPhysics/LHCHXSWGNMSSM`.

[329] M. Carena *et al.*, Phys. Rev. **D93**, 3, 035013 (2016), [arXiv:1510.09137].

[330] P. Batra *et al.*, JHEP **02**, 043 (2004), [hep-ph/0309149].

[331] R. Huo *et al.*, Phys. Rev. **D87**, 5, 055011 (2013), [arXiv:1212.0560].

[332] J. Engel, M. J. Ramsey-Musolf and U. van Kolck, Prog. Part. Nucl. Phys. **71**, 21 (2013), [arXiv:1303.2371].

[333] S. Dimopoulos and S. D. Thomas, Nucl. Phys. **B465**, 23 (1996), [hep-ph/9510220]; S. D. Thomas, Int. J. Mod. Phys. **A13**, 2307 (1998), [hep-ph/9803420].

[334] A. Pilaftsis and C. E. M. Wagner, Nucl. Phys. **B553**, 3 (1999), [hep-ph/9902371].

[335] M. Frank *et al.*, JHEP **02**, 047 (2007), [hep-ph/0611326].

[336] M. Carena *et al.*, Nucl. Phys. **B586**, 92 (2000), [hep-ph/0003180].

[337] B. Li and C. E. M. Wagner, Phys. Rev. **D91**, 095019 (2015), [arXiv:1502.02210].

[338] M. D. Goodsell and F. Staub, Eur. Phys. J. **C77**, 1, 46 (2017), [arXiv:1604.05335]; A. Chakraborty *et al.*, Phys. Rev. **D90**, 5, 055005 (2014), [arXiv:1301.2745]; M. Carena *et al.*, JHEP **02**, 123 (2016), [arXiv:1512.00437].

[339] J. F. Gunion and H. E. Haber, Phys. Rev. **D67**, 075019 (2003), [hep-ph/0207010]; G. C. Branco *et al.*, Phys. Rept. **516**, 1 (2012), [arXiv:1106.0034].

[340] N. G. Deshpande and E. Ma, Phys. Rev. **D18**, 2574 (1978).

[341] A. Goudelis, B. Herrmann and O. Stål, JHEP **09**, 106 (2013), [arXiv:1303.3010].

[342] C. D. Froggatt and H. B. Nielsen, Nucl. Phys. **B147**, 277 (1979).

[343] K. S. Babu and S. Nandi, Phys. Rev. **D62**, 033002 (2000), [hep-ph/9907213]; G. F. Giudice and O. Lebedev, Phys. Lett. **B665**, 79 (2008), [arXiv:0804.1753].

[344] E. Accomando *et al.*, CERN Report **2006-009** (2006), [hep-ph/0608079].

[345] T. Robens and T. Stefaniak, Eur. Phys. J. **C75**, 104 (2015), [arXiv:1501.02234].

[346] S. L. Glashow and S. Weinberg, Phys. Rev. **D15**, 1958 (1977); E. A. Paschos, Phys. Rev. **D15**, 1966 (1977).

[347] G. C. Branco, W. Grimus and L. Lavoura, Phys. Lett. **B380**, 119 (1996), [hep-ph/9601383]; F. J. Botella, G. C. Branco and M. N. Rebelo, Phys. Lett. **B687**, 194 (2010), [arXiv:0911.1753].

[348] J. Schechter and J. W. F. Valle, Phys. Rev. **D22**, 2227 (1980); T. P. Cheng and L.-F. Li, Phys. Rev. **D22**, 2860 (1980).

[349] H. Georgi and M. Machacek, Nucl. Phys. **B262**, 463 (1985); M. S. Chanowitz and M. Golden, Phys. Lett. **165B**, 105 (1985); J. F. Gunion, R. Vega and J. Wudka, Phys. Rev. **D42**, 1673 (1990).

[350] P. Nath *et al.*, Nucl. Phys. Proc. Suppl. **200-202**, 185 (2010), [arXiv:1001.2693].

[351] J. Garayoa and T. Schwetz, JHEP **03**, 009 (2008), [arXiv:0712.1453].

[352] H. E. Haber and H. E. Logan, Phys. Rev. **D62**, 015011 (2000), [hep-ph/9909335]; J. F. Gunion, R. Vega and J. Wudka, Phys. Rev. **D43**, 2322 (1991); S. Kanemura and K. Yagyu, Phys. Rev. **D85**, 115009 (2012), [arXiv:1201.6287].

[353] I. Low and J. Lykken, JHEP **10**, 053 (2010), [arXiv:1005.0872]; I. Low, J. Lykken and G. Shaughnessy, Phys. Rev. **D86**, 093012 (2012), [arXiv:1207.1093].

[354] H. E. Logan and M.-A. Roy, Phys. Rev. **D82**, 115011 (2010), [arXiv:1008.4869]; A. Falkowski, S. Rychkov and A. Urbano, JHEP **04**, 073 (2012), [arXiv:1202.1532].

[355] N. Arkani-Hamed *et al.*, JHEP **07**, 034 (2002), [hep-ph/0206021]; N. Arkani-Hamed, A. G. Cohen and H. Georgi, Phys. Lett. **B513**, 232 (2001), [hep-ph/0105239].

[356] M. Perelstein, Prog. Part. Nucl. Phys. **58**, 247 (2007), [hep-ph/0512128]; M. Schmaltz and D. Tucker-Smith, Ann. Rev. Nucl. Part. Sci. **55**, 229 (2005), [hep-ph/0502182].

[357] J. A. Casas, J. R. Espinosa and I. Hidalgo, JHEP **03**, 038 (2005), [hep-ph/0502066].

[358] H.-C. Cheng and I. Low, JHEP **09**, 051 (2003), [hep-ph/0308199].

[359] M. Carena *et al.*, Phys. Rev. **D75**, 091701 (2007), [hep-ph/0610156].

[360] M. Aaboud *et al.* (ATLAS), Phys. Rev. Lett. **121**, 21, 211801 (2018), [arXiv:1808.02343]; A. M. Sirunyan *et al.* (CMS), Eur. Phys. J. **C79**, 4, 364 (2019), [arXiv:1812.09768].

[361] H. Georgi, A. E. Nelson and A. Manohar, Phys. Lett. **126B**, 169 (1983); A. E. Nelson and M. J. Strassler, JHEP **09**, 030 (2000), [hep-ph/0006251]; S. Davidson, G. Isidori and S. Uhlig, Phys. Lett. **B663**, 73 (2008), [arXiv:0711.3376].

[362] C. Csaki, A. Falkowski and A. Weiler, JHEP **09**, 008 (2008), [arXiv:0804.1954]; B. Keren-Zur *et al.*, Nucl. Phys. **B867**, 394 (2013), [arXiv:1205.5803].

[363] O. Matsedonskyi, G. Panico and A. Wulzer, JHEP **01**, 164 (2013), [arXiv:1204.6333]; M. Redi and A. Tesi, JHEP **10**, 166 (2012), [arXiv:1205.0232]; D. Marzocca, M. Serone and J. Shu, JHEP **08**, 013 (2012), [arXiv:1205.0770]; A. Pomarol and F. Riva, JHEP **08**, 135 (2012), [arXiv:1205.6434].

[364] R. Contino and G. Servant, JHEP **06**, 026 (2008), [arXiv:0801.1679]; J. Mrazek and A. Wulzer, Phys. Rev. **D81**, 075006 (2010), [arXiv:0909.3977]; A. De Simone *et al.*, JHEP **04**, 004 (2013), [arXiv:1211.5663]; A. Azatov *et al.*, Phys. Rev. **D89**, 7, 075001 (2014), [arXiv:1308.6601].

[365] A. Banfi, A. Martin and V. Sanz, JHEP **08**, 053 (2014), [arXiv:1308.4771]; A. Azatov and A. Paul, JHEP **01**, 014 (2014), [arXiv:1309.5273]; C. Grojean *et al.*, JHEP **05**, 022 (2014), [arXiv:1312.3317].

[366] A. Azatov *et al.*, Phys. Rev. **D92**, 3, 035001 (2015), [arXiv:1502.00539].

[367] K. Agashe, R. Contino and A. Pomarol, Nucl. Phys. **B719**, 165 (2005), [hep-ph/0412089]; R. Contino, L. Da Rold and A. Pomarol, Phys. Rev. **D75**, 055014 (2007), [hep-ph/0612048]; D. Pappadopulo, A. Thamm and R. Torre, JHEP **07**, 058 (2013), [arXiv:1303.3062]; M. Montull *et al.*, Phys. Rev. **D88**, 095006 (2013), [arXiv:1308.0559].

[368] M. Carena, L. Da Rold and E. Pontón, JHEP **06**, 159 (2014), [arXiv:1402.2987]; D. Liu, I. Low and C. E. M. Wagner, Phys. Rev. **D96**, 3, 035013 (2017), [arXiv:1703.07791].

[369] I. Low, R. Rattazzi and A. Vichi, JHEP **04**, 126 (2010), [arXiv:0907.5413].

[370] M. Ciuchini *et al.*, JHEP **08**, 106 (2013), [arXiv:1306.4644].

[371] C. Grojean, O. Matsedonskyi and G. Panico, JHEP **10**, 160 (2013), [arXiv:1306.4655].

[372] M. Geller and O. Telem, Phys. Rev. Lett. **114**, 191801 (2015), [arXiv:1411.2974].

[373] P. Batra and Z. Chacko, Phys. Rev. **D79**, 095012 (2009), [arXiv:0811.0394]; R. Barbieri *et al.*, JHEP **08**, 161 (2015), [arXiv:1501.07803]; M. Low, A. Tesi and L.-T. Wang, Phys. Rev. **D91**, 095012 (2015), [arXiv:1501.07890].

[374] M. Aaboud *et al.* (ATLAS), Phys. Lett. **B775**, 105 (2017), [arXiv:1707.04147].

[375] CMS Collaboration, CMS-PAS-HIG-17-13 (2017); V. Khachatryan *et al.* (CMS), Phys. Lett. **B767**, 147 (2017), [arXiv:1609.02507].

[376] A. M. Sirunyan *et al.* (CMS), Phys. Lett. **B793**, 320 (2019), [arXiv:1811.08459].

[377] CMS Collaboration, CMS-PAS-HIG-16-014 (2016).

[378] ATLAS Collaboration, ATLAS-CONF-2017-058 (2017).

[379] CMS Collaboration, CMS-PAS-HIG-16-033 (2016).

[380] CMS Collaboration, CMS-PAS-HIG-16-023 (2016).

[381] ATLAS Collaboration, ATLAS-CONF-2016-082 (2016).

[382] CMS Collaboration, CMS-PAS-HIG-16-034 (2017).

[383] ATLAS Collaboration, ATLAS-CONF-2013-067 (2013).

[384] CMS Collaboration, CMS-PAS-HIG-17-033 (2019).

[385] ATLAS Collaboration, ATLAS-CONF-2012-018 (2012).

[386] M. Aaboud *et al.* (ATLAS), Phys. Lett. **B777**, 91 (2018), [arXiv:1708.04445].

[387] G. Aad *et al.* (ATLAS), JHEP **09**, 091 (2019), [arXiv:1906.08589].

[388] M. Aaboud *et al.* (ATLAS), Phys. Rev. **D98**, 5, 052008 (2018), [arXiv:1808.02380].

[389] ATLAS Collaboration, ATLAS-CONF-2016-004 (2016); M. Aaboud *et al.* (ATLAS), JHEP **05**, 124 (2019), [arXiv:1811.11028]; M. Aaboud *et al.* (ATLAS), Eur. Phys. J. **C78**, 12, 1007 (2018), [arXiv:1807.08567].

[390] ATLAS Collaboration, ATLAS-CONF-2019-030 (2019); M. Aaboud *et al.* (ATLAS), Phys. Rev. Lett. **121**, 19, 191801 (2018), [Erratum: Phys. Rev. Lett. **122**, 089901 (2019)], [arXiv:1808.00336]; G. Aad *et al.* (ATLAS) (2019), [arXiv:1908.06765].

[391] CMS Collaboration, CMS-PAS-HIG-2017-008 (2016).

[392] V. Khachatryan *et al.* (CMS), Phys. Lett. **B755**, 217 (2016), [arXiv:1510.01181].

[393] CMS Collaboration, CMS-PAS-HIG-18-013 (2019).

[394] M. Aaboud *et al.* (ATLAS), JHEP **01**, 055 (2018), [arXiv:1709.07242].

[395] A. M. Sirunyan *et al.* (CMS), JHEP **09**, 007 (2018), [arXiv:1803.06553].

[396] V. M. Abazov *et al.* (D0), Phys. Rev. Lett. **104**, 151801 (2010), [arXiv:0912.0968].

[397] D0 Collaboration, D0Note 5974-CONF (2011).

[398] R. Aaij *et al.* (LHCb), JHEP **05**, 132 (2013), [arXiv:1304.2591].

[399] A. M. Sirunyan *et al.* (CMS), JHEP **05**, 210 (2019), [arXiv:1903.10228].

[400] M. Aaboud *et al.* (ATLAS), JHEP **07**, 117 (2019), [arXiv:1901.08144].

[401] A. M. Sirunyan *et al.* (CMS) (2019), [arXiv:1907.03152].

[402] CMS Collaboration, CMS-PAS-HIG-18-017 (2019).

[403] ATLAS Collaboration, ATLAS-CONF-2019-036 (2019).

[404] A. M. Sirunyan *et al.* (CMS), JHEP **11**, 161 (2018), [arXiv:1808.01890].

[405] G. Aad *et al.* (ATLAS), JHEP **08**, 148 (2015), [arXiv:1505.07018].

[406] A. M. Sirunyan *et al.* (CMS) (2019), [arXiv:1908.01115].

[407] G. Aad *et al.* (ATLAS) (2019), [arXiv:1907.02749].

[408] S. Chatrchyan *et al.* (CMS), Phys. Lett. **B722**, 207 (2013), [arXiv:1302.2892]; CMS Collaboration, CMS-PAS-HIG-16-025 (2016); A. M. Sirunyan *et al.* (CMS), JHEP **08**, 113 (2018), [arXiv:1805.12191].

[409] V. M. Abazov *et al.* (D0), Phys. Lett. **B698**, 97 (2011), [arXiv:1011.1931].

[410] T. Aaltonen *et al.* (CDF), Phys. Rev. **D85**, 032005 (2012), [arXiv:1106.4782].

[411] ATLAS Collaboration, ATLAS-CONF-2017-055 (2017); G. Aad *et al.* (ATLAS), Phys. Lett. **B744**, 163 (2015), [arXiv:1502.04478].

[412] A. M. Sirunyan *et al.* (CMS), Eur. Phys. J. **C79**, 7, 564 (2019), [arXiv:1903.00941].

[413] CMS Collaboration, CMS-PAS-HIG-18-012 (2019).

[414] M. Aaboud *et al.* (ATLAS), Phys. Lett. **B759**, 555 (2016), [arXiv:1603.09203].

[415] M. Aaboud *et al.* (ATLAS), JHEP **09**, 139 (2018), [arXiv:1807.07915].

[416] CMS Collaboration, CMS-PAS-HIG-16-031 (2016); A. M. Sirunyan *et al.* (CMS), JHEP **07**, 142 (2019), [arXiv:1903.04560].

[417] ATLAS Collaboration, ATLAS-CONF-2012-010 (2012).

[418] V. Khachatryan *et al.* (CMS), JHEP **12**, 178 (2015), [arXiv:1510.04252].

[419] ATLAS Collaboration, ATLAS-CONF-2016-089 (2016); M. Aaboud *et al.* (ATLAS), JHEP **11**, 085 (2018), [arXiv:1808.03599].

[420] V. Khachatryan *et al.* (CMS), JHEP **11**, 018 (2015), [arXiv:1508.07774]; A. M. Sirunyan *et al.* (CMS) (2019), [arXiv:1908.09206].

[421] G. Aad *et al.* (ATLAS), Phys. Rev. Lett. **114**, 23, 231801 (2015), [arXiv:1503.04233].

[422] A. M. Sirunyan *et al.* (CMS), Phys. Rev. Lett. **119**, 14, 141802 (2017), [arXiv:1705.02942].

[423] A. M. Sirunyan *et al.* (CMS), Phys. Rev. Lett. **123**, 13, 131802 (2019), [arXiv:1905.07453].

[424] CMS Collaboration, CMS-PAS-HIG-16-030 (2016).

[425] ATLAS Collaboration, ATLAS-CONF-2011-020 (2011).

[426] CMS Collaboration, CMS-PAS-HIG-15-009 (2016).

[427] G. Aad *et al.* (ATLAS), Phys. Rev. **D92**, 5, 052002 (2015), [arXiv:1505.01609]; ATLAS Collaboration, ATLAS-CONF-2012-079 (2012).

[428] CMS Collaboration, CMS-PAS-HIG-16-055 (2016); V. Khachatryan *et al.* (CMS), JHEP **10**, 076 (2017), [arXiv:1701.02032]; A. M. Sirunyan *et al.* (CMS), Phys. Lett. **B795**, 398 (2019), [arXiv:1812.06359]; A. M. Sirunyan *et al.* (CMS) (2019), [arXiv:1907.07235]; A. M. Sirunyan *et al.* (CMS), Phys. Lett. **B785**, 462 (2018), [arXiv:1805.10191]; A. M. Sirunyan *et al.* (CMS), JHEP **11**, 018 (2018), [arXiv:1805.04865]; CMS Collaboration, CMS-PAS-HIG-18-015 (2019).

[429] V. M. Abazov *et al.* (D0), Phys. Rev. Lett. **103**, 061801 (2009), [arXiv:0905.3381].

[430] A. M. Sirunyan *et al.* (CMS), Phys. Lett. **B796**, 131 (2019), [arXiv:1812.00380].

[431] S. Schael *et al.* (ALEPH), JHEP **05**, 049 (2010), [arXiv:1003.0705].

[432] B. Aubert *et al.* (BaBar), Phys. Rev. Lett. **103**, 081803 (2009), [arXiv:0905.4539].

[433] B. Aubert *et al.* (BaBar), Phys. Rev. Lett. **103**, 181801 (2009), [arXiv:0906.2219].

[434] ATLAS Collaboration, ATLAS-CONF-2016-051 (2016); ATLAS Collaboration, ATLAS-CONF-2017-053 (2017); M. Aaboud *et al.* (ATLAS), Eur. Phys. J. **C79**, 1, 58 (2019), [arXiv:1808.01899].

[435] CMS Collaboration, CMS-PAS-HIG-16-036 (2017).

[436] S. Schael *et al.* (ALEPH, DELPHI, L3, OPAL, LEP Working Group for Higgs Boson Searches), Eur. Phys. J. **C47**, 547 (2006), [hep-ex/0602042].

[437] ATLAS Collaboration, ATLAS-CONF-2013-027 (2013).

[438] CMS Collaboration, CMS-PAS-HIG-13-016 (2013).

[439] A. Heister *et al.* (ALEPH), Phys. Lett. **B526**, 191 (2002), [hep-ex/0201014]; P. Achard *et al.* (L3), Phys. Lett. **B545**, 30 (2002), [hep-ex/0208042].

[440] M. Carena *et al.* (1999), [hep-ph/9912223].

[441] M. M. Kado and C. G. Tully, Ann. Rev. Nucl. Part. Sci. **52**, 65 (2002).

[442] G. Abbiendi *et al.* (OPAL), Eur. Phys. J. **C23**, 397 (2002), [hep-ex/0111010]; J. Abdallah *et al.* (DELPHI), Eur. Phys. J. **C38**, 1 (2004), [hep-ex/0410017].

[443] M. Carena *et al.*, Eur. Phys. J. **C45**, 797 (2006), [hep-ph/0511023].

[444] ATLAS Collaboration, ATLAS-CONF-2016-104 (2016).

[445] S. Chatrchyan *et al.* (CMS), JHEP **09**, 029 (2012), [Erratum: JHEP **03**, 132 (2014)], [arXiv:1204.2488].

[446] M. Aaboud *et al.* (ATLAS), Phys. Rev. Lett. **119**, 19, 191803 (2017), [arXiv:1707.06025].

[447] V. Khachatryan *et al.* (CMS), Phys. Lett. **B758**, 296 (2016), [arXiv:1511.03610].

[448] A. M. Sirunyan *et al.* (CMS), JHEP **11**, 010 (2017), [arXiv:1707.07283].

[449] J. Bernon *et al.*, Phys. Rev. **D91**, 7, 075019 (2015), [arXiv:1412.3385].

[450] G. Aad *et al.* (ATLAS), Phys. Rev. Lett. **113**, 17, 171801 (2014), [arXiv:1407.6583].

[451] CMS Collaboration, CMS-PAS-HIG-14-037 (2015).

[452] CMS Collaboration, CMS-PAS-HIG-17-013 (2017).

[453] S. Heinemeyer, Int. J. Mod. Phys. **A33**, 31, 1844006 (2018).

[454] S. H. Zhu, arXiv preprint (1999), [hep-ph/9901221].

[455] H. E. Logan and S.-f. Su, Phys. Rev. **D66**, 035001 (2002), [hep-ph/0203270].

[456] A. Gutierrez-Rodriguez and O. A. Sampayo, Phys. Rev. **D62**, 055004 (2000).

[457] S. Kanemura, S. Moretti and K. Odagiri, JHEP **02**, 011 (2001), [hep-ph/0012030].

[458] M. Czakon, P. Fiedler and A. Mitov, Phys. Rev. Lett. **110**, 252004 (2013), [arXiv:1303.6254].

[459] M. Carena *et al.*, Nucl. Phys. **B577**, 88 (2000), [hep-ph/9912516].

[460] J. M. Campbell, R. K. Ellis and F. Tramontano, Phys. Rev. **D70**, 094012 (2004), [hep-ph/0408158].

[461] C. Degrande *et al.*, Phys. Lett. **B772**, 87 (2017), [arXiv:1607.05291].

[462] A. A. Barrientos Bendezu and B. A. Kniehl, Phys. Rev. **D63**, 015009 (2001), [hep-ph/0007336]; A. A. Barrientos Bendezu and B. A. Kniehl, Nucl. Phys. **B568**, 305 (2000), [hep-ph/9908385].

[463] G. Abbiendi *et al.* (ALEPH, DELPHI, L3, OPAL, LEP), Eur. Phys. J. **C73**, 2463 (2013), [arXiv:1301.6065].

[464] B. Abbott *et al.* (D0), Phys. Rev. Lett. **82**, 4975 (1999), [hep-ex/9902028]; A. Abulencia *et al.* (CDF), Phys. Rev. Lett. **96**, 042003 (2006), [hep-ex/0510065]; V. M. Abazov *et al.* (D0), Phys. Lett. **B682**, 278 (2009), [arXiv:0908.1811].

[465] J. Abdallah *et al.* (DELPHI), Eur. Phys. J. **C54**, 1 (2008), [Erratum: Eur. Phys. J. **C56**, 165 (2008)], [arXiv:0801.3586].

[466] R. Dermisek, Mod. Phys. Lett. **A24**, 1631 (2009), [arXiv:0907.0297].

[467] J. F. Gunion, JHEP **08**, 032 (2009), [arXiv:0808.2509].

[468] W. Love *et al.* (CLEO), Phys. Rev. Lett. **101**, 151802 (2008), [arXiv:0807.1427].

[469] G. Aad *et al.* (ATLAS), Eur. Phys. J. **C72**, 2244 (2012), [arXiv:1210.5070]; S. Chatrchyan *et al.* (CMS), Eur. Phys. J. **C72**, 2189 (2012), [arXiv:1207.2666].

[470] G. Aad *et al.* (ATLAS), Phys. Rev. **D89**, 3, 032002 (2014), [arXiv:1312.1956].

[471] J. de Blas *et al.*, JHEP **01**, 139 (2020), [arXiv:1905.03764].

12. CKM Quark-Mixing Matrix

Revised March 2020 by A. Ceccucci (CERN), Z. Ligeti (LBNL) and Y. Sakai (KEK).

12.1 Introduction

The masses and mixings of quarks have a common origin in the Standard Model (SM). They arise from the Yukawa interactions with the Higgs condensate,

$$\mathcal{L}_Y = -Y^d_{ij}\,\overline{Q^I_{Li}}\,\phi\,d^I_{Rj} - Y^u_{ij}\,\overline{Q^I_{Li}}\,\epsilon\,\phi^*\,u^I_{Rj} + \text{h.c.}, \tag{12.1}$$

where $Y^{u,d}$ are 3×3 complex matrices, ϕ is the Higgs field, i,j are generation labels, and ϵ is the 2×2 antisymmetric tensor. Q^I_L are left-handed quark doublets, and d^I_R and u^I_R are right-handed down- and up-type quark singlets, respectively, in the weak-eigenstate basis. When ϕ acquires a vacuum expectation value, $\langle\phi\rangle = (0, v/\sqrt{2})$, Eq. (12.1) yields mass terms for the quarks. The physical states are obtained by diagonalizing $Y^{u,d}$ by four unitary matrices, $V^{u,d}_{L,R}$, as $M^f_{\rm diag} = V^f_L\,Y^f\,V^{f\dagger}_R(v/\sqrt{2})$, $f = u, d$. As a result, the charged-current $W^\pm$ interactions couple to the physical u_{Lj} and d_{Lk} quarks with couplings given by

$$\frac{-g}{\sqrt{2}}(\overline{u_L},\,\overline{c_L},\,\overline{t_L})\gamma^\mu\,W^+_\mu\,V_{\rm CKM}\begin{pmatrix} d_L \\ s_L \\ b_L\end{pmatrix} + \text{h.c.},$$
$$V_{\rm CKM} \equiv V^u_L V^{d\dagger}_L = \begin{pmatrix} V_{ud} & V_{us} & V_{ub} \\ V_{cd} & V_{cs} & V_{cb} \\ V_{td} & V_{ts} & V_{tb}\end{pmatrix}. \tag{12.2}$$

This Cabibbo-Kobayashi-Maskawa (CKM) matrix [1,2] is a 3×3 unitary matrix. It can be parameterized by three mixing angles and the CP-violating KM phase [2]. Of the many possible conventions, a standard choice has become [3]

$$V_{\rm CKM} = \begin{pmatrix} 1 & 0 & 0 \\ 0 & c_{23} & s_{23} \\ 0 & -s_{23} & c_{23}\end{pmatrix}\begin{pmatrix} c_{13} & 0 & s_{13}e^{-i\delta} \\ 0 & 1 & 0 \\ -s_{13}e^{i\delta} & 0 & c_{13}\end{pmatrix}\begin{pmatrix} c_{12} & s_{12} & 0 \\ -s_{12} & c_{12} & 0 \\ 0 & 0 & 1\end{pmatrix}$$
$$= \begin{pmatrix} c_{12}c_{13} & s_{12}c_{13} & s_{13}e^{-i\delta} \\ -s_{12}c_{23} - c_{12}s_{23}s_{13}e^{i\delta} & c_{12}c_{23} - s_{12}s_{23}s_{13}e^{i\delta} & s_{23}c_{13} \\ s_{12}s_{23} - c_{12}c_{23}s_{13}e^{i\delta} & -c_{12}s_{23} - s_{12}c_{23}s_{13}e^{i\delta} & c_{23}c_{13}\end{pmatrix}, \tag{12.3}$$

where $s_{ij} = \sin\theta_{ij}$, $c_{ij} = \cos\theta_{ij}$, and δ is the phase responsible for all CP-violating phenomena in flavor-changing processes in the SM. The angles θ_{ij} can be chosen to lie in the first quadrant, so $s_{ij}, c_{ij} \geq 0$.

It is known experimentally that $s_{13} \ll s_{23} \ll s_{12} \ll 1$, and it is convenient to exhibit this hierarchy using the Wolfenstein parameterization. We define [4–6]

$$s_{12} = \lambda = \frac{|V_{us}|}{\sqrt{|V_{ud}|^2 + |V_{us}|^2}}\,, \qquad s_{23} = A\lambda^2 = \lambda\left|\frac{V_{cb}}{V_{us}}\right|,$$
$$s_{13}e^{i\delta} = V^*_{ub} = A\lambda^3(\rho + i\eta) = \frac{A\lambda^3(\bar\rho + i\bar\eta)\sqrt{1 - A^2\lambda^4}}{\sqrt{1-\lambda^2}\,[1 - A^2\lambda^4(\bar\rho + i\bar\eta)]}\,. \tag{12.4}$$

These relations ensure that $\bar\rho + i\bar\eta = -(V_{ud}V^*_{ub})/(V_{cd}V^*_{cb})$ is phase convention independent, and the CKM matrix written in terms of λ, A, $\bar\rho$, and $\bar\eta$ is unitary to all orders in λ. The definitions of $\bar\rho$, $\bar\eta$ reproduce all approximate results in the literature; *i.e.*, $\bar\rho = \rho(1-\lambda^2/2+\ldots)$ and $\bar\eta = \eta(1-\lambda^2/2+\ldots)$, and one can write $V_{\rm CKM}$ to $\mathcal{O}(\lambda^4)$ either in terms of $\bar\rho, \bar\eta$ or, traditionally,

$$V_{\rm CKM} = \begin{pmatrix} 1-\lambda^2/2 & \lambda & A\lambda^3(\rho - i\eta) \\ -\lambda & 1-\lambda^2/2 & A\lambda^2 \\ A\lambda^3(1-\rho-i\eta) & -A\lambda^2 & 1\end{pmatrix} + \mathcal{O}(\lambda^4)\,. \tag{12.5}$$

The CKM matrix elements are fundamental parameters of the SM, so their precise determination is important. The unitarity of the CKM matrix imposes $\sum_i V_{ij}V^*_{ik} = \delta_{jk}$ and $\sum_j V_{ij}V^*_{kj} = \delta_{ik}$. The six vanishing combinations can be represented as triangles in a complex plane, of which those obtained by taking scalar products of neighboring rows or columns are nearly degenerate. The areas of all triangles are the same, half of the Jarlskog invariant, J [7], which is a phase-convention-independent measure of CP violation, defined by $\text{Im}\left[V_{ij}V_{kl}V^*_{il}V^*_{kj}\right] = J\sum_{m,n}\varepsilon_{ikm}\varepsilon_{jln}$.

The most commonly used unitarity triangle arises from

$$V_{ud}\,V^*_{ub} + V_{cd}\,V^*_{cb} + V_{td}\,V^*_{tb} = 0\,, \tag{12.6}$$

by dividing each side by the best-known one, $V_{cd}V^*_{cb}$ (see Fig. 12.1). Its vertices are exactly $(0,0)$, $(1,0)$, and, due to the definition in Eq. (12.4), $(\bar\rho, \bar\eta)$. An important goal of flavor physics is to overconstrain the CKM elements, and many measurements can be conveniently displayed and compared in the $\bar\rho, \bar\eta$ plane. While

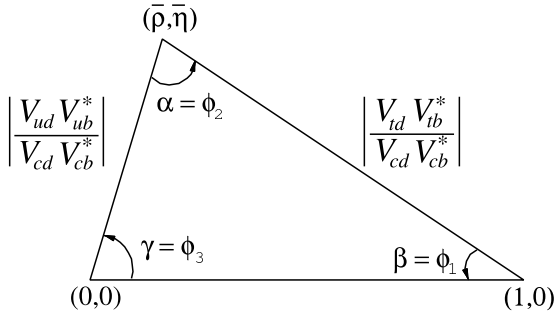

Figure 12.1: Sketch of the unitarity triangle.

the Lagrangian in Eq. (12.1) is renormalized, and the CKM matrix has a well known scale dependence above the weak scale [8], below $\mu = m_W$ the CKM elements can be treated as constants, with all μ-dependence contained in the running of quark masses and higher-dimension operators.

Unless explicitly stated otherwise, we describe all measurements assuming the SM, to extract magnitudes and phases of CKM elements in Sec. 12.2 and 12.3. Processes dominated by loop-level contributions in the SM are particularly sensitive to new physics beyond the SM (BSM). We give the global fit results for the CKM elements in Sec. 12.4, and discuss some implications for beyond standard model physics in Sec. 12.5.

12.2 Magnitudes of CKM elements

12.2.1 $|V_{ud}|$

The most precise determination of $|V_{ud}|$ comes from the study of superallowed $0^+ \to 0^+$ nuclear beta decays, which are pure vector transitions. Taking the average of the fourteen most precise determinations [9] yields [10]

$$|V_{ud}| = 0.97370 \pm 0.00014\,. \tag{12.7}$$

This value is about 2σ smaller than in the review two years ago, mainly due to adopting a recent calculation of electroweak corrections based on dispersion relations [11]. The dominant and comparable uncertainties are the experimental ones, and from the estimates of the radiative corrections. A less precise determination of $|V_{ud}|$ can be obtained from the measurement of the neutron lifetime. The theoretical uncertainties are very small, but the determination is limited by the knowledge of the ratio of the axial-

vector and vector couplings, $g_A = G_A/G_V$ [10]. The PIBETA experiment [12] has improved the measurement of the $\pi^+ \to \pi^0 e^+ \nu$ branching ratio to 0.6%, and quotes $|V_{ud}| = 0.9739 \pm 0.0029$, in agreement with the more precise result listed above. The interest in this measurement is that the determination of $|V_{ud}|$ is very clean theoretically, because it is a pure vector transition and is free from nuclear-structure uncertainties.

12.2.2 $|V_{us}|$

The product of $|V_{us}|$ and the form factor at $q^2 = 0$, $|V_{us}|\, f_+(0)$, has been extracted traditionally from $K^0_L \to \pi e \nu$ decays in order to avoid isospin-breaking corrections ($\pi^0 - \eta$ mixing) that affect $K^\pm$ semileptonic decay, and the complications induced by a second (scalar) form factor present in the muonic decays. The last round of measurements has led to enough experimental constraints to justify the comparison between different decay modes. Systematic errors related to the experimental quantities, *e.g.*, the lifetime of neutral or charged kaons, and the form factor determinations for electron and muonic decays, differ among decay modes, and the consistency between different determinations enhances the confidence in the final result. For this reason, we follow the prescription [13] to average $K^0_L \to \pi e \nu$, $K^0_L \to \pi \mu \nu$, $K^\pm \to \pi^0 e^\pm \nu$, $K^\pm \to \pi^0 \mu^\pm \nu$ and $K^0_S \to \pi e \nu$. The average of these five decay modes yields $|V_{us}|\, f_+(0) = 0.2165 \pm 0.0004$. Results obtained from each decay mode, and exhaustive references to the experimental data, are listed for instance in Ref. [10]. The form factor average $f_+(0) = 0.9706 \pm 0.0027$ [14] from $N_f = 2+1+1$ lattice QCD calculations gives $|V_{us}| = 0.2231 \pm 0.0007$ [10].[1] The broadly used classic calculation of $f_+(0)$ [16] is in good agreement with this value, while other calculations [18] differ by as much as 2%.

The calculation of the ratio of the kaon and pion decay constants enables one to extract $|V_{us}/V_{ud}|$ from $K \to \mu\nu(\gamma)$ and $\pi \to \mu\nu(\gamma)$, where (γ) indicates that radiative decays are included [19]. The value of $\Gamma(K \to \mu\nu(\gamma))$ [10] derived from the KLOE measurement of the corresponding branching ratio [20], combined with the lattice QCD result, $f_K/f_\pi = 1.1932 \pm 0.0019$ [14], leads to $|V_{us}| = 0.2252 \pm 0.0005$, where the accuracy is limited by the knowledge of the ratio of the decay constants. The average of these two determinations, with the error scaled according to the PDG prescription [21] by $\sqrt{\chi^2} = 2.0$, is quoted as [10]

$$|V_{us}| = 0.2245 \pm 0.0008\,. \tag{12.8}$$

It is important to include both QED and QCD isospin violations in the lattice QCD calculations.

The latest determination from hyperon decays can be found in Ref. [22]. The authors focus on the analysis of the vector form factor, protected from first order $SU(3)$ breaking effects by the Ademollo-Gatto theorem [23], and treat the ratio between the axial and vector form factors g_1/f_1 as experimental input, thus avoiding first order $SU(3)$ breaking effects in the axial-vector contribution. They find $|V_{us}| = 0.2250 \pm 0.0027$, although this does not include an estimate of the theoretical uncertainty due to second-order $SU(3)$ breaking, contrary to Eq. (12.8). Concerning hadronic τ decays to strange particles, averaging the inclusive decay and the exclusive $\tau \to h\nu$ ($h = \pi$, K) measurements yields $|V_{us}| = 0.2221 \pm 0.0013$ [24].

12.2.3 $|V_{cd}|$

The magnitude of V_{cd} can be extracted from semileptonic charm decays, using theoretical knowledge of the form factors. In semileptonic D decays, lattice QCD calculations have predicted the normalization of the $D \to \pi\ell\nu$ and $D \to K\ell\nu$ form factors [14]. The dependence on the invariant mass of the lepton pair, q^2, is determined from lattice QCD and theoretical constraints from analyticity [15]. Using $N_f = 2+1+1$ lattice QCD calculations for $D \to \pi\ell\nu$, $f_+^{D\pi}(0) = 0.612 \pm 0.035$ [14], and the average [24] of the measurements of $D \to \pi\ell\nu$ decays by *BABAR* [25], BESIII [26,27], CLEO-c [28], and Belle [29], one obtains $|V_{cd}| = 0.2330 \pm 0.0029 \pm 0.0133$, where the first uncertainty is experimental, and the second is from the theoretical uncertainty of the form factor.

The determination of $|V_{cd}|$ is also possible from the leptonic decay $D^+ \to \mu^+\nu$. The experimental uncertainties have not decreased significantly recently. Averaging the BESIII [30] and earlier CLEO [31] measurements, and using the $N_f = 2+1+1$ lattice QCD result, $f_D = 212.0 \pm 0.7$ MeV [14], yields $|V_{cd}| = 0.2173 \pm 0.0051 \pm 0.0007$ [24].[2]

Earlier determinations of $|V_{cd}|$ came from neutrino scattering data. The difference of the ratio of double-muon to single-muon production by neutrino and antineutrino beams is proportional to the charm cross section off valence d quarks, and therefore to $|V_{cd}|^2$ times the average semileptonic branching ratio of charm mesons, $\mathcal{B}_\mu$. The method was used first by CDHS [32] and then by CCFR [33,34] and CHARM II [35]. Averaging these results is complicated, because it requires assumptions about the scale of the QCD corrections, and because $\mathcal{B}_\mu$ is an effective quantity, which depends on the specific neutrino beam characteristics. With no recent experimental input available, we quote the average from a past review, $\mathcal{B}_\mu |V_{cd}|^2 = (0.463 \pm 0.034) \times 10^{-2}$ [36]. Analysis cuts make these experiments insensitive to neutrino energies smaller than 30 GeV. Thus, $\mathcal{B}_\mu$ should be computed using only neutrino interactions with visible energy larger than 30 GeV. An appraisal [37] based on charm-production fractions measured in neutrino interactions [38,39] gives $\mathcal{B}_\mu = 0.088 \pm 0.006$. Data from the CHORUS experiment [40] are sufficiently precise to extract $\mathcal{B}_\mu$ directly, by comparing the number of charm decays with a muon to the total number of charmed hadrons found in the nuclear emulsions. Requiring the visible energy to be larger than 30 GeV, CHORUS found $\mathcal{B}_\mu = 0.085 \pm 0.009 \pm 0.006$. We use the average of these two determinations, $\mathcal{B}_\mu = 0.087 \pm 0.005$, and obtain $|V_{cd}| = 0.230 \pm 0.011$. Averaging the three determinations above, we find

$$|V_{cd}| = 0.221 \pm 0.004\,. \tag{12.9}$$

12.2.4 $|V_{cs}|$

The direct determination of $|V_{cs}|$ is possible from semileptonic D or leptonic D_s decays, using lattice QCD calculations of the semileptonic D form factor or the D_s decay constant. For muonic decays, the average of Belle [41], CLEO-c [42], *BABAR* [43], and BESIII [44,45] is $\mathcal{B}(D_s^+ \to \mu^+\nu) = (5.51 \pm 0.16) \times 10^{-3}$ [24]. For decays to τ leptons, the average of CLEO-c [42,46,47], *BABAR* [43], Belle [41], and BESIII [44] gives $\mathcal{B}(D_s^+ \to \tau^+\nu) = (5.52 \pm 0.24) \times 10^{-2}$ [24]. From each of these values, determinations of $|V_{cs}|$ can be obtained using the PDG values for the mass and lifetime of the D_s, the masses of the leptons, and $f_{D_s} = (249.9 \pm 0.5)$ MeV [14]. The average of these determinations gives $|V_{cs}| = 0.992 \pm 0.012$, where the error is dominated by the experimental uncertainty. In semileptonic D decays, lattice QCD calculations of the $D \to K\ell\nu$ form factor are available [14]. Using $f_+^{DK}(0) = 0.765 \pm 0.031$ and the average [24] of CLEO-c [28], Belle [29], *BABAR* [48], and recent BESIII [26,49] measurements of $D \to K\ell\nu$ decays, one obtains $|V_{cs}| = 0.939 \pm 0.038$, where the dominant uncertainty is from the theoretical calculation of the form factor. Averaging the determinations from leptonic and semileptonic decays, we find

$$|V_{cs}| = 0.987 \pm 0.011\,. \tag{12.10}$$

Measurements of on-shell $W^\pm$ decays sensitive to $|V_{cs}|$ were made by LEP-2. The W branching ratios depend on the six CKM elements involving quarks lighter than m_W. The W branching ratio to each lepton flavor is $1/\mathcal{B}(W \to \ell\bar{\nu}_\ell) = 3\big[1 + \sum_{u,c,d,s,b} |V_{ij}|^2\,(1 + \alpha_s(m_W)/\pi) + \ldots\big]$. Assuming lepton universality, the measurement $\mathcal{B}(W \to \ell\bar{\nu}_\ell) = (10.83 \pm 0.07 \pm 0.07)\,\%$ [50] implies $\sum_{u,c,d,s,b} |V_{ij}|^2 = 2.002 \pm 0.027$. This is a precise test of unitarity; however, only flavor-tagged W-decays determine $|V_{cs}|$

[1] For lattice QCD inputs, we use the averages from Ref. [14], unless the minireviews [10,15] choose different values. We only use unquenched results, and if both $N_f = 2+1+1$ and $2+1$ calculations are available, we use the former.

[2] Hereafter the first error is statistical and the second is systematic, unless mentioned otherwise.

directly, such as DELPHI's tagged $W^+ \to c\bar{s}$ analysis, yielding $|V_{cs}| = 0.94^{+0.32}_{-0.26} \pm 0.13$ [51].

12.2.5 $|V_{cb}|$

This matrix element can be determined from exclusive and inclusive semileptonic decays of B mesons to charm. The inclusive determinations use the semileptonic decay rate measurement, together with (certain moments of) the lepton energy and the hadronic invariant-mass spectra. The theoretical basis is the operator product expansion [52, 53], which allows calculation of the decay rate and various spectra as expansions in α_s and inverse powers of the heavy-quark mass. The dependence on m_b, m_c, and the parameters that occur at subleading order is different for different moments, and a large number of measured moments overconstrain all the parameters, and tests the consistency of the determination. The precise extraction of $|V_{cb}|$ requires using a "threshold" quark mass definition [54, 55]. Inclusive measurements have been performed using B mesons from Z^0 decays at LEP, and at e^+e^- machines operated at the $\Upsilon(4S)$. At LEP, the large boost of B mesons from the Z^0 decay allows the determination of the moments throughout phase space, which is not possible otherwise, but the large statistics available at the B factories lead to more precise determinations. An average of the measurements and a compilation of the references are provided in Ref. [15]: $|V_{cb}| = (42.2 \pm 0.8) \times 10^{-3}$.

Complementary determinations are based on exclusive semileptonic B decays to D and D^*. In the $m_{b,c} \gg \Lambda_{\rm QCD}$ limit, all form factors are given by a single Isgur-Wise function [56], which depends on the product of the four-velocities of the B and $D^{(*)}$ mesons, $w = v \cdot v'$. Heavy-quark symmetry determines the rate at $w = 1$, the maximum momentum transfer to the $\ell\bar{\nu}$ pair, and $|V_{cb}|$ is obtained from an extrapolation to $w = 1$. The current update of the V_{cb} and V_{ub} minireview quotes from exclusive decays $|V_{cb}| = (39.5 \pm 0.9) \times 10^{-3}$ [15], based on the only unfolded measurement of $B \to D^*$ semileptonic decay distributions [57], and using a more general fit [58] than in earlier B factory measurements. With the uncertainty scaled by $\sqrt{\chi^2} = 2.4$, this yields the combination [15],

$$|V_{cb}| = (41.0 \pm 1.4) \times 10^{-3} \,. \tag{12.11}$$

Less precise measurements of $|V_{cb}|$, not included in this average, can be obtained from $\mathcal{B}(B \to D^{(*)}\tau\bar{\nu})$. The most precise data involving τ leptons are the $|V_{cb}|$-independent ratios, $\mathcal{B}(B \to D^{(*)}\tau\bar{\nu})/\mathcal{B}(B \to D^{(*)}\ell\bar{\nu})$ measured by BaBar, Belle, and LHCb. If the current, approximately $3\,\sigma$ [24], hint of lepton non-universality prevails, the determination of $|V_{cb}|$ becomes more complicated.

12.2.6 $|V_{ub}|$

The determination of $|V_{ub}|$ from inclusive $B \to X_u\ell\bar{\nu}$ decay is complicated due to large $B \to X_c\ell\bar{\nu}$ backgrounds. In most regions of phase space where the charm background is kinematically forbidden, the hadronic physics enters via unknown nonperturbative functions, so-called shape functions. (In contrast, the nonperturbative physics for $|V_{cb}|$ is encoded in a few parameters.) At leading order in $\Lambda_{\rm QCD}/m_b$, there is only one shape function, which can be extracted from the photon energy spectrum in $B \to X_s\gamma$ [59, 60], and applied to several spectra in $B \to X_u\ell\bar{\nu}$. The subleading shape functions are modeled in the current determinations. Phase space cuts for which the rate has only subleading dependence on the shape function are also possible [61]. The measurements of both the hadronic and the leptonic systems are important for an optimal choice of phase space. A different approach is to make the measurements more inclusive by extending them deeper into the $B \to X_c\ell\bar{\nu}$ region, and thus reduce the theoretical uncertainties. Analyses of the electron-energy endpoint from CLEO [62], *BABAR* [63], and Belle [64] quote $B \to X_u e\bar{\nu}$ partial rates for $|\vec{p}_e| \geq 2.0\,\text{GeV}$ and $1.9\,\text{GeV}$, which are well below the charm endpoint. The large and pure $B\overline{B}$ samples at the B factories permit the selection of $B \to X_u\ell\bar{\nu}$ decays in events where the other B is fully reconstructed [65]. With this full-reconstruction tag method, the four-momenta of both the leptonic and the hadronic final states can be measured. It also gives access to a wider kinematic region, because of improved signal purity. Ref. [15] quotes the inclusive average, $|V_{ub}| = (4.25 \pm 0.12\ ^{+0.15}_{-0.14} \pm 0.23) \times 10^{-3}$, where the first error is experimental, the second arises from the model dependence quoted by the individual measurements, and the third is an additional one estimated in Ref. [15].

To extract $|V_{ub}|$ from exclusive decays, the form factors have to be known. Experimentally, better signal-to-background ratios are offset by smaller yields. The $B \to \pi\ell\bar{\nu}$ branching ratio is now known to 5%. Lattice QCD calculations of the $B \to \pi\ell\bar{\nu}$ form factor are available [66] for the high q^2 region ($q^2 > 16$ or $18\,\text{GeV}^2$). A fit to the experimental partial rates and lattice QCD results versus q^2 yields $|V_{ub}| = (3.70 \pm 0.10 \pm 0.12) \times 10^{-3}$ [24]. Light-cone QCD sum rules are supposed to be applicable for $q^2 < 12\,\text{GeV}^2$ [67], yielding a combination, $|V_{ub}| = (3.67 \pm 0.09 \pm 0.12) \times 10^{-3}$ [15, 24].

The uncertainties in extracting $|V_{ub}|$ from inclusive and exclusive decays are different to a large extent. An average of these determinations, with the uncertainty scaled by $\sqrt{\chi^2} = 1.6$, is [15]

$$|V_{ub}| = (3.82 \pm 0.24) \times 10^{-3} \,. \tag{12.12}$$

A determination of $|V_{ub}|$ not included in this average can be obtained from $\mathcal{B}(B \to \tau\bar{\nu}) = (1.06 \pm 0.19) \times 10^{-4}$ [24]. Using $f_B = (190.0 \pm 1.3)\,\text{MeV}$ [14] and $\tau_{B^\pm} = (1.638 \pm 0.004)\,\text{ps}$ [68], we find the remarkably consistent result, $|V_{ub}| = (4.05 \pm 0.36) \times 10^{-3}$. This decay is sensitive, for example, to tree-level charged Higgs contributions, and the measured rate is consistent with the SM expectation. The LHCb measurement $|V_{ub}/V_{cb}| = 0.079 \pm 0.006$ [69] from the ratio of $\Lambda_b \to p^+\mu^-\bar{\nu}$ and $\Lambda_b \to \Lambda_c^+\mu^-\bar{\nu}$ in different regions of q^2, provides another complementary determination.

12.2.7 $|V_{td}|$ *and* $|V_{ts}|$

The CKM elements $|V_{td}|$ and $|V_{ts}|$ are not likely to be precisely measurable in tree-level processes involving top quarks, so one has to rely on determinations from B–$\overline{B}$ oscillations dominated by box diagrams with top quarks, or loop-mediated rare K and B decays. Theoretical uncertainties in hadronic effects limit the accuracy of the current determinations. These can be reduced by taking ratios of processes that are equal in the flavor $SU(3)$ limit to determine $|V_{td}/V_{ts}|$.

The mixing of the two B^0 mesons was discovered by ARGUS [70], and the mass difference is now precisely measured as $\Delta m_d = (0.5065 \pm 0.0019)\,\text{ps}^{-1}$ [71]. In the B_s^0 system, Δm_s was first measured significantly by CDF [72] and the world average, dominated by an LHCb measurement [73], is $\Delta m_s = (17.749 \pm 0.020)\,\text{ps}^{-1}$ [71]. Neglecting corrections suppressed by $|V_{tb}| - 1$, and using the lattice QCD results $f_{B_d}\sqrt{\widehat{B}_{B_d}} = (225 \pm 9)\,\text{MeV}$ and $f_{B_s}\sqrt{\widehat{B}_{B_s}} = (274 \pm 8)\,\text{MeV}$ [14],

$$|V_{td}| = (8.0 \pm 0.3) \times 10^{-3} \,, \qquad |V_{ts}| = (38.8 \pm 1.1) \times 10^{-3} \,. \tag{12.13}$$

The uncertainties are dominated by lattice QCD. Several uncertainties are reduced in the calculation of the ratio $\xi = \left(f_{B_s}\sqrt{\widehat{B}_{B_s}}\right)/\left(f_{B_d}\sqrt{\widehat{B}_{B_d}}\right) = 1.206 \pm 0.038$ [14] and therefore the constraint on $|V_{td}/V_{ts}|$ from $\Delta m_d/\Delta m_s$ is more reliable theoretically. These provide a theoretically clean and significantly improved determination,

$$\left|V_{td}/V_{ts}\right| = 0.205 \pm 0.001 \pm 0.006 \,. \tag{12.14}$$

The inclusive branching ratio $\mathcal{B}(B \to X_s\gamma) = (3.32 \pm 0.15) \times 10^{-4}$ extrapolated to $E_\gamma > E_0 = 1.6\,\text{GeV}$ [24] is also sensitive to $|V_{tb}V_{ts}|$. In addition to t-quark penguins, a substantial part of the rate comes from charm contributions proportional to $V_{cb}V_{cs}^*$ via the application of 3×3 CKM unitarity (which is used here). With the NNLO calculation of $\mathcal{B}(B \to X_s\gamma)_{E_\gamma > E_0}/\mathcal{B}(B \to X_c e\bar{\nu})$ [74], we obtain $|V_{ts}/V_{cb}| = 0.98 \pm 0.04$. The $B_s \to \mu^+\mu^-$ rate is also proportional to $|V_{tb}V_{ts}|^2$ in the SM, and the world average, $\mathcal{B}(B_s \to \mu^+\mu^-) = (3.1 \pm 0.6) \times 10^{-9}$ [24], is consistent with the SM, with sizable uncertainties.

A complementary determination of $|V_{td}/V_{ts}|$ is possible from the ratio of $B \to \rho\gamma$ and $K^*\gamma$ rates. The ratio of the neutral modes

is theoretically cleaner than that of the charged ones, because the poorly known spectator-interaction contribution is expected to be smaller (W-exchange vs. weak annihilation). For now, because of low statistics, we average the charged and neutral rates assuming the isospin symmetry and heavy-quark limit motivated relation, $|V_{td}/V_{ts}|^2/\xi_\gamma^2 = [\Gamma(B^+ \to \rho^+\gamma) + 2\Gamma(B^0 \to \rho^0\gamma)]/[\Gamma(B^+ \to K^{*+}\gamma) + \Gamma(B^0 \to K^{*0}\gamma)] = (3.37 \pm 0.49)\%$ [24]. Here ξ_γ contains the poorly known hadronic physics. Using $\xi_\gamma = 1.2 \pm 0.2$ [75] gives $|V_{td}/V_{ts}| = 0.220 \pm 0.016 \pm 0.037$, where the first uncertainty is experimental and the second is theoretical.

A theoretically clean determination of $|V_{td}V_{ts}^*|$ is possible from $K^+ \to \pi^+\nu\bar{\nu}$ decay [76]. Experimentally, only a handful of events have been observed [77, 78] and the rate is consistent with the SM with large uncertainties. Much more data are needed for a precision measurement.

12.2.8 $|V_{tb}|$

The determination of $|V_{tb}|$ from top decays uses the ratio of branching fractions $R = \mathcal{B}(t \to Wb)/\mathcal{B}(t \to Wq) = |V_{tb}|^2/(\sum_q |V_{tq}|^2) = |V_{tb}|^2$, where $q = b, s, d$. The CDF and DØ measurements performed on data collected during Run II of the Tevatron give $|V_{tb}| > 0.78$ [79] and $0.99 > |V_{tb}| > 0.90$ [80], respectively, at 95% CL. CMS measured the same quantity at 8 TeV and obtained $|V_{tb}| > 0.975$ [81] at 95% CL.

The direct determination of $|V_{tb}|$, without assuming unitarity, is possible from the single top quark production cross section. The $(3.30^{+0.52}_{-0.40})$ pb combined cross section [82] of DØ and CDF measurements implies $|V_{tb}| = 1.02^{+0.06}_{-0.05}$. The LHC experiments, ATLAS and CMS, have measured single top quark production cross sections (and extracted $|V_{tb}|$) in t-channel, Wt-channel, and s-channel at 7 TeV, 8 TeV, and 13 TeV [83]. The average of these $|V_{tb}|$ values is calculated to be $|V_{tb}| = 1.010 \pm 0.036$, where all systematic errors and theoretical errors are treated to be fully correlated. The average of Tevatron and LHC values gives

$$|V_{tb}| = 1.013 \pm 0.030\,. \tag{12.15}$$

The experimental systematic uncertainties dominate, and a dedicated combination would be welcome.

A weak constraint on $|V_{tb}|$ can be obtained from precision electroweak data, where top quarks enter in loops. The sensitivity is best in $\Gamma(Z \to b\bar{b})$ and yields $|V_{tb}| = 0.77^{+0.18}_{-0.24}$ [84].

12.3 Phases of CKM elements

As can be seen from Fig. 12.1, the angles of the unitarity triangle are

$$\beta = \phi_1 = \arg\left(-\frac{V_{cd}V_{cb}^*}{V_{td}V_{tb}^*}\right),$$
$$\alpha = \phi_2 = \arg\left(-\frac{V_{td}V_{tb}^*}{V_{ud}V_{ub}^*}\right),$$
$$\gamma = \phi_3 = \arg\left(-\frac{V_{ud}V_{ub}^*}{V_{cd}V_{cb}^*}\right). \tag{12.16}$$

Since CP violation involves phases of CKM elements, many measurements of CP-violating observables can be used to constrain these angles and the $\bar{\rho}, \bar{\eta}$ parameters.

12.3.1 ϵ *and* ϵ'

The measurement of CP violation in K^0–$\overline{K}^0$ mixing, $|\epsilon| = (2.228 \pm 0.011) \times 10^{-3}$ [85], provides important information about the CKM matrix. The phase of ϵ is determined by long-distance physics, $\epsilon = \frac{1}{2}\, e^{i\phi_\epsilon} \sin\phi_\epsilon \arg(-M_{12}/\Gamma_{12})$, where $\phi_\epsilon = \arctan|2\Delta m_K/\Delta\Gamma_K| \simeq 43.5°$. The SM prediction can be written as

$$\epsilon = \kappa_\epsilon\, e^{i\phi_\epsilon} \frac{G_F^2 m_W^2 m_K}{12\sqrt{2}\,\pi^2 \Delta m_K} f_K^2 \widehat{B}_K \left\{ \eta_{tt} S(x_t) \,\mathrm{Im}[(V_{ts}V_{td}^*)^2] + 2\eta_{ct} S(x_c, x_t) \,\mathrm{Im}(V_{cs}V_{cd}^* V_{ts}V_{td}^*) + \eta_{cc}\, x_c \,\mathrm{Im}[(V_{cs}V_{cd}^*)^2] \right\}, \tag{12.17}$$

where $\kappa_\epsilon \simeq 0.94 \pm 0.02$ [86] includes the effects of strangeness changing $\Delta s = 1$ operators and additional dependence on $\phi_\epsilon \neq \pi/4$ (see also Ref. [87]). The displayed terms are the short-distance $\Delta s = 2$ contribution to $\mathrm{Im}M_{12}$ in the usual phase convention, S is an Inami-Lim function [88], $x_q = m_q^2/m_W^2$, and η_{ij} are perturbative QCD corrections. The constraint from ϵ in the $\bar{\rho}, \bar{\eta}$ plane is bounded by approximate hyperbolas. Lattice QCD determined the bag parameter $\widehat{B}_K = 0.717 \pm 0.024$ [14], and the main uncertainties are from $(V_{ts}V_{td}^*)^2$ (approximately given by that of $|V_{cb}|^4$ or A^4), the η_{ij} coefficients, and estimates of κ_ϵ.

The measurement of $6\,\mathrm{Re}(\epsilon'/\epsilon) = 1 - |\eta_{00}/\eta_{+-}|^2$, where each $\eta_{ij} = \langle\pi^i\pi^j|\mathcal{H}|K_L\rangle/\langle\pi^i\pi^j|\mathcal{H}|K_S\rangle$ violates CP, provides a qualitative test of the CKM mechanism, and strong constraints on many BSM scenarios. Its nonzero value, $\mathrm{Re}(\epsilon'/\epsilon) = (1.67 \pm 0.23) \times 10^{-3}$ [85], demonstrated the existence of direct CP violation, a prediction of the KM ansatz. While $\mathrm{Re}(\epsilon'/\epsilon) \propto \mathrm{Im}(V_{td}V_{ts}^*)$, this quantity cannot easily be used to extract CKM parameters, because cancellations between the electromagnetic and gluonic penguin contributions for large m_t [89] enhance the hadronic uncertainties. Most SM estimates [90] agree with the observed value, indicating that $\bar{\eta}$ is positive. Progress in lattice QCD [91] may yield a precise SM prediction in the future, and trigger new work on assessing the consistency of the SM with the measured value [92, 93].

12.3.2 β / ϕ_1

12.3.2.1 *Charmonium modes*

CP-violation measurements in B-meson decays provide direct information on the angles of the unitarity triangle, shown in Fig. 12.1. These overconstraining measurements serve to improve the determination of the CKM elements, and to reveal possible effects beyond the SM.

The time-dependent CP asymmetry of neutral B decays to a final state f common to B^0 and $\overline{B}^0$ is given by [94–96]

$$\mathcal{A}_f = \frac{\Gamma(\overline{B}^0(t) \to f) - \Gamma(B^0(t) \to f)}{\Gamma(\overline{B}^0(t) \to f) + \Gamma(B^0(t) \to f)}\,, = S_f \sin(\Delta m_d\, t) - C_f \cos(\Delta m_d\, t)\,, \tag{12.18}$$

where

$$S_f = \frac{2\,\mathrm{Im}\lambda_f}{1 + |\lambda_f|^2}\,, \qquad C_f = \frac{1 - |\lambda_f|^2}{1 + |\lambda_f|^2}\,, \qquad \lambda_f = \frac{q}{p}\frac{\bar{A}_f}{A_f}\,. \tag{12.19}$$

Here, q/p describes B^0–$\overline{B}^0$ mixing and, to a good approximation in the SM, $q/p = V_{tb}^* V_{td}/V_{tb}V_{td}^* = e^{-2i\beta + \mathcal{O}(\lambda^4)}$ in the usual phase convention. A_f ($\bar{A}_f$) is the amplitude of the $B^0 \to f$ ($\overline{B}^0 \to f$) decay. If f is a CP eigenstate, and amplitudes with one CKM phase dominate the decay, then $|A_f| = |\bar{A}_f|$, $C_f = 0$, and $S_f = \sin(\arg\lambda_f) = \eta_f \sin 2\phi$, where η_f is the CP eigenvalue of f and 2ϕ is the phase difference between the $B^0 \to f$ and $B^0 \to \overline{B}^0 \to f$ decay paths. A contribution of another amplitude to the decay with a different CKM phase makes the value of S_f sensitive to relative strong-interaction phases between the decay amplitudes (it also makes $C_f \neq 0$ possible).

The $b \to c\bar{c}s$ decays to CP eigenstates ($B^0 \to$ charmonium $K^0_{S,L}$) are the theoretically cleanest examples, measuring $S_f = -\eta_f \sin 2\beta$. The $b \to s$ penguin amplitudes have dominantly the same weak phase as the $b \to c\bar{c}s$ tree amplitude. Since only λ^2-suppressed penguin amplitudes introduce a different CP-violating phase, amplitudes with a single weak phase dominate, and we expect $\left||\bar{A}_{\psi K}/A_{\psi K}| - 1\right| < 0.01$. The e^+e^- asymmetric-energy B-factory experiments, *BABAR* [97] and Belle [98], and LHCb [99] provided precise measurements. The world average, including some other measurements, is [24]

$$\sin 2\beta = 0.699 \pm 0.017\,. \tag{12.20}$$

This measurement has a four-fold ambiguity in β, which can be resolved by a global fit as mentioned in Sec. 12.4. Experimentally, the two-fold ambiguity $\beta \to \pi/2 - \beta$ (but not $\beta \to \pi + \beta$) can be resolved by a time-dependent angular analysis of $B^0 \to J/\psi K^{*0}$ [100,101], or a time-dependent Dalitz plot analysis of $B^0 \to \overline{D}^0 h^0$. The time-dependent Dalitz plot analysis of $B^0 \to \overline{D}^0 h^0$ ($h^0 = \pi^0, \eta, \omega$) with $\overline{D}^0 \to K^0_S\pi^+\pi^-$, jointly performed by Belle and *BABAR*, excludes the $\pi/2 - \beta$ solution with 7.3σ confidence level

[102]. These results indicate that negative $\cos 2\beta$ solutions are very unlikely, in agreement with the global CKM fit result.

The $b \to c\bar{c}d$ mediated transitions, such as $B^0 \to J/\psi\pi^0$ and $B^0 \to D^{(*)+}D^{(*)-}$, also measure approximately $\sin 2\beta$. However, the dominant component of the $b \to d$ penguin amplitude has a different CKM phase ($V_{tb}^* V_{td}$) than the tree amplitude ($V_{cb}^* V_{cd}$), and their magnitudes are of the same order in λ. Therefore, the effect of penguins could be large, resulting in $S_f \neq -\eta_f \sin 2\beta$ and $C_f \neq 0$. Such decay modes have been measured by *BABAR*, Belle, and LHCb. The world averages [24], $S_{J/\psi\pi^0} = -0.86 \pm 0.14$, $S_{J/\psi\rho^0} = -0.66^{+0.16}_{-0.12}$, $S_{D^+D^-} = -0.84 \pm 0.12$, and $S_{D^{*+}D^{*-}} = -0.71 \pm 0.09$ (where $\eta_f = +1$ for the $J/\psi\pi^0$ and D^+D^- modes, while $J/\psi\rho^0$ and $D^{*+}D^{*-}$ are mixtures of CP even and odd states), are consistent with $\sin 2\beta$ obtained from $B^0 \to$ charmonium K^0 decays, and the C_f's are consistent with zero, although the uncertainties are sizable.

The $b \to c\bar{u}d$ decays $B^0 \to \overline{D}^{0(*)}h^0$, with $\overline{D}^0 \to CP$ eigenstates and $\overline{D}^0 \to K^0_S\pi^+\pi^-$ with Dalitz plot analysis, have no penguin contributions, and provide theoretically clean $\sin 2\beta$ measurements. The average of joint analyses of *BABAR* and Belle data [102, 103] give $\sin 2\beta = 0.71 \pm 0.09$ [24, 104].

12.3.2.2 *Penguin-dominated modes*

The $b \to s\bar{q}q$ penguin-dominated decays have the same CKM phase as the $b \to c\bar{c}s$ tree level decays, up to corrections suppressed by λ^2, since $V_{tb}^* V_{ts} = -V_{cb}^* V_{cs}[1 + \mathcal{O}(\lambda^2)]$. Therefore, decays such as $B^0 \to \phi K^0$ and $\eta' K^0$ provide $\sin 2\beta$ measurements in the SM. Any BSM contribution to the amplitude with a different weak phase would give rise to $S_f \neq -\eta_f \sin 2\beta$, and possibly $C_f \neq 0$. Therefore, the main interest in these modes is not simply to measure $\sin 2\beta$, but to search for new physics. Measurements of many other decay modes in this category, such as $B \to \pi^0 K^0_S$, $K^0_S K^0_S K^0_S$, *etc.*, have also been performed by *BABAR* and Belle. The results and their uncertainties are summarized in Fig. 12.3 and Table 12.1 of Ref. [95]. The comparison of CP violation measurements between tree-dominated and penguin-dominated modes in B^0_s decays provides similar sensitivity to new physics.

12.3.3 α / ϕ_2

Since α is the phase between $V_{tb}^* V_{td}$ and $V_{ub}^* V_{ud}$, only time-dependent CP asymmetries in decay modes dominated by $b \to u\bar{u}d$ transition can directly measure $\sin 2\alpha$, in contrast to $\sin 2\beta$, where several different quark-level transitions can be used. Since $b \to d$ penguin amplitudes have a different CKM phase than $b \to u\bar{u}d$ tree amplitudes, and their magnitudes are of the same order in λ, the penguin contribution can be sizable, which makes the determination of α complicated. To date, α has been measured in $B \to \pi\pi$, $\rho\pi$ and $\rho\rho$ decay modes.

12.3.3.1 $B \to \pi\pi$

It is well established from the data that there is a sizable contribution of $b \to d$ penguin amplitudes in $B \to \pi\pi$ decays. Thus, $S_{\pi^+\pi^-}$ in the time-dependent $B^0 \to \pi^+\pi^-$ analysis does not measure $\sin 2\alpha$, but

$$S_{\pi^+\pi^-} = \sqrt{1 - C^2_{\pi^+\pi^-}}\, \sin(2\alpha + 2\Delta\alpha)\,, \tag{12.21}$$

where $2\Delta\alpha$ is the phase difference between $e^{2i\gamma}\bar{A}_{\pi^+\pi^-}$ and $A_{\pi^+\pi^-}$. The value of $\Delta\alpha$, and hence α, can be extracted using the isospin relation among the amplitudes of $B^0 \to \pi^+\pi^-$, $B^0 \to \pi^0\pi^0$, and $B^+ \to \pi^+\pi^0$ decays [105],

$$\frac{1}{\sqrt{2}}\, A_{\pi^+\pi^-} + A_{\pi^0\pi^0} - A_{\pi^+\pi^0} = 0\,, \tag{12.22}$$

and a similar expression for the $\bar{A}_{\pi\pi}$'s. This method utilizes the fact that a pair of pions from $B \to \pi\pi$ decay must be in a zero angular momentum state, and, because of Bose statistics, they must have even isospin. Consequently, $\pi^\pm\pi^0$ is in a pure isospin-2 state, while the penguin amplitudes only contribute to the isospin-0 final state. The latter does not hold for the electroweak penguin amplitudes, but their effect is expected to be small. The isospin analysis uses the world averages of *BABAR*, Belle, and LHCb measurements, $S_{\pi^+\pi^-} = -0.63 \pm 0.04$, $C_{\pi^+\pi^-} = -0.32 \pm 0.04$, the decay widths of all three modes, and the direct CP asymmetry $C_{\pi^0\pi^0} = -0.33 \pm 0.22$ [24]. This analysis leads to 16 mirror solutions for $0 \leq \alpha < 2\pi$. Because of this, and due to the experimental uncertainties, some of these solutions are not well separated [96].

12.3.3.2 $B \to \rho\rho$

The decay $B^0 \to \rho^+\rho^-$ contains two vector mesons in the final state, and so in general is a mixture of CP-even and CP-odd components. Therefore, it was thought that extracting α from this mode would be complicated.

However, the longitudinal polarization fractions in $B^+ \to \rho^+\rho^0$ and $B^0 \to \rho^+\rho^-$ decays were measured to be close to unity [106], which implies that the final states are almost purely CP-even. Furthermore, $\mathcal{B}(B^0 \to \rho^0\rho^0) = (0.95 \pm 0.16) \times 10^{-6}$ is much smaller than $\mathcal{B}(B^0 \to \rho^+\rho^-) = (27.7 \pm 1.9) \times 10^{-6}$ and $\mathcal{B}(B^+ \to \rho^+\rho^0) = (24.0^{+1.9}_{-2.0}) \times 10^{-6}$ [24], which implies that the effect of the penguin contributions is small. The isospin analysis using the world averages, $S_{\rho^+\rho^-} = -0.14 \pm 0.13$ and $C_{\rho^+\rho^-} = 0.00 \pm 0.09$ [24], together with the time-dependent CP asymmetry, $S_{\rho^0\rho^0} = -0.3 \pm 0.7$ and $C_{\rho^0\rho^0} = -0.2 \pm 0.9$ [107], and the above mentioned branching fractions and longitudinal polarization fractions, gives two solutions (with mirror solutions at $3\pi/2 - \alpha$) [96]. A possible small violation of Eq. (12.22) due to the finite width of the ρ [108] is so far neglected.

12.3.3.3 $B \to \rho\pi$

The final state in $B^0 \to \rho^+\pi^-$ decay is not a CP eigenstate, but this decay proceeds via the same quark-level diagrams as $B^0 \to \pi^+\pi^-$, and both B^0 and $\overline{B}^0$ can decay to $\rho^+\pi^-$, while the final state in $B^0 \to \rho^0\pi^0$ is a CP eigenstate. Consequently, mixing-induced CP violation can occur in B^0 and $\overline{B}^0$ decays to $\rho^\pm\pi^\mp$ and $\rho^0\pi^0$. The time-dependent Dalitz plot analysis of $B^0 \to \pi^+\pi^-\pi^0$ decays permits the extraction of α with a single discrete ambiguity, $\alpha \to \alpha + \pi$, since one knows the variation of the strong phases in the interference regions of the $\rho^+\pi^-$, $\rho^-\pi^+$, and $\rho^0\pi^0$ amplitudes in the Dalitz plot [109]. The combination of Belle [110] and *BABAR* [111] measurements gives only moderate constraints [96].

Combining the $B \to \pi\pi$, $\rho\pi$, and $\rho\rho$ decay modes [24, 96], α is constrained as

$$\alpha = \left(84.9^{+5.1}_{-4.5}\right)^\circ\,. \tag{12.23}$$

Similar results can be found in Refs. [112, 113].

12.3.4 γ / ϕ_3

By virtue of Eq. (12.16), γ does not depend on CKM elements involving the top quark, so it can be measured in tree-level B decays. This is an important distinction from the measurements of α and β, and implies that measurements of γ are unlikely to be affected by physics beyond the SM.

12.3.4.1 $B_{(s)} \to D_{(s)}K^{(*)}$

The interference of $B^- \to D^0K^-$ ($b \to c\bar{u}s$) and $B^- \to \overline{D}^0K^-$ ($b \to u\bar{c}s$) transitions can be studied in final states accessible in both D^0 and $\overline{D}^0$ decays [94]. In principle, it is possible to extract the B and D decay amplitudes, the relative strong phases, and the weak phase γ from the data [96].

A practical complication is that the precision depends sensitively on the ratio of the interfering amplitudes

$$r_B = \left|A(B^- \to \overline{D}^0K^-)\big/A(B^- \to D^0K^-)\right|, \tag{12.24}$$

which is around 0.1. The original GLW method [114, 115] considers D decays to CP eigenstates, such as $B^\pm \to D^{(*)}_{CP}(\to \pi^+\pi^-)K^{(*)\pm}$. To alleviate the smallness of r_B and make the interfering amplitudes (which are products of the B and D decay amplitudes) comparable in magnitude, the ADS method [116] considers final states where Cabibbo-allowed $\overline{D}^0$ and doubly-Cabibbo-suppressed D^0 decays interfere. Measurements have been made by the B factories, CDF, and LHCb, using both methods [24]. The GLW method currently gives only a loose constraint on γ, $14.9^\circ < \gamma < 30.8^\circ$, $69.9^\circ < \gamma < 87.9^\circ$, $92.1^\circ < \gamma < 110.1^\circ$,

and $149.2^\circ < \gamma < 165.1^\circ$ at 68% CL; while the ADS method provides $\gamma = (72^{+12}_{-14})^\circ$ [24, 104].

The BPGGSZ method [117, 118] utilizes that both D^0 and $\overline{D}^0$ can have large branching fractions to CP self-conjugate three-body final states, such as $K^0_S\pi^+\pi^-$, and the analysis can be optimized by studying the Dalitz plot dependence of the interferences. The best present determination of γ comes from this method. Combining the measurements by Belle [119], *BABAR* [120] and LHCb [121], $\gamma = (73.8^{+6.8}_{-7.0})^\circ$ is obtained [24, 104]. The error is sensitive to the central value of the amplitude ratio r_B (and r^*_B for the D^*K mode), for which Belle found somewhat larger central values than *BABAR* and LHCb. The same values of $r_B^{(*)}$ enter the ADS analyses, and the data can be combined to fit for $r_B^{(*)}$ and γ. The effect of D^0–$\overline{D}^0$ mixing on γ is far below the present experimental accuracy [122], unless D^0–$\overline{D}^0$ mixing is due to CP-violating new physics, in which case it can be included in the analysis [123].

The amplitude ratio is much larger in the analogous $B^0_s \to D^\pm_s K^\mp$ decays, which allows a model-independent extraction of $\gamma - 2\beta_s$ [124] (here $\beta_s = \arg(-V_{ts}V^*_{tb}/V_{cs}V^*_{cb})$ is related to the phase of B_s mixing). A recent measurement by LHCb [125] gives $\gamma = (127^{+17}_{-22})^\circ$ using a constraint on $2\beta_s$ (see Sec. 12.5).

Combining all the above measurements [24,96], γ is constrained as

$$\gamma = \left(72.1^{+4.1}_{-4.5}\right)^\circ . \qquad (12.25)$$

Similar results can be found in Refs. [112, 113].

12.3.4.2 $B^0 \to D^{(*)\pm}\pi^\mp$

The interference of $b \to u$ and $b \to c$ transitions can be studied in $\overline{B}^0 \to D^{(*)+}\pi^-$ ($b \to c\bar{u}d$) and $\overline{B}^0 \to B^0 \to D^{(*)+}\pi^-$ ($\bar{b} \to \bar{u}cd$) decays and their CP conjugates, since both B^0 and $\overline{B}^0$ decay to $D^{(*)\pm}\pi^\mp$ (or $D^\pm\rho^\mp$, *etc.*). Since there are only tree and no penguin contributions to these decays, in principle, it is possible to extract from the four time-dependent rates the magnitudes of the two hadronic amplitudes, their relative strong phase, and the weak phase between the two decay paths, which is $2\beta + \gamma$.

A complication is that the ratio of the interfering amplitudes is very small, $r_{D\pi} = A(B^0 \to D^+\pi^-)/A(\overline{B}^0 \to D^+\pi^-) = \mathcal{O}(0.01)$ (and similarly for $r_{D^*\pi}$ and $r_{D\rho}$), and therefore it has not been possible to measure it. To obtain $2\beta + \gamma$, $SU(3)$ flavor symmetry and dynamical assumptions have been used to relate $A(\overline{B}^0 \to D^-\pi^+)$ to $A(\overline{B}^0 \to D^-_s\pi^+)$, so this measurement is not model independent at present. Combining the $D^\pm\pi^\mp$, $D^{*\pm}\pi^\mp$ and $D^\pm\rho^\mp$ measurements [126] gives $\sin(2\beta+\gamma) > 0.68$ at 68% CL [112], consistent with the previously discussed results for β and γ.

12.4 Global fit in the Standard Model

Using the independently measured CKM elements mentioned in the previous sections, the unitarity of the CKM matrix can be checked. We obtain $|V_{ud}|^2 + |V_{us}|^2 + |V_{ub}|^2 = 0.9985 \pm 0.0005$ (1st row), $|V_{cd}|^2 + |V_{cs}|^2 + |V_{cb}|^2 = 1.025 \pm 0.022$ (2nd row), $|V_{ud}|^2 + |V_{cd}|^2 + |V_{td}|^2 = 0.9970 \pm 0.0018$ (1st column), and $|V_{us}|^2 + |V_{cs}|^2 + |V_{ts}|^2 = 1.026 \pm 0.022$ (2nd column), respectively. Due to the recent reduction of the value of $|V_{ud}|$, there is a 3σ tension with unitarity in the 1st row, leading also to poor consistency of the SM fit below. The uncertainties in the second row and column are dominated by that of $|V_{cs}|$. For the second row, another check is obtained from the measurement of $\sum_{u,c,d,s,b} |V_{ij}|^2$ in Sec. 12.2.4, minus the sum in the first row above: $|V_{cd}|^2 + |V_{cs}|^2 + |V_{cb}|^2 = 1.002 \pm 0.027$. These provide strong tests of the unitarity of the CKM matrix. With the significantly improved direct determination of $|V_{tb}|$, the unitarity checks for the third row and column have also become fairly precise, leaving decreasing room for mixing with other states. The sum of the three angles of the unitarity triangle, $\alpha + \beta + \gamma = \left(179^{+7}_{-6}\right)^\circ$, is also consistent with the SM expectation.

The CKM matrix elements can be most precisely determined using a global fit to all available measurements and imposing the SM constraints (*i.e.*, three generation unitarity). The fit must also use theory predictions for hadronic matrix elements, which sometimes have significant uncertainties. There are several approaches to combining the experimental data. CKMfitter [6, 112] and Ref. [127] (which develops [128, 129] further) use frequentist statistics, while UTfit [113, 130] uses a Bayesian approach. These approaches provide similar results.

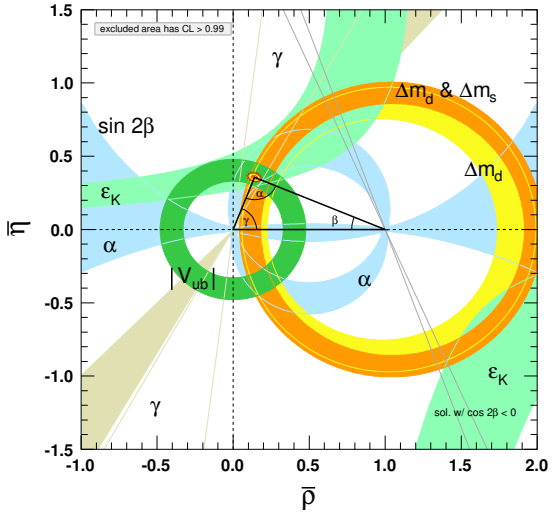

Figure 12.2: Constraints on the $\bar{\rho}, \bar{\eta}$ plane. The shaded areas have 99% CL.

The constraints implied by the unitarity of the three generation CKM matrix significantly reduce the allowed range of some of the CKM elements. The fit for the Wolfenstein parameters defined in Eq. (12.4) gives

$$\lambda = 0.22650 \pm 0.00048\,, \qquad A = 0.790^{+0.017}_{-0.012}\,,$$
$$\bar{\rho} = 0.141^{+0.016}_{-0.017}\,, \qquad \bar{\eta} = 0.357 \pm 0.011\,. \qquad (12.26)$$

These values are obtained using the method of Refs. [6,112]. Using the prescription of Refs. [113, 130] gives $\lambda = 0.22658 \pm 0.00044$, $A = 0.818 \pm 0.012$, $\bar{\rho} = 0.139 \pm 0.014$, $\bar{\eta} = 0.356 \pm 0.010$ [131]. The fit results for the magnitudes of all nine CKM elements are

$$V_{\rm CKM} = \begin{pmatrix} 0.97401 \pm 0.00011 & 0.22650 \pm 0.00048 & 0.00361^{+0.00011}_{-0.00009} \\ 0.22636 \pm 0.00048 & 0.97320 \pm 0.00011 & 0.04053^{+0.00083}_{-0.00061} \\ 0.00854^{+0.00023}_{-0.00016} & 0.03978^{+0.00082}_{-0.00060} & 0.999172^{+0.000024}_{-0.000035} \end{pmatrix}, \qquad (12.27)$$

and the Jarlskog invariant is $J = \left(3.00^{+0.15}_{-0.09}\right) \times 10^{-5}$. The parameters in Eq. (12.3) are

$$\sin\theta_{12} = 0.22650 \pm 0.00048\,, \qquad \sin\theta_{13} = 0.00361^{+0.00011}_{-0.00009}\,,$$
$$\sin\theta_{23} = 0.04053^{+0.00083}_{-0.00061}\,, \qquad \delta = 1.196^{+0.045}_{-0.043}\,. \qquad (12.28)$$

Fig. 12.2 illustrates the constraints on the $\bar{\rho}, \bar{\eta}$ plane from various measurements, and the global fit result. The CL of each of the shaded regions was increased from 95% to 99% for this edition, because the reduction in $|V_{ud}|$ discussed above leads to poor consistency between the fit result (for $\bar{\rho}$ and $\bar{\eta}$) and the individual constraints shown in the plot. The shaded 99% CL regions all overlap consistently around the global fit region.

If one uses only tree-level inputs (magnitudes of CKM elements not coupling to the top quark and the angle γ), the resulting fit is almost identical for λ in Eq. (12.26), while the other parameters' central values can change by about a sigma and their uncertainties double, yielding $\lambda = 0.22653 \pm 0.00048$, $A = 0.799^{+0.027}_{-0.028}$, $\bar{\rho} = 0.123^{+0.032}_{-0.028}$, and $\bar{\eta} = 0.382^{+0.029}_{-0.028}$. This illustrates how the constraints can be less tight in the presence of BSM physics.

12.5 Implications beyond the SM

The effects in B, B_s, K, and D decays and mixings due to high-scale physics (W, Z, t, H in the SM, and unknown heavier particles) can be parameterized by operators composed of SM fields, obeying the $SU(3)\times SU(2)\times U(1)$ gauge symmetry. Flavor-changing neutral currents, suppressed in the SM, are especially sensitive to beyond SM contributions. Processes studied in great detail, both experimentally and theoretically, include neutral meson mixings, $B_{(s)} \to X\gamma$, $X\ell^+\ell^-$, $\ell^+\ell^-$, $K \to \pi\nu\bar{\nu}$, etc. The BSM contributions to these operators are suppressed by powers of the scale at which they are generated. Already at lowest order, there are many dimension-6 operators, and the observable effects of BSM interactions are encoded in their coefficients. In the SM, these coefficients are determined by just the four CKM parameters, and the W, Z, and quark masses. For example, Δm_d, $\Gamma(B \to \rho\gamma)$, $\Gamma(B \to \pi\ell^+\ell^-)$, and $\Gamma(B \to \ell^+\ell^-)$ are all proportional to $|V_{td}V_{tb}|^2$ in the SM, however, they may receive unrelated BSM contributions. These BSM contributions may or may not obey the SM relations. (For example, the flavor sector of the MSSM contains 69 CP-conserving parameters and 41 CP-violating phases, *i.e.*, 40 new ones [132]). Thus, similar to the measurements of $\sin 2\beta$ in tree- and loop-dominated decay modes, overconstraining measurements of the magnitudes and phases of flavor-changing neutral-current amplitudes gives good sensitivity to BSM.

To illustrate the level of suppression required for BSM contributions, consider a class of models in which the unitarity of the CKM matrix is maintained, and the dominant BSM effects modify the neutral meson mixing amplitudes [133] by $(z_{ij}/\Lambda^2)(\bar{q}_i\gamma^\mu P_L q_j)^2$, where z_{ij} is an unknown coefficient and Λ is the scale suppressing this BSM contribution (see, [134, 135]). It is only known since the measurements of γ and α that the SM gives the leading contribution to $B^0-\overline{B}^0$ mixing [6, 136]. Nevertheless, new physics with a generic weak phase may still contribute to neutral meson mixings at a significant fraction of the SM [130, 137, 138]. The existing data imply that $\Lambda/|z_{ij}|^{1/2}$ has to exceed about 10^4 TeV for $K^0-\overline{K}^0$ mixing, 10^3 TeV for $D^0-\overline{D}^0$ mixing, 500 TeV for $B^0-\overline{B}^0$ mixing, and 100 TeV for $B_s^0-\overline{B}_s^0$ mixing [130, 135]. (Some other operators are even better constrained [130].) The constraints are the strongest in the kaon sector, because the CKM suppression is the most severe. Thus, if there is new physics at the TeV scale, $|z_{ij}| \ll 1$ is required. Even if $|z_{ij}|$ are suppressed by a loop factor and $|V_{ti}^*V_{tj}|^2$ (in the down quark sector), similar to the SM, one expects percent-level effects, which may be observable in forthcoming flavor physics experiments. To constrain such extensions of the SM, many measurements irrelevant for the SM-CKM fit, such as the CP asymmetry in semileptonic $B_{d,s}^0$ decays, $A_{\rm SL}^{d,s}$, are important [139]. The current world averages [24] are consistent with the SM, with experimental uncertainties far greater than those of the theory predictions.

There are many key measurements sensitive to BSM physics, which do not constrain the unitarity triangle in Fig. 12.1. For example, a key quantity in the B_s system is $\beta_s = \arg(-V_{ts}V_{tb}^*/V_{cs}V_{cb}^*)$, which is the small, λ^2-suppressed, angle of a "squashed" unitarity triangle, obtained by taking the scalar product of the second and third columns of the CKM matrix. This angle can be measured via time-dependent CP violation in $B_s^0 \to J/\psi\,\phi$, similar to β in $B^0 \to J/\psi K^0$. Since the $J/\psi\,\phi$ final state is not a CP eigenstate, an angular analysis of the decay products is needed to separate the CP-even and CP-odd components, which give opposite asymmetries. In the SM, the asymmetry for the CP-even part is $2\beta_s$, when one neglects subdominant amplitudes with a weak phase V_{ub}. (Sometimes the notation $\phi_s = -2\beta_s$ plus a possible BSM contribution to the B_s mixing phase is used.) Testing if the data agree with the SM prediction, $2\beta_s = 0.0383^{+0.0012}_{-0.0011}$ [112], is another sensitive probe of the SM. The current world average, dominated by LHC measurements [140] including the $B_s \to J/\psi\,K^+K^-$ and $J/\psi\,\pi^+\pi^-$ decay modes, is $2\beta_s = 0.051 \pm 0.023$ [71]. Since the uncertainty is much larger than that in the SM, a lot will be learned from more precise future measurements. Searches for CP violation in the charm sector, in particular in $D^0-\overline{D}^0$ mixing, provide complementary sensitivity to BSM.

In the kaon sector, the CP-violating observables, ϵ and ϵ', are tiny, so models in which all sources of CP violation are small were viable before the B-factory measurements. Since the measurement of $\sin 2\beta$, we know that CP violation can be an $\mathcal{O}(1)$ effect, and only flavor mixing is suppressed between the three quark generations. Thus, many models with spontaneous CP violation were excluded. In the kaon sector, clean tests of the SM can come from measurements of $K^+ \to \pi^+\nu\bar{\nu}$ [78] and $K_L^0 \to \pi^0\nu\bar{\nu}$ [141]. These loop-induced rare decays are sensitive to BSM, and will allow precise tests [142] of the CKM paradigm, independent of B decays.

The CKM elements are fundamental parameters, so they should be measured as precisely as possible. The overconstraining measurements of CP asymmetries, mixing, semileptonic, and rare decays severely constrain the magnitudes and phases of possible BSM contributions to flavor-changing interactions. If new particles are observed at the LHC, it will be important to explore their flavor parameters as precisely as possible to understand the underlying physics.

References

[1] N. Cabibbo, Phys. Rev. Lett. **10**, 531 (1963).

[2] M. Kobayashi and T. Maskawa, Prog. Theor. Phys. **49**, 652 (1973).

[3] L.-L. Chau and W.-Y. Keung, Phys. Rev. Lett. **53**, 1802 (1984).

[4] L. Wolfenstein, Phys. Rev. Lett. **51**, 1945 (1983).

[5] A. J. Buras, M. E. Lautenbacher and G. Ostermaier, Phys. Rev. **D50**, 3433 (1994), [hep-ph/9403384].

[6] J. Charles *et al.* (CKMfitter Group), Eur. Phys. J. **C41**, 1, 1 (2005), [hep-ph/0406184].

[7] C. Jarlskog, Phys. Rev. Lett. **55**, 1039 (1985).

[8] W. J. Marciano and A. Sirlin, Nucl. Phys. **B93**, 303 (1975); K. S. Babu, Z. Phys. **C35**, 69 (1987).

[9] J. Hardy and I. S. Towner, PoS **CKM2016**, 028 (2016).

[10] E. Blucher and W.J. Marciano, "V_{ud}, V_{us}, the Cabibbo Angle and CKM Unitarity," in this *Review*.

[11] C.-Y. Seng *et al.*, Phys. Rev. Lett. **121**, 24, 241804 (2018), [arXiv:1807.10197].

[12] D. Pocanic *et al.*, Phys. Rev. Lett. **93**, 181803 (2004), [hep-ex/0312030].

[13] M. Antonelli *et al.* (FlaviaNet Working Group on Kaon Decays), Eur. Phys. J. **C69**, 399 (2010), [arXiv:1005.2323]; see also `http://www.lnf.infn.it/wg/vus`.

[14] S. Aoki *et al.* (Flavour Lattice Averaging Group), Eur. Phys. J. **C80**, 2, 113 (2020), [arXiv:1902.08191]; The original papers that led to the quoted averages are cited in this reference or on the web page `http://flag.unibe.ch/`.

[15] T. Mannel and P. Urquijo, "Semileptonic b-Hadron Decays, Determination of V_{cb} and V_{ub}," in this *Review*.

[16] H. Leutwyler and M. Roos, Z. Phys. **C25**, 91 (1984); For earlier fits for $|V_{ud}|$ and $|V_{us}|$ in the 3-generation SM, see Ref. [17].

[17] R. E. Shrock and L.-L. Wang, Phys. Rev. Lett. **41**, 1692 (1978).

[18] J. Bijnens and P. Talavera, Nucl. Phys. **B669**, 341 (2003), [hep-ph/0303103]; M. Jamin, J. A. Oller and A. Pich, JHEP **02**, 047 (2004), [hep-ph/0401080]; V. Cirigliano *et al.*, JHEP **04**, 006 (2005), [hep-ph/0503108]; C. Dawson *et al.*, PoS **LAT2005**, 337 (2006), [hep-lat/0510018]; N. Tsutsui *et al.* (JLQCD), PoS **LAT2005**, 357 (2006), [hep-lat/0510068]; M. Okamoto (Fermilab Lattice, MILC, HPQCD), in "3rd Conference on Flavor Physics and CP Violation (FPCP 2004) Daegu, Korea, October 4-9, 2004," (2004), [hep-lat/0412044].

[19] W. J. Marciano, Phys. Rev. Lett. **93**, 231803 (2004), [hep-ph/0402299].

[20] F. Ambrosino *et al.* (KLOE), Phys. Lett. **B632**, 76 (2006), [hep-ex/0509045].

[21] See Sec. 5.2, "Averages and fits," in the Introduction to this *Review*, http://pdg.lbl.gov/2019/reviews/rpp2019-rev-rpp-intro.pdf.

[22] N. Cabibbo, E. C. Swallow and R. Winston, Ann. Rev. Nucl. Part. Sci. **53**, 39 (2003), [hep-ph/0307298]; N. Cabibbo, E. C. Swallow and R. Winston, Phys. Rev. Lett. **92**, 251803 (2004), [hep-ph/0307214].

[23] M. Ademollo and R. Gatto, Phys. Rev. Lett. **13**, 264 (1964).

[24] Y. S. Amhis *et al.* (HFLAV) (2019), [arXiv:1909.12524]; and updates at https://hflav.web.cern.ch/.

[25] J. P. Lees *et al.* (BaBar), Phys. Rev. **D91**, 5, 052022 (2015), [arXiv:1412.5502].

[26] M. Ablikim *et al.* (BESIII), Phys. Rev. **D92**, 7, 072012 (2015), [arXiv:1508.07560].

[27] M. Ablikim *et al.* (BESIII), Phys. Rev. **D96**, 1, 012002 (2017), [arXiv:1703.09084].

[28] D. Besson *et al.* (CLEO), Phys. Rev. **D80**, 032005 (2009), [arXiv:0906.2983].

[29] L. Widhalm *et al.* (Belle), Phys. Rev. Lett. **97**, 061804 (2006), [hep-ex/0604049].

[30] M. Ablikim *et al.* (BESIII), Phys. Rev. **D89**, 5, 051104 (2014), [arXiv:1312.0374].

[31] B. I. Eisenstein *et al.* (CLEO), Phys. Rev. **D78**, 052003 (2008), [arXiv:0806.2112].

[32] H. Abramowicz *et al.*, Z. Phys. **C15**, 19 (1982).

[33] S. A. Rabinowitz *et al.*, Phys. Rev. Lett. **70**, 134 (1993).

[34] A. O. Bazarko *et al.* (CCFR), Z. Phys. **C65**, 189 (1995), [hep-ex/9406007].

[35] P. Vilain *et al.* (CHARM II), Eur. Phys. J. **C11**, 19 (1999).

[36] F. J. Gilman, K. Kleinknecht and B. Renk (2004).

[37] G. De Lellis, P. Migliozzi and P. Santorelli, Phys. Rept. **399**, 227 (2004), [Erratum: Phys. Rept.411,323(2005)].

[38] N. Ushida *et al.* (Fermilab E531), Phys. Lett. **B206**, 380 (1988).

[39] T. Bolton (1997), [hep-ex/9708014].

[40] A. Kayis-Topaksu *et al.* (CHORUS), Phys. Lett. **B626**, 24 (2005).

[41] A. Zupanc *et al.* (Belle), JHEP **09**, 139 (2013), [arXiv:1307.6240].

[42] J. P. Alexander *et al.* (CLEO), Phys. Rev. **D79**, 052001 (2009), [arXiv:0901.1216].

[43] P. del Amo Sanchez *et al.* (BaBar), Phys. Rev. **D82**, 091103 (2010), [Erratum: Phys. Rev.D91,no.1,019901(2015)], [arXiv:1008.4080].

[44] M. Ablikim *et al.* (BESIII), Phys. Rev. **D94**, 7, 072004 (2016), [arXiv:1608.06732].

[45] M. Ablikim *et al.* (BESIII), Phys. Rev. Lett. **122**, 7, 071802 (2019), [arXiv:1811.10890].

[46] P. U. E. Onyisi *et al.* (CLEO), Phys. Rev. **D79**, 052002 (2009), [arXiv:0901.1147].

[47] P. Naik *et al.* (CLEO), Phys. Rev. **D80**, 112004 (2009), [arXiv:0910.3602].

[48] B. Aubert *et al.* (BaBar), Phys. Rev. **D76**, 052005 (2007), [arXiv:0704.0020].

[49] M. Ablikim *et al.* (BESIII), Phys. Rev. Lett. **122**, 1, 011804 (2019), [arXiv:1810.03127].

[50] LEP W branching fraction results for this Review of Particle Physics, LEPEWWG/XSEC/2005-01, http://lepewwg.web.cern.ch/LEPEWWG/lepww/4f/Winter05.

[51] P. Abreu *et al.* (DELPHI), Phys. Lett. **B439**, 209 (1998).

[52] I. I. Y. Bigi *et al.*, Phys. Rev. Lett. **71**, 496 (1993), [hep-ph/9304225].

[53] A. V. Manohar and M. B. Wise, Phys. Rev. **D49**, 1310 (1994), [hep-ph/9308246].

[54] I. I. Y. Bigi *et al.*, Phys. Rev. **D56**, 4017 (1997), [hep-ph/9704245].

[55] A. H. Hoang, Z. Ligeti and A. V. Manohar, Phys. Rev. **D59**, 074017 (1999), [hep-ph/9811239]; A. H. Hoang, Z. Ligeti and A. V. Manohar, Phys. Rev. Lett. **82**, 277 (1999), [hep-ph/9809423]; A. H. Hoang and T. Teubner, Phys. Rev. **D60**, 114027 (1999), [hep-ph/9904468].

[56] N. Isgur and M. B. Wise, Phys. Lett. **B237**, 527 (1990); N. Isgur and M. B. Wise, Phys. Lett. **B232**, 113 (1989).

[57] A. Abdesselam *et al.* (Belle) (2017), [arXiv:1702.01521].

[58] C. G. Boyd, B. Grinstein and R. F. Lebed, Phys. Rev. **D56**, 6895 (1997), [hep-ph/9705252]; C. G. Boyd, B. Grinstein and R. F. Lebed, Nucl. Phys. **B461**, 493 (1996), [hep-ph/9508211].

[59] M. Neubert, Phys. Rev. **D49**, 3392 (1994), [hep-ph/9311325]; M. Neubert, Phys. Rev. **D49**, 4623 (1994), [hep-ph/9312311].

[60] I. I. Y. Bigi *et al.*, Int. J. Mod. Phys. **A9**, 2467 (1994), [hep-ph/9312359].

[61] C. W. Bauer, Z. Ligeti and M. E. Luke, Phys. Lett. **B479**, 395 (2000), [hep-ph/0002161]; C. W. Bauer, Z. Ligeti and M. E. Luke, Phys. Rev. **D64**, 113004 (2001), [hep-ph/0107074].

[62] A. Bornheim *et al.* (CLEO), Phys. Rev. Lett. **88**, 231803 (2002), [hep-ex/0202019].

[63] B. Aubert *et al.* (BaBar), Phys. Rev. **D73**, 012006 (2006), [hep-ex/0509040].

[64] A. Limosani *et al.* (Belle), Phys. Lett. **B621**, 28 (2005), [hep-ex/0504046].

[65] P. Urquijo *et al.* (Belle), Phys. Rev. Lett. **104**, 021801 (2010), [arXiv:0907.0379]; J. P. Lees *et al.* (BaBar), Phys. Rev. **D86**, 032004 (2012), [arXiv:1112.0702].

[66] J. A. Bailey *et al.* (Fermilab Lattice, MILC), Phys. Rev. **D92**, 1, 014024 (2015), [arXiv:1503.07839]; J. M. Flynn *et al.*, Phys. Rev. **D91**, 7, 074510 (2015), [arXiv:1501.05373]; B. Colquhoun *et al.*, Phys. Rev. **D93**, 3, 034502 (2016), [arXiv:1510.07446].

[67] P. Ball and R. Zwicky, Phys. Rev. **D71**, 014015 (2005), [hep-ph/0406232]; A. Khodjamirian *et al.*, Phys. Rev. **D83**, 094031 (2011), [arXiv:1103.2655].

[68] Particle listing, in this *Review*.

[69] R. Aaij *et al.* (LHCb), Nature Phys. **11**, 743 (2015), [arXiv:1504.01568].

[70] H. Albrecht *et al.* (ARGUS), Phys. Lett. **B192**, 245 (1987).

[71] O. Schneider, "B^0–$\overline{B}^0$ mixing," in this *Review*.

[72] A. Abulencia *et al.* (CDF), Phys. Rev. Lett. **97**, 242003 (2006), [hep-ex/0609040].

[73] R. Aaij *et al.* (LHCb), New J. Phys. **15**, 053021 (2013), [arXiv:1304.4741].

[74] M. Misiak *et al.*, Phys. Rev. Lett. **114**, 22, 221801 (2015), [arXiv:1503.01789]; M. Czakon *et al.*, JHEP **04**, 168 (2015), [arXiv:1503.01791].

[75] B. Grinstein and D. Pirjol, Phys. Rev. **D62**, 093002 (2000), [hep-ph/0002216]; A. Ali, E. Lunghi and A. Ya. Parkhomenko, Phys. Lett. **B595**, 323 (2004), [hep-ph/0405075]; M. Beneke, T. Feldmann and D. Seidel, Nucl. Phys. **B612**, 25 (2001), [hep-ph/0106067]; S. W. Bosch and G. Buchalla, Nucl. Phys. **B621**, 459 (2002), [hep-ph/0106081]; Z. Ligeti and M. B. Wise, Phys. Rev. **D60**, 117506 (1999), [hep-ph/9905277]; D. Becirevic *et al.*, JHEP **05**, 007 (2003), [hep-lat/0301020]; P. Ball, G. W. Jones and R. Zwicky, Phys. Rev. **D75**, 054004 (2007), [hep-ph/0612081]; W. Wang, R.-H. Li and C.-D. Lu (2007), [arXiv:0711.0432]; C.-D. Lu, W. Wang and Z.-T. Wei, Phys. Rev. **D76**, 014013 (2007), [hep-ph/0701265].

[76] A. J. Buras *et al.*, Phys. Rev. Lett. **95**, 261805 (2005), [hep-ph/0508165].

[77] A. V. Artamonov *et al.* (E949), Phys. Rev. Lett. **101**, 191802 (2008), [arXiv:0808.2459]; A. V. Artamonov *et al.* (BNL-E949), Phys. Rev. **D79**, 092004 (2009), [arXiv:0903.0030].

[78] E. Cortina Gil *et al.* (NA62), Phys. Lett. **B791**, 156 (2019), [arXiv:1811.08508].

[79] D. Acosta *et al.* (CDF), Phys. Rev. Lett. **95**, 102002 (2005), [hep-ex/0505091].

[80] V. M. Abazov *et al.* (D0), Phys. Rev. Lett. **107**, 121802 (2011), [arXiv:1106.5436].

[81] V. Khachatryan *et al.* (CMS), Phys. Lett. **B736**, 33 (2014), [arXiv:1404.2292].

[82] T. A. Aaltonen *et al.* (CDF, D0), Phys. Rev. Lett. **115**, 15, 152003 (2015), [arXiv:1503.05027].

[83] LHC Top Working Group summary plots, single top quark production, Nov. 2017, `https://twiki.cern.ch/twiki/bin/view/LHCPhysics/LHCTopWGSummaryPlots`.

[84] J. Swain and L. Taylor, Phys. Rev. **D58**, 093006 (1998), [hep-ph/9712420].

[85] "K^0_L meson" particle listing, in this *Review*.

[86] A. J. Buras, D. Guadagnoli and G. Isidori, Phys. Lett. **B688**, 309 (2010), [arXiv:1002.3612]; For earlier discussions, see Ref. [87].

[87] E. A. Andriyash, G. G. Ovanesyan and M. I. Vysotsky, Phys. Lett. **B599**, 253 (2004), [hep-ph/0310314]; K. Anikeev *et al.*, in "Workshop on B Physics at the Tevatron: Run II and Beyond Batavia, Illinois, September 23-25, 1999," (2001), [hep-ph/0201071]; A. J. Buras and D. Guadagnoli, Phys. Rev. **D78**, 033005 (2008), [arXiv:0805.3887].

[88] T. Inami and C. S. Lim, Prog. Theor. Phys. **65**, 297 (1981), [Erratum: Prog. Theor. Phys.65,1772(1981)].

[89] J. M. Flynn and L. Randall, Phys. Lett. **B224**, 221 (1989), [Erratum: Phys. Lett.B235,412(1990)]; G. Buchalla, A. J. Buras and M. K. Harlander, Nucl. Phys. **B337**, 313 (1990).

[90] M. Ciuchini *et al.*, Phys. Lett. **B301**, 263 (1993), [hep-ph/9212203]; A. J. Buras, M. Jamin and M. E. Lautenbacher, Nucl. Phys. **B408**, 209 (1993), [hep-ph/9303284]; T. Hambye *et al.*, Nucl. Phys. **B564**, 391 (2000), [hep-ph/9906434]; S. Bertolini, J. O. Eeg and M. Fabbrichesi, Phys. Rev. **D63**, 056009 (2001), [hep-ph/0002234]; V. Cirigliano *et al.*, Phys. Rev. Lett. **91**, 162001 (2003), [hep-ph/0307030].

[91] Z. Bai *et al.* (RBC, UKQCD), Phys. Rev. Lett. **115**, 21, 212001 (2015), [arXiv:1505.07863].

[92] A. J. Buras *et al.*, JHEP **11**, 202 (2015), [arXiv:1507.06345].

[93] V. Cirigliano *et al.*, JHEP **02**, 032 (2020), [arXiv:1911.01359].

[94] A. B. Carter and A. I. Sanda, Phys. Rev. Lett. **45**, 952 (1980); A. B. Carter and A. I. Sanda, Phys. Rev. **D23**, 1567 (1981).

[95] A more detailed discussion and references can be found in: T. Gershon and Y. Nir, "CP violation in meson decays," in this *Review*.

[96] T. Gershon, M. Kenzie and K. Trabelsi, "Determination of CKM angles from B hadrons," in this *Review*.

[97] B. Aubert *et al.* (BaBar), Phys. Rev. **D79**, 072009 (2009), [arXiv:0902.1708].

[98] I. Adachi *et al.* (Belle), Phys. Rev. Lett. **108**, 171802 (2012), [arXiv:1201.4643].

[99] R. Aaij *et al.* (LHCb), Phys. Rev. Lett. **115**, 3, 031601 (2015), [arXiv:1503.07089].

[100] B. Aubert *et al.* (BaBar), Phys. Rev. **D71**, 032005 (2005), [hep-ex/0411016].

[101] R. Itoh *et al.* (Belle), Phys. Rev. Lett. **95**, 091601 (2005), [hep-ex/0504030].

[102] I. Adachi *et al.* (BaBar, Belle), Phys. Rev. Lett. **121**, 26, 261801 (2018), [arXiv:1804.06152]; I. Adachi *et al.* (BaBar, Belle), Phys. Rev. **D98**, 11, 112012 (2018), [arXiv:1804.06153].

[103] A. Abdesselam *et al.* (BaBar, Belle), Phys. Rev. Lett. **115**, 12, 121604 (2015), [arXiv:1505.04147].

[104] Heavy Flavor Averaging Group [24], Moriond 2020 updates for Unitarity Triangle Parameters: `https://hflav-eos.web.cern.ch/hflav-eos/triangle/PDG2020/`.

[105] M. Gronau and D. London, Phys. Rev. Lett. **65**, 3381 (1990).

[106] J. Zhang *et al.* (Belle), Phys. Rev. Lett. **91**, 221801 (2003), [hep-ex/0306007]; A. Somov *et al.* (Belle), Phys. Rev. Lett. **96**, 171801 (2006), [hep-ex/0601024]; B. Aubert *et al.* (BaBar), Phys. Rev. Lett. **97**, 261801 (2006), [hep-ex/0607092]; B. Aubert *et al.* (BaBar), Phys. Rev. **D76**, 052007 (2007), [arXiv:0705.2157].

[107] B. Aubert *et al.* (BaBar), Phys. Rev. **D78**, 071104 (2008), [arXiv:0807.4977].

[108] A. F. Falk *et al.*, Phys. Rev. **D69**, 011502 (2004), [hep-ph/0310242].

[109] A. E. Snyder and H. R. Quinn, Phys. Rev. **D48**, 2139 (1993).

[110] A. Kusaka *et al.* (Belle), Phys. Rev. Lett. **98**, 221602 (2007), [hep-ex/0701015].

[111] J. P. Lees *et al.* (BaBar), Phys. Rev. **D88**, 1, 012003 (2013), [arXiv:1304.3503].

[112] A. Hocker *et al.*, Eur. Phys. J. **C21**, 225 (2001), [hep-ph/0104062]; and updates at `http://ckmfitter.in2p3.fr/`.

[113] M. Bona *et al.* (UTfit), JHEP **07**, 028 (2005), [hep-ph/0501199]; and updates at `http://www.utfit.org`.

[114] M. Gronau and D. London, Phys. Lett. **B253**, 483 (1991).

[115] M. Gronau and D. Wyler, Phys. Lett. **B265**, 172 (1991).

[116] D. Atwood, I. Dunietz and A. Soni, Phys. Rev. Lett. **78**, 3257 (1997), [hep-ph/9612433]; D. Atwood, I. Dunietz and A. Soni, Phys. Rev. **D63**, 036005 (2001), [hep-ph/0008090].

[117] A. Bondar, talk at the Belle analysis workshop, Novosibirsk, September 2002; A. Poluektov *et al.* (Belle), Phys. Rev. **D70**, 072003 (2004), [hep-ex/0406067].

[118] A. Giri *et al.*, Phys. Rev. **D68**, 054018 (2003), [hep-ph/0303187].

[119] A. Poluektov *et al.* (Belle), Phys. Rev. **D81**, 112002 (2010), [arXiv:1003.3360].

[120] P. del Amo Sanchez *et al.* (BaBar), Phys. Rev. Lett. **105**, 121801 (2010), [arXiv:1005.1096].

[121] R. Aaij *et al.* (LHCb), JHEP **10**, 097 (2014), [arXiv:1408.2748].

[122] Y. Grossman, A. Soffer and J. Zupan, Phys. Rev. **D72**, 031501 (2005), [hep-ph/0505270].

[123] A. Amorim, M. G. Santos and J. P. Silva, Phys. Rev. **D59**, 056001 (1999), [hep-ph/9807364].

[124] R. Aleksan, I. Dunietz and B. Kayser, Z. Phys. **C54**, 653 (1992).

[125] R. Aaij *et al.* (LHCb), JHEP **03**, 059 (2018), [arXiv:1712.07428].

[126] B. Aubert *et al.* (BaBar), Phys. Rev. **D71**, 112003 (2005), [hep-ex/0504035]; B. Aubert *et al.* (BaBar), Phys. Rev. **D73**, 111101 (2006), [hep-ex/0602049]; F. J. Ronga *et al.* (Belle), Phys. Rev. **D73**, 092003 (2006), [hep-ex/0604013]; S. Bahinipati *et al.* (Belle), Phys. Rev. **D84**, 021101 (2011), [arXiv:1102.0888]; R. Aaij *et al.* (LHCb), JHEP **06**, 084 (2018), [arXiv:1805.03448].

[127] G. P. Dubois-Felsmann *et al.*, *Sensitivity of CKM fits to theoretical uncertainties and their representation* (2003), [hep-ph/0308262]; G. Eigen *et al.*, Phys. Rev. **D89**, 3, 033004 (2014), [arXiv:1301.5867].

[128] D. Boutigny *et al.* (BaBar), in "Workshop on Physics at an Asymmetric B Factory (BaBar Collaboration Meeting) Pasadena, California, September 22-24, 1997," (1998), URL `http://www-public.slac.stanford.edu/sciDoc/docMeta.aspx?slacPubNumber=SLAC-R-504`.

[129] S. Plaszczynski and M.-H. Schune hf8/019 (1999), [PoShf8,019(1999)], [hep-ph/9911280].

[130] M. Bona *et al.* (UTfit), JHEP **03**, 049 (2008), [arXiv:0707.0636].

[131] We thank the CKMfitter and UTfit groups for performing fits and preparing plots using input values from this *Review*.

[132] H. E. Haber, Nucl. Phys. Proc. Suppl. **62**, 469 (1998), [hep-ph/9709450]; Y. Nir, *CP violation: A New era* (2001), [hep-ph/0109090].

[133] J. M. Soares and L. Wolfenstein, Phys. Rev. **D47**, 1021 (1993); T. Goto *et al.*, Phys. Rev. **D53**, 6662 (1996), [hep-ph/9506311]; J. P. Silva and L. Wolfenstein, Phys. Rev. **D55**, 5331 (1997), [hep-ph/9610208].

[134] Y. Grossman, Z. Ligeti and Y. Nir, Prog. Theor. Phys. **122**, 125 (2009), [arXiv:0904.4262].

[135] G. Isidori, Y. Nir and G. Perez, Ann. Rev. Nucl. Part. Sci. **60**, 355 (2010), [arXiv:1002.0900]; G. Isidori, in "Proceedings, 2012 European School of High-Energy Physics (ESHEP 2012): La Pommeraye, Anjou, France, June 06-19, 2012," 69–105 (2014), [arXiv:1302.0661].

[136] Z. Ligeti, Int. J. Mod. Phys. **A20**, 5105 (2005), [hep-ph/0408267].

[137] J. Charles *et al.*, Phys. Rev. **D89**, 3, 033016 (2014), [arXiv:1309.2293].

[138] K. Agashe *et al.* (2005), [hep-ph/0509117].

[139] S. Laplace *et al.*, Phys. Rev. **D65**, 094040 (2002), [hep-ph/0202010].

[140] R. Aaij *et al.* (LHCb), JHEP **08**, 037 (2017), [arXiv:1704.08217]; G. Aad *et al.* (ATLAS) (2020), [arXiv:2001.07115]; V. Khachatryan *et al.* (CMS), Phys. Lett. **B757**, 97 (2016), [arXiv:1507.07527].

[141] J. K. Ahn *et al.* (KOTO), Phys. Rev. Lett. **122**, 2, 021802 (2019), [arXiv:1810.09655].

[142] A. J. Buras *et al.*, JHEP **11**, 033 (2015), [arXiv:1503.02693].

13. *CP* Violation in the Quark Sector

Revised August 2019 by T. Gershon (Warwick U.) and Y. Nir (Weizmann Inst.).

The *CP* transformation combines charge conjugation C with parity P. Under C, particles and antiparticles are interchanged, by conjugating all internal quantum numbers, *e.g.*, $Q \to -Q$ for electromagnetic charge. Under P, the handedness of space is reversed, $\vec{x} \to -\vec{x}$. Thus, for example, a left-handed electron e^-_L is transformed under *CP* into a right-handed positron, e^+_R.

If *CP* were an exact symmetry, the laws of Nature would be the same for matter and for antimatter. We observe that most phenomena are C- and P-symmetric, and therefore, also *CP*-symmetric. In particular, these symmetries are respected by the gravitational, electromagnetic, and strong interactions. The weak interactions, on the other hand, violate C and P in the strongest possible way. For example, the charged W bosons couple to left-handed electrons, e^-_L, and to their *CP*-conjugate right-handed positrons, e^+_R, but to neither their C-conjugate left-handed positrons, e^+_L, nor their P-conjugate right-handed electrons, e^-_R. While weak interactions violate C and P separately, *CP* is still preserved in most weak interaction processes. The *CP* symmetry is, however, violated in certain rare processes, as discovered in neutral K decays in 1964 [1], and established later in B (2001) and D (2019) decays. A K_L meson decays more often to $\pi^- e^+ \nu_e$ than to $\pi^+ e^- \overline{\nu}_e$, thus allowing electrons and positrons to be unambiguously distinguished, but the decay-rate asymmetry is only at the 0.003 level. The *CP*-violating effects observed in the B system are larger: the parameter describing the *CP* asymmetry in the decay time distribution of $B^0/\overline{B}^0$ meson transitions to *CP* eigenstates like $J/\psi K_S$ is about 0.7 [2, 3]. These effects are related to K^0–$\overline{K}^0$ and B^0–$\overline{B}^0$ mixing, but *CP* violation arising solely from decay amplitudes has also been observed, first in $K \to \pi\pi$ decays [4–6], subsequently in B^0 [7, 8], B^+ [9–11], and B^0_s [12] decays, and most recently in charm decays [13]. Similar effects could also occur in decays of baryons, but have not yet been observed. Moreover, *CP* violation has not yet been observed in processes involving the top quark, nor in flavor-conserving processes such as electric dipole moments, nor in the lepton sector; for all of these any significant observation would be a clear indication of physics beyond the Standard Model.

In addition to parity and to continuous Lorentz transformations, there is one other spacetime operation that could be a symmetry of the interactions: time reversal T, $t \to -t$. Violations of T symmetry have been observed in neutral K decays [14]. More recently, exploiting the fact that for neutral B mesons both flavor tagging and *CP* tagging can be used [15], T violation has been observed between states that are not *CP*-conjugate [16]. Moreover, T violation is expected as a corollary of *CP* violation if the combined *CPT* transformation is a fundamental symmetry of Nature [17]. All observations indicate that *CPT* is indeed a symmetry of Nature. Furthermore, one cannot build a locally Lorentz-invariant quantum field theory with a Hermitian Hamiltonian that violates *CPT*. (At several points in our discussion, we avoid assumptions about *CPT*, in order to identify cases where evidence for *CP* violation relies on assumptions about *CPT*.)

Within the Standard Model, *CP* symmetry is broken by complex phases in the Yukawa couplings (that is, the couplings of the Higgs scalar to quarks). When all manipulations to remove unphysical phases in this model are exhausted, one finds that there is a single *CP*-violating parameter [18]. In the basis of mass eigenstates, this single phase appears in the 3×3 unitary matrix that gives the W-boson couplings to an up-type antiquark and a down-type quark. (If the Standard Model is supplemented with Majorana mass terms for the neutrinos, the analogous mixing matrix for leptons has three *CP*-violating phases.) The beautifully consistent and economical Standard-Model description of *CP* violation in terms of Yukawa couplings, known as the Kobayashi-Maskawa (KM) mechanism [18], agrees with all measurements to date. (Some measurements are in tension with the predictions, and are discussed in more detail below. Pending verification, the results are not considered to change the overall picture of agreement with the Standard Model.) Furthermore, one can fit the data allowing new physics contributions to loop processes to compete with, or even dominate over, the Standard Model amplitudes [19, 20]. Such an analysis provides model-independent proof that the KM phase is different from zero, and that the matrix of three-generation quark mixing is the dominant source of *CP* violation in meson decays.

The current level of experimental accuracy and the theoretical uncertainties involved in the interpretation of the various observations leave room, however, for additional subdominant sources of *CP* violation from new physics. Indeed, almost all extensions of the Standard Model imply that there are such additional sources. Moreover, *CP* violation is a necessary condition for baryogenesis, the process of dynamically generating the matter-antimatter asymmetry of the Universe [21]. Despite the phenomenological success of the KM mechanism, it fails (by several orders of magnitude) to accommodate the observed asymmetry [22]. This discrepancy strongly suggests that Nature provides additional sources of *CP* violation beyond the KM mechanism. The evidence for neutrino masses implies that *CP* can be violated also in the lepton sector. This situation makes leptogenesis [23,24], a scenario where *CP*-violating phases in the Yukawa couplings of the neutrinos play a crucial role in the generation of the baryon asymmetry, a very attractive possibility. The expectation of new sources motivates the large ongoing experimental effort to find deviations from the predictions of the KM mechanism.

CP violation can be experimentally searched for in a variety of processes, such as hadron decays, electric dipole moments of neutrons, electrons and nuclei, and neutrino oscillations. Hadron decays via the weak interaction probe flavor-changing *CP* violation. The search for electric dipole moments may find (or constrain) sources of *CP* violation that, unlike the KM phase, are not related to flavor-changing couplings. Following the discovery of the Higgs boson [25,26], searches for *CP* violation in the Higgs sector are becoming feasible. Future searches for *CP* violation in neutrino oscillations might provide further input on leptogenesis.

The present measurements of *CP* asymmetries provide some of the strongest constraints on the weak couplings of quarks. Future measurements of *CP* violation in K, D, B, and B^0_s meson decays will provide additional constraints on the flavor parameters of the Standard Model, and can probe new physics. In this review, we give the formalism and basic physics that are relevant to present and near future measurements of *CP* violation in the quark sector.

Before going into details, we list here the observables where *CP* violation has been observed at a level above 5σ [27–29]:

- Indirect *CP* violation in $K \to \pi\pi$ and $K \to \pi\ell\nu$ decays, and in the $K_L \to \pi^+\pi^- e^+ e^-$ decay, is given by
$$|\epsilon| = (2.228 \pm 0.011) \times 10^{-3}\,. \tag{13.1}$$
- Direct *CP* violation in $K \to \pi\pi$ decays is given by
$$\mathcal{R}e(\epsilon'/\epsilon) = (1.65 \pm 0.26) \times 10^{-3}\,. \tag{13.2}$$
- *CP* violation in the interference of mixing and decay in the tree-dominated $b \to c\bar{c}s$ transitions, such as $B^0 \to \psi K^0$, is given by (we use K^0 throughout to denote results that combine K_S and K_L modes, but use the sign appropriate to K_S):
$$S_{\psi K^0} = +0.699 \pm 0.017\,. \tag{13.3}$$
- *CP* violation in the interference of mixing and decay in modes governed by the tree-dominated $b \to c\bar{u}d$ transitions is given by
$$S_{D^{(*)}h^0} = +0.71 \pm 0.09\,, \tag{13.4}$$
- *CP* violation in the interference of mixing and decay in various modes related to $b \to c\bar{c}d$ transitions is given by
$$\begin{aligned} S_{\psi\pi^0} &= -0.86 \pm 0.14\,, \\ S_{D^+D^-} &= -0.84 \pm 0.12\,, \\ S_{D^{*+}D^{*-}} &= -0.71 \pm 0.09\,. \end{aligned} \tag{13.5}$$

- *CP* violation in the interference of mixing and decay in various modes related to $b \to q\bar{q}s$ (penguin) transitions is given by

$$\begin{aligned} S_{\phi K^0} &= +0.74\,^{+0.11}_{-0.13}\,, \\ S_{\eta' K^0} &= +0.63 \pm 0.06\,, \\ S_{f_0 K^0} &= +0.69\,^{+0.10}_{-0.12}\,, \\ S_{K^+K^-K_S} &= +0.68\,^{+0.09}_{-0.10}\,. \end{aligned} \tag{13.6}$$

- *CP* violation in the interference of mixing and decay in the $B^0 \to \pi^+\pi^-$ mode is given by

$$S_{\pi^+\pi^-} = -0.63 \pm 0.04\,. \tag{13.7}$$

- Direct *CP* violation in the $B^0 \to \pi^+\pi^-$ mode is given by

$$C_{\pi^+\pi^-} = -0.32 \pm 0.04\,. \tag{13.8}$$

- Direct *CP* violation in $B^+ \to D_+ K^+$ decays (D_+ is the *CP*-even neutral D state) is given by

$$\mathcal{A}_{B^+ \to D_+ K^+} = +0.129 \pm 0.012\,, \tag{13.9}$$

  while the corresponding quantity in the case that the neutral D meson is reconstructed in the suppressed $K^-\pi^+$ final state is

$$\mathcal{A}_{B^+ \to D_{K^-\pi^+} K^+} = -0.41 \pm 0.06\,, \tag{13.10}$$

- Direct *CP* violation has also been observed in $B^+ \to DK^+$ decays through differences between the Dalitz plot distributions of subsequent $D \to K_S\pi^+\pi^-$ decays.
- Direct *CP* violation in the $\overline{B}^0 \to K^-\pi^+$ mode is given by

$$\mathcal{A}_{\overline{B}^0 \to K^-\pi^+} = -0.084 \pm 0.004\,. \tag{13.11}$$

- Direct *CP* violation in the $\overline{B}^0_s \to K^+\pi^-$ mode is given by

$$\mathcal{A}_{\overline{B}^0_s \to K^+\pi^-} = +0.213 \pm 0.017\,. \tag{13.12}$$

- Direct *CP* violation in $B^+ \to K^+K^-\pi^+$ decays is given by

$$\mathcal{A}_{B^+ \to K^+K^-\pi^+} = -0.118 \pm 0.022\,. \tag{13.13}$$

  An amplitude analysis has established a large *CP* violation effect associated with $\pi\pi \leftrightarrow KK$ S-wave rescattering in $B^+ \to K^+K^-\pi^+$ decays.
- Large *CP* violation effects have also been observed in certain regions of the phase space of $B^+ \to K^+K^-K^+$, $\pi^+\pi^-K^+$ and $\pi^+\pi^-\pi^+$ decays.
- Direct *CP* violation has been established in the difference of asymmetries for $D^0 \to K^+K^-$ and $D^0 \to \pi^+\pi^-$ decays

$$\Delta a_{CP} = (-0.164 \pm 0.028) \times 10^{-3}\,. \tag{13.14}$$

13.1 Formalism

The phenomenology of *CP* violation for neutral flavored mesons is particularly interesting, since many of the observables can be cleanly interpreted. Although the phenomenology is superficially different for K^0, D^0, B^0, and B^0_s decays, this is primarily because each of these systems is governed by a different balance between decay rates, oscillations, and lifetime splitting. However, the general considerations presented in this section are identical for all flavored neutral pseudoscalar mesons. The phenomenology of *CP* violation for neutral mesons that do not carry flavor quantum numbers (such as the $\eta^{(\prime)}$ state) is quite different: such states are their own antiparticles and have definite *CP* eigenvalues, so the signature of *CP* violation is simply the decay to a final state with the opposite *CP*. Such decays are mediated by the electromagnetic or (OZI-suppressed) strong interaction, where *CP* violation is not expected and has not yet been observed. In the remainder of this review, we restrict ourselves to considerations of weakly decaying hadrons.

In this section, we present a general formalism for, and classification of, *CP* violation in the decay of a weakly decaying hadron, denoted M. We pay particular attention to the case that M is a K^0, D^0, B^0, or B^0_s meson. Subsequent sections describe the *CP*-violating phenomenology, approximations, and alternative formalisms that are specific to each system.

13.1.1 *Charged- and neutral-hadron decays*

We define decay amplitudes of M (which could be charged or neutral) and its *CP* conjugate $\overline{M}$ to a multi-particle final state f and its *CP* conjugate $\overline{f}$ as

$$A_f = \langle f\,|\mathcal{H}|\,M\rangle\,, \quad \overline{A}_f = \langle f\,|\mathcal{H}|\,\overline{M}\rangle\,, \tag{13.15a}$$

$$A_{\overline{f}} = \langle \overline{f}\,|\mathcal{H}|\,M\rangle\,, \quad \overline{A}_{\overline{f}} = \langle \overline{f}\,|\mathcal{H}|\,\overline{M}\rangle\,, \tag{13.15b}$$

where $\mathcal{H}$ is the Hamiltonian governing weak interactions. The action of *CP* on these states introduces phases ξ_M and ξ_f that depend on their flavor content, according to

$$CP|M\rangle = e^{+i\xi_M}\,|\overline{M}\rangle\,, \quad CP|f\rangle = e^{+i\xi_f}\,|\overline{f}\rangle\,, \tag{13.16a}$$

$$CP|\overline{M}\rangle = e^{-i\xi_M}\,|M\rangle\,, \quad CP|\overline{f}\rangle = e^{-i\xi_f}\,|f\rangle\,, \tag{13.16b}$$

so that $(CP)^2 = 1$. The phases ξ_M and ξ_f are arbitrary and unobservable because of the flavor symmetry of the strong interaction. If *CP* is conserved by the dynamics, $[CP, \mathcal{H}] = 0$, then A_f and $\overline{A}_{\overline{f}}$ have the same magnitude and an arbitrary unphysical relative phase

$$\overline{A}_{\overline{f}} = e^{i(\xi_f - \xi_M)}\,A_f\,. \tag{13.17}$$

13.1.2 *Neutral-meson mixing*

A state that is initially a superposition of M^0 and $\overline{M}^0$, say

$$|\psi(0)\rangle = a(0)|M^0\rangle + b(0)|\overline{M}^0\rangle\,, \tag{13.18}$$

will evolve in time acquiring components that describe all possible decay final states $\{f_1, f_2, \ldots\}$, that is,

$$|\psi(t)\rangle = a(t)|M^0\rangle + b(t)|\overline{M}^0\rangle + c_1(t)|f_1\rangle + c_2(t)|f_2\rangle + \cdots\,. \tag{13.19}$$

If we are interested in computing only the values of $a(t)$ and $b(t)$ (and not the values of all $c_i(t)$), and if the times t in which we are interested are much larger than the typical strong interaction scale, then we can use a much simplified formalism [30]. The simplified time evolution is determined by a 2×2 effective Hamiltonian $\mathbf{H}$ that is not Hermitian, since otherwise the mesons would only oscillate and not decay. Any complex matrix, such as $\mathbf{H}$, can be written in terms of Hermitian matrices $\mathbf{M}$ and $\mathbf{\Gamma}$ as

$$\mathbf{H} = \mathbf{M} - \frac{i}{2}\,\mathbf{\Gamma}\,. \tag{13.20}$$

$\mathbf{M}$ and $\mathbf{\Gamma}$ are associated with $(M^0, \overline{M}^0) \leftrightarrow (M^0, \overline{M}^0)$ transitions via off-shell (dispersive), and on-shell (absorptive) intermediate states, respectively. Diagonal elements of $\mathbf{M}$ and $\mathbf{\Gamma}$ are associated with the flavor-conserving transitions $M^0 \to M^0$ and $\overline{M}^0 \to \overline{M}^0$, while off-diagonal elements are associated with flavor-changing transitions $M^0 \leftrightarrow \overline{M}^0$.

The eigenvectors of $\mathbf{H}$ have well-defined masses and decay widths. To specify the components of the strong interaction eigenstates, M^0 and $\overline{M}^0$, in the light (M_L) and heavy (M_H) mass eigenstates, we introduce three complex parameters: p, q, and, for the case that both *CP* and *CPT* are violated in mixing, z:

$$|M_L\rangle \propto p\sqrt{1-z}\,|M^0\rangle + q\sqrt{1+z}\,|\overline{M}^0\rangle\,, \tag{13.21a}$$

$$|M_H\rangle \propto p\sqrt{1+z}\,|M^0\rangle - q\sqrt{1-z}\,|\overline{M}^0\rangle\,, \tag{13.21b}$$

with the normalization $|q|^2 + |p|^2 = 1$ when $z = 0$. (Another possible choice of labelling, which is in standard usage for K mesons, defines the mass eigenstates according to their lifetimes: K_S for the short-lived and K_L for the long-lived state. The K_L is experimentally found to be the heavier state. Yet another choice is often used for the D mesons [31]: the eigenstates are labelled according to their dominant *CP* content.)

The real and imaginary parts of the eigenvalues $\omega_{L,H}$ corresponding to $|M_{L,H}\rangle$ represent their masses and decay widths, respectively. The mass and width splittings are

$$\Delta m \equiv m_H - m_L = \mathcal{R}e(\omega_H - \omega_L) \,, \tag{13.22a}$$

$$\Delta\Gamma \equiv \Gamma_H - \Gamma_L = -2\,\mathcal{I}m(\omega_H - \omega_L) \,. \tag{13.22b}$$

Note that here Δm is positive by definition, while the sign of $\Delta\Gamma$ must be experimentally determined. The sign of $\Delta\Gamma$ has not yet been established for B^0 mesons, while $\Delta\Gamma < 0$ is established for K and B_s^0 mesons. The Standard Model predicts $\Delta\Gamma < 0$ for $B^0_{(s)}$ mesons; for this reason, $\Delta\Gamma = \Gamma_L - \Gamma_H$, which is still a signed quantity, is often used in the $B^0_{(s)}$ literature and is the convention used in the PDG experimental summaries.

Solving the eigenvalue problem for $\mathbf{H}$ yields

$$\left(\frac{q}{p}\right)^2 = \frac{\mathbf{M}_{12}^* - (i/2)\mathbf{\Gamma}_{12}^*}{\mathbf{M}_{12} - (i/2)\mathbf{\Gamma}_{12}} \tag{13.23}$$

and

$$z \equiv \frac{\delta m - (i/2)\delta\Gamma}{\Delta m - (i/2)\Delta\Gamma} \,, \tag{13.24}$$

where

$$\delta m \equiv \mathbf{M}_{11} - \mathbf{M}_{22} \,, \quad \delta\Gamma \equiv \mathbf{\Gamma}_{11} - \mathbf{\Gamma}_{22} \tag{13.25}$$

are the differences in effective mass and decay-rate expectation values for the strong interaction states M^0 and $\overline{M}^0$.

If either CP or CPT is a symmetry of $\mathbf{H}$ (independently of whether T is conserved or violated), then the values of δm and $\delta\Gamma$ are both zero, and hence $z = 0$. We also find that

$$\omega_H - \omega_L = 2\sqrt{\left(\mathbf{M}_{12} - \frac{i}{2}\mathbf{\Gamma}_{12}\right)\left(\mathbf{M}_{12}^* - \frac{i}{2}\mathbf{\Gamma}_{12}^*\right)} \,. \tag{13.26}$$

If either CP or T is a symmetry of $\mathbf{H}$ (independently of whether CPT is conserved or violated), then $\mathbf{\Gamma}_{12}/\mathbf{M}_{12}$ is real, leading to

$$\left(\frac{q}{p}\right)^2 = e^{2i\xi_M} \quad \Rightarrow \quad \left|\frac{q}{p}\right| = 1 \,, \tag{13.27}$$

where ξ_M is the arbitrary unphysical phase introduced in Eq. (13.16). If, and only if, CP is a symmetry of $\mathbf{H}$ (independently of CPT and T), then both of the above conditions hold, with the result that the mass eigenstates are orthogonal

$$\langle M_H | M_L \rangle = |p|^2 - |q|^2 = 0 \,. \tag{13.28}$$

13.1.3 *CP-violating observables*

All CP-violating observables in M and $\overline{M}$ decays to final states f and $\overline{f}$ can be expressed in terms of phase-convention-independent combinations of A_f, $\overline{A}_f$, $A_{\overline{f}}$, and $\overline{A}_{\overline{f}}$, together with, for neutral meson decays only, q/p. CP violation in charged meson and all baryon decays depends only on the combination $|\overline{A}_{\overline{f}}/A_f|$, while CP violation in flavored neutral meson decays is complicated by $M^0 \leftrightarrow \overline{M}^0$ oscillations, and depends, additionally, on $|q/p|$ and on $\lambda_f \equiv (q/p)(\overline{A}_f/A_f)$.

The decay rates of the two neutral kaon mass eigenstates, K_S and K_L, are different enough ($\Gamma_S/\Gamma_L \sim 500$) that one can, in most cases, actually study their decays independently. For D^0, B^0, and B_s^0 mesons, however, values of $\Delta\Gamma/\Gamma$ (where $\Gamma \equiv (\Gamma_H + \Gamma_L)/2$) are relatively small, and so both mass eigenstates must be considered in their evolution. We denote the state of an initially pure $|M^0\rangle$ or $|\overline{M}^0\rangle$ after an elapsed proper time t as $|M^0_{\rm phys}(t)\rangle$ or $|\overline{M}^0_{\rm phys}(t)\rangle$, respectively. Using the effective Hamiltonian approximation, but not assuming CPT to be a good symmetry, we obtain

$$|M^0_{\rm phys}(t)\rangle = (g_+(t) + z\,g_-(t))\,|M^0\rangle - \sqrt{1-z^2}\,\frac{q}{p}\,g_-(t)|\overline{M}^0\rangle \,, \tag{13.29a}$$

$$|\overline{M}^0_{\rm phys}(t)\rangle = (g_+(t) - z\,g_-(t))\,|\overline{M}^0\rangle - \sqrt{1-z^2}\,\frac{p}{q}\,g_-(t)|M^0\rangle \,, \tag{13.29b}$$

where

$$g_\pm(t) \equiv \frac{1}{2}\left[\exp\left(-im_H t - \frac{1}{2}\Gamma_H t\right) \pm \exp\left(-im_L t - \frac{1}{2}\Gamma_L t\right)\right] \tag{13.30}$$

and $z = 0$ if either CPT or CP is conserved.

Defining $x \equiv \Delta m/\Gamma$ and $y \equiv \Delta\Gamma/(2\Gamma)$, and assuming $z = 0$, one obtains the following time-dependent decay rates:

$$\begin{aligned}\frac{d\Gamma\left[M^0_{\rm phys}(t) \to f\right]/dt}{e^{-\Gamma t}\mathcal{N}_f} &= \left(|A_f|^2 + |(q/p)\overline{A}_f|^2\right)\cosh(y\Gamma t) \\ &+ \left(|A_f|^2 - |(q/p)\overline{A}_f|^2\right)\cos(x\Gamma t) \\ &+ 2\,\mathcal{R}e((q/p)A_f^*\overline{A}_f)\sinh(y\Gamma t) \\ &- 2\,\mathcal{I}m((q/p)A_f^*\overline{A}_f)\sin(x\Gamma t) \,,\end{aligned} \tag{13.31a}$$

$$\begin{aligned}\frac{d\Gamma\left[\overline{M}^0_{\rm phys}(t) \to f\right]/dt}{e^{-\Gamma t}\mathcal{N}_f} &= \left(|(p/q)A_f|^2 + |\overline{A}_f|^2\right)\cosh(y\Gamma t) \\ &- \left(|(p/q)A_f|^2 - |\overline{A}_f|^2\right)\cos(x\Gamma t) \\ &+ 2\,\mathcal{R}e((p/q)A_f\overline{A}_f^*)\sinh(y\Gamma t) \\ &- 2\,\mathcal{I}m((p/q)A_f\overline{A}_f^*)\sin(x\Gamma t) \,,\end{aligned} \tag{13.31b}$$

where $\mathcal{N}_f$ is a common, time-independent, normalization factor that can be determined bearing in mind that the range of t is $0 < t < \infty$. Decay rates to the CP-conjugate final state $\overline{f}$ are obtained analogously, with $\mathcal{N}_f = \mathcal{N}_{\overline{f}}$ and the substitutions $A_f \to A_{\overline{f}}$ and $\overline{A}_f \to \overline{A}_{\overline{f}}$ in Eqs. (13.31a) and (13.31b). Terms proportional to $|A_f|^2$ or $|\overline{A}_f|^2$ are associated with decays that occur without any net $M^0 \leftrightarrow \overline{M}^0$ oscillation, while terms proportional to $|(q/p)\overline{A}_f|^2$ or $|(p/q)A_f|^2$ are associated with decays following a net oscillation. The $\sinh(y\Gamma t)$ and $\sin(x\Gamma t)$ terms of Eqs. (13.31a) and (13.31b) are associated with the interference between these two cases. Note that, in multi-body decays, amplitudes are functions of variables that describe the phase-space of the final state. Interference may be present in some regions but not others, and is strongly influenced by resonant substructure.

When neutral pseudoscalar mesons are produced coherently in pairs from the decay of a vector resonance, $V \to M^0\overline{M}^0$ (for example, $\Upsilon(4S) \to B^0\overline{B}^0$, $\psi(3770) \to D^0\overline{D}^0$ or $\phi \to K^0\overline{K}^0$), the time-dependence of their subsequent decays to final states f_1 and f_2 has a similar form to Eqs. (13.31a) and (13.31b):

$$\begin{aligned}\frac{d\Gamma\left[V_{\rm phys}(t_1,t_2) \to f_1 f_2\right]/d(\Delta t)}{e^{-\Gamma|\Delta t|}\mathcal{N}_{f_1 f_2}} &= \left(|a_+|^2 + |a_-|^2\right)\cosh(y\Gamma\Delta t) \\ &+ \left(|a_+|^2 - |a_-|^2\right)\cos(x\Gamma\Delta t) \\ &- 2\,\mathcal{R}e(a_+^* a_-)\sinh(y\Gamma\Delta t) \\ &+ 2\,\mathcal{I}m(a_+^* a_-)\sin(x\Gamma\Delta t) \,,\end{aligned} \tag{13.32}$$

where $\Delta t \equiv t_2 - t_1$ is the difference in the production times, t_1 and t_2, of f_1 and f_2, respectively, and the dependence on the average decay time and on decay angles has been integrated out. The normalisation factor $\mathcal{N}_{f_1 f_2}$ can be evaluated, noting that the range of Δt is $-\infty < \Delta t < \infty$. The coefficients in Eq. (13.32) are determined by the amplitudes for no net oscillation from $t_1 \to t_2$, $\overline{A}_{f_1}A_{f_2}$, and $A_{f_1}\overline{A}_{f_2}$, and for a net oscillation, $(q/p)\overline{A}_{f_1}\overline{A}_{f_2}$ and $(p/q)A_{f_1}A_{f_2}$, via

$$a_+ \equiv \overline{A}_{f_1}A_{f_2} - A_{f_1}\overline{A}_{f_2} \,, \tag{13.33a}$$

$$\begin{aligned}a_- \equiv &-\sqrt{1-z^2}\left(\frac{q}{p}\overline{A}_{f_1}\overline{A}_{f_2} - \frac{p}{q}A_{f_1}A_{f_2}\right) \\ &+ z\left(\overline{A}_{f_1}A_{f_2} + A_{f_1}\overline{A}_{f_2}\right) \,.\end{aligned} \tag{13.33b}$$

Assuming CPT conservation, $z = 0$, and identifying $\Delta t \to t$ and $f_2 \to f$, we find that Eqs. (13.32) and (13.33) reduce to

Eq. (13.31a) with $A_{f_1} = 0$, $\overline{A}_{f_1} = 1$, or to Eq. (13.31b) with $\overline{A}_{f_1} = 0$, $A_{f_1} = 1$. Indeed, such a situation plays an important role in experiments that exploit the coherence of $V \to M^0\overline{M}^0$ production. Final states f_1 with $A_{f_1} = 0$ or $\overline{A}_{f_1} = 0$ are called tagging states, because they identify the decaying pseudoscalar meson as, respectively, $\overline{M}^0$ or M^0. Before one of M^0 or $\overline{M}^0$ decays, they evolve in phase, so that there is always one M^0 and one $\overline{M}^0$ present. A tagging decay of one meson sets the clock for the time evolution of the other: it starts at t_1 as purely M^0 or $\overline{M}^0$, with time evolution that depends only on $t_2 - t_1$.

When f_1 is a state that both M^0 and $\overline{M}^0$ can decay into, then Eq. (13.32) contains interference terms proportional to $A_{f_1}\overline{A}_{f_1} \neq 0$ that are not present in Eqs. (13.31a) and (13.31b). Even when f_1 is dominantly produced by M^0 decays rather than $\overline{M}^0$ decays, or vice versa, $A_{f_1}\overline{A}_{f_1}$ can be non-zero owing to doubly-CKM-suppressed decays (with amplitudes suppressed by at least two powers of λ relative to the dominant amplitude, in the language of Section 13.3), and these terms should be considered for precision studies of *CP* violation in coherent $V \to M^0\overline{M}^0$ decays [32]. The correlations in $V \to M^0\overline{M}^0$ decays can also be exploited to determine strong phase differences between favored and suppressed decay amplitudes [33].

13.1.4 *Classification of CP-violating effects*

We distinguish three types of *CP*-violating effects that can occur in the quark sector:

I. *CP* violation in decay is defined by

$$|\overline{A}_{\overline{f}}/A_f| \neq 1 \,. \tag{13.34}$$

In charged meson (and all baryon) decays, where mixing effects are absent, this is the only possible source of *CP* asymmetries:

$$\mathcal{A}_{f^\pm} \equiv \frac{\Gamma(M^- \to f^-) - \Gamma(M^+ \to f^+)}{\Gamma(M^- \to f^-) + \Gamma(M^+ \to f^+)} = \frac{|\overline{A}_{f^-}/A_{f^+}|^2 - 1}{|\overline{A}_{f^-}/A_{f^+}|^2 + 1} \,. \tag{13.35}$$

Note that the usual sign convention for *CP* asymmetries of hadrons is for the difference between the rate involving the particle that contains a heavy quark and that which contains an antiquark. Hence Eq. (13.35) corresponds to the definition for $B^\pm$ mesons, but the opposite sign is used for $D^\pm_{(s)}$ decays.

II. *CP* (and *T*) violation in mixing is defined by

$$|q/p| \neq 1 \,. \tag{13.36}$$

In charged-current semileptonic neutral meson decays $M, \overline{M} \to \ell^\pm X$ (taking $|A_{\ell^+X}| = |\overline{A}_{\ell^-X}|$ and $A_{\ell^-X} = \overline{A}_{\ell^+X} = 0$, as is the case in the Standard Model, to lowest order in G_F, and in most of its reasonable extensions), this is the only source of *CP* violation, and can be measured via the asymmetry of "wrong-sign" decays induced by oscillations:

$$\mathcal{A}_{\rm SL}(t) \equiv \frac{d\Gamma/dt\left[\overline{M}^0_{\rm phys}(t) \to \ell^+X\right] - d\Gamma/dt\left[M^0_{\rm phys}(t) \to \ell^-X\right]}{d\Gamma/dt\left[\overline{M}^0_{\rm phys}(t) \to \ell^+X\right] + d\Gamma/dt\left[M^0_{\rm phys}(t) \to \ell^-X\right]} \,, \tag{13.37a}$$

$$= \frac{1 - |q/p|^4}{1 + |q/p|^4} \,. \tag{13.37b}$$

Note that this asymmetry of time-dependent decay rates is actually time-independent.

III. *CP* violation in interference between a decay without mixing, $M^0 \to f$, and a decay with mixing, $M^0 \to \overline{M}^0 \to f$ (such an effect occurs only in decays to final states that are common to M^0 and $\overline{M}^0$, including all *CP* eigenstates), is defined by

$$\arg(\lambda_f) + \arg(\lambda_{\bar{f}}) \neq 0 \,, \qquad \text{with} \qquad \lambda_f \equiv \frac{q}{p}\frac{\overline{A}_f}{A_f} \,. \tag{13.38}$$

For final *CP* eigenstates, f_{CP}, the condition Eq. (13.38) simplifies to

$$\mathcal{I}m(\lambda_{f_{CP}}) \neq 0 \,, \tag{13.39}$$

This form of *CP* violation can be observed, for example, using the asymmetry of neutral meson decays into *CP* eigenstates

$$\mathcal{A}_{f_{CP}}(t) \equiv \frac{d\Gamma/dt\left[\overline{M}^0_{\rm phys}(t) \to f_{CP}\right] - d\Gamma/dt\left[M^0_{\rm phys}(t) \to f_{CP}\right]}{d\Gamma/dt\left[\overline{M}^0_{\rm phys}(t) \to f_{CP}\right] + d\Gamma/dt\left[M^0_{\rm phys}(t) \to f_{CP}\right]} \,. \tag{13.40}$$

If $\Delta\Gamma = 0$, as expected to a good approximation for B^0 mesons but not for K^0 and B^0_s mesons, and $|q/p| = 1$, then $\mathcal{A}_{f_{CP}}$ has a particularly simple form (see Eq. (13.89), below). If, in addition, the decay amplitudes fulfill $|\overline{A}_{f_{CP}}| = |A_{f_{CP}}|$, the interference between decays with and without mixing is the only source of asymmetry and $\mathcal{A}_{f_{CP}}(t) = \mathcal{I}m(\lambda_{f_{CP}})\sin(x\Gamma t)$.

Examples of these three types of *CP* violation will be given in Sections 13.4, 13.5, and 13.6.

13.2 Theoretical Interpretation: General Considerations

Consider the $M \to f$ decay amplitude A_f, and the *CP* conjugate process, $\overline{M} \to \overline{f}$, with decay amplitude $\overline{A}_{\overline{f}}$. There are two types of phases that may appear in these decay amplitudes. Complex parameters in any Lagrangian term that contributes to the amplitude will appear in complex conjugate form in the *CP*-conjugate amplitude. Thus, their phases appear in A_f and $\overline{A}_{\overline{f}}$ with opposite signs. In the Standard Model, these phases occur only in the couplings of the $W^\pm$ bosons, and hence, are often called "weak phases." The weak phase of any single term is convention-dependent. However, the difference between the weak phases in two different terms in A_f is convention-independent. A second type of phase can appear in scattering or decay amplitudes, even when the Lagrangian is real. This phase originates from the possible contribution from intermediate on-shell states in the decay process. Since such phases are generated by *CP*-invariant interactions, they are the same in A_f and $\overline{A}_{\overline{f}}$. Usually the dominant rescattering is due to strong interactions; hence the designation "strong phases" for the phase shifts so induced. Again, only the relative strong phases between different terms in the amplitude are physically meaningful.

The "weak" and "strong" phases discussed here appear in addition to the spurious *CP*-transformation phases of Eq. (13.17). Those spurious phases are due to an arbitrary choice of phase convention, and do not originate from any dynamics or induce any *CP* violation. For simplicity, we set them to zero from here on.

It is useful to write each contribution a_i to A_f in three parts: its magnitude $|a_i|$, its weak phase ϕ_i, and its strong phase δ_i. If, for example, there are two such contributions, $A_f = a_1 + a_2$, we have

$$A_f = |a_1|e^{i(\delta_1+\phi_1)} + |a_2|e^{i(\delta_2+\phi_2)} \,, \tag{13.41a}$$

$$\overline{A}_{\overline{f}} = |a_1|e^{i(\delta_1-\phi_1)} + |a_2|e^{i(\delta_2-\phi_2)} \,. \tag{13.41b}$$

Similarly, for neutral mesons, it is useful to write

$$\mathbf{M}_{12} = |\mathbf{M}_{12}|e^{i\phi_M} \,, \quad \mathbf{\Gamma}_{12} = |\mathbf{\Gamma}_{12}|e^{i\phi_\Gamma} \,. \tag{13.42}$$

Each of the phases appearing in Eqs. (13.41) and (13.42) is convention-dependent, but combinations such as $\delta_1 - \delta_2$, $\phi_1 - \phi_2$, $\phi_M - \phi_\Gamma$, and $\phi_M + \phi_1 - \overline{\phi}_1$ (where $\overline{\phi}_1$ is a weak phase contributing to $\overline{A}_f$) are physical.

It is now straightforward to evaluate the various asymmetries in terms of the theoretical parameters introduced here. We will do so with approximations that are often relevant to the most interesting measured asymmetries.

1. The *CP* asymmetry in charged meson and all baryon decays [Eq. (13.35)] is given by

$$\mathcal{A}_f = -\frac{2|a_1a_2|\sin(\delta_2 - \delta_1)\sin(\phi_2 - \phi_1)}{|a_1|^2 + |a_2|^2 + 2|a_1a_2|\cos(\delta_2 - \delta_1)\cos(\phi_2 - \phi_1)} \,. \tag{13.43}$$

The quantity of most interest to theory is the weak phase difference $\phi_2 - \phi_1$. Its extraction from the asymmetry requires, however, that the amplitude ratio $|a_2/a_1|$ and the strong phase difference $\delta_2 - \delta_1$ are known. Both quantities depend on non-perturbative hadronic parameters that are difficult to calculate, but in some cases can be obtained from experiment.

2. In the approximation that $|\mathbf{\Gamma}_{12}/\mathbf{M}_{12}| \ll 1$ (valid for B^0 and B_s^0 mesons), the *CP* asymmetry in semileptonic neutral-meson decays [Eq. (13.37)] is given by

$$\mathcal{A}_{\rm SL} = -\left|\frac{\mathbf{\Gamma}_{12}}{\mathbf{M}_{12}}\right| \sin(\phi_M - \phi_\Gamma)\,. \tag{13.44}$$

The quantity of most interest to theory is the weak phase $\phi_M - \phi_\Gamma$. Its extraction from the asymmetry requires, however, that $|\mathbf{\Gamma}_{12}/\mathbf{M}_{12}|$ is known. State of the art calculations of this quantity for the B^0 and B_s^0 mesons have uncertainties of around 15–20% [34].

3. In the approximations that only a single weak phase contributes to decay, $A_f = |a_f| e^{i(\delta_f + \phi_f)}$, and that $|\mathbf{\Gamma}_{12}/\mathbf{M}_{12}| = 0$, we obtain $|\lambda_f| = 1$, and the *CP* asymmetries in decays to a final *CP* eigenstate f [Eq. (13.40)] with eigenvalue $\eta_f = \pm 1$ are given by

$$\mathcal{A}_{f_{CP}}(t) = \mathcal{I}m(\lambda_f)\ \sin(\Delta m t)\ \text{ with }\ \mathcal{I}m(\lambda_f) = \eta_f \sin(\phi_M + 2\phi_f)\,. \tag{13.45}$$

Note that the phase measured is purely a weak phase, and no hadronic parameters are involved in the extraction of its value from $\mathcal{I}m(\lambda_f)$.

The discussion above allows us to introduce another classification of *CP*-violating effects:

1. *Indirect CP violation* is consistent with taking $\phi_M \neq 0$ and setting all other *CP* violating phases to zero. *CP* violation in mixing (type II) belongs to this class.
2. *Direct CP violation* cannot be accounted for by just $\phi_M \neq 0$. *CP* violation in decay (type I) belongs to this class.

The historical significance of this classification is related to theory. In superweak models [35], *CP* violation appears only in diagrams that contribute to $\mathbf{M}_{12}$, hence they predict that there is no direct *CP* violation. In most models and, in particular, in the Standard Model, *CP* violation is both direct and indirect. As concerns type III *CP* violation, a single observation of such an effect would be consistent with indirect *CP* violation, but observing $\eta_{f_1}\mathcal{I}m(\lambda_{f_1}) \neq \eta_{f_2}\mathcal{I}m(\lambda_{f_2})$ (for the same decaying meson and two different final *CP* eigenstates f_1 and f_2) would establish direct *CP* violation. The experimental observation of $\epsilon' \neq 0$, which was achieved by establishing that $\mathcal{I}m(\lambda_{\pi^+\pi^-}) \neq \mathcal{I}m(\lambda_{\pi^0\pi^0})$ (see Section 13.4), excluded the superweak scenario.

13.3 Theoretical Interpretation: The KM Mechanism

Of all the Standard Model quark parameters, only the Kobayashi-Maskawa (KM) phase is *CP*-violating. Having a single source of *CP* violation, the Standard Model is very predictive for *CP* asymmetries: some vanish, and those that do not are correlated.

To be precise, *CP* could be violated also by strong interactions. The experimental upper bound on the electric-dipole moment of the neutron implies, however, that $\theta_{\rm QCD}$, the non-perturbative parameter that determines the strength of this type of *CP* violation, is tiny, if not zero. (The smallness of $\theta_{\rm QCD}$ constitutes a theoretical puzzle, known as "the strong *CP* problem.") In particular, it is irrelevant to our discussion of hadron decays.

The charged current interactions (that is, the $W^\pm$ interactions) for quarks are given by

$$-\mathcal{L}_{W^\pm} = \frac{g}{\sqrt{2}}\ \overline{u_{Li}}\ \gamma^\mu\ (V_{\rm CKM})_{ij}\ d_{Lj}\ W_\mu^+ + \text{h.c.} \tag{13.46}$$

Here $i, j = 1, 2, 3$ are generation numbers. The Cabibbo-Kobayashi-Maskawa (CKM) mixing matrix for quarks is a 3×3 unitary matrix [36]. Ordering the quarks by their masses, *i.e.*, $(u_1, u_2, u_3) \to (u, c, t)$ and $(d_1, d_2, d_3) \to (d, s, b)$, the elements of $V_{\rm CKM}$ are written as follows:

$$V_{\rm CKM} = \begin{pmatrix} V_{ud} & V_{us} & V_{ub} \\ V_{cd} & V_{cs} & V_{cb} \\ V_{td} & V_{ts} & V_{tb} \end{pmatrix}\,. \tag{13.47}$$

While a general 3×3 unitary matrix depends on three real angles and six phases, the freedom to redefine the phases of the quark mass eigenstates can be used to remove five of the phases, leaving a single physical phase, the Kobayashi-Maskawa phase, that is responsible for all *CP* violation in the Standard Model.

The fact that one can parametrize $V_{\rm CKM}$ by three real and only one imaginary physical parameters can be made manifest by choosing an explicit parametrization. The Wolfenstein parametrization [37, 38] is particularly useful:

$$V_{\rm CKM} = \begin{pmatrix} 1 - \frac{1}{2}\lambda^2 - \frac{1}{8}\lambda^4 & \lambda & A\lambda^3(\rho - i\eta) \\ -\lambda + \frac{1}{2}A^2\lambda^5[1 - 2(\rho + i\eta)] & 1 - \frac{1}{2}\lambda^2 - \frac{1}{8}\lambda^4(1 + 4A^2) & A\lambda^2 \\ A\lambda^3[1 - (1 - \frac{1}{2}\lambda^2)(\rho + i\eta)] & -A\lambda^2 + \frac{1}{2}A\lambda^4[1 - 2(\rho + i\eta)] & 1 - \frac{1}{2}A^2\lambda^4 \end{pmatrix}\,. \tag{13.48}$$

Here $\lambda \approx 0.23$ (not to be confused with λ_f), the sine of the Cabibbo angle, plays the role of an expansion parameter, and η represents the *CP*-violating phase. Terms of $\mathcal{O}(\lambda^6)$ have been neglected.

The unitarity of the CKM matrix, $(VV^\dagger)_{ij} = (V^\dagger V)_{ij} = \delta_{ij}$, leads to twelve distinct complex relations among the matrix elements. The six relations with $i \neq j$ can be represented geometrically as triangles in the complex plane. Two of these,

$$V_{ud}V_{ub}^* + V_{cd}V_{cb}^* + V_{td}V_{tb}^* = 0\,, \tag{13.49a}$$
$$V_{td}V_{ud}^* + V_{ts}V_{us}^* + V_{tb}V_{ub}^* = 0\,, \tag{13.49b}$$

have terms of equal order, $\mathcal{O}(A\lambda^3)$, and so have corresponding triangles whose interior angles are all $\mathcal{O}(1)$ physical quantities that can be independently measured. The angles of the first triangle (see Fig. 13.1) are given by

$$\alpha \equiv \varphi_2 \equiv \arg\left(-\frac{V_{td}V_{tb}^*}{V_{ud}V_{ub}^*}\right) \simeq \arg\left(-\frac{1 - \rho - i\eta}{\rho + i\eta}\right)\,, \tag{13.50a}$$
$$\beta \equiv \varphi_1 \equiv \arg\left(-\frac{V_{cd}V_{cb}^*}{V_{td}V_{tb}^*}\right) \simeq \arg\left(\frac{1}{1 - \rho - i\eta}\right)\,, \tag{13.50b}$$
$$\gamma \equiv \varphi_3 \equiv \arg\left(-\frac{V_{ud}V_{ub}^*}{V_{cd}V_{cb}^*}\right) \simeq \arg\left(\rho + i\eta\right)\,. \tag{13.50c}$$

The angles of the second triangle are equal to (α, β, γ) up to corrections of $\mathcal{O}(\lambda^2)$. The notations (α, β, γ) and $(\varphi_1, \varphi_2, \varphi_3)$ are both in common usage but, for convenience, we only use the first convention in the following.

Another relation that can be represented as a triangle,

$$V_{us}V_{ub}^* + V_{cs}V_{cb}^* + V_{ts}V_{tb}^* = 0\,, \tag{13.51}$$

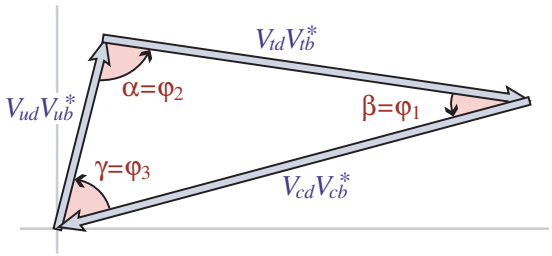

Figure 13.1: Graphical representation of the unitarity constraint $V_{ud}V_{ub}^* + V_{cd}V_{cb}^* + V_{td}V_{tb}^* = 0$ as a triangle in the complex plane.

and, in particular, its small angle, of $\mathcal{O}(\lambda^2)$,

$$\beta_s \equiv \arg\left(-\frac{V_{ts}V_{tb}^*}{V_{cs}V_{cb}^*}\right), \tag{13.52}$$

is convenient for analyzing *CP* violation in the B_s^0 sector.

All unitarity triangles have the same area, commonly denoted by $J/2$ [39]. If *CP* is violated, J is different from zero and can be taken as the single *CP*-violating parameter. In the Wolfenstein parametrization of Eq. (13.48), $J \simeq \lambda^6 A^2 \eta$.

13.4 Kaons

CP violation was discovered in $K \to \pi\pi$ decays in 1964 [1]. The same mode provided the first observation of direct *CP* violation [4–6].

The decay amplitudes actually measured in neutral K decays refer to the mass eigenstates K_L and K_S, rather than to the K and $\overline{K}$ states referred to in Eq. (13.15). The final $\pi^+\pi^-$ and $\pi^0\pi^0$ states are *CP*-even. In the *CP* conservation limit, K_S (K_L) would be *CP*-even (odd), and therefore would (would not) decay to two pions. We define *CP*-violating amplitude ratios for two-pion final states,

$$\eta_{00} \equiv \frac{\langle\pi^0\pi^0|\mathcal{H}|K_L\rangle}{\langle\pi^0\pi^0|\mathcal{H}|K_S\rangle}, \quad \eta_{+-} \equiv \frac{\langle\pi^+\pi^-|\mathcal{H}|K_L\rangle}{\langle\pi^+\pi^-|\mathcal{H}|K_S\rangle}. \tag{13.53}$$

Another important observable is the asymmetry of time-integrated semileptonic decay rates:

$$\delta_L \equiv \frac{\Gamma(K_L \to \ell^+\nu_\ell\pi^-) - \Gamma(K_L \to \ell^-\overline{\nu}_\ell\pi^+)}{\Gamma(K_L \to \ell^+\nu_\ell\pi^-) + \Gamma(K_L \to \ell^-\overline{\nu}_\ell\pi^+)}. \tag{13.54}$$

CP violation has been observed as an appearance of K_L decays to two-pion final states [27],

$$|\eta_{00}| = (2.220 \pm 0.011) \times 10^{-3}, \tag{13.55a}$$
$$|\eta_{+-}| = (2.232 \pm 0.011) \times 10^{-3}, \tag{13.55b}$$
$$|\eta_{00}/\eta_{+-}| = 0.9950 \pm 0.0007, \tag{13.55c}$$

where the phase ϕ_{ij} of the amplitude ratio η_{ij} has been determined both assuming *CPT* invariance:

$$\phi_{00} = (43.52 \pm 0.05)^\circ, \qquad \phi_{+-} = (43.51 \pm 0.05)^\circ, \tag{13.56}$$

and without assuming *CPT* invariance:

$$\phi_{00} = (43.7 \pm 0.6)^\circ, \qquad \phi_{+-} = (43.4 \pm 0.5)^\circ. \tag{13.57}$$

CP violation has also been observed in semileptonic K_L decays [27]

$$\delta_L = (3.32 \pm 0.06) \times 10^{-3}, \tag{13.58}$$

where δ_L is a weighted average of muon and electron measurements, as well as in K_L decays to $\pi^+\pi^-\gamma$ and $\pi^+\pi^-e^+e^-$ [27]. *CP* violation in $K \to 3\pi$ decays has not yet been observed [27,40].

Historically, *CP* violation in neutral K decays has been described in terms of the complex parameters ϵ and ϵ'. The observables η_{00}, η_{+-}, and δ_L are related to these parameters, and to those of Section 13.1, by

$$\eta_{00} = \frac{1-\lambda_{\pi^0\pi^0}}{1+\lambda_{\pi^0\pi^0}} = \epsilon - 2\epsilon', \tag{13.59a}$$
$$\eta_{+-} = \frac{1-\lambda_{\pi^+\pi^-}}{1+\lambda_{\pi^+\pi^-}} = \epsilon + \epsilon', \tag{13.59b}$$
$$\delta_L = \frac{1-|q/p|^2}{1+|q/p|^2} = \frac{2\mathcal{R}e(\epsilon)}{1+|\epsilon|^2}, \tag{13.59c}$$

where, in the last line, we have assumed that $\left|A_{\ell^+\nu_\ell\pi^-}\right| = \left|\overline{A}_{\ell^-\overline{\nu}_\ell\pi^+}\right|$ and $\left|A_{\ell^-\overline{\nu}_\ell\pi^+}\right| = \left|\overline{A}_{\ell^+\nu_\ell\pi^-}\right| = 0$. (The convention-dependent parameter $\tilde{\epsilon} \equiv (1-q/p)/(1+q/p)$, sometimes used in the literature, is, in general, different from ϵ but yields a similar expression, $\delta_L = 2\mathcal{R}e(\tilde{\epsilon})/(1+|\tilde{\epsilon}|^2)$.) A fit to the $K \to \pi\pi$ data yields [27]

$$|\epsilon| = (2.228 \pm 0.011) \times 10^{-3}, \tag{13.60a}$$
$$\mathcal{R}e(\epsilon'/\epsilon) = (1.66 \pm 0.23) \times 10^{-3}. \tag{13.60b}$$

In discussing two-pion final states, it is useful to express the amplitudes $A_{\pi^0\pi^0}$ and $A_{\pi^+\pi^-}$ in terms of their isospin components via

$$A_{\pi^0\pi^0} = \sqrt{\frac{1}{3}}\,|A_0|\,e^{i(\delta_0+\phi_0)} - \sqrt{\frac{2}{3}}\,|A_2|\,e^{i(\delta_2+\phi_2)}, \tag{13.61a}$$
$$A_{\pi^+\pi^-} = \sqrt{\frac{2}{3}}\,|A_0|\,e^{i(\delta_0+\phi_0)} + \sqrt{\frac{1}{3}}\,|A_2|\,e^{i(\delta_2+\phi_2)}, \tag{13.61b}$$

where we parameterize the amplitude $A_I(\overline{A}_I)$ for $K^0(\overline{K}^0)$ decay into two pions with total isospin $I = 0$ or 2 as

$$A_I \equiv \langle(\pi\pi)_I\,|\mathcal{H}|\,K^0\rangle = |A_I|\,e^{i(\delta_I+\phi_I)}, \tag{13.62a}$$
$$\overline{A}_I \equiv \langle(\pi\pi)_I\,|\mathcal{H}|\,\overline{K}^0\rangle = |A_I|\,e^{i(\delta_I-\phi_I)}. \tag{13.62b}$$

The smallness of $|\eta_{00}|$ and $|\eta_{+-}|$ allows us to approximate

$$\epsilon \simeq \frac{1}{2}(1-\lambda_{(\pi\pi)_{I=0}}), \qquad \epsilon' \simeq \frac{1}{6}(\lambda_{\pi^0\pi^0} - \lambda_{\pi^+\pi^-}). \tag{13.63}$$

The parameter ϵ represents indirect *CP* violation, while ϵ' parameterizes direct *CP* violation: $\mathcal{R}e(\epsilon')$ measures *CP* violation in decay (type I), $\mathcal{R}e(\epsilon)$ measures *CP* violation in mixing (type II), and $\mathcal{I}m(\epsilon)$ and $\mathcal{I}m(\epsilon')$ measure the interference between decays with and without mixing (type III).

The following expressions for ϵ and ϵ' are useful for theoretical evaluations:

$$\epsilon \simeq \frac{e^{i\pi/4}}{\sqrt{2}}\frac{\mathcal{I}m(\mathbf{M}_{12})}{\Delta m}, \qquad \epsilon' = \frac{i}{\sqrt{2}}\left|\frac{A_2}{A_0}\right| e^{i(\delta_2-\delta_0)}\sin(\phi_2-\phi_0). \tag{13.64}$$

The expression for ϵ is only valid in a phase convention where $\phi_2 = 0$, corresponding to a real $V_{ud}V_{us}^*$, and in the approximation that also $\phi_0 = 0$. The phase of ϵ, $\arg(\epsilon) \approx \arctan(-2\Delta m/\Delta\Gamma)$, is determined by non-perturbative QCD dynamics and is experimentally determined to be about $\pi/4$. The calculation of ϵ benefits from the fact that $\mathcal{I}m(\mathbf{M}_{12})$ is dominated by short distance physics. Consequently, the main sources of uncertainty in theoretical interpretations of ϵ are the values of matrix elements, such as $\langle K^0\,|(\bar{s}d)_{V-A}(\bar{s}d)_{V-A}|\,\overline{K}^0\rangle$. The expression for ϵ' is valid to first order in $|A_2/A_0| \sim 1/20$. The phase of ϵ' is experimentally determined, $\pi/2 + \delta_2 - \delta_0 \approx \pi/4$, and is independent of the electroweak model. Note that, accidentally, ϵ'/ϵ is real to a good approximation. Determination of weak phase information from the measurement of $\mathcal{R}e(\epsilon'/\epsilon)$ given in Eq. (13.60) has until now been precluded by uncertainties in the hadronic parameters, but recent advances in lattice QCD calculations [41,42] suggest that it may become possible [43].

A future measurement of much interest is that of *CP* violation in the rare $K \to \pi\nu\overline{\nu}$ decays. The signal for *CP* violation is simply observing the $K_L \to \pi^0\nu\overline{\nu}$ decay. The effect here is that

of interference between decays with and without mixing (type III) [44]:

$$\frac{\Gamma(K_L \to \pi^0\nu\overline{\nu})}{\Gamma(K^+ \to \pi^+\nu\overline{\nu})} = \frac{1}{2}\left[1 + |\lambda_{\pi\nu\overline{\nu}}|^2 - 2\,\mathcal{R}e(\lambda_{\pi\nu\overline{\nu}})\right] \simeq 1 - \mathcal{R}e(\lambda_{\pi\nu\overline{\nu}})\,, \tag{13.65}$$

where in the last equation we neglect *CP* violation in decay and in mixing (expected, model-independently, to be of order 10^{-5} and 10^{-3}, respectively). Such a measurement is experimentally very challenging but would be theoretically very rewarding [45]. Similar to the *CP* asymmetry in $B^0 \to J/\psi K_S$, the *CP* violation in $K \to \pi\nu\overline{\nu}$ decay is predicted to be large (that is, the ratio in Eq. (13.65) is neither CKM- nor loop-suppressed) and can be very cleanly interpreted.

Within the Standard Model, the $K_L \to \pi^0\nu\overline{\nu}$ decay is dominated by an intermediate top quark contribution and, consequently, can be interpreted in terms of CKM parameters [46]. (For the charged mode, $K^+ \to \pi^+\nu\overline{\nu}$, the contribution from an intermediate charm quark is not negligible, and constitutes a source of hadronic uncertainty.) In particular, $\mathcal{B}(K_L \to \pi^0\nu\overline{\nu})$ provides a theoretically clean way to determine the Wolfenstein parameter η [47]:

$$\mathcal{B}(K_L \to \pi^0\nu\overline{\nu}) = \kappa_L[X(m_t^2/m_W^2)]^2 A^4\eta^2\,, \tag{13.66}$$

where the hadronic parameter $\kappa_L \sim 2 \times 10^{-10}$ incorporates the value of the four-fermion matrix element which is deduced, using isospin relations, from $\mathcal{B}(K^+ \to \pi^0 e^+\nu_e)$, and $X(m_t^2/m_W^2)$ is a known function of the top mass. An explicit calculation gives $\mathcal{B}(K_L \to \pi^0\nu\overline{\nu}) = (3.00 \pm 0.30) \times 10^{-11}$ [48].

The currently tightest experimental limit is $\mathcal{B}(K_L \to \pi^0\nu\overline{\nu}) < 3.0 \times 10^{-9}$ [49], which does not yet reach the bound that can be derived from Eq. (13.65), $\mathcal{B}(K_L \to \pi^0\nu\overline{\nu}) < 4.4 \times \mathcal{B}(K^+ \to \pi^+\nu\overline{\nu})$ [44]. Significant further progress is anticipated from experiments searching for $K \to \pi\nu\overline{\nu}$ decays in the next few years [50,51].

13.5 Charm

The existence of D^0–$\overline{D}^0$ mixing is well established [52–55], with the latest experimental constraints giving [29, 56] $x \equiv \Delta m/\Gamma = (0.39\,^{+0.11}_{-0.12}) \times 10^{-2}$ and $y \equiv \Delta\Gamma/(2\Gamma) = (0.65\,^{+0.06}_{-0.07}) \times 10^{-2}$. Thus, the data clearly show that $y \neq 0$, but improved measurements are needed to be sure of the size of x. Long-distance contributions make it difficult to calculate Standard Model predictions for the D^0–$\overline{D}^0$ mixing parameters. Therefore, the goal of the search for D^0–$\overline{D}^0$ mixing is not to constrain the CKM parameters, but rather to probe new physics. Here *CP* violation plays an important role. Within the Standard Model, the *CP*-violating effects are predicted to be small, since the mixing and the relevant decays are described, to an excellent approximation, by the physics of the first two generations only. The expectation is that the Standard Model size of *CP* violation in D decays is $\mathcal{O}(10^{-3})$ or less. At present, the most sensitive searches involve the $D^0 \to K^+K^-$, $D^0 \to \pi^+\pi^-$ and $D^0 \to K^\pm\pi^\mp$ modes.

The neutral D mesons decay via a singly-Cabibbo-suppressed transition to the *CP* eigenstates K^+K^- and $\pi^+\pi^-$. These decays are dominated by Standard-Model tree diagrams. Thus, we can write, for $f = K^+K^-$ or $\pi^+\pi^-$,

$$A_f = A_f^T e^{+i\phi_f^T}\left[1 + r_f e^{i(\delta_f+\phi_f)}\right]\,, \tag{13.67a}$$

$$\bar{A}_f = A_f^T e^{-i\phi_f^T}\left[1 + r_f e^{i(\delta_f-\phi_f)}\right]\,, \tag{13.67b}$$

where $A_f^T e^{\pm i\phi_f^T}$ is the Standard Model tree-level contribution, ϕ_f^T and ϕ_f are weak, *CP* violating phases, δ_f is a strong phase difference, and r_f is the ratio between a subleading ($r_f \ll 1$) contribution with a weak phase different from ϕ_f^T and the Standard Model tree-level contribution. Neglecting r_f, λ_f is universal, and we can define an observable phase ϕ_D via

$$\lambda_f \equiv -|q/p|e^{i\phi_D}\,. \tag{13.68}$$

(In the limit of *CP* conservation, choosing $\phi_D = 0$ is equivalent to defining the mass eigenstates by their *CP* eigenvalue: $|D_\mp\rangle = p|D^0\rangle \pm q|\overline{D}^0\rangle$, with D_- (D_+) being the *CP*-odd (*CP*-even) state; that is, the state that does not (does) decay into K^+K^-.)

We define the time integrated *CP* asymmetry for a final *CP* eigenstate f as follows:

$$a_f \equiv \frac{\int_0^\infty \Gamma(D^0_{\rm phys}(t) \to f)dt - \int_0^\infty \Gamma(\overline{D}^0_{\rm phys}(t) \to f)dt}{\int_0^\infty \Gamma(D^0_{\rm phys}(t) \to f)dt + \int_0^\infty \Gamma(\overline{D}^0_{\rm phys}(t) \to f)dt}\,. \tag{13.69}$$

(This expression corresponds to the D meson being tagged at production, hence the integration goes from 0 to $+\infty$; measurements are also possible with $\psi(3770) \to D^0\overline{D}^0$, in which case the integration goes from $-\infty$ to $+\infty$ giving slightly different results; see the discussion in Section 13.1.3.) We take $x, y, r_f \ll 1$ and expand to leading order in these parameters. We can then separate the contribution to a_f into three parts [57],

$$a_f = a_f^d + a_f^m + a_f^i\,, \tag{13.70}$$

with the following underlying mechanisms:

1. a_f^d signals *CP* violation in decay (similar to Eq. (13.35)):

$$a_f^d = 2r_f \sin\phi_f \sin\delta_f\,. \tag{13.71}$$

2. a_f^m signals *CP* violation in mixing (similar to Eq. (13.44)). With our approximations, it is universal:

$$a^m = -\frac{y}{2}\left(\left|\frac{q}{p}\right| - \left|\frac{p}{q}\right|\right)\cos\phi_D\,. \tag{13.72}$$

3. a_f^i signals *CP* violation in the interference of mixing and decay (similar to Eq. (13.45)). With our approximations, it is universal:

$$a^i = \frac{x}{2}\left(\left|\frac{q}{p}\right| + \left|\frac{p}{q}\right|\right)\sin\phi_D\,. \tag{13.73}$$

One can isolate the effects of direct *CP* violation by taking the difference between the *CP* asymmetries in the K^+K^- and $\pi^+\pi^-$ modes:

$$\Delta a_{CP} \equiv a_{K^+K^-} - a_{\pi^+\pi^-} = a^d_{K^+K^-} - a^d_{\pi^+\pi^-}\,, \tag{13.74}$$

where we neglected a residual, experiment-dependent, contribution from indirect *CP* violation due to the fact that there may be a decay time-dependent acceptance function that can be different for the K^+K^- and $\pi^+\pi^-$ channels. The current average gives [29]:

$$a^d_{K^+K^-} - a^d_{\pi^+\pi^-} = (-0.164 \pm 0.028) \times 10^{-3}\,, \tag{13.75}$$

demonstrating *CP* violation in charm decay.

One can also isolate the effects of indirect *CP* violation in the following way. Consider the time-dependent decay rates in Eq. (13.31a) and Eq. (13.31b). The mixing processes modify the time dependence from a pure exponential. However, given the small values of x and y, the time dependences can be recast, to a good approximation, into purely exponential form, but with modified decay-rate parameters [58,59] (given here for the K^+K^- final state):

$$\Gamma_{D^0\to K^+K^-} = \Gamma \times [1 + |q/p|\,(y\cos\phi_D - x\sin\phi_D)]\,, \tag{13.76a}$$

$$\Gamma_{\overline{D}^0\to K^+K^-} = \Gamma \times [1 + |p/q|\,(y\cos\phi_D + x\sin\phi_D)]\,. \tag{13.76b}$$

One can define *CP*-conserving and *CP*-violating combinations of these two observables (normalized to the true width Γ):

$$y_{CP} \equiv \frac{\Gamma_{\overline{D}^0\to K^+K^-} + \Gamma_{D^0\to K^+K^-}}{2\Gamma} - 1 = (y/2)\,(|q/p| + |p/q|)\cos\phi_D - (x/2)\,(|q/p| - |p/q|)\sin\phi_D\,, \tag{13.77a}$$

$$A_\Gamma \equiv \frac{\Gamma_{D^0\to K^+K^-} - \Gamma_{\overline{D}^0\to K^+K^-}}{2\Gamma} = -(a^m + a^i)\,. \tag{13.77b}$$

In the limit of CP conservation (and, in particular, within the Standard Model), $y_{CP} = (\Gamma_+ - \Gamma_-)/2\Gamma = y$ (where $\Gamma_+(\Gamma_-)$ is the decay width of the CP-even (-odd) mass eigenstate) and $A_\Gamma = 0$. Indeed, present measurements imply that CP violation is small [29],

$$y_{CP} = (+0.72 \pm 0.11) \times 10^{-2}\,, \tag{13.78a}$$

$$A_\Gamma = (-0.032 \pm 0.026) \times 10^{-2}\,. \tag{13.78b}$$

The $K^\pm\pi^\mp$ states are not CP eigenstates, but they are still common final states for D^0 and $\overline{D}^0$ decays. Since $D^0(\overline{D}^0) \to K^-\pi^+$ is a Cabibbo-favored (doubly-Cabibbo-suppressed) process, these processes are particularly sensitive to x and/or $y = \mathcal{O}(\lambda^2)$. Taking into account that $|\lambda_{K^-\pi^+}|\,, \left|\lambda^{-1}_{K^+\pi^-}\right| \ll 1$ and $x, y \ll 1$, assuming that there is no direct CP violation (these are Standard Model tree-level decays dominated by a single weak phase, and there is no contribution from penguin-like and chromomagnetic operators), and expanding the time-dependent rates for $xt, yt \lesssim \Gamma^{-1}$, one obtains

$$\Gamma[D^0_{\rm phys}(t) \to K^+\pi^-] = e^{-\Gamma t}|\overline{A}_{K^-\pi^+}|^2 \times \left[r_d^2 + r_d\left|\frac{q}{p}\right|(y'\cos\phi_D - x'\sin\phi_D)\Gamma t + \left|\frac{q}{p}\right|^2 \frac{y^2+x^2}{4}(\Gamma t)^2\right]\,, \tag{13.79a}$$

$$\Gamma[\overline{D}^0_{\rm phys}(t) \to K^-\pi^+] = e^{-\Gamma t}|\overline{A}_{K^-\pi^+}|^2 \times \left[r_d^2 + r_d\left|\frac{p}{q}\right|(y'\cos\phi_D + x'\sin\phi_D)\Gamma t + \left|\frac{p}{q}\right|^2 \frac{y^2+x^2}{4}(\Gamma t)^2\right]\,, \tag{13.79b}$$

where

$$y' \equiv y\cos\delta - x\sin\delta \quad \text{and} \quad x' \equiv x\cos\delta + y\sin\delta\,. \tag{13.80}$$

The weak phase ϕ_D is the same as that of Eq. (13.68) (a consequence of neglecting direct CP violation) and $r_d = \mathcal{O}(\tan^2\theta_c)$ is the amplitude ratio, $r_d = \left|\overline{A}_{K^-\pi^+}/A_{K^-\pi^+}\right| = \left|A_{K^+\pi^-}/\overline{A}_{K^+\pi^-}\right|$, that is, $\lambda_{K^-\pi^+} = r_d|q/p|e^{-i(\delta-\phi_D)}$ and $\lambda^{-1}_{K^+\pi^-} = r_d|p/q|e^{-i(\delta+\phi_D)}$. The parameter δ is a strong-phase difference for these processes, that can be obtained from measurements of quantum correlated $\psi(3770) \to D^0\overline{D}^0$ decays [60,61]. By fitting to the six coefficients of the various time-dependences, one can determine r_d, $|q/p|$, (x^2+y^2), $y'\cos\phi_D$, and $x'\sin\phi_D$. In particular, finding CP violation ($|q/p| \neq 1$ and/or $\sin\phi_D \neq 0$) at a level much higher than 10^{-3} would constitute evidence for new physics. The most stringent constraints to date on CP violation in charm mixing have been obtained with this method [62] and from the A_Γ measurement [63].

A fit to all data [29], including also results from time-dependent analyses of $D^0 \to K_S\pi^+\pi^-$ decays, from which x, y, $|q/p|$ and ϕ_D can be determined directly, yields no evidence for indirect CP violation:

$$1 - |q/p| = +0.031\,^{+0.045}_{-0.050}\,, \tag{13.81a}$$

$$\phi_D = \left(-3.9\,^{+4.5}_{-4.6}\right)^\circ\,. \tag{13.81b}$$

With the additional assumption of no direct CP violation in doubly-Cabibbo-suppressed D decays [64–66], tighter constraints are obtained:

$$1 - |q/p| = +0.002 \pm 0.008\,, \tag{13.82a}$$

$$\phi_D = (+0.08 \pm 0.31)^\circ\,. \tag{13.82b}$$

More details on various theoretical and experimental aspects of D^0–$\overline{D}^0$ mixing can be found in Ref. [31].

Searches for CP violation in charged $D_{(s)}$ decays have been performed in many modes. Searches in decays mediated by Cabibbo-suppressed amplitudes are particularly interesting, since in other channels effects are likely to be too small to be observable in current experiments. Examples of relevant two-body modes are $D^+ \to \pi^+\pi^0$, K_SK^+, $\phi\pi^+$ and $D_s^+ \to K^+\pi^0$, $K_S\pi^+$, ϕK^+. The most precise results are $\mathcal{A}_{D^+\to K_SK^+} = +0.0011 \pm 0.0017$ and $\mathcal{A}_{D_s^+\to K_S\pi^+} = +0.0038 \pm 0.0048$ [29]. The precision of experiments is now sufficient that the effect from CP violation in the neutral kaon system can be seen in $D^+ \to K_S\pi^+$ decays [67,68].

Three- and four-body final states provide additional possibilities to search for CP violation, since effects may vary over the phase-space [69]. A number of methods have been proposed to exploit this feature and search for CP violation in ways that do not require modelling of the decay distribution [70–73]. Such methods are useful for analysis of charm decays since they are less sensitive to biases from production asymmetries, and are well suited to address the issue of whether or not CP violation effects are present. They can also be applied to tagged neutral D meson as well as to charged $D_{(s)}$ decays (flavor tagging is typically achieved from the charge of the pion producted in $D^{*+} \to D^0\pi^+$ decays). The results of all searches to date are consistent with the absence of CP violation, with the most significant hint at the level of 2.7σ [74].

13.6 Beauty

13.6.1 *CP violation in mixing of B^0 and B_s^0 mesons*

The upper bound on the CP asymmetry in semileptonic B decays [28] implies that CP violation in B^0–$\overline{B}^0$ mixing is a small effect (we use $\mathcal{A}_{\rm SL}/2 \approx 1 - |q/p|$, see Eq. (13.37)):

$$\mathcal{A}^d_{\rm SL} = (-2.1 \pm 1.7) \times 10^{-3} \implies |q/p| = 1.0010 \pm 0.0008\,. \tag{13.83}$$

The Standard Model prediction is

$$\mathcal{A}^d_{\rm SL} = \mathcal{O}\left[(m_c^2/m_t^2)\sin\beta\right] \lesssim 0.001\,. \tag{13.84}$$

An explicit calculation gives $(-4.7 \pm 0.6) \times 10^{-4}$ [34].

The experimental constraint on CP violation in B_s^0–$\overline{B}_s^0$ mixing is somewhat weaker than that in the B^0–$\overline{B}^0$ system [28]

$$\mathcal{A}^s_{\rm SL} = (-0.6 \pm 2.8) \times 10^{-3} \implies |q/p| = 1.0003 \pm 0.0014\,. \tag{13.85}$$

The Standard Model prediction is $\mathcal{A}^s_{\rm SL} = \mathcal{O}\left[(m_c^2/m_t^2)\sin\beta_s\right] \lesssim 10^{-4}$, with an explicit calculation giving $(2.22 \pm 0.27) \times 10^{-5}$ [34].

The fit to experimental data that results in the averages quoted above has a χ^2 probability of 4.5% indicating some tension between the different measurements [29]. This originates in part from a result from the D0 collaboration for the inclusive same-sign dimuon asymmetry that deviates from the Standard Model prediction by 3.6σ [75]. As yet, this has not been confirmed by independent studies.

In models where $\mathbf{\Gamma}_{12}/\mathbf{M}_{12}$ is approximately real, such as the Standard Model, an upper bound on $\Delta\Gamma/\Delta m \approx \mathcal{R}e(\mathbf{\Gamma}_{12}/\mathbf{M}_{12})$ provides yet another upper bound on the deviation of $|q/p|$ from one. This constraint does not hold if $\mathbf{\Gamma}_{12}/\mathbf{M}_{12}$ is approximately imaginary. (An alternative parameterization uses $q/p = (1 - \tilde{\epsilon}_B)/(1 + \tilde{\epsilon}_B)$, leading to $\mathcal{A}_{\rm SL} \simeq 4\mathcal{R}e(\tilde{\epsilon}_B)$.)

13.6.2 *CP violation in interference of B^0 decays with and without mixing*

The small deviation (less than one percent) of $|q/p|$ from 1 implies that, at the present level of experimental precision, CP violation in B^0 mixing is a negligible effect. Thus, for the purpose of analyzing CP asymmetries in hadronic B^0 decays, we can use

$$\lambda_f = e^{-i\phi_{M(B^0)}}(\overline{A}_f/A_f)\,, \tag{13.86}$$

where $\phi_{M(B^0)}$ refers to the phase of $\mathbf{M}_{12}$ appearing in Eq. (13.42) that is appropriate for B^0–$\overline{B}^0$ oscillations. Within the Standard Model, the corresponding phase factor is given by

$$e^{-i\phi_{M(B^0)}} = (V_{tb}^*V_{td})/(V_{tb}V_{td}^*)\,. \tag{13.87}$$

The class of CP violation effects in interference between mixing and decay is studied with final states that are common to B^0 and $\overline{B}^0$ decays [76–78]. It is convenient to rewrite Eq. (13.40) for B^0 decays as [79–81]

$$\mathcal{A}_f(t) = S_f\sin(\Delta mt) - C_f\cos(\Delta mt)\,, \tag{13.88}$$

$$S_f \equiv \frac{2\,\mathcal{I}m(\lambda_f)}{1+\left|\lambda_f\right|^2}\ , \quad C_f \equiv \frac{1-\left|\lambda_f\right|^2}{1+\left|\lambda_f\right|^2}\ , \tag{13.89}$$

where we assume that $\Delta\Gamma = 0$ and $|q/p| = 1$. An alternative notation in use is $A_f \equiv -C_f$ – this A_f should not be confused with the A_f of Eq. (13.15), but in the limit that $|q/p| = 1$ is equivalent with the $\mathcal{A}_f$ of Eq. (13.35).

A large class of interesting processes proceed via quark transitions of the form $\overline{b} \to \overline{q}q\overline{q}'$ with $q' = s$ or d. For $q = c$ or u, there are contributions from both tree (t) and penguin (p^{q_u}, where $q_u = u, c, t$ is the quark in the loop) diagrams (see Fig. 13.2) which carry different weak phases:

$$A_f = \left(V_{qb}^* V_{qq'}\right) t_f + \sum_{q_u=u,c,t} \left(V_{q_u b}^* V_{q_u q'}\right) p_f^{q_u}\ . \tag{13.90}$$

(The distinction between tree and penguin contributions is a heuristic one; the separation by the operator that enters is more precise. A more detailed discussion of the operator product expansion approach, which also includes higher order QCD corrections, can be found in Ref. [82] for example.) Using CKM unitarity, these decay amplitudes can always be written in terms of just two CKM combinations. For example, for $f = \pi\pi$, which proceeds via a $\overline{b} \to \overline{u}u\overline{d}$ transition, we can write

$$A_{\pi\pi} = \left(V_{ub}^* V_{ud}\right) T_{\pi\pi} + \left(V_{tb}^* V_{td}\right) P_{\pi\pi}^t\ , \tag{13.91}$$

where $T_{\pi\pi} = t_{\pi\pi} + p_{\pi\pi}^u - p_{\pi\pi}^c$ and $P_{\pi\pi}^t = p_{\pi\pi}^t - p_{\pi\pi}^c$. *CP*-violating phases in Eq. (13.91) appear only in the CKM elements, so that

$$\frac{\overline{A}_{\pi\pi}}{A_{\pi\pi}} = \frac{\left(V_{ub}V_{ud}^*\right) T_{\pi\pi} + \left(V_{tb}V_{td}^*\right) P_{\pi\pi}^t}{\left(V_{ub}^* V_{ud}\right) T_{\pi\pi} + \left(V_{tb}^* V_{td}\right) P_{\pi\pi}^t}\ . \tag{13.92}$$

For $f = J/\psi K$, which proceeds via a $\overline{b} \to \overline{c}c\overline{s}$ transition, we can write

$$A_{\psi K} = \left(V_{cb}^* V_{cs}\right) T_{\psi K} + \left(V_{ub}^* V_{us}\right) P_{\psi K}^u\ , \tag{13.93}$$

where $T_{\psi K} = t_{\psi K} + p_{\psi K}^c - p_{\psi K}^t$ and $P_{\psi K}^u = p_{\psi K}^u - p_{\psi K}^t$. A subtlety arises in this decay that is related to the fact that B^0 decays into a final $J/\psi K^0$ state while $\overline{B}^0$ decays into a final $J/\psi\overline{K}^0$ state. A common final state, *e.g.*, $J/\psi K_S$, is reached only via K^0–$\overline{K}^0$ mixing. Consequently, the phase factor (defined in Eq. (13.42)) corresponding to neutral K mixing, $e^{-i\phi_{M(K)}} = (V_{cd}^* V_{cs})/(V_{cd} V_{cs}^*)$, plays a role:

$$\frac{\overline{A}_{\psi K_S}}{A_{\psi K_S}} = -\frac{\left(V_{cb}V_{cs}^*\right) T_{\psi K} + \left(V_{ub}V_{us}^*\right) P_{\psi K}^u}{\left(V_{cb}^* V_{cs}\right) T_{\psi K} + \left(V_{ub}^* V_{us}\right) P_{\psi K}^u} \times \frac{V_{cd}^* V_{cs}}{V_{cd} V_{cs}^*}\ . \tag{13.94}$$

For $q = s$ or d, there are only penguin contributions to A_f, that is, $t_f = 0$ in Eq. (13.90). (The tree $\overline{b} \to \overline{u}u\overline{q}'$ transition followed by $\overline{u}u \to \overline{q}q$ rescattering is included below in the P^u terms.) Again, CKM unitarity allows us to write A_f in terms of two CKM combinations. For example, for $f = \phi K_S$, which proceeds via a $\overline{b} \to \overline{s}s\overline{s}$ transition, we can write

$$\frac{\overline{A}_{\phi K_S}}{A_{\phi K_S}} = -\frac{\left(V_{cb}V_{cs}^*\right) P_{\phi K}^c + \left(V_{ub}V_{us}^*\right) P_{\phi K}^u}{\left(V_{cb}^* V_{cs}\right) P_{\phi K}^c + \left(V_{ub}^* V_{us}\right) P_{\phi K}^u} \times \frac{V_{cd}^* V_{cs}}{V_{cd} V_{cs}^*}\ , \tag{13.95}$$

where $P_{\phi K}^c = p_{\phi K}^c - p_{\phi K}^t$ and $P_{\phi K}^u = p_{\phi K}^u - p_{\phi K}^t$.

Since in general the amplitude A_f involves two different weak phases, the corresponding decays can exhibit both *CP* violation in the interference of decays with and without mixing, $S_f \neq 0$, and *CP* violation in decay, $C_f \neq 0$. (At the present level of experimental precision, the contribution to C_f from *CP* violation in mixing is negligible, see Eq. (13.83).) If the contribution from a second weak phase is suppressed, then the interpretation of S_f in terms of Lagrangian *CP*-violating parameters is clean, while C_f is small. If such a second contribution is not suppressed, S_f depends on hadronic parameters and, if the relevant strong phase difference is large, C_f is large.

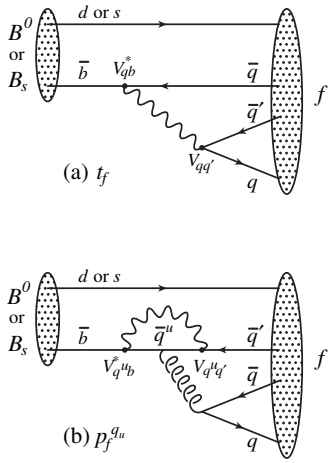

Figure 13.2: Feynman diagrams for (a) tree and (b) penguin amplitudes contributing to $B^0 \to f$ or $B_s^0 \to f$ via a $\overline{b} \to \overline{q}q\overline{q}'$ quark-level process.

A summary of $\overline{b} \to \overline{q}q\overline{q}'$ modes with $q' = s$ or d is given in Table 13.1. The $\overline{b} \to \overline{d}d\overline{q}$ transitions lead to final states that are similar to those from $\overline{b} \to \overline{u}u\overline{q}$ transitions and have similar phase dependence. Final states that consist of two vector mesons ($\psi\phi$ and $\phi\phi$) are not *CP* eigenstates, and angular analysis is needed to separate the *CP*-even from the *CP*-odd contributions.

The cleanliness of the theoretical interpretation of S_f can be assessed from the information in the last column of Table 13.1. In case of small uncertainties, the expression for S_f in terms of CKM phases can be deduced from the fourth column of Table 13.1 in combination with Eq. (13.87) (and, for $b \to q\overline{q}s$ decays, the example in Eq. (13.94)). Here we consider several interesting examples.

For $B^0 \to J/\psi K_S$ and other $\overline{b} \to \overline{c}c\overline{s}$ processes, we can neglect the P^u contribution to A_f, in the Standard Model, to an approximation that is better than one percent, giving:

$$\lambda_{\psi K_S} = -e^{-2i\beta} \ \Rightarrow\ S_{\psi K_S} = \sin 2\beta\ , \quad C_{\psi K_S} = 0\ . \tag{13.96}$$

It is important to verify experimentally the level of suppression of the penguin contribution. Methods based on flavor symmetries [83–86] allow limits to be obtained. All are currently consistent with the P^u term being negligible. Explicit calculations [86–89] also support this conclusion.

In the presence of new physics, A_f is still likely to be dominated by the T term, but the mixing amplitude might be modified. We learn that, model-independently, $C_f \approx 0$ while S_f cleanly determines the mixing phase ($\phi_M - 2\arg(V_{cb}V_{cd}^*)$). The experimental measurement [29], $S_{\psi K} = +0.699 \pm 0.017$, gave the first precision test of the Kobayashi-Maskawa mechanism, and its consistency with the predictions for $\sin 2\beta$ makes it very likely that this mechanism is indeed the dominant source of *CP* violation in the quark sector.

For $B^0 \to \phi K_S$ and other $\overline{b} \to \overline{s}s\overline{s}$ processes (as well as some $\overline{b} \to \overline{u}u\overline{s}$ processes), we can neglect the subdominant contributions, in the Standard Model, to an approximation that is good to the order of a few percent:

$$\lambda_{\phi K_S} = -e^{-2i\beta} \ \Rightarrow\ S_{\phi K_S} = \sin 2\beta\ , \quad C_{\phi K_S} = 0\ . \tag{13.97}$$

A review of explicit calculations of the effects of subleading amplitudes can be found in Ref. [90]. In the presence of new physics, both A_f and $\mathbf{M}_{12}$ can have contributions that are comparable in size to those of the Standard Model and carry new weak phases. Such a situation gives several interesting consequences for penguin-dominated $\overline{b} \to \overline{q}q\overline{s}$ decays ($q = u, d, s$) to a final state f:

1. The value of $-\eta_f S_f$ may be different from $S_{\psi K_S}$ by more than a few percent, where η_f is the *CP* eigenvalue of the final state.

Table 13.1: Summary of $\bar{b} \to \bar{q}q\bar{q}'$ modes with $q' = s$ or d. The second and third columns give examples of hadronic final states (usually those which are experimentally most convenient to study). The fourth column gives the CKM dependence of the amplitude A_f, using the notation of Eqs. ((13.91), (13.93), (13.95)), with the dominant term first and the subdominant second. The suppression factor of the second term compared to the first is given in the last column. "Loop" refers to a penguin versus tree-suppression factor (it is mode-dependent and roughly $\mathcal{O}(0.2-0.3)$) and $\lambda \simeq 0.23$ is the expansion parameter of Eq. (13.48).

$\bar{b} \to \bar{q}q\bar{q}'$	$B^0 \to f$	$B_s^0 \to f$	CKM dependence of A_f	Suppression
$\bar{b} \to \bar{c}c\bar{s}$	ψK_S	$\psi\phi$	$(V_{cb}^* V_{cs})T + (V_{ub}^* V_{us})P^u$	loop $\times \lambda^2$
$\bar{b} \to \bar{s}s\bar{s}$	ϕK_S	$\phi\phi$	$(V_{cb}^* V_{cs})P^c + (V_{ub}^* V_{us})P^u$	λ^2
$\bar{b} \to \bar{u}u\bar{s}$	$\pi^0 K_S$	K^+K^-	$(V_{cb}^* V_{cs})P^c + (V_{ub}^* V_{us})T$	λ^2/loop
$\bar{b} \to \bar{c}c\bar{d}$	D^+D^-	ψK_S	$(V_{cb}^* V_{cd})T + (V_{tb}^* V_{td})P^t$	loop
$\bar{b} \to \bar{s}s\bar{d}$	$K_S K_S$	ϕK_S	$(V_{tb}^* V_{td})P^t + (V_{cb}^* V_{cd})P^c$	$\lesssim 1$
$\bar{b} \to \bar{u}u\bar{d}$	$\pi^+\pi^-$	$\rho^0 K_S$	$(V_{ub}^* V_{ud})T + (V_{tb}^* V_{td})P^t$	loop
$\bar{b} \to \bar{c}u\bar{d}$	$D_{CP}\pi^0$	$D_{CP}K_S$	$(V_{cb}^* V_{ud})T + (V_{ub}^* V_{cd})T'$	λ^2
$\bar{b} \to \bar{c}u\bar{s}$	$D_{CP}K_S$	$D_{CP}\phi$	$(V_{cb}^* V_{us})T + (V_{ub}^* V_{cs})T'$	$\lesssim 1$

2. The values of $\eta_f S_f$ for different final states f may be different from each other by more than a few percent (for example, $S_{\phi K_S} \neq S_{\eta' K_S}$).
3. The value of C_f may be different from zero by more than a few percent.

While a clear interpretation of such signals in terms of Lagrangian parameters will be difficult because, under these circumstances, hadronic parameters play a role, any of the above three options will clearly signal new physics. In addition flavor symmetry relations, such as those which relate observables in $B \to K\pi$ decays [91,92] can be used to provide further tests of the Standard Model. Fig. 13.3 summarizes the present experimental results: none of the possible signatures listed above is unambiguously established, but there is definitely still room for new physics.

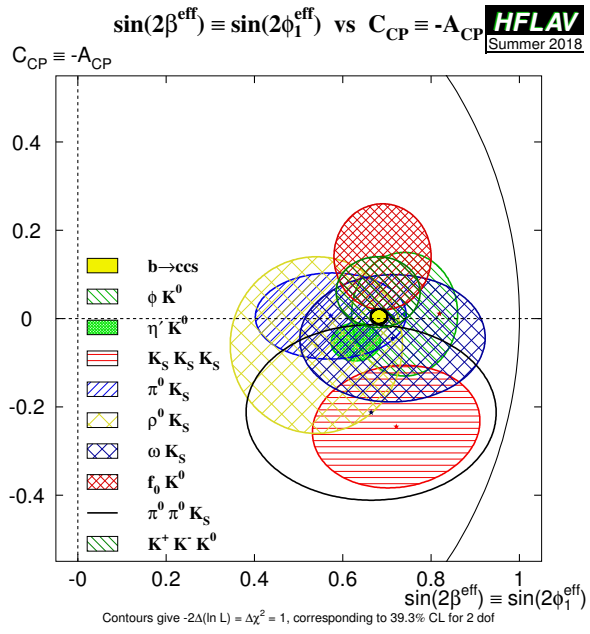

Figure 13.3: Summary of the results [29] of time-dependent analyses of $b \to q\bar{q}s$ decays, which are potentially sensitive to new physics.

For the $\bar{b} \to \bar{u}u\bar{d}$ process $B \to \pi\pi$ and other related channels, the penguin-to-tree ratio can be estimated using SU(3) relations and experimental data on related $B \to K\pi$ decays. The result (for $\pi\pi$) is that the suppression is at the level of $0.2-0.3$ and so cannot be neglected. The expressions for $S_{\pi\pi}$ and $C_{\pi\pi}$ to leading order in $R_{PT} \equiv (|V_{tb}V_{td}|\, P^t_{\pi\pi})/(|V_{ub}V_{ud}|\, T_{\pi\pi})$ are:

$$\lambda_{\pi\pi} = e^{2i\alpha}\left[(1 - R_{PT}e^{-i\alpha})/(1 - R_{PT}e^{+i\alpha})\right] \;\Rightarrow \qquad (13.98)$$

$$S_{\pi\pi} \approx \sin 2\alpha + 2\,\mathcal{R}e(R_{PT})\cos 2\alpha \sin\alpha\ , \quad C_{\pi\pi} \approx 2\,\mathcal{I}m(R_{PT})\sin\alpha\ . \qquad (13.99)$$

Note that R_{PT} is mode-dependent and, in particular, could be different for $\pi^+\pi^-$ and $\pi^0\pi^0$. If strong phases can be neglected, then R_{PT} is real, resulting in $C_{\pi\pi} = 0$. The size of $C_{\pi\pi}$ is an indicator of how large the strong phase is. The present experimental average is $C_{\pi^+\pi^-} = -0.32 \pm 0.04$ [29]. As concerns $S_{\pi\pi}$, it is clear from Eq. (13.99) that the relative size or strong phase of the penguin contribution must be known to extract α. This is the problem of penguin pollution.

The cleanest solution involves isospin relations among the $B \to \pi\pi$ amplitudes [93]:

$$\frac{1}{\sqrt{2}}A_{\pi^+\pi^-} + A_{\pi^0\pi^0} = A_{\pi^+\pi^0}\ . \qquad (13.100)$$

The method exploits the fact that the penguin contribution to $P^t_{\pi\pi}$ is pure $\Delta I = 1/2$ (this is not true for the electroweak penguins which, however, are expected to be small), while the tree contribution to $T_{\pi\pi}$ contains pieces that are both $\Delta I = 1/2$ and $\Delta I = 3/2$. A simple geometric construction then allows one to find R_{PT} and extract α cleanly from $S_{\pi^+\pi^-}$. The key experimental difficulty is that one must measure accurately the separate rates for B^0 and $\overline{B}^0 \to \pi^0\pi^0$.

CP asymmetries in $B \to \rho\pi$ and $B \to \rho\rho$ can also be used to determine α. In particular, the $B \to \rho\rho$ measurements are presently very significant in constraining α. The extraction proceeds via isospin analysis similar to that of $B \to \pi\pi$. There are, however, several important differences. First, due to the finite width of the ρ mesons, a final $(\rho\rho)_{I=1}$ state is possible [94]. The effect is, however, of the order of $(\Gamma_\rho/m_\rho)^2 \sim 0.04$. Second, due to the presence of three helicity states for the two vector mesons, angular analysis is needed to separate the *CP*-even and *CP*-odd components. The theoretical expectation is that the *CP*-odd component is small, which is supported by experiments which find that the $\rho^+\rho^-$ and $\rho^\pm\rho^0$ modes are dominantly longitudinally polarized. Third, an important advantage of the $\rho\rho$ modes is that the penguin contribution is expected to be small due to different hadronic dynamics. This expectation is confirmed by the smallness of $\mathcal{B}(B^0 \to \rho^0\rho^0) = (0.95 \pm 0.16) \times 10^{-6}$ [29,95] compared to $\mathcal{B}(B^0 \to \rho^+\rho^-) = (24.2 \pm 3.1) \times 10^{-6}$ [29]. Thus, $S_{\rho^+\rho^-}$ is not far from $\sin 2\alpha$. Finally, both $S_{\rho^0\rho^0}$ and $C_{\rho^0\rho^0}$ are experimentally accessible, which may allow a precision determination of α. However, a full isospin analysis should allow that the fractions of longitudinal polarisation in B and $\overline{B}$ decays may differ, which has not yet been done by the experiments.

Detailed discussion of the determination of α with these methods, and the latest world average, can be found in Refs. [36,96]. The consistency between the range of α determined by the $B \to \pi\pi$, $\rho\pi$ and $\rho\rho$ measurements and the range allowed by CKM fits (excluding these direct determinations) provides further support to the Kobayashi-Maskawa mechanism.

All modes discussed in this Section so far have possible contributions from penguin amplitudes. As shown in Table 13.1, *CP* violation can also be studied with final states, typically containing charmed mesons, where no such contribution is possible. The neutral charmed meson must be reconstructed in a final state, such as a *CP* eigenstate, common to D^0 and $\overline{D}^0$ so that the am-

plitudes for the B and $\overline{B}$ meson decays interfere. Although there is a second tree amplitude with a different weak phase, the contributions of the different diagrams can in many cases be separated experimentally (for example by exploiting different decays of the neutral D mesons) making these channels very clean theoretically. The first determination of $\sin(2\beta)$, with significance of *CP* violation over 5σ, with this method has recently been reported [97]. Moreover, the interference between the two tree diagrams gives sensitivity to γ, as will be discussed in Section 13.6.4.

13.6.3 *CP violation in interference of B_s^0 decays with and without mixing*

As discussed in Section 13.6.1, the world average for $|q/p|$ in the B_s^0 system currently deviates from the Standard Model expectation due to an anomalous value of the dimuon asymmetry. Attributing the dimuon asymmetry result to a fluctuation, we again neglect the deviation of $|q/p|$ from 1, and use

$$\lambda_f = e^{-i\phi_M(B_s^0)}(\overline{A}_f/A_f)\,. \tag{13.101}$$

Within the Standard Model,

$$e^{-i\phi_{M(B_s^0)}} = (V_{tb}^* V_{ts})/(V_{tb} V_{ts}^*)\,. \tag{13.102}$$

Note that $\Delta\Gamma/\Gamma = 0.132 \pm 0.008$ [29] and therefore y should not be put to zero in Eqs. (13.31a) and (13.31b). However, $|q/p| = 1$ is expected to hold to an even better approximation than for B^0 mesons. One therefore obtains

$$\mathcal{A}_f(t) = \frac{S_f \sin(\Delta m t) - C_f \cos(\Delta m t)}{\cosh(\Delta\Gamma t/2) - A_f^{\Delta\Gamma}\sinh(\Delta\Gamma t/2)}\,, \tag{13.103}$$

$$A_f^{\Delta\Gamma} \equiv \frac{-2\,\mathcal{R}e(\lambda_f)}{1+\left|\lambda_f\right|^2}\,. \tag{13.104}$$

The presence of the $A_f^{\Delta\Gamma}$ term implies that information on λ_f can be obtained from analyses that do not use tagging of the initial flavor, through so-called effective lifetime measurements [98].

The $B_s^0 \to J/\psi\phi$ decay proceeds via the $\overline{b} \to \overline{c}c\overline{s}$ transition. The *CP* asymmetry in this mode thus determines (with angular analysis to disentangle the *CP*-even and *CP*-odd components of the final state) $\sin 2\beta_s$, where β_s is defined in Eq. (13.52) [99]. The $B_s^0 \to J/\psi\pi^+\pi^-$ decay, which has a large contributions from $J/\psi f_0(980)$ and is assumed to also proceed dominantly via the $\overline{b} \to \overline{c}c\overline{s}$ transition, has also been used to determine β_s. In this case no angular analysis is necessary, since the final state has been shown to be dominated by the *CP*-odd component [100]. The combination of measurements yields [29]

$$-2\beta_s = -0.021 \pm 0.031\,, \tag{13.105}$$

consistent with the Standard Model prediction, $\beta_s = 0.0184 \pm 0.0004$ [19].

The experimental investigation of *CP* violation in the B_s^0 sector is still at a relatively early stage, and far fewer modes have been studied than in the B^0 system. First results on the $\overline{b} \to \overline{q}q\overline{s}$ decays $B_s^0 \to \phi\phi$, K^+K^- and $K^{*0}\overline{K}^{*0}$ have been reported. More channels are expected to be studied in the near future.

13.6.4 *Direct CP violation in the B system*

An interesting class of decay modes is that of the tree-level decays $B^\pm \to D^{(*)}K^\pm$. These decays provide golden methods for a clean determination of the angle γ [101–106]. The method uses the decays $B^+ \to D^0K^+$, which proceeds via the quark transition $\overline{b} \to \overline{u}c\overline{s}$, and $B^+ \to \overline{D}^0K^+$, which proceeds via the quark transition $\overline{b} \to \overline{c}u\overline{s}$, with the D^0 and $\overline{D}^0$ decaying into a common final state. The decays into common final states, such $(\pi^0K_S)_DK^+$, involve interference effects between the two amplitudes, with sensitivity to the relative phase, $\delta+\gamma$ (δ is the relevant strong phase difference). The *CP*-conjugate processes are sensitive to $\delta-\gamma$. Measurements of branching ratios and *CP* asymmetries allow the determination of γ and δ from amplitude triangle relations. The method suffers from discrete ambiguities but, since all hadronic parameters can be determined from the data, has negligible theoretical uncertainty [107].

Unfortunately, the smallness of the CKM-suppressed $b \to u$ transitions makes it difficult to use the simplest methods alone [101–103] to determine γ. These difficulties are overcome (and the discrete ambiguities are removed) by performing a Dalitz plot analysis for multi-body D decays [104–106]. Detailed discussion of the determination of γ with these methods can be found in Ref. [36].

Constraints on γ from combinations of results on various $B \to D^{(*)}K^{(*)}$ processes have been obtained by experiments [108,109]. The latest world average is [29]:

$$\gamma = \left(71.1\,^{+4.6}_{-5.3}\right)^\circ\,. \tag{13.106}$$

The consistency between the range of γ determined by the $B \to DK$ measurements and the range allowed by CKM fits (excluding these direct determinations) provides further support to the Kobayashi-Maskawa mechanism. As more data become available, determinations of γ from $B_s^0 \to D_s^\mp K^\pm$ [110, 111] and $B^0 \to DK^{*0}$ [112–115] are expected to also give competitive measurements.

Decays to the final state $K^\mp\pi^\pm$ provided the first observations of direct *CP* violation in both B^0 and B_s^0 systems. The asymmetry arises due to interference between tree and penguin diagrams [116], similar to the effect discussed in Section 13.6.2. In principle, measurements of $\mathcal{A}_{\overline{B}^0 \to K^-\pi^+}$ and $\mathcal{A}_{\overline{B}_s^0 \to K^+\pi^-}$ could be used to determine the weak phase difference γ, but lack of knowledge of the relative magnitude and strong phase of the contributing amplitudes limits the achievable precision. The uncertainties on these hadronic parameters can be reduced by exploiting flavor symmetries, which predict a number of relations between asymmetries in different modes. One such relation is that the partial rate differences for B^0 and B_s^0 decays to $K^\mp\pi^\pm$ are expected to be approximately equal and opposite [117], which is consistent with current data. It is also expected that the partial rate asymmetries for $\overline{B}^0 \to K^-\pi^+$ and $B^- \to K^-\pi^0$ should be approximately equal; however, the experimental results currently show a significant discrepancy [29]:

$$\mathcal{A}_{\overline{B}^0 \to K^-\pi^+} = -0.084 \pm 0.004\,, \quad \mathcal{A}_{B^- \to K^-\pi^0} = +0.040 \pm 0.021\,. \tag{13.107}$$

It is therefore of great interest to understand whether this originates from Standard Model QCD corrections, or whether it is a signature of new dynamics. Improved tests of a more precise relation between the partial rate differences of all four $K\pi$ final states [118–121], currently limited by knowledge of the *CP* asymmetry in $\overline{B}^0 \to K_S\pi^0$ decays, may help to resolve the situation.

It is also of interest to investigate whether similar patterns appear among the *CP* violating asymmetries in B meson decays to final states containing one pseudoscalar and one vector meson. Since the vector resonance decays to two particles, such channels can be studied through Dalitz plot analysis of the three-body final state. Model-independent analyses of $B^+ \to K^+K^-K^+$, $\pi^+\pi^-K^+$, $\pi^+\pi^-\pi^+$ and $K^+K^-\pi^+$ decays have revealed large *CP* violation effects in certain regions of phase space [122]. For the $B^+ \to K^+K^-\pi^+$ decay, an amplitude analysis has established a large *CP* violation effect associated with $\pi\pi \leftrightarrow KK$ S-wave rescattering [123]. For the other channels it remains to be seen whether the *CP* violation effects are associated to particular resonances or to interference effects, which will be necessary to understand the underlying dynamics.

13.7 Summary and Outlook

CP violation has been experimentally established in K, D and B meson decays. A full list of *CP* asymmetries that have been measured at a level higher than 5σ is given in the introduction to this review. In Section 13.1.4 we introduced three types of *CP*-violating effects. Examples of these three types include the following:

1. All three types of *CP* violation have been observed in $K \to \pi\pi$

decays:

$$\begin{aligned}\mathcal{R}e(\epsilon') &= \frac{1}{6}\left(\left|\frac{\overline{A}_{\pi^0\pi^0}}{A_{\pi^0\pi^0}}\right| - \left|\frac{\overline{A}_{\pi^+\pi^-}}{A_{\pi^+\pi^-}}\right|\right) \\ &= (2.5 \pm 0.4) \times 10^{-6}\,, \qquad \text{(I)} \qquad (13.108a)\\ \mathcal{R}e(\epsilon) &= \frac{1}{2}\left(1 - \left|\frac{q}{p}\right|\right) \\ &= (1.66 \pm 0.02) \times 10^{-3}\,, \qquad \text{(II)} \qquad (13.108b)\\ \mathcal{I}m(\epsilon) &= -\frac{1}{2}\mathcal{I}m(\lambda_{(\pi\pi)_{I=0}}) \\ &= (1.57 \pm 0.02) \times 10^{-3}\,. \qquad \text{(III)} \qquad (13.108c)\end{aligned}$$

2. For D mesons, CP violation in decay has been established in the difference of asymmetries for $D^0 \to K^+K^-$ and $D^0 \to \pi^+\pi^-$ decays.

$$\begin{aligned}\Delta a_{CP} &= \frac{|\overline{A}_{K^+K^-}/A_{K^+K^-}|^2 - 1}{|\overline{A}_{K^+K^-}/A_{K^+K^-}|^2 + 1} - \frac{|\overline{A}_{\pi^+\pi^-}/A_{\pi^+\pi^-}|^2 - 1}{|\overline{A}_{\pi^+\pi^-}/A_{\pi^+\pi^-}|^2 + 1} \\ &= (-0.164 \pm 0.028) \times 10^{-3}\,, \quad \text{(I)} \end{aligned} \qquad (13.109)$$

3. In the B meson system, CP violation in decay has been observed in, for example, $B^0 \to K^+\pi^-$ transitions, while CP violation in interference of decays with and without mixing has been observed in, for example, the $B^0 \to J/\psi K_S$ channel:

$$\begin{aligned}\mathcal{A}_{K^+\pi^-} &= \frac{|\overline{A}_{K^-\pi^+}/A_{K^+\pi^-}|^2 - 1}{|\overline{A}_{K^-\pi^+}/A_{K^+\pi^-}|^2 + 1} \\ &= -0.084 \pm 0.004\,, \qquad \text{(I)} \qquad (13.110a)\\ S_{\psi K} &= \mathcal{I}m(\lambda_{\psi K}) \\ &= +0.699 \pm 0.017\,. \qquad \text{(III)} \qquad (13.110b)\end{aligned}$$

Based on Standard Model predictions, further observations of CP violation in B^0, B^+ and B_s^0 decays seem likely in the near future, at both LHCb and its upgrades [124–126] as well as the Belle II experiment [127]. The first observation of CP violation in b baryons is also likely to be within reach of LHCb. Further improvements in the sensitivity to CP violation effects in the charm sector can also be anticipated, though uncertainty in the Standard Model predictions makes it difficult to forecast whether or not additional discoveries will be forthcoming. A number of upcoming experiments have potential to make significant progress on rare kaon decays. Observables that are subject to clean theoretical interpretation, such as β from $S_{\psi K_S}$, β_s from $B_s^0 \to J/\psi\phi$, $\mathcal{B}(K_L \to \pi^0\nu\overline{\nu})$ and γ from CP violation in $B \to DK$ decays, are of particular value for constraining the values of the CKM parameters and probing the flavor sector of extensions to the Standard Model. Progress in lattice QCD calculations is also needed to complement the anticipated experimental results. Other probes of CP violation now being pursued experimentally include the electric dipole moments of the neutron and electron, and the decays of tau leptons. Additional processes that are likely to play an important role in future CP studies include top-quark production and decay, Higgs boson decays and neutrino oscillations.

All measurements of CP violation to date are consistent with the predictions of the Kobayashi-Maskawa mechanism of the Standard Model. In fact, it is now established that the KM mechanism plays a major role in the CP violation measured in the quark sector. However, a dynamically-generated matter-antimatter asymmetry of the universe requires additional sources of CP violation, and such sources are naturally generated by extensions to the Standard Model. New sources might eventually reveal themselves as small deviations from the predictions of the KM mechanism, or else might not be observable in the quark sector at all, but observable with future probes such as neutrino oscillations or electric dipole moments. The fundamental nature of CP violation demands a vigorous search.

A number of excellent reviews of CP violation are available [128–135], where the interested reader may find a detailed discussion of the various topics that are briefly reviewed here.

We thank David Kirkby for significant contributions to earlier versions of this review.

References

[1] J. H. Christenson *et al.*, Phys. Rev. Lett. **13**, 138 (1964).

[2] B. Aubert *et al.* (BaBar), Phys. Rev. Lett. **87**, 091801 (2001), [hep-ex/0107013].

[3] K. Abe *et al.* (Belle), Phys. Rev. Lett. **87**, 091802 (2001), [hep-ex/0107061].

[4] H. Burkhardt *et al.* (NA31), Phys. Lett. **B206**, 169 (1988).

[5] V. Fanti *et al.* (NA48), Phys. Lett. **B465**, 335 (1999), [hep-ex/9909022].

[6] A. Alavi-Harati *et al.* (KTeV), Phys. Rev. Lett. **83**, 22 (1999), [hep-ex/9905060].

[7] B. Aubert *et al.* (BaBar), Phys. Rev. Lett. **93**, 131801 (2004), [hep-ex/0407057].

[8] Y. Chao *et al.* (Belle), Phys. Rev. Lett. **93**, 191802 (2004), [hep-ex/0408100].

[9] A. Poluektov *et al.* (Belle), Phys. Rev. **D81**, 112002 (2010), [arXiv:1003.3360].

[10] P. del Amo Sanchez *et al.* (BaBar), Phys. Rev. **D82**, 072004 (2010), [arXiv:1007.0504].

[11] R. Aaij *et al.* (LHCb), Phys. Lett. **B712**, 203 (2012), [Erratum: Phys. Lett.B713,351(2012)], [arXiv:1203.3662].

[12] R. Aaij *et al.* (LHCb), Phys. Rev. Lett. **110**, 22, 221601 (2013), [arXiv:1304.6173].

[13] R. Aaij *et al.* (LHCb), Phys. Rev. Lett. **122**, 21, 211803 (2019), [arXiv:1903.08726].

[14] See results on the "Time reversal invariance," within the review on "Tests of Conservation Laws," in this *Review*.

[15] J. Bernabeu, F. Martinez-Vidal and P. Villanueva-Perez, JHEP **08**, 064 (2012), [arXiv:1203.0171].

[16] J. P. Lees *et al.* (BaBar), Phys. Rev. Lett. **109**, 211801 (2012), [arXiv:1207.5832].

[17] See, for example, R. F. Streater and A. S. Wightman, *CPT, Spin and Statistics, and All That,* reprinted by Addison-Wesley, New York (1989).

[18] M. Kobayashi and T. Maskawa, Prog. Theor. Phys. **49**, 652 (1973).

[19] J. Charles *et al.* (CKMfitter Group), Eur. Phys. J. **C41**, 1, 1 (2005), updated results and plots available at: `http://ckmfitter.in2p3.fr`, [hep-ph/0406184].

[20] M. Bona *et al.* (UTfit), JHEP **10**, 081 (2006), updated results and plots available at: `http://www.utfit.org/UTfit`, [hep-ph/0606167].

[21] A. D. Sakharov, Pisma Zh. Eksp. Teor. Fiz. **5**, 32 (1967), [Usp. Fiz. Nauk161,no.5,61(1991)].

[22] A. Riotto, in "Proceedings, Summer School in High-energy physics and cosmology: Trieste, Italy, June 29-July 17, 1998," 326–436 (1998), [hep-ph/9807454].

[23] M. Fukugita and T. Yanagida, Phys. Lett. **B174**, 45 (1986).

[24] S. Davidson, E. Nardi and Y. Nir, Phys. Rept. **466**, 105 (2008), [arXiv:0802.2962].

[25] G. Aad *et al.* (ATLAS), Phys. Lett. **B716**, 1 (2012), [arXiv:1207.7214].

[26] S. Chatrchyan *et al.* (CMS), Phys. Lett. **B716**, 30 (2012), [arXiv:1207.7235].

[27] See the K-meson Listings in this *Review*.

[28] See the B-meson Listings in this *Review*.

[29] Y. Amhis *et al.* (HFLAV), Eur. Phys. J. **C77**, 12, 895 (2017), [arXiv:1612.07233].

[30] V. Weisskopf and E. P. Wigner, Z. Phys. **63**, 54 (1930).

[31] See the review on "$D^0 - \overline{D}^0$ Mixing" in this *Review*.

[32] O. Long *et al.*, Phys. Rev. **D68**, 034010 (2003), [hep-ex/0303030].

[33] M. Gronau, Y. Grossman and J. L. Rosner, Phys. Lett. **B508**, 37 (2001), [hep-ph/0103110].

[34] M. Artuso, G. Borissov and A. Lenz, Rev. Mod. Phys. **88**, 4, 045002 (2016), [arXiv:1511.09466].

[35] L. Wolfenstein, Phys. Rev. Lett. **13**, 562 (1964).

[36] See the review on "Cabibbo-Kobayashi-Maskawa Mixing Matrix," in this *Review*.

[37] L. Wolfenstein, Phys. Rev. Lett. **51**, 1945 (1983).

[38] A. J. Buras, M. E. Lautenbacher and G. Ostermaier, Phys. Rev. **D50**, 3433 (1994), [hep-ph/9403384].

[39] C. Jarlskog, Phys. Rev. Lett. **55**, 1039 (1985).

[40] See the review on "CP violation in $K_S \to 3\pi$," in this *Review*.

[41] T. Blum *et al.*, Phys. Rev. **D91**, 7, 074502 (2015), [arXiv:1502.00263].

[42] Z. Bai *et al.* (RBC, UKQCD), Phys. Rev. Lett. **115**, 21, 212001 (2015), [arXiv:1505.07863].

[43] A. J. Buras *et al.*, JHEP **11**, 202 (2015), [arXiv:1507.06345].

[44] Y. Grossman and Y. Nir, Phys. Lett. **B398**, 163 (1997), [hep-ph/9701313].

[45] L. S. Littenberg, Phys. Rev. **D39**, 3322 (1989).

[46] A. J. Buras, Phys. Lett. **B333**, 476 (1994), [hep-ph/9405368].

[47] G. Buchalla and A. J. Buras, Nucl. Phys. **B400**, 225 (1993).

[48] A. J. Buras *et al.*, JHEP **11**, 033 (2015), [arXiv:1503.02693].

[49] J. K. Ahn *et al.* (KOTO), Phys. Rev. Lett. **122**, 2, 021802 (2019), [arXiv:1810.09655].

[50] T. Yamanaka (KOTO), PTEP **2012**, 02B006 (2012).

[51] M. Mirra [NA62 Collab.], Nuovo Cimento **C038**, 13 (2015).

[52] B. Aubert *et al.* (BaBar), Phys. Rev. Lett. **98**, 211802 (2007), [hep-ex/0703020].

[53] M. Staric *et al.* (BELLE), Phys. Rev. Lett. **98**, 211803 (2007), [,65(2007)], [hep-ex/0703036].

[54] T. Aaltonen *et al.* (CDF), Phys. Rev. Lett. **100**, 121802 (2008), [arXiv:0712.1567].

[55] R. Aaij *et al.* (LHCb), Phys. Rev. Lett. **110**, 10, 101802 (2013), [arXiv:1211.1230].

[56] See the D-meson Listings in this *Review*.

[57] Y. Grossman, A. L. Kagan and Y. Nir, Phys. Rev. **D75**, 036008 (2007), [hep-ph/0609178].

[58] S. Bergmann *et al.*, Phys. Lett. **B486**, 418 (2000), [hep-ph/0005181].

[59] M. Gersabeck *et al.*, J. Phys. **G39**, 045005 (2012), [arXiv:1111.6515].

[60] D. M. Asner *et al.* (CLEO), Phys. Rev. **D78**, 012001 (2008), [arXiv:0802.2268].

[61] M. Ablikim *et al.* (BESIII), Phys. Lett. **B734**, 227 (2014), [arXiv:1404.4691].

[62] R. Aaij *et al.* (LHCb), Phys. Rev. Lett. **111**, 25, 251801 (2013), [arXiv:1309.6534].

[63] R. Aaij *et al.* (LHCb), Phys. Rev. Lett. **118**, 26, 261803 (2017), [arXiv:1702.06490].

[64] M. Ciuchini *et al.*, Phys. Lett. **B655**, 162 (2007), [hep-ph/0703204].

[65] Y. Grossman, Y. Nir and G. Perez, Phys. Rev. Lett. **103**, 071602 (2009), [arXiv:0904.0305].

[66] A. L. Kagan and M. D. Sokoloff, Phys. Rev. **D80**, 076008 (2009), [arXiv:0907.3917].

[67] Y. Grossman and Y. Nir, JHEP **04**, 002 (2012), [arXiv:1110.3790].

[68] B. R. Ko *et al.* (Belle), Phys. Rev. Lett. **109**, 021601 (2012), [Erratum: Phys. Rev. Lett.109,119903(2012)], [arXiv:1203.6409].

[69] See the "Review of Multibody Charm Analyses" in this *Review*.

[70] B. Aubert *et al.* (BaBar), Phys. Rev. **D78**, 051102 (2008), [arXiv:0802.4035].

[71] I. Bediaga *et al.*, Phys. Rev. **D80**, 096006 (2009), [arXiv:0905.4233].

[72] I. Bediaga *et al.*, Phys. Rev. **D86**, 036005 (2012), [arXiv:1205.3036].

[73] M. Williams, Phys. Rev. **D84**, 054015 (2011), [arXiv:1105.5338].

[74] R. Aaij *et al.* (LHCb), Phys. Lett. **B769**, 345 (2017), [arXiv:1612.03207].

[75] V. M. Abazov *et al.* (D0), Phys. Rev. **D82**, 032001 (2010), [arXiv:1005.2757].

[76] A. B. Carter and A. I. Sanda, Phys. Rev. Lett. **45**, 952 (1980).

[77] A. B. Carter and A. I. Sanda, Phys. Rev. **D23**, 1567 (1981).

[78] I. I. Y. Bigi and A. I. Sanda, Nucl. Phys. **B193**, 85 (1981).

[79] I. Dunietz and J. L. Rosner, Phys. Rev. **D34**, 1404 (1986).

[80] Y. I. Azimov, N. G. Uraltsev and V. A. Khoze, Sov. J. Nucl. Phys. **45**, 878 (1987), [Yad. Fiz.45,1412(1987)].

[81] I. I. Y. Bigi and A. I. Sanda, Nucl. Phys. **B281**, 41 (1987).

[82] G. Buchalla, A. J. Buras and M. E. Lautenbacher, Rev. Mod. Phys. **68**, 1125 (1996), [hep-ph/9512380].

[83] R. Fleischer, Eur. Phys. J. **C10**, 299 (1999), [hep-ph/9903455].

[84] M. Ciuchini, M. Pierini and L. Silvestrini, Phys. Rev. Lett. **95**, 221804 (2005), [hep-ph/0507290].

[85] S. Faller *et al.*, Phys. Rev. **D79**, 014030 (2009), [arXiv:0809.0842].

[86] M. Jung, Phys. Rev. **D86**, 053008 (2012), [arXiv:1206.2050].

[87] H.-n. Li and S. Mishima, JHEP **03**, 009 (2007), [hep-ph/0610120].

[88] K. De Bruyn and R. Fleischer, JHEP **03**, 145 (2015), [arXiv:1412.6834].

[89] P. Frings, U. Nierste and M. Wiebusch, Phys. Rev. Lett. **115**, 6, 061802 (2015), [arXiv:1503.00859].

[90] L. Silvestrini, Ann. Rev. Nucl. Part. Sci. **57**, 405 (2007), [arXiv:0705.1624].

[91] R. Fleischer *et al.*, Phys. Rev. **D78**, 111501 (2008), [arXiv:0806.2900].

[92] R. Fleischer *et al.*, Eur. Phys. J. **C78**, 11, 943 (2018), [arXiv:1806.08783].

[93] M. Gronau and D. London, Phys. Rev. Lett. **65**, 3381 (1990).

[94] A. F. Falk *et al.*, Phys. Rev. **D69**, 011502 (2004), [hep-ph/0310242].

[95] R. Aaij *et al.* (LHCb), Phys. Lett. **B747**, 468 (2015), [arXiv:1503.07770].

[96] J. Charles *et al.*, Eur. Phys. J. **C77**, 8, 574 (2017), [arXiv:1705.02981].

[97] A. Abdesselam *et al.* (BaBar, Belle), Phys. Rev. Lett. **115**, 12, 121604 (2015), [arXiv:1505.04147].

[98] R. Fleischer and R. Knegjens, Eur. Phys. J. **C71**, 1789 (2011), [arXiv:1109.5115].

[99] A. S. Dighe, I. Dunietz and R. Fleischer, Eur. Phys. J. **C6**, 647 (1999), [hep-ph/9804253].

[100] R. Aaij *et al.* (LHCb), Phys. Rev. **D89**, 9, 092006 (2014), [arXiv:1402.6248].

[101] M. Gronau and D. London, Phys. Lett. **B253**, 483 (1991).

[102] M. Gronau and D. Wyler, Phys. Lett. **B265**, 172 (1991).

[103] D. Atwood, I. Dunietz and A. Soni, Phys. Rev. Lett. **78**, 3257 (1997), [hep-ph/9612433].

[104] D. Atwood, I. Dunietz and A. Soni, Phys. Rev. **D63**, 036005 (2001), [hep-ph/0008090].

[105] A. Giri *et al.*, Phys. Rev. **D68**, 054018 (2003), [hep-ph/0303187].

[106] A. Bondar, *Proceedings of BINP special analysis meeting on Dalitz analysis*, 24-26 Sep. 2002, unpublished.

[107] J. Brod and J. Zupan, JHEP **01**, 051 (2014), [arXiv:1308.5663].

[108] J. P. Lees *et al.* (BaBar), Phys. Rev. **D87**, 5, 052015 (2013), [arXiv:1301.1029].

[109] R. Aaij *et al.* (LHCb), JHEP **12**, 087 (2016), [arXiv:1611.03076].

[110] R. Aleksan, I. Dunietz and B. Kayser, Z. Phys. **C54**, 653 (1992).

[111] R. Fleischer, Nucl. Phys. **B671**, 459 (2003), [hep-ph/0304027].

[112] I. Dunietz, Phys. Lett. **B270**, 75 (1991).

[113] M. Gronau, Phys. Lett. **B557**, 198 (2003), [hep-ph/0211282].

[114] T. Gershon, Phys. Rev. **D79**, 051301 (2009), [arXiv:0810.2706].

[115] T. Gershon and M. Williams, Phys. Rev. **D80**, 092002 (2009), [arXiv:0909.1495].

[116] M. Bander, D. Silverman and A. Soni, Phys. Rev. Lett. **43**, 242 (1979).

[117] X.-G. He, Eur. Phys. J. **C9**, 443 (1999), [hep-ph/9810397].

[118] D. Atwood and A. Soni, Phys. Rev. **D58**, 036005 (1998), [hep-ph/9712287].

[119] M. Gronau and J. L. Rosner, Phys. Rev. **D59**, 113002 (1999), [hep-ph/9809384].

[120] H. J. Lipkin, Phys. Lett. **B445**, 403 (1999), [hep-ph/9810351].

[121] M. Gronau, Phys. Lett. **B627**, 82 (2005), [hep-ph/0508047].

[122] R. Aaij *et al.* (LHCb), Phys. Rev. **D90**, 11, 112004 (2014), [arXiv:1408.5373].

[123] R. Aaij *et al.* (LHCb) (2019), [arXiv:1905.09244].

[124] A. A. Alves, Jr. *et al.* (LHCb), JINST **3**, S08005 (2008).

[125] I. Bediaga *et al.* (LHCb) (2012).

[126] R. Aaij *et al.* [LHCb Collab.], CERN-LHCC-2017-003.

[127] T. Aushev *et al.* (2010), [arXiv:1002.5012].

[128] G. C. Branco, L. Lavoura and J. P. Silva, Int. Ser. Monogr. Phys. **103**, 1 (1999).

[129] I. I. Bigi and A. I. Sanda (2000), [Camb. Monogr. Part. Phys. Nucl. Phys. Cosmol.9,1(2009)].

[130] A. J. Bevan *et al.* (BaBar, Belle), Eur. Phys. J. **C74**, 3026 (2014), [arXiv:1406.6311].

[131] H.R. Quinn and Y. Nir, *"The Mystery of the Missing Antimatter,"* Princeton University Press, Princeton (2008).

[132] T. E. Browder *et al.*, Rev. Mod. Phys. **81**, 1887 (2009), [arXiv:0802.3201].

[133] M. Ciuchini and A. Stocchi, Ann. Rev. Nucl. Part. Sci. **61**, 491 (2011), [arXiv:1110.3920].

[134] R. Aaij *et al.* (LHCb), Eur. Phys. J. **C73**, 4, 2373 (2013), [arXiv:1208.3355].

[135] T. Gershon and V. V. Gligorov, Rept. Prog. Phys. **80**, 4, 046201 (2017), [arXiv:1607.06746].

14. Neutrino Masses, Mixing, and Oscillations

Written August 2019 by M.C. Gonzalez-Garcia (YITP, Stony Brook; ICREA, Barcelona; ICC, U. of Barcelona) and M. Yokoyama (Tokyo U.; Kavli IPMU (WPI), U. Tokyo).

14.1 Neutrinos in the Standard Model: Massless Neutrinos

The gauge symmetry principle is one of the pillars of the great success of modern particle physics as it establishes an unambiguous connection between local (gauge) symmetries and forces mediated by spin-1 particles. In the Standard Model (SM) of particle physics the strong, weak, and electromagnetic interactions are connected to gauge symmetry under $SU(3)_{\rm C} \times SU(2)_L \times U(1)_Y$ where C stands for colour, L for left-handedness, and Y for hypercharge. The SM gauge symmetry is spontaneously broken to $SU(3)_{\rm C} \times U(1)_{\rm EM}$ where $U(1)_{\rm EM}$ couples to the electromagnetic charge $Q_{\rm EM} = T_{L3} + Y$ (T_{L3} is the weak isospin which is the third generator of $SU(2)_L$). The model explains all the interactions of the known fermions once they are assigned to well defined representation of the gauge group. The construction and tests of the Standard Model as a gauge theory are covered in the review sections on "Quantum chromodynamics" and "Electroweak model and constraints on new physics" respectively. In here we emphasize that the gauge invariance principle requires that all terms in the Lagrangian, including the mass terms, respect the local symmetry. This has important implications for the neutrino and in particular for the question of the neutrino mass [1].

In the SM, neutrinos are fermions that do not have strong nor electromagnetic interactions. Consequently they are singlets of the subgroup $SU(3)_C \times U(1)_{\rm EM}$. They are part of the lepton doublets $L_{L\ell} = \begin{pmatrix} \nu_\ell \\ \ell \end{pmatrix}_L$ where f_L is the left-handed component of the fermion f, $f_L = P_L f \equiv \frac{1-\gamma_5}{2} f$. In what follows we will refer as *active* neutrinos to neutrinos that are part of these lepton doublets. In the SM there is one active neutrino for each charged leptons, $\ell = e, \mu, \tau$. $SU(2)_L$ gauge invariance dictates the form of weak charged current (CC) interactions between the neutrinos and their corresponding charged leptons and neutral current (NC) among themselves to be:

$$-\mathcal{L}_{\rm CC} = \frac{g}{\sqrt{2}} \sum_\ell \bar{\nu}_{L\ell} \gamma^\mu \ell_L^- W_\mu^+ + \text{h.c.}\,, \tag{14.1}$$

$$-\mathcal{L}_{\rm NC} = \frac{g}{2\cos\theta_W} \sum_\ell \bar{\nu}_{L\ell} \gamma^\mu \nu_{L\ell} Z_\mu^0\,. \tag{14.2}$$

In the above equations g is the coupling constant associated to $SU(2)$ and θ_W is the Weinberg angle.

Equations(14.1) and (14.2) describe all the neutrino interactions in the SM. In particular, Eq.(14.2) determines the decay width of the Z^0 boson into light ($m_\nu \leq m_{Z^0}/2$) left-handed neutrinos states. Thus from the measurement of the total decay width of the Z^0 one can infer the number of such states. At present the measurement implies $N_\nu = 2.984 \pm 0.008$ (see Particle Listing). As a result any extension of the SM should contain three, and only three, light active neutrinos.

Sterile neutrinos are defined as having no SM gauge interactions, that is, they are singlets of the complete SM gauge group. Thus the SM, as the gauge theory able to describe all known particle interactions, contains no sterile neutrinos.

The SM with its gauge symmetry and the particle content required for the gauge interactions, that is, in the absence of SM singlets, respects an accidental global symmetry which is not imposed but appears as consequence of the gauge symmetry and the representation of the matter fields:

$$G_{\rm SM}^{\rm global} = U(1)_B \times U(1)_{L_e} \times U(1)_{L_\mu} \times U(1)_{L_\tau}\,, \tag{14.3}$$

where $U(1)_B$ is the baryon number symmetry, and $U(1)_{L_e,L_\mu,L_\tau}$ are the three lepton flavour symmetries. The total lepton number, $L_e + L_\mu + L_\tau$, is then also an accidental symmetry since is a subgroup of $G_{\rm SM}^{\rm global}$. This fact has consequences which are relevant to the question of the neutrino mass as we argue next.

In the SM, the masses of the fermions are generated via a Yukawa coupling of the scalar Higgs doublet ϕ with a fermion right-handed and left-handed component. The former is an $SU(2)_L$ singlet, the latter is part of a doublet. For leptons, we can one can build such term coupling the left-handed lepton doublets L_L with the right-handed charged lepton fields E_R:

$$-\mathcal{L}_{\rm Yukawa,lep} = Y_{ij}^\ell \bar{L}_{Li} \phi E_{Rj} + \text{h.c.}\,. \tag{14.4}$$

After spontaneous symmetry breaking these terms lead to charged lepton masses

$$m_{ij}^\ell = Y_{ij}^\ell \frac{v}{\sqrt{2}}\,, \tag{14.5}$$

where v is the vacuum expectation value of the Higgs field. However, since the model does not contain right-handed neutrinos, no such Yukawa interaction can be built for the neutrinos, which are consequently massless at the Lagrangian level.

In principle, a neutrino mass term could be generated at loop level. With the particle content of the SM the only possible neutrino mass term that could be constructed is the bilinear $\bar{L}_L L_L^c$, where L_L^c is the charge conjugated field, $L_L^c = C\bar{L_L}^T$ and C is the charge conjugation matrix. However this term is forbidden in the SM because it violates the total lepton symmetry by two units and therefore it cannot be induced by loop corrections because it breaks the accidental symmetry of the model. Also, because $U(1)_{B-L}$ is a non-anomalous subgroup of $G_{\rm SM}^{\rm global}$, the bilinear $\bar{L}_L L_L^c$, cannot be induced by nonperturbative corrections either since it breaks $B - L$.

We conclude that within the SM neutrinos are precisely massless. Consequently one must go beyond the SM in order to add a mass to the neutrino.

14.2 Extending the Standard Model to Introduce Massive Neutrinos

From the above discussion we conclude that it is not possible to construct a renormalizable mass term for the neutrinos with the

[1] The physics of massive neutrinos has been the subject of excellent books such as [1–5] and multiple review articles. The contents of the present review is built upon the structure and the contents of the review articles [6, 7].

fermionic content and gauge symmetry of the SM. The obvious consequence is that in order to introduce a neutrino mass in the theory one must extend the particle content of the model, depart from gauge invariance and/or renormalizability, or do both.

As a matter of fact, neutrino mass terms can be constructed in different ways. In the following we shall assume to maintain the gauge symmetry and explore the different possibilities to introduce a neutrino mass term adding to the SM an arbitrary number of sterile neutrinos ν_{si} $(i = 1, \dots m)$.

In the SM extended with the addition of m number of sterile neutrinos one can construct two gauge invariant renormalizable operators leading to two type of mass terms

$$-\mathcal{L}_{M_\nu} = M_{D\,ij}\bar{\nu}_{si}\nu_{Lj} + \frac{1}{2}M_{N\,ij}\bar{\nu}_{si}\nu^c_{sj} + \text{h.c.}\,, \tag{14.6}$$

where ν^c is the neutrino charge conjugated field (defined in section 14.1). M_D is a complex matrix of dimension $m \times 3$ and M_N is a symmetric $m \times m$ matrix.

The first term is generated after spontaneous electroweak symmetry breaking from Yukawa interactions,

$$Y^\nu_{ij}\bar{\nu}_{si}\tilde{\phi}^\dagger L_{Lj} \Rightarrow M_{D\,ij} = Y^\nu_{ij}\frac{v}{\sqrt{2}}\,, \tag{14.7}$$

in similarity to Eqs.(14.4) and (14.5) for the charged fermion masses. It is correspondingly called a Dirac mass term. It conserves total lepton number but it can break the lepton flavour number symmetries.

The second term in Eq.(14.6) is a Majorana mass term and it differs from the Dirac mass terms in several relevant aspects. First, it is a singlet of the SM gauge group and, as such, it can appear as a bare mass term in the Lagrangian. Second, since it involves two neutrino fields (right-handed in this case), it breaks lepton number by two units. In general such a term is not allowed if the neutrinos carry any additive conserved charge.

It is possible to rewrite Eq.(14.6) as:

$$-\mathcal{L}_{M_\nu} = \frac{1}{2}(\overline{\vec{\nu}^c_L}, \overline{\vec{\nu}_s})\begin{pmatrix} 0 & M_D^T \\ M_D & M_N \end{pmatrix}\begin{pmatrix} \vec{\nu}_L \\ \vec{\nu}^c_s \end{pmatrix} + \text{h.c.} \equiv \overline{\vec{\nu}^c}M_\nu\vec{\nu} + \text{h.c.}\,, \tag{14.8}$$

where $\vec{\nu} = (\vec{\nu}_L,\, \vec{\nu^c_s})^T$ is a $(3+m)$-dimensional vector. The matrix M_ν is complex and symmetric [2]. Thus it can be diagonalized by a unitary matrix V^ν of dimension$(3+m)$, so

$$(V^\nu)^T M_\nu V^\nu = \text{diag}(m_1, m_2, \dots, m_{3+m})\,. \tag{14.9}$$

One can express the original weak eigenstates in terms of the resulting $3+m$ mass eigenstates

$$\vec{\nu}_{\text{mass}} = (V^\nu)^\dagger\vec{\nu}\,, \tag{14.10}$$

and in terms of the mass eigenstates Eq.(14.8) takes the form:

$$\begin{aligned} -\mathcal{L}_{M_\nu} &= \frac{1}{2}\sum_{k=1}^{3+m} m_k\left(\bar{\nu}^c_{\text{mass},k}\nu_{\text{mass},k} + \bar{\nu}_{\text{mass},k}\nu^c_{\text{mass},k}\right) \\ &= \frac{1}{2}\sum_{k=1}^{3+m} m_k\bar{\nu}_{Mk}\nu_{Mk}\,, \end{aligned} \tag{14.11}$$

where

$$\nu_{Mk} = \nu_{\text{mass},k} + \nu^c_{\text{mass},k} = (V^{\nu\,\dagger}\vec{\nu})_k + (V^{\nu\,\dagger}\vec{\nu})^c_k\,. \tag{14.12}$$

So these states obey the Majorana condition

$$\nu_M = \nu^c_M\,, \tag{14.13}$$

and are referred to as Majorana neutrinos. The Majorana condition implies that only one field describes both neutrino and antineutrino states, unlike in the case of a charge for which particle and antiparticle are described by two different fields. So a Majorana neutrino can be described by a two-component spinor unlike the charged fermions, which are Dirac particles, and are represented by four-component spinors.

[2] Notice that Eq.(14.8) corresponds to the tree-level neutrino mass matrix. Corrections are induced at the loop level, which in particular lead to non-vanishing $\bar{\nu}^c_L\nu_L$ entry [8].

Inverting Eq.(14.12) we can write the weak-doublet components of the neutrino fields as:

$$\nu_{Li} = P_L\sum_{j=1}^{3+m} V^\nu_{ij}\nu_{Mj} \quad i = 1, 2, 3\,, \tag{14.14}$$

where P_L is the left projector.

In what follows we will discuss some interesting particular cases of this general framework: light Dirac neutrinos in Sec.14.2.1, and light Majorana neutrinos and the see-saw mechanism in Sec.14.2.2. A special case of the second one is the possibility of light-sterile neutrinos discussed in Sec.14.2.3. In Sec.14.2.4 we shall discuss the effective generation of neutrino masses from non-renormalizable operators (of which the see-saw mechanism is a particular realization).

14.2.1 *Dirac Neutrinos*

Imposing $M_N = 0$ is equivalent to imposing lepton number symmetry on the model. Doing so only the first term in Eq.(14.6), the Dirac mass term, is allowed. If sterile neutrinos are three ($m = 3$), we can identify them with the right-handed component of a four-spinor neutrino field. In this case the Dirac mass term can be diagonalized with two 3×3 unitary matrices, V^ν and V^ν_R as:

$$V^{\nu\,\dagger}_R M_D V^\nu = \text{diag}(m_1, m_2, m_3)\,. \tag{14.15}$$

The neutrino mass term can be written as:

$$-\mathcal{L}_{M_\nu} = \sum_{k=1}^{3} m_k\bar{\nu}_{Dk}\nu_{Dk}\,, \tag{14.16}$$

where

$$\nu_{D\,k} = (V^{\nu\,\dagger}\vec{\nu}_L)_k + (V^{\nu\,\dagger}_R\vec{\nu}_s)_k\,, \tag{14.17}$$

so the weak-doublet components of the neutrino fields are

$$\nu_{Li} = P_L\sum_{j=1}^{3} V^\nu_{ij}\nu_{Dj}\,. \qquad i = 1, 2, 3\,. \tag{14.18}$$

Let's stress that in this case both the low energy matter content and the assumed symmetries are different from those of the SM. Consequently the SM is not even a good low-energy effective theory. Furthermore, this scenario does not explain the fact that neutrinos are much lighter than the corresponding charged fermions, because all acquire their mass via the same mechanism.

14.2.2 *The See-saw Mechanism*

If the mass eigenvalues of M_N are much higher than the scale of electroweak symmetry breaking v, the diagonalization of M_ν leads to three light neutrinos, ν_l, and m heavy neutrinos, N:

$$-\mathcal{L}_{M_\nu} = \frac{1}{2}\bar{\nu}_l M^l\nu_l + \frac{1}{2}\bar{N}M^h N\,, \tag{14.19}$$

with

$$M^l \simeq -V_l^T M_D^T M_N^{-1} M_D V_l, \qquad M^h \simeq V_h^T M_N V_h\,, \tag{14.20}$$

and

$$V^\nu \simeq \begin{bmatrix} \left(1 - \frac{1}{2} M_D^\dagger {M_N^*}^{-1} M_N^{-1} M_D\right) V_l & M_D^\dagger {M_N^*}^{-1} V_h \\ -M_N^{-1} M_D V_l & \left(1 - \frac{1}{2} {M_N}^{-1} M_D M_D^\dagger {M_N^*}^{-1}\right) V_h \end{bmatrix} , \tag{14.21}$$

where V_l and V_h are 3×3 and $m \times m$ unitary matrices respectively. From Eq.(14.20) we see that the masses of the heavier states are proportional to M_N while those of the lighter ones to M_N^{-1}, hence the name of *see-saw mechanism* [9–13]. Also, as seen from Eq.(14.21), the heavy states are mostly right-handed while the light ones are mostly left-handed. Both the light and the heavy neutrinos are Majorana particles. Two well-known examples of extensions of the SM leading to a see-saw mechanism for neutrino masses are SO(10) Grand Unified Theories [10, 11] and left-right symmetry [13].

In this case the SM is a good effective low energy theory. Indeed the see-saw mechanism is a particular example of a full theory whose low energy effective realization is the SM with three light Majorana neutrinos which we describe in Sec.14.2.4.

14.2.3 *Light Sterile Neutrinos*

If the scale of some $n_s \leq m$ eigenvalues of M_N are not higher than the electroweak scale, the low energy spectrum contains n_s additional light states with large admixture of sterile component. As in the case with Dirac Neutrinos, the SM is not a good low energy effective theory: there are more than three $(3+n_s)$ light neutrinos, and they are admixtures of doublet and singlet fields. As in the general case, both light and heavy neutrinos are Majorana particles.

14.2.4 *Neutrino Masses from Generic New Physics*

Under the generic hypothesis that new physics (NP) beyond the SM only manifests itself directly above some scale $\Lambda_{\rm NP}$, we can consider that the SM is an effective low energy theory which is valid to describe the physical world at energies well below $\Lambda_{\rm NP}$ with the same gauge group, fermionic spectrum, and the pattern of spontaneous symmetry breaking of the SM. However, this is an effective theory, holding only till energy below $\Lambda_{\rm NP}$, and consequently does not need to be renormalizable. In this case the low energy Lagrangian can contain non-renormalizable higher dimensional terms whose effect will be suppressed by powers $1/\Lambda_{\rm NP}^{\text{dim-4}}$.

In this approach, the least suppressed NP effects at low energy are expected to come from dim= 5 operators. With the SM fields an gauge symmetry one can only construct the following set of dimension-five terms

$$\mathcal{O}_5 = \frac{Z^\nu_{ij}}{\Lambda_{\rm NP}} \left(\bar{L}_{Li} \tilde{\phi}\right) \left(\tilde{\phi}^T L^C_{Lj}\right) + \text{h.c.} . \tag{14.22}$$

This set violates (14.3) which poses no problem since in general there is no reason for the NP to respect the accidental symmetries of the SM. In particular it violates total lepton number by two units and after spontaneous symmetry breaking it generates a bilinear neutrino field term:

$$-\mathcal{L}_{M_\nu} = \frac{Z^\nu_{ij}}{2} \frac{v^2}{\Lambda_{\rm NP}} \bar{\nu}_{Li} \nu^c_{Lj} + \text{h.c.} . \tag{14.23}$$

This is a Majorana mass term (see Eq.(14.8)). It is built with the left-handed neutrino fields and with mass matrix:

$$(M_\nu)_{ij} = Z^\nu_{ij} \frac{v^2}{\Lambda_{\rm NP}} . \tag{14.24}$$

We conclude that Eq.(14.24) would arise in a generic extension of the SM and that neutrino masses are very likely to appear if there is NP. Comparing Eq.(14.24) and Eq.(14.5), we also find that the scale of neutrino masses is suppressed by $v/\Lambda_{\rm NP}$ when compared to the scale of charged fermion masses providing an explanation for their smallness. Furthermore, both total lepton number and the lepton flavour symmetry $U(1)_e \times U(1)_\mu \times U(1)_\tau$ are broken by Eq.(14.24) which means that, generically, in the absence of additional symmetries on the coefficients Z_{ij}, we can expect lepton flavour mixing and CP violation as we discuss in next section.

Finally, we notice that, as mentioned in Sec.14.2.2, a theory where the NP is composed of m heavy sterile neutrinos, provides an specific example of a theory which at low energy theory contains three light mass eigenstates with an effective dim-5 interaction of the form (14.22) with $\Lambda_{\rm NP} = M_N$. This is, in this case the NP scale is the characteristic mass scale of the heavy sterile neutrinos.

14.3 Lepton Mixing

Let us start by considering $n = 3 + m$ massive neutrino states and denote the neutrino mass eigenstates by $(\nu_1, \nu_2, \nu_3, \ldots, \nu_n)$. The neutrino interaction eigenstates are denoted by $\vec{\nu} = (\nu_{Le}, \nu_{L\mu}, \nu_{L\tau}, \nu_{s1}, \ldots, \nu_{sm})$. We label the corresponding mass and interaction eigenstates for the charged leptons as (e, μ, τ) and (e^I, μ^I, τ^I) respectively. The Lagrangian for the leptonic charged current interactions in the mass basis takes the form:

$$-\mathcal{L}_{\rm CC} = \frac{g}{\sqrt{2}} (\bar{e}_L, \bar{\mu}_L, \bar{\tau}_L) \gamma^\mu U \begin{pmatrix} \nu_1 \\ \nu_2 \\ \nu_3 \\ \vdots \\ \nu_n \end{pmatrix} W^+_\mu + \text{h.c.} , \tag{14.25}$$

where U is a $3 \times n$ matrix [14–16]. It satisfies the unitary condition

$$U U^\dagger = I_{3\times 3} . \tag{14.26}$$

However, in general $U^\dagger U \neq I_{n\times n}$.

In the interaction basis, the mass terms for the leptons are:

$$-\mathcal{L}_M = [(\bar{e}^I_L, \bar{\mu}^I_L, \bar{\tau}^I_L) M_\ell \begin{pmatrix} e^I_R \\ \mu^I_R \\ \tau^I_R \end{pmatrix} + \text{h.c.}] - \mathcal{L}_{M_\nu} , \tag{14.27}$$

with $\mathcal{L}_{M_\nu}$ given in Eq.(14.8). M_ℓ can be diagonalize with two 3×3 unitary matrices V^ℓ and V^ℓ_R which satisfy

$$V^{\ell\dagger} M_\ell V^\ell_R = \text{diag}(m_e, m_\mu, m_\tau) . \tag{14.28}$$

Then for the charged leptons we have

$$-\mathcal{L}_{M_\ell} = \sum_{k=1}^{3} m_{\ell_k} \bar{\ell}_k \ell_k , \tag{14.29}$$

with

$$\ell_k = (V^{\ell\dagger} \ell^I_L)_k + (V^{\ell\dagger}_R \ell^I_R)_k . \tag{14.30}$$

Inverting the equation above we find that the weak-doublet components of the charged lepton fields are

$$\ell^I_{Li} = P_L \sum_{j=1}^{3} V^\ell_{ij} \ell_j . \qquad i = 1, 2, 3 \tag{14.31}$$

From Eqs.(14.14), (14.18) and (14.31) we find that the mixing matrix U can be expressed as:

$$U_{ij} = \mathcal{P}_{\ell,ii} \, {V^\ell_{ik}}^\dagger \, V^\nu_{kj} \, (\mathcal{P}_{\nu,jj}). \tag{14.32}$$

The matrix $V^{\ell\dagger} V^\nu$ contains a number of phases that are not physical. Three of them are eliminated by the diagonal 3×3 phase matrix $\mathcal{P}_\ell$ that absorbs them in the charged lepton mass eigenstates. If neutrinos are Dirac states, further $n - 1$ are similarly eliminated by absorbing them in the neutrino mass eigenstates with the diagonal $n \times n$ phase matrix $\mathcal{P}_\nu$. For Majorana neutrinos, $\mathcal{P}_\nu = I_{n\times n}$ because one cannot rotate by an arbitrary phase a Majorana field without physical effects. If one rotates a Majorana neutrino by a phase, this phase will appear in its mass term which will no longer be real. Consequently the number of phases

that can be absorbed by redefining the mass eigenstates depends on whether the neutrinos are Dirac or Majorana particles. Altogether for $n \geq 3$ Majorana [Dirac] neutrinos the U matrix contains a total of $6(n-2)$ [$5n-11$] real parameters, of which $3(n-2)$ are angles and $3(n-2)$ [$2n-5$] can be interpreted as physical phases.

The possibility of arbitrary mixing between massive neutrino states was first discussed in the context of two neutrinos introduced in Ref. [17] (the possibility of two mixed massless flavour neutrino states had been previously considered in the literature [18], and even before the possibility of mixing between neutrino and antineutrino states in the seminal paper of Pontecorvo [19]). For that case, in which only mixing between two generations is considered with $n = 2$ distinct neutrino masses, the U matrix is 2×2 and contains one mixing angle if the neutrinos are Dirac and an additional physical phase if they are Majorana.

If there are only $n = 3$ Majorana neutrinos, U is a 3×3 matrix analogous to the CKM matrix for the quarks [20,21] but due to the Majorana nature of the neutrinos it depends on six independent parameters: three mixing angles and three phases. In this case the mixing matrix can be conveniently parametrized as:

$$U = \begin{pmatrix} 1 & 0 & 0 \\ 0 & c_{23} & s_{23} \\ 0 & -s_{23} & c_{23} \end{pmatrix} \cdot \begin{pmatrix} c_{13} & 0 & s_{13}e^{-i\delta_{\rm CP}} \\ 0 & 1 & 0 \\ -s_{13}e^{i\delta_{\rm CP}} & 0 & c_{13} \end{pmatrix} \cdot \begin{pmatrix} c_{21} & s_{12} & 0 \\ -s_{12} & c_{12} & 0 \\ 0 & 0 & 1 \end{pmatrix} \cdot \begin{pmatrix} e^{i\eta_1} & 0 & 0 \\ 0 & e^{i\eta_2} & 0 \\ 0 & 0 & 1 \end{pmatrix} , \tag{14.33}$$

where $c_{ij} \equiv \cos\theta_{ij}$ and $s_{ij} \equiv \sin\theta_{ij}$. The angles θ_{ij} can be taken without loss of generality to lie in the first quadrant, $\theta_{ij} \in [0, \pi/2]$ and the phases $\delta_{\rm CP},\ \eta_i \in [0, 2\pi]$. This is to be compared to the case of three Dirac neutrinos. In this case the Majorana phases, η_1 and η_2, can be absorbed in the neutrino states so number of physical phases is one (similar to the CKM matrix). Thus we can write U as:

$$U = \begin{pmatrix} c_{12}\, c_{13} & s_{12}\, c_{13} & s_{13}\, e^{-i\delta_{\rm CP}} \\ -s_{12}\, c_{23} - c_{12}\, s_{13}\, s_{23}\, e^{i\delta_{\rm CP}} & c_{12}\, c_{23} - s_{12}\, s_{13}\, s_{23}\, e^{i\delta_{\rm CP}} & c_{13}\, s_{23} \\ s_{12}\, s_{23} - c_{12}\, s_{13}\, c_{23}\, e^{i\delta_{\rm CP}} & -c_{12}\, s_{23} - s_{12}\, s_{13}\, c_{23}\, e^{i\delta_{\rm CP}} & c_{13}\, c_{23} \end{pmatrix} . \tag{14.34}$$

This matrix is often called the Pontecorvo-Maki-Nakagawa-Sakata (PMNS) mixing matrix.

Notice that when the charged leptons have no other interactions that the SM ones, one can identify their interaction eigenstates with the corresponding mass eigenstates up to phase redefinition. This implies that, in this case, U is just a $3\times n$ sub-matrix of the unitary neutrino mass diagonalizing matrix V^ν.

Finally, let us point out that for the case of 3 light Dirac neutrinos the procedure above leads to a unitary U matrix for the light states. But for three light Majorana neutrinos this is not the case when the full spectrum contains states which are heavy and are not in the low energy spectrum as seen, for example, in Eq.(14.21). This implies that, strictly speaking, the parametrization in Eq.(14.33) is not valid to describe the flavour mixing of the three light Majorana neutrinos in the see-saw mechanism. The violation of unitarity, however, is rather small, of the order $\mathcal{O}(M_D/M_N)$ as seen in Eq.(14.21). It is also severely constrained experimentally [22,23]. For all these reasons, for all practical purposes, we will consider the U matrix for the 3ν mixing case to be unitary independently of whether neutrinos are Dirac or Majorana particles.

14.4 Mass-Induced Flavour Oscillations in Vacuum

If neutrinos have masses and lepton flavours are mixed in the weak CC interactions, lepton flavour is not conserved in neutrino propagation [19, 24]. This phenomenon is usually referred to as *neutrino oscillations*. In brief, a weak eigenstates, ν_α, which by default is the state produced in the weak CC interaction of a charged lepton ℓ_α, is the linear combination determined by the mixing matrix U

$$|\nu_\alpha\rangle = \sum_{i=1}^{n} U^*_{\alpha i} |\nu_i\rangle \,, \tag{14.35}$$

where ν_i are the mass eigenstates and here n is the number of light neutrino species (implicit in our definition of the state $|\nu\rangle$ is its energy-momentum and space-time dependence). After travelling a distance L ($L \simeq ct$ for relativistic neutrinos), that state evolves as:

$$|\nu_\alpha(t)\rangle = \sum_{i=1}^{n} U^*_{\alpha i} |\nu_i(t)\rangle \,. \tag{14.36}$$

This neutrino can then undergo a charged-current (CC) interaction producing a charge lepton ℓ_β, $\nu_\alpha(t)N' \to \ell_\beta N$, with a probability

$$P_{\alpha\beta} = |\langle\nu_\beta|\nu_\alpha(t)\rangle|^2 = |\sum_{i=1}^{n}\sum_{j=1}^{n} U^*_{\alpha i} U_{\beta j} \langle\nu_j|\nu_i(t)\rangle|^2 \,. \tag{14.37}$$

Assuming that $|\nu\rangle$ is a plane wave, $|\nu_i(t)\rangle = e^{-i\,E_i t}|\nu_i(0)\rangle$, [3] with $E_i = \sqrt{p_i^2 + m_i^2}$ and m_i being, respectively, the energy and the mass of the neutrino mass eigenstate ν_i. In all practical cases neutrinos are very relativistic ,so $p_i \simeq p_j \equiv p \simeq E$. We can then write

$$E_i = \sqrt{p_i^2 + m_i^2} \simeq p + \frac{m_i^2}{2E} \,, \tag{14.38}$$

and use the orthogonality of the mass eigenstates, $\langle\nu_j|\nu_i\rangle = \delta_{ij}$, to arrive to the following form for $P_{\alpha\beta}$:

$$P_{\alpha\beta} = \delta_{\alpha\beta} - 4\sum_{i<j}^{n} {\rm Re}[U_{\alpha i} U^*_{\beta i} U^*_{\alpha j} U_{\beta j}] \sin^2 X_{ij} + 2\sum_{i<j}^{n} {\rm Im}[U_{\alpha i} U^*_{\beta i} U^*_{\alpha j} U_{\beta j}] \sin 2X_{ij} \,, \tag{14.39}$$

where

$$X_{ij} = \frac{(m_i^2 - m_j^2)L}{4E} = 1.267\, \frac{\Delta m^2_{ij}}{{\rm eV}^2}\, \frac{L/E}{\rm m/MeV} \,. \tag{14.40}$$

If we had made the same derivation for antineutrino states we would have ended with a similar expression but with the exchange $U \to U^*$. Consequently we conclude that the first term in the right-hand-side of Eq.(14.39) is CP conserving since it is the same for neutrinos and antineutrinos, while the last one is CP violating because it has opposite sign for neutrinos and antineutrinos.

Equation (14.39) oscillatory in distance with oscillation lengths

$$L^{\rm osc}_{0,ij} = \frac{4\pi E}{|\Delta m^2_{ij}|} \,, \tag{14.41}$$

and with amplitudes proportional to products of elements in the mixing matrix. Thus, neutrinos must have different masses

[3] For a pedagogical discussion of the quantum mechanical description of flavour oscillations in the wave package approach see for example Ref. [3]. A recent review of the quantum mechanical aspects and subtleties on neutrino oscillations can be found in in Ref. [25].

($\Delta m^2_{ij} \neq 0$) and they must have not vanishing mixing ($U_{\alpha_i} U_{\beta i} \neq 0$) in order to undergo flavour oscillations. Also, from Eq.(14.39) we see that the Majorana phases cancel out in the oscillation probability. This is expected because flavour oscillation is a total lepton number conserving process.

Ideally, a neutrino oscillation experiment would like to measure an oscillation probability over a distance L between the source and the detector, for neutrinos of a definite energy E. In practice, neutrino beams, both from natural or artificial sources, are never monoenergetic, but have an energy spectrum $\Phi(E)$. In addition each detector has a finite energy resolution. Under these circumstances what is measured is an average probability

$$\begin{aligned}\langle P_{\alpha\beta}\rangle &= \frac{\int dE \frac{d\Phi}{dE}\sigma(E) P_{\alpha\beta}(E)\epsilon(E)}{\int dE \frac{d\Phi}{dE}\sigma_{CC}(E)\epsilon(E)} \\ &= \delta_{\alpha\beta} - 4\sum_{i<j}^{n} \mathrm{Re}[U_{\alpha i}U^*_{\beta i}U^*_{\alpha j}U_{\beta j}]\langle \sin^2 X_{ij}\rangle \\ &+ 2\sum_{i<j}^{n} \mathrm{Im}[U_{\alpha i}U^*_{\beta i}U^*_{\alpha j}U_{\beta j}]\langle \sin 2X_{ij}\rangle\,.\end{aligned} \tag{14.42}$$

σ is the cross section for the process in which the neutrino flavour is detected, and $\epsilon(E)$ is the detection efficiency. The minimal range of the energy integral is determined by the energy resolution of the experiment.

It is clear from the above expression that if $(E/L) \gg |\Delta m^2_{ij}|$ ($L \ll L^{\rm osc}_{0,ij}$) so $\sin^2 X_{ij} \ll 1$, the oscillation phase does not give any appreciable effect. Conversely if $L \gg L^{\rm osc}_{0,ij}$, many oscillation cycles occur between production and detection so the oscillating term is averaged to $\langle \sin^2 X_{ij}\rangle = 1/2$.

We summarize in Table 14.1. the typical values of L/E for different types of neutrino sources and experiments and the corresponding ranges of Δm^2 to which they can be most sensitive.

Table 14.1: Characteristic values of L and E for experiments performed using various neutrino sources and the corresponding ranges of $|\Delta m^2|$ to which they can be most sensitive to flavour oscillations in vacuum. SBL stands for Short Baseline and LBL for Long Baseline.

Experiment		L (m)	E (MeV)	$\lvert\Delta m^2\rvert$ (eV^2)
Solar		10^{10}	1	10^{-10}
Atmospheric		$10^4 - 10^7$	10^2–10^5	$10^{-1} - 10^{-4}$
Reactor	SBL	$10^2 - 10^3$	1	$10^{-2} - 10^{-3}$
	LBL	$10^4 - 10^5$		$10^{-4} - 10^{-5}$
Accelerator	SBL	10^2	10^3–10^4	> 0.1
	LBL	$10^5 - 10^6$	$10^3 - 10^4$	$10^{-2} - 10^{-3}$

Historically, the results of neutrino oscillation experiments were interpreted assuming two-neutrino states so there is only one oscillating phase, the mixing matrix depends on a single mixing angle θ and no CP violation effect in oscillations is possible. At present, as we will discuss in Sec.14.7, we need at least the mixing among three-neutrino states to fully describe the bulk of experimental results. However, in many cases, the observed results can be understood in terms of oscillations dominantly driven by one Δm^2. In this limit $P_{\alpha\beta}$ of Eq.(14.39) takes the form [24]

$$P_{\alpha\beta} = \delta_{\alpha\beta} - (2\delta_{\alpha\beta} - 1)\sin^2 2\theta \sin^2 X\,. \tag{14.43}$$

In this effective $2-\nu$ limit, changing the sign of the mass difference, $\Delta m^2 \to -\Delta m^2$, and changing the octant of the mixing angle, $\theta \to \frac{\pi}{2} - \theta$, is just redefining the mass eigenstates, $\nu_1 \leftrightarrow \nu_2$: $P_{\alpha\beta}$ must be invariant under such transformation. So the physical parameter space can be covered with either $\Delta m^2 \geq 0$ with $0 \leq \theta \leq \frac{\pi}{2}$, or, alternatively, $0 \leq \theta \leq \frac{\pi}{4}$ with either sign for Δm^2.

However, from Eq.(14.43) we see that $P_{\alpha\beta}$ is actually invariant under the change of sign of the mass splitting *and* the change of octact of the mixing angle separately. This implies that there is a two-fold discrete ambiguity since the two different sets of physical parameters, $(\Delta m^2, \theta)$ and $(\Delta m^2, \frac{\pi}{2} - \theta)$, give the same transition probability in vacuum. In other words, one could not tell from a measurement of, say, $P_{e\mu}$ in vacuum whether the larger component of ν_e resides in the heavier or in the lighter neutrino mass eigenstate. This symmetry is broken when one considers mixing of three or more neutrinos in the flavour evolution and/or when the neutrinos traverse regions of dense matter as we describe in Sec.14.7.1 and Sec.14.5 respectively.

14.5 Propagation of Massive Neutrinos in Matter

Neutrinos propagating in a dense medium can interact with the particles in the medium. The probability of an incoherent inelastic scattering is very small. For example the characteristic cross section for ν-proton scattering is of the order

$$\sigma \sim \frac{G_F^2 s}{\pi} \sim 10^{-43}\ \mathrm{cm}^2 \left(\frac{E}{\mathrm{MeV}}\right)^2, \tag{14.44}$$

where G_F is the Fermi constant and s is the square of the center of mass energy of the collision.

But when neutrinos propagate in dense matter, they can also interact coherently with the particles in the medium. By definition, in coherent interactions, the medium remains unchanged so it is possible to have interference of the forward scattered and the unscattered neutrino waves which enhances the effect of matter in the neutrino propagation. In this case the effect of the medium is not on the intensity of the propagating neutrino beam, which remains unchanged, but on the phase velocity of the neutrino wave, and for this reason the effect is proportional to G_F, instead of the G_F^2 dependence of the incoherent scattering. Coherence also allows decoupling the evolution equation of the neutrinos from those of the medium. In this limit the effect of the medium is introduced in the evolution equation for the neutrinos in the form of an effective potential which depends on the density and composition of the matter [26].

As an example, let us consider the evolution of ν_e in a medium with electrons, protons and neutrons with corresponding n_e, n_p and n_n number densities. The effective low-energy Hamiltonian describing the relevant neutrino interactions at point x is given by

$$H_W = \frac{G_F}{\sqrt{2}}\left[J^{(+)\alpha}(x)J^{(-)}_\alpha(x) + \frac{1}{4}J^{(N)\alpha}(x)J^{(N)}_\alpha(x)\right], \tag{14.45}$$

where the J_α's are the standard fermionic currents

$$J^{(+)}_\alpha(x) = \bar\nu_e(x)\gamma_\alpha(1-\gamma_5)e(x)\,, \tag{14.46}$$

$$J^{(-)}_\alpha(x) = \bar e(x)\gamma_\alpha(1-\gamma_5)\nu_e(x)\,, \tag{14.47}$$

$$\begin{aligned}J^{(N)}_\alpha(x) &= \bar\nu_e(x)\gamma_\alpha(1-\gamma_5)\nu_e(x) \\ &- \bar e(x)[\gamma_\alpha(1-\gamma_5) - 4\sin^2\theta_W\gamma_\alpha]e(x) \\ &+ \bar p(x)[\gamma_\alpha(1-g^{(p)}_A\gamma_5) - 4\sin^2\theta_W\gamma_\alpha]p(x) \\ &- \bar n(x)\gamma_\alpha(1-g^{(n)}_A\gamma_5)n(x)\,,\end{aligned} \tag{14.48}$$

and $g^{(n,p)}_A$ are the axial couplings for neutrons and protons, respectively.

Let as focus first on the the effect of the charged current interactions. The effective CC Hamiltonian due to electrons in the medium is

$$H_C^{(e)} = \frac{G_F}{\sqrt{2}} \int d^3p_e f(E_e,T) \times \left\langle \langle e(s,p_e)\,|\,\bar{e}(x)\gamma^\alpha(1-\gamma_5)\nu_e(x)\bar{\nu}_e(x)\gamma_\alpha(1-\gamma_5)e(x)\,|\,e(s,p_e)\rangle \right\rangle$$
$$= \frac{G_F}{\sqrt{2}}\bar{\nu}_e(x)\gamma_\alpha(1-\gamma_5)\nu_e(x) \int d^3p_e f(E_e,T) \left\langle \langle e(s,p_e)\,|\,\bar{e}(x)\gamma_\alpha(1-\gamma_5)e(x)\,|\,e(s,p_e)\rangle \right\rangle . \tag{14.49}$$

In the above equation we denote by s the electron spin, and by p_e its momentum and $f(E_e,T)$, is the energy distribution function of the electrons in the medium which is assumed to be homogeneous and isotropic and is normalized as

$$\int d^3p_e f(E_e,T) = 1\,. \tag{14.50}$$

We denote by $\left\langle \ldots \right\rangle$ the averaging over electron spinors and summing over all electrons in the medium. Coherence dictates that s, p_e are the same for initial and final electrons. The axial current reduces to the spin in the non-relativistic limit and therefore averages to zero for a background of non-relativistic electrons. The spatial components of the vector current cancel because of isotropy. Therefore the only non trivial average is

$$\int d^3p_e f(E_e,T) \left\langle \langle e(s,p_e)\,|\,\bar{e}(x)\gamma_0 e(x)\,|\,e(s,p_e)\rangle \right\rangle = n_e(x)\,, \tag{14.51}$$

which gives a contribution to the effective Hamiltonian

$$H_C^{(e)} = \sqrt{2}G_F n_e \bar{\nu}_{eL}(x)\gamma_0\nu_{eL}(x)\,. \tag{14.52}$$

This can be interpreted as a contribution to the ν_{eL} potential energy

$$V_C = \sqrt{2}G_F n_e\,. \tag{14.53}$$

Should we have considered antineutrino states we would have ended up with $V_C = -\sqrt{2}G_F n_e$ For a more detailed derivation of the matter potentials see, for example, Ref. [3].

With an equivalent derivation we find that for ν_μ and ν_τ, the potential due to its CC interactions is zero for most media since neither μ's nor $\tau's$ are present, while the effective potential for any active neutrino due to the neutral current interactions is found to be

$$V_{NC} = \frac{\sqrt{2}}{2}G_F\left[-n_e(1-4\sin^2\theta_w) + n_p(1-4\sin^2\theta_w) - n_n\right]\,. \tag{14.54}$$

In neutral matter $n_e = n_p$ and the contribution from electrons and protons cancel each other. So we are left only with the neutron contribution

$$V_{NC} = -1/\sqrt{2}G_F n_n\,. \tag{14.55}$$

After including these effects, the evolution equation for n ultrarelativistic neutrinos propagating in matter written in the mass basis is (see for instance Ref. [27–29] for the derivation):

$$i\frac{d\vec{\nu}}{dx} = H\,\vec{\nu}, \qquad H = H_m + U^{\nu\,\dagger}\,V\,U^\nu\,. \tag{14.56}$$

Here $\vec{\nu} \equiv (\nu_1,\,\nu_2,\,\ldots,\,\nu_n)^T$, H_m is the the kinetic Hamiltonian,

$$H_m = \frac{1}{2E}\,\mathrm{diag}(m_1^2,\,m_2^2,\,\ldots,\,m_n^2), \tag{14.57}$$

and V is the effective neutrino potential in the interaction basis. U^ν is the $n\times n$ submatrix of the unitary V^ν matrix corresponding to the n ultrarelativistic neutrino states. For the three SM active neutrinos with purely SM interactions crossing a neutral medium with electrons, protons and neutrons, the evolution equation takes the form (14.56) with $U^\nu \equiv U$, and the effective potential:

$$V = \mathrm{diag}\left(\pm\sqrt{2}G_F n_e(x),\,0,\,0\right) \equiv \mathrm{diag}\,(V_e,\,0,\,0)\,. \tag{14.58}$$

The sign + (−) in Eq.(14.58) applies to neutrinos (antineutrinos), and $n_e(x)$ is the electron number density in the medium, which in general is not constant along the neutrino trajectory so the potential is not constant. Characteristic value of the potential at the Earth core is $V_e \sim 10^{-13}$ eV while at the solar core $V_e \sim 10^{-12}$ eV. Since the neutral current potential Eq.(14.55) is flavour diagonal, it can be eliminated from the evolution equation as it only contributes to an overall unobservable phase.

The instantaneous mass eigenstates in matter, ν_i^m, are the eigenstates of the Hamiltonian H in (14.56) for a fixed value of x, and they are related to the interaction basis by

$$\vec{\nu} = \tilde{U}(x)\nu^{\vec{m}}\,. \tag{14.59}$$

The corresponding instantaneous eigenvalues of H are $\mu_i(x)^2/(2E)$ with $\mu_i(x)$ being the instantaneous effective neutrino masses.

Let us take for simplicity a neutrino state which is an admixture of only two neutrino species $|\nu_\alpha\rangle$ and $|\nu_\beta\rangle$, so the two instantaneous mass eigenstates in matter ν_1^m and ν_2^m have instantaneous effective neutrino masses

$$\mu_{1,2}^2(x) = \frac{m_1^2+m_2^2}{2} + E[V_\alpha + V_\beta]$$
$$\mp\,\frac{1}{2}\sqrt{\left[\Delta m^2\cos 2\theta - A\right]^2 + \left[\Delta m^2\sin 2\theta\right]^2}\,, \tag{14.60}$$

and $\tilde{U}(x)$ is a 2x2 rotation matrix with the instantaneous mixing angle in matter given by

$$\tan 2\theta_m = \frac{\Delta m^2\sin 2\theta}{\Delta m^2\cos 2\theta - A}\,. \tag{14.61}$$

In the Eqs.(14.60) and (14.61) A is

$$A \equiv 2E(V_\alpha - V_\beta)\,, \tag{14.62}$$

and its sign depends on depends on the composition of the medium and on the flavour composition of the neutrino state considered. From the expressions above we see that for a given sign of A the mixing angle in matter is larger(smaller) than in vacuum if this last one is in the first (second) octant. We see that the symmetry about 45 degrees which existing in vacuum oscillations between two neutrino states is broken by the matter potential in propagation in a medium. The expressions above show that very important effects are present when A, is close to $\Delta m^2\cos 2\theta$. In particular, as seen in Eq.(14.61), the tangent of the mixing angle changes sign if, along its path, the neutrino passes by some matter density region satisfying, for its energy, the *resonance condition*

$$A_R = \Delta m^2\cos 2\theta\,. \tag{14.63}$$

This implies that if the neutrino is created in a region where the relevant potential satisfies $A_0 > A_R$ (A_0 here is the value of the relevant potential at the production point), then the effective mixing angle in matter at the production point is such that $\mathrm{sgn}(\cos 2\theta_{m,0}) = -\,\mathrm{sgn}(\cos 2\theta)$. So the flavour component of the mass eigenstates is inverted as compared to their composition in vacuum. In particular, if at production point we have $A_0 = 2A_R$, then $\theta_{m,0} = \frac{\pi}{2} - \theta$. Asymptotically, for $A_0 \gg A_R$, $\theta_{m,0} \to \frac{\pi}{2}$. In other words, if in vacuum the lightest (heaviest) mass eigenstate has a larger projection on the flavour α (β), inside a matter with density and composition such that $A > A_R$, the opposite holds. So if the neutrino system is travelling across a monotonically varying matter potential, the dominant flavour component of a given mass eigenstate changes when crossing the region with $A = A_R$. This phenomenon is known as *level crossing*.

Taking the derivative of Eq.(14.59) with respect to x and using Eq.(14.56), we find that in the instantaneous mass basis the evolution equation reads:

$$i\frac{d\vec{\nu}^m}{dx} = \\ = \left[\frac{1}{2E}\ \mathrm{diag}\left(\mu_1^2(x),\, \mu_2^2(x),\, \ldots,\, \mu_n^2(x)\right) - i\,\tilde{U}^\dagger(x)\,\frac{d\tilde{U}(x)}{dx}\right]\vec{\nu}^m\,. \tag{14.64}$$

The presence of the last term, Eq.(14.64) implies that this is a system of coupled equations. So in general, the instantaneous mass eigenstates, ν_i^m are not energy eigenstates. For constant or slowly enough varying matter potential this last term can be neglected and the instantaneous mass eigenstates, ν_i^m, behave approximately as energy eigenstates and they do not mix in the evolution. This is the *adiabatic* transition approximation. On the contrary, when the last term in Eq.(14.64) cannot be neglected, the instantaneous mass eigenstates mix along the neutrino path. This implies there can be *level-jumping* [30–33] and the evolution is *non-adiabatic*.

For adiabatic evolution in matter the oscillation probability take a form very similar to the vacuum oscillation expression, Eq.(14.39). For example, neglecting CP violation:

$$P_{\alpha\beta} = \left|\sum_i \tilde{U}_{\alpha i}(0)\tilde{U}_{\beta i}(L)\exp\left(-\frac{i}{2E}\int_0^L \mu_i^2(x')dx'\right)\right|^2 . \tag{14.65}$$

To compute $P_{\alpha\beta}$ in a varying potential one can always solve the evolution equation numerically. Also several analytic approximations for specific profiles of the matter potential can be found in the literature [34].

14.5.1 *The Mihheev-Smirnov-Wolfenstein Effect for Solar Neutrinos*

The matter effects discussed in the previous section are of special relevance for solar neutrinos. As the Sun produces ν_e's in its core, here we shall consider the propagation of a $\nu_e - \nu_X$ neutrino system (X is some superposition of μ and τ, which is arbitrary because ν_μ and ν_τ have only and equal neutral current interactions) in the matter density of the Sun.

The density of solar matter is a monotonically decreasing function of the distance R from the center of the Sun, and it can be approximated by an exponential for $R < 0.9R_\odot$

$$n_e(R) = n_e(0)\exp\left(-R/r_0\right)\ , \tag{14.66}$$

with $r_0 = R_\odot/10.54 = 6.6\times10^7$ m $= 3.3\times10^{14}$ eV^{-1}.

As mentioned above, the nuclear reactions in the Sun produce electron neutrinos. After crossing the Sun, the composition of the neutrino state exiting the Sun will depend on the relative size of $\Delta m^2\cos2\theta$ versus $A_0 = 2\,E\,G_F\,n_{e,0}$ (here 0 refers to the neutrino production point which is near but no exactly at the center of the Sun, $R = 0$).

If the relevant matter potential at production is well below the resonant value, $A_R = \Delta m^2\cos2\theta \gg A_0$, matter effects are negligible. With the characteristic matter density and energy of the solar neutrinos, this condition is fulfilled for values of Δm^2 such that $\Delta m^2/E \gg L_{\mathrm{Sun-Earth}}$. So the propagation occurs as in vacuum with the oscillating phase averaged to 1/2 and the survival probability at the exposed surface of the Earth is

$$P_{ee}(\Delta m^2\cos2\theta \gg A_0) = 1 - \frac{1}{2}\sin^2 2\theta > \frac{1}{2}\,. \tag{14.67}$$

If the relevant matter potential at production is only slightly below the resonant value, $A_R = \Delta m^2\cos2\theta \gtrsim A_0$, the neutrino does not cross a region with resonant density, but matter effects are sizable enough to modify the mixing. The oscillating phase is averaged in the propagation between the Sun and the Earth. This regime is well described by an adiabatic propagation, Eq.(14.65). Using that $\tilde{U}(0)$ is a 2x2 rotation of angle $\theta_{m,0}$ – the mixing angle in matter at the neutrino production point–, and $\tilde{U}(L)$ is the corresponding rotation with vacuum mixing angle θ, we get

$$P_{ee}(\Delta m^2\cos2\theta \geq A_0) = \cos^2\theta_{m,0}\cos^2\theta + \sin^2\theta_{m,0}\sin^2\theta \\ = \frac{1}{2}\left[1 + \cos2\theta_{m,0}\cos2\theta\right]\,. \tag{14.68}$$

This expression reflects that an electron neutrino produced at A_0 is an admixture of ν_1 with fraction $P_{e1,0} = \cos^2\theta_{m,0}$ and ν_2 with fraction $P_{e2,0} = \sin^2\theta_{m,0}$. On exiting the Sun, ν_1 consists of ν_e with fraction $P_{1e} = \cos^2\theta$, and ν_2 consists of ν_e with fraction $P_{2e} = \sin^2\theta$ so $P_{ee} = P_{e1,0}P_{1e} + P_{e2,0}P_{2e} = \cos^2\theta_{m,0}\cos^2\theta + \sin^2\theta_{m,0}\sin^2\theta$ [35–37], exactly as given in Eq.(14.68). Since $A_0 < A_R$ the resonance is not crossed so $\cos2\theta_{m,0}$ has the same sign as $\cos2\theta$ and still $P_{ee} \geq 1/2$.

Finally, in the case that $A_R = \Delta m^2\cos2\theta < A_0$, the neutrino can cross the resonance on its way out. In the convention of $\Delta m^2 > 0$ this occurs if $\cos2\theta > 0$ ($\theta < \pi/4$). which means that in vacuum ν_e is a combination of ν_1 and ν_2 with larger ν_1 component, while at the production point ν_e is a combination of ν_1^m and ν_2^m with larger ν_2^m component. In particular, if the density at the production point is much higher than the resonant density, $\Delta m^2\cos2\theta \ll A_0$,

$$\theta_{m,0} = \frac{\pi}{2} \quad\Rightarrow\quad \cos2\theta_{m,0} = -1\,, \tag{14.69}$$

and the produced ν_e is purely ν_2^m.

In this regime, the evolution of the neutrino ensemble can be adiabatic or non-adiabatic depending on the particular values of Δm^2 and the mixing angle. The oscillation parameters (see Secs.14.6.1 and 14.7) happen to be such that the transition is adiabatic in all ranges of solar neutrino energies. Thus the survival probability at the exposed surface of the Earth is given by Eq.(14.68) but now with mixing angle (14.69) so

$$P_{ee}(\Delta m^2\cos2\theta < A_0) = \frac{1}{2}\left[1 + \cos2\theta_{m,0}\cos2\theta\right] = \sin^2\theta\,. \tag{14.70}$$

So in this case P_{ee} can be much smaller than 1/2 because $\cos2\theta_{m,0}$ and $\cos2\theta$ have opposite signs. This is referred to as the Mihheev-Smirnov-Wolfenstein (MSW) effect [26, 38] which plays a fundamental role in the interpretation of the solar neutrino data.

The resulting energy dependence of the survival probability of solar neutrinos is shown in Fig.14.3 (together with a compilation of data from solar experiments). The plotted curve corresponds to $\Delta m^2 \sim 7.5\times10^{-5}$ eV^2 and $\sin^2\theta \sim 0.3$ (the so-called large mixing angle, LMA, solution). The figure illustrates the regimes described above. For these values of the oscillation parameters, neutrinos with $E \ll 1$ MeV are in the regime with $\Delta m^2\cos2\theta \gg A_0$ so the curve represents the value of vacuum averaged survival probability, Eq.(14.67), and therefore $P_{ee} > 0.5$. For $E > 10$ MeV, on the contrary, $\Delta m^2\cos2\theta \ll A_0$ and the survival probability is given by Eq.(14.70), so $P_{ee} = \sin^2\theta \sim 0.3$. In between, the survival probability is given by Eq.(14.68) with θ_0 changing rapidly from its vacuum value to the asymptotic matter value (14.69), 90°.

14.6 Experimental Study of Neutrino Oscillations

Neutrino flavour transitions, or neutrino oscillations, have been experimentally studied using various neutrino sources and detection techniques. Intense sources and large detectors are mandatory because of a large distance necessary for observable oscillation effects in addition to the small cross sections. Also, the relevant neutrino flux before oscillations should be known with sufficient precision for a definitive measurement. Here, the experimental status of neutrino oscillations with the different neutrino sources, the Sun, Earth's atmosphere, accelerators and nuclear reactors, are reviewed.

14.6.1 *Solar Neutrinos*

14.6.1.1 *Solar neutrino flux*

In the Sun, electron neutrinos are produced in the thermonuclear reactions which generate the solar energy. These reac-

tions occur via two main chains, the *pp* chain and the CNO cycle. The *pp* chain includes reactions $p + p \rightarrow d + e^+ + \nu$ (*pp*), $p + e^- + p \rightarrow d + \nu$ (*pep*), $^3\mathrm{He} + p \rightarrow {}^4\mathrm{He} + e^+ + \nu$ (*hep*), $^7\mathrm{Be} + e^- \rightarrow {}^7\mathrm{Li} + \nu(+\gamma)$ (^{7}Be), and $^8\mathrm{B} \rightarrow {}^8\mathrm{Be}^* + e^+ + \nu$ (^{8}B). The CNO cycle involves $^{13}\mathrm{N} \rightarrow {}^{13}\mathrm{C} + e^+ + \nu$ (^{13}N), $^{15}\mathrm{O} \rightarrow {}^{15}\mathrm{N} + e^+ + \nu$ (^{15}O), and $^{17}\mathrm{F} \rightarrow {}^{17}\mathrm{O} + e^+ + \nu$ (^{17}F). Those reactions result in the overall fusion of protons into ^{4}He, $4p \rightarrow {}^4\mathrm{He} + 2e^+ + 2\nu_e$, where the energy released in the reaction, $Q = 4m_p - m_{^4\mathrm{He}} - 2m_e \sim 26$ MeV, is mostly radiated through the photons and only a small fraction is carried by the neutrinos, $\langle E_{2\nu_e} \rangle = 0.59$ MeV. In addition, electron capture on ^{13}N, ^{15}O, and ^{17}F produces line spectra of neutrinos called ecCNO neutrinos. Dividing the solar luminosity by the energy released per neutrino production, the total neutrino flux can be estimated. At the Earth, the *pp* solar neutrino flux is about 6×10^{10} cm^{-2}s^{-1}.

The detailed calculation of the solar neutrino fluxes has been done based on the Standard Solar Model (SSM). The SSM describes the structure and evolution of the Sun based on a variety of inputs such as the mass, luminosity, radius, surface temperature, age, and surface elemental abundances. In addition, the knowledge of the absolute nuclear reaction cross sections for the relevant fusion reactions and the radiative opacities are necessary. John Bahcall and his collaborators continuously updated the SSM calculations over several decades [39, 40]. Figure 14.1 shows the solar neutrino fluxes predicted by the SSM calculation in [41] and ecCNO neutrinos in [42].

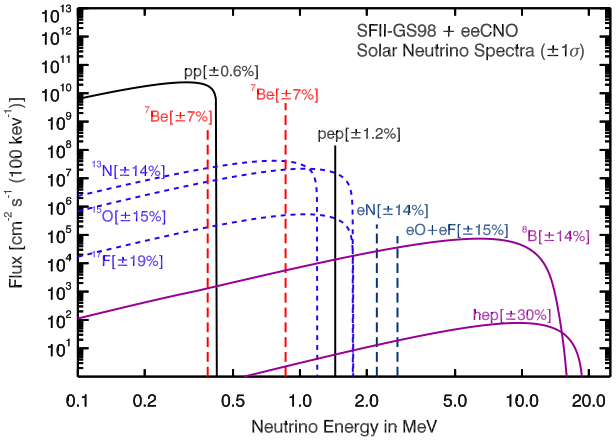

Figure 14.1: Spectrum of solar neutrino fluxes predicted by SSM calculation in [41]. In addition to standard fluxes, ecCNO neutrinos have been added based on [42]. Electron capture fluxes are given in cm^{-2}s^{-1}. Taken from [43]

14.6.1.2 *Detection of solar neutrinos and the solar neutrino problem*

Experiments which observed solar neutrinos are summarized in Table 14.2.

A pioneering solar neutrino experiment was carried out by R. Davis, Jr. and collaborators at Homestake starting in the late 1960s [44]. The Davis' experiment utilizes the reaction $\nu_e + {}^{37}\mathrm{Cl} \rightarrow e^- + {}^{37}\mathrm{Ar}$. Because this process has an energy threshold of 814 keV, the most relevant fluxes are the ^{7}Be and ^{8}B neutrinos. The detector contained ~ 615 t of C_2Cl_4. The produced ^{37}Ar, which has a half life of 34.8 d, was chemically extracted and introduced into a low-background proportional chamber every few months. The Auger electrons from electron capture of ^{37}Ar were counted to determine the reaction rate.

From the beginning, the observed number of neutrinos in the Homestake mine experiment was significantly smaller than the prediction by SSM — it was almost one third. After thorough check of both experimental and theoretical work, the discrepancy remained. This became to be known as the solar neutrino problem. The final result from Homestake experiment is $2.56 \pm 0.16 \pm 0.16$ SNU [45], where SNU (solar neutrino unit) is a unit of event rate, 1 SNU $= 10^{-36}$ captures/(s atom). On the other hand, prediction based on SSM is $8.46^{+0.87}_{-0.88}$ SNU [46].

The detection of neutrinos from other production processes was recognized as an important input to investigate the origin of the solar neutrino problem. In particular, the *pp* neutrino is most abundant, and its flux prediction has the smallest uncertainty. Using the radiochemical technique with gallium, the reaction $\nu_e + {}^{71}\mathrm{Ga} \rightarrow e^- + {}^{71}\mathrm{Ge}$ has an energy threshold of 233 keV and can be used for the *pp* neutrino detection. According to the SSM, more than a half of the events on ^{71}Ga are due to the *pp* neutrinos, with the second dominant contribution coming from the ^{7}Be neutrinos. ^{71}Ge decays via electron capture with a half life of 11.4 d. The SAGE experiment in Baksan [47] used about 50 t of liquid metallic gallium as a target. The GALLEX experiment in LNGS [48] used 101 t of $GaCl_3$, containing 30.3 t of gallium. Both experiments used natural gallium, containing 39.9% of ^{71}Ga isotope. GALLEX was followed by its successor GNO experiment. The measured capture rate is $69.3 \pm 4.1 \pm 3.6$ SNU for GALLEX+GNO [49] and $65.4^{+3.1+2.6}_{-3.0-2.8}$ SNU for SAGE [50]. A SSM prediction is $127.9^{+8.1}_{-8.2}$ SNU [46].

The radiochemical detectors measure the reaction rate integrated between extractions. The real time measurement of solar neutrino was realized by the Kamiokande experiment [51]. The Kamiokande detector was a 3,000-t water-Cherenkov detector in the Kamioka mine. An array of 50 cm diameter PMTs were attached onto the inner wall of the detector to detect Cherenkov light. Although the original purpose of the Kamiokande detector was search for nucleon decays, with an upgrade of detector Kamiokande-II achieved an energy threshold sufficiently low to allow for the observation of solar neutrinos using ν-*e* elastic scattering (ES), $\nu_x + e^- \rightarrow \nu_x + e^-$. The signal and background from radioactivity can be statistically separated by using the directional correlation between the incoming neutrino and the recoil electron. The Super-Kamiokande, the successor of Kamiokande, started operation in April 1996. It is a large upright cylindrical water Cherenkov detectorcontaining 50 kt of pure water. An inner detector volume corresponding to 32 kt water mass is viewed by more than 11,000 inward-facing 50 cm diameter PMTs.

The ES reaction occurs via both charged and neutral current interactions. Consequently, it is sensitive to all active neutrino flavours, although the cross section for ν_e, which is the only flavour to interact via charged current, is about six times larger than that for ν_μ or ν_τ. Because the energy threshold is 6.5 MeV for Kamiokande and 3.5 MeV for the present Super-Kamiokande (for the kinetic energy of recoil electron), these experiments are sensitive to primarily to ^{8}B neutrinos.

The results from Kamiokande [52, 53] and Super-Kamiokande [54, 55] showed significantly smaller numbers of observed solar neutrinos compared to the prediction. The latest ^{8}B neutrino flux measured by Super-Kamiokainde is $(2.345 \pm 0.014 \pm 0.036) \times 10^6$ cm^{-2}s^{-1} [56], while a prediction based on the SSM is $(5.46 \pm 0.66) \times 10^6$ cm^{-2}s^{-1} [57]. In addition, no significant zenith angle variation nor spectrum distortion were observed in the initial phase of Super-Kamiokande, which placed strong constraints on the solution of the solar neutrino problem [58, 59].

14.6.1.3 *Solution of the solar neutrino problem*

SNO experiment in Canada used 1,000 t of heavy water (D_2O) contained in a spherical acrylic vessel which was surrounded by an H_2O shield. An array of PMTs installed on a stainless steel structure detected Cherenkov radiation produced in both the D_2O and H_2O. The SNO detector observed ^{8}B neutrinos via three different reactions. In addition to the ES scattering with an electron, with D_2O target the charged current (CC) $\nu_e + d \rightarrow e^- + p + p$ and the neutral current (NC) $\nu_x + d \rightarrow \nu_x + p + n$ interactions are possible. The CC reaction is sensitive to only ν_e, while NC reaction is sensitive to all active flavours of neutrinos with equal cross sections. Therefore, by comparing the measurements of different reactions, SNO could provide a model independent test of the neutrino flavour change.

In 2001, SNO reported the initial result of CC measurement [62]. Combined with the high statistics measurement of ν-*e* elastic scattering from Super-Kamiokande [58], it provided a direct evidence for existence of non-ν_e component in solar neutrino flux. The result of NC measurement in 2002 [63] established it

Table 14.2: List of solar neutrino experiments

Name	Target material	Energy threshold (MeV)	Mass (ton)	Years
Homestake	C_2Cl_4	0.814	615	1970–1994
SAGE	Ga	0.233	50	1989–
GALLEX	$GaCl_3$	0.233	100 [30.3 for Ga]	1991–1997
GNO	$GaCl_3$	0.233	100 [30.3 for Ga]	1998–2003
Kamiokande	H_2O	6.5	3,000	1987–1995
Super-Kamiokande	H_2O	3.5	50,000	1996–
SNO	D_2O	3.5	1,000	1999–2006
KamLAND	Liquid scintillator	0.5/5.5	1,000	2001–2007
Borexino	Liquid scintillator	0.19	300	2007–

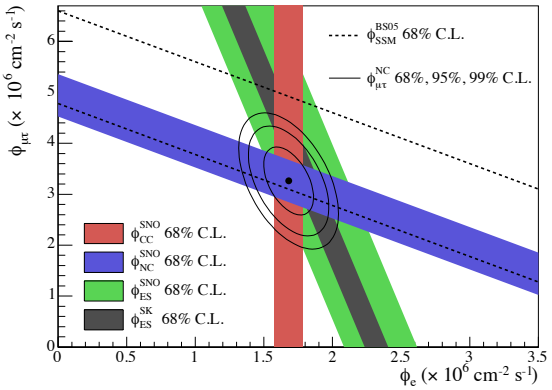

Figure 14.2: Fluxes of ^{8}B solar neutrinos, $\phi(\nu_e)$, and $\phi(\nu_{\mu,\tau})$, deduced from the SNO's CC, ES, and NC results [60]. The Super-Kamiokande ES flux is from [61]. The BS05(OP) standard solar model prediction [40] is also shown. The bands represent the 1σ error. The contours show the 68%, 95%, and 99% joint probability for $\phi(\nu_e)$ and $\phi(\nu_{\mu,\tau})$. The figure is from [60].

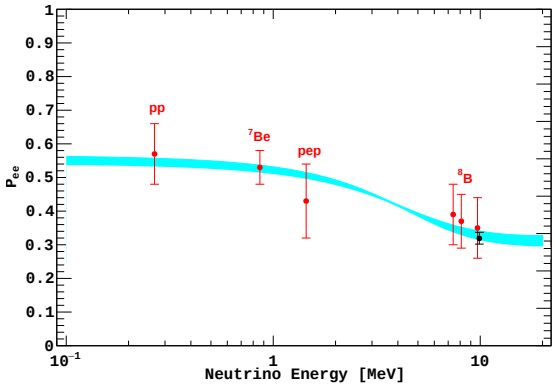

Figure 14.3: Electron neutrino survival probability as a function of neutrino energy. The points represent, from left to right, the Borexino pp, ^{7}Be, pep, and ^{8}B data (red points) and the SNO+SK ^{8}B data (black point). The three Borexino ^{8}B data points correspond, from left to right, to the low-energy (LE) range, LE+HE range, and the high-energy (HE) range. The electron neutrino survival probabilities from experimental points are determined using a high metallicity SSM from Ref. [57]. The error bars represent the $\pm1\sigma$ experimental + theoretical uncertainties. The curve corresponds to the $\pm1\sigma$ prediction of the MSW-LMA solution using the parameter values given in [65]. This figure is provided by A. Ianni.

with 5.3σ of statistical significance. Figure 14.2 shows the fluxes of electron neutrinos ($\phi(\nu_e)$) and muon and tau neutrinos ($\phi(\nu_{\mu,\tau})$) with the 68%, 95%, and 99% joint probability contours, obtained with the SNO data. Finally, together with the reactor neutrino experiment KamLAND (see Sec.14.6.4), the solution of solar neutrino problem was found to be the MSW adiabatic flavour transitions in the solar matter, the so-called large mixing angle (LMA) solution, with parameters $\Delta m^2 \sim 7.5\times10^{-5}$ eV^2 and $\sin^2\theta \sim 0.3$.

From a combined result of three phases of SNO [64], the total flux of ^{8}B solar neutrino is found to be $(5.25\pm0.16^{+0.11}_{-0.13})$ cm^{-2}s^{-1}, consistent with the SSM prediction. This consistency is one of major accomplishments of SSM.

In order to understand the SSM as well as to study the MSW effect for the solar neutrino, measurements of solar neutrinos other than ^{8}B are important. The Borexino experiment at Gran Sasso, Italy, detects solar neutrino via ν-e scattering in real time with a low energy threshold. The Borexino detector consists of 300 t of ultra-pure liquid scintillator, which achieved 0.19 MeV of energy threshold and 5% energy resolution at 1 MeV. Borexino reported the first real time detection of ^{7}Be solar neutrinos [66]. They also measured the fluxes of *pep* [67] and *pp* neutrino [68] for the first time. Together with ^{8}B [69] neutrino measurement, Borexino provides important data to study the MSW effect. The KamLAND experiment also measured ^{8}B [70] and ^{7}Be [71] solar neutrinos. Figure 14.3 shows the survival probability of solar ν_e as a function of neutrino energy. The data points are from the Borexino results [72, 73] except the SNO+SK ^{8}B data. The theoretical curve shows the prediction of the MSW-LMA solution. All the data shown in this plot are consistent with the theoretically calculated curve. This indicates that these solar neutrino measurements are consistent with the MSW-LMA solution of the solar neutrino problem.

The matter effects can also be relevant to the propagation of solar neutrinos through the Earth. Because solar neutrinos go through the Earth before interaction in the detector during the nighttime, a comparison of measured event rate between daytime and nighttime provides a clean and direct test of matter effects on neutrino oscillations. Super-Kamiokande reported the first indication of the day/night asymmetry in ^{8}B solar neutrinos [74]. The measured asymmetry, defined as the difference of the average day rate and average night rate divided by the average of those two rates, is $(-3.2 \pm 1.1 \pm 0.5)\%$, corresponding to a statistical significance of 2.7σ. The measured value of the asymmetry is consistent with the LMA solution.

14.6.2 *Atmospheric Neutrinos*

14.6.2.1 *Atmospheric neutrino flux*

Atmospheric neutrinos are produced by the decays of pions and kaons generated in the interaction of cosmic rays and nucleons in the Earth's atmosphere. They have a broad range of energy (∼0.1 GeV to >TeV) and long travel distances before detection (∼10 to 1.3×10^4 km). As shown in Table 14.1, atmospheric neutrino oscillation experiments are most sensitive to flavour oscillations with $\Delta m^2 \sim 10^{-1}$ to 10^{-4} eV^2.

Considering their dominant production modes, some generic relations for flux ratios of different flavour of neutrinos can be derived without detailed calculations. From the decay chain of a charged pion $\pi^+ \to \mu^+\nu_\mu$ followed by $\mu^+ \to e^+\nu_e\bar{\nu}_\mu$ (and the charge conjugate for π^-), the ratio $(\nu_\mu+\bar{\nu}_\mu)/(\nu_e+\bar{\nu}_e)$ is expected to be around 2 at low energies (∼ 1 GeV) where most muons decay in the atmosphere. For higher energies, some of muons reach the Earth before they decay and the ratio increases. One can also expect that the zenith angle distributions of atmospheric neutrinos are symmetric between upward-going and downward-going

neutrinos. It is true for the energy above 1 GeV, but at lower energies, the Earth's geomagnetic field induces up-down asymmetries in the the primary cosmic ray. The zenith angle corresponds to the flight length of atmospheric neutrinos. Vertically upward-going neutrinos come from the other side of the Earth with flight lengths of $\sim 10^4$ km, while downward-going neutrinos produced just above the experimental site travel ∼10 km before detection.

The atmospheric neutrino fluxes are calculated in detail based on the energy spectrum and composition of primary cosmic rays and their hadronic interactions in the atmosphere. The effects of solar activity and geomagnetic field should be also taken into account. Results of calculations by several groups are available [75–78]. A typical uncertainty of the absolute flux is 10–20%, while the ratio of fluxes between different flavour has much smaller uncertainty (< 5%).

14.6.2.2 *Observation of atmospheric neutrino oscillations*

The first detection of atmospheric neutrinos was reported in the 1960's by the underground experiments in the Kolar Gold Field experiment in India [79] and in South Africa [80]. In the 1980's, experiments searching for nucleon decays started operation. They used large underground detectors which could also observe atmospheric neutrinos. In these experiments, atmospheric neutrinos were studied as backgrounds to nucleon decays. Among the early experiments were Kamiokande [81] and IMB [82] using water Cherenkov detectors, and Frejus [83] and NUSEX [84] using iron tracking calorimeters.

The flavour of atmospheric neutrino can be identified in charged current interaction with nuclei, which produces the corresponding charged lepton. In order to study the neutrino oscillations, the identification of charged lepton is essential. Those detectors originally designed for nucleon decay search had capability to distinguish muons and electrons. For example, a water Cherenkov detector can utilize the information from Cherenkov ring patterns for particle identification; e-like particles ($e^{\pm}$, γ) produce more diffuse ring than μ-like particles ($\mu^{\pm}$, $\pi^{\pm}$) because of electromagnetic cascades and multiple Coulomb scattering effects.

To reduce the uncertainty, in early results the flux ratio $\nu_\mu/\nu_e \equiv (\nu_\mu + \bar{\nu}_\mu)/(\nu_e + \bar{\nu}_e)$ was measured, and the double ratio between observation and expectation $(\nu_\mu/\nu_e)_{\rm obs}/(\nu_\mu/\nu_e)_{\rm exp}$ was reported. The Kamiokande experiment reported an indication of a deficit of $(\nu_\mu + \bar{\nu}_\mu)$ flux [81]. IMB also observed similar deficit [82], but measurements by Frejus [83] and NUSEX [84] were consistent with the expectations. This was the original formulation of the atmospheric neutrino anomaly. Kamiokande reported studies with an increased data set of the sub-GeV (< 1.33 GeV) [85] as well as the multi-GeV (> 1.33 GeV) [86] samples. In the latter, they reported an analysis of zenith angle distributions, which showed an indication that the muon disappearance probability is dependent on the zenith angle, hence the travel length of neutrinos. However, the statistical significance was not sufficient to provide a conclusive interpretation.

The solution to the atmospheric neutrino anomaly was brought by Super-Kamiokande, which reported compelling evidence for neutrino oscillations in atmospheric neutrinos in 1998 [87]. The zenith angle (θ_z, with $\theta_z = 0$ for vertically downward-going) distributions of μ-like events showed a clear deficit of upward-going events, while no significant asymmetry was observed for e-like events. The asymmetry is defined as $A = (U-D)/(U+D)$, where U is the number of upward-going ($-1 < \cos\theta_z < -0.2$) events and D is the number of downward-going ($0.2 < \cos\theta_z < 1.0$) events. With multi-GeV (visible energy > 1.33 GeV) μ-like events alone, the measured asymmetry was $A = -0.296 \pm 0.048 \pm 0.001$, deviating from zero by more than 6σ. The sub-GeV (< 1.33 GeV) μ-like, upward through going, and upward stopping μ samples, which correspond to different energy range of neutrino, show the consistent behaviour, strengthening the credibility of the observation. The corresponding oscillation parameters were found to be $\Delta m^2 \sim 2.5 \times 10^{-3}$ eV^2 and $\theta \sim 45°$. Super-Kamiokande's results were confirmed by other atmospheric neutrino observations MACRO [88] and Soudan2 [89].

Although the energy and zenith-angle dependent muon neutrino disappearance observed with atmospheric neutrinos could be consistently explained by the neutrino oscillations between ν_μ and ν_τ, other exotic explanations such as neutrino decay or decoherence were not initially ruled out. By using a selected sample from Super-Kamiokande's atmospheric data with good L/E resolution, the L/E dependence of the survival probability was measured [90]. The observed dip in the L/E distribution was consistent with the expectation from neutrino oscillation, while alternative models were strongly disfavored.

As an experimental proof of ν_μ-ν_τ oscillation, appearance signal of ν_τ was searched for in the atmospheric neutrino data. Because of the high energy threshold (> 3.5 GeV) of ν_τ CC interaction and the short lifetime of τ lepton (0.3 ps), the identification of ν_τ appearance is experimentally very difficult. Super-Kamiokande reported evidence of tau neutrino appearance using atmospheric neutrino data with 4.6σ significance [91]. The definitive observation of ν_τ appearance was made by the long-baseline experiment, OPERA [92] (See Sec.14.6.3.3), and recently IceCube also reported the ν_τ appearance analysis [93] using atmospheric neutrinos.

14.6.2.3 *Neutrino oscillation measurements using atmospheric neutrinos*

Figure 14.4 shows the zenith angle distributions of atmospheric neutrino data from Super-Kamiokande. For wide range of neutrino energy and path length, the observed distributions are consistent with the expectation from neutrino oscillation. Atmospheric neutrinos in the energy region of a few to ∼10 GeV provide information for the determination of the neutrino mass ordering [94].

The neutrino telescopes primarily built for the high energy neutrino astronomy such as ANTARES [95] and IceCube [96] can also measure neutrino oscillations with atmospheric neutrinos. ANTARES consists of a sparse array of PMTs deployed under the Mediterranean Sea at a depth of about 2.5 km to to instrument a 10^5 m^3 volume. IceCube is a detector deployed in ice in Antarctica at the South Pole, at depth between 1.45 and 2.45 km. In the bottom center of IceCube there is a region of $\sim 10^7$ m^3 volume with denser PMT spacing called DeepCore to extend the observable energies to lower energy region. By observing the charged current interaction of up-going ν_μ, they measure the ν_μ disappearance. ANTARES reported a measurement of ν_μ disappearance with 20 GeV threshold [97]. With analysis of events with 6–56 GeV energy range, the results on ν_μ disappearance measurements from IceCube DeepCore [98] provided a precision comparable to the measurements by Super-Kamiokande and long-baseline experiments.

There are several projects for atmospheric neutrino observations either proposed or under preparation. The atmospheric neutrino observation program is included in the plans for future neutrino telescopes, ORCA in the second phase of KM3NeT project [99] in the Mediterranean Sea, and PINGU in the upgrade of IceCube [100]. In India, a 50 kt magnetized iron tracking calorimeter ICAL is planned at the INO [101]. Future large underground detectors, Hyper-Kamiokande in Japan [102] and DUNE in US [103] can also study the atmospheric neutrinos.

14.6.3 *Accelerator Neutrinos*

14.6.3.1 *Accelerator neutrino beams*

A comprehensive description of the accelerator neutrino beams is found in [104]. Conventional neutrino beams from accelerators are produced by colliding high energy protons onto a target, producing π and K which then decay into neutrinos, and stopping undecayed mesons and muons in the beam dump and soil. Because pions are the most abundant product in the high energy collisions, a conventional neutrino beam contains dominantly muon-type neutrinos (or antineutrinos).

Focusing devices called magnetic horns are used to concentrate the neutrino beam flux towards the desired direction. A magnetic horn is a pulsed electromagnet with toroidal magnetic fields to focus charged particles that are parents of neutrinos. One can choose the dominant component of the beam to be either neutrinos or antineutrinos by selecting the direction of current in the magnetic horns. Even with the focusing with horns, *wrong sign* neutrinos contaminate in the beam. Also, there is small amount of contamination of ν_e and $\bar{\nu}_e$ coming primarily from kaon and

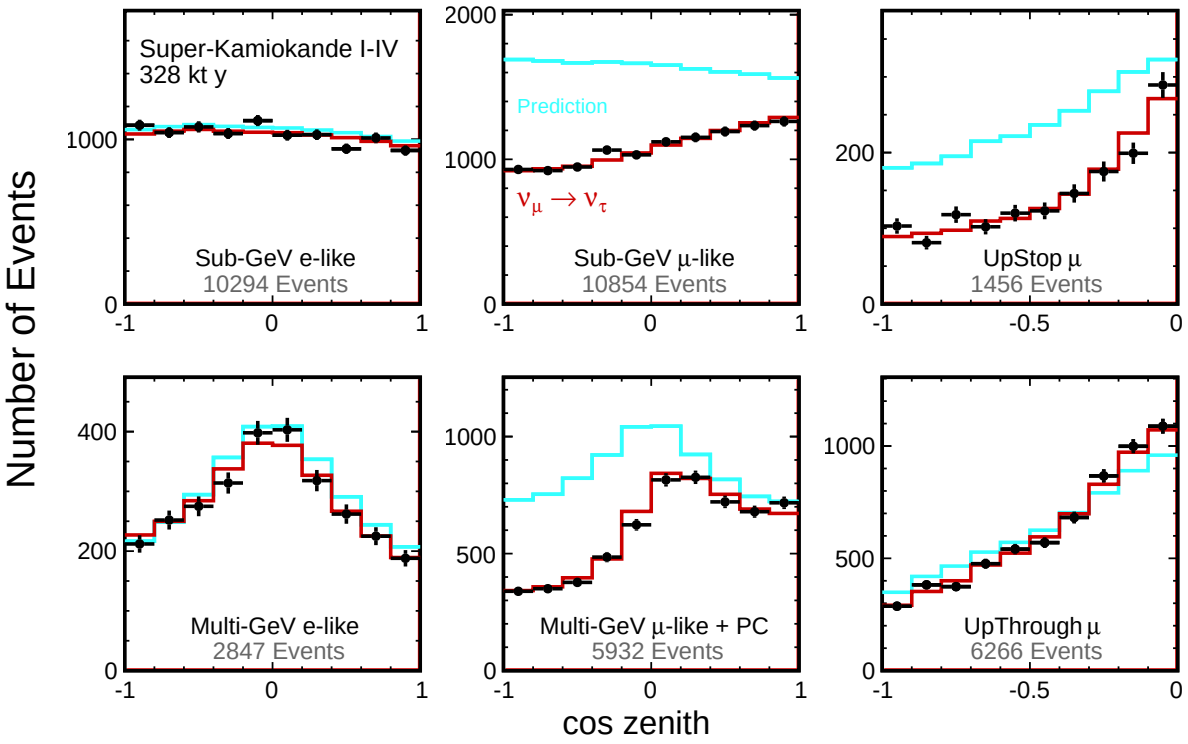

Figure 14.4: The zenith angle distributions of Super-Kamiokande atmospheric neutrino events. Fully contained 1-ring e-like and μ-like events with visible energy < 1.33 GeV (sub-GeV) and > 1.33 GeV (multi-GeV), as well as upward stopping and upward stopping μ samples are shown. Partially contained (PC) events are combined with multi-GeV μ-like events. The blue histograms show the non-oscillated Monte Carlo events, and the red histograms show the best-fit expectations for ν_μ-ν_τ oscillations. (This figure is provided by the Super-Kamiokande Collaboration)

Table 14.3: List of long-baseline neutrino oscillation experiments

Name	Beamline	Far Detector	L (km)	E_ν (GeV)	Year
K2K	KEK-PS	Water Cherenkov	250	1.3	1999–2004
MINOS	NuMI	Iron-scintillator	735	3	2005–2013
MINOS+	NuMI	Iron-scintillator	735	7	2013–2016
OPERA	CNGS	Emulsion	730	17	2008–2012
ICARUS	CNGS	Liquid argon TPC	730	17	2010–2012
T2K	J-PARC	Water Cherenkov	295	0.6	2010–
NOvA	NuMI	Liquid scint. tracking calorimeter	810	2	2014–

muon decays.

In order to maximize the sensitivity of the experiment, the ratio of baseline and neutrino energy (L/E) should be chosen to match the oscillation effects to be studied. In addition to maximizing the flux of neutrinos with relevant energy, neutrinos with irrelevant energy that result in unwanted background process should be suppressed. The energy of neutrino from a pion decay is

$$E_\nu = \frac{[1-(m_\mu/m_\pi)^2]E_\pi}{1+\gamma^2\theta^2}, \qquad (14.71)$$

where E_ν and E_π are the energy of neutrino and pion, respectively, θ is the angle between the pion and neutrino direction, and $\gamma = E_\pi/m_\pi$. For $\theta = 0$, the energy of neutrino is linearly proportional to the energy of pion. In this case, a narrow band beam can be made by selecting the momentum of pions. On the other hand, for $\theta \neq 0$, the energy of neutrino is not strongly dependent on the parent energy for a wide range of pion energy, but dependent on the off-axis angle θ. Using this relation, a neutrino beam with narrow energy spectrum, around the energy determined by θ, can be produced. This off-axis beam method was first introduced for BNL E889 proposal [105] and adopted in T2K and NOvA experiments. For a list of neutrino beamlines, see also the review 32. Neutrino Beam Lines at High-Energy Proton Synchrotrons.

As indicated in Table 14.1, there are two different scales of baselines for accelerator-based experiments to study different ranges of Δm^2. The atmospheric mass splitting $\Delta m^2 \sim 2.5 \times 10^{-3}$ eV^2 gives rise to the first oscillation maximum at $L/E \sim 500$ GeV/km. In order to study this parameter region with ~ 1 GeV accelerator neutrino beam, a long baseline of a few hundreds to thousand km is necessary. On the other hand, there have been reports of possible neutrino oscillations at ~ 1 eV scale, which can be studied at ~ 1 km baseline with neutrinos from accelerators. These experiments are called short-baseline oscillation experiments.

The flux of a neutrino beam is calculated using Monte Carlo simulation based on the configuration of the beamline. An important ingredient of the neutrino flux prediction is the hadron production cross section. Data from dedicated hadron production experiments [106–108] are used to tune the beam simulation and constrain the uncertainty. The uncertainty of predicted neutrino flux for the most relevant energy region is ∼5–10% with the latest hadron production data.

14.6.3.2 *Near detectors and neutrino interaction cross sections*

Many long-baseline experiments use two detectors to reduce the systematic uncertainties arising from neutrino flux and neutrino-nucleus interactions. The near detectors either use the same technology as the far detector or consist of sub-detectors with complementary functions to obtain detailed information of the neutrino beam and interactions. The near detectors provide information

for the neutrino flux, energy spectrum, and the interaction cross sections, which is used as an input to make predictions of observables at the far detector. However, even with the two-detector configuration, one should note that the neutrino flux is inevitably different between the near and the far detectors. In addition to the fact that the neutrino source looks like a line source for the near detector while it looks as a point source for the far detector, the neutrino oscillations alter the flavour composition of the neutrino beam quite significantly, as the design of a neutrino oscillation experiment requires.

For the precision measurements of neutrino oscillations with long-baseline experiments, the understanding of the neutrino-nucleus interaction becomes crucial. Because heavy nuclei are used as the interaction target, the nuclear effects complicate the understanding of the neutrino-nucleus interaction. For more information on the neutrino cross sections, see also the review 50. Neutrino Cross Section Measurements.

14.6.3.3 *Long-baseline experiments*

The first long-baseline experiment was the K2K experiment which used a neutrino beam from the KEK 12 GeV proton synchrotron directed towards Super-Kamiokande with a baseline of 250 km [109]. The beam had an average energy of 1.3 GeV. The K2K near detectors, located 300 m downstream of the production target, consisted of a combination of a 1 kt water Cherenkov detector and a set of fine grained detectors. K2K reported the confirmation of muon neutrino disappearance originally reported by Super-Kamiokande atmospheric neutrino observation [110].

The MINOS experiment used a beam from Fermilab and a detector in Soudan mine 735 km away [111]. The neutrino beam is produced in NuMI beamline [112] with 120 GeV proton beam from the Main Injector. The MINOS detectors are both iron-scintillator tracking calorimeters with toroidal magnetic fields. The far detector was 5.4 kt, while the near detector had a total mass of 0.98 kt and was located 1 km downstream of the production target. The NuMI beamline can vary the neutrino energy spectrum by changing the relative position of target and horns. Most of MINOS data were taken with the "low energy" configuration with the peak energy of around 3 GeV. MINOS combined accelerator and atmospheric neutrino data in both disappearance and appearance modes to measure oscillation parameters [113, 114]. Utilizing the separation of μ^- and μ^+ with the magnetic field in the far detector, MINOS also reported separate measurements of atmospheric neutrinos and antineutrinos [115].

When the NuMI beamline started operation for the NOvA experiment in 2013, it was set to the "medium energy" configuration which provided a beam with the peak neutrino energy of around 7 GeV to the MINOS+ experiment, which used the same MINOS near and far detectors. MINOS+ verified the energy dependence of ν_μ disappearance at energies above the first oscillation maximum. Utilizing the wide neutrino energy spectrum and high intensity in the medium energy configuration, limits on sterile neutrinos is reported [116].

In Europe, the CNGS neutrino beamline provided a beam with mean energy of 17 GeV from CERN to LNGS for long-baseline experiments with 732 km of baseline. The beam energy was chosen so that charged current (CC) interaction of ν_τ can occur for direct confirmation of ν_τ appearance. There was no near detector in CNGS because it was not necessary for the ν_τ appearance search. The OPERA experiment used a detector consisted of an emulsion/lead target with about 1.25 kt total mass complemented by electronic detectors. The excellent spatial resolution of emulsion enabled the event-by-event identification of τ leptons. OPERA observed ten ν_τ CC candidate events with 2.0 ± 0.4 expected background [92] and confirmed $\nu_\mu \to \nu_\tau$ oscillation in appearance mode with a statistical significance of 6.1σ. Another neutrino experiment, ICARUS [117], which used 600 t liquid argon time projection chambers, was operated in Gran Sasso from 2010 to 2012.

The first generation of long-baseline experiments confirmed the existence of neutrino oscillation. The major initial goal of second generation experiments was the observation of $\nu_\mu \to \nu_e$ oscillation. Using this appearance mode, by comparison of neutrino and antineutrino oscillation probabilities, search for CP violation in the neutrino mixing becomes possible.

The T2K experiment started in 2010 using a newly constructed high-intensity proton synchrotron J-PARC and the Super-Kamiokande detector. It is the first long-baseline experiment to employ the off-axis neutrino beam. The off-axis angle of 2.5° was chosen to set the peak of neutrino energy spectrum at 0.6 GeV, matching the first maximum of oscillation probability at the 295 km baseline for $\Delta m^2 \sim 2.5 \times 10^{-3}$ eV^2. T2K employs a set of near detectors at about 280 m from the production target. The on-axis detector, called INGRID, is an array of iron-scintillator sandwich trackers to monitor the beam intensity, direction and profile. The off-axis detector ND280, consisting of several sub-detectors inside a magnet, is placed in the direction of far detector to measure the neutrino beam properties and to study neutrino interactions.

In 2011, T2K reported the first indication of $\nu_\mu \to \nu_e$ oscillation with a statistical significance of 2.5σ [118]. In the framework of 3ν mixing, it corresponds to detecting non-zero amplitude generated by the mixing angle θ_{13} (see Eq.14.33). Later $\nu_\mu \to \nu_e$ oscillation was established by T2K with more than 7σ in 2014 [119]. Figure 14.5 shows the reconstructed energy distributions from T2K, for neutrino and anti-neutrino beam mode and also for muon and electron candidates. The muon type events show clear deficit in both neutrino and antineutrino mode, consistent with the energy-dependent disappearance probability expected from neutrino oscillations. By a combined analysis of the neutrino and antineutrino data, T2K reported a hint of CP violation with more than 2σ [120, 121].

The NOvA experiment uses the NuMI beamline with an off-axis configuration. The 14 kt NOvA far detector is located near Ash River, Minnesota, 810 km away from the source. At 14.6 mrad off-axis from the central axis of the NuMI beam, the neutrino energy spectrum at the far detector has a peak around 2 GeV, corresponding to the first oscillation maximum at 810 km baseline. The near detector, located around 1 km from the source, has a functionally identical design to the far detector with a total active mass of 193 t. Both detectors are tracking calorimeters consisting of planes of polyvinyl chloride cells alternating in vertical and horizontal orientation filled with liquid scintillator.

The physics run of NOvA was started in 2014. Although the initial data indicated non-maximal mixing [122], later analysis with increased data and improved analysis resulted in the allowed region consistent with maximal mixing [123]. After confirmation of ν_e appearance from ν_μ beam [124, 125], NOvA started data taking with antineutrino beam in 2016. Using the antineutrino beam data, NOvA has sreported the observation of $\bar{\nu}_e$ appearance from $\bar{\nu}_\mu$ beam with 4.4σ significance [126]. Figure 14.6 shows the reconstructed neutrino energy distributions from NOvA. Some values of the CP-violating phase $\delta_{\rm CP}$ (see Eq.14.33) have been excluded for the inverted mass ordering ($m_3 < m_2 < m_1$, see Sec.14.7 for definitions), while no significant limit has been set for the case of normal mass ordering ($m_1 < m_2 < m_3$, see Sec.14.7 for definitions).

Two large-scale long-baseline experiments are under preparation or proposed in future. DUNE [103] will be a 1,300 km long-baseline experiment based in US. The DUNE far detector will consist of four modules of at least 10 kt fiducial mass liquid argon time projection chambers, located 1.5 km underground at the Sanford Underground Research Facility in South Dakota. The beamline for DUNE, 1.2 MW at start and upgradable to 2.4 MW, as well as the facility for near detectors will be newly constructed at Fermilab. In Japan, Hyper-Kamiokande [102] is proposed as the successor of the Super-Kamiokande detector. It will be a water Cherenkov detector with 260 (190) kt total (fiducial) mass. With upgrade of existing accelerator and beamline, J-PARC will provide a 1.3 MW neutrino beam to Hyper-Kamiokande. Both DUNE and Hyper-Kamiokande will have a rich physics program besides the long-baseline experiment, such as searches for nucleon decays and study of supernova neutrinos.

14.6.3.4 *Short-baseline experiments*

The LSND experiment searched for neutrino oscillation using neutrinos from stopped pions at Los Alamos. A 800 MeV linac was used to produce pions which stopped in the target. Most of

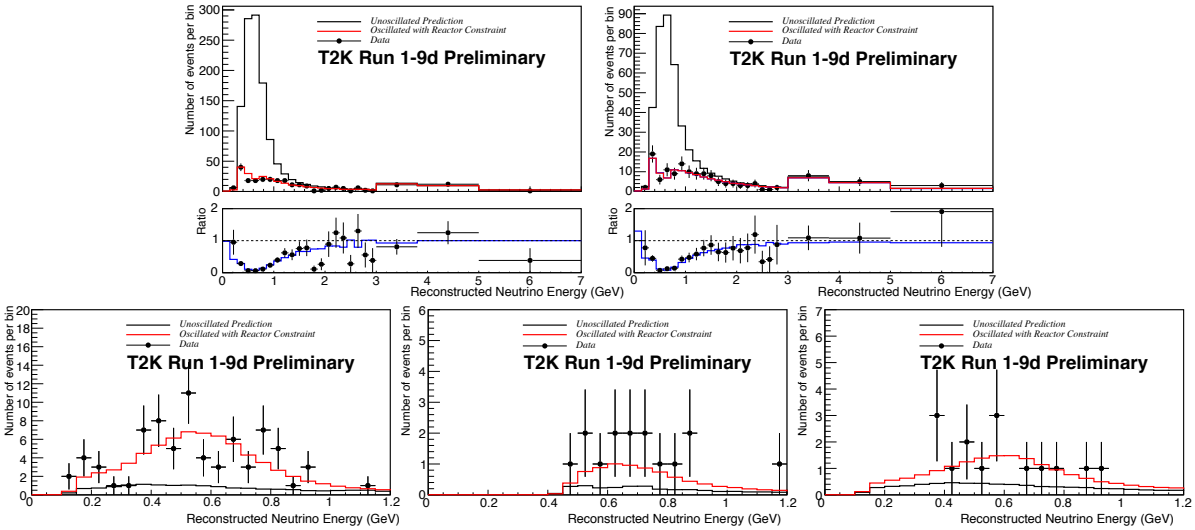

Figure 14.5: Reconstructed neutrino energy distributions from T2K. Data points with statistical error bars are shown together with the prediction without (black line) and including (red line) neutrino oscillation. Top: Single ring μ-like events. The left and right plot is for neutrino and antineutrino beam mode, respectively. Below each plot, the ratio to the prediction without oscillation is also shown. Bottom: Single ring e-like events. From left to right, 0 decay electron sample for neutrino beam, 1 decay electron sample for neutrino beam, and 0 decay electron sample for antineutrino beam. (This figure is provided by the T2K Collaboration)

π^-s are absorbed by the nuclei inside the target, while π^+s and their daughter μ^+s decay and produce neutrinos. Therefore, the produced neutrinos are mostly ν_μ, $\bar{\nu}_\mu$, and ν_e with very small contamination of $\bar{\nu}_e$. The detector was a tank filled with 167 t of diluted liquid scintillator, located about 30 m from the neutrino source. LSND searched for $\bar{\nu}_\mu \to \bar{\nu}_e$ appearance using the inverse beta decay process, $\bar{\nu}_e + p \to e^+ + n$, and found an excess of $87.9 \pm 22.4 \pm 6.0$ events over the expected background [127].

The KARMEN experiment was performed at the neutron spallation facility ISIS of the Rutherford Appleton Laboratory. The KARMEN 2 detector was a segmented liquid scintillation calorimeter with total volume of 65 m^3 located at a mean distance of 17.7 m from the ISIS target. KARMEN found a number of events consistent with the total background expectation, showing no signal for $\bar{\nu}_\mu \to \bar{\nu}_e$ oscillations [128]. The resulting limits exclude large regions of the parameter area favored by LSND.

The MiniBooNE experiment at Fermilab used a conventional neutrino beam to search for ν_e and $\bar{\nu}_e$ appearance in the same parameter region as LSND. The booster neutrino beamline (BNB) with a single magnetic horn uses a 8 GeV proton beam from the Fermilab booster to produce a neutrino (antineutrino) beam with energy spectrum peak of 600 (400) MeV. The MiniBooNE detector consists of a 12.2 m diameter sphere filled with 818 t of mineral and oil located 541 m from the target. MiniBooNE reported ν_e and $\bar{\nu}_e$ event excess in both neutrino and antineutrino running modes. In total, 460.5 ± 99.0 excess events are observed over the expected backgrounds, corresponding to 4.7σ significance [129].

Both LSND and MiniBooNE are single detector experiments. The reported excess will be further investigated with the multi-detector short-baseline neutrino (SBN) program at Fermilab BNB [130]. The SBN program comprises three liquid argon time projection chambers at different baselines in the same neutrino beamline. The 112 t Short-Baseline Near Detector will be located at 110 m from the target. The 85 t MicroBooNE detector has been operated at 470 m from the target. The ICARUS detector has been transported from Europe after refurbishment at CERN and is located at a baseline of 600 m.

JSNS^2 experiment at J-PARC will search for neutrino oscillations with $\Delta m^2 \sim 1$ eV^2 [131]. 1MW proton beam from the 3 GeV Rapid Cycling Synchrotron of J-PARC will produce neutrinos from muon decay at rest. With a detector filled with gadolinium loaded liquid scintillator of 17 t fiducial mass at 24 m from the target, JSNS^2 is aiming to provide a direct test of the LSND anomaly.

14.6.4 *Reactor Antineutrinos*

14.6.4.1 *Reactor antineutrino flux*

Nuclear reactors are very intense sources of $\bar{\nu}_e$'s in the MeV energy region, which are generated in nuclear fission of heavy isotopes (mainly ^{235}U, ^{238}U, ^{239}Pu, and ^{241}Pu). The $\bar{\nu}_e$ flux from a reactor can be estimated based on the thermal power output and fuel composition as a function of time. On average, about six $\bar{\nu}_e$'s are emitted and about 200 MeV of energy is released per fission. Therefore, a 1 GW_{th} (thermal power) reactor produces about 2×10^{20} $\bar{\nu}_e$'s per second.

The detailed estimate of $\bar{\nu}_e$ flux and energy spectrum can be obtained by either summing up the spectra of beta decays involved using available nuclear data information of each fission fragment and its decays, or using measurements of cumulative electron spectra associated with the beta decays of fission fragments. Because the fission of four main fuel isotopes involves thousands of beta-decay branches, a completely *ab initio* calculation is challenging. The cumulative electron spectra for ^{235}U, ^{239}Pu, and ^{241}Pu were measured at the Institut Laue-Langevin (ILL) reactor in Grenoble, France in the 1980s [132–134]. For the prediction of $\bar{\nu}_e$ flux from ^{238}U, a summation calculation in [135] was often used together with the ILL results.

A recent calculation of the reactor $\bar{\nu}_e$ flux [136] uses an improved *ab initio* approach for ^{238}U and combined information from nuclear databases and electron spectra measured at ILL for ^{235}U, ^{239}Pu, and ^{241}Pu. Another calculation [137] is provided for ^{235}U, ^{239}Pu, and ^{241}Pu based on the ILL measurement of electron spectra, taking into account higher order corrections and minimizing the use of nuclear databases. Both calculations predict about 3% higher normalization for the energy-averaged antineutrino fluxes of ^{235}U, ^{239}Pu, and ^{241}Pu compared to the original analyses of ILL data. However, the reactor antineutrino flux measurement at Daya Bay [138] is consistent with the old flux predictions and the flux measurement results. Also, an excess of $\bar{\nu}_e$ flux around 5 MeV, compared to the prediction, has been observed by recent reactor experiments [139–142]. Measurements of a fuel-dependent reactor $\bar{\nu}_e$ rate by Daya Bay [143] and RENO [144], and individual antineutrino spectra from ^{235}U and ^{239}Pu by Daya Bay [145] showed a discrepancy between the observed and predicted rate and spectrum from ^{235}U.

14.6.4.2 *Reactor antineutrino oscillation experiments*

Charged current interaction cannot happen if a reactor $\bar{\nu}_e$ changes its flavour to $\bar{\nu}_\mu$ or $\bar{\nu}_\tau$, because its energy is not sufficient to produce heavier charged leptons. Thus, $\bar{\nu}_e$ disappearance is the

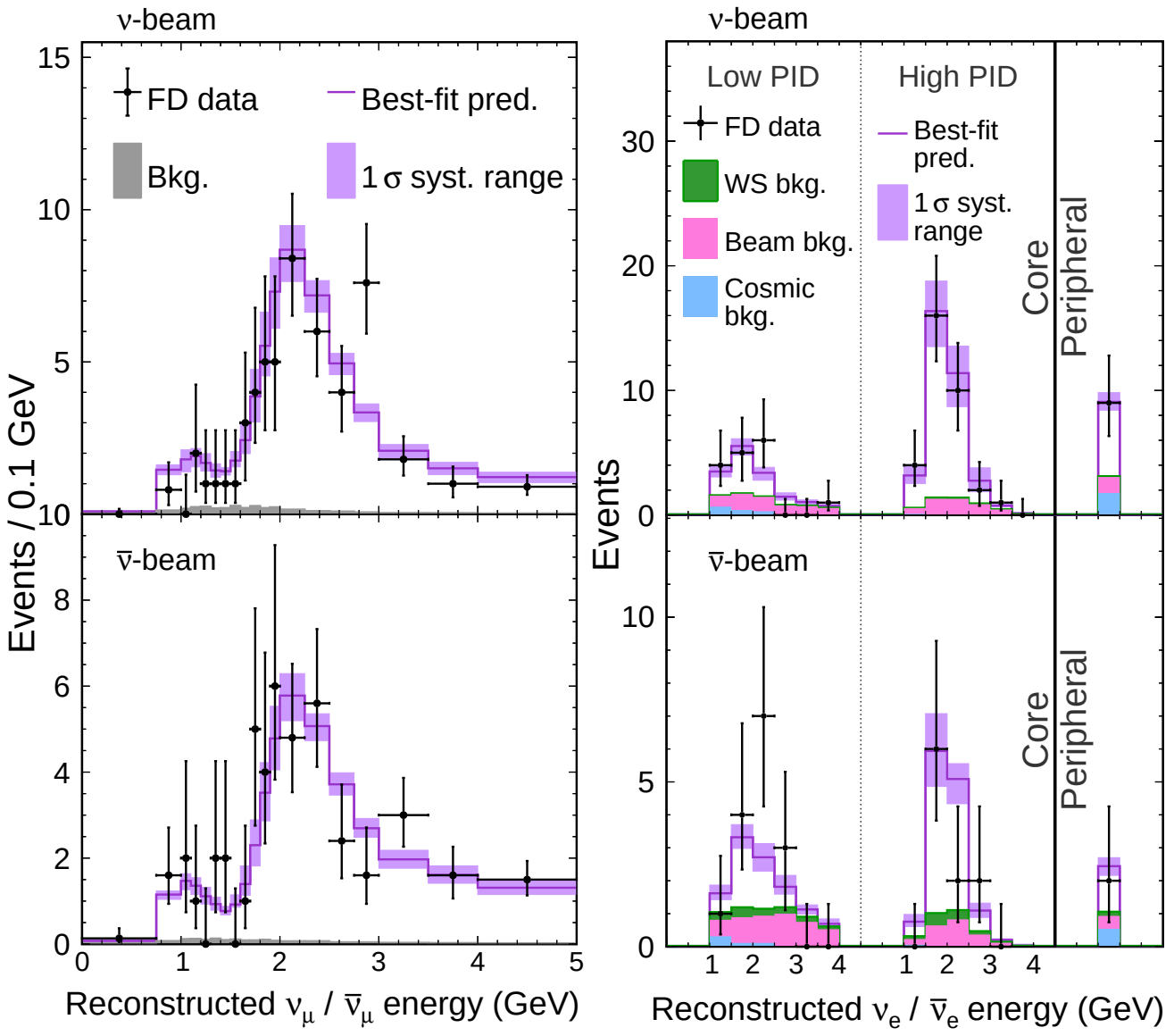

Figure 14.6: Reconstructed neutrino energy distributions from the NOvA far detector [126]. Top plots are for neutrino beam mode and bottom plots are for antineutrino beam mode. Left: muon-type candidates. Right: electron-type candidates, split into a low and high purity sample as well as the event counts in the peripheral sample which occurred near the edge of the detector.

Table 14.4: List of reactor antineutrino oscillation experiments

Name	Reactor power (GW_{th})	Baseline (km)	Detector mass (t)	Year
KamLAND	various	180 (ave.)	1,000	2001–
Double Chooz	4.25×2	1.05	8.3	2011–2018
Daya Bay	2.9×6	1.65	20×4	2011–
RENO	2.8×6	1.38	16	2011–
JUNO	26.6 (total)	53	20,000	

only channel to study neutrino flavour change with reactor experiments. The inverse beta decay $\bar{\nu}_e + p \to e^+ + n$ provides a way to detect $\bar{\nu}_e$ in the relevant energy region. The energy of prompt signal from e^+, E_p, is related to the energy of $\bar{\nu}_e$, $E_{\bar{\nu}} \sim E_p + 0.8$ MeV. The delayed coincidence with the signal from γ ray emitted by neutron capture on nucleus after thermalization very efficiently suppresses the backgrounds. Liquid scintillator is often used to realize large detectors containing hydrogen as the target of inverse beta decay. In order to increase the neutron detection efficiency, liquid scintillator is sometimes loaded with gadolinium because of large neutron capture cross section and higher energy of emitted γ rays, the total energy of about 8 MeV, by gadolinium, in contrast to 2.2 MeV for the capture by hydrogen.

Early reactor experiments that searched for neutrino oscillations at short or intermediate baselines reported negative results. The CHOOZ [146] and Palo Verde [147] experiments in 1990's searched for neutrino oscillations in the $\Delta m^2 \sim 10^{-2}$–10^{-3} eV^2 range and set a limit on the corresponding mixing angle $\sin^2 2\theta < 0.1$ at 90% CL.

Table 14.4 shows a list of reactor antineutrino experiments measuring neutrino oscillation. As was also shown in Table 14.1, experiments are designed with different baselines because of the different scale of mass splittings found by solar and atmospheric neutrino experiments. Experiments with O(100) km baseline are

sensitive to Δm^2 of 10^{-4}–10^{-5} eV^2, while $\sim$ 1 km of baseline results in a sensitivity in a range of 10^{-2}–10^{-3} eV^2.

The KamLAND detector consists of 1,000 t of ultra-pure liquid scintillator contained in a 13-m diameter spherical balloon [148]. The detector is located in the original Kamiokande cavern, where the $\bar{\nu}_e$ flux was dominated by a few reactors at an average distance of ∼180 km until 2011. KamLAND reported the first results in 2002 showing that the ratio of the observed number of $\bar{\nu}_e$ events and expectation without disappearance is $0.611 \pm 0.085 \pm 0.041$, evidence for reactor $\bar{\nu}_e$ disappearance at the 99.95% confidence level [148]. It confirmed a large value of the mixing angle corresponding to the LMA solution, which was reported by solar neutrino experiments. It is noted that there is a $\sim 2\sigma$ level tension between the global solar neutrino data and KamLAND reactor data regarding the best-fit value of Δm^2, while the mixing angle is consistent. KamLAND also showed the evidence of $\bar{\nu}_e$ spectrum distortion consistent with the expectation from neutrino oscillations [149]. Figure 14.7 shows the ratio of observed $\bar{\nu}_e$ spectrum to the expectation for no-oscillation as a function of L_0/E (L_0 = 180 km) for the KamLAND data. A clear oscillatory signature can be seen.

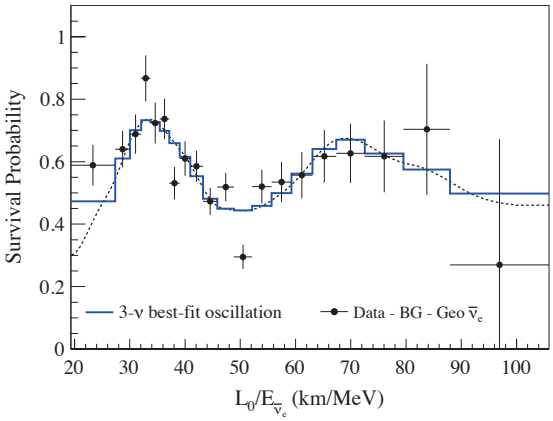

Figure 14.7: Ratio of the observed $\bar{\nu}_e$ spectrum to the expectation for no-oscillation versus L_0/E for the KamLAND data. L_0 = 180 km is the flux-weighted average reactor baseline. The 3-ν histogram is the best-fit survival probability curve from the three-flavour unbinned maximum-likelihood analysis using only the KamLAND data. This figure is taken from [150].

Following the establishment of neutrino oscillations with atmospheric, solar, accelerator, and reactor experiments, the measurement of the remaining mixing angle θ_{13} was recognized as the next major milestone. A reactor neutrino experiment with a baseline of ∼1 km can make an almost pure measurement of $\sin^2 2\theta_{13}$ from disappearance of $\bar{\nu}_e$. To be sensitive to a small value below the limit set by CHOOZ and Palo Verde, experiments with two detectors were proposed. Among several proposals, three experiments have been realized: Double Chooz in France [151], Daya Bay in China [152], and RENO in Korea [153].

These three experiments employ similar detector design optimized for the precise measurement of reactor antineutrino. An antineutrino detector consists of a cylindrical stainless steel vessel that houses two nested acrylic cylindrical vessels. The innermost vessel is filled with gadolinium-doped liquid scintillator as the primary antineutrino target. It is surrounded by a liquid scintillator layer to contain γ rays from the target volume. A buffer layer of mineral oil is placed an outside to shield inner volumes from radioactivity of PMTs and surrounding rock. The light from liquid scintillator is detected by an array of PMTs mounted on the stainless steel vessel. Optically separated by the stainless steel vessel, outside region is instrumented as a veto detector with either liquid scintillator (Double Chooz) or water Cherenkov (Daya Bay and RENO) detector.

The Double Chooz detector has gadolinium-doped liquid scintillator with mass of 8.3 t. The far detector at a baseline of ∼1050 m from the two 4.25 GW$_{\rm th}$ reactors started physics data taking in

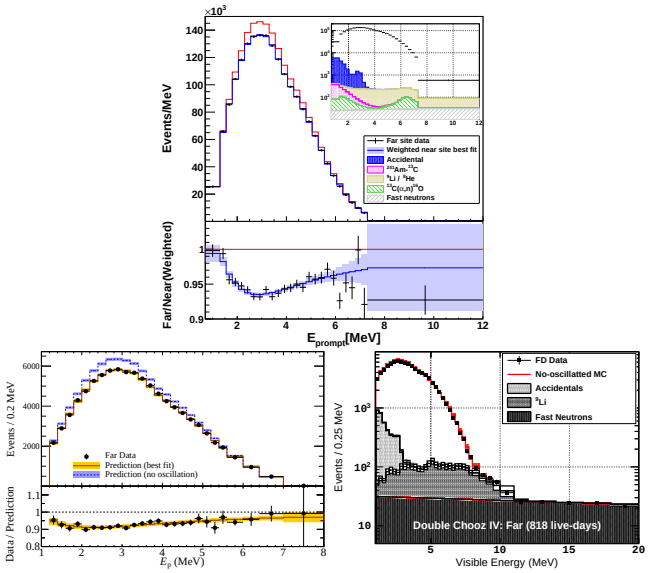

Figure 14.8: Energy spectra for prompt events at the far detectors for Daya Bay [139], RENO [140], and Double Chooz [141].

2011. The near detector, located at ∼400 m from the reactors, was completed in the end of 2014. Double Chooz finished data taking in early 2018. Daya Bay has two near (flux-weighted baseline 470 m and 576 m) and one far (1648 m) underground experimental halls near six reactors with 2.9 GW$_{\rm th}$ each. Daya Bay has eight antineutrino detectors in total; two detectors in each of the near detector halls, and four detectors in the far detector hall. Each detector contains 20 t of gadolinium-loaded liquid scintillator. RENO has two identical detectors located at 294 m and 1383 m from the center of an array of six 2.8 GW$_{\rm th}$ reactors. The mass of gadolinium-loaded liquid scintillator is 16 t per detector. RENO started data taking with both near and far detectors from August 2011.

All the three reactor neutrino experiments published first results in 2012. First, Double Chooz reported an indication of reactor electron antineutrino disappearance with the ratio of observed to expected events of $R = 0.944 \pm 0.016 \pm 0.04$, ruling out the no-oscillation hypothesis at the 94.6% CL [154]. Daya Bay observed $R = 0.940 \pm 0.011 \pm 0.004$, corresponding to 5.2σ significance of non-zero value of θ_{13} [155]. RENO also reported $R = 0.920 \pm 0.009 \pm 0.014$, indicating a non-zero value of θ_{13} with a significance of 4.9σ [156]. These results established non-zero value of θ_{13}.

In the latest analysis, both Daya Bay [139] and RENO [140] report results constraining mass-squared difference as well as the mixing angle by using both relative $\bar{\nu}_e$ rate and energy spectra information. Double Chooz has reported the first analysis based on both far and near detectors [141] for the mixing angle, using neutron capture on any elements (primarily gadolinium and hydrogen) to increase the effective target mass. Figure 14.8 shows the energy spectra of the prompt signals observed in the far detector of three experiments.

In all three experiments as well as in the NEOS experiment [142], an excess of $\bar{\nu}_e$ events over expected energy spectrum have been observed around 5 MeV as mentioned earlier. This excess is observed in both near and far detectors and scales with the reactor power. Thanks to the cancellation between the near and far detectors, the neutrino oscillation measurements are not affected in multi-detector setup.

With a baseline of ∼50 km and an excellent energy measurement, reactor antineutrino experiments have significant sensitivity to the mass ordering. The JUNO experiment [157] aims to determine the mass ordering with this technique as its primary goal. It can also provide precision measurements of neutrino mixing parameters as well as a broad non-oscillation science program. The JUNO detector, which is under construction, will consist of 20 kt

Table 14.5: List of reactor antineutrino experiments for O(eV^2) oscillations

Name	Reactor power (MW_{th})	Baseline (m)	Detector mass (t)	Detector technology	S/B
NEOS	2,800	24	1	Gd-LS	22
DANSS	3,100	10–12	0.9	Gd-PS	∼30
STEREO	57	9–11	1.7	Gd-LS	0.9
PROSPECT	85	7–9	4	^{6}Li-LS	1.3
NEUTRINO-4	100	6–12	1.5	Gd-LS	0.5
SoLid	80	6–9	1.6	^{6}Li-PS	

liquid scintillator and be located at 53 km from two nuclear power plants in China.

14.6.4.3 *New reactor experiments sensitive to O(1) eV^2 oscillations*

Possible hints of neutrino oscillation at a scale of $\Delta m^2 \sim 1$ eV^2 (see Sec.14.8) have motivated reactor experiments at a distance of ∼10 m from the core. Recent experiments searching for ∼1 eV^2 oscillation at reactors are summarized in Table 14.5.

As the antineutrino source, some use industrial reactors which can provide a large flux leading to a high statistical precision. On the other hand, though the flux is orders of magnitude smaller, a research reactor could have favorable conditions, such as relatively easier access to a short baseline, simpler fuel composition, and compact size of the core.

The detectors are based on organic scintillators, either liquid scintillator (LS) or solid plastic scintillator (PS), which contain hydrogen as the target for inverse beta decay ($\bar{\nu}_e + p \to e^+ + n$). To identify the signal, neutron capture on either gadolinium (Gd) or ^{6}Li is detected with delayed coincidence. When a neutron is captured by Gd, γ rays with a total energy of 8 MeV are emitted. After neutron capture, ^{6}Li decays into triton and α. The effect of neutrino oscillation appears as a distortion of energy spectrum. To be independent from the reactor neutrino spectrum uncertainties, some experiments compare the spectra at different baselines by using a segmented detector or moving the detector.

The NEOS [142] uses about 1 t of gadolinium-loaded liquid scintillator in an unsegmented detector. It is located at 23.7 m from the center of a commercial reactor and covered by an overburden of about 20 meters of water equivalent. Thanks to the high power reactor, NEOS observes antineutrino events at a rate of 1976 per day, with a signal to background ratio of about 22. The energy resolution is 5% at 1 MeV.

DANSS [158] is another experiment using a commercial reactor. The detector is highly segmented, consisting of 2,500 plastic scintillator strips, each with the size of $1 \times 4 \times 100$ cm^3 and coated with a thin gadolinium-loaded reflective layer. The detector is placed on a movable platform below the reactor core. The overburden of 50 m water-equivalent reduces the cosmic muon flux by a factor of six. Data are taken with three baselines, 10.7, 11.7, and 12.7 m for a comparison between different baselines. The energy resolution of $\sigma_E/E \sim 34\%$ at 1 MeV and the large size of the reactor core, 3.7 m in height and 3.2 m in diameter, somewhat smear the oscillation pattern. However it is compensated by high statistics due to the high power reactor. The observed event rate is 4899 events per day, with less than 3% cosmic background contamination, at 10.7 m position.

The STEREO detector [159] has six identical target cells of 37 cm length, ∼ 2m^3 of volume in total, filled with gadolinium-loaded liquid scintillator. They are placed from 9.4 to 11.1 m from the compact (80 cm high, 40 cm diameter) core of the ILL research reactor. The reconstructed energy resolution (σ_E/E) is about 9% at 0.835 MeV. The antineutrino event rate is 396 events per day with a signal to background ratio of about 0.9.

The PROSPECT detector [160] consists of a segmented 4 t ^{6}Li-doped liquid scintillator detector covering a baseline range of 7–9 m from the reactor core. Thin reflecting panels divide the LS volume into an 11 × 14 two-dimensional array of 154 optically isolated rectangular segments ($14.5 \times 14.5 \times 117.6$ cm^3). The energy resolution is 4.5% at 1 MeV. The detector is placed on the ground floor with an overburden of less than 1 m water-equivalent. With efficient background suppression by using pulse shape discrimination and 3D position reconstruction, a signal to background ratio of 1.3 is achieved. The antineutrino rate is 771 events per day.

NEUTRINO-4 [161] uses a gadolinium-loaded liquid scintillator detector segmented in 10×5 sections with a total volume of 1.8 m^3. The detector is installed on a movable platform and moved to various positions with baselines of 6–12 m. With the detector location close to the surface and no pule shape discrimination capability, the signal to background ratio is about 0.5. The energy resolution is 16% at 1 MeV.

The SoLid detector [162] is a finely segmented detector made of $5 \times 5 \times 5$ cm^3 plastic scintillator cubes and ^{6}LiF:ZnS sheets. A detector with 1.6 t of active volume is installed at a distance of 6–9 m from the research reactor core with an overburden of 10 m water-equivalent. The triton and α from neutron capture by ^{6}Li are detected by scintillation of ZnS. A high n-γ separation capability is achieved using the difference of time constant of scintillation between ZnS and plastic scintillator. Very fine segmentation of the detector allows 3D reconstruction of events, which also provide effective background discrimination. The energy resolution (σ_E/E) is expected to be ∼ 14% at 1 MeV.

14.7 Combined Analysis of Experimental Results: The 3ν Paradigm

From the experimental situation described in Sec.14.6 we conclude that

- Atmospheric ν_μ and $\bar{\nu}_\mu$ disappear most likely converting to ν_τ and $\bar{\nu}_\tau$. The results show an energy and distance dependence perfectly described by mass-induced oscillations.
- Accelerator ν_μ and $\bar{\nu}_\mu$ disappear over distances of ∼ 200 to 800 km. The energy spectrum of the results show a clear oscillatory behaviour also in accordance with mass-induced oscillations with wavelength in agreement with the effect observed in atmospheric neutrinos.
- Accelerator ν_μ and $\bar{\nu}_\mu$ appear as ν_e and $\bar{\nu}_e$ at distances ∼ 200 to 800 km.
- Solar ν_e convert to ν_μ and/or ν_τ. The observed energy dependence of the effect is well described by massive neutrino conversion in the Sun matter according to the MSW effect
- Reactor $\bar{\nu}_e$ disappear over distances of ∼ 200 km and ∼ 1.5 km with different probabilities. The observed energy spectra show two different mass-induced oscillation wavelengths: at short distances in agreement with the one observed in accelerator ν_μ disappearance, and a long distance compatible with the required parameters for MSW conversion in the Sun.

The minimum scenario to describe these results requires the mixing between the three flavour neutrinos of the standard model in three distinct mass eigenstates. In this case U in Eq. (14.32) is a 3×3 matrix analogous to the CKM matrix for the quarks [21] but due to the possible Majorana nature of the neutrinos it can depend on six independent parameters: three mixing angles and three phases. There are several possible conventions for the ranges of the angles and ordering of the states. The community finally agreed to a parametrization of the leptonic mixing matrix as in Eq. (14.33). The angles θ_{ij} can be taken without loss of generality to lie in the first quadrant, $\theta_{ij} \in [0, \pi/2]$, and the phase $\delta_{\rm CP} \in [0, 2\pi]$. Values of $\delta_{\rm CP}$ different from 0 and π imply CP violation in neutrino oscillations in vacuum [163–165]. The Majorana phases η_1 and η_2 play no role in neutrino oscillations [164, 166].

Hence for the study of neutrino oscillations in the 3ν mixing scenario one can use the parametrization in Eq. (14.34) irrespective of whether neutrinos are Dirac or Majorana particles. Indeed, Majorana phases are very hard to measure since they are only physical if neutrino mass is non-zero and therefore the amplitude of any process involving them is suppressed a factor m_ν/E to some power where E is the energy involved in the process which is typically much larger than the neutrino mass. The most sensitive experimental probe of Majorana phases is the rate of neutrinoless $\beta\beta$ decay as discussed in Secs. 14.9.3 and 14.9.2.

In this convention there are two non-equivalent orderings for the spectrum of neutrino masses:

- Spectrum with Normal Ordering (NO) with $m_1 < m_2 < m_3$
- Spectrum Inverted ordering (IO) with $m_3 < m_1 < m_2$.

Furthermore the data show a hierarchy between the mass splittings, $\Delta m^2_{21} \ll |\Delta m^2_{31}| \simeq |\Delta m^2_{32}|$ with $\Delta m^2_{ij} \equiv m^2_i - m^2_j$.

In this section we follow the convention used in the listing section of the PDG and discuss the results for both, NO and IO, using Δm^2_{21}, which is always the smallest mass splitting, and Δm^2_{32} which, up to a sign, is the largest mass splitting for IO, while for NO the largest mass splitting is $\Delta m^2_{31} = \Delta m^2_{32} + \Delta m^2_{21}$.

With what we know of the mass differences (see table 14.7) and the neutrino mass scale (see Sec. 14.9), depending on the value of the lightest neutrino mass, the neutrino mass spectrum can be further classified in:

- Normal Hierarchical Spectrum (NH): $m_1 \ll m_2 < m_3$, $\Rightarrow m_2 \simeq \sqrt{\Delta m^2_{21}} \sim 8.6\times10^{-3}\text{eV}, m_3 \simeq \sqrt{\Delta m^2_{32} + \Delta m^2_{21}} \sim 0.05\text{eV}$,
- Inverted Hierarchical Spectrum (IH): $m_3 \ll m_1 < m_2$, $\Rightarrow m_1 \simeq \sqrt{|\Delta m^2_{32} + \Delta m^2_{21}|} \sim 0.0492\text{eV}, m_2 \simeq \sqrt{|\Delta m^2_{32}|} \sim 0.05\text{eV}$,
- Quasidegenerate Spectrum (QD): $m_1 \simeq m_2 \simeq m_3 \gg \sqrt{|\Delta m^2_{32}|}$.

Sometimes in the literature the determination of the neutrino mass spectrum is refered to as determination of the neutrino hierarchy. However, as described above, with what we know so far of the neutrino mass scale, the neutrino spectrum may or may not be hierarchical. Therefore determination of neutrino mass ordering is a more precise expression and it is the one used in this review.

In total the 3-ν oscillation analysis of the existing data involves six parameters: 2 mass differences (one of which can be positive or negative), 3 mixing angles, and the CP phase. The different experiments described in Sec.14.6 provide information on different subsets of these parameters. The precise statistical analysis of the data requires the numerical evaluation of the corresponding oscillation probabilities by solving the evolution equation of the neutrino ensemble from their source to the experiment. Nevertheless the dominant effects in the different experiments can be qualitatively understood in terms of approximate expressions for the oscillation probabilities which, for convenience, we briefly summarize here.

14.7.1 *3ν Oscillation Probabilities*

The relevant survival probabilities for solar and KamLAND experiments in the framework of three neutrino oscillations can be written as:

$$P^{3\nu}_{ee} = \sin^4\theta_{13} + \cos^4\theta_{13} P^{2\nu}_{ee}(\Delta m^2_{21}, \theta_{12})\,, \tag{14.72}$$

where we have used the fact that $L^{\rm osc}_{0,32} = 4\pi E_\nu/\Delta m^2_{32}$ is much shorter than the distance travelled by both solar and KamLAND neutrinos, so that the oscillations related to $L^{\rm osc}_{0,32}$ are averaged. In presence of matter effects $P^{2\nu}_{ee}(\Delta m^2_{21}, \theta_{12})$ should be calculated taking into account the evolution in an effective matter density $n^{\rm eff}_e = n_e \cos^2\theta_{13}$. For $10^{-5} \lesssim \Delta m^2/\text{eV}^2 \lesssim 10^{-4}$, $P^{2\nu}_{ee}(\Delta m^2_{21}, \theta_{12})$ presents the following asymptotic behaviours [167]:

$$P^{2\nu,\rm sun}_{ee} \simeq 1 - \frac{1}{2}\sin^2(2\theta_{12}) \qquad \text{for } E_\nu \lesssim \text{few} \times 100 \text{ keV}\,, \tag{14.73}$$

$$P^{2\nu,\rm sun}_{ee} \simeq \sin^2(\theta_{12}) \qquad \text{for } E_\nu \gtrsim \text{few} \times 1 \text{ MeV}\,, \tag{14.74}$$

$$P^{2\nu,\rm kam}_{ee} = 1 - \frac{1}{2}\sin^2(2\theta_{12})\sin^2\frac{\Delta m^2_{21} L}{2E_\nu}. \tag{14.75}$$

At present most of the precision of the solar analysis is provided by SNO and SK for which the relevant MSW survival probability provides a direct measurement of $\sin^2\theta_{12}$, as seen in Eq. (14.74). In the MSW regime the determination of Δm^2_{21} in solar experiments comes dominantly from the ratio between the solar potential and the Δm^2_{21} term required to simultaneously describe the CC/NC data at SNO and the undistorted spectra of ^{8}B neutrinos as measured in both SK and SNO. Conversely, KamLAND $\bar\nu_e$ survival probability proceeds dominantly as vacuum oscillations and provides a most precise determination of Δm^2_{21} via the strong effect of the oscillating phase in the distortion of the reactor energy spectrum. On the contrary it yields a weaker constraint on θ_{12} as the vacuum oscillation probability depends on the double-valued and "flatter" function $\sin^2(2\theta_{12})$.

In what respects the interpretation of ν_μ disappearance data at LBL experiments, the ν_μ survival probability can be expanded in the small parameters $\sin\theta_{13}$ and $\alpha \equiv \Delta m^2_{21}/\Delta m^2_{31}$ to good accuracy as [168, 169]

$$\begin{aligned} P_{\nu_\mu\to\nu_\mu} &\approx 1 - \sin^2 2\theta_{\mu\mu}\sin^2\frac{\Delta m^2_{\mu\mu} L}{4E_\nu} \\ &\approx 1 - \cos^2\theta_{13}\sin^2(2\theta_{23})\sin^2\frac{\Delta m^2_{32} L}{4E_\nu} + \mathcal{O}(\alpha, s^2_{13})\,, \end{aligned} \tag{14.76}$$

with

$$\begin{aligned} \sin^2\theta_{\mu\mu} &= \cos^2\theta_{13}\sin^2\theta_{23}\,, \\ \Delta m^2_{\mu\mu} &= \sin^2\theta_{12}\Delta m^2_{31} + \cos^2\theta_{12}\Delta m^2_{32} \\ &\quad + \cos\delta_{\rm CP}\sin\theta_{13}\sin 2\theta_{12}\tan\theta_{23}\Delta m^2_{21}. \end{aligned}$$

At present ν_μ disappearance results at LBL provide the best determination of $|\Delta m^2_{32}|$ and θ_{23} but as seen above, the probability is symmetric with respect to the octant of $\theta_{\mu\mu}$ which implies symmetry around $s^2_{23} = 0.5/c^2_{13}$.

The relevant oscillation probability for ν_e appearance at LBL experiments can be expanded at the second order in the small parameters $\sin\theta_{13}$ and α, and assuming a constant matter density it takes the form [170–172]:

$$\begin{aligned} P_{\nu_\mu\to\nu_e,(\bar\nu_\mu\to\bar\nu_e)} &\approx 4\,\sin^2\theta_{13}\,\sin^2\theta_{23}\frac{\sin^2\Delta}{(1-A)^2} \\ &\quad + \alpha^2\sin^2 2\theta_{12}\,\cos^2\theta_{23}\frac{\sin^2 A\Delta}{A^2} \\ &\quad + 8\,\alpha\,J^{\rm max}_{\rm CP}\cos(\Delta \pm \delta_{\rm CP})\,\frac{\sin\Delta A}{A}\,\frac{\sin\Delta(1-A)}{1-A}\,, \end{aligned} \tag{14.77}$$

with

$$J^{\rm max}_{\rm CP} = \cos\theta_{12}\sin\theta_{12}\cos\theta_{23}\sin\theta_{23}\cos^2\theta_{13}\sin\theta_{13}\,, \tag{14.78}$$

and

$$\Delta \equiv \frac{\Delta m^2_{31} L}{4E_\nu}\,, \quad A \equiv \frac{2E_\nu V}{\Delta m^2_{31}}\,, \tag{14.79}$$

where V is the effective matter potential in the Earth crust. Results on ν_e appearance at LBL provide us with the dominant information on leptonic CP violation. Furthermore α, Δ, and A are sensitive to the sign of Δm^2_{32} (*i.e.*, the type of the neutrino mass ordering). The plus (minus) sign in Eq. (14.77) applies for

neutrinos (antineutrinos), and for antineutrinos $V \to -V$, which implies $A \to -A$. Numerically one finds for a typical Earth crust matter density of 3 g/cm^3 that at T2K with $E \sim 0.7$ GeV, matter effects are of order few percent, whereas in NOvA with $E \sim 2$ GeV we can have $|A| \sim 0.2$. Also $\alpha^2 \approx 10^{-3}$, which implies that the second term in the first line of Eq. (14.77) gives a very small contribution compared to the other terms. Also, the first term in Eq. (14.77) (which dominates for large θ_{13}) depends on $\sin^2\theta_{23}$ and therefore is sensitive to the octant.

The ν_e survival probability relevant for reactor experiments with medium baseline (MBL), $L \sim 1$ km, can be approximated as [169, 173]:

$$P_{\nu_e \to \nu_e} = 1 - \sin^2 2\theta_{13} \sin^2 \frac{\Delta m^2_{ee} L}{4E_\nu} + \mathcal{O}(\alpha^2)\,, \tag{14.80}$$

where

$$\Delta m^2_{ee} = \cos^2\theta_{12}\Delta m^2_{31} + \sin^2\theta_{12}\Delta m^2_{32}\,. \tag{14.81}$$

These MBL reactor experiments provide the most precise determination of θ_{13}. Furthermore there is an additional effect sensitive to the mass ordering when comparing the disappearance of ν_μ at LBL experiments – which is symmetric with respect to the sign of $\Delta m^2_{\mu\mu}$ given in Eq.(14.7.1)– , with that of ν_e disappearance at MBL reactors which is symmetric with respect to the slightly different effective mass-squared difference Δm^2_{ee} given in Eq. (14.81)

Finally for atmospheric neutrinos the fluxes contain ν_e, ν_μ, $\bar\nu_e$ and $\bar\nu_\mu$ and for a good fraction of the events, neutrinos travel through the Earth matter. In the context of 3ν mixing, the dominant oscillation channel of atmospheric neutrinos is $\nu_\mu \to \nu_\tau$ driven by $|\Delta m^2_{32}|$ with an amplitude controlled by θ_{23} with subleading oscillation modes, triggered by Δm^2_{21} and/or θ_{13}, which depend on the octant of θ_{23}, on the mass ordering and on $\delta_{\rm CP}$. In that respect an interesting observable is the deviation of e-like events relative to the no-oscillation prediction N^0_e, since in the two-flavour limit one expects $N_e = N^0_e$. Such deviation can be written in the following way (see, *e.g.*, [174]):

$$\begin{aligned}\frac{N_e}{N^0_e} - 1 \approx\ & (r\sin^2\theta_{23} - 1) P_{2\nu}(\Delta m^2_{32}, \theta_{13}) \\ & + (r\cos^2\theta_{23} - 1) P_{2\nu}(\Delta m^2_{21}, \theta_{12}) \\ & - \sin\theta_{13}\sin 2\theta_{23}\, r\, \Re(A^*_{ee} A_{\mu e})\,.\end{aligned} \tag{14.82}$$

Here $r \equiv \Phi_\mu/\Phi_e$ is the flux ratio with $r \approx 2$ in the sub-GeV range and $r \approx 2.6 \to 4.5$ in the multi-GeV range. $P_{2\nu}(\Delta m^2, \theta)$ is an effective two-flavour oscillation probability and $A_{ee}, A_{\mu e}$ are elements of a transition amplitude matrix. The three terms appearing in Eq. (14.82) have a well defined physical interpretation. The first term is important in the multi-GeV range and is controlled by the mixing angle θ_{13} in $P_{2\nu}(\Delta m^2_{32}, \theta_{13})$. This probability can be strongly affected by resonant matter effects [175–180]. Depending on the mass ordering the resonance will occur either for neutrinos or antineutrinos. The second term is important for sub-GeV events and it takes into account the effect of oscillations due to Δm^2_{21} and θ_{12} [181–184]. Via the pre-factor containing the flux ratio r both, the first and second terms in Eq. (14.82) depend on the octant of θ_{23}, though in opposite directions: the multi-GeV (sub-GeV) excess is suppressed (enhanced) for $\theta_{23} < 45°$. Finally, the last term in Eq. (14.82) is an interference term between θ_{13} and Δm^2_{21} amplitudes and this term shows also dependence on the CP phase $\delta_{\rm CP}$ [174, 184].

Subdominant three neutrino effects can also affect μ-like events. For example for multi-GeV muon events one can write the excess in μ-like events as [185, 186]

$$\begin{aligned}\frac{N_\mu}{N^0_\mu} - 1 \approx\ & \sin^2\theta_{23}\left(\frac{1}{r} - \sin^2\theta_{23}\right) P_{2\nu}(\Delta m^2_{32}, \theta_{13}) \\ & - \frac{1}{2}\sin^2 2\theta_{23}\,[1 - \Re(A_{33})]\,.\end{aligned} \tag{14.83}$$

The first term is controlled by θ_{13} and is subject to resonant matter effects, similar to the first term in Eq. (14.82), though with a different dependence on θ_{23} and the flux ratio. In the second term, A_{33} is a probability amplitude satisfying $P_{2\nu}(\Delta m^2_{32}, \theta_{13}) = 1 - |A_{33}|^2$. In the limit $\theta_{13} = 0$ we have $\Re(A_{33}) = \cos(\Delta m^2_{32} L/2E)$, such that the second term in Eq. (14.83) just describes two-flavour $\nu_\mu \to \nu_\mu$ vacuum oscillations.

14.7.2 *3ν Oscillation Analysis*

We summarize in Table 14.6 the different experiments which dominantly contribute to the present determination of the different parameters in the chosen convention.

The table illustrates that the determination of the leptonic parameters requires global analysis of the data from the different experiments. Over the years these analyses have been in the hands of a few phenomenological groups. We show in Table 14.7 the results from the latest analyses in Refs. [187–190]. For the sake of comparison all results are presented in the convention of the listing section as described above.

The table illustrates the dependence of the present determination of the parameters on variations of the statistical analysis performed by the different groups and on the data samples included. In that last respect the main difference resides on the results from Super-Kamiokande atmospheric data [94] which, at present, can only be included in these analysis by directy adding the χ^2 tabulated χ^2 map provided by the experiment.

Altogether the different analysis find consistent results, in particular on the better known parameters, θ_{12}, θ_{13} and Δm^2_{21} and $|\Delta m^2_{32}|$. The issues which still require clarification are: the mass ordering discrimination, the determination of θ_{23} and the leptonic CP phase $\delta_{\rm CP}$:

- In all analyses the best fit is for the normal mass ordering. Inverted ordering is disfavoured with a $\Delta\chi^2$ which ranges from slightly above 2σ – driven by the interplay of long-baseline accelerator and short-baseline reactor data – to 3σ when adding the atmospheric χ^2 table from Ref. [94].
- All analyses find some preference for the second octant of θ_{23} but with statistical significance still well below 3σ.
- The best fit for the complex phase in NO is at $\delta_{\rm CP} \sim 120°$ but CP conservation (for $\delta_{\rm CP} \sim 180°$) is still allowed at a confidence level (CL) of 1-2σ. We notice that, at present, the significance of CP violation in the global analysis is reduced with respect to that reported by T2K [191] because NOvA data does not show a significant indication of CP violation.

14.7.3 *Convention-independent Measures of Leptonic CP Violation in 3ν Mixing*

In the framework of 3ν mixing leptonic CP violation can also be quantified in terms of the leptonic Jarlskog invariant [192], defined by:

$$\begin{aligned}\Im\left[U_{\alpha i} U^*_{\alpha j} U^*_{\beta i} U_{\beta j}\right] &\equiv \sum_{\gamma=e,\mu,\tau}\sum_{k=1,2,3} J_{\rm CP}\,\epsilon_{\alpha\beta\gamma}\,\epsilon_{ijk} \\ &\equiv J^{\rm max}_{\rm CP}\,\sin\delta_{\rm CP}\,.\end{aligned} \tag{14.84}$$

With the convention in Eq. (14.33) $J^{\rm max}_{\rm CP}$ is the combination of mixing angles in Eq. (14.78). For example from the analysis in Ref. [187, 188]

$$J^{\rm max}_{\rm CP} = 0.03359 \pm 0.0006\,(\pm 0.0019)\,, \tag{14.85}$$

at 1σ (3σ) for both orderings, and the preference of the present data for non-zero $\delta_{\rm CP}$ implies a non-zero best fit value $J^{\rm best}_{\rm CP} = -0.019$.

The status of the determination of leptonic CP violation can also be graphically displayed by projecting the results of the global analysis in terms of leptonic unitarity triangles [193–195]. Since in the analysis U is unitary by construction, any given pair of rows or columns can be used to define a triangle in the complex plane. There a total of six possible triangles corresponding to the unitary conditions

$$\sum_{i=1,2,3} U_{\alpha i} U^*_{\beta i} = 0 \text{ with } \alpha \neq \beta\,, \qquad \sum_{\alpha=e,\mu,\tau} U_{\alpha i} U^*_{\alpha j} = 0 \text{ with } i \neq j\,. \tag{14.86}$$

Table 14.6: Experiments contributing to the present determination of the oscillation parameters.

Experiment	Dominant	Important
Solar Experiments	θ_{12}	Δm^2_{21} , θ_{13}
Reactor LBL (KamLAND)	Δm^2_{21}	θ_{12} , θ_{13}
Reactor MBL (Daya-Bay, Reno, D-Chooz)	θ_{13}, $\lvert\Delta m^2_{31,32}\rvert$	
Atmospheric Experiments (SK, IC-DC)		θ_{23},$\lvert\Delta m^2_{31,32}\rvert$, θ_{13},$\delta_{\rm CP}$
Accel LBL ν_μ,$\bar\nu_\mu$, Disapp (K2K, MINOS, T2K, NOνA)	$\lvert\Delta m^2_{31,32}\rvert$, θ_{23}	
Accel LBL ν_e,$\bar\nu_e$ App (MINOS, T2K, NOνA)	$\delta_{\rm CP}$	θ_{13} , θ_{23}

Table 14.7: 3ν oscillation parameters obtained from different global analysis of neutrino data. In all cases the numbers labeled as NO (IO) are obtained assuming NO (IO), *i.e.*, relative to the respective local minimum. SK-ATM makes reference to the tabulated χ^2 map from the Super-Kamiokande analysis of their data in Ref. [94].

	Ref. [188] w/o SK-ATM		Ref. [188] w SK-ATM		Ref. [189] w SK-ATM		Ref. [190] w SK-ATM	
NO	Best Fit Ordering		Best Fit Ordering		Best Fit Ordering		Best Fit Ordering	
Param	bfp $\pm1\sigma$	3σ range	bfp $\pm1\sigma$	3σ range	bfp $\pm1\sigma$	3σ range	bfp $\pm1\sigma$	3σ range
$\frac{\sin^2\theta_{12}}{10^{-1}}$	$3.10^{+0.13}_{-0.12}$	$2.75 \to 3.50$	$3.10^{+0.13}_{-0.12}$	$2.75 \to 3.50$	$3.04^{+0.14}_{-0.13}$	$2.65 \to 3.46$	$3.20^{+0.20}_{-0.16}$	$2.73 \to 3.79$
$\theta_{12}/^\circ$	$33.82^{+0.78}_{-0.76}$	$31.61 \to 36.27$	$33.82^{+0.78}_{-0.76}$	$31.61 \to 36.27$	$33.46^{+0.87}_{-0.88}$	$30.98 \to 36.03$	$34.5^{+1.2}_{-1.0}$	$31.5 \to 38.0$
$\frac{\sin^2\theta_{23}}{10^{-1}}$	$5.58^{+0.20}_{-0.33}$	$4.27 \to 6.09$	$5.63^{+0.18}_{-0.24}$	$4.33 \to 6.09$	$5.51^{+0.19}_{-0.80}$	$4.30 \to 6.02$	$5.47^{+0.20}_{-0.30}$	$4.45 \to 5.99$
$\theta_{23}/^\circ$	$48.3^{+1.2}_{-1.9}$	$40.8 \to 51.3$	$48.6^{+1.0}_{-1.4}$	$41.1 \to 51.3$	$47.9^{+1.1}_{-4.0}$	$41.0 \to 50.9$	$47.7^{+1.2}_{-1.7}$	$41.8 \to 50.7$
$\frac{\sin^2\theta_{13}}{10^{-2}}$	$2.241^{+0.066}_{-0.065}$	$2.046 \to 2.440$	$2.237^{+0.066}_{-0.065}$	$2.044 \to 2.435$	$2.14^{+0.09}_{-0.07}$	$1.90 \to 2.39$	$2.160^{+0.083}_{-0.069}$	$1.96 \to 2.41$
$\theta_{13}/^\circ$	$8.61^{+0.13}_{-0.13}$	$8.22 \to 8.99$	$8.60^{+0.13}_{-0.13}$	$8.22 \to 8.98$	$8.41^{+0.18}_{-0.14}$	$7.9 \to 8.9$	$8.45^{+0.16}_{-0.14}$	$8.0 \to 8.9$
$\delta_{\rm CP}/^\circ$	222^{+38}_{-28}	$141 \to 370$	221^{+39}_{-28}	$144 \to 357$	238^{+41}_{-33}	$149 \to 358$	218^{+38}_{-27}	$157 \to 349$
$\frac{\Delta m^2_{21}}{10^{-5}\ \mathrm{eV}^2}$	$7.39^{+0.21}_{-0.20}$	$6.79 \to 8.01$	$7.39^{+0.21}_{-0.20}$	$6.79 \to 8.01$	$7.34^{+0.17}_{-0.14}$	$6.92 \to 7.91$	$7.55^{+0.20}_{-0.16}$	$7.05 \to 8.24$
$\frac{\Delta m^2_{32}}{10^{-3}\ \mathrm{eV}^2}$	$2.449^{+0.032}_{-0.030}$	$2.358 \to 2.544$	$2.454^{+0.029}_{-0.031}$	$2.362 \to 2.544$	$2.419^{+0.035}_{-0.032}$	$2.319 \to 2.521$	2.424 ± 0.03	$2.334 \to 2.524$
IO	$\Delta\chi^2 = 6.2$		$\Delta\chi^2 = 10.4$		$\Delta\chi^2 = 9.5$		$\Delta\chi^2 = 11.7$	
$\frac{\sin^2\theta_{12}}{10^{-1}}$	$3.10^{+0.13}_{-0.12}$	$2.75 \to 3.50$	$3.10^{+0.13}_{-0.12}$	$2.75 \to 3.50$	$3.03^{+0.14}_{-0.13}$	$2.64 \to 3.45$	$3.20^{+0.20}_{-0.16}$	$2.73 \to 3.79$
$\theta_{12}/^\circ$	$33.82^{+0.78}_{-0.76}$	$31.61 \to 36.27$	$33.82^{+0.78}_{-0.75}$	$31.62 \to 36.27$	$33.40^{+0.87}_{-0.81}$	$30.92 \to 35.97$	$34.5^{+1.2}_{-1.0}$	$31.5 \to 38.0$
$\frac{\sin^2\theta_{23}}{10^{-1}}$	$5.63^{+0.19}_{-0.26}$	$4.30 \to 6.12$	$5.65^{+0.17}_{-0.22}$	$4.36 \to 6.10$	$5.57^{+0.17}_{-0.24}$	$4.44 \to 6.03$	$5.51^{+0.18}_{-0.30}$	$4.53 \to 5.98$
$\theta_{23}/^\circ$	$48.6^{+1.1}_{-1.5}$	$41.0 \to 51.5$	$48.8^{+1.0}_{-1.2}$	$41.4 \to 51.3$	$48.2^{+1.0}_{-1.4}$	$41.8 \to 50.9$	$47.9^{+1.0}_{-1.7}$	$42.3 \to 50.7$
$\frac{\sin^2\theta_{13}}{10^{-2}}$	$2.261^{+0.067}_{-0.064}$	$2.066 \to 2.461$	$2.259^{+0.065}_{-0.065}$	$2.064 \to 2.457$	$2.18^{+0.08}_{-0.07}$	$1.95 \to 2.43$	$2.220^{+0.074}_{-0.076}$	$1.99 \to 2.44$
$\theta_{13}/^\circ$	$8.65^{+0.13}_{-0.12}$	$8.26 \to 9.02$	$8.64^{+0.12}_{-0.13}$	$8.26 \to 9.02$	$8.49^{+0.15}_{-0.14}$	$8.0 \to 9.0$	$8.53^{+0.14}_{-0.15}$	$8.1 \to 9.0$
$\delta_{\rm CP}/^\circ$	285^{+24}_{-26}	$205 \to 354$	282^{+23}_{-25}	$205 \to 348$	247^{+26}_{-27}	$193 \to 346$	281^{+23}_{-27}	$202 \to 349$
$\frac{\Delta m^2_{21}}{10^{-5}\ \mathrm{eV}^2}$	$7.39^{+0.21}_{-0.20}$	$6.79 \to 8.01$	$7.39^{+0.21}_{-0.20}$	$6.79 \to 8.01$	$7.34^{+0.17}_{-0.14}$	$6.92 \to 7.91$	$7.55^{+0.20}_{-0.16}$	$7.05 \to 8.24$
$\frac{\Delta m^2_{32}}{10^{-3}\ \mathrm{eV}^2}$	$-2.509^{+0.032}_{-0.032}$	$-2.603 \to -2.416$	$-2.510^{+0.030}_{-0.031}$	$-2.601 \to -2.419$	$-2.478^{+0.035}_{-0.033}$	$-2.577 \to -2.375$	$-2.50\pm^{+0.04}_{-0.03}$	$-2.59 \to -2.39$

As illustration we show in Fig. 14.9 the recasting of the allowed regions of the analysis in Ref. [187, 188] in terms of one leptonic unitarity triangle. We show the triangle corresponding to the unitarity conditions on the first and third columns (after the shown rescaling) which is the equivalent to the one usually shown for the quark sector. In this figure the absence of CP violation would imply a flat triangle, *i.e.*, $\Im(z) = 0$. So the CL at which leptonic CP violation is being observed would be given by the CL at which the region crosses the horizontal axis. Notice however, that this representation is made *under the assumption of a unitary U matrix* and therefore does not provide any test of unitarity in the leptonic sector.

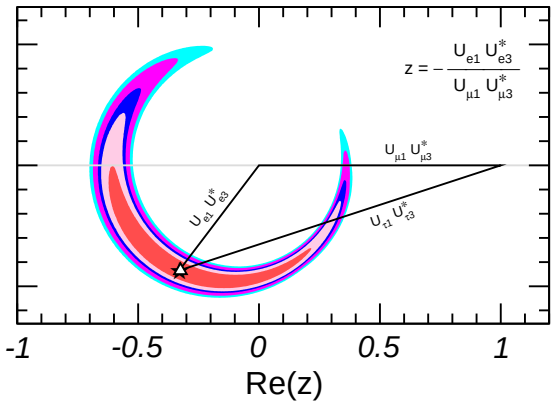

Figure 14.9: Leptonic unitarity triangle for the first and third columns of the mixing matrix. After scaling and rotating the triangle so that two of its vertices always coincide with $(0, 0)$ and $(1, 0)$ the figure shows the 1σ, 90%, 2σ, 99%, 3σ CL (2 dof) allowed regions of the third vertex for the NO from the analysis in Ref. [187, 188].

14.8 Beyond 3ν: Additional Neutrinos at the eV Scale

Besides the huge success of three-flavour oscillations described in Sec.14.7, as mentioned in Secs.14.6.3 and 14.6.4, there are some anomalies which cannot be explained within the 3ν framework and which might point towards the existence of additional neutrino states with masses at the eV scale. In brief:

- the LSND experiment [127] reports evidence for $\bar{\nu}_\mu \to \bar{\nu}_e$ transitions with $E/L \sim 1$ eV^2, where E and L are the neutrino energy and the distance between source and detector, respectively (see *Short Baseline Experiments* subsection of Sec.14.6.3).
- this effect has also been searched for by the MiniBooNE experiment [196], which reports a yet unexplained event excess in the low-energy region of the electron neutrino and anti-neutrino event spectra. No significant excess is found at higher neutrino energies. Interpreting the data in terms of oscillations, parameter values consistent with the ones from LSND are obtained, but the test is not definitive;
- radioactive source experiments at the Gallium solar neutrino experiments both in SAGE and GALLEX/GNO have obtained an event rate which is somewhat lower than expected. If not due to uncertainties in the interaction cross section, this effect can be explained by the hypothesis of ν_e disappearance due to oscillations with $\Delta m^2 \gtrsim 1$ eV^2 ("Gallium anomaly") [197, 198];
- new calculations of the neutrino flux emitted by nuclear reactors [136, 137] predict a neutrino rate which is a few percent higher than observed in short-baseline ($L \lesssim 100$ m) reactor experiments [4]. If not due to systematic or theoretical uncertainties, a decrease rate at those distances can be explained by assuming $\bar{\nu}_e$ disappearance due to oscillations with $\Delta m^2 \sim 1$ eV^2 ("reactor anomaly") [200]. This reactor anomaly is under study both by the experimental community – with a set of follow-up measurements performed at SBL both at reactors and accelerators (see the corresponding subsections in Sec.14.6.4 and Sec.14.6.3)– , and by the theory community for improvements of the reactor flux calculations.

As mentioned in Sec.14.1 whatever the extension of the SM we want to consider it must contain only three light active neutrinos. Therefore if we need more than three light massive neutrinos we must add sterile neutrinos to the particle content of the model.

The most immediate question as these anomalies were reported was whether they could all be consistently described in combination with the rest of the neutrino data – in particular with the negative results on disappearance of ν_μ at short distances – if one adds those additional sterile states. Quantitatively one can start by adding a fourth massive neutrino state to the spectrum, and perform a global data analysis to answer this question. Although the answer is always the same the physical reason behind it depends on ordering assumed for the states. In brief, there are six possible four-neutrino schemes which can in principle accommodate the results of solar+KamLAND and atmospheric+LBL neutrino experiments as well as the SBL result. They can be divided in two classes: (2+2) and (3+1). In the (3+1) schemes, there is a group of three close-by neutrino masses (as on the 3ν schemes described in the previous section) that is separated from the fourth one by a gap of the order of 1 eV, which is responsible for the SBL oscillations. In (2+2) schemes, there are two pairs of close masses (one pair responsible for solar results and the other for atmospheric [201]) separated by the $\mathcal{O}(\text{eV})$ gap. The main difference between these two classes is the following: if a (2+2)-spectrum is realized in nature, the transition into the sterile neutrino is a solution of either the solar or the atmospheric neutrino problem, or the sterile neutrino takes part in both. Consequently a (2+2)-spectrum is easier to test because the required mixing of sterile neutrinos in either solar and/or atmospheric oscillations would modify their effective matter potential in the Sun and in the Earth and giving distinctive effects in the solar and/or atmospheric neutrino observables. Those distinctive effects were not observed so oscillations into sterile neutrinos did not describe well either solar or atmospheric data. Consequently as soon as the early 2000's 2+2 spectra could be ruled out already beyond 3-4 σ as seen in the left panel in Fig.14.10 taken from Ref. [202].

On the contrary, for a (3+1)-spectrum (and more generally for a $3+N$-spectrum with an arbitrary N number of sterile states), the sterile neutrino(s) could be only slightly mixed with the active ones and mainly provide a description of the SBL results. In this case the oscillation probabilities for experiments working at $E/L \sim 1$ eV^2 take a simple form:

$$P_{\alpha\alpha} = 1 - \sin^2 2\theta_{\alpha\alpha} \sin^2 \Delta\,, \qquad P_{\mu e} = \sin^2 2\theta_{\mu e} \sin^2 \Delta\,, \quad (14.87)$$

where $\Delta \equiv \Delta m^2_{41} L/4E$ and one can define effective mixing angles

$$\sin^2 2\theta_{\alpha\alpha} \equiv 4|U_{\alpha 4}|^2(1 - |U_{\alpha 4}|^2)\,, \qquad \sin^2 2\theta_{\mu e} \equiv 4|U_{\mu 4}|^2|U_{e4}|^2\,. \quad (14.88)$$

In here $\alpha = e, \mu$ and $U_{\alpha 4}$ are the elements of the lepton mixing matrix describing the mixing of the 4th neutrino mass state with the electron and muon flavour. In this scenario there is no sensitivity to CP violation in the the Δ driven oscillations, so the relations above are valid for both neutrinos and antineutrinos. At linear order in the mixing elements one can derive a relation between the amplitudes of appearance and disappearance probabilities:

$$4 \sin^2 2\theta_{\mu e} \approx \sin^2 2\theta_{ee} \sin^2 2\theta_{\mu\mu}\,. \quad (14.89)$$

This relation implies a constraint between the possible results in disappearance and appearance experiments. Consequently it is not trivial to find a consistent description to all the SBL anomalies. Over the years, different groups have performed a variety of such global analysis leading to quantitative different conclusions on the statistical quality of the global fit (see for example [203–208], see also Refs. [209, 210] for recent reviews on the subject). Generically the results of the global analysis show that there is significant tension between groups of different data sets – in particular between appearance and disappearance results – and Eq.(14.89) makes it difficult to obtain a good global fit as illustrated in the right panel in Fig.14.10 taken from Ref. [203] which concluded that 3+1 scenario is excluded at 4.7σ level.

A straightforward question to ask is whether the situation improves if more neutrino states at the eV scale are introduced. Simplest extension is the introduction of 2 states with eV scale mass splittings, ν_4 and ν_5. The ordering of the states can be such that Δm^2_{41} and Δm^2_{51} are both positive ("3+2") or one of them is negative ("1+3+1"). From the point of view of the description of the data the most important new qualitative feature in that now non-zero CP violation at $E/L \sim$ eV^2 is possibly observable [206, 211–213]. This allows some additional freedom in fitting neutrino versus anti-neutrino data from LSND and MiniBooNE together. However, it still holds that a non-zero $\nu_\mu \to \nu_e$ appearance at SBL necessarily predicts SBL disappearance for both ν_e and ν_μ. So, generically, the tension between appearance and disappearance results remains, thought differences in the methodology of statistical quantification of the degree of agreement/disagreement in these scenarios can lead to different conclusions on whether they can provide a successful description of all the data [203,209,210]. Cosmological observations can provide complementary information on the number of relativistic neutrino states in thermal equilibrium in the early Universe and on the sum of their masses which sets further constrains on light sterile neutrino scenarios (see Section 26, Neutrinos in cosmology).

[4] However, as discussed in Sec.14.6.4, the reactor antineutrino flux measurement at Daya Bay [143, 199] is consistent with the old flux predictions and the flux measurement results in the previous short-baseline reactor neutrino oscillation experiments.

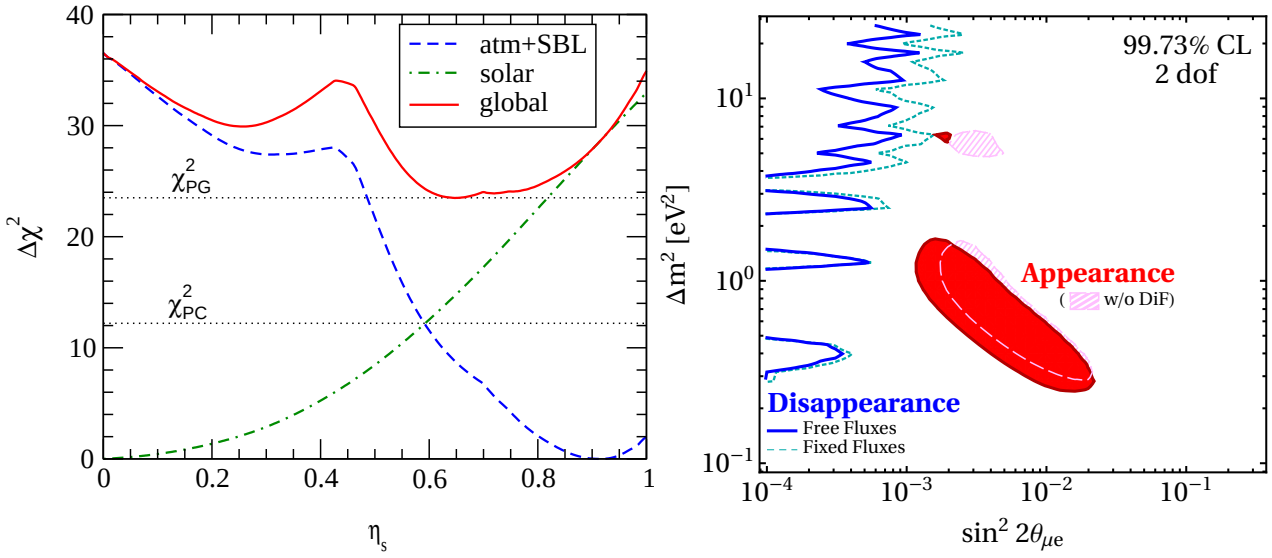

Figure 14.10: *Left*: Status of the 2+2 oscillation scenarios from Ref. [202] ($\eta_S = \sum_i |U_{is}|^2$ where i runs over the two massive states mostly relevant for solar neutrino oscillations). In the figure also shown are the values of $\chi^2_{\rm PC}$ and $\chi^2_{\rm PG}$ relevant for parameter consistency test and parameter goodness of fit respectively. *Right*: Present status of 3+1 oscillation scenarios from Ref. [203].

14.9 Laboratory Probes of ν Mass Scale and its Nature

As described in Secs.14.4 and 14.5 neutrino flavour oscillations in vacuum and flavour transitions in matter only depend on the differences between the neutrino masses-squared, Δm^2_{ij}, and on the mixing matrix elements, U_{ij}. But they are insensitive to the absolute mass scale for the neutrinos, m_i. They also give us no information on whether they are Dirac or Majorana particles.

Clearly the observation of flavour oscillations imply a lower bound on the mass of the heavier neutrino in Δm^2_{ij}, $|m_i| \geq \sqrt{\Delta m^2_{ij}}$ for $\Delta m^2_{ij} > 0$. But there is no upper bound on m_i. In particular, oscillation results allow neutrino spectrum to be approximately degenerate at a mass scale that is much higher than the $\sqrt{\Delta m^2_{ij}}$ that they determine. Information of the mass scale of the neutrino is provided by other type of experiments. In here we briefly summarize the most sensitive laboratory probes of the neutrino mass scale and on whether they are Dirac or Majorana particles. Cosmological observations provide, albeit indirectly, complementary information on the neutrino mass scale as it is reviewed in Section 26, Neutrinos in cosmology.

14.9.1 *Constraints from Kinematics of Weak Decays*

The only model independent information on the neutrino masses, rather than mass differences, can be extracted from energy-momentum conservation relation in reactions in which a neutrino or an anti-neutrino is involved.

Historically these bounds were labeled as limits on the mass of the flavour neutrino states corresponding to the charged flavour involved in the decay. Fermi proposed in 1933 such a kinematic search for the ν_e neutrino mass (which we will label here as $m^{\rm eff}_{\nu_e}$) in the end part of the beta spectra in ^{3}H beta decay $^3{\rm H} \rightarrow {}^3{\rm He} + e^- + \bar{\nu}_e$.

Because ^{3}H beta decay is a superallowed transition, the nuclear matrix elements are energy independent so the electron spectrum is determined exclusively by the phase space

$$\begin{aligned} \frac{dN}{dE} &= C\, p\, E\, (Q-T)\sqrt{(Q-T)^2 - (m^{\rm eff}_{\nu_e})^2}\, F(E) \\ &\equiv R(E)\sqrt{(E_0-E)^2 - (m^{\rm eff}_{\nu_e})^2}\,. \end{aligned} \tag{14.90}$$

E_0 is the mass difference between the inital and final nucleus, $E = T + m_e$ is the total electron energy, p its momentum, $Q \equiv E_0 - m_e$ is the maximum kinetic energy of the electron and Final state Coulomb interactions are contained in the Fermi function $F(E)$. $R(E)$ in the second equality contains all the m_ν-independent factors.

The Kurie function is defined as $K(T) \equiv \sqrt{\frac{dN}{dE}\frac{1}{pEF(E)}}$. From Eq.(14.90) we see that if $m^{\rm eff}_{\nu_e}$=0 $K(T)$ would depend linearly on T. A non-vanishing neutrino mass then provokes a distortion from the straight-line T-dependence at the end point, So for $m^{\rm eff}_{\nu_e} = 0$, $T_{\rm max} = Q$, while for $m^{\rm eff}_{\nu_e} \neq 0$, $T_{\rm max} = Q - m^{\rm eff}_{\nu_e}$. In ^{3}H beta decay $Q = 18.6$ KeV is very small and therefore this decay is more sensitive to this $m^{\rm eff}_{\nu_e}$-induced distorsion.

The most recent result on the kinematic search for neutrino mass in tritium decay is from KATRIN [214], experiment which has found so far no indication of $m_{\nu_e} \neq 0$ and sets an upper limit

$$m^{\rm eff}_{\nu_e} < 1.1 \text{ eV}\,, \tag{14.91}$$

at 90% CL improving over the previous bound from the Mainz [215] and Troitsk [216] experiments which constrained $m^{\rm eff}_{\nu_e} < 2.2$ eV at 95% CL. KATRIN continues running with an estimated sensitivity limit of $m^{\rm eff}_{\nu_e} \sim 0.2$ eV. Project 8 is exploring a new technique for β-spectrometry based on cyclotron radiation [217].

An alternative isotope to Tritium is ^{163}Ho [218] which presents the advantage of a smaller $Q = 2.8$ KeV. It decays via electron-capture to ^{163}Dy. Currently, there are three experiments exploring this decay to probe the neutrino mass: ECHo [219], HOLMES [220], and NuMECS [221]. These experiments are complementary to tritium-based searches from a technical point-of-view. Also the decay of ^{163}Ho determines the effective electron neutrino mass as opposed to anti-neutrino in Tritium.

For the other flavours the present limits compiled in the listing section of the PDG read

$$m^{\rm eff}_{\nu_\mu} < 190 \text{ keV (90\% CL)} \quad \text{from} \quad \pi^- \rightarrow \mu^- + \bar{\nu}_\mu\,, \tag{14.92}$$

$$m^{\rm eff}_{\nu_\tau} < 18.2 \text{ MeV (95\% CL)} \quad \text{from} \quad \tau^- \rightarrow n\pi + \nu_\tau\,. \tag{14.93}$$

In the presence of mixing and for neutrinos with small mass differences the distortion of the beta spectrum is given by the sum of the individual spectra generated incoherently by each neutrino massive state weighted with the relevant mixing matrix element squared [222]:

$$\frac{dN}{dE} = R(E)\sum_i |U_{ei}|^2 \sqrt{(E_0-E)^2 - m_i^2}\,\Theta(E_0 - E - m_i)\,. \tag{14.94}$$

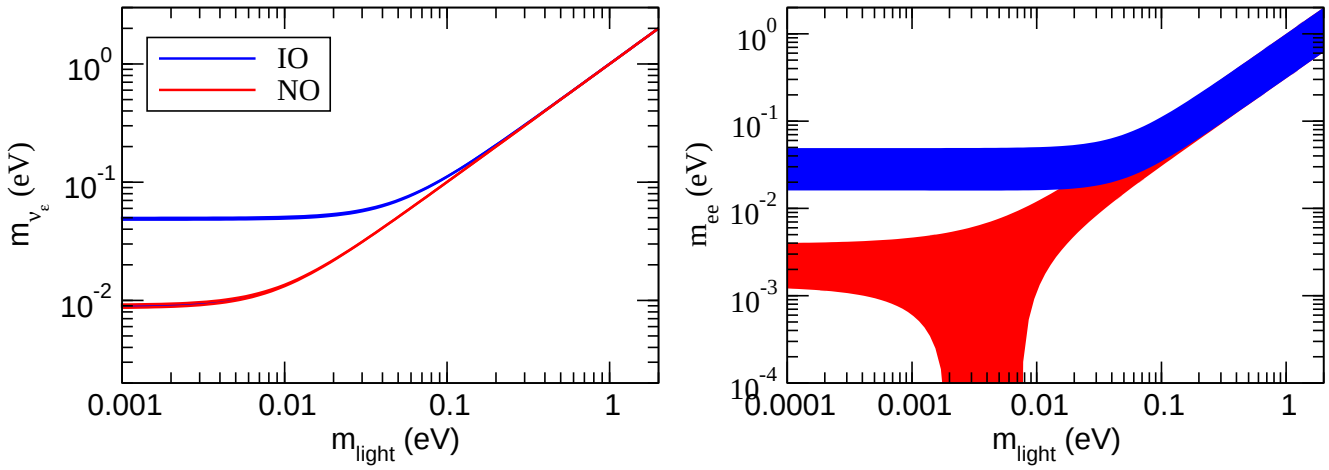

Figure 14.11: Allowed 95% CL ranges (1 dof) for the neutrino mass observable determined in ^{3}H beta decay (left panel) and in $0\nu\beta\beta$ (right panel) in the framework of 3ν mixing as a function of the lightest neutrino mass. The ranges are obtained by projecting the results of the global analysis of oscillation data (w/o SK-atm) in Ref. [187]. The region for each ordering is defined with respect to its local minimum.

The step function, $\Theta(E_0 - E - m_i)$ arises because a neutrino with a given mass m_i can only be produced if the available energy is larger than its mass. Equation (14.94) shows the two main effects of the neutrino masses and mixings on the electron energy spectrum: First kinks appear at the electron energies $E_e^{(i)} = E \sim E_0 - m_i$ with sizes that are determined by $|U_{ei}|^2$. Second the end point shifts to $E_{\rm ep} = E_0 - m_0$, where m_0 is the lightest neutrino mass. Corrections are induced once the the energy resolution of the experiment is considered [223, 224]

In the 3-ν mixing scenario the distortion of the spectrum can still be effectively described by a single parameter – which we will still denote as m_{ν_e} – if for all neutrino states $E_0 - E = Q - T \gg m_i$. In this case one can expand Eq.(14.94) as:

$$\frac{dN}{dE} \simeq R(E) \sum_i |U_{ei}|^2 \sqrt{(E_0 - E)^2 - (m_{\nu_e}^{\rm eff})^2}\,, \qquad (14.95)$$

with

$$(m_{\nu_e}^{\rm eff})^2 = \frac{\sum_i m_i^2 |U_{ei}|^2}{\sum_i |U_{ei}|^2} = \sum_i m_i^2 |U_{ei}|^2\,, \qquad (14.96)$$

where unitarity is assumed in the second equality. In this approximation the distortion of the end point of the spectrum is described by a single parameter, and with the present results from KATRIN it is bounded to be

$$1.1 \text{ eV} \geq m_{\nu_e}^{\rm eff} = \sqrt{\sum_i m_i^2 |U_{ei}|^2} = \begin{cases} \sqrt{m_0^2 + \Delta m_{21}^2 (1 - c_{13}^2 c_{12}^2) + \Delta m_{32}^2 s_{13}^2} & \text{in NO}\,, \\ \sqrt{m_0^2 + \Delta m_{21}^2 c_{13}^2 c_{12}^2 - \Delta m_{32}^2 c_{13}^2} & \text{in IO}\,, \end{cases} \qquad (14.97)$$

where $m_0 = m_1$ (m_3) is the lightest neutrino mass in NO (IO) spectrum. Correspondingly the bounds in Eqs.(14.92) and (14.93) apply to the combinations $\sum_i m_i^2 |U_{\alpha i}|^2$ for $\alpha = \mu$ and τ respectively. So with the values known of the mixing matrix elements the strongest constraint on the absolute value of the neutrino mass comes from Tritium beta decay.

From Eq.(14.97) we see that, given the present knowledge of the neutrino mass differences and their mixing from oscillation experiments, it is possible to translate the experimental information of m_{ν_e} on a corresponding range for the lightest neutrino mass and that such relation depends on the ordering of the states. We plot in Fig.14.11 the recasting of the allowed regions of the analysis in Ref. [187] in terms of the allowed range m_{ν_e} as a function of $m_{\rm light} \equiv m_0$. In particular one finds that the results of oscillation experiments imply a lower bound on $m_{\nu_e} > 0.048$ (0.0085) eV for IO (NO) at 95% CL.

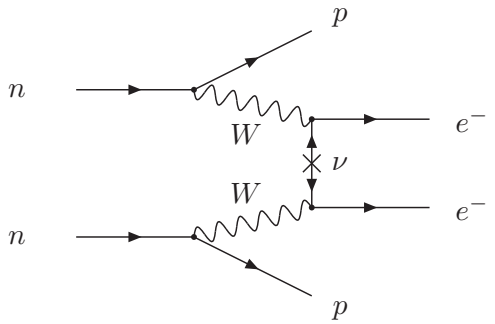

Figure 14.12: Feynman diagram for neutrinoless double-beta decay.

14.9.2 *Dirac vs Majorana: Neutrinoless Double-beta Decay*

The most sensitive probe to whether neutrinos are Dirac or Majorana states is the neutrinoless double beta decay ($0\nu\beta\beta$):

$$(A, Z) \to (A, Z + 2) + e^- + e^-. \qquad (14.98)$$

In the presence of neutrino masses and mixing the process in Eq.(14.98) can be generated at lower order in perturbation theory by the term represented in Fig.14.12. The corresponding amplitude is proportional to the product of the two leptonic currents

$$M_{\alpha\beta} \propto [\bar{e}\gamma_\alpha(1 - \gamma_5)\nu_e] \left[\bar{e}\gamma_\beta(1 - \gamma_5)\nu_e\right] \propto \sum_i (U_{ei})^2 [\bar{e}\gamma_\alpha(1 - \gamma_5)\nu_i] \left[\bar{e}\gamma_\beta(1 - \gamma_5)\nu_i\right]\,. \qquad (14.99)$$

The neutrino propagator in Fig.14.12 can only arise from the contraction $\langle 0 \,|\, \nu_i(x)\nu_i(y)^T \,|\, 0\rangle$. But if the neutrino is a Dirac particle ν_i field annihilates a neutrino states and creates an antineutrino state which are different, so the contraction $\langle 0 \,|\, \nu_i(x)\nu_i(y)^T \,|\, 0\rangle = 0$ and $M_{\alpha\beta} = 0$. On the other hand, if ν_i is a Majorana particle, neutrino and antineutrino are described by the same field and $\langle 0 \,|\, \nu_i(x)\nu_i(y)^T \,|\, 0\rangle \neq 0$.

The conclusion is that in order to induce the $0\nu\beta\beta$ decay, neutrinos must be Majorana particles. This is consistent with the fact that the process (14.98) violates total lepton number by two

units. Conversely, if $0\nu\beta\beta$ decay is observed, massive neutrinos cannot be Dirac states [225].

It is important to stress that neutrinoless double beta decay could be dominantly induced by other new physics effects beyond that of Majorana neutrino masses, Consequently the connection between the observation or limitation of the neutrinoless double beta decay and the neutrino mass can only be made under some assumption about the source of total lepton number violation in the model.

The observable determined by the experiments is the half-life of the decay. Under the assuption that the Majorana neutrino mass is the only source of lepton number violation at low energies, the decay half-life is given by:

$$(T^{0\nu}_{1/2})^{-1} = G^{0\nu} \left| M^{0\nu} \right|^2 \left(\frac{m_{ee}}{m_e} \right)^2 , \tag{14.100}$$

where $G^{0\nu}$ is the phase space integral taking into account the final atomic state, $|M^{0\nu}|$ is the nuclear matrix element of the transition, and m_{ee} is the *effective Majorana mass of* ν_e,

$$m_{ee} = \left| \sum_i m_i U^2_{ei} \right|$$
$$= \begin{cases} \left| m_0 c^2_{12} c^2_{13} + \sqrt{\Delta m^2_{21} + m^2_0}\, s^2_{12} c^2_{13} e^{2i(\eta_2 - \eta_1)} + \sqrt{\Delta m^2_{32} + \Delta m^2_{21} + m^2_0}\, s^2_{13} e^{-2i(\delta_{\rm CP} + \eta_1)} \right| & \text{in NO}\,, \\ \left| m_0 s^2_{13} + \sqrt{m^2_0 - \Delta m^2_{32}}\, s^2_{12} c^2_{13} e^{2i(\eta_2 + \delta_{\rm CP})} + \sqrt{m^2_0 - \Delta m^2_{32} - \Delta m^2_{21}}\, c^2_{12} c^2_{13} e^{2i(\eta_1 + \delta_{\rm CP})} \right| & \text{in IO}\,, \end{cases}$$

which, in addition to the masses and mixing parameters that affect the tritium beta decay spectrum, depends also on the leptonic CP violating phases. We plot in Fig.14.11 the the recasting of the allowed regions of the analysis in Ref. [187] in terms of the allowed range m_{ee} as a function of $m_{\rm light} \equiv m_0$ for the two orderings. As a consquence of the dependence on the unknown Majorana phases, the allowed range of m_{ee} for a given value of $m_{\rm light}$ and ordering is substantially broader than that of m_{ν_e}. Nevertheless, the results of oscillation experiments imply a lower bound on the effective Majorana mass for the IO, which at 95%CL reads $m_{ee} > 0.016$ eV.

From Eq.(14.100) we see that nuclear structure details enter relation between the decay rate (or lifetime) and the effective Majorana mass. As a consequence uncertainties in the nuclear structure calculations result in a spread of m_{ee} values for a given $T^{0\nu}_{1/2}$ by a factor of 2–3 [226].

We present in Sec.14.9.3 a brief description of the experimental searches for neutrinoless double-beta decay. At the time of writing of this review the strongest bound on $0\nu\beta\beta$ decay lifetime comes from the search in KamLAND-Zen experiment [227] (see Sec.14.9.3) which uses 13 Tons of Xe-loaded liquid scintillator to search for the decay $0\nu\beta\beta$ of ^{136}Xe and has set a bound on the half-life of $T^{0\nu}_{1/2} > 1.07 \times 10^{26}$ yr at 90% CL. Using a variety of nuclear matrix element calculations, the corresponding upper bound on the effective Majorana mass is

$$m_{ee} < 61 - 165 \text{ meV} . \tag{14.101}$$

14.9.3 *Experimental Search for Neutrinoless Double-beta Decay*

The signature of $0\nu\beta\beta$ is that the sum of energy of two electrons is equal to the Q-value of the nuclear transition. Various requirements must be met to achieve high sensitivity such as a large source mass with isotopic enrichment, underground location to shield cosmic-ray induced background, and ultra-low background techniques to reduce radioactive background. The sensitivity to the half-life is proportional to $\varepsilon M t$ in the case of a background-free measurement and $\varepsilon \sqrt{\frac{Mt}{b\Delta E}}$ for the case background exists, where ε is the detection efficiency of the signal, M is the source mass, t is the measurement time, b is the background rate, and ΔE is the energy resolution.

There are 35 candidate nuclei for double-beta decay. Currently, experiments using ^{136}Xe and ^{76}Ge have reported the most sensitive results of $0\nu\beta\beta$ search. Because of the uncertainties related to the nuclear matrix element, complementarity of technologies, different background, and the investigation of the mechanism behind the $0\nu\beta\beta$ in case of a positive signal, it is important to pursue the searches with various isotopes.

The energy from electrons is measured with either ionization, scintillation, or through phonons. In some experiments a combination of two techniques is used. Among those using ionization detection, ultra-high-purity germanium detector provides the best sensitivity thanks to high energy resolution and low background. GERDA uses total 20.0 kg of broad energy germanium (BEGe) and 15.6 kg of coaxial detectors, both enriched in ^{76}Ge, for the second phase. Background levels of $(5.6^{+3.4}_{-2.4}) \times 10^{-4}$ counts/(keV·kg·year) for BEGe detectors and $(5.7^{+4.1}_{-2.6}) \times 10^{-4}$ counts/(keV·kg·year) for coaxial detectors have been achieved [228], which enable a background-free search. The Majorana-Demonstrator [229] consists of 44.1 kg of Ge (29.7 kg enriched to 88% in ^{76}Ge) detectors split between two modules. It has achieved energy resolution of 2.5 keV FWHM at the Q-value (2.039 MeV).

Liquid scintillator detectors have simple structure and can utilize existing large detectors with low background environments. By adding an inner balloon to contain xenon-loaded liquid scintillator to the KamLAND detector, KamLAND-Zen used 380 kg of xenon with 90.1% enrichment in ^{136}Xe. Reducing the background level by purification of scintillator, KamLAND-Zen reported the half-life limit above 10^{26} years at 90% CL [227]. The SNO detector has been also upgraded to be filled with liquid scintillator in SNO+ experiment [230]. The SNO+ detector will be loaded with 0.5% natural tellurium, corresponding to approximately 1330 kg of ^{130}Te to search for $0\nu\beta\beta$.

With a time projection chamber, one can utilize both ionization and scintillation. EXO-200 uses a liquid xenon time projection chamber with enrichment to 80.6%, corresponding to 74.7 kg of ^{136}Xe in the fiducial mass [231]. An energy resolution of 1.15% (σ/E) is achieved at the Q-value of ^{136}Xe $0\nu\beta\beta$. The NEXT collaboration has been developing a high-pressure xenon gas time projection chamber with electroluminescent amplification and optical readouts. An energy resolution of 1% FWHM at the Q-value of ^{136}Xe $0\nu\beta\beta$ is demonstrated with NEXT-White detector [232].

CUORE uses cryogenic bolometer to measure the energy in a calorimetric way. The detector is located in Gran Sasso and composed of 988 TeO_2 bolometers for a total mass of 742 kg, corresponding to 206 kg of ^{130}Te. An effective energy resolution of (7.7±0.5) keV FWHM is achieved for the first result [233]. For further reduction of background towards future search based on the CUORE technology, CUPID proposes to simultaneously measure the calorimetric signal and the scintillation light. Using the prototype CUPID-0, the technology is demonstrated and also $0\nu\beta\beta$ is searched for with ^{82}Se [234].

AMoRE also uses the simultaneous detection of heat and scintillation. Six ^{100}Mo-enriched and ^{48}Ca-depleted $CaMoO_4$ crystals with a total mass of 1.9 kg (AMoRE-Pilot) are operated in Yangyang underground laboratory located in South Korea, searching for $0\nu\beta\beta$ of ^{100}Mo [235].

A tracker-calorimeter technique is employed in NEMO. Source isotopes are hosted in thin foils surrounded by a tracking detector, which in turn is surrounded by a calorimeter. Full topological event reconstruction with this configuration enables background rejection and gives additional information after discovery. The

NEMO-3 experiment used 7 isotopes, with the largest mass comprised of ^{100}Mo (7 kg) [236]. NEMO-3 also reported a first search for neutrinoless quadruple-β decay of ^{150}Nd [237].

References

[1] J. N. Bahcall, *NEUTRINO ASTROPHYSICS* (1989), ISBN 9780521379755.

[2] R. N. Mohapatra and P. B. Pal, World Sci. Lect. Notes Phys. **60**, 1 (1998), [World Sci. Lect. Notes Phys.72,1(2004)].

[3] C. W. Kim and A. Pevsner, Contemp. Concepts Phys. **8**, 1 (1993).

[4] B. Kayser, F. Gibrat-Debu and F. Perrier, World Sci. Lect. Notes Phys. **25**, 1 (1989).

[5] C. Giunti and C. W. Kim, *Fundamentals of Neutrino Physics and Astrophysics* (2007), ISBN 9780198508717.

[6] M. C. Gonzalez-Garcia and Y. Nir, Rev. Mod. Phys. **75**, 345 (2003), [hep-ph/0202058].

[7] M. C. Gonzalez-Garcia and M. Maltoni, Phys. Rept. **460**, 1 (2008), [arXiv:0704.1800].

[8] A. Pilaftsis, Z. Phys. **C55**, 275 (1992), [hep-ph/9901206].

[9] P. Minkowski, Phys. Lett. **67B**, 421 (1977).

[10] P. Ramond, in "International Symposium on Fundamentals of Quantum Theory and Quantum Field Theory Palm Coast, Florida, February 25-March 2, 1979," 265–280 (1979), [hep-ph/9809459].

[11] M. Gell-Mann, P. Ramond and R. Slansky, Conf. Proc. **C790927**, 315 (1979), [arXiv:1306.4669].

[12] T. Yanagida, Conf. Proc. **C7902131**, 95 (1979).

[13] R. N. Mohapatra and G. Senjanovic, Phys. Rev. Lett. **44**, 912 (1980), [,231(1979)].

[14] J. Schechter and J. W. F. Valle, Phys. Rev. **D21**, 309 (1980).

[15] J. Schechter and J. W. F. Valle, Phys. Rev. **D22**, 2227 (1980).

[16] J. Schechter and J. W. F. Valle, Phys. Rev. **D24**, 1883 (1981), [Erratum: Phys. Rev.D25,283(1982)].

[17] Z. Maki, M. Nakagawa and S. Sakata, Prog. Theor. Phys. **28**, 870 (1962), [,34(1962)].

[18] Y. Katayama *et al.*, Prog. Theor. Phys. **28**, 675 (1962).

[19] B. Pontecorvo, Sov. Phys. JETP **26**, 984 (1968), [Zh. Eksp. Teor. Fiz.53,1717(1967)].

[20] N. Cabibbo, Phys. Rev. Lett. **10**, 531 (1963), [,648(1963)].

[21] M. Kobayashi and T. Maskawa, Prog. Theor. Phys. **49**, 652 (1973).

[22] S. Antusch *et al.*, JHEP **10**, 084 (2006), [hep-ph/0607020].

[23] S. Antusch and O. Fischer, JHEP **10**, 094 (2014), [arXiv:1407.6607].

[24] V. N. Gribov and B. Pontecorvo, Phys. Lett. **28B**, 493 (1969).

[25] E. Akhmedov, in "International Conference on History of the Neutrino: 1930-2018 Paris, France, September 5-7, 2018," (2019), [arXiv:1901.05232].

[26] L. Wolfenstein, Phys. Rev. **D17**, 2369 (1978), [,294(1977)].

[27] A. Halprin, Phys. Rev. **D34**, 3462 (1986).

[28] A. J. Baltz and J. Weneser, Phys. Rev. **D37**, 3364 (1988).

[29] P. D. Mannheim, Phys. Rev. **D37**, 1935 (1988).

[30] L. Landau, Phys. Z. Sov. **2**, 46 (1932).

[31] C. Zener, Proc. Roy. Soc. Lond. **A137**, 696 (1932).

[32] E. Majorana, Nuovo Cim. **9**, 43 (1932).

[33] E. C. G. Stueckelberg, Helv. Phys. Acta **5**, 369 (1932).

[34] T.-K. Kuo and J. T. Pantaleone, Rev. Mod. Phys. **61**, 937 (1989).

[35] S. J. Parke, Phys. Rev. Lett. **57**, 1275 (1986), [,328(1986)].

[36] W. C. Haxton, Phys. Rev. Lett. **57**, 1271 (1986), [,332(1986)].

[37] S. T. Petcov, Phys. Lett. **B191**, 299 (1987), [,427(1987)].

[38] S. P. Mikheyev and A. Yu. Smirnov, Sov. J. Nucl. Phys. **42**, 913 (1985), [,305(1986)].

[39] J. N. Bahcall *et al.*, Rev. Mod. Phys. **54**, 767 (1982).

[40] J. N. Bahcall, A. M. Serenelli and S. Basu, Astrophys. J. **621**, L85 (2005), [arXiv:astro-ph/0412440].

[41] A. M. Serenelli, W. C. Haxton and C. Pena-Garay, Astrophys. J. **743**, 24 (2011), [arXiv:1104.1639].

[42] F. L. Villante, Phys. Lett. **B742**, 279 (2015), [arXiv:1410.2796].

[43] A. Serenelli, Eur. Phys. J. **A52**, 4, 78 (2016), [arXiv:1601.07179].

[44] R. Davis, Jr., D. S. Harmer and K. C. Hoffman, Phys. Rev. Lett. **20**, 1205 (1968).

[45] B. T. Cleveland *et al.*, Astrophys. J. **496**, 505 (1998).

[46] C. Pena-Garay and A. Serenelli (2008), [arXiv:0811.2424].

[47] J. N. Abdurashitov *et al.* (SAGE), J. Exp. Theor. Phys. **95**, 181 (2002), [Zh. Eksp. Teor. Fiz.122,211(2002)], [arXiv:astro-ph/0204245].

[48] W. Hampel *et al.* (GALLEX), Phys. Lett. **B447**, 127 (1999).

[49] M. Altmann *et al.* (GNO), Phys. Lett. **B616**, 174 (2005), [hep-ex/0504037].

[50] J. N. Abdurashitov *et al.* (SAGE), Phys. Rev. **C80**, 015807 (2009), [arXiv:0901.2200].

[51] K. S. Hirata *et al.* (Kamiokande-II), Phys. Rev. Lett. **63**, 16 (1989).

[52] K. S. Hirata *et al.* (Kamiokande-II), Phys. Rev. **D44**, 2241 (1991), [Erratum: Phys. Rev.D45,2170(1992)].

[53] Y. Fukuda *et al.* (Kamiokande), Phys. Rev. Lett. **77**, 1683 (1996).

[54] Y. Fukuda *et al.* (Super-Kamiokande), Phys. Rev. Lett. **81**, 1158 (1998), [Erratum: Phys. Rev. Lett.81,4279(1998)], [hep-ex/9805021].

[55] Y. Fukuda *et al.* (Super-Kamiokande), Phys. Rev. Lett. **82**, 2430 (1999), [hep-ex/9812011].

[56] K. Abe *et al.* (Super-Kamiokande), Phys. Rev. **D94**, 5, 052010 (2016), [arXiv:1606.07538].

[57] N. Vinyoles *et al.*, Astrophys. J. **835**, 2, 202 (2017), [arXiv:1611.09867].

[58] S. Fukuda *et al.* (Super-Kamiokande), Phys. Rev. Lett. **86**, 5651 (2001), [hep-ex/0103032].

[59] S. Fukuda *et al.* (Super-Kamiokande), Phys. Rev. Lett. **86**, 5656 (2001), [hep-ex/0103033].

[60] B. Aharmim *et al.* (SNO), Phys. Rev. **C72**, 055502 (2005), [arXiv:nucl-ex/0502021].

[61] S. Fukuda *et al.* (Super-Kamiokande), Phys. Lett. **B539**, 179 (2002), [hep-ex/0205075].

[62] Q. R. Ahmad *et al.* (SNO), Phys. Rev. Lett. **87**, 071301 (2001), [arXiv:nucl-ex/0106015].

[63] Q. R. Ahmad *et al.* (SNO), Phys. Rev. Lett. **89**, 011301 (2002), [arXiv:nucl-ex/0204008].

[64] B. Aharmim *et al.* (SNO), Phys. Rev. **C88**, 025501 (2013), [arXiv:1109.0763].

[65] J. Bergstrom *et al.*, JHEP **03**, 132 (2016), [arXiv:1601.00972].

[66] C. Arpesella *et al.* (Borexino), Phys. Lett. **B658**, 101 (2008), [arXiv:0708.2251].

[67] G. Bellini *et al.* (Borexino), Phys. Rev. Lett. **108**, 051302 (2012), [arXiv:1110.3230].

[68] M. Agostini *et al.* (BOREXINO), Nature **562**, 7728, 505 (2018).

[69] G. Bellini *et al.* (Borexino), Phys. Rev. **D82**, 033006 (2010), [arXiv:0808.2868].

[70] S. Abe *et al.* (KamLAND), Phys. Rev. **C84**, 035804 (2011), [arXiv:1106.0861].

[71] A. Gando *et al.* (KamLAND), Phys. Rev. **C92**, 5, 055808 (2015), [arXiv:1405.6190].

[72] M. Agostini *et al.* (Borexino) (2017), [arXiv:1707.09279].

[73] M. Agostini *et al.* (Borexino) (2017), [arXiv:1709.00756].

[74] A. Renshaw *et al.* (Super-Kamiokande), Phys. Rev. Lett. **112**, 9, 091805 (2014), [arXiv:1312.5176].

[75] M. Honda *et al.*, Phys. Rev. **D92**, 2, 023004 (2015), [arXiv:1502.03916].

[76] G. D. Barr *et al.*, Phys. Rev. **D74**, 094009 (2006), [arXiv:astro-ph/0611266].

[77] G. Battistoni *et al.*, Astropart. Phys. **19**, 269 (2003), [Erratum: Astropart. Phys.19,291(2003)], [hep-ph/0207035].

[78] J. Evans *et al.*, Phys. Rev. **D95**, 2, 023012 (2017), [arXiv:1612.03219].

[79] C. V. Achar *et al.*, Phys. Lett. **18**, 196 (1965).

[80] F. Reines *et al.*, Phys. Rev. Lett. **15**, 429 (1965).

[81] K. S. Hirata *et al.* (Kamiokande-II), Phys. Lett. **B205**, 416 (1988), [,447(1988)].

[82] D. Casper *et al.*, Phys. Rev. Lett. **66**, 2561 (1991).

[83] K. Daum *et al.* (Frejus), Z. Phys. **C66**, 417 (1995).

[84] M. Aglietta *et al.* (NUSEX), Europhys. Lett. **8**, 611 (1989).

[85] K. S. Hirata *et al.* (Kamiokande-II), Phys. Lett. **B280**, 146 (1992).

[86] Y. Fukuda *et al.* (Kamiokande), Phys. Lett. **B335**, 237 (1994).

[87] Y. Fukuda *et al.* (Super-Kamiokande), Phys. Rev. Lett. **81**, 1562 (1998), [hep-ex/9807003].

[88] M. Ambrosio *et al.* (MACRO), Phys. Lett. **B517**, 59 (2001), [hep-ex/0106049].

[89] M. C. Sanchez *et al.* (Soudan 2), Phys. Rev. **D68**, 113004 (2003), [hep-ex/0307069].

[90] Y. Ashie *et al.* (Super-Kamiokande), Phys. Rev. Lett. **93**, 101801 (2004), [hep-ex/0404034].

[91] Z. Li *et al.* (Super-Kamiokande), Phys. Rev. **D98**, 5, 052006 (2018), [arXiv:1711.09436].

[92] N. Agafonova *et al.* (OPERA), Phys. Rev. Lett. **120**, 21, 211801 (2018), [Erratum: Phys. Rev. Lett.121,no.13,139901(2018)], [arXiv:1804.04912].

[93] M. G. Aartsen *et al.* (IceCube), Phys. Rev. **D99**, 3, 032007 (2019), [arXiv:1901.05366].

[94] K. Abe *et al.* (Super-Kamiokande), Phys. Rev. **D97**, 7, 072001 (2018), [arXiv:1710.09126].

[95] M. Ageron *et al.* (ANTARES), Nucl. Instrum. Meth. **A656**, 11 (2011), [arXiv:1104.1607].

[96] M. G. Aartsen *et al.* (IceCube), JINST **12**, 03, P03012 (2017), [arXiv:1612.05093].

[97] A. Albert *et al.* (ANTARES), JHEP **06**, 113 (2019), [arXiv:1812.08650].

[98] M. G. Aartsen *et al.* (IceCube), Phys. Rev. Lett. **120**, 7, 071801 (2018), [arXiv:1707.07081].

[99] S. Adrian-Martinez *et al.* (KM3Net), J. Phys. **G43**, 8, 084001 (2016), [arXiv:1601.07459].

[100] M. G. Aartsen *et al.* (IceCube), J. Phys. **G44**, 5, 054006 (2017), [arXiv:1607.02671].

[101] S. Ahmed *et al.* (ICAL), Pramana **88**, 5, 79 (2017), [arXiv:1505.07380].

[102] K. Abe *et al.* (Hyper-Kamiokande) (2018), [arXiv:1805.04163].

[103] B. Abi *et al.* (DUNE) (2018), [arXiv:1807.10334].

[104] S. E. Kopp, Phys. Rept. **439**, 101 (2007), [arXiv:physics/0609129].

[105] D. Beavis *et al.* (E899) (1995).

[106] M. G. Catanesi *et al.* (HARP), Nucl. Instrum. Meth. **A571**, 527 (2007).

[107] J. M. Paley *et al.* (MIPP), Phys. Rev. **D90**, 3, 032001 (2014), [arXiv:1404.5882].

[108] N. Abgrall *et al.* (NA61), JINST **9**, P06005 (2014), [arXiv:1401.4699].

[109] S. H. Ahn *et al.* (K2K), Phys. Lett. **B511**, 178 (2001), [hep-ex/0103001].

[110] M. H. Ahn *et al.* (K2K), Phys. Rev. **D74**, 072003 (2006), [hep-ex/0606032].

[111] D. G. Michael *et al.* (MINOS), Nucl. Instrum. Meth. **A596**, 190 (2008), [arXiv:0805.3170].

[112] P. Adamson *et al.*, Nucl. Instrum. Meth. **A806**, 279 (2016), [arXiv:1507.06690].

[113] P. Adamson *et al.* (MINOS), Phys. Rev. Lett. **110**, 25, 251801 (2013), [arXiv:1304.6335].

[114] P. Adamson *et al.* (MINOS), Phys. Rev. Lett. **112**, 191801 (2014), [arXiv:1403.0867].

[115] P. Adamson *et al.* (MINOS), Phys. Rev. **D86**, 052007 (2012), [arXiv:1208.2915].

[116] P. Adamson *et al.* (MINOS+), Phys. Rev. Lett. **122**, 9, 091803 (2019), [arXiv:1710.06488].

[117] C. Rubbia *et al.*, JINST **6**, P07011 (2011), [arXiv:1106.0975].

[118] K. Abe *et al.* (T2K), Phys. Rev. Lett. **107**, 041801 (2011), [arXiv:1106.2822].

[119] K. Abe *et al.* (T2K), Phys. Rev. Lett. **112**, 061802 (2014), [arXiv:1311.4750].

[120] K. Abe *et al.* (T2K), Phys. Rev. Lett. **121**, 17, 171802 (2018), [arXiv:1807.07891].

[121] K. Abe *et al.* (T2K) (2019), [arXiv:1910.03887].

[122] P. Adamson *et al.* (NOvA), Phys. Rev. Lett. **118**, 15, 151802 (2017), [arXiv:1701.05891].

[123] M. A. Acero *et al.* (NOvA), Phys. Rev. **D98**, 032012 (2018), [arXiv:1806.00096].

[124] P. Adamson *et al.* (NOvA), Phys. Rev. Lett. **116**, 15, 151806 (2016), [arXiv:1601.05022].

[125] P. Adamson *et al.* (NOvA), Phys. Rev. Lett. **118**, 23, 231801 (2017), [arXiv:1703.03328].

[126] M. A. Acero *et al.* (NOvA), Phys. Rev. Lett. **123**, 151803 (2019), [arXiv:1906.04907].

[127] A. Aguilar-Arevalo *et al.* (LSND), Phys. Rev. **D64**, 112007 (2001), [hep-ex/0104049].

[128] B. Armbruster *et al.* (KARMEN), Phys. Rev. **D65**, 112001 (2002), [hep-ex/0203021].

[129] A. A. Aguilar-Arevalo *et al.* (MiniBooNE), Phys. Rev. Lett. **121**, 22, 221801 (2018), [arXiv:1805.12028].

[130] M. Antonello *et al.* (MicroBooNE, LAr1-ND, ICARUS-WA104) (2015), [arXiv:1503.01520].

[131] S. Ajimura *et al.* (2017), [arXiv:1705.08629].

[132] F. Von Feilitzsch, A. A. Hahn and K. Schreckenbach, Phys. Lett. **118B**, 162 (1982).

[133] K. Schreckenbach *et al.*, Phys. Lett. **160B**, 325 (1985).

[134] A. A. Hahn *et al.*, Phys. Lett. **B218**, 365 (1989).

[135] P. Vogel *et al.*, Phys. Rev. **C24**, 1543 (1981).

[136] T. A. Mueller *et al.*, Phys. Rev. **C83**, 054615 (2011), [arXiv:1101.2663].

[137] P. Huber, Phys. Rev. **C84**, 024617 (2011), [Erratum: Phys. Rev.C85,029901(2012)], [arXiv:1106.0687].

[138] D. Adey *et al.* (Daya Bay), Phys. Rev. **D100**, 5, 052004 (2019), [arXiv:1808.10836].

[139] D. Adey *et al.* (Daya Bay), Phys. Rev. Lett. **121**, 24, 241805 (2018), [arXiv:1809.02261].

[140] G. Bak *et al.* (RENO), Phys. Rev. Lett. **121**, 20, 201801 (2018), [arXiv:1806.00248].

[141] H. de Kerret *et al.* (Double Chooz) (2019), [arXiv:1901.09445].

[142] Y. J. Ko *et al.* (NEOS), Phys. Rev. Lett. **118**, 12, 121802 (2017), [arXiv:1610.05134].

[143] F. P. An *et al.* (Daya Bay), Phys. Rev. Lett. **118**, 25, 251801 (2017), [arXiv:1704.01082].

[144] G. Bak *et al.* (RENO), Phys. Rev. Lett. **122**, 23, 232501 (2019), [arXiv:1806.00574].

[145] D. Adey *et al.* (Daya Bay), Phys. Rev. Lett. **123**, 11, 111801 (2019), [arXiv:1904.07812].

[146] M. Apollonio *et al.* (CHOOZ), Eur.Phys.J. **C27**, 331 (2003), [hep-ex/0301017].

[147] F. Boehm *et al.*, Phys. Rev. **D64**, 112001 (2001), [hep-ex/0107009].

[148] K. Eguchi *et al.* (KamLAND), Phys. Rev. Lett. **90**, 021802 (2003), [hep-ex/0212021].

[149] T. Araki *et al.* (KamLAND), Phys. Rev. Lett. **94**, 081801 (2005), [hep-ex/0406035].

[150] A. Gando *et al.* (KamLAND), Phys. Rev. **D88**, 3, 033001 (2013), [arXiv:1303.4667].

[151] F. Ardellier *et al.* (Double Chooz) (2006), [hep-ex/0606025].

[152] X. Guo *et al.* (Daya Bay) (2007), [hep-ex/0701029].

[153] J. K. Ahn *et al.* (RENO) (2010), [arXiv:1003.1391].

[154] Y. Abe *et al.* (Double Chooz), Phys. Rev. Lett. **108**, 131801 (2012), [arXiv:1112.6353].

[155] F. P. An *et al.* (Daya Bay), Phys. Rev. Lett. **108**, 171803 (2012), [arXiv:1203.1669].

[156] J. K. Ahn *et al.* (RENO), Phys. Rev. Lett. **108**, 191802 (2012), [arXiv:1204.0626].

[157] F. An *et al.* (JUNO), J. Phys. **G43**, 3, 030401 (2016), [arXiv:1507.05613].

[158] I. Alekseev *et al.* (DANSS), Phys. Lett. **B787**, 56 (2018), [arXiv:1804.04046].

[159] H. Almazán *et al.* (STEREO), Phys. Rev. Lett. **121**, 16, 161801 (2018), [arXiv:1806.02096].

[160] J. Ashenfelter *et al.* (PROSPECT), Phys. Rev. Lett. **121**, 25, 251802 (2018), [arXiv:1806.02784].

[161] A. P. Serebrov *et al.* (NEUTRINO-4), Pisma Zh. Eksp. Teor. Fiz. **109**, 4, 209 (2019), [JETP Lett.109,no.4,213(2019)], [arXiv:1809.10561].

[162] Y. Abreu *et al.* (SoLid), JINST **12**, 04, P04024 (2017), [arXiv:1703.01683].

[163] N. Cabibbo, Phys. Lett. **72B**, 333 (1978).

[164] S. M. Bilenky, J. Hosek and S. T. Petcov, Phys. Lett. **94B**, 495 (1980).

[165] V. D. Barger, K. Whisnant and R. J. N. Phillips, Phys. Rev. Lett. **45**, 2084 (1980).

[166] P. Langacker *et al.*, Nucl. Phys. **B282**, 589 (1987).

[167] S. Goswami and A. Yu. Smirnov, Phys. Rev. **D72**, 053011 (2005), [hep-ph/0411359].

[168] N. Okamura, Prog. Theor. Phys. **114**, 1045 (2006), [hep-ph/0411388].

[169] H. Nunokawa, S. J. Parke and R. Zukanovich Funchal, Phys. Rev. **D72**, 013009 (2005), [hep-ph/0503283].

[170] A. Cervera *et al.*, Nucl. Phys. **B579**, 17 (2000), [Erratum: Nucl. Phys.B593,731(2001)], [hep-ph/0002108].

[171] M. Freund, Phys. Rev. **D64**, 053003 (2001), [hep-ph/0103300].

[172] E. K. Akhmedov *et al.*, JHEP **04**, 078 (2004), [hep-ph/0402175].

[173] H. Minakata *et al.*, Phys. Rev. **D74**, 053008 (2006), [hep-ph/0607284].

[174] O. L. G. Peres and A. Yu. Smirnov, Nucl. Phys. **B680**, 479 (2004), [hep-ph/0309312].

[175] S. Petcov, Phys.Lett. **B434**, 321 (1998), [hep-ph/9805262].

[176] E. K. Akhmedov *et al.*, Nucl.Phys. **B542**, 3 (1999), [hep-ph/9808270].

[177] E. K. Akhmedov, Nucl.Phys. **B538**, 25 (1999), [hep-ph/9805272].

[178] M. Chizhov, M. Maris and S. Petcov (1998), [hep-ph/9810501].

[179] M. Chizhov and S. Petcov, Phys.Rev.Lett. **83**, 1096 (1999), [hep-ph/9903399].

[180] E. K. Akhmedov, M. Maltoni and A. Y. Smirnov, JHEP **0705**, 077 (2007), [hep-ph/0612285].

[181] C. Kim and U. Lee, Phys.Lett. **B444**, 204 (1998), [hep-ph/9809491].

[182] O. Peres and A. Y. Smirnov, Phys.Lett. **B456**, 204 (1999), [hep-ph/9902312].

[183] M. Gonzalez-Garcia, M. Maltoni and A. Y. Smirnov, Phys.Rev. **D70**, 093005 (2004), [hep-ph/0408170].

[184] E. K. Akhmedov, M. Maltoni and A. Y. Smirnov, JHEP **0806**, 072 (2008), [arXiv:0804.1466].

[185] J. Bernabeu, S. Palomares Ruiz and S. Petcov, Nucl.Phys. **B669**, 255 (2003), [hep-ph/0305152].

[186] S. Petcov and T. Schwetz, Nucl.Phys. **B740**, 1 (2006), [hep-ph/0511277].

[187] I. Esteban *et al.*, JHEP **01**, 106 (2019), [arXiv:1811.05487].

[188] I. Esteban *et al.*, "Nufit4.1 at nufit webpage," `http://www.nu-fit.org`.

[189] F. Capozzi *et al.*, Prog. Part. Nucl. Phys. **102**, 48 (2018), [arXiv:1804.09678].

[190] P. F. de Salas *et al.*, Phys. Lett. **B782**, 633 (2018), [arXiv:1708.01186].

[191] M. Friend, "Updated Results from the T2K Experiment with 3.13×10^{21} Protons on Target," (2019), KEK/J-PARC Physics seminar, January 10, 2019, URL `https://t2k.org/docs/talk/335/2019kekseminar`.

[192] C. Jarlskog, Phys. Rev. Lett. **55**, 1039 (1985).

[193] M. C. Gonzalez-Garcia, M. Maltoni and T. Schwetz, JHEP **11**, 052 (2014), [arXiv:1409.5439].

[194] Y. Farzan and A. Yu. Smirnov, Phys. Rev. **D65**, 113001 (2002), [hep-ph/0201105].

[195] A. Dueck, S. Petcov and W. Rodejohann, Phys. Rev. **D82**, 013005 (2010), [arXiv:1006.0227].

[196] A. Aguilar-Arevalo *et al.* (MiniBooNE) (2012), [arXiv:1207.4809].

[197] M. A. Acero, C. Giunti and M. Laveder, Phys. Rev. **D78**, 073009 (2008), [arXiv:0711.4222].

[198] C. Giunti and M. Laveder, Phys. Rev. **C83**, 065504 (2011), [arXiv:1006.3244].

[199] F. P. An *et al.* (Daya Bay), Phys. Rev. Lett. **116**, 6, 061801 (2016), [Erratum: Phys. Rev. Lett.118,no.9,099902(2017)], [arXiv:1508.04233].

[200] G. Mention *et al.*, Phys. Rev. **D83**, 073006 (2011), [arXiv:1101.2755].

[201] J. J. Gomez-Cadenas and M. C. Gonzalez-Garcia, Z. Phys. **C71**, 443 (1996), [hep-ph/9504246].

[202] M. Maltoni *et al.*, Nucl. Phys. **B643**, 321 (2002), [hep-ph/0207157].

[203] M. Dentler *et al.*, JHEP **08**, 010 (2018), [arXiv:1803.10661].

[204] C. Giunti and M. Laveder, Phys. Rev. **D84**, 093006 (2011), [arXiv:1109.4033].

[205] J. M. Conrad *et al.*, Adv. High Energy Phys. **2013**, 163897 (2013), [arXiv:1207.4765].

[206] J. Kopp *et al.*, JHEP **05**, 050 (2013), [arXiv:1303.3011].

[207] G. H. Collin *et al.*, Phys. Rev. Lett. **117**, 22, 221801 (2016), [arXiv:1607.00011].

[208] S. Gariazzo *et al.*, JHEP **06**, 135 (2017), [arXiv:1703.00860].

[209] A. Diaz *et al.* (2019), [arXiv:1906.00045].

[210] S. Böser *et al.* (2019), [arXiv:1906.01739].

[211] G. Karagiorgi *et al.*, Phys. Rev. **D75**, 013011 (2007), [Erratum: Phys. Rev.D80,099902(2009)], [hep-ph/0609177].

[212] M. Maltoni and T. Schwetz, Phys. Rev. **D76**, 093005 (2007), [arXiv:0705.0107].

[213] C. Giunti and M. Laveder, Phys. Rev. **D84**, 073008 (2011), [arXiv:1107.1452].

[214] M. Aker *et al.* (KATRIN) (2019), [arXiv:1909.06048].

[215] J. Bonn *et al.*, Nucl. Phys. Proc. Suppl. **91**, 273 (2001), [PoShep2001,192(2001)].

[216] V. M. Lobashev *et al.*, Nucl. Phys. Proc. Suppl. **91**, 280 (2001), [,280(2001)].

[217] B. Monreal and J. A. Formaggio, Phys. Rev. **D80**, 051301 (2009), [arXiv:0904.2860].

[218] A. De Rujula and M. Lusignoli, Phys. Lett. **118B**, 429 (1982).

[219] L. Gastaldo *et al.*, J. Low Temp. Phys. **176**, 5-6, 876 (2014), [arXiv:1309.5214].

[220] B. Alpert *et al.*, Eur. Phys. J. **C75**, 3, 112 (2015), [arXiv:1412.5060].

[221] M. P. Croce *et al.*, J. Low. Temp. Phys. **184**, 3-4, 958 (2016), [arXiv:1510.03874].

[222] R. E. Shrock, Phys. Lett. **96B**, 159 (1980).

[223] F. Vissani, Nucl. Phys. Proc. Suppl. **100**, 273 (2001), [,273(2000)], [hep-ph/0012018].

[224] Y. Farzan, O. L. G. Peres and A. Yu. Smirnov, Nucl. Phys. **B612**, 59 (2001), [hep-ph/0105105].

[225] J. Schechter and J. W. F. Valle, Phys. Rev. **D25**, 2951 (1982), [,289(1981)].

[226] J. Engel and J. Menendez, Rept. Prog. Phys. **80**, 4, 046301 (2017), [arXiv:1610.06548].

[227] A. Gando *et al.* (KamLAND-Zen), Phys. Rev. Lett. **117**, 8, 082503 (2016), [Addendum: Phys. Rev. Lett.117,no.10,109903(2016)], [arXiv:1605.02889].

[228] M. Agostini *et al.* (GERDA), Science **365**, 1445 (2019), [arXiv:1909.02726].

[229] S. I. Alvis *et al.* (Majorana) (2019), [arXiv:1902.02299].

[230] S. Andringa *et al.* (SNO+), Adv. High Energy Phys. **2016**, 6194250 (2016), [arXiv:1508.05759].

[231] G. Anton *et al.* (EXO-200) (2019), [arXiv:1906.02723].

[232] J. Renner *et al.* (NEXT), JINST **13**, 10, P10020 (2018), [arXiv:1808.01804].

[233] C. Alduino *et al.* (CUORE), Phys. Rev. Lett. **120**, 13, 132501 (2018), [arXiv:1710.07988].

[234] O. Azzolini *et al.* (CUPID), Phys. Rev. Lett. **123**, 3, 032501 (2019), [arXiv:1906.05001].

[235] V. Alenkov *et al.*, Eur. Phys. J. **C79**, 9, 791 (2019), [arXiv:1903.09483].

[236] R. Arnold *et al.* (NEMO-3), Phys. Rev. **D92**, 7, 072011 (2015), [arXiv:1506.05825].

[237] R. Arnold *et al.* (NEMO-3), Phys. Rev. Lett. **119**, 4, 041801 (2017), [arXiv:1705.08847].

15. Quark Model

Revised August 2019 by C. Amsler (Stefan Meyer Inst.), T. DeGrand (Colorado U., Boulder) and B. Krusche (Basel U.).

15.1 Quantum numbers of the quarks

Quantum chromodynamics (QCD) is the theory of strong interactions. QCD is a quantum field theory and its constituents are a set of fermions, the quarks, and gauge bosons, the gluons. Strongly interacting particles, the hadrons, are bound states of quark and gluon fields. As gluons carry no intrinsic quantum numbers beyond color charge, and because color is believed to be permanently confined, most of the quantum numbers of strongly interacting particles are given by the quantum numbers of their constituent quarks and antiquarks. The description of hadronic properties which strongly emphasizes the role of the minimum-quark-content part of the wave function of a hadron is generically called the quark model. It exists on many levels: from the simple, almost dynamics-free picture of strongly interacting particles as bound states of quarks and antiquarks, to more detailed descriptions of dynamics, either through models or directly from QCD itself. The different sections of this review survey the many approaches to the spectroscopy of strongly interacting particles which fall under the umbrella of the quark model.

Quarks are strongly interacting fermions with spin 1/2 and, by convention, positive parity. Antiquarks have negative parity. Quarks have the additive baryon number 1/3, antiquarks -1/3. Table 15.1 gives the other additive quantum numbers (flavors) for the three generations of quarks. They are related to the charge Q (in units of the elementary charge e) through the generalized Gell-Mann-Nishijima formula

$$\mathsf{Q} = \mathsf{I}_z + \frac{\mathcal{B} + \mathsf{S} + \mathsf{C} + \mathsf{B} + \mathsf{T}}{2} , \qquad (15.1)$$

where $\mathcal{B}$ is the baryon number. The convention is that the quark *flavor* (I_z, S, C, B, or T) has the same sign as its *charge* Q. With this convention, any flavor carried by a charged meson has

Table 15.1

	d	u	s	c	b	t
Q – electric charge	$-\frac{1}{3}$	$+\frac{2}{3}$	$-\frac{1}{3}$	$+\frac{2}{3}$	$-\frac{1}{3}$	$+\frac{2}{3}$
I – isospin	$\frac{1}{2}$	$\frac{1}{2}$	0	0	0	0
I_z – isospin z-component	$-\frac{1}{2}$	$+\frac{1}{2}$	0	0	0	0
S – strangeness	0	0	-1	0	0	0
C – charm	0	0	0	$+1$	0	0
B – bottomness	0	0	0	0	-1	0
T – topness	0	0	0	0	0	$+1$

the same sign as its charge, *e.g.*, the strangeness of the K^+ is $+1$, the bottomness of the B^+ is $+1$, and the charm and strangeness of the D_s^- are each -1. Antiquarks have the opposite flavor signs. The hypercharge is defined as

$$\mathsf{Y} = \mathcal{B} + \mathsf{S} - \frac{\mathsf{C} - \mathsf{B} + \mathsf{T}}{3} . \qquad (15.2)$$

Thus Y is equal to $\frac{1}{3}$ for the u and d quarks, $-\frac{2}{3}$ for the s quark, and 0 for all other quarks. More details and derivations on the quark structure of mesons and baryons can be found in Ref. [1].

15.2 Mesons

Mesons have baryon number $\mathcal{B} = 0$. In the quark model, they are $q\bar{q}'$ bound states of quarks q and antiquarks $\bar{q}'$ (the flavors of q and q' may be different). If the orbital angular momentum of the $q\bar{q}'$ state is ℓ, then the parity P is $(-1)^{\ell+1}$. The meson spin J is given by the usual relation $|\ell - s| \le J \le |\ell + s|$, where s is 0 (antiparallel quark spins) or 1 (parallel quark spins). The charge conjugation, or C-parity $C = (-1)^{\ell+s}$, is defined only for the $q\bar{q}$ states made of quarks and their own antiquarks. The C-parity can be generalized to the G-parity $G = (-1)^{I+\ell+s}$ for mesons made of quarks and their own antiquarks (isospin $\mathsf{I}_z = 0$), and for the charged $u\bar{d}$ and $d\bar{u}$ states (isospin $\mathsf{I} = 1$).

The mesons are classified in J^{PC} multiplets. The $\ell = 0$ states are the pseudoscalars (0^{-+}) and the vectors (1^{--}). The orbital excitations $\ell = 1$ are the scalars (0^{++}), the axial vectors (1^{++}) and (1^{+-}), and the tensors (2^{++}). Assignments for many of the known mesons are given in Tables 15.2, 15.3 and 15.4. Radial excitations are denoted by the principal quantum number n. The very short lifetime of the t quark makes it likely that bound-state hadrons containing t quarks and/or antiquarks do not exist.

States in the natural spin-parity series $P = (-1)^J$ must, according to the above, have $s = 1$ and hence, $CP = +1$. Thus, mesons with natural spin-parity and $CP = -1$ (0^{+-}, 1^{-+}, 2^{+-}, 3^{-+}, *etc.*) are forbidden in the $q\bar{q}'$ model. The $J^{PC} = 0^{--}$ state is forbidden as well. Mesons with such *exotic* quantum numbers may exist, but would lie outside the $q\bar{q}'$ model (see section below on exotic mesons).

Following SU(3), the nine possible $q\bar{q}'$ combinations containing the light u, d, and s quarks are grouped into an octet and a singlet of light quark mesons:

$$\mathbf{3} \otimes \bar{\mathbf{3}} = \mathbf{8} \oplus \mathbf{1} . \qquad (15.3)$$

A fourth quark such as charm c can be included by extending SU(3) to SU(4). However, SU(4) is badly broken owing to the much heavier c quark. Nevertheless, in an SU(4) classification, the sixteen mesons are grouped into a 15-plet and a singlet:

$$\mathbf{4} \otimes \bar{\mathbf{4}} = \mathbf{15} \oplus \mathbf{1} . \qquad (15.4)$$

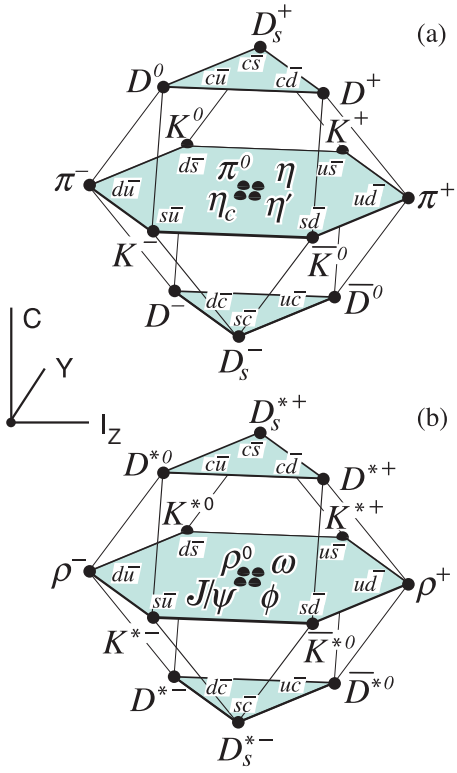

Figure 15.1: SU(4) weight diagram showing the 16-plets for the pseudoscalar (a) and vector mesons (b) made of the u, d, s, and c quarks as a function of isospin I_z, charm C, and hypercharge $\mathsf{Y} = \mathcal{B} + \mathsf{S} - \frac{\mathsf{C}}{3}$. The nonets of light mesons occupy the central planes to which the $c\bar{c}$ states have been added.

The *weight diagrams* for the ground-state pseudoscalar (0^{-+}) and vector (1^{--}) mesons are depicted in Fig. 15.1. The light quark mesons are members of nonets building the middle plane in Fig. 15.1(a) and (b).

Isoscalar states with the same J^{PC} mix, but mixing between the two light quark isoscalar mesons, and the much heavier charmonium or bottomonium states, are generally assumed to be negligible. In the following, we shall use the generic names a for the $\mathsf{I} = 1$, K for the $\mathsf{I} = 1/2$, and f and f' for the $\mathsf{I} = 0$ members of

Table 15.2: Suggested $q\bar{q}$ quark-model assignments for some of the observed light mesons. Mesons in bold face are included in the Meson Summary Table. The wave functions f and f' are given in the text (Eqn. 15.9). The singlet-octet mixing angles from the linear mass formula (15.12) and its quadratic version (in which the masses are squared) are also given for the well established nonets. The classification of the 0^{++} mesons is tentative: the light scalars $a_0(980)$, $f_0(980)$, $f_0(500)$ and $K_0^*(700)$ are often considered to be four-quark states, and are omitted from the table, see Eqn. (15.26) below. The isoscalar 0^{++} mesons $f_0(1370)$, $f_0(1500)$ (not shown) and $f_0(1710)$ are expected to mix, see the "Note on Non-$q\bar{q}$ mesons" and the "Note on Scalar Mesons below 2 GeV" in the Meson Listings for details. The isoscalar assignments in the 2^1S_0 (0^{-+}) nonet are also tentative. The $\eta(1405)$ (not shown) and $\eta(1475)$ may be manifestations of the same state, see the "Note on Pseudoscalar and Pseudovector Mesons in the 1400 MeV Region" in the Meson Listings.
† The $1^{+\pm}$ and $2^{-\pm}$ isospin $\frac{1}{2}$ states mix. In particular, the K_{1A} and K_{1B} are nearly equal (45°) mixtures of the $K_1(1270)$ and $K_1(1400)$ (see [2] and references therein).
‡ The physical vector mesons may be mixtures of 1^3D_1 and 2^3S_1 [3].

$n^{2s+1}\ell_J$	J^{PC}	I = 1 $u\bar{d}$, $\bar{u}d$, $\frac{1}{\sqrt{2}}(d\bar{d}-u\bar{u})$	I = $\frac{1}{2}$ $u\bar{s}$, $d\bar{s}$; $\bar{d}s$, $\bar{u}s$	I = 0 f'	I = 0 f	$\theta_{\rm quad}$ [°]	$\theta_{\rm lin}$ [°]
1^1S_0	0^{-+}	$\boldsymbol{\pi}$	$\boldsymbol{K}$	$\boldsymbol{\eta}$	$\boldsymbol{\eta'}(958)$	−11.3	−24.5
1^3S_1	1^{--}	$\boldsymbol{\rho(770)}$	$\boldsymbol{K^*(892)}$	$\boldsymbol{\phi(1020)}$	$\boldsymbol{\omega(782)}$	39.2	36.5
1^1P_1	1^{+-}	$\boldsymbol{b_1(1235)}$	$\boldsymbol{K_{1B}}$†	$\boldsymbol{h_1(1415)}$	$\boldsymbol{h_1(1170)}$		
1^3P_0	0^{++}	$\boldsymbol{a_0(1450)}$	$\boldsymbol{K_0^*(1430)}$	$\boldsymbol{f_0(1710)}$	$\boldsymbol{f_0(1370)}$		
1^3P_1	1^{++}	$\boldsymbol{a_1(1260)}$	$\boldsymbol{K_{1A}}$†	$\boldsymbol{f_1(1420)}$	$\boldsymbol{f_1(1285)}$		
1^3P_2	2^{++}	$\boldsymbol{a_2(1320)}$	$\boldsymbol{K_2^*(1430)}$	$\boldsymbol{f_2'(1525)}$	$\boldsymbol{f_2(1270)}$	29.6	28.0
1^1D_2	2^{-+}	$\boldsymbol{\pi_2(1670)}$	$\boldsymbol{K_2(1770)}$†	$\boldsymbol{\eta_2(1870)}$	$\boldsymbol{\eta_2(1645)}$		
1^3D_1	1^{--}	$\boldsymbol{\rho(1700)}$	$\boldsymbol{K^*(1680)}$‡		$\boldsymbol{\omega(1650)}$		
1^3D_2	2^{--}		$\boldsymbol{K_2(1820)}$†				
1^3D_3	3^{--}	$\boldsymbol{\rho_3(1690)}$	$\boldsymbol{K_3^*(1780)}$	$\boldsymbol{\phi_3(1850)}$	$\boldsymbol{\omega_3(1670)}$	31.8	30.8
1^3F_4	4^{++}	$\boldsymbol{a_4(1970)}$	$\boldsymbol{K_4^*(2045)}$	$f_4(2300)$	$\boldsymbol{f_4(2050)}$		
1^3G_5	5^{--}	$\rho_5(2350)$	$K_5^*(2380)$				
2^1S_0	0^{-+}	$\boldsymbol{\pi(1300)}$	$K(1460)$	$\boldsymbol{\eta(1475)}$	$\boldsymbol{\eta(1295)}$		
2^3S_1	1^{--}	$\boldsymbol{\rho(1450)}$	$\boldsymbol{K^*(1410)}$‡	$\boldsymbol{\phi(1680)}$	$\boldsymbol{\omega(1420)}$		
2^3P_1	1^{++}	$\boldsymbol{a_1(1640)}$					
2^3P_2	2^{++}	$\boldsymbol{a_2(1700)}$	$K_2^*(1980)$	$\boldsymbol{f_2(1950)}$	$f_2(1640)$		

Table 15.3: $c\bar{c}$ quark-model assignments for the charmonium and open charm mesons with established J^{PC}. Mesons in bold face are included in the Meson Summary Table. The open flavor states in the 1^{+-} and 1^{++} rows are mixtures of the $1^{+\pm}$ states.
† The masses are considerably smaller than most theoretical predictions.
These states have also been considered as four-quark states.
‡ Mixtures of the 1^3D_1 and 2^3S_1 states.

$n^{2s+1}\ell_J$	J^{PC}	I = 0 $c\bar{c}$	I = $\frac{1}{2}$ $c\bar{u}$, $c\bar{d}$; $\bar{c}u$, $\bar{c}d$	I = 0 $c\bar{s}$; $\bar{c}s$
1^1S_0	0^{-+}	$\boldsymbol{\eta_c(1S)}$	$\boldsymbol{D}$	$\boldsymbol{D_s^{\pm}}$
1^3S_1	1^{--}	$\boldsymbol{J/\psi(1S)}$	$\boldsymbol{D^*}$	$\boldsymbol{D_s^{*\pm}}$
1^3P_0	0^{++}	$\boldsymbol{\chi_{c0}(1P)}$	$\boldsymbol{D_0^*(2300)}$	$\boldsymbol{D_{s0}^*(2317)^{\pm}}$†
1^3P_1	1^{++}	$\boldsymbol{\chi_{c1}(1P)}$	$D_1(2430)$	$\boldsymbol{D_{s1}(2460)^{\pm}}$†
1^1P_1	1^{+-}	$\boldsymbol{h_c(1P)}$	$\boldsymbol{D_1(2420)}$	$\boldsymbol{D_{s1}(2536)^{\pm}}$
1^3P_2	2^{++}	$\boldsymbol{\chi_{c2}(1P)}$	$\boldsymbol{D_2^*(2460)}$	$\boldsymbol{D_{s2}^*(2573)}$
2^1S_0	0^{-+}	$\boldsymbol{\eta_c(2S)}$		
2^3S_1	1^{--}	$\boldsymbol{\psi(2S)}$		$\boldsymbol{D_{s1}^*(2700)^{\pm}}$‡
1^3D_1	1^{--}	$\boldsymbol{\psi(3770)}$		$D_{s1}^*(2860)^{\pm}$‡
1^3D_2	2^{--}	$\boldsymbol{\psi_2(3823)}$		
2^3P_J	$0, 1^{++}$	$\chi_{c0}(3860)$		
	2^{++}	$\boldsymbol{\chi_{c2}(3930)}$		
3^3S_1	1^{--}	$\boldsymbol{\psi(4040)}$		
2^3D_1	1^{--}	$\boldsymbol{\psi(4160)}$		
4^3S_1	1^{--}	$\boldsymbol{\psi(4415)}$		
1^3D_3	3^{--}		$D_3^*(2750)$	$D_{s3}^*(2860)^{\pm}$

Table 15.4: $b\bar{b}$ quark-model assignments for the bottomonium and B mesons with established J^{PC}.

$n^{2s+1}\ell_J$	J^{PC}	I = 0 $b\bar{b}$	I = $\frac{1}{2}$ $b\bar{u}$, $b\bar{d}$; $\bar{b}u$, $\bar{b}d$	I = 0 $b\bar{s}$; $\bar{b}s$	I = 0 $b\bar{c}$; $\bar{b}c$
$1\,^1S_0$	0^{-+}	$\boldsymbol{\eta_b(1S)}$	$\boldsymbol{B}$	$\boldsymbol{B_s^0}$	$\boldsymbol{B_c^\pm}$
$1\,^3S_1$	1^{--}	$\boldsymbol{\Upsilon(1S)}$	$\boldsymbol{B^*}$	$\boldsymbol{B_s^*}$	
$1\,^3P_0$	0^{++}	$\boldsymbol{\chi_{b0}(1P)}$			
$1\,^3P_1$	1^{++}	$\boldsymbol{\chi_{b1}(1P)}$			
$1\,^1P_1$	1^{+-}	$\boldsymbol{h_b(1P)}$	$\boldsymbol{B_1(5721)}$	$\boldsymbol{B_{s1}(5830)^0}$	
$1\,^3P_2$	2^{++}	$\boldsymbol{\chi_{b2}(1P)}$	$\boldsymbol{B_2^*(5747)}$	$\boldsymbol{B_{s2}^*(5840)^0}$	
$2\,^1S_0$	0^{-+}	$\eta_b(2S)$			$B_c(2S)^\pm$
$2\,^3S_1$	1^{--}	$\boldsymbol{\Upsilon(2S)}$			$B_c^*(2S)^\pm$
$1\,^3D_2$	2^{--}	$\boldsymbol{\Upsilon_2(1D)}$			
$2\,^3P_J$	$0,1,2^{++}$	$\boldsymbol{\chi_{b0,1,2}(2P)}$			
$2\,^1P_1$	1^{+-}	$h_b(2P)$			
$3\,^3S_1$	1^{--}	$\boldsymbol{\Upsilon(3S)}$			
$3\,^3P_J$	$0,1,2^{++}$	$\boldsymbol{\chi_{b1,2}(3P)}$			
$4\,^3S_1$	1^{--}	$\boldsymbol{\Upsilon(4S)}$			

the light quark nonets. Thus, the physical isoscalars are mixtures of the SU(3) wave function ψ_8 and ψ_1:

$$f' = \psi_8 \cos\theta - \psi_1 \sin\theta \ , \tag{15.5}$$

$$f = \psi_8 \sin\theta + \psi_1 \cos\theta \ , \tag{15.6}$$

where θ is the nonet mixing angle and

$$\psi_8 = \frac{1}{\sqrt{6}}(u\bar{u} + d\bar{d} - 2s\bar{s}) \ , \tag{15.7}$$

$$\psi_1 = \frac{1}{\sqrt{3}}(u\bar{u} + d\bar{d} + s\bar{s}) \ . \tag{15.8}$$

These mixing relations are often rewritten to exhibit the $u\bar{u} + d\bar{d}$ and $s\bar{s}$ components which decouple for the "ideal" mixing angle θ_i, such that $\tan\theta_i = 1/\sqrt{2}$ (or $\theta_i = 35.3°$). Defining $\alpha = \theta + 54.7°$, one obtains the physical isoscalar in the flavor basis

$$f' = \frac{1}{\sqrt{2}}(u\bar{u} + d\bar{d})\cos\alpha - s\bar{s} \ \sin\alpha \ , \tag{15.9}$$

and its orthogonal partner f (replace α by α –90°). Thus for ideal mixing ($\alpha_i = 90°$), the f' becomes pure $s\bar{s}$ and the f pure $u\bar{u} + d\bar{d}$. The mixing angle θ can be derived by diagonalizing the mass matrix

$$\begin{pmatrix} m_8 & m_{81} \\ m_{18} & m_1 \end{pmatrix} \tag{15.10}$$

The mass eigenvalues are $m_{f'}$ and m_f. The mixing angle is given by

$$\tan\theta = \frac{m_8 - m_{f'}}{m_{81}} \ . \tag{15.11}$$

Calculating m_8 and m_{81} from the wave functions Eq. 15.7 and Eq. 15.8, and expressing the quark masses as a function of the I = 1/2 and I = 1 meson masses, one obtains

$$\tan\theta = \frac{4m_K - m_a - 3m_{f'}}{2\sqrt{2}(m_a - m_K)} \ , \tag{15.12}$$

which also determines the sign of θ. Alternatively, one can express the mixing angle as a function of all nonet masses. The octet mass is given by

$$m_8 = m_{f'}\cos^2\theta + m_f \sin^2\theta \tag{15.13}$$

whence

$$\tan^2\theta = \frac{4m_K - m_a - 3m_{f'}}{-4m_K + m_a + 3m_f} \ . \tag{15.14}$$

Eliminating θ from Eq. (15.12) and Eq. (15.14) leads to the sum rule [4]

$$(m_f + m_{f'})(4m_K - m_a) - 3m_f m_{f'} = 8m_K^2 - 8m_K m_a + 3m_a^2. \tag{15.15}$$

This relation is verified for the ground-state vector mesons. We identify the $\phi(1020)$ with the f' and the $\omega(783)$ with the f. Thus

$$\phi(1020) = \psi_8 \cos\theta_V - \psi_1 \sin\theta_V \ ,$$
$$\omega(782) = \psi_8 \sin\theta_V + \psi_1 \cos\theta_V \ , \tag{15.16}$$

with the vector mixing angle $\theta_V = 36.4°$ from Eq. (15.14), very close to ideal mixing. Thus $\phi(1020)$ is nearly pure $s\bar{s}$. For ideal mixing, Eq. (15.12) and Eq. (15.14) lead to the relations

$$m_K = \frac{m_f + m_{f'}}{2} \ , \quad m_a = m_f \ , \tag{15.17}$$

which are satisfied for the vector mesons.

The situation for the pseudoscalar and scalar mesons is not so clear cut, either theoretically or experimentally. For the pseudoscalars, the mixing angle is small. This can be understood qualitatively via gluon-line counting of the mixing process. The size of the mixing process between the nonstrange and strange mass bases scales as α_s^2, not α_s^3, because of two rather than three gluon exchange as it does for the vector mesons. It may also be that the lightest isoscalar pseudoscalars mix more strongly with excited states or with states of substantial non-$\bar{q}q$ content, as will be discussed below.

A variety of analysis methods lead to similar results: First, for these states, Eqn. 15.15 is satisfied only approximately. Then Eqn. 15.12 and Eqn. 15.14 lead to somewhat different values for the mixing angle. Identifying the η with the f' one gets

$$\eta = \psi_8 \cos\theta_P - \psi_1 \sin\theta_P \ , \tag{15.18}$$

$$\eta' = \psi_8 \sin\theta_P + \psi_1 \cos\theta_P \ . \tag{15.19}$$

Following chiral perturbation theory, the meson masses in the mass formulae (Eq. (15.12) and Eq. (15.14)) might be replaced by their squares. Table 15.5 lists the mixing angle $\theta_{\rm lin}$ from Eqn. 15.14 (using the neutral members of the nonets) and the corresponding $\theta_{\rm quad}$ obtained by replacing the meson masses by their squares throughout.

Table 15.5: Singlet-octet mixing angles for the well established nonets from the linear mass formula (15.12) and its quadratic version in which the masses are squared.

$n^{2s+1}\ell_J$	J^{PC}	$\theta_{\rm quad}$ [°]	$\theta_{\rm lin}$ [°]
$1\,^1S_0$	0^{-+}	−11.3	−24.5
$1\,^3S_1$	1^{--}	39.2	36.5
$1\,^3P_2$	2^{++}	29.6	28.0
$1\,^3D_3$	3^{--}	31.8	30.8

The pseudoscalar mixing angle θ_P can also be measured by comparing the partial widths for radiative J/ψ decay into a vector and a pseudoscalar [5], radiative $\phi(1020)$ decay into η and η' [6], radiative decays between pseudoscalar and vector mesons [7], or $\bar{p}p$ annihilation at rest into a pair of vector and pseudoscalar or into two pseudoscalars [8,9] One obtains a mixing angle between –10° and –20°. More recently, a lattice QCD simulation, Ref. [10], has successfully reproduced the masses of the η and η', and as a byproduct find a mixing angle $\theta_{lin} = -14.1(2.8)°$. We return to this point in Sec. 15.6.

The nonet mixing angles can be measured in $\gamma\gamma$ collisions, *e.g.*, for the 0^{-+}, 0^{++}, and 2^{++} nonets. In the quark model, the amplitude for the coupling of neutral mesons to two photons is proportional to $\sum_i Q_i^2$, where Q_i is the charge of the i-th quark. The 2γ partial width of an isoscalar meson with mass m is then given in terms of the mixing angle α by

$$\Gamma_{2\gamma} = C(5\cos\alpha - \sqrt{2}\sin\alpha)^2 m^3 \ , \qquad (15.20)$$

- for f' and f ($\alpha \to \alpha - 90°$). The coupling C may depend on the meson mass. It is often assumed to be a constant in the nonet. For the isovector a, one then finds $\Gamma_{2\gamma} = 9\ C\ m^3$. Thus the members of an ideally mixed nonet couple to 2γ with partial widths in the ratios $f : f' : a = 25 : 2 : 9$. For tensor mesons, one finds from the ratios of the measured 2γ partial widths for the $f_2(1270)$ and $f_2'(1525)$ mesons a mixing angle α_T of $(81\pm 1)°$, or $\theta_T = (27 \pm 1)°$, in accord with the linear mass formula. For the pseudoscalars, one finds from the ratios of partial widths $\Gamma(\eta' \to 2\gamma)/\Gamma(\eta \to 2\gamma)$ a mixing angle $\theta_P = (-18 \pm 2)°$, while the ratio $\Gamma(\eta' \to 2\gamma)/\Gamma(\pi^0 \to 2\gamma)$ leads to $\sim$ –24 °. SU(3) breaking effects for pseudoscalars are discussed in [11].

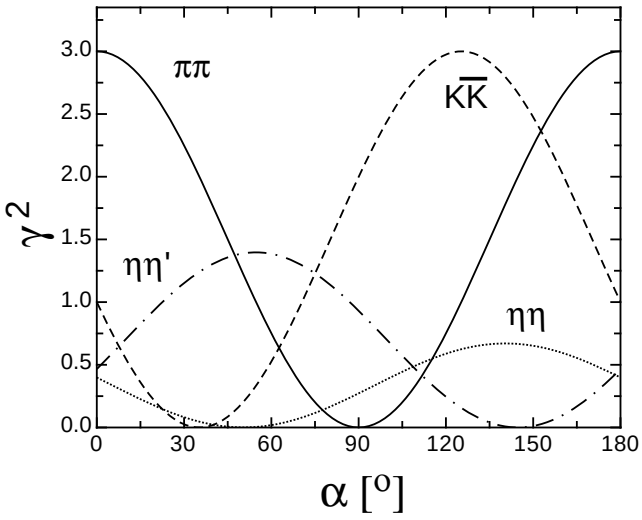

Figure 15.2: SU(3) couplings as a function of mixing angle α for isoscalar decays, up to a common multiplicative factor C and for $\theta_P = -17.3°$.

The partial width for the decay of a scalar or a tensor meson into a pair of pseudoscalar mesons is model-dependent. Following Ref. [13],

$$\Gamma = C \times \gamma^2 \times |F(q)|^2 \times q \ . \qquad (15.21)$$

C is a nonet constant, q the momentum of the decay products, $F(q)$ a form factor, and γ^2 the SU(3) coupling. The model-dependent form factor may be written as

$$|F(q)|^2 = q^{2\ell} \times \exp\left(-\frac{q^2}{8\beta^2}\right), \qquad (15.22)$$

where ℓ is the relative angular momentum between the decay products. The decay of a $q\bar{q}$ meson into a pair of mesons involves the creation of a $q\bar{q}$ pair from the vacuum, and SU(3) symmetry assumes that the matrix elements for the creation of $s\bar{s}$, $u\bar{u}$, and $d\bar{d}$ pairs are equal. The couplings γ^2 are given in Table 15.6, and their dependence upon the mixing angle α is shown in Fig. 15.2 for isoscalar decays. The generalization to unequal $s\bar{s}$, $u\bar{u}$, and $d\bar{d}$ couplings is given in Ref. [13]. An excellent fit to the tensor meson decay widths is obtained assuming SU(3) symmetry, with $\beta \simeq 0.5$ GeV/c, $\theta_V \simeq 26$ ° and $\theta_P \simeq -17$ ° [13].

Table 15.6: SU(3) couplings γ^2 for quarkonium decays as a function of nonet mixing angle α, up to a common multiplicative factor C ($\phi = 54.7° + \theta_P$).

Isospin	Decay channel	γ^2
0	$\pi\pi$	$3\cos^2\alpha$
	$K\overline{K}$	$(\cos\alpha - \sqrt{2}\sin\alpha)^2$
	$\eta\eta$	$(\cos\alpha\cos^2\phi - \sqrt{2}\sin\alpha\sin^2\phi)^2$
	$\eta\eta'$	$\frac{1}{2}\sin^2 2\phi\ (\cos\alpha + \sqrt{2}\sin\alpha)^2$
1	$\eta\pi$	$2\cos^2\phi$
	$\eta'\pi$	$2\sin^2\phi$
	$K\overline{K}$	1
$\frac{1}{2}$	$K\pi$	$\frac{3}{2}$
	$K\eta$	$(\sin\phi - \frac{\cos\phi}{\sqrt{2}})^2$
	$K\eta'$	$(\cos\phi + \frac{\sin\phi}{\sqrt{2}})^2$

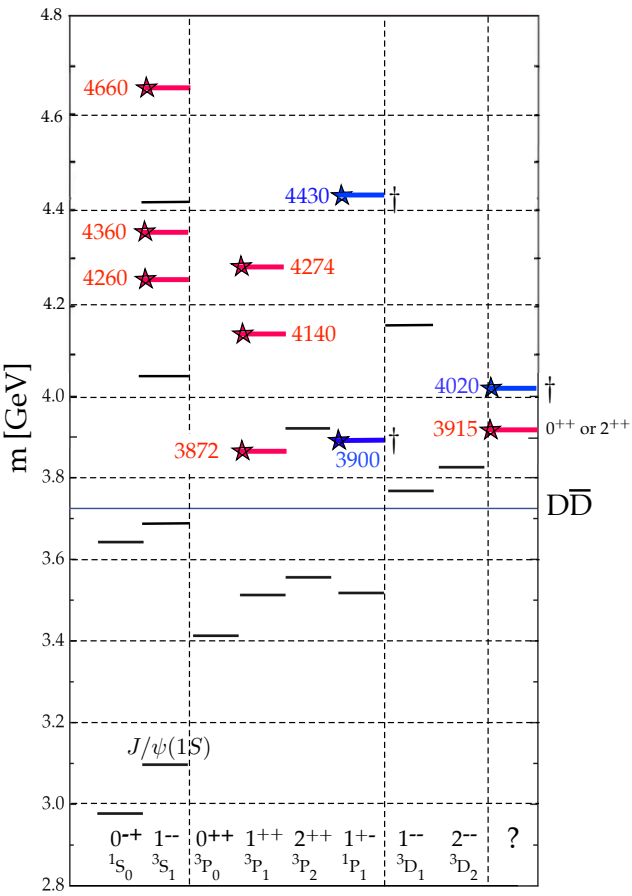

Figure 15.3: Established states populating the charmonium spectrum that are listed in the Summary Tables. The $c\bar{c}$ states are shown in black, the exotic ones are tagged by stars (red for the isoscalars, blue for the isovectors). The quantum numbers of the two states in the right colum are not firmly established.

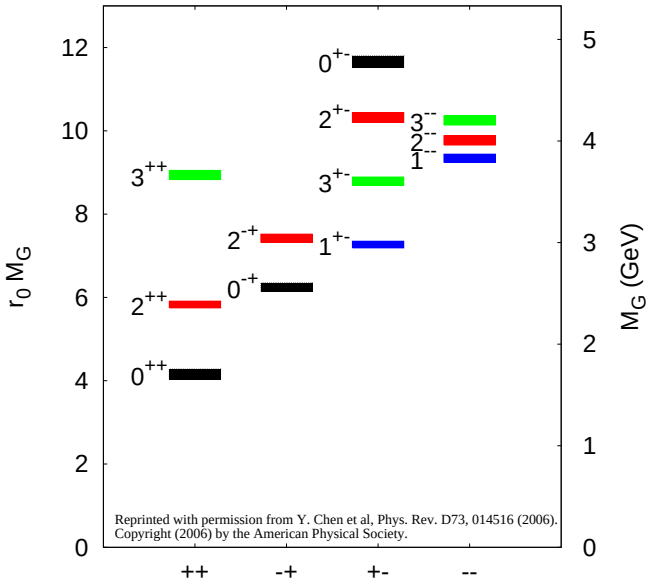

Figure 15.4: Predicted glueball mass spectrum from the lattice in quenched approximation (from [12]).

15.3 Exotic mesons

The existence of a light nonet composed of four quarks (tetraquarks) with masses below 1 GeV was suggested a long time ago [14] [15]. Coupling two triplets of light quarks u, d, and s, one obtains nine states, of which the six symmetric (uu, dd, ss, $ud+du$, $us+su$, $ds+sd$) form the six dimensional representation $\mathbf{6}$, while the three antisymmetric ($ud-du$, $us-su$, $ds-sd$) form the three dimensional representation $\overline{\mathbf{3}}$ of SU(3):

$$\mathbf{3} \otimes \mathbf{3} = \mathbf{6} \oplus \overline{\mathbf{3}} \ . \tag{15.23}$$

Hence for tetraquarks one gets the reduction

$$\begin{aligned} &\mathbf{3} \otimes \mathbf{3} \otimes \overline{\mathbf{3}} \otimes \overline{\mathbf{3}} \\ &= \mathbf{6} \oplus \overline{\mathbf{3}} \otimes \overline{\mathbf{6}} \otimes \mathbf{3} \\ &= \overline{\mathbf{3}} \otimes \mathbf{3} \oplus \mathbf{6} \otimes \overline{\mathbf{6}} \oplus \mathbf{6} \otimes \mathbf{3} \oplus \overline{\mathbf{3}} \otimes \overline{\mathbf{6}} \\ &= \mathbf{9} \oplus \mathbf{36} \oplus \mathbf{18} \oplus \overline{\mathbf{18}}. \end{aligned} \tag{15.24}$$

(15.25)

Combining with spin and color and requiring antisymmetry for diquarks and antidiquarks, one finds for ground states (zero angular momenta) that the most deeply bound tetraquarks (and hence the lightest ones) lie in the nonet and are scalar mesons (see also [1]). The average mass is estimated to be around 900 MeV from the mass differences between the ρ and π masses. Letting the strange quark determine the mass splittings one obtains a mass inverted spectrum with a light isosinglet, a medium heavy isodoublet and a heavy isotriplet + isosinglet. It is then tempting to identify these mesons as the lightest scalars

$$\begin{aligned} &f_0(500) = \bar{u}\bar{d}ud, \quad K_0^*(700) = (\bar{s}\bar{d}ud, \bar{s}\bar{u}ud) \ \text{ and } \ (\bar{u}\bar{d}us, \bar{u}\bar{d}ds), \\ &a_0(980) = (us\bar{d}\bar{s}, \frac{1}{\sqrt{2}}[u\bar{u} - d\bar{d}]s\bar{s}, \bar{u}\bar{s}ds), \\ &f_0(980) = \frac{1}{\sqrt{2}}[u\bar{u} + d\bar{d}]s\bar{s}. \end{aligned} \tag{15.26}$$

A plethora of new states have been reported in the charmonium and bottomonium spectra. The most prominent one is the $\chi_{c1}(3872)$ (formerly $X(3872)$), first observed in 2003 in B-decays in the final state $J/\psi\,\pi^+\pi^-$ (see Fig. 15.3). Even more remarkable is the observation of isosovector (charged) mesons decaying into $c\bar{c}$ plus a charged pion, such as the $Z^{\pm}(4430)$ decaying into $\psi(2S)\pi^{\pm}$, which a priori excludes an interpretation as true $c\bar{c}$ (charmonium) state. Similar states are also observed in the bottomonium spectrum. Some of these states may be tetraquarks (e.g. $cq\bar{c}\bar{q}$), molecular structures (e.g. $c\bar{q}\bar{c}q$) made of pairs of mesons such as D, D_s and D^*, D_s^* excitations, or their B and B^* counterparts. They could also be mimicked by kinematical effects. Details and references can be found in recent reviews [16], [17] and in the "Note on Non-$q\bar{q}$ Mesons" in the Meson Listings.

QCD predicts the existence of extra isoscalar mesons. In the pure gauge theory they contain only gluons, and are called glueballs. The ground state glueball is predicted by lattice gauge theories to be 0^{++}, the first excited state 2^{++}. Errors on the mass predictions are large. From Ref. [18] one obtains 1750 (50) (80) MeV for the mass of the lightest 0^{++} glueball from quenched QCD. As an example for the glueball mass spectrum, we show in Fig. 15.4 a calculation from Ref. [12]. A mass of 1710 MeV is predicted for the ground state, also with an error of about 100 MeV. Earlier work by other groups produced masses at 1650 MeV [19] and 1550 MeV [20] (see also [21]. The first excited state has a mass of about 2.4 GeV, and the lightest glueball with exotic quantum numbers (2^{+-}) has a mass of about 4 GeV.

These calculations are made in the so-called "quenched approximation" which neglects $q\bar{q}$ loops. However, both glue and $q\bar{q}$ states couple to singlet scalar mesons. Therefore glueballs will mix with nearby $q\bar{q}$ states of the same quantum numbers. For example, the two isoscalar 0^{++} mesons around 1500 MeV will mix with the pure ground state glueball to generate the observed physical states $f_0(1370)$, $f_0(1500)$, and $f_0(1710)$ [13, 22]. The first results from lattice calculations, which include these effects, indicate that the mass shifts are small. We return to a discussion of this point in Sec. 15.6.

The existence of three singlet scalar mesons around 1.5 GeV suggests additional degrees of freedom such as glue, since only two mesons are predicted in this mass range. The $f_0(1500)$ [13,22] or, alternatively, the $f_0(1710)$ [19], have been proposed as candidates for the scalar glueball, both states having considerable mixing also with the $f_0(1370)$. Other mixing schemes, in particular with the $f_0(500)$ and the $f_0(980)$, have also been proposed [23]. According to a holographic model of low-energy QCD scalar glueballs decay strongly into kaons and η mesons, in good agreement with data on the $f_0(1710)$ [24]. Details can be found in the "Note on Non-$q\bar{q}$ Mesons" in the Meson Listings and in Ref. [25]. See also the "Note on Scalar Mesons below 2 GeV".

Mesons made of $q\bar{q}$ pairs bound by excited gluons g, the hybrid states $q\bar{q}g$, are also predicted. They should lie in the 1.9 GeV mass region, according to gluon flux tube models [26]. Lattice QCD also predicts the lightest hybrid, an exotic 1^{-+}, at a mass of 1.8 to 1.9 GeV [27]. However, the bag model predicts four nonets, among them an exotic 1^{-+} around or above 1.4 GeV [28,29]. There are so far two candidates for exotic states with quantum numbers 1^{-+}, the $\pi_1(1400)$ and $\pi_1(1600)$, which could be hybrids or four-quark states (see the "Note on Non-$q\bar{q}$ Mesons" in the Meson Listings and in [25]).

15.4 Baryons: qqq states

Baryons are fermions with baryon number $\mathcal{B} = 1$, *i.e.*, in the most general case, they are composed of three quarks plus any number of quark - antiquark pairs. Until recently, all established baryons were 3-quark (qqq) configurations, which we mainly discuss in this section. However, in 2015 the LHCb collaboration published first evidence for charmed 'pentaquark' states of minimal quark content $c\bar{c}uud$ at invariant masses close to 4.4 GeV [30] More refined LHCb experiments have revealed evidence for three such states called $P_c(4312)^+$, $P_c(4440)^+$, and $P_c(4457)^+$ [31]. These states are located close to the thresholds of the production of ordinary baryon-meson pairs like $\Sigma_c^+\bar{D}^0$ and $\Sigma_c^+\bar{D}^{\star 0}$ and are discussed in terms of molecular-like states. A nice overview on the discussion of pentaquark and tetraquark states is given in Ref. [32].

The color part of baryon state functions is an SU(3) singlet, a completely antisymmetric state of the three colors. Since the quarks are fermions, the state function must be antisymmetric under interchange of any two equal-mass quarks (up and down quarks in the limit of isospin symmetry). Thus it can be written as

$$|\,qqq\,\rangle_A = |\,\text{color}\,\rangle_A \times |\,\text{space, spin, flavor}\,\rangle_S, \tag{15.27}$$

where the subscripts S and A indicate symmetry or antisymme-

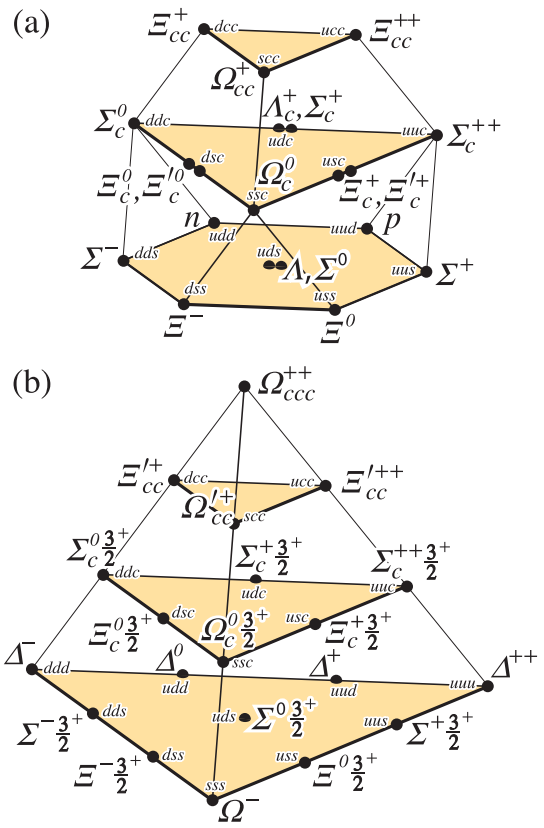

Figure 15.5: SU(4) multiplets of baryons made of u, d, s, and c quarks. (a) The spin 1/2 20-plet with an SU(3) octet. (b) The spin 3/2 20-plet with an SU(3) decuplet.

try under interchange of any two equal-mass quarks. Note the contrast with the state function for the three nucleons in ^{3}H or ^{3}He:

$$|\,NNN\,\rangle_A = |\,\text{space, spin, isospin}\,\rangle_A. \tag{15.28}$$

This difference has major implications for internal structure, magnetic moments, *etc.* (For a nice discussion, see Ref. [33].)

The "ordinary" baryons are made up of u, d, and s quarks. The three flavors imply an approximate flavor SU(3), which requires that baryons made of these quarks belong to the multiplets on the right side of

$$\mathbf{3}\otimes\mathbf{3}\otimes\mathbf{3} = \mathbf{10}_S \oplus \mathbf{8}_M \oplus \mathbf{8}_M \oplus \mathbf{1}_A \tag{15.29}$$

(see the section on "SU(n) Multiplets and Young Diagrams"). Here the subscripts indicate symmetric, mixed-symmetry, or antisymmetric states under interchange of any two quarks. The **1** is a uds state (Λ_1), and the octet contains a similar state (Λ_8). If these have the same spin and parity, they can mix. The mechanism is the same as for the mesons (see above). In the ground state multiplet, the SU(3) flavor singlet Λ_1 is forbidden by Fermi statistics. The section on "SU(3) Isoscalar Factors and Representation Matrices," shows how relative decay rates in, say, $\mathbf{10} \to \mathbf{8}\otimes\mathbf{8}$ decays may be calculated.

The addition of the c quark to the light quarks extends the flavor symmetry to SU(4). However, due to the large mass of the c quark, this symmetry is much more strongly broken than the SU(3) of the three light quarks. Figures 15.5(a) and 15.5(b) show the SU(4) baryon multiplets that have as their bottom levels an SU(3) octet, such as the octet that includes the nucleon, or an SU(3) decuplet, such as the decuplet that includes the $\Delta(1232)$. All particles in a given SU(4) multiplet have the same spin and parity. The charmed baryons are discussed in more detail in the "Note on Charmed Baryons" in the Particle Listings. The same multiplets as shown in Fig. 15.5 can be constructed when the c quark is replaced by the b quark, or they can be embedded in a larger SU(5) group that accounts for all baryons that can be constructed from the five quark flavors. The existence of baryons with t-quarks is very unlikely due to the short lifetime of the t-quark. The heavy quark baryons have recently gained a lot of interest [34]. Their relatively narrow widths allow to isolate the states much easier than the light quark baryon resonances which require intricate partial wave analyses. The only problem on the experimental side are the small production cross sections, but the recent measurements at the e^+e^- colliding B factories, at the $p\bar{p}$ Tevatron collider, and at LHCb at CERN have boosted this field. The LHCb collaboration has published evidence for five new narrow Ω_c^0 states (css) [35] and for a doubly charmed Ξ_{cc}^{++} (ccu) [36] baryon. Doubly charmed baryons have a much different structure from light baryons, more resembling a heavy 'double-star' system with an attached light 'planet' and open a new window for QCD properties. Another candidate for a doubly charmed baryon (Ξ_{cc}^+, (ccd)) had been earlier reported by the SELEX experiment [37, 38] but could so far not be confirmed by other experiments and the difference in mass between the LHCb Ξ_{cc}^{++} and the SELEX Ξ_{cc}^+ would be much larger than predicted. Quark model predictions for baryons with two heavy quarks are given in Ref. [39] and lattice results for doubly and triply charmed states are discussed in Sec. 15.6 of this review.

For the "ordinary" baryons (no c or b quark), flavor and spin may be combined in an approximate flavor-spin SU(6), in which the six basic states are $d\uparrow$, $d\downarrow$, $\cdots$, $s\downarrow$ ($\uparrow$, $\downarrow$ = spin up, down). Then the baryons belong to the multiplets on the right side of

$$\mathbf{6}\otimes\mathbf{6}\otimes\mathbf{6} = \mathbf{56}_S \oplus \mathbf{70}_M \oplus \mathbf{70}_M \oplus \mathbf{20}_A.$$

These SU(6) multiplets decompose into flavor SU(3) multiplets as follows:

$$\mathbf{56} = {}^4\mathbf{10} \oplus {}^2\mathbf{8} \tag{15.30}$$

$$\mathbf{70} = {}^2\mathbf{10} \oplus {}^4\mathbf{8} \oplus {}^2\mathbf{8} \oplus {}^2\mathbf{1} \tag{15.31}$$

$$\mathbf{20} = {}^2\mathbf{8} \oplus {}^4\mathbf{1}, \tag{15.32}$$

where the superscript $(2S+1)$ gives the net spin S of the quarks for each particle in the SU(3) multiplet. The $J^P = 1/2^+$ octet containing the nucleon and the $J^P = 3/2^+$ decuplet containing the $\Delta(1232)$ together make up the "ground-state" 56-plet, in which the orbital angular momenta between the quark pairs are zero (so that the spatial part of the state function is trivially symmetric). The **70** and **20** require some excitation of the spatial part of the state function in order to make the overall state function symmetric. States with nonzero orbital angular momenta are classified in SU(6)⊗O(3) supermultiplets.

It is useful to classify the baryons into bands that have the same number N of quanta of excitation. Each band consists of a number of supermultiplets, specified by (D, L_N^P), where D is the dimensionality of the SU(6) representation, L is the total quark orbital angular momentum, and P is the total parity. Supermultiplets contained in bands up to N = 12 are given in Ref. [40]. The N = 0 band, which contains the nucleon and $\Delta(1232)$, consists only of the $(56,0_0^+)$ supermultiplet. The N = 1 band consists only of the $(70,1_1^-)$ multiplet and contains the negative-parity baryons with masses below about 1.9 GeV. The N = 2 band contains five supermultiplets: $(56,0_2^+)$, $(70,0_2^+)$, $(56,2_2^+)$, $(70,2_2^+)$, and $(20,1_2^+)$.

The wave functions of the non-strange baryons in the harmonic oscillator basis are often labeled by $|X^{2S+1}L_\pi J^P\rangle$, where S, L, J, P are as above, $X = N$ or Δ, and $\pi = S, M$ or A denotes the symmetry of the spatial wave function. The possible model states for the bands with N=0,1,2 are given in Table 15.8. The assignment of experimentally observed states is only complete and well established up to the N=1 band. Some more tentative assignments for higher multiplets are suggested in [41].

In Table 15.7, quark-model assignments are given for many of the established baryons whose SU(6)⊗O(3) compositions are relatively unmixed. One must, however, keep in mind that apart from the mixing of the Λ singlet and octet states, states with same J^P but different L, S combinations can also mix. In the quark model with one-gluon exchange motivated interactions, the size of the mixing is determined by the relative strength of the tensor term with respect to the contact term (see below). The

Table 15.7: Quark-model assignments for some of the known baryons in terms of a flavor-spin SU(6) basis. Only the dominant representation is listed. Assignments for several states, especially for the $\Lambda(1810)$, $\Lambda(2350)$, $\Xi(1820)$, and $\Xi(2030)$, are merely educated guesses.
† suggestions for assignments and re-assignments from Ref. [42]. For assignments of the charmed baryons, see the "Note on Charmed Baryons" in the Particle Listings.

J^P	(D, L^P_N)	S	Octet members				Singlets
$1/2^+$	$(56,0^+_0)$	1/2	$N(939)$	$\Lambda(1116)$	$\Sigma(1193)$	$\Xi(1318)$	
$1/2^+$	$(56,0^+_2)$	1/2	$N(1440)$	$\Lambda(1600)$	$\Sigma(1660)$	$\Xi(1690)^\dagger$	
$1/2^-$	$(70,1^-_1)$	1/2	$N(1535)$	$\Lambda(1670)$	$\Sigma(1620)$	$\Xi(?)$	$\Lambda(1405)$
					$\Sigma(1560)^\dagger$		
$3/2^-$	$(70,1^-_1)$	1/2	$N(1520)$	$\Lambda(1690)$	$\Sigma(1670)$	$\Xi(1820)$	$\Lambda(1520)$
$1/2^-$	$(70,1^-_1)$	3/2	$N(1650)$	$\Lambda(1800)$	$\Sigma(1750)$	$\Xi(?)$	
					$\Sigma(1620)^\dagger$		
$3/2^-$	$(70,1^-_1)$	3/2	$N(1700)$	$\Lambda(?)$	$\Sigma(1940)^\dagger$	$\Xi(?)$	
$5/2^-$	$(70,1^-_1)$	3/2	$N(1675)$	$\Lambda(1830)$	$\Sigma(1775)$	$\Xi(1950)^\dagger$	
$1/2^+$	$(70,0^+_2)$	1/2	$N(1710)$	$\Lambda(1810)$	$\Sigma(1880)$	$\Xi(?)$	$\Lambda(1810)^\dagger$
$3/2^+$	$(56,2^+_2)$	1/2	$N(1720)$	$\Lambda(1890)$	$\Sigma(?)$	$\Xi(?)$	
$5/2^+$	$(56,2^+_2)$	1/2	$N(1680)$	$\Lambda(1820)$	$\Sigma(1915)$	$\Xi(2030)$	
$7/2^-$	$(70,3^-_3)$	1/2	$N(2190)$	$\Lambda(?)$	$\Sigma(?)$	$\Xi(?)$	$\Lambda(2100)$
$9/2^-$	$(70,3^-_3)$	3/2	$N(2250)$	$\Lambda(?)$	$\Sigma(?)$	$\Xi(?)$	
$9/2^+$	$(56,4^+_4)$	1/2	$N(2220)$	$\Lambda(2350)$	$\Sigma(?)$	$\Xi(?)$	

			Decuplet members			
$3/2^+$	$(56,0^+_0)$	3/2	$\Delta(1232)$	$\Sigma(1385)$	$\Xi(1530)$	$\Omega(1672)$
$3/2^+$	$(56,0^+_2)$	3/2	$\Delta(1600)$	$\Sigma(1690)^\dagger$	$\Xi(?)$	$\Omega(?)$
$1/2^-$	$(70,1^-_1)$	1/2	$\Delta(1620)$	$\Sigma(1750)^\dagger$	$\Xi(?)$	$\Omega(?)$
$3/2^-$	$(70,1^-_1)$	1/2	$\Delta(1700)$	$\Sigma(?)$	$\Xi(?)$	$\Omega(?)$
$5/2^+$	$(56,2^+_2)$	3/2	$\Delta(1905)$	$\Sigma(?)$	$\Xi(?)$	$\Omega(?)$
$7/2^+$	$(56,2^+_2)$	3/2	$\Delta(1950)$	$\Sigma(2030)$	$\Xi(?)$	$\Omega(?)$
$11/2^+$	$(56,4^+_4)$	3/2	$\Delta(2420)$	$\Sigma(?)$	$\Xi(?)$	$\Omega(?)$

Table 15.8: N and Δ states in the N=0,1,2 harmonic oscillator bands. L^P denotes angular momentum and parity, S the three-quark spin and 'sym'=A,S,M the symmetry of the spatial wave function. Listed are all possible spin/parity combinations and assignments of experimentally observed states. Only dominant components are indicated. Assignments in the N=2 band are partly tentative.

N	sym	L^P	S	$N(I=1/2)$			
2	A	1^+	1/2	$1/2^+$	$3/2^+$	-	-
2	M	2^+	3/2	$1/2^+$	$3/2^+$	$5/2^+$	$7/2^+$
2	M	2^+	1/2	-	$3/2^+$	$5/2^+$	-
2	M	0^+	3/2	-	$3/2^+$	-	-
2	M	0^+	1/2	$1/2^+$ $N(1710)$	-	-	-
2	S	2^+	3/2	-	-	-	-
2	S	2^+	1/2	-	$3/2^+$ $N(1720)$	$5/2^+$ $N(1680)$	-
2	S	0^+	3/2	-	-	-	-
2	S	0^+	1/2	$1/2^+$ $N(1440)$	-	-	-
1	M	1^-	3/2	$1/2^-$ $N(1650)$	$3/2^-$ $N(1700)$	$5/2^-$ $N(1675)$	-
1	M	1^-	1/2	$1/2^-$ $N(1535)$	$3/2^-$ $N(1520)$	-	-
0	S	0^+	3/2	-	-	-	-
0	S	0^+	1/2	$1/2^+$ $N(938)$	-	-	-
N	sym	L^P	S	$\Delta(I=3/2)$			
2	A	1^+	1/2	-	-	-	-
2	M	2^+	3/2	-	-	-	-
2	M	2^+	1/2	-	$3/2^+$	$5/2^+$	-
2	M	0^+	3/2	-	-	-	-
2	M	0^+	1/2	$1/2^+$ $\Delta(1750)$	-	-	-
2	S	2^+	3/2	$1/2^+$ $\Delta(1910)$	$3/2^+$ $\Delta(1920)$	$5/2^+$ $\Delta(1905)$	$7/2^+$ $\Delta(1950)$
2	S	2^+	1/2	-	-	-	-
2	S	0^+	3/2	-	$3/2^+$ $\Delta(1600)$	-	-
2	S	0^+	1/2	-	-	-	-
1	M	1^-	3/2	-	-	-	-
1	M	1^-	1/2	$1/2^-$ $\Delta(1620)$	$3/2^-$ $\Delta(1700)$	-	-
0	S	0^+	3/2	-	$3/2^+$ $\Delta(1232)$	-	
0	S	0^+	1/2	-	-	-	-

mixing is more important for the decay patterns of the states than for their positions. An example are the lowest lying $(70, 1_1^-)$ states with J^P=1/2$^-$ and 3/2$^-$. The physical states are:

$$|\,N(1535)1/2^-\rangle = \cos(\Theta_S)|N^2P_M1/2^-\rangle - \sin(\Theta_S)|N^4P_M1/2^-\rangle \quad (15.33)$$

$$|\,N(1520)3/2^-\rangle = \cos(\Theta_D)|N^2P_M3/2^-\rangle - \sin(\Theta)_D|N^4P_M3/2^-\rangle \quad (15.34)$$

and the orthogonal combinations for $N(1650)1/2^-$ and $N(1700)3/2^-$. The mixing is large for the J^P=1/2$^-$ states ($\Theta_S \approx$ -32^o), but small for the J^P=3/2$^-$ states ($\Theta_D \approx +6^o$) [43–45].

All baryons of the ground state multiplets are known. Many of their properties, in particular their masses, are in good agreement even with the most basic versions of the quark model, including harmonic (or linear) confinement and a spin-spin interaction, which is responsible for the octet - decuplet mass shifts. A consistent description of the ground-state electroweak properties, however, requires refined relativistic constituent quark models.

The situation for the excited states is much less clear. The assignment of some experimentally observed states with strange quarks to model configurations is only tentative and in many cases candidates are completely missing. Melde, Plessas and Sengl [42] have calculated baryon properties in relativistic constituent quark models, using one-gluon exchange and Goldstone-boson exchange for the modeling of the hyperfine interactions (see Sec. 15.5 on Dynamics). Both types of models give qualitatively comparable results, and underestimate in general experimentally observed decay widths. Nevertheless, in particular on the basis of the observed decay patterns, the authors have assigned some additional states with strangeness to the SU(3) multiplets and suggest reassignments for a few others. Among the new assignments are states with weak experimental evidence (two or three star ratings) and partly without firm spin/parity assignments, so that further experimental efforts are necessary before final conclusions can be drawn. We have added their suggestions in Table 15.7.

In the non-strange sector there are two main problems which are illustrated in Fig. 15.6, where the experimentally observed excitation spectrum of the nucleon (N and Δ resonances) is compared to the results of a typical quark model calculation [46]. The lowest states from the N=2 band, the $N(1440)1/2^+$, and the $\Delta(1600)3/2^+$, appear lower than the negative parity states from the N=1 band (see Table 15.8) and much lower than predicted by most models. Also negative parity Δ states from the N=3 band ($\Delta(1900)1/2^-$, $\Delta(1940)3/2^-$, and $\Delta(1930)5/2-$) are too low in energy. Part of the problem could be experimental. Among the negative parity Δ states, only the $\Delta(1930)5/2^-$ has three stars and the uncertainty in the position of the $\Delta(1600)3/2^+$ is large (1550 - 1700 MeV).

Furthermore, many more states are predicted than observed. This has been known for a long time as the 'missing resonance' problem [43]. Up to an excitation energy of 2.4 GeV, about 45 N states are predicted, but only 20 are established (four- or three-star; see Note on N and Δ Resonances for the rating of the status of resonances) and 5 are tentative (two- or one-star). Even for the N=2 band, up to now only half of the predicted states have been observed. However, there is some recent progress. The total number of states has not much changed but the number of states with four- or three-star rating has increased from 14 to 20 compared to the 2018 PDG particle listings. Most of this progress is due to the programs concentrating on the study of meson photoproduction reactions, while the most recent partial wave analysis of elastic pion scattering and charge exchange data by Arndt and collaborators [47] found no evidence for almost half of the states listed in this review (and included in Fig. 15.6). Such analyses are of course biased against resonances which couple only weakly to the $N\pi$ channel. Quark model predictions for the couplings to other hadronic channels and to photons are given in Ref. [46]. The large experimental effort ongoing at several electron accelerators to study the baryon resonance spectrum with real and virtual photon-induced meson production reactions includes the search for as-yet-unobserved states, as well as detailed studies of the properties of the low lying states (decay patterns, electromagnetic couplings, magnetic moments, *etc.*) (see Ref. [48] for reviews). There are two major new aspects of this program. The investigation of single and double polarization observables allows via the study of interference terms access to small partial waves that do not leave a footprint in unpolarized cross sections. An example for the impact of such data is given by a comparison of results from different multipole analyses of pion photoproduction [49]. It shows clearly that with the inclusion of polarization observables the reaction model results start to converge. This will in the near future much improve the data basis for excited baryons in the light quark sector.

The other aspect is the study of final states with meson pairs, in particular $\pi\pi$ and $\pi\eta$ pairs, which made large progress during the last few years. This is important for higher lying states, which in the quark model may have both possible oscillations excited. Such states can be expected to decay in sequential processes de-exciting the two oscillations step-by-step so that they couple strongly to multiple-meson final states but not to single-meson production. Detailed analyses of such data are for example given in [50, 51] and had already significant impact on partial wave analyses.

In quark models, the number of excited states is determined by the effective degrees of freedom, while their ordering and decay properties are related to the residual quark - quark interaction. An overview of quark models for baryons is given in [52], recent discussions of baryon spectroscopy are given in [34, 41]. The effective degrees of freedom in the standard nonrelativistic quark model are three equivalent valence quarks with one-gluon exchange-motivated, flavor-independent color-magnetic interactions. The QCD aspect of gluon-gluon interactions is emphasized by the hypercentral quark model [53, 54], which includes in a natural way three-body forces between the quarks. A different class of models uses interactions which give rise to a quark - diquark clustering of the baryons: for a review see [55]. If there is a tightly bound diquark, only two degrees of freedom are available at low energies, and thus *fewer* states are predicted. Furthermore, selection rules in the decay pattern may arise from the quantum numbers of the diquark. *More* states are predicted by collective models of the baryon like the algebraic approach in [56]. In this approach, the quantum numbers of the valence quarks are distributed over a Y-shaped string-like configuration, and additional states arise *e.g.*, from vibrations of the strings. *More* states are also predicted in the framework of flux-tube models, see [57], which are motivated by lattice QCD. In addition to the quark degrees of freedom, flux-tubes responsible for the confinement of the quarks are considered as degrees of freedom. These models include hybrid baryons containing explicit excitations of the gluon fields. However, since all half integral J^P quantum numbers are possible for ordinary baryons, such 'exotics' will be very hard to identify, and probably always mix with ordinary states. So far, the experimentally observed number of states is still far lower even than predicted by the quark–diquark models.

The influence of chiral symmetry on the excitation spectrum of the nucleon has been debated from a somewhat different perspective. Chiral symmetry, the fundamental symmetry of QCD, is strongly broken for the low lying states, resulting in large mass differences of parity partners like the J^P=1/2$^+$ $N(938)1/2^+$ ground state and the J^P=1/2$^-$ $N(1535)1/2^-$ excitation. However, at higher excitation energies there is some evidence for parity doublets and even some very tentative suggestions for full chiral multiplets of $N^\star$ and Δ resonances. An effective restoration of chiral symmetry at high excitation energies due to a decoupling from the quark condensate of the vacuum has been discussed (see Ref. [58] for recent reviews) as a possible cause. In this case, the mass generating mechanisms for low and high lying states would be essentially different. As a further consequence, the parity doublets would decouple from pions, so that experimental bias would be worse. However, parity doublets might also arise from the spin-orbital dynamics of the 3-quark system. Presently, the status of data does not allow final conclusions.

The most recent developments on the theory side are the first unquenched lattice calculations for the excitation spectrum discussed in Sec15.6. The results are basically consistent with the level counting of SU(6)⊗O(3) in the standard non-relativistic quark model and show no indication for quark-diquark structures

or parity doubling. Consequently, there is as yet no indication from lattice that the mis-match between the excitation spectrum predicted by the standard quark model and experimental observations is due to inappropriate degrees of freedom in the quark model.

15.5 Dynamics

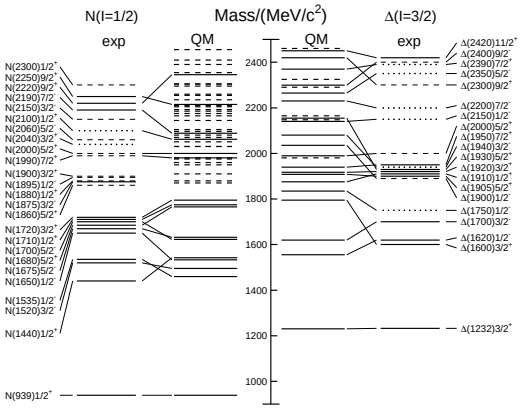

Figure 15.6: Excitation spectrum of the nucleon. Compared are the positions of the excited states identified in experiment, to those predicted by a relativized quark model calculation. Left hand side: isospin $I = 1/2$ N-states, right hand side: isospin $I = 3/2$ Δ-states. Experimental: (columns labeled 'exp'), three- and four-star states are indicated by full lines (two-star dashed lines, one-star dotted lines). At the very left and right of the figure, the spectroscopic notation of these states is given. Quark model [46, 59]: (columns labeled 'QM'), all states for the N=1,2 bands, low-lying states for the N=3,4,5 bands. Full lines: at least tentative assignment to observed states, dashed lines: so far no observed counterparts. Many of the assignments between predicted and observed states are highly tentative.

Quantum chromodynamics (QCD) is well-established as the theory for the strong interactions. As such, one of the goals of QCD is to predict the spectrum of strongly-interacting particles. To date, the only first-principles calculations of spectroscopy from QCD use lattice methods. These are the subject of Sec. 15.6. These calculations are difficult and unwieldy, and many interesting questions do not have a good lattice-based method of solution. Therefore, it is natural to build models, whose ingredients are abstracted from QCD, or from the low-energy limit of QCD (such as chiral Lagrangians) or from the data itself. The words "quark model" are a shorthand for such phenomenological models. Many specific quark models exist, but most contain a similar basic set of dynamical ingredients. These include:

1. A confining interaction, which is generally spin-independent (*e.g.*, harmonic oscillator or linear confinement);
2. Different types of spin-dependent interactions:

   a) commonly used is a color-magnetic flavor-independent interaction modeled after the effects of gluon exchange in QCD (see *e.g.*, Ref. [60]). For example, in the S-wave states, there is a spin-spin hyperfine interaction of the form

   $$H_{HF} = -\alpha_S M \sum_{i>j} (\vec{\sigma}\lambda_a)_i (\vec{\sigma}\lambda_a)_j, \qquad (15.35)$$

   where M is a constant with units of energy, λ_a ($a = 1, \cdots, 8,$) is the set of SU(3) unitary spin matrices, defined in the review "SU(3) Isoscalar Factors and Representation Matrices," and the sum runs over constituent quarks or antiquarks. Spin-orbit interactions, although allowed, seem to be small in general, but a tensor term is responsible for the mixing of states with the same J^P but different L, S combinations.

   b) other approaches include flavor-dependent short-range quark forces from instanton effects (see *e.g.*, [61, 62]). This interaction acts only on scalar, isoscalar pairs of quarks in a relative S-wave state:

   $$\langle q^2; S, L, T | W | q^2; S, L, T \rangle = -4g\delta_{S,0}\delta_{L,0}\delta_{I,0}\mathcal{W} \qquad (15.36)$$

   where $\mathcal{W}$ is the radial matrix element of the contact interaction.

   c) a rather different and controversially discussed approach is based on flavor-dependent spin-spin forces arising from one-boson exchange. The interaction term is of the form:

   $$H_{HF} \propto \sum_{i<j} V(\vec{r}_{ij}) \lambda_i^F \cdot \lambda_j^F \vec{\sigma}_i \cdot \vec{\sigma}_j \qquad (15.37)$$

   where the λ_i^F are in flavor space (see *e.g.*, Ref. [63]).
3. A strange quark mass somewhat larger than the up and down quark masses, in order to split the SU(3) multiplets;
4. In the case of spin-spin interactions (iia,c), a flavor-symmetric interaction for mixing $q\bar{q}$ configurations of different flavors (*e.g.*, $u\bar{u} \leftrightarrow d\bar{d} \leftrightarrow s\bar{s}$), in isoscalar channels, so as to reproduce *e.g.*, the η - η' and ω - ϕ mesons.

These ingredients provide the basic mechanisms that determine the hadron spectrum in the standard quark model.

15.6 Lattice Calculations of Hadronic Spectroscopy

Lattice calculations are a major source of information about QCD masses and matrix elements. The necessary theoretical background is given in Sec. 17 of this *Review*. Here we confine ourselves to some general comments and illustrations of lattice calculations for spectroscopy.

In general, the cleanest lattice results come from computations of processes in which there is only one particle in the simulation volume. These quantities include masses of hadrons, simple decay constants, like pseudoscalar meson decay constants, and semileptonic form factors (such as the ones appropriate to $B \to Dl\nu$, $Kl\nu$, $\pi l\nu$). The cleanest predictions for masses are for states which have narrow decay widths and are far below any thresholds to open channels, since the effects of final state interactions are not yet under complete control on the lattice. As a simple corollary, the lightest state in a channel is easier to study than the heavier ones. "Difficult" states for the quark model (such as exotics) are also difficult for the lattice because of the lack of simple operators which couple well to them.

Good-quality modern lattice calculations will present multi-part error budgets with their predictions. A small part of the uncertainty is statistical, from sample size. Typically, the quoted statistical uncertainty includes uncertainty from a fit: it is rare that a simulation computes one global quantity which is the desired observable. Simulations which include virtual quark-antiquark pairs (also known as "dynamical quarks" or "sea quarks") are often done at up and down quark mass values heavier than the experimental ones, and it is then necessary to extrapolate in these quark masses. Simulations can work at the physical values of the heavier quarks' masses. They are always done at nonzero lattice spacing, and so it is necessary to extrapolate to zero lattice spacing. Some theoretical input is needed to do this. Much of the uncertainty in these extrapolations is systematic, from the choice of fitting function. Other systematics include the effect of finite simulation volume, the number of flavors of dynamical quarks actually simulated, and technical issues with how these dynamical quarks are included. The particular choice of a fiducial mass (to normalize other predictions) is not standardized; there are many possible choices, each with its own set of strengths and weaknesses, and determining it usually requires a second lattice simulation from that used to calculate the quantity under consideration.

A systematic error of major historical interest is the "quenched approximation," in which dynamical quarks are simply left out of the simulation. This was done because the addition of these

virtual pairs presented an expensive computational problem. No generally-accepted methodology has ever allowed one to correct for quenching effects, short of redoing all calculations with dynamical quarks. Recent advances in algorithms and computer hardware have rendered it obsolete.

With these brief remarks, we turn to examples. The field of lattice QCD simulations is vast, and so it is not possible to give a comprehensive review of them in a small space. The history of lattice QCD simulations is a story of thirty years of incremental improvements in physical understanding, algorithm development, and ever faster computers, which have combined to bring the field to a present state where it is possible to carry out very high quality calculations. We present a few representative illustrations, to show the current state of the art.

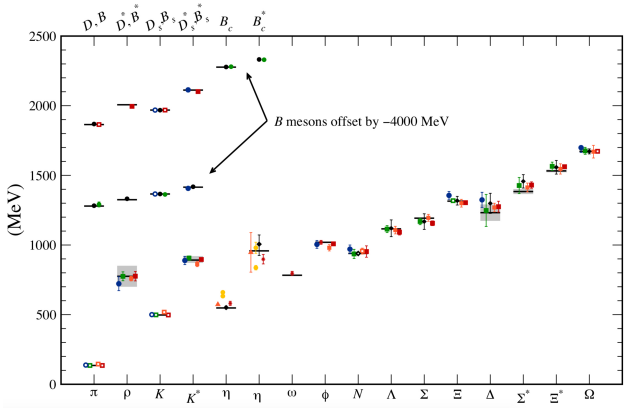

Figure 15.7: Hadron spectrum from lattice QCD. Comprehensive results for mesons and baryons are from MILC [64, 65], PACS-CS [66], BMW [67], QCDSF [68], and ETM [69]. Results for η and η' are from RBC & UKQCD [10], Hadron Spectrum [70] (also the only ω mass), UKQCD [71], and Michael, Ottnad, and Urbach [72]. Results for heavy-light hadrons from Fermilab-MILC [73], HPQCD [74,75], and Mohler and Woloshyn [76]. Circles, squares, diamonds, and triangles stand for staggered, Wilson, twisted-mass Wilson, and chiral sea quarks, respectively. Asterisks represent anisotropic lattices. Open symbols denote the masses used to fix parameters. Filled symbols (and asterisks) denote results. Red, orange, yellow, green, and blue stand for increasing numbers of ensembles (i.e., lattice spacing and sea quark mass) Black symbols stand for results with 2+1+1 flavors of sea quarks. Horizontal bars (gray boxes) denote experimentally measured masses (widths). b-flavored meson masses are offset by -4000 MeV.

By far, the major part of all lattice spectroscopy is concerned with that of the light hadrons, and so we illustrate results in Fig. 15.7, a comprehensive summary provided by A. Kronfeld (private communication; see also [77]).

Flavor singlet mesons are at the frontier of lattice QCD calculations, because one must include the effects of "annihilation graphs," for the valence q and $\bar{q}$. Recently, several groups, Refs. [10,71,78], have reported calculations of the η and η' mesons. The numbers of [10] are typical, finding masses of 573(6) and 947(142) MeV for the η and η'. The singlet-octet mixing angle (in the conventions of Table 15.2) is $\theta_{lin} = -14.1(2.8)^\circ$.

The spectroscopy of mesons containing heavy quarks has become a truly high-precision endeavor. These simulations use Non-Relativistic QCD (NRQCD) or Heavy Quark Effective Theory (HQET), systematic expansions of the QCD Lagrangian in powers of the heavy quark velocity, or the heavy quark mass. Terms in the Lagrangian have obvious quark model analogs, but are derived directly from QCD. For example, the heavy quark potential is a derived quantity, extracted from simulations. Fig. 15.8 shows the mass spectrum for mesons containing at least one heavy (b or c) quark from Ref. [75]. It also contains results from Ref. [79, 80]. The calculations uses a discretization of nonrelativistic QCD for bottom quarks with charm and lighter quarks being handled with an improved relativistic action. Four flavors (u, d, s, c) of dynamical quarks are included.

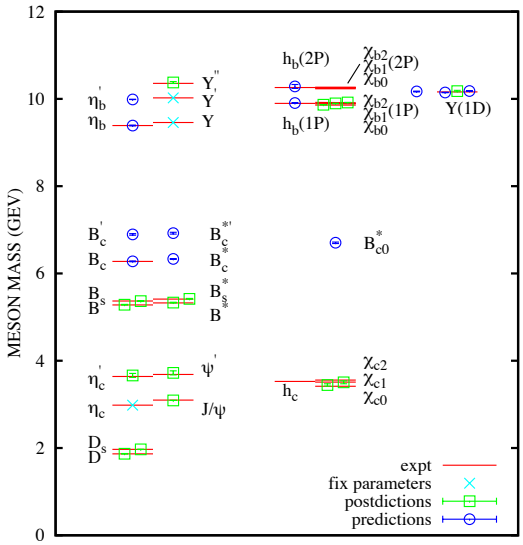

Figure 15.8: Spectroscopy for mesonic systems containing one or more heavy quarks (adapted from Ref. [75]. Particles whose masses are used to fix lattice parameters are shown with crosses; the authors distinguish between "predictions" and "postdictions" of their calculation. Lines represent experiment.

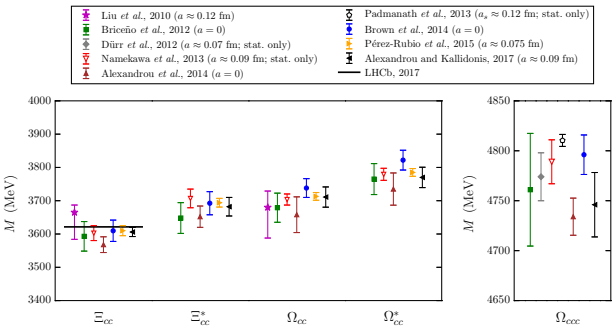

Figure 15.9: Comparison of lattice QCD results for the doubly and triply charmed baryon masses. Labels are Liu, *et al.*, [81]; Briceno, *et al.*, [82]; Namekawa, *et al.*, [83]; Padmanath, *et al.*, [84]; Alexandrou, *et al.*, [69]; Brown, *et al.*, [85]; Perez-Rubio et al., [86]; Alexandrou and Kallidonis 2017, [87]. Only calculations with dynamical light quarks are included; for the doubly charmed baryons, only calculations were performed at or extrapolated to the physical pion mass are shown. Results without estimates of systematic uncertainties are labeled "stat. only". The lattice spacing values used in the calculations are also given; $a = 0$ indicates that the results have been extrapolated to the continuum limit. In the plot of the doubly charmed baryons, the recently announced experimental result for the Ξ_{cc}^+ mass from LHCb [36] is shown with a horizontal line.

Fig. 15.9 shows a compilation of recent lattice results for doubly and triply charmed baryons, provided by S. Meinel [88]. The state recently announced by LHCb [36] is also shown. Note that the lattice calculations for the mass of this state were predictions, not postdictions.

Recall that lattice calculations take operators which are interpolating fields with quantum numbers appropriate to the desired states, compute correlation functions of these operators, and fit the correlation functions to functional forms parametrized by a set of masses and matrix elements. As we move away from hadrons which can be created by the simplest quark model operators (appropriate to the lightest meson and baryon multiplets) we encounter a host of new problems: either no good interpolating fields, or too many possible interpolating fields, and many states

with the same quantum numbers. Techniques for dealing with these interrelated problems vary from collaboration to collaboration, but all share common features: typically, correlation functions from many different interpolating fields are used, and the signal is extracted in what amounts to a variational calculation using the chosen operator basis. In addition to mass spectra, wave function information can be garnered from the form of the best variational wave function. Of course, the same problems which are present in the spectroscopy of the lightest hadrons (the need to extrapolate to infinite volume, physical values of the light quark masses, and zero lattice spacing) are also present. We briefly touch on three different kinds of hadrons: excited states of mesons (including hybrids), excited states of baryons, and glueballs. The quality of the data is not as good as for the ground states, and so the results continue to evolve.

Modern calculations use a large bases of trial states, which allow them to probe many quantum number channels simultaneously. This is vital for studying "difficult sectors" of QCD, such as the isoscalar mesons. A recent example of meson spectroscopy where this is done, by [89], is shown in Fig. 15.10. The quark masses are still heavier than their physical values, so the pion is at 392 MeV. The authors can assign a relative composition of nonstrange and strange quark content to their states, observing, for example, a nonstrange ω and a strange ϕ. Some states also have a substantial component of gluonic excitation. Note especially the three exotic channels $J^{PC} = 1^{-+}$, 0^{+-}, and 2^{+-}, with states around 2 GeV. These calculations will continue to improve as the quark masses are carried lower.

The interesting physics questions of excited baryon spectroscopy to be addressed are precisely those enumerated in the last section. An example of a recent calculation, due to Ref. [90] is shown in Fig. 15.11. Notice that the pion is not yet at its physical value. The lightest positive parity state is the nucleon, and the Roper resonance has not yet appeared as a light state.

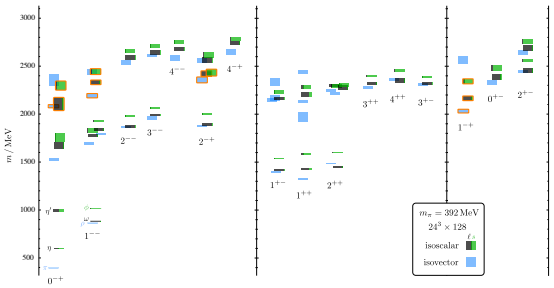

Figure 15.10: Isoscalar (green and black) and isovector (blue) spectrum from Ref. [89]. States are labeled J^{PC}. The quark mass is heavier than its physical value; $m_\pi = 392$ MeV. The vertical height of each box indicates the statistical uncertainty in the mass. Black and green indicate relative nonstrange and strange composition. Orange outlines show states with a large chromomagnetic component to their wave function, which the authors argue are hybrid states. Note the exotic states in the three rightmost columns.

Most hadrons are resonances, and lattice calculations will have to deal with this fact as the quark masses are taken ever smaller. The actual calculation is of the combined mass of two (or more) hadrons in a box of finite size. The combined mass is shifted from being the sum of the individual masses because the finite box forces the hadrons to interact with each other. The volume-dependent mass shift yields the phase shift for the continuum scattering amplitude, which in turn can be used to extract the resonance mass and width, with some degree of modeling. So far only two-body resonances, the rho meson and a few others, have been well studied. This is an active research area. A recent review, [91], summarizes the situation, and example of a calculation of the rho meson decay width is [92]. The mass and decay width of the $f_0(500)$ have recently been computed in [93]. Ref. [94] studies the decay width of the $\Delta(1238)$. Lattice calculations relevant to the extra states observed in the charmonium spectrum (Sec. 15.3)

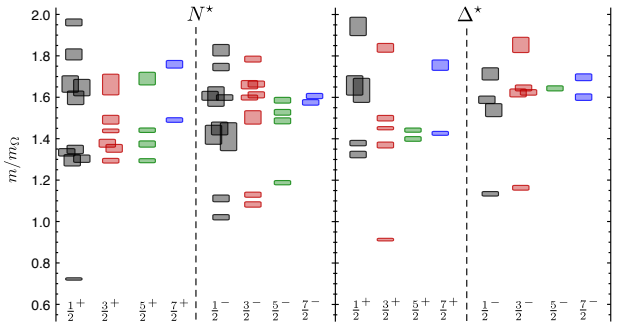

Figure 15.11: Spin-identified spectrum of nucleons and deltas, from lattices where $m_\pi = 396$ MeV, in units of the calculated Ω mass, from Ref. [90]. The colors just correspond to the different J assignments: grey for $J = 1/2$, red for $J = 3/2$, green for 5/2, blue for $J = 7/2$.

are difficult, because the states sit high in the spectrum of most channels and due to the number of nearby multiparticle states.

In Fig. 15.4 we showed a figure from [12] presenting a lattice prediction for the glueball mass spectrum in quenched approximation. A true QCD prediction of the glueball spectrum requires dynamical light quarks and (because glueball operators are intrinsically noisy) high statistics. Only recently have the first useful such calculations appeared, in [95, 96]. Fig. 15.12 shows results from [95], done with dynamical u, d and s quarks at two lattice spacings, 0.123 and 0.092 fm, along with comparisons to the quenched lattice calculation of [18] and to experimental isosinglet mesons. The dynamical simulation is, of course, not the last word on this subject, but it shows that the effects of quenching seem to be small.

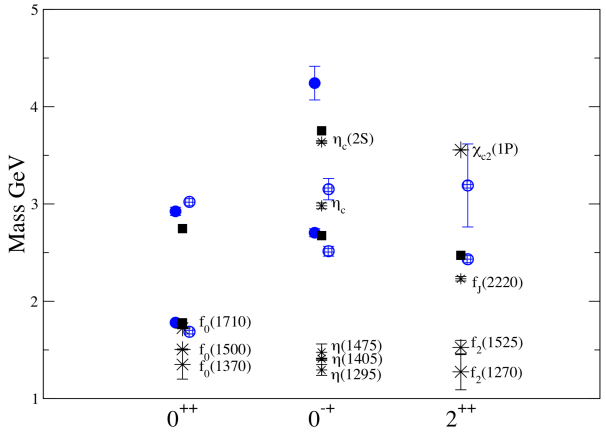

Figure 15.12: Lattice QCD predictions for glueball masses. The open and closed circles are the larger and smaller lattice spacing data of the full QCD calculation of glueball masses of Ref. [95]. Squares are the quenched data for glueball masses of Ref. [18]. The bursts labeled by particle names are experimental states with the appropriate quantum numbers.

As a final part of spectroscopy we mention electromagnetic mass splittings (such as the neutron - proton mass difference). They are interesting but difficult. These calculations are important for determining the values of the quark masses (for a discussion see the review in the PDG). Knowing that the neutron is heavier than the proton tells us that these splittings have a complicated origin. One part of the shift is because the up and down quarks have slightly different masses. The second is that the quarks have (different) charges. Phenomenologists (compare Ref. [97]) combine Coulomb forces and spin-dependent electromagnetic hyperfine interactions to model their charge effects. In order to compute hadronic mass differences on the lattice, electromagnetic interactions must be included in the simulations. This creates a host of technical is-

sues. An important one is that electromagnetic interactions are long range, but lattice simulations are done in finite volumes. The theoretical situation is summarized in the recent review [98]. A recent calculation, Ref. [99], has presented the first results for electromagnetic mass splittings in the baryon octet, with good agreement with observation. Ref. [100] has calculations for meson splittings.

References

[1] C. Amsler in the Quark Structure of Hadrons, Lecture Notes in Physics **949** (2018), ed. Springer.

[2] K.-C. Yang, Nucl. Phys. **B776**, 187 (2007), [arXiv:0705.0692].

[3] L. Burakovsky and J. T. Goldman, Nucl. Phys. **A625**, 220 (1997), [hep-ph/9703272].

[4] J. Schwinger, Phys. Rev. **135**, B816 (1964).

[5] A. Bramon, R. Escribano and M. D. Scadron, Phys. Lett. **B403**, 339 (1997), [hep-ph/9703313].

[6] A. Aloisio *et al.* (KLOE), Phys. Lett. **B541**, 45 (2002), [hep-ex/0206010].

[7] F. Ambrosino *et al.*, JHEP **07**, 105 (2009), [arXiv:0906.3819].

[8] C. Amsler *et al.* (Crystal Barrel), Phys. Lett. **B294**, 451 (1992).

[9] C. Amsler, Rev. Mod. Phys. **70**, 1293 (1998), [hep-ex/9708025].

[10] N. H. Christ *et al.*, Phys. Rev. Lett. **105**, 241601 (2010), [arXiv:1002.2999].

[11] T. Feldmann, Int. J. Mod. Phys. **A915**, 159 (2000).

[12] Y. Chen *et al.*, Phys. Rev. **D73**, 014516 (2006), [hep-lat/0510074].

[13] C. Amsler and F. E. Close, Phys. Rev. **D53**, 295 (1996), [hep-ph/9507326].

[14] R. L. Jaffe, Phys. Rev. **D15**, 267 (1977).

[15] R. L. Jaffe, Phys. Rev. **D15**, 281 (1977).

[16] S.L. Olsen, Front. Phys. **10**, 121 (2015).

[17] S. L. Olsen, T. Skwarnicki and D. Zieminska, Rev. Mod. Phys. **90**, 1, 015003 (2018), [arXiv:1708.04012].

[18] C. J. Morningstar and M. J. Peardon, Phys. Rev. **D60**, 034509 (1999), [hep-lat/9901004].

[19] W.-J. Lee and D. Weingarten, Phys. Rev. **D61**, 014015 (2000), [hep-lat/9910008].

[20] G. S. Bali *et al.* (UKQCD), Phys. Lett. **B309**, 378 (1993), [hep-lat/9304012].

[21] C. Michael, AIP Conf. Proc. **432**, 1, 657 (1998), [hep-ph/9710502].

[22] F. E. Close and A. Kirk, Eur. Phys. J. **C21**, 531 (2001), [hep-ph/0103173].

[23] W. Ochs, J. Phys. **G40**, 043001 (2013), [arXiv:1301.5183].

[24] F. Brünner and A. Rebhan, Phys. Rev. Lett. **115**, 13, 131601 (2015), [arXiv:1504.05815].

[25] C. Amsler and N. A. Tornqvist, Phys. Rept. **389**, 61 (2004).

[26] N. Isgur and J. E. Paton, Phys. Rev. **D31**, 2910 (1985).

[27] P. Lacock *et al.* (UKQCD), Phys. Lett. **B401**, 308 (1997), [hep-lat/9611011].

[28] M. S. Chanowitz and S. R. Sharpe, Nucl. Phys. **B222**, 211 (1983), [Erratum: Nucl. Phys.B228,588(1983)].

[29] T. Barnes *et al.*, Nucl. Phys. **B224**, 241 (1983).

[30] R. Aaij *et al.* (LHCb), Phys. Rev. Lett. **115**, 072001 (2015), [arXiv:1507.03414].

[31] R. Aaij *et al.* (LHCb), Phys. Rev. Lett. **122**, 22, 222001 (2019), [arXiv:1904.03947].

[32] Y.-R. Liu *et al.*, Prog. Part. Nucl. Phys. **107**, 237 (2019), [arXiv:1903.11976].

[33] F.E. Close, in *Quarks and Nuclear Forces* (Springer-Verlag, 1982), p. 56.

[34] V. Crede and W. Roberts, Rept. on Prog. in Phys. **76**, 076301 (2013).

[35] R. Aaij *et al.* (LHCb), Phys. Rev. Lett. **118**, 18, 182001 (2017), [arXiv:1703.04639].

[36] R. Aaij *et al.* (LHCb), Phys. Rev. Lett. **119**, 11, 112001 (2017), [arXiv:1707.01621].

[37] M. Mattson *et al.* (SELEX), Phys. Rev. Lett. **89**, 112001 (2002), [hep-ex/0208014].

[38] A. Ocherashvili *et al.* (SELEX), Phys. Lett. **B628**, 18 (2005), [hep-ex/0406033].

[39] M. Karliner and J. L. Rosner, Phys. Rev. **D90**, 9, 094007 (2014), [arXiv:1408.5877].

[40] R.H. Dalitz and L.J. Reinders, in "Hadron Structure as Known from Electromagnetic and Strong Interactions," *Proceedings of the Hadron '77 Conference* (Veda, 1979), p. 11.

[41] E. Klempt and J.-M. Richard, Rev. Mod. Phys. **82**, 1095 (2010), [arXiv:0901.2055].

[42] T. Melde, W. Plessas and B. Sengl, Phys. Rev. **D77**, 114002 (2008), [arXiv:0806.1454].

[43] N. Isgur and G. Karl, Phys. Rev. **D18**, 4187 (1978).

[44] N. Isgur and G. Karl, Phys. Rev. **D19**, 2653 (1979), [Erratum: Phys. Rev.D23,817(1981)].

[45] S. Capstick and W. Roberts, Prog. Part. Nucl. Phys. **45**, S241 (2000), [arXiv:nucl-th/0008028].

[46] S. Capstick and W. Roberts, Phys. Rev. **D58**, 074011 (1998), [arXiv:nucl-th/9804070].

[47] R. A. Arndt *et al.*, Phys. Rev. **C74**, 045205 (2006), [arXiv:nucl-th/0605082].

[48] B. Krusche and S. Schadmand, Prog. Part. Nucl. Phys. **51**, 399 (2003), [arXiv:nucl-ex/0306023].

[49] A. V. Anisovich *et al.*, Eur. Phys. J. **A52**, 9, 284 (2016), [arXiv:1604.05704].

[50] E. Gutz *et al.* (CBELSA/TAPS), Eur. Phys. J. **A50**, 74 (2014), [arXiv:1402.4125].

[51] V. Sokhoyan *et al.* (CBELSA/TAPS), Eur. Phys. J. **A51**, 8, 95 (2015), [Erratum: Eur. Phys. J.A51,no.12,187(2015)], [arXiv:1507.02488].

[52] S. Capstick and W. Roberts, Prog. in Part. Nucl. Phys. **45**, 241 (2000).

[53] M. Ferraris *et al.*, Phys. Lett. **B364**, 231 (1995).

[54] M. M. Giannini and E. Santopinto, Chin. J. Phys. **53**, 020301 (2015), [arXiv:1501.03722].

[55] M. Anselmino *et al.*, Rev. Mod. Phys. **65**, 1199 (1993).

[56] R. Bijker, F. Iachello and A. Leviatan, Annals Phys. **236**, 69 (1994), [arXiv:nucl-th/9402012].

[57] S. Capstick and P. R. Page, Phys. Rev. **C66**, 065204 (2002), [arXiv:nucl-th/0207027].

[58] R. L. Jaffe, D. Pirjol and A. Scardicchio, Phys. Rept. **435**, 157 (2006), [hep-ph/0602010].

[59] S. Capstick, Phys. Rev. **D46**, 2864 (1992).

[60] A. De Rujula, H. Georgi and S. L. Glashow, Phys. Rev. **D12**, 147 (1975).

[61] W. H. Blask *et al.*, Z. Phys. **A337**, 327 (1990).

[62] U. Loring *et al.*, Eur. Phys. J. **A10**, 309 (2001), [hep-ph/0103287].

[63] L. Ya. Glozman and D. O. Riska, Phys. Rept. **268**, 263 (1996), [hep-ph/9505422].

[64] C. Aubin *et al.*, Phys. Rev. **D70**, 094505 (2004), [hep-lat/0402030].

[65] A. Bazavov *et al.* (MILC), Rev. Mod. Phys. **82**, 1349 (2010), [arXiv:0903.3598].

[66] S. Aoki *et al.* (PACS-CS), Phys. Rev. **D79**, 034503 (2009), [arXiv:0807.1661].

[67] S. Durr *et al.*, Science **322**, 1224 (2008), [arXiv:0906.3599].

[68] W. Bietenholz *et al.*, Phys. Rev. **D84**, 054509 (2011), [arXiv:1102.5300].

[69] C. Alexandrou *et al.*, Phys. Rev. **D90**, 7, 074501 (2014), [arXiv:1406.4310].

[70] J. J. Dudek *et al.*, Phys. Rev. **D83**, 111502 (2011), [arXiv:1102.4299].

[71] E. B. Gregory *et al.* (UKQCD), Phys. Rev. **D86**, 014504 (2012), [arXiv:1112.4384].

[72] C. Michael, K. Ottnad and C. Urbach (ETM), Phys. Rev. Lett. **111**, 18, 181602 (2013), [arXiv:1310.1207].

[73] C. Bernard *et al.* (Fermilab Lattice, MILC), Phys. Rev. **D83**, 034503 (2011), [arXiv:1003.1937].

[74] E. B. Gregory *et al.*, Phys. Rev. **D83**, 014506 (2011), [arXiv:1010.3848].

[75] R. J. Dowdall *et al.*, Phys. Rev. **D86**, 094510 (2012), [arXiv:1207.5149].

[76] D. Mohler and R. M. Woloshyn, Phys. Rev. **D84**, 054505 (2011), [arXiv:1103.5506].

[77] A. S. Kronfeld, Ann. Rev. Nucl. Part. Sci. **62**, 265 (2012), [arXiv:1203.1204].

[78] K. Ottnad, C. Urbach and F. Zimmermann (OTM), Nucl. Phys. **B896**, 470 (2015), [arXiv:1501.02645].

[79] J. O. Daldrop, C. T. H. Davies and R. J. Dowdall (HPQCD), Phys. Rev. Lett. **108**, 102003 (2012), [arXiv:1112.2590].

[80] G. C. Donald *et al.*, Phys. Rev. **D86**, 094501 (2012), [arXiv:1208.2855].

[81] L. Liu *et al.*, Phys. Rev. **D81**, 094505 (2010), [arXiv:0909.3294].

[82] R. A. Briceno, H.-W. Lin and D. R. Bolton, Phys. Rev. **D86**, 094504 (2012), [arXiv:1207.3536].

[83] Y. Namekawa *et al.* (PACS-CS), Phys. Rev. **D87**, 9, 094512 (2013), [arXiv:1301.4743].

[84] M. Padmanath *et al.*, Phys. Rev. **D90**, 7, 074504 (2014), [arXiv:1307.7022].

[85] Z. S. Brown *et al.*, Phys. Rev. **D90**, 9, 094507 (2014), [arXiv:1409.0497].

[86] P. Pérez-Rubio, S. Collins and G. S. Bali, Phys. Rev. **D92**, 3, 034504 (2015), [arXiv:1503.08440].

[87] C. Alexandrou and C. Kallidonis, Phys. Rev. **D96**, 3, 034511 (2017), [arXiv:1704.02647].

[88] S. Meinel, private comunication .

[89] J. J. Dudek *et al.* (Hadron Spectrum), Phys. Rev. **D88**, 9, 094505 (2013), [arXiv:1309.2608].

[90] R. G. Edwards *et al.*, Phys. Rev. **D84**, 074508 (2011), [arXiv:1104.5152].

[91] R. A. Briceno, J. J. Dudek and R. D. Young, Rev. Mod. Phys. **90**, 2, 025001 (2018), [arXiv:1706.06223].

[92] J. Bulava *et al.*, Nucl. Phys. **B910**, 842 (2016), [arXiv:1604.05593].

[93] R. A. Briceno *et al.*, Phys. Rev. Lett. **118**, 2, 022002 (2017), [arXiv:1607.05900].

[94] C. W. Andersen *et al.*, Phys. Rev. **D97**, 1, 014506 (2018), [arXiv:1710.01557].

[95] C. M. Richards *et al.* (UKQCD), Phys. Rev. **D82**, 034501 (2010), [arXiv:1005.2473].

[96] E. Gregory *et al.*, JHEP **10**, 170 (2012), [arXiv:1208.1858].

[97] M. Karliner and J. L. Rosner (2019), [arXiv:1906.07799].

[98] A. Patella, PoS **LATTICE2016**, 020 (2017), [arXiv:1702.03857].

[99] S. Borsanyi *et al.*, Science **347**, 1452 (2015), [arXiv:1406.4088].

[100] D. Giusti *et al.*, Phys. Rev. **D95**, 11, 114504 (2017), [arXiv:1704.06561].

16. Heavy-Quark and Soft-Collinear Effective Theory

Revised August 2019 by C.W. Bauer (LBNL) and M. Neubert (PRISMA, Mainz Inst. for Theor. Physics, JG U.).

16.1 Effective Field Theories

Quantum field theories provide the most precise computational tools for describing physics at the highest energies. One of their characteristic features is that they almost inevitably involve multiple length scales. When trying to determine the value of an observable, quantum field theory demands that all possible virtual states and hence all particles be included in the calculation. Since these particles have widely different masses, the final prediction is sensitive to many scales. This fact represents a formidable challenge from a practical point of view. No realistic quantum field theories can be solved exactly, so that one needs to resort to approximation schemes; these, however, are typically most straightforward when only a single scale is involved at a time.

Effective field theories (EFTs) provide a general theoretical framework to deal with the multi-scale problems of realistic quantum field theories. This framework aims at reducing such problems to a combination of separate and simpler single-scale problems; simultaneously, however, it provides an organization scheme whereby the other scales are not omitted but allowed to play their role in a separate step of the computation. The philosophy and basic principles of this approach are very generic, and correspondingly EFTs represent a widely used method in many different areas of high-energy physics, from the low-energy scales of atomic and nuclear physics to the high-energy scales of (partly yet unknown) elementary-particle physics, see [1–3] for some early references. EFTs can play a role both within analytic perturbative computations and in the context of non-perturbative numerical simulations; One of the simplest applications of EFTs to particle physics concerns the description of an underlying theory that is only probed at energy scales $E < \Lambda$. Any particle with mass $m > \Lambda$ cannot be produced as a real state and therefore only leads to short-distance virtual effects. Thus, one can construct an effective theory in which the quantum fluctuations of such heavy particles are "integrated out" from the generating functional for Green functions. This results in a simpler theory containing only those degrees of freedom that are relevant to the energy scales under consideration. In fact, the standard model of particle physics itself is widely viewed as an EFT of some yet unknown, more fundamental theory.

The development of any effective theory starts by identifying the degrees of freedom that are relevant to describe the physics at a given energy (or length) scale and constructing the Lagrangian describing the interactions among these fields. Short-distance quantum fluctuations associated with much smaller length scales are absorbed into the coefficients of the various operators in the effective theory. These coefficients are determined in a matching procedure, by requiring that the EFT reproduces the matrix elements of the full theory up to power corrections. In many cases the effective Lagrangian exhibits enhanced symmetries compared with the fundamental theory, allowing for simple and sometimes striking predictions relating different observables.

16.2 Heavy-Quark Effective Theory

Heavy-quark systems provide prime examples for applications of the EFT technology, because the hierarchy $m_Q \gg \Lambda_{\rm QCD}$ (with $Q = b, c$) provides a natural separation of scales. Physics at the scale m_Q is of a short-distance nature and can be treated perturbatively, while for heavy-quark systems there is always also some hadronic physics governed by the confinement scale $\Lambda_{\rm QCD}$ of the strong interaction. Being able to separate the short-distance and long-distance effects associated with these two scales is crucial for any quantitative description. For instance, if the long-distance hadronic matrix elements are obtained from lattice QCD, then it is necessary to analytically compute the effects of short-wavelength modes that do not fit on the lattice. In many other instances, the long-distance physics can be encoded in a small number of hadronic parameters.

16.2.1 *General idea and derivation of the effective Lagrangian*

The simplest effective theory for heavy-quark systems is the heavy-quark effective theory (HQET) [4–7] (see [8, 9] for detailed discussions). It provides a simplified description of the soft interactions of a single heavy quark with light partons. This includes the interactions that bind the heavy quark with other light partons inside heavy mesons and baryons.

A softly interacting heavy quark is nearly on-shell. Its momentum may be decomposed as $p_Q = m_Q v + k$, where v is the 4-velocity of the hadron containing the heavy quark. The "residual momentum" k results from the soft interactions of the heavy quark with its environment and satisfies $v \cdot k \sim \Lambda_{\rm QCD}$ and $k^2 \sim \Lambda^2_{\rm QCD}$, which in the rest frame of the heavy hadron reduces to $k^\mu \sim \Lambda_{\rm QCD}$. In the limit $m_Q \gg \Lambda_{\rm QCD}$, the soft interactions do not change the 4-velocity of the heavy quark, which is therefore a conserved quantum number that is often used as a label on the effective heavy-quark fields. A nearly on-shell Dirac spinor has two large and two small components. We define

$$Q(x) = e^{-im_Q v\cdot x}\,[h_v(x) + H_v(x)]\,, \tag{16.1}$$

where

$$h_v(x) = e^{im_Q v\cdot x}\,\frac{1+\not{v}}{2}\,Q(x)\,, \qquad H_v(x) = e^{im_Q v\cdot x}\,\frac{1-\not{v}}{2}\,Q(x) \tag{16.2}$$

are the large ("upper") and small ("lower") components of the spinor field, respectively. The extraction of the phase factor in (16.1) implies that the fields h_v and H_v carry the residual momentum k. The field H_v is $1/m_Q$ suppressed relative to h_v and describes quantum fluctuations far off the mass shell. Integrating it out using its equations of motion yields the HQET Lagrangian

$$\mathcal{L}_{\rm HQET} = \bar h_v\, iv\cdot D_s\, h_v + \frac{1}{2m_Q}\left[\bar h_v (iD_s)^2 h_v + C_{\rm mag}(\mu)\,\frac{g}{2}\,\bar h_v\,\sigma_{\mu\nu}\,G_s^{\mu\nu} h_v\right] + \dots\,. \tag{16.3}$$

The covariant derivative $iD_s^\mu = i\partial^\mu + gA_s^\mu$ and the field strength $G_s^{\mu\nu}$ contain only the soft gluon field. Hard gluons have been integrated out, and their effects are contained in the Wilson coefficients of the operators in the effective Lagrangian. From the leading operator one derives the Feynman rules of HQET. The new operators entering at subleading order are referred to as the "kinetic energy" and "chromo-magnetic interaction". The kinetic-energy operator corresponds to the first correction term in the Taylor expansion of the relativistic energy $E = m_Q + \vec p^{\,2}/2m_Q + \dots$. Lorentz invariance, which is encoded as a reparametrization invariance of the effective Lagrangian [10], ensures that its Wilson coefficient is not renormalized ($C_{\rm kin} \equiv 1$). The coefficient $C_{\rm mag}$ of the chromo-magnetic operator receives corrections starting at one-loop order.

16.2.2 *Spin-flavor symmetry*

The leading term in the HQET Lagrangian exhibits a global spin-flavor symmetry. Its physical meaning is that, in the infinite mass limit, the properties of hadronic systems containing a single heavy quark are insensitive to the spin and flavor of the heavy quark [11, 12]. The spin symmetry results from the fact that there are no Dirac matrices in the leading term of the effective Lagrangian in (16.3), implying that the interactions of the heavy quark with soft gluons leave its spin unchanged. The flavor symmetry arises since the mass of the heavy quark does not appear at leading order. For n_Q heavy quarks moving at the same velocity, one can simply extend (16.3) by summing over n_Q identical terms for heavy-quark fields h_v^i. The result is invariant under rotations in flavor space. When combined with the spin symmetry, the symmetry group becomes promoted to $SU(2n_Q)$. These symmetries are broken by the operators at subleading power in the $1/m_Q$ expansion.

The spin-flavor symmetry leads to many interesting relations between the properties of hadrons containing a heavy quark. The most direct consequences concern the spectroscopy of such states

[13]. In the heavy-quark limit, the spin of the heavy quark and the total angular momentum j of the light degrees of freedom are separately conserved by the strong interactions. Because of heavy-quark symmetry, the dynamics is independent of the spin and mass of the heavy quark. Hadronic states can thus be classified by the quantum numbers (flavor, spin, parity, etc.) of the light degrees of freedom. The spin symmetry predicts that, for fixed $j \neq 0$, there is a doublet of degenerate states with total spin $J = j \pm \frac{1}{2}$. The flavor symmetry relates the properties of states with different heavy-quark flavor.

16.2.3 *Weak decay form factors*

Of particular interest are the relations between the weak decay form factors of heavy mesons, which parametrize hadronic matrix elements of currents between two mesons containing a heavy quark. These relations have been derived by Isgur and Wise [12], generalizing ideas developed by Nussinov and Wetzel [14] and Voloshin and Shifman [15]. For the purpose of this discussion, it is convenient to work with a mass-independent normalization of meson states and use velocity rather than momentum variables.

Consider the elastic scattering of a pseudoscalar meson, $P(v) \to P(v')$, induced by an external vector current coupled to the heavy quark contained in P, which acts as a color source moving with the meson's velocity v. The action of the current is to replace instantaneously the color source by one moving at velocity v'. Soft gluons need to be exchanged in order to rearrange the light degrees of freedom and build up the final state meson moving at velocity v'. This rearrangement leads to a form-factor suppression. The important observation is that, in the $m_Q \to \infty$ limit, the form factor can only depend on the Lorentz boost $\gamma = v \cdot v'$ connecting the rest frames of the initial and final-state mesons (as long as $\gamma = \mathcal{O}(1)$). In the effective theory the hadronic matrix element describing the scattering process can therefore be written as

$$\langle P(v')|\,\bar h_{v'}\gamma^\mu h_v\,|P(v)\rangle = \xi(v\cdot v')(v+v')^\mu, \tag{16.4}$$

with a form factor $\xi(v \cdot v')$ that is real and independent of m_Q. By flavor symmetry, the form factor remains identical when one replaces the heavy quark Q in one of the meson states by a heavy quark Q' of a different flavor, thereby turning P into another pseudoscalar meson P'. At the same time, the current becomes a flavor-changing vector current. This universal form factor is called the Isgur-Wise function [12]. For equal velocities the vector current $J^\mu = \bar h_v \gamma^\mu h_v$ is conserved in the effective theory, irrespective of the flavor of the heavy quarks. The corresponding conserved charges are the generators of the flavor symmetry. It follows that the Isgur-Wise function is normalized at the point of equal velocities: $\xi(1) = 1$. Since the recoil energy of the daughter meson P' in the rest frame of the parent meson P is $E_{\rm recoil} = m_{P'}\,(v\cdot v'-1)$, the point $v \cdot v' = 1$ is referred to as the zero-recoil limit. The heavy-quark spin symmetry leads to additional relations among weak decay form factors. It can be used to relate matrix elements involving vector mesons to those involving pseudoscalar mesons, which once again can be described completely in terms of the universal Isgur-Wise function.

The form factor relations imposed by heavy-quark symmetry describe the semileptonic decay processes $\bar B \to D\,\ell\,\bar\nu$ and $\bar B \to D^*\ell\,\bar\nu$ in the limit of infinite heavy-quark masses. They are model-independent consequences of QCD. The known normalization of the Isgur-Wise function at zero recoil can be used to obtain a model-independent measurement of the element $|V_{cb}|$ of the Cabibbo-Kobayashi-Maskawa (CKM) matrix. The semileptonic decay $\bar B \to D^*\ell\,\bar\nu$ is particularly well suited for this purpose [16]. Experimentally this is a very clean mode, since the reconstruction of the D^* meson mass provides a powerful rejection against background. From the theoretical point of view, it is ideal since the decay rate at zero recoil is protected by Luke's theorem against first-order power corrections in $1/m_Q$ [17]. This is described in more detail in Section 12. Corrections to the heavy-quark symmetry relations for the $\bar B \to D^{(*)}$ form factors near zero recoil can also be constrained using sum rules derived in the small-velocity limit [18,19].

16.2.4 *Decoupling transformation*

At leading order in $1/m_Q$, the couplings of soft gluons to heavy quarks in the effective Lagrangian (16.3) can be removed by the field redefinition $h_v(x) = Y_v(x)\,h_v^{(0)}(x)$, where $Y_v(x)$ is a soft Wilson line along the direction of v, extending from minus infinity to the point x. In terms of the new fields the leading-order HQET Lagrangian becomes $\mathcal{L}_{\rm HQET} = \bar h_v^{(0)} iv\cdot\partial\, h_v^{(0)}$. It describes a free theory as far as the strong interactions of heavy quarks are concerned. However, the theory is nevertheless non-trivial in the presence of external sources. Consider, e.g., the case of a weak-interaction heavy-quark current

$$\bar h_{v'}\gamma^\mu(1-\gamma_5)h_v = \bar h_{v'}^{(0)}\gamma^\mu(1-\gamma_5)\,Y_{v'}^\dagger Y_v\,h_v^{(0)}, \tag{16.5}$$

where v and v' are the velocities of the heavy mesons containing the heavy quarks. Unless the two velocities are equal, corresponding to the zero-recoil limit discussed above, the object $Y_{v'}^\dagger Y_v$ is non-trivial, and hence the soft gluons do not decouple from the heavy quarks inside the current operator. One may interpret $Y_{v'}^\dagger Y_v$ as a Wilson loop with a cusp at the point x, where the two paths parallel to the different velocity vectors intersect. The presence of the cusp leads to non-trivial ultra-violet behavior (for $v \neq v'$), which is described by a cusp anomalous dimension $\Gamma_{\rm cusp}(v\cdot v')$ that was calculated at two-loop order in [20]. It coincides with the velocity-dependent anomalous dimension of heavy-quark currents, which was introduced in the context of HQET in [21]. The interpretation of heavy quarks as Wilson lines is a useful tool, which was put forward in one of the very first papers on the subject [4]. This technology will be useful in the study of the interactions of heavy quarks with collinear degrees of freedom discussed later in this review.

16.2.5 *Heavy-quark expansion for inclusive decays*

The theoretical description of inclusive decays of hadrons containing a heavy quark exploits two observations [22–26]: bound-state effects related to the initial state can be calculated using the heavy-quark expansion, and the fact that the final state consists of a sum over many hadronic channels eliminates the sensitivity to the properties of individual final-state hadrons. The second feature rests on the hypothesis of quark-hadron duality, i.e. the assumption that decay rates are calculable in QCD after a smearing procedure has been applied [27]. In semileptonic decays, the integration over the lepton spectrum provides a smearing over the invariant hadronic mass of the final state (global duality). For nonleptonic decays, where the total hadronic mass is fixed, the summation over many hadronic final states provides an averaging (local duality). Since global duality is a much weaker assumption, the theoretical control of inclusive semileptonic decays is on firmer footing.

Using the optical theorem, the inclusive decay width of a hadron H_b containing a b quark can be written in the form

$$\Gamma(H_b) = \frac{1}{M_{H_b}}\,{\rm Im}\,\langle H_b|\,i\int {\rm d}^4x\,T\,\{\mathcal{H}_{\rm eff}(x),\mathcal{H}_{\rm eff}(0)\}\,|H_b\rangle\,. \tag{16.6}$$

The effective weak Hamiltonian for b-quark decays consists of dimension-6 four-fermion operators and dipole operators [28]. Because of the large mass of the b quark, it follows that the separation of fields in the time-ordered product in (16.6) is small, of order $x \sim 1/m_b$. It is thus possible to construct an operator-product expansion (OPE) for the time-ordered product, in which it is represented as a series of local operators in HQET. The leading operator $\bar h_v h_v$ has a trivial matrix element. The next contributions arise at $\mathcal{O}(1/m_b^2)$ and give rise to two parameters $\mu_\pi^2(H_b)$ and $\mu_G^2(H_b)$, which are defined as the matrix elements of the heavy-quark kinetic energy and chromo-magnetic interaction inside the hadron H_b, respectively [29]. For the ground-state heavy mesons and baryons, one has $\mu_G^2(B) = 3(m_{B^*}^2 - m_B^2)/4 \simeq 0.36\,{\rm GeV}^2$ and $\mu_G^2(\Lambda_b) = 0$. Thus, the total inclusive decay rate of a hadron H_b

can be written as [23,24]

$$\Gamma(H_b) = \frac{G_F^2 m_b^5 |V_{cb}|^2}{192\pi^3}\left[c_1 + c_2\,\frac{\mu_\pi^2(H_b)}{2m_b^2} + c_3\,\frac{\mu_G^2(H_b)}{2m_b^2} + \mathcal{O}\Big(\frac{1}{m_b^3}\Big) + \dots\right], \tag{16.7}$$

where the prefactor arises from the loop integrations and is proportional to the fifth power of the b-quark mass. The coefficient functions c_i are calculable order by order in perturbation theory. While c_1 corresponds to the decay rate of a free heavy quark, the higher-order coefficients systematically account for bound-state effects. The coefficients of the subleading operators and of the leading operator at third order in $1/m_b$ have recently been calculated at NLO [30–34], and the heavy-quark expansion has been pushed to fifth order in $1/m_b$ [35].

From the fully inclusive width in (16.7) one can obtain the lifetime of a heavy hadron via $\tau(H_b) = 1/\Gamma(H_b)$. Due to the universality of the leading term in the heavy-quark expansion, lifetime ratios such as $\tau(B^-)/\tau(\bar B^0)$, $\tau(\bar B_s^0)/\tau(\bar B^0)$ and $\tau(\Lambda_b)/\tau(\bar B^0)$ are particularly sensitive to the hadronic parameters determining the power corrections in the expansion. In order to understand these ratios theoretically, it is necessary to include phase-space enhanced power corrections of order $(\Lambda_{\rm QCD}/m_b)^3$ [36,37] as well as short-distance perturbative effects [38] in the calculation (see [39] for a recent discussion of the status of the corresponding calculations).

A formula analogous to (16.7) can be derived for differential distributions in specific inclusive decay processes, assuming that these distributions are integrated over a sufficiently large region of phase space to ensure quark-hadron duality. Important examples are the distributions in the lepton energy and the lepton invariant mass, as well as moments of the invariant hadronic mass distribution in the semileptonic processes $\bar B \to X_u\,\ell\,\bar\nu$ and $\bar B \to X_c\,\ell\,\bar\nu$. A global fit of semileptonic decay distributions can be used to determine the CKM matrix elements $|V_{ub}|$ and $|V_{cb}|$ along with heavy-quark parameters such as the masses m_b, m_c and the hadronic parameters $\mu_\pi^2(B)$, $\mu_G^2(B)$. These determinations provide some of the most accurate values for these parameters (see e.g. [40–42]).

16.2.6 *Shape functions and non-local power corrections*

In certain regions of phase space, in which the hadronic final state in an inclusive heavy-hadron decay is made up of light energetic partons, the local OPE for inclusive decays must be replaced by a more complicated expansion involving hadronic matrix elements of non-local light-ray operators [43,44]. Prominent examples are the radiative decay $\bar B \to X_s\gamma$ for large photon energy E_γ near $m_B/2$, and the semileptonic decay $\bar B \to X_u\,\ell\,\bar\nu$ at large lepton energy or small hadronic invariant mass. In these cases, the differential decay rates at leading order in the heavy-quark expansion can be written in the factorized form $d\Gamma = H\,J\otimes S$ [45], where the hard function H and the jet function J are calculable in perturbation theory. The characteristic scales for these functions are set by m_b and $(m_b\Lambda_{\rm QCD})^{1/2}$, respectively. The soft function

$$S(\omega) = \int \frac{dt}{4\pi}\, e^{-i\omega t}\,\langle \bar B(v)|\,\bar h_v(tn) Y_n(tn) Y_n^\dagger(0) h_v(0)|\bar B(v)\rangle \tag{16.8}$$

is a non-perturbative object called the shape function [43,44]. Here Y_n are soft Wilson lines along a light-like direction n aligned with the momentum of the hadronic final-state jet. The jet function and the shape function share a common variable $\omega \sim \Lambda_{\rm QCD}$, and the symbol $\otimes$ denotes a convolution in this variable.

While the hard functions are different for the decays $\bar B \to X_s\gamma$ and $\bar B \to X_u\,\ell\bar\nu$, the jet and soft functions are identical at leading order in $\Lambda_{\rm QCD}/m_Q$. This is particularly important for the shape function, which introduces non-perturbative physics into the theoretical predictions for the decay rates in the regions of experimental interest. The fact that both processes depend on the same non-perturbative function makes it possible to use the measured shape of the $\bar B \to X_s\gamma$ photon spectrum to reduce the theoretical uncertainties in the determination of the CKM element $|V_{ub}|$ from semileptonic decays. In higher orders of the heavy-quark expansion, an increasing number of subleading jet and soft functions are required to describe the decay distributions [46]. These have been analyzed in detail at order $1/m_b$ [47–49]. In the case of $\bar B \to X_s\gamma$ (and also in the related case of $\bar B \to X_s\ell\bar\ell$), some of these non-local effects survive in the total decay rate and give rise to irreducible hadronic uncertainties [50]. The technology for deriving the corresponding factorization theorems relies on the soft-collinear effective theory, to which we now turn.

16.3 Soft-Collinear Effective Theory

As discussed in the previous section, soft gluons that bind a heavy quark inside a heavy meson cannot change the virtuality of that heavy quark by a significant amount. The ratio $\Lambda_{\rm QCD}/m_Q$ provides the expansion parameter in HQET, which is a small parameter since $m_Q \gg \Lambda_{\rm QCD}$. This obviously does not work when considering light quarks. However, if the energy Q of the quarks is large, the ratio $\Lambda_{\rm QCD}/Q$ provides a small parameter, which can be used to construct an effective theory. One major difference to HQET is that light energetic quarks cannot only emit soft gluons, but they can also emit collinear gluons (an energetic gluon in the same direction as the original quark), without parametrically changing their virtuality. Thus, to fully reproduce the long-distance physics of energetic quarks requires that one includes their interactions with both soft and collinear particles. The resulting effective theory is therefore called soft-collinear effective theory (SCET) [51–53] (see [54] for a review).

A single energetic particle can always be boosted to a frame where all momentum components have similar size, in which case there is no small expansion parameter. Thus the presence of energetic particles must refer to a reference frame defined by external kinematics. SCET has a wide range of applications; some examples are the production of energetic, light states in the decay of a heavy particle in its rest frame, the production of energetic jets in collider environments, and the scattering of energetic particles off a target at rest. In this brief review we will outline the main features of this effective theory and mention a few selected applications.

16.3.1 *General idea of the expansion*

Consider a quark with virtuality much less than its energy Q, moving along the direction $\vec n$. It is convenient to parameterize the momentum p_n of this particle in terms of its light-cone components, defined by $(p_n^-, p_n^+, p_n^\perp) = (\bar n\cdot p_n, n\cdot p_n, p_n^\perp)$, where $n^\mu = (1,\vec n)$ and $\bar n^\mu = (1,-\vec n)$ are light-like vectors, and $n\cdot p_n^\perp = \bar n\cdot p_n^\perp = 0$. The subscript n on the momentum indicates the direction of the collinear particle. In terms of these light-cone components, the virtuality satisfies $p_n^2 = p_n^+ p_n^- + p_n^{\perp 2}$. The individual components of the momentum obey

$$(p_n^-, p_n^+, p_n^\perp) \sim Q(1,\lambda^2,\lambda)\,, \tag{16.9}$$

where $\lambda^2 = p^2/Q^2$ is the expansion parameter of SCET. The virtuality of such an energetic particle remains parametrically unchanged if it interacts with energetic particles in the same direction n, or with soft particles with momentum scaling as

$$(p_s^-, p_s^+, p_s^\perp) \sim Q(\lambda^2,\lambda^2,\lambda^2)\,. \tag{16.10}$$

SCET is constructed in such a way as to reproduce the long-distance dynamics arising from the interactions of collinear and soft degrees of freedom.

In the above power counting the transverse momenta of soft degrees of freedom scale as $p_s^\perp \sim Q\lambda^2$, which is much smaller than the transverse momenta $p_c^\perp \sim Q\lambda$ of collinear fields. This theory is usually called SCET$_{\rm I}$. If the external kinematics require that the transverse momenta of both soft and collinear fields are of the same size, $p_c^\perp \sim p_s^\perp$, then the appropriate degrees of freedom have the scaling $p_c \sim Q(1,\lambda^2,\lambda)$ and $p_s \sim Q(\lambda,\lambda,\lambda)$. This theory is usually called SCET$_{\rm II}$ and is required, e.g., for exclusive hadronic decays such as $\bar B \to D\pi$, where the virtuality of both collinear and soft degrees of freedom are set by $\Lambda_{\rm QCD}$, or for the description of transverse-momentum distributions at colliders. SCET$_{\rm I}$ power counting is assumed in the following sections, while SCET$_{\rm II}$ is discussed in more detail in 16.3.6.

16.3.2 *Leading-order Lagrangian*

The derivation of the SCET Lagrangian follows similar steps as described for HQET in Section 16.2.1. One begins by deriving the Lagrangian for a theory containing only a single collinear sector. Similar to HQET, one separates the full QCD field into two components, $q_n(x) = \psi_n(x) + \Xi_n(x)$, where (with $n \cdot \bar{n} = 2$)

$$\psi_n(x) = \frac{\not{n}\bar{\not{n}}}{4}\, q_n(x)\,, \qquad \Xi_n(x) = \frac{\bar{\not{n}}\not{n}}{4}\, q_n(x)\,. \tag{16.11}$$

The degrees of freedom described by the field Ξ_n are far off shell and can therefore be eliminated using its equation of motion. This gives

$$\mathcal{L}_n = \bar{\psi}_n(x) \left[in\cdot D + i\not{D}^\perp \frac{1}{i\bar{n}\cdot D}\, i\not{D}^\perp \right] \frac{\bar{\not{n}}}{2}\, \psi_n(x)\,. \tag{16.12}$$

As a next step, one separates the large and residual momentum components by decomposing the collinear momentum into a "label" and a residual momentum, $p^\mu = P^\mu + k^\mu$ with $n \cdot P = 0$. One then performs a phase redefinition on the collinear fields, such that $\psi_n(x) = e^{iP\cdot x}\, \xi_n(x)$. Derivatives acting on the fields $\xi_n(x)$ now only pick out the residual momentum. Since unlike in HQET the label momentum in SCET is not conserved, one defines a label operator $\mathcal{P}^\mu$ acting as $\mathcal{P}^\mu \xi_n(x) = P^\mu \xi_n(x)$ [52], as well as a corresponding covariant label operator $i\mathcal{D}_n^\mu = \mathcal{P}^\mu + gA_n^\mu(x)$. Note that at leading order in power counting $i\mathcal{D}_n^\mu$ does not contain the soft gluon field. This leads to the final SCET Lagrangian [52,53,55,56]

$$\mathcal{L}_n = \bar{\xi}_n(x) \left[in\cdot D_n + gn\cdot A_s + i\not{\mathcal{P}}_n^\perp \frac{1}{i\bar{n}\cdot \mathcal{D}_n}\, i\not{\mathcal{P}}_n^\perp \right] \frac{\bar{\not{n}}}{2}\, \xi_n(x) + \dots\,, \tag{16.13}$$

where we have split $in\cdot D$ into a collinear piece $in\cdot D_n = in\cdot\partial + gn\cdot A_n$ and a soft piece $gn\cdot A_s$. This latter term gives rise to the only interaction between a collinear quark and soft gluons at leading power in λ. The ellipses represent higher-order interactions between soft and collinear particles.

The Lagrangian describing collinear fields in different light-like directions is simply given by the sum of the Lagrangians for each direction n, i.e. $\mathcal{L} = \sum_n \mathcal{L}_n$. The soft gluons are the same in each individual Lagrangian. An alternative way to understand the separation between large and small momentum components is to derive the Lagrangian of SCET in position space [56]. In this case no label operators are required, and the dependence on short-distance effects is contained in non-localities at short distances. An important difference between SCET and HQET is that the SCET Lagrangian is not corrected by short distance fluctuations. The physical reason is that in the construction described above no high-momentum modes have been integrated out [56]. Such hard modes arise when different collinear sectors are coupled via some external current (e.g. in jet production at e^+e^- or hadron colliders), or when collinear particles are produced in the rest frame of a decaying heavy object (such as in B decays). Short-distance effects are then incorporated in the Wilson coefficients of the external source operators.

16.3.3 *Collinear gauge invariance and Wilson lines*

An important aspect of SCET is the implementation of local gauge invariance. Because the effective field operators describe modes with certain momentum scalings, the effective Lagrangian respects only residual gauge symmetries. One of them satisfies the collinear scaling

$$(\bar{n}\cdot\partial, n\cdot\partial, \partial^\perp)\, U_n(x) \sim Q(1, \lambda^2, \lambda)\, U_n(x)\,, \tag{16.14}$$

and one the soft scaling

$$(\bar{n}\cdot\partial, n\cdot\partial, \partial^\perp)\, U_s(x) \sim Q(\lambda^2, \lambda^2, \lambda^2)\, U_s(x)\,. \tag{16.15}$$

While the soft gauge transformation is common for all fields, collinear fields in different directions each transform under their own collinear gauge transformation, which means that each collinear sector, containing particles with large momenta along a certain direction, has to be separately gauge invariant under its collinear gauge transformation. This requires the introduction of collinear Wilson lines [52]

$$W_n(x) = \mathrm{P} \exp\left[-ig \int_{-\infty}^0 ds\, \bar{n}\cdot A_n(s\bar{n} + x) \right], \tag{16.16}$$

which transform under collinear gauge transformations according to $W_n \to U_n W_n$. Thus, the combination $\chi_n \equiv W_n^\dagger \psi_n$ is gauge invariant. In a similar manner, one can define the gauge-invariant gluon field $B_n^\mu = g^{-1} W_n^\dagger\, iD_n^\mu\, W_n$ [57, 58]. Collinear operators in SCET are typically constructed from such collinearly gauge-invariant building blocks.

16.3.4 *Derivation of factorization theorems*

One of the important applications of SCET is to understand how to factorize cross sections involving energetic particles moving in different directions into simpler pieces that can either be calculated perturbatively or determined from data. Factorization theorems have been around for much longer than SCET (see [59] for a review). However, the effective theory allows for a conceptually simpler understanding of certain classes of factorization theorems [57], since most simplifications happen already at the level of the Lagrangian. The discussion in this section is valid to leading order in the power counting of the effective theory.

As discussed in the previous section, the Lagrangian of SCET does not involve any couplings between collinear particles moving in different directions. Soft gluons couple to collinear quarks only through the term $\bar{\xi}_n\, gn\cdot A_s\, (\bar{\not{n}}/2)\, \xi_n$ in the effective Lagrangian in (16.13). This coupling is similar to the coupling of soft gluons to heavy quarks in HQET, see Section 16.2.4. It can be removed by means of the field redefinition [53]

$$\psi_n(x) = Y_n(x)\, \psi_n^{(0)}(x)\,, \qquad A_n^a(x) = Y_n^{ab}(x)\, A_n^{b(0)}(x)\,, \tag{16.17}$$

where Y_n and Y_n^{ab} live in the fundamental and adjoint representations of $SU(3)$, respectively. This fact greatly facilitates proofs of factorization theorems in SCET. A QCD operator $O(x)$ describing the interactions of collinear partons moving in different directions can thus be written as (omitting color indices for simplicity)

$$\begin{aligned} &\langle O(x)\rangle = \\ &C_O(\mu)\, \langle \left[\mathcal{C}_{n_a}^{(0)}\, \mathcal{C}_{n_b}^{(0)}\, \mathcal{C}_{n_1}^{(0)} \dots \mathcal{C}_{n_N}^{(0)}\right](x) \left[\mathcal{Y}_{n_a}\, \mathcal{Y}_{n_b}\, \mathcal{Y}_{n_1} \dots \mathcal{Y}_{n_N}\right](x) \rangle_\mu\,. \end{aligned} \tag{16.18}$$

Here $\mathcal{C}_{n_i}^{(0)}(x)$ denotes a gauge-invariant combination of collinear fields (either quark or gluon fields) in the direction n_i. The hard matching coefficient C_O accounts for short-distance effects at the scale Q. The soft Wilson lines can either be in a color triplet or color octet representation, and are collectively denoted by $\mathcal{Y}_{n_i}$. Both the matrix elements and the coefficient C_O depend on the renormalization scale μ.

Having defined the operator mediating a given process, one can calculate the cross section by squaring the operator, taking the forward matrix element and integrating over the phase space of all final-state particles. The absence of interactions between collinear degrees of freedom moving along different directions or soft degrees of freedom implies that the forward matrix element can be factorized as

$$\begin{aligned} \left\langle \mathrm{in}\right| O(x)\, O^\dagger(0) \left|\mathrm{in}\right\rangle &= |C_O(\mu)|^2 \left\langle \mathrm{in}_a\right| \mathcal{C}_{n_a}(x)\, \mathcal{C}_{n_a}^\dagger(0) \left|\mathrm{in}_a\right\rangle_\mu \\ &\times \left\langle \mathrm{in}_b\right| \mathcal{C}_{n_b}(x)\, \mathcal{C}_{n_b}^\dagger(0) \left|\mathrm{in}_b\right\rangle_\mu \\ &\times \left\langle 0\right| \mathcal{C}_{n_1}(x)\, \mathcal{C}_{n_1}^\dagger(0) \left|0\right\rangle_\mu \cdots \left\langle 0\right| \mathcal{C}_{n_N}(x)\, \mathcal{C}_{n_N}^\dagger(0) \left|0\right\rangle_\mu \\ &\times \left\langle 0\right| \left[\mathcal{Y}_{n_a} \dots \mathcal{Y}_{n_N}\right](x) \left[\mathcal{Y}_{n_a} \dots \mathcal{Y}_{n_N}\right]^\dagger(0) \left|0\right\rangle_\mu\,. \end{aligned} \tag{16.19}$$

Thus, the matrix element can be written as a product of simpler structures, each of which can be evaluated separately.

The vacuum matrix elements of the outgoing collinear fields are determined by jet functions $J_i(\mu)$. As long as the relevant scale (for example the jet mass) is sufficiently large, these functions can

be calculated perturbatively. The matrix elements of the incoming collinear fields are non-perturbative objects $B_{p/N}(\mu)$ called beam functions for parton p in nucleon N [60]. For many applications they can be related perturbatively to the well-known parton distribution functions. Finally, the vacuum matrix element of the soft Wilson lines defines a so-called soft function $S_{ab\ldots N}(\mu)$. The shared dependence on x in the above equation implies that in momentum space the various components of the factorization theorem are convoluted with one another. Deriving this convolution requires a careful treatment of the phase-space integration and the factorization of the measurement defining the cross section of interest, in particular treating the large and residual components of each momentum appropriately.

Putting all information together, the differential cross section for a proton-proton collision with N jet-like objects can schematically be written as

$$d\sigma \sim \sum_{ab} H_{ab}(\mu) \left[B_{a/P}(\mu)\, B_{b/P}(\mu)\right] \otimes \left[J_1(\mu) \ldots J_N(\mu)\right] \otimes S_{ab\ldots N}(\mu)\,. \tag{16.20}$$

The hard function is equal to the square of the matching coefficient, $H_{ab}(\mu) = |C_O(\mu)|^2$, and the beam, jet, and soft functions and their convolution structure depend on the specific N-jet measurement. It should be mentioned that the most difficult part of traditional factorization proofs involves showing that so-called Glauber gluons do not spoil the above factorization theorem [61]. Significant progress toward the description of Glauber effects within SCET has been made in [62], where a closed form for the effective Lagrangian describing these interactions was derived. In this context, a proof of factorization requires demonstrating that this Lagrangian has no impact on a particular cross section, and such proofs have not yet been fully derived within SCET.

16.3.5 *Resummation of large logarithms*

SCET can be used to sum the large logarithms arising in perturbative calculations to all orders in the strong coupling constant α_s. In general, perturbation theory will generate a logarithmic dependence on any ratio of scales r in a problem. For processes that involve initial or final states with energy much in excess of their mass, there are two powers of logarithms for every power of α_s. These are referred to as Sudakov logarithms. For widely separated scales these large logarithms can spoil the convergence of fixed-order perturbation theory. One thus needs to reorganize the expansion in such a way that $\alpha_s L = \mathcal{O}(1)$ is kept fixed, with $L = \ln r$. More precisely, a proper resummation requires summing logarithms of the form $\alpha_s^n L^m$ with $m \le (n+1)$ in the logarithm of a cross section, by writing $\ln\sigma \sim L\, g_0(\alpha_s L) + g_1(\alpha_s L) + \alpha_s\, g_2(\alpha_s L) + \ldots$, with functions $g_n(x)$ that need to be determined.

The important ingredient in achieving this resummation is the fact that SCET factorizes a given cross section into simpler pieces, each of which depends on a single physical scale. The only dependence on that scale can arise through logarithms of its ratio with the renormalization scale μ. Thus, for each of the components in the factorization theorem one can choose a renormalization scale μ for which the large logarithmic terms are absent. Of course, the factorization formula requires a common renormalization scale μ in all its components, and one therefore has to use the renormalization group (RG) to evolve the various component functions from their preferred scale to the common scale μ. A novel feature of RG equations in SCET, as opposed to other EFTs, is that the anomalous dimensions entering the evolution equations of the hard, beam, jet and soft functions in a factorization formula such as (16.20) contain a single power of the logarithm of the relevant energy scale. For example, the anomalous dimension γ_H of the hard function has the form

$$\gamma_H(\mu) = c_H\, \Gamma_{\rm cusp}(\alpha_s)\, \ln\frac{Q^2}{\mu^2} + \gamma(\alpha_s)\,, \tag{16.21}$$

where c_H is a process-dependent coefficient and $\Gamma_{\rm cusp}$ denotes the so-called cusp anomalous dimension [20, 63]. Collinear and soft functions have similar anomalous dimensions, which also involve a cusp and a non-cusp part. The non-cusp part γ of the anomalous dimensions is process (and observable) dependent. The presence of a logarithm in the anomalous dimension is characteristic of Sudakov problems and arises since the perturbative series contains double logarithms of scale ratios.

Solving the RG equations one can systematically resum all large logarithms of scale ratios in the factorized cross section and express the functions $g_n(\alpha_s L)$ introduced above in terms of ratios of running coupling constants. In order to compute the first two terms $L\, g_0(\alpha_s L) + g_1(\alpha_s L)$ in $\ln\sigma$, corresponding to the next-to-leading logarithmic (NLL) approximation, one needs two-loop expressions for the cusp anomalous dimension and β function, one-loop expressions for the non-cusp pieces in the anomalous dimensions, and tree-level matching conditions for all component functions at their characteristic scales. To calculate the next term $\alpha_s g_2(\alpha_s L)$ in the expansion, corresponding to NNLL order, one needs to go one order higher in the loop expansion, and so on.

16.3.6 *Factorization and resummation in* $\mathbf{SCET_{II}}$

The effective theory $\mathrm{SCET_{II}}$ contains collinear and soft particles with momenta scaling as $(p_n^-, p_n^+, p_n^\perp) \sim Q(1, \lambda^2, \lambda)$ and $(p_s^-, p_s^+, p_s^\perp) \sim Q(\lambda, \lambda, \lambda)$. They have the same small virtuality ($p_n^2 \sim p_s^2 \sim Q^2\lambda^2$) but differ in their rapidities. An important class of observables, for which this scaling is relevant, contains cross sections for processes in which the transverse momenta of particles are constrained by external kinematics. The prime example are the transverse-momentum distributions of electroweak gauge bosons or Higgs bosons produced at hadron colliders. The parton transverse momenta are constrained by the fact that their vector sum must be equal and opposite to the transverse momentum q_T of the boson. Standard RG evolution in the effective theory controls the logarithms arising from the fact that the virtualities of the collinear and soft modes are much smaller than the hard scale Q in the process (the boson mass). However, additional large logarithms arise since the rapidities of collinear and soft modes are parametrically different, such that $e^{|y_c - y_s|} \sim 1/\lambda$. These logarithms can be traced to a new source of divergences and an unusual failure of dimensional regularization. They need to be factorized in the cross section and resummed by other means.

Two equivalent approaches exist for how to deal with the additional rapidity logarithms in SCET. In the approach of [64], they are interpreted as a consequence of a "collinear anomaly" of the effective theory $\mathrm{SCET_{II}}$, resulting from the fact that a classical rescaling symmetry of the effective Lagrangian is broken by quantum effects. The extra large logarithms can be resummed by means of simple differential equations, which typically state that to all orders in perturbation theory (and in an appropriate space) the logarithm of the cross section contains only a single extra logarithm of $\lambda \sim q_T/Q$ not contained in the hard function. Another approach to resum the rapidity logarithms uses the "rapidity renormalization group" [65], in which the relevant differential equations are obtained by considering a new type of scale variation in a parameter ν, which separates the phase space for collinear and soft particles along a hyperbola in the (p_-, p_+) plane. In contrast to the standard RG, there is no running coupling involved in the ν evolution, since the different contributions live at the same virtuality.

$\mathrm{SCET_{II}}$ also plays an important role in the study of factorization for a variety of exclusive B meson decays, such as $\bar B \to \pi\ell\bar\nu$, $\bar B \to K^*\gamma$ and $\bar B \to \pi\pi$, for which the virtualities of energetic (collinear) final-state particles are of order $\Lambda_{\rm QCD}$, which is also the scale for the soft light degrees of freedom contained in the initial-state B meson.

16.3.7 *Applications*

Most of the applications of SCET are either in flavor physics, where the decay of a heavy B meson can give rise to energetic light partons, or in collider physics, where the presence of jets naturally leads to collimated sets of energetic particles. For some of these applications alternative approaches existed before the invention of SCET, but the effective theory has opened up alternative ways to understand the physics of these processes. For

many examples, however, SCET has allowed new insights and new applications. The investigation of heavy-to-light form factors has been instrumental for understanding factorization in exclusive semileptonic B decays [66]. SCET has also provided a field-theoretic basis for the QCD factorization approach to exclusive, non-leptonic decays of B mesons [67]. Using SCET methods, proofs of factorization were derived for the color-allowed decay $\bar{B}^0 \to D^+\pi^-$ [68], the color-suppressed decay $\bar{B}^0 \to D^0\pi^0$ [69], and the radiative decay $\bar{B} \to K^*\gamma$ [70]. Further examples are factorization theorems and the resummation of endpoint logarithms for quarkonia production [71], the resummation of large logarithmic terms for the thrust [72] and jet broadening [73] distributions in e^+e^- annihilation beyond NLL order, the development of new factorizable observables to veto extra jets [60, 74], all-orders factorization theorems for processes containing electroweak Sudakov logarithms [75], and the resummation of threshold (soft gluon) logarithms in momentum space for several important processes at hadron colliders [76–78]. There has also been a lot of activity describing p_T-based resummation at hadron colliders. Prominent examples are the transverse-momentum distributions of electroweak bosons [64, 65, 79]. Finally, SCET has given new insights into the jet substructure methods (see [80] for a recent review). We now describe a few of these applications in more detail.

Event-shape distributions, in particular the thrust distribution, have been measured to high accuracy at LEP [81]. They can be used for a determination of the strong coupling constant α_s. SCET has increased the theoretical accuracy in the calculations of the thrust and C-parameter distributions significantly. First, it has allowed to increase the perturbative accuracy of the thrust spectrum. The resummation of logarithms of τ, which become important for $\tau \ll 1$, has been performed to $\mathrm{N^3LL}$ [72], two orders beyond what was previously available. Combining this resummation with the known two-loop spectrum [82, 83] gives precise perturbative predictions both at small and large values of τ. Second, the factorization of the cross section in SCET has made it possible to include non-perturbative physics through a shape function, in analogy with the B-physics case discussed in Section 16.2.6. Comparing the theoretical predictions to the measured thrust and C-parameter distributions yields a precise value of the strong coupling constant $\alpha_s(m_Z)$, which however is lower than the average value cited in Section 9 by several standard deviations [84, 85]. For more discussions on this, see Section 9.

The Higgs-boson production cross section in gluon fusion at the LHC, defined with a jet veto stating that no jet in the final state has transverse momentum above a threshold $p_T^{\rm veto}$, can be factorized in the form [86, 87] (see [88] for a corresponding calculation outside the SCET framework)

$$\sigma(p_T^{\rm veto}) = H(m_H,\mu)\left(\frac{\nu_B}{\nu_S}\right)^{-2F_{gg}(R,p_T^{\rm veto},\mu)} S_{gg}(R,p_T^{\rm veto},\mu,\frac{\nu_S}{p_T^{\rm veto}}) \times \int_\tau^1 \frac{dz}{z}\, B_{g/P}\Big(z,R,p_T^{\rm veto},\mu,\frac{\nu_B}{m_H}\Big)\, B_{g/P}\Big(\frac{\tau}{z},R,p_T^{\rm veto},\mu,\frac{\nu_B}{m_H}\Big), \tag{16.22}$$

where $\tau = m_H^2/s$, and $\mu \sim p_T^{\rm veto}$ is a common factorization scale. The beam functions $B_{g/P}$, the soft function S_{gg} and the exponent F_{gg} all depend on the jet radius R as well as the jet clustering algorithm. The scale dependence of the hard function H is controlled by standard RG evolution in SCET. The beam functions can be factorized further into calculable collinear kernels convoluted with parton distribution functions. In addition to the renormalization scale μ, the beam and soft functions depend on two rapidity scales $\nu_B \sim m_H$ and $\nu_S \sim p_T^{\rm veto}$, respectively. In [86] the default values $\nu_B = m_H$ and $\nu_S = p_T^{\rm veto}$ are used for these scales, and the soft function S_{gg} is absorbed into the beam functions. In [87] the exponent F_{gg} is called $-\gamma_\nu^g/2$. The second factor on the right-hand side of the factorization formula (16.22), which resums large rapidity logarithms, implies that the logarithm of the jet-veto cross section contains a single large logarithm $\ln\sigma = -2F_{gg}(R,p_T^{\rm veto},\mu)\,\ln(m_H/p_T^{\rm veto}) + \ldots$ not contained in the hard function. Its coefficient can be calculated in fixed-order perturbation theory.

Obtaining more precise fixed-order calculations has been an important goal for many years. A major difficulty in these calculations is the proper handling of the infrared singularities that arise in both virtual and real contributions. A method based on N-jettiness ($\mathcal{T}_N$) slicing [89,90] allows one to obtain the NNLO result from a much easier NLO calculation, combined with information about the singular dependence of the cross section on the $\mathcal{T}_N$ resolution variable [74]. This has been used to compute various processes with final states containing up to one hard, colored particle [91–95]. While the NLO calculations can be performed using well established techniques, the singular dependence on $\mathcal{T}_N$ can be calculated using SCET at NNLO. Calculations of the leading power corrections in $\mathcal{T}_0/Q$ [96, 97] have helped to improved the numerical stability for several processes. The N-jettiness ($\mathcal{T}_N$) slicing method has been used prior to the fixed-order application in the combination of higher order resummation with parton showers [98, 99].

More generally, there is currently a strong effort to push the applications of SCET toward factorization and resummation at subleading power in the expansion in λ. The subleading SCET Lagrangian [56, 100] and current operators arising in B-meson decays and their anomalous dimensions [55, 56, 101–103] have been studied a long time ago. More recently, the focus has shifted to subleading operators arising in important collider processes, such as Drell-Yan or Higgs production. The general set of operators for such processes have been identified [104–106], and several of their anomalous dimensions have been calculated [106, 107]. First resummed results at subleading power have been presented for event shapes [108] and the Drell-Yan process [109].

16.4 Open issues and perspectives

HQET has successfully passed many experimental tests, and there are not many open questions that still need to be addressed. One concept that has not been derived from first principles is the notion of quark-hadron duality, which underlies the application of HQET to the description of inclusive decays of B mesons. The validity of global duality (at energies even lower than those relevant in B decays) has been tested experimentally using high-precision data on semileptonic B decays and on hadronic τ decays. However, assigning a theoretical uncertainty due to possible duality violations remains a difficult task. Another known issue is that the measured values of the CKM element $|V_{ub}|$ extracted from exclusive or inclusive decays of B mesons differ from each other by several standard deviations (see Section 75). This measurement relies on the heavy-quark limit, and the uncertainty quoted includes a theoretical estimate of the effect of power corrections arising from the finite b-quark mass. It remains an open question whether the discrepancy is due to underestimated theoretical or experimental uncertainties, or whether it may hint to the existence of new physics.

SCET, on the other hand, is still an active field of research, and new results are being obtained regularly. An important example concerns the understanding of non-global logarithms arising in hadron-collider processes with jets [110, 111]. For a long time a fully factorized form of non-global jet cross sections has not been available, despite significant progress towards this goal [112, 113]. A consistent factorization formula for non-global jet observables was developed in [114, 115]. It requires the introduction of a collinear-soft mode in the SCET Lagrangian. The first application of this formalism was to the light jet mass distribution [116], and significant steps toward an extension to NLL accuracy have been taken in [117]. It is believed that the results obtained from the factorization theorem derived in [114, 115] are equivalent to those obtained using the approaches proposed in [112, 113]. The various methods differ in the way in which they organize the all-order expansion for the appearing complicated multi-Wilson-line structures.

Another active field concerns the study of Glauber gluons in SCET [118] and their relation to the BFKL equation familiar from small-x physics [119]. A systematic account of the effects of Glauber gluons in the context of the SCET Lagrangian has been developed in [62]. The formalism has been extended to Glauber quarks in [120]. These developments set the basis for

a solid understanding of the impact of Glauber exchanges on factorization theorems. Glauber gluons also play an important role in SCET-based analysis of jet propagation in dense QCD media [121, 122], which gives rise to the jet-quenching phenomenon in heavy-ion collisions. An important open question facing some applications of SCET concerns factorized expressions containing endpoint-divergent convolution integrals.

We close this short review by mentioning a particularly nice application combining the methods of heavy-particle EFTs such as HQET and non-relativistic QCD with SCET in the context of describing the interactions of heavy dark matter (with mass $M \gg v$) with SM particles. In [123] it was realized that the interactions of heavy, weakly interacting massive particles (WIMPs) with nuclear targets can be described in a model-independent way using heavy-particle EFTs. The WIMPs are charged under $SU(2)_L$ and can interact with electroweak gauge bosons and the Higgs boson. The WIMP EFT was later extended by describing the produced, highly energetic electroweak gauge bosons in terms of soft or collinear fields in SCET [124–126]. This allows one to systematically separate all relevant mass scales, resum electroweak Sudakov logarithms and disentangle the so-called Sommerfeld enhancement from the short-distance hard annihilation process.

References

[1] E. Witten, Nucl. Phys. **B122**, 109 (1977).

[2] S. Weinberg, Phys. Lett. **91B**, 51 (1980).

[3] L. J. Hall, Nucl. Phys. **B178**, 75 (1981).

[4] E. Eichten and B. R. Hill, Phys. Lett. **B234**, 511 (1990).

[5] H. Georgi, Phys. Lett. **B240**, 447 (1990).

[6] B. Grinstein, Nucl. Phys. **B339**, 253 (1990).

[7] T. Mannel, W. Roberts and Z. Ryzak, Nucl. Phys. **B368**, 204 (1992).

[8] M. Neubert, Phys. Rept. **245**, 259 (1994), [hep-ph/9306320].

[9] A. V. Manohar and M. B. Wise, Camb. Monogr. Part. Phys. Nucl. Phys. Cosmol. **10**, 1 (2000).

[10] M. E. Luke and A. V. Manohar, Phys. Lett. **B286**, 348 (1992), [hep-ph/9205228].

[11] E. V. Shuryak, Phys. Lett. **93B**, 134 (1980).

[12] N. Isgur and M. B. Wise, Phys. Lett. **B232**, 113 (1989).

[13] N. Isgur and M. B. Wise, Phys. Rev. Lett. **66**, 1130 (1991).

[14] S. Nussinov and W. Wetzel, Phys. Rev. **D36**, 130 (1987).

[15] M. A. Shifman and M. B. Voloshin, Sov. J. Nucl. Phys. **45**, 292 (1987), [Yad. Fiz.45,463(1987)].

[16] M. Neubert, Phys. Lett. **B264**, 455 (1991).

[17] M. E. Luke, Phys. Lett. **B252**, 447 (1990).

[18] I. I. Y. Bigi *et al.*, Phys. Rev. **D52**, 196 (1995), [hep-ph/9405410].

[19] N. Uraltsev, Phys. Lett. **B501**, 86 (2001), [,195(2000)], [hep-ph/0011124].

[20] G. P. Korchemsky and A. V. Radyushkin, Nucl. Phys. **B283**, 342 (1987).

[21] A. F. Falk *et al.*, Nucl. Phys. **B343**, 1 (1990).

[22] J. Chay, H. Georgi and B. Grinstein, Phys. Lett. **B247**, 399 (1990).

[23] I. I. Y. Bigi, N. G. Uraltsev and A. I. Vainshtein, Phys. Lett. **B293**, 430 (1992), [Erratum: Phys. Lett.B297,477(1992)], [hep-ph/9207214].

[24] A. V. Manohar and M. B. Wise, Phys. Rev. **D49**, 1310 (1994), [hep-ph/9308246].

[25] T. Mannel, Nucl. Phys. **B413**, 396 (1994), [hep-ph/9308262].

[26] A. F. Falk, M. E. Luke and M. J. Savage, Phys. Rev. **D49**, 3367 (1994), [hep-ph/9308288].

[27] E. C. Poggio, H. R. Quinn and S. Weinberg, Phys. Rev. **D13**, 1958 (1976).

[28] G. Buchalla, A. J. Buras and M. E. Lautenbacher, Rev. Mod. Phys. **68**, 1125 (1996), [hep-ph/9512380].

[29] A. F. Falk and M. Neubert, Phys. Rev. **D47**, 2965 (1993), [hep-ph/9209268].

[30] T. Becher, H. Boos and E. Lunghi, JHEP **12**, 062 (2007), [arXiv:0708.0855].

[31] A. Alberti, P. Gambino and S. Nandi, JHEP **01**, 147 (2014), [arXiv:1311.7381].

[32] T. Mannel, A. A. Pivovarov and D. Rosenthal, Phys. Lett. **B741**, 290 (2015), [arXiv:1405.5072].

[33] T. Mannel, A. A. Pivovarov and D. Rosenthal, Phys. Rev. **D92**, 5, 054025 (2015), [arXiv:1506.08167].

[34] T. Mannel and A. A. Pivovarov, Phys. Rev. **D100**, 9, 093001 (2019), [arXiv:1907.09187].

[35] T. Mannel, S. Turczyk and N. Uraltsev, JHEP **11**, 109 (2010), [arXiv:1009.4622].

[36] M. Neubert and C. T. Sachrajda, Nucl. Phys. **B483**, 339 (1997), [hep-ph/9603202].

[37] M. Beneke, G. Buchalla and I. Dunietz, Phys. Rev. **D54**, 4419 (1996), [Erratum: Phys. Rev.D83,119902(2011)], [hep-ph/9605259].

[38] M. Beneke *et al.*, Phys. Lett. **B459**, 631 (1999), [hep-ph/9808385].

[39] M. Kirk, A. Lenz and T. Rauh, JHEP **12**, 068 (2017), [arXiv:1711.02100].

[40] P. Gambino and C. Schwanda, Phys. Rev. **D89**, 1, 014022 (2014), [arXiv:1307.4551].

[41] Y. Amhis *et al.* (HFLAV), Eur. Phys. J. **C77**, 12, 895 (2017), [arXiv:1612.07233].

[42] P. Gambino, M. Jung and S. Schacht, Phys. Lett. **B795**, 386 (2019), [arXiv:1905.08209].

[43] M. Neubert, Phys. Rev. **D49**, 3392 (1994), [hep-ph/9311325].

[44] I. I. Y. Bigi *et al.*, Int. J. Mod. Phys. **A9**, 2467 (1994), [hep-ph/9312359].

[45] G. P. Korchemsky and G. F. Sterman, Phys. Lett. **B340**, 96 (1994), [hep-ph/9407344].

[46] C. W. Bauer, M. E. Luke and T. Mannel, Phys. Rev. **D68**, 094001 (2003), [hep-ph/0102089].

[47] K. S. M. Lee and I. W. Stewart, Nucl. Phys. **B721**, 325 (2005), [hep-ph/0409045].

[48] S. W. Bosch, M. Neubert and G. Paz, JHEP **11**, 073 (2004), [hep-ph/0409115].

[49] M. Beneke *et al.*, JHEP **06**, 071 (2005), [hep-ph/0411395].

[50] M. Benzke *et al.*, JHEP **08**, 099 (2010), [arXiv:1003.5012].

[51] C. W. Bauer, S. Fleming and M. E. Luke, Phys. Rev. **D63**, 014006 (2000), [hep-ph/0005275].

[52] C. W. Bauer and I. W. Stewart, Phys. Lett. **B516**, 134 (2001), [hep-ph/0107001].

[53] C. W. Bauer, D. Pirjol and I. W. Stewart, Phys. Rev. **D65**, 054022 (2002), [hep-ph/0109045].

[54] T. Becher, A. Broggio and A. Ferroglia, Lect. Notes Phys. **896**, pp.1 (2015), [arXiv:1410.1892].

[55] J. Chay and C. Kim, Phys. Rev. **D65**, 114016 (2002), [hep-ph/0201197].

[56] M. Beneke *et al.*, Nucl. Phys. **B643**, 431 (2002), [hep-ph/0206152].

[57] C. W. Bauer *et al.*, Phys. Rev. **D66**, 014017 (2002), [hep-ph/0202088].

[58] R. J. Hill and M. Neubert, Nucl. Phys. **B657**, 229 (2003), [hep-ph/0211018].

[59] J. C. Collins, D. E. Soper and G. F. Sterman, Adv. Ser. Direct. High Energy Phys. **5**, 1 (1989), [hep-ph/0409313].

[60] I. W. Stewart, F. J. Tackmann and W. J. Waalewijn, Phys. Rev. **D81**, 094035 (2010), [arXiv:0910.0467].

[61] J. C. Collins, D. E. Soper and G. F. Sterman, Nucl. Phys. **B261**, 104 (1985).

[62] I. Z. Rothstein and I. W. Stewart, JHEP **08**, 025 (2016), [arXiv:1601.04695].

[63] I. A. Korchemskaya and G. P. Korchemsky, Phys. Lett. **B287**, 169 (1992).

[64] T. Becher and M. Neubert, Eur. Phys. J. **C71**, 1665 (2011), [arXiv:1007.4005].

[65] J.-Y. Chiu *et al.*, JHEP **05**, 084 (2012), [arXiv:1202.0814].

[66] M. Beneke and T. Feldmann, Nucl. Phys. **B685**, 249 (2004), [hep-ph/0311335].

[67] M. Beneke *et al.*, Phys. Rev. Lett. **83**, 1914 (1999), [hep-ph/9905312].

[68] C. W. Bauer, D. Pirjol and I. W. Stewart, Phys. Rev. Lett. **87**, 201806 (2001), [hep-ph/0107002].

[69] S. Mantry, D. Pirjol and I. W. Stewart, Phys. Rev. **D68**, 114009 (2003), [hep-ph/0306254].

[70] T. Becher, R. J. Hill and M. Neubert, Phys. Rev. **D72**, 094017 (2005), [hep-ph/0503263].

[71] S. Fleming, A. K. Leibovich and T. Mehen, Phys. Rev. **D68**, 094011 (2003), [hep-ph/0306139].

[72] T. Becher and M. D. Schwartz, JHEP **07**, 034 (2008), [arXiv:0803.0342].

[73] T. Becher and G. Bell, JHEP **11**, 126 (2012), [arXiv:1210.0580].

[74] I. W. Stewart, F. J. Tackmann and W. J. Waalewijn, Phys. Rev. Lett. **105**, 092002 (2010), [arXiv:1004.2489].

[75] J.-y. Chiu, R. Kelley and A. V. Manohar, Phys. Rev. **D78**, 073006 (2008), [arXiv:0806.1240].

[76] T. Becher, M. Neubert and G. Xu, JHEP **07**, 030 (2008), [arXiv:0710.0680].

[77] V. Ahrens *et al.*, Eur. Phys. J. **C62**, 333 (2009), [arXiv:0809.4283].

[78] X. Liu, S. Mantry and F. Petriello, Phys. Rev. **D86**, 074004 (2012), [arXiv:1205.4465].

[79] M. G. Echevarria, A. Idilbi and I. Scimemi, JHEP **07**, 002 (2012), [arXiv:1111.4996].

[80] A. J. Larkoski, I. Moult and B. Nachman (2017), [arXiv:1709.04464].

[81] S. Kluth, Rept. Prog. Phys. **69**, 1771 (2006), [hep-ex/0603011].

[82] A. Gehrmann-De Ridder *et al.*, Phys. Rev. Lett. **99**, 132002 (2007), [arXiv:0707.1285].

[83] S. Weinzierl, Phys. Rev. Lett. **101**, 162001 (2008), [arXiv:0807.3241].

[84] R. Abbate *et al.*, Phys. Rev. **D83**, 074021 (2011), [arXiv:1006.3080].

[85] A. H. Hoang *et al.*, Phys. Rev. **D91**, 9, 094018 (2015), [arXiv:1501.04111].

[86] T. Becher and M. Neubert, JHEP **07**, 108 (2012), [arXiv:1205.3806].

[87] I. W. Stewart *et al.*, Phys. Rev. **D89**, 5, 054001 (2014), [arXiv:1307.1808].

[88] A. Banfi *et al.*, Phys. Rev. Lett. **109**, 202001 (2012), [arXiv:1206.4998].

[89] R. Boughezal, X. Liu and F. Petriello, Phys. Rev. **D91**, 9, 094035 (2015), [arXiv:1504.02540].

[90] J. Gaunt *et al.*, JHEP **09**, 058 (2015), [arXiv:1505.04794].

[91] R. Boughezal *et al.*, Phys. Lett. **B748**, 5 (2015), [arXiv:1505.03893].

[92] R. Boughezal *et al.*, Phys. Rev. Lett. **116**, 15, 152001 (2016), [arXiv:1512.01291].

[93] J. M. Campbell, R. K. Ellis and C. Williams, JHEP **06**, 179 (2016), [arXiv:1601.00658].

[94] J. M. Campbell *et al.*, JHEP **07**, 148 (2016), [arXiv:1603.02663].

[95] G. Heinrich *et al.*, JHEP **03**, 142 (2018), [arXiv:1710.06294].

[96] I. Moult *et al.*, Phys. Rev. **D95**, 7, 074023 (2017), [arXiv:1612.00450].

[97] R. Boughezal, X. Liu and F. Petriello, JHEP **03**, 160 (2017), [arXiv:1612.02911].

[98] S. Alioli *et al.*, JHEP **09**, 120 (2013), [arXiv:1211.7049].

[99] S. Alioli *et al.*, Phys. Rev. **D92**, 9, 094020 (2015), [arXiv:1508.01475].

[100] C. W. Bauer, D. Pirjol and I. W. Stewart, Phys. Rev. **D68**, 034021 (2003), [hep-ph/0303156].

[101] D. Pirjol and I. W. Stewart, Phys. Rev. **D67**, 094005 (2003), [Erratum: Phys. Rev.D69,019903(2004)], [hep-ph/0211251].

[102] R. J. Hill *et al.*, JHEP **07**, 081 (2004), [hep-ph/0404217].

[103] M. Beneke and D. Yang, Nucl. Phys. **B736**, 34 (2006), [hep-ph/0508250].

[104] I. Moult, I. W. Stewart and G. Vita, JHEP **07**, 067 (2017), [arXiv:1703.03408].

[105] I. Feige *et al.*, JHEP **11**, 142 (2017), [arXiv:1703.03411].

[106] M. Beneke *et al.*, JHEP **03**, 001 (2018), [arXiv:1712.04416].

[107] S. Alte, M. König and M. Neubert, JHEP **08**, 095 (2018), [arXiv:1806.01278].

[108] I. Moult *et al.*, JHEP **08**, 013 (2018), [arXiv:1804.04665].

[109] M. Beneke *et al.*, JHEP **03**, 043 (2019), [arXiv:1809.10631].

[110] M. Dasgupta and G. P. Salam, Phys. Lett. **B512**, 323 (2001), [hep-ph/0104277].

[111] R. B. Appleby and M. H. Seymour, JHEP **12**, 063 (2002), [hep-ph/0211426].

[112] S. Caron-Huot, JHEP **03**, 036 (2018), [arXiv:1501.03754].

[113] A. J. Larkoski, I. Moult and D. Neill, JHEP **09**, 143 (2015), [arXiv:1501.04596].

[114] T. Becher *et al.*, Phys. Rev. Lett. **116**, 19, 192001 (2016), [arXiv:1508.06645].

[115] T. Becher *et al.*, JHEP **11**, 019 (2016), [Erratum: JHEP05,154(2017)], [arXiv:1605.02737].

[116] T. Becher, B. D. Pecjak and D. Y. Shao, JHEP **12**, 018 (2016), [arXiv:1610.01608].

[117] M. Balsiger, T. Becher and D. Y. Shao, JHEP **04**, 020 (2019), [arXiv:1901.09038].

[118] C. W. Bauer, B. O. Lange and G. Ovanesyan, JHEP **07**, 077 (2011), [arXiv:1010.1027].

[119] S. Fleming, Phys. Lett. **B735**, 266 (2014), [arXiv:1404.5672].

[120] I. Moult *et al.*, JHEP **02**, 134 (2018), [arXiv:1709.09174].

[121] A. Idilbi and A. Majumder, Phys. Rev. **D80**, 054022 (2009), [arXiv:0808.1087].

[122] G. Ovanesyan and I. Vitev, JHEP **06**, 080 (2011), [arXiv:1103.1074].

[123] R. J. Hill and M. P. Solon, Phys. Lett. **B707**, 539 (2012), [arXiv:1111.0016].

[124] M. Bauer *et al.*, JHEP **01**, 099 (2015), [arXiv:1409.7392].

[125] M. Baumgart, I. Z. Rothstein and V. Vaidya, Phys. Rev. Lett. **114**, 211301 (2015), [arXiv:1409.4415].

[126] G. Ovanesyan, T. R. Slatyer and I. W. Stewart, Phys. Rev. Lett. **114**, 21, 211302 (2015), [arXiv:1409.8294].

17. Lattice Quantum Chromodynamics

Revised August 2019 by S. Hashimoto (KEK), J. Laiho (Syracuse U.) and S.R. Sharpe (U. Washington).

Many physical processes considered in the Review of Particle Properties (RPP) involve hadrons. The properties of hadrons—which are composed of quarks and gluons—are governed primarily by Quantum Chromodynamics (QCD) (with small corrections from Quantum Electrodynamics [QED]). Theoretical calculations of these properties require non-perturbative methods, and Lattice Quantum Chromodynamics (LQCD) is a tool to carry out such calculations. It has been successfully applied to many properties of hadrons. Most important for the RPP are the calculation of electroweak form factors, which are needed to extract Cabbibo-Kobayashi-Maskawa (CKM) matrix elements when combined with the corresponding experimental measurements. LQCD has also been used to determine other fundamental parameters of the standard model, in particular the strong coupling constant and quark masses, as well as to predict hadronic contributions to the anomalous magnetic moment of the muon, $g_\mu - 2$.

This review describes the theoretical foundations of LQCD and sketches the methods used to calculate the quantities relevant for the RPP. It also describes the various sources of error that must be controlled in a LQCD calculation. Results for hadronic quantities are given in the corresponding dedicated reviews.

17.1 Lattice regularization of QCD

Gauge theories form the building blocks of the Standard Model. While the SU(2) and U(1) parts have weak couplings and can be studied accurately with perturbative methods, the SU(3) component—QCD—is only amenable to a perturbative treatment at high energies. The growth of the coupling constant in the infrared—the flip-side of asymptotic freedom—requires the use of non-perturbative methods to determine the low energy properties of QCD. Lattice gauge theory, proposed by K. Wilson in 1974 [1], provides such a method, for it gives a non-perturbative definition of vector-like gauge field theories like QCD. In lattice regularized QCD—commonly called lattice QCD or LQCD—Euclidean space-time is discretized, usually on a hypercubic lattice with lattice spacing a, with quark fields placed on sites and gauge fields on the links between sites. The lattice spacing plays the role of the ultraviolet regulator, rendering the quantum field theory finite. The continuum theory is recovered by taking the limit of vanishing lattice spacing, which can be reached by tuning the bare coupling constant to zero according to the renormalization group.

Unlike dimensional regularization, which is commonly used in continuum QCD calculations, the definition of LQCD does not rely on the perturbative expansion. Indeed, LQCD allows non-perturbative calculations by numerical evaluation of the path integral that defines the theory.

Practical LQCD calculations are limited by the availability of computational resources and the efficiency of algorithms. Because of this, LQCD results come with both statistical and systematic errors, the former arising from the use of Monte-Carlo integration, the latter, for example, from the use of non-zero values of a. There are also different ways in which the QCD action can be discretized, and all must give consistent results in the continuum limit, $a \to 0$. It is the purpose of this review to provide an outline of the methods of LQCD, with particular focus on applications to particle physics, and an overview of the various sources of error. This should allow the reader to better understand the LQCD results that are presented in other reviews, primarily those on "Quark Masses," "Quantum Chromodynamics," "CKM quark-mixing matrix," "V_{ud}, V_{us}, Cabibbo angle and CKM Unitarity," "Leptonic Decays of Charged Pseudoscalar Mesons," "$B^0 - \bar{B}^0$ Mixing," and "Semileptonic b-Hadron Decays, Determination of V_{cb} and V_{ub}." For more extensive explanations the reader should consult the available textbooks or lecture notes, the most up-to-date of which are Refs. [2–4].

17.1.1 *Gauge invariance, gluon fields and the gluon action*

A key feature of the lattice formulation of QCD is that it preserves gauge invariance. This is in contrast to perturbative calculations, where gauge fixing is an essential step. The preservation of gauge invariance leads to considerable simplifications, e.g. restricting the form of operators that can mix under renormalization.

The gauge transformations of lattice quark fields are just as in the continuum: $q(x) \longrightarrow V(x)q(x)$ and $\bar{q}(x) \longrightarrow \bar{q}(x)V^\dagger(x)$, with $V(x)$ an arbitrary element of SU(3). The only difference is that the Euclidean space-time positions x are restricted to lie on the sites of the lattice, i.e. $x = a(n_1, n_2, n_3, n_4)$ for a hypercubic lattice, with the n_j being integers. Quark bilinears involving different lattice points can be made gauge invariant by introducing the gluon field $U_\mu(x)$. For example, for adjacent points the bilinear is $\bar{q}(x)U_\mu(x)q(x+a\hat{\mu})$, with $\hat{\mu}$ the unit vector in the μ'th direction. (This form is used in the construction of the lattice covariant derivative.) This is illustrated in Fig. 17.1. The gluon field (or "gauge link") is an element of the group, SU(3), in contrast to the continuum field A_μ which takes values in the Lie algebra. The bilinear is invariant if U_μ transforms as $U_\mu(x) \to V(x)U_\mu(x)V^\dagger(x+a\hat{\mu})$. The lattice gluon field is naturally associated with the link joining x and $x+a\hat{\mu}$, and corresponds in the continuum to a Wilson line connecting these two points, $\mathrm{P}\exp(i\int_x^{x+a\hat{\mu}} dx_\mu A_\mu^{\rm cont}(x))$ (where P indicates a path-ordered integral, and the superscript on A_μ indicates that it is a continuum field). The trace of a product of the $U_\mu(x)$ around any closed loop is easily seen to be gauge invariant and is the lattice version of a Wilson loop.

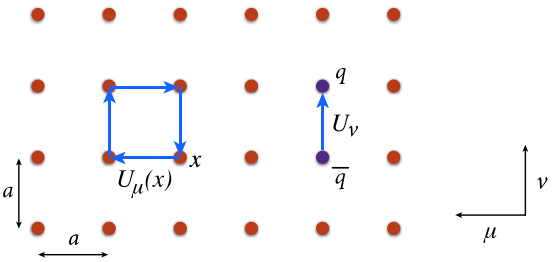

Figure 17.1: Sketch of a two-dimensional slice through the $\mu - \nu$ plane of a lattice, showing gluon fields lying on links and forming either the plaquette product appearing in the gauge action or a component of the covariant derivative connecting quark and antiquark fields.

The simplest possible gauge action, usually called the Wilson gauge action, is given by the product of gauge links around elementary plaquettes:

$$S_g = \beta \sum_{x,\mu,\nu} [1 - \frac{1}{3} \mathrm{ReTr}[U_\mu(x) U_\nu(x+a\hat{\mu}) U_\mu^\dagger(x+a\hat{\nu}) U_\nu^\dagger(x)]] \,. \quad (17.1)$$

This is illustrated in Fig. 17.1. For small a, assuming that the fields are slowly varying, one can expand the action in powers of a using $U_\mu(x) = \exp(iaA_\mu(x))$. Keeping only the leading non-vanishing term, and replacing the sum with an integral, one finds the continuum form,

$$S_g \longrightarrow \int d^4x \frac{1}{4g_{\rm lat}^2} \mathrm{Tr}[F_{\mu\nu}^2(x)] \,, (F_{\mu\nu} = \partial_\mu A_\nu - \partial_\nu A_\mu + i[A_\mu, A_\nu]) \quad (17.2)$$

as long as one chooses $\beta = 6/g_{\rm lat}^2$ for the lattice coupling. In this expression, $g_{\rm lat}$ is the bare coupling constant in the lattice scheme, which can be related (by combining continuum and lattice perturbation theory) to a more conventional coupling constant such as that in the $\overline{\rm MS}$ scheme (see Sec. 17.3.4 below).

In practice, the lattice spacing a is non-zero, leading to discretization errors. In particular, the lattice breaks Euclidean rotational invariance (which is the Euclidean version of Lorentz invariance) down to a discrete hypercubic subgroup. One wants to reduce discretization errors as much as possible. A very useful tool for understanding and then reducing discretization errors is the Symanzik effective action: the interactions of quarks and gluons with momenta low compared to the lattice cutoff ($|p| \ll 1/a$) are described by a continuum action consisting of the standard continuum terms (e.g. the gauge action given in Eq. (17.2)) augmented by higher dimensional operators suppressed by powers of a [5]. For the Wilson lattice gauge action, the leading corrections come in at $\mathcal{O}(a^2)$. They take the form $\sum_j a^2 c_j O_6^{(j)}$, with the sum running over all dimension-six operators $O_6^{(j)}$ allowed by the *lattice* symmetries, and c_j unknown coefficients. Some of these operators violate Euclidean rotational invariance, and all of them lead to discretization errors of the form $a^2\Lambda^2$, where Λ is a typical momentum scale for the quantity being calculated. These errors can, however, be reduced by adding corresponding operators to the lattice action and tuning their coefficients to eliminate the dimension-six operators in the effective action to a given order in perturbation theory or even non-perturbatively. This is the idea of the Symanzik improvement program [5]. In the case of the gauge action, one adds Wilson loops involving six gauge links (as opposed to the four links needed for the original plaquette action, Eq. (17.1)) to define the $\mathcal{O}(a^2)$ improved (or "Symanzik") action [6]. In practical implementations, the improvement is either at tree-level (so that residual errors are proportional to $\alpha_s a^2$, where the coupling is evaluated at a scale $\sim 1/a$), or at one loop order (errors proportional to $\alpha_s^2 a^2$). Another popular choice is motivated by studies of renormalization group (RG) flow. It has the same terms as the $\mathcal{O}(a^2)$ improved action but with different coefficients, and is called the RG-improved or "Iwasaki" action [7].

17.1.2 *Lattice fermions*

Discretizing the fermion action turns out to involve subtle issues, and the range of actions being used is more extensive than for gauge fields. Recall that the continuum fermion action is $S_f = \int d^4x \bar{q}[iD_\mu\gamma_\mu + m_q]q$, where $D_\mu = \partial_\mu + iA_\mu$ is the gauge-covariant derivative. The simplest discretization replaces the derivative with a symmetric difference:

$$D_\mu q(x) \longrightarrow \frac{1}{2a}[U_\mu(x) q(x+a\hat{\mu}) - U_\mu(x-a\hat{\mu})^\dagger q(x-a\hat{\mu})] \,. \quad (17.3)$$

The factors of U_μ ensure that $D_\mu q(x)$ transforms under gauge transformations in the same way as $q(x)$, so that the discretized version of $\bar{q}(x) D_\mu \gamma_\mu q(x)$ is gauge invariant. The choice in Eq. (17.3) leads to the so-called naive fermion action. This, however, suffers from the fermion doubling problem—in d dimensions it describes 2^d equivalent fermion fields in the continuum limit. The appearance of the extra "doubler" fermions is related to the deeper theoretical problem of formulating chirally symmetric fermions on the lattice. This is encapsulated by the Nielsen-Ninomiya theorem [8]: one cannot define lattice fermions having exact, continuum-like chiral symmetry without producing doublers. Naive lattice fermions do have chiral symmetry but at the cost of introducing 15 unwanted doublers (for $d = 4$).

There are a number of different strategies for dealing with the doubling problem, each with their own theoretical and computational advantages and disadvantages. Wilson fermions [1] add a term proportional to $a\bar{q}\Delta q$ to the fermion action (the "Wilson term"—in which Δ is a covariant lattice Laplacian). This gives a mass of $\mathcal{O}(1/a)$ to the doublers, so that they decouple in the continuum limit. The Wilson term, however, violates chiral symmetry, and also introduces discretization errors linear in a. A commonly used variant that eliminates the $\mathcal{O}(a)$ discretization error is the $\mathcal{O}(a)$-improved Wilson (or "clover") fermion [9]. In this application of Symanzik improvement, methods have been developed to remove $\mathcal{O}(a)$ terms non-perturbatively using auxiliary simulations to tune parameters [10]. Such "non-perturbetive improvement" is of great practical importance as it brings the discretization error from the fermion action down to the same level as that from the gauge action.

The advantages of Wilson fermions are their theoretical simplicity and relatively low computational cost. Their main disadvantage is the lack of chiral symmetry, which makes them difficult to use in cases where mixing with wrong chirality operators can occur, particularly if this involves divergences proportional to powers of $1/a$. A related problem is the presence of potential numerical instabilities due to spurious near-zero modes of the lattice Dirac operator. There are, however, studies that successfully ameliorate these problems and increase the range of quantities for which Wilson fermions can be used (see, e.g., Refs. [11–14]).

Twisted-mass fermions [15] are a variant of Wilson fermions in which two flavors are treated together with an isospin-breaking mass term (the "twisted mass" term). The main advantage of this approach is that all errors linear in a are automatically removed (without the need for tuning of parameters) by a clever choice of twisted mass and operators [16]. A disadvantage is the presence of isospin breaking effects (such as a splitting between charged and neutral pion masses even when up and down quarks are degenerate), which, however, vanish as $a^2\Lambda^2$ in the continuum limit. Strange and charm quarks can be added as a second pair, with a term added to split their masses [17, 18].

Staggered fermions are a reduced version of naive fermions in which there is only a single fermion Dirac component on each lattice site, with the full Dirac structure built up from neighboring sites [19]. They have the advantages of being somewhat faster to simulate than Wilson-like fermions, of preserving some chiral symmetry, and of having discretization errors of $\mathcal{O}(a^2)$. Their disadvantage is that they retain some of the doublers (3 for $d = 4$). The action thus describes four degenerate fermions in the continuum limit. These are usually called "tastes", to distinguish them from physical flavors, and the corresponding SU(4) symmetry is referred to as the "taste symmetry". The preserved chiral symmetry in this formulation has non-singlet taste. Practical applications usually introduce one staggered fermion for each physical flavor, and remove contributions from the unwanted tastes by taking the fourth-root of the fermion determinant appearing in the path integral. The validity of this "rooting" procedure is not obvious because taste symmetry is violated for non-zero lattice spacing. Theoretical arguments, supported by numerical evidence, suggest that the procedure is valid as long as one takes the continuum limit before approaching the light quark mass region [20]. Additional issues arise for the valence quarks (those appearing in quark propagators, as described in Sec. 17.2 below), where rooting is not possible, and one must ignore the extra tastes, or account for them by dividing by appropriate factors of four [21].

Just as for Wilson fermions, the staggered action can be improved, so as to reduce discretization errors. The Asqtad (a-squared tadpole improved) action [22] was used until recently in many large scale simulations [23]. More recent calculations use the HISQ (highly improved staggered quark) action, introduced in Ref. [24]. At tree-level it removes both $\mathcal{O}(a^2)$ errors and, to lowest order in the quark speed v/c, $\mathcal{O}([am]^4)$ errors. It also substantially reduces effects caused by taste-symmetry breaking. This makes it attractive not only for light quarks, but means that it is

also quite accurate for heavy quarks because it suppresses $(am)^n$ errors. It is being used to directly simulate charm quarks and to approach direct simulations of bottom quarks (see, e.g. [25, 26]).

There is an important class of lattice fermions, "Ginsparg-Wilson fermions," that possess a continuum-like chiral symmetry without introducing unwanted doublers. The lattice Dirac operator D for these fermions satisfies the Ginsparg-Wilson relation $D\gamma_5 + \gamma_5 D = aD\gamma_5 D$ [27]. In the continuum, the right-hand-side vanishes, leading to chiral symmetry. On the lattice, it is non-vanishing, but with a particular form (with two factors of D) that restricts the violations of chiral symmetry in Ward-Takahashi identities to short-distance terms that do not contribute to physical matrix elements [28]. In fact, one can define a modified chiral transformation on the lattice (by including dependence on the gauge fields) such that Ginsparg-Wilson fermions have an exact chiral symmetry for on-shell quantities [29]. The net result is that such fermions essentially have the same properties under chiral transformations as do continuum fermions, including the index theorem [28]. Their leading discretization errors are of $\mathcal{O}(a^2)$.

Two types of Ginsparg-Wilson fermions are currently being used in large-scale numerical simulations. The first is Domain-wall fermions (DWF). These are defined on a five-dimensional space, in which the fifth dimension is fictitious [30]. The action is chosen so that the low-lying modes are chiral, with left- and right-handed modes localized on opposite four-dimensional surfaces. For an infinite fifth dimension, these fermions satisfy the Ginsparg-Wilson relation. In practice, the fifth dimension is kept finite, and there remains a small, controllable violation of chiral symmetry. The second type is Overlap fermions. These appeared from a completely different context and have an explicit form that exactly satisfies the Ginsparg-Wilson relation [31]. Their numerical implementation requires an approximation of the matrix sign function of a Wilson-like fermion operator, and various approaches are being used. In fact, it is possible to rewrite these approximations in terms of a five-dimensional formulation, showing that the DWF and Overlap approaches are essentially equivalent [32, 33]. Numerically, the five-dimensional approach appears to be more computationally efficient.

The various lattice fermion formulations are often combined with the technique of link smearing. Here one couples the fermions to a smoother gauge link, defined by averaging with adjacent links in a gauge invariant manner. Several closely related implementations are being used. All reduce the coupling of fermions to the short-distance fluctuations in the gauge field, leading to an improvement in the numerical stability and speed of algorithms. One cannot perform this smearing too aggressively, however, since the smearing may distort short distance physics and enhance discretization errors.

As noted above, each fermion formulation has its own advantages and disadvantages. For instance, domain-wall and overlap fermions are theoretically preferred as they have chiral symmetry without doublers, but their computational cost is greater than for other choices. If the physics application of interest and the target precision do not require near-exact chiral symmetry, there is no strong motivation to use these expensive formulations. On the other hand, there is a class of applications (including the calculation of the $\Delta I = 1/2$ amplitude for $K \to \pi\pi$ decays and the S-parameter [34]) where chiral symmetry plays an essential role and for which the use of Ginsparg-Wilson fermions is strongly favored.

17.1.3 *Heavy quarks on the lattice*

The fermion formulations described in the previous subsection can be used straightforwardly only for quarks whose masses are small compared to the lattice cutoff, $m_q \lessapprox 1/a$. This is because there are discretization errors proportional to powers of am_q, and if $am_q \gtrapprox 1$ these errors are large and uncontrolled. Present LQCD simulations typically have cutoffs in the range of $1/a = 2-4$ GeV (corresponding to $a \approx 0.1 - 0.05$ fm). Thus, while for the up, down and strange quarks one has $am_q \ll 1$, for bottom quarks (with $m_b \approx 4.5$ GeV) one must use alternative approaches. Charm quarks ($m_c \approx 1.5$ GeV) are an intermediate case, allowing simulations using both direct and alternative approaches.

For the charm quark, the straightforward approach is to simultaneously reduce the lattice spacing and to improve the fermion action so as to reduce the size of errors proportional to powers of am_c. This approach has been followed successfully using the HISQ, twisted-mass and domain-wall actions [24–26, 35, 36]. It is important to note, however, that reducing a increases the computational cost because an increased number of lattice points are needed for the same physical volume. One cannot reduce the spatial size below $2-3$ fm without introducing finite volume errors. Present lattices have typical sizes of $\sim 64^3 \times 128$ (with the long direction being Euclidean time), and thus allow a lattice cutoff up to $1/a \sim 4$ GeV.

This approach can, to some extent, be extended to the bottom quark, by the use of simulations with small lattice spacings [37]. This has been pursued with the HISQ action, using lattices of size up to $144^3 \times 288$ and lattice spacings down to $a \approx 0.03$ fm ($1/a \approx 6.6$ GeV) [38]. Extrapolation in m_b is still needed [39], however, and this makes use of the mass dependence predicted by Heavy Quark Effective Theory (HQET).

Alternative approaches for discretizing heavy quarks are motivated by effective field theories. For a bottom quark in heavy-light hadrons, one can use HQET to expand about the infinite quark-mass limit. In this limit, the bottom quark is a static color source, and one can straightforwardly write the corresponding lattice action [40]. Corrections, proportional to powers of $1/m_b$, can be introduced as operator insertions, with coefficients that can be determined non-perturbatively using existing techniques [41]. This method allows the continuum limit to be taken controlling all $1/m_b$ corrections.

Another way of introducing the $1/m_b$ corrections is to include the relevant terms in the effective action. This leads to a non-relativistic QCD (NRQCD) action, in which the heavy quark is described by a two-component spinor [42]. This approach has the advantage over HQET that it can also be used for heavy-heavy systems, such as the Upsilon states. Moreover, the bottom quark can be treated without any extrapolation in m_b. A disadvantage is that some of the parameters in this effective theory are determined perturbatively (originally at tree-level, but more recently at one-loop [43]), which limits the precision of the final results. Although discretization effects can be controlled with good numerical precision for a range of lattice spacings, these artifacts cannot be extrapolated away by taking the lattice spacing to zero. This is because NRQCD is a nonrelativistic effective field theory and so ceases to work when the cutoff π/a becomes much larger than the heavy-quark mass. In practice these effects are accounted for in the error budget.

This problem can be avoided if one uses HQET power counting to analyze and reduce discretization effects for heavy quarks while using conventional fermion actions [44]. For instance, one can tune the parameters of an improved Wilson quark action so that the leading HQET corrections to the static quark limit are correctly accounted for. As the lattice spacing becomes finer, the action smoothly goes over to that of a light Wilson quark action, where the continuum limit can be taken as usual. In principle, one can improve the action in the heavy quark regime up to arbitrarily high orders using HQET, but so far large-scale simulations have typically used clover improved Wilson quarks, where tuning the parameters of the action corresponds to including all corrections through next-to-leading order in HQET. Three different methods for tuning the parameters of the clover action are being used: the Fermilab [44], Tsukuba [45] and Columbia [46] approaches. An advantage of this HQET approach is that the c and b quarks can be treated on the same footing. Parameter tuning has typically been done perturbatively, as in NRQCD, but recent work using the Columbia approach has used non-perturbative tuning of some of the parameters [47, 48]. One can improve the effective theory including the terms beyond the next-to-leading order. The Oktay-Kronfeld action that includes dimension-six and -seven operators has been constructed [49] and recently used in large-scale numerical calculations [50].

Another approach is the "ratio method" introduced in Ref. [51]. Here one uses quarks with masses lying at, or slightly above, the charm mass m_c, which can be simulated with a relativistic action, and extrapolates to m_b incorporating the behavior predicted by

HQET. The particular implementation relies on the use of ratios. As an example, consider the B meson decay constant f_B. According to HQET, this scales as $1/\sqrt{m_B}$ for $m_B \gg \Lambda_{\rm QCD}$, up to a logarithmic dependence that is calculable in perturbative QCD (but will be suppressed in the following). Here m_B is the B meson mass, which differs from m_b by $\sim \Lambda_{\rm QCD}$. One considers the ratio $y(\lambda, m_{b'}) \equiv f_{B''}\sqrt{m_{B''}}/f_{B'}\sqrt{m_{B'}}$ for fictitious B mesons containing b quarks with unphysical masses $m_{b'}$ and $m_{b''} = \lambda m_{b'}$. HQET implies that $y(\lambda, m_{b'})$ approaches unity for large $m_{b'}$ and any fixed $\lambda > 1$. The ratios are evaluated on the lattice for the sequence of masses $m_{b'} = m_c$, λm_c, $\lambda^2 m_c$, all well below the physical m_b, and for each the continuum limit is taken. The form of the ratio for larger values of $m_{b'}$ is obtained by fitting, incorporating the constraints implied by HQET. The result for $f_B\sqrt{m_B}$ is then obtained as a product of y's with $f_D\sqrt{m_D}$.

17.1.4 *QED on the lattice*

Quarks in nature are electrically charged, and the resultant coupling to photons leads to shifts in the properties of hadrons that are generically of $\mathcal{O}(\alpha_{\rm EM})$. Thus, for example, the proton mass is increased by ~ 1 MeV relative to that of the neutron due to its overall charge although this effect is more than compensated for by the ~ 2.5 MeV relative decrease due to the up quark being lighter than the down quark [52]. This example shows that once pure QCD, isospin-symmetric lattice calculations reach percent level accuracy, further improvement requires the inclusion of effects due to both electromagnetism and the up-down mass difference. This level of accuracy has in fact been obtained for various quantities, e.g. light hadron masses and decay constants (see Ref. [53]), and simulations including QED in addition to QCD are becoming more common.

The extension of lattice methods to include QED is straightforward, although some new subtleties arise. The essential change is that the quark must now propagate through a background field containing both gluons and photons. The gauge field U_μ that appears in the covariant derivative of Eq. (17.3) is extended from an SU(3) matrix to one living in U(3): $U_\mu \to U_\mu e^{iaqeA_\mu^{\rm EM}}$. Here $A_\mu^{\rm EM}$ is the photon field, e the electromagnetic coupling, and q the charge of the quark, *e.g.* $q = 2/3$ for up and $-1/3$ for down and strange quarks. The lattice action for the photon that is typically used is a discretized version of the continuum action Eq. (17.2), rather than the form used for the gluons, Eq. (17.1). This "non-compact" action has the advantage that it is quadratic in $A_\mu^{\rm EM}$, which simplifies the QED part of the generation of configurations.

One subtlety that arises is that Gauss' law forbids a charged particle in a box with periodic boundary conditions. This finite volume effect can be overcome by including a uniform background charge, and this can be shown to be equivalent to removing the zero-momentum mode from the photon field. This is an example of the enhanced finite-volume effects that arise in the presence of the massless photon.

Simulations including QED have progressed over the last few years, and now a full inclusion of QED has been achieved with almost physical quark masses [52,54]. Alternative approaches have also been used: reweighting the QCD fields *a posteriori* [55,56], and keeping only the linear term in an expansion in $\alpha_{\rm EM}$ about the QCD only case [57]. In addition, some calculations have included QED effects for the valence quarks but not the sea quarks (the "electroquenched approximation")—for a recent example see Ref. [58].

The QED corrections to processes including leptons, such as the leptonic and semileptonic decays of hadrons, involve additional diagrams in which a photon propagator bridges between a hadron and a lepton. Such diagrams induce infrared divergences that cancel against soft photon radiation (Bloch-Nordsieck theorem [59]). Methods have been developed to implement this cancellation in lattice calculations, treating the soft photon analytically [60], with first results reported recently for leptonic pion and kaon decays [61,62].

17.1.5 *Basic inputs for lattice calculations*

Since LQCD is nothing but a regularization of QCD, the renormalizability of QCD implies that the number of input parameters in LQCD is the same as for continuum QCD—the strong coupling constant $\alpha_s = g^2/(4\pi)$, the quark masses for each flavor, and the CP violating phase θ. The θ parameter is usually assumed to be zero, while the other parameters must be determined using experimental inputs.

17.1.5.1 *Lattice spacing*

In QCD, the coupling constant is a function of scale. With lattice regularization, this scale is the inverse lattice spacing $1/a$, and choosing the bare coupling constant is equivalent to fixing the lattice spacing.

In principle, a can be determined using any dimensionful quantity measured by experiments. For example, using the mass of hadron H one has $a = (am_H)^{\rm lat}/m_H^{\rm exp}$. One chooses quantities that can be calculated accurately on the lattice, and that are only weakly dependent on the light quark masses. The latter property minimizes errors from extrapolating or interpolating to the physical light quark masses or from mistuning of these masses.

Commonly used choices are the spin-averaged 1S-1P or 1S-2S splittings in the Upsilon system, the mass of the Ω^- baryon, and the pion decay constant f_π. Ultimately, all choices must give consistent results for a, and that this is the case provides a highly non-trivial check of both the calculational method and of QCD.

17.1.5.2 *Light quark masses*

In LQCD simulations, the up, down and strange quarks are usually referred to as the light quarks, in the sense that $m_q < \Lambda_{\rm QCD}$. (The standard definition of $\Lambda_{\rm QCD}$ is given in the "Quantum Chromodynamics" review; in this review we are using it only to indicate the approximate non-perturbative scale of QCD.) This condition is stronger than that used above to distinguish quarks with small discretization errors, $m_q < 1/a$. Loop effects from light quarks must be included in the simulations to accurately represent QCD. At present, most simulations are done in the isospin symmetric limit $m_u = m_d \equiv m_\ell < m_s$, and are often referred to as "$N_f = 2 + 1$" simulations. Increasingly, simulations also include loops of charm quarks (denoted $N_f = 2 + 1 + 1$ simulations), although the effect of charmed sea quarks on low-energy physics is generically expected to be at the sub-percent level [63–66]. Precision is now reaching the point where isospin breaking effects must be included. To do so without approximation requires simulating with nondegenerate up and down quarks (leading to $N_f = 1{+}1{+}1$ or $1{+}1{+}1{+}1$ simulations) as well as including electromagnetism (as described above). This has been done in Ref. [52]. Alternatively, one can use a perturbative approach, expanding about the isospin symmetric theory and working to linear order in $\alpha_{\rm EM}$ and $m_u - m_d$ [57,67].

We now describe the tuning of m_ℓ, m_s and m_c to their physical values. (For brevity, we ignore isospin violation in the following discussion.) The most commonly used quantities for these tunings are, respectively, m_π, m_K and m_{η_c}. If the scale is being set by m_Ω, then one adjusts the lattice quark masses until the ratios m_π/m_Ω, m_K/m_Ω and m_{η_c}/m_Ω take their physical values. In the past, most calculations needed to extrapolate to the physical value of m_ℓ (typically using forms based on chiral perturbation theory [ChPT]), while simulating directly at or near to the physical values of m_s and m_c. Present calculations are increasingly done with physical or near physical values of m_ℓ, requiring at most only a short extrapolation.

17.1.5.3 *Heavy quark masses*

The b quark is usually treated only as a valence quark, with no loop effects included. The errors introduced by this approximation can be estimated to be $\sim \alpha_s(m_b)\Lambda_{\rm QCD}^2/m_b^2$ and are likely to be very small. In the past, the same approximation has been made for the c quark, leading to errors $\sim \alpha_s(m_c)\Lambda_{\rm QCD}^2/m_c^2$. (See Ref. [63] for a quantitative estimate of the effects of including the charm quark on some low energy physical quantities, and Ref. [68] for similar estimates for B-meson matrix elements.) For high precision, however, dynamical charm quarks are necessary, and some of the most recent simulations now include them.

The b quark mass can be tuned by setting heavy-heavy (Υ) or heavy-light (B) meson masses to their experimental values. Consistency between these two determinations provides an important check that the determination of parameters in the heavy quark lat-

tice formulations is being done correctly (see, e.g., Ref. [37,69,70])

17.1.6 *Sources of systematic error*

Lattice results have statistical and systematic errors that must be quantified for any calculation in order for the result to be a useful input to phenomenology. The statistical error is due to the use of Monte Carlo importance sampling to evaluate the path integral (a method discussed below). There are, in addition, a number of systematic errors that are always present to some degree in lattice calculations, although the size of any given error depends on the particular quantity under consideration and the parameters of the ensembles being used. The most common lattice errors are reviewed below.

Although not strictly a systematic error, it is important to note that the presence of long autocorrelations in the sequence of lattice configurations generated by the Monte Carlo method can lead to underestimates of statistical errors [71]. It is known that the global topological charge of the gauge fields decorrelates very slowly with certain algorithms [71, 72]. The effect of poorly sampling topological charge is expected to be most significant for the pion mass and related quantities [73, 74]. This issue becomes more relevant as the precision of the final results increases.

17.1.6.1 *Continuum limit*

Physical results are obtained in the limit that the lattice spacing a goes to zero. The Symanzik effective theory determines the scaling of lattice artefacts with a. Most lattice calculations use improved actions with leading discretizations errors of $\mathcal{O}(a^2\Lambda^2)$, $\mathcal{O}(\alpha_s a^2\Lambda^2)$, or $\mathcal{O}(\alpha_s a\Lambda)$, where Λ is a typical momentum scale in the system. Knowledge of the scaling of the leading discretization errors allows controlled extrapolation to $a = 0$ when multiple lattice spacings are available, as in current state-of-the-art calculations. Residual errors arise from the exclusion of subleading a dependence from the fits.

For many quantities the typical momentum scale in the system is $\sim \Lambda_{\rm QCD} \approx 300$ MeV. Discretization errors are expected to be larger for quantities involving larger scales, for example form factors or decays involving particles with momenta larger than $\Lambda_{\rm QCD}$.

17.1.6.2 *Infinite volume limit*

LQCD calculations are necessarily carried out in finite space-time boxes, leading to departures of physical quantities (masses, decay constants, etc.) from their measured, infinite volume values. These finite-volume shifts are an important systematic that must be estimated and minimized.

Typical lattices are asymmetric, with N_s points in the three spatial directions and N_t in the (Euclidean) temporal direction. The spatial and temporal sizes in physical units are thus $L_s = aN_s$ and $L_t = aN_t$, respectively. (Anisotropic lattice spacings are also sometimes used, as discussed below in Sec. 17.2.2.) Typically, $L_t \geq 2L_s$, a longer temporal direction being used to allow excited-state contributions to correlators to decay. This means that the dominant impact of using finite volume is from the presence of a finite spatial box.

High-precision LQCD calculations are of quantities involving no more than a single particle in initial and final states (with the exception of the $K \to \pi\pi$ decay amplitudes). For such quantities, once the volume exceeds about 2 fm (so that the particle is not "squeezed"), the dominant finite-volume effect comes from virtual pions wrapping around the lattice in the spatial directions. This effect is exponentially suppressed as the volume becomes large, roughly as $\sim \exp(-m_\pi L_s)$, and has been estimated using ChPT [75] or other methods [76]. The estimates suggest that finite volume shifts are sub-percent effects when $m_\pi L_s \gtrsim 4$, and most large-scale simulations use lattices satisfying this condition. This becomes challenging as one approaches the physical pion mass, for which $L_s \gtrsim 5$ fm is required.

Finite volume errors are usually determined by repeating the simulations on two or more different volumes (with other parameters fixed). If different volumes are not available, the ChPT estimate can be used, often inflated to account for the fact that the ChPT calculation is truncated at some order.

In the future, LQCD calculations involving more than a single hadron will become increasingly precise. Examples include the calculation of resonance parameters and the above-mentioned $K \to \pi\pi$ amplitudes. Finite volume effects are much larger in these cases, with power-law terms (e.g. $1/L_s^3$) in addition to exponential dependence. Indeed, as will be discussed in Sec. 17.2.4, one can use the volume dependence to indirectly extract infinite-volume quantities such as scattering lengths. Doing so, however, requires a set of lattice volumes satisfying $m_\pi L_s \gtrsim 4$ and is thus more challenging than for single-particle quantities.

17.1.6.3 *Chiral extrapolation*

Until recently, an important source of systematic error in LQCD calculations was the need to extrapolate in m_u and m_d (or, equivalently, in m_π). This extrapolation was usually done using functional forms based on ChPT, or with analytic functions, with the difference between different fits used as an estimate of the systematic error, which was often substantial. Increasingly, however, calculations work directly at, or very close to, the physical quark masses. This either removes entirely, or greatly reduces, the uncertainties in the extrapolation, such that this error is subdominant.

17.1.6.4 *Operator matching*

Many of the quantities that LQCD can precisely calculate involve hadronic matrix elements of operators from the electroweak Hamiltonian. Examples include the pion and kaon decay constants, semileptonic form factors and the kaon mixing parameter B_K (the latter defined in Eq. (17.13)). The operators in the lattice matrix elements are defined in the lattice regularization scheme. To be used in tests of the Standard Model, however, they must be matched to the continuum regularization scheme in which the corresponding Wilson coefficients have been calculated. The only case in which such matching is not needed is if the operator is a conserved or partially conserved current. Similar matching is also needed for the conversion of lattice bare quark masses to those in the continuum $\overline{\rm MS}$ scheme.

Several methods are used to calculate the matching factors: perturbation theory (usually to one- or two-loop order), non-perturbative renormalization (NPR) using Landau-gauge quark and gluon external states [77], NPR using gauge-invariant methods based on the Schrödinger functional [78], NPR using gauge-invariant short-distance hadron correlators [79], and NPR using gauge-invariant heavy-heavy correlators [26,80]. The NPR methods replace truncation errors (which can only be approximately estimated) by statistical and systematic errors that can be determined reliably and systematically reduced.

An issue that arises in some of such calculations (e.g. for quark masses and B_K) is that, using NPR with Landau-gauge quark and gluon external states, one ends up with operators regularized in a MOM-like scheme (or a Schrödinger-functional scheme), rather than the $\overline{\rm MS}$ scheme mostly used for calculating the Wilson coefficients. To make contact with this scheme requires a purely continuum perturbative matching calculation. The resultant truncation error can, however, be minimized by pushing up the momentum scale at which the matching is done using step-scaling techniques as part of the NPR calculation [81]. It should also be noted that this final step in the conversion to the $\overline{\rm MS}$ scheme could be avoided if continuum calculations used a MOM-like scheme or if one imposes a renormalization condition for quantities that are calculable both in the $\overline{\rm MS}$ scheme and in LQCD, such as the hadron correlators at short distances (see, e.g., Ref. [82]).

17.2 Methods and status

Once the lattice action is chosen, it is straightforward to define the quantum theory using the path integral formulation. The Euclidean-space partition function is

$$Z = \int [dU] \prod_f [dq_f][d\bar{q}_f] e^{-S_g[U] - \sum_f \bar{q}_f (D[U] + m_f) q_f} , \quad (17.4)$$

where link variables are integrated over the SU(3) manifold, q_f and $\bar{q}_f$ are Grassmann (anticommuting) quark and antiquark fields of flavor f, and $D[U]$ is the chosen lattice Dirac operator with m_f the quark mass in lattice units. Integrating out the quark

and antiquark fields, one arrives at a form suitable for simulation:

$$Z = \int [dU] e^{-S_g[U]} \prod_f \det(D[U] + m_f)\,. \qquad (17.5)$$

The building blocks for calculations are expectation values of multi-local gauge-invariant operators, also known as "correlation functions",

$$\langle \mathcal{O}(U,q,\bar{q})\rangle = (1/Z)\int [dU]\prod_f [dq_f][d\bar{q}_f]\mathcal{O}(U,q,\bar{q}) e^{-S_g[U]-\sum_f \bar{q}_f (D[U]+m_f) q_f}\,. \qquad (17.6)$$

If the operators depend on the (anti-)quark fields q_f and $\bar{q}_f$, then integrating these fields out leads not only to the fermion determinant but also, through Wick's theorem, to a series of quark "propagators", $(D[U]+m_f)^{-1}$, connecting the positions of the fields.

This set-up allows one to choose, by hand, the masses of the quarks in the determinant (the sea quarks) differently from those in the propagators (valence quarks). This is called "partial quenching", and is used by some calculations as a way of obtaining more data points from which to extrapolate both sea and valence quarks to their physical values.

17.2.1 *Monte-Carlo method*

Since the number of integration variables U is huge ($N_s^3 \times N_t \times 4 \times 9$), direct numerical integration is impractical and one has to use Monte-Carlo techniques. In this method, one generates a Markov chain of gauge configurations (a "configuration" being the set of U's on all links) distributed according to the probability measure $[dU]e^{-S_g[U]}\prod_f \det(D[U]+m_f)$. Once the configurations are generated, expectation values $\langle \mathcal{O}(U,q,\bar{q})\rangle$ are calculated by averaging over those configurations. In this way the configurations can be used repeatedly for many different calculations, and there are several large collections of ensembles of configurations (with a range of values of a, lattice sizes and quark masses) that are publicly available through the International Lattice Data Grid (ILDG). As the number of the configurations, N, is increased, the error decreases as $1/\sqrt{N}$.

The most challenging part of the generation of gauge configurations is the need to include the fermion determinant. Direct evaluation of the determinant is not feasible, as it requires $\mathcal{O}((N_s^3 \times N_t)^3)$ computations. Instead, one rewrites it in terms of "pseudofermion" fields ϕ (auxiliary fermion fields with bosonic statistics). For example, for two degenerate quarks one has

$$\det(D[U]+m_f)^2 = \int [d\phi] e^{-\phi^\dagger (D[U]+m_f)^{-2}\phi}\,. \qquad (17.7)$$

By treating the pseudofermions as additional integration variables in the path integral, one obtains a totally bosonic representation. The price one pays is that the pseudofermion effective action is highly non-local since it includes the inverse Dirac operator $(D[U]+m_f)^{-1}$. Thus, the large sparse matrix $(D[U]+m)$ has to be inverted every time one needs an evaluation of the effective action.

Present simulations generate gauge configurations using the Hybrid Monte Carlo (HMC) algorithm [83], or variants thereof. This algorithm combines molecular dynamics (MD) evolution in a fictitious time (which is also discretized) with a Metropolis "accept-reject" step. It makes a global update of the configuration, and is made exact by the Metropolis step. In its original form it can be used only for two degenerate flavors, but extensions (particularly the rational HMC [84]) are available for single flavors. Considerable speed-up of the algorithms has been achieved over the last two decades using a variety of techniques.

All these algorithms spend the bulk of their computational time on the repeated inversion of $(D[U]+m)$ acting on a source (which is required at every step of the MD evolution). Inversions are done using a variety of iterative algorithms, *e.g.* the conjugate gradient algorithm. In this class of algorithms, computational cost is proportional to the condition number of the matrix, which is the ratio of maximum and minimum eigenvalues. For $(D[U]+m)$ the smallest eigenvalue is $\approx m$, so the condition number and cost are inversely proportional to the quark mass. This is a major reason why simulations at the physical quark mass are challenging.

Recent algorithmic improvements have significantly reduced this problem. The main idea is to separate different length scales. Since the low eigenvalues of $(D[U]+m)$ are associated with long wavelength quark modes, one may project the problem onto that of a coarse-grained lattice by averaging the field within a block of sublattices and carrying out the inversion on this coarse lattice. The result is then fed back to the original lattice as an efficient *preconditioner* for the iterative solver, and the whole procedure may be nested multiple times. Variants of such methods have been implemented, specifically domain-decomposition [11,12], deflation [85–88] and multigrid [89,90]. They are increasingly used in large-scale lattice simulations.

A practical concern is the inevitable presence of correlations between configurations in the Markov chain. These are characterized by an autocorrelation length in the fictitious MD time. One aims to use configurations separated in MD time by greater than this autocorrelation length. In practice, it is difficult to measure this length accurately, see, e.g., [91], and this leads to some uncertainty in the resulting statistical errors, as well as the possibility of insufficient equilibration.

For most of the applications of LQCD discussed in this review, the cost of generating gauge configurations is larger than or similar to that of performing the "measurements" on those configurations. The computational cost of gauge generation grows with the lattice volume, $V_{\rm lat} = N_s^3 N_t$, as $V_{\rm lat}^{1+\delta}$. Here $\delta = 1/4$ for the HMC algorithm [92] and can be reduced slightly using modern variants. Such growth with $V_{\rm lat}$ provides a (time-dependent) limit on the largest lattice volumes that can be simulated. At present, the largest lattices being used have $N_s = 144$ and $N_t = 288$. Typically one aims to create an ensemble of $\sim 10^3$ statistically independent configurations at each choice of parameters (a, m_q and $V_{\rm lat}$). For most physical quantities of interest, this is sufficient to make the resulting statistical errors smaller than or comparable to the systematic errors.

17.2.2 *Two-point functions*

One can extract properties of stable hadrons using two-point correlation functions, $\langle O_X(x) O_Y^\dagger(0)\rangle$. Here $O_{X,Y}(x)$ are operators that have non-zero overlaps with the hadronic state of interest $|H\rangle$, *i.e.* $\langle 0|O_{X,Y}(x)|H\rangle \neq 0$. One usually Fourier transforms in the spatial directions and considers correlators as a function of Euclidean time:

$$C_{XY}(t;\vec{p}) = \sum_{\vec{x}} \langle O_X(t,\vec{x}) O_Y^\dagger(0)\rangle e^{-i\vec{p}\cdot\vec{x}}. \qquad (17.8)$$

(Here and throughout this section all quantities are expressed in dimensionless lattice units, so that, for example, $\vec{p} = a\vec{p}_{\rm phys}$.) By inserting a complete set of states having spatial momentum $\vec{p}$, the two-point function can be written as

$$C_{XY}(t;\vec{p}) = \sum_{i=0}^{\infty} \frac{1}{2E_i(\vec{p})} \langle 0|O_X(0)|H_i(\vec{p})\rangle \langle H_i(\vec{p})|O_Y^\dagger(0)|0\rangle e^{-E_i(\vec{p})t}, \qquad (17.9)$$

where the energy of the i-th state $E_i(\vec{p})$ appears as an eigenvalue of the time evolution operator e^{-Ht} in the Euclidean time direction. The factor of $1/[2E_i(\vec{p})]$ is due to the relativistic normalization used for the states. For large enough t, the dominant contribution

is that of the lowest energy state $|H_0(\vec{p})\rangle$:

$$C_{XY}(t) \overset{t\to\infty}{\longrightarrow} \frac{1}{2E_0(\vec{p})} \langle 0|O_X(0)|H_0(\vec{p})\rangle\langle H_0(\vec{p})|O_Y^\dagger(0)|0\rangle e^{-E_0(\vec{p})t} \,. \tag{17.10}$$

One can thus obtain the energy $E_0(\vec{p})$, which equals the hadron mass m_H when $\vec{p} = 0$, and the product of matrix elements $\langle 0|O_X(0)|H_i(\vec{p})\rangle\langle H_i(\vec{p})|O_Y^\dagger(0)|0\rangle$.

This method can be used to determine the masses of all the stable mesons and baryons by making appropriate choices of operators. For example, if one uses the axial current, $O_X = O_Y = A_\mu = \bar{d}\gamma_\mu\gamma_5 u$, then one can determine m_{π^+} from the rate of exponential fall-off, and in addition the decay constant f_π from the coefficient of the exponential. A complication arises for states with high spins ($j \geq 4$ for bosons) because the spatial rotation group on the lattice is a discrete subgroup of the continuum group SO(3). This implies that lattice operators, even when chosen to lie in irreducible representations of the lattice rotation group, have overlap with states that have a number of values of j in the continuum limit [93]. For example $j = 0$ operators can also create mesons with $j = 4$. Methods to overcome this problem in practice are available [94, 95] and have been used successfully.

The expression given above for the correlator $C_{XY}(t;\vec{p})$ shows how, in principle, one can determine the energies of the excited hadron states having the same quantum numbers as the operators $O_{X,Y}$, by fitting the correlation function to a sum of exponentials, which is also important to precisely determine the ground-state exponential. In practice, in order to reliably identify the excited state, one often needs to use a large basis of operators and to adopt the variational approach such as that of Ref. [96]. One can also use an anisotropic lattice in which a_t, the lattice spacing in the time direction, is smaller than its spatial counterpart a_s. Using a combination of these and other technical improvements extensive excited-state spectra have been obtained [95, 97–100].

17.2.3 *Three-point functions*

Hadronic matrix elements needed to calculate semileptonic form factors and neutral meson mixing amplitudes can be computed from three-point correlation functions. We discuss here, as a representative example, the $D \to K$ amplitude. As in the case of two-point correlation functions one constructs operators O_D and O_K having overlap, respectively, with the D and K mesons. We are interested in calculating the matrix element $\langle K|V_\mu|D\rangle$, with $V_\mu = \bar{c}\gamma_\mu s$ the vector current calculations of this contribution.

To obtain this, we use the three-point correlator

$$C_{KV_\mu D}(t_x, t_y; \vec{p}) = \sum_{\vec{x},\vec{y}} \langle O_K(t_x,\vec{x}) V_\mu(0) O_D^\dagger(t_y,\vec{y})\rangle e^{-i\vec{p}\cdot\vec{x}} \,, \tag{17.11}$$

and focus on the limit $t_x \to \infty$, $t_y \to -\infty$. In this example we set the D-meson at rest while the kaon carries three-momentum $\vec{p}$. Momentum conservation then implies that the weak operator V_μ inserts three-momentum $-\vec{p}$. Inserting a pair of complete sets of states between each pair of operators, we find

$$C_{KV_\mu D}(t_x, t_y; \vec{p}) = \sum_{i,j} \frac{1}{2m_{D_i} 2E_{K_j}(\vec{p})} e^{-m_{D_i} t_x - E_{K_j}(\vec{p})|t_y|}$$
$$\langle 0|O_K(0)|K_i(\vec{p})\rangle\langle K_i(\vec{p})|V_\mu(0)|D_j(\vec{0})\rangle\langle D_j(\vec{0})|O_D^\dagger(0)|0\rangle. \tag{17.12}$$

The matrix element $\langle K_i(\vec{p})|V_\mu(0)|D_j(\vec{0})\rangle$ can then be extracted, since all other quantities in this expression can be obtained from two-point correlation functions. Typically one is interested in the weak matrix elements of ground states, such as the lightest pseudoscalar mesons. In the limit of large separation between the three operators in Euclidean time, the three-point correlation function yields the weak matrix element of the transition between ground states.

17.2.4 *Scattering amplitudes and resonances*

The methods described thus far yield matrix elements involving single, stable particles (where by stable we mean here absolutely stable to strong interaction decays). Most of the particles listed in the Review of Particle Properties are, however, unstable—they are resonances decaying into final states consisting of multiple strongly interacting particles. LQCD simulations cannot directly calculate resonance properties, but methods have been developed to do so indirectly for resonances coupled to two-particle final states in the elastic regime, starting from the seminal work of Lüscher [101].

The difficulty faced by LQCD calculations is that, to obtain resonance properties, or, more generally, scattering phase-shifts, one must calculate multiparticle scattering amplitudes in momentum space and put the external particles on their mass-shells. This requires analytically continuing from Euclidean to Minkowski momenta. Although it is straightforward in LQCD to generalize the methods described above to calculate four- and higher-point correlation functions, one necessarily obtains them at a discrete and finite set of Euclidean momenta. Analytic continuation to $p_E^2 = -m^2$ is then an ill-posed and numerically unstable problem. The same problem arises for single-particle states, but can be largely overcome by picking out the exponential fall-off of the Euclidean correlator, as described above. With a multi-particle state there is no corresponding trick, except for two particles at threshold [102], although recent ideas using smeared correlators and advanced spectral-reconstruction methods offer hope for future progress [103–105].

What LQCD can calculate are the energies of the eigenstates of the QCD Hamiltonian in a finite box. The energies of states containing two stable particles, e.g. two pions, clearly depend on the interactions between the particles. It is possible to invert this dependence and, with plausible assumptions, determine the scattering phase-shifts at a discrete set of momenta from a calculation of the two-particle energy levels for a variety of spatial volumes [101]. This is a challenging calculation, but it has recently been carried through in several channels with quark masses approaching physical values. Channels studied include $\pi\pi$ (for $I = 2$, 1 and 0), $\bar{K}K$, $K\pi$, $\pi\omega$, $\pi\phi$, KD, DD^* and $B\pi$. For recent comprehensive reviews see [106, 107]. Extensions to nucleon interactions are also being actively studied [108]. The generalization of the formalism to the case of three particles is under active development [109–111]. For a recent review, see [112].

It is also possible to extend the methodology to calculate electroweak decay amplitudes to two particles below the inelastic threshold, e.g. $\Gamma(K \to \pi\pi)$ [113]. Results for both the $\Delta I = 3/2$ and 1/2 amplitudes with physical quark masses have been obtained [114,115], the former now including a controlled continuum limit [116]. First results for the CP-violating quantity ϵ' have been obtained [115].

Partial extensions of the formalism above the elastic threshold have been worked out, in particular for the case of multiple two-particle channels [117]. Another theoretical extension is to allow the calculation of form factors between a stable particle and a resonance [118] , and between two resonances [119]. The former has been used to calculate the $\gamma\pi \to \rho$ amplitude, albeit for unphysically large quark masses [120].

While a systematic extension to decays with many multiparticle channels, e.g. hadronic B decays, has, however, yet to be formulated, some interesting new ideas have been recently proposed [121, 122].

17.2.5 *Recent advances*

In some physics applications, one is interested in the two-point correlation function $\langle O_X(x) O_Y^\dagger(0)\rangle$ for all values of the separation x, not just its asymptotic form for large separations (which is used to determine the hadron spectrum as sketched above). A topical example is the hadronic vacuum polarization function $\Pi_{\mu\nu}(x) = \langle V_\mu(x) V_\nu(0)\rangle$ and its Fourier transform $\Pi_{\mu\nu}(q^2)$. Since the lattice is in Euclidean space-time, only space-like momenta, $q^2 = -Q^2 < 0$, are accessible. Nevertheless, this quantity is of significant interest. It is related by a dispersion relation to the cross section for $e^+e^- \to$ hadrons, and is needed for a first-principles calculation of the "hadronic vacuum polarization" contribution to the muon anomalous magnetic moment a_μ. This is the contribution with the largest theoretical uncertainty at present. There are a number of lattice calculations of this contribution (see, e.g., Refs. [123–138] following the pioneering work Ref. [139]). Since the relevant scale is set by the muon mass m_μ, this quantity is

most sensitive to the low-energy region $Q^2 \simeq m_\mu^2$ of $\Pi_{\mu\nu}(-Q^2)$, where the long-range contribution of multibody states become relevant. The lattice calculation is challenging because of this and also because the necessary precision is high (below 1%). Many systematic effects must be carefully studied and controlled in order to achieve this precision, including finite volume errors and QED corrections.

Calculations of the light-by-light scattering contribution to a_μ are also underway. These involve the calculations of four-point correlation functions with various external momenta. Clever ways to sum over them to evaluate the contribution to a_μ are developed and first results have been reported [140–144]. Another approach to the light-by-light scattering is to decompose the amplitude to components using ChPT or phenomenological models, and to calculate the components in LQCD. Calculations of the $\pi \to \gamma^*\gamma^*$ amplitudes follow similar directions [145–147].

There are other processes for which lattice calculations can make a significant contribution to establishing a quantitative understanding. One example is the long-distance contribution to the neutral kaon mass splitting, ΔM_K. This also requires the evaluation of a four-point function, constructed from the two-point functions described above by the insertion of two electroweak Hamiltonians [148]. Rare kaon decays $K \to \pi\ell^+\ell^-$ and $K \to \pi\nu\bar{\nu}$ are also important processes for which first lattice studies have recently appeared [149–153].

17.2.6 *Status of LQCD simulations*

Until the 1990s, most large-scale lattice simulations were limited to the "quenched" approximation, wherein the fermion determinant is omitted from the path integral. While much of the basic methodology was developed in this era, the results obtained had uncontrolled systematic errors and were not suitable for use in placing precision constraints on the Standard Model. During the 1990s, more extensive simulations including the fermion determinant (also known as simulations with "dynamical" fermions) were begun, but with unphysically heavy quark masses ($m_\ell \sim 50 - 100$ MeV), such that the extrapolation to the physical light quark masses was a source of large systematic errors [154]. During the 2000s, advances in both algorithms and computers allowed simulations to reach much smaller quark masses ($m_\ell \sim 10 - 20$ MeV) such that LQCD calculations of selected quantities with all sources of error controlled and small became available. Their results played an important role in constraints on the CKM matrix and other phenomenological analyses. In the last few years, simulations directly at the physical isospin-symmetric light quark masses have become standard, removing the need for a chiral extrapolation and thus significantly reducing the overall error. The present frontier, as noted above, is the inclusion of isospin breaking. This will be needed to push the accuracy of calculations below the percent level.

On a more qualitative level, analytic and numerical results from LQCD have demonstrated that QCD confines color and spontaneously breaks chiral symmetry. Confinement can be seen as a linearly rising potential between heavy quark and anti-quark in the absence of quark loops. Analytically, this can be shown in the strong coupling limit $g_{\rm lat} \to \infty$ [1]. At weaker couplings there are precise numerical calculations of the potential that clearly show that this behavior persists in the continuum limit [155–157].

Chiral symmetry breaking was also demonstrated in the strong coupling limit on the lattice [19,158], and there have been a number of numerical studies showing that this holds also in the continuum limit. The accumulation of low-lying modes of the Dirac operator, which is the analog of Cooper pair condensation in superconductors, has been observed, yielding a determination of the chiral condensate [159–164]. Many relations among physical quantities that can be derived under the assumption of broken chiral symmetry have been confirmed by a number of lattice groups [165].

17.3 Physics applications

In this section we describe the main applications of LQCD that are both computationally mature and relevant for the determination of particle properties.

A general feature to keep in mind is that, since there are many different choices for lattice actions, all of which lead to the same continuum theory, a crucial test is that results for any given quantity are consistent. In many cases, different lattice calculations are completely independent and often have very different systematic errors. Thus final agreement, if found, is a highly non-trivial check, just as it is for different experimental measurements.

The number, variety and precision of the calculations has progressed to the point that an international "Flavour Lattice Averaging Group" (FLAG) has been formed. The main aims of FLAG include collecting all lattice results of relevance for a variety of phenomenologically interesting quantities and providing averages of those results which pass appropriate quality criteria. The averages attempt to account for possible correlations between results (which can arise, for example, if they use common gauge configurations). The quantities considered are those we discuss in this section, with the exception of the hadron spectrum. The most recent FLAG review is from 2019 [53] (see also an older edition, Ref. [165]). The interested reader can consult this review for very extensive discussions of the details of the calculations and of the sources of systematic errors.

We stress that the results we quote below are those obtained using the physical complement of light quarks (i.e. $N_f = 2+1$ or $2+1+1$ simulations).

17.3.1 *Spectrum*

The most basic prediction of LQCD is of the hadron spectrum. Once the input parameters are fixed as described in Sec. 17.1.5, the masses or resonance parameters of all other states can be predicted. This includes hadrons composed of light (u, d and s) quarks, as well as heavy-light and heavy-heavy hadrons. It also includes quark-model exotics (e.g. $J^{PC} = 1^{-+}$ mesons) and glueballs. Thus, in principle, LQCD calculations should be able to reproduce many of the experimental results compiled in the Review of Particle Properties. Doing so would test both that the error budgets of LQCD calculations are accurate and that QCD indeed describes the strong interactions in the low-energy domain. The importance of the latter test can hardly be overstated.

What is the status of this fundamental test? As discussed in Sec. 1.2, LQCD calculations are most straightforward for stable, low-lying hadrons. Calculations of the properties of resonances that can decay into only two particles are more challenging, though substantial progress has been made. First theoretical work on decays to more than two particles has begun, but the methodology is not yet practical. It is also more technically challenging to calculate masses of flavor singlet states (which can annihilate into purely gluonic intermediate states) than those of flavor non-singlets, although again algorithmic and computational advances have begun to make such calculations accessible, although not yet for physical quark masses. The present status for light hadrons is that fully controlled results are available for the masses of the octet light baryons, while results with less than complete control are available for the decuplet baryon resonances, the vector meson resonances and the η and η'. In addition, it has been possible to calculate the isospin splitting in light mesons and baryons (due to the up-down mass difference and the incorporation of QED). There are also extensive results for heavy-light (D and B systems) and heavy-heavy (J/ψ and Υ systems). All present results, which are discussed in the "Quark Model" review, are consistent with experimental values, and several predictions have been made. We refer the reader to that review for references to the relevant work.

17.3.2 *Decay constants and bag parameters*

The pseudoscalar decay constants can be determined from two-point correlation functions involving the axial-vector current, as discussed in Sec. 17.2.2. The decay constant f_P of a meson P is extracted from the weak matrix element involving the axial-vector current using the relation $\langle 0|A_\mu(x)|P(\vec{p})\rangle = f_P p_\mu \exp(-ip\cdot x)$, where p_μ is the momentum of P and $A_\mu(x)$ is the axial-vector current. Since they are among the simplest quantities to calculate, decay constants provide good benchmarks for lattice methods, in addition to being important inputs for flavor physics phenomenology in their own right. Results from many lattice groups for the pion and kaon decay constants now have errors at the percent level or better. The decay constants in the charm and bottom sectors,

f_D, f_{D_s}, f_B, and f_{B_s}, have also been calculated to high precision. Lattice results for all of these decay constants are discussed in detail in the review "Leptonic Decays of Charged Pseudoscalar Mesons."

Another important lattice quantity is the kaon bag parameter, B_K, which is needed to turn the precise measurement of CP-violation in kaon mixing into a constraint on the Standard Model. It is defined by

$$\frac{8}{3}m_K^2 f_K^2 B_K(\mu) = \langle \overline{K}^0 | Q_{\Delta S=2}(\mu) | K^0 \rangle, \quad (17.13)$$

where m_K is the kaon mass, f_K is the kaon decay constant, $Q_{\Delta S=2} = \bar{s}\gamma_\mu(1-\gamma_5)d\bar{s}\gamma_\mu(1-\gamma_5)d$ is the four-quark operator of the effective electroweak Hamiltonian and μ is the renormalization scale. The short distance contribution to the electroweak Hamiltonian can be calculated perturbatively, but the hadronic matrix element parameterized by B_K must be computed using non-perturbative methods. In order to be of use to phenomenology, the renormalization factor of the four-quark operator must be matched to a continuum renormalization scheme, e.g. to $\overline{\rm MS}$, as described in Sec. 17.1.6.4. Determinations with percent-level precision using different fermion actions and $N_f = 2+1$ light sea quarks are now available using DWF [166] , staggered fermions [167], DWF valence on staggered sea quarks [168], and Wilson fermions [13]. The results are all consistent, and the present FLAG average is $\hat{B}_K = 0.7625(97)$ [53].

The bag parameters for B and B_s meson mixing are defined analogously to that for kaon mixing. The B and B_s mesons contain a valence b-quark so that calculations of these quantities must use one of the methods for heavy quarks described above. Calculations with $N_f = 2+1$ light fermions have been done using NRQCD [169], the Fermilab formalism [68], and static heavy quarks [170]. All results are consistent. The FLAG averages for the quantities relevant for B_s and B mixing are $f_{B_s}\sqrt{B_{B_s}} = 274(8)$ MeV and $f_B\sqrt{B_B} = 225(9)$ MeV, with their ratio (which is somewhat better determined) being $\xi = 1.206(17)$ [53]. Note that the errors for quantities involving b quarks are larger than those for quantities involving only light quarks, although the difference has decreased over the last two years.

For the K, D and B systems, one can also consider the matrix elements of four-fermion operators that arise in beyond-the-standard-model (BSM) theories, which can have a different chiral structure. Knowledge of these matrix elements allows one to constrain the parameters of the BSM theories, and is complementary to direct searches at the LHC. Reliable results are now available from lattice calculations, and are reviewed by FLAG in the case of kaon mixing [53]. Complete results for D and B mixing are presented in Ref. [171] and Ref. [68], respectively.

The results for mixing matrix elements are used in the reviews "The CKM Quark-Mixing Matrix," and "$B^0 - \bar{B}^0$ Mixing."

17.3.3 *Form factors ($K \to \pi\ell\nu$, $D \to K\ell\nu$, $B \to \pi\ell\nu$, $B \to D^{(*)}\ell\nu$)*

Semileptonic decay rates can be used to extract CKM matrix elements once the semileptonic form factors are known from lattice calculations. For example, the matrix element of a pseudoscalar meson P undergoing semileptonic decay to another pseudoscalar meson D is mediated by the vector current, and can be written in terms of form factors as

$$\langle D(p_D)|V_\mu|P(p_P)\rangle = f_+(q^2)(p_D+p_P-\Delta)_\mu + f_0(q^2)\Delta_\mu\,, \quad (17.14)$$

where $q = p_D - p_P$, $\Delta_\mu = (m_D^2 - m_P^2)q_\mu/q^2$ and V_μ is the quark vector current. The shape of the form factor is typically well determined by experiment, and the value of $f_+(q^2)$ at some reference value of q^2 is needed from the lattice in order to extract CKM matrix elements. Typically $f_+(q^2)$ dominates the decay rate, since the contribution from $f_0(q^2)$ is suppressed when the final state lepton is light.

The form factor $f_+(0)$ for $K \to \pi\ell\nu$ decays is highly constrained by the Ademollo-Gatto theorem [172] and chiral symmetry. Old estimates using chiral perturbation theory combined with quark models quote sub-percent precision [173], though they suffer from some model dependence. Utilizing the constraint from the vector current conservation that $f_+(0)$ is normalized to unity in the limit of degenerate up and strange quark masses, the lattice calculation can be made very precise and has now matched the precision of the phenomenological estimates [174–181]. The present FLAG average (from $N_f = 2+1$ simulations) is $f_+(0) = 0.9677(27)$ [53].

Charm meson semileptonic decays have been calculated by different groups using methods similar to those used for charm decay constants, and results are steadily improving in precision [182–185]. For semileptonic decays involving a bottom quark, one uses HQET or NRQCD to control the discretization errors of the bottom quark. The form factors for the semileptonic decay $B \to \pi\ell\nu$ have been calculated in unquenched lattice QCD by a number of groups [186–191]. These B semileptonic form factors are difficult to calculate at low q^2, *i.e.* when the mass of the B-meson must be balanced by a large pion momentum, in order to transfer a large momentum to the lepton pair. The low q^2 region has large discretization errors and very large statistical errors, while the high q^2 region is much more accessible to the lattice. For experiment, the opposite is true. To combine lattice and experimental results it has proved helpful to use the z-parameter expansion [192]. This provides a theoretically constrained parameterization of the entire q^2 range, and allows one to obtain $|V_{ub}|$ without model dependence [193, 194].

The semileptonic decays $B \to D\ell\nu$ and $B \to D^*\ell\nu$ can be used to extract $|V_{cb}|$ once the corresponding form factors are known. The lattice calculation is most precise at zero recoil since the bulk of the systematic error cancels for appropriate ratios between $B \to D^{(*)}$ and $B \to B$ or $D^{(*)} \to D^{(*)}$ [195, 196]. The unquenched calculation of the $B \to D^{(*)}\ell\nu$ form factor at zero recoil has been performed with various formulations for the heavy quark [197–201]. Calculations at non-zero recoil have also been performed to constrain the functional form of the form factor, which can be used to extrapolate the experimental data to the zero-recoil point or to determine $|V_{cb}|$ directly at the non-zero recoil points [202–205]. Semileptonic decays of the Λ_b baryon can also be used to constrain $|V_{cb}|$ and $|V_{ub}|$ using lattice calculations of the relevant form factors [206, 207].

The rare decays $B \to K^{(*)}\ell^+\ell^-$ involve matrix elements similar to those needed for semileptonic decays, Eq. (17.14), except that the vector current V_μ is replaced by the operators $\bar{s}\gamma^\mu(1-\gamma_5)b$ or $\bar{s}\sigma^{\mu\nu}(1+\gamma_5)b$. Lattice calculations of the corresponding form factors involve similar techniques to those for the semileptonic form factors. The values of q^2 for which lattice calculations can be done are limited as for B semileptonic decays, and, in addition, the region of $c\bar{c}$ resonances has to be avoided. Recent lattice calculations [190, 208–210] have been used to constrain the standard model and new physics contributions.

The results discussed in this section are used in the reviews "The CKM Quark-Mixing Matrix," "V_{ud}, V_{us}, the Cabibbo Angle and CKM Unitarity," and "V_{cb} and V_{ub} CKM Matrix Elements."

17.3.4 *Strong coupling constant*

As explained in Sec. 17.1.5.1, for a given lattice action, the choice of bare lattice coupling constant, $g_{\rm lat}$, determines the lattice spacing a. If one then calculates a as described in Sec. 17.1.5.1, one knows the strong coupling constant in the bare lattice scheme at the scale $1/a$, $\alpha_{\rm lat} = g_{\rm lat}^2/(4\pi)$. This is not, however, useful for comparing to results for α_s obtained from other inputs, such as deep inelastic scattering or jet shape variables. This is because the latter results give α_s in the $\overline{\rm MS}$ scheme, which is commonly used in such analyses, and the conversion factor between these two schemes is known to converge extremely poorly in perturbation theory. Instead one must use a method which directly determines α_s on the lattice in a scheme closer to $\overline{\rm MS}$.

Several such methods have been used, all following a similar strategy. One calculates a short-distance quantity K both perturbatively ($K^{\rm PT}$) and non-perturbatively ($K^{\rm NP}$) on the lattice, and requires equality: $K^{\rm NP} = K^{\rm PT} = \sum_{i=0}^{n} c_i \alpha_s^i$. Solving this equation one obtains α_s at a scale related to the quantity being used. Often, α_s thus obtained is not defined in the conventional $\overline{\rm MS}$ scheme, and one has to convert among the different schemes using perturbation theory. Unlike for the bare lattice scheme, the required conversion factors are reasonably convergent. As a fi-

nal step, one uses the renormalization group to run the resulting coupling to a canonical scale (such as M_Z).

In the work of the HPQCD collaboration [211, 212], the short-distance quantities are Wilson loops of several sizes and their ratios. These quantities are perturbatively calculated through $\mathcal{O}(\alpha_s^3)$ using the V-scheme defined through the heavy quark potential. The coefficients of even higher orders are estimated using the data at various values of a. In addition, this work obtains a result for α_s by matching with $\alpha_{\rm lat}$ in a tadpole-improved scheme that improves convergence.

Another choice of short-distance quantities is to use current-current correlators. Appropriate moments of these correlators are ultraviolet finite, and by matching lattice results to the *continuum* perturbative predictions, one can directly extract the $\overline{\rm MS}$ coupling. The method can be applied for light meson correlators [213,214] as well as heavy meson correlators [36,212,215–217]. Yet another choice of short-distance quantity is the static-quark potential, where the lattice result for the potential is compared to perturbative calculations; this method was used to compute α_s within 2+1 flavor QCD [218–222]. There is also a determination of α_s from a comparison of lattice data for the ghost-gluon coupling with that of perturbation theory [223, 224].

With a definition of α_s given using the Schrödinger functional, one can non-perturbatively control the evolution of α_s to high-energy scales, such as 100 GeV, where the perturbative expansion converges very well. This method developed by the ALPHA collaboration [81] has been applied to 2+1-flavor QCD in [225–227].

The various lattice methods for calculating α_s have significantly different sources of systematic error. The FLAG review [53] reported an estimate $\alpha_{\overline{\rm MS}}^{(5)}(M_Z) = 0.11823(81)$ based on these various lattice calculations. A comparison to other phenomenological determinations can be found in the "Quantum Chromodynamics" review.

17.3.5 *Quark masses*

Once the quark mass parameters are tuned in the lattice action, the remaining task is to convert them to those of the conventional definition. Since the quarks do not appear as asymptotic states due to confinement, the pole mass of the quark propagator is not a physical quantity. Instead, one defines the quark mass after subtracting the ultra-violet divergences in some particular way. The conventional choice is again the $\overline{\rm MS}$ scheme at a canonical scale such as 2 or 3 GeV. Ratios such as m_c/m_s and m_b/m_c are also useful as they are free from multiplicative renormalization (in a mass-independent scheme).

As discussed in Sec. 17.1.6.4, one must convert the lattice bare quark mass to that in the $\overline{\rm MS}$ scheme. Older calculations did so directly using perturbation theory; most recent calculations use an intermediate NPR method (e.g. RI/MOM or RI/SMOM) which is then converted to the $\overline{\rm MS}$ scheme using perturbation theory (see, e.g., [166, 228, 229]).

Alternatively, one can use a definition based on the Schrödinger functional, which allows one to evolve the quark mass to a high scale non-perturbatively [230]. In practice, one can reach scales as high as ∼100 GeV, at which matching to the $\overline{\rm MS}$ scheme can be reliably calculated in perturbation theory.

Another approach available for heavy quarks is to match current-current correlators at short distances calculated on the lattice to those obtained in continuum perturbation theory in the $\overline{\rm MS}$ scheme [36, 212, 215–217]. This has allowed an accurate determination of m_c and m_b [80, 212, 216].

The ratio method for heavy quarks (discussed earlier) can also be used to determine m_b [231].

Results are summarized in the review of "Quark Masses."

17.3.6 *Other applications*

In this review we have concentrated on applications of LQCD that are relevant to the quantities discussed in the Review of Particle Properties. We have not discussed at all several other applications that are being actively pursued by simulations. Here we list the major such applications. The reader can consult the aforementioned texts [2–4] for further details, as well as the proceedings of recent lattice conferences [232], and several recent white papers [233–239].

LQCD can be used, in principle, to simulate QCD at non-zero temperature and density, and in particular to study how confinement and chiral-symmetry breaking are lost as T and μ (the chemical potential) are increased. This is of relevance to heavy-ion collisions, the early Universe and neutron-star structure. In practice, finite temperature simulations are computationally tractable and relatively mature, while simulations at finite μ suffer from a "sign problem" and are at a rudimentary stage.

Another topic under active investigation is nucleon structure and inter-nucleon interactions. The simplest nucleon matrix elements are calculable with a precision that is now starting to rival that for some mesonic quantities. Of particular interest are those of the axial current (leading to g_A) and of the scalar density (with $\langle N|\bar{s}s|N\rangle$ needed for dark matter searches). Other such matrix elements provide information on the parton distribution functions (PDFs) including their low moments. More recently, methods to directly access PDFs are being developed (see, e.g., Ref. [233] for a recent summary).

Finally, we note that there is much recent interest in studying QCD-like theories with more fermions, possibly in other representations of the gauge group (see, e.g., [235]). The main interest is to find nearly conformal theories which might be candidates for "walking technicolor" models.

17.4 Outlook

While LQCD calculations have made major strides in the last decade, and are now playing an important role in constraining the Standard Model, there are many calculations that could be done in principle but are not yet mature due to limitations in computational resources. As we move to exascale resources (10^{18} floating point operations per second), the list of mature calculations will grow. Examples that we expect to mature in the next few years are results for B meson and Λ_b baryon form factors covering the full range of q^2; results for excited hadrons, including quark-model exotics, at close to physical light-quark masses; results for moments of structure functions; results for the simplest nucleon matrix elements; $K \to \pi\pi$ amplitudes (allowing a prediction of ϵ'/ϵ from the Standard Model); hadronic vacuum polarization contributions to $g_\mu - 2$, the running of $\alpha_{\rm EM}$ and α_s; $\pi \to \gamma\gamma$ and related amplitudes; long-distance contributions to $\overline{K} \leftrightarrow K$ mixing; the light-by-light contribution to $g_\mu - 2$; and determinations of long distance contributions to rare kaon decays such as $K \to \pi\nu\bar{\nu}$. There will also be steady improvement in the precision attained for the mature quantities discussed above. As already noted, this will ultimately require simulations with $m_u \neq m_d$ and including electromagnetic effects.

References

[1] K. G. Wilson, Phys. Rev. **D10**, 2445 (1974).

[2] T. Degrand & C. DeTar, "Lattice Methods for Quantum Chromodynamics," World Scientific (2006).

[3] C. Gattringer & C.B. Lang, "Quantum Chromodynamics on the Lattice: An Introductory Presentation," Springer (2009).

[4] "Modern Pespectives in Lattice QCD: quantum field theory and high performance computing" (Lecture notes of the Les Houches Summer School, Vol. 93) eds. L. Lellouch *et al.*, Oxford Univ. Press. (Aug. 2011).

[5] W. Zimmermann, in "Lectures on Elementary Particles and Quantum Field Theory", ed. S. Deser et al., MIT Press, Cambridge, MA (1971); K. Symanzik, Nucl. Phys. **B226**, 187 (1983); K. Symanzik, Nucl. Phys. **B226**, 205 (1983).

[6] M. Luscher and P. Weisz, Commun. Math. Phys. **97**, 59 (1985), [Erratum: Commun. Math. Phys.98,433(1985)].

[7] Y. Iwasaki, UT-HEP-118.

[8] H. B. Nielsen and M. Ninomiya, Phys. Lett. **105B**, 219 (1981).

[9] B. Sheikholeslami and R. Wohlert, Nucl. Phys. **B259**, 572 (1985).

[10] K. Jansen *et al.*, Phys. Lett. **B372**, 275 (1996), [hep-lat/9512009].

[11] M. Luscher, JHEP **05**, 052 (2003), [hep-lat/0304007].

[12] M. Luscher, Comput. Phys. Commun. **156**, 209 (2004), [hep-lat/0310048]; M. Luscher, Comput. Phys. Commun. **165**, 199 (2005), [hep-lat/0409106]; M. Hasenbusch, Phys. Lett. **B519**, 177 (2001), [hep-lat/0107019]; C. Urbach *et al.*, Comput. Phys. Commun. **174**, 87 (2006), [hep-lat/0506011].

[13] S. Durr *et al.*, Phys. Lett. **B705**, 477 (2011), [arXiv:1106.3230].

[14] N. Ishizuka *et al.*, Phys. Rev. **D92**, 7, 074503 (2015), [arXiv:1505.05289].

[15] R. Frezzotti *et al.* (Alpha), JHEP **08**, 058 (2001), [hep-lat/0101001].

[16] R. Frezzotti and G. C. Rossi, JHEP **08**, 007 (2004), [hep-lat/0306014].

[17] R. Frezzotti and G. C. Rossi, Nucl. Phys. Proc. Suppl. **128**, 193 (2004), [hep-lat/0311008].

[18] R. Frezzotti and G. C. Rossi, JHEP **10**, 070 (2004), [hep-lat/0407002].

[19] L. Susskind, Phys. Rev. **D16**, 3031 (1977).

[20] M. Golterman, PoS **CONFINEMENT8**, 014 (2008).

[21] C. Bernard, Phys. Rev. **D73**, 114503 (2006), [hep-lat/0603011]; S. R. Sharpe, PoS **LAT2006**, 022 (2006), [hep-lat/0610094].

[22] G. P. Lepage, Phys. Rev. **D59**, 074502 (1999), [hep-lat/9809157].

[23] A. Bazavov *et al.* (MILC), Rev. Mod. Phys. **82**, 1349 (2010), [arXiv:0903.3598].

[24] E. Follana *et al.* (HPQCD, UKQCD), Phys. Rev. **D75**, 054502 (2007), [hep-lat/0610092].

[25] C. T. H. Davies *et al.*, Phys. Rev. **D82**, 114504 (2010), [arXiv:1008.4018].

[26] G. C. Donald *et al.*, Phys. Rev. **D86**, 094501 (2012), [arXiv:1208.2855].

[27] P. H. Ginsparg and K. G. Wilson, Phys. Rev. **D25**, 2649 (1982).

[28] P. Hasenfratz, V. Laliena and F. Niedermayer, Phys. Lett. **B427**, 125 (1998), [hep-lat/9801021].

[29] M. Luscher, Phys. Lett. **B428**, 342 (1998), [hep-lat/9802011].

[30] D. B. Kaplan, Phys. Lett. **B288**, 342 (1992), [hep-lat/9206013]; Y. Shamir, Nucl. Phys. **B406**, 90 (1993), [hep-lat/9303005]; Y. Shamir, Nucl. Phys. **B417**, 167 (1994), [hep-lat/9310006].

[31] H. Neuberger, Phys. Lett. **B417**, 141 (1998), [hep-lat/9707022]; H. Neuberger, Phys. Lett. **B427**, 353 (1998), [hep-lat/9801031].

[32] A. Borici, NATO Sci. Ser. C **553**, 41 (2000), [hep-lat/9912040].

[33] A. D. Kennedy (2006), [hep-lat/0607038].

[34] E. Shintani *et al.* (JLQCD), Phys. Rev. Lett. **101**, 242001 (2008), [arXiv:0806.4222].

[35] P. A. Boyle *et al.*, JHEP **12**, 008 (2017), [arXiv:1701.02644].

[36] K. Nakayama, B. Fahy and S. Hashimoto, Phys. Rev. **D94**, 5, 054507 (2016), [arXiv:1606.01002].

[37] C. McNeile *et al.*, Phys. Rev. **D85**, 031503 (2012), [arXiv:1110.4510].

[38] A. Bazavov *et al.*, Phys. Rev. **D98**, 7, 074512 (2018), [arXiv:1712.09262].

[39] A. Bazavov *et al.* (Fermilab Lattice, MILC, TUMQCD), Phys. Rev. **D98**, 5, 054517 (2018), [arXiv:1802.04248].

[40] E. Eichten and B. R. Hill, Phys. Lett. **B234**, 511 (1990).

[41] J. Heitger and R. Sommer (ALPHA), JHEP **02**, 022 (2004), [hep-lat/0310035]; B. Blossier *et al.* (ALPHA), JHEP **12**, 039 (2010), [arXiv:1006.5816].

[42] B. A. Thacker and G. P. Lepage, Phys. Rev. **D43**, 196 (1991); G. P. Lepage *et al.*, Phys. Rev. **D46**, 4052 (1992), [hep-lat/9205007].

[43] R. J. Dowdall *et al.* (HPQCD), Phys. Rev. **D85**, 054509 (2012), [arXiv:1110.6887].

[44] A. X. El-Khadra, A. S. Kronfeld and P. B. Mackenzie, Phys. Rev. **D55**, 3933 (1997), [hep-lat/9604004].

[45] S. Aoki, Y. Kuramashi and S.-i. Tominaga, Prog. Theor. Phys. **109**, 383 (2003), [hep-lat/0107009].

[46] N. H. Christ, M. Li and H.-W. Lin, Phys. Rev. **D76**, 074505 (2007), [hep-lat/0608006].

[47] Y. Aoki *et al.* (RBC, UKQCD), Phys. Rev. **D86**, 116003 (2012), [arXiv:1206.2554].

[48] N. H. Christ *et al.*, Phys. Rev. **D91**, 5, 054502 (2015), [arXiv:1404.4670].

[49] M. B. Oktay and A. S. Kronfeld, Phys. Rev. **D78**, 014504 (2008), [arXiv:0803.0523].

[50] J. A. Bailey *et al.*, Eur. Phys. J. **C77**, 11, 768 (2017), [arXiv:1701.00345].

[51] B. Blossier *et al.* (ETM), JHEP **04**, 049 (2010), [arXiv:0909.3187].

[52] S. Borsanyi *et al.*, Science **347**, 1452 (2015), [arXiv:1406.4088].

[53] S. Aoki *et al.* (Flavour Lattice Averaging Group) (2019), [arXiv:1902.08191].

[54] R. Horsley *et al.*, J. Phys. G **43**, no. 10, 10LT02 (2016).

[55] S. Aoki *et al.* [PACS-CS Collab.], PTEP **2012**, 01A102 (2012).

[56] T. Ishikawa *et al.*, Phys. Rev. Lett. **109**, 072002 (2012), [arXiv:1202.6018].

[57] G. M. de Divitiis *et al.* (RM123), Phys. Rev. **D87**, 11, 114505 (2013), [arXiv:1303.4896].

[58] P. Boyle *et al.*, JHEP **09**, 153 (2017), [arXiv:1706.05293].

[59] F. Bloch and A. Nordsieck, Phys. Rev. **52**, 54 (1937).

[60] N. Carrasco *et al.*, Phys. Rev. **D91**, 7, 074506 (2015), [arXiv:1502.00257].

[61] D. Giusti *et al.*, Phys. Rev. Lett. **120**, 7, 072001 (2018), [arXiv:1711.06537].

[62] M. Di Carlo *et al.* (2019), [arXiv:1904.08731].

[63] M. Bruno *et al.* (ALPHA), Phys. Rev. Lett. **114**, 10, 102001 (2015), [arXiv:1410.8374].

[64] F. Knechtli *et al.* (ALPHA), Phys. Lett. **B774**, 649 (2017), [arXiv:1706.04982].

[65] A. Athenodorou *et al.* (ALPHA), Nucl. Phys. **B943**, 114612 (2019), [arXiv:1809.03383].

[66] S. Cali, F. Knechtli and T. Korzec, Eur. Phys. J. **C79**, 7, 607 (2019), [arXiv:1905.12971].

[67] D. Giusti *et al.*, Phys. Rev. **D95**, 11, 114504 (2017), [arXiv:1704.06561].

[68] A. Bazavov *et al.* (Fermilab Lattice, MILC), Phys. Rev. **D93**, 11, 113016 (2016), [arXiv:1602.03560].

[69] R. J. Dowdall *et al.*, Phys. Rev. **D86**, 094510 (2012), [arXiv:1207.5149].

[70] C. McNeile *et al.*, Phys. Rev. **D86**, 074503 (2012), [arXiv:1207.0994].

[71] S. Schaefer, R. Sommer and F. Virotta (ALPHA), Nucl. Phys. **B845**, 93 (2011), [arXiv:1009.5228].

[72] M. Luscher, PoS **LATTICE2010**, 015 (2010), [arXiv:1009.5877].

[73] R. Brower *et al.*, Phys. Lett. **B560**, 64 (2003), [hep-lat/0302005].

[74] S. Aoki *et al.*, Phys. Rev. **D76**, 054508 (2007), [arXiv:0707.0396].

[75] G. Colangelo, S. Durr and C. Haefeli, Nucl. Phys. **B721**, 136 (2005), [hep-lat/0503014].

[76] M. Luscher, Commun. Math. Phys. **104**, 177 (1986).

[77] G. Martinelli *et al.*, Nucl. Phys. **B445**, 81 (1995), [hep-lat/9411010].

[78] M. Luscher *et al.*, Nucl. Phys. **B384**, 168 (1992), [hep-lat/9207009].

[79] G. Martinelli *et al.*, Phys. Lett. **B411**, 141 (1997), [hep-lat/9705018].

[80] B. Colquhoun *et al.*, Phys. Rev. **D91**, 7, 074514 (2015), [arXiv:1408.5768].

[81] M. Luscher *et al.*, Nucl. Phys. **B413**, 481 (1994), [hep-lat/9309005]; M. Della Morte *et al.* (ALPHA), Nucl. Phys. **B713**, 378 (2005), [hep-lat/0411025].

[82] M. Tomii *et al.* (JLQCD), Phys. Rev. **D94**, 5, 054504 (2016), [arXiv:1604.08702].

[83] S. Duane *et al.*, Phys. Lett. **B195**, 216 (1987).

[84] M. A. Clark and A. D. Kennedy, Phys. Rev. Lett. **98**, 051601 (2007), [hep-lat/0608015].

[85] M. Luscher, JHEP **07**, 081 (2007), [arXiv:0706.2298].

[86] M. Luscher, JHEP **12**, 011 (2007), [arXiv:0710.5417].

[87] A. Stathopoulos and K. Orginos, SIAM J. Sci. Comput. **32**, 439 (2010), [arXiv:0707.0131].

[88] P. A. Boyle (2014), [arXiv:1402.2585].

[89] R. Babich *et al.*, Phys. Rev. Lett. **105**, 201602 (2010), [arXiv:1005.3043].

[90] A. Frommer *et al.*, SIAM J. Sci. Comput. **36**, A1581 (2014), [arXiv:1303.1377].

[91] M. Bruno, S. Schaefer and R. Sommer (ALPHA), JHEP **08**, 150 (2014), [arXiv:1406.5363].

[92] M. Creutz, Phys. Rev. **D38**, 1228 (1988); R. Gupta, G. W. Kilcup and S. R. Sharpe, Phys. Rev. **D38**, 1278 (1988).

[93] J. E. Mandula, G. Zweig and J. Govaerts, Nucl. Phys. **B228**, 91 (1983); J. E. Mandula and E. Shpiz, Nucl. Phys. **B232**, 180 (1984).

[94] H. B. Meyer and M. J. Teper, Nucl. Phys. **B658**, 113 (2003), [hep-lat/0212026].

[95] J. J. Dudek *et al.*, Phys. Rev. **D82**, 034508 (2010), [arXiv:1004.4930]; J. J. Dudek *et al.*, Phys. Rev. **D83**, 111502 (2011), [arXiv:1102.4299]; R. G. Edwards *et al.*, Phys. Rev. **D84**, 074508 (2011), [arXiv:1104.5152].

[96] M. Luscher and U. Wolff, Nucl. Phys. **B339**, 222 (1990).

[97] G. P. Engel *et al.* (BGR [Bern-Graz-Regensburg]), Phys. Rev. **D82**, 034505 (2010), [arXiv:1005.1748]; D. Mohler *et al.*, Phys. Rev. Lett. **111**, 22, 222001 (2013), [arXiv:1308.3175].

[98] M. S. Mahbub *et al.*, Annals Phys. **342**, 270 (2014), [arXiv:1310.6803].

[99] J. Bulava *et al.*, Nucl. Phys. **B910**, 842 (2016), [arXiv:1604.05593].

[100] R. Brett *et al.*, Nucl. Phys. **B932**, 29 (2018), [arXiv:1802.03100].

[101] M. Luscher, Commun. Math. Phys. **105**, 153 (1986); M. Luscher, Nucl. Phys. **B364**, 237 (1991).

[102] L. Maiani and M. Testa, Phys. Lett. **B245**, 585 (1990).

[103] M. T. Hansen, H. B. Meyer and D. Robaina, Phys. Rev. **D96**, 9, 094513 (2017), [arXiv:1704.08993].

[104] M. Hansen, A. Lupo and N. Tantalo, Phys. Rev. **D99**, 9, 094508 (2019), [arXiv:1903.06476].

[105] J. Bulava and M. T. Hansen (2019), [arXiv:1903.11735].

[106] R. A. Briceno, J. J. Dudek and R. D. Young, Rev. Mod. Phys. **90**, 2, 025001 (2018), [arXiv:1706.06223].

[107] N. Brambilla *et al.* (2019), [arXiv:1907.07583].

[108] M. J. Savage, Prog. Part. Nucl. Phys. **67**, 140 (2012), [arXiv:1110.5943]; T. Inoue *et al.* (HAL QCD), Phys. Rev. **C91**, 1, 011001 (2015), [arXiv:1408.4892].

[109] K. Polejaeva and A. Rusetsky, Eur. Phys. J. **A48**, 67 (2012), [arXiv:1203.1241]; R. A. Briceno and Z. Davoudi, Phys. Rev. **D87**, 9, 094507 (2013), [arXiv:1212.3398]; M. T. Hansen and S. R. Sharpe, Phys. Rev. **D90**, 11, 116003 (2014), [arXiv:1408.5933]; M. T. Hansen and S. R. Sharpe, Phys. Rev. **D92**, 11, 114509 (2015), [arXiv:1504.04248]; R. A. Briceño, M. T. Hansen and S. R. Sharpe, Phys. Rev. **D95**, 7, 074510 (2017), [arXiv:1701.07465]; H. W. Hammer, J. Y. Pang and A. Rusetsky, JHEP **10**, 115 (2017), [arXiv:1707.02176].

[110] R. A. Briceno, M. T. Hansen and S. R. Sharpe, Phys. Rev. **D99**, 1, 014516 (2019), [arXiv:1810.01429].

[111] M. Mai and M. Döring, Eur. Phys. J. **A53**, 12, 240 (2017), [arXiv:1709.08222].

[112] M. T. Hansen and S. R. Sharpe (2019), [arXiv:1901.00483].

[113] L. Lellouch and M. Luscher, Commun. Math. Phys. **219**, 31 (2001), [hep-lat/0003023].

[114] T. Blum *et al.*, Phys. Rev. Lett. **108**, 141601 (2012), [arXiv:1111.1699]; T. Blum *et al.*, Phys. Rev. **D86**, 074513 (2012), [arXiv:1206.5142].

[115] Z. Bai *et al.* (RBC, UKQCD), Phys. Rev. Lett. **115**, 21, 212001 (2015), [arXiv:1505.07863].

[116] T. Blum *et al.*, Phys. Rev. **D91**, 7, 074502 (2015), [arXiv:1502.00263].

[117] V. Bernard *et al.*, JHEP **01**, 019 (2011), [arXiv:1010.6018]; M. Doring *et al.*, Eur. Phys. J. **A47**, 139 (2011), [arXiv:1107.3988]; M. T. Hansen and S. R. Sharpe, Phys. Rev. **D86**, 016007 (2012), [arXiv:1204.0826]; R. A. Briceno and Z. Davoudi, Phys. Rev. **D88**, 9, 094507 (2013), [arXiv:1204.1110].

[118] R. A. Briceño, M. T. Hansen and A. Walker-Loud, Phys. Rev. **D91**, 3, 034501 (2015), [arXiv:1406.5965].

[119] R. A. Briceño and M. T. Hansen, Phys. Rev. **D94**, 1, 013008 (2016), [arXiv:1509.08507].

[120] R. A. Briceño *et al.*, Phys. Rev. **D93**, 11, 114508 (2016), [arXiv:1604.03530].

[121] D. Agadjanov *et al.*, JHEP **06**, 043 (2016), [arXiv:1603.07205].

[122] S. Hashimoto, PTEP **2017**, 5, 053B03 (2017), [arXiv:1703.01881].

[123] X. Feng *et al.*, Phys. Rev. Lett. **107**, 081802 (2011), [arXiv:1103.4818].

[124] P. Boyle *et al.*, Phys. Rev. **D85**, 074504 (2012), [arXiv:1107.1497].

[125] M. Della Morte *et al.*, JHEP **03**, 055 (2012), [arXiv:1112.2894].

[126] F. Burger *et al.* (ETM), JHEP **02**, 099 (2014), [arXiv:1308.4327].

[127] B. Chakraborty *et al.* (HPQCD), Phys. Rev. **D89**, 11, 114501 (2014), [arXiv:1403.1778].

[128] F. Burger, K. Jansen, M. Petschlies and G. Pientka, Eur. Phys. J. **C76**, 464 (2016).

[129] B. Chakraborty *et al.*, Phys. Rev. **D93**, 7, 074509 (2016), [arXiv:1512.03270].

[130] B. Chakraborty *et al.*, Phys. Rev. **D96**, 3, 034516 (2017), [arXiv:1601.03071].

[131] T. Blum *et al.* (RBC/UKQCD), JHEP **04**, 063 (2016), [Erratum: JHEP05,034(2017)], [arXiv:1602.01767].

[132] S. Borsanyi *et al.*, Phys. Rev. **D96**, 7, 074507 (2017), [arXiv:1612.02364].

[133] M. Della Morte *et al.*, JHEP **10**, 020 (2017), [arXiv:1705.01775].

[134] S. Borsanyi *et al.* (Budapest-Marseille-Wuppertal), Phys. Rev. Lett. **121**, 2, 022002 (2018), [arXiv:1711.04980].

[135] T. Blum *et al.* (RBC, UKQCD), Phys. Rev. Lett. **121**, 2, 022003 (2018), [arXiv:1801.07224].

[136] B. Chakraborty *et al.*, Phys. Rev. **D98**, 9, 094503 (2018), [arXiv:1806.08190].

[137] D. Giusti, F. Sanfilippo and S. Simula, Phys. Rev. **D98**, 11, 114504 (2018), [arXiv:1808.00887].

[138] C. T. H. Davies *et al.* (Fermilab Lattice, LATTICE-HPQCD, MILC) (2019), [arXiv:1902.04223].

[139] T. Blum, Phys. Rev. Lett. **91**, 052001 (2003), [hep-lat/0212018].

[140] T. Blum *et al.*, Phys. Rev. Lett. **114**, 1, 012001 (2015), [arXiv:1407.2923].

[141] T. Blum *et al.*, Phys. Rev. **D93**, 1, 014503 (2016), [arXiv:1510.07100].

[142] J. Green *et al.*, Phys. Rev. Lett. **115**, 22, 222003 (2015), [arXiv:1507.01577].

[143] T. Blum *et al.*, Phys. Rev. Lett. **118**, 2, 022005 (2017), [arXiv:1610.04603].

[144] T. Blum *et al.*, Phys. Rev. **D96**, 3, 034515 (2017), [arXiv:1705.01067].

[145] X. Feng *et al.*, Phys. Rev. Lett. **109**, 182001 (2012), [arXiv:1206.1375].

[146] A. Gérardin, H. B. Meyer and A. Nyffeler, Phys. Rev. **D94**, 7, 074507 (2016), [arXiv:1607.08174].

[147] A. Gérardin *et al.*, Phys. Rev. **D98**, 7, 074501 (2018), [arXiv:1712.00421].

[148] Z. Bai *et al.*, Phys. Rev. Lett. **113**, 112003 (2014), [arXiv:1406.0916].

[149] N. H. Christ *et al.* (RBC, UKQCD), Phys. Rev. **D92**, 9, 094512 (2015), [arXiv:1507.03094].

[150] N. H. Christ *et al.* (RBC, UKQCD), Phys. Rev. **D93**, 11, 114517 (2016), [arXiv:1605.04442].

[151] N. H. Christ *et al.*, Phys. Rev. **D94**, 11, 114516 (2016), [arXiv:1608.07585].

[152] Z. Bai *et al.*, Phys. Rev. Lett. **118**, 25, 252001 (2017), [arXiv:1701.02858].

[153] Z. Bai *et al.*, Phys. Rev. **D98**, 7, 074509 (2018), [arXiv:1806.11520].

[154] C. Bernard *et al.*, Nucl. Phys. Proc. Suppl. **119**, 170 (2003), [hep-lat/0209086].

[155] S. Perantonis and C. Michael, Nucl. Phys. **B347**, 854 (1990).

[156] G. S. Bali and K. Schilling, Phys. Rev. **D46**, 2636 (1992).

[157] S. Necco and R. Sommer, Nucl. Phys. **B622**, 328 (2002), [hep-lat/0108008].

[158] J. M. Blairon *et al.*, Nucl. Phys. **B180**, 439 (1981).

[159] H. Fukaya *et al.* (JLQCD), Phys. Rev. Lett. **104**, 122002 (2010), [Erratum: Phys. Rev. Lett.105,159901(2010)], [arXiv:0911.5555].

[160] H. Fukaya *et al.* (JLQCD, TWQCD), Phys. Rev. **D83**, 074501 (2011), [arXiv:1012.4052].

[161] L. Giusti and M. Luscher, JHEP **03**, 013 (2009), [arXiv:0812.3638].

[162] K. Cichy, E. Garcia-Ramos and K. Jansen, JHEP **10**, 175 (2013), [arXiv:1303.1954].

[163] G. P. Engel *et al.*, Phys. Rev. Lett. **114**, 11, 112001 (2015), [arXiv:1406.4987].

[164] G. P. Engel *et al.*, Phys. Rev. **D91**, 5, 054505 (2015), [arXiv:1411.6386].

[165] S. Aoki *et al.*, Eur. Phys. J. **C77**, 2, 112 (2017), [arXiv:1607.00299].

[166] T. Blum *et al.* (RBC, UKQCD), Phys. Rev. **D93**, 7, 074505 (2016), [arXiv:1411.7017].

[167] B. J. Choi *et al.* (SWME), Phys. Rev. **D93**, 1, 014511 (2016), [arXiv:1509.00592].

[168] J. Laiho and R. S. Van de Water, PoS **LATTICE2011**, 293 (2011), [arXiv:1112.4861].

[169] E. Gamiz *et al.* (HPQCD), Phys. Rev. **D80**, 014503 (2009), [arXiv:0902.1815].

[170] Y. Aoki *et al.*, Phys. Rev. **D91**, 11, 114505 (2015), [arXiv:1406.6192].

[171] A. Bazavov *et al.*, Phys. Rev. **D97**, 3, 034513 (2018), [arXiv:1706.04622].

[172] M. Ademollo and R. Gatto, Phys. Rev. Lett. **13**, 264 (1964).

[173] H. Leutwyler and M. Roos, Z. Phys. **C25**, 91 (1984).

[174] P. A. Boyle *et al.*, Phys. Rev. Lett. **100**, 141601 (2008), [arXiv:0710.5136].

[175] V. Lubicz *et al.* (ETM), Phys. Rev. **D80**, 111502 (2009), [arXiv:0906.4728]; V. Lubicz *et al.* (ETM), PoS **LATTICE2010**, 316 (2010), [arXiv:1012.3573].

[176] P. A. Boyle *et al.* (RBC-UKQCD), Eur. Phys. J. **C69**, 159 (2010), [arXiv:1004.0886].

[177] A. Bazavov *et al.*, Phys. Rev. **D87**, 073012 (2013), [arXiv:1212.4993].

[178] T. Kaneko *et al.* (JLQCD), PoS **LATTICE2012**, 111 (2012), [arXiv:1211.6180].

[179] P. A. Boyle *et al.*, JHEP **08**, 132 (2013), [arXiv:1305.7217].

[180] P. A. Boyle *et al.* (RBC/UKQCD), JHEP **06**, 164 (2015), [arXiv:1504.01692].

[181] N. Carrasco *et al.*, Phys. Rev. **D93**, 11, 114512 (2016), [arXiv:1602.04113].

[182] H. Na *et al.*, Phys. Rev. **D82**, 114506 (2010), [arXiv:1008.4562].

[183] H. Na *et al.*, Phys. Rev. **D84**, 114505 (2011), [arXiv:1109.1501].

[184] V. Lubicz *et al.* (ETM), Phys. Rev. **D96**, 5, 054514 (2017), [Erratum: Phys. Rev.D99,no.9,099902(2019)], [arXiv:1706.03017].

[185] T. Kaneko *et al.* (JLQCD), EPJ Web Conf. **175**, 13007 (2018), [arXiv:1711.11235].

[186] E. Dalgic *et al.*, Phys. Rev. **D73**, 074502 (2006), [Erratum: Phys. Rev.D75,119906(2007)], [hep-lat/0601021].

[187] J. M. Flynn *et al.*, Phys. Rev. **D91**, 7, 074510 (2015), [arXiv:1501.05373].

[188] J. A. Bailey *et al.* (Fermilab Lattice, MILC), Phys. Rev. **D92**, 1, 014024 (2015), [arXiv:1503.07839].

[189] B. Colquhoun *et al.*, Phys. Rev. **D93**, 3, 034502 (2016), [arXiv:1510.07446].

[190] Z. Gelzer *et al.*, EPJ Web Conf. **175**, 13024 (2018), [arXiv:1710.09442].

[191] B. Colquhoun, S. Hashimoto and T. Kaneko, PoS **LATTICE2018**, 274 (2018), [arXiv:1811.00227].

[192] C. Bourrely, B. Machet and E. de Rafael, Nucl. Phys. **B189**, 157 (1981); C. G. Boyd, B. Grinstein and R. F. Lebed, Phys. Rev. Lett. **74**, 4603 (1995), [hep-ph/9412324]; T. Becher and R. J. Hill, Phys. Lett. **B633**, 61 (2006), [hep-ph/0509090]; C. Bourrely, I. Caprini and L. Lellouch, Phys. Rev. **D79**, 013008 (2009), [Erratum: Phys. Rev.D82,099902(2010)], [arXiv:0807.2722].

[193] M. C. Arnesen *et al.*, Phys. Rev. Lett. **95**, 071802 (2005), [hep-ph/0504209].

[194] J. A. Bailey *et al.*, Phys. Rev. **D79**, 054507 (2009), [arXiv:0811.3640].

[195] S. Hashimoto *et al.*, Phys. Rev. **D61**, 014502 (1999), [hep-ph/9906376].

[196] S. Hashimoto *et al.*, Phys. Rev. **D66**, 014503 (2002), [hep-ph/0110253].

[197] C. Bernard *et al.*, Phys. Rev. **D79**, 014506 (2009), [arXiv:0808.2519].

[198] J. A. Bailey *et al.* (Fermilab Lattice, MILC), Phys. Rev. **D89**, 11, 114504 (2014), [arXiv:1403.0635].

[199] J. Harrison, C. Davies and M. Wingate (HPQCD), Phys. Rev. **D97**, 5, 054502 (2018), [arXiv:1711.11013].

[200] E. McLean *et al.*, Phys. Rev. **D99**, 11, 114512 (2019), [arXiv:1904.02046].

[201] T. Bhattacharya *et al.* (LANL/SWME), PoS **LATTICE2018**, 283 (2018).

[202] J. A. Bailey *et al.* (MILC), Phys. Rev. **D92**, 3, 034506 (2015), [arXiv:1503.07237].

[203] H. Na *et al.* (HPQCD), Phys. Rev. **D92**, 5, 054510 (2015), [Erratum: Phys. Rev.D93,no.11,119906(2016)], [arXiv:1505.03925].

[204] A. V. Avilés-Casco *et al.* (Fermilab Lattice, MILC), PoS **LATTICE2018**, 282 (2019), [arXiv:1901.00216].

[205] T. Kaneko *et al.* (JLQCD), PoS **LATTICE2018**, 311 (2018), [arXiv:1811.00794].

[206] W. Detmold, C. Lehner and S. Meinel, Phys. Rev. **D92**, 3, 034503 (2015), [arXiv:1503.01421].

[207] W. Detmold and S. Meinel, Phys. Rev. **D93**, 7, 074501 (2016), [arXiv:1602.01399].

[208] R. R. Horgan *et al.*, Phys. Rev. **D89**, 9, 094501 (2014), [arXiv:1310.3722].

[209] J. A. Bailey *et al.*, Phys. Rev. **D93**, 2, 025026 (2016), [arXiv:1509.06235].

[210] D. Du *et al.*, Phys. Rev. **D93**, 3, 034005 (2016), [arXiv:1510.02349].

[211] C. T. H. Davies *et al.* (HPQCD), Phys. Rev. **D78**, 114507 (2008), [arXiv:0807.1687].

[212] C. McNeile *et al.*, Phys. Rev. **D82**, 034512 (2010), [arXiv:1004.4285].

[213] E. Shintani *et al.*, Phys. Rev. **D82**, 7, 074505 (2010), [Erratum: Phys. Rev.D89,no.9,099903(2014)], [arXiv:1002.0371].

[214] R. J. Hudspith *et al.*, Mod. Phys. Lett. **A31**, 32, 1630037 (2016).

[215] I. Allison *et al.* (HPQCD), Phys. Rev. **D78**, 054513 (2008), [arXiv:0805.2999].

[216] B. Chakraborty *et al.*, Phys. Rev. **D91**, 5, 054508 (2015), [arXiv:1408.4169].

[217] Y. Maezawa and P. Petreczky, Phys. Rev. **D94**, 3, 034507 (2016), [arXiv:1606.08798].

[218] Q. Mason *et al.* (HPQCD, UKQCD), Phys. Rev. Lett. **95**, 052002 (2005), [hep-lat/0503005].

[219] A. Bazavov *et al.*, Phys. Rev. **D86**, 114031 (2012), [arXiv:1205.6155].

[220] A. Bazavov *et al.*, Phys. Rev. **D90**, 7, 074038 (2014), [arXiv:1407.8437].

[221] F. Karbstein, M. Wagner and M. Weber, Phys. Rev. **D98**, 11, 114506 (2018), [arXiv:1804.10909].

[222] H. Takaura *et al.*, JHEP **04**, 155 (2019), [arXiv:1808.01643].

[223] B. Blossier *et al.*, Phys. Rev. **D85**, 034503 (2012), [arXiv:1110.5829]; B. Blossier *et al.*, Phys. Rev. Lett. **108**, 262002 (2012), [arXiv:1201.5770].

[224] S. Zafeiropoulos *et al.*, Phys. Rev. Lett. **122**, 16, 162002 (2019), [arXiv:1902.08148].

[225] S. Aoki *et al.* (PACS-CS), JHEP **10**, 053 (2009), [arXiv:0906.3906].

[226] P. Fritzsch *et al.*, PoS **LATTICE2014**, 291 (2014), [arXiv:1411.7648].

[227] M. Bruno *et al.* (ALPHA), Phys. Rev. Lett. **119**, 10, 102001 (2017), [arXiv:1706.03821].

[228] S. Durr *et al.*, Phys. Lett. **B701**, 265 (2011), [arXiv:1011.2403].

[229] S. Durr *et al.*, JHEP **08**, 148 (2011), [arXiv:1011.2711].

[230] S. Capitani *et al.*, Nucl. Phys. **B544**, 669 (1999), [Erratum: Nucl. Phys.B582,762(2000)], [hep-lat/9810063].

[231] A. Bussone *et al.* (ETM), Phys. Rev. **D93**, 11, 114505 (2016), [arXiv:1603.04306].

[232] SISSA, *Proceedings, 36th International Symposium on Lattice Field Theory (Lattice 2018)*, volume LATTICE2018, SISSA (2019), URL `https://pos.sissa.it/334/`.

[233] W. Detmold *et al.* (USQCD) (2019), [arXiv:1904.09512].

[234] A. S. Kronfeld *et al.* (USQCD) (2019), [arXiv:1904.09931].

[235] R. C. Brower *et al.* (USQCD) (2019), [arXiv:1904.09964].

[236] C. Lehner *et al.* (USQCD) (2019), [arXiv:1904.09479].

[237] A. Bazavov *et al.* (USQCD) (2019), [arXiv:1904.09951].

[238] V. Cirigliano *et al.* (USQCD) (2019), [arXiv:1904.09704].

[239] B. Joó *et al.* (USQCD) (2019), [arXiv:1904.09725].

18. Structure Functions

Revised August 2019 by E.C. Aschenauer (BNL), R.S. Thorne (UCL) and R. Yoshida (Jefferson Lab).

18.1 Deep inelastic scattering

High-energy lepton-nucleon scattering plays a key role in determining the partonic structure of the proton. The process $\ell N \to \ell' X$ is illustrated in Fig. 18.1. The filled circle in this figure represents the internal structure of the proton which can be expressed in terms of structure functions.

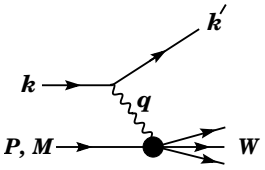

Figure 18.1: Kinematic quantities for the description of deep inelastic scattering. The quantities k and k' are the four-momenta of the incoming and outgoing leptons, P is the four-momentum of a nucleon with mass M, and W is the mass of the recoiling system X. The exchanged particle is a γ, $W^{\pm}$, or Z; it transfers four-momentum $q = k - k'$ to the nucleon.

Invariant quantities:

$\nu = \frac{q\cdot P}{M} = E - E'$ is the lepton's energy loss in the nucleon rest frame (in earlier literature sometimes $\nu = q \cdot P$). Here, E and E' are the initial and final lepton energies in the nucleon rest frame.

$Q^2 = -q^2 = 2(EE' - \vec{k}\cdot\vec{k}') - m_\ell^2 - m_{\ell'}^2$ where $m_\ell(m_{\ell'})$ is the initial (final) lepton mass. If $EE'\sin^2(\theta/2) \gg m_\ell^2,\, m_{\ell'}^2$, then

$\approx 4EE'\sin^2(\theta/2)$, where θ is the lepton's scattering angle with respect to the lepton beam direction.

$x = \frac{Q^2}{2M\nu}$ where, in the parton model, x is the fraction of the nucleon's momentum carried by the struck quark. Beyond leading order the equation remains the definition of x, but this is no longer identical to nucleon momentum fraction.

$y = \frac{q\cdot P}{k\cdot P} = \frac{\nu}{E}$ is the fraction of the lepton's energy lost in the nucleon rest frame.

$W^2 = (P+q)^2 = M^2 + 2M\nu - Q^2$ is the mass squared of the system X recoiling against the scattered lepton.

$s = (k+P)^2 = \frac{Q^2}{xy} + M^2 + m_\ell^2$ is the center-of-mass energy squared of the lepton-nucleon system.

The process in Fig. 18.1 is called deep ($Q^2 \gg M^2$) inelastic ($W^2 \gg M^2$) scattering (DIS). In what follows, the masses of the initial and scattered leptons, m_ℓ and $m_{\ell'}$, are neglected.

18.1.1 *DIS cross sections*

The double-differential cross section for deep inelastic scattering can be expressed in terms of kinematic variables in several ways.

$$\frac{d^2\sigma}{dx\,dy} = x\,(s-M^2)\,\frac{d^2\sigma}{dx\,dQ^2} = \frac{2\pi\,M\nu}{E'}\frac{d^2\sigma}{d\Omega_{\rm Nrest}\,dE'}\,. \qquad (18.1)$$

In lowest-order perturbation theory, the cross section for the scattering of polarized leptons on polarized nucleons can be expressed in terms of the products of leptonic and hadronic tensors associated with the coupling of the exchanged bosons at the upper and lower vertices in Fig. 18.1 (see Refs. [1–4])

$$\frac{d^2\sigma}{dxdy} \;=\; \frac{2\pi y\alpha^2}{Q^4}\,\sum_j\,\eta_j\,L_j^{\mu\nu}\,W_{\mu\nu}^j\,. \qquad (18.2)$$

For neutral-current processes, the summation is over $j = \gamma, Z$ and γZ representing photon and Z exchange and the interference between them, whereas for charged-current interactions there is only W exchange, $j = W$. (For transverse nucleon polarization, there is a dependence on the azimuthal angle of the scattered lepton.) The lepton tensor $L_{\mu\nu}$ is associated with the coupling of the exchange boson to the leptons. For incoming leptons of charge $e = \pm 1$ and helicity $\lambda = \pm 1$,

$$\begin{aligned}
L^{\gamma}_{\mu\nu} &= 2\left(k_\mu k'_\nu + k'_\mu k_\nu - (k\cdot k' - m_\ell^2)g_{\mu\nu} - i\lambda\varepsilon_{\mu\nu\alpha\beta}k^\alpha k'^\beta\right),\\
L^{\gamma Z}_{\mu\nu} &= (g_V^e + e\lambda g_A^e)\,L^{\gamma}_{\mu\nu}, \quad L^{Z}_{\mu\nu} = (g_V^e + e\lambda g_A^e)^2\,L^{\gamma}_{\mu\nu},\\
L^{W}_{\mu\nu} &= (1+e\lambda)^2\,L^{\gamma}_{\mu\nu},
\end{aligned} \qquad (18.3)$$

where $g_V^e = -\frac{1}{2} + 2\sin^2\theta_W$, $\quad g_A^e = -\frac{1}{2}$.

Although here the helicity formalism is adopted, an alternative approach is to express the tensors in Eq. (18.3) in terms of the polarization of the lepton.

The factors η_j in Eq. (18.2) denote the ratios of the corresponding propagators and couplings to the photon propagator and coupling squared

$$\begin{aligned}
\eta_\gamma &= 1\;;\;\eta_{\gamma Z} = \left(\frac{G_F M_Z^2}{2\sqrt{2}\pi\alpha}\right)\left(\frac{Q^2}{Q^2+M_Z^2}\right);\\
\eta_Z &= \eta_{\gamma Z}^2\;;\;\eta_W = \tfrac{1}{2}\left(\frac{G_F M_W^2}{4\pi\alpha}\,\frac{Q^2}{Q^2+M_W^2}\right)^2.
\end{aligned} \qquad (18.4)$$

The hadronic tensor, which describes the interaction of the appropriate electroweak currents with the target nucleon, is given by

$$W_{\mu\nu} \;=\; \frac{1}{4\pi}\int d^4z\,e^{iq\cdot z}\,\left\langle P,S\left|\left[J_\mu^\dagger(z),J_\nu(0)\right]\right|P,S\right\rangle, \qquad (18.5)$$

where J_α is the hadronic contribution to the electromagnetic, or weak current and S denotes the nucleon-spin 4-vector, with $S^2 = -M^2$ and $S\cdot P = 0$.

18.2 Structure functions of the proton

The structure functions are defined in terms of the hadronic tensor (see Refs. [1–3])

$$\begin{aligned}
W_{\mu\nu} &= \left(-g_{\mu\nu} + \frac{q_\mu q_\nu}{q^2}\right)F_1(x,Q^2) + \frac{\hat{P}_\mu\hat{P}_\nu}{P\cdot q}\,F_2(x,Q^2)\\
&- i\varepsilon_{\mu\nu\alpha\beta}\,\frac{q^\alpha P^\beta}{2P\cdot q}\,F_3(x,Q^2)\\
&+ i\varepsilon_{\mu\nu\alpha\beta}\,\frac{q^\alpha}{P\cdot q}\left[S^\beta g_1(x,Q^2) + \left(S^\beta - \frac{S\cdot q}{P\cdot q}\,P^\beta\right)g_2(x,Q^2)\right]\\
&+ \frac{1}{P\cdot q}\left[\tfrac{1}{2}\left(\hat{P}_\mu\hat{S}_\nu + \hat{S}_\mu\hat{P}_\nu\right) - \frac{S\cdot q}{P\cdot q}\,\hat{P}_\mu\hat{P}_\nu\right]g_3(x,Q^2)\\
&+ \frac{S\cdot q}{P\cdot q}\left[\frac{\hat{P}_\mu\hat{P}_\nu}{P\cdot q}\,g_4(x,Q^2) + \left(-g_{\mu\nu} + \frac{q_\mu q_\nu}{q^2}\right)g_5(x,Q^2)\right]
\end{aligned} \qquad (18.6)$$

where

$$\hat{P}_\mu \;=\; P_\mu - \frac{P\cdot q}{q^2}\,q_\mu, \qquad \hat{S}_\mu \;=\; S_\mu - \frac{S\cdot q}{q^2}\,q_\mu\,. \qquad (18.7)$$

In [2],the definition of $W_{\mu\nu}$ with $\mu \leftrightarrow \nu$ is adopted, which changes the sign of the $\varepsilon_{\mu\nu\alpha\beta}$ terms in Eq. (18.6), although the formulae given below are unchanged. Ref. [1] tabulates the relation between the structure functions defined in Eq. (18.6) and other choices available in the literature.

The cross sections for neutral- and charged-current deep inelastic scattering on unpolarized nucleons can be written in terms of

the structure functions in the generic form

$$\frac{d^2\sigma^i}{dxdy} = \frac{4\pi\alpha^2}{xyQ^2}\,\eta^i \left\{ \left(1 - y - \frac{x^2y^2M^2}{Q^2}\right) F_2^i + y^2 x F_1^i \mp \left(y - \frac{y^2}{2}\right) xF_3^i \right\}, \tag{18.8}$$

where i = NC, CC corresponds to neutral-current ($eN \to eX$) or charged-current ($eN \to \nu X$ or $\nu N \to eX$) processes, respectively. For incoming neutrinos, $L^W_{\mu\nu}$ of Eq. (18.3) is still true, but with e, λ corresponding to the outgoing charged lepton. In the last term of Eq. (18.8), the $-$ sign is taken for an incoming e^+ or $\overline{\nu}$ and the $+$ sign for an incoming e^- or ν. The factor $\eta^{\rm NC} = 1$ for unpolarized $e^\pm$ beams, whereas

$$\eta^{\rm CC} = (1 \pm \lambda)^2 \eta_W \tag{18.9}$$

with $\pm$ for $\ell^\pm$; and where λ is the helicity of the incoming lepton and η_W is defined in Eq. (18.4); for incoming neutrinos $\eta^{\rm CC} = 4\eta_W$. The CC structure functions, which derive exclusively from W exchange, are

$$F_1^{\rm CC} = F_1^W,\ F_2^{\rm CC} = F_2^W,\ xF_3^{\rm CC} = xF_3^W. \tag{18.10}$$

The NC structure functions $F_2^\gamma, F_2^{\gamma Z}, F_2^Z$ are, for $e^\pm N \to e^\pm X$, given by [5],

$$F_2^{\rm NC} = F_2^\gamma - (g_V^e \pm \lambda g_A^e)\eta_{\gamma Z} F_2^{\gamma Z} + ({g_V^e}^2 + {g_A^e}^2 \pm 2\lambda g_V^e g_A^e)\,\eta_Z F_2^Z \tag{18.11}$$

and similarly for $F_1^{\rm NC}$, whereas

$$xF_3^{\rm NC} = -(g_A^e \pm \lambda g_V^e)\eta_{\gamma Z} xF_3^{\gamma Z} + [2g_V^e g_A^e \pm \lambda({g_V^e}^2 + {g_A^e}^2)]\eta_Z xF_3^Z\,. \tag{18.12}$$

The polarized cross-section difference

$$\Delta\sigma = \sigma(\lambda_n = -1, \lambda_\ell) - \sigma(\lambda_n = 1, \lambda_\ell)\,, \tag{18.13}$$

where λ_ℓ, λ_n are the helicities (± 1) of the incoming lepton and nucleon, respectively, may be expressed in terms of the five structure functions $g_{1,\ldots 5}(x, Q^2)$ of Eq. (18.6). Explicitly,

$$\frac{d^2\Delta\sigma^i}{dxdy} = \frac{8\pi\alpha^2}{xyQ^2}\,\eta^i \left\{ -\lambda_\ell y \left(2 - y - 2x^2y^2\frac{M^2}{Q^2}\right) xg_1^i + \lambda_\ell 4x^3y^2\,\frac{M^2}{Q^2}\,g_2^i + 2x^2y\frac{M^2}{Q^2}\left(1 - y - x^2y^2\frac{M^2}{Q^2}\right) g_3^i - \left(1 + 2x^2y\frac{M^2}{Q^2}\right)\left[\left(1 - y - x^2y^2\frac{M^2}{Q^2}\right) g_4^i + xy^2 g_5^i\right] \right\} \tag{18.14}$$

with i = NC or CC as before. The Eq. (18.13) corresponds to the difference of antiparallel minus parallel spins of the incoming particles for e^- or ν initiated reactions, but the difference of parallel minus antiparallel for e^+ or $\overline{\nu}$ initiated processes. For longitudinal nucleon polarization, the contributions of g_2 and g_3 are suppressed by powers of M^2/Q^2. These structure functions give an unsuppressed contribution to the cross section for transverse polarization [1],but in this case the cross-section difference vanishes as $M/Q \to 0$.

Because the same tensor structure occurs in the spin-dependent and spin-independent parts of the hadronic tensor of Eq. (18.6) in the $M^2/Q^2 \to 0$ limit, the differential cross-section difference of Eq. (18.14) may be obtained from the differential cross section Eq. (18.8) by replacing

$$F_1 \to -g_5\,, \quad F_2 \to -g_4\,, \quad F_3 \to 2g_1\,, \tag{18.15}$$

and multiplying by two, since the total cross section is the average over the initial-state polarizations. In this limit, Eq. (18.8) and Eq. (18.14) may be written in the form

$$\frac{d^2\sigma^i}{dxdy} = \frac{2\pi\alpha^2}{xyQ^2}\,\eta^i \left[Y_+ F_2^i \mp Y_- xF_3^i - y^2 F_L^i\right],$$

$$\frac{d^2\Delta\sigma^i}{dxdy} = \frac{4\pi\alpha^2}{xyQ^2}\,\eta^i \left[-Y_+ g_4^i \mp Y_- 2xg_1^i + y^2 g_L^i\right], \tag{18.16}$$

with i = NC or CC, where $Y_\pm = 1 \pm (1-y)^2$ and

$$F_L^i = F_2^i - 2xF_1^i\,, \qquad g_L^i = g_4^i - 2xg_5^i\,. \tag{18.17}$$

In the naive quark-parton model, the analogy with the Callan-Gross relations [6] $F_L^i = 0$, are the Dicus relations [7] $g_L^i = 0$. Therefore, there are only two independent polarized structure functions: g_1 (parity conserving) and g_5 (parity violating), in analogy with the unpolarized structure functions F_1 and F_3.

18.2.1 *Structure functions in the quark-parton model*

In the naive quark-parton model [8, 9], contributions to the structure functions F^i and g^i can be expressed in terms of the quark distribution functions $q(x, Q^2)$ of the proton, where $q = u, \overline{u}, d, \overline{d}$ etc. The quantity $q(x, Q^2)dx$ is the number of quarks (or antiquarks) of designated flavor that carry a momentum fraction between x and $x + dx$ of the proton's momentum in a frame in which the proton momentum is large.

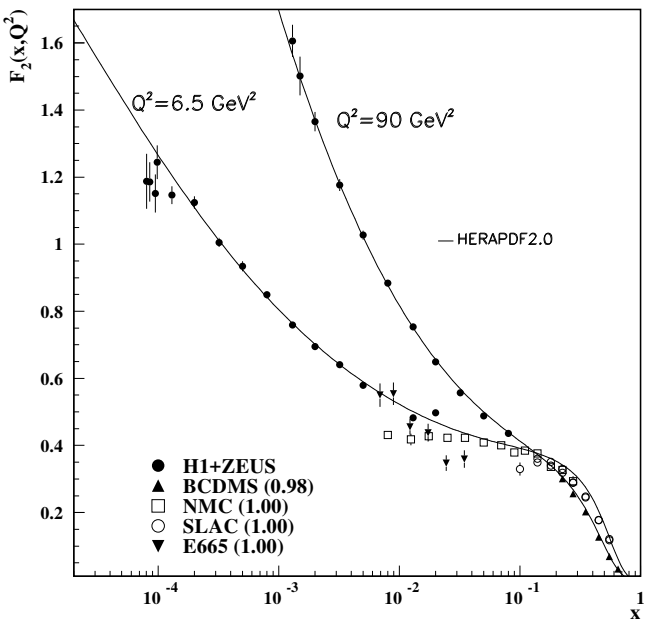

Figure 18.2: The proton structure function F_2^p given at two Q^2 values (6.5 GeV^2 and 90 GeV^2), which exhibit scaling at the 'pivot' point $x \sim 0.14$. See the captions in Fig. 18.8 and Fig. 18.10 for the references of the data. The various data sets have been renormalized by the factors shown in brackets in the key to the plot, which were globally determined in a previous HERAPDF analysis [10]. The curves were obtained using the PDFs from the HERAPDF analysis [11]. In practice, data for the reduced cross section, $F_2(x, Q^2) - (y^2/Y_+)F_L(x, Q^2)$, were fitted, rather than F_2 and F_L separately. The agreement between data and theory at low Q^2 and x can be improved by a positive higher-twist correction to $F_L(x, Q^2)$ [12, 13] (see Fig. 8 of Ref. [13]), or small-x resummation [14, 15].

For the neutral-current processes $ep \to eX$,

$$\begin{aligned}
\left[F_2^\gamma,\ F_2^{\gamma Z},\ F_2^Z\right] &= x\sum_q \left[e_q^2,\ 2e_q g_V^q,\ {g_V^q}^2 + {g_A^q}^2\right]\ (q+\overline{q})\ , \\
\left[F_3^\gamma,\ F_3^{\gamma Z},\ F_3^Z\right] &= \sum_q \left[0,\ 2e_q g_A^q,\ 2g_V^q g_A^q\right]\ (q-\overline{q})\ , \\
\left[g_1^\gamma,\ g_1^{\gamma Z},\ g_1^Z\right] &= \tfrac{1}{2}\sum_q \left[e_q^2,\ 2e_q g_V^q,\ {g_V^q}^2 + {g_A^q}^2\right]\ (\Delta q+\Delta\overline{q})\ , \\
\left[g_5^\gamma,\ g_5^{\gamma Z},\ g_5^Z\right] &= \sum_q \left[0,\ e_q g_A^q,\ g_V^q g_A^q\right]\ (\Delta\overline{q}-\Delta q)\ ,
\end{aligned} \tag{18.18}$$

where $g_V^q = \pm\frac{1}{2} - 2e_q \sin^2\theta_W$ and $g_A^q = \pm\frac{1}{2}$, with $\pm$ according to whether q is a $u-$ or $d-$type quark respectively. The quantity Δq is the difference $q\uparrow - q\downarrow$ of the distributions with the quark spin parallel and antiparallel to the proton spin.

For the charged-current processes $e^- p \to \nu X$ and $\overline{\nu} p \to e^+ X$, the structure functions are:

$$\begin{aligned}
F_2^{W^-} &= 2x(u + \overline{d} + \overline{s} + c\ldots)\ , \\
F_3^{W^-} &= 2(u - \overline{d} - \overline{s} + c\ldots)\ , \\
g_1^{W^-} &= (\Delta u + \Delta\overline{d} + \Delta\overline{s} + \Delta c\ldots)\ , \\
g_5^{W^-} &= (-\Delta u + \Delta\overline{d} + \Delta\overline{s} - \Delta c\ldots)\ ,
\end{aligned} \tag{18.19}$$

where only the active flavors have been kept and where CKM mixing has been neglected. For $e^+ p \to \overline{\nu} X$ and $\nu p \to e^- X$, the structure functions F^{W^+}, g^{W^+} are obtained by the flavor interchanges $d \leftrightarrow u, s \leftrightarrow c$ in the expressions for F^{W^-}, g^{W^-}. The structure functions for scattering on a neutron are obtained from those of the proton by the interchange $u \leftrightarrow d$. For both the neutral- and charged-current processes, the quark-parton model predicts $2xF_1^i = F_2^i$ and $g_4^i = 2xg_5^i$.

Neglecting masses, the structure functions g_2 and g_3 contribute only to scattering from transversely polarized nucleons, and have no simple interpretation in terms of the quark-parton model. They arise from off-diagonal matrix elements $\langle P,\lambda'|[J_\mu^\dagger(z), J_\nu(0)]|P,\lambda\rangle$, where the proton helicities satisfy $\lambda' \neq \lambda$. In fact, the leading-twist contributions to both g_2 and g_3 are both twist-2 and twist-3, which contribute at the same order of Q^2. The Wandzura-Wilczek relation [16] expresses the twist-2 part of g_2 in terms of g_1 as

$$g_2^i(x) \ = \ -g_1^i(x) \ + \ \int_x^1 \frac{dy}{y}\ g_1^i(y)\ . \tag{18.20}$$

However, the twist-3 component of g_2 is unknown. Similarly, there is a relation expressing the twist-2 part of g_3 in terms of g_4. A complete set of relations, including M^2/Q^2 effects, can be found in [17].

18.2.2 *Structure functions and QCD*

One of the most striking predictions of the quark-parton model is that the structure functions F_i, g_i *scale*, i.e., $F_i(x,Q^2) \to F_i(x)$ in the Bjorken limit that Q^2 and $\nu \to \infty$ with x fixed [18]. This property is related to the assumption that the transverse momentum of the partons in the infinite-momentum frame of the proton is small. In QCD, however, the radiation of hard gluons from the quarks violates this assumption, leading to logarithmic scaling violations, which are particularly large at small x, see Fig. 18.2. The radiation of gluons produces the evolution of the structure functions. As Q^2 increases, more and more gluons are radiated, which in turn split into $q\overline{q}$ pairs. This process leads both to the softening of the initial quark momentum distributions and to the growth of the gluon density and the $q\overline{q}$ sea as x decreases.

In QCD, the above processes are described in terms of scale-dependent parton distributions $f_a(x,\mu^2)$, where $a = g$ or q and, typically, μ is the scale of the probe Q. For parton distributions x always refers to the nucleon momentum fraction of the parton, whereas for structure functions it retains the definition in Sec. 18.1. For $Q^2 \gg M^2$, the structure functions are of the form

$$F_i = \sum_a C_i^a \otimes f_a + \mathcal{O}(M^2/Q^2), \tag{18.21}$$

where $\otimes$ denotes the convolution integral

$$C \ \otimes \ f \ = \ \int_x^1 \frac{dy}{y}\ C(y)\ f\left(\frac{x}{y}\right)\ , \tag{18.22}$$

and where the coefficient functions C_i^a are given as a power series in α_s. The parton distribution f_a corresponds, at a given x, to the density of parton a in the proton integrated over transverse momentum k_t up to μ. Its evolution in μ is described in QCD by a DGLAP equation (see Refs. [19–22]) which has the schematic form

$$\frac{\partial f_a}{\partial \ln\mu^2} \sim \frac{\alpha_s(\mu^2)}{2\pi}\sum_b (P_{ab} \otimes f_b)\ , \tag{18.23}$$

where the P_{ab}, which describe the parton splitting $b \to a$, are also given as a power series in α_s. Although perturbative QCD can predict, via Eq. (18.23), the evolution of the parton distribution functions from a particular scale, μ_0, these DGLAP equations cannot predict them *a priori* at any particular μ_0. Thus they must be measured at a starting point μ_0 before the predictions of QCD can be compared to the data at other scales, μ. In general, all observables involving a hard hadronic interaction (such as structure functions) can be expressed as a convolution of calculable, process-dependent coefficient functions and these universal parton distributions, e.g. Eq. (18.21).

It is often convenient to write the evolution equations in terms of the gluon, non-singlet (q^{NS}) and singlet (q^S) quark distributions, such that

$$q^{NS} \ = \ q_i - \overline{q}_i \quad (\text{or } q_i - q_j), \qquad q^S \ = \ \sum_i (q_i + \overline{q}_i)\ . \tag{18.24}$$

The non-singlet distributions have non-zero values of flavor quantum numbers, such as isospin and baryon number. The DGLAP evolution equations then take the form

$$\frac{\partial q^{NS}}{\partial \ln\mu^2} = \frac{\alpha_s(\mu^2)}{2\pi}\ P_{qq} \ \otimes \ q^{NS}\ ,$$

$$\frac{\partial}{\partial \ln\mu^2}\ \begin{pmatrix} q^S \\ g \end{pmatrix} = \frac{\alpha_s(\mu^2)}{2\pi}\ \begin{pmatrix} P_{qq} & 2n_f\ P_{qg} \\ P_{gq} & P_{gg} \end{pmatrix} \otimes \begin{pmatrix} q^S \\ g \end{pmatrix}, \tag{18.25}$$

where P are splitting functions that describe the probability of a given parton splitting into two others, and n_f is the number of (active) quark flavors. The leading-order Altarelli-Parisi [21]

Table 18.1: The main processes relevant to global PDF analyses, ordered in three groups: fixed-target experiments, HERA and the $p\bar{p}$ Tevatron / pp LHC. For each process we give an indication of their dominant partonic subprocesses, the primary partons which are probed and the approximate range of x constrained by the data.

Process	Subprocess	Partons	x range
$\ell^\pm \{p,n\} \to \ell^\pm X$	$\gamma^* q \to q$	$q, \bar{q}, g$	$x \gtrsim 0.01$
$\ell^\pm n/p \to \ell^\pm X$	$\gamma^* d/u \to d/u$	d/u	$x \gtrsim 0.01$
$pp \to \mu^+\mu^- X$	$u\bar{u}, d\bar{d} \to \gamma^*$	$\bar{q}$	$0.015 \lesssim x \lesssim 0.35$
$pn/pp \to \mu^+\mu^- X$	$(u\bar{d})/(u\bar{u}) \to \gamma^*$	$\bar{d}/\bar{u}$	$0.015 \lesssim x \lesssim 0.35$
$\nu(\bar{\nu})\, N \to \mu^-(\mu^+)\, X$	$W^* q \to q'$	$q, \bar{q}$	$0.01 \lesssim x \lesssim 0.5$
$\nu\, N \to \mu^-\mu^+\, X$	$W^* s \to c$	s	$0.01 \lesssim x \lesssim 0.2$
$\bar{\nu}\, N \to \mu^+\mu^-\, X$	$W^* \bar{s} \to \bar{c}$	$\bar{s}$	$0.01 \lesssim x \lesssim 0.2$
$e^\pm\, p \to e^\pm\, X$	$\gamma^* q \to q$	$g, q, \bar{q}$	$10^{-4} \lesssim x \lesssim 0.1$
$e^+\, p \to \bar{\nu}\, X$	$W^+ \{d,s\} \to \{u,c\}$	d, s	$x \gtrsim 0.01$
$e^\pm p \to e^\pm\, c\bar{c}X, e^\pm\, b\bar{b}X$	$\gamma^* c \to c$, $\gamma^* g \to c\bar{c}$	c, b, g	$10^{-4} \lesssim x \lesssim 0.01$
$e^\pm p \to$ jet$+X$	$\gamma^* g \to q\bar{q}$	g	$0.01 \lesssim x \lesssim 0.1$
$p\bar{p}, pp \to$ jet$+X$	$gg, qg, qq \to 2j$	g, q	$0.00005 \lesssim x \lesssim 0.5$
$p\bar{p} \to (W^\pm \to \ell^\pm\nu)\, X$	$ud \to W^+, \bar{u}\bar{d} \to W^-$	$u, d, \bar{u}, \bar{d}$	$x \gtrsim 0.05$
$pp \to (W^\pm \to \ell^\pm\nu)\, X$	$u\bar{d} \to W^+, d\bar{u} \to W^-$	$u, d, \bar{u}, \bar{d}, g$	$x \gtrsim 0.001$
$p\bar{p}(pp) \to (Z \to \ell^+\ell^-)X$	$uu, dd, ..(u\bar{u}, ..) \to Z$	$u, d, ..(g)$	$x \gtrsim 0.001$
$pp \to W^- c,\ W^+\bar{c}$	$gs \to W^- c$	$s, \bar{s}$	$x \sim 0.01$
$pp \to (\gamma^* \to \ell^+\ell^-)X$	$u\bar{u}, d\bar{d}, .. \to \gamma^*$	$\bar{q}, g$	$x \gtrsim 10^{-5}$
$pp \to (\gamma^* \to \ell^+\ell^-)X$	$u\gamma, d\gamma, .. \to \gamma^*$	γ	$x \gtrsim 10^{-2}$
$pp \to b\bar{b}\, X,\quad t\bar{t}X$	$gg \to b\bar{b},\quad t\bar{t}$	g	$x \gtrsim 10^{-5}, 10^{-2}$
$pp \to$ exclusive J/ψ, Υ	$\gamma^*(gg) \to J/\psi$, Υ	g	$x \gtrsim 10^{-5}, 10^{-4}$
$pp \to \gamma\, X$	$gq \to \gamma q$, $g\bar{q} \to \gamma\bar{q}$	g	$x \gtrsim 0.005$

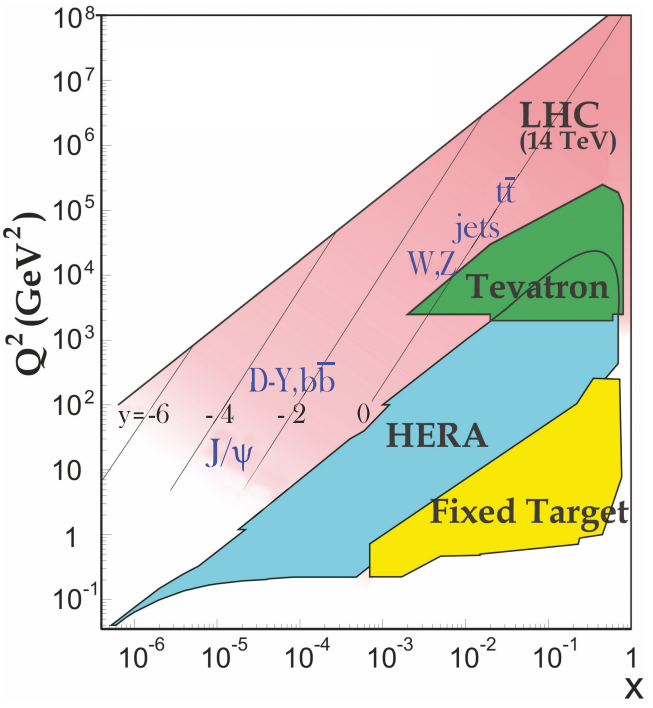

Figure 18.3: Kinematic domains in x and Q^2 probed by fixed-target and collider experiments, where here Q^2 can refer either the literal Q^2 for deep inelastic scattering, or the hard scale of the process in hadron-hadron collisions, e.g. invariant mass or transverse momentum p_T^2. Some of the final states accessible at the LHC are indicated in the appropriate regions, where y is the rapidity. The incoming partons have $x_{1,2} = (Q/14\ \text{TeV})e^{\pm y}$ where Q is the hard scale of the process shown in blue in the figure. For example, open charm production [23] and exclusive J/ψ and Υ production [24] at high $|y|$ at the LHC may probe the gluon PDF down to $x \sim 10^{-5}$.

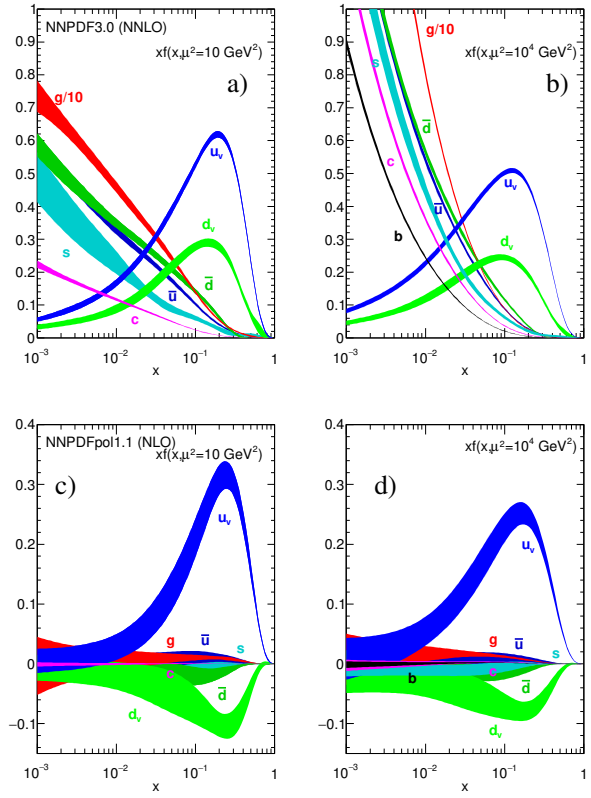

Figure 18.4: The bands are x times the unpolarized (a,b) parton distributions $f(x)$ (where $f = u_v, d_v, \overline{u}, \overline{d}, s \simeq \bar{s}, c = \bar{c}, b = \bar{b}, g$) obtained in NNLO NNPDF3.0 global analysis [25] at scales $\mu^2 = 10\ \text{GeV}^2$ (left) and $\mu^2 = 10^4\ \text{GeV}^2$ (right), with $\alpha_s(M_Z^2) = 0.118$. The analogous results obtained in the NNLO MMHT analysis can be found in Fig. 1 of Ref [26].The corresponding polarized parton distributions are shown (c,d), obtained in NLO with NNPDFpol1.1 [27].

splitting functions are

$$P_{qq} = \frac{4}{3}\left[\frac{1+x^2}{(1-x)}\right]_+ = \frac{4}{3}\left[\frac{1+x^2}{(1-x)_+}\right] + 2\delta(1-x)\ , \qquad (18.26)$$

$$P_{qg} = \frac{1}{2}\left[x^2+(1-x)^2\right]\ ,\ P_{gq} = \frac{4}{3}\left[\frac{1+(1-x)^2}{x}\right]\ , \qquad (18.27)$$

$$P_{gg} = 6\left[\frac{1-x}{x} + x(1-x) + \frac{x}{(1-x)_+}\right] + \left[\frac{11}{2} - \frac{n_f}{3}\right]\delta(1-x), \qquad (18.28)$$

where the notation $[F(x)]_+$ defines a distribution such that for any sufficiently regular test function, $f(x)$,

$$\int_0^1 dx f(x)[F(x)]_+ = \int_0^1 dx\ (f(x) - f(1))F(x)\ . \qquad (18.29)$$

In general, the splitting functions can be expressed as a power series in α_s. The series contains both terms proportional to $\ln\mu^2$ and to $\ln(1/x)$ and $\ln(1-x)$. The leading-order DGLAP evolution sums up the $(\alpha_s \ln\mu^2)^n$ contributions, while at next-to-leading order (NLO) the sum over the $\alpha_s(\alpha_s \ln\mu^2)^{n-1}$ terms is included [28, 29]. The NNLO contributions to the splitting functions and the DIS coefficient functions are also all known [30–32].

In the kinematic region of very small x, one may also sum leading terms in $\ln(1/x)$, independent of the value of $\ln\mu^2$. At leading order, LLx, this is done by the BFKL equation for the unintegrated distributions (see Refs. [33, 34].) The leading-order $(\alpha_s \ln(1/x))^n$ terms result in a power-like growth, $x^{-\omega}$ with $\omega = (12\alpha_s \ln 2)/\pi$, at asymptotic values of $\ln 1/x$. The next-to-leading $\ln 1/x$ (NLLx) contributions are also available [35, 36]. They are so large (and negative) that the results initially appeared to be perturbatively unstable. Methods, based on a combination of collinear and small-x resummations, have been developed which reorganize the perturbative series into a more stable hierarchy [37–40], and this has been used as the basis for a framework for including the corrections in phenomenological studies [41, 42]. There are some limited indications that small-x resummations become necessary for sufficient precision for $x \lesssim 10^{-3}$ at low scales [14, 15]. There is not yet any very convincing indication for a 'non-linear' regime, for $Q^2 \gtrsim 2\ \text{GeV}^2$, in which the gluon density would be so high that gluon-gluon recombination effects would become significant.

The precision of the experimental data demands that at least NLO, and preferably NNLO, DGLAP evolution be used in comparisons between QCD theory and experiment. Beyond the leading order, it is necessary to specify, and to use consistently, both a renormalization and a factorization scheme. The renormalization scheme used almost universally is the modified minimal subtraction ($\overline{\text{MS}}$) scheme [43, 44]. The most popular choices for the factorization scheme is also $\overline{\text{MS}}$ [45]. However, sometimes the DIS [46] scheme is adopted, in which there are no higher-order corrections to the F_2 structure function. The two schemes differ in how the non-divergent pieces are assimilated in the parton distribution functions.

The discussion above relates to the Q^2 behavior of leading-twist (twist-2) contributions to the structure functions. Higher-twist terms, which involve their own non-perturbative input, exist. These die off as powers of Q; specifically twist-n terms are damped by $1/Q^{n-2}$. Provided a cut, say $W^2 > 15\ \text{GeV}^2$ is imposed, the

higher-twist terms appear to be numerically unimportant for Q^2 above a few GeV^2, except possibly for very small x and more definitely for x close to 1 [47–49], though it is important to note that they are likely to be larger in $xF_3(x,Q^2)$ than in $F_2(x,Q^2)$ (see e.g. [50])due to a lack of a constraining sum rule for $xF_3(x,Q^2)$.

18.3 Determination of parton distributions

The parton distribution functions (PDFs) can be determined from an analysis of data for deep inelastic lepton-nucleon scattering and for related hard-scattering processes initiated by nucleons; see Refs. [51–56] for reviews. Table 18.1 highlights some of the processes, where LHC data are playing an increasing role [57], and their primary sensitivity to PDFs. Fixed-target and collider experiments have complementary kinematic reach (as is shown in Fig. 18.3), which enables the determination of PDFs over a wide range in x and μ^2. As more precise LHC data for $W^{\pm}$, Z, γ, jet, $b\bar{b}$, $t\bar{t}$ and J/ψ production become available, tighter constraints on the PDFs are expected in a wider kinematic range.

Recent determinations and releases of the unpolarized PDFs up to NNLO have been made by six groups: MMHT [26], NNPDF [58], CT(EQ) [59], HERAPDF [11], ABMP [60] and JR [61]. JR generate 'dynamical' PDFs from a valence-like input at a very low starting scale, $Q_0^2 = 0.5$ GeV^2, whereas other groups start evolution at $Q_0^2 = 1-4$ GeV^2. Most groups use input PDFs of the form $xf = x^a(...)(1-x)^b$ with 14-28 free parameters in total. In these cases the PDF uncertainties are made available using the "Hessian" formulation. The free parameters are expanded around their best fit values, and orthogonal eigenvector sets of PDFs depending on linear combinations of the parameter variations are obtained. The uncertainty is then the quadratic sum of the uncertainties arising from each eigenvector. The NNPDF group combines a Monte Carlo representation of the probability measure in the space of PDFs with the use of neural networks. Fits are performed to a number of "replica" data sets obtained by allowing individual data points to fluctuate randomly by amounts determined by the size of the data uncertainties. This results in a set of replicas of unbiased PDF sets. In this case the best prediction is the average obtained using all PDF replicas and the uncertainty is the standard deviation over all replicas. It is now possible to convert the eigenvectors of Hessian-based PDFs to Monte Carlo replicas [62] and *vice versa* [63].

In these analyses, the u, d and s quarks are taken to be massless, but the treatment of the heavy c and b quark masses, m_Q, differs, and has a long history, which may be traced from Refs. [64–75]. The MSTW, CT, NNPDF and HERAPDF analyses use different variants of the General-Mass Variable-Flavour-Number Scheme (GM-VFNS). This combines fixed-order contributions to the coefficient functions (or partonic cross sections) calculated with the full m_Q dependence, with the all-order resummation of contributions via DGLAP evolution in which the heavy quarks are treated as massless after starting evolution at some transition point. Transition matrix elements are computed, following [67], which provide the boundary conditions between n_f and n_f+1 PDFs. The ABMP and JR analyses use a FFNS where only the three light (massless) quarks enter the evolution, while the heavy quarks enter the partonic cross sections with their full m_Q dependence. The GM-VFNS and FFNS approaches yield different results: in particular $\alpha_s(M_Z^2)$ and the large-x gluon PDF at large Q^2 are both significantly smaller in the FFNS. It has been argued [48,49,74] that the difference is due to the slow convergence of the $\ln^n(Q^2/m_Q^2)$ terms in certain regions in a FFNS. The final HERA combination of heavy flavour structure function data has recently been published [76], and the evolution of these measurements and their interpretation may be traced in [77].

The most recent determinations of the groups fitting a variety of data and using a GM-VFNS (MMHT, NNPDF and CT) have converged, so that now a good agreement has been achieved between the resulting PDFs. Indeed, the CT14 [59], MMHT2014 [26], and NNPDF3.0 [25] PDF sets have been combined [78] using the Monte Carlo approach [62] mentioned above. The single combined set of PDFs is discussed in detail in Ref. [78].

For illustration, we show in Fig. 18.4 the PDFs obtained in the NNLO NNPDF analysis [25] at scales $\mu^2 = 10$ and 10^4 GeV^2. The values of α_s found by MMHT [79] may be taken as representative of those resulting from the GM-VFNS analyses

$$\text{NLO}: \alpha_s(M_Z^2) = 0.1201 \pm 0.0015,$$

$$\text{NNLO}: \alpha_s(M_Z^2) = 0.1172 \pm 0.0012,$$

where the error (at 68% C.L.) corresponds to the uncertainties resulting from the data fitted (the uncertainty that might be expected from the neglect of higher orders is at least as large). A similar results is found by the NNPDF group [80], who find $\alpha_s(M_Z^2) = 0.1185 \pm 0.0005$ at NNLO. The ABMP analysis [60],which uses a FFNS, finds $\alpha_s(M_Z^2) = 0.1147 \pm 0.0011$ at NNLO.

As a first step towards the inclusion of higher order electroweak corrections a recent development has been a vastly increased understanding of the photon content of the proton. Sets of PDFs with a photon contribution were first considered in Ref. [81] and then in subsequent PDF sets [82,83]. However, due to weak data constraints, the uncertainty was extremely large. Subsequently, there has been a much improved understanding of the separation into elastic and inelastic contributions [84–86]. This gives much more theoretical precision, since the elastic contribution, arising from coherent emission of a photon from the proton, can be directly related to the well-known proton electric and magnetic form factors; the model dependence of the inelastic (incoherent) contribution, related to the quark PDFs, is at the level of tens of percent. A final development directly relating the entire photon contribution to the proton structure function [87] resulted in a determination of the photon content of the proton as precise as that of the light quarks. The framework has been applied within global fits to PDFs via an iterative procedure in [88] and to provide the low-scale input photon PDF in [89].

Nuclear PDFs: The study of the parton distributions for nucleons within nuclei, so-called nuclear parton distribution functions (nPDFs), is now reaching a level of maturity and sophistication similar to nucleon PDFs. The PDFs are now also a function of the nucleon number of the nucleus, A. The nPDFs are obtained via fits to deep inelastic scattering data and dilepton (Drell-Yan) and pion production from proton-nucleus. There are a number of recent examples of NLO analyses, DSSZ [90], nCTEQ15 [91], EPPS16 [92], while an NNLO analysis with a smaller selection of data types now also exists [93]. Much of the heavy-nucleus data included are in the form of ratios to proton or deuteron measurements. And most nuclear PDFs are related to a particular proton PDF via a nuclear modification factor, i.e.

$$f_i^{p/A}(x,Q^2) = R_i^A(x,Q^2) f_i^p(x,Q^2). \qquad (18.30)$$

An exception is the PDFs in [91] which parameterise the nuclear PDFs directly but are equal to proton PDFs in the limit $A = 1$. There is some variation in whether charged current neutrino DIS data is used as well as neutral current DIS data since there is no clear compatibility in the modification factors obtained [94, 95]. Recently, LHC data from vector boson production [96, 97] in proton-lead collisions has been studied [98] or used directly [92], and LHC jet data [99] has been included [92], giving extra constraint on the gluon within nuclei. Further information at smaller x values should soon be extracted from heavy meson production at LHCb [100] and pion production [101]. All the PDF extractions above are based on the Hessian formulation, but the first NNPDF study of nPDFs has appeared [102], so far based on neutral current DIS data only. As well as improved constraints from further LHC data, nPDFs would be significantly improved by data from a potential high-energy Electron-Ion Collider [103].

Polarized PDFs: For spin-dependent structure functions, data exists for a more restricted range of Q^2 and has lower precision, so that the scaling violations are not seen so clearly. However, spin-dependent (or polarized) parton distributions have been extracted by comparison to data using NLO global analyses which include measurements of the g_1 structure function in inclusive polarized

DIS, 'flavour-tagged' semi-inclusive DIS data, open–charm production in DIS and results from polarized pp scattering at RHIC. There are recent results on DIS from JLAB [104] (for g_1^n/F_1^n), COMPASS [105,106] and CLAS [107]. NLO analyses are given in Refs. [108–111] and more recent extractions [112,113]. Improved parton-to-hadron fragmentation functions, needed to describe the semi-inclusive DIS (SIDIS) data, can be found in Refs. [114–117]. Only the DSSV collaboration includes in their NLO analysis to extract polarized PDFs all the world data, inclusive and semi-inclusive DIS, double spin asymmetries in jet, dijet and inclusive

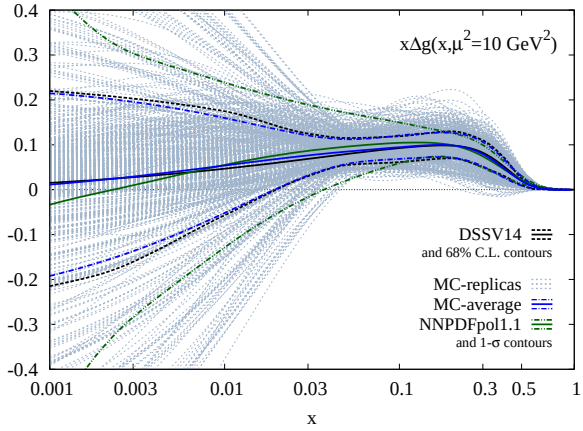

Figure 18.5: Ensemble of replicas (dotted blue lines) for the NLO gluon helicity density $\Delta g(x,Q^2)$ at $Q^2 = 10$ GeV^2 shown along with its statistical average (solid blue line) and variance (dot-dashed blue lines). The corresponding results from the DSSV14 fit (black lines) [112] and the NNPDFpol1.1 analysis (green lines) [27] are shown for comparison. Figure taken from Ref. [118].

π^0-production as well as the single spin asymmetries in $W^\pm, Z^0$ production. A determination [119], using the NNPDF methodology, concentrates just on the inclusive polarized DIS data, and finds the uncertainties on the polarized gluon PDF have been underestimated in the earlier analyses. An update to this [27], where jet and $W^\pm$ data from pp collisions and open–charm DIS data have been included via reweighting, reduces the uncertainty and suggests a positive polarized gluon PDF. The DSSV group has recently implemented a Monte Carlo sampling strategy to extract helicity parton densities and their uncertainties from a reference set of longitudinally polarized scattering data [118].

A comparison of the polarized gluon PDFs obtained in the NLO analyses of NNPDF [27] and DSSV [118] is shown in Fig. 18.5 at scale $\mu^2 = 10$ GeV^2. The world data of the inclusive structure function g_1 for proton and deuterium included in these analysis are shown in Fig. 18.14 and Fig. 18.15.

Comprehensive sets of PDFs are available from the LHAPDF library [120], which can be linked directly into a user's programme to provide access to recent PDFs in a standard format.

18.4 The hadronic structure of the photon

Besides the *direct* interactions of the photon, it is possible for it to fluctuate into a hadronic state via the process $\gamma \to q\bar{q}$. While in this state, the partonic content of the photon may be *resolved*, for example, through the process $e^+e^- \to e^+e^-\gamma^\star\gamma \to e^+e^-X$, where the virtual photon emitted by the DIS lepton probes the hadronic structure of the quasi-real photon emitted by the other lepton. The perturbative LO QED contributions to this process with $\gamma \to q\bar{q}$ in conjunction with $\gamma^\star q(\bar{q}) \to q(\bar{q})$, are subject to QCD corrections due to the radiation of gluons from these quarks.

Often the equivalent-photon approximation is used to express the differential cross section for deep inelastic electron–photon scattering in terms of the structure functions of the transverse quasi-real photon times a flux factor N_γ^T (for these incoming quasi-real photons of transverse polarization)

$$\frac{d^2\sigma}{dxdQ^2} = N_\gamma^T \frac{2\pi\alpha^2}{xQ^4}\left[\left(1+(1-y)^2\right)F_2^\gamma(x,Q^2) - y^2 F_L^\gamma(x,Q^2)\right], \tag{18.31}$$

where we have used $F_2^\gamma = 2xF_T^\gamma + F_L^\gamma$ (where F_T is the transverse structure function), not to be confused with F_2^γ of Sec. 18.2. Complete formulae are given, for example, in the comprehensive review of [121].

The hadronic photon structure function, F_2^γ, evolves with increasing Q^2 from the 'hadron-like' behavior, calculable via the vector-meson-dominance model, to the dominating 'point-like' behaviour, calculable in perturbative QCD. Due to the point-like coupling, the logarithmic evolution of F_2^γ with Q^2 has a *positive* slope for all values of x, see Fig. 18.16. The 'loss' of quarks at large x due to gluon radiation is over-compensated by the 'creation' of quarks via the point-like $\gamma \to q\bar{q}$ coupling. The logarithmic evolution was first predicted in the quark–parton model ($\gamma^\star\gamma \to q\bar{q}$) [122,123], and then an improved expression was obtained using QCD corrections in the limit of large Q^2 [124]. The evolution is now known to NLO [125–127]. The NLO data analyses to determine the parton densities of the photon can be found in Refs. [128–130].

18.5 Diffractive DIS (DDIS)

Some 10% of DIS events are diffractive, $\gamma^* p \to X + p$, in which the slightly deflected proton and the cluster X of outgoing hadrons are well-separated in rapidity [131]. Besides x and Q^2, two extra

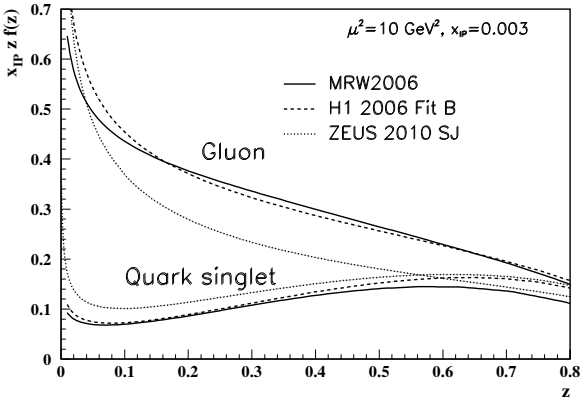

Figure 18.6: Diffractive parton distributions, $x_{I\!P}\, z f^{\rm D}_{a/p}$, obtained from fitting to the ZEUS data with $Q^2 > 5$ GeV^2 [132],H1 data with $Q^2 > 8.5$ GeV^2 assuming Regge factorization [133], and from MRW2006 [134] using a more perturbative QCD approach [134]. Only the Pomeron contributions are shown and not the secondary Reggeon contributions, which are negligible at the value of $x_{I\!P} = 0.003$ chosen here. The H1 2007 Jets distribution [135] is similar to H1 2006 Fit B.

variables are needed to describe a DDIS event: the fraction $x_{I\!P}$ of the proton's momentum transferred across the rapidity gap and t, the square of the 4-momentum transfer of the proton. The DDIS data [136,137] are usually analysed using two levels of factorization. First, the diffractive structure function $F_2^{\rm D}$ satisfies *collinear factorization*, and can be expressed as the convolution [138]

$$F_2^{\rm D} = \sum_{a=q,g} C_2^a \otimes f^{\rm D}_{a/p}, \tag{18.32}$$

with the same coefficient functions as in DIS (see Eq. (18.21)), and where the diffractive parton distributions $f^{\rm D}_{a/p}$ ($a = q, g$) satisfy DGLAP evolution. Second, *Regge factorization* is assumed [139],

$$f^{\rm D}_{a/p}(x_{I\!P}, t, z, \mu^2) = f_{I\!P/p}(x_{I\!P}, t)\, f_{a/I\!P}(z, \mu^2), \tag{18.33}$$

where $f_{a/I\!P}$ are the parton densities of the Pomeron, which itself is treated like a hadron, and $z \in [x/x_{I\!P}, 1]$ is the fraction of the Pomeron's momentum carried by the parton entering the

hard subprocess. The Pomeron flux factor $f_{I\!P/p}(x_{I\!P}, t)$ is taken from Regge phenomenology. There are also secondary Reggeon contributions to Eq. (18.33). A sample of the t-integrated diffractive parton densities, obtained in this way, is shown in Fig. 18.6. A more recent extraction of the parton densities may be found in [140].

Although collinear factorization holds as $\mu^2 \to \infty$, there are non-negligible corrections for finite μ^2 and small $x_{I\!P}$. Besides the *resolved* interactions of the Pomeron, the perturbative QCD Pomeron may also interact *directly* with the hard subprocess, giving rise to an inhomogeneous evolution equation for the diffractive parton densities analogous to the photon case. The results of the MRW analysis [134],which includes these contributions, are also shown in Fig. 18.6.

Unlike the inclusive case, the diffractive parton densities cannot be directly used to calculate diffractive hadron-hadron cross sections, since account must first be taken of "soft" rescattering effects.

18.6 Generalized parton distributions

The parton distributions of the proton of Sec. 18.3 are given by the diagonal matrix elements $\langle P, \lambda | \hat{O} | P, \lambda \rangle$, where P and λ are the 4-momentum and helicity of the proton, and $\hat{O}$ is a twist-2 quark or gluon operator. However, there is new information in the so-called generalised parton distributions (GPDs) defined in terms of the off-diagonal matrix elements $\langle P', \lambda' | \hat{O} | P, \lambda \rangle$; see Refs. [141–146] for reviews. Unlike the diagonal PDFs, the GPDs cannot be regarded as parton densities, but are to be interpreted as probability amplitudes.

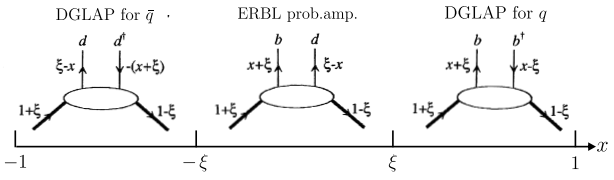

Figure 18.7: Schematic diagrams of the three distinct kinematic regions of the imaginary part of H_q. The proton and quark momentum fractions refer to $\bar{P}^+$, and x covers the interval (-1,1). In the ERBL domain the GPDs are generalisations of distribution amplitudes which occur in processes such as $p\bar{p} \to J/\psi$.

The physical significance of GPDs is best seen using light-cone coordinates, $z^\pm = (z^0 \pm z^3)/\sqrt{2}$, and in the light-cone gauge, $A^+ = 0$. It is conventional to define the generalised quark distributions in terms of quark operators at light-like separation

$$F_q(x,\xi,t) = \frac{1}{2}\int \frac{dz^-}{2\pi} e^{ix\bar{P}^+ z^-} \langle P'|\bar{\psi}(-z/2)\gamma^+\psi(z/2)|P\rangle \Big|_{z^+=z^1=z^2=0} = \frac{1}{2\bar{P}^+} \times \left(H_q(x,\xi,t)\ \bar{u}(P')\gamma^+ u(P) + E_q(x,\xi,t)\ \bar{u}(P')\frac{i\sigma^{+\alpha}\Delta_\alpha}{2m}u(P)\right) \quad (18.34)$$

with $\bar{P} = (P + P')/2$ and $\Delta = P' - P$, and where we have suppressed the helicity labels of the protons and spinors. We now have two extra kinematic variables:

$$t = \Delta^2, \qquad \xi = -\Delta^+/(P + P')^+. \quad (18.35)$$

We see that $-1 \le \xi \le 1$. Similarly, we may define GPDs $\tilde{H}_q$ and $\tilde{E}_q$ with an additional γ_5 between the quark operators in Eq. (18.34); and also an analogous set of gluon GPDs, H_g, E_g, $\tilde{H}_g$ and $\tilde{E}_g$. After a Fourier transform with respect to the transverse components of Δ, we are able to describe the spatial distribution of partons in the impact parameter plane in terms of GPDs [147, 148].

For $P' = P$, $\lambda' = \lambda$ the matrix elements reduce to the ordinary PDFs of Sec. 18.2.1

$$H_q(x,0,0) = q(x), \quad H_q(-x,0,0) = -\bar{q}(x), \quad H_g(x,0,0) = xg(x), \quad (18.36)$$

$$\tilde{H}_q(x,0,0) = \Delta q(x),\ \tilde{H}_q(-x,0,0) = \Delta\bar{q}(x),\ \tilde{H}_g(x,0,0) = x\Delta g(x), \quad (18.37)$$

where $\Delta q = q\uparrow - q\downarrow$ as in Eq. (18.18). No corresponding relations exist for E, $\tilde{E}$ as they decouple in the forward limit, $\Delta = 0$.

The functions H_g, E_g are even in x, and $\tilde{H}_g, \tilde{E}_g$ are odd functions of x. We can introduce valence and 'singlet' quark distributions which are even and odd functions of x respectively. For example

$$H_q^V(x,\xi,t) \equiv H_q(x,\xi,t) + H_q(-x,\xi,t) = H_q^V(-x,\xi,t), \quad (18.38)$$

$$H_q^S(x,\xi,t) \equiv H_q(x,\xi,t) - H_q(-x,\xi,t) = -H_q^S(-x,\xi,t). \quad (18.39)$$

All the GPDs satisfy relations of the form

$$H(x,-\xi,t) = H(x,\xi,t) \qquad \text{and} \qquad H(x,-\xi,t)^* = H(x,\xi,t), \quad (18.40)$$

and so are real-valued functions. Moreover, the moments of GPDs, that is the x integrals of $x^n H_q$ etc., are *polynomials* in ξ of order $n+1$. Another important property of GPDs are Ji's sum rule [141]

$$\frac{1}{2}\int_{-1}^{1} dx\ x\,(H_q(x,\xi,t) + E_q(x,\xi,t)) = J_q(t), \quad (18.41)$$

where $J_q(0)$ is the total angular momentum carried by quarks and antiquarks of flavour q, with a similar relation for gluons.

To visualize the physical content of H_q, we Fourier expand ψ and $\bar{\psi}$ in terms of quark, antiquark creation (b, d) and annihilation ($b^\dagger, d^\dagger$) operators, and sketch the result in Fig. 18.7. There are two types of domain: (i) the time-like or 'annihilation' domain, with $|x| < |\xi|$, where the GPDs describe the wave functions of a t-channel $q\bar{q}$ (or gluon) pair and evolve according to modified ERBL equations [149,150]; (ii) the space-like or 'scattering' domain, with $|x| > |\xi|$, where the GPDs generalise the familiar $\bar{q}$, q (and gluon) PDFs and describe processes such as 'deeply virtual Compton scattering' ($\gamma^* p \to \gamma p$), $\gamma p \to J/\psi p$, etc., and evolve according to modified DGLAP equations. The splitting functions for the evolution of GPDs are known to NLO [151–153].

GPDs describe new aspects of proton structure and must be determined from experiment. We can parametrise them in terms of 'double distributions' [154,155], which reduce to diagonal PDFs as $\xi \to 0$. Alternatively, flexible $SO(3)$-based parametrisations have been used to determine GPDs from DVCS data [156,157]; a more recent summary may be found in Ref. [158,159].

18.7 Transverse momentum dependent distributions

Transverse momentum dependent distributions (TMDs) are complementary to GPDs. Together, they describe the three-dimensional structure of hadrons. In contrast to GPDs that encode the transverse position of a parton in a nucleon, TMDs encompassing both the parton distributions (TMD PDF) and fragmentation functions (TMD FF) encode the transverse momenta and lead to observable transverse momenta in the final state. Both TMDs and GPDs derive, via integration over the appropriate variable, from Wigner distributions [160–162] that depend on the average transverse momentum and position of partons.

For a proton, there are eight independent TMD PDFs, at leading twist, three of which correspond to the usual unpolarized, longitudinally polarized and transversely polarized quark parton distributions [163, 164]. The novel TMD PDFs have physical interpretations. For example, the Sivers function [165] represents the distribution of unpolarized partons inside a transversely polarized hadron. For (pseudo)scalar particles, such as kaon and pions, there are two independent leading-twist TMD FFs, one being the ordinary unpolarized fragmentation function and the other the Collins FF [166] which is related to the probability of a polarized quark fragmenting into an unpolarized hadron.

Factorization of TMDs have been shown for semi-inclusive DIS, for the Drell-Yan process as well as for electron-position annihilation into dihadrons [167–172]. Recently first TMD global fits have become available [173–180], although problems with consistent descriptions still remain [181, 182].

Because TMD PDFs encode nonperturbative information about transverse momentum and polarization degrees of freedom, they are important for descriptions of multi-scale, non-inclusive collider observables, for example, production of electroweak gauge bosons at LHC [183] and can have an effect on determination of the W boson mass [184]. The combination of TMD PDFs an FFs can give consistent global description of spin and azimuthal asymmetries and provide predictions. Some recent reviews of this rapidly developing field are given here [183, 185–187].

References

[1] J. Blumlein and N. Kochelev, Nucl. Phys. **B498**, 285 (1997), [hep-ph/9612318].

[2] S. Forte, M. L. Mangano and G. Ridolfi, Nucl. Phys. **B602**, 585 (2001), [hep-ph/0101192].

[3] M. Anselmino, P. Gambino and J. Kalinowski, Z. Phys. **C64**, 267 (1994), [hep-ph/9401264].

[4] M. Anselmino, A. Efremov and E. Leader, Phys. Rept. **261**, 1 (1995), [Erratum: Phys. Rept.281,399(1997)], [hep-ph/9501369].

[5] M. Klein and T. Riemann, Z. Phys. **C24**, 151 (1984).

[6] C. G. Callan, Jr. and D. J. Gross, Phys. Rev. Lett. **22**, 156 (1969).

[7] D. A. Dicus, Phys. Rev. **D5**, 1367 (1972).

[8] J. D. Bjorken and E. A. Paschos, Phys. Rev. **185**, 1975 (1969).

[9] R.P. Feynman, Photon Hadron Interactions (Benjamin, New York, 1972).

[10] A.M. Cooper-Sarkar, private communication.

[11] H. Abramowicz *et al.* (H1, ZEUS), Eur. Phys. J. **C75**, 12, 580 (2015), [arXiv:1506.06042].

[12] L. A. Harland-Lang *et al.*, Eur. Phys. J. **C76**, 4, 186 (2016), [arXiv:1601.03413].

[13] I. Abt *et al.*, Phys. Rev. **D94**, 3, 034032 (2016), [arXiv:1604.02299].

[14] R. D. Ball *et al.*, Eur. Phys. J. **C78**, 4, 321 (2018), [arXiv:1710.05935].

[15] H. Abdolmaleki *et al.* (xFitter Developers' Team), Eur. Phys. J. **C78**, 8, 621 (2018), [arXiv:1802.00064].

[16] S. Wandzura and F. Wilczek, Phys. Lett. **72B**, 195 (1977).

[17] J. Blumlein and A. Tkabladze, Nucl. Phys. **B553**, 427 (1999), [hep-ph/9812478].

[18] J. D. Bjorken, Phys. Rev. **179**, 1547 (1969).

[19] V. N. Gribov and L. N. Lipatov, Sov. J. Nucl. Phys. **15**, 438 (1972), [Yad. Fiz.15,781(1972)].

[20] L.N. Lipatov, Sov. J. Nucl. Phys. **20**, 95 (1975).

[21] G. Altarelli and G. Parisi, Nucl. Phys. **B126**, 298 (1977).

[22] Y. L. Dokshitzer, Sov. Phys. JETP **46**, 641 (1977), [Zh. Eksp. Teor. Fiz.73,1216(1977)].

[23] O. Zenaiev *et al.* (PROSA), Eur. Phys. J. **C75**, 8, 396 (2015), [arXiv:1503.04581].

[24] R. Aaij *et al.* (LHCb), J. Phys. **G41**, 055002 (2014), [arXiv:1401.3288].

[25] R. D. Ball *et al.* (NNPDF), JHEP **04**, 040 (2015), [arXiv:1410.8849].

[26] L. A. Harland-Lang *et al.*, Eur. Phys. J. **C75**, 5, 204 (2015), [arXiv:1412.3989].

[27] E. R. Nocera *et al.* (NNPDF), Nucl. Phys. **B887**, 276 (2014), [arXiv:1406.5539].

[28] G. Curci, W. Furmanski and R. Petronzio, Nucl. Phys. **B175**, 27 (1980); W. Furmanski and R. Petronzio, Phys. Lett. **97B**, 437 (1980).

[29] R.K. Ellis *et al.*, QCD and Collider Physics (Cambridge UP, 1996).

[30] W. L. van Neerven and E. B. Zijlstra, Phys. Lett. **B272**, 127 (1991); E. B. Zijlstra and W. L. van Neerven, Phys. Lett. **B273**, 476 (1991); E. B. Zijlstra and W. L. van Neerven, Phys. Lett. **B297**, 377 (1992); E. B. Zijlstra and W. L. van Neerven, Nucl. Phys. **B383**, 525 (1992).

[31] S. Moch and J. A. M. Vermaseren, Nucl. Phys. **B573**, 853 (2000), [hep-ph/9912355].

[32] S. Moch, J. A. M. Vermaseren and A. Vogt, Nucl. Phys. **B688**, 101 (2004), [hep-ph/0403192]; A. Vogt, S. Moch and J. A. M. Vermaseren, Nucl. Phys. **B691**, 129 (2004), [hep-ph/0404111]; S. Moch, J. A. M. Vermaseren and A. Vogt, Phys. Lett. **B606**, 123 (2005), [hep-ph/0411112]; J. A. M. Vermaseren, A. Vogt and S. Moch, Nucl. Phys. **B724**, 3 (2005), [hep-ph/0504242].

[33] V. S. Fadin, E. A. Kuraev and L. N. Lipatov, Phys. Lett. **60B**, 50 (1975); E. A. Kuraev, L. N. Lipatov and V. S. Fadin, Sov. Phys. JETP **44**, 443 (1976), [Zh. Eksp. Teor. Fiz.71,840(1976)]; E. A. Kuraev, L. N. Lipatov and V. S. Fadin, Sov. Phys. JETP **45**, 199 (1977), [Zh. Eksp. Teor. Fiz.72,377(1977)].

[34] I. I. Balitsky and L. N. Lipatov, Sov. J. Nucl. Phys. **28**, 822 (1978), [Yad. Fiz.28,1597(1978)].

[35] V. S. Fadin and L. N. Lipatov, Phys. Lett. **B429**, 127 (1998), [hep-ph/9802290].

[36] G. Camici and M. Ciafaloni, Phys. Lett. **B412**, 396 (1997), [Erratum: Phys. Lett.B417,390(1998)], [hep-ph/9707390]; M. Ciafaloni and G. Camici, Phys. Lett. **B430**, 349 (1998), [hep-ph/9803389].

[37] M. Ciafaloni, D. Colferai and G. P. Salam, Phys. Rev. **D60**, 114036 (1999), [hep-ph/9905566]; M. Ciafaloni, D. Colferai and G. P. Salam, JHEP **07**, 054 (2000), [hep-ph/0007240].

[38] M. Ciafaloni *et al.*, Phys. Lett. **B576**, 143 (2003), [hep-ph/0305254]; M. Ciafaloni *et al.*, Phys. Rev. **D68**, 114003 (2003), [hep-ph/0307188].

[39] G. Altarelli, R. D. Ball and S. Forte, Nucl. Phys. **B742**, 1 (2006), [hep-ph/0512237]; G. Altarelli, R. D. Ball and S. Forte, Nucl. Phys. **B799**, 199 (2008), [arXiv:0802.0032].

[40] C. D. White and R. S. Thorne, Phys. Rev. **D75**, 034005 (2007), [hep-ph/0611204].

[41] M. Bonvini, S. Marzani and T. Peraro, Eur. Phys. J. **C76**, 11, 597 (2016), [arXiv:1607.02153].

[42] M. Bonvini, S. Marzani and C. Muselli, JHEP **12**, 117 (2017), [arXiv:1708.07510].

[43] G. 't Hooft and M. J. G. Veltman, Nucl. Phys. **B44**, 189 (1972).

[44] G. 't Hooft, Nucl. Phys. **B61**, 455 (1973).

[45] W. A. Bardeen *et al.*, Phys. Rev. **D18**, 3998 (1978).

[46] G. Altarelli, R. K. Ellis and G. Martinelli, Nucl. Phys. **B143**, 521 (1978), [Erratum: Nucl. Phys.B146,544(1978)].

[47] A. D. Martin *et al.*, Eur. Phys. J. **C35**, 325 (2004), [hep-ph/0308087].

[48] R. D. Ball *et al.* (NNPDF), Phys. Lett. **B723**, 330 (2013), [arXiv:1303.1189].

[49] R. S. Thorne, Eur. Phys. J. **C74**, 7, 2958 (2014), [arXiv:1402.3536].

[50] M. Dasgupta and B. R. Webber, Phys. Lett. **B382**, 273 (1996), [hep-ph/9604388].

[51] A. De Roeck and R. S. Thorne, Prog. Part. Nucl. Phys. **66**, 727 (2011), [arXiv:1103.0555].

[52] S. Forte and G. Watt, Ann. Rev. Nucl. Part. Sci. **63**, 291 (2013), [arXiv:1301.6754].

[53] J. Blumlein, Prog. Part. Nucl. Phys. **69**, 28 (2013), [arXiv:1208.6087].

[54] E. Perez and E. Rizvi, Rept. Prog. Phys. **76**, 046201 (2013), [arXiv:1208.1178].

[55] R. D. Ball *et al.*, JHEP **04**, 125 (2013), [arXiv:1211.5142].

[56] J. Gao, L. Harland-Lang and J. Rojo, Phys. Rept. **742**, 1 (2018), [arXiv:1709.04922].

[57] J. Rojo *et al.*, J. Phys. **G42**, 103103 (2015), [arXiv:1507.00556].

[58] R. D. Ball *et al.* (NNPDF), Eur. Phys. J. **C77**, 10, 663 (2017), [arXiv:1706.00428].

[59] CT_{14}, S. Dulat *et al.*, Phys. Rev. **D93**, 3, 033006 (2016), [arXiv:1506.07443].

[60] S. Alekhin *et al.*, Phys. Rev. **D96**, 1, 014011 (2017), [arXiv:1701.05838].

[61] P. Jimenez-Delgado and E. Reya, Phys. Rev. **D89**, 7, 074049 (2014), [arXiv:1403.1852].

[62] G. Watt and R. S. Thorne, JHEP **08**, 052 (2012), [arXiv:1205.4024].

[63] S. Carrazza *et al.*, Eur. Phys. J. **C75**, 8, 369 (2015), [arXiv:1505.06736].

[64] J. C. Collins, F. Wilczek and A. Zee, Phys. Rev. **D18**, 242 (1978).

[65] E. Laenen *et al.*, Nucl. Phys. **B392**, 162 (1993).

[66] M. A. G. Aivazis *et al.*, Phys. Rev. **D50**, 3102 (1994), [hep-ph/9312319].

[67] M. Buza *et al.*, Eur. Phys. J. **C1**, 301 (1998), [hep-ph/9612398].

[68] J. C. Collins, Phys. Rev. **D58**, 094002 (1998), [hep-ph/9806259].

[69] A. Chuvakin, J. Smith and W. L. van Neerven, Phys. Rev. **D61**, 096004 (2000), [hep-ph/9910250].

[70] R. S. Thorne, Phys. Rev. **D73**, 054019 (2006), [hep-ph/0601245].

[71] R. S. Thorne and W. K. Tung, in "Proceedings, HERA and the LHC Workshop Series on the implications of HERA for LHC physics: 2006-2008," 332–351 (2008), [,2(2008)], [arXiv:0809.0714].

[72] S. Alekhin and S. Moch, Phys. Lett. **B699**, 345 (2011), [arXiv:1011.5790].

[73] S. Forte *et al.*, Nucl. Phys. **B834**, 116 (2010), [arXiv:1001.2312].

[74] R. S. Thorne, Phys. Rev. **D86**, 074017 (2012), [arXiv:1201.6180].

[75] E. G. de Oliveira *et al.*, Eur. Phys. J. **C73**, 10, 2616 (2013), [arXiv:1307.3508].

[76] H. Abramowicz *et al.* (H1, ZEUS), Eur. Phys. J. **C78**, 6, 473 (2018), [arXiv:1804.01019].

[77] O. Behnke, A. Geiser and M. Lisovyi, Prog. Part. Nucl. Phys. **84**, 1 (2015), [arXiv:1506.07519].

[78] J. Butterworth *et al.*, J. Phys. **G43**, 023001 (2016), [arXiv:1510.03865].

[79] L. A. Harland-Lang *et al.*, Eur. Phys. J. **C75**, 9, 435 (2015), [arXiv:1506.05682].

[80] R. D. Ball *et al.* (NNPDF), Eur. Phys. J. **C78**, 5, 408 (2018), [arXiv:1802.03398].

[81] A. D. Martin *et al.*, Eur. Phys. J. **C39**, 155 (2005), [hep-ph/0411040].

[82] R. D. Ball *et al.* (NNPDF), Nucl. Phys. **B877**, 290 (2013), [arXiv:1308.0598].

[83] C. Schmidt *et al.*, Phys. Rev. **D93**, 11, 114015 (2016), [arXiv:1509.02905].

[84] M. Gluck, C. Pisano and E. Reya, Phys. Lett. **B540**, 75 (2002), [hep-ph/0206126].

[85] A. D. Martin and M. G. Ryskin, Eur. Phys. J. **C74**, 3040 (2014), [arXiv:1406.2118].

[86] L. A. Harland-Lang, V. A. Khoze and M. G. Ryskin, Phys. Rev. **D94**, 7, 074008 (2016), [arXiv:1607.04635].

[87] A. Manohar *et al.*, Phys. Rev. Lett. **117**, 24, 242002 (2016), [arXiv:1607.04266].

[88] V. Bertone *et al.* (NNPDF), SciPost Phys. **5**, 1, 008 (2018), [arXiv:1712.07053].

[89] L. A. Harland-Lang *et al.*, Eur. Phys. J. **C79**, 10, 811 (2019), [arXiv:1907.02750].

[90] D. de Florian *et al.*, Phys. Rev. **D85**, 074028 (2012), [arXiv:1112.6324].

[91] K. Kovarik *et al.*, Phys. Rev. **D93**, 8, 085037 (2016), [arXiv:1509.00792].

[92] H. Paukkunen, Nucl. Phys. **A967**, 241 (2017), [arXiv:1704.04036].

[93] H. Khanpour and S. Atashbar Tehrani, Phys. Rev. **D93**, 1, 014026 (2016), [arXiv:1601.00939].

[94] K. Kovarik *et al.*, Phys. Rev. Lett. **106**, 122301 (2011), [arXiv:1012.0286].

[95] H. Paukkunen and C. A. Salgado, Phys. Rev. Lett. **110**, 21, 212301 (2013), [arXiv:1302.2001].

[96] G. Aad *et al.* (ATLAS), Phys. Rev. **C92**, 4, 044915 (2015), [arXiv:1507.06232].

[97] V. Khachatryan *et al.* (CMS), Phys. Lett. **B750**, 565 (2015), [arXiv:1503.05825].

[98] A. Kusina *et al.*, Eur. Phys. J. **C77**, 7, 488 (2017), [arXiv:1610.02925].

[99] S. Chatrchyan *et al.* (CMS), Eur. Phys. J. **C74**, 7, 2951 (2014), [arXiv:1401.4433].

[100] R. Aaij *et al.* (LHCb), JHEP **10**, 090 (2017), [arXiv:1707.02750].

[101] S. Acharya *et al.* (ALICE), Eur. Phys. J. **C78**, 8, 624 (2018), [arXiv:1801.07051].

[102] R. Abdul Khalek, J. J. Ethier and J. Rojo (NNPDF), Eur. Phys. J. **C79**, 6, 471 (2019), [arXiv:1904.00018].

[103] E. C. Aschenauer *et al.*, Phys. Rev. **D96**, 11, 114005 (2017), [arXiv:1708.05654].

[104] D. Flay *et al.* (Jefferson Lab Hall A), Phys. Rev. **D94**, 5, 052003 (2016), [arXiv:1603.03612].

[105] C. Adolph *et al.* (COMPASS), Phys. Lett. **B753**, 18 (2016), [arXiv:1503.08935].

[106] C. Adolph *et al.* (COMPASS), Phys. Lett. **B769**, 34 (2017), [arXiv:1612.00620].

[107] R. Fersch *et al.* (CLAS), Phys. Rev. **C96**, 6, 065208 (2017), [arXiv:1706.10289].

[108] M. Hirai and S. Kumano (Asymmetry Analysis), Nucl. Phys. **B813**, 106 (2009), [arXiv:0808.0413].

[109] D. de Florian *et al.*, Phys. Rev. Lett. **101**, 072001 (2008), [arXiv:0804.0422]; D. de Florian *et al.*, Phys. Rev. **D80**, 034030 (2009), [arXiv:0904.3821].

[110] E. Leader, A. V. Sidorov and D. B. Stamenov, Phys. Rev. **D82**, 114018 (2010), [arXiv:1010.0574].

[111] J. Blumlein and H. Bottcher, Nucl. Phys. **B841**, 205 (2010), [arXiv:1005.3113].

[112] D. de Florian *et al.*, Phys. Rev. Lett. **113**, 1, 012001 (2014), [arXiv:1404.4293].

[113] N. Sato *et al.* (Jefferson Lab Angular Momentum), Phys. Rev. **D93**, 7, 074005 (2016), [arXiv:1601.07782].

[114] D. de Florian *et al.*, Phys. Rev. **D91**, 1, 014035 (2015), [arXiv:1410.6027].

[115] D. de Florian *et al.*, Phys. Rev. **D95**, 9, 094019 (2017), [arXiv:1702.06353].

[116] V. Bertone *et al.* (NNPDF), Eur. Phys. J. **C77**, 8, 516 (2017), [arXiv:1706.07049].

[117] V. Bertone *et al.* (NNPDF), Eur. Phys. J. **C78**, 8, 651 (2018), [arXiv:1807.03310].

[118] D. De Florian *et al.* (2019), [arXiv:1902.10548].

[119] R. D. Ball *et al.* (NNPDF), Nucl. Phys. **B874**, 36 (2013), [arXiv:1303.7236].

[120] A. Buckley *et al.*, Eur. Phys. J. **C75**, 132 (2015), [arXiv:1412.7420].

[121] R. Nisius, Phys. Rept. **332**, 165 (2000), [hep-ex/9912049].

[122] T. F. Walsh and P. M. Zerwas, Phys. Lett. **44B**, 195 (1973).

[123] R. L. Kingsley, Nucl. Phys. **B60**, 45 (1973).

[124] E. Witten, Nucl. Phys. **B120**, 189 (1977).

[125] W. A. Bardeen and A. J. Buras, Phys. Rev. **D20**, 166 (1979), [Erratum: Phys. Rev.D21,2041(1980)].

[126] M. Fontannaz and E. Pilon, Phys. Rev. **D45**, 382 (1992).

[127] M. Gluck, E. Reya and A. Vogt, Phys. Rev. **D45**, 3986 (1992).

[128] F. Cornet, P. Jankowski and M. Krawczyk, Phys. Rev. **D70**, 093004 (2004), [hep-ph/0404063].

[129] P. Aurenche, M. Fontannaz and J. P. Guillet, Eur. Phys. J. **C44**, 395 (2005), [hep-ph/0503259].

[130] W. Slominski, H. Abramowicz and A. Levy, Eur. Phys. J. **C45**, 633 (2006), [hep-ph/0504003].

[131] H. Abramowicz and A. Caldwell, Rev. Mod. Phys. **71**, 1275 (1999), [hep-ex/9903037].

[132] S. Chekanov *et al.* (ZEUS), Nucl. Phys. **B831**, 1 (2010), [arXiv:0911.4119].

[133] A. Aktas *et al.* (H1), Eur. Phys. J. **C48**, 715 (2006), [hep-ex/0606004].

[134] A. D. Martin, M. G. Ryskin and G. Watt, Phys. Lett. **B644**, 131 (2007), [hep-ph/0609273].

[135] A. Aktas *et al.* (H1), JHEP **10**, 042 (2007), [arXiv:0708.3217].

[136] F. D. Aaron *et al.* (H1, ZEUS), Eur. Phys. J. **C72**, 2175 (2012), [arXiv:1207.4864].

[137] F. D. Aaron *et al.* (H1), Eur. Phys. J. **C72**, 2074 (2012), [arXiv:1203.4495].

[138] J. C. Collins, Phys. Rev. **D57**, 3051 (1998), [Erratum: Phys. Rev.D61,019902(2000)], [hep-ph/9709499].

[139] G. Ingelman and P. E. Schlein, Phys. Lett. **152B**, 256 (1985).

[140] M. Goharipour, H. Khanpour and V. Guzey, Eur. Phys. J. **C78**, 4, 309 (2018), [arXiv:1802.01363].

[141] X.-D. Ji, J. Phys. **G24**, 1181 (1998), [hep-ph/9807358].

[142] K. Goeke, M. V. Polyakov and M. Vanderhaeghen, Prog. Part. Nucl. Phys. **47**, 401 (2001), [hep-ph/0106012].

[143] M. Diehl, Phys. Rept. **388**, 41 (2003), [hep-ph/0307382].

[144] A. V. Belitsky and A. V. Radyushkin, Phys. Rept. **418**, 1 (2005), [hep-ph/0504030].

[145] S. Boffi and B. Pasquini, Riv. Nuovo Cim. **30**, 387 (2007), [arXiv:0711.2625].

[146] K. Kumericki, S. Liuti and H. Moutarde, Eur. Phys. J. **A52**, 6, 157 (2016), [arXiv:1602.02763].

[147] M. Burkardt, Int. J. Mod. Phys. **A18**, 173 (2003), [hep-ph/0207047].

[148] M. Diehl, Eur. Phys. J. **C25**, 223 (2002), [Erratum: Eur. Phys. J.C31,277(2003)], [hep-ph/0205208].

[149] A. V. Efremov and A. V. Radyushkin, Phys. Lett. **94B**, 245 (1980).

[150] G. P. Lepage and S. J. Brodsky, Phys. Rev. **D22**, 2157 (1980).

[151] A. V. Belitsky, A. Freund and D. Mueller, Phys. Lett. **B493**, 341 (2000), [hep-ph/0008005].

[152] A. V. Belitsky, A. Freund and D. Mueller, Nucl. Phys. **B574**, 347 (2000), [hep-ph/9912379].

[153] V. M. Braun *et al.*, JHEP **06**, 037 (2017), [arXiv:1703.09532].

[154] A. V. Radyushkin, Phys. Rev. **D59**, 014030 (1999), [hep-ph/9805342].

[155] A. V. Radyushkin, Phys. Lett. **B449**, 81 (1999), [hep-ph/9810466].

[156] K. Kumerički and D. Mueller, Nucl. Phys. **B841**, 1 (2010), [arXiv:0904.0458].

[157] N. d'Hose, S. Niccolai and A. Rostomyan, Eur. Phys. J. **A52**, 6, 151 (2016).

[158] M. Guidal, H. Moutarde and M. Vanderhaeghen, Rept. Prog. Phys. **76**, 066202 (2013), [arXiv:1303.6600].

[159] M. Anselmino, M. Guidal and P. Rossi, The European Physical Journal A **52**, 6, 149 (2016), ISSN 1434-601X, URL `https://doi.org/10.1140/epja/i2016-16164-4`.

[160] X. Ji, Phys. Rev. Lett. **91**, 062001 (2003), [hep-ph/0304037].

[161] A. V. Belitsky, X. Ji and F. Yuan, Phys. Rev. **D69**, 074014 (2004), [hep-ph/0307383].

[162] C. Lorce, B. Pasquini and M. Vanderhaeghen, JHEP **05**, 041 (2011), [arXiv:1102.4704].

[163] P. J. Mulders and R. D. Tangerman, Nucl. Phys. **B461**, 197 (1996), [Erratum: Nucl. Phys.B484,538(1997)], [hep-ph/9510301].

[164] D. Boer and P. J. Mulders, Phys. Rev. **D57**, 5780 (1998), [hep-ph/9711485].

[165] D. W. Sivers, Phys. Rev. **D41**, 83 (1990).

[166] J. C. Collins, Nucl. Phys. **B396**, 161 (1993), [hep-ph/9208213].

[167] X. Ji, J. Ma and F. Yuan, Phys. Rev. **D71**, 034005 (2005), [hep-ph/0404183].

[168] J. Collins, Foundations of perturbative QCD Camb. Monogr. Part. Phys. Nucl. Phys. Cosmol. 32 (2011) 1-624 and references therein.

[169] S. M. Aybat and T. C. Rogers, Phys. Rev. **D83**, 114042 (2011), [arXiv:1101.5057].

[170] M. G. Echevarria, A. Idilbi and I. Scimemi, JHEP **07**, 002 (2012), [arXiv:1111.4996].

[171] M. G. A. Buffing, A. Mukherjee and P. J. Mulders, Phys. Rev. **D88**, 054027 (2013), [arXiv:1306.5897].

[172] T. C. Rogers and P. J. Mulders, Phys. Rev. **D81**, 094006 (2010), [arXiv:1001.2977].

[173] A. Signori *et al.*, JHEP **11**, 194 (2013), [arXiv:1309.3507].

[174] M. Anselmino *et al.*, JHEP **04**, 005 (2014), [arXiv:1312.6261].

[175] U. D'Alesio *et al.*, JHEP **11**, 098 (2014), [arXiv:1407.3311].

[176] M. G. Echevarria *et al.*, Phys. Rev. **D89**, 074013 (2014), [arXiv:1401.5078].

[177] P. Sun *et al.*, Int. J. Mod. Phys. **A33**, 11, 1841006 (2018), [arXiv:1406.3073].

[178] A. Bacchetta *et al.*, JHEP **06**, 081 (2017), [Erratum: JHEP06,051(2019)], [arXiv:1703.10157].

[179] I. Scimemi and A. Vladimirov, Eur. Phys. J. **C78**, 2, 89 (2018), [arXiv:1706.01473].

[180] V. Bertone, I. Scimemi and A. Vladimirov, JHEP **06**, 028 (2019), [arXiv:1902.08474].

[181] J. O. Gonzalez-Hernandez *et al.*, Phys. Rev. **D98**, 11, 114005 (2018), [arXiv:1808.04396].

[182] A. Bacchetta *et al.*, Phys. Rev. **D100**, 1, 014018 (2019), [arXiv:1901.06916].

[183] R. Angeles-Martinez *et al.*, Acta Phys. Polon. **B46**, 12, 2501 (2015), [arXiv:1507.05267].

[184] A. Bacchetta *et al.*, Phys. Lett. **B788**, 542 (2019), [arXiv:1807.02101].

[185] M. Diehl, Eur. Phys. J. **A52**, 6, 149 (2016), [arXiv:1512.01328].

[186] A. Bacchetta, Eur. Phys. J. **A52**, 6, 163 (2016).

[187] `http://hepdata.cedar.ac.uk/pdfs`.

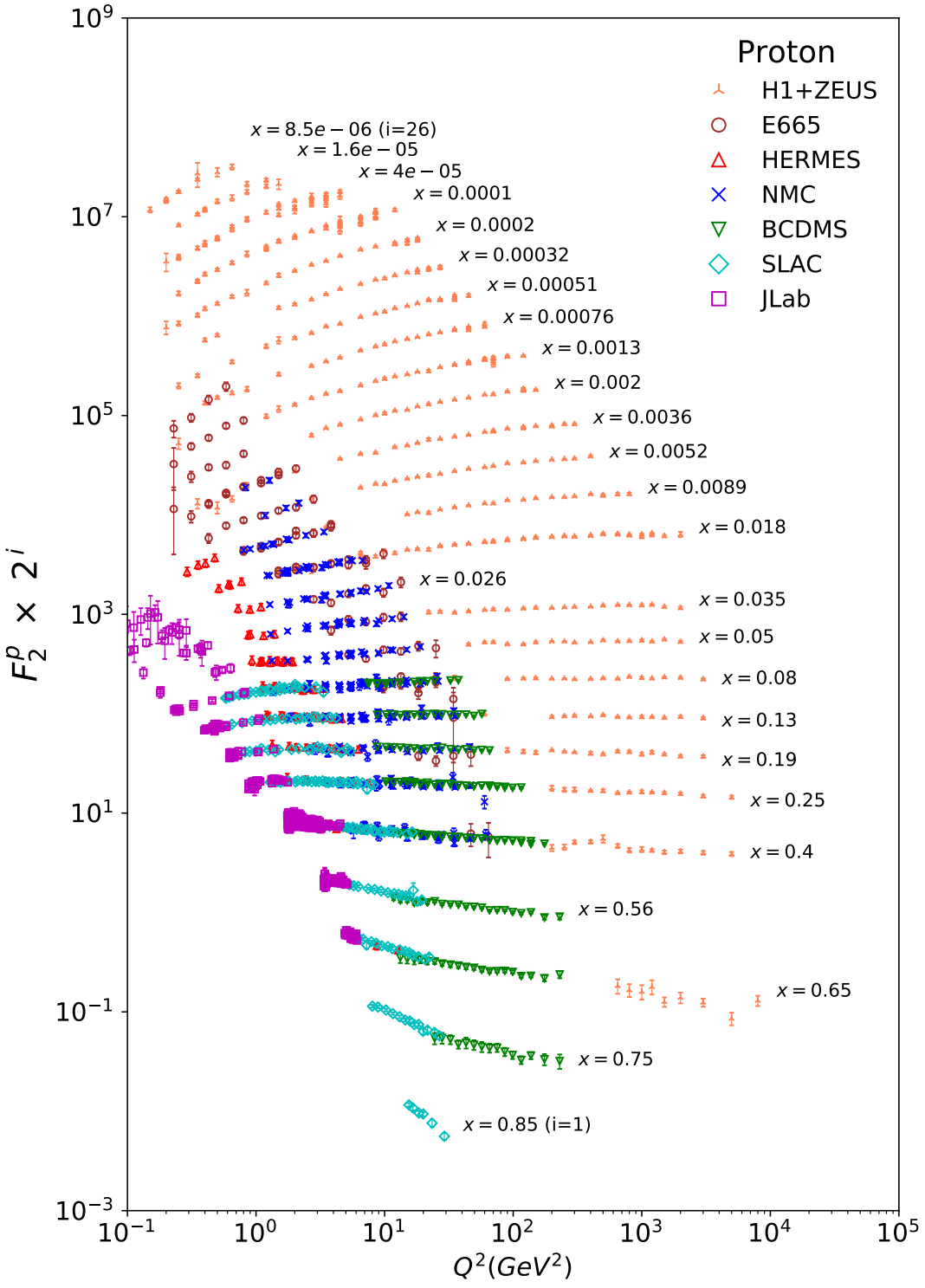

Figure 18.8: The proton structure function F_2^p measured in electromagnetic scattering of electrons and positrons on protons, and for electrons/positrons (SLAC,HERMES,JLAB) and muons (BCDMS, E665, NMC) on a fixed target. Statistical and systematic errors added in quadrature are shown. The H1+ZEUS combined values are obtained from the measured reduced cross section and converted to F_2^p with a HERAPDF NLO fit, for all measured points where the predicted ratio of F_2^p to reduced cross-section was within 10% of unity. The data are plotted as a function of Q^2 in bins of fixed x. Some points have been slightly offset in Q^2 for clarity. The H1+ZEUS combined binning in x is used in this plot; all other data are rebinned to the x values of these data. For the purpose of plotting, F_2^p has been multiplied by 2^{i_x}, where i_x is the number of the x bin, ranging from $i_x = 1$ ($x = 0.85$) to $i_x = 26$ ($x = 0.0000085$). Only data with $W^2 > 3.5$ GeV^2 is included. Plot from CJ collaboration (Shujie Li – private communication). References: **H1 and ZEUS**—H. Abramowicz *et al.*, Eur. Phys. J. **C75**, 580 (2015) (for both data and HERAPDF parameterization); **BCDMS**—A.C. Benvenuti *et al.*, Phys. Lett. **B223**, 485 (1989) (as given in [187]} **E665**—M.R. Adams *et al.*, Phys. Rev. **D54**, 3006 (1996); **NMC**—M. Arneodo *et al.*, Nucl. Phys. **B483**, 3 (1997); **SLAC**—L.W. Whitlow *et al.*, Phys. Lett. **B282**, 475 (1992); **HERMES**—A. Airapetian *et al.*, JHEP **1105**, 126 (2011);**JLAB**—Y. Liang *et al.*, Jefferson Lab Hall C E94-110 collaboration, nucl-ex/0410027, M.E. Christy *et al.*, Jefferson Lab Hall C E94-110 Collaboration, Phys. Rev. **C70**, 015206 (2004), S. Malace *et al.*, Jefferson Lab Hall C E00-116 Collaboration, Phys. Rev. **C80**, 035207 (2009), V. Tvaskis *et al.*, Jefferson Lab Hall C E99-118 Collaboration, Phys. Rev. **C81**, 055207 (2010), M. Osipenko *et al.*, Jefferson Lab Hall B CLAS6 Collaboration, Phys. Rev. **D67**, 092001 (2003).

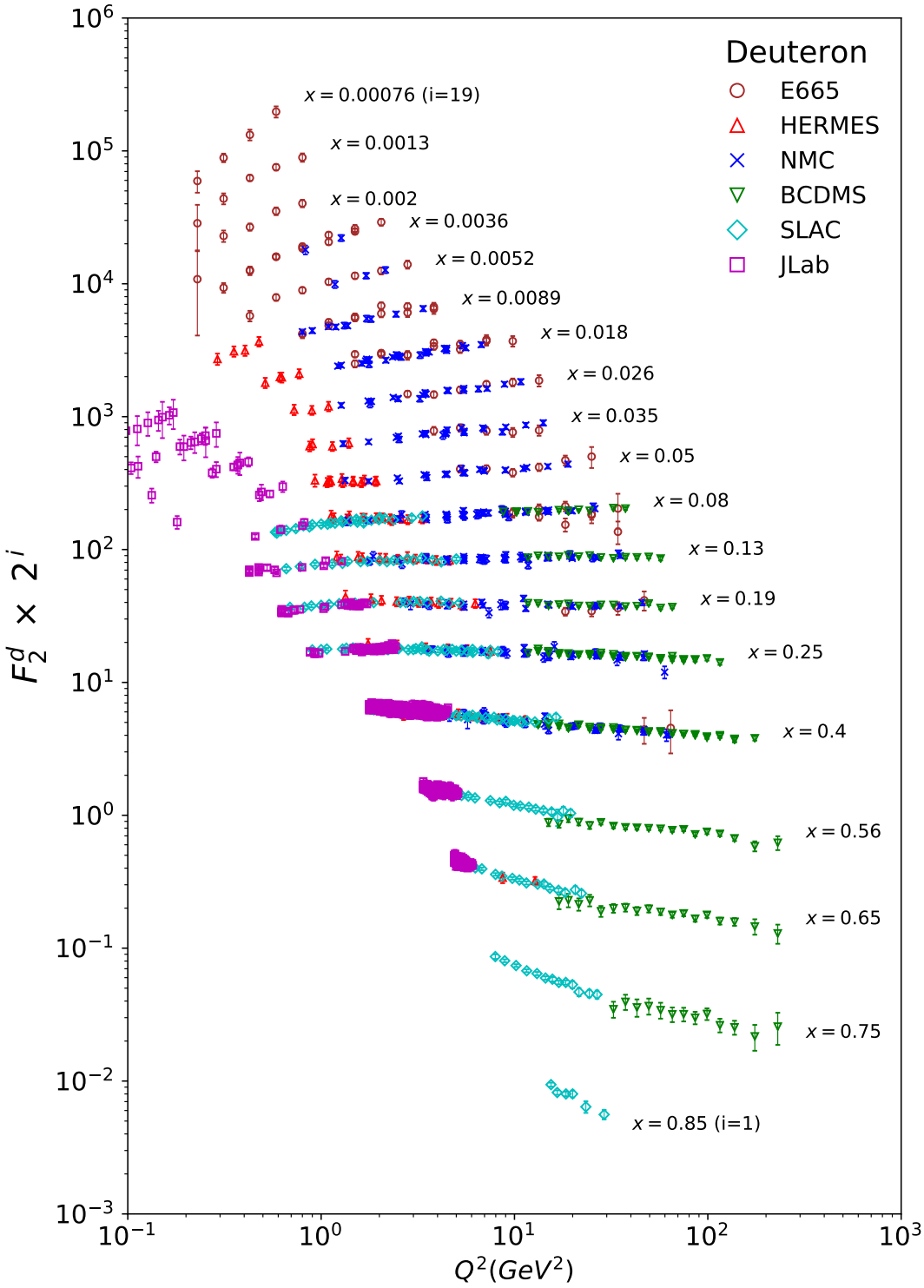

Figure 18.9: The deuteron structure function F_2^d measured in electromagnetic scattering of electrons/positrons (SLAC,HERMES,JLAB) and muons (BCDMS, E665, NMC) on a fixed target, shown as a function of Q^2 for bins of fixed x. Statistical and systematic errors added in quadrature are shown. For the purpose of plotting, F_2^d has been multiplied by 2^{i_x}, where i_x is the number of the x bin, ranging from 1 ($x = 0.85$) to 29 ($x = 0.00076$). Only data with $W^2 > 3.5$ GeV^2 is included. Plot from CJ collaboration (Shujie Li – private communication) References: **BCDMS**—A.C. Benvenuti *et al.*, Phys. Lett. **B237**, 592 (1990). **E665, NMC, SLAC,HERMES**—same references as Fig. 18.8; **JLAB**—S. Malace *et al.*, Jefferson Lab Hall C E00-116 Collaboration, Phys. Rev. **C80**, 035207 (2009), V. Tvaskis *et al.*, Jefferson Lab Hall C E99-118 Collaboration, Phys. Rev. **C81**, 055207 (2010), J. Seely (MIT, LNS) *et al.*, Jefferson Lab Hall C E03-103 Collaboration, Phys. Rev. Lett. **103**, 202301 (2009), M. Osipenko *et al.*, Jefferson Lab Hall B CLAS6 Collaboration, Phys. Rev. **C73**, 045205 (2006).

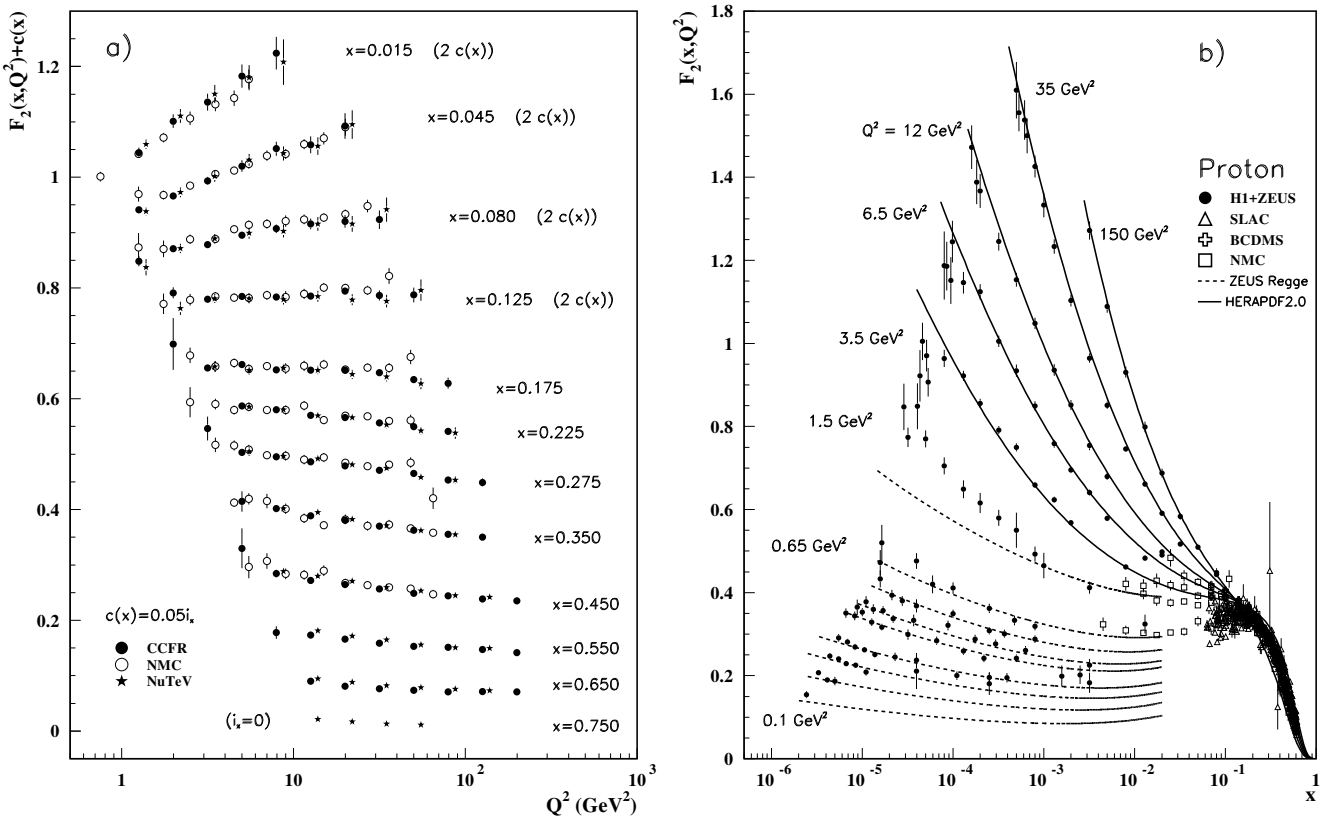

Figure 18.10: a) The deuteron structure function F_2 measured in deep inelastic scattering of muons on a fixed target (NMC) is compared to the structure function F_2 from neutrino-iron scattering (CCFR and NuTeV) using $F_2^\mu = (5/18)F_2^\nu - x(s+\bar{s})/6$, where heavy-target effects have been taken into account. The data are shown versus Q^2, for bins of fixed x. The NMC data have been rebinned to CCFR and NuTeV x values. For the purpose of plotting, a constant $c(x) = 0.05i_x$ is added to F_2, where i_x is the number of the x bin, ranging from 0 ($x = 0.75$) to 7 ($x = 0.175$). For $i_x = 8$ ($x = 0.125$) to 11 ($x = 0.015$), $2c(x)$ has been added. References: **NMC**—M. Arneodo *et al.*, Nucl. Phys. **B483**, 3 (1997); **CCFR/NuTeV**—U.K. Yang *et al.*, Phys. Rev. Lett. **86**, 2741 (2001); **NuTeV**—M. Tzanov *et al.*, Phys. Rev. **D74**, 012008 (2006).

b) The proton structure function F_2^p mostly at small x and Q^2, measured in electromagnetic scattering of electrons and positrons (H1, ZEUS), electrons (SLAC), and muons (BCDMS, NMC) on protons. Lines are ZEUS Regge and HERAPDF parameterizations for lower and higher Q^2, respectively. The width of the bins can be up to 10% of the stated Q^2. Some points have been slightly offset in x for clarity. The H1+ZEUS combined values for $Q^2 \geq 3.5$ GeV^2 are obtained from the measured reduced cross section and converted to F_2^p with a HERAPDF NLO fit, for all measured points where the predicted ratio of F_2^p to reduced cross-section was within 10% of unity. A turn-over is visible in the low-x points at medium Q^2 (3.5 GeV^2 and 6 GeV^2) for the H1+ZEUS combined values. In order to obtain F_2^p from the measured reduced cross-section, F_L must be estimated; for the points shown, this estimate is obtained from HERAPDF2.0. No F_L value consistent with the HERA data can eliminate the turn-over. This may indicate that at low x and Q^2 there are contributions to the structure functions that cannot be described in standard DGLAP evolution.

References: **H1 and ZEUS**—F.D. Aaron *et al.*, JHEP **1001**, 109 (2010) (data for $Q^2 < 3.5$ GeV^2), H. Abramowicz *et al.*, Eur. Phys. J. **C75**, 580 (2015) (data for $Q^2 \geq 3.5$ GeV^2 and HERAPDF parameterization); **ZEUS**—J. Breitweg *et al.*, Phys. Lett. **B487**, 53 (2000) (ZEUS Regge parameterization); **BCDMS, NMC, SLAC**—same references as Fig. 18.8.

Statistical and systematic errors added in quadrature are shown for both plots.

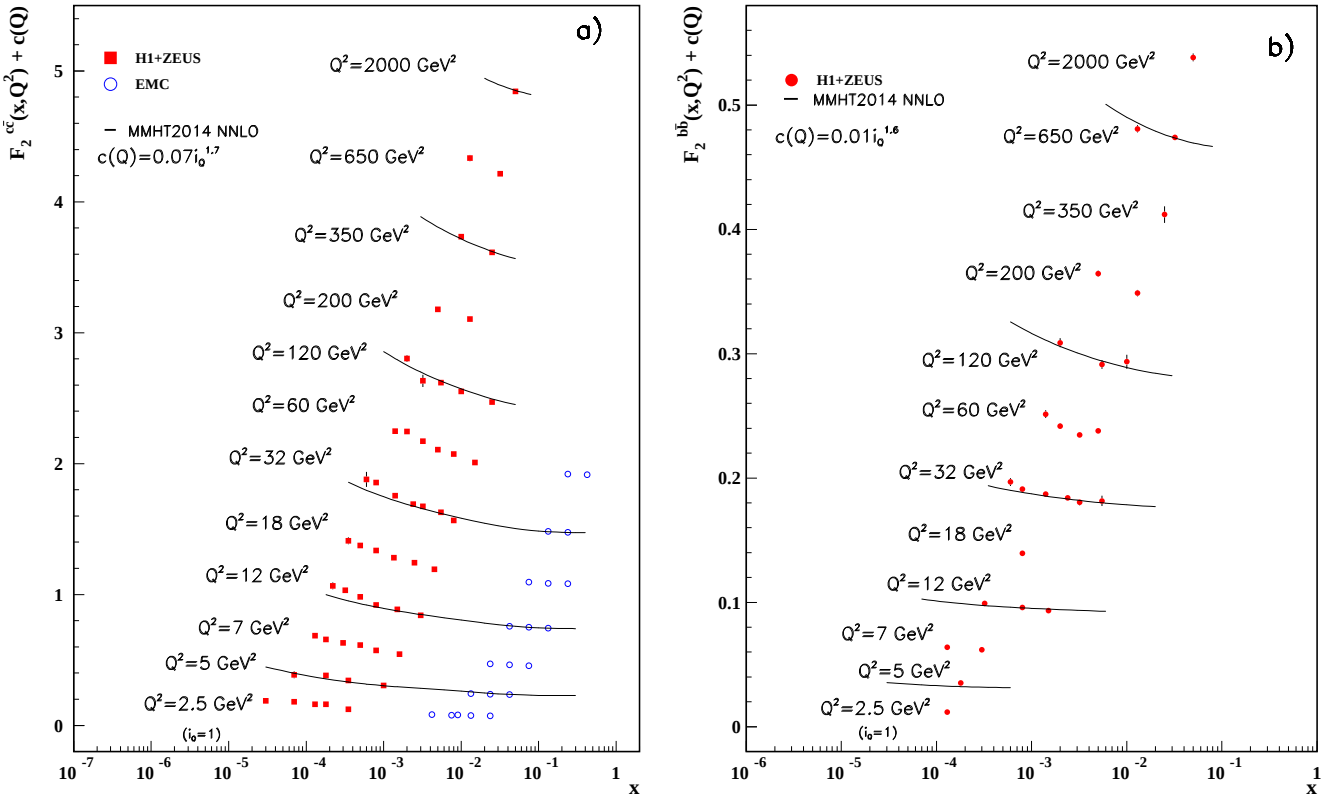

Figure 18.11: a) The charm-quark structure function $F_2^{c\bar{c}}(x)$, i.e. that part of the inclusive structure function F_2^p arising from the production of charm quarks, measured in electromagnetic scattering of positrons on protons (H1, ZEUS) (the values are obtained from the measured reduced cross section and converted to $F_2^{c\bar{c}}$ using the PDFs from the MMHT NNLO fit) and muons on iron (EMC). For the purpose of plotting, a constant $c(Q) = 0.07 i_Q{}^{1.7}$ is added to $F_2^{c\bar{c}}$ where i_Q is the number of the Q^2 bin, ranging from 1 ($Q^2 = 2.5$ GeV^2) to 12 ($Q^2 = 2000$ GeV^2). References: **H1 and ZEUS run I +II combination**—H. Abramowicz *et al.*, Eur. Phys. J. **C78**, 473 (2018); **EMC**—J.J. Aubert *et al.*, Nucl. Phys. **B213**, 31 (1983).

b) The bottom-quark structure function $F_2^{b\bar{b}}(x)$. For the purpose of plotting, a constant $c(Q) = 0.01 i_Q^{1.6}$ is added to $F_2^{b\bar{b}}$ where i_Q is the number of the Q^2 bin, ranging from 1 ($Q^2 = 2.5$ GeV^2) to 12 ($Q^2 = 2000$ GeV^2). References: **H1 and ZEUS run I combination**—H. Abramowicz *et al.*, Eur. Phys. J. **C78**, 473 (2018).

For both plots, statistical and systematic errors added in quadrature are shown. The data are given as a function of x in bins of Q^2. Points may have been slightly offset in x for clarity. Some data have been rebinned to common Q^2 values. Also shown is the MMHT2014 parameterization given at several Q^2 values (L. A. Harland-Lang *et al.*, Eur. Phys. J. **C75**, 204 (2015)).

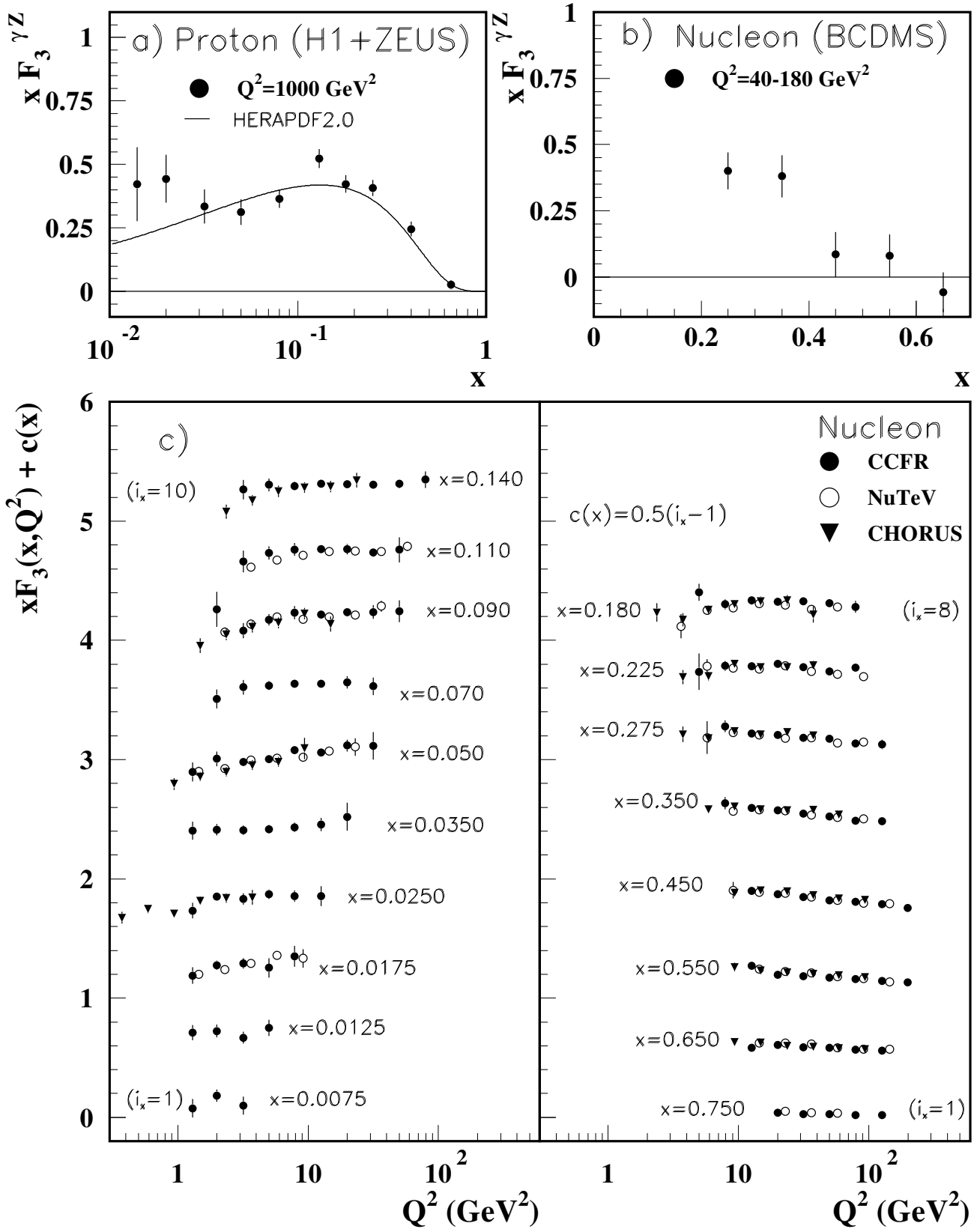

Figure 18.12: The structure function $xF_3^{\gamma Z}$ measured in electroweak scattering of **a)** electrons on protons (H1 and ZEUS) and **b)** muons on carbon (BCDMS). The line in **a)** is the HERAPDF parameterization. References: **H1 and ZEUS**—H. Abramowicz *et al.*, Eur. Phys. J. **C75**, 580 (2015) (for both data and HERAPDF parameterization); **BCDMS**—A. Argento *et al.*, Phys. Lett. **B140**, 142 (1984).
c) The structure function xF_3 of the nucleon measured in ν-Fe scattering. The data are plotted as a function of Q^2 in bins of fixed x. For the purpose of plotting, a constant $c(x) = 0.5(i_x - 1)$ is added to xF_3, where i_x is the number of the x bin as shown in the plot. The NuTeV and CHORUS points have been shifted to the nearest corresponding x bin as given in the plot and slightly offset in Q^2 for clarity. References: **CCFR**—W.G. Seligman *et al.*, Phys. Rev. Lett. **79**, 1213 (1997); **NuTeV**—M. Tzanov *et al.*, Phys. Rev. **D74**, 012008 (2006); **CHORUS**—G. Önengüt *et al.*, Phys. Lett. **B632**, 65 (2006).

Statistical and systematic errors added in quadrature are shown for all plots.

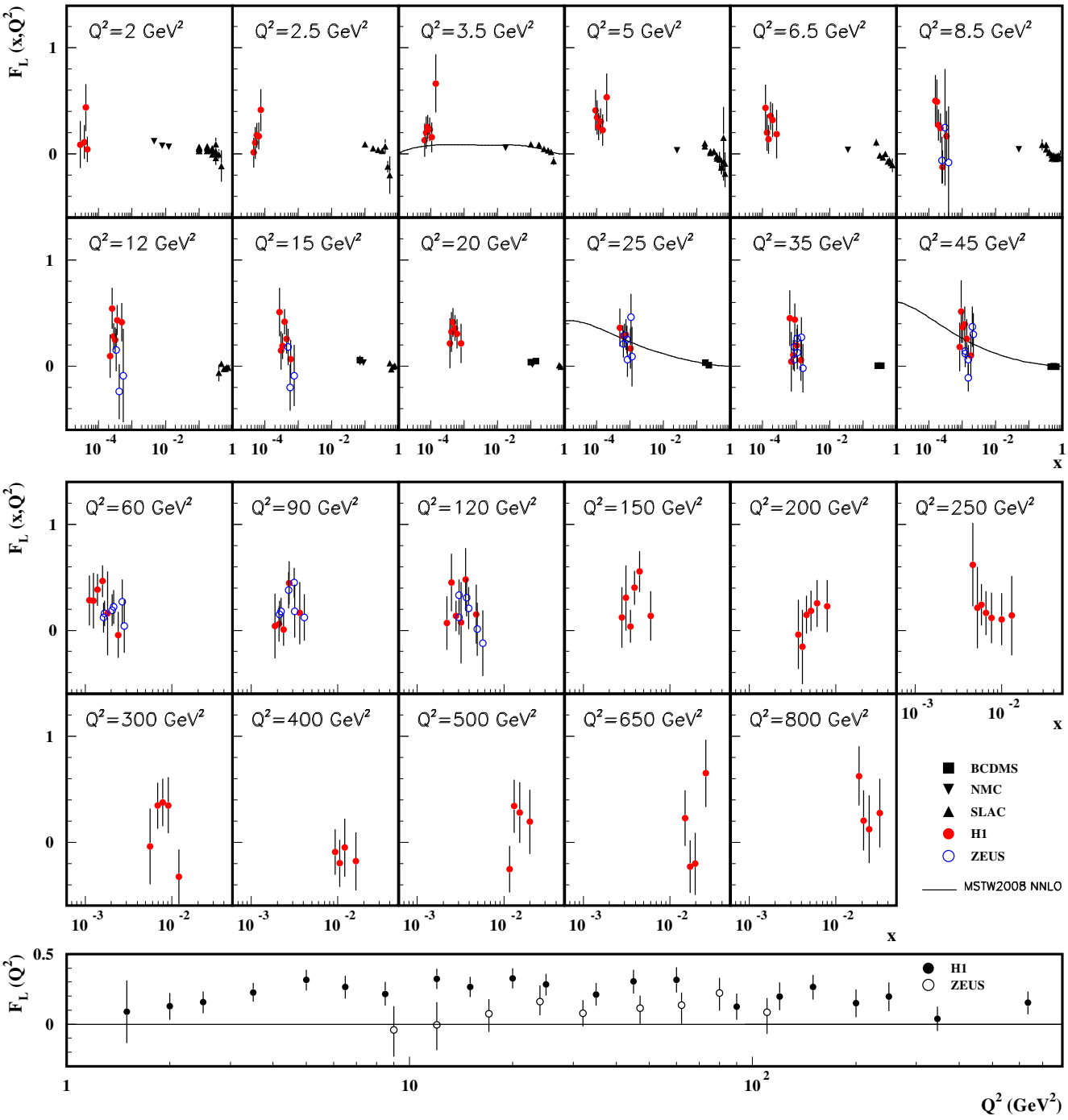

Figure 18.13: Top panels: The longitudinal structure function F_L as a function of x in bins of fixed Q^2 measured on the proton (except for the SLAC data which also contain deuterium data). BCDMS, NMC, and SLAC results are from measurements of R (the ratio of longitudinal to transverse photon absorption cross sections) which are converted to F_L by using the BDCMS parameterization of F_2 (A.C. Benvenuti *et al.*, Phys. Lett. **B223**, 485 (1989)). It is assumed that the Q^2 dependence of the fixed-target data is small within a given Q^2 bin. Some of the other data may have been rebinned to common Q^2 values. Some points have been slightly offset in x for clarity. Also shown is the MSTW2008 parameterization given at three Q^2 values (A.D. Martin *et al.*, Eur. Phys. J. **C63**, 189 (2009)). References: **H1**—V. Andreev *et al.*, Eur. Phys. J. **C74**, 2814 (2014); **ZEUS**—S. Chekanov *et al.*, Phys. Lett. **B682**, 8 (2009); H. Abramowicz et al., Phys. Rev. **D90**, 072002 (2014); **BCDMS**—A. Benvenuti *et al.*, Phys. Lett. **B223**, 485 (1989); **NMC**—M. Arneodo *et al.*, Nucl. Phys. **B483**, 3 (1997); **SLAC**—L.W. Whitlow *et al.*, Phys. Lett. **B250**, 193 (1990) and numerical values from the thesis of L.W. Whitlow (SLAC-357).
Bottom panel: The longitudinal structure function F_L as a function of Q^2. Some points have been slightly offset in Q^2 for clarity. References: **H1**—V. Andreev *et al.*, Eur. Phys. J. **C74**, 2814 (2014); **ZEUS**—H. Abramowicz et al., Phys. Rev. **D90**, 072002 (2014).
The results shown in the bottom plot require the assumption of the validity of the QCD form for the F_2 structure function in order to extract F_L. Statistical and systematic errors added in quadrature are shown for both plots.

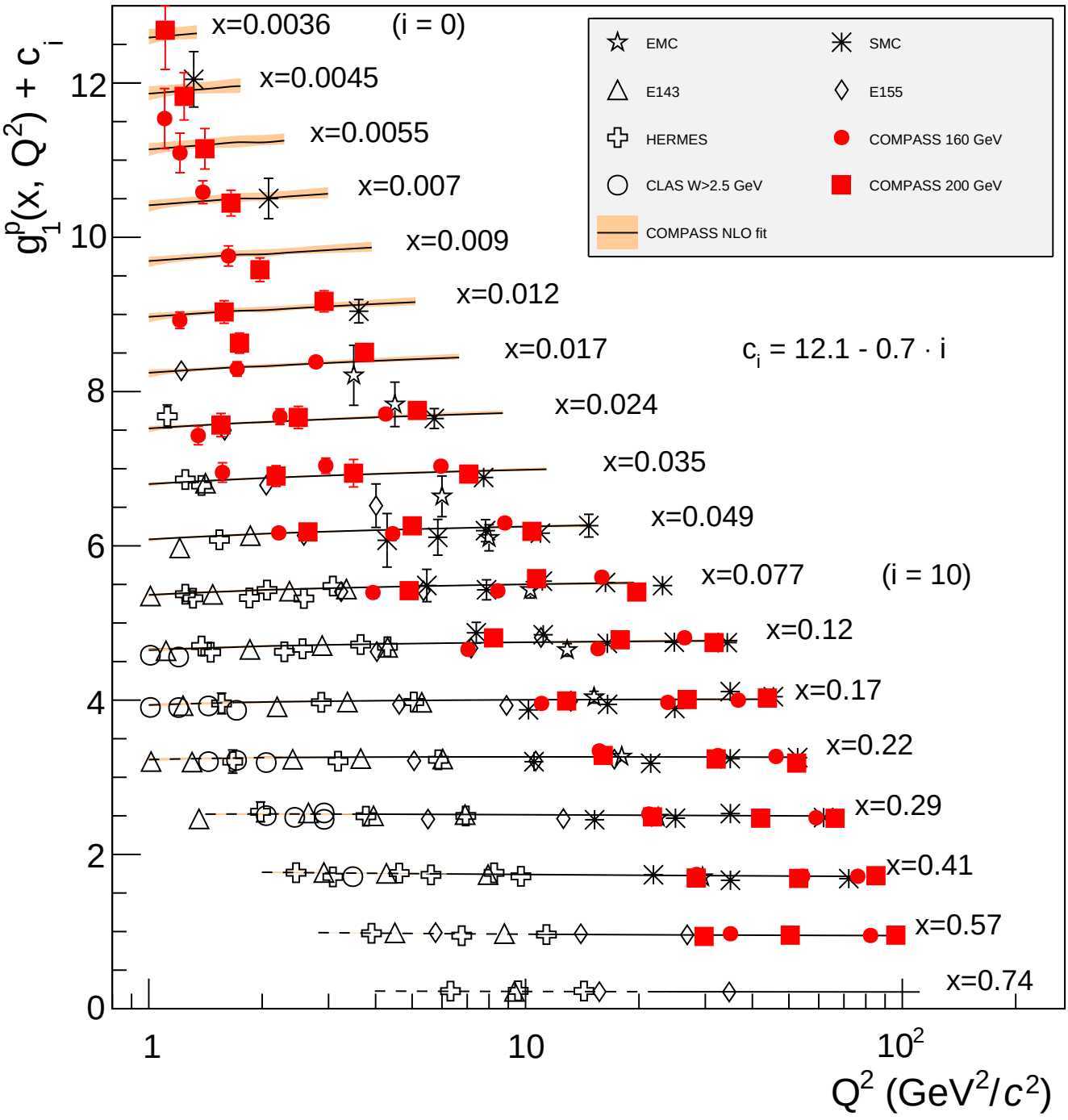

Figure 18.14: World data on the spin-dependent structure function g_1^p as a function of Q^2 for various values of x The lines represent the Q^2 dependence for each value of x, as determined from a NLO QCD fit. The dashed ranges represent the region with $W^2 < 10$ $(\mathrm{GeV/c^2})^2$. References: **EMC**—J. Ashman *et al.*, Phys. Lett. **B206**, 363 (1988); Nucl. Phys. **B328**, 1 (1989); **E143**—K. Abe *et al.*, Phys. Rev. **D58**, 112003 (1998); **SMC**—B. Adeva *et al.*, Phys. Rev. **D58**, 112001 (1998); **HERMES**—A. Airapetian *et al.*, Phys. Rev. **D75**, 012007 (2007); **E155**—P.L. Anthony *et al.*, Phys. Lett. **B493**, 19 (2000); **COMPASS**—M.G. Alekseev *et al.*, Phys. Lett. **B690**, 466 (2010), C. Adolph, *et al.*, Phys. Lett. **B753**, 18 (2016); **CLAS**—K.V. Dharmawardane *et al.*, Phys. Lett. **B641**, 11 (2006) (which also includes resonance region data not shown on this plot — there is also low W^2 CLAS data in Y. Prok *et al.*, Phys. Rev. **C90**, 025212 (2014) and N. Guler *et al.*, Phys. Rev. **C92**, 055201 (2015)).

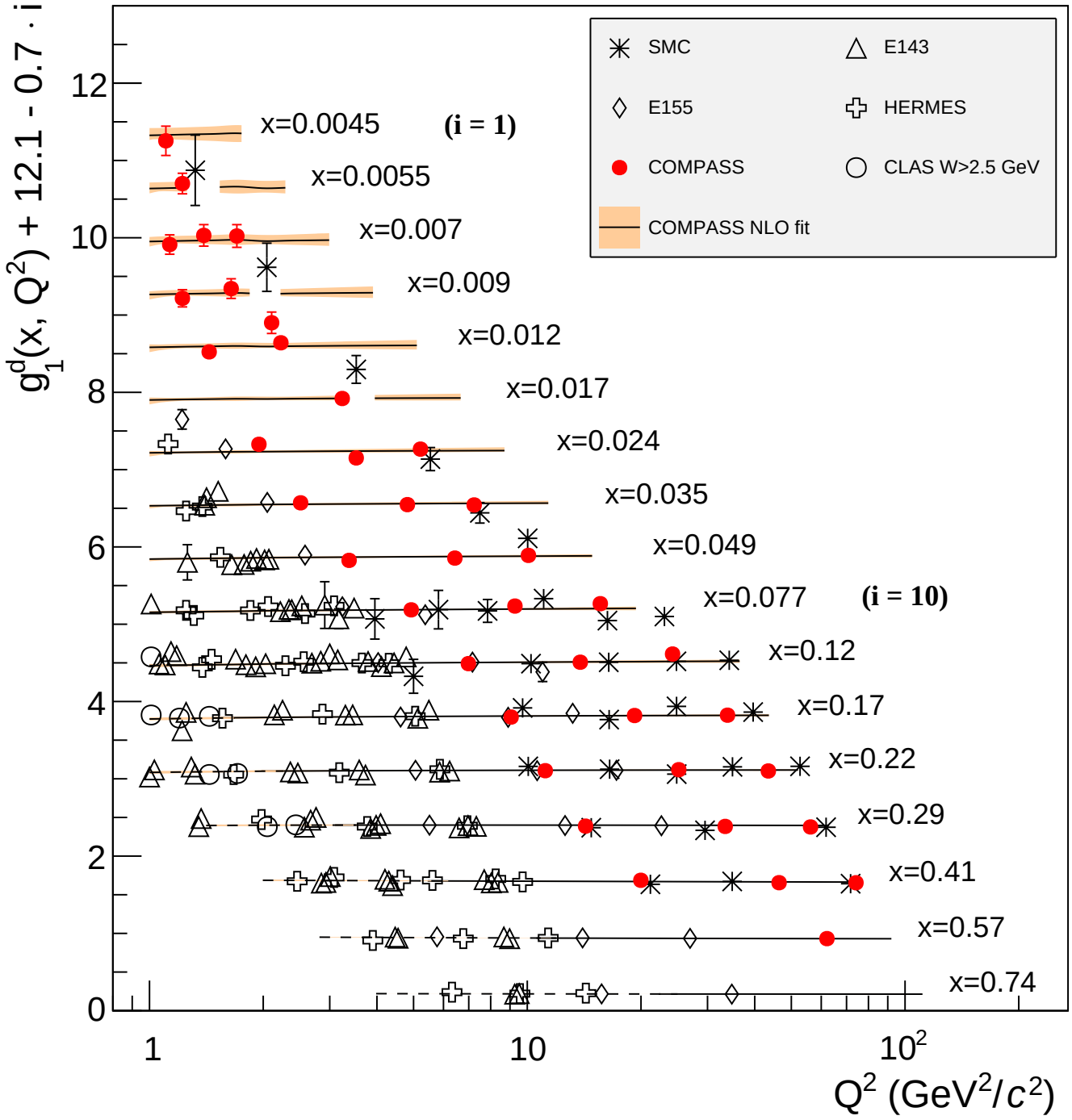

Figure 18.15: World data on the spin-dependent structure function g_1^d as a function of Q^2 for various values of x The lines represent the Q^2 dependence for each value of x, as determined from a NLO QCD fit. The dashed ranges represent the region with $W^2 < 10$ (GeV/c^2)^2. **CLAS**—K.V. Dharmawardane *et al.*, Phys. Lett. **B641**, 11 (2006) **HERMES**—A. Airapetian *et al.*, Phys. Rev. **D75**, 012007 (2007); **SMC**—B. Adeva *et al.*, Phys. Rev. **D58**, 112001 (1998); **E155**—P.L. Anthony *et al.*, Phys. Lett. **B463**, 339 (1999); **E143**—K. Abe *et al.*, Phys. Rev. **D58**, 112003 (1998); **COMPASS**—C. Adolph, *et al.*, Phys. Lett. **B769**, 34 (2017);

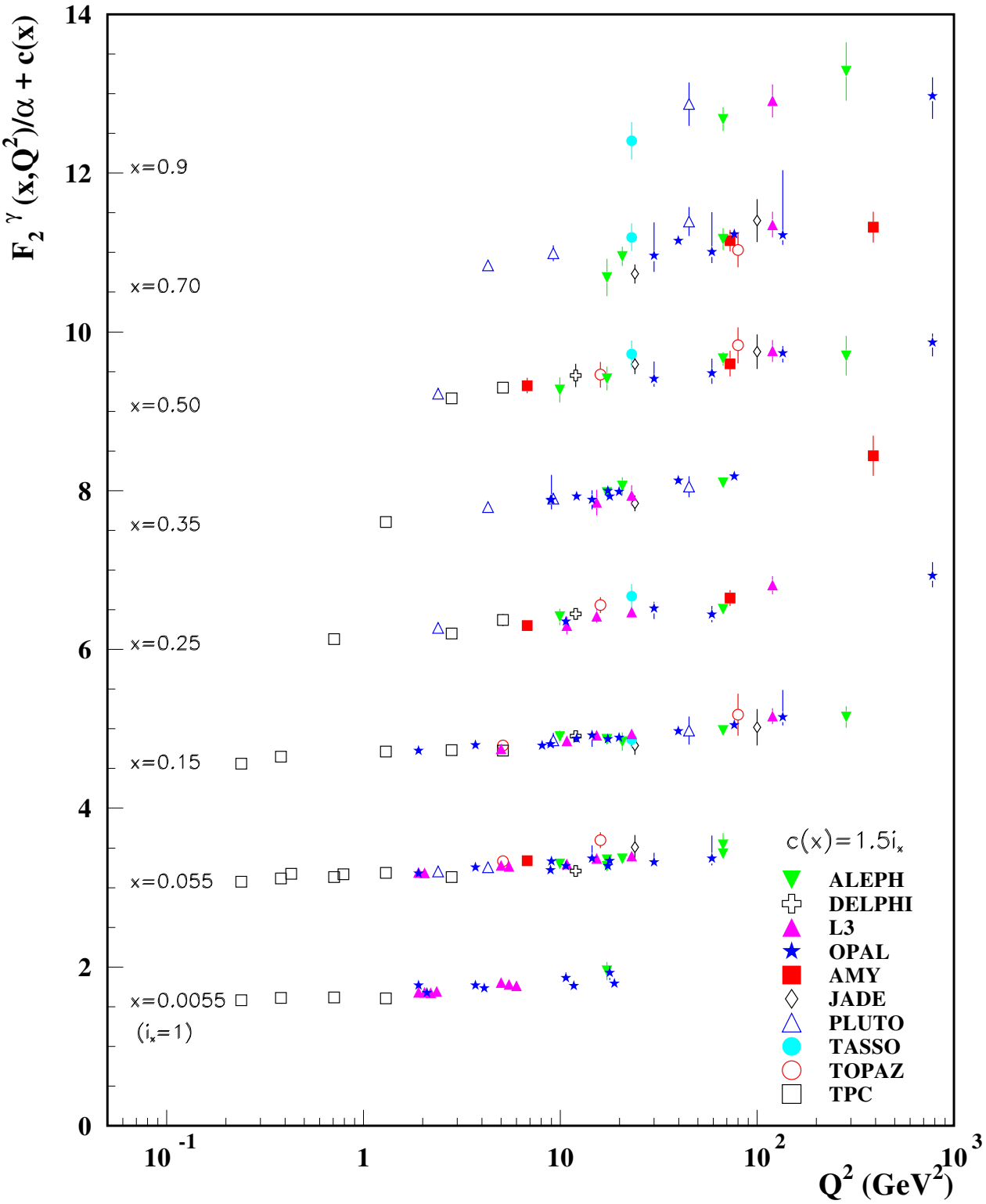

Figure 18.16: The hadronic structure function of the photon F_2^γ divided by the fine structure constant α measured in e^+e^- scattering, shown as a function of Q^2 for bins of x. Data points have been shifted to the nearest corresponding x bin as given in the plot. Some points have been offset in Q^2 for clarity. Statistical and systematic errors added in quadrature are shown. For the purpose of plotting, a constant $c(x) = 1.5i_x$ is added to F_2^γ/α where i_x is the number of the x bin, ranging from 1 ($x = 0.0055$) to 8 ($x = 0.9$). References: **ALEPH**–R. Barate *et al.*, Phys. Lett. **B458**, 152 (1999); A. Heister *et al.*, Eur. Phys. J. **C30**, 145 (2003);**DELPHI**–P. Abreu *et al.*, Z. Phys. **C69**, 223 (1995); **L3**–M. Acciarri *et al.*, Phys. Lett. **B436**, 403 (1998); M. Acciarri *et al.*, Phys. Lett. **B447**, 147 (1999); M. Acciarri *et al.*, Phys. Lett. **B483**, 373 (2000); **OPAL**–A. Ackerstaff *et al.*, Phys. Lett. **B411**, 387 (1997); A. Ackerstaff *et al.*, Z. Phys. **C74**, 33 (1997); G. Abbiendi *et al.*, Eur. Phys. J. **C18**, 15 (2000); G. Abbiendi *et al.*, Phys. Lett. **B533**, 207 (2002) (note that there is overlap of the data samples in these last two papers); **AMY**–S.K. Sahu *et al.*, Phys. Lett. **B346**, 208 (1995); T. Kojima *et al.*, Phys. Lett. **B400**, 395 (1997); **JADE**–W. Bartel *et al.*, Z. Phys. **C24**, 231 (1984); **PLUTO**–C. Berger *et al.*, Phys. Lett. **142B**, 111 (1984); C. Berger *et al.*, Nucl. Phys. **B281**, 365 (1987); **TASSO**–M. Althoff *et al.*, Z. Phys. **C31**, 527 (1986); **TOPAZ**–K. Muramatsu *et al.*, Phys. Lett. **B332**, 477 (1994); **TPC/Two Gamma**–H. Aihara *et al.*, Z. Phys. **C34**, 1 (1987).

19. Fragmentation Functions in e^+e^-, ep, and pp Collisions

Revised August 2019 by O. Biebel (Ludwig-Maximilians U.), D. de Florian (ICAS and ICIFI, UNSAM), D. Milstead (Stockholm U.) and W. Vogelsang (Tübingen U.).

19.1 Introduction to fragmentation

Quarks and gluons produced in hard-scattering reactions will ultimately give rise to the colorless hadronic bound states that may be observed in the detector. The associated hadronization process is described by fragmentation functions $D_i^h(x,\mu^2)$ $(i = q, \bar{q}, g)$ which are universal functions representing, in the simplest picture, a measure of the probability density that an outgoing parton produces a hadron h. Here, x is the fraction of the parton's momentum transferred to the hadron, and μ is a 'resolution' scale known as factorization scale. The $D_i^h(x,\mu^2)$ may be viewed as the final-state analogs of the initial-state parton distribution functions (PDFs) addressed in Section 18 of this *Review*. They are also sometimes referred to as *timelike* distributions since they are primarily accessed in e^+e^- annihilation via a timelike intermediate boson. (See Refs. [1,2] for introductory reviews, and Refs. [3–5] for summaries of experimental and theoretical research in this field).

The cleanest laboratory for the study of fragmentation functions is provided by semi-inclusive electron-positron annihilation, $e^+e^- \to \gamma/Z \to h+X$. The cross section for this reaction may be expressed in terms of 'fragmentation structure functions' $F_{T,L,A}$ that are directly related to the fragmentation functions. At center-of-mass (CM) energy $\sqrt{s} = q^2$ we have

$$\frac{1}{\sigma_0}\frac{d^2\sigma^h}{dx\,d\cos\theta} = \frac{3}{8}(1+\cos^2\theta)F_T^h(x,q^2) + \frac{3}{4}\sin^2\theta\,F_L^h(x,q^2) + \frac{3}{4}\cos\theta\,F_A^h(x,q^2)\,. \tag{19.1}$$

Here, q is the four-momentum of the intermediate photon or Z-boson, with $q^2 > 0$, and $x = 2P_h \cdot q/q^2$ with the hadron's four-momentum P_h is the fragmentation counterpart of the familiar DIS Bjorken variable. (Note that $x = 2E_h/\sqrt{s} \le 1$ in terms of the energy E_h of the produced hadron in the CM frame of the electron positron pair.) Furthermore, in the same frame, θ is the hadron's angle relative to the electron beam direction. Eq. (19.1) is the most general form for unpolarized inclusive single-particle production via vector bosons [6]. The fragmentation structure functions F_T and F_L represent the contributions from γ/Z polarizations transverse or longitudinal with respect to the direction of motion of the hadron. The parity-violating term with the asymmetric fragmentation function F_A arises from the interference between vector and axial-vector contributions. Various normalization factors σ_0 are used in the literature, ranging from the total cross section $\sigma_{\rm tot}$ for $e^+e^- \to$ hadrons, including all weak and QCD contributions, to $\sigma_0 = 4\pi\alpha^2 N_c/3s$ with $N_c = 3$, the lowest-order QED cross section for $e^+e^- \to \mu^+\mu^-$ times the number of colors N_c. LEP1 measurements of the three fragmentation structure functions are shown in Fig. 19.1.

Integration of Eq. (19.1) over all θ yields the total fragmentation structure function $F^h = F_T^h + F_L^h$:

$$\frac{1}{\sigma_0}\frac{d\sigma^h}{dx} = F^h(x,q^2) = \sum_i \int_x^1 \frac{dz}{z}\,C_i\left(z,\alpha_s(\mu),\frac{q^2}{\mu^2}\right) D_i^h\left(\frac{x}{z},\mu^2\right)\,. \tag{19.2}$$

On the right we have written the factorized expression for the structure function in terms of a sum over convolutions of the fragmentation functions D_i^h for partons $i = u,\ \bar{u},\ d,\ \bar{d},\ \ldots,\ g$ with perturbative coefficient functions C_i. Since photons and Z bosons do not distinguish between quarks and antiquarks, e^+e^- annihilation primarily constrains the combinations $D_q^h + D_{\bar{q}}^h$. Gluon fragmentation contributes only at higher order in perturbation theory or by scaling violations. Corrections to the factorized expression in Eq. (19.2) are suppressed by inverse powers of q^2. They arise from quark and hadron mass terms and from non-perturbative effects.

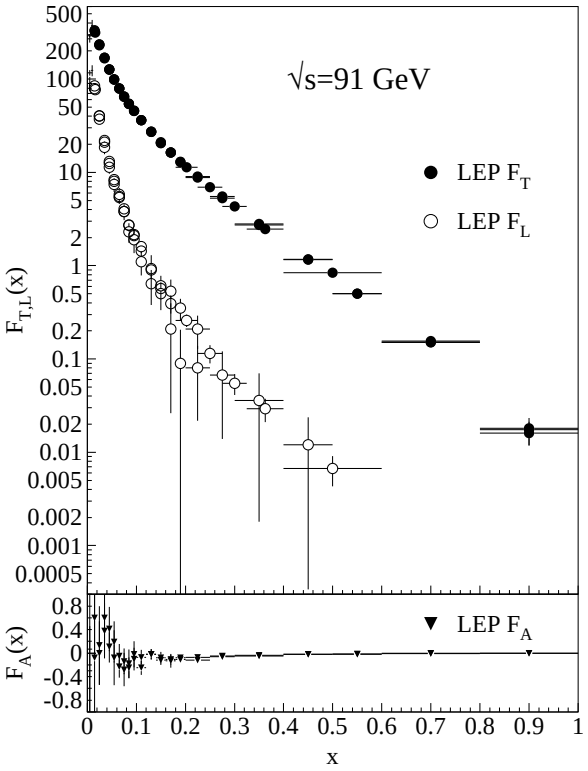

Figure 19.1: LEP1 measurements of total transverse (F_T), longitudinal (F_L), and asymmetric (F_A) fragmentation structure functions [7]. Data points with relative errors greater than 100% are omitted.

Analogous factorized expressions as in Eq. (19.2) may be written for each of the structure functions $F_{T,L,A}$ individually.

The fragmentation functions obey the momentum sum rule constraint

$$\sum_h \int_0^1 dx\,x\,D_i^h(x,\mu^2) = 1\,, \tag{19.3}$$

separately for each flavor i. Note that the sum rule involves a sum over all possible produced hadrons. The dependence of the functions D_i^h on the factorization scale μ^2 will be discussed in the next section.

Measurements of hadron production in deeply-inelastic lepton-proton scattering and hadron-hadron scattering are complementary to those in e^+e^- annihilation. The former process, $\ell p \to \ell' + h + X$, is known as *semi-inclusive deep-inelastic scattering (SIDIS)*. Here, in analogy with Eq. (19.2), the high virtuality of the photon in DIS also permits factorization of the cross section in terms of fragmentation functions, PDFs for the incoming proton, and perturbative hard-scattering cross sections. Likewise, factorization also occurs for $pp \to h + X$ at large transverse momentum of the produced hadron, and for $pp \to {\rm jet}(h) + X$, where the hadron is part of a fully reconstructed jet. The fragmentation functions contributing to $e^+e^- \to h + X$, $\ell p \to \ell' + h + X$, and $pp \to h + X$, $pp \to {\rm jet}(h) + X$ are universal in the sense that the same functions appear in the factorized expressions for the three reactions. Modern QCD analyses of fragmentation functions "globally" take into account experimental data sets for all three types of processes in order to obtain optimal sets of fragmentation functions.

Electron-positron annihilation has the advantage that there is no hadronic initial state and hence no beam remnant. This is in contrast to $\ell p \to \ell' + h + X$ or $pp \to h + X$, which are affected by hadron remnant contributions associated with the partons of the initial-state hadron(s) which are collaterally involved in the hard lepton-parton or parton-parton collision. On the other hand,

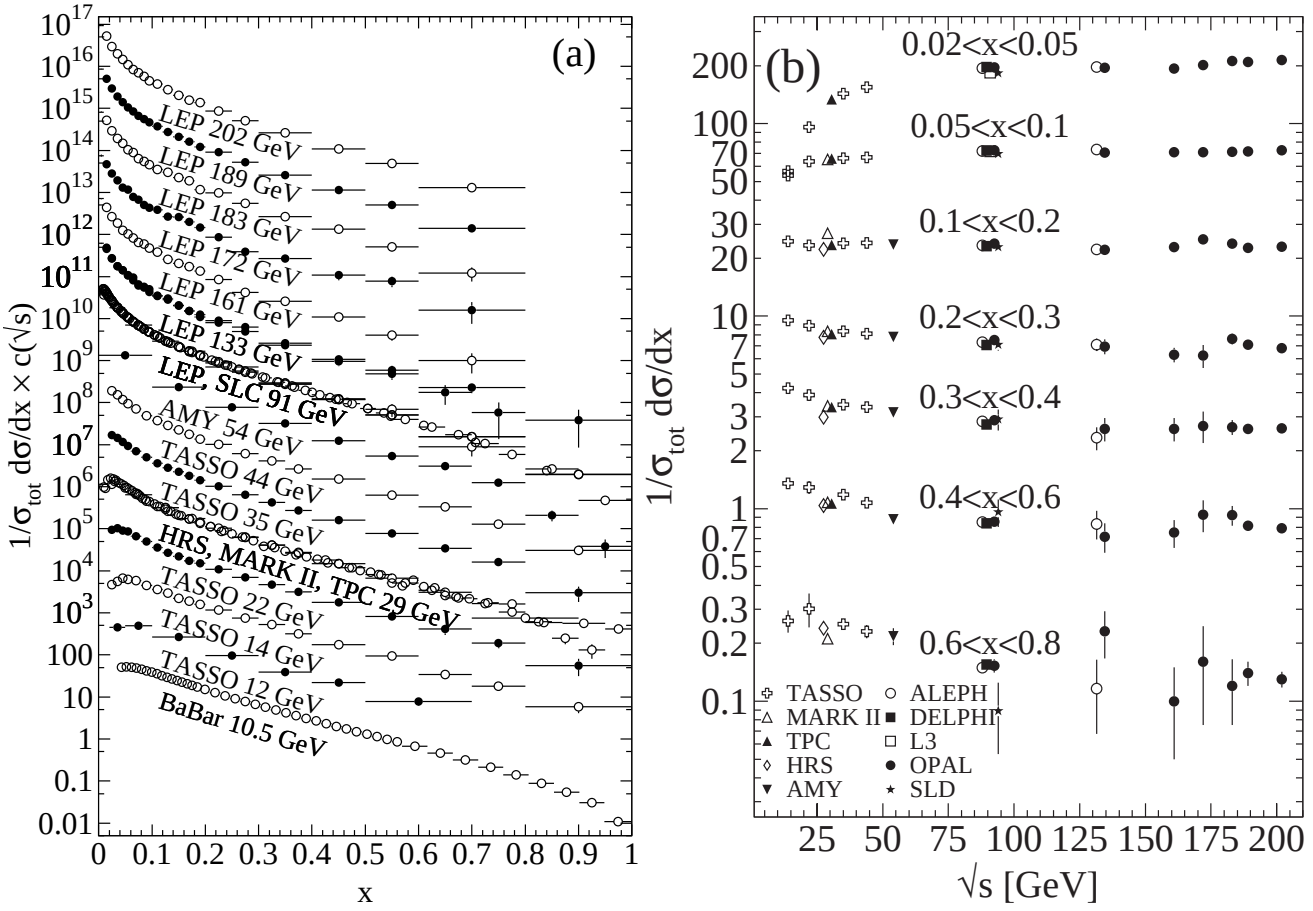

Figure 19.2: Cross section for $e^+e^- \to h + X$ for all charged hadrons [8–26], (a) for different CM energies $\sqrt{s}$ versus x, and (b) for various ranges of x versus $\sqrt{s}$. For (a) the distributions have been scaled by $c(\sqrt{s}) = 10^i$ with i ranging from $i = 0$ ($\sqrt{s} = 12$ GeV) to $i = 13$ ($\sqrt{s} = 202$ GeV).

$e^+e^- \to h + X$ has little sensitivity to D_g^h and is insensitive to the charge asymmetries $D_q^h - D_{\bar{q}}^h$. These quantities are best constrained in proton–(anti-)proton and electron-proton scattering, respectively. Especially the latter provides an environment that allows the study of the influence of initial-state QCD radiation on the fragmentation process, of the partonic and spin structure of the hadron target, and of the target remnant system. (See Ref. [27] for a comprehensive review of the measurements and models of fragmentation in lepton-hadron scattering).

Moreover, unlike e^+e^- annihilation where $q^2 = s$ is fixed by the collider energy, lepton-hadron scattering has two independent scales, $Q^2 = -q^2$ and the invariant mass squared, $W^2 \approx Q^2(1-x)/x$, of the hadronic final state, which both can vary by several orders of magnitudes for a given CM energy, thus allowing the study of fragmentation in different environments by a single experiment. For example, in photoproduction the exchanged photon is quasi-real ($Q^2 \approx 0$), leading to processes akin to hadron-hadron scattering. In DIS ($Q^2 \gg 1$ GeV^2), using factorization, the hadronic fragments of the struck quark can be directly compared with quark fragmentation in e^+e^- in a suitable frame. Results from lepton-hadron experiments quoted in this report primarily concern fragmentation in the DIS regime. Studies performed by lepton-hadron experiments of fragmentation with photoproduction data containing high transverse momentum jets or particles are also reported, when these are directly comparable to DIS and e^+e^- results.

Fragmentation studies in lepton-hadron collisions are usually performed in one of two frames in which the target hadron and the exchanged boson are collinear. The hadronic center-of-mass frame (HCMS) is defined as the rest system of the exchanged boson and incoming hadron, with the z^*-axis defined along the direction of the exchanged boson. The positive z^* direction defines the so-called current fragmentation region. Fragmentation measurements performed in the HCMS often use the Feynman-x variable $x_F = 2p_z^*/W$, where p_z^* is the longitudinal momentum of the particle in this frame. As W is the invariant mass of the hadronic final state, x_F ranges between -1 and 1.

The Breit system [28, 29] is related to the HCMS by a longitudinal boost such that the time component of q vanishes, i.e, $q = (0, 0, 0, -Q)$. In the parton model, the struck parton then has the longitudinal momentum $Q/2$ which becomes $-Q/2$ after the collision. As compared with the HCMS, the current fragmentation region of the Breit frame is more closely matched to the partonic scattering process, and is thus appropriate for direct comparisons of fragmentation functions in DIS with those from e^+e^- annihilation. The variable $x_p = 2p^*/Q$, where p^* is the particle's momentum in the current region of the Breit frame, is used at HERA for measurements in the Breit frame, enabling rather direct comparisons of DIS and e^+e^- results.

19.2 Scaling violations and QCD corrections

As mentioned, the coefficient functions for the fragmentation structure functions in $e^+e^- \to h + X$ are amenable to QCD perturbation theory. For each of the structure functions $F_{T,L,A}(x, q^2)$ in Eq. (19.1) (and hence for the total structure function F^h in Eq. (19.2)) the coefficient function has an expansion of the form

$$C_{a,i}\left(z, \alpha_s(\mu), \frac{q^2}{\mu^2}\right) = (1 - \delta_{aL})\,\delta_{iq}\,\delta(1-z) + \frac{\alpha_s(\mu)}{2\pi}\,c_{a,i}^{(1)}\left(z, \frac{q^2}{\mu^2}\right) + \left(\frac{\alpha_s(\mu)}{2\pi}\right)^2 c_{a,i}^{(2)}\left(z, \frac{q^2}{\mu^2}\right) + . \quad (19,4)$$

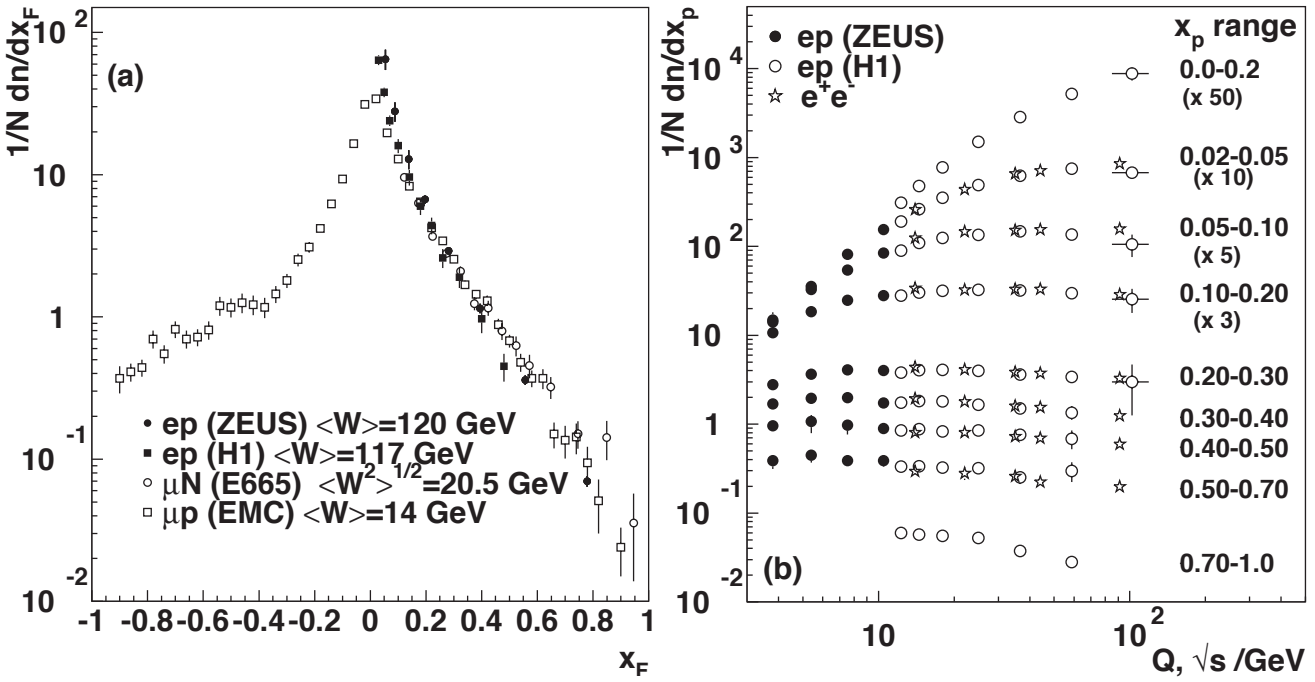

Figure 19.3: (a) The distribution $1/N \cdot dN/dx_F$ for all charged particles in DIS lepton-hadron experiments at different values of W, measured in the HCMS [30–33]. (b) Scaling violations of the fragmentation structure function for all charged particles in the current region of the Breit frame of DIS [34, 35] and in e^+e^- interactions [19, 36]. The data are shown as a function of $\sqrt{s}$ for e^+e^- results, and as a function of Q for the DIS results, each within the same indicated intervals of the scaled momentum x_p. The data for the four lowest intervals of x_p are multiplied by factors 50, 10, 5, and 3, respectively for better visibility.

where $a = T, L, A$. At the zeroth order in the strong coupling α_s the coefficient functions C_g for gluons vanish, while for (anti-) quarks $C_i = g_i(s)\,\delta(1-z)$ (except for F_L for which the leading contribution is of order α_s, as indicated in Eq. (19.4)). Here $g_i(s)$ is the appropriate electroweak coupling. In particular, $g_i(s)$ is proportional to the squared charge of the quark i at $s \ll M_Z^2$, when weak effects can be neglected. The full electroweak prefactors $g_i(s)$ can be found in Ref. [6]. The first-order QCD corrections to the coefficient functions have been calculated in Refs. [37,38], and the second-order terms in [39–41]. Thus, the coefficient functions are known to NNLO, except for F_L. We note that beyond the leading order the coefficient functions, and hence the fragmentation functions, start to depend on the choice of factorization scheme. The standard choice in the literature is the $\overline{\rm MS}$ scheme.

The simplest parton-model approach would predict scale-independent ('scaling') x-distributions for both the structure function F^h and the parton fragmentation functions D_i^h. Perturbative QCD corrections lead to logarithmic scaling violations via the evolution equations [42]

$$\frac{\partial}{\partial \ln \mu^2}\, D_i^h(x,\mu^2) \;=\; \sum_j \int_x^1 \frac{dz}{z}\, P_{ji}\Big(z, \alpha_s(\mu^2)\Big) D_j^h\left(\frac{x}{z}, \mu^2\right) \;, \tag{19.5}$$

where the functions $P_{ij}(z, \alpha_s(\mu^2))$ describe the splitting process $i \to j + X$, where parton j carries the longitudinal momentum fraction z of parton i. Note that for fragmentation the relevant splitting functions are P_{ji} (rather than P_{ij} as for the PDFs) since D_j^h represents the fragmentation of the final parton. Usually the system of evolution equations is decomposed into a 2×2 flavor-singlet sector comprising the gluon and the sum of all quark and antiquark fragmentation functions, and scalar ('non-singlet') equations for quark-antiquark and flavor differences.

The splitting functions in Eq. (19.5) have the perturbative expansion

$$P_{ji}(z, \alpha_s) \;=\; \frac{\alpha_s}{2\pi}\, P_{ji}^{(0)}(z) + \left(\frac{\alpha_s}{2\pi}\right)^2 P_{ji}^{(1)}(z) + \left(\frac{\alpha_s}{2\pi}\right)^3 P_{ji}^{(2)}(z) + \ldots \;, \tag{19.6}$$

where the leading-order (LO) functions $P^{(0)}(z)$ [42, 43] are the same as those for the initial-state parton distributions. The next-to-leading order (NLO) corrections $P^{(1)}(z)$ have been calculated in Refs. [44–48] (there are well-known misprints in the journal version of Ref. [45]). Ref. [48] also includes the spin-dependent case. The timelike functions are different from, but related to, their spacelike counterparts, see also Ref. [49]. The connections between the two sets of functions has facilitated recent calculations of the next-to-next-to-leading order (NNLO) quantities $P_{qq}^{(2)}(z)$ and $P_{gg}^{(2)}(z)$ in Eq. (19.6) [40,50]. In the same way, the corresponding off-diagonal quantities $P_{qg}^{(2)}$ and $P_{gq}^{(2)}$ were recently obtained in Ref. [51] with the help of constraints from the momentum sum rule Eq. (19.3) [50] and of the limit of $C_A = C_F = n_f$ for which QCD becomes supersymmetric. An uncertainty still remains for the $P_{qg}^{(2)}$ kernel, which however does not affect the logarithmic behavior at small and large momentum fractions. With the exception of Ref. [47], all these higher-order results refer to the standard $\overline{\rm MS}$ scheme with a fixed number n_f of light flavors. When the threshold for the production of a heavier quark flavor is crossed in the course of the scale evolution, fragmentation functions change. The NLO treatment of these flavor thresholds in the evolution has been addressed in Ref. [52].

The phenomenological effect of scale evolution is similar in the timelike and spacelike cases: As the scale increases, one observes a scaling violation in which the x-distribution is shifted towards lower values. This can be seen from Fig. 19.2 where a set of measurements of the total fragmentation structure function in e^+e^- annihilation are shown. In particular, the figure on the right exhibits the dependence on $\sqrt{q^2} = \sqrt{s}$ at fixed values of x. QCD analyses of these data are discussed in Section 19.5 below.

The NLO coefficient functions for SIDIS, $ep \to e + h + X$, have been presented in Refs. [37, 38] Corresponding results have also been obtained for the case that a non-vanishing hadron transverse momentum is required in the HCMS frame [53, 54].

Scaling violations in DIS are shown in Fig. 19.3 for both the HCMS and the Breit frames. In Fig. 1.3(a) the distribution in terms of $x_F = 2p_z^*/W$ shows a steeper slope in ep data than for the lower-energy μp data for $x_F > 0.15$, indicating the scaling

violations. At smaller values of x_F in the current jet region, the multiplicity of particles substantially increases with W, owing to the increased phase space available for the fragmentation process. The EMC data access both the current region and the region of the fragmenting target remnant system. At higher values of $|x_F|$, due to the extended nature of the remnant, the multiplicity in the target region far exceeds that in the current region. For acceptance reasons the remnant hemisphere of the HCMS is only accessible by the lower-energy fixed-target experiments.

Using hadrons from the current hemisphere in the Breit frame, measurements of fragmentation functions and the production properties of particles in ep scattering have been reported in Refs. [34, 35, 55–58]. Fig. 19.3(b) compares results from ep scattering and e^+e^- experiments; the latter results have been divided by two as they cover both event hemispheres. The agreement between the DIS and e^+e^- results is fairly good. However, processes in DIS which are not present in e^+e^- annihilation, such as boson-gluon fusion and initial-state QCD radiation, can depopulate the current region. These effects become most prominent at low values of Q and x_p. Hence, when compared with e^+e^- annihilation data at $\sqrt{s} = 5.2$, 6.5 GeV [59] not shown here, the DIS particle rates tend to lie below those observed in e^+e^- annihilation. A ZEUS study [60] finds that the direct comparability of the ep data to e^+e^- results at low scales is improved if twice the energy in the current hemisphere of the Breit frame, $2E_B^{\rm cr}$, is used instead of $Q/2$ as the fragmentation scale. Choosing $2E_B^{\rm cr}$ for the fragmentation scale approximates QCD radiation effects relevant at low scales, as detailed in Ref. [29].

19.3 Fragmentation functions for small particle momenta

The higher-order timelike splitting functions in Eq. (19.6) are singular at small values of x. They show a double-logarithmic enhancement, with leading terms of the form $\alpha_{\rm s}^k\left(\ln^{2k-2}x\right)/x$ at the kth order of perturbation theory, corresponding to poles $\alpha_{\rm s}^k\,(N-1)^{1-2k}$ for the Mellin moments

$$P^{(k)}(N) \;=\; \int_0^1 dx\; x^{N-1}\; P^{(k)}(x)\;. \qquad (19.7)$$

Despite large cancellations between leading and non-leading logarithms at non-asymptotic values of x, the resulting small-x rise in the timelike splitting functions dwarfs that of their spacelike counterparts for the evolution of the parton distributions in Section 18 of this *Review*, see Fig. 1 of Ref. [50]. Consequently, in fragmentation the fixed-order approximation to the evolution breaks down orders of magnitude earlier in x than in DIS.

The pattern of the known coefficients and other considerations suggest that the double-logarithmic terms sum to all-order expressions without any pole at $N = 1$, such as [61, 62]

$$P_{gg}^{\rm LL}(N) \;=\; -\frac{1}{4}\left(N - 1 - \sqrt{(N-1)^2 \cdot 24\,\alpha_{\rm s}/\pi}\right) \qquad (19.8)$$

for the gluon-to-gluon splitting function at leading logarithmic order. Keeping the first three terms in the resulting expansion of Eq. (19.5) around $N = 1$ and taking the Mellin inverse yields a Gaussian in the variable $\xi = \ln(1/x)$ for the small-x fragmentation functions,

$$xD(x, q^2 = s) \;\propto\; \exp\left[-\frac{1}{2\sigma^2}(\xi - \xi_p)^2\right]\;, \qquad (19.9)$$

with the peak position and width varying with the energy as [63] (see also Ref. [2])

$$\xi_p \;\simeq\; \frac{1}{4}\ln\left(\frac{s}{\Lambda^2}\right)\;,\quad \sigma \;\propto\; \left[\ln\left(\frac{s}{\Lambda^2}\right)\right]^{3/4}\;. \qquad (19.10)$$

Next-to-leading logarithmic corrections to the above predictions have been calculated [64]. In the method of Ref. [65], see also Refs. [66, 67], the corrections are included in an analytical form known as the 'modified leading logarithmic approximation' (MLLA). Alternatively they can be used to compute higher-moment corrections to the shape in Eq. (19.9) [68]. The small-x resummation of the coefficient functions for semi-inclusive e^+e^- annihilation and of the timelike spitting functions in the standard $\overline{\rm MS}$ scheme was extended in Refs. [69–73] and has reached full next-to-next-to-leading logarithmic accuracy. Applications of these results to gluon and quark jet multiplicities have been presented in Refs. [74].

Fig. 19.4 shows the ξ distribution for charged particles produced in the current region of the Breit frame in DIS and in e^+e^- annihilation. Consistently with Eq. (19.9) (the 'hump backed plateau') and Eq. (19.10) the distributions have a Gaussian shape, with the peak position and area increasing with CM energy (e^+e^-) and Q^2 (DIS).

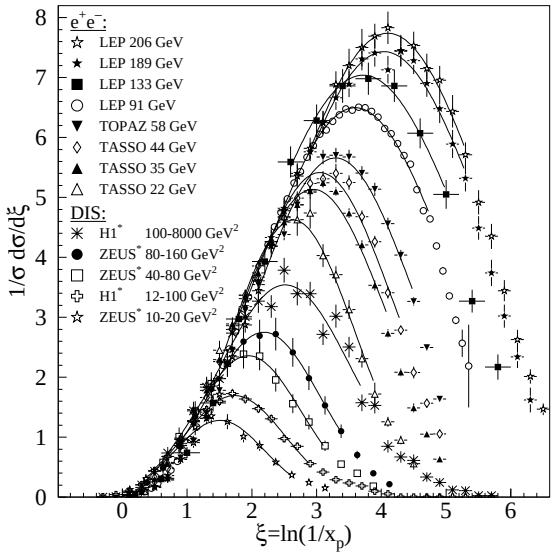

Figure 19.4: Distribution of the normalized fragmentation cross sections in $\xi = \ln(1/x_p)$ at several CM energies (e^+e^-) [10,11,16–19,57,58,75–78] and for intervals of Q^2 (DIS). At each energy only one representative measurement is displayed. For clarity some measurements at intermediate CM energies (e^+e^-) or Q^2 ranges (DIS) are not shown. The DIS measurements ($*$) have been scaled by a factor of 2 for direct comparability with the e^+e^- results. Fits of simple Gaussian functions are overlaid for illustration.

The predicted energy dependence of the peak in the ξ distribution (see Eq. (19.10)) is explained by soft gluon coherence (angular ordering), *i.e.*, the destructive interference of the color wavefunction of low energy gluon radiation, which correctly predicts the suppression of hadron production at small x. Of course, a decrease at very small x is expected on purely kinematical grounds, but this would occur at particle energies proportional to their masses, *i.e.*, at $x \propto m/\sqrt{s}$ and hence $\xi \sim \frac{1}{2}\ln s$. Thus, if the suppression were purely kinematic, the peak position ξ_p would vary twice as rapidly with the energy, which is ruled out by the data in Fig. 19.5. The e^+e^- and DIS data agree well with each other, demonstrating the universality of hadronization and the MLLA prediction. Measurements of the higher moments of the ξ distribution in e^+e^- [19,78–80] and DIS [58] have also been performed and show consistency with each other.

The average charged-particle multiplicity is another observable sensitive to fragmentation functions for small particle momenta. Perturbative predictions using both NLO [89] and MLLA [90, 91] have been obtained by solving Eq. (19.5) yielding

$$\left\langle n_G(Q^2)\right\rangle \propto \alpha_{\rm s}^b(Q^2)\cdot\exp\left[\frac{c}{4\pi b_0\sqrt{\alpha_{\rm s}(Q^2)}}\cdot\left(1 + 6a_2\frac{\alpha_{\rm s}(Q^2)}{\pi}\right)\right]\,, \qquad (19.11)$$

where $b = \frac{1}{4} + \frac{10}{27}\frac{n_f}{4\pi b_0}$, $c = \sqrt{96\pi}$, with $b_0 = (33 - 2n_f)/(12\pi)$, cf. Section 9 of this *Review*, for n_f contributing quark flavors. Higher-order corrections to Eq. (19.11) are known up to next-to-next-to-next-to-leading order ($\rm N^3LO$), for details and references

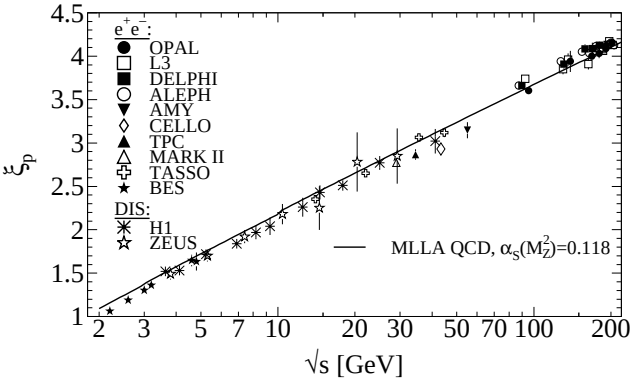

Figure 19.5: Evolution of the peak position, ξ_p, of the ξ distribution with the CM energy $\sqrt{s}$. The MLLA QCD prediction using $\alpha_s(s = M_Z^2) = 0.118$ is superimposed to the data of Refs. [10, 12, 15, 19, 56, 57, 76, 77, 80–88].

see [92]. The term proportional to $a_2 \approx -0.502 + 0.0421\, n_f - 0.00036\, n_f^2$ in Eq. (19.11) is the contribution due to NNLO corrections [93]. The quantity $\langle n_G(Q^2)\rangle$ refers to the average number of gluons, while for $\langle n_q(Q^2)\rangle$ for quarks a correction factor $1/r$ is required due to the different color factors in quark and gluon couplings, so that $\langle n_q(Q^2)\rangle = \langle n_G(Q^2)\rangle/r$. The correction factor depends only weakly on Q^2; higher-order corrections up to N^{3}LO on the asymptotic value $r = C_A/C_F = 9/4$ [94] are quoted in [92].

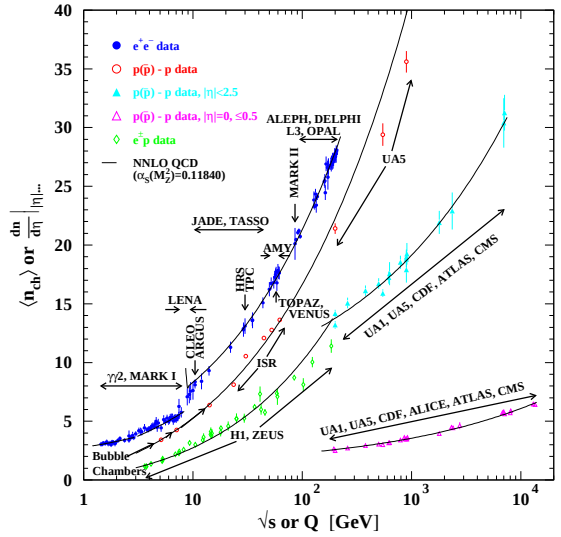

Figure 19.6: Average charged-particle multiplicity $\langle n_{\rm ch}\rangle$ as a function of $\sqrt{s}$ or Q for e^+e^- and $p\overline{p}$ annihilations, and pp and ep collisions. The indicated errors are statistical and systematic uncertainties added in quadrature, except when no systematic uncertainties are given. All NNLO QCD curves are from Eq. (19.11) with fitted normalization, $K_{\rm LHPD}$, and offset, n_0, using a fixed $\alpha_s(M_Z^2) = 0.1184$ [95] and for e^+e^- annihilation data $n_f = 3$, 4, or 5 depending on $\sqrt{s}$, else $n_f = 3$. $\mathbf{e^+e^-}$: Contributions from K^0_S and Λ decays included. Data compiled from Refs. [8,10,16,16,22,77,83,96–106]; $\mathbf{e^\pm p}$: Multiplicities have been measured in the current fragmentation region of the Breit frame. Data compiled from Refs. [35, 57, 58, 60, 107]; $\mathbf{p(\overline{p})}$: Measured values above 20 GeV refer to non-single diffractive (NSD) processes. Central pseudorapidity multiplicities $(\mathrm{d}n/\mathrm{d}\eta)|_{|\eta|...}$ refer to either $|\eta| < 2.5$ (CMS: $|\eta| < 2.4$) or $|\eta| = 0$ (UA5, CMS, ALICE: $|\eta| < 0.5$). Data compiled from Refs. [108–123].

Employing the hypothesis of 'Local Parton-Hadron Duality' (LPHD) [90], *i.e.*, that the color charge of partons is balanced locally in phase space and, hence, their hadronization occurs locally such that (Mellin transformed) parton and hadron inclusive distributions directly correspond, Eq. (19.11) can be applied to describe average charged particle multiplicities obtained in e^+e^- annihilation. The equation can also be applied to $e^\pm p$ scattering if the current fragmentation region of the Breit frame is considered for measuring the average charged-particle multiplicity. Fig. 19.6 shows corresponding data and fits of Eq. (19.11) where apart from an LPHD normalization factor a constant offset has been allowed for, so that $\langle n_{\rm ch}(Q)\rangle = K_{\rm LHPD} \cdot \langle n_G(Q)\rangle/r + n_0$.

In hadron-hadron collisions beam remnants, e.g. from single-diffractive (SD) scattering where one colliding proton is negligibly deflected while hadrons related with the other colliding proton are well-separated in rapidity from the former proton, contribute to the measurement of the hadron multiplicity from a hard parton-parton scattering, making interpretation of the data more model dependent. Experimental results are usually given for inelastic processes or for non-single diffractive processes (NSD). Due to the large beam particle momenta at Tevatron and LHC, not all final state particles can be detected within the limited detector acceptance. Therefore, experiments at Tevatron and LHC quote particle multiplicities for limited ranges of pseudo-rapidity $\eta = -\ln\tan(\vartheta/2)$ or at central rapidity, i.e. $\eta = 0$, as shown in Fig. 19.6.

A universality of the average particle multiplicities in e^+e^- and $p(\overline{p})$ processes has been reported in Ref. [124] when considering an effective collision energy $Q_{\rm eff} = \sqrt{s}/k$ in $p(\overline{p})$ reduced by a factor of $k \approx 3$, plus a constant offset of $n_0 \approx 2$. A more detailed review is available in Ref. [125]. According to the investigations presented in Ref. [126] the universality of the energy dependence of average particle multiplicities also applies to hadron-hadron and nucleus-nucleus collisions for both full and central rapidity multiplicities. Evidence for this universality is given by the good agreement for the energy dependence of Eq. (19.11) when fit to the $p(\overline{p})$ data as shown in Fig. 19.6.

19.4 Fragmentation models

Although the scaling violations can be calculated perturbatively, the actual form of the parton fragmentation functions is non-perturbative. Perturbative evolution gives rise to a shower of quarks and gluons (partons). Multi-parton final states from leading and higher order matrix element calculations are linked to these parton showers using factorization prescriptions, also called matching schemes, see Ref. [127] for an overview.

Phenomenological schemes are then used to model the carry-over of parton momenta and flavor to the hadrons. Implemented in Monte Carlo event generators (see Section 42 of this *Review*), these schemes have been tuned using e^+e^- data and provide good description of hadron collisions as well, thus providing evidence of the universality of fragmentation. However, e^+e^- mainly fix the quark jet fragmentation while it provides less constraints for modelling the gluon jet fragmentation.

19.5 Phenomenology of quark and gluon fragmentation functions

The fragmentation functions are solutions to the evolution equations Eq. (19.5), but need to be specified at some initial scale μ_0^2 (usually around 1 GeV^2 for light quarks and gluons, and at m_Q^2 for heavy quarks). A typical parameterization for a given light hadron is [128, 129, 131–137]

$$D_i^h(x,\mu_0^2) = N_i\, x^{\alpha_i}(1-x)^{\beta_i}\left(1+\gamma_i(1-x)^{\delta_i}\right)\,, \qquad (19.12)$$

where as indicated the normalization N_i, and the parameters α_i, β_i, γ_i and δ_i depend on the type i of the fragmenting parton. Heavy flavor fragmentation into heavy mesons is discussed in Sec. 19.8 below. The parameters of Eq. (19.12) are obtained by performing global fits to data on various hadron types for different combinations of partons and hadrons in e^+e^-, lepton-hadron and hadron-hadron collisions. We note that the choice of parameterization of the fragmentation functions at the initial scale necessarily introduces a bias since it imposes a certain form of the functions. This bias is largely avoided in neural network approaches which offer a wide flexibility of the initial functions and have recently been applied to fragmentation functions as well [130]. Sets of fragmentation functions are now available for

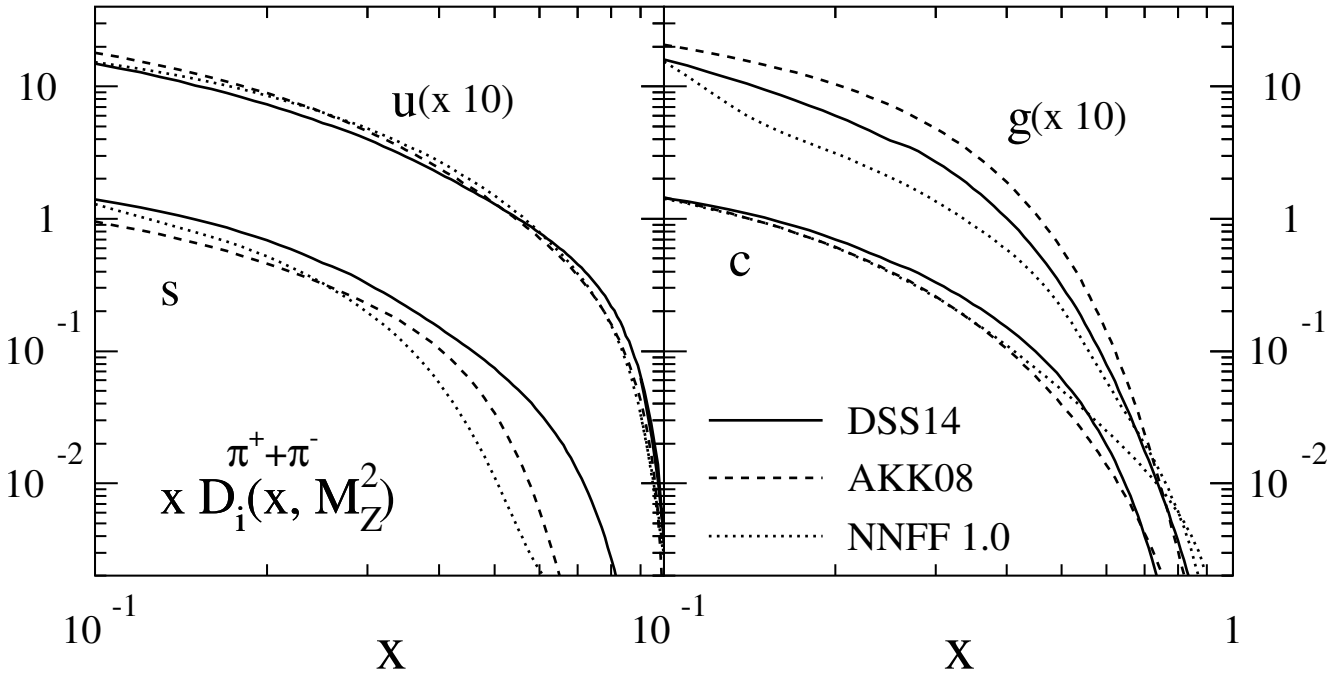

Figure 19.7: Comparison of up, strange, charm and gluon NLO fragmentation functions for $\pi^+ + \pi^-$ at the mass of the Z. The different lines correspond to the results of the analyses performed in Refs. [128–130].

pions, kaons, protons, neutrons, η mesons, Λ baryons, and charged hadrons [128–130, 132–140]. They are all at NLO level, except for Refs. [130, 139] which have been performed at NNLO level. The latter sets are restricted to the analysis of e^+e^- annihilation data. Recently, data from hadron-hadron collisions have been added in the framework of the neural network approach at NLO accuracy for charged hadrons [141]. It is noteworthy that the NNLO effects lead to an improvement in the theoretical description of the data in e^+e^- annihilation.

Data from e^+e^- annihilation present the cleanest experimental source for the measurement of fragmentation functions, but cannot be used to disentangle quark from antiquark fragmentation. Since the bulk of the e^+e^- annihilation data is obtained at the mass of the Z-boson, where the electroweak couplings are roughly the same for the different partons, it provides the most precise determination of the flavor-singlet combination of quark and antiquark fragmentation functions. Flavor-tagged results [142], distinguishing between the light quark, charm and bottom contributions are of particular value for flavor decomposition, even though those measurements cannot be unambiguously interpreted in perturbative QCD.

The most relevant source for quark-antiquark (and also flavor) separation is provided by SIDIS data. Semi-inclusive measurements are usually performed at much lower scales than for e^+e^- annihilation. The inclusion of SIDIS data in global fits allows for a wider coverage in the evolution of the fragmentation functions, resulting at the same time in a stringent test of the universality of the distributions. Charged-hadron production data in hadronic collisions also have sensitivity to (anti-)quark fragmentation functions.

The gluon fragmentation function $D_g^h(x)$ can be extracted, in principle, from the longitudinal fragmentation structure function F_L in Eq. (19.2), as the coefficient functions $C_{L,i}$ for quarks and gluons are comparable at order α_s. However at NLO, *i.e.*, including the $\mathcal{O}(\alpha_s^2)$ coefficient functions $C_{L,i}^{(2)}$ [39], quark fragmentation is dominant in F_L over a large part of the kinematic range, reducing the sensitivity to D_g^h. This distribution could be determined also by analyzing the scale evolution of the fragmentation functions. This possibility is limited by the lack of sufficiently precise data at energy scales away from the Z-resonance and the dominance of the quark contributions at medium and large values of x. In e^+e^- annihilation, D_g^h can also be deduced from the study

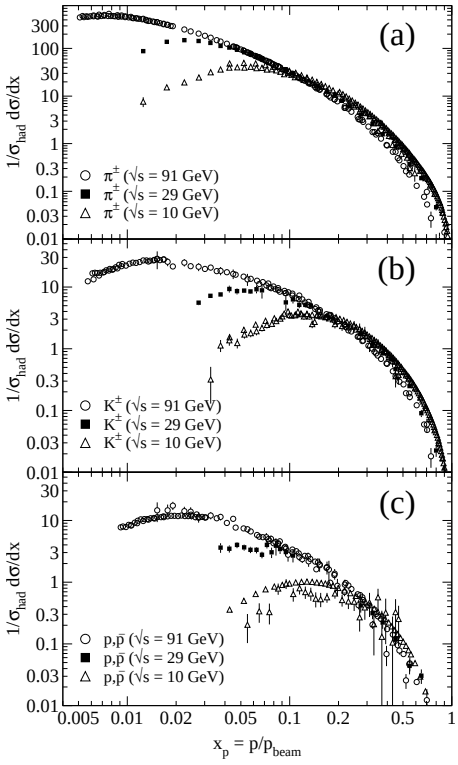

Figure 19.8: Scaled momentum spectra of (a) $\pi^\pm$, (b) $K^\pm$, and (c) $p, \overline{p}$ at $\sqrt{s} = 10$, 29, and 91 GeV [24, 26, 85, 143, 144].

of three-jet events in which the gluon jet is identified, for example, by tagging the other two jets with heavy quark decays. To leading order, the measured distributions of $x = E_{\rm had}/E_{\rm jet}$ for particles in gluon jets can be identified directly with the gluon fragmentation function $D_g^h(x)$.

Data for $p(\overline{p}) \to h + X$ provide much more direct constraint on D_g^h. At variance with e^+e^- annihilation and SIDIS, here gluon

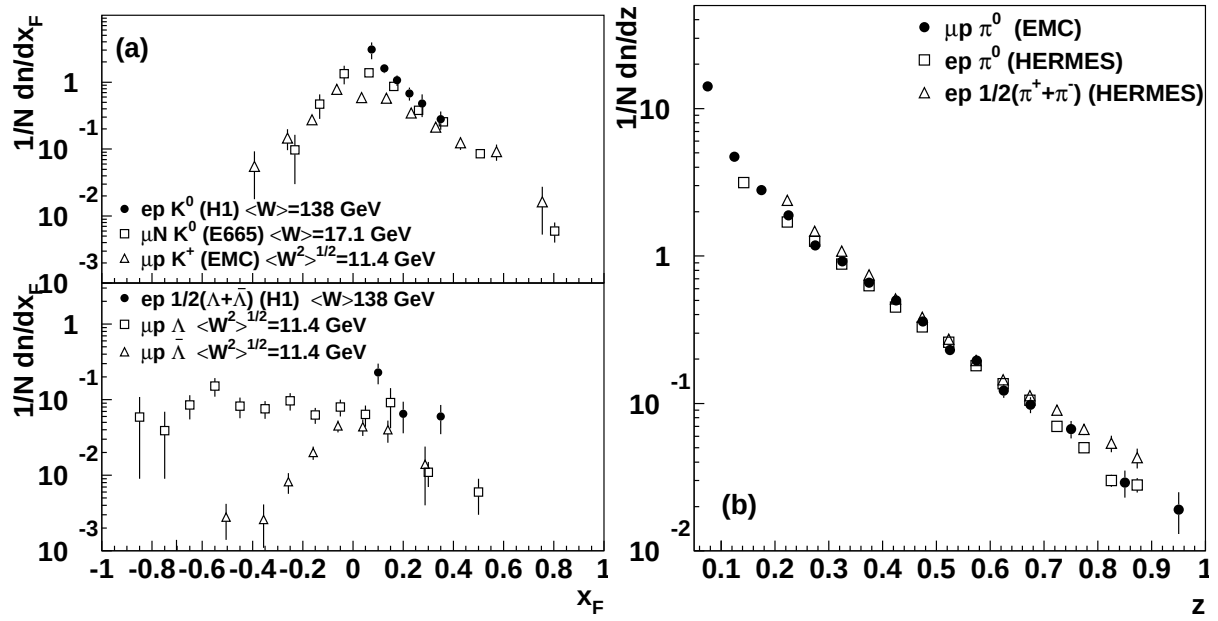

Figure 19.9: (a) $1/N \cdot dn/dx_F$ for identified strange particles in DIS at various values of W [145–147]. (b) $1/N \cdot dn/dz$ for measurements of pions in fixed-target DIS experiments [148–150].

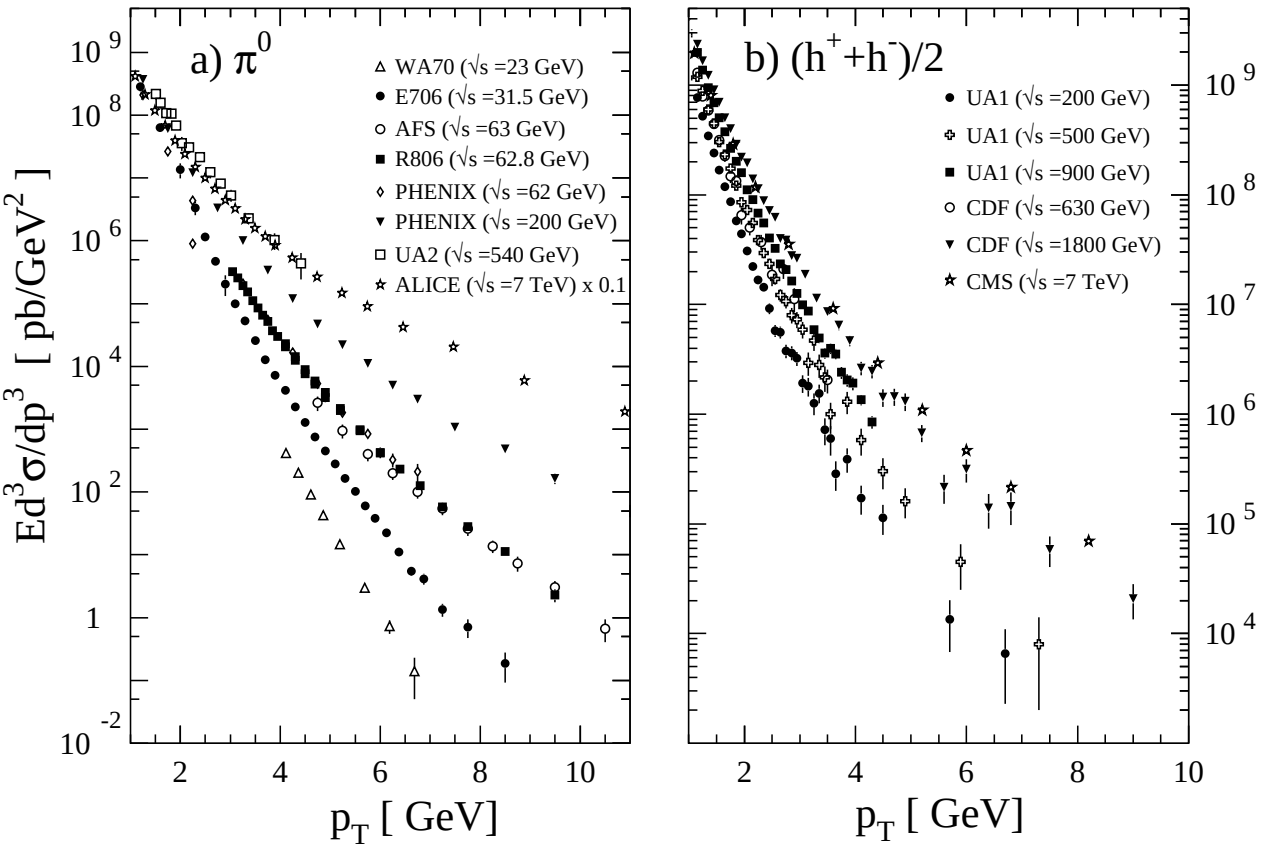

Figure 19.10: Selection of inclusive (a) π^0 and (b) charged-hadron production data from pp [118, 151–156] and $p\bar{p}$ [114, 157, 158] collisions.

fragmentation contributes already at the lowest order in the coupling constant. At large $x \gtrsim 0.5$, where information from e^+e^- is sparse, data from hadronic colliders significantly improve extractions of D_g^h [128, 129, 131, 138]. Recent LHC data has been included in the NLO analyses [129,137] of pion-fragmentation functions; see Sec.(17.7) for more details. Note that these analyses are currently the only ones that 'globally' incorporate available data from all sources, $e^+e^- \to h + X$, $ep \to e'h + X$ and $pp \to h + X$.

We note that recently a 'hybrid' type of high-p_T jet/hadron observable has also been considered both theoretically [159–165] and experimentally [166–173]. It is defined by an identified specific hadron found inside a fully reconstructed jet. This gives rise to a *same-side* hadron-jet momentum correlation that may be addressed using perturbative methods. One of several rele-

Table 19.1: Classification of spin- and transverse-momentum dependent quark fragmentation functions. For simplicity we have left out the ubiquitous label for flavor i of the fragmenting quark and for hadron species h. Each of the functions carries the argument $(x, x^2k_T^2)$ (plus dependence on a factorization scale), where $xk_T = p_T^h$ is the hadron's transverse momentum. λ and Λ are the quark's and hadron's helicities, respectively, and $\vec{s}_T$ and $\vec{S}_T$ are their transverse spin vectors. We have defined $\left[\vec{a} \times \vec{b}\right] \equiv a^1 b^2 - a^2 b^1$. Finally, m_h is the mass of the produced hadron.

	quark polarization		
hadron pol.	unpolarized	long. polarized	transv. polarized
unpol.	D	–	$\frac{\left[\vec{k}_T \times \vec{s}_T\right]}{m_h} H^\perp$
long. pol.	–	$\lambda \Lambda G_L$	$\frac{\vec{k}_T \cdot \vec{s}_T}{m_h} \Lambda H_L^\perp$
transv. pol.	$\frac{\left[\vec{k}_T \times \vec{S}_T\right]}{m_h} D_T^\perp$	$\frac{\vec{k}_T \cdot \vec{S}_T}{m_h} \lambda G_T^\perp$	$(\vec{s}_T \cdot \vec{S}_T) H_T + \frac{\vec{k}_T \cdot \vec{S}_T}{m_h} \frac{\vec{k}_T \cdot \vec{s}_T}{m_h} H_T^\perp$

vant kinematical variables (see [164] for an overview) is $z_h \equiv (\vec{p}_T^{\,h} \cdot \vec{p}_T^{\,\rm jet})/(p_T^{\rm jet})^2$, where $\vec{p}_T^{\,h}$ and $\vec{p}_T^{\,\rm jet}$ are the transverse momenta of the hadron and the jet, respectively. The observable provides an alternative window on fragmentation functions in a more exclusive setting, enabling novel tests of the universality of fragmentation functions. Varying z_h and/or the hadron species, one can map out the fragmentation functions 'locally' as functions of x. This is in contrast to the single-inclusive observable $pp \to h + X$, which inevitably samples over a broad range of x. Although hadron-in-jet data are not yet routinely included in analyses of fragmentation functions, a 'proof-of-principle' analysis does exist [174] that shows the potential of the observable in providing constraint on fragmentation functions.

A comparison of recent NLO fits of fragmentation functions for $\pi^+ + \pi^-$ obtained by DSS14 [129], AKK08 [128] and NNPDF1.0 [130] is shown in Fig. 19.7. Differences among the functions for these sets are large, especially for the gluon fragmentation function over the full range of x and for the quark functions at large momentum fractions. The differences are even larger for other species of hadrons like kaons and protons [128, 131, 135, 138]. Recent analyses [129,130,135,137,175,176] estimate the uncertainties involved in the extraction of fragmentation functions.

Photonic fragmentation functions play a relevant role in the theoretical understanding of inclusive photon production in (leptonic and hadronic) high energy processes. In the sprit of the analogy between parton fragmentation functions and parton distribution functions, also photonic fragmentation functions are analogous to the photon structure function F_2^γ and to the proton's photonic parton distributions (see review on structure functions in Section 18 of this *Review*). Since photons have a pointlike coupling to quarks [177], the corresponding fragmentation functions obey inhomogeneous evolution equations and are generally decomposed into a perturbative and a non-perturbative component [134, 178, 179]. The hadronic part, sometimes approximated by the Vector Meson Dominance Model, can in principle be obtained by performing a global analysis to the available prompt photon production data [7,12,15,19–21,85,143,180,181], although in practice this has not been done. We note that also the cross section for photons produced in fully reconstructed jets has been proposed [182] as a new tool for obtaining access to photon fragmentation functions, in analogy to the hadron-in-jet cross section discussed above.

19.6 Identified particles in e^+e^- and semi-inclusive DIS

There is a great wealth of measurements of e^+e^- fragmentation into identified particles. A collection of references for data on fragmentation into identified particles is provided in Table 52.1 of this *Review*. As a representative example, Figure 19.8 shows differential charged-hadron spectra as functions of the scaled hadron momentum at several CM energies.

Quantitative results of studies of scaling violations in e^+e^- fragmentation have been reported in [7,21,183,184]. Scaling violations may be used to extract a value of α_s; the values obtained are consistent with the world average (see review on QCD in Section 9 of this *Review*).

Many studies have been made of production of identified particles in lepton-hadron scattering, although fewer particle species have been measured than in e^+e^- collisions. References [145, 146, 148–150, 185–187] and [147, 188–193] are representative of the data from fixed target and ep collider experiments, respectively. QCD calculations performed at NLO provide an overall good description of the HERA data [33, 34, 58, 193–195], both for SIDIS [196] and for the hadron transverse momentum distribution [53,197] in the kinematic regions in which the calculations are predictive. A first step towards an NNLO calculation for SIDIS has been presented in [198].

Fig. 19.9(a) compares lower-energy fixed-target and HERA data on strangeness production, showing that the HERA spectra have substantially increased multiplicities, albeit with statistical precision that is insufficient to study scaling violations. The fixed-target data show that the Λ rate substantially exceeds the $\overline{\Lambda}$ rate in the remnant region, owing to the conserved baryon number from the baryon target. Fig. 19.9(b) shows $1/N \cdot dn/dz$ for neutral and charged pion production, where z is defined as the ratio of the pion energy to that of the exchanged boson, both measured in the laboratory frame. Results are shown from the HERMES and the EMC experiments, where the HERMES data have been evolved to $\langle Q^2 \rangle = 25$ GeV^2 at NLO QCD, in order to be comparable with the EMC data. Each of the experiments uses various kinematic cuts to ensure that the measured particles lie in the region that is expected to be associated with the struck quark. In the DIS kinematic regime accessed at these experiments, and over the range in z shown in Fig. 19.9, the z and x_F variables have similar values [30]. The precision data on identified particles can be used in the study of the quark flavor content of the proton [175, 214, 215].

Data on identified particle production can aid the investigation of the universality of jet fragmentation in e^+e^- and DIS. The strangeness suppression factor γ_s, as derived principally from tuning the Lund string model [216] within JETSET [217], is typically found to be around 0.3 in e^+e^- experiments [75], although values closer to 0.2 [218] have also been obtained. A number of measurements of so-called V^0-particles (K^0, Λ^0) and the relative rates of V^0's and inclusively produced charged particles have been performed at HERA [147,188,219] and fixed target experiments [145]. These typically favour a stronger suppression ($\gamma_s \approx 0.2$) than usually obtained from e^+e^- data, although values close to 0.3 have also been obtained [220, 221].

However, when comparing the description of QCD-based models for lepton-hadron interactions and e^+e^- collisions, it is important to note that the overall description by event generators of inclusively produced hadronic final states is more accurate in e^+e^- collisions than in lepton-hadron interactions [222]. Predictions of particle rates in lepton-hadron scattering are affected by uncertainties in the modelling of the parton composition of the

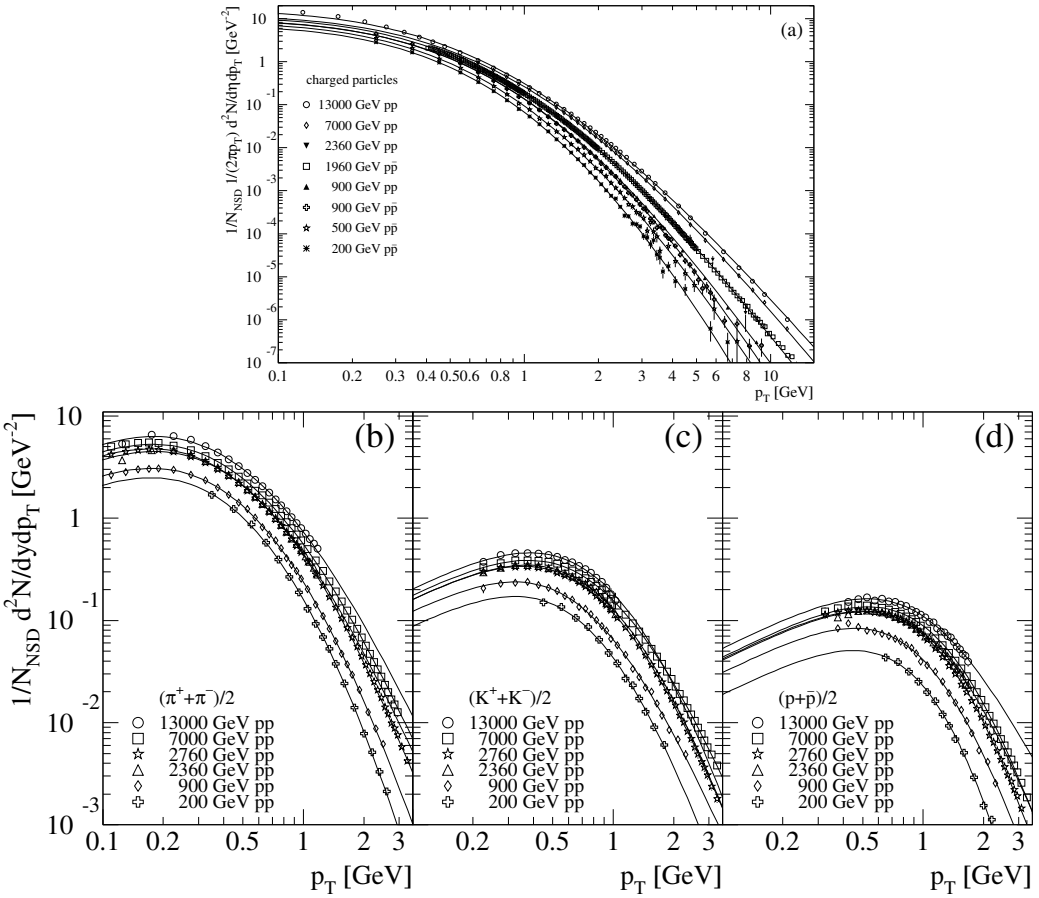

Figure 19.11: (a) Selection of inclusive charged-particle transverse momentum spectra [114, 117, 119, 121, 157, 199, 200], normalized to the non-single diffractive cross section (NSD). (b)-(d) Selection of identified charged-particle transverse momentum spectra [201–206] normalized to the NSD cross section. All spectra are scaled to the NSD cross-section using measurements of total, inelastic, elastic, single, or non-single diffractive cross sections from [207–211, 211–213]. The overall normalization uncertainty of about 3% is not shown. Superimposed are fits of the Tsallis distribution in Eq. (19.13).

proton and photon, the extended target remnant, and initial and final-state QCD radiation. Furthermore, the tuning of event generators for e^+e^- collisions is typically based on a larger set of parameters and uses more observables [75] than are used when optimizing models for lepton-hadron data [223].

19.7 Fragmentation in hadron-hadron collisions

An extensive set on high-transverse momentum (p_T) single-inclusive hadron data has been collected in $h_1h_2 \to hX$ scattering processes, both at high energy colliders and fixed-target experiments [151–158, 181, 224–246]. Fig. 19.10 shows the invariant cross sections $E\mathrm{d}^3\sigma/\mathrm{d}p^3$ for a compilation of neutral-pion and charged-hadron production data for energies in the range $\sqrt{s} \approx 23$ - 7000 GeV.

The differential cross section for high-transverse momentum hadron production has been computed to NLO accuracy in perturbative QCD [247]. The NLO corrections are typically large and can even double the prediction for the cross section at fixed-target energies. Nevertheless, the NLO calculations significantly under-predict the cross-section for several fixed-target energy data sets [242, 248, 249]. Different strategies have been developed to ameliorate the theoretical description at fixed-target energies. A possible phenomenological approach involves the introduction of a non-perturbative intrinsic partonic transverse momentum [156, 242, 250, 251]. Furthermore, the resummation of the dominant higher order corrections at threshold produces an enhancement of the theoretical calculation that significantly improves the description of the data [252, 253].

Data collected at high energy colliders are either included in global fit analyses or used as a test for the universality of fragmentation functions. A certain tension has been observed between data sets from RHIC and the LHC [254]. The tension can be largely resolved [129] by excluding data with transverse momentum smaller than ~ 5 GeV from the analysis, where fixed-order pQCD calculations are not expected to provide an accurate description of the process. Still, after removing these smaller p_T values where the data sets appear to be mutually exclusive in the global fit, the RHIC data show a preference towards harder gluon fragmentation at large x than the LHC data.

Transverse momentum distributions can usually be fit by power laws [255]. An approach to describe the low p_T particle spectra is the Tsallis distribution [256–258], which is based on a non-extensive generalization of the Boltzmann-Gibbs statistics. The functional form [259]

$$\frac{\mathrm{d}^2N}{\mathrm{d}p_T\mathrm{d}y} = p_T\frac{\mathrm{d}N}{\mathrm{d}y}\frac{(n-1)(n-2)}{nT(nT+m_0(n-2))}\left[1+\frac{m_T-m_0}{nT}\right]^{-n} \tag{19.13}$$

is frequently used to fit the transverse momentum spectra, where $\mathrm{d}N/\mathrm{d}y$ is the particle's multiplicity, T and n are fit parameters of the Tsallis distribution, m_0 is the either the mass of the most abundant particle, i.e. the pion for inclusive spectra, or the mass of an identified particle, and $m_T = \sqrt{p_T^2+m_0^2}$. The parameter n is related to the non-extensive parameter $q = n/(n-1)$ of the original Tsallis formula [260], and T is connected to the temperature in the Boltzmann-Gibbs statistics. The Tsallis distribution has been very successfully fit to measured transverse momentum distributions of both inclusive charged particles and identified particle spectra for hadron-hadron collisions, see for example [261–263], for collisions of heavy nuclei, see for example [264], and also for e^+e^- collisions, see for example [265]. The energy dependence of

the fitted Tsallis parameters has also been investigated in detail, see [259, 266]. Fig. 19.11 shows examples of hadron production data in pp and $p\bar{p}$ collisions compared to Tsallis distributions.

Hadron production provides a critical observable for probing the high energy-density matter produced in heavy-ion collisions. Measurements at colliders show a suppression of inclusive hadron yields at high transverse momentum for AA collisions compared to pp scattering, indicating the formation of a dense medium opaque to quark and gluons, see e.g. [267].

19.8 Heavy quark fragmentation

It was recognized very early [268] that a heavy flavored meson should retain a large fraction of the momentum of the primordial heavy quark, and therefore its fragmentation function should be much harder than that of a light hadron. In the limit of a very heavy quark, one expects the fragmentation function for a heavy quark to go into any heavy hadron to be peaked near $x = 1$.

When the heavy quark is produced at a momentum much larger than its mass, one expects important perturbative effects, enhanced by powers of the logarithm of the transverse momentum over the heavy quark mass, to intervene and modify the shape of the fragmentation function. In leading logarithmic order (*i.e.*, including all powers of $\alpha_s \log(m_Q/p_T)$), the total (*i.e.*, summed over all hadron types) perturbative fragmentation function is simply obtained by solving the leading evolution equation for fragmentation functions, Eq. (19.5), with the initial condition due to the finite mass of the heavy quark given by $D_Q(x,\mu^2)\Big|_{\mu^2=m_Q^2} = \delta(1-x)$ and $D_i(x,\mu^2)\Big|_{\mu^2=m_Q^2} = 0$ for $i \neq Q$ (here $D_i(x,\mu^2)$, stands for the probability to produce a heavy quark Q from parton i with a fraction x of the parton momentum).

Several extensions of the leading logarithmic result have appeared in the literature. Next-to-leading-log (NLL) order results for the perturbative heavy quark fragmentation function have been obtained in [272]. The resummation of the dominant logarithmic contributions at large x was performed in [273] to next-to-leading-log accuracy. Fixed-order calculations of the fragmentation function at order α_s^2 in e^+e^- annihilation have appeared in [274] while the initial condition for the perturbative heavy quark fragmentation function has been extended to NNLO in [275].

Inclusion of non-perturbative effects in the calculation of the heavy-quark fragmentation function is done by convoluting the perturbative result with a phenomenological non-perturbative form. This form follows from the simple kinematical consideration that the formation of a hadron by attaching light quarks/antiquarks to the heavy quark will slightly decelerate the heavy quark. Thus its shape will show a peak that becomes increasingly centered next to $x = 1$ the higher the quark mass. Among the most popular parameterizations we have the following:

$$\text{Peterson } \textit{et al.}\ [276]: \quad D_{\rm np}(x) \propto \frac{1}{x}\left(1-\frac{1}{x}-\frac{\epsilon}{1-x}\right)^{-2}, \tag{19.14}$$

$$\text{Kartvelishvili } \textit{et al.}\ [277]: \quad D_{\rm np}(x) \propto x^{\alpha}(1-x), \tag{19.15}$$

$$\text{Collins \& Spiller } [278]: \quad D_{\rm np}(x) \propto \left(\frac{1-x}{x}+\frac{(2-x)\epsilon_C}{1-x}\right)\times (1+x^2)\times \left(1-\frac{1}{x}-\frac{\epsilon_C}{1-x}\right)^{-2} \tag{19.16}$$

$$\text{Colangelo \& Nason } [279]: \quad D_{\rm np}(x) \propto (1-x)^{\alpha}x^{\beta} \tag{19.17}$$

$$\text{Bowler } [280]: \quad D_{\rm np}(x) \propto x^{-(1+bm_{h,\perp}^2)} \times (1-x)^a \exp\left(-\frac{bm_{h,\perp}^2}{x}\right) \tag{19.18}$$

$$\text{Braaten } \textit{et al.}\ [281]: \quad \text{(see Eqs. (31), (32) in [281])} \tag{19.19}$$

where ϵ, ϵ_C, a, $bm_{h,\perp}^2$, α, and β are non-perturbative parameters that depend on the heavy hadron considered. The parameters entering the non-perturbative forms are fitted together with some model of hard radiation, which can be either a shower Monte Carlo, a leading-log or NLL calculation (which may or may not include Sudakov resummation), or a fixed order calculation. In [274], for example, the Peterson *et al.* [276] ϵ parameter for charm and bottom production is fitted from the measured distributions of Refs. [282, 283] for charm, and of [284] for bottom. If the leading-logarithmic approximation (LLA) is used for the perturbative part, one finds $\epsilon_c \approx 0.05$ and $\epsilon_b \approx 0.006$; if a second order calculation is used one finds $\epsilon_c \approx 0.035$ and $\epsilon_b \approx 0.0033$; if a NLL improved fixed order $\mathcal{O}(\alpha_s^2)$ calculation is used instead of NLO $\mathcal{O}(\alpha_s)$ one finds $\epsilon_c \approx 0.022$ and $\epsilon_b \approx 0.0023$. The larger values found in the LL approximation are consistent with what is obtained in the context of parton shower models [285], as expected. The ϵ parameter for charm and bottom scales roughly with the inverse square of the heavy flavor mass. This behavior can be justified by several arguments [268, 286, 287]. It can be used to relate the non-perturbative parts of the fragmentation functions of charm and bottom quarks [274, 279, 288].

A more conventional approach [289] involves the introduction of a unique set of heavy quark fragmentation functions of non-perturbative nature that obey the usual massless evolution equations in Eq. (19.5). Finite mass terms of the form $(m_Q/p_T)^n$ are kept in the corresponding short distance coefficient function for each scattering process. Within this approach, the initial condition for the perturbative fragmentation function provides the term needed to define the correct subtraction scheme to match the massless limit for the coefficient function (see e.g. [290]). Such an implementation is in line with the variable flavor number scheme introduced for parton distributions functions, as described in Section 18 of this *Review*.

High statistics data for charmed-meson production near the Υ resonance (excluding decay products of B mesons) have been published [269, 270]. They include results for D and D^*, D_s (see also [291, 292]) and Λ_c. Shown in Fig. 19.12(a) are the CLEO and BELLE inclusive cross-sections times branching ratio $\mathcal{B}$, $s\mathcal{B}d\sigma/dx_p$, for the production of D^0 and D^{*+}. The variable x_p approximates the light-cone momentum fraction x, but is not identical to it. The two measurements are consistent with each other.

The branching ratio $\mathcal{B}$ represents $D^0 \to K^-\pi^+$ for the D^0 results and for the D^{*+} the product of the branching fractions for $D^{*+} \to D^0\pi^+$ and $D^0 \to K^-\pi^+$. Given the high precision of CLEO's and BELLE's data, a superposition of different parametric forms for the non-perturbative contribution is needed to obtain a good fit [52]. Older studies are reported in Refs. [283, 293, 294]. Charmed meson spectra on the Z peak have been published by OPAL and ALEPH [295, 296].

Charm quark production has also been extensively studied at HERA by the H1 and ZEUS collaborations. Measurements have been made of $D^{*\pm}$, $D^{\pm}$, and $D_s^{\pm}$ mesons and the Λ_c baryon. See, for example, Refs. [297, 298].

Experimental studies of the fragmentation function for b quarks, shown in Fig. 19.12(b), have been performed at LEP and SLD [271, 284, 299]. Commonly used methods identify the B meson through its semileptonic decay or based upon tracks emerging from the B secondary vertex. Heavy flavor contributions from gluon splitting are usually explicitly removed before fitting for the fragmentation functions. The studies in [271] fit the B spectrum using a Monte Carlo shower model supplemented with non-perturbative fragmentation functions yielding consistent results.

The experiments measure primarily the spectrum of B mesons. This defines a fragmentation function that includes the effect of the decay of higher mass excitations, like the B^* and B^{**}. In the literature (cf. details in Ref. [300]), there is sometimes ambiguity in what is defined to be the bottom fragmentation function. Instead of using what is directly measured (*i.e.*, the B meson spectrum), in some cases corrections are applied to account for B^* or B^{**} production.

Heavy-flavor production in e^+e^- collisions is the primary source of information for the role of fragmentation effects in heavy-flavor production in hadron-hadron and lepton-hadron collisions. The

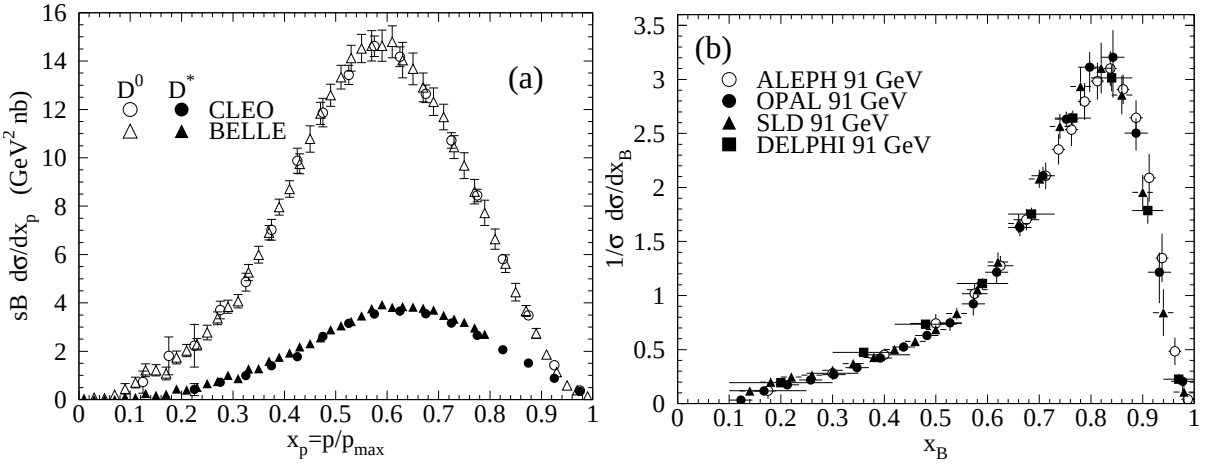

Figure 19.12: (a) Efficiency-corrected inclusive cross-section measurements for the production of D^0 and D^{*+} in e^+e^- measurements at $\sqrt{s} \approx 10.6$ GeV, excluding B decay products [269] [270]. (b) Measured e^+e^- fragmentation function of b quarks into B hadrons at $\sqrt{s} \approx 91$ GeV [271].

QCD calculations tend to underestimate the data in certain regions of phase space. Some experimental results from LHC summarized in [301] show such deviations e.g. at high transverse jet momentum and also at low di-jet separation angles, see [302] for details, and were already theoretically investigated in [303].

Both bottomed- and charmed-meson spectra have been measured at the Tevatron with unprecedented accuracy [304]. The measured spectra are in good agreement with QCD calculations (including non-perturbative fragmentation effects inferred from e^+e^- data [305]).

The HERA collaborations have produced a number of measurements of beauty production; see, for example, Refs. [297,306–309]. As for the Tevatron data, the HERA results are described well by QCD-based calculations using fragmentation models optimised with e^+e^- data.

Besides degrading the fragmentation function by gluon radiation, QCD evolution can also generate soft heavy quarks, increasing in the small x region as $\sqrt{s}$ increases. Several theoretical studies are available on the issue of how often $b\bar{b}$ or $c\bar{c}$ pairs are produced indirectly via a gluon splitting mechanism [310–312]. Experimental results from studies on charm and bottom production via gluon splitting, given in [296, 313–317], yield weighted averages of $\overline{n}_{g\to c\bar{c}} = 3.05 \pm 0.45\%$ and $\overline{n}_{g\to b\bar{b}} = 0.277 \pm 0.072\%$, respectively. The production of bottom-antibottom quark pairs via gluon splitting has also been investigated at hadron colliders, see for example [318–320].

19.9 Spin-dependent and transverse-momentum dependent fragmentation functions

The fragmentation functions we have considered so far apply to the spin-averaged case in which the polarization of the produced hadron is not observed, or the hadron has spin-0. We have also only considered 'collinear' fragmentation functions $D_i^h(x, \mu^2)$ which carry only one kinematical variable, the momentum fraction x. New insights into fragmentation and hadronization become available when also the dependence of fragmentation functions on the spin of the produced hadron and/or its relative transverse momentum with respect to the fragmenting parton are considered. In the latter case, one refers to the fragmentation functions as 'transverse-momentum dependent (TMD)' fragmentation functions.

Staying first with collinear fragmentation functions, two types of spin-dependent fragmentation functions to spin-1/2 hadrons can be considered. The helicity-dependent fragmentation function measures the transfer of longitudinal spin from the fragmenting parton to the hadron [38, 321–324]. It is given by

$$\Delta D_i^h(x, \mu^2) \equiv D_{i+}^{h^+}(x, \mu^2) - D_{i+}^{h^-}(x, \mu^2)\,, \qquad (19.20)$$

where the superscripts $\pm$ refer to the helicities of the parton and hadron. Λ hyperons are ideally suited for measurements of the ΔD_i^h, thanks to their self-analyzing weak decay $\Lambda \to \pi p$. Measurements of the longitudinal spin transfer to Lambda hyperons have been presented in e^+e^- (on the Z resonance), ℓp, and pp scattering in Refs. [325–331]. One may readily extend Eq. (19.20) to the case of transverse polarization of hadrons and quarks [332], where the corresponding fragmentation functions are known as 'transversity' fragmentation functions. There are also measurements constraining these fragmentation functions [326, 333, 334].

If the transverse-momentum (k_T) dependence of fragmentation functions is considered, there are eight types of leading-twist functions, defined by the correlations among the hadronic and partonic spin vectors and transverse-momentum vectors they represent. (For review, see [5]). We note that the eight fragmentation functions given in the table below exist separately for each quark and antiquark flavor, and a similar set may be introduced for gluons. Upon integration over the transverse momentum k_T the collinear unpolarized, helicity, and transversity fragmentation functions are reproduced.

The various fragmentation functions may be obtained from spin asymmetries and angular distributions in hadron production processes. There is a large body of precision data by now on transverse-momentum distributions in e^+e^- annihilation [335] and SIDIS [186, 336] that provide constraints on the unpolarized TMD fragmentation functions D_i^h, which have been analyzed theoretically, partly also including TMD evolution effects and high orders of perturbation theory [337–342].

Besides the unpolarized functions D most of the attention in experiment and theory has been on the function $H^\perp$ which describes the production of unpolarized (or spin-0) hadrons by transversely polarized quarks. This function is known as the 'Collins function' [343]. Its importance also derives from the fact that it may be used to probe the quark transversity PDF of the nucleon [344] which gives the probability of finding a transversely polarized quark with its spin aligned or anti-aligned with the spin of a transversely polarized nucleon. The transversity function is chiral-odd, and therefore not accessible through measurements of inclusive lepton-hadron scattering. The Collins effect in semi-inclusive DIS, on the other hand, provides an avenue for accessing transversity. The Collins fragmentation function is chiral-odd and T-odd, leading to a characteristic single-spin asymmetry in the azimuthal angular distribution of the produced hadron in the hadron scattering plane. A number of SIDIS [345–356] and e^+e^- experiments [357–361] have performed measurements of the Collins effect, for charged pions and kaons. These have been analyzed theoretically [362, 363], leading to an extraction of the nucleon's transversity distributions [363]. The Collins effect has also been studied in pp scattering, where one considers azimuthal transverse single-spin asymmetries for distributions of hadrons inside

jets [173, 364, 365].

In the context of extractions of transversity PDFs also fragmentation functions for same-side pairs of hadrons with small invariant mass, *dihadrons*, have been introduced and studied [366–374]. Compared to the Collins effect, dihadron fragmentation functions have the advantage that they may be defined purely in collinear factorization. The relevant spin-dependent dihadron fragmentation function exploits a correlation between the transverse polarization of the fragmenting quark and the relative momentum of the two hadrons. In SIDIS with a transversely polarized hadron beam, the dihadron cross section then contains a specific modulation in the azimuthal orientation of the plane containing the momenta of the two hadrons. The coefficient of this modulation is a product of the spin-dependent dihadron fragmentation function and the target's transversity PDF. The dihadron fragmentation functions may be separately extracted from measurements in e^+e^- annihiliation, and the Belle experiment has presented data [375] that have been analyzed theoretically [376, 377]. In lepton scattering, HERMES [378] and COMPASS [379, 380] have reported data sensitive to the spin-dependent dihadron fragmentation functions, and recently the STAR experiment at RHIC has presented data in the azimuthal distribution of $\pi^+\pi^-$ pairs produced in pp scattering with one transversely polarized proton [381]. The results have been successfully used for the extraction of transversity PDFs [377, 382–384].

References

[1] G. Altarelli, Phys. Rept. **81**, 1 (1982).

[2] R.K. Ellis *et al.*, *QCD and Collider Physics*, Cambridge University Press (1996).

[3] S. Albino *et al.* (2008), [arXiv:0804.2021].

[4] F. Arleo, Eur. Phys. J. **C61**, 603 (2009), [arXiv:0810.1193].

[5] A. Metz and A. Vossen, Prog. Part. Nucl. Phys. **91**, 136 (2016), [arXiv:1607.02521].

[6] P. Nason and B. R. Webber, Nucl. Phys. **B421**, 473 (1994), [Erratum: Nucl. Phys.B480,755(1996)].

[7] D. Buskulic *et al.* (ALEPH), Phys. Lett. **B357**, 487 (1995), [Erratum: Phys. Lett.B364,247(1995)].

[8] P. Abreu *et al.* (DELPHI), Eur. Phys. J. **C6**, 19 (1999).

[9] R. Barate *et al.* (ALEPH), Phys. Rept. **294**, 1 (1998).

[10] D. Buskulic *et al.* (ALEPH), Z. Phys. **C73**, 409 (1997).

[11] B. Adeva *et al.* (L3), Phys. Lett. **B259**, 199 (1991).

[12] Y. K. Li *et al.* (AMY), Phys. Rev. **D41**, 2675 (1990).

[13] D. Bender *et al.*, Phys. Rev. **D31**, 1 (1985).

[14] G. S. Abrams *et al.*, Phys. Rev. Lett. **64**, 1334 (1990).

[15] A. Petersen *et al.*, Phys. Rev. **D37**, 1 (1988).

[16] G. Alexander *et al.* (OPAL), Z. Phys. **C72**, 191 (1996).

[17] K. Ackerstaff *et al.* (OPAL), Z. Phys. **C75**, 193 (1997).

[18] G. Abbiendi *et al.* (OPAL), Eur. Phys. J. **C16**, 185 (2000), [hep-ex/0002012].

[19] W. Braunschweig *et al.* (TASSO), Z. Phys. **C47**, 187 (1990).

[20] K. Ackerstaff *et al.* (OPAL), Eur. Phys. J. **C7**, 369 (1999), [hep-ex/9807004].

[21] P. Abreu *et al.* (DELPHI), Phys. Lett. **B398**, 194 (1997).

[22] G. Abbiendi *et al.* (OPAL), Eur. Phys. J. **C37**, 1, 25 (2004), [hep-ex/0404026].

[23] R. Brandelik *et al.* (TASSO), Phys. Lett. **114B**, 65 (1982).

[24] K. Abe *et al.* (SLD), Phys. Rev. **D69**, 072003 (2004), [hep-ex/0310017].

[25] H. Aihara *et al.* (TPC/Two Gamma), Phys. Rev. Lett. **61**, 1263 (1988).

[26] M. Leitgab *et al.* (Belle), Phys. Rev. Lett. **111**, 062002 (2013), [arXiv:1301.6183].

[27] W. Kittel and E.A. De Wolf, *Soft Multihadron Dynamics*, World Scientific (2005).

[28] H.F. Jones, Nuovo Cimento **40A**, 1018 (1965).

[29] K. H. Streng, T. F. Walsh and P. M. Zerwas, Z. Phys. **C2**, 237 (1979).

[30] M. R. Adams *et al.* (E-665), Phys. Lett. **B272**, 163 (1991).

[31] M. Arneodo *et al.* (European Muon), Z. Phys. **C35**, 417 (1987).

[32] I. Abt *et al.* (H1), Z. Phys. **C63**, 377 (1994).

[33] M. Derrick *et al.* (ZEUS), Z. Phys. **C70**, 1 (1996), [hep-ex/9511010].

[34] J. Breitweg *et al.* (ZEUS), Phys. Lett. **B414**, 428 (1997), [hep-ex/9710011].

[35] F. D. Aaron *et al.* (H1), Phys. Lett. **B654**, 148 (2007), [arXiv:0706.2456].

[36] P. Abreu *et al.* (DELPHI), Phys. Lett. **B311**, 408 (1993).

[37] G. Altarelli *et al.*, Nucl. Phys. **B160**, 301 (1979); R. Baier and K. Fey, Z. Phys. **C2**, 339 (1979).

[38] D. de Florian, M. Stratmann and W. Vogelsang, Phys. Rev. **D57**, 5811 (1998), [hep-ph/9711387].

[39] P. J. Rijken and W. L. van Neerven, Phys. Lett. **B386**, 422 (1996), [hep-ph/9604436]; P. J. Rijken and W. L. van Neerven, Phys. Lett. **B392**, 207 (1997), [hep-ph/9609379]; P. J. Rijken and W. L. van Neerven, Nucl. Phys. **B487**, 233 (1997), [hep-ph/9609377].

[40] A. Mitov, S. Moch and A. Vogt, Phys. Lett. **B638**, 61 (2006), [hep-ph/0604053].

[41] A. Mitov and S.-O. Moch, Nucl. Phys. **B751**, 18 (2006), [hep-ph/0604160].

[42] V. N. Gribov and L. N. Lipatov, Sov. J. Nucl. Phys. **15**, 438 (1972), [Yad. Fiz.15,781(1972)]; V. N. Gribov and L. N. Lipatov, Sov. J. Nucl. Phys. **15**, 675 (1972), [Yad. Fiz.15,1218(1972)]; L.N. Lipatov, Sov. J. Nucl. Phys. **20**, 95 (1975); Yu.L. Dokshitzer, Sov. Phys. JETP Lett. **46**, 641 (1977); G. Altarelli and G. Parisi, Nucl. Phys. **B126**, 298 (1977).

[43] H. Georgi and H. D. Politzer, Nucl. Phys. **B136**, 445 (1978); J. F. Owens, Phys. Lett. **76B**, 85 (1978); T. Uematsu, Phys. Lett. **79B**, 97 (1978).

[44] G. Curci, W. Furmanski and R. Petronzio, Nucl. Phys. **B175**, 27 (1980).

[45] W. Furmanski and R. Petronzio, Phys. Lett. **97B**, 437 (1980).

[46] E. G. Floratos, C. Kounnas and R. Lacaze, Nucl. Phys. **B192**, 417 (1981).

[47] J. Kalinowski, K. Konishi and T. R. Taylor, Nucl. Phys. **B181**, 221 (1981).

[48] M. Stratmann and W. Vogelsang, Nucl. Phys. **B496**, 41 (1997), [hep-ph/9612250].

[49] Yu. L. Dokshitzer, G. Marchesini and G. P. Salam, Phys. Lett. **B634**, 504 (2006), [hep-ph/0511302].

[50] S. Moch and A. Vogt, Phys. Lett. **B659**, 290 (2008), [arXiv:0709.3899].

[51] A. A. Almasy, S. Moch and A. Vogt, Nucl. Phys. **B854**, 133 (2012), [arXiv:1107.2263].

[52] M. Cacciari, P. Nason and C. Oleari, JHEP **04**, 006 (2006), [hep-ph/0510032]; M. Cacciari, P. Nason and C. Oleari, JHEP **10**, 034 (2005), [hep-ph/0504192].

[53] P. Aurenche *et al.*, Eur. Phys. J. **C34**, 277 (2004), [hep-ph/0312359]; A. Daleo, D. de Florian and R. Sassot, Phys. Rev. **D71**, 034013 (2005), [hep-ph/0411212]; B. A. Kniehl, G. Kramer and M. Maniatis, Nucl. Phys. **B711**, 345 (2005), [Erratum: Nucl. Phys.B720,231(2005)], [hep-ph/0411300].

[54] B. Wang *et al.*, Phys. Rev. **D99**, 9, 094029 (2019), [arXiv:1903.01529].

[55] S. Aid *et al.* (H1), Nucl. Phys. **B445**, 3 (1995), [hep-ex/9505003].

[56] M. Derrick *et al.* (ZEUS), Z. Phys. **C67**, 93 (1995), [hep-ex/9501012].

[57] C. Adloff *et al.* (H1), Nucl. Phys. **B504**, 3 (1997), [hep-ex/9707005].

[58] J. Breitweg *et al.* (ZEUS), Eur. Phys. J. **C11**, 251 (1999), [hep-ex/9903056].

[59] J. F. Patrick *et al.*, Phys. Rev. Lett. **49**, 1232 (1982).

[60] S. Chekanov *et al.* (ZEUS), JHEP **06**, 061 (2008), [arXiv:0803.3878].

[61] A. H. Mueller, Phys. Lett. **104B**, 161 (1981).

[62] A. Bassetto *et al.*, Nucl. Phys. **B207**, 189 (1982).

[63] Yu.L. Dokshitzer *et al.*, Z. Phys. **C15**, 324 (1982).

[64] A. H. Mueller, Nucl. Phys. **B213**, 85 (1983); A. H. Mueller, Nucl. Phys. **B241**, 141 (1984).

[65] Y. L. Dokshitzer, V. A. Khoze and S. I. Troian, Int. J. Mod. Phys. **A7**, 1875 (1992).

[66] Yu.L. Dokshitzer *et al.*, *Basics of Perturbative QCD*, Editions Frontières (1991).

[67] V. A. Khoze and W. Ochs, Int. J. Mod. Phys. **A12**, 2949 (1997), [hep-ph/9701421].

[68] C. P. Fong and B. R. Webber, Nucl. Phys. **B355**, 54 (1991).

[69] S. Albino *et al.*, Phys. Rev. Lett. **95**, 232002 (2005), [hep-ph/0503170].

[70] S. Albino *et al.*, Phys. Rev. **D73**, 054020 (2006), [hep-ph/0510319].

[71] S. Albino *et al.*, Nucl. Phys. **B851**, 86 (2011), [arXiv:1104.3018]; S. Albino *et al.*, Nucl. Phys. **B855**, 801 (2012), [arXiv:1108.3948].

[72] A. Vogt, JHEP **10**, 025 (2011), [arXiv:1108.2993]; C. H. Kom, A. Vogt and K. Yeats, JHEP **10**, 033 (2012), [arXiv:1207.5631].

[73] D. P. Anderle *et al.*, Phys. Rev. **D95**, 5, 054003 (2017), [arXiv:1611.03371].

[74] P. Bolzoni, B. A. Kniehl and A. V. Kotikov, Phys. Rev. Lett. **109**, 242002 (2012), [arXiv:1209.5914]; P. Bolzoni, B. A. Kniehl and A. V. Kotikov, Nucl. Phys. **B875**, 18 (2013), [arXiv:1305.6017].

[75] P. Abreu *et al.* (DELPHI), Z. Phys. **C73**, 11 (1996).

[76] P. Abreu *et al.* (DELPHI), Z. Phys. **C73**, 229 (1997).

[77] P. Achard *et al.* (L3), Phys. Rept. **399**, 71 (2004), [hep-ex/0406049].

[78] R. Itoh *et al.* (TOPAZ), Phys. Lett. **B345**, 335 (1995), [hep-ex/9412015].

[79] M. Althoff *et al.* (TASSO), Z. Phys. **C22**, 307 (1984).

[80] M. Z. Akrawy *et al.* (OPAL), Phys. Lett. **B247**, 617 (1990).

[81] W. Dunwoodie *et al.* (BES), Phys. Rev. **D69**, 072002 (2004), [hep-ex/0306055].

[82] D. Buskulic *et al.* (ALEPH), Z. Phys. **C55**, 209 (1992).

[83] A. Heister *et al.* (ALEPH), Eur. Phys. J. **C35**, 457 (2004).

[84] P. Abreu *et al.* (DELPHI), Phys. Lett. **B275**, 231 (1992).

[85] P. Abreu *et al.* (DELPHI), Eur. Phys. J. **C5**, 585 (1998).

[86] P. Abreu *et al.* (DELPHI), Phys. Lett. **B459**, 397 (1999).

[87] M. Acciarri *et al.* (L3), Phys. Lett. **B444**, 569 (1998).

[88] TPC/TWO-GAMMA Collab.: H. Aihara *et al.*, LBL 23737.

[89] B. R. Webber, Phys. Lett. **143B**, 501 (1984).

[90] Y. I. Azimov *et al.*, Z. Phys. **C27**, 65 (1985).

[91] Y. I. Azimov *et al.*, Z. Phys. **C31**, 213 (1986).

[92] I. M. Dremin and J. W. Gary, Phys. Rept. **349**, 301 (2001), [hep-ph/0004215].

[93] I. M. Dremin and V. A. Nechitailo, Mod. Phys. Lett. **A9**, 1471 (1994), [hep-ex/9406002].

[94] S. J. Brodsky and J. F. Gunion, Phys. Rev. Lett. **37**, 402 (1976).

[95] J. Beringer *et al.* (Particle Data Group), Phys. Rev. **D86**, 010001 (2012).

[96] R. Akers *et al.* (OPAL), Z. Phys. **C68**, 203 (1995).

[97] P. D. Acton *et al.* (OPAL), Z. Phys. **C53**, 539 (1992).

[98] D. Buskulic *et al.* (ALEPH), Z. Phys. **C69**, 15 (1995).

[99] P. Abreu *et al.* (DELPHI), Phys. Lett. **B372**, 172 (1996).

[100] P. Abreu *et al.* (DELPHI), Phys. Lett. **B416**, 233 (1998).

[101] P. Abreu *et al.* (DELPHI), Eur. Phys. J. **C18**, 203 (2000), [Erratum: Eur. Phys. J.C25,493(2002)], [hep-ex/0103031].

[102] M. Acciarri *et al.* (L3), Phys. Lett. **B371**, 137 (1996).

[103] M. Acciarri *et al.* (L3), Phys. Lett. **B404**, 390 (1997).

[104] K. Nakabayashi *et al.* (TOPAZ), Phys. Lett. **B413**, 447 (1997).

[105] K. Okabe *et al.* (VENUS), Phys. Lett. **B423**, 407 (1998).

[106] H. Albrecht *et al.* (ARGUS), Z. Phys. **C54**, 13 (1992).

[107] S. Chekanov *et al.* (ZEUS), Phys. Lett. **B510**, 36 (2001), [hep-ex/0104036].

[108] J. Benecke *et al.* (Bonn-Hamburg-Munich), Nucl. Phys. **B76**, 29 (1974).

[109] W. M. Morse *et al.*, Phys. Rev. **D15**, 66 (1977).

[110] W. Thome *et al.* (Aachen-CERN-Heidelberg-Munich), Nucl. Phys. **B129**, 365 (1977).

[111] A. Breakstone *et al.* (Ames-Bologna-CERN-Dortmund-Heidelberg-Warsaw), Phys. Rev. **D30**, 528 (1984).

[112] G. J. Alner *et al.* (UA5), Phys. Rept. **154**, 247 (1987).

[113] R. E. Ansorge *et al.* (UA5), Z. Phys. **C43**, 357 (1989).

[114] C. Albajar *et al.* (UA1), Nucl. Phys. **B335**, 261 (1990).

[115] F. Abe *et al.* (CDF), Phys. Rev. **D41**, 2330 (1990), [,119(1989)].

[116] K. Aamodt *et al.* (ALICE), Eur. Phys. J. **C68**, 89 (2010), [arXiv:1004.3034].

[117] V. Khachatryan *et al.* (CMS), JHEP **02**, 041 (2010), [arXiv:1002.0621].

[118] V. Khachatryan *et al.* (CMS), JHEP **01**, 079 (2011), [arXiv:1011.5531].

[119] V. Khachatryan *et al.* (CMS), Phys. Rev. Lett. **105**, 022002 (2010), [arXiv:1005.3299].

[120] G. Aad *et al.* (ATLAS), Eur. Phys. J. **C76**, 7, 403 (2016), [arXiv:1603.02439].

[121] M. Aaboud *et al.* (ATLAS), Eur. Phys. J. **C76**, 9, 502 (2016), [arXiv:1606.01133].

[122] J. Adam *et al.* (ALICE), Phys. Lett. **B753**, 319 (2016), [arXiv:1509.08734].

[123] J. Adam *et al.* (ALICE), Eur. Phys. J. **C77**, 1, 33 (2017), [arXiv:1509.07541].

[124] P. V. Chliapnikov and V. A. Uvarov, Phys. Lett. **B251**, 192 (1990).

[125] J. F. Grosse-Oetringhaus and K. Reygers, J. Phys. **G37**, 083001 (2010), [arXiv:0912.0023].

[126] E. K. G. Sarkisyan and A. S. Sakharov (2004), [hep-ph/0410324]; E. K. G. Sarkisyan and A. S. Sakharov, AIP Conf. Proc. **828**, 1, 35 (2006), [hep-ph/0510191]; E. K. G. Sarkisyan and A. S. Sakharov, Eur. Phys. J. **C70**, 533 (2010), [arXiv:1004.4390].

[127] S. Hoeche *et al.*, in "HERA and the LHC: A Workshop on the implications of HERA for LHC physics: Proceedings Part A," 288–289 (2005), [hep-ph/0602031]; S. Mrenna and P. Richardson, JHEP **05**, 040 (2004), [hep-ph/0312274]; J. Alwall *et al.*, Eur. Phys. J. **C53**, 473 (2008), [arXiv:0706.2569].

[128] S. Albino, B. A. Kniehl and G. Kramer, Nucl. Phys. **B803**, 42 (2008), [arXiv:0803.2768].

[129] D. de Florian *et al.*, Phys. Rev. **D91**, 1, 014035 (2015), [arXiv:1410.6027].

[130] V. Bertone *et al.* (NNPDF), Eur. Phys. J. **C77**, 8, 516 (2017), [arXiv:1706.07049].

[131] D. de Florian, R. Sassot and M. Stratmann, Phys. Rev. **D76**, 074033 (2007), [arXiv:0707.1506].

[132] S. Kretzer, E. Leader and E. Christova, Eur. Phys. J. **C22**, 269 (2001), [hep-ph/0108055].

[133] S. Kretzer, Phys. Rev. **D62**, 054001 (2000), [hep-ph/0003177].

[134] L. Bourhis *et al.*, Eur. Phys. J. **C19**, 89 (2001), [hep-ph/0009101].

[135] M. Hirai *et al.*, Phys. Rev. **D75**, 094009 (2007), [hep-ph/0702250].

[136] C. A. Aidala *et al.*, Phys. Rev. **D83**, 034002 (2011), [arXiv:1009.6145].

[137] D. de Florian *et al.*, Phys. Rev. **D95**, 9, 094019 (2017), [arXiv:1702.06353].

[138] D. de Florian, R. Sassot and M. Stratmann, Phys. Rev. **D75**, 114010 (2007), [hep-ph/0703242].

[139] D. P. Anderle, F. Ringer and M. Stratmann, Phys. Rev. **D92**, 11, 114017 (2015), [arXiv:1510.05845].

[140] E. Leader, A. V. Sidorov and D. B. Stamenov, Phys. Rev. **D93**, 7, 074026 (2016), [arXiv:1506.06381].

[141] V. Bertone *et al.* (NNPDF), Eur. Phys. J. **C78**, 8, 651 (2018), [arXiv:1807.03310].

[142] R. Barate *et al.* (ALEPH), Eur. Phys. J. **C17**, 1 (2000); R. Akers *et al.* (OPAL), Z. Phys. **C68**, 179 (1995); G. Abbiendi *et al.* (OPAL), Eur. Phys. J. **C11**, 217 (1999), [hep-ex/9903027].

[143] K. Abe *et al.* (SLD), Phys. Rev. **D59**, 052001 (1999), [hep-ex/9805029].

[144] D. Buskulic *et al.* (ALEPH), Z. Phys. **C66**, 355 (1995); H. Albrecht *et al.* (ARGUS), Z. Phys. **C44**, 547 (1989); R. Akers *et al.* (OPAL), Z. Phys. **C63**, 181 (1994).

[145] M. R. Adams *et al.* (E665), Z. Phys. **C61**, 539 (1994).

[146] M. Arneodo *et al.* (European Muon), Z. Phys. **C34**, 283 (1987).

[147] S. Aid *et al.* (H1), Nucl. Phys. **B480**, 3 (1996), [hep-ex/9607010].

[148] J. J. Aubert *et al.* (European Muon), Z. Phys. **C18**, 189 (1983).

[149] A. Airapetian *et al.* (HERMES), Eur. Phys. J. **C21**, 599 (2001), [hep-ex/0104004].

[150] T. P. McPharlin *et al.*, Phys. Lett. **90B**, 479 (1980).

[151] S. S. Adler *et al.* (PHENIX), Phys. Rev. Lett. **91**, 241803 (2003), [hep-ex/0304038].

[152] B. Abelev *et al.* (ALICE), Phys. Lett. **B717**, 162 (2012), [arXiv:1205.5724].

[153] M. Bonesini *et al.* (WA70), Z. Phys. **C38**, 371 (1988).

[154] T. Akesson *et al.* (Axial Field Spectrometer), Sov. J. Nucl. Phys. **51**, 836 (1990), [Yad. Fiz.51,1314(1990)].

[155] C. Kourkoumelis *et al.*, Z. Phys. **C5**, 95 (1980).

[156] L. Apanasevich *et al.* (Fermilab E706), Phys. Rev. **D68**, 052001 (2003), [hep-ex/0204031].

[157] F. Abe *et al.* (CDF), Phys. Rev. Lett. **61**, 1819 (1988).

[158] M. Banner *et al.* (UA2), Phys. Lett. **115B**, 59 (1982).

[159] M. Procura and I. W. Stewart, Phys. Rev. **D81**, 074009 (2010), [Erratum: Phys. Rev.D83,039902(2011)], [arXiv:0911.4980].

[160] A. Jain, M. Procura and W. J. Waalewijn, JHEP **05**, 035 (2011), [arXiv:1101.4953].

[161] M. Procura and W. J. Waalewijn, Phys. Rev. **D85**, 114041 (2012), [arXiv:1111.6605].

[162] F. Arleo *et al.*, JHEP **04**, 147 (2014), [arXiv:1311.7356].

[163] M. Ritzmann and W. J. Waalewijn, Phys. Rev. **D90**, 5, 054029 (2014), [arXiv:1407.3272].

[164] T. Kaufmann, A. Mukherjee and W. Vogelsang, Phys. Rev. **D92**, 5, 054015 (2015), [arXiv:1506.01415].

[165] Y.-T. Chien *et al.*, JHEP **05**, 125 (2016), [arXiv:1512.06851].

[166] F. Abe *et al.* (CDF), Phys. Rev. Lett. **65**, 968 (1990).

[167] T. A. collaboration (ATLAS) (2015).

[168] S. Chatrchyan *et al.* (CMS), JHEP **10**, 087 (2012), [arXiv:1205.5872].

[169] X. Lu (ALICE), Nucl. Phys. **A931**, 428 (2014), [arXiv:1407.8385].

[170] C. Bianchin (ALICE), J. Phys. Conf. Ser. **612**, 1, 012020 (2015).

[171] F. Krizek (ALICE), J. Phys. Conf. Ser. **668**, 1, 012018 (2016), [arXiv:1509.02024].

[172] M. Aaboud *et al.* (ATLAS), Nucl. Phys. **A978**, 65 (2018), [arXiv:1706.02859].

[173] L. Adamczyk *et al.* (STAR), Phys. Rev. **D97**, 3, 032004 (2018), [arXiv:1708.07080].

[174] D. P. Anderle *et al.*, Phys. Rev. **D96**, 3, 034028 (2017), [arXiv:1706.09857].

[175] N. Sato *et al.* (JAM) (2019), [arXiv:1905.03788].

[176] M. Epele *et al.*, Phys. Rev. **D86**, 074028 (2012), [arXiv:1209.3240].

[177] E. Witten, Nucl. Phys. **210**, 189 (1977).

[178] L. Bourhis, M. Fontannaz and J. P. Guillet, Eur. Phys. J. **C2**, 529 (1998), [hep-ph/9704447].

[179] M. Gluck, E. Reya and A. Vogt, Phys. Rev. **D48**, 116 (1993), [Erratum: Phys. Rev.D51,1427(1995)]; Erratum *ibid.* **D51**, 1427 (1995).

[180] G. Abbiendi *et al.* (OPAL), Eur. Phys. J. **C27**, 467 (2003), [hep-ex/0209048].

[181] G. Bocquet *et al.*, Phys. Lett. **B366**, 434 (1996).

[182] T. Kaufmann, A. Mukherjee and W. Vogelsang, Phys. Rev. **D93**, 11, 114021 (2016), [arXiv:1604.07175].

[183] P. Abreu *et al.* (DELPHI), Eur. Phys. J. **C13**, 573 (2000).

[184] B. A. Kniehl, G. Kramer and B. Potter, Phys. Rev. Lett. **85**, 5288 (2000), [hep-ph/0003297].

[185] M. Arneodo *et al.* (European Muon), Z. Phys. **C33**, 167 (1986).

[186] A. Airapetian *et al.* (HERMES), Phys. Rev. **D87**, 074029 (2013), [arXiv:1212.5407].

[187] C. Adolph *et al.* (COMPASS), Phys. Lett. **B764**, 1 (2017), [arXiv:1604.02695].

[188] F. D. Aaron *et al.* (H1), Phys. Lett. **B673**, 119 (2009), [arXiv:0901.0477].

[189] M. Derrick *et al.* (ZEUS), Z. Phys. **C68**, 29 (1995), [hep-ex/9505011].

[190] S. Chekanov *et al.* (ZEUS), Phys. Lett. **B553**, 141 (2003), [hep-ex/0211025].

[191] S. Chekanov *et al.* (ZEUS), Nucl. Phys. **B786**, 181 (2007), [arXiv:0705.3770].

[192] F. D. Aaron *et al.* (H1), Eur. Phys. J. **C61**, 185 (2009), [arXiv:0810.4036].

[193] A. Aktas *et al.* (H1), Eur. Phys. J. **C36**, 413 (2004), [hep-ex/0403056].

[194] P. Dixon, D. Kant and G. Thompson, J. Phys. **G25**, 1453 (1999).

[195] C. Adloff *et al.* (H1), Phys. Lett. **B462**, 440 (1999), [hep-ex/9907030].

[196] D. Graudenz, Fortsch. Phys. **45**, 629 (1997), [hep-ph/9701334].

[197] P. M. Nadolsky, D. R. Stump and C. P. Yuan, Phys. Rev. **D61**, 014003 (2000), [Erratum: Phys. Rev.D64,059903(2001)], [hep-ph/9906280].

[198] D. de Florian *et al.*, Phys. Rev. **D95**, 0334027 (2017).

[199] T. Aaltonen *et al.* (CDF), Phys. Rev. **D79**, 112005 (2009), [Erratum: Phys. Rev.D82,119903(2010)], [arXiv:0904.1098].

[200] G. Aad *et al.* (ATLAS), New J. Phys. **13**, 053033 (2011), [arXiv:1012.5104].

[201] B. I. Abelev *et al.* (STAR), Phys. Rev. **C75**, 064901 (2007), [arXiv:nucl-ex/0607033].

[202] K. Aamodt *et al.* (ALICE), Eur. Phys. J. **C71**, 1655 (2011), [arXiv:1101.4110].

[203] B. B. Abelev *et al.* (ALICE), Phys. Lett. **B736**, 196 (2014), [arXiv:1401.1250].

[204] J. Adam *et al.* (ALICE), Eur. Phys. J. **C75**, 5, 226 (2015), [arXiv:1504.00024].

[205] S. Chatrchyan *et al.* (CMS), Eur. Phys. J. **C72**, 2164 (2012), [arXiv:1207.4724].

[206] A. M. Sirunyan *et al.* (CMS), Phys. Rev. **D96**, 11, 112003 (2017), [arXiv:1706.10194].

[207] G. J. Alner *et al.* (UA5), Z. Phys. **C32**, 153 (1986).

[208] B. Abelev *et al.* (ALICE), Eur. Phys. J. **C73**, 6, 2456 (2013), [arXiv:1208.4968].

[209] G. Antchev *et al.* (TOTEM), EPL **101**, 2, 21004 (2013).

[210] A. M. Sirunyan *et al.* (CMS), JHEP **07**, 161 (2018), [arXiv:1802.02613].

[211] F. Abe *et al.* (CDF), Phys. Rev. **D50**, 5550 (1994).

[212] F. Abe *et al.* (CDF), Phys. Rev. **D50**, 5518 (1994).

[213] S. S. Adler *et al.* (PHENIX), Phys. Rev. **C74**, 024904 (2006), [arXiv:nucl-ex/0603010].

[214] S. Albino *et al.*, Phys. Rev. **D75**, 034018 (2007), [hep-ph/0611029].

[215] I. Borsa, R. Sassot and M. Stratmann, Phys. Rev. **D96**, 9, 094020 (2017), [arXiv:1708.01630].

[216] B. Andersson *et al.*, Phys. Rept. **97**, 31 (1983).

[217] T. Sjostrand and M. Bengtsson, Comput. Phys. Commun. **43**, 367 (1987); T. Sjostrand, Comput. Phys. Commun. **82**, 74 (1994).

[218] P. D. Acton *et al.* (OPAL), Phys. Lett. **B305**, 407 (1993).

[219] J. Breitweg *et al.* (ZEUS), Eur. Phys. J. **C2**, 77 (1998), [hep-ex/9711018].

[220] D. DeProspo *et al.* (E632), Phys. Rev. **D50**, 6691 (1994).

[221] S. Chekanov *et al.* (ZEUS), Eur. Phys. J. **C51**, 1 (2007), [hep-ex/0612023].

[222] G. Grindhammer *et al.*, in: *Proceedings of the Workshop on Monte Carlo Generators for HERA Physics*, Hamburg, Germany, 1998/1999.

[223] N. Brook *et al.*, in: *Proceedings of the Workshop for Future HERA Physics at HERA*, Hamburg, Germany, 1996.

[224] D. Acosta *et al.* (CDF), Phys. Rev. **D72**, 052001 (2005), [hep-ex/0504048].

[225] G. Arnison *et al.* (UA1), Phys. Lett. **118B**, 167 (1982).

[226] M. Banner *et al.* (UA2), Phys. Lett. **122B**, 322 (1983).

[227] M. Banner *et al.* (UA2, Bern-CERN-Copenhagen-Orsay-Pavia-Saclay), Z. Phys. **C27**, 329 (1985).

[228] A. Adare *et al.* (PHENIX), Phys. Rev. **D76**, 051106 (2007), [arXiv:0704.3599].

[229] A. Adare *et al.* (PHENIX), Phys. Rev. **D83**, 032001 (2011), [arXiv:1009.6224].

[230] A. Adare *et al.* (PHENIX), Phys. Rev. **D86**, 092006 (2012), [arXiv:1202.4020].

[231] A. Adare *et al.* (PHENIX), Phys. Rev. **D88**, 3, 032006 (2013), [arXiv:1209.3283].

[232] A. Adare *et al.* (PHENIX), Phys. Rev. **D91**, 3, 032001 (2015), [arXiv:1409.1907].

[233] A. Adare *et al.* (PHENIX), Phys. Rev. **D90**, 7, 072008 (2014), [arXiv:1406.3541].

[234] A. Adare *et al.* (PHENIX), Phys. Rev. **D93**, 1, 011501 (2016), [arXiv:1510.02317].

[235] I. Arsene *et al.* (BRAHMS), Phys. Rev. Lett. **98**, 252001 (2007), [hep-ex/0701041].

[236] J. Adams *et al.* (STAR), Phys. Rev. Lett. **97**, 152302 (2006), [arXiv:nucl-ex/0602011].

[237] J. Adams *et al.* (STAR), Phys. Lett. **B637**, 161 (2006), [arXiv:nucl-ex/0601033].

[238] B. I. Abelev *et al.* (STAR), Phys. Rev. **D80**, 111108 (2009), [arXiv:0911.2773].

[239] G. Agakishiev *et al.* (STAR), Phys. Rev. Lett. **108**, 072302 (2012), [arXiv:1110.0579].

[240] L. Adamczyk *et al.* (STAR), Phys. Rev. **D89**, 1, 012001 (2014), [arXiv:1309.1800].

[241] B. B. Abelev *et al.* (ALICE), Eur. Phys. J. **C73**, 12, 2662 (2013), [arXiv:1307.1093].

[242] L. Apanasevich *et al.* (Fermilab E706), Phys. Rev. Lett. **81**, 2642 (1998), [hep-ex/9711017].

[243] G. Ballocchi *et al.* (UA6), Phys. Lett. **B436**, 222 (1998).

[244] K. Aamodt *et al.* (ALICE), Eur. Phys. J. **C71**, 1594 (2011), [arXiv:1012.3257].

[245] R. Aaij *et al.* (LHCb), Phys. Lett. **B703**, 267 (2011), [arXiv:1107.3935].

[246] G. Aad *et al.* (ATLAS), Phys. Lett. **B758**, 67 (2016), [arXiv:1602.01633].

[247] F. Aversa *et al.*, Nucl. Phys. **B327**, 105 (1989); D. de Florian, Phys. Rev. **D67**, 054004 (2003), [hep-ph/0210442]; B. Jager *et al.*, Phys. Rev. **D67**, 054005 (2003), [hep-ph/0211007].

[248] U. Baur *et al.*, in "QCD and weak boson physics in Run II. Proceedings, Batavia, USA, March 4-6, June 3-4, November 4-6, 1999," 115–164 (2000), [,115(2000)], [hep-ph/0005226], URL `http://lss.fnal.gov/archive/preprint/fermilab-conf-00-411-ae.shtml`.

[249] P. Aurenche *et al.*, Eur. Phys. J. **C13**, 347 (2000), [hep-ph/9910252].

[250] L. Apanasevich *et al.*, Phys. Rev. **D59**, 074007 (1999), [hep-ph/9808467].

[251] U. D'Alesio and F. Murgia, Phys. Rev. **D70**, 074009 (2004), [hep-ph/0408092].

[252] D. de Florian and W. Vogelsang, Phys. Rev. **D71**, 114004 (2005), [hep-ph/0501258].

[253] P. Hinderer *et al.*, Phys. Rev. **D99**, 5, 054019 (2019), [arXiv:1812.00915].

[254] D. d'Enterria *et al.*, Nucl. Phys. **B883**, 615 (2014), [arXiv:1311.1415].

[255] G. Wilk and Z. Wlodarczyk, Eur. Phys. J. **A40**, 299 (2009), [arXiv:0810.2939].

[256] C. Tsallis, J. Statist. Phys. **52**, 479 (1988).

[257] C. Tsallis, Braz. J. Phys. **29**, 1 (1999).

[258] C. Tsallis, Eur. Phys. J. **A40**, 257 (2009), [arXiv:0812.4370].

[259] M. D. Azmi and J. Cleymans, J. Phys. **G41**, 065001 (2014), [arXiv:1401.4835].

[260] G. Wilk and Z. Wlodarczyk, Phys. Rev. Lett. **84**, 2770 (2000), [hep-ph/9908459].

[261] T. Bhattacharyya *et al.*, J. Phys. **G45**, 5, 055001 (2018), [arXiv:1709.07376].

[262] S. Grigoryan, Phys. Rev. **D95**, 5, 056021 (2017), [arXiv:1702.04110].

[263] T. Wibig, Int. J. Mod. Phys. **A29**, 1450021 (2014).

[264] K. Saraswat, P. Shukla and V. Singh, J. Phys. Comm. **2**, 3, 035003 (2018), [arXiv:1706.04860].

[265] K. Urmossy, G. G. Barnafoldi and T. S. Biro, Phys. Lett. **B701**, 111 (2011), [arXiv:1101.3023].

[266] A. S. Parvan, O. V. Teryaev and J. Cleymans, Eur. Phys. J. **A53**, 5, 102 (2017), [arXiv:1607.01956].

[267] K. Adcox *et al.* (PHENIX), Phys. Rev. Lett. **88**, 022301 (2002), [arXiv:nucl-ex/0109003]; C. Adler *et al.* (STAR), Phys. Rev. Lett. **90**, 082302 (2003), [arXiv:nucl-ex/0210033].

[268] V.A. Khoze *et al.*, *Proceedings, Conference on High-Energy Physics, Tbilisi 1976*; J. D. Bjorken, Phys. Rev. **D17**, 171 (1978).

[269] M. Artuso *et al.* (CLEO), Phys. Rev. **D70**, 112001 (2004), [hep-ex/0402040].

[270] R. Seuster *et al.* (Belle), Phys. Rev. **D73**, 032002 (2006), [hep-ex/0506068].

[271] A. Heister *et al.* (ALEPH), Phys. Lett. **B512**, 30 (2001), [hep-ex/0106051]; J. Abdallah *et al.* (DELPHI), Eur. Phys. J. **C71**, 1557 (2011), [arXiv:1102.4748]; G. Abbiendi *et al.* (OPAL), Eur. Phys. J. **C29**, 463 (2003), [hep-ex/0210031]; K. Abe *et al.* (SLD), Phys. Rev. **D65**, 092006 (2002), [Erratum: Phys. Rev.D66,079905(2002)], [hep-ex/0202031].

[272] B. Mele and P. Nason, Phys. Lett. **B245**, 635 (1990); B. Mele and P. Nason, Nucl. Phys. **B361**, 626 (1991), [Erratum: Nucl. Phys.B921,841(2017)].

[273] M. Cacciari and S. Catani, Nucl. Phys. **B617**, 253 (2001), [hep-ph/0107138].

[274] P. Nason and C. Oleari, Phys. Lett. **B418**, 199 (1998), [hep-ph/9709358]; P. Nason and C. Oleari, Phys. Lett. **B447**, 327 (1999), [hep-ph/9811206]; P. Nason and C. Oleari, Nucl. Phys. **B565**, 245 (2000), [hep-ph/9903541].

[275] K. Melnikov and A. Mitov, Phys. Rev. **D70**, 034027 (2004), [hep-ph/0404143].

[276] C. Peterson *et al.*, Phys. Rev. **D27**, 105 (1983).

[277] V. G. Kartvelishvili, A. K. Likhoded and V. A. Petrov, Phys. Lett. **78B**, 615 (1978).

[278] P. D. B. Collins and T. P. Spiller, J. Phys. **G11**, 1289 (1985).

[279] G. Colangelo and P. Nason, Phys. Lett. **B285**, 167 (1992).

[280] M. G. Bowler, Z. Phys. **C11**, 169 (1981).

[281] E. Braaten *et al.*, Phys. Rev. **D51**, 4819 (1995), [hep-ph/9409316].

[282] R. Akers *et al.* (OPAL), Z. Phys. **C67**, 27 (1995).

[283] H. Albrecht *et al.* (ARGUS), Z. Phys. **C52**, 353 (1991).

[284] D. Buskulic *et al.* (ALEPH), Phys. Lett. **B357**, 699 (1995).

[285] J. Chrin, Z. Phys. **C36**, 163 (1987).

[286] R. L. Jaffe and L. Randall, Nucl. Phys. **B412**, 79 (1994), [hep-ph/9306201].

[287] M. Cacciari and E. Gardi, Nucl. Phys. **B664**, 299 (2003), [hep-ph/0301047].

[288] L. Randall and N. Rius, Nucl. Phys. **B441**, 167 (1995), [hep-ph/9405217].

[289] J. C. Collins, Phys. Rev. **D58**, 094002 (1998), [hep-ph/9806259].

[290] B. A. Kniehl *et al.*, Eur. Phys. J. **C41**, 199 (2005), [hep-ph/0502194].

[291] S. Ahmed *et al.* (CLEO), Phys. Rev. **D62**, 112003 (2000), [hep-ex/0008015].

[292] B. Aubert *et al.* (BaBar), Phys. Rev. **D65**, 091104 (2002), [hep-ex/0201041].

[293] D. Bortoletto *et al.* (CLEO), Phys. Rev. **D37**, 1719 (1988), [Erratum: Phys. Rev.D39,1471(1989)].

[294] H. Albrecht *et al.* (ARGUS), Z. Phys. **C54**, 1 (1992).

[295] G. Alexander *et al.* (OPAL), Z. Phys. **C69**, 543 (1996).

[296] A. Heister *et al.* (ALEPH), Phys. Lett. **B561**, 213 (2003), [hep-ex/0302003].

[297] F. D. Aaron *et al.* (H1), Eur. Phys. J. **C65**, 89 (2010), [arXiv:0907.2643].

[298] S. Chekanov *et al.* (ZEUS), JHEP **07**, 074 (2007), [arXiv:0704.3562]; ZEUS Collab: H. Abramowicz *et al.*, JHEP , 1309 (2013); A. Aktas *et al.* (H1), Eur. Phys. J. **C51**, 271 (2007), [hep-ex/0701023]; F. D. Aaron *et al.* (H1), Eur. Phys. J. **C59**, 589 (2009), [arXiv:0808.1003].

[299] B. Adeva *et al.* (L3), Phys. Lett. **B261**, 177 (1991).

[300] O. Biebel, P. Nason and B. R. Webber (2001), [hep-ph/0109282].

[301] H. Evans (ALICE, ATLAS, CMS, LHCb), in "Proceedings, 14th International Conference on Hadron spectroscopy (Hadron 2011): Munich, Germany, June 13-17, 2011," (2011), [arXiv:1110.5294]; E. Aguilo, in "Proceedings, 47th Rencontres de Moriond on QCD and High Energy Interactions: La Thuile, France, March 10-17, 2012," 115–120 (2012), [arXiv:1205.5678]; F. Simonetto, Journal of Physics: Conference Series **347**, 012014 (2012).

[302] V. Khachatryan *et al.* (CMS), JHEP **03**, 136 (2011), [arXiv:1102.3194]; G. Aad *et al.* (ATLAS), Eur. Phys. J. **C71**, 1846 (2011), [arXiv:1109.6833]; S. Chatrchyan *et al.* (CMS), JHEP **04**, 084 (2012), [arXiv:1202.4617]; G. Aad *et al.* (ATLAS), Eur. Phys. J. **C73**, 2, 2301 (2013), [arXiv:1210.0441].

[303] H. Jung *et al.*, Phys. Rev. **D85**, 034035 (2012), [arXiv:1111.1942].

[304] D. Acosta *et al.* (CDF), Phys. Rev. Lett. **91**, 241804 (2003), [hep-ex/0307080]; D. Acosta *et al.* (CDF), Phys. Rev. **D71**, 032001 (2005), [hep-ex/0412071].

[305] M. Cacciari and P. Nason, JHEP **09**, 006 (2003), [hep-ph/0306212]; M. Cacciari *et al.*, JHEP **07**, 033 (2004), [hep-ph/0312132]; B. A. Kniehl *et al.*, Phys. Rev. Lett. **96**, 012001 (2006), [hep-ph/0508129].

[306] H. Abramowicz *et al.* (ZEUS), Eur. Phys. J. **C71**, 1573 (2011), [arXiv:1101.3692].

[307] S. Chekanov *et al.* (ZEUS), Phys. Rev. **D78**, 072001 (2008), [arXiv:0805.4390].

[308] S. Chekanov *et al.* (ZEUS), JHEP **02**, 032 (2009), [arXiv:0811.0894].

[309] F. D. Aaron *et al.* (H1), Eur. Phys. J. **C72**, 2148 (2012), [arXiv:1206.4346].

[310] M. L. Mangano and P. Nason, Phys. Lett. **B285**, 160 (1992).

[311] M. H. Seymour, Nucl. Phys. **B436**, 163 (1995).

[312] D. J. Miller and M. H. Seymour, Phys. Lett. **B435**, 213 (1998), [hep-ph/9805414].

[313] R. Barate *et al.* (ALEPH), Phys. Lett. **B434**, 437 (1998).

[314] P. Abreu *et al.* (DELPHI), Phys. Lett. **B405**, 202 (1997).

[315] M. Acciarri *et al.* (L3), Phys. Lett. **B476**, 243 (2000), [hep-ex/9911016].

[316] G. Abbiendi *et al.* (OPAL), Eur. Phys. J. **C13**, 1 (2000), [hep-ex/9908001].

[317] K. Abe *et al.* (SLD) (1999), [hep-ex/9908028], URL `http://www-public.slac.stanford.edu/sciDoc/docMeta.aspx?slacPubNumber=SLAC-PUB-8157`.

[318] C. Albajar *et al.* (UA1 Collaboration), Z. Phys. C **61**, 41 (1993), URL `http://cds.cern.ch/record/253028`.

[319] R. Aaij *et al.* (LHCb), JHEP **11**, 030 (2017), [arXiv:1708.05994].

[320] M. Aaboud *et al.* (ATLAS), Phys. Rev. **D99**, 5, 052004 (2019), [arXiv:1812.09283].

[321] M. Burkardt and R. L. Jaffe, Phys. Rev. Lett. **70**, 2537 (1993), [hep-ph/9302232].

[322] P. J. Mulders and R. D. Tangerman, Nucl. Phys. **B461**, 197 (1996), [Erratum: Nucl. Phys.B484,538(1997)], [hep-ph/9510301].

[323] R. Jakob, Nucl. Phys. **A711**, 35 (2002), [hep-ph/0206271].

[324] D. de Florian, M. Stratmann and W. Vogelsang, Phys. Rev. Lett. **81**, 530 (1998), [hep-ph/9802432].

[325] D. Buskulic *et al.* (ALEPH), Phys. Lett. **B374**, 319 (1996).

[326] K. Ackerstaff *et al.* (OPAL), Eur. Phys. J. **C2**, 49 (1998), [hep-ex/9708027].

[327] G. Abbiendi *et al.* (OPAL), Phys. Lett. **B444**, 539 (1998), [hep-ex/9808006].

[328] M. Alekseev *et al.* (COMPASS), Eur. Phys. J. **C64**, 171 (2009), [arXiv:0907.0388].

[329] A. Airapetian *et al.* (HERMES), Phys. Rev. **D74**, 072004 (2006), [hep-ex/0607004].

[330] G. Karyan (HERMES), Int. J. Mod. Phys. Conf. Ser. **40**, 1660067 (2016).

[331] J. Adam *et al.* (STAR), Phys. Rev. **D98**, 11, 112009 (2018), [arXiv:1808.07634].

[332] R. L. Jaffe, Phys. Rev. **D54**, 11, R6581 (1996), [hep-ph/9605456].

[333] A. Airapetian *et al.* (HERMES), Phys. Rev. **D76**, 092008 (2007), [arXiv:0704.3133].

[334] A. Moretti (COMPASS), PoS **SPIN2018**, 138 (2018), [arXiv:1901.01735].

[335] R. Seidl *et al.* (Belle), Phys. Rev. **D99**, 11, 112006 (2019), [arXiv:1902.01552].

[336] C. Adolph *et al.* (COMPASS), Eur. Phys. J. **C73**, 8, 2531 (2013), [Erratum: Eur. Phys. J.C75,no.2,94(2015)], [arXiv:1305.7317].

[337] A. Signori *et al.*, JHEP **11**, 194 (2013), [arXiv:1309.3507].

[338] M. Anselmino *et al.*, JHEP **04**, 005 (2014), [arXiv:1312.6261].

[339] M. G. Echevarria *et al.*, Phys. Rev. **D89**, 074013 (2014), [arXiv:1401.5078].

[340] M. G. Echevarria, I. Scimemi and A. Vladimirov, Phys. Rev. **D93**, 1, 011502 (2016), [Erratum: Phys. Rev.D94,no.9,099904(2016)], [arXiv:1509.06392].

[341] M. G. Echevarria, I. Scimemi and A. Vladimirov, JHEP **09**, 004 (2016), [arXiv:1604.07869].

[342] A. Bacchetta *et al.*, JHEP **06**, 081 (2017), [Erratum: JHEP06,051(2019)], [arXiv:1703.10157].

[343] J. C. Collins, Nucl. Phys. **B396**, 161 (1993), [hep-ph/9208213].

[344] J. P. Ralston and D. E. Soper, Nucl. Phys. **B152**, 109 (1979).

[345] H. Avakian *et al.* (CLAS), Phys. Rev. **D69**, 112004 (2004), [hep-ex/0301005].

[346] A. Airapetian *et al.* (HERMES), Phys. Rev. Lett. **84**, 4047 (2000), [hep-ex/9910062].

[347] A. Airapetian *et al.* (HERMES), Phys. Rev. **D64**, 097101 (2001), [hep-ex/0104005].

[348] A. Airapetian *et al.* (HERMES), Phys. Rev. Lett. **94**, 012002 (2005), [hep-ex/0408013].

[349] A. Airapetian *et al.* (HERMES), Phys. Lett. **B693**, 11 (2010), [arXiv:1006.4221].

[350] V. Yu. Alexakhin *et al.* (COMPASS), Phys. Rev. Lett. **94**, 202002 (2005), [hep-ex/0503002].

[351] E. S. Ageev *et al.* (COMPASS), Nucl. Phys. **B765**, 31 (2007), [hep-ex/0610068].

[352] M. Alekseev *et al.* (COMPASS), Phys. Lett. **B673**, 127 (2009), [arXiv:0802.2160].

[353] M. G. Alekseev *et al.* (COMPASS), Phys. Lett. **B692**, 240 (2010), [arXiv:1005.5609].

[354] M. G. Alekseev *et al.* (COMPASS), Eur. Phys. J. **C70**, 39 (2010), [arXiv:1007.1562].

[355] C. Adolph *et al.* (COMPASS), Phys. Lett. **B717**, 376 (2012), [arXiv:1205.5121].

[356] C. Adolph *et al.* (COMPASS), Phys. Lett. **B744**, 250 (2015), [arXiv:1408.4405].

[357] K. Abe *et al.* (Belle), Phys. Rev. Lett. **96**, 232002 (2006), [hep-ex/0507063].

[358] R. Seidl *et al.* (Belle), Phys. Rev. **D78**, 032011 (2008), [Erratum: Phys. Rev.D86,039905(2012)], [arXiv:0805.2975].

[359] J. P. Lees *et al.* (BaBar), Phys. Rev. **D90**, 5, 052003 (2014), [arXiv:1309.5278].

[360] J. P. Lees *et al.* (BaBar), Phys. Rev. **D92**, 11, 111101 (2015), [arXiv:1506.05864].

[361] M. Ablikim *et al.* (BESIII), Phys. Rev. Lett. **116**, 4, 042001 (2016), [arXiv:1507.06824].

[362] M. Anselmino *et al.*, Phys. Rev. **D92**, 11, 114023 (2015), [arXiv:1510.05389].

[363] Z.-B. Kang *et al.*, Phys. Rev. **D93**, 1, 014009 (2016), [arXiv:1505.05589].

[364] F. Yuan, Phys. Rev. Lett. **100**, 032003 (2008), [arXiv:0709.3272].

[365] Z.-B. Kang *et al.*, JHEP **11**, 068 (2017), [arXiv:1705.08443].

[366] K. Konishi, A. Ukawa and G. Veneziano, Phys. Lett. **78B**, 243 (1978).

[367] I. Vendramin, Nuovo Cim. **A66**, 339 (1981).

[368] J. C. Collins, S. F. Heppelmann and G. A. Ladinsky, Nucl. Phys. **B420**, 565 (1994), [hep-ph/9305309].

[369] R. L. Jaffe, X.-m. Jin and J. Tang, Phys. Rev. Lett. **80**, 1166 (1998), [hep-ph/9709322].

[370] R. L. Jaffe, X.-m. Jin and J.-a. Tang, Phys. Rev. **D57**, 5920 (1998), [hep-ph/9710561].

[371] A. Bianconi *et al.*, Phys. Rev. **D62**, 034008 (2000), [hep-ph/9907475].

[372] M. Radici, R. Jakob and A. Bianconi, Phys. Rev. **D65**, 074031 (2002), [hep-ph/0110252].

[373] D. de Florian and L. Vanni, Phys. Lett. **B578**, 139 (2004), [hep-ph/0310196].

[374] A. Bacchetta and M. Radici, Phys. Rev. **D67**, 094002 (2003), [hep-ph/0212300].

[375] A. Vossen *et al.* (Belle), Phys. Rev. Lett. **107**, 072004 (2011), [arXiv:1104.2425].

[376] A. Courtoy *et al.*, Phys. Rev. **D85**, 114023 (2012), [arXiv:1202.0323].

[377] M. Radici *et al.*, JHEP **05**, 123 (2015), [arXiv:1503.03495].

[378] A. Airapetian *et al.* (HERMES), JHEP **06**, 017 (2008), [arXiv:0803.2367].

[379] C. Adolph *et al.* (COMPASS), Phys. Lett. **B713**, 10 (2012), [arXiv:1202.6150].

[380] C. Adolph *et al.* (COMPASS), Phys. Lett. **B736**, 124 (2014), [arXiv:1401.7873].

[381] L. Adamczyk *et al.* (STAR), Phys. Rev. Lett. **115**, 242501 (2015), [arXiv:1504.00415].

[382] A. Bacchetta, A. Courtoy and M. Radici, Phys. Rev. Lett. **107**, 012001 (2011), [arXiv:1104.3855].

[383] A. Bacchetta, A. Courtoy and M. Radici, JHEP **03**, 119 (2013), [arXiv:1212.3568].

[384] M. Radici and A. Bacchetta, Phys. Rev. Lett. **120**, 19, 192001 (2018), [arXiv:1802.05212].

20. High Energy Soft QCD and Diffraction

Written February 2020 by V.A. Khoze (Durham U.; Petersburg Nuclear Phys. Inst.), M. Ryskin (Petersburg Nuclear Phys. Inst.) and M. Taševský (Prague, Inst. Phys.).

20.1 Introduction

Despite the enormous successes of Quantum Chromodynamics (QCD) (see Section 9 in [1] and [2]) there remain a number of deep questions to be answered in the domain of strong interaction physics. These concern first of all small momentum transfer processes which are generically called soft interactions.

One of the most challenging problems is the high-energy behaviour of hadronic scattering processes. At high collision energies, $\sqrt{s}$, soft interactions play a dominant role. Unfortunately, soft interactions cannot be described in terms of perturbative QCD. These are non-perturbative phenomena related to confinement which are generally considered in the context of the analytic S-matrix, based on *first principles*, such as analyticity, crossing symmetry and unitarity of partial waves, see e.g. [3, 4]. At high energies the most self-consistent way to perform the calculations and to describe the data is the Regge approach (see for example [5–7]), which will be considered below. As discussed in Section 20.5, this formalism could be smoothly matched with perturbative QCD calculations at larger transverse momenta. Therefore, here we will concentrate on the properties of high energy soft interactions that can be expected from the extension of the perturbative QCD domain.

The main aim of this review is to present the well-established theoretical framework, based on Regge theory and QCD, used for describing high-energy collisions. A limited number of some new experimental results, mainly from the LHC, are shown in order to demonstrate that the gross features of the data are in agreement with this approach. We are not focussing on any particular phenomenological or Monte Carlo model, which are covered in the dedicated reviews and books, see e.g. Section 41 in [1], [2, 8–14] and Chapter 2 in [15].

Typically, in multiparticle production, the secondaries[1] fill the whole available rapidity interval.[2] However, there exists an important class of events in which a large interval of rapidity (typically at least 4 units) is devoid of any hadronic activity. Such an interval is called a Large Rapidity Gap (LRG). The most frequent case with a LRG is elastic scattering. There are also events in which one of the incoming protons (or both) is transformed (dissociates) into a set of two or more final state particles with the mass $M \ll \sqrt{s}$ and proton quantum number. All these events have properties similar to those of the well-known from optics pattern of diffraction of a beam of light on an obstacle. By analogy, in high-energy physics, the corresponding processes are usually called diffractive. The classic example is the elastic scattering of hadrons on nuclei (see e.g. [16]), which manifests an angular distribution with a series of minima and maxima, analogous to the diffraction of light on a black disk. At LHC energies diffractive processes constitute up to 40% of the total (pp) cross section, $\sigma_{\rm tot}$. Therefore, we will pay special attention to the description of the elastic scattering amplitude and proton diffractive dissociation. Diffraction dissociation can be considered as a quantum mechanical process caused by the fact that different components of the incoming hadron wave function have different probabilities for interaction with a target [17]. This feature allows us to probe the transverse size of the interaction region.

Note that besides being of a fundamental interest in their own right for understanding the high energy behaviour of the QCD amplitude, there are several reasons why it is important to study soft and diffractive processes. Firstly, soft interactions unavoidably give an underlying component to rare 'hard' events, from which we hope to extract signals for New Physics. Secondly, we should be able to estimate the probability that rapidity gaps, which occur in 'hard' diffractive events, survive rescattering effects, that is, survive the population of the gaps by the secondary particles from the underlying event. Thirdly, an understanding of diffractive processes is very important for evaluation of pile-up backgrounds in high-luminosity pp collisions, which have a direct impact on various experimental measurements. Pile-up corresponds to soft independent interactions in the same bunch crossing whose number rises with increasing instantaneous luminosity. And, finally, studies of diffractive processes should help in the understanding of the structure of high-energy cosmic ray cascades, which requires a very detailed knowledge of the spectra of particles carrying a large fraction x of the incoming momentum in proton-air and nucleus-air interactions, see for instance [18].

Experimentally, diffractive processes are selected using two distinct features:

1. large regions (typically at least $\Delta\eta > 4$) in the detector are devoid of hadronic activity (LRG) and/or
2. one or both incoming particles stay intact after collision and are registered by the dedicated forward detectors placed a few hundred meters from the interaction point. The momentum loss of the initial particle, $\xi = 1 - x$, is typically smaller than 0.15.

Thus, in the case of proton-proton collisions, diffractive events correspond to elastic $pp \to pp$ scattering and to $pp \to p + X$ (Single Dissociation, SD) and $pp \to X + Y$ (Double Dissociation, DD) processes, where the + sign denotes a large rapidity gap. Note that strictly speaking in high energy physics it is impossible to define (and select) rigorously purely diffractive events. We can always have some admixture of events of different origin. As a rule we call 'diffractive' the events with sufficiently large gap (with say $\Delta y > 4$, see above) and the vacuum quantum numbers transferred across the gap. Typically at the LHC the integrated cross sections of diffractive dissociation, $\sigma_{\rm SD}$, $\sigma_{\rm DD}$, are of the order of 5–10 mb depending on the gap size. Schematic diagrams of all discussed processes are shown in Fig. 20.1.

20.2 Regge pole approach

In pre-QCD times, in order to describe the behaviour of scattering amplitudes at high energy, $\sqrt{s}$, and small momentum-transfer squared, $-t$, Regge theory was developed and successfully applied in a wide range of energies. The Regge approach [5–7] is based on the singularities of amplitudes in the complex angular momentum, j, plane.

For instance, the measured $\pi^- p \to \pi^0 n$ amplitude behaves as

$$T_{\pi p}(s,t) \propto s^{\alpha_\rho(t)}, \tag{20.1}$$

where the process is described by the exchange of the ρ-trajectory, $j = \alpha_\rho(t) \simeq 0.5 + 0.9t$ (with $t = (p_{\pi^-} - p_{\pi^0})^2$ in GeV^2). This trajectory passes through the spin-1 ρ-meson resonance in the 'crossed' t-channel $\pi^-\pi^0 \to \bar{p}n$; that is, $\alpha_\rho(t = m_\rho^2) = 1$. The corresponding cross section decreases with increasing s.

On the other hand, high-energy total and elastic pp cross sections are observed to grow slowly with energy (see e.g. Section 52 in [1]) and in terms of Regge theory are dominated by the exchange of a trajectory with vacuum quantum numbers, $\sigma_{\rm tot} \propto s^{j-1}$. The simplest possibility is to assume that the rightmost singularity in the j-plane, which drives the high-energy behaviour of the cross section, is the leading (at $t \le 0$) Regge pole at $j = \alpha(t)$. Then the pp elastic amplitude reads

$$T_{\rm el}(s,t) \propto s^{\alpha_{\mathbb{P}}(t)} \ . \tag{20.2}$$

The total cross section can then be conveniently expressed using the so called optical theorem which states that

$$s\sigma_{\rm tot} = {\rm Im}T_{\rm el}(s, t = 0), \tag{20.3}$$

as illustrated in the upper part of Fig. 20.2, and thus

$$\sigma_{\rm tot} \propto s^{\alpha_{\mathbb{P}}(0)-1}. \tag{20.4}$$

[1] Here and in what follows, we call secondaries the new particles produced in the course of the interaction.

[2] For definition of particle rapidity (pseudorapidity), see Section 48.5.2 in [1]; $y = \frac{1}{2}\ln\frac{E+p_z}{E-p_z}$ ($\eta = -\ln(\tan(\theta/2))$; the correct variable is the rapidity y, however, experimentally it is simpler to use the pseudorapidity η which does not require identifying the particles, setting $m = 0$. For $p_T \gg m$, $\eta \simeq y$.

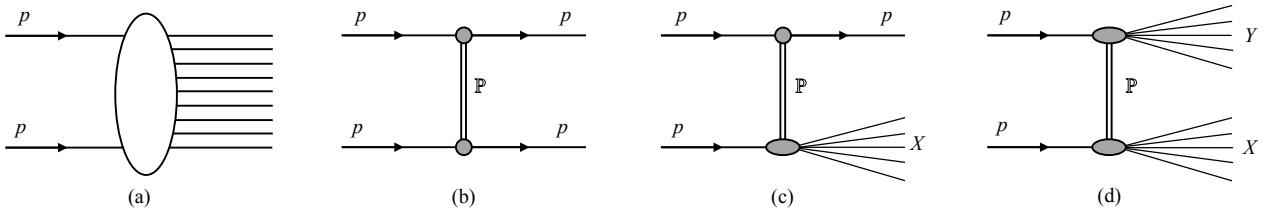

Figure 20.1: Schematic diagrams of soft pp processes. (a) non-diffractive processes, (b) elastic scattering, (c) single dissociation and (d) double dissociation. The double line corresponds to the Pomeron exchange.

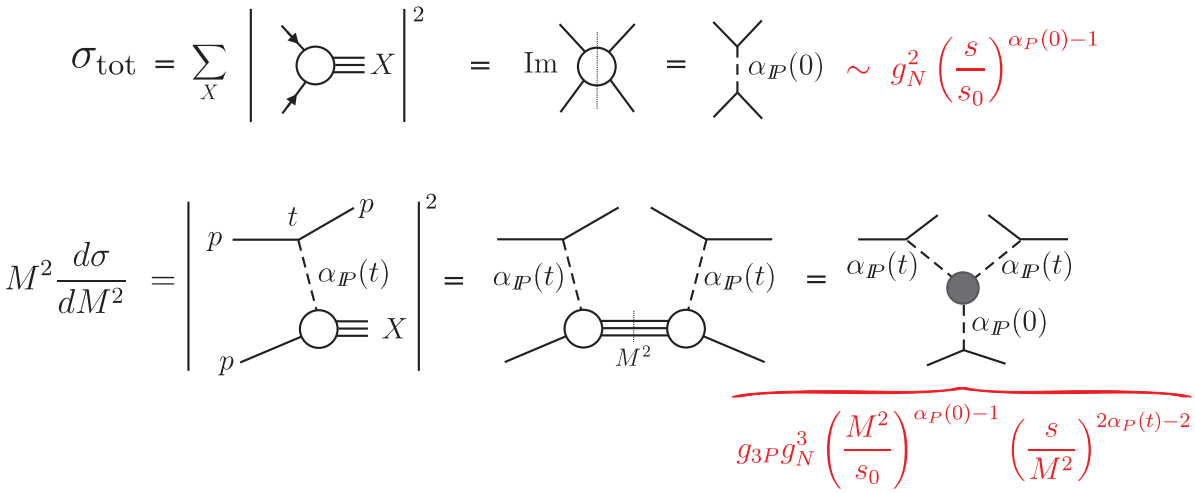

Figure 20.2: Illustration of the optical theorem for the total cross section and for high-mass diffractive dissociation in the absence of absorptive corrections.

The pole with the largest intercept, originally assumed to be $\alpha_{\mathbb{P}}(0) = 1$ since high-energy total cross sections were thought to have a constant asymptotic behaviour, is called the *Pomeron*[3]

Prior to the LHC, the energy behaviour of $pp, p\bar{p}, \pi p, Kp$ cross sections was satisfactorily reproduced by the sum of the Pomeron and secondary Reggeons (the poles at lower values of j, typically with $\alpha_\rho(0) \simeq 0.5$, see [22, 23] and Section 51 in [24]). However, above Tevatron energies the secondary Reggeon contributions (which all have intercepts $\alpha(0) \simeq 0.5$) are highly suppressed, which enables us to study the properties of the Pomeron only.

A popular parameterization of the elastic pp-scattering amplitude by Donnachie-Landshoff (DL) is the Regge form [25]

$$T_{\rm el}(s,t) = \eta_P \sigma_0 F_1^2(t) s^{\alpha_{\mathbb{P}}(t)}, \tag{20.5}$$

where $\sigma_0 = 21.7$ mb [26] and η_P is the signature factor

$$\eta_P = \frac{1 + \exp(-i\pi\alpha_{\mathbb{P}}(t))}{\sin(-\pi\alpha_{\mathbb{P}}(t))}, \tag{20.6}$$

F_1 is the Dirac electromagnetic form factor of the proton and the *effective* Pomeron trajectory

$$\alpha_{\mathbb{P}}(t) = 1 + \Delta + \alpha' t \;\simeq\; 1 + 0.0808 + 0.25t, \tag{20.7}$$

with t given in GeV^2. The intercept $\alpha_{\mathbb{P}}(0)$ just above 1 reproduces the observed slow growth of the total hadron-hadron cross sections at high energies.

However, this simple parameterization is becoming increasingly deficient at higher energies. This is because due to unitarity we have to take into account not only Regge poles, but also the cuts in the j-plane [27, 28], which correspond to the multiple exchange of Regge poles in the t-channel, see for instance [29–31]. A powerful technique to evaluate Reggeon diagrams was developed by Gribov [7, 32] (Reggeon calculus or Reggeon Field Theory (RFT)), which allows us to calculate the multi-Pomeron contributions.

[3]Pomeron pole was named after I. Y. Pomeranchuk. The history of the Pomeron is discussed in [19–21].

20.3 Theoretical description of high-energy diffraction

Diffractive processes (see e.g. reviews [33–37]) represent a rich testing ground for the dynamics of soft interactions as well as Monte Carlo models for soft hadron-hadron physics (see for reviews e.g. [8], Section 41 in [1] and Chapter 2 in [15]).

There is no universally agreed definition of diffractive processes. Theoretically, diffraction is the effect caused by the absorption of the incoming plane-wave in some region of impact parameter, b. After a decomposition of the distorted plane-wave over the outgoing momentum, q, due to absorption we arrive at some set of plane-waves with non-zero transverse momentum, $q_t \neq 0$. Experimentally, we call diffractive the events with large rapidity gaps (LRG) in the distribution of the final state particles. However, this definition is appropriate only for the events with very large gap sizes ($\Delta\eta > 4 - 5$); otherwise gaps can also be caused by fluctuations in the hadronization process [38].

In the case of proton-proton collisions, diffraction corresponds to elastic $pp \to pp$ scattering and to the $pp \to p + X$ and $pp \to X_1 + X_2$ processes where one or both protons are allowed to dissociate into a system X with the quantum numbers of the proton. The $p \to X$ dissociation is caused by the fact that the individual components of the incoming proton wave function interact differently with the target (see Section 20.3.1).

Theoretically, high-energy diffraction may be studied from either the s-channel or the t-channel viewpoint.

20.3.1 *Diffraction from the s-channel viewpoint*

Unitarity plays a central role in diffractive processes. To discuss unitarity effects it is convenient to work in terms of impact parameter, b. The total cross section is closely related to the elastic scattering amplitude and the scattering into inelastic final states via the s-channel unitarity of the S-matrix (see Sections 49 and 52 in [1]), $SS^\dagger = I$, or

$$disc\; T \equiv T - T^\dagger = iT^\dagger T \tag{20.8}$$

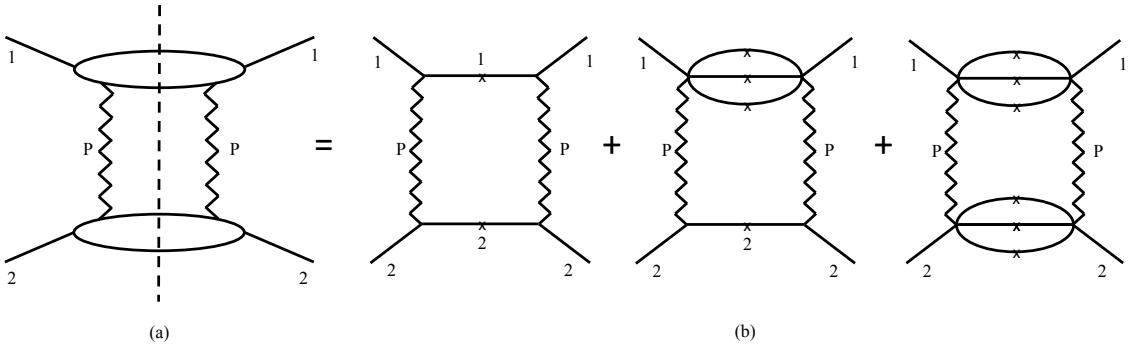

Figure 20.3: Two-Pomeron exchange in the t channel expressed as a sum over all diffractive intermediate states in the s-channel. The crosses indicate that the particles are on the mass shell.

with $S = I + iT$. If we were to focus, for example, on the unitarity for elastic and quasielastic processes, then *disc* T would simply denote a cut in s-channel between incoming and outgoing particles as visualized by crosses in Fig. 20.3.

At high energies, the s-channel unitarity relation is diagonal in the b basis such that

$$2\mathrm{Im}\, T_{\rm el}(s,b) = |T_{\rm el}(s,b)|^2 + G_{\rm inel}(s,b) \tag{20.9}$$

with

$$\sigma_{\rm tot} = 2\int d^2b\, \mathrm{Im}\, T_{\rm el}(s,b) \tag{20.10}$$

$$\sigma_{\rm el} = \int d^2b\, |T_{\rm el}(s,b)|^2 \tag{20.11}$$

$$\sigma_{\rm inel} = \int d^2b\, \left[2\mathrm{Im}\, T_{\rm el}(s,b) - |T_{\rm el}(s,b)|^2\right]. \tag{20.12}$$

The general solution of Eq. (20.9) is

$$T_{\rm el}(b) \;=\; i(1 - e^{-\Omega(b)/2}) \tag{20.13}$$

and

$$G_{\rm inel}(s,b) = 1 - \mathrm{e}^{-\mathrm{Re}\Omega(b)} = 1 - P_{\rm nointer}(s,b), \tag{20.14}$$

where $G_{\rm inel}$ is the sum over all inelastic intermediate states and $P_{\rm nointer}$ is a probability to have no inelastic interactions. $G_{\rm inel}(s,b)$ describes the b-profile of inelastic particle collisions. It satisfies the condition $0 \le G_{\rm inel} \le 1$ and determines how absorptive the interaction region is at a given impact parameter (with $G_{\rm inel}$= 1 for full absorption and $G_{\rm inel}$= 0 for the complete dominance of elastic scattering). As seen from Eq. (20.14), $\exp(-\mathrm{Re}\Omega(s,b))$ is the probability that no inelastic interactions occur at impact parameter b. Ω ($\mathrm{Re}\Omega \ge 0$) is called the opacity (optical density) or eikonal. The quantity

$$S^2(b) \equiv e^{-\mathrm{Re}\Omega(b)} \;=\; P_{\rm nointer}(b) \tag{20.15}$$

is the so-called survival factor, which enables us to calculate the probability that the LRG survives soft rescattering.

In terms of the opacity the elastic cross section takes the form

$$\frac{\mathrm{d}\sigma_{\rm el}}{\mathrm{d}t} = \frac{1}{16\pi s^2}\,|T_{\rm el}(s,t)|^2 = \frac{1}{4\pi}\left|\int \mathrm{d}^2b\; e^{i\vec{q}_t\cdot\vec{b}}(1 - e^{-\Omega(b)/2})\right|^2$$
$$= \pi\left|\int b\mathrm{d}b\; J_0(q_t b)(1 - e^{-\Omega(b)/2})\right|^2, \tag{20.16}$$

where $q_t = \sqrt{|t|}$ and J_0 is the zeroth-order Bessel function.

To describe the elastic scattering at one fixed energy we can always find an appropriate parameterization for the opacity $\Omega(b)$ and tune the parameters to reproduce the observed $\mathrm{d}\sigma_{\rm el}/\mathrm{d}t$ cross section. Moreover, we can fix the form of the parameterization, but choose, at each particular energy, the corresponding values of parameters; see, e.g. [39]. Alternatively, we may simply take the Fourier-Bessel transform from the experimental data [33, 40, 41]

$$\mathrm{Im}T_{\rm el}(b) \;=\; \int \frac{q_t \mathrm{d}q_t}{4\pi}\sqrt{\frac{\mathrm{d}\sigma_{\rm el}}{\mathrm{d}t}\frac{16\pi}{1+\rho^2}}\; J_0(q_t b), \tag{20.17}$$

where the square root represents $\mathrm{Im}T_{\rm el}(q_t)$, with $\rho \equiv \mathrm{Re}T_{\rm el}/\mathrm{Im}T_{\rm el}$. In this way, we first determine $T_{\rm el}$ from the data for $\mathrm{d}\sigma_{\rm el}/\mathrm{d}t$, and then calculate $\Omega(b)$ using Eq. (20.13), assuming in accordance with data that ρ is small (or $\rho(t)$ = constant).

At high energies $\rho^2 \ll 1$, which is usually well justified except in the diffractive dip region (see Section 20.3.3.1 for discussion of the dip region).

The value of ρ can be derived via the dispersion relation, see [3]:

$$\frac{1}{s}\mathrm{Re}T_{\rm el}(s) \;=\; \frac{1}{\pi}\int_{-\infty}^{+\infty}\frac{\mathrm{d}s'}{s'-s}\sigma_{\rm tot}(|s'|) \;=\; \frac{1}{\pi}\int_0^{\infty}\sigma_{\rm tot}(s')\frac{2s\mathrm{d}s'}{s'^2 - s^2}. \tag{20.18}$$

Since we consider just the charge-parity C-even amplitude, here for negative s' we put $\sigma_{p\bar{p}} = \sigma_{pp}$. That is, for negative s', which corresponds to the interaction with an *anti*particle, we use the same $\sigma_{pp}(|s'|)$. The major contribution comes from $s' \simeq s$. Thus, with a good accuracy we can evaluate $\rho(t=0)$ as

$$\rho \;\simeq\; \frac{\pi}{2}\,\frac{\partial \ln \sigma_{\rm tot}(s)}{\partial \ln s}. \tag{20.19}$$

20.3.2 *Diffractive dissociation*

The elastic cross section probes the optical density of the proton. The well known example of scattering on a black disk, with $G_{\rm inel} = 1$ for $b < R$, gives $\sigma_{\rm el} = \sigma_{\rm inel} = \pi R^2$ and $\sigma_{\rm tot} = 2\pi R^2$. In general, the absorption of the initial wave (due to inelastic channels) leads, via s-channel unitarity, to elastic scattering.

Inelastic diffraction (i.e. proton dissociation) is a consequence of the *internal structure* of hadrons. This can be conveniently described at high energies, where the lifetimes of each particular Fock component of the incoming hadron/proton wave function (the hadronic fluctuations) are large, $\tau \sim E/m^2$, and during these time intervals the corresponding Fock states can be considered as 'frozen'. Each hadronic constituent can undergo a scattering with its own probability and thus destroys coherence of the fluctuations[4]. As a result, the outgoing superposition of states will be different from the incident particle, and will most likely contain multiparticle states, so we will have *inelastic*, as well as elastic scattering.

To calculate diffractive dissociation we can enlarge the set of intermediate states (p, N_a^*), from just the single elastic channel, and introduce a multichannel eikonal. However, it is more convenient

[4] At high energies the configurations with different transverse separation, r, between the quarks (valence partons) can serve as an example of such Fock states. An interaction with the QCD Pomeron does not change the value of r, while the cross section $\sigma \propto \alpha_s^2 \cdot r^2$ (see Section 20.4.2 and [42–44]).

to follow Good and Walker [45], and to introduce states ϕ_k diagonalising the T matrix (which e.g. in the proton case describes different $p \to N^*$, $N_a^* \to N_b^*$ transitions). Such eigenstates only undergo elastic scattering. Since there are no off-diagonal transitions,

$$\langle \phi_i | T | \phi_k \rangle = 0 \qquad \text{for } i \neq k, \tag{20.20}$$

a state k cannot diffractively dissociate into a state $j \neq k$. Working in terms of the Good-Walker eigenstates ϕ_i, we have a simple one-channel eikonal for each state. We denote the orthogonal matrix which diagonalizes T by a, so that

$$T \;=\; aFa^T \qquad \text{with} \qquad \langle \phi_i | F | \phi_k \rangle \;=\; F_k \, \delta_{ik}, \tag{20.21}$$

where F_k is the probability amplitude of the hadronic process proceeding via the diffractive eigenstate ϕ_k.

Now consider the diffractive dissociation of an incoming state $|h\rangle$. We can write

$$|h\rangle \;=\; \sum_k a_{hk} \, |\phi_k\rangle. \tag{20.22}$$

The elastic scattering amplitude satisfies

$$\langle h|T|h\rangle \;=\; \sum_k |a_{hk}|^2 \, F_k \;=\; \langle F \rangle, \tag{20.23}$$

where $F_k \equiv \langle \phi_k | F | \phi_k \rangle$ and where the brackets of $\langle F \rangle$ mean that we take the average of F over the initial probability distribution of diffractive eigenstates. After the diffractive scattering described by T_{fh}, the final state $|f\rangle$ will, in general, be a different superposition of eigenstates from that of $|h\rangle$, which was shown in Eq. (20.22). Neglecting the real parts, for the cross sections at a given impact parameter b, we have

$$\begin{aligned}
\frac{\mathrm{d}\sigma_{\rm tot}}{\mathrm{d}^2 b} &= 2\,\mathrm{Im}\langle h|T|h\rangle \;=\; 2\sum_k |a_{hk}|^2 \,\mathrm{Im} F_k \;=\; 2\langle \mathrm{Im} F\rangle \\
\frac{\mathrm{d}\sigma_{\rm el}}{\mathrm{d}^2 b} &= |\langle h|T|h\rangle|^2 \;=\; \left| \sum_k |a_{hk}|^2 \, F_k \right|^2 \;=\; \langle |F| \rangle^2 \\
\frac{\mathrm{d}\sigma_{\rm el\,+\,SD}}{\mathrm{d}^2 b} &= \sum_k |\langle \phi_k | T | h \rangle|^2 \;=\; \sum_k |a_{hk}|^2 \, |F_k^2| \;=\; \langle |F^2| \rangle.
\end{aligned} \tag{20.24}$$

It follows that the cross section for the single diffractive dissociation of a proton,

$$\frac{\mathrm{d}\sigma_{\rm SD}}{\mathrm{d}^2 b} \;=\; \langle |F^2| \rangle \;-\; \langle |F| \rangle^2, \tag{20.25}$$

is given by the statistical dispersion in the absorption probabilities of the diffractive eigenstates. Here the average is taken over the components k of the incoming proton which dissociates. If the averages are taken over the components of both of the incoming particles, then Eq. (20.25) is the sum of the cross sections for single and double dissociation, see Fig. 20.3.

Note that if all the components ϕ_k of the incoming proton $|h\rangle$ were absorbed equally, then the diffracted superposition would be proportional to the incident one and the probability of the inelastic diffraction would be zero. Thus if, at very high energies, the amplitudes F_k at small impact parameters are equal to the black disk limit, $F_k = i$, then diffractive production will be equal to zero in this impact parameter domain, and so will only occur in the peripheral b region where the edge of the disk becomes not completely black. Hence the impact parameter structure of diffractive dissociation and elastic scattering is drastically different in the presence of absorptive s-channel unitarity effects (see the $G_{\rm inel}$ term in Eq. (20.9)). Under the assumption that amplitudes F_k at high energies cannot exceed the black disk limit, Im $F_k \leq 1$, equations 20.24 lead to the following bound

$$\frac{\mathrm{d}\sigma_{\rm el\,+\,SD_1+SD_2+DD}}{\mathrm{d}^2 b} \leq \frac{1}{2} \frac{\mathrm{d}\sigma_{\rm tot}}{\mathrm{d}^2 b} \, . \tag{20.26}$$

known as the Pumplin bound [46] [5].

20.3.3 *Diffraction from the t-channel viewpoint*

The t-channel approach is based on the Regge model (see Section 20.2), where high-energy diffractive processes are mediated by the exchange of a Pomeron ($\mathbb{P}$). In the case of the elastic pp-scattering amplitude in the eikonal model (see Eq. (20.13)), the opacity corresponding to the exchange of one Pomeron is

$$\Omega(s,b) = \int \frac{\mathrm{d}^2 q_t}{4\pi^2} \; \Omega(s,q_t) \; e^{i\vec{q}_t \cdot \vec{b}} \tag{20.27}$$

with

$$\Omega(s,q_t) = \frac{1}{s} T'_{\rm el} = -i\eta_P(t) g_N(t) g_N(t) \left(\frac{s}{s_0} \right)^{\alpha_{\mathbb{P}}(t)-1}, \tag{20.28}$$

where $T'_{\rm el}$ is the two-particle s-channel irreducible elastic amplitude, cf. Eq. (20.5), and $g_N(t)$ is the proton-Pomeron coupling.

If we assume an exponential t-dependence of the coupling, $g_N(t) = g_N(0) \exp(B_0 t)$, and neglect the Pomeron phase, then the opacity is

$$\Omega(s,q_t) = g_N(0) g_N(0) \left(\frac{s}{s_0} \right)^{\alpha_{\mathbb{P}}(0)-1} e^{Bt}, \tag{20.29}$$

with the t-slope given by

$$B \;=\; 2B_0 + \alpha'_{\mathbb{P}} \ln\left(\frac{s}{s_0} \right). \tag{20.30}$$

At high energies the opacity has a Gaussian form in the b-space:

$$\Omega(s,b) = \frac{g_N^2(0)}{4\pi B} \left(\frac{s}{s_0} \right)^{\alpha_{\mathbb{P}}(0)-1} e^{-b^2/4B} \, . \tag{20.31}$$

In terms of opacity the effective radius of interaction increases at high energies as $\sqrt{\alpha'_{\mathbb{P}} \ln(s/s_0)}$. This means that with energy increasing the differential cross section becomes steeper (the so called *shrinkage* of the diffractive peak).

If we were to take for the Pomeron the DL parametrisation [25, 26], that is to keep just the first, $T(b) = \Omega(b)/2$, term in the elastic amplitude (Eq. (20.13)) then, at LHC energies, the Gaussian would exceed the black disk limit at small b. However, the eikonal unitarization reduces the power growth of the one-Pomeron exchange cross section. Thus, in Eq. (20.31) $\Omega(s,b) \propto (s/s_0)^{\alpha_{\mathbb{P}}-1}$ gives an amplitude Im $T_{\rm el}(s,b) = 1 - e^{-\Omega/2} < 1$. Hence the total cross section is limited by the size of the effective interaction area $\sigma_{\rm tot} < 2\pi R^2$, where the interaction radius R can be estimated from Eq. (20.31) as the value of b where Re$\Omega(b)$ becomes ~ 1.

For the parameterization of Eq. (20.31) the corresponding radius grows at very large energies as

$$b^2 = R^2 = 4B \ln \left[\frac{g_N^2(0)}{4\pi B} \left(\frac{s}{s_0} \right)^{\alpha_{\mathbb{P}}(0)-1} \right] \simeq 4\Delta \alpha'_{\mathbb{P}} \ln^2(s/s_0) \, . \tag{20.32}$$

That is for $\Delta = 0.1$ and $\alpha'_{\mathbb{P}}$=0.25 GeV^{-2} we may expect that the cross section increases as

$$\sigma_{\rm tot} = 2\pi R^2 \simeq c \cdot \ln^2 s \, , \tag{20.33}$$

with $c = 8\pi\Delta\alpha'_{\mathbb{P}} = 0.24$ mb. This value is close to that obtained by the COMPETE parameterization ($c = 0.27$ mb [22, 24]) but much smaller than the Froissart-Lukaszuk-Martin (FLM) bound [47–49]. With $c^{\rm FLM} = \pi/m_\pi^2 \simeq 60$ mb, see Section 20.7,

$$\sigma_{\rm tot} \leq \frac{\pi}{m_\pi^2} \ln^2 \left(\frac{s}{s_0} \right). \tag{20.34}$$

[5] Strictly speaking the proof of the Pumplin bound is justified only for low mass dissociation. When the masses $M_{1,2}$ become so large (say, $M_i^2 > \sqrt{s s_0}$) that the Good-Walker states $|\phi_i\rangle$, corresponding to two incoming protons overlap, we may face double counting. Therefore, the high mass dissociation will be considered in the next Section, in terms of the multi-Pomeron diagram. Here and in what follows s_0 is a constant which should be defined for a particular theoretical model or fitted from experiment.

The fact that $c = (0.24–0.27)$ mb $\ll c^{\rm FLM} = 60$ mb demonstrates that even at the LHC we are very far from true high-energy asymptotics [6], and the observed growth of the cross section is driven by the interactions at relatively large transverse momenta $k_t \gg m_\pi$ rather than the smallest hadron mass m_π in the denominator of Eq. (20.34).

20.3.3.1 *The t-slope and dip in the elastic cross section*

We first start with a relatively small one-Pomeron amplitude and consider the two-Pomeron contribution corresponding to the Ω^2 term in the expansion of the eikonal $1 - \exp(-\Omega/2)$. In this term the momentum transferred, $q_t = \sqrt{|t|}$, is divided between the two Pomerons so that each Pomeron carries about a momentum $q_t/2$. Correspondingly, the t dependence of the whole 'two-Pomeron' amplitude will be $\exp(2B(t/4)) = \exp(Bt/2)$ [7].

Since the two-Pomeron contribution has an opposite sign in comparison with the one-Pomeron exchange, their interference will result in the appearance of the first diffractive minimum which moves to smaller $|t|$ with energy increasing. Such interference effects are largely responsible for the zero in the imaginary part of the amplitude (with the minimum filled by the real part).

It is worth mentioning that the one-channel eikonal discussed so far is a rather oversimplified approximation. It provides some indications about the behaviour we may expect for the elastic cross section, but clearly it does not give the whole story. Moreover, even within the framework of the one-channel eikonal, the expectation for the elastic slope t-dependence could be masked by other effects. Firstly, there is no reason why the t-dependence of the proton-Pomeron coupling $g_N(t)$ has to be a pure exponent. Next, there exists a two-pion singularity at $t = 4m_\pi^2$ (close to the physical region) in the Pomeron trajectory which generates some curvature in the behaviour of $\mathrm{d}\sigma_{\rm el}/\mathrm{d}t$ [50–52]. So there may be some compensation between the effects caused by the eikonal (arising from the interference between the different multi-Pomeron contributions), and the curvatures coming from the form of the proton-Pomeron coupling and the two-pion singularity of the Pomeron trajectory. However, an exact compensation looks quite non-trivial and a *pure* exponential behaviour of $\mathrm{d}\sigma_{\rm el}/\mathrm{d}t$ looks highly unlikely.

Indeed, the measurements by the TOTEM collaboration at 8 TeV [53] and at 13 TeV [54] clearly demonstrate that the local slope of the elastic pp cross section,

$$B = \mathrm{d}[\ln(\mathrm{d}\sigma_{\rm el}/\mathrm{d}t)]/\mathrm{d}t, \tag{20.35}$$

at $-t \lesssim 0.3$ GeV^2 varies with t.

20.3.3.2 *High mass dissociation*

Let us turn to inelastic diffractive processes that is, to single and double proton dissociations, $pp \to X + p$ and $pp \to X_1 + X_2$, where the + sign denotes the presence of a LRG in the distribution of final state particles. For example, for the diffractive dissociation of a proton into a system of mass M, the rapidity gap between the incoming proton and the remaining hadrons is

$$\Delta y = \ln\left(\frac{s}{M^2}\right) = \ln\left(\frac{1}{\xi}\right), \tag{20.36}$$

where $\xi = 1 - x$ and x is the initial momentum fraction (Feynman variable) carried by the outgoing proton. The masses, M, of the diffractively excited states, produced in high $\sqrt{s}$ collisions, can be large. To separate dissociation from the common inelastic process, usually the condition $M^2 \ll s$ is imposed.

The simplest multi-Pomeron diagram used to describe the diffractive dissociation is the so-called triple-Pomeron graph, shown at the end of Fig. 20.2.

In the Regge pole model, the cross section for the inclusive single diffractive (SD) dissociation process [55–57] can be written in the form (see Fig. 20.2)

$$\frac{\xi \mathrm{d}\sigma_{\rm SD}}{\mathrm{d}t\mathrm{d}\xi} = \frac{M^2 \mathrm{d}\sigma_{\rm SD}}{\mathrm{d}t\mathrm{d}M^2} = \frac{g_{3\mathbb{P}}(t) g_N(0) g_N^2(t)}{16\pi^2} \left(\frac{s}{M^2}\right)^{2\alpha_{\mathbb{P}}(t)-2} \left(\frac{M^2}{s_0}\right)^{\alpha_{\mathbb{P}}(0)-1}, \tag{20.37}$$

where $g_{3\mathbb{P}}(t)$ is the triple-Pomeron coupling. The value of the coupling $g_{3\mathbb{P}}$ is usually obtained from a triple-Regge analysis of lower energy data (see e.g. [34]) .

In an analogous way the cross section for double dissociation reads

$$\frac{\xi_1\xi_2 \mathrm{d}\sigma_{\rm DD}}{\mathrm{d}t\mathrm{d}\xi_1\xi_2} = \frac{M_1^2 M_2^2 \mathrm{d}\sigma_{\rm DD}}{\mathrm{d}t\mathrm{d}M_1^2\mathrm{d}M_2^2} = \frac{g_{3\mathbb{P}}^2(t) g_N^2(0)}{16\pi^3} \left(\frac{s s_0}{M_1^2 M_2^2}\right)^{2\alpha_{\mathbb{P}}(t)-2} \left(\frac{M_1^2 M_2^2}{s_0^2}\right)^{\alpha_{\mathbb{P}}(0)-1}, \tag{20.38}$$

where t is the momentum squared transferred through the LRG. As discussed in Section 20.5, from a microscopic point of view the

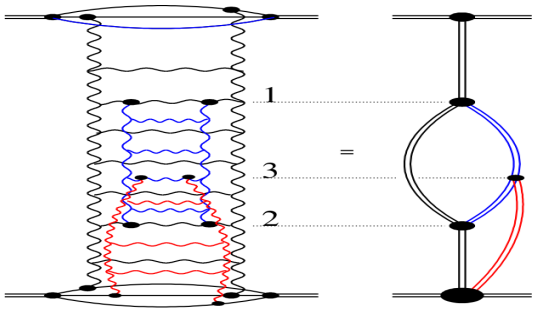

Figure 20.4: Pomeron exchange with schematic diagrams for the enhanced and semi-enhanced exchanges.

Pomeron exchange is described by a set of ladder-type diagrams (see [58–60]), which can lead to a rescattering of the intermediate partons (produced inside this ladder during the evolution), see Fig. 20.4. The left plot shows the Pomeron exchange complemented with the rescattering of partons 1 and 2 and the scattering of a parton 3 on the target. In terms of multi-Pomeron exchanges this corresponds to the diagram on the right hand side, where the Pomeron exchange is shown by the double line of a corresponding colour. The blue one is called "enhanced" (its contribution is integrated over the rapidities of both upper and lower vertices, i.e. of partons 1 and 2). The loop formed by the Pomerons shown in red is called "semi-enhanced" (it is integrated over the rapidity of one intermediate parton).

While the rescattering of the incoming hadron (proton) is already embedded in the eikonal formula (Eq. (20.13)), the rescattering of the intermediate partons in RFT is accounted for by the so-called enhanced diagrams [8] with multi-Pomeron vertices, g_m^n, which couple m to n Pomerons. It is quite a challenging task to resum all the enhanced diagrams, however this was successfully performed within the framework of the QGSJET Monte Carlo [61]. An elegant approach to sum up all enhanced diagrams in the case when each extra effective Pomeron contribution is very large was proposed in [62], assuming the analyticity of the g_m^n vertices in n and m in the right half of the complex n- and m-planes. The resulting amplitude becomes a black disk.

The simplest triple-Pomeron vertex $g_2^1 = g_{3\mathbb{P}}$ produces the first multi-Pomeron graph considered above (see the end of Fig. 20.2). However, numerically the multi-Pomeron vertices are relatively small. Note also that the value of $g_{3\mathbb{P}}$, determined from the fit to

[6] As usual, we assume $s_0 = 1$ GeV^2, but the qualitative conclusion does not depend on any realistic choice of s_0.

[7] The two-Pomeron contribution has a factor of two smaller t-slope, and in terms of the impact parameter, the $\Omega^2(b)$ term is concentrated in the domain of a smaller radius. In such a simplified picture, the impact parameters corresponding to an exchange of n Pomerons will rapidly decrease with n increasing.

[8] This contribution is *enhanced* due to the large parton multiplicity.

experimental data (e.g. [63]), is actually an effective vertex with coupling

$$g_{\rm eff} \;=\; g_{3\mathbb{P}}\,\langle S^2\rangle, \tag{20.39}$$

which already includes the survival factor $S^2(b)$, see Eq. (20.15).

Since the opacity Ω increases with energy, at large Ω the number of multiple interactions grows as $N \propto \Omega$, leading to a smaller S^2. An explicit analysis [64] accounting for the survival effects gives a coupling $g_{3\mathbb{P}}$ about a factor of 3 larger than $g_{\rm eff}$, namely $g_{3\mathbb{P}} \simeq 0.2 g_N$.

Recall that the Pomeron exchange simultaneously describes both the elastic scattering amplitude, $T_{\rm el}$, and the multiparticle production cross section, $G_{\rm inel}$. The discontinuity (*disc* $T_{\rm el}$) of the ladder diagram corresponds to the production of secondary particles, practically homogeneously distributed over the whole available rapidity interval covered by the Pomeron, as illustrated by the right-hand diagram in Fig. 20.5.

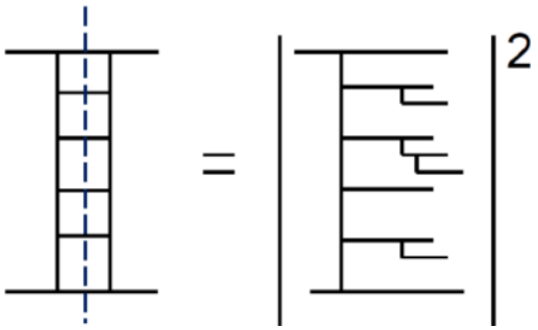

Figure 20.5: Cut Pomeron contribution to the inelastic cross section.

For the one-Pomeron case this discontinuity is called the "cut Pomeron". Correspondingly each multi-Pomeron diagram describes a series of different processes. Cutting k Pomerons in the diagram with n Pomerons we get the inelastic interaction with the multiplicity (density of secondaries) k times larger than that, N_0, produced by one cut Pomeron, $\mathrm{d}N/\mathrm{d}y = k \cdot N_0$. The remaining $n-k$ (elastic) Pomerons account for the absorptive corrections to the subprocess with k cut Pomerons. Indeed, the contribution of the diagram with n Pomerons includes also the processes with larger, $(k+i)\cdot N_0$ multiplicities (cut Pomerons), where $(i = 1, 2, ..., n-k)$. Absorptive corrections, described by the remaining elastic Pomerons, play a role of the survival factor S^2 for the process with the fixed particle density $k \cdot N_0$. They ensure probability conservation (the sum of the probabilities of all possible different channels is equal to one) and restore unitarity. Note that the multi-Pomeron diagrams represent all possible interactions between partons from the protons and partons from the Pomerons. In the case of Monte Carlo generators, the non-enhanced multi-Pomeron contributions are included in terms of the multiple parton interaction (MPI) option, see [13,65] and Section 7.2 in [2]. However, as a rule, this option accounts mainly for the multiple interactions between the partons from the protons (incoming hadrons). The energy-momentum sharing between the various inelastic rescattering processes (including the cut and uncut Pomerons) was performed at the amplitude level within the EPOS Monte Carlo [66].

20.3.3.3 *AGK cutting rules*

The relation between the cross sections of subprocesses with a different number of cut Pomerons within a given diagram with n Pomerons) is given by the AGK (Abramovsky-Gribov-Kancheli [67]) cutting rules. These rules include also the cut *between* the Pomerons with $k = 0$ which corresponds to the contribution of the particular diagram to the elastic cross section. By applying these rules, it is possible to show the self-consistency of the approach, which was lacking in the pure Regge-pole model.

Consider a diagram where the elastic scattering amplitude is mediated by an exchange of n Pomerons. The AGK cutting rules specify the coefficients c_n^k arising when k of these Pomerons are cut. Recall that the Pomeron cut discontinuities give the corresponding inelastic contributions to $\sigma_{\rm tot}$. The terms with $k = 0$ correspond to the diffractive cutting of the diagram (that is, the cut is between the Pomeron exchanges, and not through the Pomerons themselves), while the terms with $k = 1, 2, ...$ describe the processes with k cut Pomerons. The coefficients $c_n^k = \sigma_n^k/|\sigma_{\rm tot}^{(n)}|$ are [9]

$$c_n^{k=0} = (-1)^n(2^{n-1}-1), \qquad c_n^{k\neq 0} \;=\; (-2)^{n-1}\,\frac{(-1)^{k-1}n!}{k!(n-k)!} \tag{20.40}$$

where $\sigma_{\rm tot}^{(n)}$ denotes the contribution of the n-Pomeron diagram to the total cross section. Note the alternating sign of $\sigma_{\rm tot}^{(n)}$ expressed as $(-1)^{n-1}$.

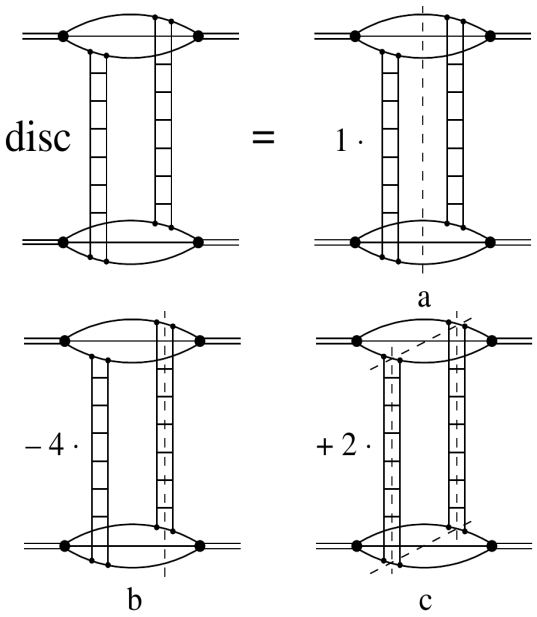

Figure 20.6: Two-Pomeron exchange diagram as a sum of different AGK cuts shown by the dashed lines.

For the two-Pomeron exchange, $n = 2$, the coefficients are $+1$, -4, or $+2$ according to whether $k = 0$, 1 or 2 Pomerons are cut, respectively. As shown in Fig. 20.6, the amplitude of the two-Pomeron exchange corresponds to a sum of three processes: i) inelastic interaction with particle density twice that caused by one Pomeron (see Fig. 20.6(c)) which enters with the coefficient '2', ii) shadowing (absorptive) correction to the one-Pomeron exchange contribution, which corresponds to events with a single Pomeron density (only one Pomeron is cut), see Fig. 20.6 (b), which enters with a factor '-4', and iii) diffractive elastic scattering or proton dissociation (when different components of the proton wave function correspond to different interaction cross sections), caused by the distortion of the incoming plane wave, see Fig. 20.6(a).

Note that the inclusive cross section is not affected by the multi-Pomeron contribution: $2 \times (2) + 1 \times (-4) = 0$. This is a general property of the AGK rules valid for any number of Pomerons n. Thus in order to calculate the inclusive single-particle cross section, it is sufficient to consider just the *one*-Pomeron exchange diagram.

Let us emphasize that the AGK rules provide a framework to consistently work with multi-Pomeron diagrams, that is, with the Regge cuts, accounting for their contributions to different processes (elastic scattering and diffractive dissociation, inelastic events with different densities, $\mathrm{d}N/\mathrm{d}y$, of secondaries, etc.).

Measurements of diffractive dissociation cross sections have been made in a wide range of pre-LHC energies, see e.g. [68–73]. At the LHC, cross sections of events with a LRG were measured by the ATLAS, CMS and ALICE collaborations at 7 and 8 TeV,

[9] In their complete form the AGK cutting rules were implemented in the QGSJET Monte Carlo [61].

see [74–77]. ATLAS [78] and CMS and TOTEM [79] presented first measurements of SD cross sections at 8 TeV with a tagged forward proton. While ATLAS measured inclusive SD cross section, CMS and TOTEM studied SD dijet production. Note that in [78] the measured slope $B = 7.65 \pm 0.34$ GeV^{-2} of the inclusive SD cross section as well as the differential distributions $\frac{\xi \mathrm{d}\sigma_{\mathrm{SD}}}{\mathrm{d}t\mathrm{d}\xi}$ for $0.0001 \leq \xi \leq 0.025$ are (within the experimental uncertainties) in a good agreement with the theoretical expectations [29,80]. Moreover a relatively small (in comparison with the $\mathrm{d}\sigma_{\mathrm{el}}/\mathrm{d}t$) slope B indicates that the size of the triple-Pomeron vertex is much smaller than the proton size.

20.3.4 *Central Diffractive processes*

Processes $pp \to p + X + p$, where an object X, produced in the central rapidity region, is separated from the outgoing protons by a LRG on each side, are called Central Exclusive Production (CEP). They are described by the double Pomeron exchange (DPE) diagrams. When the mass of the central system, M_X, is large and the interaction in the M_X region can be described by Pomeron exchange, the corresponding cross section reads

$$\frac{\xi_1\xi_2 \mathrm{d}\sigma^{\mathrm{CEP}}}{\mathrm{d}\xi_1 \mathrm{d}t_1 \mathrm{d}\xi_2 \mathrm{d}t_2} = \frac{g_N^2(t_1) g_N^2(t_2)}{(16\pi^2)^2} \left(\frac{1}{\xi_1}\right)^{2\alpha_{\mathbb{P}}(t_1)-2} \left(\frac{1}{\xi_2}\right)^{2\alpha_{\mathbb{P}}(t_2)-2} \times g_{3\mathbb{P}}^2(0) \left(\frac{M_X^2}{s_0}\right)^{\alpha_{\mathbb{P}}(0)-1} . \tag{20.41}$$

If the mass M_X is not too large or for the cases (such as exclusive Higgs boson or dijet production) where the mass M_X is comparable with the corresponding hard scale, the last factor $g_{3\mathbb{P}}^2(0)(M_X^2/s_0)^{\alpha_{\mathbb{P}}(0)-1}$ should be replaced by the corresponding 'Pomeron-Pomeron cross section', see for instance [81,82].

Note that equations (20.37), (20.38) and (20.41) are written in a simplified way without accounting for absorptive corrections. That is, the cross sections in equations (20.37) (20.38) and (20.41) should be multiplied by the gap survival factor S^2 (see Eq. (20.15)).

Since the QCD Pomeron is built mainly from gluons it is natural to search for glueballs in double Pomeron exchange processes, and in particular, in CEP.

Resonance production in the Pomeron-Pomeron fusion was extensively studied at the CERN ISR at $\sqrt{s}$ from 22 GeV to 63 GeV (see for reviews [82–84]) and, after the ISR closure in 1983, in fixed target experiments at the CERN SPS [85] and E690 at the Tevatron [86, 87]. Glueballs were actively searched for and the properties of the f_0 and f_2 production studied in detail using multiparticle spectrometers, such as the Omega facility at the CERN SPS experiments (WA76, WA91 and WA102), see for a review [85].

An important property of CEP processes, which can be expected from matching with the perturbative QCD LO (leading order) calculation, is the $J_z = 0$ dominance. Perturbatively, for the CEP of a heavy object, the leading contribution comes from a configuration with the projection of this object spin onto the beam axis $J_z = 0$ [81]. Note that the CEP cross section is suppressed at large M_X by a strong bremsstrahlung off the incoming gluons (from the Pomeron) which would violate the 'exclusivity'. The small probability of not having such radiation is described by the Sudakov suppression factor, T_{Sud}, [88], see [81] for details.

20.3.5 *Diffractive parton distributions*

Selecting in Deep Inelastic Scattering (DIS) events with a LRG (see e.g. [89,90]) or detecting the leading proton (see Section V.C. in the review [91]) we can study the parton (quark and gluon) distributions of the Pomeron [10]. In other words, such events can be treated as DIS on the Pomeron target with the incoming Pomeron flux given by

$$f_{\mathbb{P}}(x_{\mathbb{P}}) = \int \mathrm{d}t \frac{g_N^2(t)}{16\pi^2} x_{\mathbb{P}}^{2(1-\alpha_{\mathbb{P}}(t))} , \tag{20.42}$$

where the proton momentum fraction transferred through the Pomeron $x_{\mathbb{P}} = \xi = M^2/s$.

These Pomeron PDFs were extracted from the HERA measurements of ep scattering with leading protons or a LRG and can be used to describe the inclusive production of high E_T dijets or another hard process based on the collinear factorization theorem in the same way as that in non-diffractive collisions (see [91]). The inclusive measurements of these PDFs are described in [92–94], with the combined H1 and ZEUS data using tagged protons analyzed in [95]. The impact of diffractive jet measurements is addressed e.g. in [96] and the measured charm contribution is presented in [97, 98]. As far as the parton distributions are known, we can calculate the corresponding inelastic cross section of the Pomeron-proton interaction using one of the 'general purpose' Monte Carlo generators (see e.g. [13]), multiply it by the Pomeron flux and compare the obtained result with the Regge formula in Eq. (20.37). This approach provides another way to evaluate the triple-Pomeron vertex $g_{3\mathbb{P}}$. The corresponding analysis was performed in [99] and leads to practically the same (within the error bars) value of $g_{3\mathbb{P}} = 0.2 g_N(0)$.

It is worth mentioning that in DIS at large Q^2 we are dealing with small-size objects and the rescattering effects are small. Therefore, the survival factor $S^2 \simeq 1$ and does not affect the results.

20.4 Experimental data on diffraction at high energies

20.4.1 *Total and elastic cross sections*

The elastic scattering of protons is a process with a special and rather simple experimental signature: the central detector is empty while the incoming protons after the collisions are detected in the dedicated forward proton detectors (FPD) placed far from the interaction point (IP). Elastic scattering data are taken in special runs in order to be able to reach different ranges of t-values and thanks to the very large value of the cross section the data can be collected with a relatively low instantaneous luminosity and hence a negligible pile-up.[11]

These special runs usually have very few proton bunches and differ in the t range covered, which is governed roughly by the relation $t_{\min} \propto d^2/\beta^*$. Here d is the distance, expressed in multiples of the beam size at the detector, from the centre of the LHC beam and β^* is defined as the distance from the IP to the point where the transverse area of the beam is twice as wide as that at the IP (see Section 31 in [1]). Note that if we work at large β^*, the incoming protons have very small angular divergence leading to small average transverse momentum, which allows us to measure very small $|t|$ values. The lowest $|t|$ values measured so far at the LHC are 4×10^{-4} GeV^2 (ALFA) and 6×10^{-4} GeV^2 (TOTEM) reached with the 8 TeV LHC beam configured with β^*=1 km optics. The largest t values of about 4 GeV^2 were measured by TOTEM at 8 and 13 TeV with $\beta^* = 90$ m thanks to special triggers. Other β^* values used in special runs are 3.5 m, 11 m and 2.5 km.

There are four ways to determine the σ_{tot} value:

1. **Elastic and Inelastic.** This method does not require the optical theorem and hence no extrapolation of $\mathrm{d}\sigma_{\mathrm{el}}/\mathrm{d}t$ to $t = 0$ and no ρ (defined below Eq. (20.17)) but rather the luminosity and measuring rates N_{el} (elastic) and N_{inel} (inelastic). The total cross section is then simply:
$$\sigma_{\mathrm{tot}} = \frac{1}{\mathcal{L}}(N_{\mathrm{el}} + N_{\mathrm{inel}}). \tag{20.43}$$
Of course, both N_{el} and N_{inel} should be corrected for the detector acceptance and efficiency. This is especially important for N_{inel} since the detectors never cover the whole rapidity region (i.e. the whole 4π).
2. **Elastic only.** This approach necessitates measuring $\mathrm{d}\sigma_{\mathrm{el}}/\mathrm{d}t$ and using the optical theorem with a known value of ρ. As explained in Section 20.2, the optical theorem states that

[10] see also Section 18.5 in [1]

[11] The pile-up is formed by additional pp collisions which typically produce low-p_T particles. These may affect the signal sample and worsen various reconstruction and identification efficiencies.

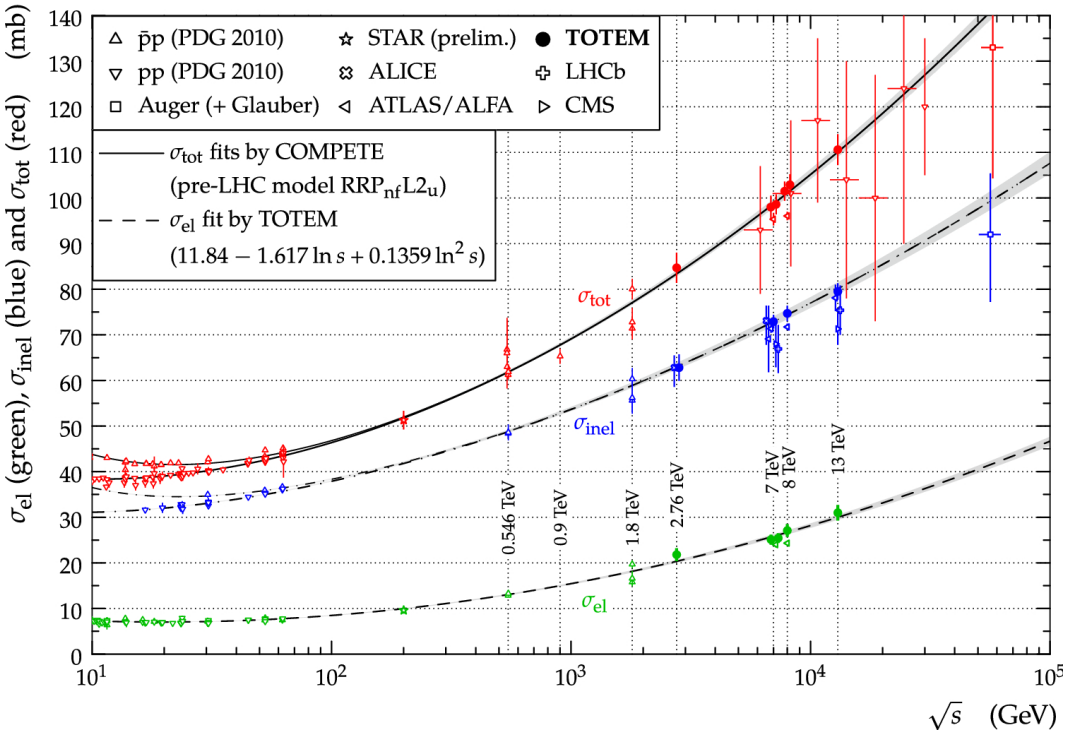

Figure 20.7: Overview of elastic ($\sigma_{\rm el}$), inelastic ($\sigma_{\rm inel}$) and total ($\sigma_{\rm tot}$) cross section data for pp and $p\bar{p}$ collisions as a function of $\sqrt{s}$. The continuous black lines (lower for pp, upper for $p\bar{p}$) represent the best fits of the total cross section data by the COMPETE collaboration [22]. The dashed line is a fit of the elastic cross section data. The dashed-dotted lines refer to the inelastic cross section and are obtained from the difference between the continuous and dashed lines. Figure from Ref. [100].

$\sigma_{\rm tot} \propto {\rm Im}[T_{\rm el}(t \to 0)]$, see Eq. (20.3). Since in practice it is not possible to measure down to $t = 0$, we need to extrapolate. To minimize the model dependence when extrapolating, it is vital to measure down to as low $|t|$ values as possible (i.e. high β^*). This method requires an independent luminosity measurement. Once the luminosity is known, $\mathrm{d}\sigma_{\rm el}/\mathrm{d}t$ can be normalized and used to extract $\sigma_{\rm tot}$ using the formula:

$$\sigma_{\rm tot}^2 = \frac{16\pi}{1+\rho^2} \left.\frac{\mathrm{d}\sigma_{\rm el}}{\mathrm{d}t}\right|_{t\to 0} . \qquad (20.44)$$

3. **Coulomb normalization.** Similarly to the previous method, this approach relies on the elastic observables only and requires a measurement of the elastic cross section at very low values of $|t|$, where it is sensitive to the theoretically well known Coulomb QED contribution $4\pi\alpha_{\rm QED}^2/t^2$. The normalization of $\mathrm{d}\sigma_{\rm el}/\mathrm{d}t$ is then determined by fitting the experimental data at very low $|t|$ using a formula including the Coulomb amplitude and its interference with the strongly interacting (the so-called nuclear) term. This method has been successfully used by UA4/2 [101] and TOTEM [102].
4. **Luminosity-independent.** This method does not rely on the knowledge of luminosity but rather on the knowledge of $N_{\rm el}$ and $N_{\rm inel}$ and on the optical theorem: combining equations (20.43) and (20.44) with $\frac{\mathrm{d}\sigma_{\rm el}}{\mathrm{d}t} = \frac{1}{\mathcal{L}} \frac{\mathrm{d}N_{\rm el}}{\mathrm{d}t}$ we get

$$\sigma_{\rm tot} = \frac{16\pi}{1+\rho^2} \frac{\left.\mathrm{d}N_{\rm el}/\mathrm{d}t\right|_{t=0}}{N_{\rm el}+N_{\rm inel}}, \qquad (20.45)$$

where $\left.\mathrm{d}N_{\rm el}/\mathrm{d}t\right|_{t=0}$ corresponds to the extrapolation to $t = 0$ of the nuclear term only. By independently and simultaneously measuring $N_{\rm el}$ and $N_{\rm inel}$, and applying the optical theorem, we can also determine the luminosity.

The TOTEM [100, 103–105] and ATLAS [106, 107] collaborations at CERN have covered an energy range from $\sqrt{s}$=2.76 TeV to 13 TeV. A compilation of high energy total pp and $p\bar{p}$ cross section measurements is shown in Fig. 20.7 (for discussion of the pre-LHC elastic scattering data see review [108]).

Despite some tension between the Tevatron CDF [109] and E811 [110] data [12] and to a lesser extent between the TOTEM [104, 105] and ATLAS [106, 107] measurements, the data clearly indicate that in the Tevatron – LHC energy interval the total cross section starts to grow *faster* than the power-law parametrization [26] describing the data below the Tevatron energy. In particular, while the DL fit [26] predicts $\sigma_{\rm tot} = 90.7$ mb at $\sqrt{s} = 7$ TeV, the TOTEM experiment observes 98.6±2.2 mb [104].

A compilation of the high-energy data on the elastic slope is shown in Fig. 20.8. It is clearly seen that in the TeV energy range the slope increases with $\sqrt{s}$ more rapidly than the logarithmic behaviour expected in the case of one-Pomeron exchange, see Eq. (20.30). Such an acceleration of the t-slope derivative, $\mathrm{d}B/\mathrm{d}\ln s$, is a clear manifestation of the increasing role of the multi-Pomeron exchanges, where asymptotically the slope should rise as $\ln^2 s$, see [117]. Finally, Fig. 20.9 illustrates the energy dependence of the differential elastic pp cross section. As expected (see Section 20.3.3.1), the diffractive dip moves to smaller $|t|$ with increasing energy.

20.4.2 *Diffractive vector meson production*

The exclusive production of vector mesons was studied in detail at HERA (see for a review [91]). It is well described within the 'dipole model' (see for review and references [120]), where the incoming photon first fluctuates into a quark-antiquark, which then interacts with the target proton and, finally, with the probability given by the overlap integral between the vector meson wave function and the outgoing $q\bar{q}$-pair, the vector meson is produced. The crucial quantity is the value of cross section, $\sigma(q\bar{q} - p)$, of elastic scattering of the $q\bar{q}$-pair on the proton. The energy behaviour of $\sigma(q\bar{q} - p)$ is driven by the intercept, $\alpha_{\rm eff}(0)$, of the effective Pomeron [13] (rightmost singularity in the j-plane), while

[12] The CDF 1.8 TeV point [109] is 2.8 σ higher than the corresponding E811 result [110].

[13] Effective Pomeron means that this is not an original pole in the j-plane, but it includes the corrections (renormalizations) caused by the enhanced diagrams (see e.g. [121]).

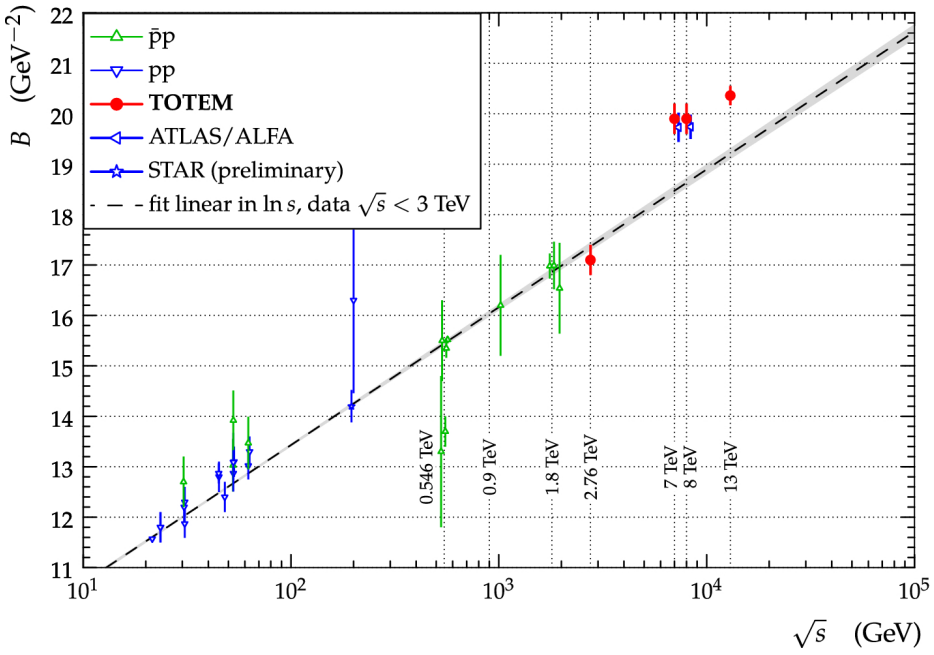

Figure 20.8: The diffractive slope B for pp and $p\bar{p}$ elastic scattering as a function of $\sqrt{s}$. The experimental uncertainties represent the quadratic sum of statistical and systematic uncertainties. The dashed line is a result of a linear fit to data at $\sqrt{s} < 3$ TeV. The data points come from [103–107, 111–113]. Figure from Ref. [100].

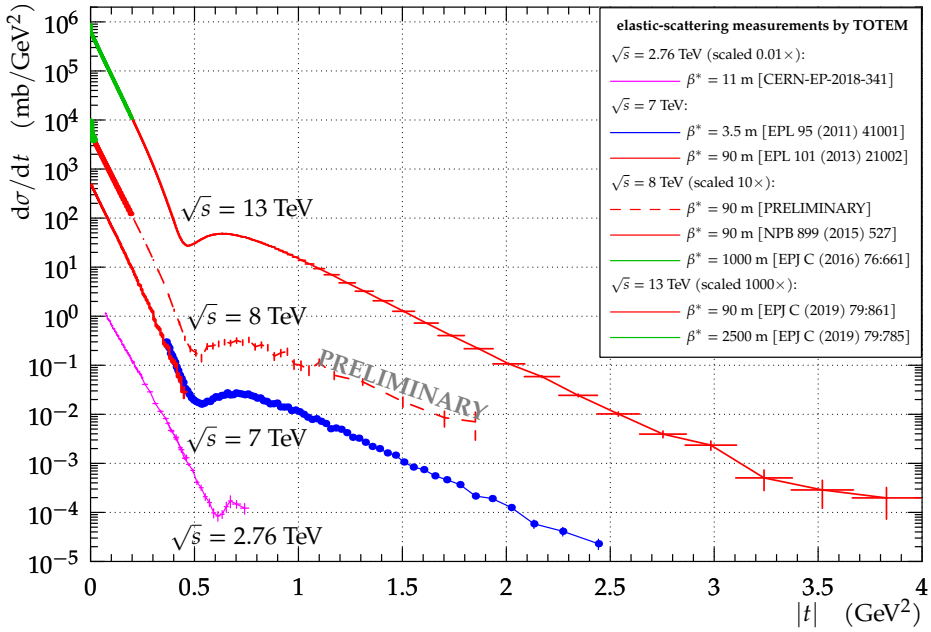

Figure 20.9: The t-dependence of the pp elastic cross section for collision energies $\sqrt{s}$ = 2.76 TeV [103], 7 TeV [104, 114], 8 TeV [53,115,116] and 13 TeV [54,102]. The experimental uncertainties represent the quadratic sum of statistical and systematic uncertainties. Figure from Ref. [116].

the value of the cross section depends on the quark separation, r, in the transverse plane, $\sigma(q\bar{q}-p) \propto \alpha_s^2\langle r^2\rangle$ [43, 44]. Thus different processes with the same $\langle r^2\rangle$ are driven by the same $\sigma(q\bar{q}-p)$ cross section.

In the DIS case this separation in turn is controlled by the photon virtuality, Q^2, and the quark mass, m_q: $\langle r^2\rangle \simeq 1/(z(1-z)Q^2 + m_q^2)$ (z is the photon momentum fraction carried by the quark). Indeed, the cross section of the ρ meson diffractive production in DIS at $Q^2 = M^2_{J/\psi}$ is close (up to the difference in the quark electric charges) to that for the J/ψ photoproduction, see Fig. 20.10 (Left).

The production cross section depends non-trivially on W, the energy of the $\gamma^* p$ center of mass system. It increases with W as W^n, where $n = 0.2$ for ρ, ω and ϕ (light quark)-mesons but $n = 0.8$ for J/ψ. Note that in the J/ψ case the energy dependence is close to that of the BFKL (Balitsky-Fadin-Kuraev-Lipatov) Pomeron [59,122,123], that is, the singularity calculated within the leading (and next-to-leading) approximation in perturbative QCD. But at lower scales the absorptive (multi-Pomeron) corrections tame the growth which leads to smaller values of n ([124–127]), see Fig. 20.10 (Right).

A similar situation reveals in the dependence of $\alpha_{\rm eff}$ on Q^2, as can be seen in Fig. 47 of [91]. At a large scale $\mu^2 = (Q^2 + M_V^2)/4$ the value of $\alpha_{\rm eff} \simeq 1.3$ is close to the prediction for the QCD

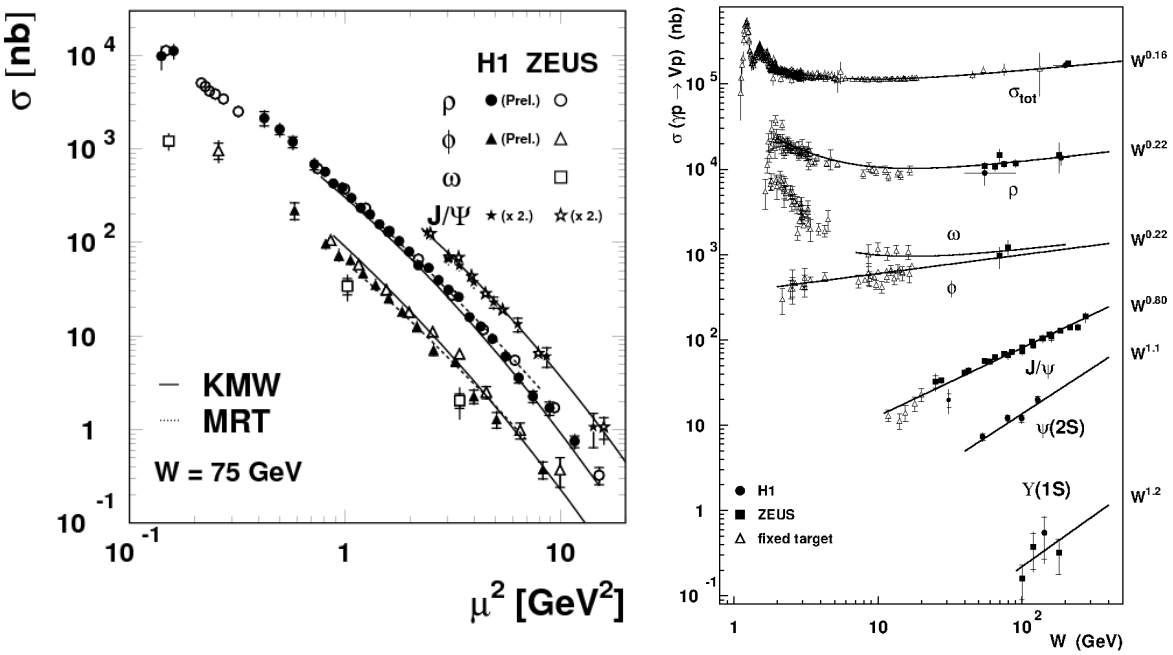

Figure 20.10: (Left) The ρ, ω, ϕ and J/ψ elastic production cross sections as a function of the scale $\mu^2 = (Q^2 + M_V^2)/4$. For readability of the figure, the J/ψ cross sections are multiplied by a factor 2. Figure from Ref. [118]. (Right) Compilation of photoproduction cross section measurements as a function of the γp centre-of-mass energy, W. The total cross section and various vector meson production cross sections are included, with the approximate power law dependences $\sigma \propto W^\delta$ indicated for each process. Figure from Ref. [119].

Pomeron, while for a smaller scale, the absorptive corrections described by the multi-Pomeron diagrams start to reduce the cross section, and $\alpha_{\rm eff}$ decreases.

20.5 Pomeron in QCD

All features described in the previous Sections were based on *first principles*, such as analyticity (based on causality), unitarity, crossing symmetry, etc. Since QCD theory satisfies all these principles it should reveal a corresponding "Regge" behaviour. Indeed, within perturbative QCD there is a Pomeron: an even-signature singularity in the j-plane with vacuum quantum numbers. While in the old Regge theory the Regge trajectories and their couplings were phenomenological numbers fitted from experiment, perturbative QCD allows one to calculate the positions of the singularities and the corresponding couplings with $O(\alpha_s)$ and even with $O(\alpha_s^2)$ accuracy [59, 122, 123, 128–131].

In terms of Feynman diagrams, the QCD Pomeron may be viewed as a sum of multi-particle ladders built by the exchange of two t-channel (reggeized [14]) gluons, see the left-hand side of Fig. 20.5.

The sum of ladder diagrams of the type of Fig. 20.5 is the simplest multiparticle structure which reproduces the power-like s^α behaviour of the Pomeron pole. In other words it corresponds to a sum of completely inelastic $2 \to n$ processes, that is, to the last term $G_{\rm inel} = 1 - \exp(-\Omega)$ in the unitarity equation (20.9). This set of diagrams was resummed in the limit of a small QCD coupling, $\alpha_s \ll 1$, but large energy, such that $\alpha_s \ln(s/s_0) \sim O(1)$ [59]. The summation results in the rightmost singularity at $j = 1 + \omega_0 > 1$. After accounting for the next-to-leading logarithmic (NLL) corrections, the position of the singularity (Pomeron intercept) corresponds to $\omega_0 = 0.25$–0.3 depending only weakly on the scale [122, 123, 132–136], whose value is characterized by the transverse momentum, k_t, of gluons in the ladder.

It was demonstrated (see e.g. [137]) that the resummation of the $(\alpha_s \ln(1/x))^n$ terms based on the QCD Pomeron results essentially improves the description of low-x inclusive HERA data within the framework of the NNLO DGLAP evolution.

At this stage the singularity is the cut in the j-plane. However we have to account for the boundary conditions at relatively small k_t. Imposing a reasonable boundary, we arrive at a series of Regge poles in the interval from $j = 1$ to $j = 1 + \omega_0$ instead of the cut [134]. Note that the first (corresponding to the rightmost pole in the j-plane, i.e. to the pole with the largest Re j) eigenfunction consists of gluons with relatively small k_t, while for the next poles the k_t increases. DIS inclusive $\gamma^* p$ cross sections were fitted in [135] using the QCD based approach in which Pomeron is represented by series of Regge poles obtained within the perturbative QCD BFKL approach. It was concluded that the first pole has a small coupling to the proton. It is possible that this small value of the coupling to the proton is related to the fact that the enhanced multi-Pomeron diagrams (i.e. the rescattering of intermediate partons) were neglected in the fit. The main effect of this enhanced contribution is the "renormalization" of the intercept which diminishes the effective value of ω_0. Besides this, the enhanced diagrams provide a saturation by reducing the rise of the parton densities in the (b, k_t, y)-space (see e.g. [138, 139]).

Note that perturbative QCD allows us to understand why the values of the phenomenological multi-Pomeron vertices and the shift, ω_0, of the intercept, are small (due to $\alpha_s \ll 1$ and some numerical factors such as N_c and π). Indeed, at the lowest α_s orders we get for the ω_0 value and the simplest multi-Pomeron vertices (see e.g. [59, 139, 140]):

$$\omega_0 \propto \frac{N_c \alpha_s}{\pi}, \quad g_{3\mathbb{P}} \propto \frac{N_c \alpha_s^2}{(N_c^2-1)\pi^2} \quad \text{and} \quad g_2^2 \propto \frac{N_c \alpha_s}{(N_c^2-1)^2}\ , \tag{20.46}$$

where g_2^2 is the coupling corresponding to the transition of 2 into 2 Pomerons.

20.5.1 *BFKL evolution in the 'dipole' representation*

It was shown in [141–144] that the LO BFKL Pomeron equation [59] can be written in terms of the evolution of the dipole

[14] That is, the virtual loop corrections to the one-gluon exchanges are included. These corrections are important in order to provide infrared stability of the results.

density, $N(x_d, y_d; y)$, in rapidity y (here x_d and y_d are the transverse coordinates of two t-channel gluons which form the colour singlet dipole). Indeed, after the emission of a new gluon at point z_d, the initial colour dipole with coordinates (x_d, y_d) turns into a pair of dipoles (x_d, z_d) and (z_d, y_d). This can be considered as a development of a 'dipole cascade'. Moreover in this formalism it is easy to include the non-linear absorptive corrections (last term in the square brackets in Eq. (20.47)), which accounts for the rescattering of the intermediate partons (gluons) on the target proton. The corresponding contribution is described by the so-called "fan" diagrams and these are the most important corrections to the linear DGLAP (Dokshitzer-Gribov-Lipatov-Altarelli-Parisi) evolution [145] in the case of DIS at not large scales but at very small momentum fraction [139].

The resulting non-linear evolution (Balitsky-Kovchegov equation [146–148]) reads

$$\frac{\mathrm{d}}{\mathrm{d}y}N(x_d, y_d; y) = \frac{\alpha_s N_c}{2\pi^2}\int \mathrm{d}^2 z_d \frac{(x_d - y_d)^2}{(x_d - z_d)^2(y_d - z_d)^2} \times [N(x_d, z_d; y) + N(y_d, z_d; y) - N(x_d, y_d; y) - N(x_d, z_d; y)N(y_d, z_d; y)] \ . \tag{20.47}$$

For a small density N the last term in the square brackets can be neglected, and the first three terms in Eq. (20.47) reproduce the conventional BFKL equation in the coordinate representation. However, for large $N \to 1$ the right-hand side of Eq. (20.47) vanishes and we reach the saturation $N = 1$. It is worth mentioning that, as shown in [149], in terms of 'dipole' formalism, with the triple-Pomeron vertex generated by the 'one dipole to two dipoles' transition, it is possible to relate the Good-Walker approach to high mass diffraction with the triple-Pomeron diagram.

20.5.2 *Distribution of secondaries: theory versus experiment*

As already discussed, in terms of Feynman diagrams the cut Pomeron can be viewed as a set of ladder diagrams corresponding to a sum of completely inelastic $2 \to n$ processes, that is, to the last term $G_{\mathrm{inel}} = 1 - \exp(-\Omega)$ in the unitarity equation (20.9). Here $n > 2$ means the production of additional $(n-2)$ gluons which, after hadronization, form minijets. [15] Therefore, in the final state driven by one Pomeron, we expect to observe gluon minijets with a flat rapidity distribution in the central (plateau) rapidity region. This would correspond to a flat pseudorapidity distribution of produced particles if they were massless. A typical pseudorapidity distribution of charged particles in inclusive events (up to $|\eta| = 7$) is shown in Fig. 20.11 (left) [150] (see also Fig. 52.1 in [1]). The central part ($|\eta| < 2.5$) was measured by CMS, while the forward region was covered by TOTEM. The dip observed at $\eta = 0$ is explained by the presence of massive particles (the Jacobian $J(p_T, m, \eta) = p_T/E \to p_T/\sqrt{p_T^2 + m^2}$ at $\eta = 0$). A photon energy spectrum is shown in Fig. 20.11 (right) [151], measured by LHCf inclusively and in events with a diffraction topology, i.e. no charged particles with $p_T > 100$ MeV and $|\eta| < 2.5$ observed by ATLAS. As expected in diffractive events the energy flow decreases with E_γ more slowly than that in the inclusive case.

The energy dependence of the particle density $\mathrm{d}N_{\mathrm{ch}}/\mathrm{d}\eta$ at $\eta = 0$ is shown in Fig. 20.12 (left). Neglecting absorptive corrections given by the enhanced diagrams (which mainly change ('renormalize') the effective Pomeron intercept $\alpha_{\mathrm{eff}}(0) = 1 + \Delta$ [121]), we conclude that according to the AGK rules the plateau height $\mathrm{d}\sigma/\mathrm{d}\eta \propto s^{\Delta}$ is driven just by the one-Pomeron exchange with effective $\Delta \sim 0.2$ (see Section 20.3.3.3). That is, the density of secondaries observed in the inclusive process increases with increasing energy faster than the total cross section, whose growth is tamed by the multi-Pomeron diagrams. Indeed, as is seen from Fig. 20.12 (left), in the interval of collider energies $\mathrm{d}N_{\mathrm{ch}}/\mathrm{d}\eta = (1/\sigma_{\mathrm{inel}})\mathrm{d}\sigma/\mathrm{d}\eta \propto s^{0.115}$ (i.e. $\mathrm{d}\sigma/\mathrm{d}\eta \propto s^{0.215}$), while $\sigma_{\mathrm{inel}} \propto s^{0.1}$.

[15] Minijets result from hadronization of partons emitted from the cut QCD Pomeron. Typically these are groups of hadrons with comparatively low overall $E_T \lesssim$ 5–10 GeV.

Contrary to the 'old' Regge theory where it was *assumed* (based on the experimental data existing in the 1950s and 1960s) that all transverse momenta are limited, in QCD the k_t distributions of jets (charged particles) have a long k_t tail ($\mathrm{d}\sigma/\mathrm{d}k_t^2 \propto \alpha_s^2(k_t^2)/k_t^4$ at large k_t and very large energy $s \gg k_t^2$). An example of the p_T distribution of charged secondaries is shown in Fig. 20.12 (right).

Note that the mean transverse momentum of secondaries, produced via jet fragmentation, slowly increases with collision energy, see Fig. 20.13 (right). This is caused by the stronger absorption (at larger $\sqrt{s}$) of the gluons with a smaller k_t ($\sigma^{\mathrm{abs}} \propto 1/k_t^2$). The growth of $\langle p_T \rangle$ with multiplicity (see Fig. 20.13 (left)) can be explained by the fact that events with larger N_{ch} correspond to a smaller impact parameter, b, where the absorption of a low k_t component is stronger and, next, larger multiplicity can be originated by the events with jets/minijets with higher p_T. Since the mean p_T of secondaries grows with $\sqrt{s}$, the increase with $\sqrt{s}$ of transverse energy flow is a bit faster than that of particle density.

The model [162] based on a modification of the classic RFT allows one to trace the smooth transition from the pure perturbative, large k_t, region into the *soft* domain. A strong absorption of the low k_t partons plays a crucial role here since it produces an effective infrared cutoff, k_{sat}, and provides the possibility of extending the parton approach, used for 'hard' processes, to also describe high-energy soft and semihard interactions. This approach combines a description of soft physics and diffraction with jet physics in a coherent self-consistent way.

Another way is to include the soft and hard components independently [37, 66, 163, 164]. In this approach the soft part is described in terms of RFT with the phenomenological "soft" Pomeron pole while the hard part is calculated in terms of the parton model for minijet production with the energy dependent cutoff $k_t > k_0(s)$. A combined description of soft and hard processes in hadronic collisions is reached within the QGSJET Monte Carlo model (e.g. [61]) in the framework of the so-called "semihard Pomeron" approach (see e.g. [165]).

In [166] a model was constructed, which incorporated the attractive features of the two successful theoretical approaches to high energy QCD: BFKL Pomeron calculus [59,60] and the Colour Glass Condensate/saturation [167].

20.5.2.1 *Correlations*

All LHC experiments routinely measure tracks with $p_T > p_{\mathrm{min}}$, where p_{min} can vary in different studies. Typically, $p_{\mathrm{min}} =$ 200 MeV, where tracking reconstruction efficiencies are larger than 70%. In order to identify particle species, each experiment has sophisticated identification procedures usually based on the ionization energy loss, $\mathrm{d}E/\mathrm{d}x$, or other techniques, with different regions of applicability for different particle species. Thanks to usually relatively large cross sections of soft QCD processes, most of the results below come from event samples with very low or negligible pile-up.

Following the notation in [168], symmetrized inclusive particle number densities for q points at $y_1, ..., y_q$ (where y_i represents the 4-momentum of the ith particle), $\rho_q(y_1, ..., y_q)$, are related to the inclusive differential cross section by

$$\frac{1}{\sigma_{\mathrm{inel}}}\mathrm{d}\sigma = \rho_1(y)\mathrm{d}y, \quad \frac{1}{\sigma_{\mathrm{inel}}}\mathrm{d}^2\sigma = \rho_2(y_1, y_2)\mathrm{d}y_1\mathrm{d}y_2 \quad \text{etc.} \tag{20.48}$$

By integrating we get

$$\int \rho_1(y)\mathrm{d}y = \langle n \rangle, \quad \int\int \rho_2(y_1, y_2)\mathrm{d}y_1\mathrm{d}y_2 = \langle n(n-1) \rangle \quad \text{etc.}, \tag{20.49}$$

where the angular brackets denote averaging over the event sample and n is the particle multiplicity.

Since the inclusive q-particle densities in general contain trivial contributions from lower-order densities, it is convenient to consider quantities C_q which vanish when one of their arguments becomes statistically independent of (uncorrelated with) the others. These quantities C_q, called correlation functions (or cumulant

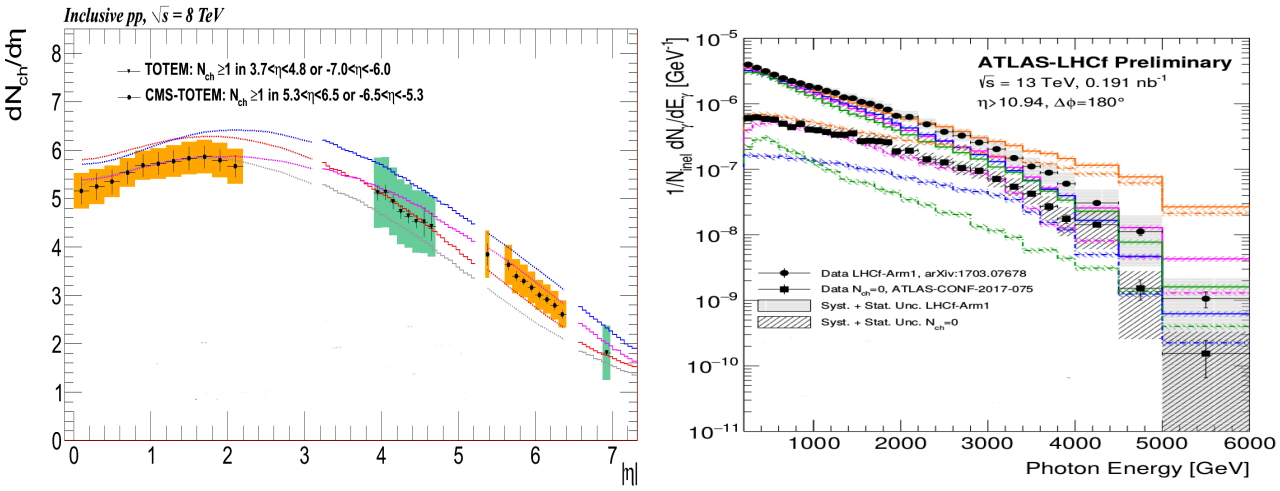

Figure 20.11: (Left) Charged-particle pseudorapidity distribution for inclusive events measured by CMS and TOTEM [150]. The error bars represent the statistical and uncorrelated systematic uncertainties between neighboring bins, while the shaded areas denote the combined statistical and full systematic uncertainties. The coloured lines indicate model predictions. (Right) Photon energy spectrum measured by LHCf at $|\eta|$ >10.94. The filled circles show the inclusive photon spectrum measured by LHCf [152] and filled squares the spectrum for $N_{\rm ch} = 0$ events where no charged particles with $p_T > 100$ MeV and $|\eta|$ <2.5 are observed by ATLAS [153]. The coloured lines indicate model predictions. The error bars correspond to the statistical uncertainties and the shaded areas denote the combined statistical and systematic uncertainties. Figure from Ref. [151].

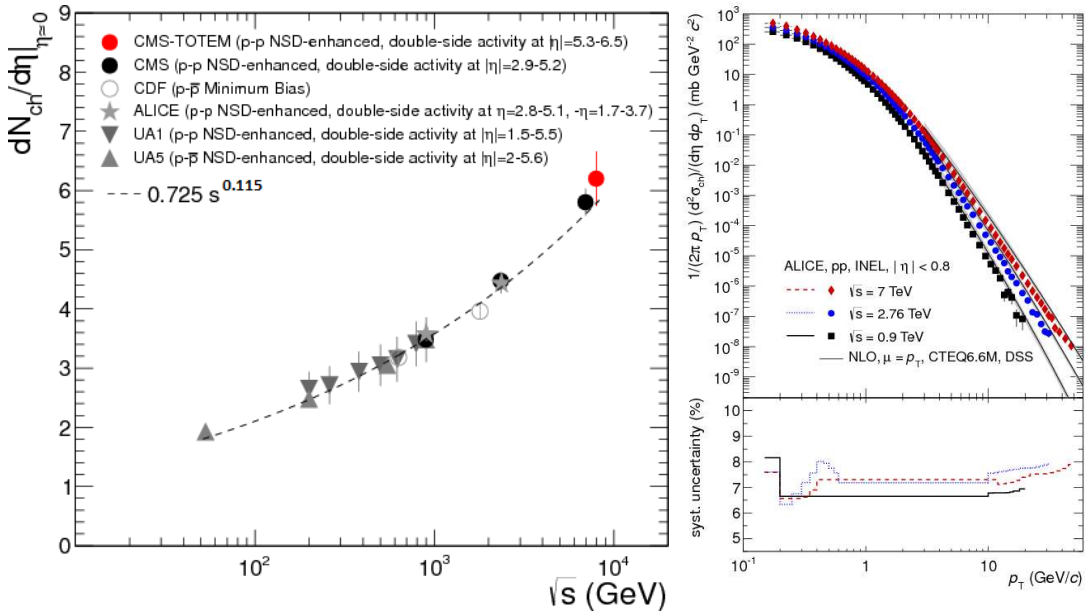

Figure 20.12: (Left) Energy dependence of the charged particle density $\mathrm{d}N_{\rm ch}/\mathrm{d}\eta$ at $\eta \approx 0$ for pp and $p\bar{p}$ collisions. Shown are measurements performed with different Non-SD event selections from UA1 [154], UA5 [155], CDF [156,157], ALICE [158] and CMS [159]. The dashed line is a power-law fit to the data. Figure from Ref. [150]. (Right) Differential cross section of charged particles with $|\eta| < 0.8$ in inelastic pp collisions at $\sqrt{s} = 0.9, 2.76$ and 7 TeV as a function of p_T. Only statistical uncertainties are shown. Figure from Ref. [160].

functions), are defined as:

$$C_2(1,2) = \rho_2(1,2) - \rho_1(1)\rho_1(2), \quad C_3(1,2,3) = \rho_3(1,2,3) - \sum_{(3)} \rho_1(1)\rho_2(2,3) + 2\rho_1(1)\rho_1(2)\rho_1(3),$$

$$C_4(1,2,3,4) = \rho_4(1,2,3,4) - \sum_{(4)} \rho_1(1)\rho_3(1,2,3) - \sum_{(3)} \rho_2(1,2)\rho_2(3,4) + 2\sum_{(6)} \rho_1(1)\rho_1(2)\rho_2(3,4) - 6\rho_1(1)\rho_1(2)\rho_1(3)\rho_1(4). \tag{20.50}$$

The 2D two-particle correlation function is defined as

$$C(\Delta\eta, \Delta\phi) = \frac{\rho_2(\Delta\eta, \Delta\phi)}{\rho_1(\eta_a, \phi_a)\rho_1(\eta_b, \phi_b)}. \tag{20.51}$$

The distribution $\rho_2(\Delta\eta, \Delta\phi)$ is usually interpreted as a conditional probability to observe a particle a at the phase-space point (η_a, ϕ_a) if a particle b at (η_b, ϕ_b) is observed as well, and $\Delta\eta = \eta_a - \eta_b$ and $\Delta\phi = \phi_a - \phi_b$. The distributions $\rho_1(\eta_a, \phi_a)$ and $\rho_1(\eta_b, \phi_b)$ are probabilities to observe a single particle at (η_a, ϕ_a) and (η_b, ϕ_b), respectively. The denominator of Eq. (20.51) is constructed as a product of two single-particle distributions using an event mixing technique, where each particle in the pair comes from a different event. Experimentally, each reconstructed track

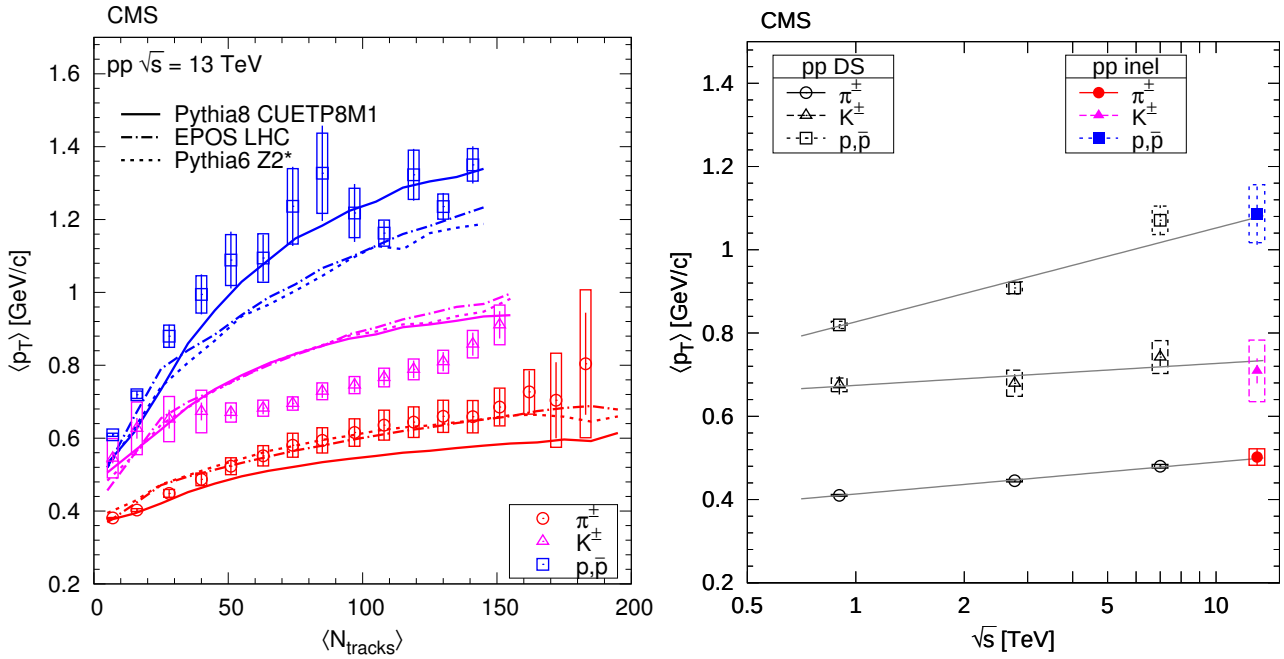

Figure 20.13: Average p_T of pions, kaons and protons in the range $|\eta| < 1.0$ as a function of (left) track multiplicity at $|\eta| < 2.4$ and (right) of center-of-mass energy where the curves show linear fits using ln$s$. The error bars indicate the uncorrelated combined uncertainties, while the boxes show the uncorrelated systematic uncertainties. Figures from Ref. [161].

is weighted by the inverse of an efficiency factor which accounts for the detector acceptance, the reconstruction and particle identification efficiencies, the contamination by secondary particles and the fraction of misreconstructed tracks.

An example of two-particle correlation functions measured in pp collisions at 7 TeV is shown in Fig. 20.14 for identical-particle pairs (right panel) and for particle–anti-particle pairs (left panel) [169].

We observe two distinct features which can be explained by short-range (in rapidity) correlations: 1) a near-side peak at $\Delta\phi \approx 0$ and 2) an away-side peak or rather a ridge at $\Delta\phi \approx \pi$. The near-side peak is considered to be caused by at least three effects:

- *fragmentation of partons scattered at a hard scale.* These relatively high p_T partons produce showers which after the hadronization form the mini-jets which create a broad structure extending over at least one unit in $\Delta\eta$ and $\Delta\phi$.
- *resonance decays.* The decay of resonances contributes to the near-side peak at $\Delta\eta \sim 0$ and extended in $\Delta\phi$ [170–172], depending on the released kinetic energy of the given resonance. This effect is mostly visible for unlike-sign particle pairs.
- *femtoscopic correlations.* The term "femtoscopic" refers to a length scale of the order of 10^{-15} m. These correlations are present at low relative momenta of the particles in a pair (representing a very small phase-space corner, so they are practically invisible in terms of $(\Delta\eta, \Delta\phi)$) and give rise to an enhancement of the correlation function (due to Bose-Einstein quantum statistics for identical bosons) or its suppression (due to Fermi-Dirac quantum statistics for identical fermions). Besides this, at low relative momenta there are correlations caused by Coulomb and/or other final state interactions. The shape of all these effects in $(\Delta\eta, \Delta\phi)$ space depend strongly on the mass of the particle type as well as on the size of the particle-emitting system. The latter is traditionally measured in Bose-Einstein correlation (BEC) analyses and is not part of this review.

The away-side peak originates from energy-momentum conservation which manifests itself by the quark and the anti-quark going back-to-back in ϕ. In this case the rapidity width of the away-side peak is much larger than the near-side peak since in the original matrix element the quark and the antiquark can be separated by some $\Delta\eta$ interval.

As discussed in Sections 20.3.3.2 and 20.3.3.3, there may be several cut Pomerons in the same event, each giving rise to particle sets which are, in general, independent of each other (except for small Bose-Einstein correlations). This leads to long-range (in rapidity) correlations. Since the density of secondaries, $\mathrm{d}N/\mathrm{d}y$, is proportional to the number of cut Pomerons, k, the probability to observe at least one particle is proportional to $\langle k \rangle$, while the probability to observe simultaneously two particles separated by some (rather large) rapidity interval is proportional to $\langle k^2 \rangle$. Thus the long-range correlations are pedicted to be $C_2 = \langle k^2 \rangle / \langle k \rangle^2 - 1 > 0$ which depends weakly on the separation $\Delta\eta$ between the two particles [173, 174]. In the case of the pure eikonal approach, neglecting the enhanced diagrams and the conservation law effects in the proton fragmentation region, we expect that these long-range correlations,

$$C_2(\Delta y) = \frac{\sigma_{\mathrm{inel}} \mathrm{d}^2\sigma/\mathrm{d}y_1\mathrm{d}y_2}{\mathrm{d}\sigma/\mathrm{d}y_1 \; \mathrm{d}\sigma/\mathrm{d}y_2} - 1 \sim \mathrm{const}, \qquad (20.52)$$

do not depend on the rapidity separation, $\Delta y = |y_1 - y_2|$, between the two particles. The contribution of the processes with more cut Pomerons also results in a much wider multiplicity distribution and in a larger density of soft particles coming from the 'underlying event'.

20.5.2.2 *Color reconnection*

In this context, we have to mention also the so-called 'colour reconnection' phenomenon. This is a pure 'soft QCD' effect. The point is that after a number of coloured secondary partons are produced, there are different possibilities to form the colour flow between these partons and to group the partons into colourless clusters. In the process of reconnection, one rearranges the colour flow in such a way as to minimize the size of the clusters. This is especially important when dealing with MPI contributions. The reconnection between the different cut Pomerons diminishes the final multiplicity and can change the form of the N_{ch} distributions (see e.g. Section 41.3.3 of [1] and [2, 13, 177, 178]).

20.5.2.3 *Double parton scattering*

The probability of MPI depends on the spatial distribution of partons in the incoming protons. The effects of MPI are suppressed if the density of partons is low and the partons from the incoming beam particles are separated from each other by a large

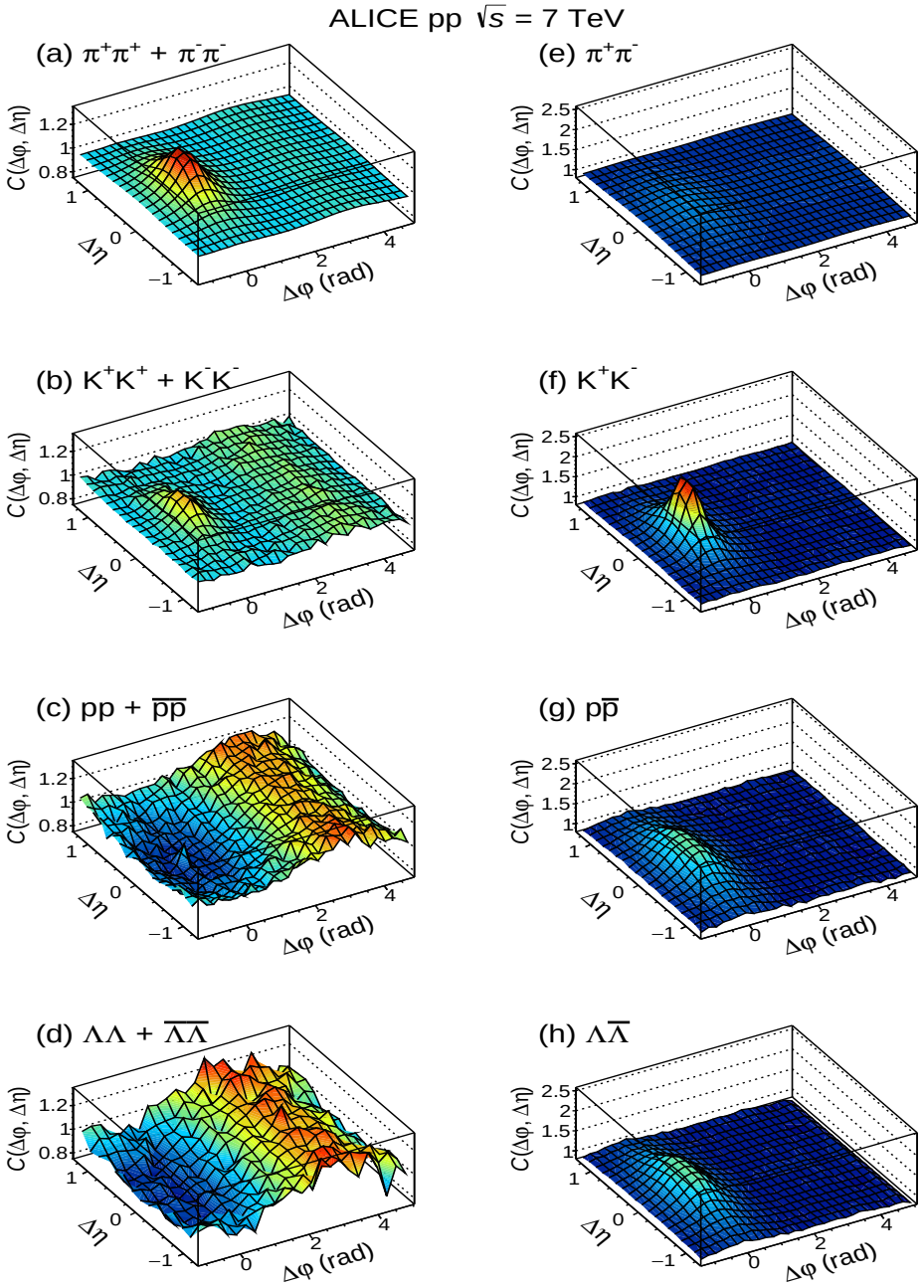

Figure 20.14: Two-particle correlation functions for identical-particle pairs: $\pi^+\pi^+ + \pi^-\pi^-$, $K^+K^+ + K^-K^-$, $pp + \bar{p}\bar{p}$, and $\Lambda\Lambda + \bar{\Lambda}\bar{\Lambda}$ (left panel) and particle–anti-particle pairs: $\pi^+\pi^-$, K^+K^-, $p\bar{p}$ and $\Lambda\bar{\Lambda}$ (right panel). Figure from Ref. [169].

interval in transverse coordinate space $\vec{x}_t$. Events in which two hard subprocesses, caused by interactions of two different parton pairs (say, (a_1b_1) and (a_2b_2)), take place simultaneously, are called Double Parton Scattering (DPS). The DPS cross section is driven by the 'double parton distributions', $D(y_{a_1}, y_{a_2}, ...)$, where y_{a_1} and y_{a_2} are momentum fractions carried by the partons from the proton a and the dots denote all other coordinates. As a rule, experiments study DPS processes at relatively small momentum fractions y_i. Here, correlations due to momentum conservation (like $y_{a_1} + y_{a_2} < 1$) are not so important, and with a reasonable accuracy we can assume a factorization

$$D(y_{a_1}, y_{a_2}, ...) \propto F(y_{a_1}) \cdot F(y_{a_2}) \ , \tag{20.53}$$

where $F(y_{a_i})$ are the single parton distributions. In such a case the DPS cross section takes the form

$$\sigma^{\rm DPS} \ = \ c \cdot \frac{\sigma_{a_1b_1}\sigma_{a_2b_2}}{\sigma_{\rm eff}} \ , \tag{20.54}$$

where $\sigma_{a_1b_1}$ and $\sigma_{a_2b_2}$ are cross sections for the two *independent* hard processes, while $\sigma_{\rm eff}$ characterizes the mean area occupied by the partons a_1 and b_1; the constant factor $c = 1/2$ if both hard processes (a_1b_1) and (a_2b_2) are identical, otherwise $c = 1$. Thus the DPS cross section is sensitive to the spatial separations between partons in the proton (see Section 7.2.3 in [2] and [179, 180] for more explanations and reviews).

One problem is that within this approach we *assume* that the partons a_1 and a_2 are produced by two independent parton showers (and similarly for the other incoming proton). On the other hand, there is a probability that from the beginning we start with the evolution of a single shower which further splits into two different branches. In this case the separation between the two partons (two shower branches) becomes very small – of the order of the inverse scale ($\sim 1/\sqrt{q^2}$) at which the splitting occurs. The exact value of this 'splitting' scale q^2 depends on the particular kinematics of the DPS process. So, different experiments (with

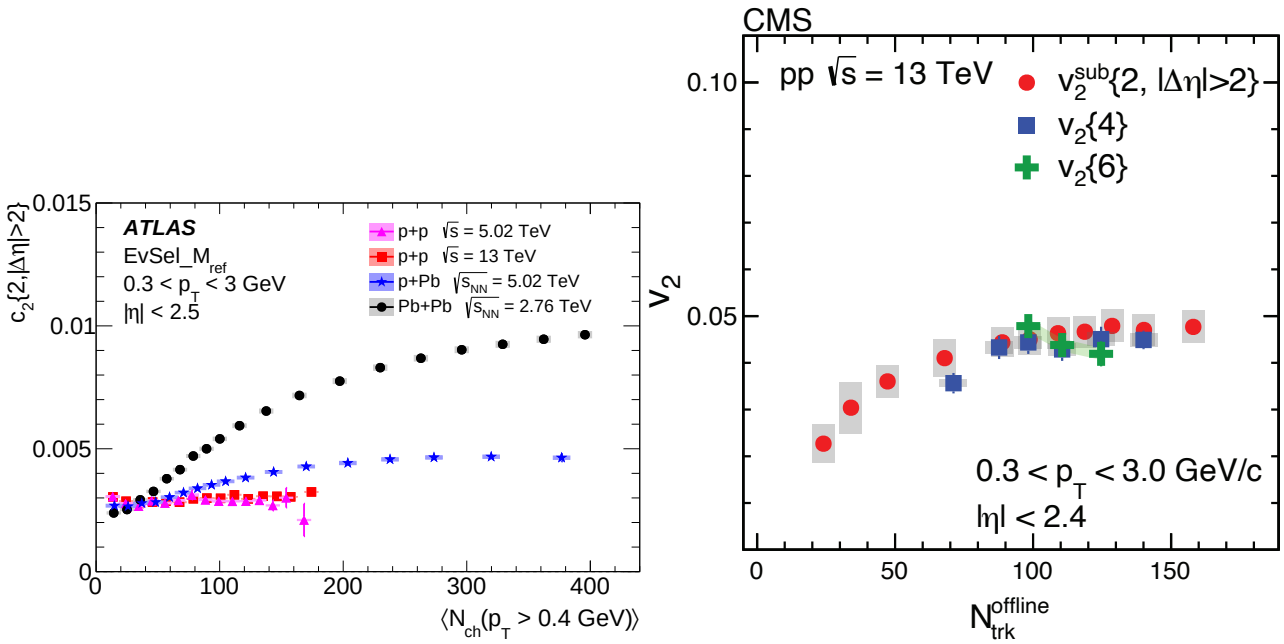

Figure 20.15: (Left) The two-particle cumulant, $c_2\{2, |\Delta\eta| > 2\}$, as a function of $\langle N_{\rm ch}(p_T > 0.4\ {\rm GeV})\rangle$ for pp collisions at $\sqrt{s} = 5.02$ and 13 TeV, pPb collisions at $\sqrt{s_{NN}} = 5.02$ TeV and low-multiplicity $PbPb$ collisions at $\sqrt{s_{NN}} = 2.76$ TeV. The data are constructed from particles with $0.3 < p_T < 3.0$ GeV. Figure from Ref. [175]. (Right) The $v_2\{2, |\Delta\eta| > 2\}$, $v_2\{4\}$ and $v_2\{6\}$ values as a function of number of charged particles, averaged over $0.3 < p_T < 3.0$ GeV and $|\eta| < 2.4$, in pp collisions at $\sqrt{s} = 13$ TeV. Figure from Ref. [176]. The error bars correspond to the statistical uncertainties, while the shaded areas denote the systematic uncertainties.

different kinematical conditions) can give somewhat different values of $\sigma_{\rm eff}$. In general, the value of $\sigma_{\rm eff}$ depends on the following features: a) on the measured process since the spatial (b_t) distributions of different incoming partons (light quarks, heavy quarks, gluons) can be different; b) on the splitting scale, $\sqrt{q^2}$, of one parton cascade into two branches. The typically high value of the splitting scale then explains the fact that the experimentally measured values of $\sigma_{\rm eff} \sim 7$–25 mb (see Fig. 4 of [181]) are smaller than $\sigma_{\rm tot}$ or mostly even lower than the proton area $\pi R_p^2 \sim 22$–24 mb (see e.g. [182]); c) on the p_T balance, k_T, in the individual hard process (e.g. for two dijet productions $k_T = |\overrightarrow{p_{T1}} + \overrightarrow{p_{T2}}|$ where p_{T1} and p_{T2} are jet p_T's of the first hard process (similarly for the second hard process). A small value of k_T indicates that there were no splittings or the splitting scale $\sqrt{q^2}$ was small and, therefore, we expect larger $\sigma_{\rm eff}$; d) on the contribution of single parton scatterings misidentified as DPS. For a lower scale of the hard process this contribution is larger (see [183] for more detailed discussion).

20.5.2.4 *Final state interactions*

The formalism of the RFT does not include 'final state interactions' [16]. Therefore, besides the correlations considered in the previous Section 20.5.2.1 we have to expect the correlation caused by partons and hadrons rescattering in the final state. These effects are not crucial at lower energies, but become more important at high LHC energies, in particular in heavy-ion collisions where the particle density is large. For example, the final state interactions (FSI) lead to the formation of the collective flow of secondaries (see e.g. [185] for a review), especially in high-multiplicity events. To study the collective flow experimentally, one has to subtract correlations coming from few-particle sources such as resonance decays, mini-jets, multi-jets and BEC (so called "non-flow"). The non-flow can efficiently be suppressed using the sub-event method, that is by studying the azimuthal correlations between particles separated in η [186], or subtracted using the multi-particle correlation (or cumulant) techniques.

The cumulant method is based on calculating $2k$-particle azimuthal correlations, ${\rm corr}_n\{2k\}$, and cumulants $c_n\{2k\}$ (where $k = 1, 2, ...$), for nth Fourier harmonics. The ${\rm corr}_n\{2k\}$ are defined as [187, 188]:

$\langle\langle {\rm corr}_n\{2\}\rangle\rangle = \langle\langle e^{in(\phi_1-\phi_2)}\rangle\rangle$, $\langle\langle {\rm corr}_n\{4\}\rangle\rangle = \langle\langle e^{in(\phi_1+\phi_2-\phi_3-\phi_4)}\rangle\rangle$,
$\langle\langle {\rm corr}_n\{6\}\rangle\rangle = \langle\langle e^{in(\phi_1+\phi_2+\phi_3-\phi_4-\phi_5-\phi_6}\rangle\rangle$

and similarly for higher numbers of correlated particles. The double-brackets $\langle\langle\rangle\rangle$ denote averaging first over particles in an event and then over events within a given event class. For every event, the average is taken over all possible combinations of azimuthal angles ϕ_l ($l = 1, ..., 2k$) of the $2k$ particles. The cumulants are then obtained from multi-particle azimuthal correlations after subtracting correlations between $2(k-1)$ particles according to the following formulae [187, 188]:

$c_n\{2\} = \langle\langle {\rm corr}_n\{2\}\rangle\rangle$, $c_n\{4\} = \langle\langle {\rm corr}_n\{4\}\rangle\rangle - 2\langle\langle {\rm corr}_n\{2\}\rangle\rangle^2$, $c_n\{6\} = \langle\langle {\rm corr}_n\{6\}\rangle\rangle - 9\langle\langle {\rm corr}_n\{2\}\rangle\rangle \times \langle\langle {\rm corr}_n\{4\}\rangle\rangle + 12\langle\langle {\rm corr}_n\{2\}\rangle\rangle^3$.

The cumulants for higher particle multiplicities are calculated in [187, 188]. The cumulants then serve to estimate the Fourier harmonics v_n as follows [187]:

$v_n\{2\} = \sqrt{c_n\{2\}}$, $v_n\{4\} = \sqrt[4]{-c_n\{4\}}$, $v_n\{6\} = \sqrt[6]{c_n\{6\}/4}$.

Some of the long-range correlation ($|\Delta\eta| > 2$) results obtained on a sample of charged particles with $0.3 < p_T < 3.0$ GeV and $|\eta| < 2.4$ are summarized in Fig. 20.15. The left plot shows the cumulant c_2 measured for pp, pPb and $PbPb$ collisions [175], while the right plot shows the elliptical harmonics v_2 measured for pp collisions [176], both as functions of multiplicities of charged particles. The two-particle correlations are observed to be strongest and rising with $N_{\rm ch}$ for $PbPb$ collisions, and weakest and rather flat for pp collisions. The elliptical-flow harmonics for 4- and 6-particle correlations show again a rather flat multiplicity dependence (at least for large multiplicities). Within experimental uncertainties, the values of $v_2\{2\}, v_2\{4\}$ and $v_2\{6\}$ measured in pp collisions at 13 TeV are consistent with each other. The similarity between $v_2\{4\}$ and $v_2\{6\}$ suggests that some collective effects are occurring in pp collisions at high multiplicity and the obser-

[16] In general, final state interactions can be included into the detailed structure of the multi-Pomeron vertices. However these vertices are phenomenological objects which are not well known experimentally.

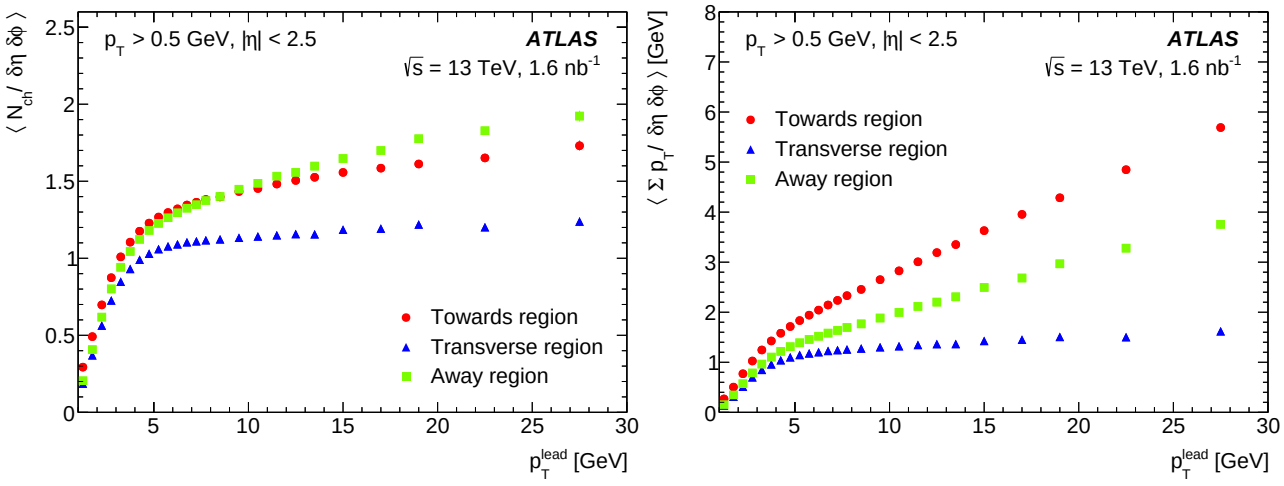

Figure 20.16: Mean charged particle density (left) and the sum of transverse momenta of secondaries (right) in events with the 'leading' high p_T particle as a function of $p_T^{\rm lead}$ in the transverse, towards and away azimuthal regions. Secondaries with $p_T > 0.5$ GeV and $|\eta| < 2.5$ are registered. The error bars (mostly hidden by the data markers) represent combined statistical and systematic uncertainties. Figures from [184].

vations are similar to those in $PbPb$ collisions, where the $v_2\{4\}$ values were measured to be close to $v_2\{6\}$ but they are both lower than $v_2\{2\}$ (not shown here)).

Another example of long-range correlations is the so-called "ridge effect". Here not only the 'back-to-back' jet correlations are registered, but also an excess of particles going in the same (in the azimuthal plane) direction as the leading (relatively high p_T) hadron. Moreover, this excess is seen at the rapidities separated from the leading hadron by a rather large interval (see e.g. [189] for a review).

It is popular to describe such FSI effects within the hydrodynamic model [190], which operates with collective (thermodynamic) variables. In terms of microscopic interactions, the collective flow can be caused by the geometry of a particular collision (the absorption is smaller for the secondaries flying in the direction orthogonal to the impact parameter vector $\vec{b}$ [191, 192]), or by the colour reconnection at the hadronization stage [193], or accounting for the rescattering of secondaries directly, as was done, for example, in the AMPT model [194].

20.5.3 *The underlying event*

Except for the exclusive case, any 'hard' subprocess is accompanied by soft secondaries coming from initial state radiation (ISR), final state radiation (FSR) and multiple parton interaction (MPI), see Subsection 7.2.2 in [2]. These extra particles distort the signal we are looking for. In particular, they affect the isolation criteria applied to photons and charged leptons and the vertex reconstruction efficiency. In general, also the effects of colour reconnection (discussed in Section 20.5.2.2) contribute to the underlying event.

The usual procedure of estimating the amount of underlying event (UE) is to spatially divide tracks in each event according to their azimuthal angle into the Toward region (where the highest p_T jet points), the Away region (opposite to the Toward region) and to two Transverse regions. The standard observables are the average track multiplicity per unit area and the average scalar sum of track p_T per unit area. Figure 20.16 shows the particle density and the sum of p_T for the UE in ATLAS events containing at least one charged particle with $p_T > 0.5$ GeV and $|\eta| < 2.5$ [184].

Note that by construction the largest values of $\langle p_T \rangle$ are observed in the 'Toward' region, while in the 'Away' region we observe a slightly larger density than in the Toward region. These are results of the 'leading' and 'backward' jet fragmentation. In the transverse region, mostly filled by particles from the UE, the particle density and sum of p_T per unit $(\Delta\eta, \Delta\phi)$ area practically do not depend on the $p_T^{\rm lead}$ since these secondaries come from the other cut Pomeron(s), that is, from other 'multiple interactions'. For low $p_T^{\rm lead} < 2$ GeV the distributions in all three regions are close to each other. These events actually do not contain a 'hard' subprocess. Moreover, for a very small $p_T^{\rm lead} \to 1$ GeV we start to select soft events with abnormally low $p_T < p_T^{\rm lead}$ particles. Since only particles with $p_T > 0.5$ GeV are registered, the signal drops fast for $p_T^{\rm lead} \to 1$ GeV. As a function of collision energy $\sqrt{s}$, the energy flow in the transverse region increases as $\sum p_T \sim s^{0.2}$ (as follows from Fig. 7 (right) in [184]) due to the larger number of MPI collisions and larger $\langle p_T \rangle$ in each collision [17]. As follows from this and other UE-dedicated LHC studies [195], from the comparisons of the data to the models with and without MPI, the necessity of MPI is convincingly demonstrated.

20.6 The Odderon

Apart from the even-signature singularity (Pomeron), in QCD with $N_c = 3$ there exists its counterpart, the odd-signature singularity placed at $j \simeq 1$ and formed by three t-channel reggeized gluons connected in colour space by the symmetric d^{abc} tensor of the colour $SU(3)$ group [196, 197]. This object is called the Odderon. The Odderon exchange amplitude has opposite sign for pp and $p\bar{p}$ scatterings. Its intercept is predicted to be very close to $j = 1$ [198–200], while according to perturbative estimates the coupling to the nucleon is rather small [201,202]. The corresponding amplitude is mainly real and is about 100 times smaller than the imaginary part of the Pomeron exchange amplitude. Calculating the elastic amplitude via the eikonal formula (20.13) we have to replace the opacity $\Omega(b)$ by the sum $\Omega = \Omega_{\rm even} + \Omega_{\rm odd}$, where $\Omega_{\rm even}$ is mainly real and $\Omega_{\rm odd}$ is imaginary. Note that at $t = 0$ this QCD Odderon does not couple to mesons, and the t-slope of the Odderon amplitude is expected to be smaller than that for the Pomeron; instead of the singularity at $t = 4m_\pi^2$ in the Pomeron case, the nearest singularity in the Odderon channel is at $t = 9m_\pi^2$, see for instance [200]. Thus, in the impact parameter b space the QCD Odderon occupies an area of a smaller radius, see e.g. [203].

Experimentally an indication in favour of a manifestation of the high energy C-odd amplitude was observed by comparing the elastic pp and $p\bar{p}$ cross sections in the dip region (where the contribution from the C-even amplitude has a minimum) at the CERN-ISR [205], see Fig. 20.17 (left) [18].

To get a better understanding of the Odderon effects it would be very instructive to have the $d\sigma_{el}/dt$ data for both pp and $p\bar{p}$ reactions at the same but higher energy ~ 1 TeV (ideally in the same apparatus) and, in the ideal case, to study the energy de-

[17] Recall the stronger absorption of the low k_t partons.

[18] Note that a qualitatively similar behaviour to the $p\bar{p}$ ISR data, namely a filling in of the dip in the t-distribution, was observed by the UA4 collaboration at the CERN S$p\bar{p}$S collider at $\sqrt{s}$=546 and 630 GeV(see [208,209] and in particular Fig. 2 in [209]) and by the $D0$ collaboration at the Tevatron at 1.96 TeV [207].

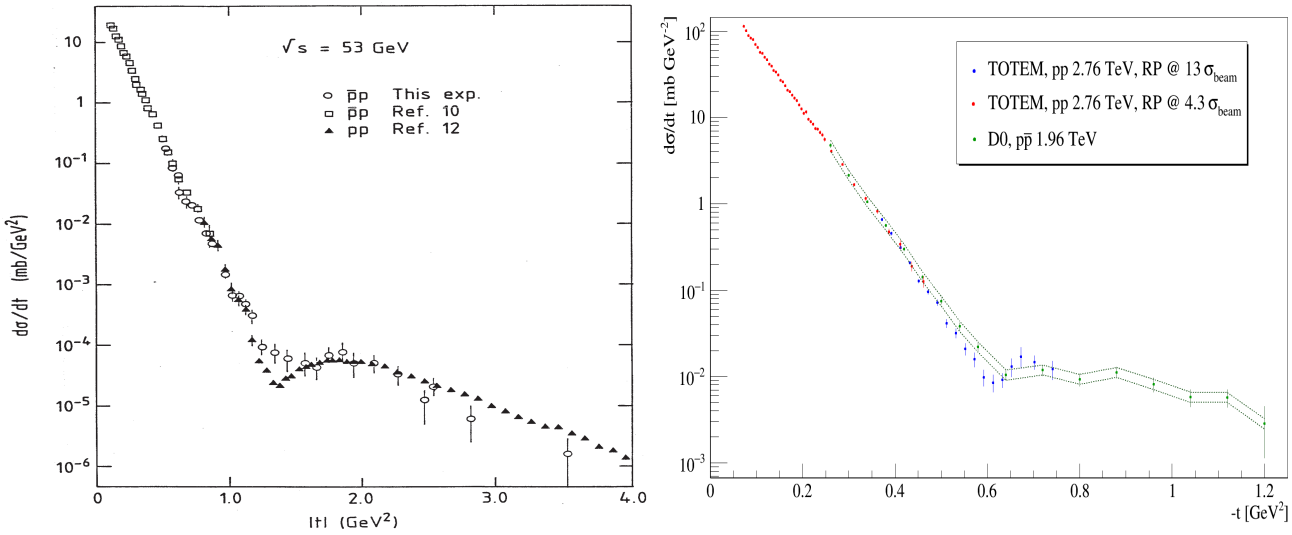

Figure 20.17: Comparison of the t-dependence of the elastic cross sections from pp and $p\bar{p}$ collisions. (Left) Data from the ISR energy of 53 GeV are shown by closed triangles [204] for pp collisions and by open circles [205] and open squares [206] for $p\bar{p}$ collisions. Only t-dependent uncertainties are shown and the systematic scale uncertainty is estimated to be ±30%. Figure from Ref. [205]. (Right) Data from the D0 experiment at 1.96 TeV [207] are compared with data from the TOTEM experiment [103]. The green dashed line indicates the normalization uncertainty of the D0 measurement. Figure from Ref. [103].

pendence.

At the moment we can only compare the pp cross section measured by TOTEM at $\sqrt{s} = 2.76$ TeV [103] with the $\mathrm{d}\sigma/\mathrm{d}t$ values measured by the D0 collaboration at 1.96 TeV in $p\bar{p}$ collisions [207], see Fig. 20.17 (right).

The situation looks quite intriguing, but needs further investigation. Note that in the TeV energy range the ω, ρ and ωP, ρP exchange contributions, which may be responsible for the difference between the pp and $p\bar{p}$ cross sections in the dip region at the ISR energies, are practically negligible.

Another way to search for the Odderon is to measure the real part of the elastic pp scattering amplitude via the interference with the pure QED one-photon exchange. Since the one-photon exchange amplitude contribution is sizeable only at very small $|t|$, this way we can study the Odderon at or near to $t = 0$. Indeed, the value of the ratio $\rho \equiv \mathrm{Re}T_{\mathrm{el}}/\mathrm{Im}T_{\mathrm{el}}$, obtained by TOTEM at 13 TeV ($\rho = 0.10 \pm 0.01$ [102]), turns out to be smaller than that expected for the pure even-signature amplitude, see Fig. 20.18.

Based on dispersion relations and assuming the C-even contribution only, from the known total cross sections we would rather expect $\rho \simeq 0.13$–0.14. The difference could indicate that the rise of the total cross section at energies above those of the LHC slows down (see the dispersion relation, Eq. (20.19)) or this could be attributed to an Odderon contribution (see e.g. [210]). However, the Odderon exchange amplitude extracted in this analysis has opposite sign to that for the lowest-α_s-order QCD Odderon, see e.g. [201, 202, 211, 212]. Besides this, the Odderon contribution to ρ, obtained in [210], grows with $\sqrt{s}$ (for $\sqrt{s} > 0.5$ TeV), while in QCD we expect that the Odderon contribution to ρ decreases with energy, since the QCD Odderon intercept is smaller than that of the QCD Pomeron.

It is worth mentioning also that the Odderon contribution is strongly screened by the multi-Pomeron diagrams, which facilitate the falling-off of ρ with energy increasing, see [213, 214]. On the other hand, analyzing the whole ensemble of high energy elastic pp ($p\bar{p}$) low $|t|$ data, a reasonable description can be obtained using the even-signature amplitude only, that is, without the Odderon. In particular, the RR(PL2)qc model/version of the COMPETE parameterization is consistent with the TOTEM 13 TeV data on σ_{tot} and ρ within 1σ [19]. Another example is the recent analysis in [212] of the low $|t| < 0.1$ GeV^2 elastic data. Fitting all the low-t pp and $p\bar{p}$ data in the range of $\sqrt{s}$ between 13 GeV and 13 TeV without Odderon, Donnachie and Landshoff [212] succeeded to describe the TOTEM cross section with less than 1σ deviation in each $\mathrm{d}\sigma_{\mathrm{el}}/\mathrm{d}t$ point (see Fig. 8 of [212]). Note that in this analysis, they get a larger value of ρ close to 0.14 at 13 TeV.

It was proposed also to search for the Odderon in exclusive C-even meson (π^0, η, f_2, η_c, ...) photoproduction (see e.g. [215,216]). However the expected cross sections are small (e.g. for η_c) and in each channel there is a large background caused either by Pomeron-Pomeron fusion (such as CEP of the f_2 meson production in pp or pPb collisions) or due to the vector meson radiative decay (such as $\omega \to \pi^0\gamma$ for the case of pion) [217]. Up to now, no definitive Odderon signal in the C-even meson production has been observed. At the moment there exist only upper limits on the photoproduction cross sections obtained in the measurements at HERA at $\sqrt{s} \simeq 200$ GeV [218–220].

To conclude, let us emphasize that the existence of the C-odd singularity with intercept
$\alpha_{\mathrm{odd}}(0) \simeq 1$ is a firm prediction of QCD. At least in the high k_t region there is a well established C-odd three-gluon contribution to the scattering amplitude. However the expected coupling of such an Odderon singularity is numerically very small. Therefore it is quite challenging to observe its manifestation experimentally. Currently it seems to be a bit premature to draw any definite conclusion about an experimental observation of the Odderon signal.

20.7 Asymptotics

The high-energy behaviour of total hadronic cross sections has been one of the oldest problems of strong interactions over many decades, beginning from Heisenberg [221]. The most important bound obtained based on general analytical properties of scattering amplitudes is the FLM bound [47–49]. It states that the growth of the total hadronic cross section with energy does not exceed $\ln^2 s$, see Eq. (20.34).

Recall that we neglected the photon contribution as well as the whole electro-weak sector, and that the parameter in Eq. (20.34) s_0 is an *a priori* unknown scale. However, if we were to assume a reasonable hadronic scale, $s_0 \simeq 1\,\mathrm{GeV}^2$, we would find that Eq. (20.34) implies an unrealistically high upper bound in comparison with the cross sections observed at present collider energies. Nevertheless there is a common trend in the literature (see for instance, reviews [222, 223] and references therein) to fit phenomenologically the total cross section with $\ln^2 s$, keeping in mind the saturation of the FLM bound. Such an asymptotic behaviour is assumed also by the COMPETE collaboration [22], which achieved a comprehensive description of all soft pre-LHC data measured at $\sqrt{s} \geq 4$ GeV as well as total pp cross sections

[19] We thank Jean-Rene Cudell for clarifying this issue.

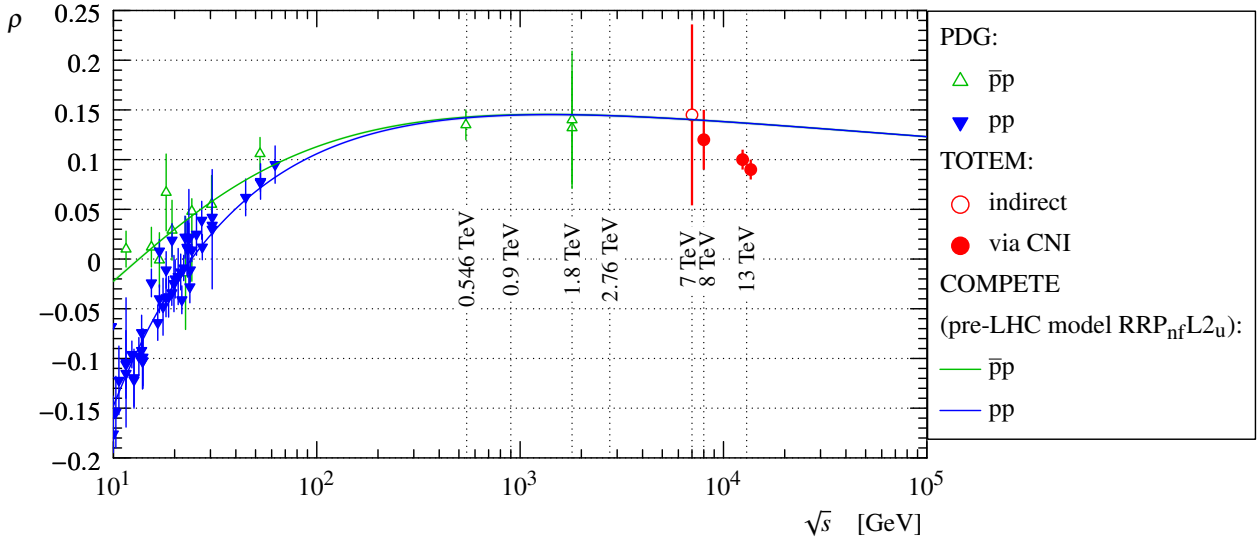

Figure 20.18: The dependence of the ρ parameter on the collision energy. The pp (blue) and $p\bar{p}$ (green) data are taken from [1]. The TOTEM measurements are marked in red. The two points at 13 TeV correspond to two fit cases, discussed in [102], using the same data. The lines represent fits to the data using the COMPETE parameterization [22]. Figure from Ref. [102].

from the LHC available in the first half of 2015 (see Section 51 in [24]).

It is interesting that the Froissart-type $\ln^2 s$ asymptotics of the pp total cross section are also supported by numerical results in lattice QCD [224]. Such a behaviour is also observed in the approach [225] based on Colour Glass Condensate saturation.

Finally, it is worth mentioning that the possibility that *asymptotically* the Pomeron intercept becomes smaller than 1, $\alpha_{\mathbb{P}}(0) < 1$, and at very high energies the total cross section starts to decrease with energy, though highly unlikely, is not yet completely rejected. For instance, such a behaviour is expected in a theory with only the triple-Pomeron coupling, $g_{3\mathbb{P}}$, and which neglects the more complicated multi-Pomeron vertices g_m^n, such as the $2 \to 2$ Pomeron coupling [226, 227].

It was also argued that in the case of an increasing (with energy) cross section the only regime consistent asymptotically with both the s- and the t-channel unitarities is that of a *black* disc whose radius increases as $R = c \cdot \ln s$ [228] (i.e. $R \propto (\ln s)^\gamma$, with $\gamma = 1$ exactly).

20.8 Acknowledgements

It is a pleasure to thank Michael Albrow, Robert Cahn, Robert Ciesielski, Per Grafstrom, Frank Krauss, Paul Newman, Sergey Ostapchenko and Edward Sarkisyan-Grinbaum for discussions, suggestions and comments on this review. Special thanks to Graeme Watt who read the article through and helped to improve the presentation. MT is supported by MEYS of the Czech Republic within project LTT17018. VAK thanks the Institute of Physics of the Czech Academy of Sciences in Prague for hospitality.

References

[1] M. Tanabashi *et al.* (Particle Data Group), Phys. Rev. **D98**, 3, 030001 (2018).

[2] J. Campbell, J. Huston and F. Krauss, *The Black Book of Quantum Chromodynamics*, Oxford University Press (2017), ISBN 9780199652747, URL `https://global.oup.com/academic/product/the-black-book-of-quantum-chromodynamics-9780199652747`.

[3] R. J. Eden *et al.*, *The analytic S-matrix*, Cambridge Univ. Press, Cambridge (1966).

[4] A. Martin, Lect. Notes Phys. **3**, 1 (1969).

[5] P. D. B. Collins, *An Introduction to Regge Theory and High-Energy Physics*, Cambridge Monographs on Mathematical Physics, Cambridge Univ. Press, Cambridge, UK (2009), ISBN 9780521110358, URL `http://www-spires.fnal.gov/spires/find/books/www?cl=QC793.3.R4C695`.

[6] S. Donnachie *et al.*, Camb. Monogr. Part. Phys. Nucl. Phys. Cosmol. **19**, 1 (2002).

[7] V. N. Gribov, *The theory of complex angular momenta: Gribov lectures on theoretical physics*, Cambridge Monographs on Mathematical Physics, Cambridge University Press (2007), ISBN 9780521037037, 9780521818346, 9780511055041, URL `http://www.cambridge.org/uk/catalogue/catalogue.asp?isbn=0521307848`.

[8] S. Ostapchenko, in "25th European Cosmic Ray Symposium (ECRS 2016) Turin, Italy, September 04-09, 2016," (2016), [arXiv:1612.09461].

[9] T. Sjostrand, Int. J. Mod. Phys. **A3**, 751 (1988).

[10] B. Andersson, Camb. Monogr. Part. Phys. Nucl. Phys. Cosmol. **7**, 1 (1997).

[11] W. Kittel and E. A. De Wolf, *Soft multihadron dynamics* (2005), ISBN 9789812562951.

[12] I. M. Dremin and A. B. Kaidalov, Phys. Usp. **49**, 263 (2006), [Usp. Fiz. Nauk176,275(2006)].

[13] A. Buckley *et al.*, Phys. Rept. **504**, 145 (2011), [arXiv:1101.2599].

[14] R. Ciesielski and K. Goulianos, PoS **ICHEP2012**, 301 (2013), [arXiv:1205.1446].

[15] K. Akiba *et al.* (LHC Forward Physics Working Group), J. Phys. **G43**, 110201 (2016), [arXiv:1611.05079].

[16] G. D. Alkhazov, S. L. Belostotsky and A. A. Vorobev, Phys. Rept. **42**, 89 (1978).

[17] E. L. Feinberg and I. Y. Pomeranchuk, Doklady Akad. Nauk SSSR **93**, 439 (1953); E. L. Feinberg and I. Y. Pomeranchuk, Suppl. Nuovo Cimento **III**, serie X, 652 (1956).

[18] R. Engel, D. Heck and T. Pierog, Ann. Rev. Nucl. Part. Sci. **61**, 467 (2011).

[19] M. Gell-Mann, in "High-energy physics. Proceedings, 11th International Conference, ICHEP'62, Geneva, Switzerland, Jul 4-11, 1962," 533–542 (1962).

[20] S. Frautschi, M. Gell-Mann and F. Zachariasen, Phys. Rev. **126**, 6, 2204 (1962).

[21] K. G. Boreskov, A. B. Kaidalov and O. V. Kancheli, Phys. Atom. Nucl. **69**, 1765 (2006), [Yad. Fiz.69,1802(2006)].

[22] J. R. Cudell *et al.* (COMPETE), Phys. Rev. Lett. **89**, 201801 (2002), [hep-ph/0206172].

[23] C. Bourrely, J. Soffer and T. T. Wu, Eur. Phys. J. **C28**, 97 (2003), [hep-ph/0210264].

[24] C. Patrignani *et al.* (Particle Data Group), Chin. Phys. **C40**, 10, 100001 (2016).

[25] A. Donnachie and P. V. Landshoff, Nucl. Phys. **B231**, 189 (1984).

[26] A. Donnachie and P. V. Landshoff, Phys. Lett. **B296**, 227 (1992), [hep-ph/9209205].

[27] S. Mandelstam, Nuovo Cim. **30**, 1148 (1963).

[28] V. N. Gribov, I. Ya. Pomeranchuk and K. A. Ter-Martirosian, Phys. Lett. **9**, 269 (1964).

[29] V. A. Khoze, A. D. Martin and M. G. Ryskin, Int. J. Mod. Phys. **A30**, 08, 1542004 (2015), [arXiv:1402.2778].

[30] E. Gotsman, E. Levin and U. Maor, Int. J. Mod. Phys. **A30**, 08, 1542005 (2015), [arXiv:1403.4531].

[31] S. Ostapchenko, Phys. Rev. **D81**, 114028 (2010), [arXiv:1003.0196].

[32] V. N. Gribov, Sov. Phys. JETP **26**, 414 (1968), [Zh. Eksp. Teor. Fiz.53,654(1967)].

[33] U. Amaldi, M. Jacob and G. Matthiae, Ann. Rev. Nucl. Part. Sci. **26**, 385 (1976).

[34] A. B. Kaidalov, Phys. Rept. **50**, 157 (1979).

[35] V. Barone and E. Predazzi, *High-Energy Particle Diffraction*, volume v.565 of *Texts and Monographs in Physics*, Springer-Verlag, Berlin Heidelberg (2002), ISBN 3540421076, URL `http://www-spires.fnal.gov/spires/find/books/www?cl=QC794.6.C6B37::2002`.

[36] A. B. Kaidalov *et al.*, Acta Phys. Polon. **B34**, 3163 (2003), [hep-ph/0303111].

[37] L. Frankfurt and M. Strikman, in E. M. Henley and S. D. Ellis, editors, "100 Years of Subatomic Physics," 363–423 (2013), [arXiv:1304.4308].

[38] V. A. Khoze *et al.*, Eur. Phys. J. **C69**, 85 (2010), [arXiv:1005.4839].

[39] D. A. Fagundes *et al.*, Phys. Rev. **D88**, 9, 094019 (2013), [arXiv:1306.0452].

[40] R. Fiore *et al.*, Int. J. Mod. Phys. **A24**, 2551 (2009), [arXiv:0810.2902].

[41] I. M. Dremin, Phys. Usp. **56**, 3 (2013), [Usp. Fiz. Nauk 183, 3 (2013)], [arXiv:1206.5474].

[42] L. Frankfurt *et al.*, Phys. Rev. Lett. **101**, 202003 (2008), [arXiv:0808.0182].

[43] G. Bertsch *et al.*, Phys. Rev. Lett. **47**, 297 (1981).

[44] B. Z. Kopeliovich, L. I. Lapidus and A. B. Zamolodchikov, JETP Lett. **33**, 595 (1981), [Pisma Zh. Eksp. Teor. Fiz. 33, 612 (1981)].

[45] M. L. Good and W. D. Walker, Phys. Rev. **120**, 1855 (1960).

[46] J. Pumplin, Phys. Rev. **D8**, 2899 (1973).

[47] M. Froissart, Phys. Rev. **123**, 1053 (1961).

[48] A. Martin, Nuovo Cim. **A42**, 930 (1965).

[49] L. Lukaszuk and A. Martin, Nuovo Cim. **A52**, 122 (1967).

[50] A. A. Anselm and V. N. Gribov, Phys. Lett. **40B**, 487 (1972).

[51] G. Cohen-Tannoudji, V. V. Ilyin and L. L. Jenkovszky, Lett. Nuovo Cim. **5S2**, 957 (1972), [Lett. Nuovo Cim.5,957(1972)].

[52] V. A. Khoze, A. D. Martin and M. G. Ryskin, Eur. Phys. J. **C18**, 167 (2000), [hep-ph/0007359].

[53] G. Antchev *et al.* (TOTEM), Nucl. Phys. **B899**, 527 (2015), [arXiv:1503.08111].

[54] G. Antchev *et al.* (TOTEM), Eur. Phys. J. **C79**, 10, 861 (2019), [arXiv:1812.08283].

[55] L. Caneschi and A. Pignotti, Phys. Rev. Lett. **22**, 1219 (1969).

[56] O. V. Kancheli, JETP Lett. **11**, 267 (1970), [Pisma Zh. Eksp. Teor. Fiz. 11, 397 (1970)].

[57] A. H. Mueller, Phys. Rev. **D4**, 150 (1971).

[58] D. Amati, A. Stanghellini and S. Fubini, Nuovo Cim. **26**, 896 (1962).

[59] V. S. Fadin, E. A. Kuraev and L. N. Lipatov, Phys. Lett. **60B**, 50 (1975); E. A. Kuraev, L. N. Lipatov and V. S. Fadin, Sov. Phys. JETP **44**, 443 (1976), [Zh. Eksp. Teor. Fiz.71,840(1976)]; E. A. Kuraev, L. N. Lipatov and V. S. Fadin, Sov. Phys. JETP **45**, 199 (1977), [Zh. Eksp. Teor. Fiz.72,377(1977)]; I. I. Balitsky and L. N. Lipatov, Sov. J. Nucl. Phys. **28**, 822 (1978), [Yad. Fiz.28,1597(1978)].

[60] B. L. Ioffe, V. S. Fadin and L. N. Lipatov, *Quantum chromodynamics: Perturbative and nonperturbative aspects*, volume 30, Cambridge Univ. Press (2010), ISBN 9781107424753, 9780521631488, 9780511717444, URL `http://www.cambridge.org/de/knowledge/isbn/item2710695`.

[61] S. Ostapchenko, Phys. Rev. **D83**, 014018 (2011), [arXiv:1010.1869].

[62] J. L. Cardy, Nucl. Phys. **B75**, 413 (1974).

[63] A. B. Kaidalov *et al.*, Phys. Lett. **45B**, 493 (1973).

[64] E. G. S. Luna *et al.*, Eur. Phys. J. **C59**, 1 (2009), [arXiv:0807.4115].

[65] T. Sjöstrand, Adv. Ser. Direct. High Energy Phys. **29**, 191 (2018), [arXiv:1706.02166].

[66] K. Werner, F.-M. Liu and T. Pierog, Phys. Rev. **C74**, 044902 (2006), [hep-ph/0506232].

[67] V. A. Abramovsky, V. N. Gribov and O. V. Kancheli, Yad. Fiz. **18**, 595 (1973), [Sov. J. Nucl. Phys. 18, 308 (1974)].

[68] G. Alberi and G. Goggi, Phys. Rept. **74**, 1 (1981).

[69] K. A. Goulianos, Phys. Rept. **101**, 169 (1983).

[70] D. Bernard *et al.* (UA4), Phys. Lett. **B186**, 227 (1987).

[71] R. E. Ansorge *et al.* (UA5), Z. Phys. **C33**, 175 (1986).

[72] N. A. Amos *et al.* (E710), Phys. Lett. **B301**, 313 (1993).

[73] F. Abe *et al.* (CDF), Phys. Rev. **D50**, 5535 (1994).

[74] G. Aad *et al.* (ATLAS), Eur. Phys. J. **C72**, 1926 (2012), [arXiv:1201.2808].

[75] V. Khachatryan *et al.* (CMS), Phys. Rev. **D92**, 1, 012003 (2015), [arXiv:1503.08689].

[76] B. Abelev *et al.* (ALICE), Eur. Phys. J. **C73**, 6, 2456 (2013), [arXiv:1208.4968].

[77] G. Aad *et al.* (ATLAS), Phys. Lett. **B754**, 214 (2016), [arXiv:1511.00502].

[78] G. Aad *et al.* (ATLAS), JHEP **02**, 042 (2020), [arXiv:1911.00453].

[79] A. M. Sirunyan *et al.* (CMS and TOTEM) (2020), [arXiv:2002.12146].

[80] V. A. Khoze, A. D. Martin and M. G. Ryskin, Eur. Phys. J. **C73**, 2503 (2013), [arXiv:1306.2149].

[81] V. A. Khoze, A. D. Martin and M. G. Ryskin, Eur. Phys. J. **C23**, 311 (2002), [hep-ph/0111078].

[82] M. G. Albrow, T. D. Coughlin and J. R. Forshaw, Prog. Part. Nucl. Phys. **65**, 149 (2010), [arXiv:1006.1289].

[83] M. Albrow, Int. J. Mod. Phys. **A29**, 1402006 (2014).

[84] H. G. Fischer, W. Geist and M. Makariev, Int. J. Mod. Phys. **A29**, 28, 1446005 (2014).

[85] A. Kirk, Int. J. Mod. Phys. **A29**, 28, 1446001 (2014), [arXiv:1408.1196].

[86] M. A. Reyes *et al.* (E690), Phys. Rev. Lett. **81**, 4079 (1998).

[87] G. Gutierrez and M. A. Reyes, Int. J. Mod. Phys. **A29**, 28, 1446008 (2014), [arXiv:1409.8243].

[88] Y. L. Dokshitzer, D. Diakonov and S. I. Troian, Phys. Rept. **58**, 269 (1980).

[89] M. Derrick *et al.* (ZEUS), Phys. Lett. **B315**, 481 (1993).

[90] T. Ahmed *et al.* (H1), Nucl. Phys. **B429**, 477 (1994).

[91] P. Newman and M. Wing, Rev. Mod. Phys. **86**, 3, 1037 (2014), [arXiv:1308.3368].

[92] A. Aktas *et al.* (H1), Eur. Phys. J. **C48**, 715 (2006), [hep-ex/0606004].

[93] S. Chekanov *et al.* (ZEUS), Nucl. Phys. **B816**, 1 (2009), [arXiv:0812.2003].

[94] F. D. Aaron *et al.* (H1), Eur. Phys. J. **C72**, 2074 (2012), [arXiv:1203.4495].

[95] F. D. Aaron *et al.* (H1, ZEUS), Eur. Phys. J. **C72**, 2175 (2012), [arXiv:1207.4864].

[96] A. Aktas *et al.* (H1), JHEP **10**, 042 (2007), [arXiv:0708.3217].

[97] A. Aktas *et al.* (H1), Eur. Phys. J. **C50**, 1 (2007), [hep-ex/0610076].

[98] S. Chekanov *et al.* (ZEUS), Nucl. Phys. **B672**, 3 (2003), [hep-ex/0307068].

[99] E. G. de Oliveira, A. D. Martin and M. G. Ryskin, Phys. Lett. **B695**, 162 (2011), [arXiv:1010.1366].

[100] G. Antchev *et al.* (TOTEM), Eur. Phys. J. **C79**, 2, 103 (2019), [arXiv:1712.06153].

[101] C. Augier *et al.* (UA4/2), Phys. Lett. **B316**, 448 (1993).

[102] G. Antchev *et al.* (TOTEM), Eur. Phys. J. **C79**, 9, 785 (2019), [arXiv:1812.04732].

[103] G. Antchev *et al.* (TOTEM), Eur. Phys. J. **C80**, 2, 91 (2020), [arXiv:1812.08610].

[104] G. Antchev *et al.* (TOTEM), EPL **101**, 2, 21002 (2013).

[105] G. Antchev *et al.* (TOTEM), Phys. Rev. Lett. **111**, 1, 012001 (2013).

[106] G. Aad *et al.* (ATLAS), Nucl. Phys. **B889**, 486 (2014), [arXiv:1408.5778].

[107] M. Aaboud *et al.* (ATLAS), Phys. Lett. **B761**, 158 (2016), [arXiv:1607.06605].

[108] M. M. Block and R. N. Cahn, Rev. Mod. Phys. **57**, 563 (1985).

[109] F. Abe *et al.* (CDF), Phys. Rev. **D50**, 5550 (1994).

[110] C. Avila *et al.* (E811), Phys. Lett. **B445**, 419 (1999).

[111] W. Guryn, "Invited talk at the Workshop on Diffraction and Low-x Physics, Reggio Calabria, Italy, August 26th–September 1st, 2018," .

[112] K. Nakamura *et al.* (Particle Data Group), J. Phys. **G37**, 075021 (2010).

[113] F. J. Nemes, PoS **DIS2017**, 059 (2018).

[114] G. Antchev *et al.* (TOTEM), EPL **95**, 4, 41001 (2011), [arXiv:1110.1385].

[115] G. Antchev *et al.* (TOTEM), Eur. Phys. J. **C76**, 12, 661 (2016), [arXiv:1610.00603].

[116] J. Kaspar, "Invited talk at the meeting of the LHC Working Group on Forward Physics and Diffraction, CERN, Switzerland, December 16-17th, 2019," .

[117] V. A. Schegelsky and M. G. Ryskin, Phys. Rev. **D85**, 094024 (2012), [arXiv:1112.3243].

[118] A. Bruni, X. Janssen and P. Marage, in "Proceedings, HERA and the LHC Workshop Series on the implications of HERA for LHC physics: 2006-2008," 427–439 (2008), [arXiv:0812.0539].

[119] A. Levy, in "Proceedings, 17th International Workshop on Deep-Inelastic Scattering and Related Subjects (DIS 2009): Madrid, Spain, April 26-30, 2009," 177 (2009), [arXiv:0907.2178].

[120] J. R. Forshaw, R. Sandapen and G. Shaw, JHEP **11**, 025 (2006), [hep-ph/0608161].

[121] A. Capella *et al.*, Nucl. Phys. **B593**, 336 (2001), [hep-ph/0005049].

[122] V. S. Fadin and L. N. Lipatov, Phys. Lett. **B429**, 127 (1998), [hep-ph/9802290].

[123] M. Ciafaloni and G. Camici, Phys. Lett. **B430**, 349 (1998), [hep-ph/9803389].

[124] F. D. Aaron *et al.* (H1), JHEP **05**, 032 (2010), [arXiv:0910.5831].

[125] C. Adloff *et al.* (H1), Eur. Phys. J. **C13**, 371 (2000), [hep-ex/9902019].

[126] J. Breitweg *et al.* (ZEUS), Eur. Phys. J. **C6**, 603 (1999), [hep-ex/9808020].

[127] S. Chekanov *et al.* (ZEUS), PMC Phys. **A1**, 6 (2007), [arXiv:0708.1478].

[128] M. Ciafaloni, Nucl. Phys. **B296**, 49 (1988).

[129] S. Catani, F. Fiorani and G. Marchesini, Phys. Lett. **B234**, 339 (1990).

[130] S. Catani, F. Fiorani and G. Marchesini, Nucl. Phys. **B336**, 18 (1990).

[131] G. Marchesini, Nucl. Phys. **B445**, 49 (1995), [hep-ph/9412327].

[132] G. P. Salam, JHEP **07**, 019 (1998), [hep-ph/9806482].

[133] M. Ciafaloni and D. Colferai, Phys. Lett. **B452**, 372 (1999), [hep-ph/9812366].

[134] H. Kowalski, L. N. Lipatov and D. A. Ross, Eur. Phys. J. **C76**, 1, 23 (2016), [arXiv:1508.05744].

[135] H. Kowalski *et al.*, Eur. Phys. J. **C77**, 11, 777 (2017), [arXiv:1707.01460].

[136] S. J. Brodsky *et al.*, JETP Lett. **70**, 155 (1999), [hep-ph/9901229].

[137] R. D. Ball *et al.*, Eur. Phys. J. **C78**, 4, 321 (2018), [arXiv:1710.05935].

[138] E. M. Levin and M. G. Ryskin, Phys. Rept. **189**, 267 (1990).

[139] L. V. Gribov, E. M. Levin and M. G. Ryskin, Phys. Rept. **100**, 1 (1983).

[140] E. M. Levin, M. G. Ryskin and A. G. Shuvaev, Nucl. Phys. **B387**, 589 (1992).

[141] A. H. Mueller, Phys. Rept. **73**, 237 (1981).

[142] A. H. Mueller, Nucl. Phys. **B415**, 373 (1994).

[143] A. H. Mueller and B. Patel, Nucl. Phys. **B425**, 471 (1994), [hep-ph/9403256].

[144] N. N. Nikolaev, B. G. Zakharov and V. R. Zoller, JETP Lett. **59**, 6 (1994), [hep-ph/9312268].

[145] V. N. Gribov and L. N. Lipatov, Sov. J. Nucl. Phys. **15**, 438 (1972), [Yad. Fiz.15,781(1972)]; G. Altarelli and G. Parisi, Nucl. Phys. **B126**, 298 (1977); Y. L. Dokshitzer, Sov. Phys. JETP **46**, 641 (1977), [Zh. Eksp. Teor. Fiz. 73, 1216 (1977)].

[146] I. Balitsky, Nucl. Phys. **B463**, 99 (1996), [hep-ph/9509348].

[147] I. Balitsky, Phys. Rev. **D60**, 014020 (1999), [hep-ph/9812311].

[148] Y. V. Kovchegov, Phys. Rev. **D60**, 034008 (1999), [hep-ph/9901281].

[149] G. Gustafson, Phys. Lett. **B718**, 1054 (2013), [arXiv:1206.1733].

[150] S. Chatrchyan *et al.* (CMS, TOTEM), Eur. Phys. J. **C74**, 10, 3053 (2014), [arXiv:1405.0722].

[151] Q.-D. Zhou (LHCF, ATLAS), EPJ Web Conf. **208**, 05008 (2019).

[152] O. Adriani *et al.* (LHCf), Phys. Lett. **B780**, 233 (2018), [arXiv:1703.07678].

[153] M. Aaboud *et al.* (ATLAS) , ATLAS-CONF-2017-075.

[154] C. Albajar *et al.* (UA1), Nucl. Phys. **B335**, 261 (1990).

[155] G. J. Alner *et al.* (UA5), Z. Phys. **C33**, 1 (1986).

[156] T. Aaltonen *et al.* (CDF), Phys. Rev. **D79**, 112005 (2009), [Erratum: Phys. Rev.D82,119903(2010)], [arXiv:0904.1098].

[157] F. Abe *et al.* (CDF), Phys. Rev. **D41**, 2330 (1990), [,119(1989)].

[158] K. Aamodt *et al.* (ALICE), Eur. Phys. J. **C68**, 89 (2010), [arXiv:1004.3034].

[159] V. Khachatryan *et al.* (CMS), Phys. Rev. Lett. **105**, 022002 (2010), [arXiv:1005.3299].

[160] B. B. Abelev *et al.* (ALICE), Eur. Phys. J. **C73**, 12, 2662 (2013), [arXiv:1307.1093].

[161] A. M. Sirunyan *et al.* (CMS), Phys. Rev. **D96**, 11, 112003 (2017), [arXiv:1706.10194].

[162] M. G. Ryskin, A. D. Martin and V. A. Khoze, Eur. Phys. J. **C71**, 1617 (2011), [arXiv:1102.2844].

[163] X.-N. Wang, Phys. Rept. **280**, 287 (1997), [hep-ph/9605214].

[164] S. Ostapchenko and M. Bleicher, Universe **5**, 5, 106 (2019).

[165] F. M. Liu *et al.*, J. Phys. **G28**, 2597 (2002), [hep-ph/0109104].

[166] E. Gotsman, E. Levin and U. Maor, Acta Phys. Polon. Supp. **8**, 777 (2015).

[167] Y. V. Kovchegov and E. Levin, Camb. Monogr. Part. Phys. Nucl. Phys. Cosmol. **33**, 1 (2012).

[168] E. A. De Wolf, I. M. Dremin and W. Kittel, Phys. Rept. **270**, 1 (1996), [hep-ph/9508325].

[169] J. Adam *et al.* (ALICE), Eur. Phys. J. **C77**, 8, 569 (2017), [arXiv:1612.08975].

[170] V. Khachatryan *et al.* (CMS), JHEP **09**, 091 (2010), [arXiv:1009.4122].

[171] K. Eggert *et al.*, Nucl. Phys. **B86**, 201 (1975).

[172] B. Alver *et al.* (PHOBOS), Phys. Rev. **C75**, 054913 (2007), [arXiv:0704.0966].

[173] E. M. Levin and M. G. Ryskin, Sov. J. Nucl. Phys. **20**, 280 (1975), [Yad. Fiz.20,519(1974)].

[174] A. Capella and A. Krzywicki, Phys. Rev. **D18**, 4120 (1978).

[175] M. Aaboud *et al.* (ATLAS), Eur. Phys. J. **C77**, 6, 428 (2017), [arXiv:1705.04176].

[176] V. Khachatryan *et al.* (CMS), Phys. Lett. **B765**, 193 (2017), [arXiv:1606.06198].

[177] S. Gieseke, "Invited talk at the Workshop on Multiple Partonic Interactions at the LHC, Prague, Czech Republic, November 18th–26th, 2019," .

[178] S. Kundu, B. Mohanty and D. Mallick (2019), [arXiv:1912.05176].

[179] M. Diehl, D. Ostermeier and A. Schafer, JHEP **03**, 089 (2012), [Erratum: JHEP03,001(2016)], [arXiv:1111.0910].

[180] T. Sjostrand and P. Z. Skands, JHEP **03**, 053 (2004), [hep-ph/0402078].

[181] M. Aaboud *et al.* (ATLAS), Phys. Lett. **B790**, 595 (2019), [Phys. Lett.790,595(2019)], [arXiv:1811.11094].

[182] M. G. Ryskin and A. M. Snigirev, Phys. Rev. **D83**, 114047 (2011), [arXiv:1103.3495].

[183] B. Blok *et al.*, Eur. Phys. J. **C74**, 2926 (2014), [arXiv:1306.3763].

[184] M. Aaboud *et al.* (ATLAS), JHEP **03**, 157 (2017), [arXiv:1701.05390].

[185] R. Snellings, New J. Phys. **13**, 055008 (2011), [arXiv:1102.3010].

[186] M. Aaboud *et al.* (ATLAS), Phys. Rev. **C97**, 2, 024904 (2018), [arXiv:1708.03559].

[187] N. Borghini, P. M. Dinh and J.-Y. Ollitrault, Phys. Rev. **C63**, 054906 (2001), [arXiv:nucl-th/0007063].

[188] A. Bilandzic, R. Snellings and S. Voloshin, Phys. Rev. **C83**, 044913 (2011), [arXiv:1010.0233].

[189] W. Li, Mod. Phys. Lett. **A27**, 1230018 (2012), [arXiv:1206.0148].

[190] B. Schenke, J. Phys. **G38**, 124009 (2011), [arXiv:1106.6012].

[191] K. G. Boreskov, A. B. Kaidalov and O. V. Kancheli, Eur. Phys. J. **C58**, 445 (2008), [arXiv:0809.0625].

[192] K. G. Boreskov, A. B. Kaidalov and O. V. Kancheli, Phys. Atom. Nucl. **72**, 361 (2009), [Yad. Fiz.72,390(2009)].

[193] C. Bierlich and J. R. Christiansen, Phys. Rev. **D92**, 9, 094010 (2015), [arXiv:1507.02091].

[194] Z.-W. Lin *et al.*, Phys. Rev. **C72**, 064901 (2005), [arXiv:nucl-th/0411110].

[195] V. Khachatryan *et al.* (CMS) , CMS-PAS-FSQ-16-008.

[196] J. Bartels, Nucl. Phys. **B175**, 365 (1980).

[197] J. Kwiecinski and M. Praszalowicz, Phys. Lett. **94B**, 413 (1980).

[198] M. A. Braun (1998), [hep-ph/9805394].

[199] J. Bartels, L. N. Lipatov and G. P. Vacca, Phys. Lett. **B477**, 178 (2000), [hep-ph/9912423].

[200] C. Ewerz (2003), [hep-ph/0306137].

[201] M. Fukugita and J. Kwiecinski, Phys. Lett. **83B**, 119 (1979), [,625(1979)].

[202] M. G. Ryskin, Sov. J. Nucl. Phys. **46**, 337 (1987), [Yad. Fiz.46,611(1987)].

[203] J. Bartels, C. Contreras and G. P. Vacca (2019), [arXiv:1910.04588].

[204] E. Nagy *et al.*, Nucl. Phys. **B150**, 221 (1979).

[205] A. Breakstone *et al.*, Phys. Rev. Lett. **54**, 2180 (1985).

[206] A. Breakstone *et al.* (AMES-BOLOGNA-CERN-DORTMUND-HEIDELBERG-WARSAW), Nucl. Phys. **B248**, 253 (1984).

[207] V. M. Abazov *et al.* (D0), Phys. Rev. **D86**, 012009 (2012), [arXiv:1206.0687].

[208] M. Bozzo *et al.* (UA4), Phys. Lett. **155B**, 197 (1985).

[209] D. Bernard *et al.* (UA4), Phys. Lett. **B171**, 142 (1986).

[210] E. Martynov and B. Nicolescu, Eur. Phys. J. **C79**, 6, 461 (2019), [arXiv:1808.08580].

[211] A. Donnachie and P. V. Landshoff, Phys. Lett. **123B**, 345 (1983).

[212] A. Donnachie and P. V. Landshoff, Phys. Lett. **B798**, 135008 (2019), [arXiv:1904.11218].

[213] J. Finkelstein *et al.*, Phys. Lett. **B232**, 257 (1989).

[214] V. A. Khoze, A. D. Martin and M. G. Ryskin, Phys. Lett. **B780**, 352 (2018), [arXiv:1801.07065].

[215] W. Kilian and O. Nachtmann, Eur. Phys. J. **C5**, 317 (1998), [hep-ph/9712371].

[216] J. Bartels *et al.*, Eur. Phys. J. **C20**, 323 (2001), [hep-ph/0102221].

[217] L. A. Harland-Lang *et al.*, Phys. Rev. **D99**, 3, 034011 (2019), [arXiv:1811.12705].

[218] J. Olsson (H1), in "New trends in high-energy physics: Experiment, phenomenology, theory. Proceedings, International Conference, Yalta, Crimea, Ukraine, September 22-29, 2001," 79–87 (2001), [hep-ex/0112012].

[219] C. Adloff *et al.* (H1), Phys. Lett. **B544**, 35 (2002), [hep-ex/0206073].

[220] T. Berndt (H1), Acta Phys. Polon. **B33**, 3499 (2002), [,182(2002)].

[221] W. Heisenberg, Z. Phys. **133**, 65 (1952).

[222] G. Pancheri and Y. N. Srivastava, Eur. Phys. J. **C77**, 3, 150 (2017), [arXiv:1610.10038].

[223] M. M. Block, Phys. Rept. **436**, 71 (2006), [hep-ph/0606215].

[224] M. Giordano, E. Meggiolaro and N. Moretti, JHEP **09**, 031 (2012), [arXiv:1203.0961].

[225] E. Ferreiro *et al.*, Nucl. Phys. **A710**, 373 (2002), [hep-ph/0206241].

[226] P. Grassberger and K. Sundermeyer, Phys. Lett. **77B**, 220 (1978).

[227] K. G. Boreskov, in M. Olshanetsky and A. Vainshtein, editors, "Multiple facets of quantization and supersymmetry," 322–351 (2001), [hep-ph/0112325].

[228] V. A. Khoze, A. D. Martin and M. G. Ryskin, Phys. Lett. **B787**, 167 (2018), [arXiv:1809.10406].